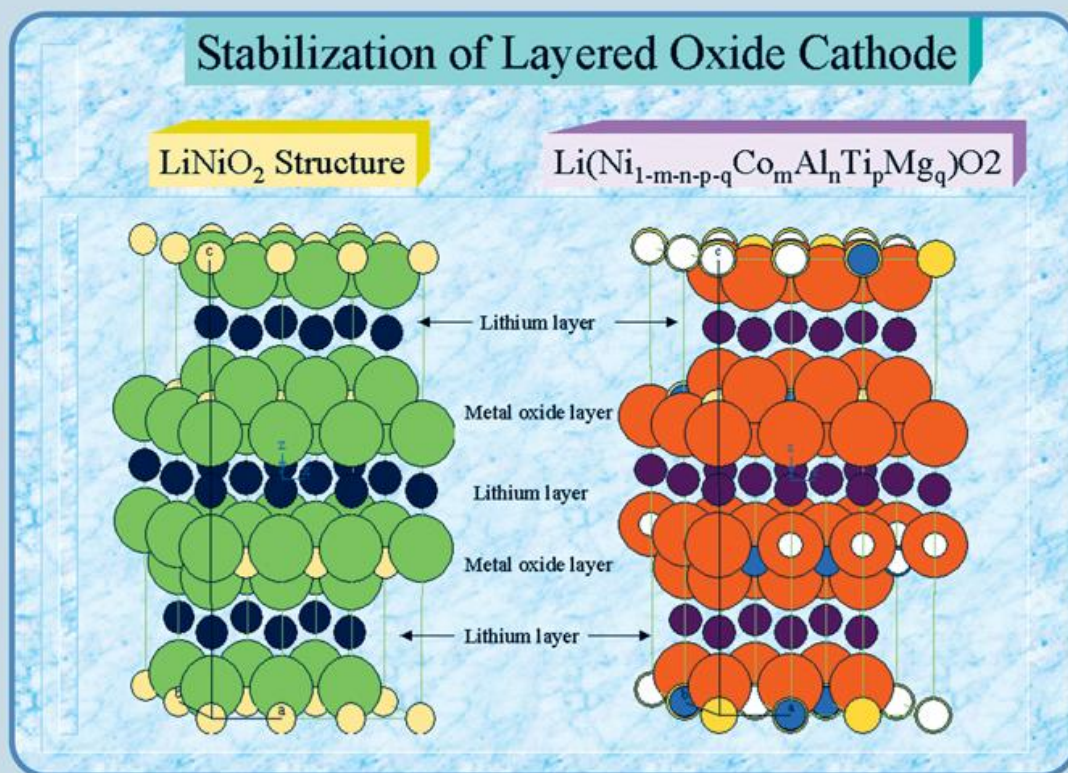


LITHIUM BATTERIES

Science and Technology

Gholam-Abbas Nazri
Gianfranco Pistoia
(Eds.)



LITHIUM BATTERIES

Science and Technology

LITHIUM BATTERIES

Science and Technology

Edited by

Gholam-Abbas Nazri

*General Motors Research & Development Center
Warren, Michigan, U.S.A.*

Gianfranco Pistoia

*Consultant
Rome, Italy*



Springer

Editors

Gholam-Abbas Nazri
General Motors R&D and Planning Center
MC 480-102-RCEL
30500 Mound Road
Warren, MI 48090-9055
USA

Gianfranco Pistoia
Via G. Scalia, 10
00136 Rome
Italy

ISBN: 978-1-4020-7628-2 (hardcover)

ISBN: 978-0-387-92674-2 (softcover)

e-ISBN: 978-0-387-92675-9

Library of Congress Control Number: 2008941279

© Springer Science+Business Media, LLC 2003, First softcover printing 2009

All rights reserved. This work may not be translated or copied in whole or in part without the written permission of the publisher (Springer Science+Business Media, LLC, 233 Spring Street, New York, NY 10013, USA), except for brief excerpts in connection with reviews or scholarly analysis. Use in connection with any form of information storage and retrieval, electronic adaptation, computer software, or by similar or dissimilar methodology now known or hereafter developed is forbidden.

The use in this publication of trade names, trademarks, service marks, and similar terms, even if they are not identified as such, is not to be taken as an expression of opinion as to whether or not they are subject to proprietary rights.

Printed on acid-free paper

springer.com

Contents

List of Contributors	xv
Preface	xvii

I. Fundamentals

1. Materials Aspects: An Overview

A. Manthiram

1.1. Introduction	3
1.2. Basic Concepts of Rechargeable Lithium Batteries	3
1.3. Cells with Insertion Compounds as Both Anode and Cathode	8
1.4. Layered Oxide Cathodes	11
1.4.1. Layered LiCoO_2	12
1.4.2. Layered LiNiO_2	19
1.4.3. Other Layered Oxides	24
1.5. Spinel Oxide Cathodes	25
1.5.1. Spinel Manganese Oxides	26
1.5.2. Other Spinel Oxides	30
1.6. Oxide Cathodes with Polyanions	32
1.7. Other Oxide Cathodes	33
1.8. Anode hosts	35
1.9. Conclusions	36
References	37

2. The Role of Electronic Properties in the Electrochemical Behavior of Intercalation Compounds from a First Principles Vantage Point

A. Van der Ven and G. Ceder

2.1. Introduction	42
2.2. General Electronic Structure of Octahedral Transition Metal Ions	45
2.3. First Principles Method	48
2.3.1. The Local Density Approximation (LDA)	54
2.3.2. The Generalized Gradient Approximation (GGA)	54
2.3.3. Spin Polarization	55
2.3.4. Caveats About Approximations to DFT	55
2.3.5. Different Numerical Schemes	57
2.4. Electronic Structure of Li_xCoO_2	58
2.4.1. Covalent Bonding in Li_xCoO_2	58
2.4.2. Experimental Evidence for Shift in Covalency	62
2.4.3. The Role of Covalency in Determining Thermodynamic, Kinetic and Structural Properties of Li_xCoO_2	64
2.5. Electronic Properties in LiNiO_2 : the 180° Interaction	67
2.6. Layered to Spinel Transformation in Li_xMnO_2	71
2.6.1. The Crystallography and Thermodynamics of the Layered to Spinel Phase Transformation	71
2.6.2. A Two Stage Transformation Mechanism	73
2.6.3. Suppressing the Layered to Spinel Transformation	78
2.7. Conclusions	79
References	80

3. Synthesis of Battery Materials

M.S. Whittingham

3.1. Introduction	85
3.2. The Synthesis and Manufacture of Titanium Disulfide	86
3.3. Synthesis of Alkali Ion Intercalates by Insertion into the Host Lattice (and the Reverse)	88
3.4. High Temperature Synthesis of Layered Oxides	90
3.5. Hydrothermal and Solvothermal Synthesis of Cathode Materials	93
3.6. Ion Exchange Methodes for Lithium Manganese Oxides Synthesis	95
3.7. Stabilization of Layered LiMnO_2 and the Mixed Metal Oxides $\text{Li}(\text{Ni}, \text{Mn}, \text{Co})\text{O}_2$	97
3.8. Addition of Carbon Conductive Diluents Post-Synthesis and <i>in-situ</i> : LiFePO_4	99
3.9. Synthesis of Anode Materials	102
3.10. Mechanochemistry and Mechanical Grinding	103
References	105

II. Anode Materials

4. Anodes and Composite Anodes: An Overview

L.F. Nazar and O. Crosnier

4.1. Introduction: Lithium Metal and Carbon Based Materials	112
4.1.1. Issue of Safety, A Brief History	113
4.1.2. Carbonaceous Materials	114
4.1.3. Looking to the Future	115
4.2. Compounds and Composites of Sn, Sb and Al	116
4.2.1. Intermetallics Composites and Binary Phases Comprised of Sn, Sb and Al	117
4.2.2. Silicides	127
4.3. Metal Oxides	129
4.3.1. Transition Metal Oxides Where Insertion Governs the Process	130
4.3.2. Transition Metal Oxides Where Reduction of Metal Oxide to Metallic or Semi-metal Occurs	130
4.3.3. Mixed Transition Metal Oxides – Where Both Reduction and alloying are Responsible for Li Capacity	132
4.4. Nitrides and Phosphides	132
4.4.1. Nitrides	132
4.4.2. Phosphides	134
4.5. Conclusions	138
References	139

5. Carbonaceous and Graphitic Anodes

M. Winter, K.-C. Moeller and J. O. Besenhard

5.1. Carbons in Ion Transfer Batteries	144
5.2. History of Lithiated Carbons	146
5.3. Electrochemical Li Storage in Carbon	148
5.3.1. Carbonaceous Host Materials and Their Properties	148
5.3.2. Electrochemical Li Storage in Graphitic Carbons	153
5.3.3. Electrochemical Li Storage in Non-Graphitic Carbons	160
5.4. Reactions of Lithiated Carbons with the Electrolyte	167

5.4.1. Interphase Formation – Metallic Li Anode vs. Li_xC_6 Anode and Oxide Cathode	168
5.4.2. Unsolvated and Solvated Lithium Intercalation	171
5.5. What is Special About Lithiated Carbons?	179
References	180
6. Graphite-Electrolyte Interface in Lithium-Ion Batteries	
<i>M. Nazri, B. Yebka, and G.-A. Nazri</i>	
6.1. Introduction	195
6.2. Experimental Set Up to Evaluate Surface Reactions of Graphite Anodes	198
6.2.1. Graphite Types	198
6.2.2. A General Procedure to Fabricate Carbon Anodes and their Evaluation	200
6.3. Graphite Cycling and Film Formation	203
6.3.1. Gas Generation on Graphites	207
6.3.2. Infrared Spectroscopy of SEI Layer on Graphite Anodes	208
6.3.3. Thermal Analysis of SEI Layer on Graphite Anodes	216
6.4. Conclusions	217
References	218
7. The Key Role of Nanoparticles in Reactivity of 3d Metal Oxides Towards Li	
<i>J.-M. Tarascon, S. Grugeon, S. Laruelle, D. Larcher and P. Poizot</i>	
7.1. Introduction	220
7.2. Experimental	221
7.3. Results and Discussion	222
7.3.1. Reactivity of 3d Metal Oxides Towards Li	222
7.3.2. Rationalization and Potential Applications	226
7.3.3. Practical Application Considerations	234
7.3.4. Acting on Reaction Paths Through Particle Size	236
7.4. Conclusions	244
References	245
8. Nitride and Silicide Negative Electrodes	
<i>G.G. Amatucci and N. Pereira</i>	
8.1. Introduction	247
8.2. The Nitrides	248
8.2.1. The Ternary Nitrides	248
8.2.2. The Binary Nitrides	254
8.2.3. Summary – Nitrides	258
8.3. Silicides	259
8.3.1. Introduction	259
8.3.2. Ternary Li-Si-M Systems at Elevated Temperature	260
8.3.3. Silicides at Ambient Temperature	262
8.3.4. Summary – Silicides	267
References	268
9. Alloys and Intermetallic Anodes	
<i>R. A. Huggins</i>	
9.1. Introduction	270
9.2. Alloys as an Alternative to Pure Lithium	271

9.2.1. Lithium – Carbon Alloys	271
9.3. Principles Determining the Potentials and Capacities of Alloy Electrodes Under Equilibrium Conditions	272
9.3.1. Relations Between Phase Diagrams, the Composition-Dependence of the Potential, and the Capacity of Electrodes	273
9.3.2. An Example, The Lithium-Antimony System	275
9.3.3. Relation Between the Potentials and Thermodynamic Data	278
9.3.4. Temperature Dependence of the Equilibrium Potential	279
9.3.5. Experiments at Ambient Temperature	283
9.4. Liquid Binary Alloys	283
9.5. Mixed-Conductor Matrix Electrodes	286
9.6. Decrepitation	290
9.7. Formation of Amorphous Products at Ambient Temperature	293
9.8. Summary	294
References	295
10. Current Issues of Metallic Lithium Anode	
<i>M. Ishikawa and M. Morita</i>	
10.1. Intrinsic Advantages and Drawbacks of Metallic Lithium Anode	297
10.2. Historical Aspects in Rechargeable Metallic Lithium Batteries	298
10.3. Recent Trends in the Development of Batteries with a Li Anode	300
10.4. Optimization of the Lithium Anode Interface	300
10.4.1. Fundamentals	300
10.4.2. Effect of Additives	303
10.5. Physical Factors Affecting the Lithium Interface	303
10.6 Recent Advances in the Research on Metallic Lithium Anode	304
References	311
III. Cathode Materials	
11. Trends in Cathode Materials for Rechargeable Batteries	
<i>M. Pasquali, S. Passerini and G. Pistoia</i>	
11.1. Introduction	315
11.2. Methods of Synthesis	317
11.3. Effect of Particle Size and Morphology on Cathode Behavior	321
11.4. Natural vs. Artificial Cathodic Films	324
11.5. Specific Cathode Materials	327
11.5.1. LiNiO_2 and LiCoO_2	327
11.5.2. Manganese Spinels	335
11.5.3. Layered Li_xMnO_2 and Similar Cathodes	341
11.5.4. 3 V Cathodes	344
11.5.5. A Special Case: LiFePO_4	347
11.5.6. Sulphur and Organic or Inorganic Sulphides	350
11.5.7. High Voltage Materials	351
11.6. Concluding Remarks	352
References	353
12. Spinel Cathode Materials for Lithium-Ion Batteries	
<i>Y. Xia and M. Yoshio</i>	

12.1. Introduction	361
12.2. LiMn_2O_4 and Metal-Ion Doped Spinel $\text{LiM}_x\text{Mn}_{2-x}\text{O}_4$	362
12.3. Optimizing the Capacity and Rechargeability by Using a Li-Mn-O Phase Diagram	366
12.4. Capacity Fading on Cycling	369
12.5. Oxygen-Deficient Spinel $\text{LiMn}_2\text{O}_{4-y}$	373
12.5.1. Charge/Discharge Profile of Spinel with Different Li/Mn Ratios and Oxygen Contents	373
12.5.2. Phase Transitions During Charge/Discharge	374
12.5.3. Phase Transition at Low Temperature	375
12.6. Summary	377
References	377
13. Layered Manganese Oxides as Cathodes	
<i>B. Ammundsen</i>	
13.1. Introduction	381
13.2. Overview of the Structure and Stability of Layered Manganese Oxides	383
13.2.1. Layered vs. Orthorhombic Structure of LiMnO_2	383
13.2.2. Instability with Respect to the Spinel Structure	384
13.2.3. Alternative Layered Structures	387
13.2.4. Layered Lithium Manganese Oxides with Tetravalent Manganese	388
13.3. Layered Manganese Oxides Based on LiMnO_2	389
13.3.1. Orthorhombic LiMnO_2	389
13.3.2. Lithium Manganese Oxide with the O3 Layered Structure Prepared by “Soft Chemistry” Routes	390
13.3.3. Substituted LiMnO_2 with the O3 Layered Structure Prepared by High Temperature Processing	392
13.3.4. O2 Layered Structures	395
13.4. Layered Solid Solution Cathode Materials Based on Tetravalent Manganese	397
13.4.1. Overview of Solid Solution Approaches	397
13.4.2. Solid Solutions with LiCrO_2	399
13.4.3. Lithium-Rich Solid Solutions with LiCrO_2	402
13.4.4. Solid Solutions with LiNiO_2 and $\text{LiCo}_x\text{Ni}_{1-x}\text{O}_2$	402
13.4.5. Further Work	406
13.5. Summary and Outlook	406
References	407
14. Cathodes Based on LiCoO_2 and LiNiO_2	
<i>B. Park, Y. J. Kim and J. Cho</i>	
14.1. LiCoO_2 Cathode Materials	410
14.1.1. Introduction	410
14.1.2. Capacity Fading Mechanisms in LiCoO_2 Cathode Materials	414
14.1.3. Electrochemical Properties of LiCoO_2 Cathodes	416
14.1.4. Doping the LiCoO_2 Cathode	420
14.2. LiNiO_2 Cathode Materials	422
14.2.1. Introduction	422
14.2.2. Structure of LiNiO_2	422

14.2.3. Electrochemical Properties and Capacity Fading Mechanisms of LiNiO ₂	423
14.3. Metal-Oxide Coating on LiCoO ₂ Powders	426
14.3.1. Introduction	426
14.3.2. Preparation of Metal-Oxide Coated LiCoO ₂ Powders	426
14.3.3. Cycle-Life Performance of Metal-Oxide Coated LiCoO ₂	427
14.4. Thin-Film LiCoO ₂ Cathodes	431
14.4.1. Introduction	431
14.4.2. Electrochemical Properties of Al ₂ O ₃ -Coated LiCoO ₂ Thin Films	431
14.4.3. Future Work	441
References	442
15. Polyanion-Based Positive Electrode Materials	
<i>C. Masquelier, S. Patoux, C. Wurm, M. Morcrette</i>	
15.1. Introduction: from Oxides to Ionically Conducting Polyanionic Frameworks	445
15.2. Tuning the M ⁿ⁺ /M ⁽ⁿ⁻¹⁾⁺ Redox Couple in the NASICON structure by Changing the Chemical Nature of the XO ₄ ⁿ⁻ Groups: Inductive Effect	448
15.2.1. Relative Position of Various M ⁿ⁺ /M ⁽ⁿ⁻¹⁾⁺ Redox Couples (M = Fe, Ti, V, Nb) in NASICON Phosphates	450
15.2.2. Position of the Ti ⁴⁺ /Ti ³⁺ Couple vs. Li ⁺ /Li and Na ⁺ /Na	451
15.2.3. Relative Positions of the Ti ⁴⁺ /Ti ³⁺ , Fe ³⁺ /Fe ²⁺ , Nb ⁵⁺ /Nb ⁴⁺ , Nb ⁴⁺ /Nb ³⁺ , V ⁴⁺ /V ³⁺ and V ³⁺ /V ²⁺ Couples vs. Na ⁺ /Na and Li ⁺ /Li in the NASICON Structure	453
15.3. Extension of the Concept to Other Polyanionic Structures	456
15.3.1. The Monoclinic Forms of Fe ₂ (SO ₄) ₃ and Li ₃ M ₂ (XO ₄) ₃ (M = Fe, V, X = P, As)	457
15.3.2. The Rhombohedral Form of Li ₃ Fe ₂ (AsO ₄) ₃	460
15.3.3. The Diphosphates and Diarsenates Li _x MX ₂ O ₇ (M = Fe, V, Ti; X = P, As)	461
15.3.4. Amorphous or Crystalline Iron Phosphates: FePO ₄ ·nH ₂ O and Fe ₄ (P ₂ O ₇) ₃ ·4H ₂ O	463
15.3.5. V ⁵⁺ /V ⁴⁺ and V ⁴⁺ /V ³⁺ Couples in Li _x VOXO ₄ (X = P, As)	466
15.3.6. Nb ⁵⁺ /Nb ⁴⁺ Couple in Li _x NbPO ₅	467
15.3.7. The Olivine LiMPO ₄ (M = Fe, Mn, Co)	469
15.4. Conclusions	473
References	474
16. Understanding Phase Transformations in Lithium Battery Materials by Transmission Electron Microscopy	
<i>Y. Shao-Horn</i>	
16.1. Introduction	478
16.2. Transmission Electron Microscopy	481
16.2.1. Electron Diffraction of Crystals	481
16.2.2. TEM Imaging	483
16.2.3. TEM Sample Preparation	484
16.2.4. Caveat to TEM Techniques	484
16.3. Lithium and Vacancy Ordering	484
16.3.1. Lithium and Vacancy Ordering in O ₃ Li _x NiO ₂	485

16.3.2. Lithium and Vacancy Ordering in O3 Li_xCoO_2	487
16.3.3. Lithium Ordering in O2 derived Li_xCoO_2	489
16.4. Spatially Localized Phase Transitions	492
16.4.1. Jahn-Teller Induced Phase Transition in $\text{Li}_x[\text{Mn}_2]\text{O}_4$	493
16.5. Phase Transformation Between 2D Layered and 3D Spinel Related Configurations	494
16.5.1. Intermediate Layered-Spinel Cation Configurations in LT- LiCoO_2	497
16.5.2. Layered to Spinel Transformation in Cycled Li_xMnO_2	499
16.6. Perspectives	500
16.6.1. High-Resolution TEM Imaging and Simulation	500
16.6.2. EELS Analysis and Imaging	502
16.6.3. In-Situ TEM Imaging	502
References	503

IV. Electrolytes

17. Liquid Electrolytes: Some Theoretical and Practical Aspects

M. Nazri

17.1. Introduction to Solvents	509
17.2. Coulombic Forces Between Ions and Dipolar Solvents	511
17.2.1. Ion-Dipole Forces	511
17.2.2. Dipole-Dipole Interactions	513
17.2.3. Dipole-Induced Dipole Interactions	513
17.2.4. Instantaneous Dipole-Induced Dipole Interaction Forces	514
17.2.5. Hydrogen Bonding	515
17.3. Electron Pair Donor-Electron Pair Acceptor Interactions (EPD/EPA Interactions)	516
17.4. Solvation	517
17.4.1. Solvation Number	518
17.4.2. Selective or Preferred Solvation	518
17.5. The Basic Requirements of Electrolytes for Lithium Batteries	519
17.5.1. Electrolyte Conductivity	520
17.5.2. The Electrochemical Stability of Organic Electrolytes	525
17.6. Conclusions	527
References	527

18. Advanced Liquid Electrolyte Solutions

D. Aurbach and A. Schechter

18.1. Introduction	530
18.1.1. Types of Advanced Liquid Electrolyte Solutions	530
18.1.2. Scope of Subjects of Interest	532
18.2. General Properties of Liquid Electrolyte Solutions	532
18.2.1. On the Physical Properties of Polar Aprotic Electrolyte Solutions	532
18.2.2. How to Evaluate Solvents for Electrolyte Solutions	535
18.2.3. On the Conductivity of Polar Aprotic Solutions and Diffusion of Ions in Them	539
18.3. Electrochemical Windows of Nonaqueous Electrolyte Solutions	541
18.3.1. On Cathodic Reactions of Polar Aprotic Electrolyte Solutions	545

18.3.2. Oxidation Reactions in Polar Aprotic Electrolyte Solutions	547
18.3.3. A Short Summary of the Anodic Limit of Nonaqueous Electrolyte Solutions	552
18.4. Liquid Electrolytes Solutions for Rechargeable Li (Metal) Batteries	553
18.4.1. Problems with the Use of Li Metal Anodes	553
18.4.2. On the Choice of Electrolyte Solutions for Rechargeable Li (Metal) Batteries	556
18.5. Liquid Electrolyte Solutions for Rechargeable Li-Ion Batteries	560
18.5.1. The Requirements of Suitable Solutions for Li-Ion Batteries	560
18.5.2. Standard Electrolyte Solutions for Li-Ion Batteries	561
18.5.3. Advanced Electrolyte Solutions for Li-Ion Batteries	564
18.6. Molten Salts	567
18.6.1. Introduction	567
18.6.2. Electrochemical Properties of Molten Salt Solutions and Battery Applications	568
References	568
19. Polymeric Electrolytes: An Overview	
<i>J.B. Kerr</i>	
19.1. Introduction	574
19.2. Lithium Transport in Lithium Batteries	575
19.2.1. Solvent-free, Ion-Coupled Systems	577
19.2.2. Effect of Polymer Molecular Structure (Architecture)	579
19.2.3. Effect of Polymer Solvation Structure	582
19.2.4. Effect of Surfaces on Polymer Electrolyte Behavior	587
19.2.5. Gel Polymer Systems	591
19.3. Polymer Electrolytes in Lithium Batteries	592
19.3.1. The Effect of Transport Properties on Cell Performance	595
19.3.2. Polyelectrolyte Single-Ion Conductors	602
19.3.3. Chemical and Electrochemical Stability of Polymer Electrolytes	604
19.3.4. Dendrite Growth	609
19.3.5. Mechanical Properties	613
19.4. Conclusions	615
References	617
20. Glass and Ceramic Electrolytes for Lithium and Lithium-Ion Batteries	
<i>N. J. Dudney</i>	
20.1. Introduction	623
20.2. Glass Electrolytes	625
20.2.1. Oxide Glasses	626
20.2.2. Oxynitride Glasses and Lipon	626
20.2.3. Sulfide and Oxysulfide Glasses	628
20.2.4. Thionitride Glasses	629
20.2.5. Lithium Halide Doped Glasses	629
20.3. Crystalline Ceramic Electrolytes	630
20.3.1. Perovskite Electrolytes	631
20.3.2. Nasicon-Type Phosphates	632
20.3.3. Lisicon-Type Materials	633

20.3.4. Lithium Metal Halides, Nitrides, and Phosphides	633
20.3.5. Other Compositions	634
20.4. Models for Ion Conduction	634
20.5. Conclusion	635
References	637

V. Battery Systems and Applications

21. Li-Ion Batteries for EV, HEV and Other Industrial Applications

M. Broussely

21.1. Introduction	645
21.1.1. Specific Properties Required of Industrial Li-Ion Batteries	646
21.2. Which Li-Ion Chemistry for a Large Battery?	646
21.2.1. Positive Materials	646
21.2.2. Negative Materials	651
21.3. General Technology and Manufacturing Processes	651
21.3.1. General Considerations for Battery Assembly	652
21.4. EV Applications	652
21.4.1. EV Battery Requirements and Technology Comparison	653
21.4.2. Battery Monitoring and Management	654
21.4.3. Li-Ion Technology for EV	655
21.5. HEV Applications	663
21.5.1. Application Requirements	663
21.5.2. Competing Battery Technologies	664
21.5.3. High Power Li-Ion Technology Challenges	664
21.6. Stationary Applications	671
21.6.1. Standby (Float) Operations	671
21.6.2. Intermittent Charging (Cycling) Applications	673
21.6.3. Buffer Operation	673
21.6.4. Stationary Battery Trials	674
21.7. Space Applications	674
21.7.1. Battery Requirements for Satellites	675
21.7.2. Competing Technologies	676
21.7.3. Saft Cell and Battery Design	677
21.7.4. Other Battery Designs	680
21.7.5. Launchers	683
21.8. Conclusions	684
References	684

22. Lithium Batteries for Medical Applications

E. S. Takeuchi, R. A. Leising, D. M. Spillman,

R. Rubino, H. Gan, K. J. Takeuchi and A. C. Marschilok

22.1 Introduction	686
22.2 Primary Batteries	687
22.2.1. The Use of Lithium Metal as an Anode	687
22.2.2. Lithium/Iodine Systems and their Medical Applications	688
22.2.3. Lithium/Thionyl Chloride Systems and their Medical Applications	689
22.2.4. Lithium/CF _x Systems and their Medical Applications	691
22.2.5. Lithium/Silver-Vanadium-Oxide Systems and their Medical Applications	691
22.2.6. Lithium/MnO ₂ Systems and their Medical Applications	694

22.3. Secondary Batteries	694
22.3.1. Lithium-Ion Systems – General Considerations	694
22.3.2. Lithium-Ion Systems – Current and future Medical Applications	697
22.4. Summary	699
References	699
23. Current Issues and Market Trends of Li-Ion Batteries for Consumer Applications	
<i>D. MacArthur</i>	
23.1. Introduction	701
23.2. Lithium-Ion batteries	702
23.2.1. The Market	702
23.2.2. Different Technologies	704
23.2.3. Targets: Small and Large Batteries	705
References	706
Subject Index	707

List of Contributors

Name	Chapter	Name	Chapter
G. G. Amatucci	8	M. Morita	10
B. Ammundsen	13	L. F. Nazar	4
D. Aurbach	18	G. A. Nazri	6
J. O. Besenhard	5	M. Nazri	6, 17
M. Broussely	21	B. Park	14
G. Ceder	2	P. Poizot	7
J. Cho	14	M. Pasquali	11
O. Crosnier	4	S. Passerini	11
N. J. Dudney	20	S. Patoux	15
H. Gan	22	N. Pereira	8
S. Grugeon	7	G. Pistoia	11
R. A. Huggins	9	R. Rubino	22
M. Ishikawa	10	A. Schechter	18
J. B. Kerr	19	Y. Shao-Horn	16
Y. J. Kim	14	D. M. Spillman	22
D. Larcher	7	E. S. Takeuchi	22
S. Laruelle	7	J.-M. Tarascon	7
R. A. Leising	22	A. Van der Ven	2
D. MacArthur	23	M. S. Whittingham	3
A. Manthiram	1	M. Winter	5
A. C. Marschilok	22	C. Wurm	15
C. Masquelier	15	Y. Xia	12
K.-C. Moeller	5	B. Yebka	6
M. Morcrette	15	M. Yoshio	12

Preface:

The science and technology of lithium batteries have dominated the field of advanced power sources and replaced many other batteries in the market, particularly in the areas of communications, computers, electronics, and in more power demanding devices such as power tools and transportation. The significant progress of lithium batteries is mainly due to the numerous innovations in materials, design and safety aspects of the batteries. Solid-state chemists, material physicists, materials scientists and electrochemists are among the main contributors to the field of advanced lithium batteries. Potential improvements in performance and application of lower cost yet safer materials in lithium batteries are in near horizon.

This book provides the most current knowledge and recent concepts on advanced lithium batteries. The book is designed to serve the researchers in the field also as a text for academic teaching. The emphasis is on materials aspects of advanced lithium batteries. Applications of the lithium batteries in medical field and transportation also have been reviewed. The general concepts of the device are discussed first and detailed electrode and electrolyte materials are covered in the subsequent chapters.

Chapter one is providing a general background for the advanced lithium batteries and an over view of electrode materials, electrode performances, and materials engineering. This chapter is highly recommended for students and practitioners in the field. Chapter two is a general overview of advanced theoretical approaches currently in use for better understanding of lithium battery electrodes and provides a guide for designing new electrode materials. The pros and cons of each theoretical method, and the mechanism of charge transfer and structural modification of intercalation electrodes and contribution of anions are discussed. Chapter three provides a general overview of advanced synthesis for electrode materials. Both traditional methods such as ceramic and solution techniques and nontraditional methods such as hydrothermal and mechanochemistry methods are covered in this chapter.

Part two of this book is a comprehensive discussion on alternative anodes materials for lithium batteries. Chapter four provides a general background on alternative anodes with a detailed analysis of intermetallics, composites, metal oxides, nitrides and phosphides anodes. Chapter five covers chemistry and physics of lithium intercalation into graphitic anode. Application of carbonaceous materials and various graphitic materials are also discussed. Chapter six is an overview of carbonaceous materials with emphasis on reactivity of lithiated graphite with organic electrolytes. Electrolyte decomposition on reactive anodes and formation of SEI layer and gaseous species are also discussed. Chapter seven is covering the role of nano particles in reactivity of transition metal oxides anodes. This chapter provides a comprehensive discussion on mechanism, thermodynamics and

kinetics of the reversible redox process in transition metal oxide with lithium. The equilibrium voltage values and overpotentials for various metal oxides are mapped in this chapter. The reaction pathways and mechanism of transition metal oxides reaction with lithium are clearly illustrated by in-situ x-ray diffraction, magnetic and electrochemical measurements. Chapter eight deals with most recent advances in metal nitrides and metal silicides anodes. Mechanism of reversible lithium insertion – extraction process in these classes of materials is discussed. The role of nano-particle in enhanced reactivity of transition metal nitrides are also presented. Chapter nine is covering the fundamentals of lithium alloys and intermetallic anodes. The phase diagrams of alloys also complement the voltage profiles of this class of active anodes. Chapter ten provides a general background on metallic lithium anode and reviewed recent progresses made in understanding the nature of lithium anode – electrolyte interface. The role of various additives, stack pressure and temperature are also discussed in this chapter.

In part three the cathode materials are reviewed. Chapter eleven provides a general background and trends in rechargeable cathode materials. Chapter twelve deals with synthesis, characterization and performance of manganese oxide spinel as cathode materials. Potentials and limitations of spinel cathodes, particularly their performances at elevated temperatures are discussed in this chapter. Chapter thirteen is a comprehensive review of the development of advanced layered transition metal oxide based on manganese system. Chapter fourteen is covering the structure, and performance of the layered lithium cobalt and lithium nickel oxide cathodes. Various synthesis routes for preparation of layered transition metal oxides are also presented. Chapter sixteen is covering the electrochemical performances of layered molybdenum oxides. The role of hydrated water molecules on electrochemical performance of the hydrated molybdenum oxide are presented. Thermodynamic parameters are extracted from temperature dependent voltage profiles of the molybdenum oxide-based cathodes. Chapter seventeen is covering the microstructure of various cathode materials and providing a general background on application of transmission electron microscopy for analysis of battery electrodes.

Part three deals with various aspects of non-aqueous, polymeric and ceramic electrolytes. Chapter eighteen is a general overview of fundamentals of non-aqueous electrolytes. The conductivity of various multi-blend organic carbonates is presented. The dynamic nature of solvent-solvent and lithium ion –solvent molecule interactions is discussed. Numerous tables with physical properties of organic solvents are presented. This chapter also serves as a reference for physical properties of aprotic solvents. Chapter nineteen provides a comprehensive analysis of liquid electrolyte and fundamentals of electrode-electrolyte interface. A general over view of polymeric electrolytes are presented in chapter twenty. Recent advances are discussed and older concepts are challenged. Chapter twenty-one deals with synthesis, fabrication

and performances of ceramic electrolytes. Physical methods for preparing thin-film electrodes and micro-batteries are also presented in this chapter.

Part five is devoted to the application of lithium batteries in transportation and medical field. The market analysis of lithium batteries and their future prospects are also presented in part five. Chapter twenty-two is a general review of lithium battery for transportation with an emphasis on high power lithium ion technology for hybrid electric vehicles. The lithium ion technology based on advanced nickel oxide based cathode and graphitic anodes are presented. Application of lithium batteries in medical fields and its miniaturization are discussed in chapter twenty-three. Chapter twenty-four provides current market trends and future prospects for the lithium ion batteries.

Authors would like to thank all contributors to this book and many thanks to the Kluwer Publishing Company, particularly Mr. Alex Greene for his guidance and patience during the course of preparing this book. We also like to thank our families for their continuous support while we were working on this manuscript.

Gholam-Abbas Nazri
GM Res. & Dev. Center
Warren, Michigan, USA

Gianfranco Pistoia
Battery Consultant
Rome, Italy

Chapter 1

MATERIALS ASPECTS: AN OVERVIEW

A. Manthiram

*Materials Science and Engineering Program, The University of Texas at Austin,
Austin, TX 78712, USA*

1.1. INTRODUCTION

The exponential growth in portable electronic devices such as cellular phones and laptop computers during the past decade has created enormous interest in compact, light-weight batteries offering high energy densities. Also, growing environmental concerns around the globe are driving the development of advanced batteries for electric vehicles. Lithium-ion batteries are appealing for these applications as they provide higher energy density compared to the other rechargeable battery systems such as lead-acid, nickel-cadmium, and nickel-metal hydride batteries as shown in Figure 1.1.¹ The higher volumetric and gravimetric energy densities of the lithium-ion cells in Figure 1.1 are due to the higher cell voltages (~ 4 V) achievable by the use of non-aqueous electrolytes, which also allow a wider temperature of operation. Lithium-ion cells have become a commercial reality after the initial announcement by Sony in the early 1990s because of an intense world-wide activity on lithium insertion compounds (electrode materials) during the past three decades. This chapter provides an overview of the electrode materials aspects of rechargeable lithium batteries. A more detailed discussion of the specific cathode and anode materials systems as well as the electrolytes is presented by various authors in the subsequent chapters.

1.2. BASIC CONCEPTS OF RECHARGEABLE LITHIUM BATTERIES

Rechargeable lithium batteries involve a reversible insertion/extraction of lithium ions (guest species) into/from a host matrix

(electrode material), called lithium insertion compound, during the discharge/charge process. The lithium insertion/extraction process occurring with a flow of ions through the electrolyte is accompanied by a reduction/oxidation (redox) reaction of the host matrix assisted with a flow of electrons through the external circuit. This concept of rechargeable lithium batteries was first illustrated with a transition metal sulfide, TiS_2 , as the cathode, metallic lithium as the anode, and a non-aqueous electrolyte.² The TiS_2 cathode has a layer structure as shown in Figure 1.2. During discharge, the lithium ions are inserted into the van der Waals gap between the sulfide layers and the charge balance is maintained by a reduction of the Ti^{4+} ions to Ti^{3+} . During charge, exactly the reverse process involving the extraction of lithium from the van der Waals gap and an oxidation of Ti^{3+} to Ti^{4+} occurs. During the lithium insertion/extraction (discharge/charge) process, the layer structure is maintained, resulting in good reversibility.

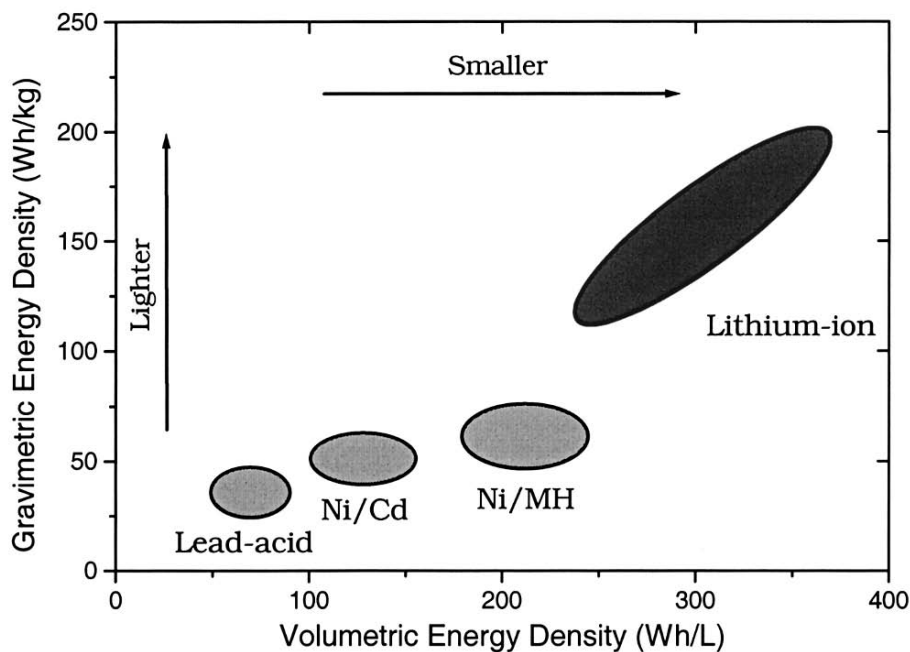


Figure 1.1. Comparison of the gravimetric and volumetric energy densities of various rechargeable battery systems.

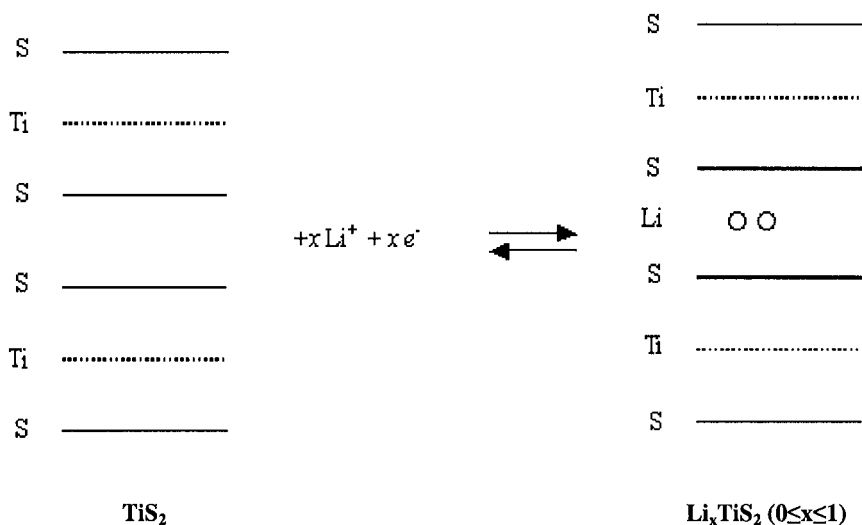


Figure 1.2. Illustration of lithium insertion/extraction into/from the layered TiS_2 during the discharge/charge process.

The open-circuit voltage V_{oc} of such a lithium cell is given by the difference in the lithium chemical potential between the cathode ($\mu_{\text{Li}(c)}$) and the anode ($\mu_{\text{Li}(a)}$) as:

$$V_{oc} = \frac{\mu_{\text{Li}(c)} - \mu_{\text{Li}(a)}}{F} \quad (1.1)$$

where F is the Faraday constant. Figure 1.3 shows a schematic energy diagram of a cell at open circuit. The cell voltage V_{oc} is determined by the energies involved in both the electron transfer and the Li^+ transfer. While the energy involved in electron transfer is related to the work functions of the cathode and anode, that involved in Li^+ transfer is determined by the crystal structure and the coordination geometry of the site into/from which Li^+ ions are inserted/extracted.³ Thermodynamic stability considerations require the redox energies of the cathode (E_c) and anode (E_a) to lie within the band gap E_g of the electrolyte, as shown in Figure 1.3, so that no unwanted reduction or oxidation of the electrolyte occurs during the charge-discharge process. Thus the electrochemical stability requirement imposes a limitation on the cell voltage as:

$$eV_{oc} = \mu_{\text{Li}(c)} - \mu_{\text{Li}(a)} < E_g \quad (1.2)$$

Although the concept is simple, the lithium insertion compound should satisfy several criteria in order for it to be a successful cathode material in a rechargeable lithium cell:

- The insertion compound $\text{Li}_x\text{M}_y\text{X}_z$ ($\text{X} = \text{anion}$) should have a high lithium chemical potential ($\mu_{\text{Li(c)}}$) to maximize the cell voltage. This implies that the transition metal ion M^{n+} in $\text{Li}_x\text{M}_y\text{X}_z$ should have a high oxidation state.

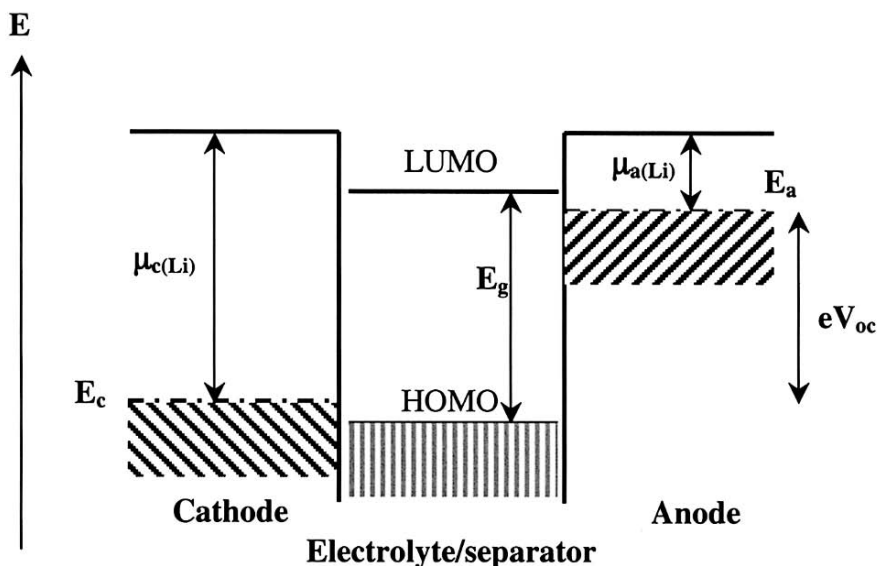


Figure 1.3. Schematic energy diagram of a lithium cell at open circuit. HOMO and LUMO refer, respectively, to the highest occupied molecular orbital and lowest unoccupied molecular orbital in the electrolyte.

- The insertion compound $\text{Li}_x\text{M}_y\text{X}_z$ should allow an insertion/extraction of a large amount of lithium, x , to maximize the cell capacity. This depends on the number of available lithium sites and the accessibility of multiple valences for M in the insertion host. A combination of high capacity and cell voltage can maximize the energy density, which is given by a product of the capacity and voltage.
- The lithium insertion/extraction process should be reversible with no or minimal changes in the host structure over the entire range x of lithium

insertion/extraction in order to provide a good cycle life for the cell. This implies that the insertion compound $\text{Li}_x\text{M}_y\text{X}_z$ should have good structural stability without breaking any M-X bonds.

- The insertion compound should support mixed conduction. It should have good electronic conductivity σ_e and lithium-ion conductivity σ_{Li} to minimize polarization losses during the discharge/charge process and thereby to support a high current density and power density. This depends on the crystal structure, arrangement of the MX_n polyhedra, geometry and interconnection of the lithium sites, nature and electronic configuration of the M^{n+} ion, and the relative positions of the M^{n+} and X^{n-} energies.
- The insertion compound should be chemically stable without undergoing any reaction with the electrolyte over the entire range, x , of lithium insertion/extraction.
- The redox energy of the cathode in the entire range, x , of lithium insertion/extraction should lie within the band gap of the electrolyte as shown in Figure 1.3 to prevent any unwanted oxidation or reduction of the electrolyte.
- From a commercial point of view, the insertion compound should be inexpensive, environmentally benign, and lightweight. This implies that the M^{n+} ion should preferably be from the 3d transition series.

Following the initial demonstration of the concept of rechargeable lithium batteries with the layered TiS_2 ,² several other sulfides and chalcogenides were pursued during the 1970s and 1980s as cathodes.⁴ However, most of them exhibit a lower cell voltage of <2.5 V versus metallic lithium anode. This limitation in cell voltage is due to an overlap of the higher valent $\text{M}^{n+}:\text{d}$ band with the top of the nonmetal:p band – for example, with the top of the $\text{S}:\text{3p}$ band as shown in Figure 1.4. Such an overlap results in an introduction of holes into (or removal of electrons from) the $\text{S}^{2-}:\text{3p}$ band and the formation of molecular ions such as S_2^{2-} , which in turn leads to an inaccessibility of higher oxidation states for M^{n+} in a sulfide $\text{Li}_x\text{M}_y\text{S}_z$. The stabilization of higher oxidation state is essential to maximize the cell voltage. Recognizing this difficulty with chalcogenides, Goodenough's group at the University of Oxford focused on oxide cathodes during the 1980s.⁵⁻⁷ The location of the top of the $\text{O}^{2-}:\text{2p}$ band much below the top of the $\text{S}^{2-}:\text{3p}$ band and a larger raising of the $\text{M}^{n+}:\text{d}$ energies in an oxide compared to that in a sulfide due to a larger Madelung energy (Figure 1.4), make the higher valent states accessible in oxides. For example, while Co^{3+} can be readily stabilized in an oxide, it is difficult to stabilize Co^{3+} in a

sulfide since the $\text{Co}^{2+/3+}$ redox couple lies within the $\text{S}^{2-}3\text{p}$ band as seen in Figure 1.4. Accordingly, several transition metal oxide hosts crystallizing in a variety of structures (2-dimensional layered and 3-dimensional framework structures) have been pursued during the past two decades and Figure 1.5 compares the electrochemical potential ranges of some selected lithium insertion compounds versus metallic lithium. Cell voltages of as high as 5 V versus metallic lithium have been achieved with oxide insertion compounds as seen in Figure 1.5. The readers may refer to some of the review articles and books⁸⁻¹⁶ in the field to get a more detailed account of the various lithium insertion compounds that have been investigated over the past three decades.

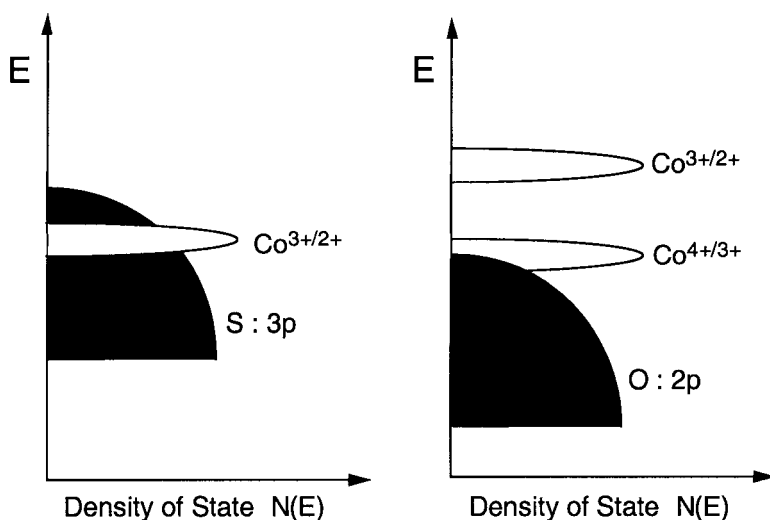


Figure 1.4. Relative energies of metal:d (for example, $\text{Co}:3\text{d}$) and nonmetal:p in (a) a sulfide and (b) an oxide.

1.3. CELLS WITH INSERTION COMPOUNDS AS BOTH ANODE AND CATHODE

Despite the development of several lithium insertion compounds during the 1970s and 1980s, the commercialization of rechargeable lithium batteries was hindered for many years until the announcement by Sony in the early 1990s. The delay was mainly because of the difficulties posed by the metallic lithium anodes. As an alkali metal, lithium is chemically reactive with the non-aqueous electrolyte, which results in the formation of

a passivating film on the metallic lithium anode. Although the passivating film on the surface prevents the bulk from further corrosion, it leads to a non-uniform plating of lithium during charging. This results not only in a total cell failure due to dendritic short circuiting, but also in serious safety problems due to local over heating. The difficulties associated with the metallic lithium anode prompted to pursue a strategy in which a lithium insertion compound instead of metallic lithium could be used as an anode.

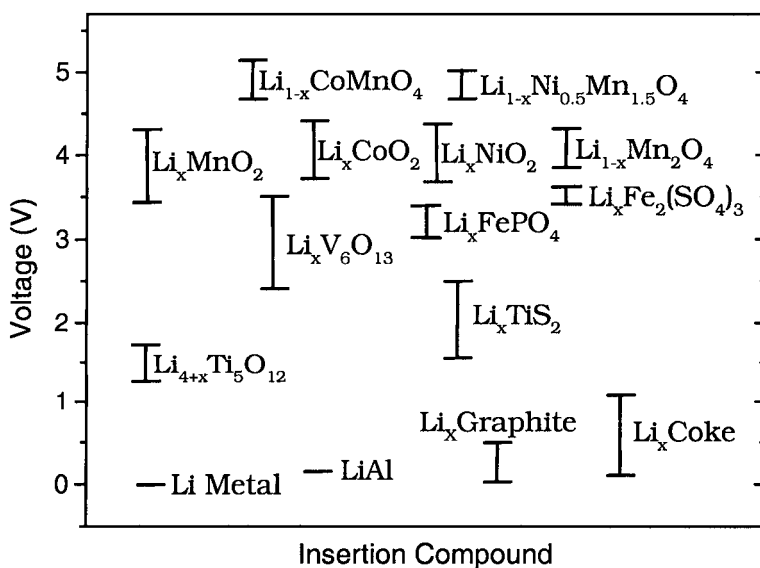


Figure 1.5. Electrochemical potential ranges of some lithium insertion compounds in reference to metallic lithium.

Such cells consisting of lithium insertion compounds as both cathodes and anodes are called lithium-ion cells or rocking-chair cells since the lithium ion shuttles or rocks between the cathode and anode hosts during the charge/discharge process as illustrated in Figure 1.6. This strategy, however, requires a careful selection of cathode and anode pairs in order to maintain an acceptable cell voltage of at least 3 V and to realize a reasonable energy density without unduly increasing the weight or volume of the cell through the insertion compound anode.

With this strategy, the anode and cathode insertion hosts should have, respectively, the lowest and highest voltages versus metallic lithium in order to maximize the cell voltage while satisfying the other required criteria. Accordingly, among the various known lithium insertion

compounds, LiCoO_2 , LiNiO_2 and LiMn_2O_4 oxides having a high electrode potential of 4 V versus metallic lithium, have become attractive cathodes for lithium-ion cells. Although one might tend to prefer a cathode like LiMnCoO_4 offering 5 V versus lithium (Figure 1.5), the long-term stability of both the electrolyte and the cathodes under such a high voltage need to be fully assessed before they could be considered for commercial cells (see later). On the other hand, graphite and coke having a lower electrode potential of <1 V versus metallic lithium and lightweight have become attractive anodes. The lithium-ion cells are presently made with LiCoO_2 cathodes and carbon anodes as shown in Figure 1.6. In such a cell, the lithium ions migrate from LiCoO_2 cathode to the Li_xC_6 anode through the electrolyte and the electron flows through the external circuit from the cathode to the anode during the charge process. An exactly reverse reaction occurs during the discharge process. Although the replacement of metallic lithium having a huge capacity of 3860 mAh/g by carbon having a capacity

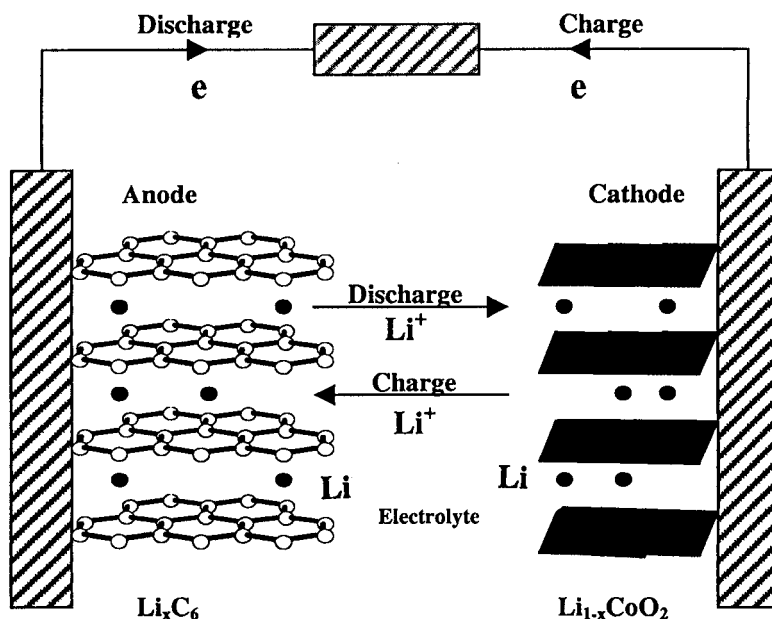


Figure 1.6. Schematic illustration of the charge/discharge process in a lithium-ion cell consisting of lithium insertion compounds as both anode and cathode.

of 372 mAh/g causes an important sacrifice in energy density, the lithium-ion cells involving the shuttling of lithium ions between the two insertion hosts without any metallic lithium offer significant advantages in terms of safety and cycle life.

From a materials design point of view, the anode insertion

compound $\text{Li}_x\text{M}_y\text{X}_z$ should also satisfy several important criteria like the cathode insertion host: a large degree x of lithium insertion/extraction (high capacity), high electronic and ionic conductivity, good chemical and structural stabilities (reversibility), and affordable cost. The main difference between the anode and cathode insertion hosts is that the former should have a low lithium chemical potential ($\mu_{\text{Li(a)}}$) in order to maximize the cell voltage, which implies that the M^{n+} ion in the $\text{Li}_x\text{M}_y\text{X}_z$ anode should have low oxidation state.

Apart from the various intrinsic characteristics of the insertion electrode materials discussed, several other criteria are important in designing a good lithium-ion cell that can offer high performance with long cycle life. The electrolyte should have high lithium-ion conductivity, but should be an electronic insulator in order to avoid internal short-circuiting. A high ionic conductivity in the electrolyte is essential to minimize IR drop or ohmic polarization and achieve good rate capability. With a given electrolyte, the IR drop due to electrolyte resistance can be reduced and the rate capability can be improved by having a higher electrode interfacial area and thin separators. The electrolyte should also have good chemical stability and should not undergo any direct reaction with the electrodes. Additionally, the engineering involved in cell design and fabrication plays a critical role in the overall cell performance.¹² For example, high electronic conductivity and lithium-ion diffusion rate in the electrodes are essential to minimize cell polarizations and the electronic conductivity of the electrodes can be improved by adding electronically conducting additives such as carbon. However, the amount of additive should be minimized to avoid any undue sacrifice in gravimetric or volumetric capacity. Finally, cell safety, environmental factors, and raw material and fabrication costs are additional important considerations in both materials selection and cell design.

1.4. LAYERED OXIDE CATHODES

Several oxides with a general formula LiMO_2 ($\text{M} = \text{V}, \text{Cr}, \text{Co}, \text{and Ni}$) crystallize in a layered structure in which the Li^+ and M^{3+} ions occupy the alternate (111) planes of the rock salt structure to give a layer sequence of -O-Li-O-M-O- along the c axis as shown in Figure 1.7 for LiCoO_2 . The structure has an oxygen stacking sequence of ...ABCABC... along the c axis and the Li^+ and M^{3+} ions occupy the octahedral interstitial sites of the cubic close-packed oxygen array. This structure is designated as the O3 layer structure since the Li^+ ions occupy the octahedral sites (O referring to octahedral) and there are three MO_2 sheets per unit cell. The structure with a strongly (covalently) bonded MO_2 layers allows a reversible extraction/insertion of lithium ions from/into the lithium planes. The interconnected lithium-ion sites through the edge-shared LiO_6 octahedral

arrangement between the MO_2 layers provide fast two-dimensional lithium-ion diffusion leading to high σ_{Li} . On the other hand, the edge-shared MO_6 octahedral arrangement with a direct M-M interaction can provide good electronic conductivity σ_e depending on the electronic configuration of the M^{3+} ion. As a result, the LiMO_2 oxides crystallizing in the O3 structure have become attractive candidates as cathodes and they are discussed below.

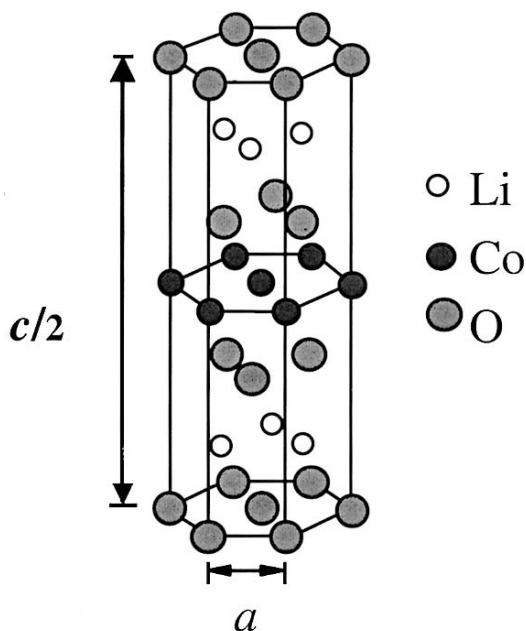


Figure 1.7. Crystal structure of LiCoO_2 having the O3 layered structure.

1.4.1. Layered LiCoO_2

LiCoO_2 synthesized by conventional high temperature procedures at $T > 800^\circ\text{C}$ adopts the O3 layer structure (Figure 1.7) with an excellent ordering of the Li^+ and Co^{3+} ions on the alternate (111) planes of the rock salt lattice. In contrast, synthesis at lower temperatures ($\sim 400^\circ\text{C}$) results in a considerable disordering of the Li^+ and Co^{3+} ions leading to the formation of a lithiated spinel-like LiCoO_2 phase with a cation distribution of $\{\text{Li}_2\}_{16c}[\text{Co}_2]_{16d}\text{O}_4$ as indicated by X-ray diffraction and single crystal electron diffraction studies.¹⁷⁻²⁰ This low-temperature form is designated as LT- LiCoO_2 and it exhibits poor electrochemical properties, making it an unattractive cathode.²¹ Thus heating the LiCoO_2 sample at high temperatures ($T > 800^\circ\text{C}$) is essential to have a good mobility for the cations and a

subsequent ordering of the Li^+ and Co^{3+} ions on cooling to give the desired O3 layered structure.

The O3-type LiCoO_2 obtained by the high temperature procedure exhibits good electrochemical properties and most of the commercial lithium-ion cells are currently made with the LiCoO_2 cathodes. A high lithium chemical potential $\mu_{\text{Li(c)}}$ associated with the highly oxidized $\text{Co}^{3+/4+}$ couple provides a high cell voltage of around 4 V,⁵ and the discharge voltage does not change significantly with the degree of lithium extraction/insertion x in $\text{Li}_{1-x}\text{CoO}_2$ (Figure 1.8). The direct Co-Co interaction with a partially filled t_{2g}^{6-x} band associated with the $\text{Co}^{3+/4+}$ couple leads to high electronic conductivity for $\text{Li}_{1-x}\text{CoO}_2$. Additionally, a strong preference of the low-spin Co^{3+} ($t_{2g}^6 e_g^0$) and Co^{4+} ($t_{2g}^5 e_g^0$) ions for the octahedral sites provides good structural stability for $\text{Li}_{1-x}\text{CoO}_2$ without encountering a migration of the $\text{Co}^{3+/4+}$ ions from the octahedral sites of the cobalt plane to the octahedral sites of the lithium plane via the neighboring tetrahedral sites (see later). These features have made LiCoO_2 an excellent cathode for the lithium-ion cells.

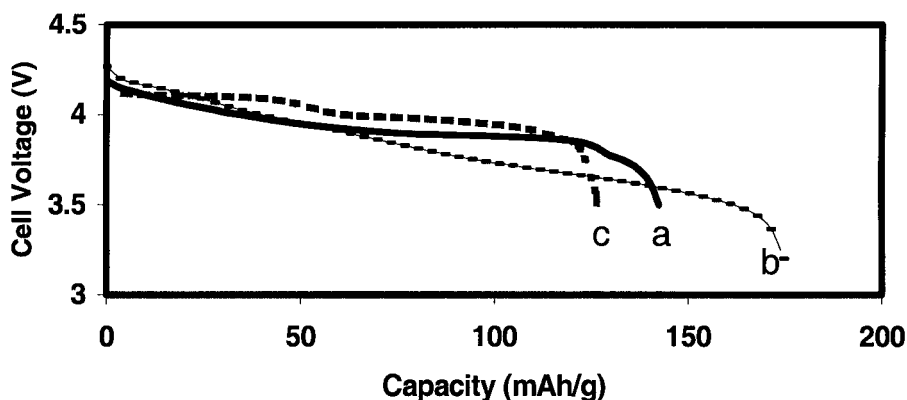


Figure 1.8. Typical discharge curves of (a) layered LiCoO_2 , (b) layered $\text{LiNi}_{0.85}\text{Co}_{0.85}\text{O}_2$, and (c) spinel LiMn_2O_4 .

However, only 0.5 lithium ions per LiCoO_2 formula could be reversibly extracted/inserted and cycling to $(1-x) < 0.5$ in $\text{Li}_{1-x}\text{CoO}_2$ results in capacity fade. This translates into a practical capacity of around 140 mAh/g, which is 50% of the theoretical capacity. The limitation in practical capacity has been attributed in the literature to an ordering of lithium ions and consequent structural distortions (hexagonal to monoclinic transformation) around $x=0.5$ in $\text{Li}_{1-x}\text{CoO}_2$ ²² and side reactions at >4.2 V (versus metallic

lithium).²³ However, it has been found recently that the cyclability of the $\text{Li}_{1-x}\text{CoO}_2$ cathodes could be improved significantly down to $(1-x)\approx 0.3$, offering reversible capacities of close to 200 mAh/g, by modifying its surface with other oxides such as Al_2O_3 , ZrO_2 , and TiO_2 .²⁴⁻²⁹ For example, Figure 1.9 compares the cyclability of Al_2O_3 -modified LiCoO_2 cathode with that of unmodified LiCoO_2 cathode to various cut-off voltages.²⁹ As can be seen, the surface modified samples exhibit good capacity retention to higher cut-off voltages with practical capacities of close to 200 mAh/g. Cho *et al.*^{26,27} attributed the improved cyclability from *ex-situ* X-ray diffraction data to a suppression of both the changes in the c axis with $(1-x)$ and the hexagonal to monoclinic phase transition arising from an ordering of the lithium ions around $(1-x)=0.5$. However, *in-situ* X-ray diffraction data indicate that the surface modified samples also exhibit changes in c axis with $(1-x)$ and the hexagonal to monoclinic phase transition around $(1-x)=0.5$ just like the uncoated $\text{Li}_{1-x}\text{CoO}_2$.³⁰ Also, Transmission electron microscopic (TEM) studies show that the coating oxides such as Al_2O_3 and ZrO_2 are present as loose nanoparticles on the surface of LiCoO_2 .^{29,30} These findings suggest that the capacity fade commonly encountered by the LiCoO_2 cathodes (uncoated) on cycling to $(1-x)<0.5$ may not be simply due to the hexagonal to monoclinic transition at $(1-x)=0.5$ and some other factors may play a role.

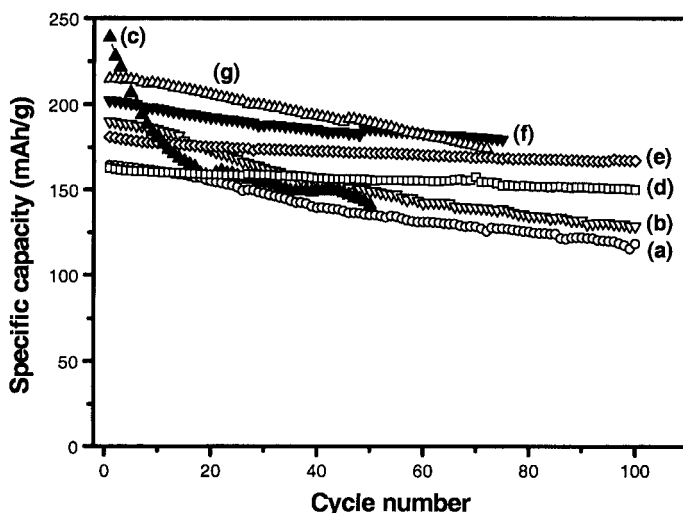


Figure 1.9. Comparison of the cyclability data of unmodified and Al_2O_3 -modified LiCoO_2 cathodes in different voltage ranges at C/5 rate: (a) unmodified LiCoO_2 (4.3 to 3.2 V), (b) unmodified LiCoO_2 (4.5 to 3.2 V), (c) unmodified LiCoO_2 (4.7 to 3.2 V), (d) Al_2O_3 -modified LiCoO_2 (4.3 to 3.2 V), (e) Al_2O_3 -modified LiCoO_2 (4.5 to 3.2 V), (f) Al_2O_3 -modified LiCoO_2 (4.6 to 3.2 V), and (g) Al_2O_3 -modified LiCoO_2 (4.7 to 3.2 V).

The lack of a clear understanding of the factors that limit the practical capacity of the LiCoO_2 (uncoated) cathode to 140 mAh/g is partly due to the fact that most of the investigations in the literature^{22,31-34} have focused mainly on the structural characterization (both *in-situ* and *ex-situ*) of the electrochemically charged $\text{Li}_{1-x}\text{CoO}_2$ samples. No chemical characterization data such as the variations of the oxidation state of Co and the oxygen content with lithium content were available since it is difficult to chemically characterize the electrochemically charged samples as they are contaminated with carbon, binder, and electrolyte. To overcome these difficulties and to develop a better understanding of the factors that control the practical capacities, recent investigation by our group³⁵⁻³⁸ has focused on both the chemical and structural characterizations of the $\text{Li}_{1-x}\text{CoO}_2$ samples that were obtained by chemical delithiation. The chemical delithiation reactions were carried out by stirring the LiCoO_2 powder under argon atmosphere with an acetonitrile solution of an oxidizing agent such as NO_2PF_6 (or NO_2BF_4) that has a reduction potential of around 5 V versus metallic lithium³⁹ and is strong enough to extract all the lithium from LiCoO_2 :

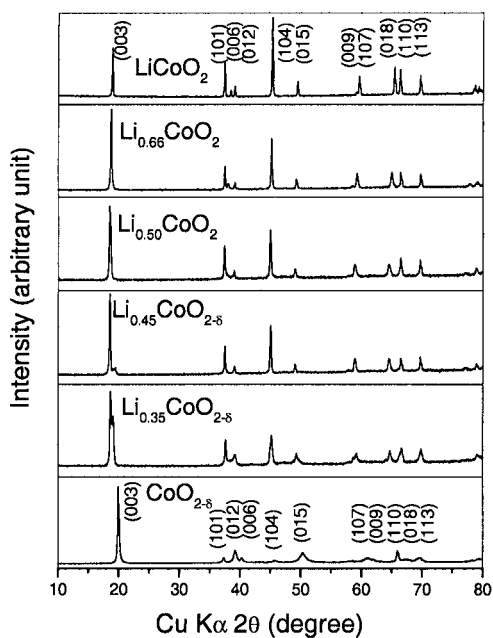


Figure 1.10. X-ray diffraction patterns of the $\text{Li}_{1-x}\text{CoO}_2$ phases obtained by chemical delithiation.

Figure 1.10 shows the evolution of the X-ray diffraction patterns of the chemically delithiated $\text{Li}_{1-x}\text{CoO}_2$ samples.³⁸ The $\text{Li}_{1-x}\text{CoO}_2$ system maintains the initial O3-type structure for $0.5 \leq (1-x) \leq 1.0$ and a new phase begins to form around $(1-x)=0.45$ as indicated by the appearance of a shoulder to the right of the (003) reflection. The new phase continues to grow with decreasing lithium content and the end member CoO_2 consists of reflections corresponding to only the new phase, which could be indexed on the basis of a P3-type structure. In the intermediate region $0 < (1-x) \leq 0.45$, both the O3-type and the P3-type phases coexist (Figure 1.11). The observation of a P3-type structure for CoO_2 is in contrast to the O1-type structure reported in the literature³²⁻³⁴ for the electrochemically synthesized samples. However, the P3-type structure observed for the chemically synthesized CoO_2 sample is metastable and it transforms slowly to the O1-type structure with increasing reaction time of >2 days with the oxidizer NO_2PF_6 .³⁷ The formation of the metastable P3-type phase during chemical delithiation is due to the rapid extraction of lithium in <15 min, which translates into an extremely high charging rate of $>4\text{C}$, compared to the much slower electrochemical charging ($<1\text{C}/10$ rate) process normally used.^{32,34} The P3- and O1-type phases have an oxygen stacking sequence of, respectively, ...AABBCC... and ...ABABAB... along the c axis compared to a stacking sequence of ...ABCABC... in the initial O3-type LiCoO_2 phase (Figure 1.12). The P3- and O1-type phases are formed from the initial O3-type structure by a sliding

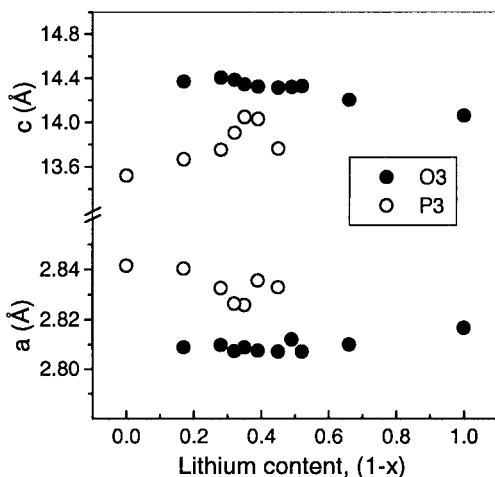


Figure 1.11. Variations of the a and c lattice parameters of the chemically delithiated $\text{Li}_{1-x}\text{CoO}_2$ with $(1-x)$.

of some CoO_2 sheets as shown in Figure 1.13 without involving the breaking of any Co-O bonds. The O3-, P3- and O1-type structures have, respectively, 3, 3, and 1 CoO_2 sheets per unit cell. While the alkali metal ions have an octahedral coordination in both the O3- and O1- type structures (O referring to octahedral), they have prismatic coordination in the P3-type phase (P referring to prismatic).

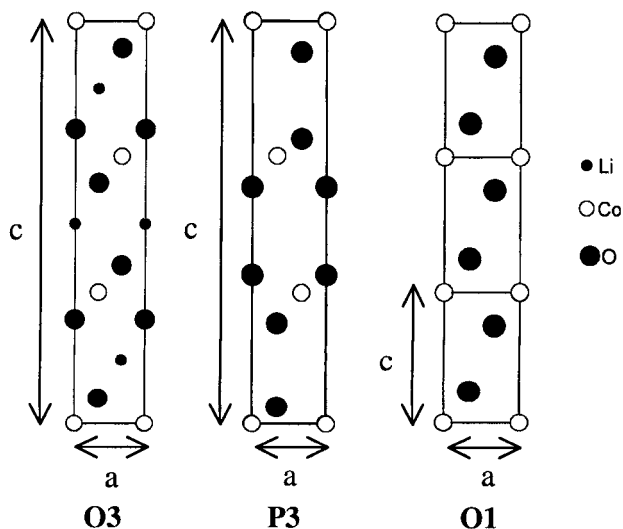


Figure 1.12. Crystal structures of O3-type LiCoO_2 , P3-type CoO_2 , and O1-type CoO_2 viewed along the (100) plane.

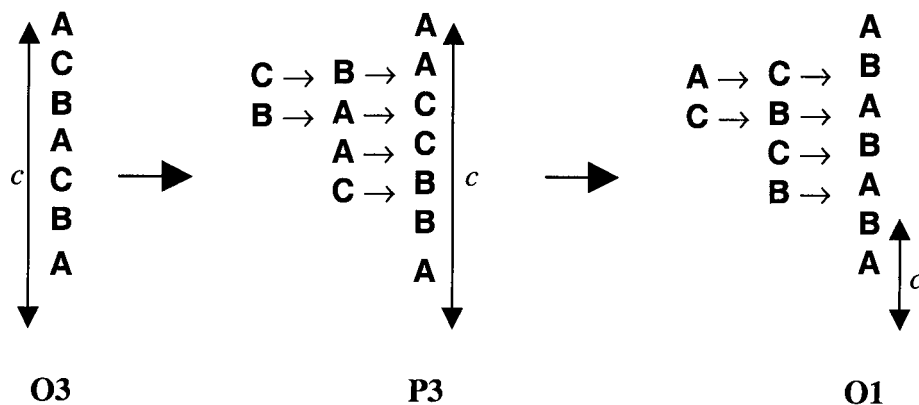


Figure 1.13. Schematics of the sliding of some CoO_2 sheets leading to the transformation of the O3 structure to P3 and O1 structures. The letters refer to oxygen stacking sequence along the c axis.

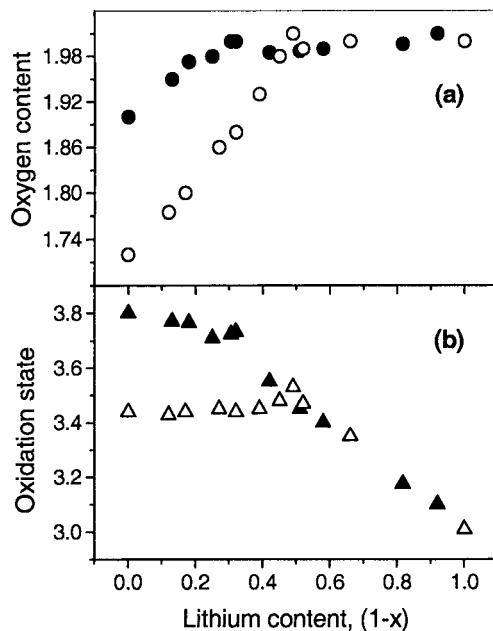


Figure 1.14. Variations of the (a) oxidation state of Co and ($\text{Ni}_{0.85}\text{Co}_{0.15}$) and (b) oxygen content with lithium content ($1-x$) in $\text{Li}_{1-x}\text{CoO}_2$ and in $\text{Li}_{1-x}\text{Ni}_{0.85}\text{Co}_{0.15}\text{O}_2$.

Figure 1.14 shows the variations of the oxidation state of Co and the oxygen content with lithium content for the chemically delithiated $\text{Li}_{1-x}\text{CoO}_2$ samples.³⁸ The data in Figure 1.14 were obtained by a wet-chemical analysis involving iodometric titration⁴⁰ and the application of charge neutrality principle. The oxidation state of cobalt increases linearly with $(1-x)$ and the oxygen content remains around 2 for $0.5 \leq (1-x) \leq 1.0$ in $\text{Li}_{1-x}\text{CoO}_{2-\delta}$. For $0 \leq (1-x) < 0.5$, the oxidation state of cobalt remains nearly constant and the charge compensation is achieved by a loss of oxygen from the lattice with a $\delta=0.28$ for the end-member $\text{CoO}_{2-\delta}$. The loss of oxygen from the lattice signals a chemical instability for $(1-x) < 0.5$ in $\text{Li}_{1-x}\text{CoO}_{2-\delta}$, which may be the factor limiting its reversible capacity. The increased reversible capacity for the surface modified samples in Figure 1.9 is due to a more stable electrode-electrolyte interface and the consequent improvement in the chemical stability. Interestingly, the lithium content ($1-x$) at which the oxygen loss begins to occur coincides with the lithium content at which the new phase P3 begins to form (Figures 1.10 and 1.11). The results indicate that the P3 phase is oxygen deficient with a shorter O-O distance across the van der Waals gap between the CoO_2 sheets, signaling an increased O-O interaction.

1.4.2. Layered LiNiO₂

LiNiO₂ crystallizes in the O3 layered structure shown in Figure 1.7 like LiCoO₂. The Ni^{3+/4+} couple with a high lithium chemical potential $\mu_{\text{Li(c)}}$ provides a high cell voltage of around 4 V⁶ like LiCoO₂ as seen in Figure 1.8. LiNiO₂ provides an important advantage compared to LiCoO₂ since Ni is less expensive and less toxic than Co, but it suffers from a few problems: (i) difficulty to synthesize LiNiO₂ with all Ni³⁺ and as a perfectly ordered phase without a mixing of Li⁺ and Ni³⁺ ions in the lithium plane,⁴¹⁻⁴³ (ii) Jahn-Teller distortion (tetragonal structural distortion) associated with the low spin Ni³⁺:d⁷ ($t_{2g}^6 e_g^1$) ion,^{44,45} (iii) irreversible phase transitions occurring during the charge-discharge process,^{32,46} and (iv) exothermic release of oxygen at elevated temperatures and safety concerns in the charged state.⁴⁷ As a result, LiNiO₂ is not a promising material for lithium-ion cells. However, some of these difficulties have been overcome by a partial substitution of Co for Ni. For example, the composition LiNi_{0.85}Co_{0.15}O₂ has been found to show a reversible capacity of around 180 mAh/g (Figure 1.8) with excellent cyclability.⁴⁹ This capacity is 30% higher than that of LiCoO₂ and it corresponds to a reversible extraction/insertion of 0.65 lithium per transition metal ion (65% of the theoretical capacity). *In situ* X-ray absorption fine structure studies have shown that the substitution of Co for Ni suppresses the cation disorder and Jahn-Teller distortion.^{44,45} The substitution also suppresses the phase transitions commonly encountered with lithium extraction from LiNiO₂ and LiNi_{1-y}Co_yO₂ (0.15 ≤ y ≤ 0.2) is intensively being pursued particularly for electric vehicles due to its lower cost compared to LiCoO₂.

However, the LiNi_{1-y}Co_yO₂ (0.15 ≤ y ≤ 0.2) cathodes have been found to develop impedance during cycling particularly at elevated temperatures.⁵⁰ The reason for the impedance development is not fully understood, but it could be related to the migration of the nickel ions from the nickel plane to the lithium plane during cycling. The nickel-rich Li_{1-x}Ni_{1-y}Co_yO₂ samples obtained by both chemical delithiation⁵¹ and electrochemical charging⁵² have been found to exhibit a decrease in *c/a* ratio on heating at T > 50°C while the Li_{1-x}CoO₂ system does not suffer from such a difficulty.⁵³ Rietveld analysis has shown that the decrease in the *c/a* ratio is due to a migration of the nickel ions from the octahedral sites of the nickel plane to the octahedral sites of the lithium plane via the neighboring tetrahedral sites as illustrated in Figure 1.15. The tendency for such a migration in Li_{1-x}Ni_{1-y}Co_yO₂ and its absence in Li_{1-x}CoO₂ is due to a lower octahedral-site stabilization energy (OSSE) associated with the low-spin Ni³⁺:d⁷ ($t_{2g}^6 e_g^1$) ions compared to that for the low-spin Co³⁺:d⁶ (t_{2g}^6) ion (Table 1.1).^{53,54} While a moderate

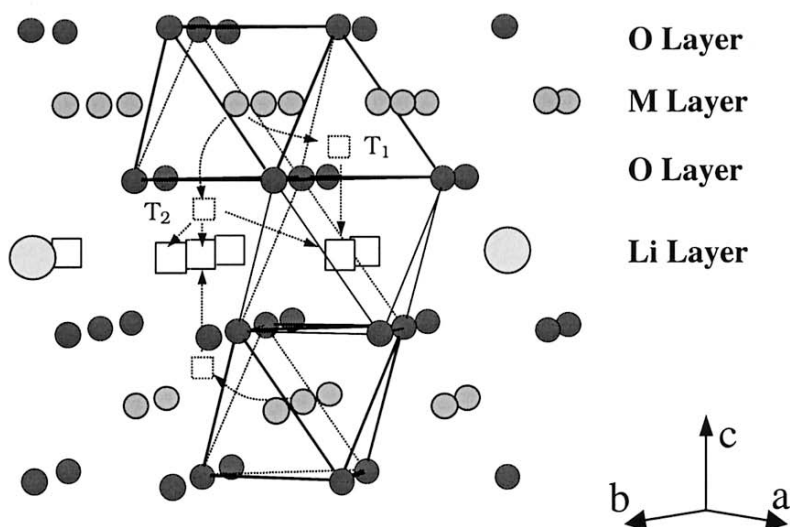


Figure 1.15. Schematic representation of the paths for the migration of M^{3+} ions in layered $Li_{1-x}MO_2$ ($M = Mn, Co$ and Ni). The open squares and the dotted squares refer, respectively, to lithium ion vacancies and tetrahedral sites. T_1 and T_2 refer to tetrahedral sites at $(0, 0, 0.125)$ and $(0, 0, 0.375)$ respectively.

OSSE allows the Ni^{3+} ions to migrate through the tetrahedral sites under mild heat, the stronger OSSE of Co^{3+} hinders such a migration.

Nevertheless, the $LiNi_{0.85}Co_{0.15}O_2$ cathodes exhibit a higher reversible capacity of 180 mAh/g compared to that of the analogous $LiCoO_2$ (140 mAh/g) cathodes. However, the reason for the difference in capacity is not fully understood in the literature. With an objective to develop a better understanding, our group has focused on the structural and chemical characterizations of the chemically delithiated $Li_{1-x}Ni_{0.85}Co_{0.15}O_2$ samples and a comparison of the results with those of $Li_{1-x}CoO_2$. Figures 1.16 and 1.17 show the X-ray diffraction patterns of the chemically delithiated $Li_{1-x}Ni_{0.85}Co_{0.15}O_2$ samples and the lattice parameter variations with the lithium content $(1-x)$. The $Li_{1-x}Ni_{0.85}Co_{0.15}O_2$ system maintains the initial O3-type structure over a wide lithium content of $0.3 \leq (1-x) \leq 1$ and a new phase begins to form at a much lower lithium content of around $(1-x)=0.25$ compared to that found around $(1-x)=0.45$ in the $Li_{1-x}CoO_2$ system (Figure 1.10) as indicated by the small shoulder to the right of the (003) reflection. The new phase grows with decreasing lithium content and the end member $Ni_{0.85}Co_{0.15}O_2$ consists of only the new phase. However, the new phase could also be indexed on the basis of an O3-type structure in contrast to the P3-type structure found for CoO_2 . The new O3-type phase of $Ni_{0.85}Co_{0.15}O_2$ has

Table 1.1. Crystal field stabilization energies (CFSE) and octahedral site stabilization energies (OSSE) of some 3d transition metal ions.

Ion	Octahedral coordination		Tetrahedral coordination		OSSE ^d
	Configuration ^a	CFSE ^b	Configuration ^a	CFSE ^{b,c}	
V ³⁺ :3d ²	$t_{2g}^2 e_g^0$	-8 Dq	$e^2 t_2^0$	-5.33 Dq	-2.67 Dq
Cr ³⁺ :3d ³	$t_{2g}^3 e_g^0$	-12 Dq	$e^2 t_2^1$ (HS)	-3.56 Dq	-8.44 Dq
Mn ³⁺ :3d ⁴	$t_{2g}^3 e_g^1$ (HS)	-6 Dq	$e^2 t_2^2$ (HS)	-1.78 Dq	-4.22 Dq
Fe ³⁺ :3d ⁵	$t_{2g}^3 e_g^2$ (HS)	0 Dq	$e^2 t_2^3$ (HS)	0 Dq	0 Dq
Co ³⁺ :3d ⁶	$t_{2g}^6 e_g^0$ (LS)	-24 Dq	$e^3 t_2^3$ (HS)	-2.67 Dq	-21.33 Dq
Ni ³⁺ :3d ⁷	$t_{2g}^6 e_g^1$ (LS)	-18 Dq	$e^4 t_2^3$ (HS)	-5.33 Dq	-12.67 Dq

^a LS and HS refer, respectively, to low-spin and high-spin configurations.

^b Pairing energies are neglected for simplicity.

^c Obtained by assuming $\Delta_t = 0.444 \Delta_o$; Δ_t and Δ_o refer, respectively, to tetrahedral and octahedral splittings.

^d Obtained by taking the difference between the CFSE values for octahedral and tetrahedral coordinations.

a smaller c parameter than the initial O3 phase as evident in Figure 1.17, and we have designated this new O3 phase as O3' phase.³⁸ In the intermediate region $0 < (1-x) \leq 0.25$, both the O3 and O3' phases coexist. The lower c parameter of the O3' phase may again signal a stronger O-O interaction across the van der Waals gap between the (Co,Ni)O₂ sheets like in the P3-type CoO₂. The overall trends in the c parameter variations of both the Li_{1-x}CoO₂ and the Li_{1-x}Ni_{0.85}Co_{0.15}O₂ systems are in general agreement with that reported for the electrochemically charged samples, despite the slight differences in the type of phases observed for the two delithiation processes.^{31,32,55}

Figure 1.14 compares the variations with lithium content of the average oxidation state of Ni_{0.85}Co_{0.15} and the oxygen content in Li_{1-x}Ni_{0.85}Co_{0.15}O₂ with those of Li_{1-x}CoO₂. The Li_{1-x}Ni_{0.85}Co_{0.15}O_{2-δ} system loses

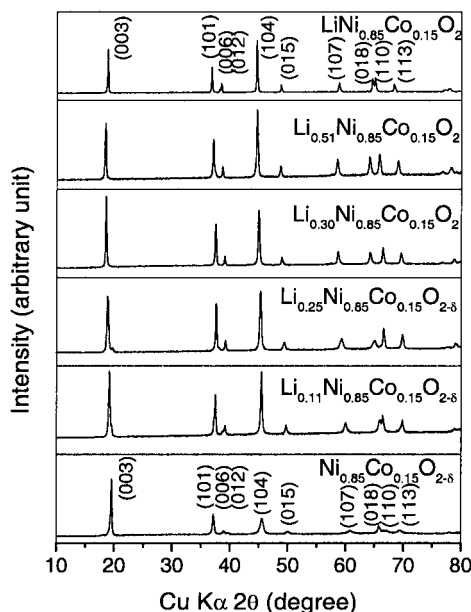


Figure 1.16. X-ray diffraction patterns of the $\text{Li}_{1-x}\text{Ni}_{0.85}\text{Co}_{0.15}\text{O}_2$ phases obtained by chemical delithiation.

oxygen at a much lower lithium content of around $(1-x)=0.25$, and the end-member $\text{Ni}_{0.85}\text{Co}_{0.15}\text{O}_{2-\delta}$ has a much smaller $\delta=0.1$ compared to that in the $\text{Li}_{1-x}\text{CoO}_{2-\delta}$ system. However, similar to that observed in the $\text{Li}_{1-x}\text{CoO}_{2-\delta}$ system, the lithium content $(1-x)$ at which the oxygen loss begins to occur coincides with the lithium content at which the new phase O3' begins to form, indicating that the O3' phase is oxygen deficient with a shorter O-O distance across the van der Waals gap and an increased O-O interaction. More importantly, the realization of a higher capacity for the $\text{LiNi}_{0.85}\text{Co}_{0.15}\text{O}_{2-\delta}$ system (180 mAh/g) compared to the LiCoO_2 system (140 mAh/g) could be due to the better chemical stability of the former without tending to lose oxygen from the lattice down to a lower lithium content of around 0.3. Although the data presented in Figure 1.14 are for chemically delithiated samples, the data collected with the electrochemically charged samples also show a similar trend.³⁸ However, it should be noted that neutral oxygen may not be evolved during an over-charge of lithium-ion cells, but rather the cathode might undergo a slow reduction reaction with the electrolyte during cycling.

The differences in the chemical stability (oxygen loss) between the $\text{Li}_{1-x}\text{CoO}_2$ and the $\text{Li}_{1-x}\text{Ni}_{0.85}\text{Co}_{0.15}\text{O}_2$ systems can be understood

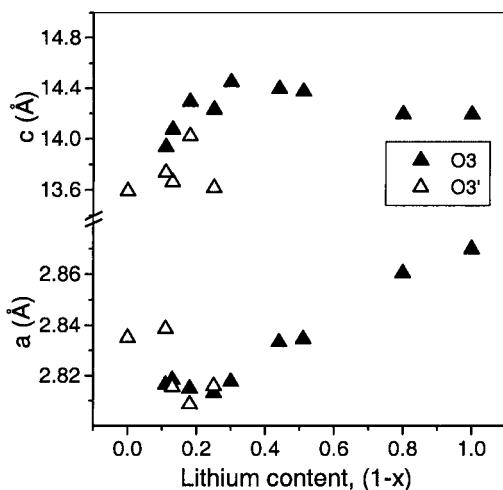


Figure 1.17. Variations of the a and c lattice parameters of the chemically delithiated $\text{Li}_{1-x}\text{Ni}_{0.85}\text{Co}_{0.15}\text{O}_2$ with $(1-x)$.

by considering the qualitative band diagrams for the $\text{Li}_{1-x}\text{CoO}_2$ and $\text{Li}_{1-x}\text{NiO}_2$ systems (Figure 1.18). With a low-spin $\text{Co}^{3+}:3d^6$ configuration, the t_{2g} band is completely filled and the e_g band is empty ($t_{2g}^6 e_g^0$) in LiCoO_2 . As lithium is extracted from LiCoO_2 , the Co^{3+} ions are oxidized to Co^{4+} by a removal of electrons from the t_{2g} band. However, at deeper lithium extraction with $(1-x) < 0.5$, removal of electrons may occur from the $\text{O}^{2-}:2p$ band (creation of holes) as well since the t_{2g} band overlaps with the top of the $\text{O}^{2-}:2p$ band. The removal of significant amount of electron density from the $\text{O}^{2-}:2p$ band will result in an oxidation of the O^{2-} ions and an ultimate loss of oxygen from the lattice. In contrast, the LiNiO_2 system with a low-spin $\text{Ni}^{3+}:t_{2g}^6 e_g^1$ configuration involves the removal of electrons only from the e_g band. Since the e_g band barely touches the top of the $\text{O}^{2-}:2p$ band, the $\text{Li}_{1-x}\text{NiO}_2$ system loses a small amount of oxygen only towards the end of lithium extraction with $(1-x) < 0.2$.³⁵ In the case of $\text{LiNi}_{0.85}\text{Co}_{0.15}\text{O}_2$ with a small amount of Co, it loses oxygen slightly earlier for $(1-x) < 0.3$. For a comparison, the band diagram of the $\text{Li}_{1-x}\text{Mn}_2\text{O}_4$ spinel system is also shown in Figure 1.18. With a high-spin $\text{Mn}^{3+}:t_{2g}^3 e_g^1$ configuration, the removal of electrons occurs only from the e_g band in $\text{Li}_{1-x}\text{Mn}_2\text{O}_4$. Since the e_g band lies well above the top of the $\text{O}:2p$ band, the $\text{Li}_{1-x}\text{Mn}_2\text{O}_4$ system has been found by chemical analysis data not to lose any oxygen.⁵⁶ Also, while the partially filled t_{2g} band leads to metallic conductivity for $(1-x) < 0.77$ in $\text{Li}_{1-x}\text{CoO}_2$, the completely filled t_{2g} band leads to semiconducting behavior for $0 \leq (1-x) \leq 1$ in both $\text{Li}_{1-x}\text{NiO}_2$ and $\text{Li}_{1-x}\text{Ni}_{0.85}\text{Co}_{0.15}\text{O}_2$.³⁵

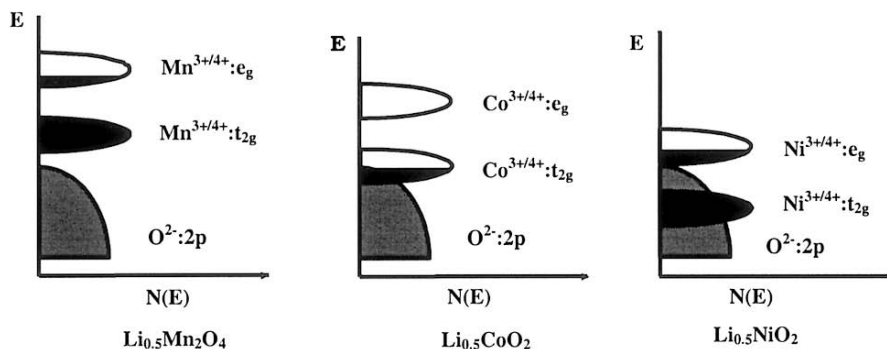


Figure 1.18. Comparison of the energy diagrams of $\text{Li}_{0.5}\text{CoO}_2$, $\text{Li}_{0.5}\text{NiO}_2$, and $\text{Li}_{0.5}\text{Mn}_2\text{O}_4$.

The qualitative band diagrams shown in Figure 1.18 and the observed oxygen loss behavior are consistent with (i) the spectroscopic data that holes are introduced into the $\text{O}^{2-}:2p$ band rather than into the $\text{Co}:3d$ band in $\text{Li}_{1-x}\text{CoO}_2$, but into the $\text{Ni}:e_g$ band in $\text{Li}_{1-x}\text{NiO}_2$ and $\text{Li}_{1-x}\text{Ni}_{0.85}\text{Co}_{0.15}\text{O}_2$ during electrochemical charging,⁵⁷⁻⁵⁹ and (ii) the theoretical calculations that the average charge on oxygen decreases with decreasing lithium content in $\text{Li}_{1-x}\text{CoO}_2$.^{60,61} Furthermore, the introduction of holes into the $\text{O}^{2-}:2p$ band facilitates the O-O interaction across the van der Waals gap between the MO_2 sheets, which could in turn be the driving force for the formation of the P3 or O3' phases with smaller c parameters than the O3 phase (Figures 1.11 and 1.17). In fact, the P3 phase is generally believed to be inaccessible since the oxide ions lie one above the other along the c axis (Figure 1.12), and the formation of the P3 phase only in the case of $\text{CoO}_{2.8}$ could very well be due to the presence of significant amount of holes in the $\text{O}^{2-}:2p$ band and considerable amount of oxygen vacancies.

1.4.3. Other Layered Oxides

Both LiVO_2 and LiCrO_2 crystallize in the O3 structure (Figure 1.7), but the vanadium ions migrate to the lithium planes for $(1-x) < 0.67$ in $\text{Li}_{1-x}\text{VO}_2$ ⁶² due to the low OSSE (Table 1.1), while it is difficult to extract lithium from LiCrO_2 . So, both LiVO_2 and LiCrO_2 are not promising cathode materials. LiTiO_2 is difficult to synthesize and both LiMnO_2 and LiFeO_2 synthesized by high temperature procedures do not adopt the O3 structure. Nevertheless, the sodium analogs NaMO_2 ($M = \text{Mn}$ and Fe) adopt the O3 structure and the O3-type LiMnO_2 and LiFeO_2 have been obtained by ion-

exchange reactions of NaMO_2 .⁶³⁻⁶⁵ Also, a partial substitution of Cr or Al for Mn has been found to access the O3-type LiMnO_2 by direct ceramic procedures.^{53,66-68} Unfortunately, the O3-type LiMnO_2 transforms to spinel-like phases during cycling due to the low OSSE of Mn^{3+} (Table 1.1) and the consequent migration of the Mn^{3+} ions from the Mn plane to the Li plane. Similarly, the orthorhombic LiMnO_2 that is obtained by conventional procedures also transforms to spinel-like phase,⁶⁹ leading to poor cyclability. The O3-type LiFeO_2 also exhibits poor electrochemical cycling properties due to structural instabilities since the high-spin $\text{Fe}^{3+}3d^5$ with an OSSE value of zero (Table 1.1) can readily migrate from the octahedral to tetrahedral sites.

1.5. SPINEL OXIDE CATHODES

A few oxides with the general formula LiM_2O_4 ($\text{M} = \text{Ti}, \text{V}, \text{and Mn}$) crystallize in the normal spinel structure (Figure 1.19) in which the Li^+ and the $\text{M}^{3+/4+}$ ions occupy, respectively, the 8a tetrahedral and 16d octahedral sites of the cubic close-packed oxygen array to give a cation distribution of $(\text{Li})_{8a}[\text{M}_2]_{16d}\text{O}_4$. A strong edge-shared octahedral $[\text{M}_2]\text{O}_4$ array permits

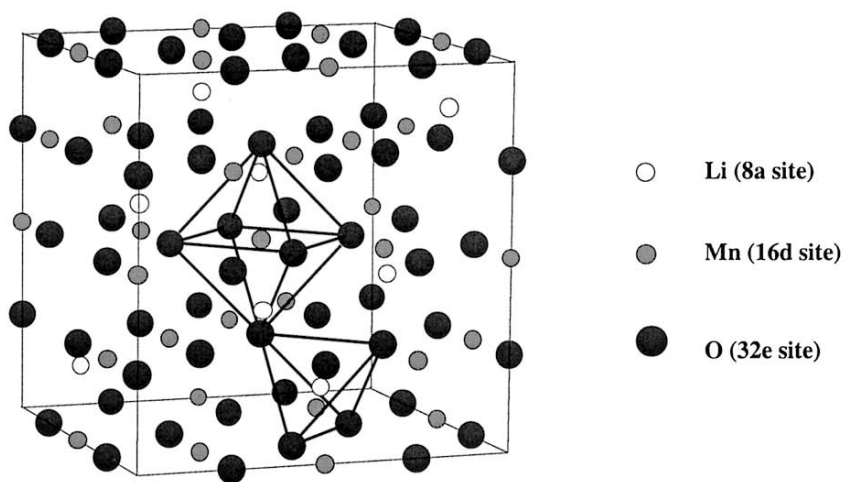


Figure 1.19. Crystal structure of spinel LiMn_2O_4 .

reversible extraction of the Li^+ ions from the tetrahedral sites without collapsing the 3-dimensional $[\text{M}_2]\text{O}_4$ spinel framework. An additional

lithium can also be inserted in to the empty 16c octahedral sites of the spinel framework to give the lithiated spinel $\text{Li}_2[\text{M}_2]\text{O}_4$. However, an electrostatic repulsion between the Li^+ ions in the 8a tetrahedral and 16c octahedral sites, which share common faces, causes a displacement of the tetrahedral Li^+ ions into the neighboring empty 16c sites to give an ordered rock salt structure having a cation distribution of $\{\text{Li}_2\}_{16\text{c}}[\text{M}_2]_{16\text{d}}\text{O}_4$. Thus theoretically two lithium ions per LiM_2O_4 formula unit could be reversibly inserted/extracted. While the edge shared MO_6 octahedral arrangement with direct M-M interaction, as in the layered LiMO_2 oxides, provides good electrical conductivity σ_e , the interconnected interstitial (lithium) sites in the three-dimensional spinel framework provide good lithium-ion conductivity σ_{Li} . As a result, the spinel LiM_2O_4 oxides have also become attractive candidates and they are discussed below.

1.5.1. Spinel Manganese Oxides

Mn is inexpensive and environmentally benign compared to Co and Ni and, therefore, the spinel LiMn_2O_4 cathodes have become appealing for lithium-ion cells. The extraction/insertion of two lithium ions from/into the $\text{Li}[\text{Mn}_2]\text{O}_4$ spinel framework occurs in two distinct steps.⁷ While the lithium extraction/insertion from/into the 8a tetrahedral sites occurs at around 4 V (Figure 1.8) with the maintenance of the initial cubic spinel symmetry, that from/into the 16c octahedral sites occurs at around 3 V by a two-phase mechanism involving the cubic spinel $\text{Li}[\text{Mn}_2]\text{O}_4$ and the tetragonal lithiated spinel $\text{Li}_2[\text{Mn}_2]\text{O}_4$. Although both involve the same $\text{Mn}^{3+/4+}$ couple, the 1 V difference between the two processes is a reflection of the differences in the site energies.³ A deep energy well for the 8a tetrahedral Li^+ ions and a high activation energy required for the Li^+ ions to move from one 8a tetrahedral site to another via an energetically unfavorable neighboring 16c site lead to a higher voltage of 4 V. The cubic to tetragonal transition on going from $\text{Li}[\text{Mn}_2]\text{O}_4$ to $\text{Li}_2[\text{Mn}_2]\text{O}_4$ is due to the Jahn-Teller distortion associated with the single electron in the e_g orbitals of a high spin $\text{Mn}^{3+}:3d^4 (t_{2g}^3 e_g^1)$ ion (Figure 1.20). A cooperative distortion of the MnO_6 octahedra with long Mn-O bonds along the c axis and short Mn-O bonds along the a and b axes as shown in Figure 1.20 results in a macroscopic tetragonal symmetry for $\text{Li}_2[\text{Mn}_2]\text{O}_4$.

The cubic to tetragonal transition is accompanied by a 16% increase in the c/a ratio and 6.5% increase in the unit cell volume. This change is too severe for the electrodes to maintain structural integrity during the discharge-charge cycle and so LiMn_2O_4 exhibits rapid capacity fade in the 3 V region.

Therefore, LiMn_2O_4 could be used only in the 4 V region with a limited practical capacity of around 120 mAh/g (Figure 1.8), which corresponds to an extraction/insertion of 0.4 lithium per Mn. Unfortunately, even with a limited capacity, LiMn_2O_4 tends to exhibit capacity fade in the

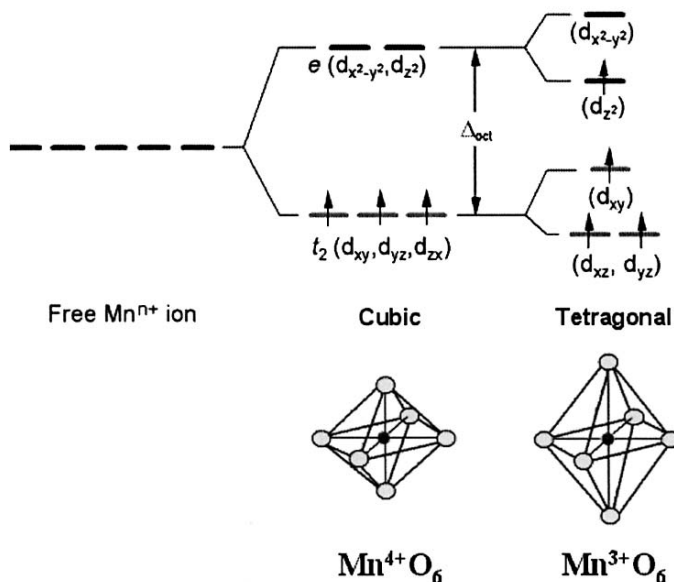


Figure 1.20. Illustration of the Jahn-Teller distortion in manganese oxides: (left) $\text{Mn}^{4+}:3d^3$ with cubic symmetry (no Jahn-Teller distortion) and (right) $\text{Mn}^{3+}:3d^4$ with tetragonal symmetry (Jahn-Teller distortion).

4 V region as well particularly at elevated temperatures (50°C). Several factors such as Jahn-Teller distortion occurring on the surface of the particles under conditions of nonequilibrium cycling^{70,71} manganese dissolution into the electrolyte,⁷²⁻⁷⁴ formation of two cubic phases in the 4 V region,⁷⁵ loss of crystallinity,^{76,77} and development of micro-strain⁷⁸ during cycling have been suggested to be the source of capacity fade.

Several strategies have been pursued to overcome the capacity fade of LiMn_2O_4 . For example, increasing the oxidation state of Mn via (i) an increase in the oxygen content to give the defect spinel $\text{LiMn}_2\text{O}_{4+\delta}$ (or $\text{Li}_2\text{Mn}_4\text{O}_{9.8}$)⁷⁹⁻⁸¹ which is actually a cation-deficient spinel $\text{Li}_{1-y}\text{Mn}_{2-2y-3y}\text{O}_4$, and (ii) cationic substitutions to give $\text{LiMn}_{2-y}\text{M}_y\text{O}_4$ ($\text{M} = \text{Li}, \text{Cr}, \text{Co}, \text{Ni}$ and Cu)⁸²⁻⁸⁹ have been pursued with an aim to suppress the difficulties of Jahn-Teller distortion since $\text{Mn}^{4+}:3d^3$ ($t_{2g}^3 e_g^0$) does not undergo Jahn-Teller distortion. However, such a strategy leads to a decrease in capacity in the 4 V region. For example, the end member $(\text{Li})[\text{Mn}_{1.67}\text{Li}_{0.33}]\text{O}_4$ (or $\text{Li}_4\text{Mn}_5\text{O}_{12}$)

with $M = \text{Li}$ has an average oxidation state of 4+ for Mn and does not exhibit any capacity in the 4 V region corresponding to the extraction of lithium from the 8a tetrahedral sites.⁸²⁻⁸⁵ It exhibits capacity only in the 3 V region corresponding to an insertion of an additional lithium into the 16c octahedral sites to give $\{\text{Li}_2\}_{16c}[\text{Li}_{0.33}\text{Mn}_{1.67}]_{16d}\text{O}_4$. On the other hand, the $\text{LiMn}_{2-y}\text{M}_y\text{O}_4$ spinel oxides with $M = \text{Cr}, \text{Co}, \text{Ni},$ and Cu exhibit two plateaus for the extraction/insertion of lithium from/into the 8a tetrahedral sites⁸⁶⁻⁸⁹: one around 4 V corresponding to the oxidation of Mn^{3+} to Mn^{4+} and the other around 5 V corresponding to the oxidation of the other transition metal ions.

It is interesting to note that while the $M = \text{Co}^{3+/4+}$ and $\text{Ni}^{3+/4+}$ couples offer around 4 V corresponding to the extraction/insertion of lithium from/into the octahedral sites of the layered LiMO_2 , they offer 5 V corresponding to the extraction/insertion of lithium from/into the tetrahedral sites of the spinel $\text{LiMn}_{2-y}\text{M}_y\text{O}_4$. The 1 V difference is due to the differences in the site energies as discussed earlier.³ However, the 5 V capacity has generally been observed only when the other transition metal ions are present along with Mn in the spinel lattice.⁹⁰⁻⁹³ For example, both $\text{LiNi}_{0.5}\text{Ge}_{1.5}\text{O}_4$ ^{90, 91} and LiCo_2O_4 ²¹ do not show any capacity above 4.5 V. These observations together with an examination in the 5 V region of spinel oxides such as $\text{LiMn}_{2-y}\text{Li}_y\text{O}_4$, $\text{Li}_2\text{Mn}_4\text{O}_{9-\delta}$, and $\text{Li}_4\text{Mn}_5\text{O}_{12}$ that contain no transition metal ions other than Mn suggest that the participation of $\text{O}^{2-/1-}$ and possibly $\text{Mn}^{4+/5+}$ couples could be involved in imparting the 5 V capacity.^{93,94} Also, it has been found that good crystallinity for the $\text{LiMn}_{2-y}\text{M}_y\text{O}_4$ samples by synthesizing at higher temperatures $T > 500^\circ\text{C}$ is essential to realize capacities in the 5 V region.⁹⁴ Finally, although cathodes with 5 V are appealing from an energy and power density points of view, the $\text{LiMn}_{2-y}\text{M}_y\text{O}_4$ oxides may be prone to suffer from oxygen loss from the lattice similar to that observed for the layered $\text{Li}_{1-x}\text{CoO}_2$ for $(1-x) < 0.5$ (Figure 1.14) and consequent safety concerns in the 5 V region. However, the oxygen loss problems may be minimized for $M = \text{Ni}$ since the $\text{Ni}^{3+/4+}:\text{e}_g$ band barely touches the top of the $\text{O}^{2-}:\text{2p}$ band (Figure 1.18).

Another strategy that has been pursued to improve the cyclability of the LiMn_2O_4 spinel is the modification or coating of its surface with other oxides such as LiCoO_2 , V_2O_5 , Al_2O_3 , or MgO ^{77,95-97} with an aim to suppress the dissolution of manganese in contact with the electrolyte. The modified samples exhibit improved cyclability at both ambient and elevated temperatures. However, firing at higher temperatures ($\sim 800^\circ\text{C}$) after coating leads to much better capacity retention compared to firing at lower temperatures ($\sim 400^\circ\text{C}$) in contrast to the coated LiCoO_2 samples²⁹ discussed earlier that requires firing only at low temperatures ($\sim 300^\circ\text{C}$). This suggests that (i) a diffusion of the coating or modifying oxides M_yO_z into LiMn_2O_4 is essential to achieve good cyclability and (ii) the improved cyclability need not be simply due to the protection of the cathode surface from the

electrolyte and the consequent suppression of manganese dissolution. Clearly, additional factors other than manganese dissolution could be playing a role in improving the cyclability on coating/modifying the LiMn_2O_4 cathodes.

With an aim to fully understand the factors that cause capacity fading in LiMn_2O_4 , our group has recently focused on a number of $\text{LiMn}_{2-y}\text{M}_y\text{O}_4$ and $\text{LiMn}_{2-2y}\text{Li}_y\text{M}_y\text{O}_4$ ($\text{M} = \text{Co}, \text{Ni}, \text{and Ti}$) compositions.⁹⁸ Our data reveal a clear relationship between the lattice parameter difference Δa between the two cubic phases formed in the 4 V region and the % capacity loss (Figure 1.21). The % capacity loss decreases with decreasing lattice parameter difference Δa . For example, compositions such as $\text{LiMn}_{1.85}\text{Li}_{0.075}\text{Ni}_{0.075}\text{O}_4$ exhibit excellent capacity retention at elevated temperatures (Figure 1.22) with a small sacrifice in reversible capacity (100 mAh/g). The $\text{LiMn}_{1.85}\text{Li}_{0.075}\text{Ni}_{0.075}\text{O}_4$ sample also exhibits superior rate capability (Figure 1.22) and excellent capacity retention after storage at 60°C at different depths of discharge (DOD) compared to LiMn_2O_4 .^{98,99} The compositions that exhibit good capacity retention and rate capability are found to maintain good crystallinity with sharp diffraction peaks after extended cycling,^{98,99} suggesting a suppression of the development of micro-strain that is normally encountered during the cycling of LiMn_2O_4 .^{77,78} The study reveals that the volume changes and lattice strain arising from the difference in lattice parameters between the two cubic phases formed in the 4 V region play a

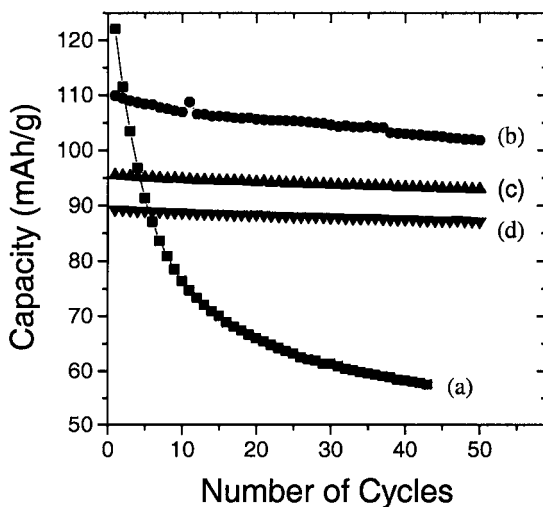


Figure 1.21. Cyclability data of $\text{LiMn}_{2-y}\text{Li}_y\text{Ni}_y\text{O}_4$ at 60°C: (a) LiMn_2O_4 , (b) $\text{LiMn}_{1.9}\text{Li}_{0.05}\text{Ni}_{0.05}\text{O}_4$, (c) $\text{LiMn}_{1.85}\text{Li}_{0.075}\text{Ni}_{0.075}\text{O}_4$, and (d) $\text{LiMn}_{1.8}\text{Li}_{0.1}\text{Ni}_{0.1}\text{O}_4$.

critical role in the capacity fading of LiMn_2O_4 , which could be overcome with optimum cationic substitutions such as $\text{LiMn}_{1.85}\text{Li}_{0.075}\text{Ni}_{0.075}\text{O}_4$. These findings are encouraging and with optimum cationic substitutions, it could become possible to employ the spinel manganese oxides for electric vehicle applications.

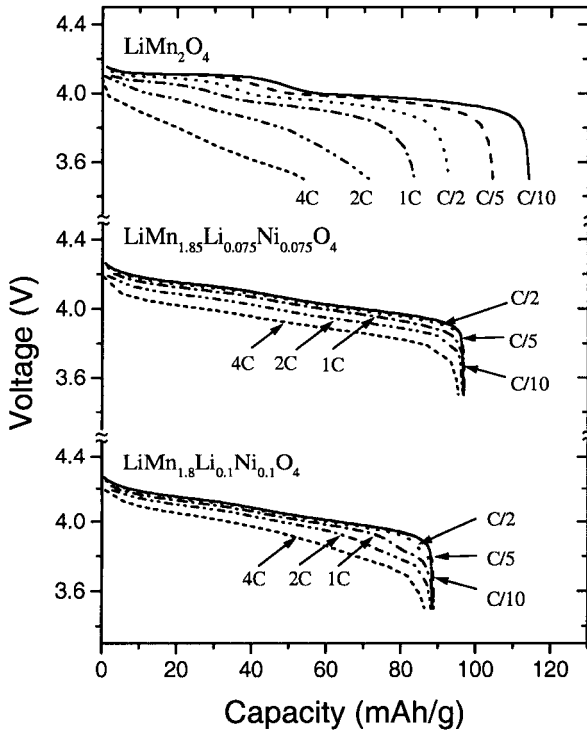


Figure 1.22. Discharge profiles of $\text{LiMn}_{2-2y}\text{Li}_y\text{Ni}_y\text{O}_4$ at various C rates (C/10, C/5, C/2, 1C, 2C, and 4C).

1.5.2. Other Spinel Oxides

Both LiTi_2O_4 and LiV_2O_4 crystallize in the normal spinel structure $(\text{Li})_{8a}[\text{M}_2]_{16d}\text{O}_4$ ($\text{M} = \text{Ti}$ and V) and are metallic due to the direct M-M interactions with a partially filled t_{2g} band. LiTi_2O_4 inserts an additional lithium into the empty 16c octahedral sites to give the lithiated spinel $\{\text{Li}_2\}_{16c}[\text{Ti}_2]_{16d}\text{O}_4$, which occurs with a flat discharge profile (two-phase reaction) at a much lower voltage of around 1.5 V.¹⁰⁰ Accordingly, $(\text{Li})_{8a}[\text{Ti}_{1.67}\text{Li}_{0.33}]_{16d}\text{O}_4$ (or $\text{Li}_4\text{Ti}_5\text{O}_{12}$), which is much easier to synthesize due to all Ti^{4+} than LiTi_2O_4 , has become appealing as an anode [101]. $(\text{Li})_{8a}[\text{Ti}_{1.67}\text{Li}_{0.33}]_{16d}\text{O}_4$ and the lithiated spinel $\{\text{Li}_2\}_{16c}[\text{Ti}_{1.67}\text{Li}_{0.33}]_{16d}\text{O}_4$ differ

in their unit cell volume by 0.1%, which is attractive to maintain good electrode integrity and capacity retention unlike in the case of LiMn_2O_4 . However, the higher voltage (1.5 V) and lower capacity (175 mAh/g) of $\text{Li}_4\text{Ti}_5\text{O}_{12}$ make it difficult to compete with the currently used carbon anodes. LiV_2O_4 also inserts an additional lithium into the 16c sites. The lithium

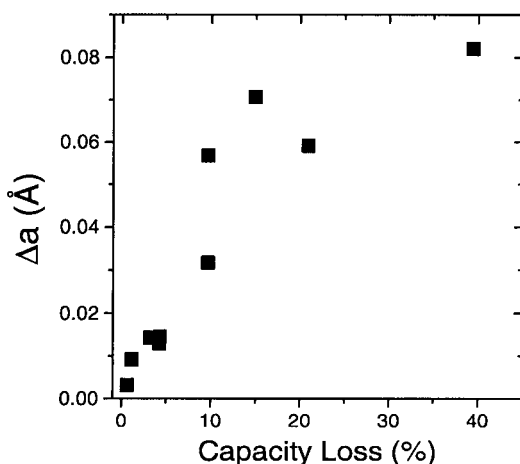


Figure 1.23. Relationship between % capacity loss and lattice parameter difference (Δa) between the two cubic phases in $\text{Li}_{1-x}\text{Mn}_{2-y}\text{M}_y\text{O}_4$ and $\text{Li}_{1-x}\text{Mn}_{2-2y}\text{Li}_y\text{M}_y\text{O}_4$ ($\text{M} = \text{Li, Ti, Co and Ni}$).

ions could also be extracted from the 8a tetrahedral sites of LiV_2O_4 .^{102,103} However, LiV_2O_4 suffers from a migration of the vanadium ions during these processes, which leads to poor capacity retention.

Both LiCr_2O_4 and LiFe_2O_4 are not known. LiCo_2O_4 could not be made by conventional high temperature methods, but it could be accessed as a normal spinel $(\text{Li})_{8a}[\text{Co}_2]_{16d}\text{O}_4$ by chemically extracting 50% of lithium with aqueous acid²⁰ or NO_2PF_6 in acetonitrile medium^{21,104} from the low temperature form of LiCoO_2 that has a lithiated spinel structure.¹⁷⁻¹⁹ LiCo_2O_4 spinel is metallic due to the direct Co-Co interaction and the partially filled t_{2g} band associated with the low-spin $\text{Co}^{3+/4+}$.¹⁰⁴ While the extraction of lithium from the 8a sites occurs around 3.9 V, the insertion of an additional lithium into the 16c sites occurs around 3.5 V.²¹ However, the system suffers from a huge polarization loss as indicated by a large separation between the discharge and charge profiles, which could possibly be related to the low-temperature synthesis. Attempts to make LiNi_2O_4 spinel by chemically extracting 50% of lithium from LiNiO_2 followed by heating at $T \leq 200^\circ\text{C}$ result in a spinel-like cubic phase, but with the $\text{Ni}^{3+/4+}$ ions in both the 16c and 16d sites. Heating at $T > 200^\circ\text{C}$ results in a disproportionation to give LiNiO_2 and NiO .⁵³

1.6. OXIDE CATHODES WITH POLYANIONS

Iron oxides offer significant advantages compared to other 3d transition metal oxides from both cost and toxicity points of view. Unfortunately, the high spin $\text{Fe}^{3+}3d^5$ ion with a zero OSSE value (Table 1.1) tends to migrate readily from octahedral to tetrahedral sites as discussed earlier with respect to the layered LiFeO_2 , causing structural instabilities. This problem could, however, be overcome by designing complex iron oxides consisting of poly ions such as $(\text{SO}_4)^{2-}$ and $(\text{MoO}_4)^{2-}$.^{105,106} For example, $\text{Fe}_2(\text{SO}_4)_3$ crystallizing in NASICON-related 3-dimensional framework structures was shown in the 1980s to exhibit a capacity of around 110 mAh/g with a flat discharge voltage of 3.6 V.¹⁰⁵ In these structures, the FeO_6

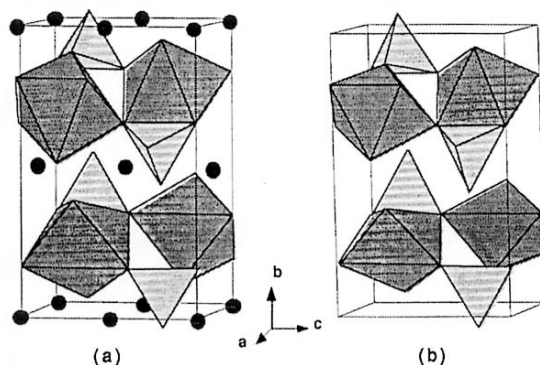


Figure 1.24. Crystal structure of olivine (a) LiFePO_4 and (b) FePO_4 consisting of FeO_6 octahedra and PO_4 tetrahedra (Ref. 62). The circles refer to lithium ions.

octahedra share corners with the SO_4 tetrahedra with a Fe-O-S-O-Fe linkage and lithium ions could be inserted into the interstitial voids of the framework. The higher voltage of 3.6 V observed with the $\text{Fe}^{2+/3+}$ couple in $\text{Fe}_2(\text{SO}_4)_3$ compared to that found in simple iron oxide is due to the inductive effect caused by the counter cation S^{6+} . A stronger S-O covalent bonding weakens the π -bond Fe-O covalence through inductive effect, which results in a lowering of the $\text{Fe}^{2+/3+}$ redox couple and an increase in the cell voltage. However, a poor electronic conductivity associated with the Fe-O-X-O-Fe ($\text{X} = \text{S}$ or P) linkages leads to poor rate capability.

Following this initial concept of using poly anions, several phosphates have been investigated in recent years.¹⁰⁷⁻¹⁰⁹ Among them, LiFePO_4 crystallizing in the olivine structure with FeO_6 octahedra and PO_4 tetrahedra

(Figure 1.24) has been shown to be a promising material exhibiting a flat discharge voltage of around 3.3 V.¹⁰⁹ However, LiFePO_4 also suffers from limited rate capability due to poor electronic (σ_e) and lithium-ion (σ_{Li}) conductivity compared to the layered and spinel oxide cathodes discussed earlier. While only around 0.6 lithium per iron could be reversibly extracted with the samples synthesized by conventional solid-state synthesis, nearly one lithium ion per iron could be reversibly extracted with materials synthesized by low temperature procedures and having a good atomic scale mixing of carbon.¹¹⁰⁻¹¹² Unlike in the case of layered LiMO_2 ($M = \text{Co}, \text{Ni}$ or Mn) oxides, the presence of covalently bonded PO_4 units as well as the operation of $\text{Fe}^{2+/3+}$ couple rather than $M^{3+/4+}$ couples leads to good structural and chemical stabilities resulting in good safety features. However, the low rate capability may limit its use to low power applications. Recent experiments involving a doping of LiFePO_4 with Nb or Zr have been claimed to improve the electronic conductivity by several orders of magnitude,¹¹³ but further studies are needed to confirm the finding and to understand the mechanism of improvement in conductivity.

1.7. OTHER OXIDE CATHODES

The cation migration and structural instability encountered by ions with low OSSE values such as Fe^{3+} and Mn^{3+} in close-packed structures (layered and spinel structures) could also be overcome by having non-close-packed structures. For example, $\text{Na}_{0.5}\text{MnO}_2$ – designated as $\text{Na}_{0.44}\text{MnO}_2$ in the literature – adopting a non-close-packed tunnel structure does not transform to spinel-like phases and shows extraordinary structural stability to temperatures as high as 300°C.^{114,115} Although only a small amount of lithium could be extracted from the ion-exchanged sample $\text{Na}_{0.5-x}\text{Li}_x\text{MnO}_2$, additional lithium could be inserted into $\text{Na}_{0.5-x}\text{Li}_x\text{MnO}_2$, exhibiting good cyclability.

Although both layered LiVO_2 and spinel LiV_2O_4 suffer from structural instability and poor cyclability, a number of other vanadium oxides such as $\text{VO}_2(\text{B})$ – a metastable form of VO_2 ¹¹⁶ – and V_6O_{13} ¹¹⁷ exhibit high capacity with good cyclability. They can be considered to have shear structures derived from the hypothetical VO_3 having the ReO_3 structure.^{118,119} The structure consists of distorted VO_6 octahedra sharing corners and edges. For example, the structure of V_6O_{13} (Figure 1.25) consists of edge shared octahedra forming single zig-zag strings (denoted as I) and double zig-zag ribbons (denoted as II), which are then joined together by sharing corners to give a 3-dimensional lattice. The resulting structure contains tricapped cavities joined through shared square faces with the three open faces of the cavity permitting lithium-ion diffusion along (010). On the other hand, $\text{VO}_2(\text{B})$ contains one dimensional tunnel. Additionally, both

V_2O_5 ^{120,121} and LiV_3O_8 ¹²² having layered structures have been shown to exhibit high capacity. The vanadium oxides generally exhibit good chemical stability with better safety characteristics without releasing oxygen from the lattice compared to the cobalt or nickel oxides as the $V^{4+/5+}$ and $V^{3+/4+}$ couples lie well above the top of the $O^{2-}2p$ band.

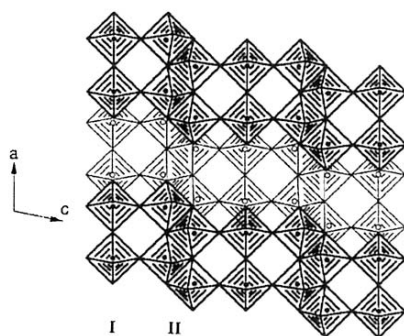


Figure 1.25. Crystal structure of V_6O_{13} consisting of single strings (I) and double ribbons (II).

Although it is difficult to charge the layered $LiCrO_2$, a few chromium oxides such as Cr_2O_5 , Cr_6O_{15} and Cr_3O_8 having oxidation states of $\geq 5+$ for Cr show high capacities.¹²³ However, the synthesis of these oxides generally requires decomposition of CrO_3 in an autoclave or under high oxygen pressure and the products are often contaminated with undecomposed CrO_3 .

In addition to the various crystalline cathode hosts discussed so far, a number of amorphous and nanocrystalline oxide compositions $Li_xM_yO_z$ with $M = V$ ^{116,124,125}, Cr ^{126,127}, Mn ¹²⁸⁻¹³³, Fe ¹³⁴, and $Fe_{1-\eta}Cu_\eta$ ¹³⁵ have been shown to exhibit good cyclability. Among them, the manganese and vanadium oxides exhibit remarkably high capacities of around 300 mAh/g. However, the capacity occurs over a wide voltage range of 4.3 to 1.5 V with a sloping discharge profile as the lithium insertion is not limited to specific crystallographic sites and grain boundaries are involved in amorphous and nanocrystalline oxides. Nevertheless, a moderate capacity of around 200 mAh/g could be readily utilized with these oxides. Also, the amorphous manganese oxides have been found (i) to accommodate the lattice (Jahn-Teller) distortions more smoothly compared to the crystalline manganese oxides as indicated by spectroscopic studies¹³⁶ and (ii) not to transform to spinel-like phases during electrochemical cycling. However, the large surface area associated with the smaller particle size may aggravate unwanted electrode-electrolyte reactions, which could become an issue for long-term cyclability and charge efficiency particularly at elevated temperatures. Surface modifications that can provide a more robust

electrode-electrolyte interface could help in this regard. Also, more in-depth characterizations by spectroscopic and other techniques are needed to fully understand the mechanism of lithium insertion/extraction and the origin of the high capacities in the amorphous and nanocrystalline hosts.

Although some of the oxides discussed in this section are appealing as they exhibit high capacities with good safety characteristics compared to LiCoO_2 , most of them do not contain extractable lithium. The as-synthesized oxides are in the charged state and they are not suitable for fabricating lithium-ion cells with carbon anodes. However, development of new lithium-containing anodes may make these cathodes viable for lithium-ion cells. Also, these cathodes may be attractive for lithium polymer batteries employing metallic lithium anode as the lower discharge voltage associated with many of them is advantageous to achieve good stability with the polymer electrolytes.

1.8. ANODE HOSTS

Carbon has become the material of choice for anode in the present generation of lithium-ion cells.^{137,138} The lightweight and low electrochemical potential lying close to that of metallic lithium (Figure 1.5) have made carbon an attractive anode. It has a theoretical capacity of 372 mAh/g, which corresponds to an insertion of one lithium per 6 carbon atoms ($x=1$ in Li_xC_6). One of the drawbacks with the carbon anodes is the occurrence of significant amount of irreversible capacity during the first discharge-charge cycle due to unwanted, irreversible side reactions with electrolyte. Also, with electrolytes consisting of propylene carbonate (PC), natural graphite cannot be charged as it leads to an evolution of gas at around 1 V. However, with electrolytes consisting of other solvents such as ethylene carbonate (EC) and diethyl carbonate (DEC), the side reactions are suppressed and it can be cycled without much difficulty.

Carbon materials can be classified into soft carbon (graphitic carbon) and hard carbon (glassy carbon). The hard carbons are typically obtained by a thermal decomposition of phenolic and epoxy resins and products from petroleum pitch. They have significant amount of open micropores, which tend to become closed on heating at higher temperatures, and some of them consist of single graphene sheets. Generally, hard carbons show higher capacities than graphite, which is thought to be due to the adsorption of lithium on both sides of the single graphene sheets, accommodation of extra lithium into nanometer size cavities, and storage of additional lithium at the edges and surfaces. Also, hard carbons can be used with PC-based electrolytes unlike graphite. However, the hard carbons show a sloping discharge profile between 0 and 1 V unlike graphite, which shows a nearly flat discharge profile between 0 and 0.3 V. With an aim to improve the

performance of carbon anodes, structural modifications such as texture control, surface modification by mild oxidation and coating, and incorporation of other elements such as B, O, Si, and P have been studied.

A few oxides, nitrides, phosphides, and intermetallic compounds have also been investigated as anode hosts. Metal nitrides and phosphides offer lower voltages versus lithium due to the covalent character and the stabilization of lower oxidation states. As discussed earlier in section 5.2, spinel $\text{Li}_4\text{Ti}_5\text{O}_{12}$ offers 175 mAh/g at around 1.5 V,¹⁰¹ but it is less attractive compared to carbon due to its lower capacity and higher voltage. SnO_2 shows a reversible capacity of as high as 600 mAh/g at 0 to 2 V, but it exhibits a high irreversible capacity loss during the first cycle.¹³⁹ Rutile-type MoO_2 and WO_2 ^{140,141}, Fe_2O_3 ¹⁴², MnP_4 ¹⁴³ and intermetallic compounds¹⁴⁴ such as Cu_6Sn_5 having NiAs-type structure have also been investigated. These anodes, including carbon, do not contain Li and they can be coupled only with cathodes such as LiCoO_2 and LiMn_2O_4 that already contain lithium. With respect to finding anodes that could be coupled with cathodes free from lithium, some lithiated transition metal nitrides^{137,145} and intermetallic compounds¹⁴⁶ have become appealing. For example, $\text{Li}_{7-x}\text{MnN}_4$ and $\text{Li}_{3-x}\text{FeN}_2$ exhibit capacities of around 200 mAh/g with a flat discharge voltage of around 1.2 V. $\text{Li}_{2.6-x}\text{Co}_{0.4}\text{N}$, $\text{Li}_{2.6-x}\text{Cu}_{0.4}\text{N}$, and $\text{Li}_{2.7-x}\text{Fe}_{0.3}\text{N}$ that have structures similar to that of Li_3N exhibit much higher capacities of around 500 mAh/g at 0.2 to 1.3 V due to the formation of an amorphous phase during the initial stages. Two lithium per formula unit could be reversibly extracted from Li_2CuSn .¹⁴⁶ However, further work is necessary to assess the full potential of these anodes. If successful, they have the possibility of being coupled with some of the lithium-free cathodes discussed in Section 1.7.

1.9. CONCLUSIONS

After providing a brief introduction to the basic concepts of rechargeable lithium batteries, this chapter presented an overview of the various cathode and anode materials. In view of maximizing the cell voltage and energy density, transition metal oxides offering around 4 V versus lithium have emerged as the choice for cathodes while the light-weight carbon with an electrochemical potential close to that of metallic lithium has become the anode. With carbon anode that does not contain lithium, the layered LiMO_2 ($\text{M} = \text{Co}$ and Ni), spinel LiMn_2O_4 , and olivine LiFePO_4 containing lithium have emerged as the leading cathode candidates. However, only 40 to 65% of the theoretical capacity of the layered LiMO_2 and spinel LiMn_2O_4 could be practically utilized due to the chemical and structural instabilities encountered by these cathodes at deep lithium extraction. Although recent studies indicate that 100% of the theoretical

capacity of LiFePO_4 can be utilized, the added weight of the PO_4 units and the poor electronic conductivity lower the energy and power densities significantly.

The future challenge is to develop simple oxide cathodes without other elements such as P in which at least one lithium ion per transition metal ion could be reversibly extracted/inserted to give close to 300 mAh/g while keeping the materials cost and toxicity low. Such cathodes can double the energy density compared to the present level. There are also possibilities to increase the capacity of anodes perhaps by focusing on amorphous materials and metal nitrides, pnictides, borides, and carbides with significant covalent character. An alternative approach is to develop cells with lithium-containing anodes and lithium-free cathodes. This strategy will allow the use of some of the already known high capacity cathodes such as the vanadium oxides and nanocrystalline manganese oxides that offer higher capacity with better chemical stability and safety characteristics compared to the currently used LiCoO_2 cathode. From a safety, and cycle and shelf life points of view, cathodes with a lower voltage (3 to 4 V), but with an increased capacity are desirable for future applications. Such cathodes would also be attractive for polymer batteries from a stability point of view.

ACKNOWLEDGMENT

Financial support by the Welch Foundation Grant F-1254 is gratefully acknowledged.

REFERENCES

1. Lithium Battery Energy Storage (LIBES) Publication, Technological Research Association, Tokyo (1994).
2. M. S. Whittingham, *Science* 192 (1976) 1126.
3. M. K. Aydinol, G. J. Ceder, J. *Electrochem. Soc.* 144 (1997) 3832.
4. M. S. Whittingham, A. J. Jacobson, *Intercalation Chemistry*, Academic Press, New York (1982).
5. K. Mizushima, P.C. Jones, P.J. Wiseman, J.B. Goodenough, *Mat. Res. Bull.* 15 (1980) 783.
6. J.B. Goodenough, K. Mizushima, T. Takeda, *Jap. J. Appl. Phys.* 19 (1983) 305.
7. M.M. Thackeray, W.I.F. David, P.G. Bruce, J.B. Goodenough, *Mat. Res. Bull.* 18 (1983) 461.
8. J.P. Gabano, (Ed.) *Lithium Batteries*, Academic Press, London (1983).
9. H.V. Venkatesetty, (Ed.) *Lithium Battery Technology*, John Wiley, New York (1984).
10. G. Pistoia, (Ed.) *Lithium Batteries: New Materials, Developments and Perspectives*, Industrial Chemistry Library, Vol. 5, Elsevier, Amsterdam (1994).
11. C. Julien, G.A. Nazri, *Solid State Batteries: Materials Design and Optimization*, Kluwer, Boston (1994).
12. D. Linden, (Ed.) *Handbook of Batteries*, second edition, McGraw Hill, New York (1995).

13. M. Wakihara, O. Yamamoto, (Eds.) *Lithium Ion Batteries: Fundamentals and Performance*, Wiley-VCH, Weinheim (1998).
14. M.M. Thackeray, *Prog. Solid State Chem.* 25 (1997) 1.
15. A. Manthiram, J. Kim, *Chem. Mat.* 10 (1998) 2895.
16. A. Manthiram, J. Kim, *Recent Res. Dev. Electrochem.* 2 (1999) 31.
17. R.J. Gummow, M.M. Thackeray, W.I.F. David, S. Hull, *Mat. Res. Bull.* 27 (1992) 327.
18. R.J. Gummow, D.C. Liles, M.M. Thackeray, *Mat. Res. Bull.* 28 (1993) 235.
19. R.J. Gummow, D.C. Liles, M.M. Thackeray, *Mat. Res. Bull.* 28 (1993) 1177.
20. Y. Shao-Horn, S.A. Hackney, C.S. Johnson, A.J. Kahaian, M.M. Thackeray, *J. Solid State Chem.* 140 (1998) 116.
21. S. Choi, A. Manthiram, *J. Electrochem. Soc.* 149 (2002) A162.
22. J.N. Reimers, J.R. Dahn, *J. Electrochem. Soc.* 139 (1992) 2091.
23. G.G. Amatucci, J.M. Tarascon, L.C. Klein, *Solid State Ionics* 83 (1996) 167.
24. J. Cho, C. Kim, S.I. Yoo, *Electrochem. Solid-State Lett.* 3 (2000) 362.
25. J. Cho, Y.I. Kim, B. Park, *Chem. Mater.* 12 (2000) 3788.
26. J. Cho, Y.I. Kim, B. Park, *J. Electrochem. Soc.* 148 (2001) A1110.
27. J. Cho, Y.I. Kim, T.J. Kim, B. Park, *Angew. Chem. Int. Ed. Engl.* 40 (2001) 3367.
28. Z. Liu, H. Wang, L. Fang, J.Y. Lee, L.M. Gan, *J. Power Sources* 104 (2002) 101.
29. A.M. Kannan, L. Rabenberg, A. Manthiram, *Electrochem. Solid-State Lett.* 6 (2003) A16.
30. Z. Chen, J.R. Dahn, *Electrochem. Solid-State Lett.* 5 (2002) A213.
31. T. Ohzuku, A. Ueda, M. Nagayama, *J. Electrochem. Soc.* 140 (1993) 1862.
32. G.G. Amatucci, J.M. Tarascon, L.C. Klein, *J. Electrochem. Soc.* 143 (1996) 1114.
33. J.M. Tarascon, G. Vaughan, Y. Chabre, L. Seguin, M. Anne, P. Strobel, G.G. Amatucci, *J. Solid State Chem.* 147 (1999) 410.
34. X.Q. Yang, X. Sun, J. McBreen, *Electrochem. Comm.* 2 (2000) 100.
35. R.V. Chebiam, F. Prado, A. Manthiram, *Chem. Mater.* 13 (2001) 2951.
36. R.V. Chebiam, F. Prado, A. Manthiram, *J. Solid State Chem.* 163 (2002) 5.
37. S. Venkatraman, A. Manthiram, *Chem. Mater.* 14 (2002) 3907.
38. S. Venkatraman, Y. Shin, A. Manthiram, *Electrochem. Solid-State Lett.* 6 (2003) A9.
39. A.R. Wizansky, P.E. Rauch, F.J. DiSalvo, *J. Solid State Chem.* 81 (1989) 203.
40. A. Manthiram, J.S. Swinnea, Z.T. Sui, H. Steinfink, J.B. Goodenough, *J. Amer. Chem. Soc.* 109 (1987) 6667.
41. G. Dutta, A. Manthiram, J.B. Goodenough, *J. Solid State Chem.* 96 (1992) 123.
42. A. Hirano, R. Kanno, Y. Kawamoto, Y. Takeda, K. Yamamura, M. Takano, K. Ohyama, M. Ohashi, Y. Yamaguchi, *Solid State Ionics* 78 (1995) 123.
43. R. Kanno, H. Kubo, Y. Kawamoto, T. Kamiyama, F. Izumi, Y. Takeda, M. Takano, *J. Solid State Chem.* 110 (1994) 216.
44. I. Nakai, T. Nakagome, *Electrochem. Solid-State Lett.* 1 (1998) 259.
45. I. Nakai, K. Takahashi, Y. Shiraishi, T. Nakagome, F. Nishikawa, *J. Solid State Chem.* 140 (1998) 145.
46. T. Ohzuku, A. Ueda, M. Nagayama, Y. Iwakashi, H. Komori, *Electrochim. Acta* 38 (1993) 1159.
47. J.R. Dahn, E.W. Fuller, M. Obrovac, U. von Sacken, *Solid State Ionics* 69 (1994) 265.
48. Z. Zhang, D. Fouchard, J.R. Rea, *J. Power Sources* 70 (1998) 16.
49. W. Li, J. Curie, *J. Electrochem. Soc.* 144 (1997) 2773.
50. G. Nagasubramanian, *Proceedings of the 40th Power Sources Conference*, Cherry Hill, NJ, June 10-13, 2002, p. 434.
51. R.V. Chebiam, F. Prado, A. Manthiram, *J. Electrochem. Soc.* 148 (2001) A49.
52. A.M. Kannan, A. Manthiram, *J. Electrochem. Soc.* 150 (2003) A349.
53. S. Choi, A. Manthiram, *J. Electrochem. Soc.* 149 (2002) A1157.
54. J.E. Huheey, *Inorganic Chemistry*, second edition, Harper and Row, New York, 1978, p. 348.
55. F. Ronci, B. Scrosati, V.R. Albertini, P. Perfetti, *Electrochem. Solid-State Lett.* 3 (2000) 174.

56. R.V. Chebiam, A.M. Kannan, F. Prado, A. Manthiram, *Electrochem. Commun.* 3 (2001) 624.
57. L.A. Montoro, M. Abbate, J.M. Rosolen, *Electrochem. Solid-State Lett.* 3 (2000) 410.
58. A.N. Mansour, X.Q. Yang, X. Sun, J. McBreen, L. Croguennec, C. Delmas, *J. Electrochem. Soc.* 147 (2000) 2104.
59. M. Balasubramanian, X. Sun, X.Q. Yang, J. McBreen, *J. Electrochem. Soc.* 147 (2000) 2903.
60. G. Ceder, Y.M. Chiang, D.R. Sadoway, M.K. Aydinol, Y.I. Jang, B. Hunny, *Nature* 392 (1998) 695.
61. A. Van der Ven, M.K. Aydinol, G. Ceder, G. Kresse, J. Hafner, *Phys. Rev. B* 58 (1998) 2975.
62. L.A. de Picciotto, M.M. Thackeray, W.I.F. David, P.G. Bruce, J.B. Goodenough, *Mat. Res. Bull.* 19 (1984) 1497.
63. A.R. Armstrong, P.G. Bruce, *Nature* 381 (1996) 499.
64. F. Capitaine, P. Gravereau, C. Delmas, *Solid State Ionics* 89 (1996) 197.
65. B. Fuchs, S. Kemmler-Sack, *Solid State Ionics* 68 (1994) 279.
66. I.J. Davidson, R.S. McMillan, J.J. Murray, *J. Power Sources* 54 (1995) 205.
67. J. Davidson, R.S. McMillan, H. Sleg, B. Luan, I. Kargina, J.J. Murray, I.P. Swainson, *J. Power Sources* 81-82 (1999) 406.
68. H. Wang, Y.I. Jang, Y.M. Chiang, *Electrochem. Solid-State Lett.* 2 (1999) 490.
69. R.J. Gummow, D.C. Liles, M.M. Thackeray, *Mat. Res. Bull.* 28 (1993) 1249.
70. T. Ohzuku, M. Kitagawa, T. Hirai, *J. Electrochem. Soc.* 137 (1990) 769.
71. M.M. Thackeray, Y. Shao-Horn, A.J. Kahaian, K.D. Kepler, E. Skinner, J.T. Vaughey, S.A. Hackney, *Electrochem. Solid-State Lett.* 1 (1998) 7.
72. D.H. Jang, Y.J. Shin, S.M. Oh, *J. Electrochem. Soc.* 143 (1996) 2204.
73. T. Inoue, M. Sano, *J. Electrochem. Soc.* 145 (1998) 3704.
74. A. Du Pasquier, A. Blyr, P. Courjal, D. Larcher, G. Amatucci, B. Gerand, J.M. Tarascon, *J. Electrochem. Soc.* 146 (1999) 428.
75. Y. Xia, M. Yoshio, *J. Electrochem. Soc.* 143 (1996) 825.
76. H. Huang, C.A. Vincent, P.G. Bruce, *J. Electrochem. Soc.* 146 (1999) 3649.
77. A.M. Kannan, A. Manthiram, *Electrochem. Solid-State Lett.* 5 (2002) A167.
78. Y. Shin, A. Manthiram, *Electrochem. Solid-State Lett.* 5 (2002) A55.
79. M.M. Thackeray, A. de Kock, M.H. Rossouw, D.C. Liles, D. Hoge, R. Bittihn, *J. Electrochem. Soc.* 139 (1992) 363.
80. R.J. Gummow, A. de Kock, M.M. Thackeray, *Solid State Ionics* 69 (1994) 59.
81. S. Choi, A. Manthiram, *J. Electrochem. Soc.* 147 (2000) 1623.
82. M.M. Thackeray, M.F. Mansuetto, D.W. Dees, D.R. Vissers, *Mater. Res. Bull.* 31 (1996) 133.
83. Y. Gao, J.R. Dahn, *J. Electrochem. Soc.* 143 (1996) 1783.
84. M.M. Thackeray, M.F. Mansuetto, C.S. Johnson, *J. Solid State Chem.* 125 (1996) 274.
85. J. Kim, A. Manthiram, *J. Electrochem. Soc.* 145 (1998), L53.
86. C. Sigala, D. Guyomard, A. Verbaere, Y. Piffard, M. Tournoux, *Solid State Ionics* 81 (1995) 167.
87. H. Kawai, M. Nagata, H. Takamoto, A.R. West, *Electrochem. Solid-State Lett.* 1 (1998) 212.
88. Q. Zhong, A. Bonakdarpour, M. Zhang, Y. Gao, J.R. Dahn, *J. Electrochem. Soc.* 144 (1997) 205.
89. Y. Ein-Eli, W.F. Howard, Jr., S.H. Lu, S. Mukerjee, J. McBreen, J.T. Vaughey, M.M. Thackeray, *J. Electrochem. Soc.* 145 (1998) 1238.
90. H. Kawai, M. Tabuchi, M. Nagata, H. Tukamoto, A.R. West, *J. Mater. Chem.* 8 (1998) 1273.
91. H. Kawai, M. Nagata, H. Tukamoto, A.R. West, *J. Power Sources* 81-82 (1999) 67.
92. Y. Shao-Horn, R. L. Middaugh, *Solid State Ionics*, 139 (2001) 13.

93. A.R. West, H. Kawai, H. Kageyama, M. Tabuchi, M. Nagata, H. Tukamoto, *J. Mater. Chem.* 11 (2001) 1662.
94. Y. Shin, A. Manthiram, *Electrochim. Acta* (submitted).
95. S. Park, Y. Han, Y. Kang, P.S. Lee, S. Ahn, H. Lee, J. Lee, *J. Electrochem. Soc.* 148 (2001) A680.
96. J. Cho, G.B. Kim, H.S. Lim, C. Kim, S. Yoo, *Electrochem. Solid State Lett.* 2 (1999) 607.
97. H. Kweon, G. Kim, D. Park, US Patent No. 6,183,911 (2001).
98. Y. Shin, A. Manthiram, *Electrochem. Solid-State Lett.* 6 (2002) A34.
99. Y. Shin, A. Manthiram, *J. Electrochem. Soc.* (submitted).
100. D.W. Murphy, R.J. Cava, S.M. Zahurak, A. Santoro, *Solid State Ionics* 9 & 10 (1983) 413.
101. E. Ferg, R.J. Gummow, A. de Kock, M.M. Thackeray, *J. Electrochem. Soc.* 141 (1994) L147.
102. L.A. de Picciotto, M.M. Thackeray, *Mat. Res. Bull.* 20 (1985) 1409.
103. A. Manthiram, J.B. Goodenough, *Can. J. Phys.* 65 (1987) 1309.
104. S. Choi, A. Manthiram, *J. Solid State Chem.* 164 (2002) 332.
105. A. Manthiram, J.B. Goodenough, *J. Power Sources* 26 (1989) 403.
106. A. Manthiram, J.B. Goodenough, *J. Solid State Chem.* 71 (1987) 349.
107. A.K. Padhi, K.S. Nanjundaswamy, C. Masquelier, S. Okada, J.B. Goodenough, *J. Electrochem. Soc.* 144 (1997) 1609.
108. A.K. Padhi, K.S. Nanjundaswamy, C. Masquelier, J.B. Goodenough, *J. Electrochem. Soc.* 144 (1997) 2581.
109. A.K. Padhi, K.S. Nanjundaswamy, J.B. Goodenough, *J. Electrochem. Soc.* 144 (1997) 1188.
110. A. Yamada, S.C. Chung, K. Hinokuma, *J. Electrochem. Soc.* 148 (2001) A224.
111. H. Huang, S-C. Yin, L.F. Nazar, *Electrochem. Solid-State Lett.* 4 (2001) A170.
112. P.P. Prosini, M. Carewska, S. Scaccia, P. Wisniewski, S. Passerini, M. Pasquali, *J. Electrochem. Soc.* 149 (2002) A886.
113. S.Y. Chung, J.T. Bloking, Y.M. Chiang, *Nature Materials* 1 (2002) 123.
114. M.M. Doeff, T.J. Richardson, L. Kepley, *J. Electrochem. Soc.* 143 (1996) 2507.
115. Y.U. Jeong, A. Manthiram, *Electrochem. Solid-State Lett.* 2 (1999) 421.
116. C. Tsang, A. Manthiram, *J. Electrochem. Soc.* 144 (1997) 520.
117. C. Lampe-Onnerud, J.O. Thomas, M. Hardgrave, S. Yde-Andersen, *J. Electrochem. Soc.* 142 (1995) 3648.
118. K. Wilhelm, K. Waltersson, L. Kihlberg, *Acta Chem. Scand.* 25 (1971) 2675.
119. F. Theobald, R. Cabala, J. Bernard, *J. Solid State Chem.* 17 (1976) 431.
120. A.L. Tipton, S. Passerini, B.B. Owens, W.H. Smyrl, *J. Electrochem. Soc.* 143 (1996) 3473.
121. A.M. Kannan, A. Manthiram, *J. Electrochem. Soc.* (in press).
122. N. Kumagai, A. Yu, *J. Electrochem. Soc.* 144 (1997) 830.
123. Y. Takeda, R. Kanno, Y. Tsuji, O. Yamamoto, *J. Power Sources* 9 (1983) 325.
124. B.B. Owens, S. Passerini, W.H. Smyrl, *Electrochim. Acta* 45 (1999) 215.
125. A.M. Kannan, A. Manthiram, *Solid State Ionics* (in press).
126. O. Yamamoto, Y. Takeda, R. Kanno, Y. Oyabe, Y. Shinya, *J. Power Sources* 20 (1987) 151.
127. J. Kim, A. Manthiram, *J. Electrochem. Soc.* 144 (1997) 3077.
128. J. Kim, A. Manthiram, *Nature* 390 (1997) 265.
129. J.J. Xu, A.J. Kinsler, B.B. Owens, W.H. Smyrl, *Electrochem. Solid-State Lett.* 1 (1998) 1.
130. J. Kim, A. Manthiram, *Electrochem. Solid-State Lett.* 2 (1999) 55.
131. D. Im, A. Manthiram, *J. Electrochem. Soc.* 149 (2002) A1001.
132. D. Im, A. Manthiram, *J. Electrochem. Soc.* (in press).
133. D. Im, A. Manthiram, *Solid State Ionics* (in press).
134. J. Kim, A. Manthiram, *J. Electrochem. Soc.* 146 (1999) 4371.

135. S. Choi, A. Manthiram, *J. Electrochem. Soc.* 149 (2002) A570.
136. C.R. Horne, U. Bergmann, J. Kim, K.A. Streibel, A. Manthiram, S.F. Cramer, E.J. Cairns, *J. Electrochem. Soc.* 147 (2000) 395.
137. N. Imanishi, Y. Takeda, O. Yamamoto, in *Lithium Ion Batteries: Fundamentals and Performance* (M. Wakihara and O. Yamamoto, Eds.), 1998, p. 98, Wiley-VCH, Weinheim.
138. M. Winter, J.O. Besenhard, in *Lithium Ion Batteries: Fundamentals and Performance* (M. Wakihara and O. Yamamoto, Eds.), 1998, p. 127, Wiley-VCH, Weinheim.
139. W. Liu, X. Huang, Z. Wang, H. Li, L. Chen, *J. Electrochem. Soc.* 145 (1998) 59.
140. J.J. Auborn, Y.L. Barbeiro, *J. Electrochem. Soc.* 134 (1987) 638.
141. K.M. Abraham, D.M. Pasquariello, E.B. Willstaedt, *J. Electrochem. Soc.* 137 (1990) 743.
142. S. Morzilli, B. Scrosati, F. Sgarlatta, *Electrochim. Acta* 30 (1985) 1271.
143. D.C.S. Souza, V. Pralong, A.J. Jacobson, L.F. Nazar, *Science* 296 (2002) 2012.
144. K.D. Kepler, J.T. Vaughey, M.M. Thackeray, *Electrochem. Solid-State Lett.* 2 (1999) 307.
145. J.L.C. Rowsell, V. Pralong, L.F. Nazar, *J. Amer. Chem. Soc.* 123 (2001) 8598.
146. J.T. Vaughey, K.D. Kepler, R. Benedek, M.M. Thackeray, *Electrochem. Comm.* 1 (1999) 517.

Chapter 2

THE ROLE OF ELECTRONIC PROPERTIES IN THE ELECTROCHEMICAL BEHAVIOR OF INTERCALATION COMPOUNDS FROM A FIRST PRINCIPLES VANTAGE POINT

A. Van der Ven and G. Ceder

Department of Materials Science and Engineering,

Massachusetts Institute of Technology, Cambridge, MA, U.S.A.

2.1. INTRODUCTION

Lithium transition metal oxides are remarkable intercalation compounds, exhibiting an array of intriguing electronic and phase transformation phenomena. Their ability to undergo large variations in lithium concentration, often without suffering irreversible changes, makes these materials ideal electrodes for rechargeable lithium batteries. Lithium transition metal oxides consist of a metal oxide host with a crystal structure in which lithium ions occupy a relatively open network of interstitial sites. While some lithium transition metal oxides can serve as an anode in rechargeable lithium batteries, most are more suited for the role of cathode as they typically exhibit a high voltage with respect to a metallic lithium anode, the ideal theoretical reference electrode. In a rechargeable lithium battery, lithium ions are shuttled between an anode and a cathode, whereby lithium ions are removed from and inserted into the electrodes. During deintercalation of a lithium transition metal oxide, vacancies are created on the lithium sites of the host. During intercalation, these sites are refilled by lithium. Removal and insertion of lithium ions can lead to several phenomena that can significantly affect the electrochemical properties of the compound. For one, variations in lithium concentration alter the electronic properties of the

transition metal oxide host. The valence electron of each lithium ion is generally donated to the host where it can either shift the valence state of the transition metal ion and/or alter the nature of the bonds between the transition metal and the oxygen ions. Simultaneously, lithium removal from the host may structurally destabilize the metal oxide structure or may lead to order-disorder phase transitions between lithium and vacancies once a critical vacancy concentration is reached. These phenomena often affect the voltage characteristic or the lattice parameters of the compound in important ways.

Within the last decade, much attention has been devoted to understanding the properties of Li_xCoO_2 , Li_xNiO_2 , Li_xMnO_2 , $\text{Li}_x\text{Mn}_2\text{O}_4$ ¹ and Li_xFePO_4 ², currently among the most important candidate cathode materials for rechargeable lithium batteries. Other compounds receiving attention are typically doped variants of the Co, Ni and Mn compounds. While many lithium transition metal oxides have similar crystal structures, either a layered form or one derived from the spinel structure (Li_xFePO_4 has the olivine crystal structure), they are often characterized by very different electrochemical properties owing to the unique electronic structure of each transition metal. Li_xCoO_2 , for example undergoes a concentration driven metal-insulator phase transformation whereby the electrons over much of the lithium concentration range ($x < 0.75$) are delocalized and exhibit metallic properties.³ In contrast, the $\text{Li}_x\text{Mn}_2\text{O}_4$ compound in important lithium concentration regions is characterized by more localized electrons with large magnetic moments leading to phenomena such as charge ordering and Jahn-Teller distortions.⁴⁻⁶ Often, phenomena such as these can be rationalized with crude crystal-field and molecular orbital models. More subtle properties such as the relative stability of similar crystal structures, stable ordered lithium-vacancy arrangements and charge-ordered and magnetic-ordered electronic states are more difficult to predict or rationalize with intuition based on simple electronic structure models. It is here that first-principles numerical-schemes for solving the Schrödinger equation of solids are proving invaluable. The record of the last decade of first principles studies of lithium transition metal

oxides has demonstrated that these methods are an important new tool in predicting and understanding the properties of these materials.⁷⁻⁴⁰

The state of the art in first principles electronic structure methods for solids is based on density functional theory (DFT).⁴¹⁻⁴³ Density functional theory casts the problem of solving the many-body Schrödinger equation of the solid into an equivalent problem of solving for the electronic charge density of the solid. While density functional theory is exact in principle, its practical implementation for real solids requires approximations, the most common of which are referred to as the local density approximation (LDA) and the generalized gradient approximation (GGA). The properties that can be directly derived with density functional theory are the charge (or spin) density and the total energy of the solid. Other properties can only be calculated if physical models relating them to energies or charge densities exist. By using thermodynamic and statistical mechanical models, voltages^{7,8,10,12,15,17}, relative stabilities^{11,14,18,27} and kinetic properties such as atomic migration mechanisms and rates^{31,33,36} can be predicted. The first principles study of lithium transition metal oxides has also received an important boost with developments in alloy theory during the last twenty years, most notably the development of the cluster expansion^{27,44,45} which enables the statistical mechanical treatment of solids with significant configurational disorder. In intercalation compounds this capability is critical due to the many degrees of freedom of distributing lithium ions and vacancies over the interstitial sites. Similarly, the disorder in mixed compounds with multiple transition metal elements can only be described properly with cluster expansion techniques.²⁸ The combination of accurate DFT calculations with sophisticated statistical mechanics techniques have enabled accurate calculations of phase diagrams of intercalation compounds,^{18,28,39} voltage intercalation curves^{12,15,17} and lithium diffusion coefficients.^{31,36}

In this chapter, we focus on a description of important electronic properties of Li_xCoO_2 , Li_xNiO_2 and Li_xMnO_2 . Most of our information will be derived from first principles calculations. The chapter starts with an overview

of ligand-field and molecular orbital theory, and continues with a description of first principles density functional theory. We next illustrate how each theory can be used to *understand* and, in the case of density functional theory, *predict* the electronic properties of Li_xCoO_2 , Li_xNiO_2 and Li_xMnO_2 . We emphasize the electronic properties that are predicted by density functional theory but would not be *a priori* expected from ligand field or molecular orbital models. In the case of Li_xCoO_2 , density functional theory has shown the important role of covalency in influencing the structural and thermodynamic properties of the host. In Li_xNiO_2 , DFT calculations have exposed the existence of an intriguing long-range attraction between lithium ions of different lithium planes mediated through a Jahn-Teller distorted Ni^{+3} octahedron. This long-range attraction, termed a 180° interaction, leads to electrochemical properties in Li_xNiO_2 that differ significantly from those observed in Li_xCoO_2 even though both compounds have the same crystal structure. Finally, in Li_xMnO_2 , DFT calculations have predicted a charge-disproportionation reaction between the Mn ions, creating Mn^{+2} that favor tetrahedral sites. This mechanism is responsible for the rapid transformation to spinel that occurs during cycling of layered Li_xMnO_2 , an irreversible transformation that has prevented commercialization of layered Li_xMnO_2 for lithium battery applications.

In all three examples, the first principles predictions expose mechanisms that play a central role in determining the electrochemical properties or stability of these materials as cathodes. Understanding the link between electrochemical properties and their electronic origins is invaluable in optimizing these materials.

2.2. GENERAL ELECTRONIC STRUCTURE OF OCTAHEDRAL TRANSITION METAL IONS

The ability of lithium transition metal oxides to undergo large variations in lithium concentration is attributable to the flexibility of the

valence electronic structure formed by the transition metal and oxygen ions. Lithium is generally completely ionized within the oxide,⁷ having donated its valence electron to the host. The electronic properties of the transition metal oxide are dictated to a large extent by the number of valence electrons and by the interaction of the d-orbitals of the transition metal with the p-orbitals of the oxygen ions.

In both the layered and spinel crystal structures, the transition metal is octahedrally coordinated by oxygen. Figure 2.1 illustrates the electronic charge densities of hydrogenic d-orbitals within an octahedral oxygen environment. Although the five d levels when occupied by a single electron outside of a closed shell core are degenerate in a free transition metal ion, in an octahedral environment, this degeneracy is broken. Crystal field theory⁴⁶⁻⁴⁹, for example, shows that the interaction of the d orbitals with the electrostatic potential due to the negatively charged oxygen ions of the octahedron produces an increase in the energy of the $d_{3z^2-r^2}$ and $d_{x^2-y^2}$ orbitals with respect to the energy of the d_{xy} , d_{xz} and d_{yz} orbitals. This occurs because the $d_{3z^2-r^2}$ and $d_{x^2-y^2}$ orbitals have lobes pointing toward the negatively charged oxygen ions while the lobes of the d_{xy} , d_{xz} and d_{yz} orbitals point between oxygen ions.

Only considering the effect of the electrostatic field of the oxygen ions neglects the important role of covalency that can exist between the transition metal and oxygen orbitals. A more accurate picture of the interaction between the transition metal ion with the surrounding oxygen ions arises from molecular orbital theory.⁴⁶⁻⁴⁹ The $d_{3z^2-r^2}$ and $d_{x^2-y^2}$ orbitals directly overlap with the p_x , p_y and p_z orbitals of oxygen forming bonding and antibonding σ levels referred to as e_g^b and e_g^* . These levels are illustrated schematically in Figure 2.2. Since the energy of the p orbitals are below the energy of the d orbitals, the bonding e_g^b levels are predominantly of oxygen p character while the antibonding e_g^* levels (frequently referred to as simply e_g) consist mainly of metal d states. This dichotomy in character between the

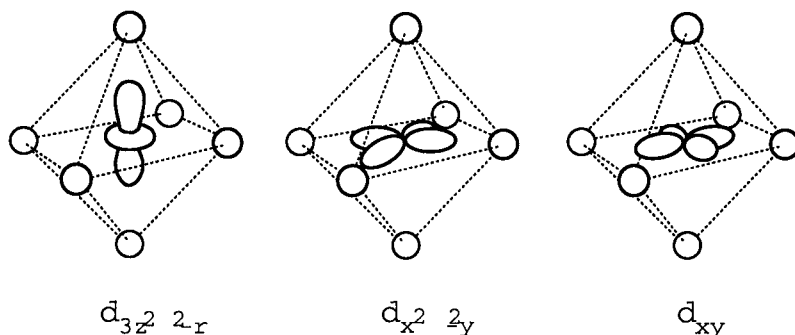


Figure 2.1. Hydrogenic d-orbitals within an octahedral oxygen environment. (a) The d_{3z^2-2r} and (b) the $d_{x^2-y^2}$ orbitals have lobes pointing toward the oxygen ions. (c) The d_{xy} orbital, which is symmetrically equivalent to the d_{xz} and d_{yz} orbitals, has lobes pointing between oxygen ions.

bonding and antibonding levels becomes more pronounced as the difference in the energy of the metal d-levels and the oxygen p-levels widens. The d_{xy} , d_{xz} and d_{yz} orbitals which do not directly overlap with oxygen p orbitals to form σ bonds, are frequently said to form a set of nonbonding levels denoted by t_{2g} .⁴⁶⁻⁴⁹ A band gap Δ_o separates the t_{2g} levels from the antibonding e_g levels. In an octahedral environment, the t_{2g} levels are below the e_g levels. Although the d_{xy} , d_{xz} and d_{yz} orbitals do not form σ bonds with the oxygen ions, they do form π bonds with the oxygen p orbitals.⁴⁶

Instead of being non-bonding levels, t_{2g} energy levels of Figure 2.2, more accurately correspond to the bonding levels of the π overlap between d_{xy} , d_{xz} and d_{yz} and the oxygen p levels. Increased covalency of this π bond will result in a lowering of the energy of the t_{2g} levels and hence an increase in the band gap Δ_o .⁴⁶

Other levels arise from the overlap of oxygen p-levels with the transition metal 4s and 4p levels. These are referred to as t_{1u} and a_{1g} . Since the energy of the oxygen p levels are again below the energy of the metal 4s and 4p levels, the bonding t_{1u} and a_{1g} levels are predominantly of oxygen character.

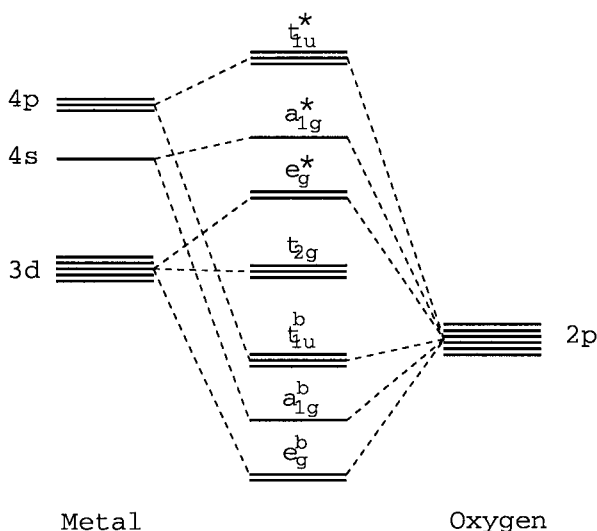


Figure 2.2. Schematic illustration of the bonding and antibonding levels that arise for a transition metal ion in an oxygen octahedral environment due to the hybridization between the valence electronic states of the transition metal ion with those of the oxygen ions.

In a crystal, the levels of Figure 2.2 become bands. Furthermore, although the transition metal ions reside in octahedral interstitial sites, the remainder of the crystal outside of the octahedral site generally does not exhibit the symmetry of a perfect octahedron. Hence the degeneracy of the levels is further broken. Nevertheless, the schematic picture of Figure 2.2 is usually still identifiable in the band structure.

While general trends can be rationalized with simple crystal field and molecular orbit models, more accurate numerical methods based on density functional theory are necessary to understand and predict the relationship between the electronic structure of a compound and specific electrochemical properties.

2.3. FIRST PRINCIPLES METHODS

Calculating properties of solids from first principles without

experimental input involves solving the many body Schrödinger equation for the solid.^{50,51} The time-independent Schrödinger equation (in this section, all equations are expressed in atomic units) is an eigenvalue equation

$$H\Psi = E\Psi \quad (2.1)$$

where H is the Hamiltonian operator for the solid, Ψ is the many body wave function describing N_e electrons and E is the total energy of the solid. Within the Born-Oppenheimer approximation, the electrons are assumed to instantaneously adjust their state to any change in the positions of the nuclei. The coordinates of the nuclei \vec{R}_n then serve only as parameters in the Schrödinger equation and the Hamiltonian can be written as

$$H = T + V_{ee} + \sum_j v(\vec{r}_j) + \sum_n \sum_{m < n} \frac{Z_n Z_m}{|\vec{R}_m - \vec{R}_n|} \quad (2.2)$$

T is the electronic kinetic energy operator

$$T = -\frac{1}{2} \sum_j \nabla_j^2 \quad (2.3)$$

and V_{ee} describes the Coulomb interactions between the different electrons

$$V_{ee} = \sum_i \sum_{j < i} \frac{1}{|\vec{r}_i - \vec{r}_j|} \quad (2.4)$$

where the \vec{r}_j refer to the positions of the electrons. The sums in Eqs. (2.2),

(2.3) and (2.4) are over all the electrons in the solid. The third term in Eq. (2.2) describes the coulomb interaction between the electrons and the nuclei of the solid and the last term is the Ewald energy arising from the coulomb interaction between the nuclei having charge Z_m . The Ewald energy is simply an additive term and does not affect the electronic wave function Ψ . It can be dropped when solving the eigenvalue equation for the electronic ground state and only needs to be added to the electronic energy to obtain the total energy of the crystal.

For solids of practical interest, solving the many-body Schrödinger equation is intractable. One approach to solving Eq. (2.1) is with density functional theory (DFT).⁴¹⁻⁴³ As was shown by Hohenberg and Kohn (and extended by Levy),^{41,52} the ground state properties of a crystal are uniquely determined by the electron density $\rho(\vec{r})$ (which is determined by the many-body wave function Ψ). The fundamental theorems of density functional theory state that the ground state energy of a solid is a functional of the electron density⁴¹

$$E[\rho] = F[\rho] + \int \rho(\vec{r}) v(\vec{r}) d\vec{r} \quad (2.5)$$

with

$$F[\rho] = \langle \Psi | T + V_{ee} | \Psi \rangle \quad (2.6)$$

a universal functional and $v(\vec{r})$ the coulomb potential due to the nuclei of the solid. The Ψ in Eq. (2.6) is the electronic wave function that minimizes $\langle \Psi | T + V_{ee} | \Psi \rangle$ subject to the constraint that Ψ produces the electron density

ρ .⁵² According to DFT, if the functional $F[\rho]$ were known, the ground state energy of the solid with external potential $v(\vec{r})$ is obtained by variationally minimizing the functional $E[\rho]$ with respect to ρ .^{41,42} The minimization proceeds over the set of all densities ρ that can be obtained with antisymmetric wave functions.⁵²

$F[\rho]$ is not known and approximations to it are therefore necessary. Formally, $F[\rho]$ can also be written as

$$F[\rho] = T[\rho] + V_{ee}[\rho] \quad (2.7)$$

where the kinetic energy and the electron-electron interaction energy are individually expressed as functionals of the electron density. Of the two terms in Eq. (2.7), the kinetic energy $T[\rho]$ is the most elusive to approximate as a functional of ρ .^{42,43} To side step this difficulty, Kohn and Sham⁵³ introduced a different separation of $F[\rho]$ by writing it as:

$$F[\rho] = T_s[\rho] + J[\rho] + E_{xc}[\rho] \quad (2.8)$$

where $T_s[\rho]$ is the kinetic energy of a system of non-interacting electrons with the same density ρ . $J[\rho]$ is often referred to as the Hartree term and is a classical Coulomb energy given by

$$J[\rho] = \frac{1}{2} \iint \frac{\rho(\vec{r})\rho(\vec{r}')}{|\vec{r} - \vec{r}'|} d\vec{r} d\vec{r}'. \quad (2.9)$$

The last term $E_{xc}[\rho]$, called the exchange-correlation energy, which can be written as

$$E_{xc}[\rho] = (T[\rho] - T_s[\rho]) + (V_{ee}[\rho] - J[\rho]) \quad (2.10)$$

E_{xc} includes the difference between the kinetic energy of the actual system of interacting electrons with density ρ and the kinetic energy of a system of independent electrons with the same density. This difference, though, is generally expected to be small⁴² and E_{xc} primarily accounts for a correction to $J[\rho]$ arising from the correlations between electrons. Since the electron density corresponds to a probability distribution and not a charge density in

the classical sense, $J[\rho]$ is a mean-field approximation to the electron-electron interactions. Embodied in $J[\rho]$ is the assumption that the probability of having two electrons at \vec{r} and \vec{r}' respectively is equal to the probability of having an electron at \vec{r} times the probability of having another electron at \vec{r}' . Neglected are the conditional probabilities resulting from the fact that if an electron is already present at \vec{r} , the probability of having another electron at \vec{r}' will be different than the average probability. These correlations between pairs of electrons are implicitly accounted for by $E_{xc}[\rho]$.

Correlations between electrons, which become more important as \vec{r} and \vec{r}' approach each other, arise from two effects. The first type of correlation results from electrostatic repulsions which ensure that electrons avoid the vicinity of other electrons. These are called *direct correlations*. The second type of correlation has its origin in the Pauli exclusion principle which forbids electrons with parallel spins from having the same spatial position coordinates. This effect does not arise from the many body Hamiltonian, but is enforced by the fact that the wave function is antisymmetric. Since the wave function is continuous, the Pauli exclusion principle implies that the probability of having electrons with the same spin approach each other is small. This correlation is referred to as an *exchange correlation*. The energy contribution of exchange correlation is typically an order of magnitude larger than that of direct correlation.⁴³

The advantage of introducing the non-interacting kinetic energy functional $T_s[\rho]$ is that it can be calculated exactly with a Slater determinant Ψ_D of independent electron orbitals $\psi_j(\vec{r})$. The independent electron kinetic energy functional then becomes⁴²

$$T_s[\rho] = \langle \Psi_D | T | \Psi_D \rangle = \sum_j^{N_e} \int \psi_j^*(\vec{r}) \left(-\frac{1}{2} \nabla^2 \right) \psi_j(\vec{r}) d\vec{r} \quad (2.11)$$

where Ψ_D and the ψ_j are such that they produce the electron density ρ .

Since it is possible that more than one Ψ_D could produce the same density, the particular Ψ_D appearing in Eq. (2.11) is the one that minimizes $\langle \Psi_D | T | \Psi_D \rangle$ for fixed ρ .

With the Ψ_D and ρ expressed in terms of the independent orbitals ψ_j , Kohn and Sham⁵³ variationally minimized the energy functional

$$E[\rho] = T_s[\rho] + J[\rho] + E_{xc}[\rho] + \int \rho(\vec{r}) v(\vec{r}) d\vec{r} \quad (2.12)$$

and obtained what are now referred to as the *self-consistent Kohn-Sham* equations

$$\left[-\frac{1}{2} \nabla^2 + v_{eff}(\vec{r}) \right] \psi_j(\vec{r}) = \epsilon_j \psi_j(\vec{r}) \quad (2.13)$$

with

$$v_{eff}(\vec{r}) = v(\vec{r}) + \int \frac{\rho(\vec{r}')}{|\vec{r} - \vec{r}'|} d\vec{r}' + v_{xc}(\vec{r}). \quad (2.14)$$

In Eq. (2.14), $v_{xc}(\vec{r})$ is the exchange correlation potential and is the variational derivative of the exchange correlation energy functional

$$v_{xc}(\vec{r}) = \frac{\delta E_{xc}[\rho]}{\delta \rho(\vec{r})} \quad (2.15)$$

An equation of the form of Eq. (2.13), exists for each electron in the solid. The Kohn-Sham procedure replaces the many body eigenvalue equation, Eqs. (2.1) and (2.2), with a set of independent-electron-like eigenvalue equations. Despite their appearance, however, the Kohn-Sham equations are not independent due to the dependence of v_{eff} on the density ρ (Eq. (2.14))

which itself is determined by *all* the orbitals ψ_j . This means that the Kohn-Sham equations are to be solved self-consistently.

2.3.1. The Local Density Approximation (LDA)

The Kohn-Sham equations as represented in Eq. (2.13) are exact provided the universal functional $E_{xc}[\rho]$ (and hence its functional derivative $v_{xc}(\vec{r})$) is known. As with $F[\rho]$ of Eqs. (2.5) and (2.6), $E_{xc}[\rho]$ is not known. The most common approximation to E_{xc} is the local density approximation (LDA).⁵³ Within LDA, E_{xc} is written as

$$E_{xc}[\rho] = \int \varepsilon_{xc}(\rho(\vec{r})) \rho(\vec{r}) d\vec{r} \quad (2.16)$$

where ε_{xc} is the exchange correlation energy per electron at \vec{r} . $\varepsilon_{xc}(\rho(\vec{r}))$ is set equal to the exchange correlation energy per electron of a homogeneous electron gas with the same density $\rho(\vec{r})$. LDA therefore assumes that ε_{xc} is local and neglects the effects of non-uniform charge densities around \vec{r} . There are different parameterizations of ε_{xc} as a function of the homogeneous electron gas density ρ . The local density approximation has proven remarkably successful considering its simplicity. Typically though, equilibrium lattice parameters, volumes and band-gaps of solids are under-predicted within LDA.

2.3.2. The Generalized Gradient Approximation (GGA)

The generalized gradient approximation (GGA) includes in the approximation to $E_{xc}[\rho]$ a term that depends on the gradient of the electron density at each point. While the inclusion of gradient corrections to the local density approximation often improves the accuracy of predictions, this is not

formally guaranteed and for some solids, properties predicted within LDA agree more with experiment than those predicted within GGA. Typically, GGA predicts lattice parameters and volumes that are slightly larger than those observed experimentally.

2.3.3. Spin Polarization

Many solids, especially transition metal oxides, are characterized by a net magnetic moment produced by an unequal electron population of $+1/2$ and $-1/2$ spin states. This is true of many atoms as well, as filling of the atomic orbitals according to Hund's rules often results in a net electronic spin. One of Hund's rules arises from exchange and correlation interactions between electrons. Due to the Pauli exclusion principle, two electrons with the same electronic spin cannot occupy the same position in space. Hence, electrons with parallel spin do not occupy atomic orbitals with the same spatial distribution, minimizing direct electrostatic repulsion. No such quantum-mechanical restriction exists on a pair of electrons with opposite spin. Electrons with opposite spin can therefore occupy atomic orbitals with identical spatial distribution but are then energetically penalized by enhanced electrostatic interactions.

To account for the possibility of spin polarization within practical implementations of density functional theory, the total electron density is separated into an electron density $\rho^\alpha(\vec{r})$ for the spin $+1/2$ electrons and an electron density $\rho^\beta(\vec{r})$ for the spin $-1/2$ electrons. While such a separation is not strictly necessary within exact density functional theory, it enables more accurate approximations to the exchange-correlation functional whereby a different exchange-correlation potential is introduced between electrons with parallel spins and electrons with opposite spin.

2.3.4. Caveats About Approximations to DFT

At this point, several caveats of DFT and LDA and GGA in particular deserve attention. The orbitals ψ_j and orbital energies ε_j of the Kohn-Sham equations do not correspond to real electronic states and electronic energy levels. It is only the total energy and electron density that have any physical meaning. Nevertheless, the Kohn-Sham energy levels often do give a good characterization of the band structure of crystalline materials and are frequently compared to quasi-particle energies measured in photo-emission experiments. The kinetic energy as expressed in terms of the ψ_j by Eq. (2.11), is not the real kinetic energy of the solid, though it is a close approximation of it.⁴² The local density approximation is exact for a uniform electron density and a good approximation for a slowly varying one. Furthermore, for many solids exhibiting rapidly varying electron densities, LDA has proven surprisingly accurate. Yet, for solids in which the electronic states are highly localized in space, we can expect LDA to break down since it cannot be expected to capture the strong correlations between the localized electrons.

For systems with well localized electrons, specific inadequacies of the local density approximation can be identified. One inadequacy is that the approximation to the exchange-correlation potential v_{xc} depends only on the local density and not on the specific orbital that a particular localized electron occupies. In the Hartree-Fock approximation for example, the exchange energy, which is exact within the approximation of the ansatz wave function (Slater determinant consisting of single electron orbitals), is a non-local integral between different electron orbitals. These integrals not only depend on the local electron density, but also on the shape of the different orbitals. Similar orbital dependencies can be expected to arise from direct correlations. Methods such as LDA+U attempt to remedy this deficiency of LDA.⁵⁴ Another major inadequacy of LDA is that it has self-interaction (see, *e.g.*, Ref. 42). In reality, electrons interact with other electrons. They do not interact electrostatically with themselves. In the Hartree term $J[\rho]$ defined by Eq. (2.9)

of the energy functional Eq. (2.12), a coulomb interaction of each electron with itself is included. For the exact $E_{xc}[\rho]$ functional, this self-interaction component is canceled out. (In the Hartree-Fock approximation, the self-interaction in the Hartree term is explicitly canceled out by an identical term in the exchange term). When an approximation for E_{xc} is used, however, the self-interaction does not cancel. This error becomes severe for well localized electronic states. LDA calculations with self-interaction corrections were pioneered by Perdew and Zunger⁵⁵ and have been used to investigate the electronic properties of several transition metal oxides⁵⁶ and semiconductors.⁵⁷ Incorporating self-interaction corrections leads to orbital dependent effective potentials⁵⁸ which complicates the numerical solution of the energy and charge density, and as a result it is rarely done.

2.3.5. Different Numerical Schemes

Many different numerical techniques exist for solving the Kohn-Sham equations. For oxides, the most reliable methods have proven to be the Linear Augmented Plane Wave (LAPW) method⁵⁹ and the pseudopotential method.^{60,61} The LAPW method is currently considered the most accurate and hence the standard, yet it is computationally the most costly. In the LAPW method, all electrons of the solid are treated and their states are expanded in a basis consisting of both local atomic-like orbitals and plane waves. In the pseudopotential method, the effect of the core electrons around the ions that do not participate in bonding are replaced by a pseudopotential. The pseudopotentials are designed such that the valence single electron pseudo-wave functions have the same scattering properties as the actual valence electrons would have with the core electrons. The pseudopotential approximation is valid as long as the core electrons do not participate in the bonding of the solid - that is the changes in their wave functions and energy levels are negligible when the atom is placed in different environments. For most solids this approximation is valid. Comparisons of energy *differences* for

the Li_xCoO_2 system has shown that the pseudopotential method and LAPW calculations⁶² agree to within 10 meV per Li_xCoO_2 formula unit. Modern pseudopotentials are determined from all electron calculations of atoms, making the pseudopotential method a first principles approach.⁶³⁻⁶⁸

The general procedure of solving the Kohn-Sham equations is to expand the orbitals $\psi_j(\vec{r})$ in terms of a set of basis functions. In pseudopotential calculations, these basis functions are usually plane waves.

2.4. ELECTRONIC STRUCTURE OF Li_xCoO_2

Li_xCoO_2 is currently the most important transition metal oxide compound for battery applications and is ubiquitous in commercial lithium-ion batteries. In this section, we describe important electronic properties of Li_xCoO_2 as predicted with DFT-LDA calculations. Striking is the important role that shifts in covalency play in determining relative stability and lattice parameter variations with lithium concentration.

2.4.1. Covalent bonding in Li_xCoO_2

Figure 2.3 illustrates the LDA-calculated electronic band structures for CoO_2 and LiCoO_2 .^{8,69} The lowest six bands correspond to the e_g^b , t_{1u} and a_{1g} levels of Figure 2.2 which we will refer to as the oxygen p-levels. The next three levels are the t_{2g} levels and the highest two levels correspond to the anti-bonding e_g bands. In LiCoO_2 , the Fermi level lies between the t_{2g} and the e_g levels, making the compound a semiconductor. This is consistent with the experimental observations of van Elp *et al.*⁷⁰ When all the lithium ions are removed, the Fermi level resides in the t_{2g} bands as one electron per CoO_2 formula unit is removed.

The band structures of LiCoO_2 and CoO_2 are qualitatively similar. An important difference between the two band structures is the distance between the oxygen p like levels and the t_{2g} levels which is larger in LiCoO_2

than in CoO_2 . The electron donated by Li when inserted in the CoO_2 host resides in a t_{2g} level. Through coulombic interaction, the addition of the extra electron to the t_{2g} levels raises the energy of the other occupied t_{2g} levels thus increasing the energy difference between the metal d-states and the oxygen p-states. This results in a reduction in the hybridization between the Co d-levels and the oxygen p-levels which translates into a change in the nature of bonding from a more covalent character in CoO_2 to a more ionic character in LiCoO_2 .

To better understand this shift in bonding characteristics with Li insertion, it is useful to inspect a charge difference plot.¹⁸ Figure 2.4 shows a charge difference plot between Li_xCoO_2 at $x=1/4$ and CoO_2 both in the layered O3 structure of Figure 2.5. Electronic charge densities were calculated with the pseudopotential method in the local density approximation for both $\text{Li}_{1/4}\text{CoO}_2$ and CoO_2 .¹⁸ The lattice parameters and the positions of Co and O were the same in the two structures to enable a point by point subtraction of the charge density of CoO_2 from $\text{Li}_{1/4}\text{CoO}_2$. The resulting difference shows how the electron distribution changes when Li is added to the host, and in particular, where the electron of the added lithium resides. The plane illustrated in Figure 2.4 corresponds to the shaded plane shown in Figure 2.5. This plane cuts through Li, Co and O ions.

The charge difference plot illustrates that lithium intercalation induces a significant redistribution of charge within the CoO_2 host.^{17,18} Figure 2.4 shows that there is an accumulation of charge density around all the Co ions in lobes pointing in directions between oxygen ions. This increase in charge results from an electron addition to the partially filled t_{2g} bands as lithium is added to the host. The charge accumulation occurs around all the cobalt ions indicating that these states are delocalized. Figure 2.4 also shows that there is a significant depletion in electron density around the Co ions closest to the lithium ions. The charge depletion occurs in regions that resemble the charge density of a $d_{x^2-y^2}$ atomic orbital (see Figure 2.1). The $d_{x^2-y^2}$ atomic orbital together with the oxygen p orbitals form the σ bonding

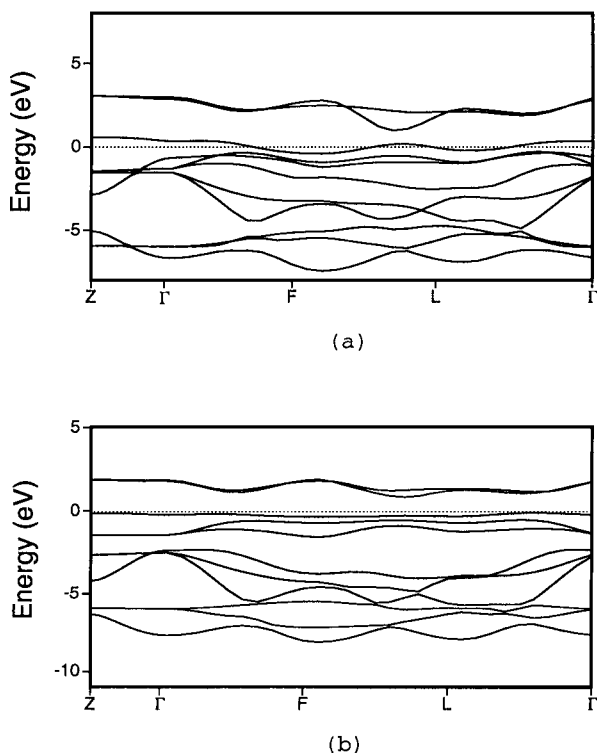


Figure 2.3. The partial band structures of (a) CoO_2 and (b) LiCoO_2 as calculated within the local density approximation. The dashed line shows the Fermi level.

e_g^b and anti-bonding e_g^* bands. The depletion around the Co ions coincides with a significant increase in charge density in atomic p-like orbitals on oxygen ions which point toward the lithium ions and also overlap with the depleted cobalt $d_{x^2-y^2}$ like lobes.

The simultaneous depletion of charge in $d_{x^2-y^2}$ like orbitals around cobalt and accumulation of charge around oxygen indicates a change in the polarization of the σ e_g bonds between oxygen and cobalt. Since the antibonding e_g^* bands are unoccupied in Li_xCoO_2 , the polarization of the σ bond reflects changes in the nature of the bonding e_g^b bands. As lithium is added, the e_g^b bands obtain more of an oxygen character and less of a Co

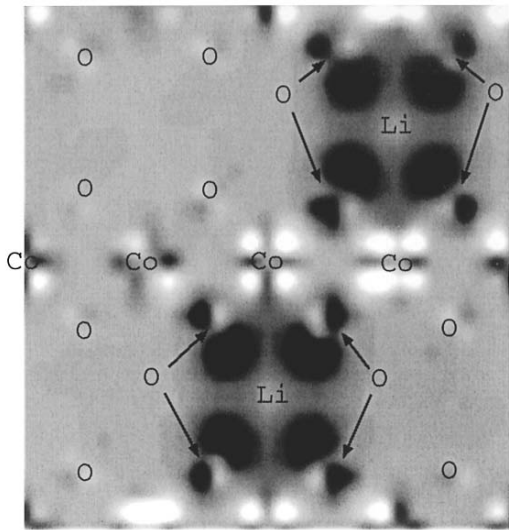


Figure 2.4. Charge difference plot between $\text{Li}_{1/4}\text{CoO}_2$ and CoO_2 . Dark shade signifies regions of charge accumulation and light areas correspond to regions of charge depletion.

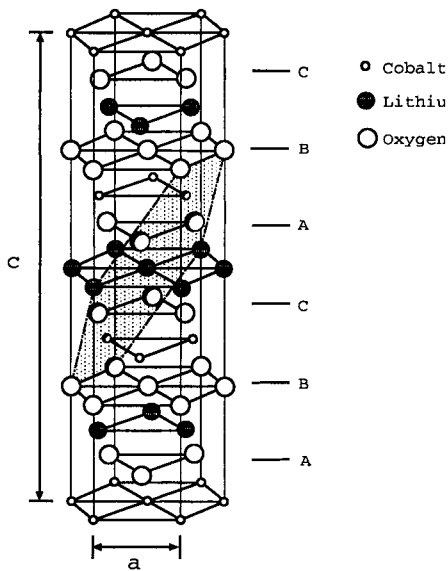


Figure 2.5. The O3 crystal of LiCoO_2 . The crystallographic plane on which the electronic charge density difference is viewed in Figure 2.4 corresponds to the shaded plane in this figure.

character. This causes the σ bond between Co and oxygen to become less covalent and more ionic with increasing x . The result is a significant increase in the electron density at the oxygen sites immediately surrounding the lithium ions. The net effect is that the electron transfer from lithium to the host is very local and occurs predominantly to the oxygen ions.^{7,8}

The conventional picture of lithium transition metal oxides is that the electron donated to the host by lithium is transferred to the transition metal where it shifts its valence state. First principles work within LDA^{7,8,17,18} show that the electronic changes of the host with x are in fact more subtle. The addition of lithium to the CoO_2 host causes a shift in the nature of the bond between oxygen and cobalt from a covalent character at low lithium concentration to a more ionic character at high x . While the electron donated by lithium is added to the t_{2g} band, which is predominantly of Co d character, the effect of this addition is to polarize the Co-O bond such that the charge around the oxygen ions actually increases upon lithium insertion (it is important to realize that oxygen is not in its fully ionized state of -2 in CoO_2). Hence, while it is reasonable to talk about formal valence changes of Co upon Li insertion/removal, one has to keep in mind that the rehybridization around the cobalt ions occurs in a manner that ensures that the local net charge around the cobalt ions remains fixed as the lithium concentration changes.¹⁷

2.4.2. Experimental Evidence for Shift in Covalency

Both X-ray absorption spectroscopy (XAS) and electron energy loss spectroscopy (EELS) have been used to study the local electronic properties of Li_xCoO_2 as a function of x and have provided evidence consistent with a shift in covalency with varying lithium concentration.⁷¹⁻⁷³ Both XAS and EELS measurements rely on transitions of core electrons to unoccupied states above the Fermi level. Of particular importance are the O K-edge, resulting from the excitation of an O 1s core electron into unoccupied O 2p states, and the Co $L_{2,3}$ edge, arising from the excitation of Co 2p electrons to unoccupied

Co 3d states. As the lowest unoccupied states in Li_xCoO_2 are those made up of the hybridization of the Co 3d and O 2p levels, the O K-edge and the Co $L_{2,3}$ -edge supply useful information about the Co-O bond. Variation of the spectrum with lithium concentration sheds light on the nature of bonding and indicates where the charge of the electron from the intercalating lithium goes. The excitations of core electrons with XAS and EELS are local phenomena and selection rules derived from electric dipole allowed transitions isolate well defined excitations. Hence the O K-edge spectra, for example, offer information about the unoccupied 2p states projected on the oxygen sites as the transition from O 1s to Co 3d is forbidden within the electric-dipole approximation.

Measurements of the Co $L_{2,3}$ -edge in Li_xCoO_2 as a function of lithium concentration show only minor variation of the spectra with lithium concentration.⁷¹⁻⁷³ The Co $L_{2,3}$ spectrum consists of two major peaks, L_2 , and, L_3 , arising from excitations of Co $2p_{3/2}$ and $2p_{1/2}$ core electrons to unoccupied Co 3d states. The splitting of Co core 2p levels is induced by spin-orbit coupling. While Graetz *et al.*⁷² were unable to discern a variation with x in the *intensity* of the $L_{2,3}$ peaks, Yoon *et al.*⁷³ were able to quantify a very slight increase to higher energy in the peak *positions* as Li_xCoO_2 is deintercalated.

The variation of the O K-edge spectra with lithium concentration is much more pronounced⁷¹⁻⁷³ than that of the Co $L_{2,3}$ -edge. Even in fully lithiated LiCoO_2 , a well defined transition from the core O 1s state to the unoccupied 2p state is observed, a feature that is absent in completely ionic oxides where the oxygen 2p states are locally fully occupied. This result indicates some degree of covalency between the Co-O bond in LiCoO_2 . As LiCoO_2 is deintercalated, the O K-edge spectra change dramatically.⁷¹⁻⁷³ Deintercalation is accompanied by an increased broadening of the O K near edge pre-peak as well as an increase in the integrated intensity of the pre-peak.⁷² In fact Yoon *et al.*⁷³ identified the growth of three new shoulder peaks upon deintercalation that emerge around the original peak corresponding to the O 1s to 2p transition of fully lithiated LiCoO_2 .

The pronounced variation of the O K-edge spectra compared to the minor variation of the Co $L_{2,3}$ -edge spectra indicates the important role that oxygen plays in the states near the Fermi level. The increase in integrated intensity of the O K near edge pre-peak upon deintercalation implies electron depletion of the O 2p states and hence a reduction in the local charge density around the oxygen ions.^{71,72}

The increase in covalence with decreasing lithium concentration plays an important role in determining the structural properties and the sequence of stable phases with x observed experimentally and predicted from first principles for layered Li_xCoO_2 . It is also of importance in understanding the non-negligible concentration dependence of the activation barrier for lithium diffusion.

2.4.3. The Role of Covalency in Determining Thermo-dynamic, Kinetic and Structural Properties of Li_xCoO_2

Delithiation of Li_xCoO_2 leads to phase transformations and lattice parameter changes that are closely linked to the accompanying changes in electronic structure. LiCoO_2 is a semiconductor⁷⁰ but within a delocalized band structure picture should become metallic upon lithium removal due to the creation of holes in the t_{2g} valence bands. Experimentally, though the removal of lithium for x ranging between 0.93 and 1.0 is found to result in the creation of electronic-hole states that are localized in space and exhibit an activated conduction mechanism.³ The actual transition from the semi-conducting state to a metallic state is obscured by a first order structural phase transformation between $x=0.93$ and 0.75.⁷⁴ Below $x=0.75$, Li_xCoO_2 exhibits metallic properties.³ It has been argued^{3,18,27} that the semi-conducting to metal transition induces the structural phase transformation between $x=0.93$ and 0.75 as the electronic transition is likely to break the convexity of the free energy in part as a result of additional configurational entropy from localized

electron-hole states in the semi-conducting state.^{18,27}

Further delithiation of Li_xCoO_2 leads to a series of ordering and structural phase transformations along with a dramatic contraction of the lattice parameter perpendicular to the oxygen planes below $x=0.5$.^{75,76} Reimers and Dahn⁷⁴ were the first to observe an ordering phase transformation at $x=1/2$ whereby rows of lithium ions are alternated by rows of vacancies. Amatucci *et al.*⁷⁶ demonstrated the stability of fully delithiated CoO_2 but observed that CoO_2 is stable in the O1 crystal structure which is characterized by an ABAB⁷⁷ oxygen stacking sequence. Comprehensive first principles investigations^{15,17,18} of phase stability in Li_xCoO_2 , confirmed the thermodynamic stability of the ordered phase at $x=1/2$ observed by Reimers and Dahn⁷⁴ as well as the O1 phase observed by Amatucci *et al.*⁷⁶ Furthermore, a staged phase in the vicinity of $x=0.15$ was also predicted to be thermodynamically stable from first principles.^{15,18} The predicted staged phase, labeled H1-3,^{15,18} is characterized by a stacking sequence that is a hybrid between O3 and O1. Alternating lithium planes in H1-3 have an O3 environment (*i.e.* lithium sites are edge sharing with Co octahedra) and are partially occupied by lithium while the remaining lithium planes have an O1 environment (lithium sites share faces with Co octahedra) and are vacant. The stability of the H1-3 phase has recently been confirmed experimentally.^{78,79}

The progression in stability in layered Li_xCoO_2 from O3 to H1-3 to O1 during delithiation can be attributed to the increased covalency of the Co-O bond with decreasing x . In the delithiated state, O3 CoO_2 is isomorphic to CdCl_2 , a relatively ionic compound, while O1 CoO_2 is isomorphic to CdI_2 , a more covalent compound. The H1-3 phase at low lithium concentrations enables accommodation of the increased covalency of the Co-O bonds in the vicinity of the O1 like stacking while simultaneously accommodating the lithium ions within the alternating planes locally having the O3 stacking. H1-3 can be thought of as a local phase separation between a delithiated O1 block and a Li-rich O3 block.

Part of the significant contraction of the lattice parameter c of layered

Li_xCoO_2 upon deintercalation can be attributed to a reduction in the number of lithium ions which electrostatically pull the O-Co-O sheets together. Another significant factor contributing to this contraction, though, is the change with x of the electronic properties of the compound. The increased covalency of the Co-O bonds with delithiation results in a contraction of the cobalt-oxygen distances and, therefore, a reduction in width of the O-Co-O slabs as x is decreased. Furthermore, the increased covalency is accompanied by a reduction in the polarization of negative charge toward the oxygen ions. Hence the electrostatic repulsion between negatively charged oxygen ions of adjacent O-Co-O slabs diminishes as lithium is removed from the host.

Kinetic properties such as the migration barrier for Li diffusion are affected by changes in the electronic properties with varying lithium concentration. First principles calculations^{31,36} predict that lithium diffusion in layered Li_xCoO_2 occurs with a divacancy mechanism whereby the lowest

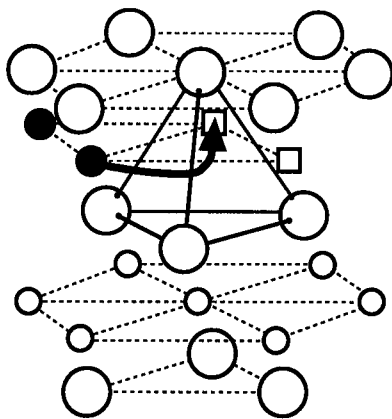


Figure 2.6. The dominant migration mechanism in layered Li_xCoO_2 is by means of a divacancy. The presence of a divacancy enables lithium to pass through an adjacent tetrahedral site as illustrated above (filled circles are lithium, empty squares are lithium vacancies, large empty circles are oxygen and small empty circles are cobalt).

energy migration path between neighboring octahedral sites passes through an adjacent tetrahedral site as illustrated in Figure 2.6. First principles calculations also predict an increase in the activation barrier upon delithiation.^{31,36}

The tetrahedral site along the lithium migration path shares a face with an adjacent octahedral site containing positively charged cobalt. The resulting electrostatic repulsion energetically penalizes the tetrahedral site relative to the octahedral site. This electrostatic repulsion is screened to some extent by the negative electronic charge on the oxygen ions. Nevertheless, the screening diminishes with decreasing lithium concentration because of the accompanying reduction of the charge on oxygen. As the Li concentration is reduced, the accompanying reduction of screening, along with the contraction of the *c* axis, which results in a reduction of volume of the tetrahedral site, leads to a dramatic increase of the activation barrier for lithium migration.

2.5. ELECTRONIC PROPERTIES IN LiNiO_2 : THE 180° INTERACTION

As is the case for LiCoO_2 , LiNiO_2 is also stable in the O3 crystal structure. Nevertheless, nickel has one extra valence electron which dramatically alters the properties of layered Li_xNiO_2 as compared to those of Li_xCoO_2 . LiCoO_2 is a semiconductor with occupied t_{2g} bands and unoccupied e_g bands. Upon delithiation, holes are introduced in the t_{2g} bands. In LiNiO_2 , the additional valence electron resides in one of the e_g bands. Within crystal field theory, the two e_g states in an octahedron are degenerate, and single occupancy of the e_g states can potentially lead to a Jahn-Teller distortion of the octahedron. The distortion lifts the degeneracy of the e_g levels lowering the energy of the occupied level while raising the energy of the unoccupied level. As described above, molecular orbital models characterize the e_g states as anti-bonding levels which are typically more localized electron states. From these simple models we can anticipate distortions of Ni octahedra in

LiNiO_2 and local charge ordering on the Ni ions upon delithiation. While collective distortion of the crystal due to Jahn-Teller activity has not been observed experimentally,⁸⁰⁻⁸³ evidence exists for the presence of uncoordinated locally distorted octahedra.^{80,81} In fact, accurate first principles calculations within the generalized gradient approximation have predicted a weak energetic preference for a collective Jahn-Teller distortion of LiNiO_2 crystal.³⁵ Furthermore, at intermediate lithium concentrations charge ordering between Ni^{+3} and Ni^{+4} ions accompanied by local Jahn-Teller distortions has been predicted from first principles.^{34,39,40}

While accurate first principles calculations confirm the conclusions that emerge from crystal field and molecular orbital models, detailed first principles calculations also predict an unexpected electronically induced long range attraction between lithium ions in different lithium planes.^{34,39,40} A systematic study³⁴ of the energies and local distortions of Ni octahedra in structures of Li_xNiO_2 with different lithium-vacancy arrangements showed a remarkable attraction between lithium ions at opposite ends of a distorted Ni

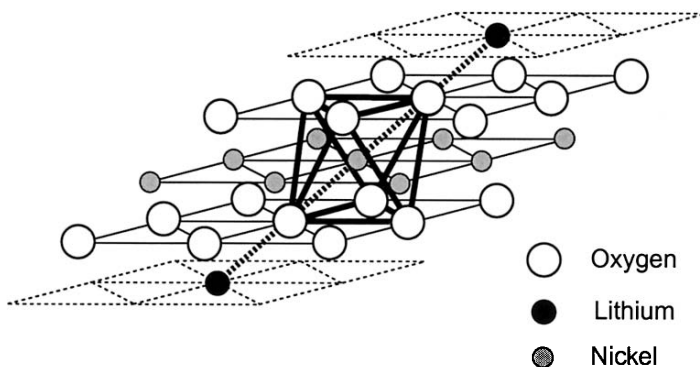


Figure 2.7. In Li_xNiO_2 a long range attraction between a pair of lithium ions of different lithium planes is mediated by a Jahn-Teller distortion of a Ni^{+3} octahedron.

octahedron as illustrated in Figure 2.7. 180° Li-O-Ni-O-Li configurations

around Ni^{+3} ions along the elongated axis of the Jahn-Teller distorted octahedra were consistently present in low energy configurations of Li_xNiO_2 .

A similar long range interaction between four lithium ions was also discerned in which four lithium 2s orbitals hybridize with the e_g molecular orbital made of Ni $d_{x^2-y^2}$ and oxygen p orbitals as illustrated in Figure 2.8.³⁴ An octahedron containing Ni^{+3} and coordinated by four lithium ions as in Figure 2.8 are characterized by a negative Jahn-Teller distortion in which the four Ni-O bonds pointing to Li ions are elongated and two Ni-O bonds pointing to Li vacancies are contracted.

The stability of the 180° Li-O- Ni^{+3} -O-Li configurations around distorted octahedra can be rationalized as follows.³⁴ The presence of lithium ions at opposite corners of an octahedron lowers the energy of an occupied e_g level due to hybridization between the Li-2s, O-2p and a Ni e_g orbital (either

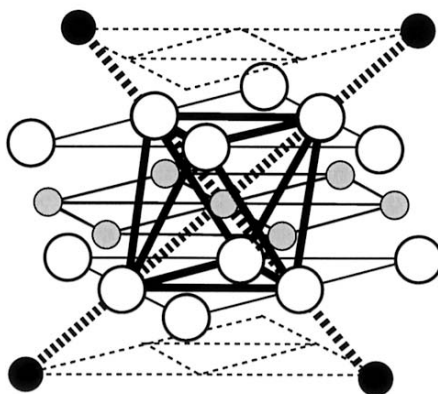


Figure 2.8. Attraction between four lithium ions over long distances in Li_xNiO_2 is mediated by a negative Jahn-Teller distortion of a Ni^{+3} octahedron (legend as in Figure 2.7).

$d_{x^2-y^2}$ or $d_{3z^2-r^2}$). Although a Jahn-Teller distortion in any environment already leads to a lowering of the energy of an e_g level, the presence of Li ions at opposite corners of the oxygen octahedra further stabilizes this e_g orbital through hybridization. Hence the occurrence of the long-range 180° Li-Li attraction and the Jahn-Teller distortions are coupled, one reinforcing the other.

The energy gain from a Jahn-Teller distortion is maximal when the occupied e_g orbital is localized. This favors localization of electronic charge around the Ni ions, which upon deintercalation leads to charge ordered states consisting of well defined Ni^{+3} and Ni^{+4} ions. Due to the 180° Li-O- Ni^{+3} -O-Li attraction, the lithium-vacancy arrangements and the Ni^{+3} and Ni^{+4} arrangements are strongly coupled.

The 180° coupling between Jahn-Teller active ions and the lithium ions of different lithium planes is in part responsible for the dramatically different electrochemical behavior between Li_xNiO_2 and Li_xCoO_2 .³⁹ Interactions between different lithium ions in a transition metal oxide are typically short-ranged due to extensive screening by the oxygen ions. The 180° coupling in Li_xNiO_2 , which is absent in Li_xCoO_2 , leads to a long range coupling between lithium ions of different lithium planes that are more than 8 Å apart. The added long range interactions favor different lithium-vacancy ordering reactions than is observed and predicted in Li_xCoO_2 . In fact, first principles calculations predict a very stable ordered phase at $x=2/5$ in Li_xNiO_2 , an unsuspected type of ordering on a triangular lattice.³⁹

In reality, synthesis of ideal $LiNiO_2$ has proven elusive, with actual specimens invariably having an excess of Ni ions.⁸⁰ The excess Ni ions occupy sites within the lithium layer. So while it is possible to make predictions from first principles about ideal Li_xNiO_2 , the presence of excess Ni in the lithium planes in experiment is likely to alter these predictions to some extent. Excess Ni ions in the lithium planes will certainly alter the topology of the phase diagram of ideal Li_xNiO_2 and may even change the types of ordered phases that occur. Nevertheless, the existence of the 180° long-range lithium attraction should persist in some form, even in the Ni excess samples.

2.6. LAYERED TO SPINEL TRANSFORMATION IN Li_xMnO_2

Most forms of Li_xCoO_2 and Li_xNiO_2 have the layered O3 crystal structure. Lithium manganese oxide, however, is generally synthesized in the spinel crystal structure with stoichiometry $\text{Li}_x\text{Mn}_2\text{O}_4$. The voltage profile of the spinel crystal structure is characterized by two plateaus, one around 4.2 V for $x < 1$ and one around 3 V between $x = 1$ and $x = 2$. The second plateau occurs as a result of a first order phase transformation. For many years, much effort was devoted to synthesizing layered Li_xMnO_2 .^{84,85} Nevertheless, successfully synthesized layered LiMnO_2 was found to transform to a phase resembling spinel upon lithium removal.⁸⁶⁻⁸⁹

2.6.1. The Crystallography and Thermodynamics of the Layered to Spinel Phase Transformation

The fact that the layered form of LiMnO_2 is observed to readily transform to the spinel variant upon delithiation is not surprising from a crystallographic point of view. Both the layered O3 crystal structure and the spinel crystal structure have the same close-packed oxygen framework with an ABCABC stacking sequence. The two phases only differ in the arrangement of the lithium and transition metal ions over the interstitial sites of the oxygen skeleton. Transformation from layered to spinel therefore only requires a reordering of the transition metal and lithium ions.

In the layered phase, the transition metal ions occupy octahedral sites in alternating layers between close-packed oxygen planes, giving the phase a rhombohedral symmetry. The lithium ions occupy the remaining octahedral sites that also form alternating layers between close-packed oxygen planes. In the spinel crystal structure, the transition metal ions are distributed more uniformly among the octahedral interstitial sites: 3/4 of the metal ions reside

in alternating layers between close-packed oxygen planes, while the remaining 1/4 of the metal ions reside in the other alternating planes. This particular metal ordering produces a transition metal oxide host structure with cubic symmetry. While the lithium ions can occupy the remaining vacant octahedral sites in the host, energetically favorable tetrahedral sites are also available; the metal ordering in spinel results in a set of tetrahedral sites that do not share faces with metal-oxygen octahedra. Upon deintercalation of the layered O3 crystal structure, channels within the oxygen framework open up that enable transition metal ions to migrate to the vacated lithium layers. For the layered phase to transform to spinel, exactly one in four transition metal ions must migrate to the lithium layer. This transformation thus can occur without reconstruction of the oxygen skeletal structure.

First principles calculations have exposed that for many transition metal oxides Li_xMO_2 ($\text{M}=\text{Ti}, \text{V}, \text{Mn}, \text{Fe}, \text{Co}, \text{Ni}$)^{16,27} the spinel crystal structure is energetically more stable than the layered crystal structure at $x=1/2$. Figure 2.9, which illustrates the calculated free energy curves of O3 and spinel Li_xCoO_2 as a function of lithium concentration,²⁰ clearly shows the thermodynamic stability of spinel around $x=1/2$ over the O3 phase. This relative stability means that for layered lithium transition metal oxides a thermodynamic driving force exists for transformation to the spinel crystal structure upon deintercalation. Nevertheless, only Li_xMnO_2 is observed to undergo this transformation at room temperature.⁸⁶⁻⁸⁹ Layered Li_xCoO_2 for example, maintains its layered structure upon continued cycling. The high mobility of Mn ions which makes the transformation of Li_xMnO_2 to a spinel structure at room temperature possible, has its origin in the particular electronic structure of the Mn ion in octahedral and tetrahedral environments.

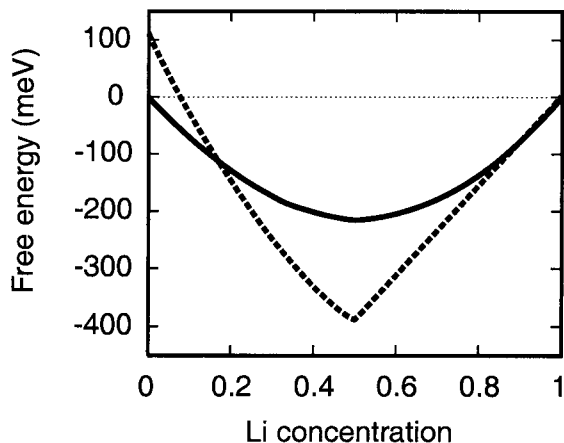


Figure 2.9. Free energy of layered O3 (solid line) and spinel (dashed line) Li_xCoO_2 as a function of lithium concentration.

2.6.2. A Two Stage Transformation Mechanism

First principles calculations have shown that the layered to spinel phase transformation in Li_xMnO_2 occurs in two stages.³³ This is consistent with experimental observations.⁹⁰⁻⁹³ The kinetics of the layered to spinel phase transformation relies crucially on the first step which is driven by a unique charge-disproportionation reaction predicted from first principles to occur only in Li_xMnO_2 and not in the Co and Ni layered compounds.³³

A first step in the transformation from layered Li_xMO_2 to the spinel variant is the migration of transition metal ions to adjacent tetrahedral sites. These tetrahedral sites share faces with an oxygen-octahedra in the transition metal layer and three octahedra in the lithium layer (Figure 2.10).

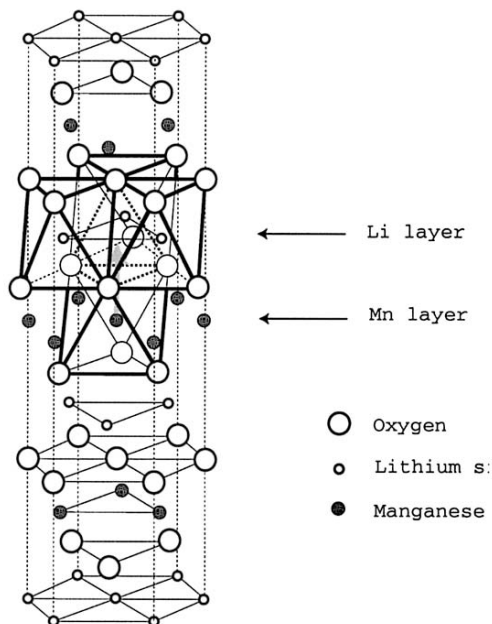


Figure 2.10. The layered O3 host and spinel have the same oxygen skeletal structure. Transformation from layered to spinel can occur by a redistribution of the transition metal ions within this structure. The first step of such a transformation involves migration of 1/4 of the metal ions to tetrahedral sites (thick dashed lines) in the lithium layer.

The migrating transition metal ion must then migrate further to an octahedral site within the lithium layer. If one in four transition metal ions migrate to the lithium layer in a coordinated manner (see Figure 2.11) accompanied by lithium rearrangement to the non-face sharing tetrahedral sites that result from the metal rearrangement, the transformation would yield a defect free spinel phase. Due to the thermal nature of such a reordering transformation, however, we can expect the transition metal rearrangement to occur in a more random way, creating a disordered spinel phase. Over time, though, the intermediate disordered phase should gradually evolve to the perfect spinel ordering as a result of continued ion rearrangement within the oxygen skeletal structure.

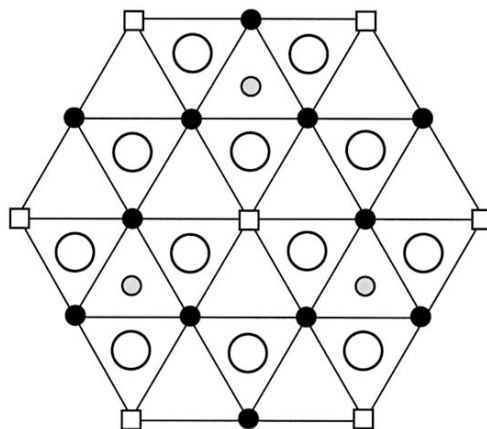


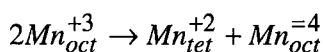
Figure 2.11. Projection of a metal layer (transition metals are the filled circles) and the oxygen layer (oxygen ions are the empty circles) above it in the O3 crystal structure. Transformation to spinel involves migration of 1/4 of the metal ions to the lithium layer. This leaves a vacant metal site (empty squares) within the metal layer. The migrated metal ions must migrate to a lithium site above a triangle of metal ions (shaded circle). In order for this rearrangement to lead to spinel, the arrangement of vacancies within each metal layer must be ordered as illustrated in the above figure.

2.6.2.1. Stage I of the Layered to Spinel Transformation in Li_xMnO_2

A tetrahedral site as in Figure 2.10 is only a viable path for transition metal migration to the lithium layer if the three adjacent octahedral sites in the lithium layer are vacant. Hence a precondition for the layered to spinel transformation is some degree of lithium deintercalation such that the simultaneous existence of three lithium vacancies around a tetrahedral site has a reasonable probability of occurring. As the lithium concentration is reduced, the concentration of such tri-vacancies increases. Typically the transition metals considered for cathode materials with stoichiometry Li_xMO_2 prefer octahedral sites over tetrahedral sites. Migrating to a tetrahedral site is then accompanied by an increase in the energy of the crystal³³ and therefore thermodynamically unfavorable. But first principles calculations predict that

Mn ions with a valence state of +2 behave differently, actually preferring tetrahedral sites over octahedral sites.

The formal valence state of transition metal ions in LiMO_2 is +3 which on average increases towards +4 as lithium is removed. Nevertheless, as the Li concentration is reduced, first principles calculations³³ predict that Mn^{+2} ions can form through a charge disproportionation reaction involving electron transfer from a neighboring Mn^{+3} ion according to



(2.17)

The above reaction equation should be interpreted as follows: Migration of a Mn^{+3} ion from an octahedral site in the metal layer to an adjacent tetrahedral site surrounded by lithium vacancies becomes energetically favorable provided that it is adjacent to another Mn^{+3} ion from which it can borrow an electron. The result of the reaction is a Mn^{+2} ion in a tetrahedral site within the lithium layer and a Mn^{+4} ion in the metal layer. First principles calculations predict that the valence electrons of the Mn^{+2} ion in the tetrahedral site have parallel spin.³³ A high spin Mn^{+2} ion has a half filled d-shell that chemically behaves similar to a closed shell ion. Hybridization with the coordinating oxygen ions then occurs predominantly with the empty 4s and 4p levels, which in a tetrahedral environment, hybridize into sp^3 orbitals. It is the ability of the Mn ions to form a closed d shell electron configuration that makes migration to adjacent tetrahedral sites energetically favorable. This unique electronic property of Mn is absent in other transition metal ions in Li_xMO_2 ($\text{M}=\text{Co}$ or Ni) and is crucial in precipitating the first step of the layered to spinel phase transformation. In the other layered transition metal oxides, migration of the transition metal to a tetrahedral site is met with an energy barrier;³³ in the Mn compound, it leads to a reduction in energy, and hence will occur spontaneously as long as sufficient vacancies exist in the

lithium layer and sufficient Mn^{+3} ions are available in the metal layer to feed the charge-disproportionation reaction of Eq. (2.17).

The availability of vacancies in the lithium layer and Mn^{+3} ions in the metal layer are requirements that have an opposite dependence on lithium concentration. Decreasing the lithium concentration increases the number of lithium vacancies but it decreases the number of Mn^{+3} ions. A maximum in the octahedral to tetrahedral migration rate can therefore be expected at intermediate lithium concentration, the concentration which also happens to coincide with the maximal thermodynamic driving force for the layered to spinel transformation.

2.6.2.2. Stage II of the Layered to Spinel Transformation in Li_xMnO_2

In layered Li_xMnO_2 , the migration of Mn to tetrahedral sites between the metal and lithium layer is predicted to occur spontaneously (without energy barrier) at intermediate lithium concentration.³³ In fact, at $x=1/2$, sufficient Mn^{+3} ions exist for 1/4 of the Mn ions to migrate from the metal layer to tetrahedral sites by means of the charge-disproportionation reaction of Eq. (2.17). The migration of Mn ions from octahedral sites in the metal layer to tetrahedral sites leads to other tetrahedral sites in the lithium layers to no longer share a face with Mn octahedra. These tetrahedral sites then become energetically favorable for lithium occupation. Spontaneous Mn migration to tetrahedral sites is predicted to be accompanied by lithium migration to tetrahedral sites.³³ While migration of Mn ions to tetrahedral sites at $x=1/2$ occurs spontaneously, this phase with 1/4 tetrahedral Mn^{+2} and some tetrahedral lithium is still intermediate in energy between the O3 phase and the perfectly ordered spinel phase (all lithium in tetrahedral sites, cubic ordering of Mn ions over octahedral sites).³³ We refer to this intermediate phase at $x=1/2$ as the "splayed" phase and emphasize that it has 1/4 of the Mn ions in tetrahedral sites distributed uniformly but in a more or less disordered arrangement. The existence of a partially transformed layered

phase with tetrahedral Mn has been observed experimentally.⁹⁰⁻⁹³ Further transformation of the splayed phase to spinel occurs by thermally activated Mn hops within the lithium layers and therefore proceeds slower than the layered to splayed transformation, which has no barrier.

In a battery, charging rarely stops at $x=1/2$ but continues to lower concentrations. Further lithium removal from the spontaneously formed splayed phase would require oxidation of Mn^{+2} ions, destabilizing the Mn ions in the tetrahedral sites. Lithium removal below $x=1/2$ therefore leads to Mn migration from tetrahedral sites back to octahedral sites. Nevertheless, a Mn ion in a tetrahedral site can migrate to four neighboring octahedral sites, one which resides in the metal layer and three which reside in the lithium layer. The higher availability of octahedral sites in the lithium layer leads to a net migration of tetrahedral Mn ions to octahedral sites in the lithium layer during further deintercalation. Repeated cycling will enhance the migration of Mn ions to the lithium layers and this is observed experimentally where cycling of the material leads to an increased spinel formation.

2.6.3. Suppressing the Layered to Spinel Transformation

The electronic origin of the layered to spinel phase transformation in Li_xMnO_2 can be exploited to suppress this transformation by appropriately doping the compound. The crucial step in the layered to spinel phase transformation is the charge-disproportionation reaction fed by the presence of Mn^{+3} ions. Doping of the compound to prevent the layered to spinel transformation should hence deprive the host of Mn^{+3} ions. This can be done with elements that are more electronegative than Mn, therefore oxidizing Mn^{+3} to Mn^{+4} , even in the fully lithiated state. This has been successfully achieved by Ammundsen *et al.*⁹⁴ who found that layered $Li_xMn_{0.4}Cr_{0.4}Li_{0.2}O_2$ cycles without transformation to spinel. Substituting half the Mn with Ni has also been shown to suppress the layered to spinel phase transformation.^{95,96} In layered $Li_xMn_{0.5}Ni_{0.5}O_2$, Ni is predicted to have a +2 valence while Mn has a

+4 valence.³⁸ Charging of the compound leads to the oxidation of Ni from the +2 state to the +4 state. The absence of Mn^{+3} ions at all lithium concentrations prevents the detrimental layered to spinel phase transformation in this compound.

2.7. CONCLUSIONS

We have reviewed theoretical models and tools that enable us to understand and predict the electronic properties of lithium transition metal oxides. We have focussed in particular on a detailed description of density functional theory (DFT), currently the most reliable and accurate approach to studying the electronic properties of complex oxides from first principles. We have also reviewed results and insights derived from DFT studies of three important lithium transition metal oxides, namely Li_xCoO_2 , Li_xNiO_2 and Li_xMnO_2 . In our discussion of these three compounds, we have focused on important electronic properties exposed by DFT calculations which have a particular bearing on the electrochemical properties of these compounds. In Li_xCoO_2 , DFT calculations have shown the importance of covalent bonding between oxygen and cobalt and the role of increased covalency with decreasing x in affecting the thermodynamic and structural properties of this compound. In Li_xNiO_2 , a DFT study has predicted a long range attraction between lithium ions of different lithium planes. This long-range attraction is mediated by a Jahn-Teller distorted oxygen octahedra containing a Ni^{+3} ion. The lithium-lithium attraction, termed the 180° interaction, is in part responsible for the very different electrochemical properties of Li_xNiO_2 as compared to those of Li_xCoO_2 . For LiMnO_2 , a DFT investigation has led to the prediction of a remarkable charge-disproportionation reaction between Mn ions, which leads to spontaneous migration of Mn ions to tetrahedral sites within the lithium layer of layered Li_xMnO_2 . It is this charge-disproportionation reaction, identified from first principles, which is responsible for the undesirable layered to spinel phase transformation that has

prevented the successful implementation of layered Li_xMnO_2 in lithium batteries.

ACKNOWLEDGMENTS

We are grateful to Elena Arroyo, John Reed, Chris Marianetti, Claude Delmas and Bing Joe Hwang for insightful discussions. We thank the Department of Energy (award no. DE-FG0296ER45571) and the National Science Foundation (award no. DMR 98-08941 and NPACI supercomputer support).

REFERENCES

1. M.M. Thackeray, J.O. Thomas, M.S. Whittingham, *MRS Bulletin* 25 (2000) 39.
2. A. K. Padhi, K. S. Nanjundaswamy, J. B. Goodenough, *J. Electrochem. Soc.* 144 (1997) 1188.
3. M. Menetrier, I. Saadoune, S. Levasseur, C. Delmas, *J. Mater. Chem.* 9 (1999) 1135.
4. E. Greedan, N.P. Raju, A.S. Will, C. Morin, S.M. Shaw, J.N. Reimers, *Chem. Mater.* 10 (1998) 3058.
5. J. Rodriguez-Carvajal, G. Rousse, C. Masquelier, M. Hervieu, *Phys. Rev. Lett.* 81 (1998) 4660.
6. G. Rousse, C. Masquelier, J. Rodriguez-Carvajal, M. Hervieu, *Electrochem. Solid -State Lett.* 2 (1999) 1.
7. G. Ceder, M.K. Aydinol, A.F. Kohan, *Comp. Mat. Sci.* 8 (1997) 161.
8. M. K. Aydinol, A.F. Kohan, G. Ceder, G. K. Cho, J. Joannopoulos, *Phys. Rev. B* 56 (1997) 1354.
9. M.K. Aydinol, G. Ceder, *J. Electrochem. Soc.* 144 (1997) 3832.
10. E. Deiss, A. Wokaun, J.L. Barras, C. Daul, P. Dufek, *J. Electrochem. Soc.* 144 (1997) 3877.
11. R. Benedek, M.M. Thackeray, L.H. Yang, *Phys. Rev. B* 56 (1997) 10707.
12. G. Ceder, A.F. Kohan, M.K. Aydinol, P.D. Tepesch, A. Van der Ven, *J. Amer. Cer. Soc.* 81

- (1998) 517.
13. G Ceder, Y.M. Chiang, D.R. Sadoway, M.K. Aydinol, Y.I. Jang, B. Huang, *Nature* 392 (1998) 694.
14. C. Wolverton, A. Zunger, *Phys. Rev. B* 57 (1998) 2242.
15. A. Van der Ven, M.K. Aydinol, G Ceder, *J. Electrochem. Soc.* 145 (1998) 2149.
16. C. Wolverton, A. Zunger, *J. Electrochem. Soc.* 145 (1998) 2424.
17. C. Wolverton, A. Zunger, *Phys. Rev. Lett.* 81 (1998) 606.
18. A. Van der Ven, M.K. Aydinol, G Ceder, G Kresse, J. Hafner, *Phys. Rev. B* 58 (1998) 2975.
19. L Benco, J.L. Barras, M. Atanasov, C.A. Daul, E. Deiss, *Solid State Ionics* 112 (1998) 225.
20. A. Van der Ven, G Ceder, *Phys. Rev. B* 59 (1999) 742.
21. L. Benco, J. L. Barras, C. A. Daul, E. Deiss, *Inorg. Chem.* 38 (1999) 20.
22. M. S. Mishra, G Ceder, *Phys. Rev. B* 59 (1999) 6120.
23. L. Benco, J. L. Barras, M. Atanasov, C. Daul, E. Deiss, *J. Solid State Chem.* 145 (1999) 503.
24. J. S. Braithwaite, C. R. A. Catlow, J. D. Gale, J. H. Harding, *Chem. Mat.* 11 (1999) 1990.
25. R. Benedek, M. M. Thackeray, L. H. Yang, *Phys. Rev. B* 60 (1999) 6335.
26. G Ceder, M. S. Mishra, *Electrochem. Solid-State Lett.* 2 (1999) 550.
27. G Ceder, A. Van der Ven, *Electrochim. Acta*, 45 (1999) 131.
28. S. Buta, D. Morgan, A. Van der Ven, M. K. Aydinol, G Ceder, *J Electrochem. Soc.* 146 (1999) 4335.
29. J. S. Braithwaite, C. R. A. Catlow, J. D. Gale, J. H. Harding, P. E. Ngoepe, *J. Mat. Chem.* 10 (2000) 239.
30. J. S. Braithwaite, C. R. A. Catlow, J. H. Harding, J. D. Gale, *Phys. Chem. Chem. Phys.* 2 (2000) 3841.
31. A. Van der Ven, G Ceder, *Electrochem. Solid-State Lett.* 3 (2000) 301.
32. A. Van der Ven, C. Marianetti, D. Morgan, G Ceder, *Solid State Ionics* 135 (2000) 21.
33. J. Reed, G Ceder, A. Van der Ven, *Electrochem. Solid-State Lett.* 4 (2001) 78.
34. M. E. Arroyo y de Dompablo, C. Marianetti, A. Van der Ven, G Ceder, *Phys. Rev. B* 63 (2001) 144107.
35. C. Marianetti, D. Morgan, G Ceder, *Phys. Rev. B* 63 (2001) 224304.

36. A. Van der Ven, G Ceder, M. Asta, P. D. Tepesch, *Phys. Rev. B* 64 184307 (2001).
37. G. E. Grechnev, R. Ahuja, B. Johansson, O. Eriksson, *Phys. Rev. B* 65 (2002) 174408.
38. J. Reed, G Ceder, *Electrochem. Solid-State Lett.* 5 (2002) A145.
39. M. E. Arroyo y de Dompablo, A. Van der Ven, G Ceder, *Phys. Rev. B* 66 (2002) 64112.
40. M. E. Arroyo y de Dompablo, G Ceder, *Chem. Mater.* 15 (2003) 63.
41. P. Hohenberg, W. Kohn, *Phys. Rev. B* 136 (1964) 864.
42. R. G Parr, W. Yang, *Density Functional Theory of Atoms and Molecules*, Oxford University Press (1989).
43. R. O. Jones, O. Gunnarsson, *Rev. Mod. Phys.* 61 (1989) 689.
44. J. M. Sanchez, F. Ducastelle, D. Gratias, *Physica* 128A (1984) 334.
45. D. de Fontaine, *Solid State Phys.* 47 (1994) 33.
46. M. C. Day, J. Selbin, *Theoretical Inorganic Chemistry*, Reinhold Pub. (1962).
47. C. J. Ballhausen, *Introduction to Ligand Field Theory*, McGraw-Hill (1962).
48. T. M. Dunn, D. S. McClure, R. G Pearson, *Crystal Field Theory*, Harper and Row (1965).
49. L. H. Hall, *Group Theory and Symmetry in Chemistry*, McGraw-Hill (1969).
50. N. W. Ashcroft, N. D. Mermin, *Solid State Physics*, Saunders College Publishing (1976).
51. O. Madelung, *Introduction to Solid State Theory*, Springer Verlag (1978).
52. M. Levy, *Proc. Natl. Acad. Sci.* 76 (1979) 6062.
53. W. Kohn, L. J. Sham, *Phys. Rev.* 140 (1965) A1133.
54. V. I. Anisimov, F. Aryasetiawan, A. I. Lichtenstein, *J. Phys. Condens. Matter* 9 (1997) 767.
55. J. P. Perdew, A. Zunger, *Phys. Rev. B* 23 (1981) 5048.
56. Z. Szotek, W. M. Temmerman, H. Winter, *Phys. Rev. B* 47 (1993) 4029.
57. M. M. Rieger, P. Vogl, *Phys. Rev. B* 52 (1995) 16567.
58. S. Goedecker, C. J. Umriga, *Phys. Rev. A* 55 (1997) 1765.
59. D. J. Singh, *Planewaves, Pseudopotentials and the LAPW Method*, Kluwer Academic Pub. (1994).
60. J. C. Phillips, L. Kleinman, *Phys. Rev.* 116 (1959) 287.
61. M. C. Payne, M. P. Teter, D. C. Allan, T. A. Arias, J. D. Joannopoulos, *Rev. Mod. Phys.* 64 (1992) 1045.
62. C. Wolverton, *private communication* (1997).
63. D. R. Hamann, M. Schluter, C. Chiang, *Phys. Rev. Lett.* 43 (1979) 1494.

64. G. B. Bachelet, D. R. Hamann, M. Schluter, *Phys. Rev. B* **26** (1982) 4199.
65. L. Kleinman, D. M. Bylander, *Phys. Rev. Lett.* **48** (1982) 1425.
66. A. M. Rappe, K. M. Rabe, E. Kaxiras, J. D. Joannopoulos, *Phys. Rev. B* **41** (1990) 1227.
67. N. Troullier, J. L. Martins, *Phys. Rev. B* **43** (1991) 1993 .
68. D. Vanderbilt, *Phys. Rev. B* **41** (1990) 7892.
69. M. T. Czyzyk, R. Potze, G. A. Sawatzky, *Phys. Rev. B* **46** (1992) 3729.
70. J. van Elp, J. L. Wieland, H. Eskes, P. Kuiper, G. A. Sawatzky, F. M. F. de Groot, T. S. Turner, *Phys. Rev. B* **44** (1991) 6090.
71. L. A. Montoro, M. Abbate, J. M. Rosolen, *Electrochem. Solid-State Lett.* **3** (2000) 410.
72. J. Graetz, A. Hightower, C. C. Ahn, R. Yazami, P. Rez, B. Fultz, *J. Phys. Chem. B* **106** (2002) 1286.
73. W.-S. Yoon, K.-B. Kim, M.-G. Kim, M.-K. Lee, H.-J. Shin, J.-M. Lee, J.-S. Lee, C.-H. Yo, *J. Phys. Chem. B* **106** (2002) 2526.
74. J. N. Reimers, J. R. Dahn, *J. Electrochem. Soc.* **139** (1992) 2091.
75. T. Ohzuku, A. Ueda, *J. Electrochem. Soc.* **141** (1994) 2972.
76. G. G. Amatucci, J. M. Tarascon, L. C. Klein, *J. Electrochem. Soc.* **143** (1996) 1114.
77. C. Delmas, C. Fouassier, P. Hagenmuller, *Physica B* **99** (1980) 81.
78. Z. H. Chen, Z. H. Lu, J. R. Dahn, *J. Electrochem. Soc.* **149** (2002) 1604.
79. L. Croguennec, S. Levasseur, M. Morcrette, J. M. Tarascon, C. Delmas, Materials Research Society (MRS) Fall meeting, Boston (MA), Dec. 2-6, 2002.
80. A. Rougier, C. Delmas, A. V. Chadwick, *Solid State Commun.* **94** (1995) 123.
81. C. Delmas, M. Menetrier, L. Croguennec, S. Levasseur, J. P. Peres, C. Pouillere, G. Prado, L. Fournes, F. Weill, *Int. J. Inorg. Mater.* **1** (1999) 11.
82. A. N. Mansour, X. Q. Yang, X. Sun, J. McBreen, L. Croguennec, C. Delmas, *J. Electrochem. Soc.* **174** (2000) 2104.
83. J. P. Peres, A. Demourgues, C. Delmas, *Solid State Ionics* **111** (1998) 135.
84. A. R. Armstrong, P. G. Bruce, *Nature* **381** (1996) 499.
85. F. Capitaine, P. Gravereau, C. Delmas, *Solid State Ionics* **89** (1996) 197.
86. A. Blyr, C. Sigala, G. Amatucci, D. Guyomard, Y. Chabre, *J. Electrochem. Soc.* **145** (1998) 194.
87. Y. -M. Chiang, D. R. Sadoway, Y. I. Jang, B. Huang, H. Wang, *Electrochem. Solid-State*

- Lett.* 2 (1999) 107.
88. Y. Shao-Horn, S. A. Hackney, A. R. Armstrong, P. G. Bruce, R. Gitsendanner, C. S. Johnson, M. M. Thackeray, *J. Electrochem. Soc.* 146 (1999) 2404.
89. G. Vitins, K. West, *J. Electrochem. Soc.* 144 (1997) 2587.
90. P. Bruce, A. Armstrong, R. Gitzendanner, *J. Mater. Chem.* 9 (1998) 193.
91. B. Ammundsen, J. Desilvestro, T. Groutso, D. Hassell, J. B. Metson, E. Regan, R. Steiner, P. J. Pickering, *J. Electrochem. Soc.* 147 (2000) 4078.
92. H. Wang, Y. I. Jang, Y. -M. Chiang, *Electrochem. Solid-State Lett.* 2 (1999) 10.
93. S. J. Hwang, H. S. Park, J. H. Choy, *Chem. Mater.* 12 (2000) 1818.
94. B. Ammundsen, J. Paulsen, I. Davidson, R. S. Liu, C. H. Shen, J. M. Chen, L. Y. Jang, J. F. Lee, *J. Electrochem. Soc.* 149 (2002) A431.
95. J. S. Kim, C. S. Johnson, M. M. Thackeray, *Electrochem. Comm.* 4 (2002) 205.
96. S. H. Kang, J. Kim, M. E. Stoll, D. Abraham, Y. K. Sun, K. Amine, *J. Power Sources* 112 (2002) 41.

Chapter 3

SYNTHESIS OF BATTERY MATERIALS

M. S. Whittingham

*Chemistry and Materials Science
State University of New York at Binghamton, Binghamton, NY 13902, U.S.A.*

3.1. INTRODUCTION

Synthesis is critical not only to the generation of new materials for exploration of new structures and fundamental properties, but also for the formation of materials with the optimum electrochemical behavior for commercial devices. The technique used is quite often very different for the above two cases. The initial synthesis of a material should provide it in a pure enough state that its intrinsic behavior and properties can be determined; it should for example be possible to accurately determine whether its structure is cubic spinel, layered or some other form. There is presently much confusion in the literature because the synthesized material was insufficiently well-characterized. Once well characterized, the material needs to be synthesized in a form suitable to be used in a battery, for example it may be doped or coated to enhance the conductivity, its particle size and morphology will be optimized for maximum reactivity but minimum corrosivity and side-reactions.

Many battery materials are metastable phases, and therefore non-traditional synthesis methods must be devised to allow kinetics to over-ride thermodynamics. Hence, many soft chemistry techniques have come to the fore such as hydrothermal, ion-exchange, intercalation, etc. In addition, to optimize the formation of the desired material frequently the reactants are finely mixed prior to final reaction by for example sol-gel formation or co-precipitation as hydroxides.

A number of critical synthetic parameters will be discussed in this chapter. The temperature of formation of the electrode material determines the defect structure, for example in all the layered structures strict ordering of the cations is desired. Thus, in TiS_2 no titanium must reside in the lithium sites or diffusion is limited. This restricts the final firing temperature to a

maximum of 600°C, otherwise there is significant titanium occupancy in the van der Waals layer. A similar behavior is observed in the layered metal oxides, such as LiNiO_2 , $\text{LiNi}_{1-y}\text{Mn}_y\text{O}_2$ and LiMnO_2 . In the nickel oxides it is typical to find about 7% nickel occupancy on the lithium sites. In the formation of layered Li_xMnO_2 , great care must be taken to avoid temperatures over 100°C otherwise manganese migrates converting the material to the spinel phase. For the mixed metal oxides, the temperature of synthesis has a marked effect on the reversible capacity of the electrode. Even in materials such as LiFePO_4 , the temperature of formation is key; too low a temperature and some of the iron migrates to the lithium sites.

The synthesis and manufacture of battery materials will be discussed by looking at a series of examples of materials that have moved from curiosity to research to development. Amongst these the concept of intercalation reactions from the 1970's will be considered, high temperature reactions, followed by hydrothermal and ion-exchange reactions, then a range of synthetic methods for conductively coating the lithium iron phosphate class of material. Finally, the synthesis of anode materials will be discussed.

Although cost is not critical in the research phase of a project, it is critical for the cost-effectiveness of batteries, that not only the electrode materials be themselves low cost, but that the process costs for synthesizing the materials also be low in cost.^{1,2}

3.2. THE SYNTHESIS AND MANUFACTURE OF TITANIUM DISULFIDE

When a battery is being commercialized, the synthesis process used in the laboratory often cannot be used because of the processing costs or cost of the starting materials. As an example, titanium disulfide will be considered where in the laboratory bulk titanium was used to provide electronic grade titanium disulfide, and sponge titanium provided research battery grade material. The latter could be produced a pound at a time in silica tubes, had a surface area of 5 m²/g, and allowed current densities of 10 mA/cm² to be achieved. However, both involved reaction with sulfur, which took from hours for the sponge to days for the bulk metal. Such material would cost more than \$100/lb. An inspection of the commercial process, shown in Figure 3.1, for sponge manufacture revealed that the precursor was titanium tetrachloride, a liquid at room temperature. This tetrachloride is available in tonnage quantities as it is used in the manufacture of titanium dioxide paint pigment. Therefore, a manufacturing process was devised by two european companies that involved the formation of stoichiometric TiS_2 by deposition

from the gas phase reaction of TiCl_4 with H_2S . This produced a sulfide with a morphology with many plates growing in three dimensions from a single central point, which shows excellent electrochemical behavior.

The stoichiometry and ordering of the titanium is critical to the electrochemical behavior of TiS_2 . Stoichiometric and ordered TiS_2 has been shown to exist³ if the temperature is kept below 600°C , and to have metallic conductivity.⁴ The titanium disorder can be readily measured by attempting to intercalate weakly bonding species such as ammonia or pyridine. In practice a slight excess, $\leq 1\%$, is beneficial in that it reduces the corrosiveness of the sulfur without significantly impacting the cell potential or the lithium diffusion coefficient. It is preferable to add this extra metal to the initial reaction medium.

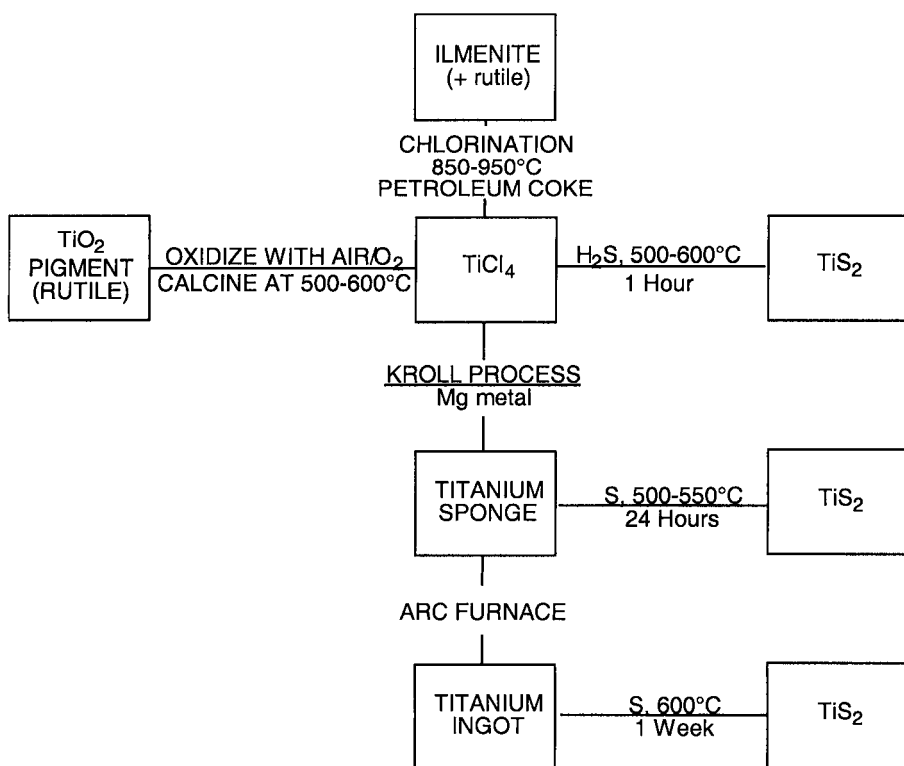


Figure 3.1. Synthesis and manufacture of titanium and titanium disulfide.

3.3. SYNTHESIS OF ALKALI ION INTERCALATES BY INSERTION INTO THE HOST LATTICE (AND THE REVERSE)

Although the heavier alkali intercalates of the transition metal oxides and chalcogenides had been extensively studied,^{5,6} the lack of a suitable lithiating agent delayed the formation and characterization of the pure lithium compounds until the early 1970's. Although lithium had been inserted by dissolution in liquid ammonia,^{7,8} this also resulted in the insertion of the ammonia, resulting in degradation of the host lattice as the sulfide or oxide layers must all shift relative to one another as indicated in Figure 3.2.⁹ In contrast when lithium is inserted by electro-intercalation,^{10,11} from butyl lithium in hexane,¹²⁻¹⁴ or from mercury amalgams no solvent is incorporated and the lattice simply expands. Just as in the case of ammonia solutions, lithium can also be incorporated from aqueous solutions either chemically or electrochemically,^{10,11,15,16} then the water must be removed. The many synthetic procedures possible for the layered dichalcogenides are shown schematically in Figure 3.3.⁹

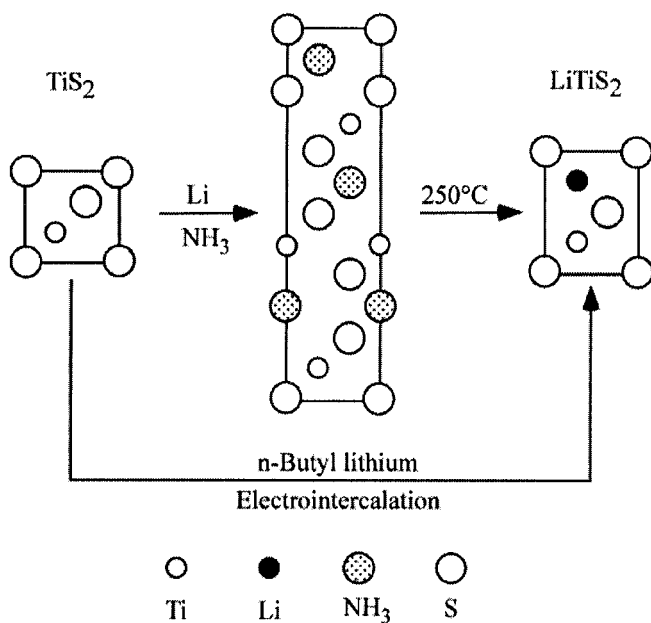


Figure 3.2. 110 projections of the structural changes occurring during the lithiation of titanium disulfide in the presence and absence of a co-intercalating solvent such as ammonia.⁹

Many materials of interest do not exist as the thermodynamically stable phase in the desired structure, and so must be prepared at low temperatures where kinetics control the path of the reaction rather than thermodynamics. For example, the stable phase of titanium disulfide is the layered structure for Li_xTiS_2 for $0 \leq x \leq 1$ and batteries can be built in either the charged state $\text{Li} // \text{TiS}_2$ or in the discharged state $\text{C} / \text{LiTiS}_2$.¹⁷ In contrast, although the layered sulfides LiVS_2 and LiCrS_2 were well-known their lithium free analogs were not, and so researchers at Bell Labs synthesized them by de-intercalation of the fully lithiated compounds.¹⁸ They developed a full range of chemical lithiating and delithiating agents.¹⁹ As noted above, the layered hexagonal close-packed form of TiS_2 is the thermodynamically stable phase; however a number of researchers²⁰⁻²² successfully synthesized the cubic form by de-intercalation of, for example, the spinel CuTi_2S_4 . This cubic structure can also be reversibly intercalated with lithium, although the diffusion coefficient is not as high as in the layered form.

The more ionic transition metal dioxides are not readily formed as layer structures in the absence of cations between the MO_2 layers, other phases being more stable such as in TiO_2 where a range of phases such as rutile, anatase and brookite are known but layered TiO_2 is not. Goodenough and co-workers, whilst investigating the magnetic behavior of LiCoO_2 recognized that it might be possible to also form a layered compound, analogous to the sulfides by lithium removal.²³ They successfully formed a layered Li_xCoO_2 by lithium de-intercalation and showed that this material could reversibly incorporate lithium over at least a range of ∂x of around 0.6. This led to the first commercially successful lithium secondary battery by Sony.²⁴ The lithium cobalt oxides can be readily prepared by the high temperature firing of materials containing lithium and cobalt in the appropriate ratio in an oxidizing environment. Amatucci *et al.*²⁵ more recently showed that all the lithium can be removed giving CoO_2 , which has the same 1T structure as TiS_2 .

A number of the layered dichalcogenides and oxides can incorporate a second lithium ion forming the phase Li_2MX_2 . This was first observed for vanadium diselenide,^{14,26} and can be accomplished either electrochemically or chemically, for example by using butyl-lithium. Li_2NiO_2 was formed²⁷ both electrochemically and chemically using lithium benzophenone in tetrahydrofuran; its structure switches from the 3R- LiNiO_2 phase to one identical to those of Li_2TiS_2 and Li_2VSe_2 , where the lithium ions sit in all the tetrahedral sites between the NiO_2 sheets forming a 1T structure. In a similar manner $\text{Li}_2\text{Mn}_{0.5}\text{Ni}_{0.5}\text{O}_2$ has also been synthesized in electrochemical cells, and both lithium ions can be cycled when part of the Mn is substituted by titanium.²⁸

Another innovative synthetic approach was developed by Haering²⁹ who showed that 2H-MoS_2 , where the molybdenum is in trigonal prismatic

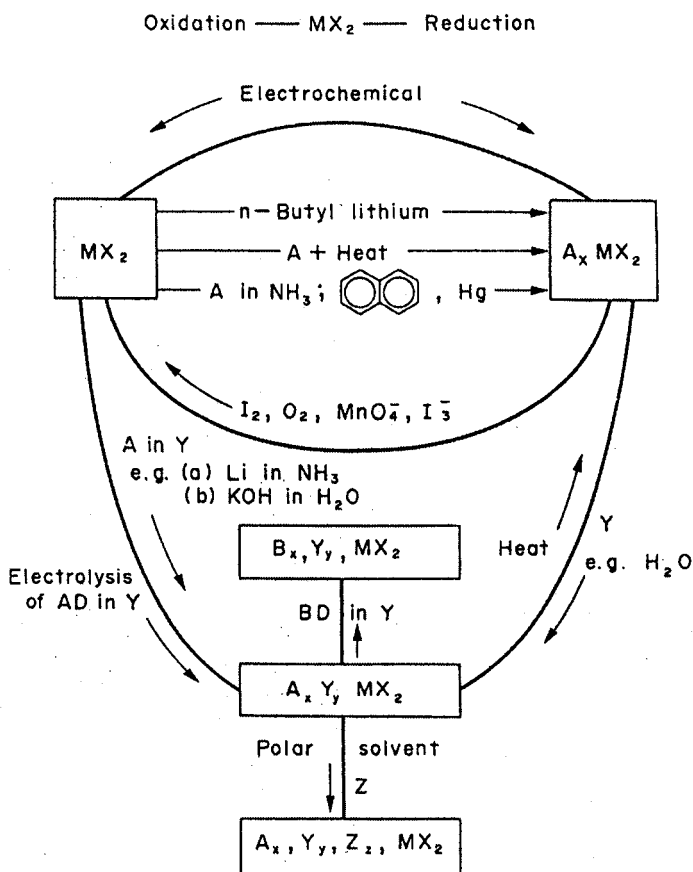


Figure 3.3. Schematic of the reactions of the dichalcogenides.⁹

coordination, could be induced to change structure to the 1T TiS_2 form by incorporation and then removal of lithium. This structural form showed much improved cyclability over the 2H form which is poorly reversible, and was the basis of the MoliEnergy MoS_2 lithium battery.³⁰

3.4. HIGH TEMPERATURE SYNTHESIS OF LAYERED OXIDES

The layered compound $LiCoO_2$ is made by the high temperature reaction in air of the carbonates at 900°C .²³ A number of other layered lithium metal dioxides, such as $LiNiO_2$ can also be formed by high temperature synthesis, but in this case there is significant nickel disorder so

that the lithium layer always contains some nickel,³¹ seven to ten % being quite typical. In contrast there is no measurable cobalt in the lithium layer when LiCoO_2 is formed at the optimum temperature. However, there is the possibility of forming spinel-like (some Co in the Li layer) or the spinel phase,³² sometimes known as LT-LiCoO_2 ,³³ when lower temperatures such as 400°C are used in the synthesis. It is not easy to distinguish between the layered and spinel forms of these layered oxides, as the X-ray diffraction patterns look almost identical at a first look. A clue to spinel formation is the c/a ratio, which is around 4.90 for the spinel, while it is closer to 5.00 for the rhombohedral layer structure; both have cubic close-packed oxygen lattices for which the ideal c/a ratio is 1.633 ($= 4.90/3$). A second clue to pure layered formation, which results from the non-ideal close packing in the layered structure, is the existence of a doublet in the X-ray powder pattern at around $66^\circ 2\theta$ associated with the 108 and 110 reflections; the spinel has a single reflection, the 440, in this region for $\text{CuK}\alpha$ radiation. The $\text{LT-Li}_x\text{Co}_{1-y}\text{Ni}_y\text{O}_2$ phases, also formed at 400°C , were found to have spinel-like structures where there is partial occupancy of the lithium sites by the transition metal ions.³⁴

The synthesis of LiCoO_2 requires firing at temperatures from $850 - 1000^\circ\text{C}$ for one to two days. However, such high temperatures may not be necessary. For example, ion exchange between CoOOH and excess LiOH results in pure LiCoO_2 after firing to 280°C to remove residual carbonate and hydroxide.³⁵ This ion-exchange was carried out in the solid state at 100°C with just a trace of water added as a transport agent. HT-LiCoO_2 was formed as evidenced by the doublet at $66^\circ 2\theta$, the c/a ratio of 5.00 and the electrochemical fingerprint. The success of the synthesis in this case can be associated with the structure of the starting reagent, CoOOH , which is layered and does not change under the low-temperature ion-exchange conditions. The electrochemical behavior was quite good, but the capacity was less than that of the high temperature formed LiCoO_2 ; it was suggested that there is some cobalt disorder, some of the lithium sites being occupied. LiNiO_2 was similarly synthesized³⁵ but no electrochemical or nickel ordering data were presented, but the rather broad X-ray lines suggest significant lattice disorder. LiCoO_2 formed hydrothermally at 230°C from cobalt nitrate, lithium hydroxide and hydrogen peroxide, had rather poor cycling characteristics, the capacity dropping by more than 70% over 20 cycles at a $\text{C}/2$ rate.³⁶

The spinel LiNi_2O_4 is also known, being formed³⁷ when $\text{Li}_{0.5}\text{NiO}_2$ formed by electrochemical removal of lithium from LiNiO_2 is annealed at 200°C ; this structural conversion begins at 150°C just as observed for layered $\text{Li}_{0.5}\text{MnO}_2$.³⁸ The coalescence of the 108 and 110 X-ray reflections is readily observed. This spinel is only stable until 300°C , when it decomposes into a mixture of products.³⁷ As noted above, neither NiO_2 nor CoO_2 has

been synthesized directly because of their thermodynamic instability. In the case of NiO_2 , the oxygen partial pressure is well over one atmosphere at 25°C , so it is inherently unsafe even under oxidizing conditions. In an attempt to reduce the possibility of explosive interactions with the electrolyte, additional elements can be used to partially replace the nickel. For example, addition of a trivalent ion such as boron or aluminum prevents the complete removal of all the lithium thus limiting the overall average oxidation state of the nickel. Alternatively, part of the nickel may be replaced by for example cobalt as in $\text{LiNi}_{1-y}\text{Co}_y\text{O}_2$, which forms a continuous solid solution. A combination of these two approaches has been extensively studied, as in $\text{LiNi}_{0.85}\text{Co}_{0.1}\text{Al}_{0.05}\text{O}_2$ ^{39,40} and $\text{LiNi}_{0.80}\text{Co}_{0.15}\text{Al}_{0.05}\text{O}_2$.⁴¹ The $\text{LiNi}_{1-y}\text{Co}_y\text{O}_2$ phases have been prepared^{42,43} by the direct reaction of Li_2CO_3 , NiO and Co_3O_4 . A finely ground mixture of the reagents is first fired at 500°C for a few hours, followed by 48 hours in oxygen at $800\text{--}1000^\circ\text{C}$. A solid solution is found over the entire range of y from 0 to 1.

Manganese has also been substituted in the cobalt oxide, $\text{LiCo}_{1-y}\text{Mn}_y\text{O}_2$ for $0 < y \leq 0.2$ using a combinatorial approach starting from an aqueous solution of lithium hydroxide, cobalt acetate and manganese acetate, followed by firing at 730°C ;⁴⁴ the lattice parameter perpendicular to the planes was found to expand with increasing manganese content. At higher manganese contents, second phases begin to be observed.

Spahr *et al.*⁴⁵ showed that the replacement of some of the nickel in LiNiO_2 by manganese also served the same purpose as cobalt in improving the cyclability and capacity of the nickel oxide electrode. They found that the composition $\text{LiNi}_{0.5}\text{Mn}_{0.5}\text{O}_2$ was optimum. The synthesis of the logical next step, $\text{LiNi}_{1-y-z}\text{Mn}_y\text{Co}_z\text{O}_2$ will be discussed below under manganese oxides.

Grenier *et al.*⁴⁶ have shown that oxygen can be electrochemically intercalated from strong basic electrolytes into some superconducting materials, thus increasing the oxidation state of the transition metal. If this technique can be extended to organic electrolytes at room temperature then it would be very useful in increasing the cell potential and possibly the capacity of cathode materials; the importance of such an oxidation was shown when the capacity of $\text{N}(\text{CH}_3)_4\text{V}_3\text{O}_7$ was tripled when it was oxidized to $\text{N}(\text{CH}_3)_4\text{V}_3\text{O}_8$.⁴⁷ Such oxidations must be performed below the decomposition temperature of the compound. A similar behavior has been observed in the formation of hexagonal MoO_3 by the thermal decomposition of its hydrate, $\text{MoO}_3 \cdot 0.6\text{H}_2\text{O}$, formed by ion-exchange of the sodium form using 6M nitric acid;⁴⁸ this molybdenum oxide reacts reversibly with about 1.5 Li/MoO_3 ⁴⁹ similar to that of MoO_3 itself.

3.5. HYDROTHERMAL AND SOLVOTHERMAL SYNTHESIS OF CATHODE MATERIALS

In this synthetic method, the reactants are dissolved in water or another solvent and then heated above the boiling point of the solvent for the desired length of time. The heating may be performed in either a conventional oven or in a microwave oven. This process is used commercially for a number of materials, including zeolites in tonnage quantities daily.

Although the technique has been used for several decades, it is only in the last ten years that much effort has been focused on transition metal compounds for battery electrode use. The early work has been reviewed^{50,51} and emphasized many tungsten, molybdenum and vanadium oxides. Thin films of tungsten oxides for electrochromic or sensor applications can be formed *in-situ* in the hydrothermal reactor.⁵² Vanadium oxides in a wide range of morphologies have been formed hydrothermally,⁴⁷ including the electrochemically active nanotubes.⁵³⁻⁵⁶ The studies of vanadium oxides showed the critical role that pH plays in determining the structure. At high pH values, the structural building blocks contain predominantly VO₄ tetrahedra, at intermediate values VO₅ square pyramids, and under the most acidic conditions VO₆ octahedra.⁵⁷ As VO₄ tetrahedra are only stable in the +5 oxidation state, materials containing these are unsuitable candidates for cathodes. In contrast the VO₆ octahedra are stable over many oxidation states, +5 to +2, and so are much more likely to provide rechargeable cathode materials. Thus, the electrochemically active δ -V₄O₁₀ phases and xerogels are all made usually at pH values less than 3. The electrochemically active H₂V₃O₈ phase has also been synthesized solvothermally,⁴⁷ and shows good electrochemically behavior.

A number of layered structure manganese oxides, M_xMnO₂, where M=Li, Na or K have been synthesized by hydrothermal and other soft chemistry approaches. When KMnO₄ aqueous solutions are hydrothermally treated at 170°C, well-crystalline layered K_{0.27}MnO₂·nH₂O is formed.⁵⁸ The water may be readily removed by heating. In this reaction, KOH is also produced and oxygen gas evolved according to the equation:



The corresponding lithium and sodium manganese oxides have also been synthesized from the permanganate.^{38,59} The alkali content of these manganese oxide compounds is very dependent on the alkali metal and the reaction medium; thus, in water x in M_xMnO₂ is 0.47, 0.35 and 0.27 for Li, Na and K respectively. In these compounds the manganese site occupancy is close to unity, and about 0.6 Li/Mn can be readily cycled in lithium cells.

Addition of cobalt or nickel to the reaction medium, allows the partial substitution of the manganese. This substitution even at the 1 to 5% level, increases the electronic conductivity by two orders of magnitude,⁶⁰ and significantly improves the recyclability.⁶¹ Heating of the lithium compound converts it to the spinel phase; this conversion reaction begins even at 150°C, and is rapidly completed on heating to 400°C.³⁸

The hydrothermal treatment of λ - MnO_2 with 0.5 M LiOH or 4 M NaOH aqueous solutions at 170°C for 24 days leads to the formation of the "spinel" $\text{Li}_{0.63}\text{Mn}_{1.73}\text{O}_4 \cdot 0.4\text{H}_2\text{O}$ with $a=8.18$ Å and the layered $\text{Na}_{0.40}\text{MnO}_{2.15} \cdot 0.6\text{H}_2\text{O}$ respectively.⁶² If the LiOH solution is stronger than 1 M, then Li_2MnO_3 was formed.

Manganese dioxides can also be prepared using a sol-gel reduction of permanganate using a reductant such as sugar⁶³ or fumaric acid.⁶⁴ The sodium compound, $\text{Na}_{0.45}\text{MnO}_2 \cdot 0.6\text{H}_2\text{O}$, has been formed by the reduction of NaMnO_4 by oxalic acid formed in-situ followed by a 600°C anneal and a water oxidation.⁶⁵ The sodium ions can then be ion-exchanged by lithium plus transition metals.⁶⁵ After annealing at 300-600°C the material shows spinel-like characteristics and cycles well on the 3V plateau; the X-ray patterns are also best fitted by a cubic spinel structure with $a=8.129$ Å, consistent with a 600°C anneal of a $\text{Li}_{0.45}\text{MnO}_2$ composition.

The layered ranceite-type manganic acid, $\text{H}_y\text{Mn}_{1.8}\text{O}_2 \cdot n\text{H}_2\text{O}$, has been formed⁶⁶ following the method of Tsuji *et al.*⁶⁷ by the acid hydrolysis of KMnO_4 at 60°C. Ion exchange of the manganic acid for two weeks in a large excess of an equimolar solutions of 1M MCl and 1M MOH, where M=Li, Na or K, leads to the alkali compounds. The alkali metal contents of these materials are very similar to those formed in the one-step hydrothermal process described above, namely 0.42 Li, 0.33 Na and 0.26 K per formula unit. Although the acid is reported to have the 1T structure with $a=2.83$ Å and $c=7.55$ Å,⁶⁷ these compounds almost certainly have the same rhombohedral structure as found for the hydrothermal compounds,⁵⁸ but their poor crystallinity precludes an effective structural analysis.

The acid leaching of layered manganates formed at elevated temperatures, such as of NaMnO_2 , results in both ion exchange and partial oxidation.⁶⁸ The degree of reduction and ion-exchange is surprisingly inversely dependent on the acid strength, for example 1M HCl leads to $\text{Na}_{0.007}\text{H}_{0.13}\text{Mn}^{\text{III}}_{0.14}\text{Mn}^{\text{IV}}_{0.86} \cdot 0.6\text{H}_2\text{O}$ whereas 0.01M HCl leads to $\text{Na}_{0.004}\text{H}_{0.27}\text{Mn}^{\text{III}}_{0.27}\text{Mn}^{\text{IV}}_{0.73} \cdot 0.6\text{H}_2\text{O}$.

3.6. ION EXCHANGE METHODES FOR LITHIUM MANGANESE OXIDE SYNTHESIS

Many sodium and potassium transition metal oxides had been synthesized using standard high temperature methods in the 1970s and early 1980s. These included K_xMnO_2 ,⁶⁹ Na_xMnO_2 ,⁷⁰ K_xCoO_2 ,⁷¹ Na_xCoO_2 ,⁷² K_xCrO_2 ⁷³ and Na_xCrO_2 .⁷² The complete phase diagrams of these systems are now well understood. Much less was known about the corresponding lithium compounds, and indeed the corresponding $LiMnO_2$ compound cannot be synthesized at elevated temperatures.

Although ion-exchange methods had been used extensively in the synthesis of solid electrolytes, in particular of beta-alumina⁷⁴⁻⁷⁶ and beta"-alumina much less effort had been made to prepare lithium based cathodes using ion-exchange until the 1990s. As noted above, layered $LiMnO_2$ cannot be synthesized at elevated temperatures because of its thermodynamic instability. Thus, a number of studies have been made on ion-exchanging the sodium analogs to the lithium form. Groups at Bordeaux^{77,78} and St. Andrews⁷⁹ showed simultaneously that layered $NaMnO_2$ could be readily exchanged to the layered form of $LiMnO_2$. In these experiments, the sodium compound is immersed in hot lithium salts dissolved in water-alcohol mixtures for periods of hours to days. Care has to be taken that the temperature is not too high, otherwise the spinel structure can be formed. Cobalt doped material has also been synthesized by the same approach of first preparing the sodium material followed by ion-exchange;^{80,81} these cobalt containing materials show much enhanced cycling⁸¹ even though they eventually convert to the spinel phase even for $LiMn_{0.5}Co_{0.5}O_2$.

The above layered $LiMnO_2$ phases have the same rhombohedral structure as the lithium, and other alkali phases formed by the hydrothermal decomposition of $LiMnO_4$,³⁸ and other permanganates.⁵⁸ However, these hydrothermal compounds have a lower alkali content, for example $Li_{0.5}MnO_2$ due to their initially being hydrates. A comparison for the potassium manganese oxides is given in Figure 3.4, which also distinguishes between the two high temperature regimes. Higher alkali contents can be obtained by carrying out the hydrothermal reactions under very high alkali hydroxide concentrations. The range of synthesis reactions and redox/intercalation reactions for the layered manganates are shown schematically in Figure 3.5. Doeff⁸²⁻⁸⁵ ion exchanged the $Na_{0.44}MnO_2$ tunnel structure⁸⁶ giving predominantly the lithium analog, which shows excellent cycling with no change of structure unlike the layered manganese dioxides. These results showed convincingly that a stable manganese dioxide can be formed. The cycling can be improved by replacing part of the manganese by titanium, but the rate capability is negatively impacted.^{87,88} Pure $Li_{0.44}MnO_2$ was prepared by ion-exchange,⁸⁹ and also showed excellent cycling.

Lithium iron oxides, such as the layered LiFeO_2 , have also been synthesized by ion exchange of the sodium compounds.⁹⁰ The sodium compound $\alpha\text{-NaFeO}_2$ was formed by hydrothermal treatment of FeOOH with a large excess of NaOH ($\text{Na}:\text{Fe} = 250$) at 220°C ; this sodium compound was then partially converted to the lithium compound by ion exchange

Hydrothermal

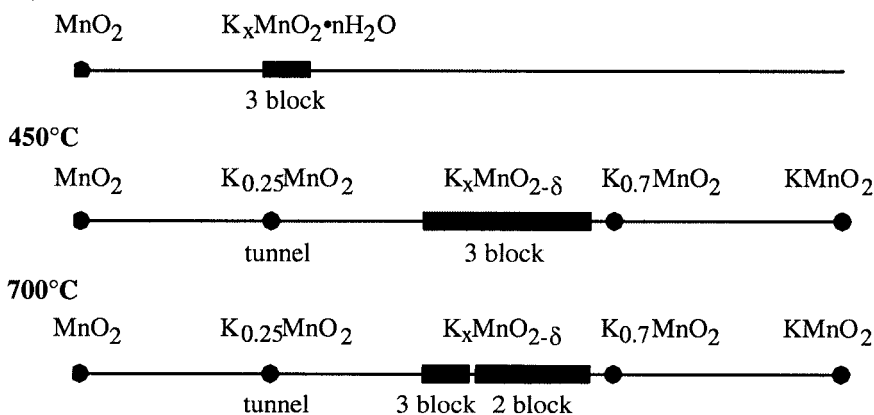


Figure 3.4. Composition of the potassium manganese oxides, both hydrothermal⁵⁸ and high temperature forms.⁶⁹

under hydrothermal conditions,⁹⁰ with 80% conversion in four hours at 140°C . Reaction between NaFeO_2 and molten lithium halides results in almost complete ion-exchange results in the formation of LiFeO_2 , but with a cubic lattice constant of 4.162 \AA indicating that the lithium and iron have become disordered giving a NaCl lattice.⁹¹ Reducing the temperature by using a eutectic mixture of LiCl and LiNO_3 resulted in the formation of a spinel phase. An extensive study of the formation of lithium-iron-oxygen phases failed to synthesize the layered LiFeO_2 compound.⁹² However, Shirane *et al.*⁹³ reported the formation of "layered" LiMnO_2 which consisted of the layered $\alpha\text{-NaFeO}_2$ phase and a spinel phase; they synthesized this by ion exchange of $\alpha\text{-NaFeO}_2$ in a LiCl/KCl molten salt at 400°C .

The electrochemically active vanadium oxide nanotubes are also synthesized by ion exchange from the initially formed alkylammonium tubes, giving the sodium⁵⁵ or manganese⁵⁶ compound.

3.7. STABILIZATION OF LAYERED LiMnO_2 AND THE MIXED METAL OXIDES $\text{Li}(\text{Ni}, \text{Mn}, \text{Co})\text{O}_2$

Although layered LiMnO_2 would be an ideal cathode material, it is unstable relative to spinel formation and so the structure must be stabilized. The layered form and the spinel form have essentially the same structure as each other with cubic close packing of the oxygen as discussed above for LiCoO_2 . The difference lies in the atomic positions the manganese ions occupy. Thus, a means must be found to prevent the manganese from

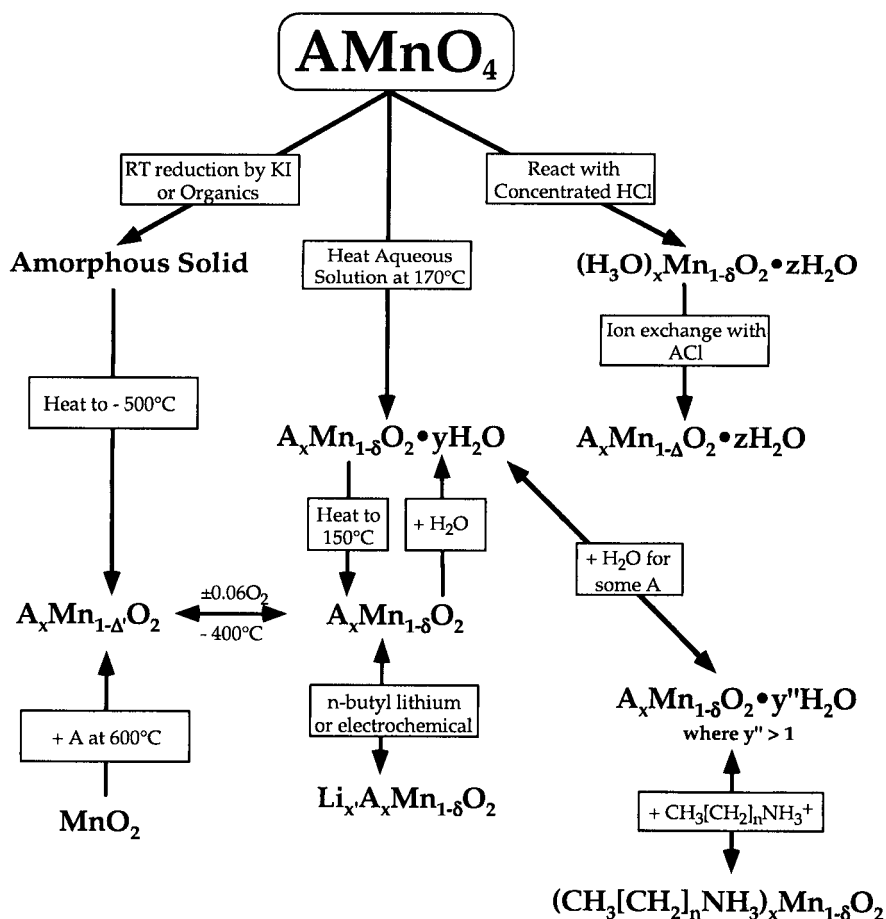


Figure 3.5. Schematic showing the synthesis, redox and intercalation reactions for MnO_2 .

diffusing. There are two distinct ways of doing this: geometric and electronic stabilization of MnO_2 layers. In the former, the structure is prevented from going to ccp, for example by placing pillars between the MnO_2 sheets, or by using a none ccp structure, such as a two-block structure. Here, one is trying to defeat thermodynamics by making the transformation difficult – kinetically controlled reaction. In the latter, the manganese is made to be more cobalt-like by doping the lattice with a transition metal to the right of cobalt such as nickel. Whichever way is chosen presents a synthetic challenge, as in many cases a metastable structure must be formed.

In the geometric approach, cations larger than lithium must be inserted between the sheets. The potassium manganese oxides, described above, where the potassium ions are in trigonal prismatic sites thus breaking-up the oxygen ccp are readily formed at elevated temperatures or by hydrothermal techniques (see Figure 3.4). Though potassium enhances the cyclability, these ions eventually diffuse out of the lattice and it reverts to a spinel structure. Thus, immobile ions must be inserted into the lattice, between the sheets. Vanadium oxide pillars, probably V-O-V groups, were successfully inserted using a combination of ion-exchange resins to form the starting material followed by hydrothermal reaction;⁹⁴ the structure is believed to be similar to that of the pillared $\text{Zn}_3(\text{OH})_2\text{V}_2\text{O}_7 \cdot 2\text{H}_2\text{O}$.⁹⁵ This vanadium pillared structure was stable and did not convert to spinel even at 5 volts; however, the rate characteristics were poor relative to LiMnO_2 itself. Leroux *et al.*⁹⁶ synthesized a similar Ranceite based compound, which also was stable but again had poor rate capabilities.

The second geometric approach again aims to prevent the formation of a ccp lattice,⁹⁷ by forming a LiMnO_2 in which the oxygen layer stacking is no longer the three-block $|\text{AB}|\text{CA}|\text{BC}|\text{AB}|$ structure, but for example is the two-block $|\text{AB}|\text{CB}|\text{AB}|$ structure or even the hexagonal close-packing found in LiTiS_2 or in CoO_2 . As none of these structures are stable for lithium at high temperatures, the sodium or potassium compounds must first be synthesized by standard high temperature techniques; these may then be ion-exchanged to give the corresponding lithium compound as discussed above. The initial composition of the sodium or potassium compound may be varied to give a wide range of stacking opportunities (see Figure 3.4); moreover, in all the potassium compounds and in some of the sodium compounds the alkali cation is in trigonal prismatic coordination; as the lithium ion must be in octahedral coordination, there will be sliding of the MnO_2 layers leading to still further stacking opportunities. All these structures are inherently thermodynamically metastable, as the MnO_2 sheets can slide relative to one another and the manganese ions are quite mobile.

In the electronic stabilization approach, the goal is to make the manganese look electronically more like cobalt where the layer structure is the thermodynamically stable phase, for example by doping with nickel.⁹⁸

Indeed, the mixed phase $\text{LiNi}_{1-y}\text{Mn}_y\text{O}_2$, can be readily synthesized for $y \leq 0.5$.⁹⁹ The composition $\text{LiNi}_{0.5}\text{Ni}_{0.5}\text{O}_2$, which is isoelectronic with LiCoO_2 , shows the optimum electrochemical behavior in the mixed nickel-manganese system,⁴⁵ and its electrochemical profile is very similar to that of LiNiO_2 . These compounds were synthesized by firing the monoxides of nickel and manganese with $\text{LiOH} \cdot \text{H}_2\text{O}$ after mechanical grinding.⁹⁹ As discussed above, the LiNiO_2 - LiCoO_2 system is completely miscible, and 20% of the cobalt can be substituted by manganese giving $\text{LiCo}_{0.8}\text{Mn}_{0.2}\text{O}_2$.⁴⁴ The logical next step was the synthesis of the system, $\text{LiNi}_{1-y-z}\text{Mn}_y\text{Co}_z\text{O}_2$.^{100,101} These compounds are best formed by mixing the metals in aqueous solution, from which the hydroxides are precipitated before being fired at between 700 and 1000°C in air. Just as with most of the other layered compounds, the synthesis conditions are important in determining the metal ordering and in the subsequent electrochemistry. Figure 3.6 shows the effect of firing temperature on the electrochemical capacity of the composition, $\text{LiNi}_{0.4}\text{Mn}_{0.4}\text{Co}_{0.2}\text{O}_2$.¹⁰²

The synthesis of the spinel LiMn_2O_4 will not be specifically discussed here. It is readily synthesized by the solid state reaction of stoichiometric quantities of Li_2CO_3 and MnO_2 .^{103,104} A number of anneals at around 800°C are necessary to produce the optimum electrochemical material.

3.8. ADDITION OF CARBON CONDUCTIVE DILUENTS POST SYNTHESIS AND *IN-SITU*: LiFePO_4

Many cathode materials, unlike the metallic conducting TiS_2 , must be admixed with a conductive diluent for use as a cathode. The challenge in these cases is to obtain an intimate mixture and contact between the active cathode, the conductive diluent, and the electrolyte as it is only at this three-phase contact that reaction can occur. Thus, it is invariably best to try and make the cathode material itself electronically conductive so that the reaction can occur at the two phase contact between cathode and electrolyte. This diluent can either be added post the electrode material synthesis or during the actual synthesis. Carbon black has been used in the synthesis of a number of vanadium oxides,^{105,106} where it was found to significantly reduce the polarization in cycling cells; the vanadium oxide is described as being coated onto the carbon with an 8 wt% carbon loading. Carbons have been extensively studied in the case of lithium iron phosphate where a reducing atmosphere is necessary during the synthesis process to prevent the oxidation of ferrous to ferric. This material, LiFePO_4 , will be discussed in some detail

here as it exemplifies well a number of synthesis procedures, some of which work and others that are less successful.

Lithium iron phosphate, LiFePO_4 , has been reported¹⁰⁷ to be an excellent cathode but with high a resistivity that limits the capacity to around 0.6 lithium. This material is normally synthesized by the high temperature heating of lithium, iron and phosphate materials for example lithium acetate, iron oxalate and ammonium phosphate. Such salts can be first dissolved making an aqueous solution that can be dehydrated forming a gel with the reactants in atomic contact with one another. This material is then fired under an inert gas, to prevent oxidation of ferrous to ferric, at

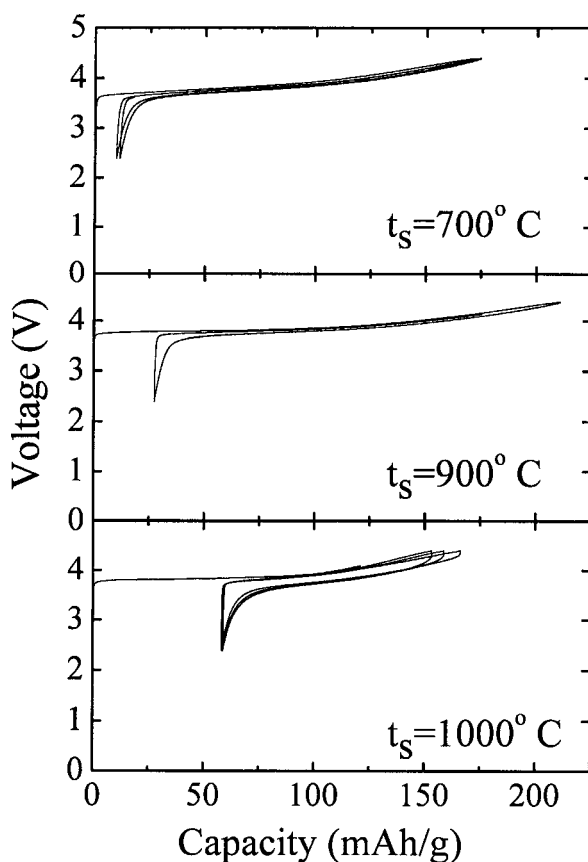


Figure 3.6. Effect of synthesis firing temperature on the electrochemical capacity of $\text{LiNi}_{0.4}\text{Mn}_{0.4}\text{Co}_{0.2}\text{O}_2$.¹⁰²

between 600 and 900°C forming LiFePO_4 . Such material has been well-characterized,¹⁰⁸ and has lattice parameters of $a=10.329 \text{ \AA}$, $b=6.007 \text{ \AA}$, $c=4.691 \text{ \AA}$ and volume = 291.0 \AA^3 . LiFePO_4 can also be synthesized by a variety of other techniques, including hydrothermal^{109,110} and microwave.

In the hydrothermal process, lithium acetate, ferrous oxalate and phosphoric acid dissolved in water are heated at around 120°C for up to 5 hours.¹¹⁰ The reaction was found to be complete in much less than an hour. It can also be carried out under microwave heating. However, X-ray analysis showed that there is some iron on the lithium sites which restricts the rate of lithium insertion and removal,¹¹¹ making the hydrothermal approach unsuitable for LiFePO_4 synthesis. Such disordering can be recognized from the lattice parameters, $a=10.403 \text{ \AA}$, $b=6.023 \text{ \AA}$, $c=4.726 \text{ \AA}$ and volume = 294.4 \AA^3 , which are significantly larger than the ordered material. A high temperature anneal appears to be necessary to cause the ordering of the lithium and iron atoms. A recent report on the microwave processing¹¹² of LiFePO_4 would seem to have the same problem, as indicated by the rather low electrochemical capacity even at elevated temperatures.

The original publication on the LiFePO_4 electrode suggested that the high resistivity of the material was the cause of the rather low electrochemical capacity, around 0.6 Li/Fe. Several efforts were directed at improving the effective electronic conductivity, including modifying the synthesis process so that a conductive coating is formed at the time of synthesis – *in-situ* coating. Such approaches have been used in the case of vanadium oxides. Ravet *et al.*^{113,114} proposed firing the initial reactants with carbonaceous materials such as sugar, so as to form a carbon coating thus enhancing the overall conductivity of the composite so formed. These composites allowed almost complete utilization of the lithium. Even more impressive results were obtained when a carbon gel was fired with the reactants,¹¹⁵ leading to complete utilization of the LiFePO_4 at 5 mg/cm^2 loadings. Masquelier¹¹⁶ showed the effectiveness of ball-milling carbon with LiFePO_4 in giving complete capacity at elevated temperatures. A comparative study of the effect of synthesis/coating procedure, including *in-situ* carbon gel, sugar and aqueous gel¹¹⁷ versus post synthesis coating using a wide range of techniques suggested that the coating procedure is not particularly important¹¹⁸ at high cathode loadings, $20 - 70 \text{ mg/cm}^2$. However, the addition of carbon at high levels is very deleterious to the already low volumetric energy density of the LiFePO_4 cell.¹¹⁹ What may be just as critical as the coating process, is the nature of the material formed, including its particle size and absence of ferric material and unlithiated phosphate so as to enhance the lithium ion diffusivity.

An alternative to the *in-situ* coating of the lithium iron phosphate during the synthesis of the cathode material is to actually modify the intrinsic electronic conductivity of the phosphate itself by doping the lattice as

described above for the layered manganese oxides.⁶⁰ Chiang *et al.*¹²⁰ have doped the lattice with for example 1 wt% niobium and showed that the resistance is reduced from around 10^9 ohm-cm in very pure LiFePO_4 to around 10^2 ohm-cm. The very low doping levels have a surprisingly large impact; the material is black, but there are apparently some carbonaceous residues present. The electrochemical capacity is around 80% at 0.4 mA/cm^2 for a 2.5 mg/cm^2 loading, significantly lower than that from the carbon gel coatings.¹¹⁵ The resistance of regular battery grade LiFePO_4 formed from reagent grade chemicals is around 10^5 - 10^6 ohm-cm,¹¹⁸ not significantly different than that of undoped manganese oxide.⁶⁰ The impact of synthesis procedure on the lithium ion conductivity is still not known and this might be just as critical if not more critical than the electronic conductivity.

3.9. SYNTHESIS OF ANODE MATERIALS

Lithium when used in the pure state is very prone to dendrite formation on electrolytic deposition, thus metal alloys have been investigated for more than 30 years in organic electrolytes. Dey first described¹²¹ the electrochemical formation in organic electrolytes of lithium alloys with a wide range of metals, including aluminum and tin. In these experiments, the cell was simply short-circuited externally or a 1 kohm external resistor was used so that the voltage profile with time could be followed. The compounds formed were shown to be same as those formed by high temperature metallurgical reaction. These intermetallic compounds are normally very brittle, so it is not easy to form an electrode out of them; thus Exxon in its LiAl/TiS_2 cells constructed the alloy anode *in-situ* by placing a sheet of lithium on top of the aluminum on cell construction. No reaction occurs until the electrolyte solution is added to the cell, immediately prior to cell closure. The formation and cycling behavior of the lithium aluminum alloys synthesized both electrochemically and thermally have been studied.¹²² Wang *et al.*¹²³ synthesized at high temperatures the lithium alloys of tin, antimony and bismuth in both a porous and dense state by melting the components together in molybdenum crucibles; they used these materials to determine the lithium diffusion coefficients and phase equilibria in organic electrolyte based cells.

Herold¹²⁴ first formed the alkali metal intercalation compounds of graphite, but the electrochemical formation of the lithium compound LiC_6 was complicated by the co-intercalation of the electrolyte solvent.^{125,126} Use of the solid electrolyte, polyethylene oxide, allowed the formation at 80°C of the solvent free sodium graphite compound NaC_{64} ; higher sodium content materials were not formed.¹²⁷ This shows the importance of choice of solvent in the synthetic process, or in the battery, where it may participate in the

reaction even if only as a solvating specie. This can be equally true for the cathode as for the anode. Thus, when propylene carbonate was used as the electrolyte solvent in the Li/TiS_2 cell, if a trace of water was present then propylene carbonate was co-intercalated with the lithium expanding the lattice three fold. The ether dioxolane was found to be a particularly effective electrolyte solvent for lithium batteries, not being co-intercalated and being very good for lithium electroplating.^{128,129} Such solvents were proposed for use with the lithium-graphite anode.¹³⁰ Carbon based anodes are now used in essentially all commercially lithium-ion batteries,¹³¹ and critical to their success is choice of solvent with ethylene carbonate being highly successful. Hard carbons rather than pure graphite are preferred for long cycle life and capacity.¹³² The batteries are constructed in the discharged state, and the lithium is electro-intercalated into the graphite on the first charge. Thus, the cathode material provides all the lithium for the anode, which means that excess anode cells are not constructed. Thus, any lithium side-reactions have an immediate negative impact on cell capacity. Fong *et al.*¹³³ showed that the graphite surface is coated with a protective film on the first synthesis of C_6Li which irreversibly consumes some of the lithium. This film is stable and so need not be reconstructed on each electrochemical cycle but it does permanently reduce the capacity of the battery. Hence, there is much interest in synthesizing other potential anode materials that have a higher capacity, and safer operation than graphite based compounds. The outstanding stability and rechargeability of graphite after the first cycle will be hard to surpass.

3.10. MECHANOCHEMISTRY AND MECHANICAL GRINDING

Much emphasis has therefore been placed on investigating other simple materials that might store lithium by a simple reaction around room temperature. A novel approach to the synthesis of new materials developed predominantly in Russia at the Institute for Solid State Chemistry and Mechanochemistry^{134,135} is that of mechanochemistry or mechanical alloying. In this approach physico-chemical transformations and chemical reactions of solids are induced by mechanical action. Although the grinding is typically performed at room temperature, the actual temperature at the particle contact is probably substantial. Although most scientists were skeptical initially about mechanochemistry the technique has now gained complete credibility.^{136,137} A number of anode materials have been synthesized by this technique, and carbon has been effectively coated onto LiFePO_4 .¹¹⁶ The precursor for LiFePO_4 has also been formed using mechanical grinding,¹³⁸ which allowed the formation of LiFePO_4 even at

400°C; the quality of the material in electrochemical cells has not been described.

A number of anode materials have been synthesized by mechanochemical reactions. Many intermetallic compounds have been proposed for anode use using different concepts, one where the structure of the intermetallic is at least in part retained during reaction with lithium such as Cu_6Sn_5 .^{139,140} A second approach is where the structure is destroyed but one component acts as a mechanical buffer and the other reacts with the lithium, an example might be Sn_2Mn . A third option is where a composite mixture of intermetallics is used.

The phase Cu_6Sn_5 phase is very well characterized, being formed at the interface when copper is soldered using tin based materials. It has been investigated as a potential lithium anode, and has been synthesized in a variety of ways. In a mechanochemical process, powders of tin and copper after hand-grinding were mixed and about 3-4 wt % of carbon was added as a solid lubricant prior to milling for 20 hours; purity of phase was shown by X-ray analysis.¹⁴⁰ On cycling lithium is inserted into this compound forming a Li_2SnCu like phase. Cu_6Sn_5 has also been prepared by reaction of copper and tin under argon at 400°C.¹⁴¹ An alternative synthesis approach has been reported by Tamura *et al.*¹⁴² They electrodeposited tin onto a copper foil, then annealed the foil at 200°C for 24 hours in vacuum to form Cu_6Sn_5 . The electrochemical behavior of some of these tin containing materials is compared in Figure 3.7, where it can be seen that the pure tin foil¹⁴³ retains the same capacity as the annealed Cu_6Sn_5 phase¹⁴² for the first ten cycles.

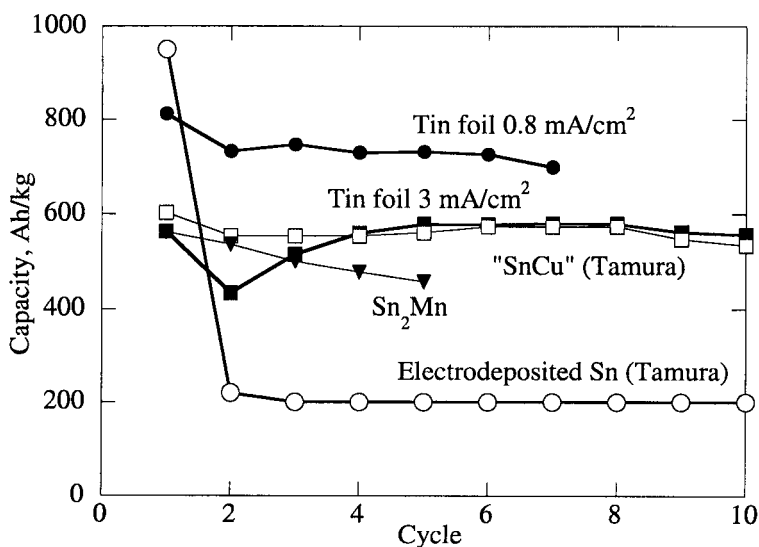


Figure 3.7. The electrochemical capacity of several tin based anodes, synthesized by different techniques.

The intermetallic InSb has also been prepared by ballmilling.¹⁴⁴ In this case indium and antimony metals in a 1:1 ratio were ballmilled in air at room temperature for 20 hours; after which the resulting powder was annealed under flowing argon at 400°C for 12 hours. This material had a capacity of 300 to 220 mAh/g for the 2nd to 20th cycle.

Mechanical alloying is particularly amenable to producing intermetallic alloys or mixtures of them. Mao *et al.*^{145,146} prepared composites of SnFe₂ and SnFe₃C. Powders of tin, iron and carbon were placed in hardened steel vials together with hardened steel balls; these were loaded in an argon environment, and then shaken for 20 hours. X-ray diffraction showed that the resulting grain size was about 10 nm. In this case only the SnFe₂ phase is electrochemically active, the carbide phase being the inert matrix; the cell capacity which exceeds 1500 mAh/cc (around 200 mAh/g) for 24% SnFe₂ can be enhanced by increasing the ratio of active component but it is at the expense of capacity retention. The same mechanical alloying process has also been used¹⁴⁷ to reduce the particle size of SnFe₂ formed by high temperature processes. A recent review of tin-based intermetallics details some of the other synthetic processes used.¹⁴⁸

ACKNOWLEDGEMENTS

This work was supported in part by the National Science Foundation and the US Department of Energy.

REFERENCES

1. L. H. Gaines, R. W. Francis, G. H. Newman, B. M. L. Rao, "Ambient Temperature Electric Vehicle Batteries Based on Lithium and Titanium Disulfide", in *11th Intersociety Energy Conversion Conference* (1976) 418. Stateline, Nevada.
2. L. Gaines, R. Cuenca, "Costs of Lithium-Ion Batteries for Vehicles", in *Argonne National Laboratory Report ANL/ESD-42*. 2000, Argonne National Laboratory, p. 57.
3. A. H. Thompson, F. R. Gamble, C. R. Symon, *Mater. Res. Bull.* 10 (1975) 915.
4. A. H. Thompson, *Phys. Rev. Lett.* 35 (1975) 1786.
5. M. Danot, A. L. Blanc, J. Rouxel, *Bull. Soc. Chim. France* (1969) 2670.
6. J. Rouxel, M. Danot, J. Bichon, *Bull. Soc. Chim. France* (1971) 3930.
7. W. Rudorff, *Chimia* 19 (1965) 489.
8. M. Danot, J. Rouxel, *Comptes Rendus Acad. Sc. Paris* C276 (1973) 1283.
9. M. S. Whittingham, *Prog. Solid State Chem.* 12 (1978) 41.
10. M. S. Whittingham, U. S. Patent 4040017 and U.K. Patent 1468244 (1973)
11. M. S. Whittingham, *J. Chem. Soc. Chem. Comm.* (1974) 328.
12. M. B. Dines, *Mater. Res. Bull.* 10 (1975) 287.
13. M. S. Whittingham, M. B. Dines, *J. Electrochem. Soc.* 124 (1977) 1387.
14. D. W. Murphy, F. J. DiSalvo, G. W. Hull, J. V. Waszczak, *Inorg. Chem.* 15 (1976) 17.
15. R. Schöllhorn, H. Meyer, *Mater. Res. Bull.* 9 (1974) 1237.

16. G. V. SubbaRao, J. C. Tsang, *Mater. Res. Bull.* 9 (1974) 921.
17. M. S. Whittingham, U.S. Patent 4009052 and U.K. Patent 1468416 (1973)
18. D. W. Murphy, J. N. Carides, F. J. DiSalvo, C. Cros, J. V. Waszczak, *Mat. Res. Bull.* 12 (1977) 825.
19. D. W. Murphy, P. A. Christian, *Science* 205 (1979) 651.
20. R. Schöllhorn, A. Payer, *Angew. Chem. Int. Ed.* 24 (1985) 67.
21. S. Sinha, D. W. Murphy, *Solid State Ionics* 20 (1986) 81.
22. J. B. Goodenough, A. Manthiram, B. Wnetrzewski, *J. Power Sources* 43-44 (1993) 269.
23. K. Mitzushima, P. C. Jones, P. J. Wiseman, J. B. Goodenough, *Mat. Res. Bull.* 15 (1980) 783.
24. K. Ozawa, *Solid State Ionics* 69 (1994) 212.
25. G. G. Amatucci, J. M. Tarascon, L. C. Klein, *J Electrochem Soc.* 143 (1996) 1114.
26. M. S. Whittingham, *Mater. Res. Bull.* 13 (1978) 959.
27. J. R. Dahn, U. v. Sacken, C. A. Michal, *Solid State Ionics* 44 (1990) 87.
28. C. S. Johnson, J.-S. Kim, A. J. Kropf, A. J. Kahaian, J. T. Vaughey, M. M. Thackeray, *Electrochem. Commun.* 4 (2002) 492.
29. M. A. Py, R. R. Haering, *Can. J. Phys.* 61 (1983) 76.
30. R. R. Haering, J. A. R. Stiles, K. Brandt, U. S. Patent 4,224,390 (1980)
31. J. N. Reimers, J. R. Dahn, *Phys. Rev. B* 46 (1992) 3236.
32. E. Rossen, J. N. Reimers, J. R. Dahn, *Solid State Ionics* 62 (1993) 53.
33. R. J. Gummow, M. M. Thackeray, W. I. F. David, S. Hull, *Mater. Res. Bull.* 27 (1992) 327.
34. R. J. Gummow, M. M. Thackeray, *J. Electrochem. Soc.* 140 (1993) 3365.
35. G. G. Amatucci, J. M. Tarascon, D. Larcher, L. C. Klein, *Solid State Ionics* 84 (1996) 169.
36. A. Burukhin, O. Brylev, P. Hany, B. R. Churagulov, *Solid State Ionics* 151 (2002) 259.
37. M. G. S. R. Thomas, W. I. F. David, J. B. Goodenough, *Mater. Res. Bull.* 20 (1985) 1137.
38. R. Chen, M. S. Whittingham, *J. Electrochem. Soc.* 144 (1997) L64.
39. S. Mudhavi, G. V. SubbaRao, B. V. R. Chowdari, S. F. Y. Li, *J. Power Sources* 93 (2001) 156.
40. S. Mudhavi, G. V. SubbaRao, B. V. R. Chowdari, S. F. Y. Li, *Solid State Ionics* 152 (2002) 199.
41. J. Liu, K. Xu, T. R. Jow, K. Amine, *Electrochemical Society Fall Meeting*, Salt Lake City (2002)
42. I. Saadoune, C. Delmas, *J. Materials Chemistry* 6 (1996) 193.
43. C. Delmas, I. Saadonne, *Solid State Ionics* 53-56 (1992) 370.
44. I. Yanase, T. Ohtaki, M. Watanabe, *Solid State Ionics* 151 (2002) 189.
45. M. E. Spahr, P. Novák, B. Schnyder, O. Haas, R. Nesper, *J. Electrochem. Soc.* 145 (1998) 1113.
46. J.-C. Grenier, M. Pouchard, A. Wettiaux, *Current Opinion in Solid State & Materials Science*, 1 (1996) 233.
47. T. A. Chirayil, P. Y. Zavalij, M. S. Whittingham, *Chem. Mater.* 10 (1998) 2629.
48. J. Guo, P. Zavalij, M. S. Whittingham, *Eur. J. Solid State Chem* 31 (1994) 833.
49. J.-D. Guo, P. Zavalij, M. S. Whittingham, *J. Solid State Chem* 117 (1995) 323.
50. M. S. Whittingham, *Current Opinion in Solid State & Materials Science*, 1 (1996) 227.
51. M. S. Whittingham, J. Guo, R. Chen, T. Chirayil, G. Janauer, P. Zavalij, *Solid State Ionics* 75 (1995) 257.
52. J. Guo, Y. J. Li, M. S. Whittingham, *J. Power Sources* 54 (1995) 461.
53. M. E. Spahr, P. Stoschitzki-Bitterli, R. Nesper, M. Müller, F. Krumeich, H. U. Nissen, *Angew. Chem. Int. Ed. Engl.* 37 (1998) 1263.
54. M. E. Spahr, P. Stoschitzki-Bitterli, R. Nesper, O. Haas, P. Novak, *J. Electrochem. Soc.* 146 (1999) 2780.
55. K. Edström, T. Gustafsson, S. Nordliner, *Electrochem. Solid-State Lett.* 4 (2001) A129.
56. A. Doble, K. Ngala, S. Yang, P. Y. Zavalij, M. S. Whittingham, *Chem. Mater.* 13 (2001)

- 4382.
57. P. Y. Zavalij, M. S. Whittingham, *Acta Cryst.* B55 (1999) 627.
58. R. Chen, P. Zavalij, M. S. Whittingham, *Chem Mater* 8 (1996) 1275.
59. R. Chen, T. Chirayil, M. S. Whittingham, *Proceedings of the 10th International Symposium on Solid State Ionics*, Singapore, December 1995. *Solid State Ionics* 86-88 (1996) 1.
60. P. Sharma, G. Moore, F. Zhang, P. Y. Zavalij, M. S. Whittingham, *Electrochem. Solid-State Lett.* 2 (1999) 494.
61. F. Zhang, M. S. Whittingham, *Electrochem. Solid-State Letters* 3 (2000) 309.
62. Q. Feng, H. Kanoh, Y. Miyai, K. Ooi, *Chem. Mater.* 7 (1995) 1226.
63. S. Ching, J. A. Landrigan, M. L. Jorgenson, N. Duan, S. L. Suib, C.-L. O'Young, *Chem. Mater.* 7 (1995) 1604.
64. S. Bach, M. Henry, N. Baffier, J. Livage, *J. Solid State Chem.* 88 (1990) 325.
65. S. Franger, S. Bach, J. P. Pereira-Ramos, N. Baffier, *J. Electrochem. Soc.* 147 (2000) 3226.
66. F. Leroux, D. Guyomard, Y. Piffard, *Solid State Ionics* 80 (1995) 299.
67. M. Tsuji, S. Komarneni, Y. Tamaura, M. Abe, *Mat. Res. Bull.* 27 (1992) 741.
68. Y. Omomo, T. Sasaki, M. Watanabe, *Solid State Ionics* 151 (2002) 243.
69. C. Delmas, C. Fouassier, *Z. Anorg. Allg. Chem.* 420 (1976) 184.
70. A. Mendiboure, C. Delmas, P. Hagenmuller, *J. Solid State Chemistry* 57 (1985) 323.
71. C. Delmas, C. Fouassier, P. Hagenmuller, *J. Solid State Chemistry* 13 (1975) 165.
72. C. Delmas, J.-J. Braconnier, C. Fouassier, P. Hagenmuller, *Solid State Ionics* 3/4 (1981) 165.
73. C. Delmas, M. Devalette, C. Fouassier, P. Hagenmuller, *Mat. Res. Bull.* 10 (1975) 393.
74. Y. Y. Yao, J. T. Kummer, *J. Inorg. Nucl. Chem.* 29 (1967) 2453.
75. M. S. Whittingham, R. A. Huggins, *J. Electrochem. Soc.* 118 (1971) 1.
76. M. S. Whittingham, R. A. Huggins, *NBS Special Publications* 364 (1972) 139.
77. C. Delmas, F. Capitaine, *8th IMLB* 8 (1996) 470.
78. F. Capitaine, P. Gravereau, C. Delmas, *Solid State Ionics* 89 (1996) 197.
79. A. R. Armstrong, P. G. Bruce, *Nature* 381 (1996) 499.
80. A. D. Robertson, A. R. Armstrong, A. J. Fowles, P. G. Bruce, *J. Mater. Chem.* 11 (2001) 113.
81. A. R. Armstrong, R. Gitzendanner, A. D. Robertson, P. G. Bruce, *Chem. Commun.* (1998) 1833.
82. M. M. Doeff, M. Y. Peng, Y. Ma, L. C. DeJonghe, *J. Electrochem. Soc.* 141 (1994) L145.
83. M. M. Doeff, T. J. Richardson, L. Kepley, *J. Electrochem. Soc.* 143 (1996) 2507.
84. M. M. Doeff, M. Y. Peng, Y. Ma, S. J. Visco, L. C. DeJonghe, US Patent 5,558,961 (1996)
85. M. M. Doeff, K.-T. Hwang, T. J. Richardson, L. C. DeJongue, *Electrochem. Soc. Proc.* 99-2 (1999) 184.
86. W. G. Mumme, *Acta Cryst.* B24 (1968) 1114.
87. M. M. Doeff, T. J. Richardson, K. T. Hwang, A. Anapolsky, *Electrochem. Soc. Proc.* 99-24 (2000) 48.
88. M. M. Doeff, T. J. Richardson, K.-T. Hwang, A. Anapolsky, *ITE Battery Lett.* 2 (2001) B.
89. A. R. Armstrong, H. Huang, R. A. Jennings, P. G. Bruce, *J. Mater. Chem.* 8 (1998) 255.
90. M. Tabuchi, C. Masquelier, T. Takeuchi, K. Ado, I. Matsubara, T. Shirane, R. Kanno, S. Nasu, H. Sakaebe, H. Okuyama, O. Nakamura, *Abstracts of the 10th Int. Conf. on Solid State Ionics*, Singapore, December 3-8 (1995) 197.
91. B. Fuchs, S. Kemmlersack, *Solid State Ionics* 68 (1994) 279.
92. M. Tabuchi, K. Ado, H. Sakaebe, C. Masquelier, H. Kageyama, O. Nakamura, *Solid State Ionics* 79 (1995) 220.
93. T. Shirane, R. Kanno, Y. Kawamoto, Y. Takeda, M. Takano, T. Kamiyama, F. Izumi, *Solid State Ionics* 79 (1995) 227.

94. F. Zhang, K. Ngala, M. S. Whittingham, *Electrochem. Commun.* 2 (2000) 445.
95. P. Y. Zavalij, F. Zhang, M. S. Whittingham, *Acta Cryst.* C53 (1997) 1738.
96. F. Leroux, A. L. G. L. Salle, D. Guyomard, Y. Piffard, *J. Materials Chem.* 11 (2001) 652.
97. M. S. Whittingham, *1996 USDOE BATT Annual Report* (1997)
98. R. Chen and M. S. Whittingham, *Proc. Annual Automotive Technology Development Customers Coordination Meeting*, DOE-OTT (Dearborn, MI, Oct. 27-30, 1997), III (1997) 301.
99. E. Rossen, C. D. W. Jones, J. R. Dahn, *Solid State Ionics* 57 (1992) 311.
100. T. Ohzuku, Y. Makimura, *Chem. Lett.* (2001) 642.
101. Z. Lu, D. D. MacNeil, J. R. Dahn, *Electrochem. Solid-State Lett.* 4 (2001) A200.
102. J. K. Ngala, N. A. Chernova, M. Ma, P. Y. Zavalij, M. S. Whittingham, *Chem. Mater.* 15 (2003) in press.
103. D. Guyomard, J. M. Tarascon, *J. Electrochem. Soc.* 139 (1992) 937.
104. J. M. Tarascon, W. R. McKinnon, F. Coowar, T. N. Bowmer, G. Amatucci, D. Guyomard, *J. Electrochem. Soc.* 141 (1994) 1421.
105. C. C. Torardi, C. R. Miao, M. E. Lewittes, Z. Li, *Electrochemical Society Proceedings*, 2000-21 (2000) 68.
106. C. C. Torardi, C. R. Miao, M. E. Lewittes, Z. Li, *J. Solid State Chem.* 163 (2002) 93.
107. A. K. Padhi, K. S. Nanjundaswamy, J. B. Goodenough, *J. Electrochem. Soc.* 144 (1997) 1188.
108. A. S. Andersson, B. Kalska, L. Häggström, J. O. Thomas, *Solid State Ionics* 130 (2000) 41.
109. M. B. Armand, *Personal Communication* (2001)
110. S. Yang, P. Y. Zavalij, M. S. Whittingham, *Electrochem. Commun.* 3 (2001) 505.
111. S. Yang, Y. Song, P. Y. Zavalij, M. S. Whittingham, *Electrochem. Commun.* 4 (2002) 239.
112. M. Higuchi, K. Katayama, Y. Azuma, M. Yukawa, M. Suhara, *J. Power Sources* (2003) in press.
113. N. Ravet, J. B. Goodenough, S. Besner, M. Simoneau, P. Hovington, M. Armand, *Electrochem. Soc. Abstracts*, 99-2 (1999) 127.
114. N. Ravet, S. Besner, M. Simoneau, A. Vallée, M. Armand, J.-F. Magnan, European Patent 1049182A2 (2000).
115. H. Huang, S.-C. Yin, L. F. Nazar, *Electrochem. Solid-State Lett.* 4 (2001) A170.
116. C. Masquelier, C. Wurm, M. Morcrette, J. Gaubicher, *Int. Meeting on Solid State Ionics*, Cairns, Australia, July 9-13, paper A-IN-06, (2001)
117. R. Dominko, M. Gaberscek, J. Drofenik, M. Bele, S. Pejovnik, *Electrochem. Solid-State Lett.* 4 (2001) A187.
118. S. Yang, Y. Song, K. Ngala, P. Y. Zavalij, M. S. Whittingham, *J. Power Sources* (2003) in press.
119. Z. Chen, J. R. Dahn, *J. Electrochem. Soc.* 149 (2002) A1184.
120. S.-Y. Chung, J. T. Bloking, Y.-M. Chiang, *Nature Materials* 1 (2002) 123.
121. A. N. Dey, *J. Electrochem. Soc.* 118 (1971) 1547.
122. B. M. L. Rao, R. W. Francis, H. A. Christopher, *J. Electrochem. Soc.* 124 (1977) 1490.
123. J. Wang, I. D. Raistrick, R. A. Huggins, *J. Electrochem. Soc.* 133 (1986) 457.
124. A. Hérol, *Bull. Soc. Chim. France* (1955) 999.
125. J. O. Besenhard, H. P. Fritz, *Electroanal. Chem. Interfac. Electrochem.* 53 (1974) 329.
126. J. O. Besenhard, *Carbon* 14 (1976) 111.
127. P. Ge, M. Foulletier, *Solid State Ionics* 28-30 (1988) 1172.
128. M. S. Whittingham, G. H. Newman, US Patent 4,086,403 (1976).
129. M. S. Whittingham, G. H. Newman, *J. Electrochem. Soc.* 128 (1981) 706.
130. S. Basu, US Patent 4,423,125 (1982).
131. M. Mohri, N. Yanagisawa, Y. Tajima, H. Tanaka, T. Mitate, S. Nakajima, M. Yoshida, Y. Yoshimoto, T. Suzuki, H. Wada, *J. Power Sources* 26 (1989) 545.

132. Y. Nishi, in: M. Wakihara and O. Yamamoto (Eds.), *Lithium Ion Batteries*, Kodansha, Tokyo, 1998, p. 181.
133. R. Fong, U. v. Sacken, J. R. Dahn, *J. Electrochem. Soc.* 137 (1990) 2009.
134. V. V. Boldyrev, *Experimental Methods in Mechanochemistry of Inorganic Solids*, 1986, Novosibirsk. Nauka (in Russian).
135. V. V. Boldyrev, *Mechanochemistry and Mechanical Activation of Solids*, 2004, World Scientific.
136. M. Senna, *Solid State Chemistry* 63-65 3.
137. E. Gutman, *Mechanochemistry of Materials*, 1997, Cambridge International Science Pub.
138. N. V. Kosova, E. T. Devyatkina, *Electrochem. Society Abstracts*, 2003-1 (2003) 1009.
139. K. D. Kepler, J. T. Vaughey, M. M. Thackeray, *Electrochem. Solid-State Lett.* 2 (1999) 307.
140. J. T. Vaughey, K. D. Kepler, C. S. Johnson, T. Sarakonsri, R. Benedek, J. O'Hara, S. Hackney, M. M. Thackeray, *Electrochem. Soc. Proc.* 99-2 (1999) 280.
141. M. M. Thackeray, J. T. Vaughey, A. J. Kahaian, K. D. Kepler, R. Benedek, *Electrochem. Comm.* 1 (1999) 111.
142. N. Tamura, R. Ohshita, M. Fujimoto, S. Fujitani, M. Kamino, I. Yonezu, *J. Power Sources* 107 (2002) 48.
143. S. Yang, P. Y. Zavalij, M. S. Whittingham, *Mater. Res. Soc. Proc.* 756 (2003) 295.
144. J. T. Vaughey, J. O'Hara, M. M. Thackeray, *Electrochem. Solid-State Lett.* 3 (2000) 13.
145. O. Mao, R. L. Turner, I. A. Courtney, B. D. Fredericksen, M. I. Buckett, L. J. Krause, J. R. Dahn, *Electrochem. Solid-State Lett.* 2 (1999) 3.
146. O. Mao, J. R. Dahn, *J. Electrochem. Soc.* 146 (1999) 414.
147. O. Mao, R. A. Dunlap, I. A. Courtney, J. R. Dahn, *J. Electrochem. Soc.* 145 (1998) 4195.
148. M. Winter, J. O. Besenhard, *Electrochim. Acta* 45 (1999) 31.

Chapter 4

ANODES AND COMPOSITE ANODES: AN OVERVIEW

L. F. Nazar and O. Crosnier

*Department of Chemistry, University of Waterloo,
Waterloo, Ontario, Canada N2L 3G1*

4.1. INTRODUCTION: LITHIUM METAL AND CARBON-BASED MATERIALS

The past years have witnessed significant improvements in the nature and capability of energy storage systems. A combination of fundamental and technologically driven studies were responsible for these advances, which have been reviewed in Chapter 1. Motivation for the advancement has been inspired by the ever-increasing demands that a multitude of applications are placing on the energy storage battery. In addition to the ever-popular needs for portable energy electronics, future demands lie in rechargeable batteries for hybrid electric vehicles, miniaturized electronics; space exploration, uninterrupted power supplies, and medical devices.^{1,2,3} These various applications differ in their requirements of the energy storage cell: some needing high power, and others needing high capacity. All demand safety, however, and most require excellent stability of the cell over long-term usage. As fuel cells are still many years away from meeting the needs in most of these areas, lithium-ion rechargeable batteries offer the only technological solution at present, and the best long-term solution for the foreseeable future in many of the areas. Developments in the positive electrode arena have produced materials capable of gravimetric energy densities in the regime of 200 mAh/g; therefore anode materials are sought to match these high-capacity cathodes. This chapter is devoted to a review of the new technologies in the field that may address these issues.

4.1.1. Issue of Safety: a Brief History

The problems of the lithium battery, and inception of the lithium-ion battery as an alternative arose from well-known problems with the anode. In the decade before 1990, lithium batteries were introduced as novel, high energy density cells whose promise lay in the low atomic weight of lithium metal and the high degree of reversibility of the systems. The first materials to undergo commercialization, TiS_2 ,⁴ and MoS_2 ,⁵ were used as positive electrodes versus lithium foil in several commercial products. These layered transition metal dichalcogenides benefited from relatively fast lithium ion diffusion, along with appealing cell voltages vs. Li (about 1.8V). The use of lithium metal as anode material in rechargeable solution-electrolyte batteries was discarded in the late 1980's, however, after a few well-documented spectacular failures of the Li/ MoS_2 cells in operating devices. The problem is now understood to arise from reaction of the solution electrolyte with the metallic lithium surface. The electrode surface, passivated by the formation of lithium alkyl carbonates, sustains repeated non-epitaxial deposition of lithium after each cycle as a result of the complex surface chemistry. This in turn, results in continuously increasing electrode surface area, and more extensive surface reactions. The insulating, complex deposits that build up on the surface of the electrode lead to the growth of uneven "fingers" or dendrites. Ultimately cell failure occurs when the dendrites reach the positive electrode surface and/or the insulating layer causes a large rise in cell impedance, leading to an internal short-circuit.

The "rocking-chair" battery, pioneered in the mid 80's, solved the safety problem by replacing the metallic lithium anode with a lithium insertion compound. These "rocking-chair" or "shuttle-cock" batteries functioned on the principle of simultaneous lithium ion de-insertion and insertion in both electrodes. Lithium ions shuttle back and forth across the electrolyte, in concert with electron transport through the external circuit. Since these cells contained no metallic lithium, they were much safer than the lithium battery. The choice of the anode is based on properties that include fast insertion kinetics, and a redox potential vs. Li which is less than that of the cathode to provide a sufficiently large cell voltage. In the earliest conception, the anode employed was a low potential lithiated insertion compound such as Li_xWO_2 .⁶ Lower density carbon-based insertion materials replaced the oxide in batteries commercialized by Sony Energytech in 1991,⁷ giving rise to a series of patents and a product called a "lithium-ion" battery. Maximal capacities and cell voltages were obtained by marrying the carbonaceous material with a lithium-containing high-voltage cathode that functioned as the lithium reservoir, *i.e.*, LiCoO_2 . These cells have since established dominance in the lithium-ion battery market. Much effort has been expended in the last decade to improve these batteries, with research devoted

to all three components of the cell.^{8,9,10,11,12} These have resulted in significant improvements in the performance (increase in energy density and rate capability by a factor of two) and cost (more than a factor of two). Aspects of the positive electrode are discussed in Part III and the electrolyte in Part IV of this book. From the anode point of view, these directions have concentrated in three areas: improvement of carbonaceous materials; utilization of metallic lithium in combination with stable electrolytes; and a search for new materials. The most suitable direction for new anode materials is not independent of the other components in the cell - for example, successful implementation of a 5V cathode and electrolyte system would allow for anodes that have working potentials above 1 V to be utilized. Similarly, directions at improving the stability of metallic lithium anodes are directed towards implementation of lower voltage cathodes that have the advantage of electrolyte stability.

4.1.2. Carbonaceous Materials

Most of the improvements in anodes actually implemented over the last decade have involved carbonaceous materials, in concert with LiCoO_2 or related layered oxides. This is partly based on the fact that graphite and graphitic carbons, well known as intercalation compounds, have been thoroughly studied in the past 30 years.¹³ The mechanism of lithium intercalation that gives rise to a maximum uptake corresponding to LiC_6 is well understood. The reasons that lie behind the commercial success of carbon-based negative electrodes include the relatively low inherent cost of carbon, its excellent reversibility for lithium insertion, and its formation of a protective surface film with many electrolyte solutions. When a graphite electrode is polarized to negative potentials during initial Li intercalation in an ethylene carbonate based solution, the organic solvent reductively decomposes on the graphite surface to form a stable surface film.^{14,15} This film, which is often called the solid electrolyte interface (SEI)¹⁶ effectively passivates the graphite surface and prevents further co-interaction and decomposition of solvent molecules, allowing only Li ion migration.¹⁷ As ethylene carbonate is quite viscous, it is often used in combination with other alkyl carbonate solvents such as dimethyl carbonate.

One form of carbon is the soft or poorly ordered carbons ("petroleum coke" products). For soft carbons heat-treated below graphitization temperatures, turbostratic disordered carbons are obtained. Lithium cannot be readily accommodated in the interlamellar graphene galleries and low capacities are observed.^{18,19,20} For graphitized soft carbons, the level of disorder has a direct effect on the mechanism of the reaction with lithium. They display complex behavior due to surface effects, internal porosity and

dangling surface bonds.^{19,21} Capacities well above the theoretical limit of 372 mAh/g are observed, but are inevitably associated with a large hysteresis.

Specific new forms of carbon which have replaced petroleum coke and given rise to high capacity/rate capability anodes include MCMB (mesocarbon microbeads or spherical graphite), MCF (microcarbon fiber), along with natural and synthetic graphite flakes. MCMB's in particular, are highly utilized. They exhibit large capacities after heat treatments at low temperatures, as well as after graphitization at higher temperatures.^{22,23,24} MCMB materials are derived from petroleum industry byproducts or coal products, but are expensive owing to low yields. They, along with other carbonaceous and graphitic anodes are discussed in detail in Chapters 5 and 6.

4.1.3. Looking to the Future

Despite the advances made in carbons, it has been recognized for some years now that new anode materials are needed. First, graphitic carbons can suffer from solvent co-intercalation resulting in large interlayer expansions and the subsequent degradation of the graphite structure. This, however, can be suppressed by the adroit choice of solvent (*i.e.*, alkyl carbonate mixture) and co-additives.²⁵ More importantly, carbons suffer from a fundamental limitation in gravimetric capacity, and particularly in volumetric capacity (theoretical limit of 1000 mAh/cc). Developments in cathode materials that have effectively doubled the capacity within the last few years demand an anode to match. An increase in the operating voltage above the current values for carbonaceous materials is highly desirable to inhibit lithium metal deposition that can occur at fast rates. To date, no new non-carbon containing anodes have been commercialized however, as they currently are not competitive with carbon in terms of cost or stability on cycling.

Nonetheless, a large number of alternative possibilities for negative electrodes have been recently reported in the literature that may lead to new directions in meeting the anode challenge. One important area is in the development of composite materials. It is apparent that promising characteristics can result from development of nanostructured domains within materials during the initial cycles of the cell. The partial disorder inherent to these materials can have a substantial impact, affecting the kinetics and/or thermodynamics of the materials in highly beneficial ways. In fact, the attempted development of materials over the past few years suggests that one component alone will not suffice. These composites fall into two categories: those created *in-situ* as mentioned above, or those deliberately constructed using various synthesis-by-design approaches. What follows is a brief overview of some developments that highlights key points in anode design based on these concepts.

4.2. COMPOUNDS AND COMPOSITES OF Sn, Sb AND Al

Amongst the first materials to be examined as electrodes for Li uptake at low potential, well before carbon gained prominence, were other members of Group IV, and the neighboring Group III and Group V elements. These include Al, Si, Ge, Sn, Pb, Sb and Bi, which all form alloys with Li at relatively low voltages vs. Li. Much of the early work concentrated on alloys with Al (Li_9Al_4 being the end member, although LiAl is observed in practice),²⁶ and Group IV elements which display stoichiometries as high as 4.4 Li/M. Studies on the Li–Sn system, carried out at elevated temperatures by Huggins and others,^{27,28} show that seven line phases exist within the phase diagram: Li_2Sn_5 , LiSn , Li_7Sn_3 , Li_5Sn_2 , $\text{Li}_{13}\text{Sn}_5$, Li_7Sn_2 and $\text{Li}_{22}\text{Sn}_5$. Based on their known structures, Courtney *et al.* recently were able to calculate the theoretical electrochemical voltage profile in the lithium–tin system using a pseudo-potential plane-wave approach.²⁹ Their results were in good agreement with experiment.³⁰ Silicon, being the lightest member of Group IV aside from carbon, shows the highest gravimetric capacities (up to 4000 mAh/g for the end member $\text{Li}_{21}\text{Si}_5$) although achieving this at ambient temperature is difficult.³¹ A detailed re-examination of the crystal structure of the end members of the Li/Group IV compounds has shown, in fact, that although the end member composition for Si is correct, the precise stoichiometry for Ge, Sn and Pb is $\text{Li}_{339}\text{Ge}_{80}$, $\text{Li}_{341}\text{Sn}_{80}$, and $\text{Li}_{340}\text{Pb}_{80}$. The proper composition can therefore be approximated as Li_{17}M_4 , not Li_{22}M_5 .³²

Regardless of the element, the formation of alloys within Groups III, IV and V is associated with a large volume expansion that results in pulverization of the electrode material and loss of electrical contact between the material grains on prolonged cycling. The degree of volume expansion depends on the element, as shown in Table 4.1. In all cases the resulting rapid capacity fade reduces their practical use as electrodes. To overcome this problem, efforts have turned to the encapsulation of the main group metal center in a matrix which is conducive to Li^+ transport (and/or ideally, to electron transport) in addition to possessing mechanical flexibility; and also to the formation of binary systems based on intermetallics.

Table 4.1. Capacities and volume changes of different elements.

Starting material	C	Al	Si	Sn	Bi
Lithiated phase	LiC_6	Li_9Al_4	$\text{Li}_{21}\text{Si}_5$	$\text{Li}_{17}\text{Sn}_4$	Li_3Bi
Theoretical specific capacity (Ah/kg)	372	2235	4010	959	385
Theoretical volumetric capacity (Ah/l)	833	6035	9340	7000	3773
Volume changes (%)	12	238	297	257	115

4.2.1. Intermetallic Composites and Binary Phases Comprised of Sn, Sb and Al

Multiphase electrode materials composed of MM' compounds, in which only one component forms an alloy with lithium, exhibit better cycling performance than a single phase host. This has been attributed to the formation of an "inactive" M' matrix that surrounds the "active alloying M metal, and helps maintain the integrity of the microstructure of the composite electrode during the (de-)alloying process. Much of this work has been carried out using a transition metal as the inactive component and a main group metal as the active alloying centre: these are termed "intermetallics" (although strictly, the name applies to Al compounds and other true metals. The concept was based on the first "matrix" approach involving main group metal oxides, in which the Li_2O that is formed on reduction acts as the inactive matrix component. Another approach is to use intermetallics MM' that show strong structural relationships to their lithiated products.

These are discussed in the following sections.

4.2.1.1. Tin Oxide Composites

TCO, a new anode material comprised of an amorphous, multi-element composite oxide glass ($\text{Sn}_x\text{Al}_y\text{B}_z\text{P}_p\text{O}_n$), containing "active" Sn^{II} centers inspired much interest in the area of main-group metal oxide materials.³³ Studies on related compounds such as SnO , SnO_2 , and Sn_2BPO_6 established that the initial Li uptake results in an irreversible reaction to form

Li_2O and metallic Sn. The subsequent Li uptake that results in the reversible capacity is based on alloying of the Li with the Sn centres, to ultimately form $\text{Li}_{4.4}\text{Sn}$ nanoparticles embedded in the Li_2O matrix.^{34,35} A similar mechanism was thought to be responsible for Li uptake in the tin-oxide composite glasses. Detailed studies which followed, based on a variety of spectroscopic and diffraction methods, revealed that the “Li-Sn” alloy nanoparticles are highly disordered at the limit of deep discharge.^{36,37,38} The proximity of oxygen in the matrix (either on the bulk of the particles or within them) may give rise to this disorder – and in any case, certainly affects the thermodynamics of the system.

The reactions occurring within the tin composite glasses take place in a size-limiting regime, where the thermodynamics are strongly affected by the high surface energy of the particles.³⁶ The reaction between Li and Sn, which forms crystalline $\text{Li}_{4.4}\text{Sn}$ under high-temperature conditions can be much more complex on a nanoscopic level. First, the kinetics of the system limit the formation of ordered “bulk” phases at ambient temperature, even in tin oxide itself, but especially in the dilute tin-based glasses. Secondly, the tin clusters formed on Li uptake are in close proximity with both lithium and oxygen as a result of these particles having a very high surface area: volume ratio. We have suggested that partial oxygen incorporation within the bulk (as an interstitial element) may be responsible for some of the disorder observed in the X-ray diffraction patterns of the fully discharged material, as well as unusually low frequency ^7Li NMR shifts indicative of Li in the proximity of both reduced Sn and oxygen.³⁶ Oxygen is present as an interstitial component in main group compounds such as $\text{Zr}_5\text{Sn}_3\text{O}$ and $\text{La}_5\text{Sn}_3\text{O}$ and is implicated in a range of intermetallics.³⁹ The possible interstitial, and surface oxygen can facilitate the reversibility of Li uptake by the Sn. The surface energy of these particles allows the “back-reaction” of lithium with oxygen to take place at a lower potential than predicted from simple considerations that exclude surface energy contributions.

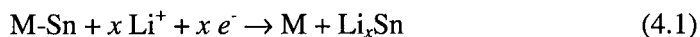
This has been corroborated by Mössbauer studies,³⁷ and EXAFS studies,³⁶ which give evidence of oxygen incorporation/disorder at low potential. The availability of matrix bound oxygen to participate (surface or interstitial) will be determined by the surface energy of the electrochemically active particles, hence the smaller the aggregates, the more reactive they will be.

Other tin oxide composites (and negative electrodes in general) are summarized in a comprehensive review article by Tirado *et al.*⁴⁰

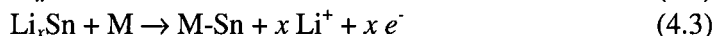
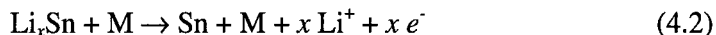
4.2.1.2. Inactive/Active Composites. Reduction-Decomposition/Alloying

4.2.1.2.1. Tin compounds

In order to reduce the irreversible capacity observed in the case of oxides, it was concluded that oxygen bonded to the electrochemically active atom M should be avoided. This approach, first suggested by Besenhard⁴¹ and Huggins⁴², has been applied to several systems based on tin intermetallics, M_xSn_y , where M is an electrochemically inactive transition metal ($M=Fe^{43,44}$, $Ni^{45,46}$, $Mn^{47,44}$, Co^{44}). The fundamental concept is simple. Li uptake/reduction induces dissociation of the starting material into an active component that will react with lithium to form Li-M alloys, and an inactive part, as described in equation 4.1:



The role of M is mainly to provide a matrix that will absorb the massive volume changes that occur within the electrode upon the lithiation (expansion)/delithiation (contraction) processes. It therefore maintains the mechanical integrity between the particles and also with the current collector. Loss of contact is a major source of capacity fade. The role of the inactive metal is also to improve the electronic conductivity of the composite electrode more effectively than the insulating Li_2O -based matrix formed in the case of oxides. However, this is at the expense of inhibiting lithium transport, which must take place upon grain boundaries. Upon charge (lithium removal), two processes can occur based on the degree of back-reaction (see Figure 4.1): either the delithiation of the Li_xSn alloys leads to metallic tin dispersed in a framework composed of the M atoms (equation 4.2); or the starting material is reformed (according to equation 4.3):



The first example of the application of this concept was in iron-tin compounds where iron forms the inactive matrix surrounding the tin atoms.⁴³ Powders of Sn_2Fe prepared by high energy ball-milling were shown by ^{57}Fe Mössbauer studies to decompose upon lithiation to nanosized iron and lithium-tin alloys, as described in Figure 4.1. Upon charge (delithiation), the Fe atoms aid lithium removal by reacting with Sn to re-form small grains of Sn_2Fe . However, due to the large volume expansion during reaction with lithium, some tin regions gradually lose connection, leading to an incomplete

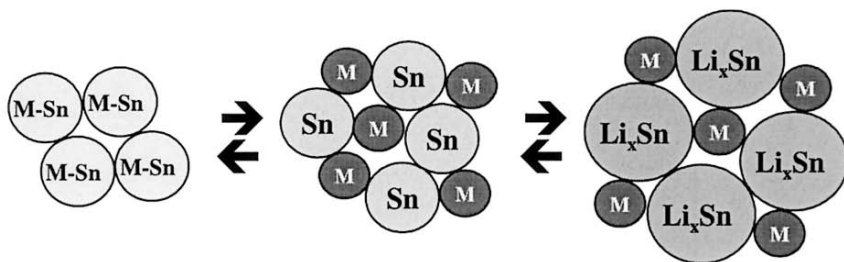


Figure 4.1. Dissociation reaction of lithium with tin-based intermetallic compounds M-Sn.

reformation of the starting material. Such compounds exhibit high specific capacities of 800 mAh/g and 650 mAh/g during the first discharge and first charge, respectively, but capacity fading on long-term cycling. As noted for tin oxide-based materials,³⁵ an improved cycle life (associated with lower capacities) of such electrodes can be obtained by reducing the voltage window between 0 and 0.55V vs. Li^+/Li .

The effects of increasing the Fe:Sn ratio were subsequently investigated by the same group. They found that increasing the Fe:Sn ratio from SnFe to Sn_3Fe_5 also resulted in dissociation. However, owing to the higher iron content, the Fe atoms form an impenetrable “skin” on the surface of the grains that inhibits complete reaction of lithium with the tin and does not allow complete dissociation of the Sn-Fe compound. The more iron in the alloy, the less reactive is the material towards lithium.

A compromise between the higher reactivity/greater fading of the Sn-rich materials and lower reactivity/lesser fading of the iron-rich materials was found by generating composites of Sn_2Fe (active component) and SnFe_3C (inactive component). These materials, prepared by mechanical alloying, show better cycling stability than the pure Sn_2Fe compound, and higher capacities than SnFe_3C . Thus the initial goal of tin atoms embedded in an electrochemically inactive iron matrix was not completely achieved, but the results obtained with the active/inactive composite electrode on the Fe/Sn/C system suggest that this concept is promising. Similar results were obtained by the same group in the Sn/Mn/C system.⁴⁷ Again, increasing the ratio of the ‘inactive’ atoms in the alloys prevents the reaction of lithium with tin and limits the capacity of these materials.

Development of nanostructured SnMn_3C led to the concept of grain-boundary storage of lithium. SnMn_3C has a perovskite structure that is inactive toward lithium. However, nanosized SnMn_3C particles (12 nm) synthesized by high energy ball milling provide a ‘host’ for the reversible insertion of lithium that can “intercalate” in the spaces between the grains. The authors showed that lithium can reversibly react at and within the grain

boundaries, delivering 150 mAh/g with a good cycling stability. The drawback is the limited capacity obtainable by this approach. The concept, however, may be also applicable to nanostructured anode materials as a source of additional Li capacity.

Nanocrystalline composite $\text{Mo}_{1-x}\text{Sn}_x$ has been prepared as a thin film by a sputtering method. The films show solid solution behavior below $x=0.45$; the coexistence of the above phase and nanocrystalline tin when $x>0.45$; and laminae of composition-modulated $\text{Mo}_{1-x}\text{Sn}_x$ and nanocrystalline tin when the overall tin content is $>40\%$.⁴⁸ Relatively stable electrochemical cycling is exhibited with promising electrochemical properties.⁴⁹

4.2.1.2.2. Antimonides

Later work continued with antimony-based intermetallic compounds. Similar to tin, antimony itself exhibits high capacities associated with alloying reactions to form Li_3Sb (theoretical capacity of 660 mAh/g).⁵⁰ It also exhibits the same expansion/contraction problems on Li cycling (see Table 4.1 above), and therefore poor capacity retention is improved by the use of an inactive network provided by a transition metal element to improve the cyclability.

In most cases, the reaction of the M_xSb compounds can be summarized by a variation of equation 4.1 above: namely simple dissociation of the starting material into M and Sb to form Li_3Sb alloys and metal particles. The dissociation reaction seems independent of the stoichiometry or structure of the starting phase, as it is observed for all transition metal antimonides. CoSb_3 , for example, crystallizes in the skutterudite structure, comprised of corner-shared CoSb_6 octahedra (similar to the ReO_3 structure except with tilting of the octahedra; see Figure 4.2).⁵¹ During the first discharge the uptake of 9 lithium takes place at *ca.* 500 mV *vs.* Li^+/Li , corresponding to a specific capacity of 800 mAh/g.^{52,53} The process leads to destruction of the crystalline structure and formation of Li_3Sb alloys dispersed in a Co matrix, as confirmed by ^{121}Sb Mössbauer spectroscopy.⁵⁴ On charge, a large irreversibility of 400 mAh/g is partially caused by the formation of a SEI layer. Upon subsequent cycles, the lithium reactions occur at higher voltages (~ 800 mV and ~ 1.2 V *vs.* Li^+/Li for discharge and charge processes respectively) and are related to the formation/dissociation of lithium antimony alloys. Despite the presence of highly dispersed cobalt clusters within the electrode, the capacity quickly fades to 200 mAh/g after 20 cycles.

Similar dissociation behavior is also observed for MSb_2 ($\text{M} = \text{Ti}, \text{V}$)⁴⁴ that crystallize in the $\theta\text{-Al}_2\text{Cu}$ structure, and MSb_2 ($\text{M} = \text{Cr}^{55}, \text{Fe}^{56}$) that crystallize in a marcasite-type structure.^{57,58} The latter is comprised of corner and edge joined MSb_6 octahedra that form small channels (see Figure 4.2).

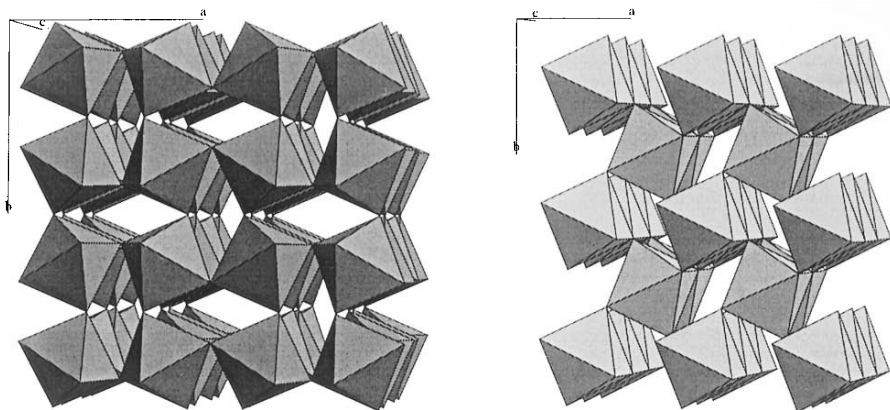


Figure 4.2. CoP_3 skutterudite structure with corner-joined CoP_6 octahedra (left) and FeP_2 marcasite structure with edge-joined FeP_6 octahedra (right).

Similar to CoSb_3 , the first reaction step (which takes place at 0.6 V and 0.35 V vs. Li^+/Li for CrSb_2 and FeSb_2 respectively), leads to a complete amorphization of the structure and the formation of Li_3Sb alloys as shown by XRD patterns (Figure 4.3).

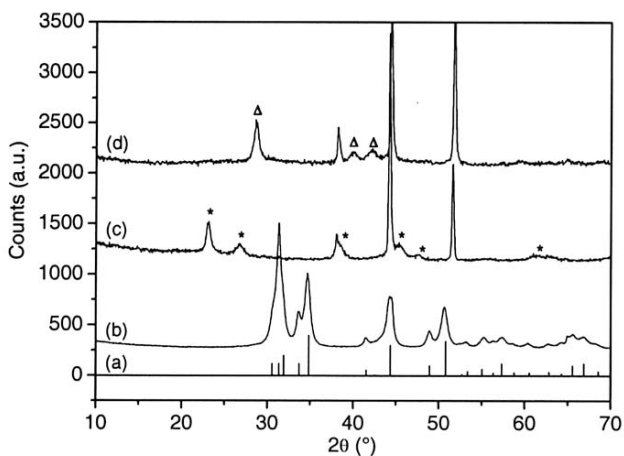


Figure 4.3. XRD patterns of FeSb_2 (a): reference, (b): pristine material synthesized by ballmilling, (c): after 5 cycles stopped at the end of discharge and (d): after 5 cycles stopped at the end of charge. (*) and (Δ) represent Li_3Sb and Sb peaks respectively.

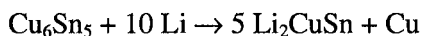
More stable cycling behavior was noted for FeSb₂ than in CoSb₃, however as a capacity of 300 mAh/g can still be obtained after 30 cycles at a C/2 rate.⁵⁶

Reversing (increasing) the M:Sb ratio provides similar outcomes, exemplified by Li uptake in Mn₂Sb which also gives simple dissociation of the starting material into Mn and Sb to form Li₃Sb alloys (equation 4.1).⁵⁹ This can be contrasted with the behavior of copper antimonides, such as the isostructural Cu₂Sb (see below), where the apparent limited region of Li-Sn (or Sb)-Cu solubility initially leads to ternary phases.

4.2.1.3. Intermetallic "Insertion" Hosts: Reduction/Insertion - Alloying

4.2.1.3.1. Cu-Sn and Cu-Sb Intermetallics

In contrast to the active/inactive concept, the copper/tin system was initially proposed by Thackeray *et al.* as a potential intermetallic Li-insertion host; *i.e.*, a host capable of topotactic Li intercalation.^{60,61} Such a compound can, in principle, exhibit high specific and volumetric capacities without the drawback of the massive volume expansion problems consecutive to an alloy formation. The mechanism of lithium insertion into η -Cu₆Sn₅, is now thought to occur in two distinct steps which are a function of the voltage; in the first step, Cu₆Sn₅ initially undergoes a phase transition involving Li insertion to form a known Li₂CuSn-type structure. This transition is observed at 400 mV vs. Li⁺/Li, corresponding to an idealized reaction that can be written as:



In fact, distinction between Li₂CuSn and "Li_{2.17}CuSn_{0.83}" is not made, as the two are probably isostructural. This process has been confirmed by *in-situ* XRD studies,⁶² recent theoretical calculations using the FP-LAPW methods⁶³ and by ¹¹⁹Sn Mössbauer spectroscopy.⁶⁴ To explain the insertion mechanism, Figure 4.4a describes the NiAs-type hexagonal structure of the starting material η -Cu₆Sn₅ in which layers of tin atoms are sandwiched between sheets of copper atoms. During the lithiation, half of the tin atoms are displaced to form columns of tin, while the copper and the other half of tin atoms remain spatially intact, creating small hexagonal channels in which lithium can be inserted to form Li₂CuSn (Figure 4.4b).

This "topotactic" reaction is associated with a 61 % volume change. When the voltage is curtailed at 0 V during discharge, the decomposition of the ternary Li₂CuSn phase occurs according to the equation:



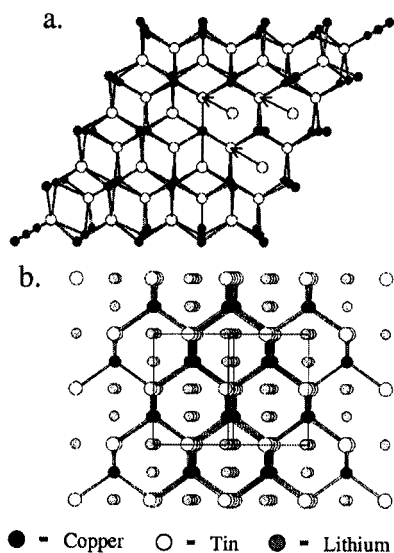


Figure 4.4. Phase transformation of η - Cu_6Sn_5 during lithiation (a) to form “ Li_2CuSn ” (b).

At deep discharge, Li_xSn alloys (*i.e.*, $\text{Li}_{4.4}\text{Sn}$) are ultimately formed, as shown by *in-situ* XRD studies.⁶² The specific capacity corresponds to 360 mAh/g for a fully lithiated electrode. As observed for the Fe/Sn/C system, only a partial reformation of the starting material occurs, and both copper extrusion and a large volume expansion lead to a poor cycling life of such electrodes.

The behavior of copper antimonide, Cu_2Sb , is related to the above process. Thackeray *et al.* demonstrated that it reacts to form Li_2CuSb (isostructural with Li_2CuSn) before transforming to Li_3Sb .⁶⁵ The transition of Cu_2Sb to Li_2CuSb takes place with extrusion of 50% of the Cu atoms, and a small structural change to yield the zinc blende phase of CuSb , and then Li_2CuSb . Further lithiation results in a $\text{Li}_{2+x}\text{Cu}_{1-x}\text{Sb}$ solid solution that terminates in the end member, Li_3Sb at $x=1$. The reaction is highly reversible, providing a capacity of 290 mAh/g that is 90% of the theoretical. The presence of the extruded copper particles is thought to impart good electronic conductivity to the electrode. Most important in this work, and that of InSb and SnSb that follow, is the principle of the reversible lithium insertion/metal displacement reactions within a face-centered cubic (fcc) Sb host structure. Therefore in the case of Cu_2Sb , the absence of significant internal displacement of the fcc Sb during the transformation aids the reversibility. The lithium and copper, of comparable sizes, can be considered to move in and out of the lattice with little disruption to the framework. This interesting

concept has been recently reviewed, and details are given elsewhere.⁶⁶

4.2.1.3.2. I_M -Sb (Where I_M is an Intermetallic)

The same principle of strong structural relationships between parent and lithiated compounds governs Li insertion into both InSb and SnSb to some degree, as noted by Thackeray *et al.*⁶⁶ Of note is that both components in these cases can partake in lithium alloying reactions, but they occur sequentially.

The zinc blende structure of InSb has a favourable three-dimensional interstitial space for lithium diffusion, and two crystallographic sites for Li insertion, as described by the first authors who reported its uptake of lithium.⁶⁷ The reaction of Li with InSb occurs in several steps which can be broadly classified as 1) a reaction of Li to form $Li_yIn_{1-y}Sb$, accompanied by extrusion of In from the framework, and 2) a second step that involves alloying of the extruded In with Li to form Li_xIn . The precise details of the electrochemical reaction during the initial stages are subject to controversy, however. The original authors have concluded, on the basis of *in-situ* XRD⁶⁸ and EXAFS studies,⁶⁹ that Li is inserted into, and In extruded from, a fixed fcc Sb framework to give $Li_{x+y}In_{1-y}Sb$ ($0 \leq x < 2$, $0 < y < 1$). They propose that, first, Li is inserted into the interstitial sites of the zinc blende structure to give Li_xInSb . Second, further reaction of lithium induces extrusion of In and replacement by Li to give $Li_{x+y+z}In_{1-y}Sb + y In$. The extent to which Li is inserted before In extrusion occurs is not yet accurately known, and is the subject of the controversy. EXAFS measurements do not support early In extrusion, but other author's detailed XRD measurements suggest that In extrusion occurs at $x=0.27$.⁷⁰ Irrespective of the details, both agree that ultimately Li_3Sb is formed at the end of the first stage, and that the last step involves formation of Li_xIn .

The good performance of the electrode (300 mAh/g after 25 cycles) has been attributed in part to the reversible lithium insertion/indium extrusion based on the fcc Sb host,⁶⁸ as described above for the Cu-Sn compounds; *i.e.* the structural similarity of InSb and Li_3Sb . The small increase in crystallographic volume of the electrode after full discharge (taking into account the extruded indium) is only 46.5%, suggesting that appropriate engineering of the materials might yield a system with good stability. Unfortunately the extensive crystal growth of the extruded indium and formation of Li_xIn alloys compromises the reversibility of the electrochemical InSb to Li_3Sb transformation.

The reaction of Li with SnSb can be described in similar terms to that involving InSb. The reaction can be summarized as Li insertion into, and tin displacement from, an fcc Sb host structure.⁶⁶ Li_3Sb is formed after the first

step, and the second step involves reaction of the extruded tin with Li to form Li_xSn alloys. A recent study⁷¹ using ^{119}Sn Mössbauer combined with ^7Li MAS NMR spectroscopy confirmed the dissociation of the starting material during the first discharge and also demonstrated that a partial recovery of the structure occurs upon charge for SnSb single phase electrodes. The good cyclability of this system can be attributed to the fact that 1) both components react sequentially: Li_3Sb formation at 700 mV vs. Li^+/Li is followed by Li_xSn alloy formation at lower voltages as shown in the first report on this system.⁴¹ Therefore at each step of the reaction, the lithiated phase is embedded in an inactive matrix;⁷² 2) the extruded tin and subsequent Li_xSn alloys are more available for reaction than in the case of InSb, since bulk tin crystallites are apparently not formed on the surface. However, low voltage reaction involving formation of tin alloys result in further electrode expansion and loss of interparticle contact between Li_3Sb and Sn, causing irreversibility and capacity fading.

The best results were obtained for a Sn/SnSb mixture with a reported charge-limited specific capacity of 360 mAh/g during 200 cycles.⁷³ However, these materials exhibit a large irreversibility during the first cycle due to the formation of a SEI layer and also because of residual impurities inherent in the synthesis process.^{74,75}

Synopsis. In summary, both tin and antimonide intermetallic compounds show high specific and volumetric capacities, but problems with irreversibility and capacity fading. Different reaction mechanisms can be observed depending on the composition. Where the materials are of type M-Sn or M-Sb (M = transition metal), inactive/active composites can be formed *in-situ* by Li uptake. The transition metal that is extruded during reduction acts as the inactive component, and the Sn or Sb participate in alloying reactions with the Li. These composites can also be prepared "by design" by ball-milling selected components. Alternatively, the binary intermetallic host can insert Li concomitant with extrusion of the inactive component, which is then followed by alloying of Li with the "active" component that generates additional capacity. When both components are "active", a combination of insertion, extrusion and alloying occurs.

Despite experimental specific capacities often lower than for graphite, the volumetric capacities obtained with intermetallic compounds are usually much higher than the 830 Ah/l observed for graphite (*i.e.*, 4500 Ah/l for Sn_2Fe , 1650 Ah/l for $\eta\text{-Cu}_6\text{Sn}_5$) due to their high density (greater than 7 g/cm³, 2.24 g/cm³ for graphite). Moreover, since 21 elements can form alloys with lithium, and up to 70 metals can form intermetallic compounds, this concept offers some future prospects. However, composite electrodes prepared *in situ* during cycling are still insufficient in terms of cycle life of the electrode. Such compounds need to be improved to replace graphitic materials

in commercial batteries.

4.2.1.4. Aluminides

Although ternary intermetallic phases are known for Al-Cu-Li, such as LiAl_2Cu , Li_3CuAl_6 , and LiAlCu , Al_2Cu is completely inactive towards Li insertion. The reasons for this were addressed in a systematic study of A_2B compounds that all have the $\theta\text{-Al}_2\text{Cu}$ structure (Sb_2Ti , Sb_2V , Sn_2Co , Sn_2Mn , Sn_2Fe , and Al_2Cu). The authors concluded that even though thermodynamics predict that the alloying reaction *should* proceed, the large activation energy needed to break an Al-transition metal bond hinders reactivity.

4.2.2. Silicides

Several efforts have also been undertaken on silicon-based electrodes. Attention has been given to Mg_2Si ,^{76,77,78,79} but despite much effort its properties have proven disappointing. More promising are silicon-based composites prepared/designed by a variety of techniques.

4.2.2.1. Mg_2Si

Many authors have investigated Mg_2Si due to its anti-fluorite structure which was reported to be amenable to Li insertion. The reaction mechanism is, however, still unclear. Moriga *et al.* proposed a lithium insertion into the vacant sites, leading to the formation of a ternary phase LiMg_2Si , followed by Li_2MgSi ,⁷⁶ along with extrusion of Mg atoms that will react to form Li/Mg alloys. This process is in conflict with the simple dissociation reaction proposed by other groups,^{78,79} followed by the formation of lithium alloys with Mg and Si. Despite a large initial specific capacity of 1370 mAh/g at an average voltage of 350 mV vs. Li^+/Li , the mechanical instability of the electrode causes a drastic fade of the capacity upon cycling, even by reducing the voltage window of the study.⁸⁰ Extended studies were also performed on isostructural compounds, such as Mg_2Sn ⁸¹ and Mg_2Ge ,⁸² showing better cycling behavior (in the case of the tin compound) than Mg_2Si with capacities of 300 mAh/g after 60 cycles in an appropriate voltage window.

4.2.2.2. Si-Based Composites

As noted above in Section 4.2.1., Si displays the highest gravimetric

and volumetric capacity of all of the Group IV/V elements. Much attention has therefore been devoted to preparing composites of Si with various compounds/elements, by different methods that allow good dispersion of the Si within the matrix. Early work in this area devoted to C/Si composites utilized chemical vapor deposition to produce highly dispersed Si clusters within a carbon matrix; these materials showed promising electrochemical behavior.⁸³

Ball-milling has since been used with varying success to prepare composites of Si with both hard and soft materials. Mechanical milling of Si with titanium nitride, known for its conductivity, mechanical strength and hardness, has recently been reported.⁸⁴ TiN plays the role of the inactive component, and also aids in preserving the morphology of the electrode. The composite obtained by high energy mechanical milling (HEMM) that exhibits the best electrochemical properties (Si:TiN ratio of 1:2), is comprised of nanocrystallites of TiN (5-7 nm) agglomerated with amorphous Si to generate particles a few hundred nanometers in diameter. It exhibits good cycling stability over 20 cycles associated with a specific capacity of 300 mAh/g. This capacity is still lower than the theoretical of 776 mAh/g (assuming reaction to form $\text{Li}_{21}\text{Si}_5$), apparently owing to a large fraction of inaccessible Si buried within the TiN matrix. However, the electrode structure is relatively stable during cycling, as little cracking/crumbling was observed after 30 cycles. Lower-energy ball-milling has been employed to prepare composite electrodes with silicon and "soft" materials such as graphite. The Si/C composites recently reported, namely $\text{C}_{1-x}\text{Si}_x$ powders with Si contents varying from 10-20% made by milling crystalline Si and graphite, were reported to contain Si microencapsulated by a thin layer of amorphous carbon. They display reversible capacities of up to 1040 mAh/g which fade to 800 mAh/g after 20 cycles.⁸⁵ The increase in Si content in those composite materials is accompanied by the coexistence of inactive SiC during their synthesis. Better materials were obtained using nanocrystalline Si, prepared by laser-induced silane decomposition, ball-milled with carbon black.⁸⁶ These were shown to exhibit high initial reversible capacities up to 2000 mAh/g, but extensive fading over 20 cycles was still observed.

Composite electrodes can also be prepared by coating or sputtering methods. The use of thermal vapour decomposition (TVD) has been recently used to obtain carbon coated graphite.⁸⁷ The resultant materials display increased rate capacities and decreased irreversibility by comparison to carbonaceous materials, where graphite layer exfoliation often limits reversibility. Thermal vapor decomposition has been more recently extended to the formation of Si/C composites.⁸⁸ Composites containing 20% carbon coating exhibit excellent performance. Up to 800 mAh/g can be obtained with an excellent cyclability. This method also inhibits the decomposition of electrolytes, which can be a problem on the surface of unprotected Si-

electrodes, and furthermore provides a conductive network.

However, in general (as noted above) obtaining stable cycling for alloy negative electrodes is an unattainable goal, unless the capacity is constrained to values near that of graphite. The reason for cycling instability is believed to be due to inhomogeneous volume expansion in coexisting regions of phases with different lithium concentrations. Another approach to anode composites described in a patent application,⁸⁹ is based on using amorphous metals and metalloids. The advantage of amorphous materials lies in the potential elimination of the two-phase regions between phases of different lithium concentration, which can lead to homogeneous volume expansions and improved charge-discharge cycling behavior. Such materials, based on amorphous Si/Sn alloys have been prepared using a magnetron sputtering method.⁹⁰ The authors showed through electrochemical and *in-situ* XRD experiments that the materials remain amorphous at all times during cycling, and that the two local environments for Si and Sn are distributed evenly throughout the bulk. These are believed to be the reasons that the materials can sustain large volume expansions without drastic cracking and pulverization. These materials were found to readily uptake up to 4 lithium per $\text{Si}_{1-x}\text{Sn}_x$ formula when cycled to 0 V vs. Li^+/Li , leading to a specific capacity of 3000 mAh/g for the composition $x=0.33$.

These materials, and the new Si-carbon composites seem amongst the most promising as negative electrodes in lithium-ion batteries, although preparation of large-scale amounts of materials by sputtering technique may prove challenging.

4.3. METAL OXIDES

Metal oxide anode materials can be divided into two classes. One is the true insertion compounds: metal oxides capable of intercalation chemistry at low potential. These materials are characterized by relatively high potentials (usually between 1.4-1.8 V), low lithium capacities and often highly reversible insertion reactions. The other class of metal oxides display Li capacities derived from reaction with the lithium to form another material, which is usually the reduced metal oxide encapsulated in a matrix of Li_2O , similar to the case of the tin oxides described above. These materials also display a relatively high average charge potential, but also a large hysteresis consistent with the necessity of oxygen transport within the bulk during oxidation. Critical to the functioning of these materials, therefore, is the intimate mixture at the nanoscale regime, of metal sub-oxide (or pure metal, depending on the degree of Li uptake) and oxygen from the lithium oxide matrix that facilitates the oxygen recovery process.

4.3.1. Transition Metal Oxides: Where Insertion Governs the Process

As these are not strictly "composite" anode materials they will be mentioned only briefly.

The most widely considered metal oxide for low potential applications is $\text{Li}_4\text{Ti}_5\text{O}_{12}$, described as a zero-strain insertion material owing to the almost negligible changes in the unit cell on insertion of up to one lithium into the structure.⁹¹ The formula can be written as $\text{Li}[\text{Li}_{1/3}\text{Ti}_{5/3}]\text{O}_4$, illustrating the mixing of Li and Ti on the octahedral 16d sites, and occupation of the remaining Li on the tetrahedral 8a sites. To account for the virtually zero changes in volume on Li insertion, Ohzuku *et al.* have suggested that Li is inserted into the unoccupied 16c sites, which are also additionally occupied owing to migration of Li from the tetrahedral sites. The combination of little structural hysteresis and rapid lithium diffusion result in good electrochemical properties for this material, despite an average insertion potential of 1.5 V. Typically, capacity values close to 150 mAh/g are observed. Materials exhibiting such capacities at very high rates can be obtained from in high surface area modifications, such as in nanocrystalline films made by sol-gel methods⁹² or in commercial nanomaterials prepared by spray drying or other techniques. $\text{Li}[\text{CrTi}]\text{O}_4$, with a related structure, also shows similar characteristics.⁹³

The other oxide that has received attention is TiO_2 as the anatase polymorph,⁹⁴ and particularly as a nanocrystalline material. Many reports have been devoted to preparing nanostructured anatase, with techniques spanning the gamut of spray drying, sol-gel chemistry, and the polyol method.⁹⁵ A synthetic polymorph of TiO_2 produced by "chimie douce" methods, known as $\text{TiO}_2(\text{B})$,⁹⁶ shows slightly better behavior than TiO_2 anatase. All these materials suffer, however, from a higher insertion potential than the spinel $\text{Li}_4\text{Ti}_5\text{O}_{12}$, and less efficient lithium mobility.⁹⁷

4.3.2. Transition Metal Oxides: Where Reduction of Metal Oxide to Metallic or Semi-metal Occurs

The first reports of a metal oxide being subjected to deep discharge involved lithium insertion in $\alpha\text{-Fe}_2\text{O}_3$ or Co_3O_4 , which were reported to lead to the extrusion of the transition metals and formation of Li_2O .⁹⁸ For the iron oxide, this occurs in a series of stages involving progressive formation of reduced spinel structures, with reversibility implied in some of the steps. Subsequent studies on metal oxides concentrated on "complex" oxides, including LiMVO_4 ($\text{M} = \text{Zn}, \text{Cd}, \text{Ni}$),⁹⁹ Li_xMO_z and $\text{Li}_x\text{M}_y\text{V}_{1-y}\text{O}_z$ ($\text{M} =$

transition metal)¹⁰⁰ and amorphous or semi-crystalline RVO_4 ($R = \text{In, Fe}$),¹⁰¹ MV_2O_6 ($M = \text{Fe, Mn, Co}$),¹⁰² and $A_x\text{MoO}_3$.¹⁰³

When these materials were first reported, the mechanism responsible for the Li uptake and reversibility was not understood; however great strides have since been made. A beneficial mix of metal and metal-oxide on the nanoscale appears to be responsible for promising properties exhibited by a growing number of transition metal oxides. The initial work on Li uptake in partially reduced molybdenum oxides such as $\text{Li}_{0.25}\text{MoO}_3$ showed by means of a combination of ^7Li NMR, XRD and XAS probes, that a complex amorphous nanocomposite is formed at low potential. It consists of a disordered, highly oxygen deficient lithium/molybdenum-oxide (a “lithium/molybdenum sub-oxide”) in intimate association with lithium oxide.¹⁰³ The latter accounts for the irreversible capacity observed by electrochemical studies. Subsequent EXAFS and XANES studies revealed that although metallic Mo is formed on deep discharge, a molybdenum oxide is regenerated on oxidation.^{104,105} The depth of discharge is important in controlling the metal-oxygen environment. At potentials deep enough to result in complete reduction of the metal, the molybdenum retains most of its oxygen coordination environment. The latter is only lost at repeated discharge to very low potential. Thus, if the voltage window is restricted above this level, the Mo essentially shuttles between oxygen poor/lithium rich (discharge) and oxygen rich/lithium poor (charge) amorphous phases with improved cyclability being the result. Complementary findings in Fe and Co vanadate systems on Li uptake have also been revealed by *in-situ* X-ray, XANES, Mössbauer and microscopy studies.¹⁰⁶ The recently reported behavior of iron borates such as Fe_3BO_6 and Fe_3BO_3 as low-potential Li-uptake materials is also based on similar principles.¹⁰⁷

These findings led to investigation of simple nano-sized metal oxides MO based on the rock-salt structure ($M = \text{Co, Fe, Ni}$). High-resolution TEM studies of the material at deep discharge demonstrated the presence of metal nanoparticles about 20 Å in diameter. Again, the highly divided, high-surface energy nature of the nanoparticles facilitates the back-reaction with oxygen from the lithium oxide matrix to reform the metal oxide on charge, this time in a semi-crystalline form.¹⁰⁸ The reaction, particularly reversible for Co, but less so for Fe and Ni, can be simplified as reaction between Li and MO to form $\text{Li}_2\text{O} + M$, which is reversible if the materials are on the nanoscale.

4.3.3. Mixed Transition Metal Oxides - Where Both Reduction and Alloying are Responsible for Li Capacity

The Sn-oxide, transition metal oxide, and Sn/Fe intermetallic studies cited above opened avenues to investigate oxide materials containing both transition metal and main-group metal active centers. An interesting class of materials based on the inherently open architecture of CaFe_2O_4 are suitable candidates.¹⁰⁹ This structure exhibits partial solid solution based on Sn substitution for Fe with accompanying removal of Ca for Li, the end member having the stoichiometry $\text{Li}_{0.6}\text{Ca}_{0.4}\text{Sn}_{0.6}\text{Fe}_{1.4}\text{O}_4$, and relatively high ionic conductivity. On introducing Sn into the structure the *reversible* capacity is substantially increased compared with the parent material, owing to the additional reaction of the Sn. Although irreversible capacity is observed that arises from the partial formation of Li_2O , reversible Li uptake is observed with good stability. The materials sustain a stable reversible capacity of >600 mAh/g for the optimized composition $\text{Li}_{0.5}\text{Ca}_{0.5}\text{Sn}_{0.5}\text{Fe}_{1.5}\text{O}_4$.¹⁰⁵ The profile of the differential capacity plots suggest there is no complete phase separation to Li/Sn alloy phases on reduction, but that a lithium-rich, oxygen deficient Sn/Fe/oxide matrix is formed. These results are also supported by XAS measurements which suggest that Sn-Fe alloy nanophases formed at intermediate potentials lie in close proximity with oxygen.

4.4. NITRIDES AND PHOSPHIDES

4.4.1. Nitrides

By contrast to metal oxides, where the high degree of electronegativity difference between the metal and the anion tends to drive the reduction to the formation of the metal on Li uptake, nitrides display more covalent bonding between the metal and anion. Different behavior is expected - and observed. In all cases, the mechanism of Li uptake/extraction is still subject to scrutiny. Numerous binary, and ternary (Li-containing) nitrides are summarized in an comprehensive review by Gregory *et al.*¹¹⁰ but most have not been found to be electrochemically active.

The first examination of the electrochemical behavior of metal nitrides was based on layered LiMoN_2 , isostructural to LiCoO_2 .¹¹¹ Despite this promising similarity in structure to a known intercalation compound, LiMoN_2 failed to show any electrochemical activity although chemical extraction of lithium was achievable using butyl-lithium. Subsequent studies involved nitrides of the first row transition metals. These Li-M-N structures follow a

predictable trend. For Ti through Fe, an antifluorite structure is favored with Li and M in the tetrahedral sites, M being present in a high oxidation state.¹¹² Metal nitrides in this class such as Li_7MnN_4 ¹¹³ and Li_3FeN_2 ¹¹⁴ display electrochemical behavior at about 1.2 V vs. lithium, with reversible capacities in the range of 300–350 mAh/g. For Co, Ni, and Cu, a structure based on α - Li_3N is formed, with M^{1+} substituting for Li^+ between the hexagonal Li_2N layers. These $\text{Li}_2(\text{Li}_{1-x}\text{M}_x)\text{N}$ compounds ($\text{M} = \text{Mn} \rightarrow \text{Cu}$) are more promising. The layered morphology is advantageous, supporting fast Li-ion conduction and low transition metal oxidation states. The first studies on $\text{Li}_2(\text{Li}_{1-x}\text{M}_x)\text{N}$ compounds ($\text{M} = \text{Co, Ni or Cu}$) suggested that the Co member showed the highest capacity (480 mAh/g) and most reversible behavior. The significantly poorer performance of the Ni and Cu members has not been explained. Other studies by Shodai reported that $\text{Li}_{2.6}\text{Co}_{0.4}\text{N}$ can exhibit a capacity up to 760 mAh/g in the voltage window 0–1.4 V.¹¹⁵

Owing to the high cost and toxicity of cobalt compounds, a better material would be based on Fe or Mn. Both are unique in their behavior which lies between the two structural extremes described above. For example, Fe forms both the antifluorite phase with iron in a high formal +3 oxidation state, and layered phases with iron in lower oxidation states. Of the latter, most reports were of single crystals isolated as minor phases from mixtures, but they indicated the possibilities of intriguing chemistry. A “metastable” layered phase Li_4FeN_2 contains layers of Li_2N with ordered Fe^{2+} and vacancies between the layers.¹¹⁶ Crystals of $\text{Li}_2(\text{Li}_{0.37}\text{Fe}_{0.67})\text{N}$ (Fe^{1+}) have been isolated from a mixture formed from decomposition of the antifluorite phase in a lithium flux.¹¹⁷ We devised a synthesis route to a novel lower iron-content nitride, layered $\text{Li}_2(\text{Li}_{0.7}\text{Fe}_{0.3})\text{N}$, that provides virtually gram-scale quantities in 100% yield within a day, by simple reaction of Fe with Li_3N at 800°C.¹¹⁸ The material is isostructural with the layered $\text{Li}_{2.6}\text{Co}_{0.4}\text{N}$ analogue. Electrochemical studies showed that $\text{Li}_2(\text{Li}_{0.7}\text{Fe}_{0.3})\text{N}$ displays a capacity of up to 550 mAh/g in a potential window of 0 → 1.3 V, with relatively good stability on cycling.

Both the antifluorite and higher capacity layered nitrides, however, are subject to three concerns: 1) They are highly hygroscopic and moisture sensitive. 2) They become amorphous on lithium extraction, making it difficult to ascertain the mechanism responsible for reversible Li extraction/uptake. Studies to determine the mechanism responsible for amorphization and Li uptake suggest that reversible migration of the N atoms occurs during charge and discharge.¹¹⁹ 3) They need to be “charged” first by the removal of lithium from the structure, and hence they act as a reservoir for lithium, not a sink. This results in problems in finding a suitable cathode material, as most of the preferred materials exist as lithiated air-stable phases. Despite these concerns, $\text{Li}_{2.6}\text{Co}_{0.4}\text{N}$ has been recently re-examined by groups at Panasonic/Matsushita¹²⁰ and proposed as an anode versus LiMn_2O_4 in

lithium-ion cells.¹²¹ In recent work, the material has also been coupled with tin-containing anode materials to compensate for irreversibility in the latter.¹²²

The electrochemical behavior of main group nitrides capable of acting as a Li "sink" have been recently described by the Telcordia group.¹²³ They report that uptake of Li by Zn_3N_2 results in formation of LiZn in a matrix of $\beta\text{-Li}_3\text{N}$. On charge, complex reactions result in the oxidation of LiZn to metallic Zn, and reaction of $\beta\text{-Li}_3\text{N}$ with LiZn to form LiZnN which is the end member phase for all subsequent cycles. This first-reported reversible Li_3N conversion gives a reversible capacity of 555 mAh/g but the cycle life was limited.

4.4.2 Phosphides

Like nitrides in some respects and antimonides in others, phosphides have recently been shown to exhibit interesting chemistry that is a combination of the other Group V members. In common is the fact that the high-lying mixed anion-metal bands, and a high degree of electron delocalization lead to a low formal oxidation state of the metal, and strong covalent character of the M-pnictogen bond.^{124,53} The materials therefore show an overall lower intercalation potential compared to the respective oxides. Differences within Group V compounds arise from the fact that phosphides display more covalent bonding than the corresponding nitrides, but less than the predominantly semi-metallic antimonides. These bonding differences are reflected in the band structure and chemistry, as shown in Figure 4.5.

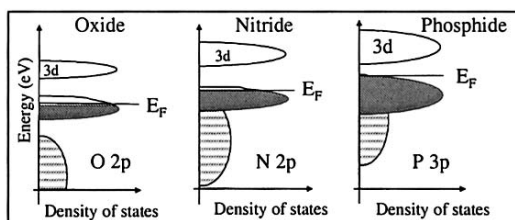


Figure 4.5. Comparison of DOS for oxides, nitrides and phosphides.

In nitrides, the uppermost band is thought to expose nitrogen-based orbitals and hence result in holes appearing in the nitrogen-dominant band upon oxidation (and evolution of N_2 on overcharge).¹²⁰ In antimonides by contrast the redox reactions involve the metal-Sb bond, and hence Li

uptake/reduction results in phase separation to form metal and Li_xSb alloys. In phosphides, the chemistry seems to lie midway between the two. Differences in the strength of the M-pnictogen (P_N) bond, and relative contribution of the P_N - P_N bond results in a paucity of transition metal-poor binary nitrides (but plethora of transition metal antimonides). For example, MnN_4 , analogous to MnP_4 , does not exist. As no binary nitrides are known that can uptake Li^+/e^- , the lithium ions must first be removed from the structure to give reversible cycling, a drawback of these materials that also results in irreversible collapse to an amorphous structure. More importantly, the negative electrode in a cell should act as a *reservoir* for Li as MnP_4 does, not a source. In this respect, phosphides have advantages over nitrides.

The electrochemistry that is responsible for reversible Li uptake varies according to element, and as to whether a lithiated ternary phase exists in the phase diagram with the same M:P stoichiometry as the binary phase. Unlike the antimonides, the mechanism is *dependent* on the stoichiometry/structure of the starting phase. The behavior exhibited can be separated into four groups: those in which the binary and ternary phases exist *i.e.*, $\text{MP} \leftrightarrow \text{LiMP}$; those in which only either the binary or ternary phase exist, *i.e.*, MP (FeP_2) or LiMP (Li_2CuP); and those in which Li uptake results in phase decomposition to the metallic state, as in CoP_3 . These are discussed below.

4.4.2.1. Binary ($\text{MP} \leftrightarrow \text{LiMP}$) Combination

Where a fully lithiated end member exists, conversion between the binary and ternary crystalline phases can occur on lithium insertion. Such a reaction is exhibited by MnP_4 , which undergoes a first-order phase transition to yield crystalline Li_7MnP_4 .¹²⁵ The mechanism by which this occurs is more complex than a typical intercalation reaction, however, as substantial structural differences exist between the two phases. The layered 8-MnP_4 structure is composed of infinite sheets of MnP_6 octahedra linked by P-P bonds both within the sheets, and between the sheets. Li_7MnP_4 has the antifluorite structure. On Li^+/e^- uptake, P-P bonds between the layers are reductively cleaved ($\text{P}^1 \rightarrow \text{P}^3$), and Li ions are inserted in the resulting interlamellar voids. Translation of Mn from an octahedral to a tetrahedral site within each coordination rhomboid provides space for additional tetrahedral interstitial sites for Li^+ , to give the antifluorite structure. A scheme illustrating the proposed mechanism is shown below. Importantly, the process can be readily reversed by reversing the voltage, resulting in “electrochemical recrystallization” of the original MnP_4 phase as a crystalline compound. The P-P bonds in the MnP_4 structure that are cleaved on Li insertion (reduction) to give Li_7MnP_4 , are reformed on re-oxidation to MnP_4 . Thereby, they act as an electron storage reservoir.

The reaction is a quasi-topotactic intercalation process that represents the first unequivocal example of reversible lithium insertion of lithium at low potential, aside from graphite. There are obvious differences, however. Li insertion in graphite cleaves only the very weak van der Waals bonding between the graphene layers, and is hence a facile process, whereas the energy required to cleave and re-form the covalent P-P bonds is significantly higher. Contrary to the pure intercalation process in graphite that can therefore proceed with little hysteresis, the phosphide reaction is kinetically limited by the structural rearrangement involved in the phase transition. The substantial volume/density change also seen in other high-capacity anodes also results in some cracking and loss of contact with the current collector. Lower reversible capacities (700 mAh/g) than theoretical (1050 mAh/g) are observed on the first cycle, that fade on cycling.

Nonetheless, reversible capacities of 550 mAh/g, stable over >25 cycles, can be sustained at C/4 rates in nano-sized particles formed by ball-milling.¹²⁶ Interestingly, Li can also be de-inserted from crystalline Li_7MnP_4 to give similar electrochemical results. However, the MnP_4 formed on oxidation is very poorly crystalline (almost amorphous), as is the Li_7MnP_4 subsequently formed on re-insertion. This is presumably due to the fact that inherent ordering of Li and Mn is implied on insertion of Li in MnP_4 . This cannot be duplicated by starting in the opposite direction, due to the perfectly random distribution of Li and Mn in Li_7MnP_4 .

Li *de*-insertion from Li_7VP_4 has also been recently reported to give reversible capacities of 550 mAh/g, on the first cycle at a C/34 rate.¹²⁷ They report unusual stability of the VP_4 framework to different lithium compositions, based on the fact that *de*-insertion of Li appeared to result in no structural change to the lattice. The authors, however, allowed for the possibility that the oxidized phase could be amorphous.

4.4.2.2. Binary MP; No Stable LiMP Ternary

Where a binary MP exists but no stable LiMP ternary phase of the same MP stoichiometry, two possibilities for Li uptake can be predicted. The reaction can either yield a metastable ternary phase, such has been proposed for lithium insertion in FeP_2 ; or decomposition to yield Li_3P and metal can occur, akin to the reaction in antimonides. The latter is exhibited by CoP_3 . In both cases, Li uptake (and subsequent extraction) results in an amorphous material, making the nature of the Li uptake process difficult to discern.

4.4.2.2.1. FeP_2

The reaction of FeP_2 with Li occurs with a remarkably low degree of irreversibility on the charge cycle as shown in Figure 4.6.¹²⁸

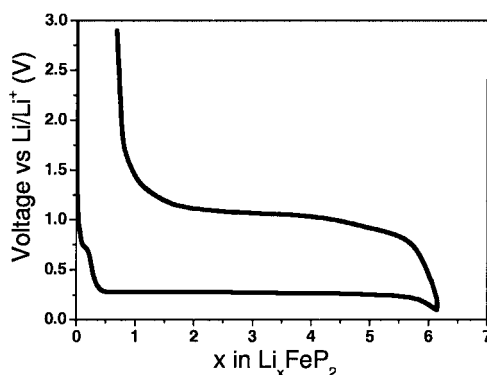


Figure 4.6. Voltage vs composition for FeP_2 cycled at a C/4 rate.

The process of Li insertion has been investigated using electrochemical studies in concert with X-ray diffraction, XAS and magnetic measurements. The uptake of six Li during the first discharge leads to a specific capacity of 1365 mAh/g, and an amorphous phase retaining substantial Fe-P bonding. It displays superparamagnetic behavior and an extremely low transition temperature below 10K. Upon charge, 5.5 lithium can be extracted from this metastable ternary “Li-Fe-P” phase, leading to a reversible capacity of 1250 mAh/g.⁵⁶ To account for the presence of Fe-P bonding observed in the XAS - EXAFS experiments, the magnetic behavior of the particles on discharge, and lack of identifiable Li_3P , it was proposed that Li uptake occurs by expansion of the phosphorus lattice, and incorporation of the additional lithium to form a disordered, stuffed metastable “ $\text{Li}_3\text{Fe}_{0.5}\text{P}$ ” lattice that still maintains Fe within the structure. The low (*ca.* 10-15%) irreversibility exhibited by FeP_2 makes it an interesting material in the search for new negative electrode materials.

Therefore, like in MnP_4 , the high degree of covalent bonding and low valence of the metal induces a transformation more akin to “insertion”, in contrast to the iron antimonide, FeSb_2 , where complete phase separation into the lithium antimonide and the metal occurs as described in Section 4.2.1.2.2

In other metal phosphides, the possibility of a transition between a ternary LiMP phase and a metastable MP phase could be envisioned. Such a transformation appears responsible for the reversible de-insertion from lithium from Li_2CuP to give “CuP” recently discovered in our lab.

4.4.2.2.2. CoP_3

Phase separation of metal phosphides into metal and Li_3P is observed for one phosphide, CoP_3 , however, as recently described by two different research groups.^{129,130} Their conclusions are similar, although they differ on the charge process. The presence of Co particles is not apparent in the XRD pattern of reduced CoP_3 due to their small dimensions (well below the broadening limit of 500 Å in XRD) but their presence was indirectly suggested by the clear presence of Li_3P in the diffraction pattern. TEM measurements revealed the presence of 10-20 Å nanoparticles embedded within the original crystallite. As the SAED pattern showed only broad, weak rings with d-spacings corresponding to Li_3P , and no interplanar spacings assignable to cobalt crystallites, it was concluded the metal must be very highly dispersed; perhaps weakly bonded to the matrix as highly metal-rich phosphide clusters.¹²⁹ The metallic state of Co was revealed in XAS measurement of Alcántara *et al.*, however, who also showed the presence of Li_3P through MAS-NMR studies.¹³⁰

The process on charge appears to involve redox reactions of Li_3P , but no participation of the cobalt. The same mechanisms as in the antimonides was suggested by Alcántara *et al.*, involving a reaction based on formation/re-formation of Li_3P from its elements, $\text{Li} + \text{P}$. A reversible capacity of 487 mAh/g was observed in this case. A slightly different mechanism was reported by Pralong *et al.*,¹²⁹ in which cycling (400 mAh/g) was attributed to the transformation between Li_3P and LiP on the basis of XPS measurements. In both cases the observed capacities are well below the theoretical.

Synopsis. The behavior of the phosphides represents a departure from that exhibited by ionic negative electrode materials such as oxides (where the high energy of the metal-localized bands drives the reduction to the metallic state on Li uptake); nitrides; and intermetallic negative electrode materials where Li uptake relies on formation of alloys Li_xM ($\text{M} = \text{Sb}, \text{Sn}$). Furthermore, facile covalent bond rearrangement and atom migration that lead to electrochemical “recrystallization” (MnP_4) or facile introconversion of amorphous phases (FeP_2) are a signature of these materials. New opportunities are hence afforded by some phosphides, if difficulties with electrolyte reactivity/SEI formation can be overcome which currently limit cycling stability.

4.5. CONCLUSIONS

The task of finding alternate materials for anodes in lithium-ion cells to

carbonaceous materials has proven to be a daunting and challenging task that has spanned more than a decade of work amongst many research groups. This overview has attempted to summarize some of the major directions that have dominated the field, both in anode materials in general and in composites in particular. It is clear that the goal of developing materials capable of insertion/uptake of large proportions of lithium is incompatible with the difficulties of the large volume changes necessitated by such reactions, and resultant capacity fading. However, clever approaches can be used to ameliorate the problem, many of which lie in the composite approach. Composites-by-design (such as carbon coated Si materials) and the concept of active/inactive materials provide good possibilities for the future, along with targeted synthesis of intermetallic compounds, nitrides, phosphides and silicides that may demand a composite (and/or combinatorial) approach to optimize their electrochemical performance. Alternatively, designed approaches to nanostructured alternatives of these materials are needed. Understanding of the mechanism of lithium uptake is critical to advancing progress in the area. Finally, attention must be given to reactions of these materials with electrolytes at low potential which can compromise electrochemical performance. SEI formation with materials aside from carbon is not well understood, and the liquid electrolytes today that are optimized for carbon may prove less than ideal for other materials.

REFERENCES

1. M. Broussely, *J. Power Sources* 82 (1999) 140.
2. M. Balkanski, *Sol. Energy Mater. Sol. Cells* 62 (2000) 21.
3. N. Terada, T. Yanagi, S. Arai, M. Yoshikawa, K. Ohta, N. Nakajima, A. Yanai, N. Arai, *J. Power Sources* 100 (2001) 80.
4. K. M. Abraham, D. M. Pasquariello, F. J. Martin, *J. Electrochem. Soc.* 133 (1986) 661.
5. A. J. Jacobson, R. R. Chianelli, M. S. Whittingham, *J. Electrochem. Soc.* 126 (1979) 2277.
6. M. Lazzari, B. Scrosati, *J. Electrochem. Soc.* 127 (1980) 773.
7. T. Nagaura, K. Tozawa, *Prog. Batt. Solar Cells* 9 (1990) 209.
8. G. Pistoia, (Ed.), *Lithium Batteries*, New York: Elsevier, 1994.
9. M. Winter, J. O. Besenhard, M. E. Spahr, P. Novak, *Adv. Mater.* 10 (1998) 725.
10. B. Scrosati, *Electrochim. Acta* 45 (2000) 2461.
11. M. Wakihara, *Mater. Sci. Eng.* R33 (2001) 109.
12. J. M. Tarascon, M. Armand, *Nature* 414 (2001) 359.
13. R. Schöllhorn, A. Payer, *Angew. Chem. Int. Ed.* 24 (1985) 67.
14. Z. Ogumi, M. Inaba, *Bull. Chem. Soc. Jpn* 71 (1998) 521.
15. M. Winter, J. O. Besenhard, M. E. Spahr, P. Novak, *Adv. Mater.* 10 (1998) 725.
16. E. Peled, *J. Electrochem. Soc.* 126 (1979) 2047.
17. E. Peled, in *Handbook of Battery Materials* J. O Besenhard Ed., Wiley-VCH Weinheim, 1999.
18. J. R. Dahn, T. Zheng, Y. Liu, J. S. Xue, *Science* 270 (1995) 590.
19. R. Alcántara, J. M. Jiménez, P. Lavela, J. Morales, J. L. Tirado, *Mater. Sci. Eng. B* 39

- (1996) 216.
20. R. Alcántara, J. M. Jiménez-Mateos, J. L. Tirado, *J. Electrochem Soc.* 149 (2002) 201.
 21. J. R. Dahn, W. Xing, Y. Gao, *Carbon* 35 (1997) 825
 22. K. Tatsumi, N. Iwashita, H. Sakaebe, H. Shioyama, S. Higuchi, A. Mabuchi, H. Fujimoto, *J. Electrochem. Soc.* 142 (1995) 716.
 23. M. Inaba, H. Yoshida, Z. Ogumi, *J. Electrochem. Soc.* 143 (1996) 2572.
 24. R. Alcántara, F. J. Fernández-Madrigal, P. Lavela, J. L. Tirado, J. M. Jiménez-Mateos, C. Gómez De Salazar, R. Stoyanova, E. Zhecheva, *Carbon* 38 (2000) 1031.
 25. M. Inaba, Z. Siroma, A. Funabiki, Z. Ogumi, T. Abe, Y. Mizutani, M. Asano, *Langmuir* 12 (1996) 1535; M. Inaba, Z. Siroma, Y. Kawatate, A. Funabiki, Z. Ogumi, *J. Power Sources* 68 (1997) 221; S. K. Jeong, M. Inaba, T. Abe, Z. Ogumi, *J. Electrochem. Soc.* 148 (2001) A989.
 26. C. J. Wen, B. A. Boukamp, R. A. Huggins, W. Weppner, *J. Electrochem. Soc.* 126 (1979) 2258; Y. Hamon, T. Brousse, F. Jousse, P. Topart, P. Buvat, D. M. Schleich, *J. Power Sources* 97 (2001) 185.
 27. M. S. Foster, C. E. Crouthamel, S. E. Wood, *J. Phys. Chem.* 70 (1966) 3042.
 28. C. J. Wen, R. A. Huggins, *J. Electrochem. Soc.* 128 (1981) 1181.
 29. I. A. Courtney, J. S. Tse, O. Mao, J. Hafner, J. R. Dahn, *Phys. Rev. B* 58 (1998) 15583.
 30. J. Chouvin, J. Olivier-Fourcade, J. C. Jumas, B. Simon, O. Godiveau, *Chem. Phys. Lett.* 308 (1999) 413; R. A. Dunlap, D. A. Small, D. D. MacNeil, M. N. Obrovac, J. R. Dahn, *J. Alloy Compd.* 289 (1999) 135.
 31. W. J. Weydanz, M. Wohlfahrt-Mehrens, R. A. Huggins, *J. Power Sources* 81–82, (1999) 237.
 32. G. R. Goward, N. J. Taylor, D. C. S. Souza, L. F. Nazar, *J. Alloy Compd.* 329 (2001) 82.
 33. Y. Iodata, T. Kubota, A. Matsufuji, Y. Maekawa, T. Miyasaka, *Science* 276 (1997) 1395.
 34. I. A. Courtney, J. R. Dahn, *J. Electrochem. Soc.* 144 (1997) 2045.
 35. I. A. Courtney, J. R. Dahn, *J. Electrochem. Soc.* 144 (1997) 2943.
 36. G. R. Goward, F. Leroux, W. P. Power, G. Ouvrard, T. Egami, W. Dmowski, L. F. Nazar, *Electrochem. Solid-State Lett.* 2 (1999) 367; G. R. Goward, L. F. Nazar, W. P. Power, *J. Mater. Chem.* 10 (2000) 1.
 37. J. Chouvin, C. Branci, J. Sarradin, J. Olivier-Fourcade, J. C. Jumas, B. Simon, Ph. Biensan, *J. Power Sources* 81 (1999) 277; J. Chouvin, J. Olivier-Fourcade, J. C. Jumas, B. Simon, O. Godiveau, *Chem. Phys. Lett.* 308 (1999) 413; A. Hightower, P. Delcroix, G. Le Caër, C-KK. Huang, B. V. Ratnakumar, C. C. Ahn, B. Fultz, *J. Electrochem. Soc.* 147 (2000) 1.
 38. I. A. Courtney, J. S. Tse, O. Mao, J. Hafner, J. R. Dahn, *Phys. Rev. B.* 58 (1998) 15583.
 39. J. D. Corbett, E. Garcia, A. M. Guloy, W-M. Hurng, Y-U. Kwon, E. A. Leon-Escamilla, *Chem. Mater.* 10 (1998) 2824.
 40. J. L. Tirado, *Mat. Sci. Eng.* R40 (2003) 103.
 41. J. Yang, M. Winter, J. O. Besenhard, *Solid State Ionics* 90 (1996) 281.
 42. R. A. Huggins, B. A. Boukamp, 1984 *U.S. Patent* 4,436,796.
 43. O. Mao, R. A. Dunlap, J. R. Dahn, *J. Electrochem. Soc.* 146 (1999) 405; J. R. Dahn, *ibid* 146 (1999) 414; O. Mao, J. R. Dahn, *ibid.*, 146 (1999) 423.
 44. D. Larcher, L. Y. Beaulieu, O. Mao, A. E. George, J. R. Dahn, *J. Electrochem. Soc.* 147 (2000) 1703.
 45. O. Crosnier, T. Brousse, X. Devaux, P. Fragnaud, D. M. Schleich, *J. Power Sources* 94 (2001) 169.
 46. G. M. Ehrlich, C. Durand, X. Chen, T. A. Hugener, F. Spiess, S. L. Suib, *J. Electrochem. Soc.* 2000 147 (2000) 886.
 47. L. Y. Beaulieu, J. R. Dahn, *J. Electrochem. Soc.* 147 (2000) 3237; L. Beaulieu, D. Larcher, R. A. Dunlap, J. R. Dahn, *J. Alloys Compd.* 297 (2000) 122.
 48. J. R. Dahn, R. L. Turner, O. Mao, R. A. Dunlap, A. E. George, M. M. Buckett, D. J. McClure, L. J. Krause, *Thin Solid Films* 408 (2002) 111.

49. R. L. Turner, D. J. McClure, L. J. Krause, M. M. Buckett, J. R. Dahn, O. Mao, *Patent Cooperative Treaty Application* 1999 WO99/49532.
50. J. Yang, I. D. Raistrick, R. A. Huggins, *J. Electrochem. Soc.* 133 (1986) 457.
51. A. Kjekshus, D. G. Nicholson, T. Rakke, *Acta. Chem. Scand.* 27 (1973) 1307.
52. R. Alcantara, F. J. Fernandez-Madrigal, P. Lavela, J. L. Tirado, J. C. Jumas, J. Olivier-Fourcade, *J. Mater. Chem.* 9 (1999) 2517.
53. I. Lefebvre-Devos, M. Lassalle, X. Wallart, J. Olivier-Fourcade, L. Monconduit, J. C. Jumas, *Phys. Rev. B* 63 (2001) 125110.
54. L. Aldon, A. Garcia, J. Olivier-Fourcade, J. C. Jumas, F. Fernández-Madrigal, P. Lavela, C. Perez Vicente, J. L. Tirado, IMLB 2002, Monterrey, USA, *Abstract* #255.
55. F. J. Fernández-Madrigal, P. Lavela, C. Perez-Vicente, J. L. Tirado, *J. Electroanal. Chem.* 501 (2001) 205.
56. O. Crosnier, D. C. S. Souza, J. E. Greedan, L. F. Nazar, *Materials Research Society Symposium* Dec 2-6, 2002, Abstract EE8.3. p 683
57. A. Kjekshus, P. G. Peterzens, T. Rakke, A. F. Andresen, *Acta. Chem. Scand.* 33 (1979) 469.
58. H. Holseth, A. Kjekshus, *Acta. Chem. Scand.* 23 (1969) 3043.
59. L. M. L. Fransson, J. T. Vaughey, K. Edström, M. M. Thackeray, *J. Electrochem. Soc.* 150 (2003) A86.
60. K. D. Kepler, J. T. Vaughey, M. M. Thackeray, *Electrochem. Solid-State Lett.* 2 (1999) 307.
61. G. X. Wang, L. Sun, D. H. Bradhurst, S. H. Dou, H. K. Liu, *J. Alloys and Compounds* 299 (2000) L12.
62. D. Larcher, L. Y. Beaulieu, D. D. MacNeil, J. R. Dahn, *J. Electrochem. Soc.* 147 (2000) 1658.
63. S. Sharma, L. Fransson, E. Sjöstedt, L. Nordström, B. Johansson, K. Edström, *J. Electrochem. Soc.* 150 (2003) A330.
64. L. Fransson, E. Nordström, K. Edström, L. Häggström, M. M. Thackeray, *J. Electrochem. Soc.* 149 (2002) A736.
65. L. M. L. Fransson, J. T. Vaughey, R. Benedek, K. Edström, J. O. Thomas, M. M. Thackeray, *Electrochem. Comm.* 3 (2001) 317.
66. M. M. Thackeray, J. T. Vaughey, C. S. Johnson, A. J. Kropf, R. Benedek, L. M. L. Fransson, K. Edstrom, *Journal of Power Sources* 113 (2003) 124.
67. J. T. Vaughey, J. O'Hara, M. M. Thackeray, *Electrochem. Sol. St. Lett.* 3 (2000) 13.
68. C. S. Johnson, J. T. Vaughey, M. M. Thackeray, T. Sarakonsri, S. A. Hackeney, L. Fransson, K. Edström, J. O. Thomas, *Electrochem. Comm.* 2 (2000) 595.
69. A. J. Kropf, H. Tostman, C. S. Johnson, J. T. Vaughey, M. M. Thackeray, *Electrochem. Comm.* 3 (2001) 244.
70. K. C. Hewitt, L. Y. Beaulieu, J. R. Dahn, *J. Electrochem. Soc.* 148 (2001) A402.
71. F. J. Fernández-Madrigal, P. Lavela, C. Perez-Vicente, J. L. Tirado, J. C. Jumas, J. Olivier-Fourcade, *Chem. Mater.* 14 (2002) 2962.
72. M. Wachtler, M. Winter, J. O. Besenhard, *J. Power Sources* 105 (2002) 160.
73. J. Yang, M. Wachtler, M. Winter, J. O. Besenhard, *Electrochem. Solid-State Lett.* 2 (1999) 161.
74. M. Wachtler, J. O. Besenhard, M. Winter, *J. Power Sources* 94 (2001) 189.
75. H. Li, L. Shi, W. Lu, X. Huang, L. Chen, *J. Electrochem. Soc.* 148 (2001) A915.
76. A. Anani, R. A. Huggins, *J. Power Sources* 38 (1992) 351.
77. T. Moriga, K. Watanabe, D. Tsuji, S. Massaki, I. Nakabayashi, *J. Sol. St. Chem.* 153 (2000) 386.
78. J. Santos-Pena, T. Brousse, D. M. Schleich, *Ionics* 6 (2000) 133.
79. H. Kim, J. Choi, H.-J. Sohn, T. Kang, *J. Electrochem. Soc.* 146 (1999) 4401.
80. G. A. Oberts, E. J. Cairns, J. A. Reimer, *J. Power Sources* 110 (2002) 424; S.-W. Song, K. A. Striebel, R. P. Reade, G. A. Roberts, E. J. Cairns, *J. Electrochem. Soc.* 150 (2003) A121

81. H. Kim, Y.-J. Kim, D.-G. Kim, H.-J. Sohn, T. Kang, *Solid State Ionics* 144 (2001) 41
82. H. Sakaguchi, H. Honda, T. Esaka, *J. Power Sources* 81 (1999) 229
83. A. M. Wilson, B. M. Way, J. R. Dahn, T. van Burren, *J. Appl. Phys.* 77 (1995) 2363.
84. I. Kim, P. N. Kumta, G. E. Blomgren, *Electrochem. Solid-State Lett.* 3 (2000) 493.
85. C. S. Wang, G. T. Wu, X. B. Zhang, Z. F. Qi, W. Z. Li, *J. Electrochem. Soc.* 145 (1998) 2751.
86. H. Li, X. Huang, L. Chen, Z. Wu, Y. Liang, *Electrochem. Solid-State Lett.* 2 (1999) 547.
87. H. Wang, M. Yoshio, A. Takeshi, Z. Ogumi, *Electrochem. Solid-State Lett.* 4 (2002) A499.
88. M. Yoshio, H. Wang, K. Fukuda, T. Umeno, N. Dimov, Z. Ogumi, *J. Electrochem. Soc.* 149 (2002) A1598.
89. R. L. Turner, *World Intellectual Property Organization Patent Application* 2000 WO00/03444.
90. L. Y. Beaulieu, K. C. Hewitt, R. L. Turner, A. Bonakdarpour, A. A. Abdo, L. Christensen, K. W. Eberman, L. J. Krause, J. R. Dahn, *J. Electrochem. Soc.* 150 (2003) A149.
91. T. Ohzuku, A. Ueda, N. Yamamoto, *J. Electrochem. Soc.* 142 (1995) 1431.
92. L. Kavan, M. Grätzel, *Electrochem. Solid State Lett.* 5 (2002) A39.
93. T. Ohzuku, K. Tatsumi, N. Matoba, K. Sawai, *J. Electrochem. Soc.* 147 (2000) 3592.
94. S. Huang, L. Kavan, I. Exnar, M. Grätzel, *J. Electrochem. Soc.* 142 (1995) L142.
95. B. O'Regan, M. Grätzel, *Nature* 353 (1991) 737
96. T. P. Feist, P. K. Davies, *J. Solid State Chem.* 101 (1992) 275; G. Nussli, K. Yoshizawa, T. Yamabe, *J. Mater. Chem.* 7 (1997) 2529.
97. M. Wagemaker, A. P. M. Kentgenst, F. M. Mulder, *Nature* 418 (2002) 397.
98. M. M. Thackeray, W. I. F. David, J. B. Goodenough, *J. Solid State Chem.* 55 (1984) 280; L. A. Picciotto, M. M. Thackeray, *Mat. Res. Bull.* 21 (1986) 583.
99. C. Sigala, D. Guyomard, Y. Piffard, M. Tournoux, *C.R. Acad. Sci. Paris.* 320 (1995) 523; D. Guyomard, C. Sigala, A. LeGal LaSalle, Y. Piffard, *J. Power Sources* 68 (1997) 692.
100. N. Kumagai, *Jap. Patent* 08-241707 (1996).
101. S. Denis, E. Baudrin, M. Touboul, J.-M. Tarascon, *J. Electrochem. Soc.* 144 (1997) 4099.
102. F. Leroux, G. Piffard, Ouvrard, J.-L. Mansot, D. M. Guyomard, *Chem. Mater.* 11 (1999) 2948.
103. F. Leroux, G. R. Goward, W. P. Power, L. F. Nazar, *Electrochem. Solid-State Lett.* 1 (1998) 201; F. Leroux, L. F. Nazar, *Solid State Ionics* 133 (2000) 37.
104. F. Leroux, L. F. Nazar, *Mat. Res. Soc. Symp. Proc. New Materials for Batteries and Fuel Cells, II*, 575 (1999) 173.
105. L. Nazar, G. Goward, F. Leroux, M. Duncan, H. Huang, T. Kerr, J. Gaubicher, *J. Int. J. Inorg. Mat.* 3 (2001) 191.
106. S. Denis, E. Baudrin, F. Orsini, G. Ouvrard, M. Touboul, J.-M. Tarascon, *J. Power Sources* 81 (1999) 79; S. Denis, E. Baudrin, F. Orsini, J.-M. Tarascon, *Chem. Mater.* 12 (2000) 3733.
107. J. Rowsell, J. Gaubicher, L. F. Nazar, *J. Power Sources* in press.
108. P. Poizot, S. Laruelle, S. Grugeon, L. Dupont, J. M. Tarascon, *Nature* 406 (2000) 407.
109. M. Duncan, L. F. Nazar, *Mat. Res. Soc. Symp. Proc. Solid State Ionics* 548 (1999) 71; M. Duncan, G. Ouvrard, L. F. Nazar, J. Gaubicher, Abstract # 235, *The Electrochemical Society Meeting Abstracts*, Hawaii, 1999.
110. D. H. Gregory, *J. Chem. Soc., Dalton Trans.* (1999) 259.
111. S. H. Elder, L. H. Doerr, F. J. DiSalvo, J. B. Parise, D. Guyomard, J. M. Tarascon, *Chem. Mater.* 4 (1992) 928.
112. R. Juza, K. Langer, K. von Benda, *Angew. Chem. Int. Ed. Engl.* 7 (1968) 360.
113. M. Nishijima, N. Tadokoro, Y. Takeda, N. Imanishi, O. Yamamoto, *J. Electrochem. Soc.* 141 (1994) 2966; S. Suzuki, T. Shodai, *Solid State Ionics* 116 (1999) 1.
114. M. Nishijima, Y. Takeda, N. Imanishi, O. Yamamoto, *J. Solid State Chem.* 113 (1994) 205.
115. T. Shodai, S. Okada, S. Tobishima, J. Yamaki, *Solid State Ionics* 86–88 (1996) 785

116. A. Gudat, R. Kniep, A. Rabenau, *Angew. Chem. Int. Ed. Engl.* 30 (1991) 199.
117. J. Klatyk, R. Z. Kniep, *Kristallogr. NCS* 214 (1999) 447.
118. J. L. C. Rowsell, V. Pralong, L. F. Nazar, *J. Am. Chem. Soc.* 123 (2001) 8598.
119. T. Y. Kim, M. G. Kim, J. M. Lee, T. Kang, H-J. Sohn, *Electrochem. Solid-State Lett.* 5 (2002) A103.
120. T. Shodai, Y. Sakurai, T. Suzuki, *Solid State Ionics* 122 (1999) 85.
121. Y. Takeda, M. Nishijima, M. Yamahata, K. Takeda, N. Imanishi, O. Yamamoto, *Solid State Ionics* 130 (2000) 61
122. J. Yang, Y. Takeda, N. Imanishi, O. Yamamoto, *J. Electrochem. Soc.* 147 (2000) 1671.
123. N. Pereira, L.C. Klein, G. G. Amatucci, *J. Electrochem. Soc.*, 149 (2002) A262
124. L. Monconduit, M. Tillard-Charbonnel, C. Belin, *J. Solid State Chem.* 156 (2001) 37.
125. D. Souza, V. Pralong, A. J. Jacobson, L. F. Nazar, *Science* 296 (2002) 2012.
126. D. Souza, V. Pralong, A. J. Jacobson, L. F. Nazar, 11th IMLB, Abstract #60, Monterey California 2002.
127. M.-L. Doublet, F. Lemoigno, F. Gillot, L. Monconduit, *Chem. Mater.* 14 (2002) 4126.
128. L. Nazar, D. Souza, V. Pralong, *Patent Cooperative Treaty International Application* 2002 PCT/CA02/00016
129. V. Pralong, D. C. Souza, L. F. Nazar, *Electrochem. Comm.* 4 (2002) 516
130. R. Alcántara, J. L. Tirado, J. C. Jumas, L. Monconduit, J. Olivier-Fourcade, *J. Power Sources* 109 (2002) 308.

Chapter 5

CARBONACEOUS AND GRAPHITIC ANODES

M. Winter, K.-C. Moeller and J. O. Besenhard

*Institute for Chemical Technology of Inorganic Materials, Graz University of Technology,
Stremayrgasse 16, A-8010 Graz, Austria, e-mail: martin.winter@tugraz.at*

5.1. CARBONS IN ION TRANSFER BATTERIES

In rechargeable lithium ion batteries the main¹ application of carbon is the use as a host anode accessible by lithium cations via electrochemical insertion, the lithium being provided by another insertion material used as host cathode (Figure 5.1A). This "electro-insertion" reaction is basically a host/guest solid state redox reaction involving electrochemical charge transfer coupled with insertion of mobile guest ions (in lithium ion batteries, these are lithium ions) into the structure of a solid host, which is a mixed electronic and ionic conductor. The major structural features of the host are kept after the insertion of the guests. A common convention in the literature is that "intercalation" is regarded as a special case of "insertion". The term "intercalation" implies the restricting condition that a *layered* host takes up guests within its interlayer gaps ("galleries"), which may result in a volume change perpendicular to the layers, but which causes no other structural changes. However, according to this strict definition, even graphite would be not a pure intercalation host, as during Li accomodation the stacking sequence changes by sliding of the graphene layers. Therefore, in this review the term intercalation will be used where the historical conventions or the present practice make its use appropriate, *i.e.*, we will use the term lithium-graphite intercalation compounds for lithiated graphites (cf. Refs. 1-16).

¹ It should be noted here, that cation and anion intercalation can also occur into carbon materials used as conductive electrode additives. At the anode, this cation intercalation is a regular reaction occurring in parallel to intercalation in the active carbonaceous anode material. At the cathode, anion intercalation can happen during overcharge of the electrode.

Graphite is a redox-amphoteric intercalation host, *i.e.*, it can be intercalated by cations and anions yielding so-called donor- and acceptor-type graphite intercalation compounds.^{11,15-17} All-graphite-based

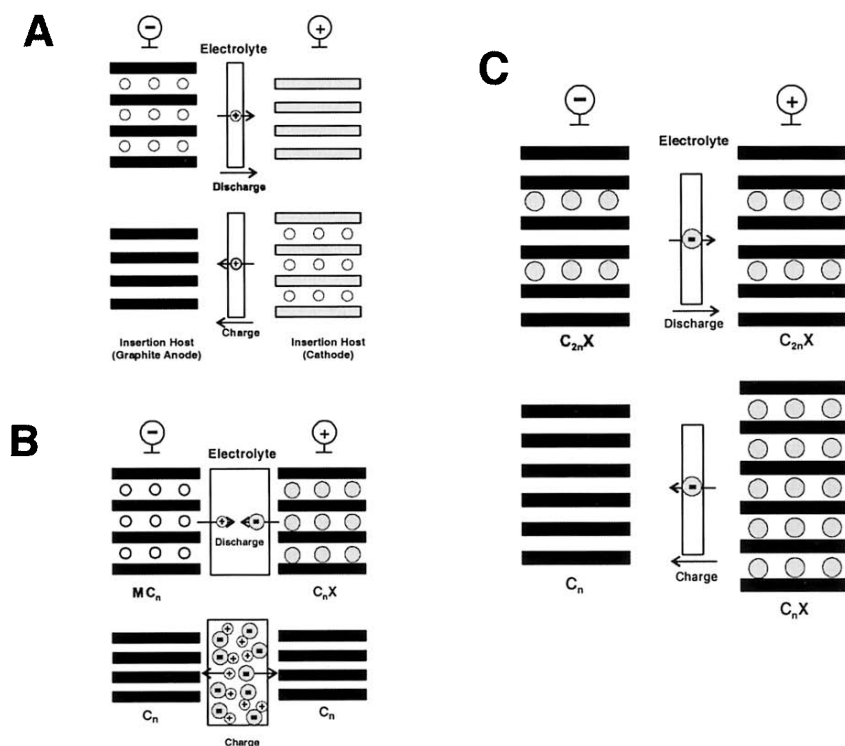


Figure 5.1. Rechargeable cells with active graphite intercalation electrodes: (A) graphite as lithium cation intercalation host anode (negative electrode) in lithium ion cells, (B) graphite as anode (accepting cations M) and cathode (positive electrode, accepting anions X) in dual graphite cells, and (C) hydrogen sulfate ion transfer cell based on graphite anode and cathode (both accepting anions $X=HSO_4^-$), C_nX denotes a stage-I, $C_{2n}X$ a stage-II hydrogensulfate/graphite intercalation compound (cf. Section 5.3.2.2).

rechargeable batteries have been investigated since decades. In these so-called "dual-graphite" cells,¹⁸⁻²² the charge/discharge reaction is the intercalation/release of electrolyte cations *and* anions into graphite (Figure 5.1B). As the ion concentration of the electrolyte changes during cycling, enough electrolyte salt (cations + anions X) must be incorporated in the cell to guarantee the electrolyte conductivity, and enough solvent must be

provided to leave the electrolyte salt dissolved at any state of charge/discharge.

In contrast with lithium ion cells, where the electrolyte is basically an ion transfer medium, this charge/discharge mechanism requires excess of electrolyte salt and solvent at the expense of energy density. Furthermore, as the cell operates at up to 5 V, the electrolyte suffers from strong electrolyte reduction and oxidation.

A very interesting example of an all-graphite-based rechargeable battery has been proposed by Rüdorff and Hofmann²³ as early as 1938. They have constructed an electrochemical cell by combining a graphite cathode, fully intercalated with $\text{HSO}_4^-(\text{H}_2\text{SO}_4)_y$ (this is a so-called stage I graphite intercalation compound, the HSO_4^- guest ion being solvated by sulfuric acid molecules; cf. Sections 5.3.2.2 and 5.4.2 for explanations) with a plain (not intercalated) graphite anode. During charge, the anions are transferred from the cathode to the anode, until both electrodes possess the same guest concentration. During discharge, the guest concentration in the cathode is re-established by the backwards ion transfer. Using today's terminology, this electrochemical set-up would be named a hydrogen sulfate ion cell. This cell is the first "ancestor" of the lithium ion cell.

5.2. HISTORY OF LITHIATED CARBONS

The first occurrence of lithiated carbons formed by reaction of lithium with carbonaceous materials is said to go back to the development of the thermonuclear hydrogen bomb in the 1940s, whose enormous energy release of 22.4 MeV is based on the strongly exothermal fusion reaction of the isotopes ^6_3Li and ^2_1H yielding two molecules of ^4_2He .²⁴

Nevertheless, the first intended and official synthesis of lithiated carbons was reported by Hérolf^{25,26} in 1955, who prepared a lithium-graphite intercalation compound (Li-GIC) from the elements via a chemical synthesis route. The formation of Li-GICs is in competition with the formation of Li carbides.²⁷⁻²⁹ Therefore, the chemical synthesis has to be carried out at moderate temperatures and lithium vapor pressures. The chemical synthesis of the GICs of the heavy alkali metals K, Rb, and Cs was reported before,^{30,31} whereas the first Na-GIC's emerged afterwards.^{32,33} Fully intercalated highly crystalline graphites have the stoichiometric formulae of MC_8 ($\text{M}=\text{K}$, Rb , and Cs) and LiC_6 .²⁶ Na hardly intercalates into graphite yielding diluted GIC's of the formulae $\approx \text{NaC}_{24} - \text{NaC}_{64}$.^{11,26} A higher Na uptake was obtained with disordered carbons.³⁴⁻³⁸ An overview about the early works on chemically prepared GICs is given in Ref. 26.

The electrochemical formation of Li-GICs was performed more than ten years after the chemical synthesis. As in the case of metals which alloy

with lithium,³⁹⁻⁴² electrochemically prepared lithiated graphites⁴³⁻⁴⁵ emerged first in room temperature lithium cells, when they were used as substrates for the electrodeposition of metallic lithium from Li^+ -containing electrolytes. It took a while until the occurring phenomenon was identified to be a reversible lithium intercalation into graphite.^{46,47} Not much later, graphite was proposed as reversible anode for nonaqueous electrolyte based rechargeable lithium batteries⁴⁸ by adapting the already known concepts of electro-insertion and electro-intercalation.¹⁻³

Though the safety problems with the dendritic lithium deposition in rechargeable nonaqueous organic electrolyte lithium batteries (cf. reviews 12,14,49-61) urgently demanded a replacement by an insertion anode, which avoided the use of Li metal, the attempts to introduce a graphitic carbon anode in a rechargeable lithium battery resulted in no practical realization for more than a decade. These attempts included the use (i) of electrolytes^{46,47} which co-intercalate into graphite (cf. Section 5.4.2), (ii) of solid polymer electrolytes,^{62,63} and (iii) of a lithiated (charged) graphite anode in molten salts^{64,65} or organic electrolytes,^{64,66} which is sensitive to air and moisture and thus complicates cell assembly.

The first two research reports on carbon anodes with practical relevance for rechargeable lithium batteries by Kanno *et al.*⁶⁷ and Mohri *et al.*⁶⁸ appeared in 1989. Mohri *et al.*⁶⁸ even constructed a complete lithium ion cell consisting of a pyrolytic carbon anode and a metal oxide cathode, which was able to deliver several hundreds of cycles at satisfactory efficiencies. In fact, several Japanese companies have investigated and patented the usage of specific carbonaceous anodes before that time.⁶⁹ The first announcement of a commercial application of a carbon insertion host anode in a so-called lithium ion cell was done by Sony in 1991.^{70,71} Their cell was based on a disordered carbon anode and a LiCoO_2 cathode, which means the electrode materials are assembled in the discharged state, the electrode materials being not very sensitive to moisture and air.

The underlying ion transfer concept was proposed⁷² and applied with alternative electrode materials⁷³⁻⁷⁷ before. However, though lithium ion cells with lithium-aluminum alloy anode⁷³ or an insertion anode based on oxidic materials⁷⁴⁻⁷⁷ were feasible in principle, they suffered from poor practical energy densities (oxides) or cycling stabilities (alloys). The superiority of lithium ion cells is chiefly connected with the use of carbonaceous anode materials.

The announcement of Sony induced a run on the research topic lithium ion batteries, which in turn produced tens of thousands of papers, patents, and other publications (cf. books and compilations⁷⁸⁻⁸² and reviews 8,12,42,54,55,57-59,61,83,84). With regard to carbonaceous anodes, this large publication output is mainly due to the variety of carbon materials investigated for lithium insertion and the various resulting lithium storage

mechanisms. In addition, the manifold interactions of the carbon material with other battery components, in particular with the electrolyte, have to be considered. The related issues will be discussed in the following sections.

5.3. ELECTROCHEMICAL Li STORAGE IN CARBON

5.3.1. Carbonaceous Host Materials and Their Properties

The quality and quantity of sites which are capable of reversible lithium accommodation and the type and extent of interaction with the electrolyte depend in a complex manner on the crystallinity, texture, (micro-) structure, and (micro-) morphology of the carbonaceous host material. The type of carbon determines the current/voltage characteristics of the electrochemical intercalation reaction and also potential side reactions. Carbonaceous materials suitable for lithium insertion or intercalation are commercially available in manifold types and qualities (cf. reviews 12,14,53,57,60,85-94). Many exotic carbons have been specially synthesized in a laboratory scale by pyrolysis of various precursors. Even fullerene¹⁴ and carbon nanotubes⁹⁵ have been evaluated, however with little practical success.

Heteroatoms, *i.e.*, atoms in the carbonaceous material different from carbon, can play an important role in the bulk (Section 5.3) and surface chemistry (Section 5.4) of carbon and furthermore have strong influence on its characteristics in the lithium ion cell. The term "carbon alloys" has been created for structurally and chemically heterogeneous carbons.⁹⁶

It has to be emphasized that the assumed suitability of a carbonaceous material for a lithium intercalation host depends strongly on the method of its evaluation. Quite a few carbons may have been rejected as anode materials due to an inadequate evaluation. As a consequence, the classification of a carbon as "good" or "poor" anode material can be sometimes only preliminary.

Due to the variety of available carbons a classification is inevitable. Most carbonaceous materials which are capable of reversible lithium storage can roughly be classified as graphitic and non-graphitic (disordered).

5.3.1.1. Graphitic Carbons

Graphitic carbons basically comprise of sp^2 -hybridized carbon atoms which are arranged in a planar "honeycomb-like" network, *i.e.*, a "graphene" layer is formed⁹⁷ (Figure 5.2). Van der Waals forces provide a weak cohesion of the graphene layers leading to the layered graphite structure.

From a strictly crystallographic point of view, the term "graphite" is only applicable to carbons having a layered lattice structure with a perfect stacking order of graphene layers, either the prevalent AB (hexagonal graphite, 2H-, or α -phase) or the less common ABC (rhombohedral graphite, 3R-, or β -phase). Due to the small energy for transformation of AB into ABC stacking (and viceversa), perfectly stacked graphite crystals are not readily available. Therefore, the term "graphite" is often used regardless of stacking order.

The ratio of hexagonal to rhombohedral contents can be varied by certain processes. Mechanical treatments, especially milling, shearing, or ultrasonic impact result in a larger extent of the β -phase,^{85,98,99} whereas thermal annealing procedures at elevated temperatures convert the material to the thermodynamically more stable α -form. By heat treatment, it is possible to create a graphite which contains 100% α -phase, whereas this could not be achieved by mechanical measures for the β -form. So far, β -phase contents up to 30% have been reported. The rhombohedral and hexagonal contents of graphites can be estimated from XRD spectra.^{85,98,100-103} It should be noted here, that in addition to a change of the stacking sequence, the mechanical milling is able to destroy carbon-carbon bonds and thus to increase the number of structural defects,¹⁰⁴⁻¹⁰⁸ the kind and extent of defects being dependent on the milling procedure.¹⁰⁹⁻¹¹¹ On the contrary, heat-treatment does "heal" the graphite structure by reducing the number of defects.^{85,101} After long term milling, graphite can develop a fully amorphous structure.^{110,112} Shorter milling times can confine the amorphization to the surface.^{101,109,111} Milling is also able to change the chemical (surface) composition of the carbon material, when done under a certain atmosphere, as the defects created by milling are highly reactive.¹¹³⁻¹¹⁶

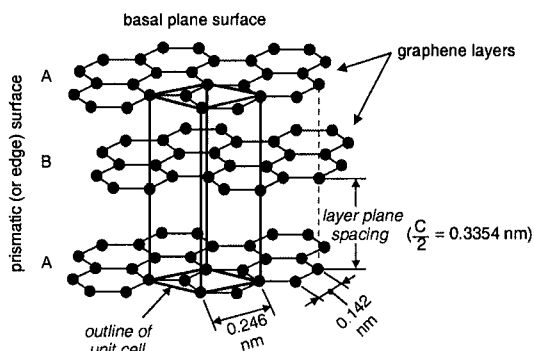


Figure 5.2. Crystal structure of hexagonal graphite showing the AB layer stacking sequence, the unit cell, and the subdivision in basal plane and prismatic surfaces.

The structure of layered graphite gives rise to basically two kinds of surfaces, prismatic (edge) surfaces and basal plane surfaces (Figure 5.2). Ideal (defect- and contaminant-free) basal plane surfaces are homogeneous and "smooth" and consist of carbon atoms. In contrast, the prismatic surfaces are heterogeneous and "rough" and apart from carbon may contain various, mostly (but not only) oxygen-containing, surface groups. The quantity and quality of surface groups for graphitic and non-graphitic carbonaceous materials can be changed by mechanical (*e.g.*, milling), thermal (*e.g.*, heat-treatment), and chemical measures (*e.g.*, exposure to reagents creating a certain surface chemistry), or a combination of these methods. For further details on carbon surface chemistry, cf. 11,117-122. The problems with the determination of the surface chemistry of carbons are discussed in Refs. 123,124.

It is well known that the prismatic and basal plane surfaces of graphite show a different electrochemical behavior in many respects.^{117,118} Intercalation, for example, proceeds via the prismatic and not via the basal plane surfaces. The interaction of graphitic materials with the electrolyte is also dependent on the respective surface and its properties. The information about the relative and absolute extents of prismatic and basal plane surface areas in a graphite material is essential for understanding and controlling the reactions of the graphite anode in lithium ion cells.

The adsorption of nitrogen at 77 K is a commonly used measurement for the determination of the total specific surface area (as m²/g) of graphites and other materials through application of the well known Brunauer-Emmett-Teller (BET) equation. The determination of the BET surface area is based on the premise that the surface of the solid adsorbent is homogeneous and thus, the whole surface adsorbs the same extent of nitrogen per area, such that the calculation of the nitrogen volume forming a mono-layer on the adsorbent allows to determine the surface area. Any surface heterogeneities leading to different degrees of (multi-layer) nitrogen adsorption at different surface sites are not accounted for in the BET theory. A more sophisticated theory than the BET theory has to be applied in order to estimate the total surface area of graphitic carbons.^{125,126} This theory also allows to individually estimate the extents of prismatic and basal plane surfaces of a graphitic material, and thus for example may disclose which part of the graphite surface is active for lithium intercalation and which not^[85,127].

The actual structure and surface of practical carbonaceous materials deviates more or less from the ideal graphite structure and surface. Even highly ordered graphites typically have a number of structural defects, such as dislocations, steps, boundaries, point defects, and cracks.^{128,129} Moreover, carbonaceous materials consisting of aggregates of graphite crystallites are named graphites as well. For instance, the terms natural, artificial, synthetic, and pyrolytic graphite are commonly used, although the meant materials are

polycrystalline.¹³⁰ The crystallites may vary considerably in size, ranging from nm to μm . In some carbons, the aggregates are large and relatively free of defects, *e.g.*, in highly oriented pyrolytic graphite (HOPG). Furthermore, texture effects can be observed as the crystallites may be differently oriented to each other. In addition to essentially graphitic crystallites, carbons may also include crystallites containing carbon layers (or packages of stacked carbon layers) with randomly distributed misfits and misorientation angles of the stacked segments to each other (turbostratic disorder¹³¹). The latter disorder can be identified from a non-uniform and on average increased interlayer spacing compared to graphite;^{130,132} the corresponding XRD patterns show relatively broad and quite asymmetric (00 l) diffraction peaks.¹³³

5.3.1.2. Non-Graphitic Carbons

When the structure disorder becomes more dominating among the crystallites, the carbonaceous material can be no longer considered graphitic but must be regarded as non-graphitic (disordered). For carbons that contain both characteristic graphitic and non-graphitic structure units, the classification in graphitic and non-graphitic types can be somehow arbitrary and in many cases only made for the sake of convenience.

In case of non-graphitic carbons most of the carbon atoms are arranged in a planar hexagonal network too. The basic structural unit (BSU) contains planar aromatic structures consisting of several tens of rings, which have different relative arrangements.¹³⁴ Though layered structure segments made from BSUs are probable, there is actually no far-reaching crystallographic order in *c* direction. This is typical of the BSUs form carbon structures which are characterized by amorphous areas embedding and partially crosslinking more graphitic-type (layered) structure segments.¹³⁵⁻¹³⁷ The number and size of these areas vary and depend both on the precursor material and on the manufacturing process, *e.g.*, manufacturing temperature and pressure. The size of the BSUs and of the structure segments made from the BSUs can be small, so that many internal edges with internal heteroatoms or unpaired electrons are possible.¹¹⁷ Most non-graphitic carbons are prepared by pyrolysis of organic polymer or hydrocarbon precursors at temperatures below $\sim 1500^\circ\text{C}$. Further heat treatment at temperatures from ~ 1500 to $\sim 3000^\circ\text{C}$ allows to distinguish between two different types of carbons.

Graphitizing carbons develop the graphite structure continuously during the heating process. The structure segments are mobile enough to form graphite-like crystallites as crosslinking between them is weak. Graphitization of these carbons is simply the disorder \rightarrow order transformation of small but disorderedly stacked carbon layers and graphite crystallites into more ordered (more graphitic) arrangements.

Non-graphitizing carbons exhibit no true development of the graphite structure, even at high temperatures (2500-3000°C), since the carbon layers are immobilized by strong crosslinking. In order to increase the number of crosslinks, organic precursors which tend to crosslink, or crosslinking agents such as oxygen¹³⁸ can be applied. Since non-graphitizing carbons are mechanically harder than graphitizing ones, it is common to divide the non-graphitic carbons into soft and hard carbons.¹³⁵ The precursors, the preparation, and assumed structures of hard carbons resemble those of glassy carbon.^{139,140} The inter-layer and intra-layer disorder in hard carbons is so strong that the carbon layer fragments building up the carbonaceous material have sizes of only ≈ 1 nm.^{141,142}

Franklin¹³⁵ reported that, compared to graphitizing carbons, non-graphitizing carbons exhibit a considerably larger fine-structure micro- and nano-porosity. The size of the pores is in the range of 1 nm.^{141,143}

The different structural features (graphitic order, disorder, and nanopores) of graphite, soft carbons, and hard carbons result in different lithium storage mechanisms (see below). Dahn and colleagues^{53,85} and Tatsumi and colleagues^{144,145} have proposed theories based on the Franklin model, which allows to correlate the complex XRD patterns of non-graphitic carbons with the relative amounts of unorganized (randomly oriented and amorphous) and organized (layered) areas. As a result, the lithium storage capacity of a specific carbon material can be approximately predicted.

Azuma and colleagues^{146,147} have developed a novel model of the structure of soft and hard carbons. The model is based on the analysis of the interlayer distances, true densities, and nearest-neighbor-interactions of single carbon layers in a carbonaceous material and allowed them to predict structural characteristics beneficial for high lithium storage capabilities. The basic difference to the Franklin model is that the model considers each single carbon layer, whereas the Franklin model considers small crystallites, each containing two or three carbon layers, with equidistant interlayer distances and equal orientation to each other.

For graphitizing carbons, Méring and colleagues¹⁴⁸ has proposed a model which assumes that each single carbon layer is disordered. Graphitization is primarily considered as an ordering of this *intra-layer* disorder. The development of *inter-layer* ordered graphite structure is a secondary effect, resulting from the intra-layer ordering process. The application of this model to the lithium intercalation behavior is reported in Refs. 85,149.

The mobility of the carbon structure units, *i.e.*, depending on the model, the mobility (i) of small graphite crystallites, (ii) of single carbon layers (or BSUs), or (iii) within the single layers, determines the degree of microstructural ordering as well as the texture of the carbonaceous material. It depends on the state of aggregation of the intermediate phase during pyrolysis, which can be solid, liquid, or gaseous.¹³⁷ Non-graphitizing carbons

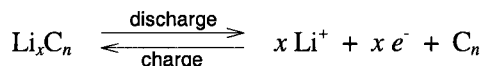
are usually products of solid-phase pyrolysis, whereas graphitizing carbons are commonly produced by liquid- or gas-phase pyrolysis. Examples of products of *solid-phase* pyrolysis are chars and glassy (vitreous) carbon. Because of the small crystal size and high structural disorder of the precursor polymers and the presence of crosslinkings, the ability of these carbons to graphitize is low. Pyrolysis of thermally stabilized polyacrylonitrile or pitch, which are the precursors for carbon fibers, yields also solid intermediate phases, but stretching of the fibrous material during the manufacturing process produces an ordered microstructure.¹³⁷ The synthesis of petroleum coke, which is the most important precursor for the manufacture of carbons and graphites, is an example of *liquid-phase* pyrolysis. Petroleum coke is produced by the pyrolysis of petroleum pitch, which is the residue from the distillation of petroleum fractions. Cokes are also products from pyrolysis of coal tar pitch and aromatic hydrocarbons at 300-500°C. Carbon black, pyrocarbon, and carbon films are examples of *gas-phase* pyrolysis products, *i.e.*, products of thermal cracking of gaseous hydrocarbon compounds which are deposited as carbon on a substrate.^{130,137}

The ability to graphitize also depends on the pre-ordering and pre-texture of the respective precursor. For example, the graphitization ability within the carbon layer should be higher (i) when the precursor material comprises highly condensed aromatic hydrocarbons, which can be considered to have a graphene-like structure and (ii) when neighboring BSUs, graphene layers or graphitic crystallites are suitably orientated to each other.

Apart from manifold structures, carbons can have various shapes, forms, and textures including powders with different particle size distributions, foams, whiskers, foils, felts, papers, fibers,^{91,150,152} spherical particles^{150,153} such as mesophase carbon microbeads (MCMB),^{87,154,160} etc. Different shapes, forms, and textures do not only influence the lithium intercalation behavior and the interactions with the electrolyte, but also may be crucial for electrode construction.^{90,91} Comprehensive overviews on carbon properties are given *e.g.*, in Refs. 130,136,137. Further information on carbonaceous materials can be found in Refs. 130,135,137,161-164.

5.3.2. Electrochemical Li Storage in Graphitic Carbons

The electro-insertion of Li⁺ cations into carbon proceeds according to:



During electrochemical reduction (charge) of the carbon host, Li cations penetrate into the carbon and form a lithiated carbon Li_xC_n . Li cation release during carbon oxidation is the anode discharge reaction.

5.3.2.1. In-Plane Ordering

In general, a maximum lithium content of one Li guest atom per 6 carbon host atoms can be reached for lithium intercalation into highly ordered, highly crystalline graphite ($n \geq 6$ in LiC_n or $x \leq 1$ in Li_xC_6) at ambient pressure. Higher lithium storage capacities into carbon can be reached with certain non-graphitic carbons and specifically treated graphites (see below).

The intercalation reaction proceeds via the prismatic surfaces (Figure 5.2). Through the basal planes, intercalation is possible at defect sites only. During intercalation the stacking order of the graphene layers shifts to AA. Thus, two neighboring graphene layers in LiC_6 directly face each other (Figure 5.3A). The energetically favored AA stacking sequence of LiC_6 has been proven by quantum mechanical calculations.^[165,166] Due to the hosted lithium the interlayer distance between the graphene layers increases moderately (10.3% has been calculated for LiC_6 ^{16,167,168}). The stacking order of the lithium interlayers is $\alpha\alpha$ (a Li-C₆-Li-C₆-Li chain exists along the *c* axis^{16,169}). In LiC_6 the lithium is distributed in-plane in such a manner that the occupation of nearest neighbor sites is avoided (Figure 5.3B).

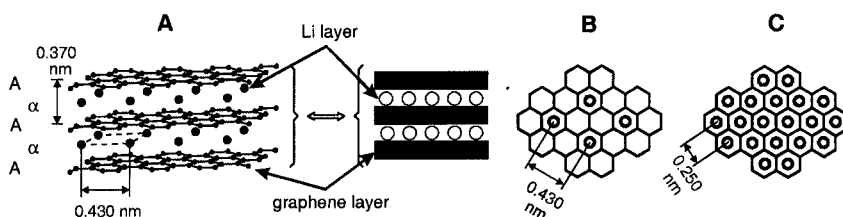


Figure 5.3. AA layer stacking sequence and the $\alpha\alpha$ interlayer ordering of the intercalated lithium in LiC_6 (A). In-plane structures of LiC_6 (B) and LiC_2 (C).

A higher lithium in-plane density by occupation of nearest neighbor sites is obtained in the phases $\text{LiC}_2 - \text{LiC}_4$, i.e., x in $\text{Li}_x\text{C}_6 = 2-3$, which are prepared chemically from graphitic carbon under high pressure (~ 60 kbar) and high temperature ($\sim 300^\circ\text{C}$) conditions.^{89,170-173} The close Li-Li distance in LiC_2 (Figure 5.3C) results in a higher chemical activity of lithium than that of lithium metal (Li-Li bond length (20°C) = 0.304 nm¹⁷⁴). Under ambient conditions LiC_2 decomposes slowly via various metastable intermediate Li/C phases to LiC_6 and metallic lithium.^{89,172} A study of the electrochemical

behavior of LiC_2 can be found in Ref. 89. For more details on the chemical synthesis of Li_xC_6 , see Refs. 26,88,89,175,176.

5.3.2.2. Stage Formation

A general feature of intercalation into graphite is the formation of a periodic array of unoccupied layer gaps (galleries) at low concentrations of guest species, called stage formation.^{11,15,16,23,25,26,177-180} This stepwise process can be described by the stage index "s" which is equal to the number of graphene layers between two nearest guest layers. Staging is a thermodynamic phenomenon related with the energy required to "open" the van der Waals gap between two graphene layers for the guests entering the hosts. The repulsive coulombic interactions between the guest ions are less effective. As a consequence, few but highly occupied van der Waals gaps are energetically favored over a random distribution of guests.

Staging phenomena as well as the degree of intercalation can be easily

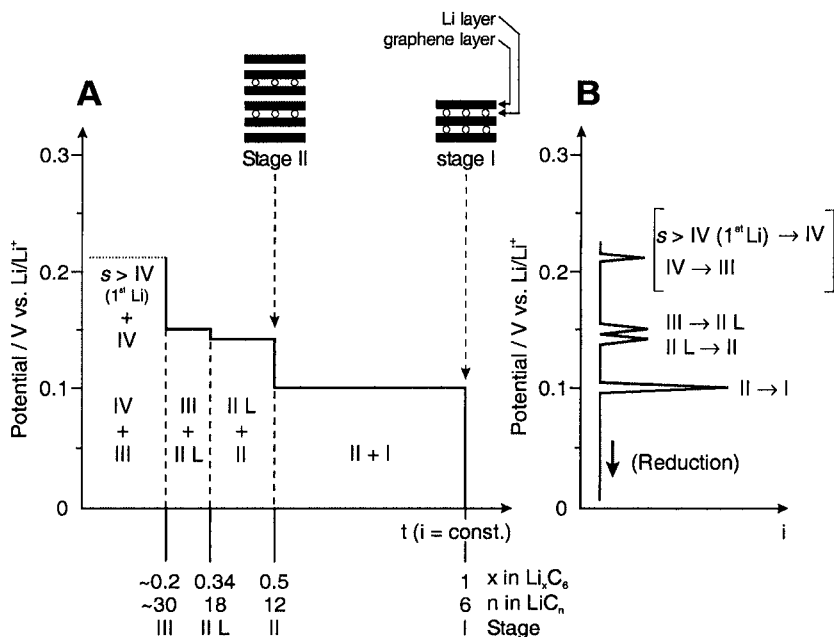


Figure 5.4. Stage formation during electrochemical lithiation of graphite. A: Schematic constant current charge curve. B: Schematic voltammetric curve.

observed during the electrochemical reduction of carbons in Li^+ containing electrolytes. Figure 5.4A shows a schematic potential/composition curve for the constant current reduction (charge) of graphite to LiC_6 corresponding to a lithium storage capacity of 372 Ah/kg with respect to the graphite mass. The potential plateaus in the curve arising during reduction indicate two-phase regions (coexistence of two phases). Under potentiodynamic control (linear potential sweep voltammetry) the two-phase regions are indicated by current peaks (Figure 5.4B).

Only within the small one-phase regions, the Li^+ transport is a diffusion process. Within the two phase regions, the stage transformation proceeds by nucleation of lithium and following phase boundary movement, *i.e.*, a reaction front propagates through the graphite.¹⁸¹⁻¹⁸³ The reaction front has a narrow width of $<5\ \mu\text{m}$ and a rate of 5–10 mm/min.¹⁸³

Apart from the stage $s = \text{I}$, other binary phases corresponding to the stages $s = \text{IV}$, III , II L , and II (which can be also obtained by chemical synthesis^{12,14,25,26,177,179,184}) were identified and confirmed by X-ray diffraction^{12,14,184-188} and Raman spectroscopy.^{189,190} The splitting of stage II into two, $s = \text{II}$ ($x=0.5$ in Li_xC_6) and $s = \text{II L}$ ($x=0.33$ in Li_xC_6), is due to different lithium packing densities. The term II L indicates a liquid like structure, which has no in-plane ordering^[191]. A phase diagram of Li_xC_6 was constructed from chemical¹⁸⁴ and electrochemical¹⁸⁸ data. There are different reports in the literature about what happens at the beginning of intercalation, *i.e.*, how the "1st lithium" is accommodated in graphite, before the stage IV compound is formed. It is reported, that the 1st lithium forms stages higher than $s = \text{IV}$.^{189,192} In contrast, it is said that the 1st lithium is randomly distributed in the graphite.^{188,193,194} The discrepancies about staging are discussed in Ref. 90.

5.3.2.3. Nature of the Bond in Li-Graphite Intercalation Compounds

In 1934-1938 Hofmann and co-workers^{23,195} have proposed that the bond in graphite intercalation compounds is of electrostatic nature, which led them to the term "graphite salts". Based on this proposal, Hennig and colleagues^{34,196} and Ubbelohde and colleagues^{197,198} have developed the "ionic model", *e.g.*, lithium is stored in cationic form in graphite, whereas the graphite host takes over the corresponding negative charge. Today, this model is still in use and may be the basis for the term "lithium ion battery". In general, GICs show a larger electronic conductivity than pure graphite (therefore GICs are called "synthetic metals"), which is an indicator for the take up of electrons by graphite. Moreover, the electrons are not homogeneously, but locally distributed over the graphene planes, the electron density being particularly high near the intercalated cationic

guests.¹⁷ ^7Li NMR spectroscopy^{143,146,199-202} as well as quantum mechanical calculations²⁰³ confirm the mostly ionic state of lithium in Li-GICs.

However, there is considerable criticism on the purely ionic model. Especially the Li-graphite bond in LiC_6 seems to be partially metallic (or covalent). Due to the $\alpha\alpha$ stacking of the lithium guest layers, the Li-Li distance along the c axis is smaller than the in-plane Li-Li distance (Figure 5.3A). On the other hand, the small increase in volume due to Li intercalation can be better explained by assuming that the lithium is stored as a small size guest, *i.e.*, in ionic form. Recently, Hightower *et al.*²⁰⁴ attributed a neutral character to the Li in stage-I LiC_6 by using transmission electron energy loss spectroscopy. Indeed, the potential of the stage-I compound (Figure 5.4A) is very close (but is not the same!) to metallic lithium, whereas the higher stage compounds and the diluted stage-I compound show more positive potentials. It is reasonable to presume that at the beginning of intercalation the lithium is accommodated into graphite in a more ionic form. This is also in agreement with the possibility of formation of solvated Li-GICs (*cf.* Section 5.4.2). During further reduction, the intercalated lithium gradually becomes more neutral. However, as there is still a small potential gap between the potential of metallic Li and that of LiC_6 , the Li in LiC_6 still should be partly ionic. Even the lithium which is stored in hard carbons at potentials of only 5 mV *vs.* Li/Li^+ is not in a fully metallic state (*cf.* Section 5.3.3). Finally, also the regular in-plane order of guests in LiC_6 (Figure 5.3B) can be better explained if the Li contains still some ionic charge which is providing repulsive coulombic interactions with its near lithium neighbors.

5.3.2.4. Reversible and Irreversible Capacity

Constant current charge/discharge curves for Li^+ intercalation/de-intercalation into/out of graphite clearly prove the staging phenomenon (Figure 5.5A). Nevertheless, there are no sharp discontinuities between the two-phase regions because (i) the packing density of Li_xC_6 slightly varies (a phase width exists),^{12,14} (ii) various types of overpotentials cause plateau-sloping in galvanostatic measurements (and peak broadening in voltammetric measurements, respectively),^{12,14} and (iii) in practical cases lithium intercalation does not proceed homogeneously over the electrode. Theoretically, the Li^+ intercalation into carbons is fully reversible. In the practical charge/discharge curve, however, the charge consumed in the first cycle significantly exceeds the theoretical specific charge for the first stage LiC_6 of 372 Ah/kg. The subsequent discharge recovers only ~80-95% of this charge. In the second and subsequent cycles the charge capacity is lower and the charge recovery is close to 100%. The excess charge consumed in the first cycle is generally ascribed to irreversible reactions (i) of Li^+ with graphite and (ii) of the (lithiated) graphite with the electrolyte.

The first reasoning is only to a minor part responsible for the excess charge. It is believed that reduction of impurities like H_2O or O_2 present on the carbon surface, reduction of surface groups at the prismatic surfaces, and irreversible lithium incorporation into the carbon matrix ("formation of residue compounds"²⁰⁵⁻²⁰⁷), *e.g.*, by reduction of heteroatom-groups located at carbon layer edges in polycrystalline carbons, take place.

The main part of the irreversible charge loss, however, is due to reactions with the electrolyte, which typically consists of a mixture of organic solvents and a highly soluble lithium salt. The strong reducing power of graphite (and other carbon anodes), at potentials where lithium intercalation proceeds, leads to reductive electrolyte decomposition.^{53,208-211} In suitable nonaqueous electrolytes, however, "passivating" films of

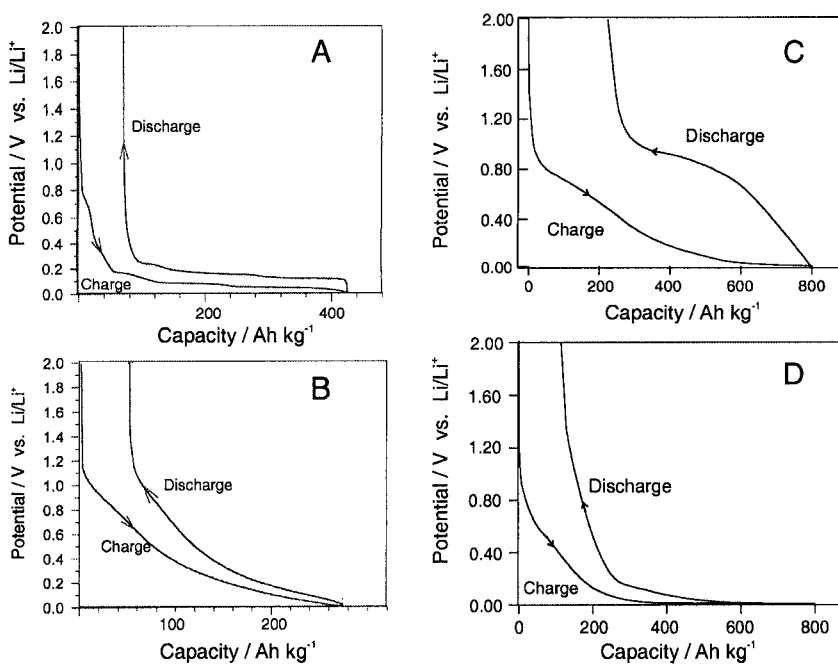


Figure 5.5. Typical schematic 1st cycle charge/discharge curve of (A) graphite, (B) soft carbon (coke), (C) soft carbon (low temperature, hydrogen containing), (D) hard carbon.

Li^+ -containing electrolyte decomposition products protect the carbon surfaces and the electrolyte against further reactions with each other. These films are considered to act as a "sieve" being selectively permeable to the electrochemically active charge carrier, the Li^+ cation, but impermeable to any other electrolyte component that would react with lithium, *i.e.*, they are

considered to behave as a electronically insulating solid electrolyte interphase (SEI).^{212,213}

Since the reactions of lithium with carbon and surface impurities as well as the film formation on Li_xC_6 are associated with the irreversible consumption of material (lithium and electrolyte), the corresponding charge loss is frequently called "irreversible specific charge" or "irreversible capacity". The reversible lithium intercalation, on the other hand, is called "reversible specific charge" or "reversible capacity". The losses have to be minimized because the charge and lithium losses are detrimental to the specific energy of the whole cell and, moreover, increase the material expenses due to the necessary excess of costly cathode material, which is the lithium source in a lithium ion cell after cell assembly.

The extent of the irreversible charge losses due to SEI formation depends to a first approximation on the surface area of the lithiated carbon which is wetted by the electrolyte.^{109,208,211,214-222} However, detailed investigations proved that the particle-size,^{223,224} -shape (fiber, flake, bead, or potato shapes, etc.),^{225,226} -thickness^{211,227,228} and -morphology²²⁹⁻²³² also influence the performance.

A third contribution to the irreversible capacity is rather related with the properties of the electrode than the properties of the active material. The high rate capability of a carbon electrode may be achieved by thin layer *composite electrodes* that are made up from small particle size carbons, with sizes in the μm range, that are mechanically bound together by an usually organic binder material^{58,215,218,233-236} which supports the compactness of the electrode. Usually, the binder amount is in the range of a few wt%. The binder/carbon composite is attached to a thin copper foil functioning as current collector.

The presence of these "inactive"² components makes the relation of material and electrode parameters with reversible and irreversible capacities quite complex. For example, the binder in the electrode on the one hand partly coats the electrochemically active surface area, so that SEI formation and solvent co-intercalation reactions are reduced.^{218,237,238} On the other hand, the rate capability is decreased because of the covered surface areas. In addition, it has to be considered that the binder reduces also the capacity because of the extra inactive mass.

Another influence of the inactive electrode components is due to the fact that they experience the same potential as the active material. On all electronically conductive electrode components (active material, conductive additive and current collector) in contact with the electrolyte, SEI formation takes place. In some cases, the binder also reacts in an irreversible reaction.

² Conductive additives like carbon blacks, which reversibly take up lithium, can not be considered as inactive.

A prominent example for the latter effect are fluorinated binders like poly(tetrafluoro ethylene) (PTFE; "teflon", $(-\text{CF}_2-\text{CF}_2-)_n$) and several poly(vinylidene fluoride) (PVdF, $(\text{CH}_2-\text{CF}_2-)_n$). Kavan²³⁹ has disclosed that fluorinated polymers can be electrochemically reduced ("electrochemical carbonization") at the conditions a graphite anode experiences in contact with an organic electrolyte in a lithium ion cell during charge. In general, perhalogenated polymers react with lithium very easily. The dehalogenation yields LiHal (LiF , $\text{LiCl}\dots$) and elemental carbon. The reduction of PTFE by lithium is well investigated as PTFE was suggested by Gabano and colleagues²⁴⁰ as cathode for lithium primary cells. PTFE can be completely converted into carbon by electrochemical reduction,²⁴¹ therefore increases the irreversible capacity²⁴² and consequently should be avoided as binder for carbon anodes. The reaction of Li with halogenated polymers containing vicinal halogen atoms is facilitated due to the formation of energetically favored products, *i.e.*, conjugated $\text{C}=\text{C}$ double bonds and LiF . Partially halogenated polymers which contain no vicinal halogen atoms, such as PVdF and poly(vinyl chloride) (PVC) usually do not react, because the C-H bond is more resistive against reaction with Li, which blocks the formation of a conjugated carbon-carbon bond system.²³⁹ In contrast, Biensan *et al.* [243] have observed a highly exothermal reaction of PVdF with lithiated graphite at elevated temperatures. It is likely that the presence of defects or irregularities in the monomer sequence, which locally lead to vicinal halogen atoms in the partially halogenated polymer, may alleviate the electrochemical reduction by lithium.

5.3.3. Electrochemical Li Storage in Non-Graphitic Carbons

Compared to graphite, non-graphitic (disordered) carbons offer a wider variety of structures and thus of sites available to lithium storage (cf. Section 5.3.1.2). This leads to different constant current charge/discharge potential profiles [Figure 5.5(B-D)]. In analogy to graphite, however, there is an irreversible part in the charge/discharge potential profile of these carbons, which again can be attributed to reactions with the electrolyte and SEI formation and to irreversible reactions of lithium with the carbon host.

It should be noted again that the use of the term intercalation is restricted to processes which involve the lithium accommodation within the interlayer gaps of a layered host like graphite. Any other Li storage process in carbons without significant layered structure is considered as insertion process.

Depending on the precursor and the heat-treatment temperature the carbonaceous materials discussed in this chapter contain heteroatoms in

addition to the prevailing carbon atoms. In particular, carbons prepared at temperatures below 1000°C do not consist of pure carbon and can contain substantial amounts of heteroatoms. Even highly crystalline graphite is saturated with heteroatoms at dislocations in the crystallites and at edges of the graphene layers (prismatic surfaces), which are supposed to affect the formation of residue compounds and the (electro-)chemistry at the electrode/electrolyte interface. From this point of view, the influence of "non-carbonaceous" elements which have been particularly added to the carbon precursor material is of great interest. If the non-carbon atoms are introduced in the carbon lattice by intention, the term "doped carbons" is used. This definition is in contrast with carbons made from "carbon precursors" which contain heteroatoms by chance.

5.3.3.1. Non-Graphitic Carbons Made from "Carbon Precursors"

Non-graphitic carbons can offer additional or simply more sites for lithium accommodation than graphites. As a result, they show a higher capability of reversible lithium storage than graphites. These so-called "high specific charge" or "high capacity" carbons are usually synthesized at rather low temperatures of ~500 to ~1000°C and can exhibit reversible capacities of ~400 to ~2000 Ah/kg, depending on the heat treatment, the organic precursor, and the electrolyte used. When lithium is stored in the bulk of non-graphitic (soft and hard) carbons, one can suppose that a higher specific charge (in Ah/kg) requires a correspondingly higher volume (lower density) of the carbonaceous matrix to accommodate the lithium. The calculated X-ray densities and average carbon layer distances of soft and hard carbons deviate from that of graphite as follows: graphite: 2.26 g/cm³ & 335.4 pm; soft carbon: ≈2.0 g/cm³ & 375 pm; hard carbon: 1.4-1.8 g/cm³ & 380-523 pm.^{85,143,146} As a consequence, the charge densities (in Ah/l, these volumetric values are important for small portable applications) of these carbons should be comparable to those of graphite.

The variety of precursor materials and of manufacture processes leads to carbonaceous host materials with various structures and compositions. This might explain the numerous models which have been suggested to explain the high capacity. Yazami *et al.*^{88,244-248} proposed the formation of non-dendritic metallic lithium multilayers on external graphene sheets and surfaces. Sato *et al.*^{249,250} suggested that Li₂ covalent molecules occupy nearest neighbor sites in intercalated carbons, *i.e.*, they assume a higher in-plane density of lithium guests. Yata's and Yamabe's groups discussed the possibility of lithium bilayer accommodation within the graphitic galleries of carbons with high interlayer spacing of ~0.400 nm.²⁵¹⁻²⁵⁶ Peled *et al.*^{213,257,258} suggested that the extra charge gained by mild oxidation of *graphite* is attributed to the accommodation of lithium at the prismatic faces between

two adjacent crystallites and in the vicinity of defects (cf. Section 5.4.2.3). In Refs. 259-264 it is assumed that small particle size carbons can store a considerable amount of lithium at graphite edges and surfaces in addition to the lithium located between the graphene layers. The existence of different Li storage sites is discussed by many other authors,²⁶⁵⁻²⁷¹ mostly however on the basis of different models. Other groups proposed that additional lithium can be accommodated in nano-cavities^{87,154,156-158} or pores,^{272,273} which are present in the carbon at temperatures below $\sim 800^{\circ}\text{C}$ and which the electrolyte can not enter.²⁷² Alternative comparisons of the models can be found in the reviews 12,14,60,85,87,90,91. The significance of the models is rather controversially discussed.²⁶⁷⁻²⁷⁸

For a systematic correlation of the lithium storage capacity with the structure of the parent carbonaceous material, we will use the considerations of Dahn's group,²⁷⁷⁻²⁸¹ which are supported by work of Fischer and colleagues^{141,142,282,283} (cf. also their recent reviews^{282,284}).

Their understanding is based on the structural model of graphitizing (soft) and non-graphitizing (hard) carbons proposed by Franklin (cf. Section 5.3.1.2 for the Franklin model and other related information). If soft and hard carbons are prepared at temperatures of ≈ 650 to 900°C , they show very high capacities, which are especially high at very low temperatures.^{274,285} In addition, they exhibit a potential hysteresis:^{252,277,278,280,281} the lithium insertion occurs close to 0 V vs. Li/Li^{+} whereas the lithium de-insertion occurs at much more positive potentials (Figure 5.5C). The hysteresis is due to kinetic hindrances,²⁸¹ as the insertion/release of Li into/from these carbons is associated with large exothermal heats.²⁸⁶

These low-temperature carbons can be considered as an intermediate material between the organic precursor compounds and carbon, as considerable hydrogen is still contained in their structure.²⁸⁷ The extent of lithium storage capacity and of potential hysteresis is assumed to be proportional to the hydrogen content in the carbon.^{274,278,288} The hydrogen is bonded at the periphery of aromatic molecules constituting the basic structure units. The ratio of hydrogen to carbon (H/C ratio) in the material is high when a substantial amount of hydrogen is present during manufacture, either because hydrogen is already incorporated in the precursor material and/or by manufacture under H_2 atmosphere. It has been suggested that lithium is bound near single proton terminated edge carbons which induces a partial bond change at the carbon from sp^2 - to sp^3 -hybridization.^{281,282} The bond change requires activation energy for both the lithium insertion and removal process leading to the observed potential hysteresis. Alternatively, a breakage-recovery model of weak C-H bonds has been suggested in Refs. 289,290. Other ideas for the lithium storage mechanism are discussed in Refs. 291-293.

With increasing temperature the electrical conductivity of the material increases by several orders of magnitude²⁹⁴ and hydrogen is removed.

Usually, all hydrogen is lost at temperatures of 1000°C,²⁹⁵ whereas oxygen and nitrogen (1500°C)²⁹⁶ and sulfur (2000°C)²⁹⁷ are lost at higher temperatures and thus may still have an effect on the lithium storage behavior. The specific charges achieved after the removal of hydrogen depend on the structure of the carbonaceous material, whether it is a soft (graphitizing) or a hard (non-graphitizing) carbon.^{157,159,202,278,281,298-301}

At temperatures $\geq 1000^\circ\text{C}$ the *graphitizing (soft) carbons* develop a disordered structure, which offers a lower number of sites for lithium intercalation as compared to graphite.^{12,14,53,85} In addition, cross-linking of carbon layers in disordered carbons hampers the shift to AA stacking, which is necessary for the accommodation of a higher lithium amount into graphitic sites.³⁰²⁻³⁰⁴ Correspondingly, rather low capacities of $\approx 150\text{--}200\text{ Ah/kg}$ are observed in soft carbons like turbostratic carbons, and more disordered carbons like cokes and certain carbon blacks. The potential profile of the 1st Li⁺ intercalation/de-intercalation cycle of a coke electrode differs from that of graphite, in the sense that the reversible intercalation of Li⁺ begins at a potential $>1\text{ V vs. Li/Li}^+$, and the curve slopes without distinguishable plateaus (Figure 5.4B). This behavior is a consequence of the disordered structure providing electronically and geometrically non-equivalent sites, whereas for a particular intercalation stage in highly crystalline graphite the sites are basically equivalent.⁵³

With increasing treatment temperature soft carbons develop more graphitic structure segments. The sites for lithium storage which were formerly determined by the disordered structure (see above) change to graphitic sites, where lithium resides in the Van der Waals gaps between ordered graphene layers. Finally, at $\sim 3000^\circ\text{C}$ the structure of graphite with its already reported electrochemical performance is achieved.^{12,14}

In contrast to soft carbons, many *non-graphitizing (hard) carbons* obtained at temperatures of $\sim 1000^\circ\text{C}$ show a high specific charge with little hysteresis. This high specific charge of several hundreds Ah/kg can be reached only at a very low potential of a few mV vs. Li/Li⁺ (Figure 5.5D). Comparing with graphitic carbons and cokes which show volume expansions and contractions in the range of $\sim 10\%$ during cycling, the hard carbons are claimed not to be subject to dimensional changes during lithium uptake and removal due to the high distance of $>\sim 0.380\text{ nm}$ between two neighboring carbon layers.¹⁴³ In order to explain the high capability of lithium storage in non-graphitizing carbons, Dahn *et al.*^{277,279,305-308} suggested that lithium is "adsorbed" on both sides of single graphene layer sheets which are arranged like a "house of cards"³⁰⁵ or like "falling cards"³⁰⁶ (Figure 5.6A). The "falling cards" model is the advanced form of the "house of cards" model and takes also into account the storage of lithium in micropores. Both the pore size and the pore openings should be small to avoid the reaction of stored lithium with the electrolyte.^{278,279,305,309} Recent studies on a hard carbon prepared at 1000°C reveal that the size of the single layers as well as the size of the

pores are in the range of 1 nm.^{141,142,282} In conclusion, a large fraction of single layer sheets and nanopores is beneficial for the lithium storage capabilities of hard carbons.

On the other hand, heat treatment higher than 1000°C leads to drastically reduced capacities of hard carbons.^{159,310} This may be related to the burn-off of material²⁷⁹ or to a slight mobility of single carbon layers,²⁸⁴ which causes the opening of the nanopores. Electrolyte can penetrate in, and the sites in the pore are no longer available for lithium storage (Figure 5.6B). This sensitiveness of nanoporous hard carbons might be a difficulty for surface treatment processes involving higher temperatures.

The existence of different lithium storage sites in these carbons have been also monitored by ⁷Li NMR spectroscopy.^{143,146,311} In conclusion, the lithium stored in soft carbons is considered as almost fully ionic, whereas the lithium in hard carbons is present in two different states, (i) a pseudo-metallic (but not metallic!) state of the lithium, which is stored at potentials close to the lithium metal potential, and (ii) an ionic state of the lithium stored at higher carbon electrode potentials. The pseudo-metallic character and thus the – compared to ionic lithium - reduced repulsive coulombic

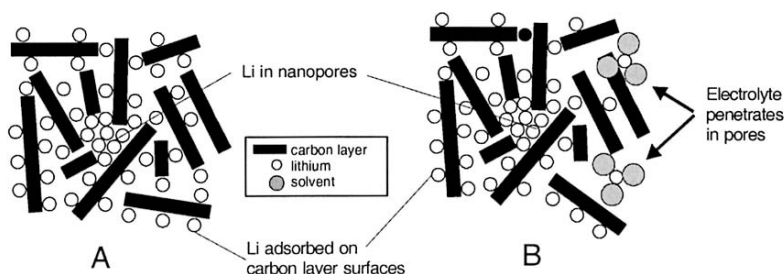


Figure 5.6. A) Mechanism of lithium storage in hard (non-graphitizing) carbons; B) Electrolyte penetration in the pores after pore opening.

interaction between neighboring lithium is an explanation for the higher lithium packing density in pores and at the single carbon layers.

Finally, it should be emphasized that the above proposed models for lithium storage in non-graphitic carbons are based on a limited number of experiments made with a limited number of carbonaceous materials (for the used precursors, cf. Refs. 85,94). This means that carbons may be synthesized which do not belong to any of the above categories. For example, it cannot be excluded that lithium storage in nanopores and near hydrogen terminated edge carbons proceeds in parallel. For another example, it was reported that milling of hard carbons alters the charge/discharge curve completely, as hysteresis is observed.³¹² This may be explained with a

lithium storage mechanism near oxygen surface groups, as carbon-carbon bond cleavages due to milling create unpaired electrons which react with oxygen from air thus creating the surface groups.

Tarascon and colleagues found that also milling of highly graphitic carbons resulted in graphites with very high reversible and irreversible capacities.¹⁰⁹⁻¹¹¹ As the milling creates structural disorder, an electrochemistry-structure relation may be indeed valid also in this case. However, the milling creates also a large number of broken bonds and therefore unpaired electrons, which react with hydrogen or oxygen present in the atmosphere during the milling process; some contribution of heteroatoms to the capacity may be taken into account, too.^{113-116,282}

Despite the fact that the high specific charge carbons show a multiple of the specific charge of graphite, there are still some problems to solve.

In many cases extremely high irreversible specific charges were observed.^{157,253,265,277-279,284,313-315} occasionally also at higher cycle numbers.^{265,278,313,314,316,317} The irreversible capacities can be correlated with the formation of the SEI.^{157,278,279,313,317} However, an "irreversible lithium incorporation" into the carbon is discussed, too.^{265,317-320} Apart from an irreversible trapping of lithium in the pore volume of disordered carbons,³²⁰ the large fraction of (internal and external) heteroatoms in the non-graphitic carbons, such as hydrogen and oxygen, can irreversibly bind a considerable amount of lithium during reduction of the carbon.^{265,284,317-319} In addition, the large amount of polar surface groups adsorbs large amounts of impurities from air, which can irreversibly react with lithium and thus have to be removed.^{93,312,321} All of the above charge losses have to be compensated by an excess of cathode material as lithium ion cells are assembled in the discharged state. As, in contrast to hydrogen-containing carbons, hard carbon has electrochemical properties suitable for application in lithium ion batteries,¹⁴³ there are attempts to reduce the irreversible capacity of hard carbons by changing the surface properties.^{284,312,315,318}

With one exception^[322], carbons exhibiting hysteresis show a low efficiency and poor cycling performance. Furthermore, they can be discharged only over a broad potential region of about 1-2 V.^{87,157,158,251-253,277-279,305,308,313} As a result the practical energy efficiency of a lithium ion cell is reduced.

The end of charge potential of non-graphitic carbons must be chosen very close to 0 V vs. Li/Li⁺ in order to obtain the available capacity. The narrow "safety gap" separating from the potential where metallic lithium is deposited on the carbon surface might give rise to some safety problems of these carbons. In particular, if fast charging is applied, there is a high risk of lithium plating at the end of charge. In some cases^{278,279,305,308} the hard carbon electrode was indeed charged below 0 V vs. Li/Li⁺ and dendritic³²³ lithium deposition on such carbons was observed. In contrast, there is a difference of

approximately 0.1 V between the potential of LiC_6 and the potential of lithium deposition (Figures 5.3A and 5.5A).

At a very low temperature, -30°C , a high polarization of the carbon electrode is observed, which is equivalent to a high overpotential. As the overpotential shifts the lithium insertion potential downwards beyond the lithium deposition potential, parts of the lithium storage capacity are not available anymore. Even the lithium intercalation capacity of graphite is very much reduced in this case.³²⁴ Cokes might benefit from their smooth change of lithium storage capacity as a function of the potential (Figure 5.5C).³²⁴ The effects of low temperature on the lithium storage capacity of hard carbons at 5 mV vs. Li/Li^+ (Figure 5.5D), however, must be dramatic.

The reported limitations of non-graphitic carbons seem to favor the use of graphitic anode materials at present. On the other hand, the charge/discharge profile of hard carbons gradually changes with time, which is advantageous for estimation of the capacity of a lithium ion cell. Hybrids of graphitic and non-graphitic carbons may be a reasonable compromise (cf. Section 5.4.2.3).

5.3.3.2. Non-Graphitic Carbons with Heteroatoms ("Doped Carbons")

The reaction of precursor materials (i) containing carbon atoms together with (various) heteroatoms or (ii) combining a "carbon precursor" with "heteroatom precursors" can result in a variety of doped carbons materials with interesting physical and (electro-)chemical properties. The "combination" of carbon and heteroatoms is done by the following methods: mechanical milling, chemical treatment of carbons with the dopant atom containing precursor at elevated temperatures, chemical vapor co-deposition, and co-pyrolysis. Doping of carbons has been originally applied in order (i) to change the chemical composition in the bulk and/or the surface, (ii) to change the electron distribution, and (iii) to enhance (catalyze) or slow the graphitization process.³²⁵⁻³²⁷ The dopant can be substituted for carbon or is additionally incorporated in the carbon. For further details, in particular regarding the synthesis and preparation of the materials, see Refs. 53,85,328,329. For the application in lithium ion cells, B, N, S, Si, and P have been preferably used as dopants.

Boron is assumed to act as an electron acceptor in a carbon host and thus to cause a shift of the intercalation potential to more positive values and an increase of the reversible capacity due to more electronic sites.^{53,85,330-335} This can enable a more rapid charging process. For HOPG it has been found that B substitution results in a more disordered structure.³³⁶ This might be the reason for the compatibility of B-doped graphites with electrolytes which are not compatible with undoped graphites. B-doped graphitized carbon fibers^{327,334,337,338} are used by Toshiba.^{339,340}

Nitrogen can be incorporated substitutionally into carbon, and a co-doping with B is also possible. N presumably functions as an electron donor and should therefore have the opposite effect on the reversible capacity and the insertion potential.^{53,341} Contrarily, others^{342,343} report that N-containing carbons can provide high specific charges of ~500 Ah/kg. Whereas the higher lithium storage capability of the above B- and N-containing anode materials is mainly explained by different electronic properties of the host^{53,331} the high specific charge of phosphorous-doped carbons,³⁴⁴⁻³⁴⁹ already observed in 1991,³⁵⁰ is discussed on the basis of steric effects.³⁴⁴ Other substituted carbons, such as layered B/C/N materials³⁵¹⁻³⁵⁷ and $C_xS^{342,358}$ have been evaluated, too.

High capacity lithium storage materials derived by pyrolysis from silicon-containing precursors like silicon-containing polymers or epoxy-silane composites have been the subject of investigations, too.³⁵⁹⁻³⁶⁸ In addition to silicon and carbon, these materials can contain a substantial amount of hydrogen and oxygen, which can lead to a large variety of compositions.^{360,361} Apart from high reversible capacities of up to 770 Ah/kg, which seem to depend on the Si content in the matrix,^{361,362} these materials usually exhibit strong potential hysteresis and large irreversible capacities (>150 Ah/kg). The interactions of the various heteroatoms with each other and with the carbon atom neighbors and their influence on reversible and irreversible lithium storage seem to be quite complex and have not been entirely clarified yet. Also, the nature of the lithium insertion mechanism is still uncertain. In some reports,^{366,367} it was proposed that carbon/silicon composite materials were prepared by above synthesis procedures. The high reversible capacities can be explained by the high Li alloying capacity of silicon in addition to the lithium incorporation in disordered carbon regions proceeding independently.^{368,369} If true, the insertion mechanism of a Si metal/carbon composite would be different from that of Si-doped carbon.

For all doped carbons based on non-graphitic low temperature carbons, there is some uncertainty about the effect of doping. In particular, in some cases it is not clear whether the structure, the chemical composition, or both are responsible for the observed lithium storage behavior.

5.4. REACTIONS OF LITHIATED CARBONS WITH THE ELECTROLYTE

The solid electrolyte interphase (SEI) concept (cf. Section 5.3.2.4) describes the filming behavior observed on the Li_xC_6 anode in a very basic and general way. In fact, SEI formation is a complex process and the formed films do obviously not have the properties of a true solid electrolyte for lithium cations with a transference number $t_{Li^+} = 1$. Nevertheless, the SEI

concept has been quite generally accepted due to its simplicity.

The first note on the solid electrolyte character of the film formed on metallic Li in organic electrolytes was made by Dey.³⁷⁰ Peled^{213,371,372} has discussed the reaction of Li and other reactive metals with organic and inorganic electrolytes in detail and has proposed the term SEI for the unique film, the term being in use until today. It should be emphasized that the original work of Peled considers the SEI as a new *phase* formed between anode phase and electrolyte phase at the electrode/electrolyte interface, *i.e.*, it is an "interphase", not an "interface". Depending on the electrolyte, other decomposition products may be liquid and dissolve or accumulate in the electrolyte or are gaseous,^{43,373-378} the latter increasing the cell pressure.

5.4.1. Interphase Formation – Metallic Li Anode vs. Li_xC_6 Anode and Oxide Cathode

Though the SEI concept has been basically adapted for carbonaceous anodes,^{208,210,212,213} there are significant differences between film formation processes on metallic lithium and lithiated carbon. Film formation on metallic Li takes place upon contact with the electrolyte. The electrolyte, which consists of various electrolyte components (solvent(s), electrolyte additives, electrolyte salt, impurities) decomposes spontaneously with low selectivity, and some of the decomposition products form the film.¹⁴ On the contrary, film formation on the surface of carbonaceous hosts takes place as a charge consuming side reaction in the first few Li^+ intercalation/de-intercalation cycles, especially during the first reduction of the carbon host material, leading to the so-called "irreversible capacity". In this case, the electrolyte components which are least stable towards reduction selectively react first. The chemical composition of the SEI on lithiated carbon varies through the depth of the film.¹⁴ In addition, the film composition and morphology is also laterally non-homogeneously distributed over the carbon anode surface.³⁷⁹ As a consequence of the difference in the reduction behavior to metallic lithium, dissimilar intermediate reduction products and different decomposition mechanisms of the electrolyte may occur in the presence of lithiated carbon.

Finally, the behavior of metallic lithium and of lithiated carbon, respectively, during battery charge and its influence on the SEI has to be discussed. Upon recharge of the Li anode, lithium plating occurs simultaneously to lithium corrosion and "passivation" (formation of SEI). Thus, lithium deposits as highly disperse, highly reactive metal particles. These dendrites are covered with SEI films, which in some cases electronically insulate them from the rest of the Li. Thus, the dendrites are

partially electrochemically inactive. This reduces the efficiency of the lithium dissolution/deposition process. Moreover, the dendrites grow to filaments upon cycling, which may short-circuit and locally overheat the cell and cause a disastrous thermal runaway due to the low melting point of highly reactive Li ($\sim 180^\circ\text{C}$) and reaction with the organic electrolyte. The above reactions imply that the surface of a metallic lithium electrode is periodically renewed during cycling, *i.e.*, a "new" SEI is formed in each cycle. Unless the Li electrode becomes inactive due to full passivation, this process can be repeated until the Li anode and/or the electrolyte are completely consumed.^{12,49-59,61}

At difference, the surface of the lithiated carbon electrode is all the time passivated by the SEI during cycling and no dendrites are formed as lithium is inserted into carbon. The film formation on lithiated carbons proceeds in several subsequent steps. These are of course influenced by the reactions taking place in parallel at the carbon anode, *e.g.*, reduction of carbon surface groups and surface impurities, unsolvated and solvated lithium insertion and self-discharge reactions. For ester-based electrolytes the following reaction sequence can be assumed: (i) electron transfer from the cathodically polarized electrode in the electrolyte solution³⁸⁰⁻³⁸² and formation of a solvated radical anion^{381,382} (and possible intermediate existence of solvated electrons^{213,383}), (ii) chain reaction of the radical with neighboring electrolyte species (*e.g.* further electron transfer) leading to insoluble products^{381,382} (iii) precipitation of these products on the carbon anode surface by nucleation and crystal growth,³⁸⁴ (iv) further precipitation until a dense, but also thicker film is formed,³⁸⁵⁻³⁸⁷ as well as further reduction of the film products deposited near the carbon anode which is becoming gradually more reductive. In contact with the highly reductive fully lithiated carbon anode only fully reduced (inorganic) species, such as LiF, LiCl, Li₂O, or Li₂CO₃ can exist. Partially reduced (organic) species can only "survive" in SEI regions far away from the reductive carbon anode surface near the electrolyte side.^{12,14,213} The inorganic part may be as thin as 2 nm.³⁸⁸

The film thickness and resistance increase during charge^{389,390} and discharge.³⁹⁰ The increase seems to be a discontinuous process proceeding in several steps.^{385,386,389,391} The film formed in the first cycle has a thickness of several tens of nm.^{208,378,385-387} The thickness of the SEI increases to several μm ^{12,14,388} during cycling or storage and the resistance increases in parallel.³⁹²⁻³⁹⁹ This process contributes to "cell aging".⁴⁰⁰ The increase of the film resistance and thus the higher overpotentials or even the electronic insulation of carbon particles by the SEI are considered as main reason for capacity fade of carbon electrodes during cycling.^{396,398,401,402} In parallel, SEI products may dissolve in the electrolyte, which is a major factor for the self-discharge of lithiated carbons.⁴⁰³⁻⁴⁰⁵ SEI formation and dissolution are in a

dynamic equilibrium.⁴⁰⁵ Peled⁴⁰⁶ accounts the breaking of the SEI due to graphite expansion/contraction during lithium uptake/release for the self-discharge phenomenon. A list of factors contributing to self-discharge is given in Ref. 405. Especially in the first cycles, self-discharge is a serious problem as the SEI is not fully developed and thus sufficiently protective. Measurements of self-discharge of sufficiently filmed lithium carbon electrodes show a linear lithium loss with storage time during ~40 d of storage. Thereafter, the reaction rate decreases, but self-discharge is still existent after even ~170 d.^{407,408} The self-discharge rate of the carbon anode increases with temperature,^{409,410} which may be associated with the increasing rate for SEI dissolution or breakdown.^{409,411,412} Broussely *et al.*^{400,410} concluded that the electronic conductivity of the SEI is the main contributor to the self-discharge of a graphite electrode. This assumption implies that the SEI is not a true solid electrolyte.

Also at the cathode an interphase consisting of reaction products of cathode material and electrolyte is formed,^{12,413-415} which shows "SEI-like" properties. The electrolyte decomposition products at the cathode are, however, formed by oxidation. Due to the fact that various cathodes, *e.g.*, LiCoO₂, LiNiO₂, LiMn₂O₄, LiFePO₄ and derivatives are used, the interphase compositions and formation mechanisms may vary more than for carbonaceous anodes, which all basically consist of carbon. It has been reported,^{392,416-419} that the cathode interphase contributes more to the overall cell resistance than the anode interphase (SEI).

It is furthermore assumed that SEI components can migrate between the anode and cathode, which would correspond to a shuttle mechanism creating self-discharge.⁴²⁰ As the transition metal oxides used for the cathode in lithium ion cells partially dissolve in the electrolyte,^{409,421-423} and then are deposited in metallic form on the carbon surface or are accumulated in the anode-SEI, Komaba and co-authors⁴²⁴ have studied the influence of manganese, cobalt, and nickel ions on the SEI formation process. They found detrimental effects both on capacity and on rechargeability. A general main conclusion to be drawn is that reactions at the cathode and anode and their interactive behavior should be considered in parallel.

The chemical composition and the properties of the films formed on graphite and the mechanisms involved with their formation have been analyzed by various sophisticated *in situ* and *ex situ* analytical tools. For space reasons, in this chapter we may only mention the works of Aurbach's group,^{413-415,425,426} Novák's group^{216,217,375-378} and Peled's and Golodnitzky's group.^{212,213,379}

The obtained information, however, has to be carefully considered. Several reports had to be withdrawn because later they were disproved by a more sophisticated method. A general limitation is also that a certain analytical method is only providing a piece of information, but does not give

the complete set of facts. Therefore, a certain property or property change of the film, which has been detected by a particular method may, but not inevitably, be related to a corresponding (change of) electrochemical performance. Furthermore, the electrolyte decomposition products are highly sensitive to reaction with moisture and other atmospheric species, which limits the meaning of *ex situ* results. On the other hand, using *in situ* or on-line methods, the relevant information may be so complex that it is not easy to extract the relevant information. The situation is getting even more complex, due to the large number of electrolyte components and their mixtures as well as due to the fact that the formed film and the other electrolyte decomposition products contain various species. Moreover, different charge/discharge regimes under various conditions, such as temperature, result in SEI films with different properties. For instance, higher charging currents result in low irreversible capacity and low SEI resistance.^{406,409} Finally, also the effect of impurities in/on the electrode and in the electrolyte,^{427,428} such as water,^{378,409,429-432} always has to be considered. This large number of effects may be the reason for the quite often inconsistent reports on the SEI film.

5.4.2. Unsolvated and Solvated Lithium Intercalation

Apart from reactions with the electrolyte at the carbon surface, the irreversible capacity is furthermore strongly affected by the possible co-intercalation of polar solvent molecules between the graphene layers of highly graphitic matrices. This so-called solvated intercalation reaction depends (i) on the composition of the electrolyte and (ii) on the crystallinity and morphology of the parent carbonaceous material.

5.4.2.1. Effects of the Electrolyte on Co-Intercalation and SEI Formation

In general, the intercalation of Li^+ from electrolytes with organic donor solvents into fairly crystalline graphitic carbons quite often yields solvated (ternary) lithium-graphite intercalation compounds, $\text{Li}_x(\text{solv})_y\text{C}_n$ (Figure 5.7B).^{12,14,46,47,59,60,208,433} The co-intercalation of the large solvent molecules is associated with extreme expansion of the graphite matrix (typically >100%), frequently leading to graphite exfoliation (shedding of single graphene layers or packages of graphene layers), and mechanical disintegration of the electrode. This large expansion is possible as the attractive interaction of the donor solvent shell with the Li^+ cation is much stronger than the Van der Waals forces between the graphene layers of

graphite. In the "best" case reduced charge storage capabilities, in the worst case complete electrode destruction are the results of this reaction.

As long as the content of lithium in the graphitic carbon is low ($x \leq 0.33$ in Li_xC_6), the ternary lithium-graphite intercalation compounds are thermodynamically favored over the unsolvated binary compounds, Li_xC_6 (Figure 5.7A). Hence, the potentials of their electrochemical formation are more positive than those for the formation of the corresponding compound Li_xC_6 . At this stage of Li^+ intercalation the coulombic interaction between the lithium guest layer (Li^+) and the balancing negative charge distributed over the graphene layers (C_n^-) is weak, and space to accommodate large solvent molecules is still available.^{12,14,59,60,434,435}

The solvated GICs are thermodynamically unstable with respect to the reduction of the co-intercalated solvent molecules.^{12,14,59,60} The kinetically controlled reduction depends on the type of co-intercalated solvent. It is slow for, *e.g.*, dimethyl sulfoxide, where even staging of solvated GICs can be observed,^{11,436,437} but very much faster for, *e.g.*, PC,^{43,46,438-441} where the electrochemical intercalation followed by fast decomposition of the intercalated $\text{Li}^+(\text{solv})_y$ can be misunderstood as simple electrolyte decomposition. The reduction of $\text{Li}^+(\text{solv})_y$ inside the graphite is associated with extra irreversible capacity.

Both effects resulting from solvent co-intercalation, the mechanical destruction and the higher irreversible capacities, seriously complicate the operation of graphitic anode materials. Due to the fact that ternary lithiated carbons are thermodynamically favored at low lithium concentrations in the graphite, *i.e.*, at the beginning of intercalation, kinetic measures have to be applied to diminish or even to completely suppress solvent co-intercalation.

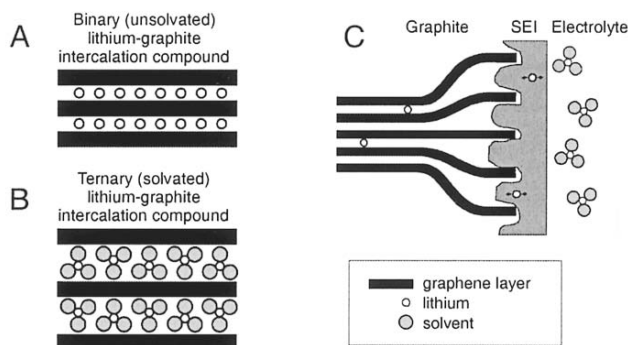


Figure 5.7. Schematic drawing (A) of binary and (B) of ternary lithium-graphite intercalation compounds, as well as (C) of the SEI formed on/in graphite via electrochemically formed solvated lithium/graphite intercalation compounds.

This can be accomplished by using electrolyte components that form effectively protecting SEI films, which are only permeable for unsolvated lithium cations. The first²⁰⁸ effective solvent in this respect was ethylene carbonate (EC).^{433,442-446} Since the viscosity of electrolytes using pure EC is rather high, mixtures of EC with low viscosity solvents such as dimethyl carbonate (DMC), diethyl carbonate (DEC), ethyl methyl carbonate (EMC) are widely used.⁴⁴⁷⁻⁴⁵³

Although the formation of binary lithium-graphite intercalation compounds prevails in EC-based electrolytes, many examinations point at a film formation mechanism, where also solvated lithiated graphites participate. Film formation in the first cycle during the first reduction of the host material is not a simple surface reaction but a rather complex three-dimensional process, taking basically place at a potential of $\sim 1 - \sim 0.6$ V vs. Li/Li⁺ (Figure 5.5A). *In situ* dilatometric,⁴⁴⁵ STM,^{454,455} and Raman¹⁸⁹ methods indicate a (partially) large expansion of the graphite host corresponding to the (intermediate) formation of Li_x(solv)_yC_n at those potentials. The reduction of Li_x(solv)_y on parts of the *internal* surfaces *between* the graphene layers results in an "extra" film, which penetrates into the bulk of the graphite host (Figure 5.7C). Correspondingly "extra" irreversible charge losses are observed.⁴⁴⁵ The penetration depth of the film into the graphite depends on how deep the reaction front of solvated lithium ions can propagate into the graphite, before the solvated lithium is reductively decomposed inside the graphite. Several investigations indicate that the film formation and solvent co-intercalation processes on/into graphite can be even more complex.^{192,385,386,389,454-456} Solvent co-intercalation in EC-based electrolytes depends on the kind of the low viscosity co-solvent⁴⁵⁷ and the kind⁴⁵⁸ and concentration⁴⁵⁹ of the electrolyte salt.

The structures of EC and PC are very similar and both solvents evolve gases, ethylene (EC)^{216,217,460} or propylene (PC)^{43,217} during reduction, but their tendency to exfoliation of graphite is dramatically different. Therefore, there is controversy about the reactions occurring in EC- and PC-based electrolytes.

Ross and colleagues⁴⁶¹ have observed a significant kinetic hindrance for PC reduction. Chung *et al.*^{462,463} have proposed a strong dependence of the solvent co-intercalation behavior on structure of the solvent, by using differently methyl-substituted PC molecules: *cis*- (*c*-BC) and *trans*-butylene carbonate (*t*-BC). *c*-BC does, *t*-BC does not co-intercalate into graphite, which is explained by steric hindrances.

Aurbach and colleagues^{425,464} attribute the exfoliation of graphite in PC electrolytes to the penetration of graphite openings such as pores and fissures by solvent molecules. Due to the fact that the graphite is only insufficiently passivated by the SEI in PC electrolytes, PC decomposes inside these openings to propylene gas, which pressure induces cracking of the graphite. The formed cracks allow massive penetration of PC molecules inside the

graphite matrix, where they are reduced. Again gas is produced, which leads to further cracking and so on. This reaction mechanism involves no PC co-intercalation step. This behavior seems to be only typical for PC electrolytes, as for electrochemical reduction or oxidation of other nonaqueous and aqueous electrolytes, which results into strong gas evolution; a similar and such rapid mechanical destruction mechanism has not been reported so far.

Takamura and colleagues⁴⁶⁵ investigated highly graphitized carbon fibers in PC based electrolytes. They found a dependence of the extent of exfoliation on the number of used carbon fibers and their relative orientation to each other. With a single fiber no exfoliation and very low irreversible capacity could be observed. With a bundle of five fibers in which the fibers have been irregularly oriented to each other, strong exfoliation takes place; the irreversible capacity is high. However, if the fibers in the bundle are arranged in parallel to each other, the extent of the exfoliation reaction is very much reduced. They attributed the exfoliation to an inhomogeneous current distribution in the bundle, which does not occur with a single carbon fiber. One might, however, also speculate that the irreversible capacity in this case is also reduced, when the current density is high and furthermore is uniform for the total surface area of the anode material.

The authors⁴⁶⁶ have investigated the reactions of graphite vs. PC by *in situ* electrochemical dilatometry. Strong macroscopic expansions of graphite occur, which can be partially reversible under certain conditions. The results suggest that PC co-intercalation into graphite is the initial step, which opens up fissures and pores in the graphite. The second step is *physical* penetration of PC electrolyte into these openings of graphite, then gas evolution inside graphite, which causes strong mechanical stress and graphite destruction. This subsequent reaction process is also supported by Chung *et al.*^{462,463,467}

5.4.2.2. Film Forming Electrolyte Additives and Electrolyte Components

The choice of solvents or solvent mixtures for a certain lithium ion battery application is usually a compromise between the desired physical (*e.g.*, electrolyte conductivity, volatility, flammability, wetting ability, etc.) and electrochemical properties (reduction and oxidation at the respective electrode/electrolyte interfaces, solid electrolyte interphase (SEI) formation behavior, etc.).^{468,469} An elegant way to overcome the inevitable limitations of this compromise is the use of electrolyte components, which even in small amounts ("additive amounts") improve the electrolyte properties in the desired direction.⁴⁶⁸ The technical realization of this concept is quite simple, as the electrolyte additive can be just added to the base electrolyte. Among many additive applications, such as safety improvement and overcharge protection, electrolyte components for improved film formation processes at

anode and cathode have found particular interest. Beside EC, significant improvements have been achieved at the anode with a large number of film forming components.

The first reports deal with gaseous electrolyte additives and components such as CO_2 ,^{390,403,433,446,470-474} N_2O ,^{390,474} and SO_2 .^{445,474-476}

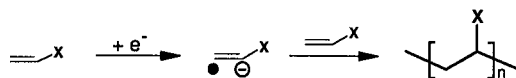
Some other prominent examples are derivatives or analogous compounds of the cyclic carbonates ethylene carbonate (EC) and propylene carbonate (PC), *e.g.*, chloro ethylene carbonate⁴⁷⁷⁻⁴⁸¹ (which evolves CO_2 during reduction^{460,482}), 4,5-dichloroethylene carbonate,⁴⁸³ fluoro ethylene carbonate,⁴⁸⁴ trifluoro propylene carbonate,^{477,481,485} vinylene carbonate (VC),⁴⁸⁶⁻⁴⁹¹ catechol carbonate,⁴⁹² ethylene sulfite^{468,493,494} and propylene sulfite.⁴⁹⁵

Other sulfur additives are: S_x ,^{2-, 390,474,496,497} sulfites (⁴⁹⁸ and *cf.* above), propane sultone,^{499,500} SO_2 (above), sulfates,⁵⁰¹ etc.⁴⁹³

Also derivatives or analogous compounds of the linear carbonates, diethyl carbonate (DEC) and dimethyl carbonate (DMC), *e.g.* dimethyl sulfite and diethyl sulfite,^{493,502} S,S-dialkyl dithiocarbonates,⁵⁰³ 2-methoxyethyl (methyl) carbonate,⁵⁰⁴ dimethyl pyrocarbonate (DMPC),^{505,506} dibutyl pyrocarbonate,⁵⁰⁶ ethyl propyl carbonate,^{182,507} ethyl methyl carbonate^{508,509} and other asymmetric alkyl methyl carbonates,^{510,511} 1-trifluoroethylmethyl carbonate,⁵¹² and other partially fluorinated linear carbonates⁵¹³ have been proven to be useful. Even Li_2CO_3 ^{406,514,515} is an effective electrolyte additive.

A third family of compounds include partially halogenated organic compounds such as bromo butyrolactone,⁵¹⁶ chloro and fluoro ethylene carbonate (see above), trifluoro propylene carbonate (see above), fluorinated noncyclic compounds as glycol ethers⁵¹⁷ and other ethers,⁵¹⁸ urethanes,⁵¹⁹ glycol esters,⁵²⁰ *N,N*-dimethylamino trifluoro acetamide,^{521,522} trifluoro ethylmethyl carbonate and other partially fluorinated linear carbonates (see above), and methyl chloroformate.⁵¹⁶ An overview on fluorinated solvents, their beneficial low-temperature and safety behavior, how they operate in the cell, etc., is given in Refs. 523,524.

A novel class of additives incorporates polymerizable unsaturated bonds. These include vinylene compounds, such as vinylene carbonate (VC, see above), acrylic acid nitrile,^{522,525-527} ethyl cinnamate,⁵²⁸ and vinylene acetate.⁵²⁹ The reaction^{526,527} is proceeding according to:



with "X" being an electron-withdrawing group (see also below).

In general, the films formed in the presence of electrolyte additives exhibit a low resistance^{390,505} and are very thin.⁴⁸⁹

Many of the above film forming compounds take advantage from the fact that they are usually reduced at quite positive graphite electrode potentials, *i.e.*, at the early stages of the first reduction of the graphite electrode, before detrimental side reactions such as solvent co-intercalation proceed. The formed films have SEI properties. Solvent co-intercalation (even as a side reaction) is suppressed. This sensitiveness towards reduction may be explained (i) by the electron-withdrawing effect of chlorine- or fluorine-groups introducing partial positive charge on the molecule (chlorinated and fluorinated solvents) or (ii) by the presence of atoms or groups in the molecule which have a high electron affinity, *e.g.*, sulfur in the oxidation state +IV (sulfites) or double bonds (vinylene compounds). The reduction behavior and the reduction potentials of film forming components may be also calculated,^{461,486} though the dependence on the chosen experimental conditions (type of electrode and co-electrolyte components, charge regime, kinetics, etc.) will inevitably make a practical test necessary.

In many cases, electrolyte additives not only improve typical lithium ion battery electrolytes, but also allow the use of PC-based electrolytes and other electrolytes not compatible with graphitic anodes. Especially, the use of PC instead of EC in a lithium ion battery electrolyte is highly desired, as PC has a large liquid range from -49°C to $+240^{\circ}\text{C}$, whereas EC is a solid at room temperature. Thus, PC-based electrolytes usually show a low-temperature performance desired for use in lithium ion cells. The low viscosity of the PC at lower temperatures is counteracted by the still high conductivity of the SEI film formed in the presence of PC.⁵³⁰

There is no universally applicable electrolyte additive or electrolyte solvent available and therefore additive/solvent mixtures are used at the moment. However, the cross-interaction of the various electrolyte components contributing to SEI formation is an issue of concern. For example, in electrolytes designed for good low temperature performance, not the still comparatively high electrolyte conductivity, but the low ionic conductivity of lithium within the SEI formed in these electrolytes,^{324,506,531,532} and especially the low conductivity within the carbon material^{324,506,533} at these temperatures, limit the low temperature performance. Similar observations were made with flame retardant or other safety-relevant electrolyte additives which may deteriorate,^{534,535} but also may improve^{536,537} the SEI formation process. Finally, electrolyte additives are desired, which are in parallel beneficial for the interphase formation at anode and cathode.

5.4.2.3. Effects of the Carbon on Co-Intercalation and SEI formation

Disordered soft and hard carbons are much less sensitive to solvent co-

intercalation than highly crystalline graphites. The crosslinking between the graphene layers and graphite crystallites by sp^3 -hybridized carbon atoms mechanically suppresses the formation of solvated lithiated graphites.^{12,14,53,59,60,85,208} As a result the gap between the layers cannot expand very much and thus there is not enough space for the solvent to co-intercalate. Furthermore, due to the presence of defects (pores, etc.) in the structure, the transport of solvated lithium ions inside the graphite particle by an insertion mechanism is hindered. Therefore, these carbons have the advantage that they can operate in electrolytes which are free of typical film forming electrolyte components.

Using thermally treated graphites with a low number of defects (and a high hexagonal phase content), *i.e.*, graphites with extremely high crystallinity, even the use of EC-based electrolytes results in a solvent co-intercalation, exfoliation and corresponding irreversible capacities.^{85,538} On the other hand, strongly milled or otherwise mechanically treated graphites with a low number of defects (and a higher rhombohedral phase content) do not show exfoliation at all.^{85,538-541} The tendency to solvent co-intercalation is primarily dependent on the defect concentration and not on the relative ratio of hexagonal to rhombohedral phase.⁵⁴¹

Composite carbonaceous materials, comprising a "core" of graphite and a thin protective "shell" of non-graphitic carbon, combine the beneficial properties of graphite (stable lithium storage potential plateau, larger gap to the metallic lithium deposition potential, high reliability of manufacturing, low cost, etc.), with the high tolerance of non-graphitic carbons to electrolyte systems not compatible with graphite.^{201,542-551} These carbons also show a lower extent of irreversible capacity with solvents having low tendency to co-intercalation, obviously due to an improved SEI formation process.

Graphitic materials with a crystalline core, but with more disordered "sub-surface structure" (*i.e.*, thin part of graphite bulk material next to the surface) yield similar results as the above composites.^{101,467,552-555} Such graphite surface and sub-surface structures can be created by mechanical milling and by high temperature gas treatment.^{101,554,555}

Polymer-coated,^{556,557} and metal-coated^{545,558-562} carbons exhibit several improvements compared to the uncoated material. In addition to impacts on SEI formation and solvent co-intercalation behavior, the metal-coated graphites benefit from better electronic conductivities and higher Li storage capacities. The latter are particularly observed when the coating consists of metals which alloy with lithium, as lithiated metals and alloys show much higher lithium storage capacities than graphite⁴² (cf. Refs. 544,563-572 and Section 5.3.4.2 for C/Si composites).

In general, surface modification has been proven to be a tool for further improvements of the carbonaceous anode materials, in particular in view of improved SEI formation. Coatings and surface modifications of hard carbons have already been discussed in Section 5.3.4.1. Takamura and his

colleagues^{93,321,465,558,562,573-575} started work on the topic "surface modification" very early. The basic intention is to control irreversible reactions with the electrolyte, such as solvent co-intercalation and SEI deposition, as well as to remove or introduce carbon surface properties (*e.g.*, certain morphologies and chemical compositions) detrimental or beneficial for performance. The interaction of anode surface properties, surface coatings and surface modifications with the electrolyte can be easily understood, when SEI formation on the carbon surface is compared with a deposition process (Figure 5.8).⁵⁷⁶⁻⁵⁷⁸

Apart from surface coatings, chemical treatments such as surface fluorination,⁵²⁴ surface oxidation, surface reduction^{579,580} or heat treatment under inert atmosphere ("outgassing"),⁵⁷³ as well as chemical bonding of certain substances to carbon surface groups and surface impurities,^{558,576} and milling under certain gas atmosphere¹¹³⁻¹¹⁶ have been investigated. Oxidation is the most commonly applied method of surface modification. It has been performed by gas (air, O₂, CO₂, O₃) treatments^{213,257,258,384,554,555,577-581} and by wet chemical measures.⁵⁸²⁻⁵⁸⁴ A most interesting phenomenon is that in some, but not all of the cases, the reversible capacity of oxidized graphites can exceed the theoretical value of the first stage compound LiC₆ by more than 10%.^{213,257,258,582} A problem remains the interpretation of the results, as for basically equal treatment procedures the results vary considerably. The

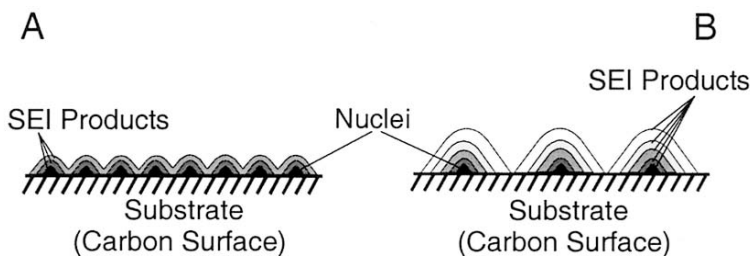


Figure 5.8. Deposition (*plating*) of SEI film products. Composition and morphology of the SEI deposit are controlled by the "plating conditions", *i.e.*, by (i) the electrolyte composition, (ii) the pretreatment (coating or modification) of the carbon surface ("substrate"), and (iii) the plating conditions (constant current or pulse plating, etc.): A) Plating conditions favoring nucleation result in a compact and dense SEI. B) Plating conditions which facilitate the crystal growth of the initially formed nuclei induce the formation of a rough SEI deposit, which requires more SEI products to get pin-hole-free, *i.e.*, consumes more irreversible capacity. These considerations can be applied to other anode and cathode materials, too.

variety of graphites and their various properties again makes the matter complex and obviously not reproducible. Generally speaking, morphology changes^{213,257,258,384,577} as well as surface chemistry changes^{213,257,258,384,582}

after treatment are accounted for the obtained results. In addition, the burn-off of reactive carbon sites or complete reactive particles, which could contribute to the irreversible capacity to a large proportion, may also be considered.

Though a comprehensive interpretation of the above effects of surface modifications is still missing, the reports have elucidated the importance of surface properties for the performance of carbon anodes.

A most critical issue is still the influence of carbon surface heterogeneities on performance. Both unsolvated and solvated intercalation take place via the prismatic surfaces. In addition, the prismatic surface and basal plane surface are different both from the viewpoint of morphology and chemistry, *i.e.*, they are very different foundations for SEI deposition (cf. Figure 5.8). Thus, not the total external surface area but rather the ratio of the prismatic and basal plane surfaces will affect the irreversible capacity^{120,127} as well as the rate capabilities of graphites. The reports of Peled and colleagues^{213,379,585} are in line with this idea, as they have detected completely different SEI compositions at the edge and basal plane surfaces of HOPG. The existence of different surface sites and their influence on irreversible capacities is discussed also in Refs. 224,515,586,587. The coverage and/or removal of detrimental or sensitive surface sites may be the main motivation for surface coatings and modifications.

5.5. WHAT IS SPECIAL ABOUT LITHIATED CARBONS?

Carbons have been and still are considered to be *the* anode material for rechargeable high energy density lithium batteries, due to a synergetic combination of properties beneficial for performance and production. These properties include: high lithium storage capacities, negative redox potentials *vs.* the cathode, long term cycling performance, low costs and large abundance. Any other anode material discussed in this book may possess several, but not all of these properties. Nevertheless, as (surface) modifications or the use in composites seem to be the perspective for future carbon anode materials, the same might be true for other anode materials, maybe in a composite together with carbon.

Two "wonders" are associated with the story of success of carbon anodes. The first wonder is strongly related with the properties of metallic lithium. Apart from having the highest capacity, among the light metals $M = \text{Li, Na, and Mg}$, solely metallic Li shows a chemical and electrochemical behavior which favors its use in high energy density batteries, because surface films with the unique SEI properties are formed. In contrast, products of electrolyte decomposition of alkali metals other than Li are

typically partially soluble and therefore do not form similarly protective films.¹² Films formed on Mg are typically highly passivating.⁵⁸⁸ Mg can be only used in combination with electrolytes which do not form films on the metal surface.⁵⁸⁹ The resulting cell, however, by far can not reach the energy densities of lithium ion batteries.⁵⁹⁰ The excellent protective properties of the films formed on lithiated carbons can be directly related to the extraordinary films formed on metallic lithium.

The second wonder is the obviously "perfect accommodation" of lithium cations inside carbon. There is no other cationic guest species, that can be inserted into carbons at such high concentrations, with such high rates and at a such low potential vs. a cathode material. The alkali metals $M = K, Rb, Cs$ form 1st stage GICs MC_8 (cf. LiC_6) and the increase in interlayer spacing due to intercalation of the large M cations is large. As a result, the charge storage capacity is poor. Sodium can hardly be intercalated into graphitic materials, but in disordered soft and hard carbons (cf. Section 5.2). However, also in this case the sodium storage capacities are significantly lower than the Li storage capacities in the same material, and the reversibility is poor, which may be related with insufficiently protective surface films.

It is a most lucky case in battery science and technology, that lithiated carbons combine all the properties necessary for an outstanding anode material. The final questions are: What comes after lithiated carbon? Will there be a third wonder in the future?

ACKNOWLEDGEMENT

We acknowledge the long term support of the Austrian Science Funds (FWF) for our work on carbon anodes and other lithium battery materials.

REFERENCES

1. M. B. Armand, in: *Fast Ion Transport in Solids*, W. van Gool, Ed., Elsevier, Amsterdam, 1973, 665.
2. B. C. H. Steele, in: *Fast Ion Transport in Solids*, W. van Gool, Ed., Elsevier, Amsterdam, 1973, 103.
3. M. S. Whittingham, *Science* 1976, 192, 1226.
4. M. S. Dresselhaus (Ed.), *Intercalation in Layered Materials*, NATO ASI Series, Plenum, New York, 1986, Vol. 148.
5. A. P. Legrand, S. Flandrois (Eds.), *Chemical Physics of Intercalation*, NATO ASI Series, Plenum, New York, 1987, Vol. 172.
6. M. S. Whittingham, A. J. Jacobsen (Eds.) *Intercalation Chemistry*, Academic Press, New York, 1982.
7. W. Müller-Warmuth, R. Schöllhorn (Eds.), *Progress in Intercalation Research*, Kluwer, Dordrecht, 1994.
8. S. S. Prasad, in: *Handbook of Solid State Batteries and Capacitors*, M. Z. A. Munshi, Ed., World Scientific, Singapore, 1995, 467.

9. R. Schöllhorn, *Angew. Chem. Int. Ed. Engl.* 19 (1980) 983.
10. J. B. Goodenough, *Solid State Ionics* 69 (1994) 184.
11. J. O. Besenhard, H. P. Fritz, *Angew. Chem. Int. Ed. Engl.* 95 (1983) 950.
12. M. Winter, J. O. Besenhard, M. E. Spahr, P. Novak, *Adv. Mat.* 10 (1998) 725.
13. W. R. McKinnon, in: *Solid State Electrochemistry*, P. G. Bruce, Ed., Cambridge University Press, 1995, 163.
14. M. Winter, J. O. Besenhard, in: *Handbook of Battery Materials*, J. O. Besenhard, Ed. Wiley-VCH, Weinheim, 1999, 383.
15. R. Schlögl, in: *Progress in Intercalation Research*, W. Müller-Warmuth, R. Schöllhorn, Eds., Kluwer, Dordrecht, 1994, 83.
16. R. Moret, in: *Intercalation in Layered Materials*, NATO ASI Series, M. S. Dresselhaus, Ed., Plenum, New York, 1986, Vol. B148, 185.
17. M. S. Dresselhaus, G. Dresselhaus, *Advances in Physics* 30 (1981) 139.
18. J. R. Dahn, J. A. Steel, *J. Electrochem. Soc.* 147 (2000) 899.
19. F. P. McCullough, U.S. Pat. No. 5532083, 1996.
20. R. T. Carlin, H. C. DeLong, J. Fuller, P. C. Trulove, *J. Electrochem. Soc.* 141 (1994) L73.
21. R. Santhanam, M. Noel, *J. Power Sources* 76 (1998) 147.
22. F. Beck, in: *Advances in Electrochemical Science and Engineering*, Wiley-VCH, Weinheim, 1997, Vol. 5, 303.
23. W. Rüdorff, U. Hofmann, *Z. Anorg. Allg. Chem.* 238 (1938) 1.
24. See: Textbooks of Inorganic Chemistry.
25. A. Hérol, *Bull. Soc. Chim. France* 187 (1955) 999.
26. A. Hérol, in: *Chemical Physics of Intercalation*, NATO ASI Series, A. P. Legrand, S. Flandrois, Eds., Plenum, New York, 1987, Vol. B172, 3.
27. D. Guérard, A. Hérol, *Carbon* 13 (1975) 337.
28. L. B. Ebert, *Ann. Rev. Mater. Sci.* 6 (1976) 181.
29. V. V. Avdeev, A. P. Savchenko, L. A. Monyakina, I. V. Nikol'skaya, A. V. Khvostov, *J. Phys. Chem. Solid* 57 (1996) 947.
30. E. Weintraub, US Pat. No. 922645, 1909, & French Pat. No. 585185, 1924.
31. K. Fredenhagen, G. Cadenbach, *Z. Anorg. Allg. Chem.* 158 (1926) 249.
32. R. C. Asher, *J. Inorg. Nucl. Chem.* 10 (1959) 238.
33. A. Métrot, D. Guérard, D. Billaud, A. Hérol, *Synth. Met.* 1(1979/89) 363.
34. G. Hennig, *J. Chem. Phys.* 19 (1951) 922.
35. M. M. Doeff, M. Y. Pengg, Y. Ma, L. C. de Jonghe, *J. Electrochem. Soc.* 141 (1994) L145.
36. D. A. Stevens, J. R. Dahn, *J. Electrochem. Soc.* 148 (2001) A803.
37. P. Thomas, D. Billaud, *Electrochim. Acta* 47 (2002) 3303.
38. R. Alcantara, J. M. Jimenez Mateos, J. L. Tirado, *J. Electrochem. Soc.* 149 (2002) A201.
39. W. S. Harris, Thesis No. UCRL-8381, University of California, 1958.
40. M. L. B. Rao, *J. Electrochem. Soc.* 114 (1967) 665.
41. N. P. Yao, E. D'Orsay, D. N. Bennion, *J. Electrochem. Soc.* 115 (1968) 999.
42. M. Winter, J. O. Besenhard, *Electrochim. Acta* 45 (1999) 31.
43. A. N. Dey, B. P. Sullivan, *J. Electrochem. Soc.* 117 (1970) 222.
44. A. Brenner, *J. Electrochem. Soc.* 118 (1971) 461.
45. J. S. Dunning, W. H. Tiedemann, L. Hsueh, D. N. Bennion, *J. Electrochem. Soc.* 118 (1971) 1886.
46. J. O. Besenhard, H. P. Fritz, *J. Electroanal. Chem.* 53 (1974) 329.
47. J. O. Besenhard, *Carbon* 14 (1976) 111.
48. M. Armand, French Pat. No. 7832977, 1978.
49. J.-P. Gabano (Ed.), *Lithium Batteries*, Academic Press, London, 1983.
50. J. O. Besenhard, G. Eichinger, *J. Electroanal. Chem.* 68 (1976) 1.
51. G. Eichinger, J. O. Besenhard, *J. Electroanal. Chem.* 72 (1976) 1.
52. S. C. Levy, P. Bro, *Battery Hazards and Accident Prevention*, Plenum, New York 1994.
53. J. R. Dahn, A. K. Sleight, H. Shi, B. M. Way, W. J. Weydanz, J. N. Reimers, Q. Zhong, U. von Sacken, in: *Lithium Batteries, New Materials, Developments and Perspectives*, G. Pistoia, Ed., Elsevier, Amsterdam 1994, 1.
54. J.-M. Tarascon, M. Armand, *Nature* 414 (2001) 359.
55. M. Broussely, P. Biensan, B. Simon, *Electrochim. Acta* 45 (1999) 3.
56. D. Aurbach, E. Zinigrad, H. Teller, P. Dan, *J. Electrochem. Soc.* 147 (2000) 1274.
57. D. Fauteux, R. Koksang, *J. Appl. Chem.* 23 (1993) 1.
58. S. Megahed, B. Scrosati, *J. Power Sources* 51 (1994) 79.
59. J. O. Besenhard, M. Winter, in: *2. Ulmer Elektrochemische Tage, Ladungsspeicherung in der Doppelschicht*, W. Schmickler, Ed., Universitätsverlag Ulm 1995, 47.

60. M. Winter, J. O. Besenhard, in: *Lithium Ion Batteries*, M. Wakihara, O. Yamamoto, Eds., Kodansha/Wiley-VCH, Tokyo/Weinheim, 1998, Chapter 6.
61. K. Brandt, *Solid State Ionics* 69 (1994) 173.
62. R. Yazami, P. Touzain, *J. Power Sources* 9 (1983) 365.
63. R. Yazami, *J. Power Sources* 97-98 (2001) 33.
64. S. Basu, *J. Power Sources* 81-82 (1999) 200.
65. S. Basu, US Pat. No. 4304825, 1981.
66. S. Basu, US Pat. No. 4423125, 1983.
67. R. Kanno, Y. Takeda, T. Ichikawa, K. Nakanishi, O. Yamamoto, *J. Power Sources* 26 (1989) 535.
68. M. Mohri, N. Yanagisawa, Y. Tajima, H. Tanaka, T. Mitate, S. Nakajima, M. Yoshida, Y. Yoshimoto, T. Suzuki, H. Wada, *J. Power Sources* 26 (1989) 545.
69. A. Yoshino, K. Sanekikawa, T. Nakajima, US Pat. No. 4668595, 1987 (Asahi Kasei), T. Suzuki, H. Wada, Y. Yoshimoto, M. Yoshida, S. Nakajima, EU Pat. Appl. No. 0346 088, 1989 (Sharp), Y. Nishi, H. Azuma, A. Omaru, EU Pat. Appl. No. 0357001, 1989 (Sony).
70. T. Nagaura, in: *Progress in Batteries and Solar Cells* (Eds: JEC Press Inc. and IBA Inc.), JEC Press Inc., Brunswick OH, 1991, Vol. 10, 218.
71. T. Nagaura, K. Tozawa, in: *Progress in Batteries and Solar Cells* (Eds.: JEC Press Inc. and IBA Inc.), JEC Press Inc., Brunswick, OH 1990, Vol. 9, 209.
72. M. B. Armand, in: *Materials for Advanced Batteries*, D. W. Murphy, J. Broadhead, B. C. H. Steele, Eds., Plenum, New York 1980, 145.
73. J. O. Besenhard, in: *Euchem Conference Proceedings, "Solid State Chemistry and Electrochemistry, Especially with Respect to its Application in Battery Research"*, Rosenheim, Germany (April 30 - May 3, 1979).
74. D. W. Murphy, F. J. DiSalvo, J. N. Cardides, J. V. Waszak *Mat. Res. Bull.* 13 (1978) 1395.
75. M. Lazzari, B. Scrosati, *J. Electrochem. Soc.* 127 (1980) 773.
76. B. Di Pietro, M. Patriarca, B. Scrosati, *J. Power Sources* 8 (1982) 289.
77. B. Di Pietro, M. Patriarca, B. Scrosati, *Synth. Met.* 5 (1982) 1.
78. G. Pistoia (Ed.), *Lithium Batteries, New Materials, Developments and Perspectives*, Elsevier, Amsterdam, 1994.
79. M. Wakihara, O. Yamamoto (Eds.), *Lithium Ion Batteries*, Kodansha/Wiley-VCH, Tokyo/Weinheim, 1998.
80. J. O. Besenhard (Ed.), *Handbook of Battery Materials*, Wiley-VCH, Weinheim, 1999.
81. D. Aurbach (Ed.): *Electrochim. Acta, Special Ed. "Li Insertion into Host Materials"*, Vol. 45, 1999.
82. W. A. van Schalkwijk, B. Scrosati (Eds.), *Advances in Lithium Ion Batteries*, Kluwer/Plenum, New York, 2002.
83. J. O. Besenhard, M. Winter, *J. Pure Appl. Chem.* 70 (1998) 603.
84. M. Wakihara, *Mat. Sci. Eng.* R33 (2001) 109.
85. J. R. Dahn, A. K. Sleight, H. Shi, J. N. Reimers, Q. Zhong, B. M. Way, *Electrochim. Acta* 38 (1993) 1179.
86. S. Flandrois, B. Simon, *Carbon* 37 (1999) 165.
87. A. Mabuchi, *Tanso* 165 (1994) 298.
88. R. Yazami, M. Z. A. Munshi, in: *Handbook of Solid State Batteries and Capacitors*, M. Z. A. Munshi, Ed., World Scientific, Singapore, 1995, 425.
89. R. Yazami, in: *Lithium Batteries, New Materials, Developments and Perspectives*, G. Pistoia, Ed., Elsevier, Amsterdam, 1994, 49.
90. N. Imanishi, Y. Takeda, O. Yamamoto, in: *Lithium Ion Batteries*, M. Wakihara, O. Yamamoto, Eds., Kodansha/Wiley-VCH, Tokyo/Weinheim 1998, Chapter 5.
91. M. Endo, C. Kim, K. Nishimura, T. Fujino, M. Miyashita, *Carbon* 38 (2000) 183.
92. T. Zheng, J. R. Dahn, in: *Carbon Materials for Advanced Technologies*, T. D. Burchell, Ed., Pergamon, Elsevier, Amsterdam, 1999, 341.
93. T. Takamura, *NPC'98 Proceedings, Annual Nagoya International Battery and Power Sources Conference* (Aug. 26-28, 1998), 49.
94. M. Noel, V. Suryanarayanan, *J. Power Sources* 111 (2002) 193.
95. E. Frackowiack, S. Gautier, H. Gaucher, S. Bonnamy, F. Béguin, *Carbon* 37 (1999) 61.
96. Y. Tanabe, E. Yasuda, *Carbon* 38 (2000) 329.
97. B. McEnaney, in: *Carbon Materials for Advanced Technologies*, T. D. Burchell, Ed., Pergamon, Elsevier, Amsterdam 1999, 1.
98. H. Gasparoux, *Carbon* 5 (1967) 441.
99. S. Flandrois, A. Fevrier, P. Biensan, B. Simon, US Pat. No. 5554462, 1996.
100. M. Inagaki, *Tanso* 94 (1978) 106.
101. W. Kohns, H. J. Santner, F. Hofer, H. Schröttner, J. Doninger, I. Barsukov, J. H. Albering,

- K.-C. Möllea, J. O. Besenhard and M. Winter., *J. Power Sources*, submitted.
102. H. Shi, J. Barker, M. Y. Saidi, R. Koksang, L. Morris, *J. Power Sources* 68 (1997) 291.
103. H. Shi, J. Barker, M. Y. Saidi, R. Koksang, *J. Electrochem. Soc.* 143 (1996) 3466.
104. T. D. Shen, W. q. Ge, K. Y. Wang, M. X. Quan, J. T. Wang, W. D. Wie, C. C. Koch, *Nanostruct. Mater.* 7 (1996) 393.
105. W. L. Zhou, Y. Ikuhara, W. Zhao, J. Tang, *Carbon* 33 (1995) 1177.
106. J. Tang, W. Zhao, L. Li, A. U. Falster, W. B. Simmons, W. L. Zhou, Y. Ikuhara, J. H. Zhang, *J. Mater. Res.* 11 (1996) 733.
107. J. B. Aladekomo, R. H. Bragg, *Carbon* 28(1990)897.
108. M. Nakamizo, H. Honda, M. Inagaki, *Carbon* 16 (1978) 281.
109. F. Disma, L. Aymard, L. Dupont, J.M. Tarascon, *J. Electrochem. Soc.* 143 (1996) 3959.
110. F. Salver-Disma, J.-M. Tarascon, C. Clinard, J.-N. Rouzaud, *Carbon* 1941 (1999) 1959.
111. F. Salver-Disma, A. du Pasquier, J.-M. Tarascon, J.-C. Lasségues, J.-N. Rouzaud, *J. Power Sources* 81-82 (1999) 291.
112. N. J. Whelman, J. S. Williams, *Carbon* 36 (1998) 1309.
113. T. S. Ong, H. Yang, *Carbon* 38 (2000) 2077.
114. F. Chevallier, L. Aymard, J.-M. Tarascon, *J. Electrochem. Soc.* 148 (2001) A1216.
115. T. S. Ong, H. Yang, *J. Electrochem. Soc.* 149 (2002) A1.
116. D. Aurbach, B. Markovsky, A. Nimberger, E. Levi, Y. Gofer, *J. Electrochem. Soc.* 149 (2002) A152.
117. B. R. Puri, in: *Chemistry and Physics of Carbon*, P. Walker, P. Thrower, Eds., Marcel Dekker, New York 1970, Vol. 6, 191.
118. J.P. Randin, in: *Encyclopedia of Electrochemistry of the Elements*, A.J. Bard, Ed., Volume VII (Carbon, Vanadium), Marcel Dekker, New York, 1976, p. 2
119. P. M. A. Sherwood, in: *Practical Surface Analysis*, 2nd Ed., D. Briggs, M. P. Seah, Eds., Wiley, Chichester, 1990, p 384.
120. P. M. A. Sherwood, *J. Elect. Spect. Relat. Phenom.* 81 (1996) 391.
121. H.-P. Boehm, E. Diehl, W. Heck, R. Sappok, *Angew. Chem.* 17 (1964) 742.
122. F. Atamny, J. Blöcker, A. Dübotzky, H. Kurt, O. Timpe, G. Loose, W. Mahidi, R. Schlögl, *Mol. Phys.* 76 (1992) 851.
123. R. I. R. Blyth, H. Buqa, F. P. Netzer, M. G. Ramsey, J. O. Besenhard, P. Golob, M. Winter, *Appl. Surf. Sci.* 167 (2001) 99.
124. R. I. R. Blyth, H. Buqa, F. P. Netzer, M. G. Ramsey, J. O. Besenhard, M. Winter, *J. Power Sources* 97-98 (2001) 171.
125. S. Ross, J.P. Olivier, *J. Phys. Chem.* 65 (1961) 608.
126. J.P. Olivier, S. Ross, *Proc. Roy. Soc. (Lond.)* 265A (1962) 447.
127. J. P. Olivier, M. Winter, *J. Power Sources* 97-98 (2001) 151.
128. S. Amelinck, P. Delavignette, M. Heerschap, in: *Chemistry and Physics of Carbon*, P.L. Walker Jr., Ed., Marcel Dekker, New York, 1965, Vol. 1, Chapter 1
129. H. Chang, A. J. Bard, *Langmuir* 7 (1991) 1143.
130. H. O. Pierson, *Handbook of Carbon, Graphite, Diamond and Fullerenes*, Noyes Publications, Mill Road, Park Ridge NJ 1993, 43.
131. B. E. Warren, *Phys. Rev.* 59 (1941) 693.
132. R. E. Franklin, *Acta Cryst.* 4 (1951) 253.
133. B. E. Warren, *J. Chem. Phys.* 2 (1934) 551.
134. A. Oberlin, in: *Chemistry and Physics of Carbon*, P. A. Thrower, Ed., Marcel Dekker, New York 1989, Vol. 22, 1.
135. R. E. Franklin, *Proc. Roy. Soc. (London)* A209 (1951) 196.
136. K. Kinoshita, *Carbon, Electrochemical and Physicochemical Properties*, Wiley, New York, 1987.
137. O. Vohler, F. von Sturm, E. Wege, H. von Kienle, M. Voll, P. Kleinschmitt, in: *Ullmann's Encyclopedia of Industrial Chemistry* (Executive Ed.: W. Gerhartz), 5th Edition, VCH, Weinheim 1986, Volume 5A, 95.
138. J. B. Barr, I. C. Lewis, *Carbon* 16 (1978) 439.
139. G. M. Jenkins, K. Kawamura, *Polymeric Carbons, Carbon Fibre, Glass and Char*, Cambridge University Press, Cambridge, 1976.
140. G. Dübgen, Z. Popp, *Werkstofftech.* 15 (1984) 331.
141. P. Zhou, P. Papanek, R. Lee, J. E. Fisher, W. A. Kamitakahara, *J. Electrochem. Soc.* 144 (1997) 1744.
142. P. Zhou, R. Lee, AS. Claye, J. E. Fisher, *Carbon* 36 (1998) 1777.
143. Y. Nishi, in: *Lithium Ion Batteries*, M. Wakihara, O. Yamamoto, Eds., Kodansha/Wiley-VCH, Tokyo/Weinheim, 1998, Chapter 8.
144. K. Tatsumi, N. Iwashita, H. Sakaebe, S. Higuchi, A. Mabuchi, H. Fujimoto,

- J. Electrochem. Soc.*, 142 (1995) 716.
145. N. Imanishi, Y. Takeda, O. Yamamoto, in: *Lithium Ion Batteries*, M. Wakihara, O. Yamamoto, Eds., Kodansha/Wiley-VCH, Tokyo/Weinheim, 1998, Chapter 5.
 146. H. Azuma, H. Imoto, S. Yamada, K. Sekai, *J. Power Sources* 81-82 (1999) 1.
 147. H. Azuma, *J. Appl. Cryst.* 31 (1998) 910.
 148. J. Maire, J. Méring, in: *Chemistry and Physics of Carbon*, P. L. Walker, Ed., Marcel Dekker, New York, 1971, Vol. 6, 193.
 149. S. Flandrois, A. Février-Bouvier, K. Guerin, B. Simon, P. Biensan, *Mol. Cryst. Liq. Cryst.* 244 (1994) 89.
 150. M. Inagaki, *Solid State Ionics* 86-88 (1996) 833.
 151. W. Ruland, *Adv. Mater.* 2 (1990) 528.
 152. M. Endo, Y. A. Kim, T. Hayashi, K. Nishimura, T. Matusita, K. Miyashita, M. S. Dresselhaus, *Carbon* 39 (2001) 1287.
 153. Z. Ma, X. Yuan, D. Li, X. Liao, H. Hu, J. Ma, J. Wang, *Electrochem. Comm.* 4 (2002) 188.
 154. K. Tokumitsu, A. Mabuchi, H. Fujimoto, T. Kasuh, *J. Electrochem. Soc.* 143 (1996) 2235.
 155. H. Fujimoto, A. Mabuchi, K. Tokumitsu, T. Kasuh, *Carbon* 38 (2000) 871.
 156. K. Tokumitsu, H. Fujimoto, A. Mabuchi, T. Kasuh, *Carbon* 37 (1999) 1599.
 157. H. Fujimoto, A. Mabuchi, K. Tokumitsu, T. Kasuh, *J. Power Sources* 54 (1995) 440.
 158. K. Tokumitsu, A. Mabuchi, H. Fujimoto, T. Kasuh, *J. Power Sources* 54 (1995) 444.
 159. A. Mabuchi, H. Fujimoto, K. Tokumitsu, T. Kasuh, *J. Electrochem. Soc.* 142 (1995) 3049.
 160. T. Kasuh, A. Mabuchi, K. Tokumitsu, H. Fujimoto, *J. Power Sources* 68 (1997) 99.
 161. B. T. Kelly, *Physics of Graphite*, Applied Science Publishers, Englewood NJ, 1981.
 162. E. Fitzer, K. Mueller, W. Schaefer, in: *Chemistry and Physics of Carbon*, P. Walker, Ed., Marcel Dekker, New York, 1971, Vol. 7, 193.
 163. H. Marsh, *Introduction to Carbon Science*, Butterworth & Co. Ltd., 1989.
 164. Book Series: *Chemistry and Physics of Carbon*, Marcel Dekker, New York.
 165. C. Hartwigsen, W. Witschel, E. Spohr, *Ber. Bunsenges. Phys. Chem.* 101 (1997) 859.
 166. M. K. Song, S. D. Hong, K. T. No, *J. Electrochem. Soc.* 148 (2001) A1159.
 167. D. Billaud, E. McRae, A. Hérol, *Mat. Res. Bull.* 14 (1979) 857.
 168. X. Y. Song, K. Kinoshita, T. D. Tran, *J. Electrochem. Soc.* 143 (1996) L120.
 169. J. Rossat-Mignod, D. Fruchart, M. J. Moran, J. W. Milliken, J. E. Fisher, *Synth. Met.* 2 (1980) 143.
 170. V. V. Avdeev, V. A. Nalimova, K. N. Semenenko, *High Pressure Research* 6 (1990) 11.
 171. D. Guerard, V. A. Nalimova, in: *Solid State Ionics IV*, G.-A. Nazri, J.-M. Tarascon, M. Schreiber, Eds., Mat. Res. Soc. Symp. Proc., 1995, 369, 155.
 172. V. A. Nalimova, G. Guerard, M. Lelaurain, O. V. Fateev, *Carbon* 33 (1995) 177.
 173. V. A. Nalimova, C. Bindra, J. E. Fisher, *Solid State Comm.* 97 (1996) 583.
 174. *Handbook of Chemistry and Physics*, 68th Edition, R. C. Weast, Ed., CRC Press, Boca Raton FL, 1987.
 175. R. Yazami, A. Cherigui, V. A. Nalimova, D. Guerard, in: *Lithium Batteries*, S. Surampudi, V. R. Koch, Eds., The Electrochemical Society, Pennington NJ, 1993, PV 93-24, 379.
 176. Y. Mizutani, T. Abe, K. Ikeda, E. Ihara, M. Asano, T. Harada, M. Inaba, Z. Ogumi, *Carbon* 1997 35 (1997) 61.
 177. N. Daumas, A. Hérol, *C. R. Acad. Sci. Paris* 268C (1969) 373.
 178. W. Rüdorff, in: *Advances in Inorganic Chemistry and Radiochemistry*, H. J. Emeléus, A. G. Sharpe, Eds., Academic Press, New York, 1959, Vol. 1, 223.
 179. N. Daumas, A. Hérol, *Bull. Soc. Chim.* 5 (1971) 1598.
 180. S. A. Safran, in: *Chemical Physics of Intercalation*, NATO ASI Series, A. P. Legrand, S. Flandrois, Eds., Plenum Press, New York, 1987, B172, 47.
 181. A. Funabiki, M. Inaba, T. Abe, Z. Ogumi, *Electrochim. Acta* 45 (1999) 865.
 182. A. Funabiki, M. Inaba, T. Abe, Z. Ogumi, *J. Electrochem. Soc.* 146 (1999) 2443.
 183. A. Funabiki, M. Inaba, T. Abe, Z. Ogumi, *Carbon* 37 (1999) 1591.
 184. J. E. Fischer, in: *Chemical Physics of Intercalation*, NATO ASI Series, A. P. Legrand, S. Flandrois, Eds., Plenum Press, New York, 1987, Vol. B172, 59.
 185. J. R. Dahn, R. Fong, M. J. Spoon, *Phys. Rev. B* 42 (1990) 6424.
 186. D. Billaud, F. X. Henry, P. Willmann, *Mat. Res. Bull.* 28 (1993) 477.
 187. A. H. Whitehead, K. Edström, N. Rao, J. R. Owen, *J. Power Sources* 63 (1996) 41.
 188. J. R. Dahn, *Phys. Rev. B* 44 (1991) 9170.
 189. W. Huang, R. Frech, *J. Electrochem. Soc.* 145 (1998) 765.
 190. M. Inaba, H. Yoshida, Z. Ogumi, T. Abe, Y. Mizutani, M. Asano, *J. Electrochem. Soc.*

- 142 (1995) 20.
191. K. C. Woo, W. A. Kamitakahara, D. P. Divincenzo, D. S. Robinson, H. Mertwoy, J. W. Milliken, J. E. Fisher, *Phys. Rev. Lett.* 50 (1983) 182.
192. S. Mori, H. Asahina, H. Suzuki, A. Yonei, E. Yasukawa, *J. Power Sources* 68 (1997) 59.
193. O. Tanaiki, M. Inagaki, *Carbon* 35(1997) 831.
194. S. A. Safran, *Phys. Rev. Lett.* 44 (1980) 937.
195. W. Rüdorff, U. Hofmann, *Z. Electrochem.* 30 (1934) 511.
196. M. L. Dzurus, G. Hennig, *J. Am. Chem. Soc.* 79 (1957) 5897.
197. F. R. McDonnell, R. C. Pink, A. R. Ubbelohde, *J. Chem. Soc. (London)* 1951, 191.
198. A. R. Ubbelohde, F. A. Lewis, *Graphite and its Crystal Compounds*, Clarendon Press, Oxford, 1960.
199. J. Conard, in: *Chemical Physics of Intercalation*, NATO ASI Series, A. P. Legrand, S. Flandrois, Eds., Plenum Press, New York 1987, Vol. B172, 357.
200. S. Yamazaki, T. Hashimoto, T. Iriyama, Y. Mori, H. Shiroki, N. Tamura, *J. Mol. Struct.* 441 (1998) 165.
201. Y. Kida, A. Kinoshita, K. Yanagida, A. Funahashi, T. Nohma, I. Yonezu, *Electrochim. Acta* 47 (2002) 1691.
202. K. Tatsumi, T. Akai, T. Imamura, K. Zhaghib, N. Iwasita, S. Higuchi, Y. Sawada, *J. Electrochem. Soc.* 143 (1996) 1923.
203. M. K. Song, S. D. Hong, K. T. No, *J. Electrochem. Soc.* 148 (2001) A1159.
204. A. Hightower, C. C. Ahn, B. Fultz, P. Rez, *Appl. Phys. Lett.* 77 (2000) 238.
205. R. Bitihn, R. Herr, D. Hoge, *J. Power Sources* 43-44 (1993) 409.
206. G. R. Hennig, *Progr. Inorg. Chem.* 1 (1959) 125.
207. J. G. Hooley, *Chem. Phys. Carbon* 5 (1969) 321.
208. R. Fong, U. von Sacken, J. R. Dahn, *J. Electrochem. Soc.* 137 (1990) 2009.
209. K. Yokoyama, N. Nagawa, in: *New Sealed Rechargeable Batteries and Supercapacitors*, B. M. Barnett, E. Dowgiallo, G. Halpert, Y. Matsuda, Z. Takehara, Eds., The Electrochemical Society, Pennington, NJ 1993, PV 93-23, 270.
210. R. Kanno, Y. Kawamoto, Y. Takeda, S. Ohashi, N. Imanishi, O. Yamamoto, *J. Electrochem. Soc.* 139 (1992) 3397.
211. M. Winter, P. Novák, A. Monnier, *J. Electrochem. Soc.* 145 (1998) 428.
212. E. Peled, D. Golodnitzky, G. Ardel, *J. Electrochem. Soc.* 144 (1997) L208.
213. E. Peled, D. Golodnitzky, J. Pencier, in: *Handbook of Battery Materials*, J. O. Besenhard, Ed., Wiley-VCH, Weinheim, 1999, Part III, Chapter 6.
214. V. Manev, I. Naidenov, B. Puresheva, G. Pistoia, *J. Power Sources* 57 (1995) 133.
215. V. Manev, I. Naidenov, B. Puresheva, G. Pistoia, *J. Power Sources* 57 (1995) 211.
216. R. Imhof, P. Novák, in: *Batteries for Portable Applications and Electric Vehicles*, C. F. Holmes, A. R. Landgrebe, Eds., The Electrochemical Society, Pennington NJ 1997, PV97-18, 313.
217. R. Imhof, P. Novák, *J. Electrochem. Soc.* 145 (1998) 1081.
218. P. Novák, W. Scheifele, M. Winter, O. Haas, *J. Power Sources* 68 (1997) 267.
219. K. Tatsumi, K. Zaghbi, H. Abe, S. Higuchi, T. Ohsaki, Y. Sawada, *J. Power Sources* 54 (1996) 425.
220. F. Joho, P. Novák, M. E. Spahr, *J. Electrochem. Soc.* 149 (2002) A1020.
221. F. Disma, C. Lenain, B. Beaudoin, L. Aymard, J.-M. Tarascon, *Solid State Ionics* 98 (1997) 145.
222. A. Du Pasquier, F. Disma, T. Bowmer, A. S. Gozdz, G. Amatucci, J.-M. Tarascon, *J. Electrochem. Soc.* 145 (1997) 472.
223. O. Yamamoto, N. Imanishi, Y. Takeda, H. Kashiwagi, *J. Power Sources* 54 (1995) 72.
224. K. Zaghbi, G. Nadeau, K. Kinoshita, *J. Electrochem. Soc.* 147 (2000) 2110.
225. C. Lampe-Onnerud, J. Shi, P. Onnerud, R. Chamberlain, B. Barnett, *J. Power Sources* 97-98 (2001) 133.
226. K. Takei, N. Terada, K. Kumai, T. Iwahori, T. Uwai, T. Miura, *J. Power Sources* 55 (1995) 191.
227. K. Fukuda, K. Kikuya, K. Isono, M. Yoshio, *J. Power Sources* 69 (1997) 165.
228. H. Wang, T. Ikeda, K. Fukuda, M. Yoshio, *J. Power Sources* 83 (1999) 141.
229. O. Yamamoto, Y. Takeda, N. Imanishi, R. Kanno, in: *New Sealed Rechargeable Batteries and Supercapacitors*, B. M. Barnett, E. Dowgiallo, G. Halpert, Y. Matsuda, Z. Takehara, Eds., The Electrochemical Society, Pennington NJ, 1993, PV 93-23, 302.
230. N. Imanishi, H. Kashiwagi, T. Ichikawa, Y. Takeda, O. Yamamoto, M. Inagaki, *J. Electrochem. Soc.* 140 (1993) 315.
231. D. Billaud, F. X. Henry, P. Willmann, *J. Power Sources* 54 (1995) 383.
232. Y.-P. Wu, C.-R. Wan, Y.-X. Li, S.-B. Fang, Y.-Y. Jiang, *Electrochem. Solid-State Lett.* 1 (1999) 118.

233. K. Zaghib, K. Tatsumi, H. Abe, T. Ohsaki, Y. Sawada, S. Higuchi, *J. Power Sources* 54 (1995) 435.
234. S. Passerini, J. M. Rosolen, B. Scrosati, *J. Power Sources* 45 (1993) 333.
235. C. E. Newnham, S. Rinne, N. Scholey, *J. Power Sources* 54 (1995) 516.
236. J.-M. Tarascon, A. S. Gozdz, C. N. Schmutz, P. C. Warren, F. Shokoohi, in *Advances in Porous Materials*, S. Komarneni, D. M. Smith, J. S. Beck, Eds., Mat. Res. Soc. Symp. Proc., 1995, 369, 595.
237. K. A. Hirasawa, K. Nishioka, T. Sato, S. Yamaguchi, S. Mori, *J. Power Sources* 69 (1997) 97.
238. R. Santhanam, M. Noel, *J. Power Sources* 63 (1996) 1.
239. L. Kavan, *Chem. Rev.* 97 (1997) 3061.
240. V. I. Decheneaux, F. Drovot, J. P. Gabano, Y. Jumeat, Ger. Pat. No. 2210370, 1971.
241. G. Li, R. Xue, L. Chen, *Solid State Ionics* 90 (1996) 221.
242. Y. Nakagawa, S. Wang, Y. Matsumura, C. Yamaguchi, *Synth. Met.* 85 (1997) 1343.
243. P. Biensan, *J. Power Sources*, 81-82 (1999) 906.
244. R. Yazami, M. Deschamps, in: *Advances in Porous Materials*, S. Komarneni, D. M. Smith, J. S. Beck, Eds., Mat. Res. Soc. Symp. Proc., 1995, 369, 165.
245. R. Yazami, M. Deschamps, *J. Power Sources* 54 (1995) 411.
246. R. Yazami, M. Deschamps, in: *Rechargeable Lithium and Lithium-Ion Batteries*, S. Megahed, B. Barnett, L. Xie, Eds., The Electrochemical Society, Pennington NJ, 1995, PV 94-28, 183.
247. M. Deschamps, R. Yazami, *J. Power Sources* 68 (1997) 236.
248. R. Yazami, M. Dechaumps, in *Progress in Batteries & Battery Materials* (Eds: ITE-JEC Press Inc. and IBA Inc.), JEC Press Inc., Brunswick OH, 1996, Vol. 15, 161.
249. K. Sato, M. Noguchi, A. Demachi, N. Oki, M. Endo, *Science* 264 (1994) 556.
250. K. Sato, M. Noguchi, A. Demachi, N. Oki, M. Endo, Y. Sasabe, *Int. Workshop on Advanced Batteries (Lithium Batteries)*, Osaka, 1995, 219.
251. S. Yata, H. Kinoshita, M. Komori, N. Ando, T. Kashiwamura, T. Harada, K. Tanaka, T. Yamabe, *Synth. Met.* 62 (1994) 153.
252. S. Yata, K. Sakurai, T. Osaki, Y. Inoue, K. Yamaguchi, *Synth. Met.* 33 (1990) 177.
253. S. Yata, Y. Hato, H. Kinoshita, N. Ando, A. Anekawa, T. Hashimoto, M. Yamaguchi, K. Tanaka, T. Yamabe, *Synth. Met.* 73 (1995) 273.
254. S. Yata, *Int. Workshop on Advanced Batteries (Lithium Batteries)*, Osaka 1995, 204.
255. S. Yata, H. Kinoshita, M. Komori, N. Ando, T. Kashiwamura, T. Harada, K. Tanaka, T. Yamabe, in: *New Sealed Rechargeable Batteries and Supercapacitors*, B. M. Barnett, E. Dowgiallo, G. Halpert, Y. Matsuda, Eds., The Electrochemical Society, Pennington NJ, 1993, PV 93-23, 502.
256. S. Yata, *Denki Kagaku* 9 (1997) 65.
257. E. Peled, C. Menachem, D. Bar-Tow, A. Melman, *J. Electrochem. Soc.* 143 (1996) L4.
258. C. Menachem, E. Peled, L. Burstein, Y. Rosenberg, *J. Power Sources* 68 (1997) 277.
259. H. Xiang, S. Fang, Y. Jiang, *J. Electrochem. Soc.* 144 (1997) L187.
260. S. Wang, Y. Matsumura, T. Maeda, *Synth. Met.* 71 (1995) 1759.
261. Y. Matsumura, S. Wang, J. Mondori, *Carbon* 33 (1995) 1457.
262. Y. Matsumura, S. Wang, T. Kasuh, T. Maeda, *Synth. Met.* 71 (1995) 1755.
263. Y. Matsumura, S. Wang, K. Shinohara, T. Maeda, *Synth. Met.* 71 (1995) 1757.
264. W. S. Li, L. C. Jiang, G. Y. Xie, X. Jiang, *J. Power Sources* 58 (1996) 235.
265. Y. Mori, T. Iriyama, T. Hashimoto, S. Yamazaki, F. Kawakami, H. Shiroki, T. Yamabe, *J. Power Sources* 56 (1995) 205.
266. N. Takami, A. Satoh, T. Ohsaka, M. Kanda, *Electrochim. Acta* 42 (1997) 2537.
267. Y. Dai, Y. Wang, V. Eshkenazi, E. Peled, S. G. Greenbaum, *J. Electrochem. Soc.* 145 (1998) 1179.
268. T. Fukutsuka, T. Abe, M. Inaba, Z. Ogumi, *J. Electrochem. Soc.* 148 (2001) A1260.
269. C. W. Park, S. Ho, S. I. Lee, S. M. Oh, *Carbon* 38 (2000) 995.
270. S. Lee, M. Nishizawa, I. Uchida, *Electrochim. Acta* 44 (1999) 2379.
271. I. Mochida, C. Ku, Y. Korai, *Carbon* 39 (2001) 399.
272. S. Morimoto, Kureha Chemical Industry Co., Ltd., personal communication.
273. A. Nagai, M. Ishikawa, J. Masuko, N. Sonobe, H. Chuman, T. Iwasaki, *Mat. Res. Soc. Symp. Proc.* 393 (1995) 339.
274. J. R. Dahn, T. Zheng, Y. Liu, J. S. Xue, *Science* 270 (1995) 590.
275. L. B. Ebert, *Carbon* 34 (1996) 671.
276. P. Zhou, P. Papanek, C. Bindra, R. Lee, J. E. Fischer, *J. Power Sources* 68 (1997) 297.
277. T. Zheng, J. S. Xue, J. R. Dahn, *Chem. Mater.* 8 (1996) 389.
278. T. Zheng, Y. Liu, E. W. Fuller, S. Tseng, U. von Sacken, J. R. Dahn, *J. Electrochem. Soc.* 142 (1995) 2581.

279. J. S. Xue, J. R. Dahn, *J. Electrochem. Soc.* 142 (1995) 3668.
280. T. Zheng, J. R. Dahn, *J. Power Sources* 68 (1997) 201.
281. T. Zheng, W. R. McKinnon, J. R. Dahn, *J. Electrochem. Soc.* 143 (1996) 2137.
282. A. Claye, J. E. Fischer, *Electrochim. Acta* 45 (1999) 107.
283. P. Papanek, M. Radosavljevic, J. E. Fischer, *Chem. Mater.* 8 (1996) 1519.
284. E. Buiel, J. R. Dahn, *Electrochim. Acta* 45 (1999) 121.
285. J. Gong, H. Wu, Q. Yang, *Carbon* 37 (1999) 1409.
286. M. Inaba, M. Fujikawa, T. Abe, Z. Ogumi, *J. Electrochem. Soc.* 147 (2000) 4008.
287. M. Noguchi, K. Miyasita, M. Endo, *Tanso* 155 (1992) 315.
288. Y. Gao, K. Myrtle, Z. Meiji, J. N. Reimers, J. R. Dahn, *Phys. Rev. B* 54 (1996) 23.
289. Z. Wang, X. Huang, R. Xue, L. Chen, *Carbon* 37 (1999) 685.
290. Z. Wang, X. Huang, R. Xue, L. Chen, *J. Power Sources* 81-82 (1999) 328.
291. S. Wang, Y. Zhang, L. Yang, Q. Liu, *Solid State Ionics* 86-88 (1996) 919.
292. N. Takami, A. Satoh, T. Ohsaki, M. Kanda, *J. Electrochem. Soc.* 145 (1998) 478.
293. H. Ago, M. Kato, K. Yahara, K. Yoshizawa, K. Tanaka, T. Yamabe, *J. Electrochem. Soc.* 146 (1999) 1262.
294. P. Delhaës, F. Carmona, in: *Chemistry and Physics of Carbon*, P.L. Walker and P. A. Thrower, Eds., Marcel Dekker, New York, 1981, Vol. 17, 89.
295. C. R. Kinney, *Proc. of 1st & 2nd Int. Conf. on Carbon*, Pergamon, New York, 1955, 83.
296. A. Marchand, J. V. Zanetta, *Carbon* 3 (1996) 483.
297. M. Cerutti, J. Übersfeld, J. Millet, J. Parisot, *J. Chim. Phys.* 57 (1960) 907.
298. A. Satoh, N. Takami, T. Ohsaki, *Solid State Ionics* 80 (1995) 291.
299. A. Satoh, N. Takami, T. Ohsaki, M. Kanda, in: *Rechargeable Lithium and Lithium-Ion Batteries*, S. Megahed, B. Barnett, L. Xie, Eds., The Electrochemical Society, Pennington NJ, 1995, PV 94-28, 143.
300. K. Tatsumi, A. Mabuchi, N. Iwashita, H. Sakaebe, H. Shioyama, H. Fujimoto, S. Higuchi, in: *Batteries and Fuel Cells for Stationary and Electric Vehicle Applications*, A. R. Landgrebe, Z. Takehara, Eds., The Electrochemical Society, Pennington NJ, 1993, PV 93-8, 64.
301. K. Tatsumi, N. Iwashita, H. Sakaebe, H. Shioyama, S. Higuchi, A. Mabuchi, H. Fujimoto, *J. Electrochem. Soc.* 142 (1995) 716.
302. T. Zheng, J. R. Dahn, *Synth. Met.* 73 (1995) 1.
303. T. Zheng, J. R. Dahn, *Phys. Rev. B* 53 (1996) 3061.
304. T. Zheng, J. N. Reimers, J. R. Dahn, *Phys. Rev. B* 51 (1995) 734.
305. W. Xing, J. S. Xue, T. Zheng, A. Gibaud, J. R. Dahn, *J. Electrochem. Soc.* 143 (1996) 3482.
306. J. R. Dahn, W. Xing, Y. Gao, *Carbon* 35 (1997) 825.
307. Y. Liu, J. S. Xue, T. Zheng, J. R. Dahn, *Carbon* 34 (1994) 193.
308. T. Zheng, Q. Zhong, J. R. Dahn, *J. Electrochem. Soc.* 142 (1994) L211.
309. H. Ago, K. Tanaka, T. Yamabe, T. Miyoshi, K. Takegoshi, T. Terao, S. Yata, Y. Hato, S. Nagaura, N. Ando, *Carbon* 12 (1997) 1781.
310. H. Iomoto, A. Omaru, A. Azuma, Y. Nishi, in: *Lithium Batteries*, S. Surampudi, V. R. Koch, Eds., The Electrochemical Society, Pennington, NJ 1993, PV 93-24, 9.
311. J. Conard, K. Tatsumi, S. Menu, P. Lauginie, *ITE Letters on Batteries, New Technologies & Medicine*, 2000, 1, B27-47, and references therein.
312. W. Xing, R. A. Dunlap, J. R. Dahn, *J. Electrochem. Soc.* 145 (1998) 62.
313. H. Imoto, M. Nagamine, Y. Nishi, in: *Rechargeable Lithium and Lithium-Ion Batteries*, S. Megahed, B. Barnett, L. Xie, Eds., The Electrochemical Society, Pennington, NJ 1995, PV 94-28, 43.
314. M. Alamgir, Q. Zuo, K. M. Abraham, *J. Electrochem. Soc.* 141 (1994) L143.
315. E. Buiel, J. R. Dahn, *J. Electrochem. Soc.* 145 (1998) 1977.
316. T. Iijima, K. Suzuki, Y. Matsuda, *Synth. Met.* 73 (1995) 9.
317. Y. Matsumura, S. Wang, J. Mondori, *J. Electrochem. Soc.* 142 (1995) 2914.
318. F. Chevallier, S. Gautier, J. P. Salvétat, C. Clinard, E. Frackowiack, J. N. Rouzaud, F. Béguin, *J. Power Sources* 97-98 (2001) 143.
319. Y. Jung, M. C. Suh, H. Lee, M. Kim, S. Lee, S. C. Shim, J. Kwak, *J. Electrochem. Soc.* 144 (1997) 4279.
320. K. Guerin, A. Fevrier-Bouvier, S. Flandrois, B. Simon, P. Biensan, *Electrochim. Acta* 45 (2000) 1607.
321. M. Kikuchi, Y. Ikezawa, T. Takamura, *J. Electroanal. Chem.* 396 (1995) 451.
322. S. Wang, S. Yata, J. Nagano, Y. Okano, H. Kinoshita, H. Kikuta, T. Yamabe, *J. Electrochem. Soc.* 147 (2000) 2498.
323. R. E. Gerald II, R. J. Klingler, G. Sandi, C. S. Johnson, L. G. Scanlon, J. W. Rathke, *J.*

- Power Sources* 89 (2000) 237
324. C. Wang, A. J. Appleby, F. E. Little, *J. Electrochem. Soc.* 149 (2002) A754.
 325. A. Marchand, in: *Chemistry and Physics of Carbon*, P.L. Walker, Ed., Marcel Dekker, New York 1971, Vol. 7, 155.
 326. V. A. Q. Tyumentsev, E. A. Belenkov, G. P. Shveikin, S. A. Podkopaev, *Carbon* 36 (1998) 845.
 327. C. Kim, T. Fujino, K. Miyashita, T. Hayashi, M. Endo, M. S. Dresselhaus, *J. Electrochem. Soc.* 147 (2000) 1257.
 328. R. Riedel, *Adv. Mater.* 6 (1994) 549.
 329. M. Kawaguchi, *Adv. Mater.* 9 (1997) 615.
 330. J. R. Dahn, J. N. Reimers, A. K. Sleight, T. Tiedje, *Phys. Rev. B* 45 (1992) 3773.
 331. B. M. Way, J. R. Dahn, *J. Electrochem. Soc.* 1994 141(1994).
 332. T. Tamaki, M. Tamaki, 8th IMLB, Ext. Abstr., Nagoya 1996, 216.
 333. B. M. Way, J. R. Dahn, T. Tiedje, K. Myrtle, M. Kasrai, *Phys. Rev. B* 1992 46 (1992).
 334. M. Endo, C. Kim, T. Karaki, Y. Nishimura, M. J. Matthews, S. D. M. Brown, M. S. Dresselhaus, *Carbon* 37 (1999) 561.
 335. U. Tanaka, T. Sogabe, H. Sakagoshi, M. Ito, T. Tojo, *Carbon* 39 (2001) 931.
 336. C. E. Lowell, *J. Am. Ceram. Soc.* 50 (1967) 142.
 337. Y. Nishimura, T. Takahashi, T. Tamaki, T. Endo, M. S. Dresselhaus, *Tanso* 172 (1996) 89.
 338. C. Kim, T. Fujino, T. Hayashi, M. Endo, M. S. Dresselhaus, *J. Electrochem. Soc.* 147 (2000) 1265.
 339. N. Takami, M. Sekino, T. Ohsaki, M. Kanda, M. Yamamoto, *J. Power Sources* 97-98 (2001) 677.
 340. N. Takami, T. Ohsaki, H. Hasebe, M. Yamamoto, *J. Electrochem. Soc.* 149 (2002) A9.
 341. W. J. Weydanz, B. M. Way, T. van Buuren, J. R. Dahn, *J. Electrochem. Soc.* 141 (1994) 900
 342. S. Ito, T. Murata, M. Hasegawa, Y. Bito, Y. Toyoguchi, *J. Power Sources* 68 (1997) 245.
 343. T. Nakajima, M. Koh, M. Takashima, *Electrochim. Acta* 43 (1998) 883.
 344. T. D. Tran, J. H. Feikert, S. T. Mayer, X. Song, K. Kinoshita, in: *Rechargeable Lithium and Lithium-Ion Batteries*, S. Megahed, B. Barnett, L. Xie, Eds., The Electrochemical Society, Pennington NJ, 1995, PV 94-28, 110.
 345. H. H. Schönfelder, K. Kitoh, H. Nemoto, *J. Power Sources* 68 (1997) 258.
 346. T. D. Tran, S. T. Mayer, R. W. Pekala, in *Advances in: Porous Materials*, S. Komarneni, D. M. Smith, J. S. Beck, Eds., Mat. Res. Soc. Symp. Proc., 1995, 369, 449.
 347. A. Omaru, H. Azuma, M. Aoki, A. Kita, Y. Nishi, in: *Lithium Batteries*, S. Surampudi, V. R. Koch, Eds., The Electrochemical Society, Pennington NJ, 1993, PV 93-24, 21.
 348. R. L. Morrison, US Pat. No. 5558954, 1996.
 349. T. D. Tran, J. H. Feikert, X. Song, K. Kinoshita, *J. Electrochem. Soc.* 142 (1995) 3297.
 350. H. Azuma, A. Omaru, Y. Nishi, *Electrochem. Soc. Japan, Fall Meeting*, Nagoya, 1991, Ext. Abstr. 132.
 351. Y. Matsuda, M. Ishikawa, T. Nakamura, M. Morita, S. Tsujioka, T. Kawashima, in: *Rechargeable Lithium and Lithium-Ion Batteries*, S. Megahed, B. Barnett, L. Xie, Eds., The Electrochemical Society, Pennington NJ, 1995, PV 94-28, 85.
 352. M. Morita, T. Hanada, H. Tsutsumi, Y. Matsuda, M. Kawaguchi, *J. Electrochem. Soc.* 139 (1992) 1227.
 353. Y. Matsuda, M. Morita, T. Hanada, M. Kawaguchi, *J. Power Sources* 43-44 (1993) 75.
 354. M. Ishikawa, T. Nakamura, M. Morita, Y. Matsuda, S. Tsujioka, T. Kawashima, *J. Power Sources* 55 (1995) 127.
 355. M. Ishikawa, T. Nakamura, M. Morita, Y. Matsuda, M. Kawaguchi, *Denki Kagaku* 62 (1994) 897.
 356. M. Morita, T. Hanada, H. Tsutsumi, Y. Matsuda, in: *High Power, Ambient Temperature Lithium Batteries*, W. D. Clark, G. Halpert, Eds., The Electrochemical Society, Pennington NJ, 1992, PV 92-15, 101.
 357. M. Ishikawa, M. Morita, T. Hanada, Y. Matsuda, M. Kawaguchi, *Denki Kagaku* 61 (1993) 1395.
 358. Y. P. Wu, S. Fang, Y. Jiang, R. Holze, *J. Power Sources* 108 (2000) 245.
 359. A. M. Wilson, J. N. Reimers, E. W. Fuller, J. R. Dahn, *Solid State Ionics* 74 (1995) 249.
 360. A. M. Wilson, G. Zank, K. Eguchi, W. Xing, J. R. Dahn, *J. Power Sources* 68 (1997) 195.
 361. W. Xing, A. M. Wilson, K. Eguchi, G. Zank, J. R. Dahn, *J. Electrochem. Soc.* 144 (1997) 2410.
 362. A. M. Wilson, G. Zank, K. Eguchi, W. Xing, B. Yates, J. R. Dahn, *Chem. Mater.* 9 (1997) 2139.

363. J. S. Xue, K. Myrtle, J. R. Dahn, *J. Electrochem. Soc.* 142 (1995) 2927.
364. R. A. Guidotti, B. J. Johnson, *Proc. 37th Power Sources Conf.*, Cherry Hill, NJ, 1996, 219.
365. W. Xing, A. M. Wilson, G. Zank, J. R. Dahn, *Solid State Ionics* 93 (1997) 239.
366. A. M. Wilson, J. R. Dahn, *J. Electrochem. Soc.* 142 (1995) 326.
367. A. M. Wilson, J. R. Dahn, in: *Rechargeable Lithium and Lithium-Ion Batteries*, S. Megahed, B. Barnett, L. Xie, Eds., The Electrochemical Society, Pennington NJ, 1995, PV 94-28, 158.
368. G. S. Wang, G. T. Wu, X. B. Zhang, Z. F. Qi, W. Z. Li, *J. Electrochem. Soc.* 145 (1998) 2751.
369. J. Niu, J. Y. Lee, *Electrochem. Solid-State Lett.* 5 (2002) A107.
370. A. N. Dey, *Electrochem. Soc. Fall Meeting*, 1970, Abstr. 62.
371. E. Peled, *J. Electrochem. Soc.* 126 (1979) 40.
372. E. Peled, in: *Lithium Batteries*, J.-P. Gabano, Ed., Academic Press, London, 1983, Chapter 3.
373. F. Joho, B. Rykart, R. Imhof, P. Novák, M. E. Spahr, A. Monnier, *J. Power Sources* 81-82 (1999) 243.
374. M. Fujimoto, Y. Kida, T. Nohma, M. Takahashi, K. Nishio, T. Saito, *J. Power Sources* 63 (1996) 127.
375. P. Novák, F. Joho, R. Imhof, J.-P. Panitz, O. Hass, *J. Power Sources* 81-82 (1999) 212.
376. M. Lanz, E. Lehmann, R. Imhof, I. Exnar, P. Novák, *J. Power Sources* 101 (2001) 177.
377. P. Novák, J.-C. Panitz, F. Joho, M. Lanz, R. Imhof, M. Coluccia, *J. Power Sources* 90 (2000) 52.
378. P. Novák, F. Joho, M. Lanz, B. Rykart, J.-C. Panitz, D. Allia, R. Kötz, O. Haas, *J. Power Sources* 97-98 (2001) 39.
379. E. Peled, D. Bar-Tow, A. Merson, A. Gladkikh, L. Burstein, D. Golodnitzky, *J. Power Sources* 97-98 (2001) 52.
380. E. Endo, K. Tanaka, K. Sekai, *J. Electrochem. Soc.* 147 (2000) 4029.
381. E. Endo, M. Ata, K. Tanaka, K. Sekai, *J. Electrochem. Soc.* 145 (1998) 3757.
382. E. Endo, M. Ata, K. Tanaka, K. Sekai, *J. Electrochem. Soc.* 146 (1999) 49.
383. D. Rahn, *J. Power Sources* 81-82 (1999) 358.
384. M. Winter, H. Buqa, B. Evers, T. Hoda, K.-C. Möller, C. Reisinger, M. V. Santis Alvarez, I. Schneider, G. H. Wrodnigg, F. P. Netzer, R. I. R. Blyth, M. G. Ramsey, P. Golob, F. Hofer, C. Grogger, W. Kern, R. Saf, J. O. Besenhard, *ITE Batt. Lett.*, 1999, 1(2), 129.
385. S.-K. Jeong, M. Inaba, T. Abe, Z. Ogumi, *J. Electrochem. Soc.* 148 (2001) A989.
386. K. A. Hirasawa, T. Sato, H. Asahina, S. Yamaguchi, S. Mori, *J. Electrochem. Soc.* 144 (1997) L81.
387. D. Allia, R. Kötz, P. Novák, H. Siegenthaler, *Electrochem. Comm.* 2 (2000) 436.
388. M. Dollé, S. Grugeon, B. Beaudoin, L. Dupont, J.-M. Tarascon, *J. Power Sources* 97-98 (2001) 104.
389. S. Yamaguchi, H. Asahina, K. A. Hirasawa, T. Sato, S. Mori, *Mol. Cryst. Liq. Cryst.* 1 322 (1998) 239.
390. J. O. Besenhard, M. W. Wagner, M. Winter, A. D. Jannakoudakis, P. D. Jannakoudakis, E. Theodoridou, *J. Power Sources* 43-44 (1993) 413.
391. S. Zhang, M. S. Ding, K. Xu, J. Allen, T. R. Jow, *Electrochem. Solid-State Lett.* 4 (2001) A206.
392. Y.-C. Chang, H.-J. Sohn, *J. Electrochem. Soc.* 147 (2000) 50.
393. D. Zhang, B. S. Haran, A. Durairajan, R. E. White, Y. Podrashanzky, B. N. Popov, *J. Power Sources* 91 (2000) 122.
394. X. Zhang, P. N. Ross, Jr., R. Kostecki, F. Kong, S. Sloop, J. B. Kerr, K. Striebel, E. J. Cairns, F. McLarnon, *J. Electrochem. Soc.* 148 (2001) A463.
395. Y. Wang, X. Guo, S. Greenbaum, J. Liu, K. Amine, *Electrochem. Solid-State Lett.* (2001) 4 A68.
396. J.-S. Kim, Y.-T. Park, *J. Power Sources* 91 (2000) 172.
397. C. Wang, A. J. Appleby, F. E. Little, *Electrochim. Acta* 46 (2001) 1793.
398. C. Wang, I. Kakwan, A. J. Appleby, F. E. Little, *J. Electroanal. Chem.* 489 (2000) 55.
399. I. Bloom, B. W. Cole, J. J. Sohn, S. A. Jones, E. G. Polzin, V. S. Battaglia, G. L. Henrikson, C. Motloch, R. Richardson, T. Unkelhauser, D. Ingersoll, H. L. Case, *J. Power Sources* 101 (2001) 238.
400. M. Broussely, in: *Advances In Lithium Ion Batteries*, W. van Schalkwijk, B. Scrosati, Eds., Kluwer/Plenum, New York, 2002, 393.
401. Y. Kobayashi, H. Miyashiro, K. Kumei, K. Takei, T. Iwahori, I. Uchida, *J. Electrochem. Soc.* 149 (2001) A978.

402. M. Koltypin, Y. S. Cohen, B. Markovsky, Y. Cohen, D. Aurbach, *Electrochem. Comm.* 4 (2002) 17.
403. B. Simon, J. P. Boeue, M. Broussely, *J. Power Sources* 43-44 (1993) 65.
404. J. M. Tranchant, R. Messina, *J. Electrochem. Soc.* 143 (1996) 391.
405. R. Yazami, Y. F. Reynier, *Electrochim. Acta* 47 (2002) 1217.
406. E. Peled, in: *Rechargeable Lithium and Lithium-Ion Batteries*, S. Megahed, B. Barnett, L. Xie, Eds., The Electrochemical Society, Pennington NJ, 1995, PV 94-28, 1.
407. M. Jean, A. Tranchant, R. Messina, *J. Electrochem. Soc.* 143 (1996) 391.
408. M. Jean, A. Chausse, R. Messina, *J. Power Sources* 68 (1997) 232.
409. G. Amatucci, A. Du Pasquier, A. Blyr, T. Zheng, J.-M. Tarascon, *Electrochim. Acta* 45 (1999) 255.
410. M. Broussely, S. Herreyre, P. Biensan, P. Kasztejna, K. Nechev, R. J. Staniewicz, *J. Power Sources* 97-98 (2001) 13.
411. A. Du Pasquier, F. Disma, T. Bowmer, A.S. Gozdz, G. Amatucci, J.-M. Tarascon, *J. Electrochem. Soc.* 145 (1998) 472.
412. K. Edström, M. Herranen, *J. Electrochem. Soc.* 147 (2000) 3628.
413. D. Aurbach, M. D. Levi, E. Levi, H. Teler, B. Markovsky, G. Salitra, U. Heider, L. Heider, *J. Electrochem. Soc.* 145 (1998) 3024.
414. D. Aurbach, B. Markovsky, M. D. Levi, E. Levi, A. Schechter, M. Moshkovich, Y. Cohen, *J. Power Sources* 81-82 (1999) 95.
415. D. Aurbach, *J. Power Sources* 89 (2000) 206.
416. G. Nagasubramanian, *J. Power Sources* 87 (2000) 226.
417. Q. Wei, W. Lu, J. Prakash, *J. Power Sources* 88 (2000) 237.
418. C. H. Chen, J. Liu, K. Amine, *Electrochem. Comm.* 3 (2001) 44.
419. K. Amine, C. H. Chen, J. Liu, M. Hammond, A. Jansen, D. Dees, I. Billom, D. Vissers, G. Henriksen, *J. Power Sources* 97-98 (2001) 684.
420. N. R. Avery, K. J. Black, *J. Power Sources* 68 (1997) 191.
421. G. G. Amatucci, J. M. Tarascon, L. C. Klein, *Solid State Ionics* 83 (1996) 167.
422. H. Mao, J. N. Reimers, Q. Zhong, U. von Sacken, in: *Rechargeable Lithium and Lithium-Ion Batteries*, S. Megahed, B. M. Barnett, L. Xie, Eds., The Electrochemical Society, Pennington NJ, 1995, PV 94-28, 245.
423. Y. Shin, A. Manthiram, *Electrochem. Solid-State-Lett.* 5 (2002) A55.
424. S. Komaba, N. Kumagi, Y. Kataoka, *Electrochim. Acta* 47 (2002) 1229.
425. D. Aurbach, B. Markovsky, I. Weissman, E. Levi, Y. Ein-Eli, *Electrochim. Acta* 45 (1999) 67.
426. D. Aurbach (Ed.), *Nonaqueous Electrochemistry*, Marcel Dekker, Basel, 1999.
427. U. Heider, R. Oesten, M. Jungnitz, *J. Power Sources* 81-82 (1999) 119.
428. Y. Ein-Eli, *Electrochem. Comm.* 4 (2002) 644.
429. A. N. Dey, *J. Electrochem. Soc.* 114 (1967) 823.
430. X. Zhang, J. K. Pugh, P. N. Ross, Jr., *Electrochem. Solid-State Lett.* 4 (2001) A82.
431. C. G. Barlow, *Electrochem. Solid-State Lett.* 2 (1999) 362.
432. F. Joho, B. Rykart, R. Imhof, P. Novák, M. E. Spahr, A. Monnier, *J. Power Sources* 81-82 (1999) 243.
433. M. Winter, J. O. Besenhard, P. Novák, *GDCh-Monographie*, 1996, 3, 438.
434. J. O. Besenhard, I. Kain, H.-F. Klein, H. Möhwald, H. Witty, in: *Intercalated Graphite*, M. S. Dresselhaus, G. Dresselhaus, J. E. Fischer, M. J. Moran, Eds., North Holland, New York, 1983, 221.
435. B. Marcus, P. Touzain, *J. Solid State Chem.* 77 (1988) 223.
436. J. O. Besenhard, H. Möhwald, J. J. Nickl, *Carbon* 18 (1980) 399.
437. P. Schoderböck, H. P. Boehm, *Synth. Met.* 44 (1991) 239.
438. M. Arakawa, K. Yamaki, *J. Electroanal. Chem.* 219 (1987) 273.
439. G. Eichinger, *J. Electroanal. Chem.* 74 (1976) 183.
440. Z. X. Shu, R. S. McMillan, J. J. Murray, *J. Electrochem. Soc.* 140 (1993) L101.
441. Z. X. Shu, R. S. McMillan, J. J. Murray, in: *New Sealed Rechargeable Batteries and Supercapacitors*, B. M. Barnett, E. Dowgiallo, G. Halpert, Y. Matsuda, Z. Takehara, Eds., The Electrochemical Society, Pennington NJ, 1993, PV 93-23, 238.
442. D. Guyomard, J. M. Tarascon, *J. Electrochem. Soc.* 139 (1992) 937.
443. T. Ohzuku, Y. Iwakoshi, K. Sawai, *J. Electrochem. Soc.* 140 (1993) 2490.
444. D. Guyomard, J. M. Tarascon, US Pat. No. 5192629, 1993.
445. J. O. Besenhard, M. Winter, J. Yang, W. Biberacher, *J. Power Sources* 54 (1995) 228.
446. D. Aurbach, Y. Ein-Eli, O. Chusid, Y. Carmeli, M. Babai, H. Yamin, *J. Electrochem. Soc.* 141 (1994) 603.
447. G. E. Blomgren, *J. Power Sources* 81-82 (1999) 112.
448. J. Barthel, H. J. Gores, in: *Handbook of Battery Materials*, J. O. Besenhard, Ed., Wiley-

- VCH, Weinheim, 1999, Part III, Ch. 7.
449. D. Guyomard, J. M. Tarascon, *J. Power Sources* 54 (1995) 92.
450. D. Guyomard, J. M. Tarascon, *Solid State Ionics* 69 (1994) 222.
451. D. Guyomard, J. M. Tarascon, *Solid State Ionics* 69 (1994) 222.
452. D. Aurbach, B. Markovsky, A. Shechter, Y. Ein-Eli, H. Cohen, *J. Electrochem. Soc.* 143 (1996) 3809.
453. D. Aurbach, A. Zaban, A. Schechter, Y. Ein-Eli, E. Zinigrad, B. Markovsky, *J. Electrochem. Soc.* 142 (1995) 2873.
454. M. Inaba, Z. Siroma, A. Funabiki, Z. Ogumi, *Langmuir* 12 (1996) 1535.
455. M. Inaba, Z. Siroma, Y. Kawadate, A. Funabiki, Z. Ogumi, *J. Power Sources* 1 68 (1997) 221.
456. D. Aurbach, Y. Ein-Eli, *J. Electrochem. Soc.* 142 (1995) 1746.
457. S. Jeong, M. Inaba, Y. Iriyama, T. Abe, Z. Ogumi, *Electrochim. Acta* 47 (2002) 1975.
458. K. Morigaki, *J. Power Sources* 103 (2002) 253.
459. S. S. Zhang, T. R. Jow, K. Amine, G. L. Henrikson, *J. Power Sources* 197 (2002) 18.
460. M. Winter, R. Imhof, F. Joho, P. Novák, *J. Power Sources* 81-82 (1999) 818.
461. X. Zhang, R. Kostecki, T. R. Richardson, J. K. Pugh, P. N. Ross, Jr., *J. Electrochem. Soc.* 148 (2001) A1341.
462. G.-C. Chung, H.-J. Kim, S.-I. Yu, S.-H. Jun, J. Choi, M.-H. Kim, *J. Electrochem. Soc.* 147 (2000) 4391.
463. G.-C. Chung, *J. Power Sources* 104 (2002) 7.
464. D. Aurbach, M. D. Levi, E. Levi, A. Schechter, *J. Phys. Chem. B* 101 (1997) 2195.
465. K. Yamaguchi, J. Suzuki, M. Saito, K. Sekine, T. Takamura, *J. Power Sources* 97-98 159.
466. M. Winter, G. H. Wrodnigg, J. O. Besenhard, W. Biberacher, P. Novák, *J. Electrochem. Soc.* 147 (2000) 2427.
467. G.-C. Chung, S.-H. Jun, K.-Y. Lee, M.-H. Kim, *J. Electrochem. Soc.* 146 (1999) 1664.
468. G. H. Wrodnigg, J. O. Besenhard, M. Winter, *J. Electrochem. Soc.* 146 (1999) 470.
469. M. Winter, W. K. Appel, B. Evers, T. Hodal, K.-C. Möller, I. Schneider, M. Wachtler, M. R. Wagner, G. H. Wrodnigg, J. O. Besenhard, *Chem. Monthly* 132 (2001) 473.
470. J. O. Besenhard, P. Castella, M. W. Wagner, *Mater. Sci. Forum* 91-93 (1992) 647.
471. Y. Ein-Eli, B. Markovsky, D. Aurbach, Y. Carmeli, H. Yamin, S. Luski, *Electrochim. Acta* 39 (1994) 2559.
472. O. Chusid, Y. Ein-Ely, D. Aurbach, *J. Power Sources* 43-44 (1993) 47.
473. J. O. Besenhard, M. Winter, J. Yang, *International Workshop on Advanced Batteries (Lithium Batteries)*, Osaka 1995, 129.
474. M. Winter, Diploma Thesis, University of Münster, Germany, 1993.
475. Y. Ein-Eli, S. R. Thomas, and V.R. Koch, *J. Electrochem. Soc.* 144 (1997) 1159.
476. Y. Ein-Eli, S. R. Thomas, and V.R. Koch, *J. Electrochem. Soc.* 144 (1997) L195.
477. Z. X. Shu, R. S. McMillan, J. J. Murray, *J. Electrochem. Soc.* 142 (1995) L161.
478. Z. X. Shu, R. S. McMillan, J. J. Murray, I. J. Davidson, *J. Electrochem. Soc.* 143 (1996) 2230.
479. Z. X. Shu, R. S. McMillan, J. J. Murray, US Pat. No. 5529859, 1996.
480. Z. X. Shu, R. S. McMillan, J. J. Murray, US Pat. No. 5571635, 1996.
481. J. Arai, H. Katayama, H. Akahoshi, *J. Electrochem. Soc.* 149 (2002) A217.
482. M. Winter, P. Novák, *J. Electrochem. Soc.* 145 (1998) L27.
483. J. Barker, F. Gao, US Pat. No. 5780182, 1998.
484. R. McMillan, H. Sleg, Z. X. Shu, W. Wang, *J. Power Sources* 81-82 (1999) 20.
485. M. Inaba, Y. Kawadate, A. Funabiki, S. Jeong, T. Abe, Z. Ogumi, *Electrochim. Acta* 45 (1999) 99.
486. C. Jehoulet, P. Biensan, J. M. Bodet, M. Broussely, C. Moteau, C. Tessier- Lescourret, in: *Batteries for Portable Applications and Electric Vehicles*, C. F. Holmes, A. R. Landgrebe, Eds., The Electrochemical Society, Pennington NJ, 1997, PV97-18, 974.
487. M. Fujimoto, M. Takahashi, K. Nishio (Sanyo) US Pat. No. 5352548, 1994; B. Simon, J.-P. Boeve (SAFT) US Pat. No. 5626981, 1997; J. Barker, F. Gao (Valence) US Pat. No. 5712059, 1998; Y. Naruse, S. Fujita, A. Omaru (Sony) US Pat. No. 5714281, 1998.
488. Y. Wang, S. Nakamura, K. Tasaki, P. B. Balbuen, *J. Am. Chem. Soc.* 124 (2002) 4408.
489. O. Matsuoka, A. Hiwara, T. Omi, M. Toriida, T. Hayashi, C. Tanaka, Y. Saito, T. Ishida, H. Tan, S. S. Ono, S. Yamamoto, *J. Power Sources* 108 (2002) 128.
490. D. Aurbach, K. Gamolsky, B. Markovsky, Y. Gofer, M. Schmidt, U. Heider, *Electrochim. Acta* 47 (2002) 1423.
491. R. Oesten, U. Heider, M. Schmidt, *Solid State Ionics* 148 (2001) 391.
492. C. Wang, H. Nakamura, H. Komatsu, M. Yoshio, H. Yoshitake, *J. Power Sources* 74 (1998) 142.

493. G. H. Wrodnigg, C. Reisinger, J. O. Besenhard, M. Winter, *ITE Batt. Lett.*, 1999, 1(1) 111.
494. H. Ota, T. Sato, H. Suzuki, T. Usami, *J. Power Sources* 97-98 (2001) 107.
495. G. H. Wrodnigg, T. M. Wrodnigg, J. O. Besenhard, M. Winter, *Electrochem. Comm.* 1 (1999) 148.
496. M. W. Wagner, C. Liebenow, J. O. Besenhard, *J. Power Sources* 68 (1997) 328.
497. M. W. Wagner, J. O. Besenhard, C. Liebenow, in: *Batteries for Portable Applications and Electric Vehicles*, C. F. Holmes, A. R. Landgrebe, Eds., The Electrochemical Society, Pennington NJ, 1997, PV97-18, 26.
498. H. Gan, E. S. Takeuchi, Eur. Pat. Appl. No. 513428, 2000.
499. J. F. Wolf, S. M. Savner, M. Maxfield, L. W. Lawrence, US Pat. No. 4528254, 1985.
500. T. Mamamoto, A. Hitaka, Y. Nakada, K. Ube, US Pat. No. 6033809, 2000.
501. H. Gan, E. S. Takeuchi, Eur. Pat. Appl. No. 4510457, 2001.
502. G. H. Wrodnigg, J. O. Besenhard, M. Winter, *J. Power Sources* 97-98 (2001) 592.
503. Y. Ein-Eli, S. F. McDevitt, *J. Solid State Electrochem.* 1 (1997) 227.
504. G. Y. Gu, S. Bouviert, C. Wu, R. Laura, M. Rzeznik, K. M. Abraham, *Electrochim. Acta* 45 (2000) 3127.
505. F. Coowar, A. M. Christie, P. G. Bruce, C. A. Vincent, *J. Power Sources* 75 (1998) 144.
506. B. V. Ratnakumar, M. C. Smart, S. Surampudi, *J. Power Sources* 97-98 (2001) 137.
507. Y. Ein-Eli, S. McDevitt, D. Aurbach, B. Markovsky, A. Schechter, *J. Electrochem. Soc.* 144 (1997) L180.
508. H. Nakamura, H. Komatsu, M. Yoshio, *J. Power Sources* 62 (1996) 219.
509. Y. Ein-Eli, S. R. Thomas, V. Koch, D. Aurbach, B. Markovsky, A. Schechter, *J. Electrochem. Soc.* 143 (1996) L273.
510. Y. Ein-Eli, *Electrochem. Solid-State Lett.* 2 (1999) 212.
511. Y. Ein-Eli, S. F. McDevitt, R. Laura, *J. Electrochem. Soc.* 145 (1998) L1.
512. S. Sakai, M. Yamamoto, US Patent 5891588, 1999.
513. M. C. Smart, B. V. Ratnakumar, V. S. Ryan, S. Surampudi, G. K. S. Prakash, J. Hu, 198th Meeting of the Electrochemical Society, 2000, Abstract No. 138.
514. J.-S. Wan, C.-H. Han, U.-H. Jung, S.-I. Lee, H.-J. Kim, K. Kim, *J. Power Sources* 109 (2002) 47.
515. Y.-K. Choi, K. Chung, W.-S. Kim, Y.-E. Sung, S.-M. Park, *J. Power Sources* 104 (2002) 132.
516. A. Naji, J. Ghanbaja, P. Willmann, D. Billaud, *Electrochim. Acta* 45 (2000) 1893.
517. J. O. Besenhard, K. v. Werner, M. Winter, US Pat. No. 5916708, 1997.
518. T. Yamamoto, H. Miura, US Pat. No. 5795677, 1998.
519. W. K. Appel, J. O. Besenhard, S. Pasenok, M. Winter, G. H. Wrodnigg, Ger Pat No. DE 19 724 709, 1998.
520. W. K. Appel, J. O. Besenhard, L. H. Lie, S. Pasenok, M. Winter, Ger. Pat. No. DE 198 58 924, 1998.
521. K.-C. Möller, T. Hodal, W. K. Appel, M. Winter, J. O. Besenhard, *J. Power Sources* 97-98 (2001) 595.
522. K.-C. Möller, S. C. Skrabl, M. Winter, J. O. Besenhard, in: *Proc. 3rd Hawaii Battery Conference*, Hawaii, USA, 2001, 228.
523. L. H. Lie, T. Hodal, K.-C. Möller, G. H. Wrodnigg, W. K. Appel, J. O. Besenhard, M. Winter, *ITE Batt. Lett.*, 1999, 1(1), 105.
524. T. Nakajima, *J. Fluorine Chemistry* 105 (2000) 229.
525. K.-C. Möller, H. J. Santner, J. O. Besenhard, M. Winter, in: *Proc. 4th Hawaii Battery Conference*, Hawaii, USA, 2002, 238.
526. K.-C. Möller, H. J. Santner, W. Kern, S. Yamaguchi, J. O. Besenhard, M. Winter, *J. Power Sources*, in press.
527. H. J. Santner, K.-C. Möller, J. Ivančo, M. G. Ramsey, F. P. Netzer, S. Yamaguchi, J. O. Besenhard, M. Winter, *J. Power Sources*, in press.
528. R. Shimizu(NEC), Jap. Pat. JP2000149989, 2000.
529. M. Yoshio, H. Yoshitake, K. Abe, T. Umeno, K. Fukuda, 11th IMLB, Monterey CA, 2002, Abstract No. 9.
530. S. S. Zhang, K. Xu, J. L. Allen, T. R. Jow, *J. Power Sources* 110 (2002) 216.
531. H. Lin, D. Chua, M. Salomon, H.-C. Shiao, M. Hendricksen, E. Plichta, S. Slane, *Electrochem. Solid-State Lett.* 4 (2001) A71.
532. E. J. Plichta, M. Hendrikson, R. Thompson, G. Au, W. K. Behl, M. C. Smart, B. V. Ratnakumar, S. Surampudi, *J. Power Sources* 94 (2001) 160.
533. C.-K. Huang, J. S. Sakamoto, J. Wolfenstine, S. Surampudi, *J. Electrochem. Soc.* 147 (2000) 2893.
534. X. Wang, E. Yasukawa, S. Kasuya, *J. Electrochem. Soc.* 148 (2001) A1058.

535. K. Xu, M. S. Ding, S. Zhang, J. L. Allen, T. R. Jow, *J. Electrochem. Soc.* 149 (2002) A622.
536. S. S. Zhang, K. Xu, T. R. Jow, *Electrochem. Solid-State Lett.* 5 (2002) A206.
537. K. Xu, S. Zhang, J. L. Allen, T. R. Jow, *J. Electrochem. Soc.* 149 (2002) A1079.
538. B. Simon, S. Flandrois, K. Guerin, A. Fevrier-Bouvier, I. Teulat, P. Biensan, *J. Power Sources* 81-82 (1999) 312.
539. S. Flandrois, A. Fevrier, P. Biensan, B. Simon, US Pat. No. 5554462, 1996.
540. F. Cao, I. V. Barsukov, H. Y. Bang, P. Zaleski, J. Prakash, *J. Electrochem. Soc.* 147 (2000) 3579.
541. K. Guerin, A. Fevrier-Bouvier, S. Flandrois, M. Couzi, B. Simon, P. Biensan, *J. Electrochem. Soc.* 146 (1999) 3660.
542. I. Kuribayashi, M. Yokoyama, M. Yamashita, *J. Power Sources* 54 (1995) 1.
543. X. Shu, L. D. Schmidt, W. H. Smyrl, in: *Rechargeable Lithium and Lithium-Ion Batteries*, S. Megahed, B. Barnett, L. Xie, Eds., The Electrochemical Society, Pennington NJ, 1995, PV 94-28, 196.
544. H. Momose, A. Funahashi, J. Aragane, K. Matsui, S. Yoshitake, I. Mitsuishi, H. Awata, T. Iwahori, in: *Batteries for Portable Applications and Electric Vehicles*, C. F. Holmes, A. R. Landgrebe, Eds., The Electrochemical Society, Pennington NJ, 1997, PV97-18, 376.
545. K. Yamada, H. Tanaka, T. Mitate, M. Yoshikawa (Sharp), US Pat. No. 5595938, 1997.
546. M. Yamasaki, T. Nohma, K. Nishio, Y. Kusumoto, Y. Shoji (Sanyo), US Pat. No. 5888671, 1999.
547. C. Natarajan, H. Fujimoto, K. Tokumitsu, A. Mabuchi, T. Kasuh, *Carbon* 39 (2001) 1409.
548. H. Wang, M. Yoshio, T. Abe, Z. Ogumi, *J. Electrochem. Soc.* 149 (2002) A499.
549. A. Funahashi, Y. Kida, K. Yanagida, T. Nohma, I. Yonezu, *J. Power Sources* 104 (2002) 248.
550. K. Yanagida, A. Yanai, Y. Kida, A. Funahashi, T. Nohma, I. Yonezu, *J. Electrochem. Soc.* 149 (2002) A804.
551. J.-S. Kim, W.-Y. Yoon, K. S. Doo, G.-S. Park, C. W. Lee, Y. Muakami, D. Shindo, *J. Power Sources* 104 (2002) 175.
552. K. Suzuki, T. Hamada, T. Sugiura, *J. Electrochem. Soc.* 146 (1999) 890.
553. K. Suzuki, T. Ijima, M. Wakihara, *Electrochim. Acta* 44 (1999) 2185.
554. M. E. Spahr, H. Wilhelm, F. Joho, J.-C. Panitz, J. Wambach, P. Novák, N. Dupont-Pavlovsky, *J. Electrochem. Soc.* 149 (2002) A960.
555. M. E. Spahr, H. Wilhelm, F. Joho, P. Novák, *ITE Letters on Batteries*, New Technologies & Medicine, 2002, 2839, B53-370-73.
556. Q. Pan, K. Guo, L. Wang, S. Fang, *J. Electrochem. Soc.* 149 (2002) A1218.
557. B. Veeraraghavan, J. Paul, B. Haran, B. Popov, *J. Power Sources* 109 (2002) 377.
558. T. Takamura, M. Kikuchi, H. Awano, T. Ura, Y. Ikezawa, *Mat. Res. Symp. Proc.* 393 (1995) 345.
559. P. Yu, J. A. Ritter, R. E. White, B. N. Popov, *J. Electrochem. Soc.* 147 (2000) 2081.
560. J. K. Lee, D. H. Ryu, J. B. Ju, Y. G. Shul, B. W. Cho, D. Park, *J. Power Sources* 107 (2002) 90.
561. B. Veeraraghavan, A. Durairajan, B. Haran, B. Popov, R. Guidotti, *J. Electrochem. Soc.* 149 (2002) A675.
562. J. Suzuki, M. Yoshida, C. Nakahar, K. Sekine, M. Kikuchi, T. Takamura, *Electrochem. Solid State Lett.* 4 (2001) A1.
563. J. Aragane, K. Matsui, H. Andoh, S. Suzuki, H. Fukada, H. Ikeya, K. Kitaba, R. Ishikawa, *J. Power Sources* 68 (1997) 13.
564. K. Nishimura, H. Honbo, S. Takeuchi, T. Horiba, M. Oda, M. Koseki, Y. Muranaka, Y. Kozono, H. Miyadera, *J. Power Sources* 68 (1997) 436.
565. H. Momose, H. Honbo, S. Takeuchi, K. Nishimura, T. Horiba, Y. Muranaka, Y. Kozono, H. Miyadera, *J. Power Sources* 68 (1997) 208.
566. J. Y. Lee, R. Zhang, Z. Liu, *Electrochem. Solid State Lett.* 3 (2000) 167.
567. J. Y. Lee, R. Zhang, Z. Liu, *J. Power Sources* 90 (2000) 70.
568. G. X. Wang, J.-H. Ahn, M. J. Lindsay, L. Sun, D. H. Bradhurst, S. X. Dhou, H. K. Liu, *J. Power Sources* 97-98 (2001) 211.
569. H. Tamai, S. Matsuoka, M. Ishihara, H. Yasuda, *Carbon* 39 (2001) 1515.
570. M. Egashira, H. Takatsuji, S. Okada, J. Yamaki, *J. Power Sources* 107 (2002) 56.
571. W. X. Chen, J. Y. Lee, Z. Liu, *Electrochem. Comm.* 4 (2002) 260.
572. A. Ulus, Y. Rosenberg, L. Burstein, E. Peled, *J. Electrochem. Soc.* 149 (2002) A635.
573. M. Kikuchi, Y. Ikezawa, T. Takamura, *J. Electroanal. Chem.* 396 (1995) 451.
574. T. Takamura, M. Kikuchi, J. Ebana, M. Nagashima, Y. Ikezawa, in: *New Sealed*

- Rechargeable Batteries and Supercapacitors*, B. M. Barnett, E. D'Agostino, G. Halpert, Y. Matsuda, Z. Takehara, Eds., The Electrochemical Society, Pennington NJ, 1993, PV 93-23, 229.
575. T. Takamura, H. Awano, T. Ura, K. Sumiya, *J. Power Sources* 68 (1997) 114.
576. H. Buqa, Ch. Grogger, M. V. Santis Alvarez, J. O. Besenhard, M. Winter, *J. Power Sources* 97-98 (2001) 126.
577. H. Buqa, P. Golob, M. Winter, J. O. Besenhard, *J. Power Sources* 97-98 (2001) 122.
578. H. Buqa, R.I.R. Blyth, P. Golob, B. Evers, I. Schneider, M. V. Santis Alvarez, F. Hofer, F. P. Netzer, M. G. Ramsey, M. Winter, J. O. Besenhard, *Ionics* 6 (2001) 172.
579. W. Lu, D. D. L. Chung, *Carbon* 39 (2001) 493.
580. T. D. Tran, L. C. Murguia, X. Soong, K. Kinoshita, in: *Batteries for Portable Applications and Electric Vehicles*, C. F. Holmes, A. R. Landgrebe, Eds., The Electrochemical Society, Pennington NJ, 1997, PV97-18, 974.
581. G. G. Tibbetts, G.-A. Nazri, B. J. Howie (GM), US Patent 5,587,257, 1996.
582. Y. Bito, S. Ito, H. Murai, M. Hasegawa, Y. Toyoguchi (Matsushita), US Pat. No. 5580538, 1996.
583. Y. Ein-Eli, V. R. Koch, *J. Electrochem. Soc.* 144 (1997) 2968.
584. Y. P. Wu, C. Jiang, C. Wan, R. Holze, *Electrochem. Comm.* 4 (2002) 483.
585. D. Bar-Tow, E. Peled, L. Burstein, *J. Electrochem. Soc.* 146 (1999) 824.
586. T. Tran, B. Yebka, YX. Song, G. Nazri, K. Kinoshita, D. Curtis, *J. Power Sources* 85 (2000) 269.
587. K. Zaghib, G. Nadeua, K. Kinoshita, *J. Power Sources* 97-98 (2002) 97.
588. P. Novák, R. Imhof, O. Haas, *Electrochim. Acta* 45 (1999) 351.
589. D. Aurbach, Z. Lu, A. Schechter, Y. Gofer, H. Giszbar, R. Turgeman, Y. Cohen, M. Moshkovich, E. Levi, *Nature* 407 (2000) 724.
590. J. O. Besenhard, M. Winter, *ChemPhysChem* 2 (2002) 155.

Chapter 6

GRAPHITE-ELECTROLYTE INTERFACE IN LITHIUM-ION BATTERIES

M.Nazri¹, B.Yebka² and G.-A. Nazri²

1. University of Windsor, Department of Chemistry, Windsor, Ontario N9B 3P4, Canada

2. GM Research and Development Center, Warren, Michigan 48090, U.S.A.

6.1. INTRODUCTION

The recent commercialization of advanced lithium batteries is mainly due to the breakthrough in the stabilization of the anode-electrolyte interface. Although metallic lithium has an energy density (3860 mAh/g) higher than that of other alternative anodes, its poor performance and safety issues related to the low melting point of lithium (180 °C), dendritic growth during lithium deposition (charge), and high reactivity toward the electrolytes have hindered the commercialization of rechargeable lithium-anode batteries.

There have been several approaches to solve the problem of lithium anode. The development of lithium alloys, particularly the binary and ternary alloys, has received considerable attention (see Chapter 9 of this book). However, the performance of these alloys is unsatisfactory mainly due to the large volume change (100-200%) during lithiation and delithiation processes. This expansion and contraction processes may cause the alloy particles to crack and lose contact with the electrode substrate. In addition, the lithium alloys with high concentration of lithium are very reactive toward the electrolytes and cause decomposition. Therefore a problem similar to that of the metallic lithium also exists for Li-alloy anodes. Recently, some success has been made using intermetallic alloys such as Cu_6Sn_5 that insert lithium topotactically over a wide composition range $\text{Li}_x\text{Cu}_6\text{Sn}_5$ ($0 < x < 13$).¹ Despite the good volumetric energy density of these alloys, their gravimetric energy density is poor and there is a significant capacity loss during multiple cycling.

The early transition metal oxide anodes have also been proposed for application in rechargeable lithium batteries -in particular, the use of lithium intercalated titanium oxide.²⁻⁷ The lithium titanium oxide anode is described

as a zero-strain insertion anode owing to negligible volume change during the lithium insertion/extraction process. In addition, titanium oxide does not decompose the organic electrolytes, hence it can be considered as a safe anode for rechargeable lithium batteries. The drawback of the lithiated titanium oxide is its high redox potential (1.5 V vs. Li). Ohzuku *et al.*⁸ have shown very good reversibility and electrochemical performance for $\text{Li}_4\text{Ti}_5\text{O}_{12}$.

Lithium transition metal nitrides and phosphides also have been considered as anodes for rechargeable lithium batteries.⁹⁻¹⁵ The voltage profiles of nitrides and phosphides during charge-discharge are between 0 to 1.5 V vs. Li. There is also a large voltage hysteresis between the charge and discharge of nitrides and phosphides. The principal mechanism is believed to be the formation of lithium nitride and phosphide during reduction of transition metal ions to the metallic state. The nano-scale transition metal clusters formed in this process are catalytically active, and during lithium extraction reaction they tend to form the original compound. The slow kinetics and large hysteresis between charge and discharge is a major drawback for the nitride and phosphide anodes.

In early 1990, a breakthrough was announced by researchers from Sony Energytech: an anode based on lithium intercalated carbon or graphite for rechargeable lithium battery was used.¹⁶ The volume change during full lithium intercalation in graphite (LiC_6) is less than 9% according to the *in-situ* X-ray diffraction study. The specific capacity of the lithiated graphite is only LiC_6 (370 mAh/g), much lower than that of metallic lithium. In spite of the lower energy density, the current rechargeable lithium battery (Li-ion battery) technology uses a lithiated carbonaceous anode.¹⁷⁻²¹ The success of the LiC_6 anode is mainly due to the fast stabilization of the anode/electrolyte interface and the high electrochemical reversibility of lithium intercalation/deintercalation process. The LiC_6 anodes have been charged and discharged over 1000 times without an appreciable capacity loss. The Li-ion battery is currently replacing all other battery types in the market, particularly in the field of electronics, computers, and communications. In recent years, the application of the Li-ion batteries for more power demanding applications such as power tools, stationary, and transportation has started. The production of Li-ion batteries in 2002 has exceeded 500 million cells, with Japan as the main producer (over 70%).

Lithium intercalation in graphite is not new and has been fully studied by physicists in search of high T_C superconductors during the last 50 years.^{22,23} The hexagonal structure of graphite in ABAB arrangement is shown in Figure 6.1. The layer B is shifted with respect to the A layer, but AA and BB layers are on exact registry with each other. When lithium intercalates between the layers, the layer B glides to make an exact AAAA structure.

Graphite has an ideal layered structure with weak van der Waals bonding between the graphene layers. Thus, Li can be inserted between the layers of graphite. According to recent ^6Li - and ^7Li - NMR studies, the nature of lithium in graphite is partly ionic. There is partial charge transfer from lithium to the π -orbitals of the graphene planes. The lithium in the graphite has also a high mobility, which is ideal for applications in high-power batteries. In addition, the graphite has very high electronic conductivity, hence electrode resistance is very low. Natural graphite is abundant, and synthetic graphite also can be made from a variety of precursors. Heat treatment of various organic polymers, particularly those with conjugated benzene rings, goes through a carbonization process around 1200-1500 °C and graphitization around 2300-3000 °C. During graphitization, the rate of growth in a and c directions is strongly temperature dependent. Therefore, graphite flakes with extended a or spherical with extended c directions can be made for different applications. The ideal graphite structure consists of

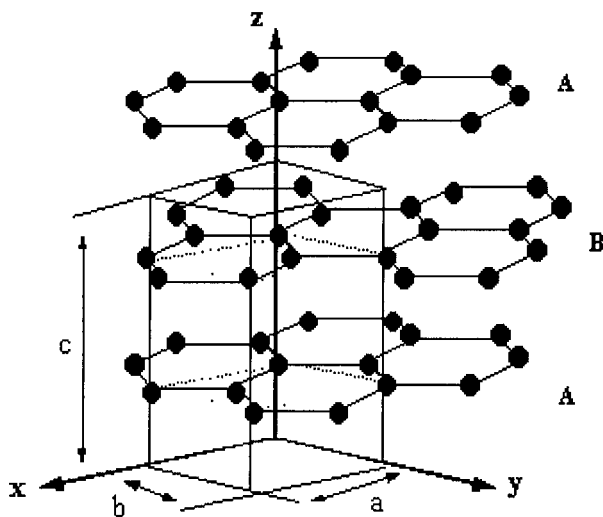


Figure 6.1. Schematic of graphite and lithium intercalated graphite.

layers of carbon atoms arranged in hexagonal rings that are stacked in an ABAB sequence (Figure 6.1). The graphite comprises planar hexagonal networks of carbon atoms (honeycombs) with two different crystalline forms, hexagonal ($2H$) and rhombohedral ($3R$). The $2H$ graphite structure is the most common and the carbon layers are arranged in the ABAB sequence,

where the B layers are shifted to a registered position with respect to the A layers. In the $3R$ (rhombohedral) structure, the stacking sequence is ABCABC, where the C layers are also shifted by the same distance with respect to the B layers, as the B layers are shifted with respect to the A layers.²⁴

The separation of the layers in well-graphitized sample is 3.35 \AA , and layers are held together with weak van der Waals bonds. The softness and the lubricity of graphite can be attributed to the easy glide of these layers over one another. Within each graphene layer only three carbon atoms surround each carbon atom. After forming one σ bond with each neighbor, each carbon atom would still have one electron and these are paired up into a system of π bonds.²⁵

6.2. EXPERIMENTAL SET UP TO EVALUATE SURFACE REACTIONS OF GRAPHITE ANODES

6.2.1. Graphite Types

Several natural and synthetic graphite samples commercially available (BG-34, BG-35, CPC, CN-39, CN-39A, SFG-15) with different morphology,

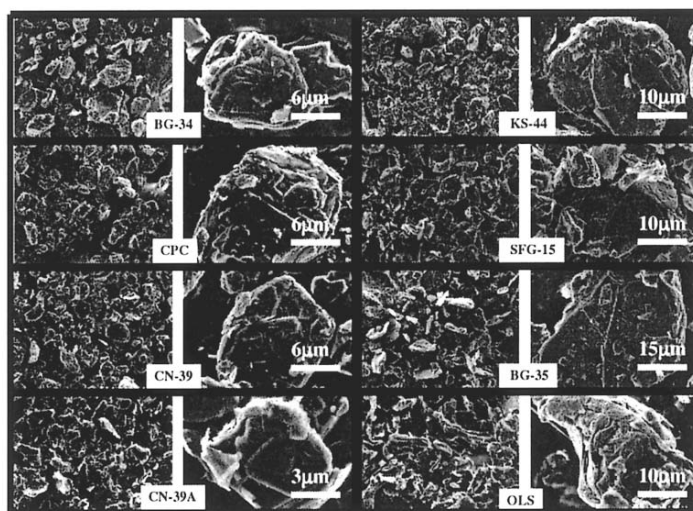


Figure 6.2. SEM morphology of natural graphites BG34, BG35, KS44, and synthetic graphite samples CPC, CN-39, CN39A, and SFG-15.

particle size, and surface area have been examined. Figure 6.2 shows the morphology of these graphite samples.

Table 6.1. Surface area of various commercial graphite samples.

Graphite	BG-35	BG-34	KS-44	CN-39	CN-39	CPC
Surface area (m^2/g)	7.0	7.8	10	10.5	12.5	7.0

The surface area of the graphites is listed in Table 6.1. These samples have low surface area and, so, may be suitable for battery applications. Because of the high reactivity of lithiated graphite, lower surface area samples are preferred.

The X-ray diffractions of the graphite samples listed above are shown in Figure 6.3. The high and narrow 002 peak is an indication of the good crystallinity of the samples.

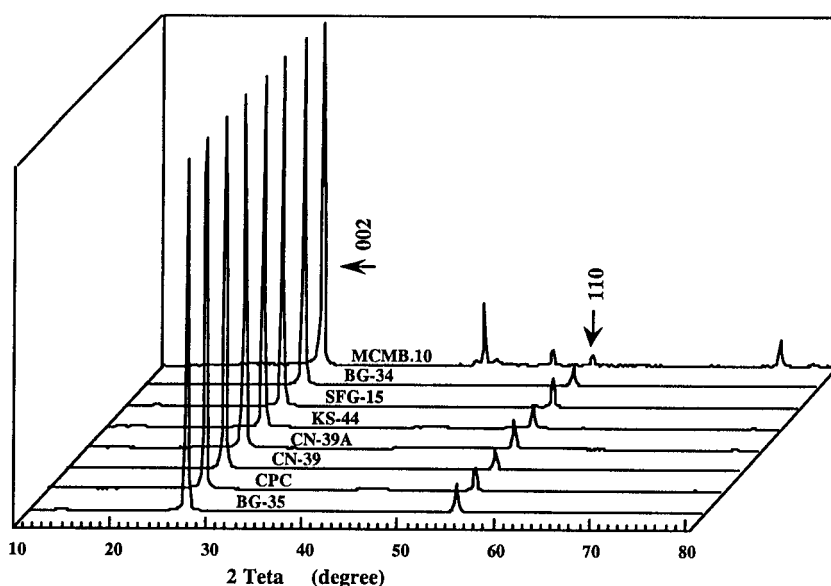


Figure 6.3. X-ray diffractions of various graphite samples.

6.2.2. A General Procedure to Fabricate Carbon Anodes and their Evaluation

The graphite samples need to be heated in vacuum between 700-900 °C to remove moisture and attached functional groups, which usually exist at the edge of graphene sheets. It is very important to remove the water molecules trapped in graphite before using it in a lithium battery. Previous temperature program desorption (TPD) study has shown that almost all surface functional groups can be removed at 700-900 °C. The heat treated graphite is then mixed with 8-10 wt% conductive diluent carbon, and to this mixture 4-5 wt% EPDM binder (in xylene) is added to make a slurry. The mixture of graphite sample, diluent carbon, and binder is ball milled using a commercial micronizer. The slurry is spread on the surface of a copper foil and dried to remove xylene. To improve the adhesion of the sample to copper, the sample is hot pressed inside of a dry box at 100°C. The coating process to make an electrode for lithium cells is shown in Figure 6.4.

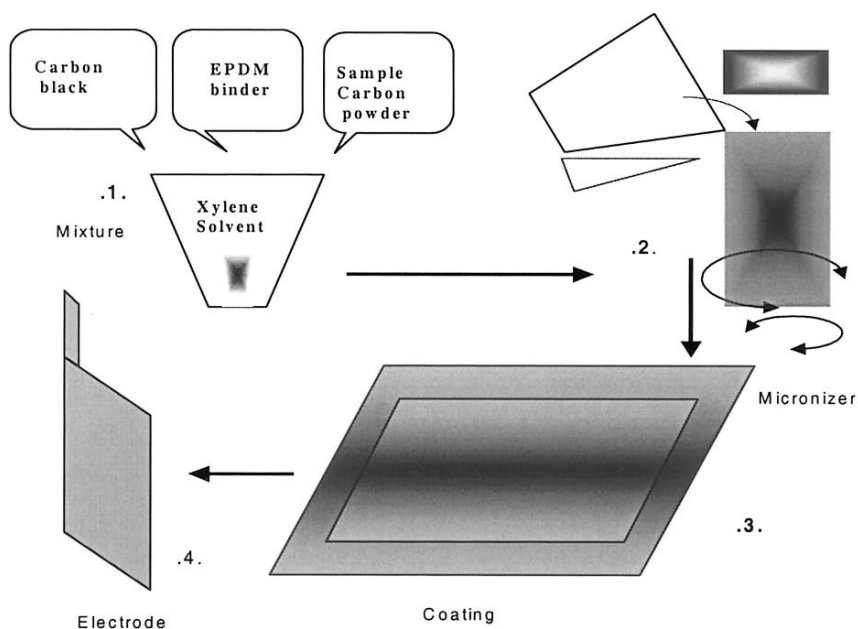


Figure 6.4. Coating process to make electrodes for lithium cells. Anode is metallic lithium, the cathode is the graphite electrode, and reference electrode is lithium wire inserted in the cell between two layers of porous separator.

From the coated foil, electrodes are cut to make the lithium cells. Two types of cells can be constructed. A $10 \times 10 \text{ cm}^2$ electrode can be used to study the surface reactions and electrolyte decomposition using a GC-MS system. Figure 6.5 shows the structure of the cell used for measuring gaseous species formed during electrolyte decomposition. The graphite electrode is separated from the metallic lithium electrode by a porous polyethylene polypropylene separator soaked with electrolyte. The cell is housed in a polyethylene coated aluminum pouch.

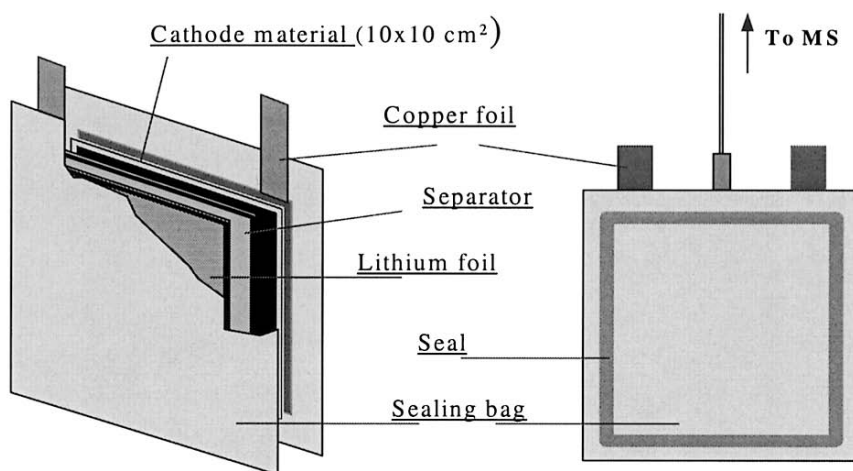


Figure 6.5. Schematic of Li/graphite cell for *in-situ* GC-MS analysis of electrolyte decomposition during lithium intercalation in graphite electrodes.

A 5 cm^2 disc electrode can be used for evaluation of capacity and cycle life tests. Figure 6.6 shows the assembly of this cell. The electrolyte decomposition occurs on the surface of graphite during initial lithium intercalation. In order to investigate the nature of the evolving gas, a special cell assembly is constructed to allow the generated gas to escape from the cell and be sampled by *in-situ* GC-MS analysis. Before sealing the cell shown in Figure 6.5, a flexible 2 mm diameter tube is inserted in the cell. The tube is connected to an on-line GC-MS system. Figure 6.7 shows the combined GC-MS equipment used for *in-situ* analysis of the gaseous products.

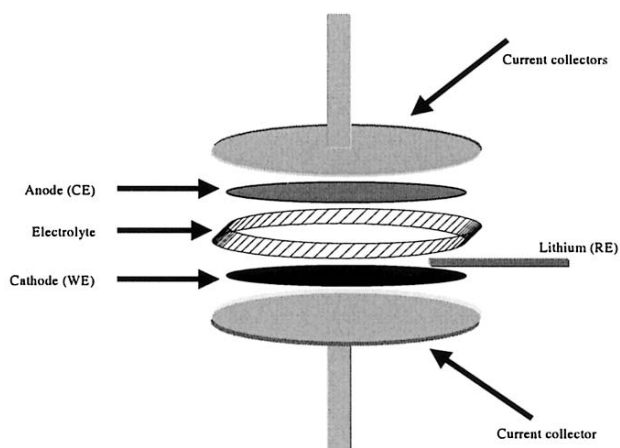


Figure 6.6. Schematic of lithium cell for evaluation of graphite anodes. WE = working electrode, CE = counter electrode and RE = reference electrode.

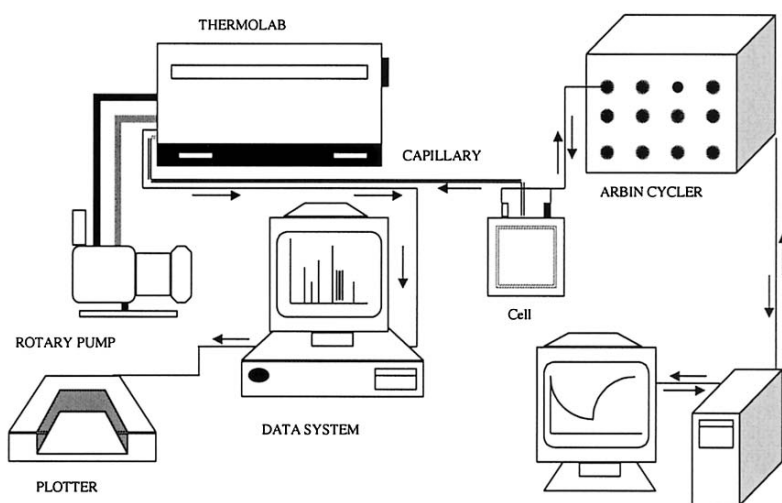


Figure 6.7. Schematic of on-line GC-MS for analysis of gases generated during lithium intercalation in graphite anodes due to electrolyte decomposition.

The Li/graphite cells, after charging and discharging cycles, are disassembled and the electrode is rinsed to remove excess salt. The IR spectra of the surface film is then obtained using a diffuse reflectance accessory that allows to install the sample inside the dry box and later transferred to the IR spectrometer for analysis.

In order to understand the thermal properties of the surface film, a sample is collected from the surface of the graphite electrode (inside the dry box) and placed in a hermetically sealed DSC pan.

6.3. GRAPHITE CYCLING AND FILM FORMATION

The lithium intercalation/deintercalation process between the graphene planes of graphitic samples is facile. The high lithium storage in graphite with a high lithium mobility, has provided a unique anode for rechargeable lithium batteries. The voltage of the lithiated graphite is very close to the voltage of metallic lithium (100-300 mV vs. Li). In addition, the voltage profile of the graphite anode during the lithium intercalation/deintercalation process is fairly flat with a very small hysteresis.

The graphite can accommodate one lithium per six carbons to form the so-called "stage one" (LiC_6) compound. High-pressure intercalation synthesis has yielded a lithium rich phase, LiC_3 . However, the LiC_3 phase is not stable at ambient pressure. It is interesting to note that the amount of lithium in 1 cm^3 of LiC_3 is higher than that of the pure metallic lithium.

The lithium intercalated graphite is highly reactive and reacts with the electrolyte solution. The by-product of the electrolyte decomposition forms a solid film on the surface of the electrode. The electrolyte decomposition during lithium intercalation occurs at about 0.8 V vs. Li. In parallel with the electrolyte decomposition, lithium intercalation in graphite also proceeds. The film formed on the graphite surface, called solid electrolyte interface (SEI layer), is electronically insulating and ionically conducting. The SEI layer protects the lithiated graphite from further reaction with electrolyte. Therefore, the electrolyte decomposition stops in subsequent charge-discharge cycles. The nature of the film formed on the surface of the carbonaceous anodes depends on the composition of electrolyte. Ethylene carbonate based electrolytes tend to form a good compact SEI layer, and in most commercial lithium batteries the electrolyte contain EC in addition to other carbonate solvents. The use of electrolyte with only propylene carbonate solvent has not been successful, due to the co-intercalation of solvent and exfoliation of the graphitic anode. In practice, usually EC in combination with other linear carbonate solvents such as dimethyl carbonate, diethyl carbonate, or methyl ethyl carbonates are used. Figure 6.8 shows the voltage profile of a graphitic anode during the lithium intercalation process.

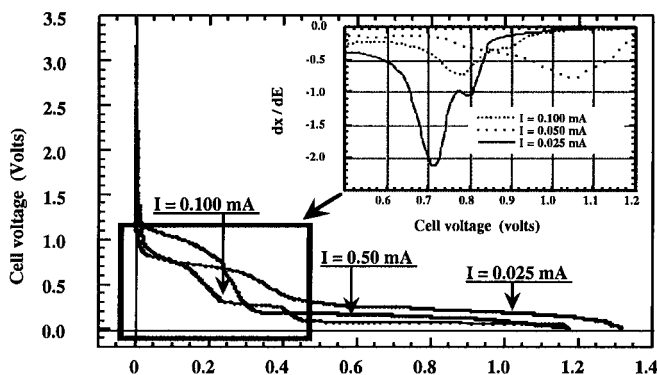


Figure 6.8. Voltage profile of graphite anode as a function of lithium concentration at 0.025 mA, 0.5 mA, and 0.1 mA constant current charging.

The voltage plateau at about 0.8 volt is due to the electrolyte decomposition. It is important to note that when charging the electrode at a higher current density, a more protective film is formed, and less electrolyte decomposition occurs. The voltage plateaus between the 0.3–0.01 V are an indication of the staging phenomena usually observed for the formation of LiC_6 , LiC_{12} , and other diluted phases of LiC_n ($n = 24, 36$, etc). The insert in Figure 6.8 shows the derivative of the voltage profile for the electrolyte decomposition part of the graph. The first charge-discharge of various graphitic electrodes is shown in Figure 6.9. After lithiation in the first cycle, the electrode/electrolyte interface is stable and does not react with the electrolyte. The voltage of the graphite drops to very low value (300 mV vs. Li) by intercalation of a small amount of lithium ($\text{Li}_{0.05}\text{C}_6$).

All samples have shown some degree of electrolyte decomposition during the first lithium intercalation. The decomposition plateau for BG-35 is lower than for the other samples. In samples with a high degree of crystallinity, the staging phenomenon is observed with better resolution, as seen for the case of highly crystalline KS-44.

The amount of electrolyte decomposition also depends on the composition of electrolyte. Figure 6.10 shows the voltage profile of an electrode made from CPC during lithium intercalation in different electrolyte compositions. The electrolyte containing EC-DEC- LiPF_6 shows less electrolyte decomposition. This suggests that the electrolyte containing cyclic ethylene carbonate and linear carbonate may provide a safer operation for the lithium battery. The interface of graphite electrode is stabilized after chemical prelithiation or during the first charge-discharge cycle.

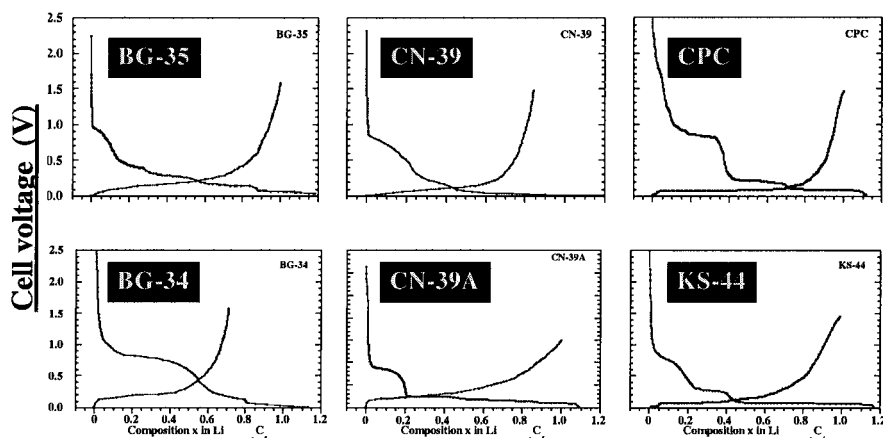


Figure 6.9. The voltage profile of graphitic electrodes (BG-35, CN-339, CPC, BG-34, CN-39A, and KS44).

Multiple charge-discharge cycles of a prelithiated graphite anode are shown in Figure 6.11. The charge-discharge cycles are very reversible and there is no sign of an electrolyte decomposition (plateau at 0.8V). At low charging

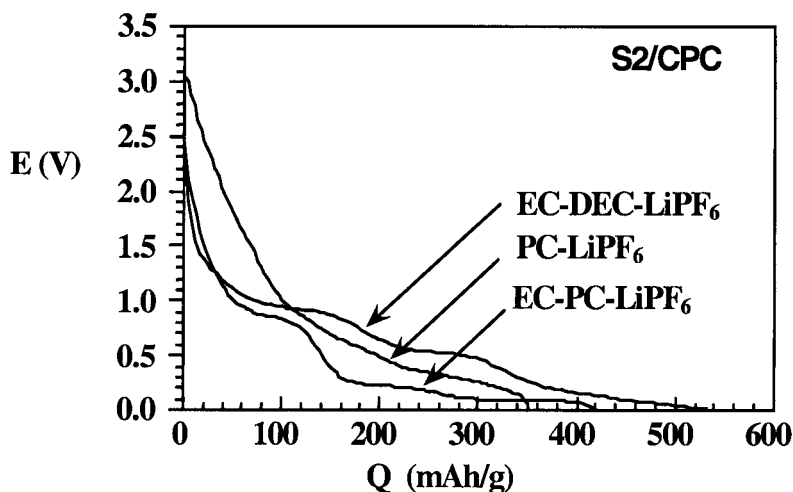


Figure 6.10. Voltage profile of CPC graphite anode in different electrolytes.

rate, capacities close to theoretical one (372 mAh/g) are achievable. The rate at which the electrode can be charged depends also on the amount of active materials loaded on the substrate. For the design of a high rate (power)

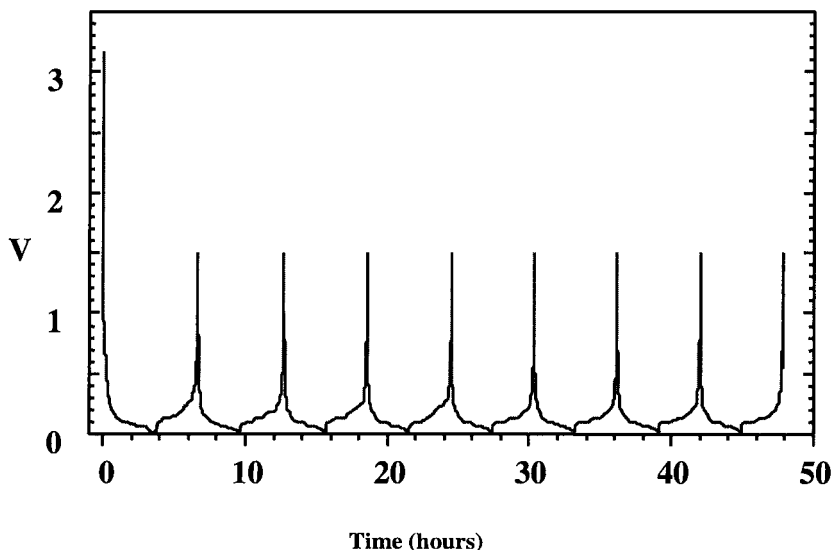


Figure 6.11. Multiple charge-discharge cycles of a graphite electrode after stabilization of the electrode/electrolyte interface and formation of the SEI layer.

battery, the coating is thinner than for the electrode designed for high-energy applications. The usual loading for high power battery is about 10-20 mg/cm² and for the high-energy cells the loading may exceed 100 mg/cm².

Disordered carbons have also been used as anodes. However, their capacity is almost half that of the graphitic anodes, and their voltage profile during lithium intercalation does not show the staging processes often observed for the graphitic anodes. Some special carbon anodes with extended single layer graphene sheets, store lithium to a higher level than the theoretical capacity. In this case, the lithium is being adsorbed on both sides of the graphene sheets and in micropores. However, the cycle life of this type of carbon is poor and there is significant capacity loss during multiple charge-discharge cycles. In addition, there is a considerable amount of voltage hysteresis between charge and discharge. The sloping charge-discharge profile also suggests that there are various sites for lithium with different affinities.

6.3.1 Gas Generation on Graphites

The structure and degree of graphitization of the carbon electrode plays a critical role in the performance and safety of Li-ion batteries. The major effort is directed to understanding the relationship between the physicochemical properties of carbonaceous materials and their

Table 6.2. Gas Chromatography and Mass Spectrometry analysis of the various gases generated on the surface of different graphite anodes during the first lithium intercalation process.

Graphite	Electrolytes	C ₂ H ₄	C ₃ H ₆	CO	H ₂
BG-35	EC-DEC	3.33	0	2.25	1.25
	EC-PC	2.36	0.98	3.33	0.98
	EC-DMC	0.56	0	3.96	1.02
	PC-DMC	0	0.66	4.58	1.21
CPC	EC-DEC	1.23	0	1.85	1.23
	EC-PC	0.39	1.11	2.98	0.21
	EC-DMC	0.69	0	3.44	0.98
	PC-DMC	0	2.03	3.99	1.20
CN-39	EC-DEC	0.11	0	2.55	0.84
	EC-PC	0.22	0.97	3.68	0.96
	EC-DMC	0.34	0	4.11	0.99
	PC-DMC	0	2.11	5.22	1.06
KS-44	EC-DEC	0.87	0	2.31	0.78
	EC-PC	0.54	1.02	2.97	0.29
	EC-DMC	0.35	0	3.33	1.00
	PC-DMC	0	1.33	3.69	1.31
SFG-15	EC-DEC	0.69	0	2.22	0.96
	EC-PC	0.68	0.97	3.09	0.56
	EC-DMC	0.35	0	2.99	1.08
	PC-DMC	0	2.02	4.21	1.04
BG-34	EC-DEC	0.98	0	3.01	0.87
	EC-PC	0.57	1.87	3.77	0.59
	EC-DMC	0.48	0	4.56	1.17
	PC-DMC	0	2.96	4.89	1.19

electrochemical performance. The crystallinity and surface area of the carbonaceous materials, and the nature of the electrolyte used are important factors for the electrochemical stability of Li-ion cells and for the nature and volume of gases generated during the lithium insertion/extraction process (see Table 6.2). Graphite anodes with high degree of crystallinity generate less gas during the first lithium intercalation cycle.

Careful analysis of various carbonaceous anodes indicates that a gel-type film is also forming on the electrode surface as a result of electrolyte decomposition. The nature of this film has a significant impact on the rate capability and the overall cell impedance.

6.3.2. Infrared Spectroscopy of SEI Layer on Graphite Anodes

The film formed on the surface of graphite anode during electrolyte decomposition can be probed using IR spectroscopy. After initial charge-discharge, the cell is opened in the dry box, and a disc is cut from the electrode. The sample is then placed in a diffuse scattering IR accessory and sealed inside the dry box and transferred to the IR spectrometer. The IR spectra of non-cycled graphite electrodes were used as a reference. The spectra of the film formed on the surface of BG-34 graphite anode after one full charge-discharge cycle in DMC-LiPF₆ is shown in Figure 6.12. The complex IR spectrum, with several absorption peaks, indicates formation of an organic moiety different from the electrolyte used. The peaks around 870-890 and 1456 cm⁻¹ are assigned to the formation of Li₂CO₃. There is also an indication of the formation of lithium-organic compounds such as CH₃OCOLi with an absorption peak around 1600-1630 cm⁻¹ assigned to the C=O stretch.

As we observed in the analysis of gaseous species generated when DMC is present in the electrolyte, the formation of CH₂=CH₂ also suggests the following decomposition reactions:

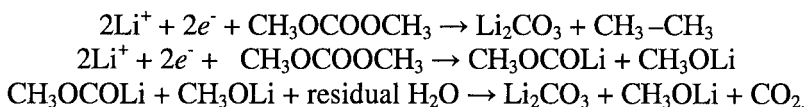


Table 6.3 reports the vibrational frequencies in DMC + 1M LiPF₆. This and the following tables are self-explanatory.

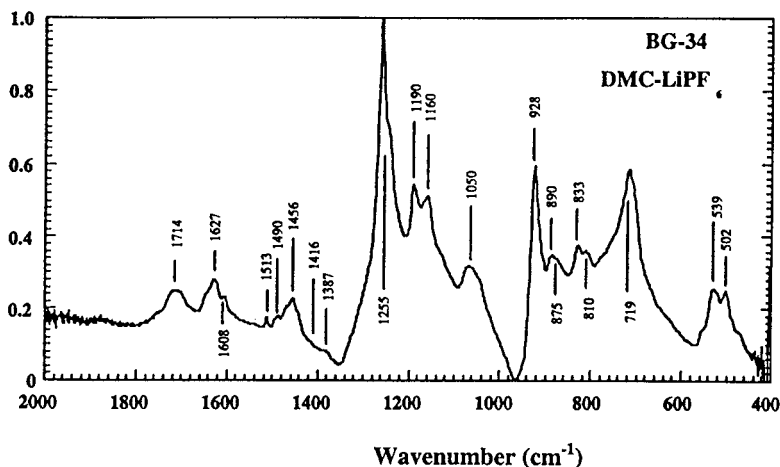


Figure 6.12. IR spectrum of the film formed on the surface of graphite anode during lithium intercalation in (DMC + 1M LiPF₆) electrolyte.

Table 6.3. Vibrational frequencies of the surface layer on BG-34 graphite in DMC-LiPF₆.

ν observed (cm ⁻¹)	ν assigned	Assignment	
		Bands	Compounds
1627br		CO ₂ stretch	
1456br	1420-1470	-	Carbonate ion
	1441	-	Li ₂ CO ₃
1255sp	1280	-	Dimethyl Carbonate
1190m		CO stretch	
1160m	1150-1170	CH stretch	LiOCH ₃
1050br	1050-1070	CH stretch	LiOCH ₃
	1020-1090	CO stretch	Carbonate ion
928sp	969-914	-	Dimethyl Carbonate
890m		-	
875sh	820-890	-	Carbonate ion
	866	-	Li ₂ CO ₃
833m	820-890	-	Carbonate ion
	846	CO ₃ bend	Li ₂ CO ₃
810sh		-	
719sp	680-750	-	Carbonate ion
	738	CO ₂ asym. bend	Li ₂ CO ₃
539m	550-650	LiO stretch	LiOCH ₃

(w: weak, m: medium, s: strong, sh: shoulder, br: broad, v: very, sp: sharp)

The IR spectrum of the film formed on BG-34 in EC-DMC(1:1mol) + LiPF_6 is more complex, indicating significant involvement of EC decomposition on the surface of lithiated graphite (Figure 6.13). The peaks corresponding to the formation of organo-lithium compounds as well as Li_2CO_3 are present. The peaks at 844 and 1483 cm^{-1} are assigned to the lithium carbonate. The peak at 1083 cm^{-1} can be assigned to CH_3OLi , and $\text{CH}_3\text{OCO}_2\text{Li}$, various C-H bending of CH_3 and CH_2 groups.

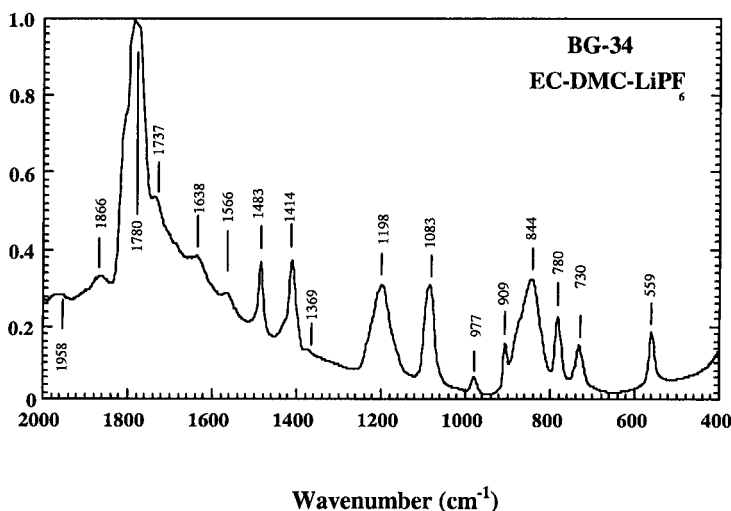


Figure 6.13. IR spectrum of the film formed on lithiated graphite during the first lithium intercalation process in EC-DMC (1:1mol) + 1M LiPF_6 electrolyte.

In Table 6.4 the vibrational frequencies in EC-DMC- LiPF_6 are reported.

The IR spectrum of film formed on graphite during first lithium intercalation in EC-DEC (1:1mol) + 1M LiPF_6 is shown in Figure 6.14. The complex spectrum with several absorption peaks shows decomposition by-products of the EC and DEC solvents. The richness of the spectrum indicated that besides $\text{Li}_2\text{CO}_3(\text{solid})$, $\text{CH}_2=\text{CH}_2(\text{gas})$, and $\text{CH}_3-\text{CH}_3(\text{gas})$ there are various other organo-lithium compounds present. The peaks at around $700\text{--}800\text{ cm}^{-1}$ are matched with the bending mode of δ_{CO_3} in ROCO_2Li . Because of the gelatinous nature of the film formed on the surface of the graphite, there is a possibility of ring opening decomposition of EC and formation of organo-lithium dimers or trimers of EC (similar to the ring opening polymerization).

Table 6.4. Vibrational frequencies on the surface layer on BG-35 graphite in EC-DMC-LiPF₆.

v observed (cm ⁻¹)	v assigned	bands	Assignment	Compounds
1958vw				
1866w	1870-1750	-	Organic Carbonate	
	1870	-	Ethylene Carbonate	
1780sp	1870-1750	-	Organic Carbonate	
	1760	-	Dimethyl Carbonate	
1737sh	1870-1750	-	Organic Carbonate	
1638sh	1629	-	LiPF ₆ ⁺	
1566sh	1580	O-C-O stretch	RCOOLi	
1483sp		CH ₂ bend		
1414sp	1441	-	Li ₂ CO ₃	
	1420	-	Li ₂ CO ₃	
1369sh	1380-1360	CH bend	LiOCH ₃	
1198br	1170-1150	CH stretch	LiOCH ₃	
1083sp	1089	CO stretch	Li ₂ CO ₃	
	1085	CO stretch	RCO ₃ Li	
	1074	-	Ethylene Carbonate	
	1083	-	LiPF ₆ ⁺	
977m	974	-	Ethylene Carbonate	
909sp		-		
844br	846	CO ₃ bending	Li ₂ CO ₃	
	858	-	Dimethyl Carbonate	
	850	-	LiF	
	832	-	LiPF ₆ ⁺	
780sp	745-789	-	LiO	
	774	-	Ethylene Carbonate	
		-		
730sp	738	CO ₂ asym.	Li ₂ CO ₃	
	740	bend	Li ₂ CO ₃	
		CO ₂ asym.		
		bend		
559sp	550	-	LiF	
	557	-	LiPF ₆ ⁺	
	552	LiO stretching	Li ₂ O ₂	

(w: weak, m: medium, s: strong, sh: shoulder, br: broad, v: very, sp: sharp)

The peak assignments for SEI layer formed on the surface of graphite during the first lithium intercalation are listed in Table 6.5. The peaks correspond to the formation of residual lithium carbonate with peaks around 1400 cm⁻¹, formation of various organo-lithium compounds as well as peaks for the C=O stretching vibrations at 1650-1800 cm⁻¹.

The IR spectrum of the film formed on the surface of graphite anode during lithium intercalation in PC-LiPF₆ solution is shown in Figure 6.15, and the frequencies and products in Table 6.6. This spectrum is rich in by-products of the PC decomposition. The IR signals of Li₂CO₃, around 850 and 1460 cm⁻¹ have also been observed. As already mentioned, the film formed in this case is much thicker than the film formed by EC decomposition, this indicating further electrolyte decomposition upon cycling.

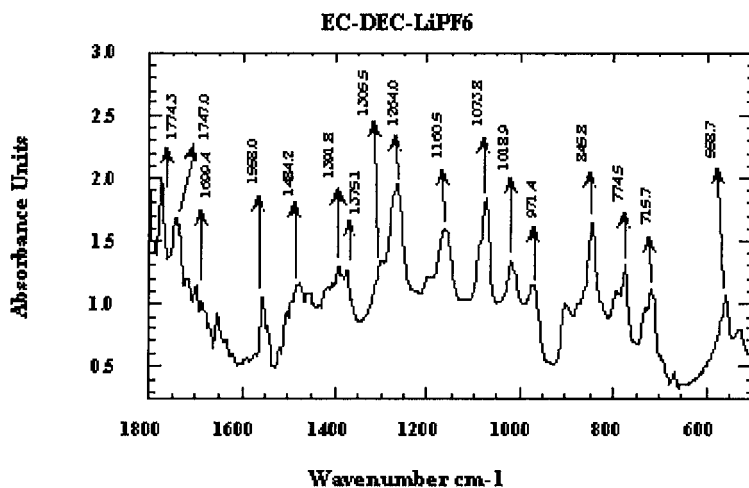


Figure 6.14. IR spectrum of the film formed on BG-34 in EC-DEC + 1MLiPF₆ during first lithiation.

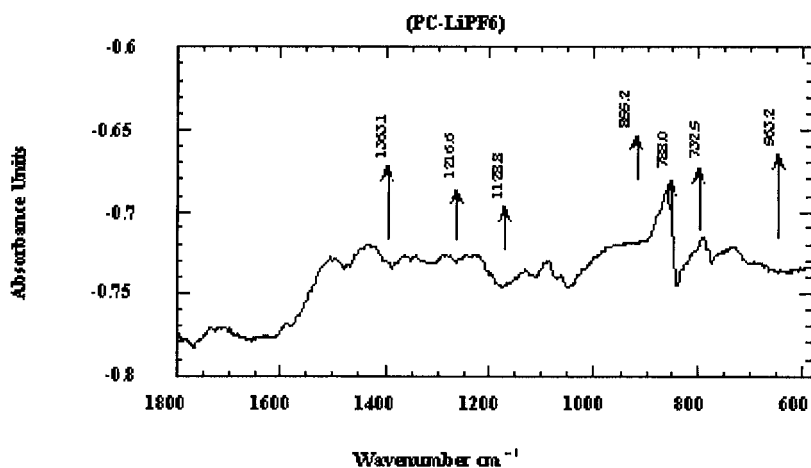


Figure 6.15. IR spectrum of the film formed on graphite anode in PC-1M LiPF₆.

Table 6.5. Vibrational frequencies on the surface layer on graphite in EC-DEC-LiPF₆.

Observed	v assigned	Assignment bands	compounds
1966sp			
1860sh	1870		Ethylene Carbonate
1809sp	-		
1771sp	1750-1870		Organic Carbonate
1746m	1750		Diethyl Carbonate
1699w	-		
1685w	-		
1652m	1650	CO ₂ stretch	RCO ₃ Li
1555sp	1580		RCOOLi
	1580		LiOH
1505sh	1500		(CH ₂ OLi) ₂
1479w	-	-	Ethylene Carbonate
1457w	1450-1480	CH bend	LiOCH ₃
	1445	CH, CH ₃ asy. bend	Ethyl-CO ₃ Li
1390w	-	-	Ethylene Carbonate
	1360-1380	CH bend	LiOCH ₃
1374w	1351	CO ₂ sym. stretch	Ethyl-CO ₃ Li
1296sh	-		
1267sp	1262	-	Diethyl Carbonate
1195sh	-	CO stretch	
1161sp	1162	-	Ethylene Carbonate
	1152	CO stretch	Ethyl-CO ₃ Li
1072sp	1074	-	Ethylene Carbonate
	1085	CO stretch	Ethyl-CO ₃ Li
	1100	CO stretch	(CH ₂ OLi) ₂
1017sp	1021	-	Diethyl Carbonate
	1010	CO stretch	Ethyl-CO ₃ Li
973m	974		Ethylene Carbonate
903sh	890		(CH ₂ OLi) ₂
844sp	858	-	Diethyl Carbonate
	826	CO ₃ bend	Ethyl-CO ₃ Li
	850	-	LiOH
774sp	774	-	Ethylene Carbonate
730sh	738		
717m	720	CO ₂ asym. bend	Ethyl-CO ₃ Li
666w	660-550	LiO stretch	LiOCH ₃
556sp	500-600	LiO stretch	Ethyl-CO ₃ Li
529w	400-500		LiOH
-	-		

(w: weak, m: medium, s: strong, sh: shoulder, br: broad, v: very, sp: sharp)

The IR spectrum of the film formed on the surface of lithiated graphite in PC-DMC-LiPF₆ is shown in Figure 6.16 (peak assignments in Table 6.7). The film formed with electrolyte containing PC was always thicker and richer in PC decomposition by-products. It is also observed that the film

formed from solutions containing EC is also rich in EC decomposition by-products.

The IR spectra of surface films formed on lithiated graphite anodes in solutions containing both the cyclic and the linear carbonates have been studied. The composition of the film is dominated by the decomposition by-products of the cyclic carbonates. This observation may suggest that the cyclic carbonates that selectively solvate the Li^+ in the electrolyte, carry their solvation shell to the graphite surface, and preferentially saturate the electrode-electrolyte interface with the cyclic carbonate. This observation may explain the beneficial effect of EC in commercial electrolytes for lithium batteries.

Table 6.6. Vibrational frequencies on the surface layer on graphite in PC-LiPF₆.

ν observed (cm^{-1})	ν assigned	Assignment bands	Compounds
1862sh			
1817sp		-	
1785sh	1760	-	Dimethyl Carbonate
1732w		-	
1715br		-	
1630w	1629	-	LiPF ₆ *
1588sh	1580	-	RCOOLi
1500br		-	
1430br	1441	-	Li ₂ CO ₃
1360br		CO ₂ sym. stretch	
1338br		-	
1289br	1280	-	Dimethyl Carbonate
1250w	1263	-	LiPF ₆ *
1233w		-	
1134m	1122	-	LiPF ₆
1088m	1089	CO stretch	Li ₂ CO ₃
	1083	-	LiPF ₆ *
1065w	1060	-	Li ₂ O
960w	969-914	-	Dimethyl Carbonate
865sp	866	CO ₃ bend	Li ₂ CO ₃
	832	-	LiPF ₆ *
	870	-	Li ₂ O
	866	-	LiO
791sp	793	-	Dimethyl Carbonate
	789-745	-	LiO
734br	738	CO ₂ asym. bend	Li ₂ CO ₃
691sh	730-689	-	LiO
562sp	557	-	LiPF ₆ *
	650-550	LiO stretch	LiOCH ₃

(w: weak, m: medium, s: strong, sh: shoulder, br: broad, v: very, sp: sharp)

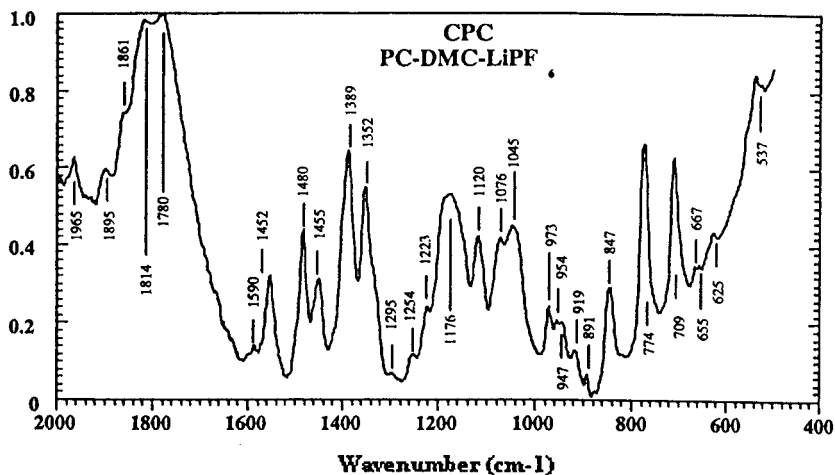


Figure 6.16. IR spectrum of the film formed on the surface of graphite anode during lithium intercalation in PC-DMC (1:1mol) + 1M LiPF₆.

Table 6.7. IR frequencies of the surface layer on cycled CPC in PC-DMC- LiPF₆.

		Assignment	
ν observed (cm ⁻¹)	ν assigned	bands	Compounds
1861sh	1750-1870	-	Organic Carbonate
1780br	1760	-	Dimethyl Carbonate
1590w	1630-1590	-	Carbonate ion
1555sp	1580	-	RCOOLi
1480sp	1480-1450	CH bend	LiOCH ₃
1455sp	1450-1480	CH bend	LiOCH ₃
	1441	-	Li ₂ CO ₃
1389sp	1380-1360	CH bend	LiOCH ₃
1254w	1250-1280	-	Organic Carbonate
1223w		-	
1176br	1170-1150	CH stretch	LiOCH ₃
1120sp		-	
1076w	1070-1050	CH stretch	LiOCH ₃
	1089	CO stretch	Li ₂ CO ₃
1045br		-	
973sp	970-1020	-	Organic Carbonate
891sp	866	CO ₃ bend	Li ₂ CO ₃
847sp	826	CO ₃ bend	Ethy-CO ₃ Li
	846	CO ₃ bend	Li ₂ CO ₃
774sp	774-793	CO ₂ asym. bend	Organic Carbonate
709sp	720	CO ₂ asym. bend	Ethy-CO ₃ Li
625w	550-650	LiO stretch	LiOCH ₃
537w	529	CO bend	

(w: weak, m: medium, s: strong, sh: shoulder, br: broad, v: very, sp: sharp)

6.3.3. Thermal Analysis of SEI Layer on Graphite Anodes

The thermal characteristics of the surface film formed on the graphite anode during lithium intercalation are very important for practical reasons.²⁶ The lithium battery may be subject to different thermal conditions during its operational life. Therefore its thermal safety characteristics must be known. A useful tool for evaluating the thermal properties of films formed on a graphite anode is the differential scanning calorimetry (DSC). The graphite electrode was charged and discharged in carbonate-based electrolytes, and the surface film formed on the anode was collected for DSC study. Figure 6.17 shows the thermal behavior of the surface film in contact with Li_xC_6 , ($x=0.2, 0.4, 0.6, 0.8, 1.0$).

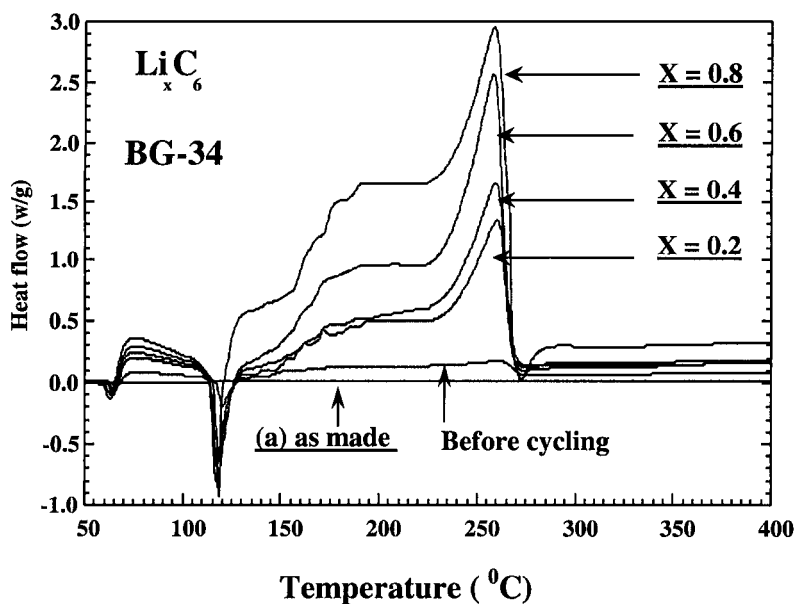


Figure 6.17. Differential scanning calorimetry of the surface film formed on graphite anode at different states of charge ($x=0.2-0.8$ in Li_xC_6).

The sample has an endothermic peak near the boiling point of DMC, and then the exothermic process starts around 150 °C. A major exotherm was observed at 220-240 °C. The intensity of the exotherm peak correlates well with the amount of lithium remaining in the graphite. It is very important to stress the safety aspects of the Li-ion cells when they are exposed to temperatures above 150 °C. Further electrolyte decomposition with massive gas generation may occur above 150°C, and cell temperature may rise to

above the flash point of the electrolyte components. Therefore care should be exercised dealing with lithium-ion batteries with graphitic anodes, particularly in the charged state (x value close to one in Li_xC_6).

A similar thermal behavior was observed for almost all graphitic anodes. The temperature-induced degradation of the SEI layers occurs first around 120-140 °C followed by an exothermic reaction and the decomposition of trapped LiPF_6 around 210-230 °C. We have found a direct correlation between the BET surface area of the graphite anode, amplitude of the DSC exothermic peak and the irreversible capacity losses measured for C/Li cells. Figure 6.18 shows the correlation between the volume of gas generated on the surface of lithiated graphite anodes and the surface area of the graphite material used.

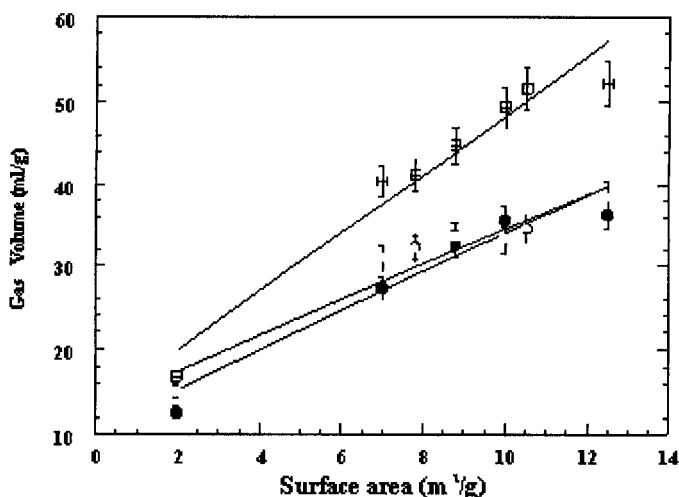


Figure 6.18. The correlation between the volumes of gas evolved during lithium intercalation in graphite anode and the surface area of the graphite. Upper line: PC-DMC; middle: EC-DMC; lower: EC-DEC (all with LiPF_6).

6.4. CONCLUSIONS

The following general conclusions can be made from this study.

1. Organic carbonates are not electrochemically stable over a lithiated graphite electrode. However, the decomposition by-products formed on the surface can protect the electrode, and the electrolyte decomposition is eliminated in subsequent charge-discharge cycles.
2. The nature of the film formed on the surface of lithiated graphite depends on the composition of electrolyte, and in the case of

- electrolyte made of organic carbonates, the by-products are organo-lithium compounds as well as some lithium carbonate.
3. The composition of the film is dominated by the by-products of cyclic carbonate decomposition, and less by the linear carbonate decomposition.
 4. The film formed from the decomposition of cyclic ethylene carbonate is denser and more protective as compared with films formed from other carbonates.
 5. The gaseous species formed during the first charge discharge are mostly flammable and care should be taken when preparing large lithium cells.
 6. The thermal analysis has shown that the film formed on the surface of lithiated graphite is not stable above 150 °C. If lithium cells are exposed to heat, or if internal heat exceeds 150 °C, the protective film could be destroyed and further electrolyte decomposition of the freshly exposed surface of lithiated graphite may occur. Therefore, it can be concluded that the current lithium-ion cells are not very safe above 150°C, and their application in such conditions must be avoided. In addition, a safer and more robust anode is needed, particularly for large size applications of high-energy and high-power lithium batteries.

REFERENCES

1. M.M. Thackeray, J.T. Vaughey, A.J. Kahaian, K.D. Kepler, R. Benedek, *Electrochem. Comm.* 1(1999) 111.
2. J. Akimoto, Y. Gotoh, Y. Oosawa, J. Akimoto, Y. Gotoh, Y. Osawa, *J. Solid State Chemistry* 7 (1997) 129.
3. J.P. Kartha, D.P. Tunstall, J.T.S. Irvine, *J. Solid State Chemistry* 152 (2000) 397.
4. M.E. Arroyo de Dompablo, A. Varez, F. Garcia-Alvarado, *J. Solid State Chemistry* 153 (2000) 132.
5. R. van de Krol, Thesis, 2000, Universal Press, Veeneddaal, Netherland.
6. S. Sodergren, H. Siegbahn, H. Rensmo, H. Lindstrom, A. Hagfeldt, S.E. Lindquist, *J. Phys. Chem. B* 101 (1997) 3087.
7. D.W. Murphy, R.J. Cava, S.M. Zahurak, A. Santoro, *Solid State Ionics* 9 (1983) 413.
8. T. Ohzuku, A. Ueda, N. Yamamoto, *J. Electrochem. Soc.* 142 (1995) 1431.
9. M. Nishijima, Y. Takeda, N. Imanishi, O. Yamamoto, *J. Electrochem. Soc.* 141 (1994) 2966.
10. T. Shodai, S. Okada, S. Tobishima, J. Yamaki, *Solid State Ionics* 86 (1996) 785.
11. S. Suzuki, T. Shodai, *Solid State Ionics* 116 (1999) 1.
12. J.L.C. Rowsell, V. Pralong, L.F. Nazar, *J. Am. Chem. Soc.* 123 (2001) 8598.
13. N. Pereira, L.C. Klein, G.G. Amatucci, *J. Electrochem. Soc.* A262 (2002) 149.
14. D. Souza, V. Pralong, A.J. Jacobson, L.F. Nazar, *Science* 296 (2002) 2012.
15. V. Pralong, D.C. Souza, L.F. Nazar, *Electrochem. Com.* 4 (2002) 516.
16. T. Nagaura, K. Tozawa, *Prog. Battery and Solar Cells* 9 (1990) 209.
17. C.F. Holmes, A.R. Landgrebe, *The Electrochemical Society Proceeding* 97 (1997) 18.
18. T. Ohzuku, A. Ueda, *J. Electrochem. Soc.* 144 (1997) 2780.

19. P. Novack, K. Miller, K.S.V. Santhanam, O. Heas, *Chem. Rev.* 97 (1997) 207.
20. P. Bicke, W.F. Chu, W. Weppner, *Solid State Ionics* 1997, 93.
21. M. Arakawa, J. Yamaki, *J. Power Sources* 54 (1995) 250.
22. S.A. Safran, *Solid State Physics* 40 (1987) 183.
23. S.E. Ulloa, G. Kirczenow, *Comments Cond. Mat. Phys.* 12 (1986) 181.
24. J.R. Dahn, A.K. Sleight, H. Shi, J.N. Reimer, Q. Zhong, B.M. Way,, *Electrochim. Acta* 38 (1993) 1179.
25. F.A. Cotton, G. Wilkinson, C.A. Murillo, M. Bochmann,,*Advanced Inorganic Chemistry*, John Wiley & Sons. Inc. NY 1999.
26. M.N. Richard, J.R. Dahn, *J. Electrochem. Soc.* 146 (1999) 2068.

Chapter 7

THE KEY ROLE OF NANOPARTICLES IN REACTIVITY OF 3d METAL OXIDES TOWARD LITHIUM

J-M. Tarascon, S. Grugeon, S. Laruelle, D. Larcher and P. Poizot

*Laboratoire de Réactivité et Chimie des Solides, Université de Picardie Jules Verne and
CNRS (UMR-6007), 33 rue Saint Leu, 80039, Amiens, France*

7.1. INTRODUCTION

In response to the needs of today's mobile society and the emergence of ecological concerns such as global warming, one of the major technological challenges in this new century is undoubtedly energy generation and storage. Ninety percent of today's electrical power generation still comes from fossil fuels, and we are constantly struggling to reduce the carbon dioxide emissions per unit of electric power so as to help curtail global warming. It is now mandatory that new and environmentally friendly energy/storage sources be found. Hence, the fast developing research in that field involving, among others, fuel cells, primary and rechargeable batteries, and supercapacitors. As a result of this worldwide ecological priority, political concerns have come into play, and science has suffered from prioritisation based on both industrial pressure and media reports, rather than on the clear and rigorous scientific identification of technological stoppers inherent in each storage system. Needless to say, this applies to battery systems as well.

In the past two decades, intensive efforts have given birth to the rechargeable Li-ion battery technology that has dominated the market place, and can be regarded as one of the great successes in modern electrochemistry to date. But these Li-based systems still suffer from the lack of suitable electrode and electrolyte materials, which they require if they are ever to accommodate the increasing user's demands. Aware of this limitation, chemists have been acting at several levels to incrementally improve the Li-ion performance. They have followed a dual approach, dealing with either positive or negative electrode materials, with efforts centered around: 1) the modification of existing materials through cationic/anionic substitution, texture modification and surface treatments, 2) the making of composite

electrodes or electrolytes made of several chemical components, and 3) the design of new electrode materials. Such approaches were pursued at the macroscopic scale on electrode materials¹⁻³ having a dual electronic-ionic conductivity, a void structure to insert/de-insert Li ions, or the ability to alloy with Li. They led to the identification of layered $\text{LiMn}_{1-x}\text{Cr}_x\text{O}_2$ oxides⁴⁻⁵ or three-dimensional iron phosphates (LiFePO_4)⁶, that stand as a possible alternative to LiCoO_2 or negative electrode materials such as tin-based oxides (SnO_2 , SnO),⁷⁻⁸ intermetallics (CuSb^9 , $\text{Cu}_6\text{Sn}_5^{10}$, ...), nitrides¹¹ and phosphides,^{12,13} which could be used as alternatives to carbonaceous materials, once their initial large irreversibility and poor cycle life have been overcome.

Recently, our research group pursued a novel approach, deviating from the conventional route aimed at searching for compounds having voids structure or alloying with Li. We obtained astonishing results with the possibility for metal oxides (MO), having an interstice-free rock-salt structure, to reversibly react with Li.¹⁴ Not only did such findings make us aware that high-performing electrode materials may have been wrongly disregarded in the past, but also they now comfort us in our approach aimed at tackling electrode materials at the microscopic rather than macroscopic scale. Through our work on metal oxides, which was extended to other metal-based anode materials, we will stress that, when working at the atomic level, new kinds of effects are apparent, and represent completely new opportunities in the unusual design of materials.

Thus, this chapter will be organized as follows. First, we will recall the key observations motivating the reactivity of 3d-metal oxides towards Li, and describe the fundamentals lying beyond such an unusual reactivity. Secondly, we will rationalize these types of reactions, and evaluate their potential with respect to applications. Thirdly, we will stress the positive attribute of nanoparticles in enhancing kinetics, therefore enabling different Li reactivity paths.

7.2. EXPERIMENTAL

The Co-based metal oxide powders used within this study were commercial products (CoO), or were synthesized in-house (Co_3O_4 , Mn_3O_4 , $\alpha\text{-Fe}_2\text{O}_3$). The other metal oxides ($\text{M} = \text{Ni}, \text{Fe}, \text{Mn}, \text{Cu}$) were used as received from commercial sources, unless otherwise specified. LiCoO_2 was also provided by the market.

Powder purity and crystallinity were examined by X-ray diffraction (XRD), operating in Bragg-Brentano geometry with a $\text{CuK}\alpha$ radiation. The powders morphology and composition were investigated by scanning electron microscopy (SEM) with a field emission gun (FEG), coupled to an instrument for energy-dispersive X-ray spectroscopy (EDS). High-

resolution transmission electron microscopy (HRTEM) was carried out using a microscope equipped with an EDS analyzer. Magnetic measurements were performed on a commercial SQUID magnetometer, at temperatures ranging from 5 to 290 K. Electrochemically-driven structural changes were followed by means of an *in situ* electrochemical cell similar to that previously described¹⁵, with the studied electrode material deposited behind a beryllium window, which acts as the positive current collector.

The materials were tested in either SwagelokTM or standard 2035-size coin cells that were assembled in an argon-filled glove box at a dew point of -80°C. If not otherwise specified, the cell consists of a plastic positive electrode disk containing 64 wt% of M_xO_y materials, 8 wt% SP carbon black and 28 wt.% PVDF-HFP copolymer binder; a 1 cm² disk of Li foil as the negative electrode member; and a Whatman GF/D borosilicate glass fibre sheet separator, saturated with a 1 M LiPF₆ electrolyte solution in a 1:1 (by wt) dimethyl carbonate/ethylene carbonate.

The cells were tested using a VMP automatic cycling/data recording system that can be operated in both galvanostatic and potentiostatic modes. Each reported curve was reproduced three times. Hardly any deviation was noted among the curves.

7.3. RESULTS AND DISCUSSION

7.3.1. Reactivity of 3d Metal Oxides Towards Li

The electrochemical reactivity of 3d metal oxides towards Li has long been studied. A few oxides, such as CuO, which converts to Cu through a decomposition reaction ($\text{CuO} \rightarrow \text{Cu} + 1/2\text{O}_2$), were spotted as attractive electrode materials, leading to the assembly of primary CuO/Li cells that are still commercialised nowadays.¹⁶⁻¹⁸ However, with the common belief that decomposition reactions cannot be electrochemically reversible, such oxides have been disregarded as reversible Li electrode. The motivation to reinvestigate them, like most materials advances, is the result of several observations/contributions going back to 1996. In 1996, Fuji's researchers⁷ reported that vanadates-based electrodes displayed, when cycled down to zero volt, reversible capacities greater than those expected, assuming a reduction of the constituting metal elements. Later, these results were reconfirmed by Guyomard's group¹⁹. Occasionally, for some LiMVO₄ (M= Zn, Ni, Co ..) phases, this group reported a surprising capacity enhancement upon cycling, which turned out not to be fortuitous, as will be seen later. In light of such intriguing results, our group launched a complete study of the vanadates, aimed at identifying the key parameters governing their unusual reactivity vs. Li. Numerous hydrated vanadates of formula $\text{RVO}_4 \cdot n\text{H}_2\text{O}$,

either crystalline or amorphous, were surveyed with special attention given to the Fe- and Co-based ones ($\text{FeVO}_4 \cdot 1.1\text{H}_2\text{O}$, $\text{Co}(\text{VO}_3)_2 \cdot n\text{H}_2\text{O}$) that displayed exceedingly large (800 mAh/gr) reversible capacities.²⁰⁻²³ Among the numerous *in situ* techniques used to study the electrochemical behaviour of $\text{Co}(\text{VO}_3)_2 \cdot n\text{H}_2\text{O}$ /Li cells, XANES turned out to be the most fruitful²⁴. Indeed, it indicated that upon charge/discharge cycles, the oxidation state of Co was surprisingly converting between 0 and 2, and that of vanadium between 3 and 5. Knowing that the electrochemical behavior of V_2O_5 proceeds through an insertion/deinsertion process, we hypothesized that the unexpected electrochemical results could be associated to the reactivity of 3d metal oxides towards Li. Thus, our study of the vanadates was narrowed-down to that of the 3d metal oxides as MO (M = Co, Ni, Fe, Mn), which were precluded to react with lithium on the basis of Li insertion-deinsertion or Li-alloying reactions.²⁵⁻³⁰

Several CoO/Li half-cells were electrochemically tested towards Li¹⁴ and, to our surprise, we found that they could sustain a nicely reversible capacity when cycled down to zero volt. During discharge (Figure 7.1), two different electrochemical processes appear, a plateau at 0.8 V with an amplitude of two Li, followed by a continuous uptake of 0.7 additional Li, down to a voltage of 0.02 V. With the following charge, only about two Li per formula unit could be removed, leading to a capacity of 700 mAh per gram of CoO, a value about twice that of today's graphite negative electrodes. Since such oxide does not contain voids, or a metallic element that alloys with Li, its reactivity had to be different from the classical Li insertion/deinsertion or Li-alloying processes. In an attempt to pin down this new mechanism, Potentiodynamic Intermittent Titration Technique (PITT), *in situ* X-ray diffraction, and XANES measurements, together with *semi in situ* TEM measurements, were carried out on CoO/Li cells.

PITT electrochemical measurements revealed two very clear and distinct processes. The first one (Figure 7.2) for which the chronoamperometry response to the voltage step ($E=0.92\text{ V}$) displays a bell curve shape, corresponds exactly to an uptake of 2 Li (*e.g.*, a full reduction of Co^{+2} in Co).

Beyond $x=2$, we observed a continuous decrease in the potential as a function of x , as observed in the galvanostatic mode, with a difference in the number of reacted Li that reached 1.8 instead of 0.7. This suggests a faradic process strongly influenced by the imposed current (*e.g.*, a kinetic influence). This $\text{CoO} \rightarrow \text{Co}$ conversion process was further confirmed by XANES measurements²⁴ at the Co K-edge, indicating that the spectrum of fully lithiated and fully delithiated samples after 10 cycles was superimposing that of metallic cobalt foil and fresh electrode, respectively.

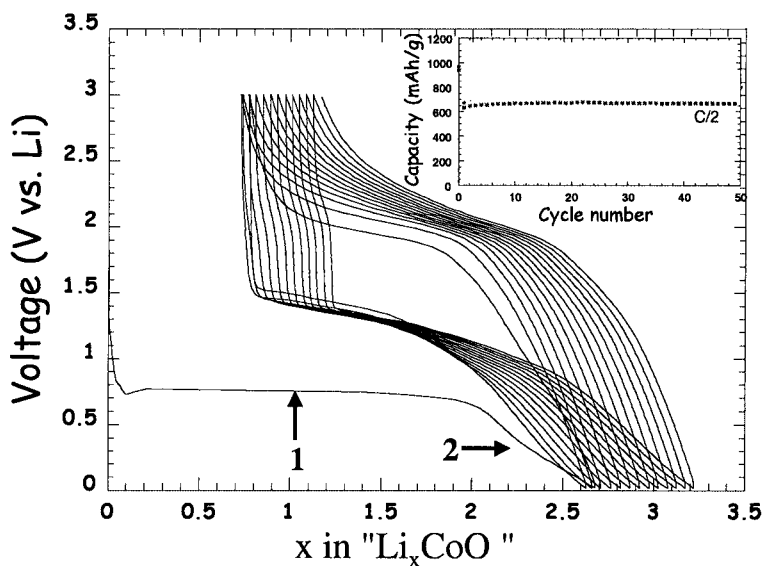


Figure 7.1. Voltage-composition traces for a CoO/Li cell cycled between 0.01 V and 3 V at a rate of $C/2$ (e.g., 1 lithium per formula unit in 2 hours) shown over several cycles. Capacity retention for the same cell shown in the inset.

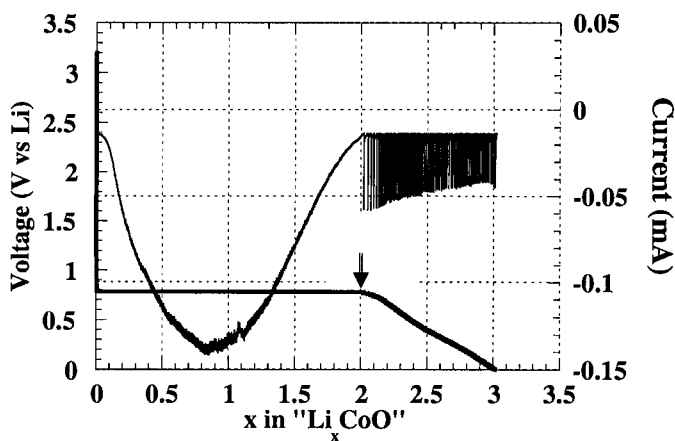


Figure 7.2. PITT measurements performed on a CoO/Li cell. The voltage steps are of 10 mV with a current limit (i_{\min}) corresponding to $C/300$ (e.g., 1 Li in 300 hours).

Through the electrochemical reduction process the samples were shown, as deduced by *in situ* X-ray measurements,¹⁴ to become amorphous, and to remain so upon subsequent cycles. Transmission electron microscopy was then used as a complementary technique to further grasp the electrode evolution morphology upon cycling. We observed (Figure 7.3) that upon cell discharge, the sintered CoO particles of dimensions ranging from 1000 to 2000 Å, decomposed into 10 to 20 Å diameter Co nanograins, dispersed into a matrix.

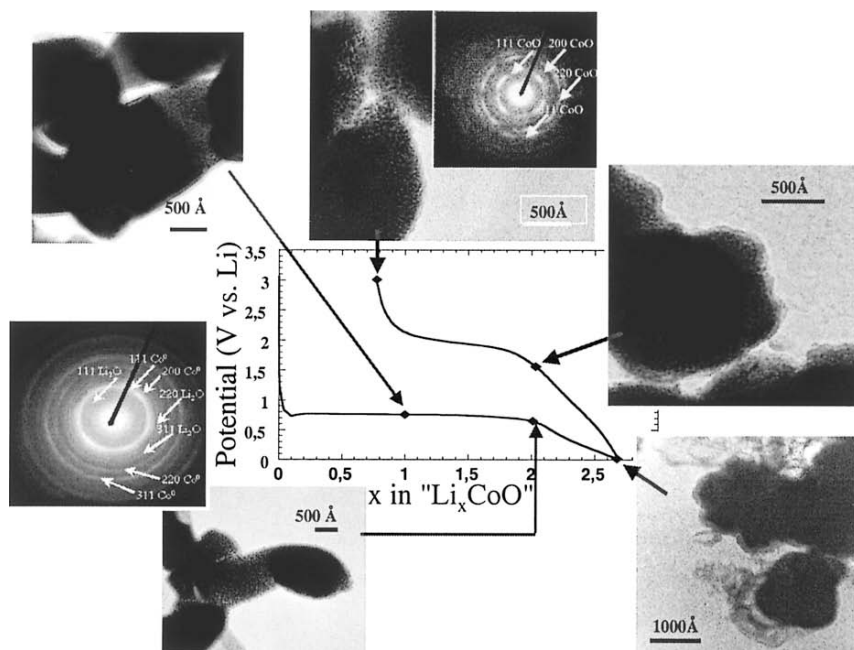


Figure 7.3. TEM observations realized on CoO electrodes recovered from CoO/Li cells that were stopped at various discharged and charged states, as indicated by the full circles on the voltage/composition curves. When necessary, the SAED patterns are joined to the micrograph as a means to indicate the electrode composition. The nanometric character of the composite together with the growth/disappearance of a polymeric layer are nicely depicted.

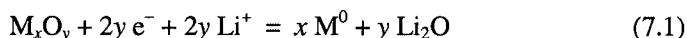
At $x=2$, the decomposition was completed, and from an indexation of the collected SAED patterns, we could clearly identify the presence of Co^0 (cubic structure) and Li_2O (antifluorine structure) matrix. Upon further lithiation (beyond $x=2$), the SAED patterns no longer evolved. Contrastingly, we noted the growth of an organic-type layer. The layer disappeared upon the following charge, and the Co deoxidised, leading to a CoO nanograin electrode, as deduced from an indexation of the collected SAED patterns. Two polymorphic forms, referred to as the high temperature

α -CoO (PDF n° 48-1719) and the low temperature β -CoO forms (PDF n° 42-1300) exist. It was separately reported, as deduced by x-rays, that metallic Co nanoparticles were converting to the low temperature CoO form (denoted α -CoO) upon oxidation.³¹ Therefore, we could not ascertain the assignment from our HRTEM measurements, since the two CoO polymorphic forms have lattice parameters differences falling within the limit of the technique itself.

7.3.2. Rationalization and Potential Applications

7.3.2.1. Thermodynamic and Kinetic Considerations of the MO \rightarrow M Conversion

Whatever the α or β forms, all the above results convey the message that the reduction of CoO through the first discharge plateau is reversible according to the following reaction.



The disappearance of the well-defined first discharge plateau at the expense of a “sloping voltage plateau” upon subsequent cycling is fully consistent with the nano-sized character of the electro-produced particles, which generate many new indefinite interfaces with various interfacial energies. Interestingly, while never observed at room temperature, an electrochemical reaction involving the formation/decomposition of Li_2O was already observed to occur during the electrochemical oxidation/reduction of Fe_2O_3 or Fe_3O_4 in molten salt at 500°C.³²⁻³³ As usual, when dealing with the feasibility of any chemical reaction, one must return to basic thermodynamics. In short, one must simply calculate the associated changes in standard Gibbs free energy. If this $\Delta_r G$ turns out to be negative, the considered reaction is thermodynamically feasible. Then, from Gibbs free enthalpy of reactions, one can predict the equilibrium potentials by using the well-known Nernst law $\Delta_r G = -nEF$, where F is Faraday’s constant. Using the thermodynamic data³⁴⁻³⁵ given in the literature for massive compounds, we can deduce for CoO a $\Delta_r G \cong -347$ kJ/mol that should correspond to a plateau located at $E_{eq} = 1.798$ V vs Li^+/Li^0 . Similar calculations can be extended to most of the 3d metal oxides,³⁶⁻³⁷ with the main result being that the tabulated Gibbs free energy values are negative. This result unambiguously proves that such oxides are, under these conditions, spontaneously reducible at E_{eq} values, as reported in Figure 7.4.

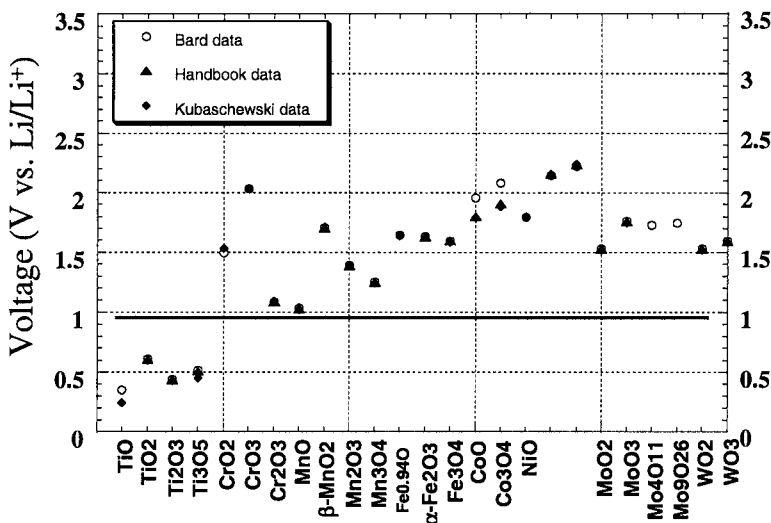


Figure 7.4. The equilibrium voltage values of $\text{MO} \leftrightarrow \text{M}$ conversion reaction are reported for various oxides. The values were obtained by first determining the reaction free energy (ΔG) and then by applying the Nernst law.

Thus, by blindly considering a thermodynamic reversible process, one should expect the reduction of CoO to occur at 1.798 V. This contrasts with the reduction potential value of 0.8V (Figure 7.1), obtained during the first discharge of a CoO/Li cell. The deviation of about 1 V is naturally of kinetic nature, and represents the important over potential needed to initiate and pursue the decomposition reaction. Assuming that the 1V over potential needed to reduce CoO is of the same amplitude as for most of the other 3d oxides considered, our difficulty encountered in reducing MnO (Figure 7.5), or our inability to reduce TiO_2 and *at fortiori* MgO, can be understood.

Since reaction (7.1) is thermodynamically allowed in the forward direction, it should also occur backwards (that is to say, from right to left), if the applied voltage exceeds the E_{eq} voltage. Thus, a legitimate question is why was this reaction never observed to proceed at room temperature, when mixtures of Li_2O and Co were mechanically made and reoxydized. The answer is of a kinetic nature, and lies in the difficult task to reconvert, through a solid-state reaction, coarse $\text{M}^0 + \text{Li}_2\text{O}$ particles into a metal oxide (M_xO_y). We believe that the reversibility experienced with various $\text{M}_x\text{O}_y/\text{Li}$ cells is mainly nested in the high chemical reactivity of the electrochemically made nanograins, after the electrode has been reduced once. Indeed, with a decreasing particle size, an increasing fraction of atoms lies near or on the surface, making the effect of surface on the chemical/electrochemical reactivity of increasing importance. Thus, the chemical diffusion path in

highly divided powders becomes close to that of a liquid state, thereby explaining why a reaction occurring at about 500 °C can be produced at room temperature. Nevertheless, electrochemically speaking, reaction (7.1) remains slow as seen by the substantial difference observed between the discharge and the charge voltage composition curves in cycling (Figure 7.5). However, caution has to be exercised, since the capacity associated with the full reduction of the 3d metal through a decomposition reaction does not fully account for the measured capacity.

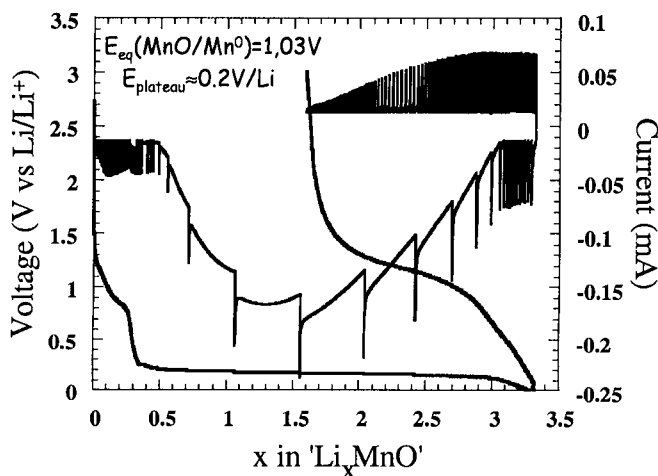


Figure 7.5. The voltage composition curves as deduced from PITT measurements for MnO/Li cells cycled between 0.02 V and 3V. The voltage steps were of 10 mV with a current limit corresponding to C/300.

7.3.2.2. The Rich Chemistry Associated to the Low Voltage Process

The above observations, while leading to a full understanding of the 0.8 V process, did not give any clue as to its origin. To further look into this low voltage process, we measured the dependence of I vs. the voltage scan speed (V/s) over the 0 to 1.8 V range (Figure 7.6), and observed a linearity that is reminiscent of a super capacitor-type behaviour. Interestingly, we showed, by TEM, that the gel-like film formed on CoO was not affected when cycling was limited to the 0–1.8 V range, while vanishing when the CoO electrode voltage was raised to 3 V. Such a finding suggested that the grown polymer film had an electrochemical activity. However, we do not have any information about its composition. In contrast, its formation is nested in the Co-catalysed electrolyte decomposition, with some of the

resulting products moving to the negative electrode, as deduced by the one-to-one correlation between the phenomena occurring at the CoO and Li electrode, as observed by AC impedance³⁸ measurements. Indeed, we noted that the reversible transition from the $\text{CoO} \rightarrow \text{Co}$ conversion process to the electrolyte decomposition process was mirrored by a reversible change in the Li electrode resistivity.

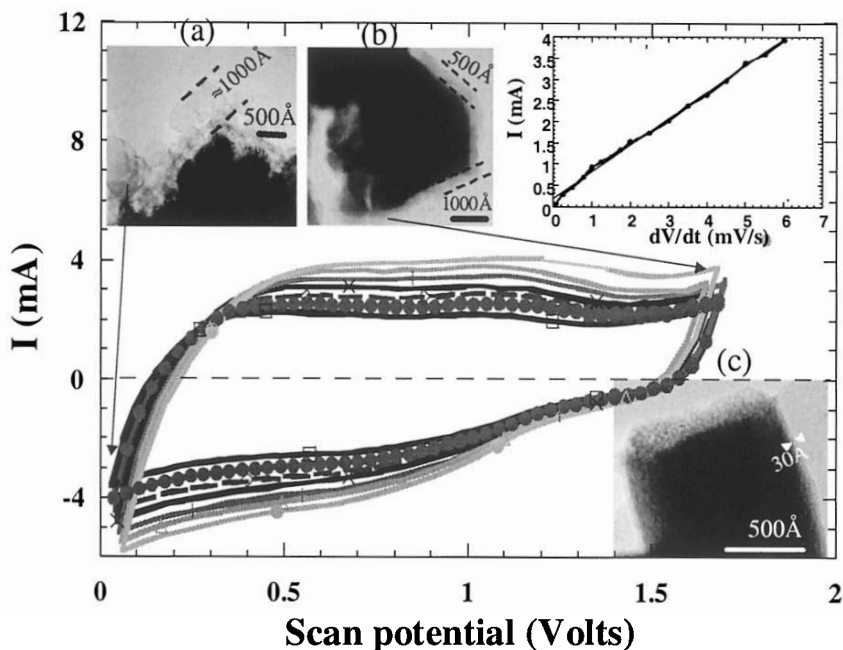


Figure 7.6. Cyclic-voltammetry data as a function of the scan rate for a CoO/Li cell that was cycled between 0.02 and 1.8 V. One inset shows the linear variation of the current as a function of the scan rate. The others, a, b, and c are micrographs of CoO electrodes recovered from CoO/Li cells that were fully discharged and fully recharged 10 times between 0.02 and 1.8 V, and fully recharged to 3 V, respectively.

Aware that the low temperature process was rooted in electrolyte decomposition reactions, we decided to study how it would depend on the nature of the electrolyte used. We went through a survey of various electrolytes encompassing the use of 1 M LiPF_6 in either a single solvent, such as EC or DMC, or solvent mixtures, such as EC-DMC and EC-PC. The use of DMC (linear alkyl carbonate) as the sole solvent resulted in fast capacity fading, as opposed to EC (cyclic alkyl carbonate), which enables sustained cyclability. The detrimental effect of DMC was considerably diminished when used in a 50/50 weight mixture, with either PC or EC

cyclic molecular structures. As cells were cycled, at least during the first cycles, we noted on oxidation the partial disappearance of the organic layer that was forming on reduction. Worth mentioning, however, was that the amount of formed polymeric film was always found to be less in presence of EC.

At this point, a legitimate question was whether such observed effects could be the simple result of the presence of carbon within our starting CoO-C electrode composite. The observed growth of the polymeric layer in cells made with thinner carbon-free CoO electrodes ruled out this possibility. The only difference between cells having carbon free (CoO/Li) or carbon containing CoO positive electrode (CoO_c/Li) cells resides in the first few cycles. The former display a lowest initial capacity that decays more rapidly over the first few cycles than the latter.

With the polymeric layer being the result of an electrolyte decomposition, one could hypothesize its growth to be strongly temperature dependent. To check this hypothesis, we studied the cycling behaviour of both CoO_c/Li and CoO/Li cells at various temperatures, namely, 55°C and 75°C (Figure 7.7).

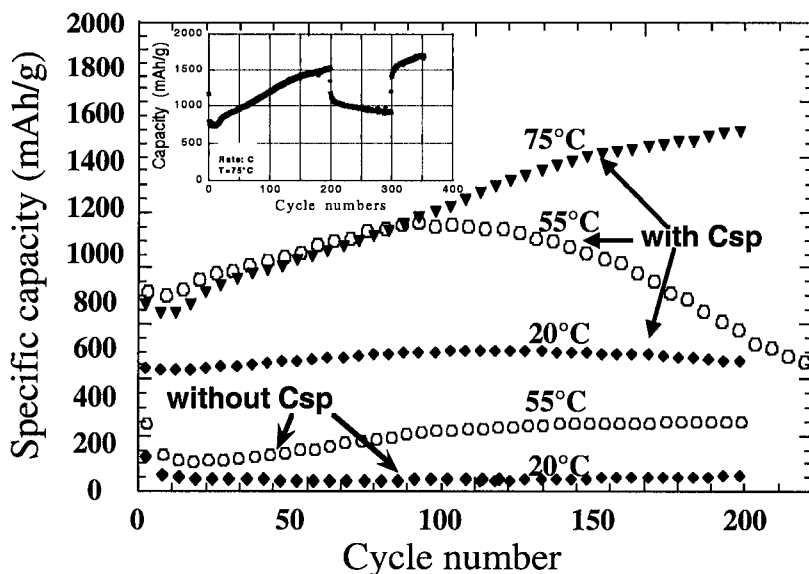


Figure 7.7. Variation of the capacity retention of CoO/Li cells, both as a function of the temperature and of the electrode content (e.g., with or without carbon). Effect of temperature sweep between 20°C and 75°C on the capacity values shown as an inset.

First, common to all the cells once the first ten cycles were achieved, we note a continuous increase in the cell capacity that was more pronounced with increasing temperature. At 75°C, a doubling of the initial capacity was reached after 200 cycles. Such a capacity was found to be reversibly temperature dependent, since a decrease in temperature resulted in a capacity decrease, which is fully recovered as the temperature return to its original value³⁹. Worth mentioning is that more than 500 cycles were achieved without any evidence of short-circuit, reminiscent of dendrite formations. Furthermore, on cells opened after 500 cycles, we noted that the polymeric layer has expanded through all the separator, suggesting at first that the polymeric layer could not be a good electronic conductor, without which the cell would have a short. The feasibility of cycling CoO/Li cells at 75°C at a 2C rate for more than 400 cycles is somewhat amazing, bearing in mind that these are the best conditions to favour dendrite formation. This can be explained either by: 1) the fact that the polymer film formed on the CoO electrode prevents dendrite penetration, and by the same token, cell short or 2) by a modification of the Li surface morphology, due to the deposit of electrolyte degradation products, to the point that it cancelled dendrite formation. Needless to say these facts could help in engineering better Li/electrolyte interfaces so that rechargeable Li batteries could finally become a commercial reality.

Finally, by conducting cycling measurements with different discharge cut-off voltages (Figure 7.7, inset), we reached the conclusion that this temperature-enhanced capacity was the result of electrochemical processes taking place at voltages close to lithium (*e.g.*, over the 0.02-0.15 V). Obviously, this result could simply be explained by assuming a temperature enhanced electrolyte degradation that would lead to an electrochemically active polymer. Therefore the amount of this polymer would increase, the capacity would increase, and should remain constant whatever the cycling temperature once the film is formed. This is not as simple, since we observed that the capacity decreases once the temperature is lowered. The fact that the temperature-driven extra capacity is located near 0 V vs. Li^+/Li^0 , indicates that one needs to decrease the cell polarization by rising the cell temperature to tap into this low potential extra capacity. Thus, the capacity swing observed with changing the temperature is the result of polarization effects, most likely associated to a limited ionic or electronic conductivity of the grown polymeric layer.

To further explain the cycling data at 70°C, we plotted the derivative curves (Figure 7.8) as a function of the cycle number. We noted the appearance of a 1.2V peak corresponding to the $\text{CoO} \rightarrow \text{Co}$ conversion process, which disappeared upon cycling at the expense of a 0.8 V peak. This implies that, upon long cycling, the $\text{CoO} \rightarrow \text{Co}$ conversion process initially corresponding to the main part of the overall cell capacity vanished.

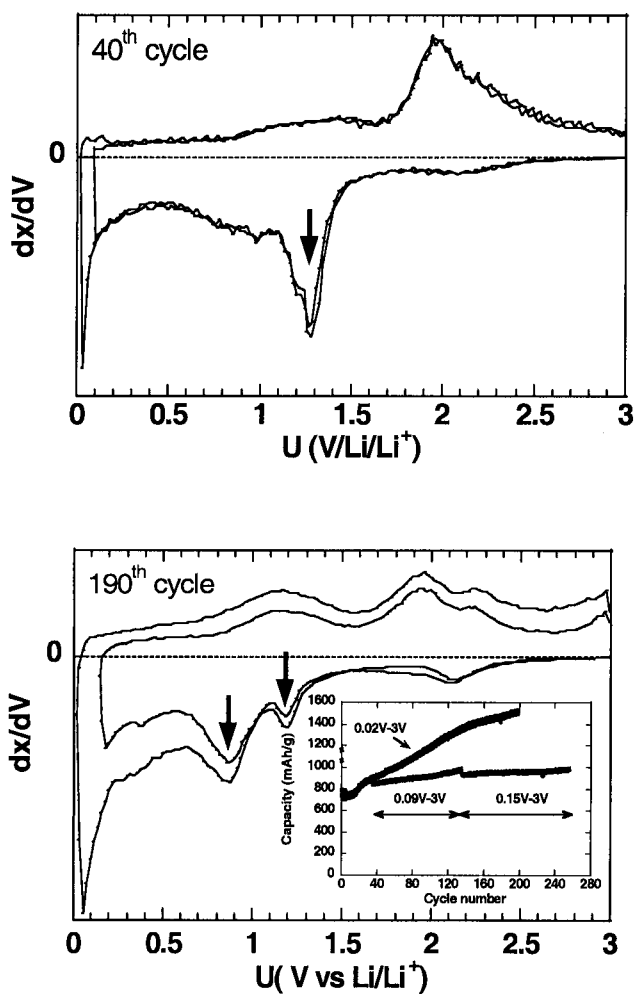


Figure 7.8. Derivative dx/dV plots as a function of the cycle number for CoO/Li cells. The cells were cycled at 75°C at a C rate. Two scanning ranges were used, 0.02 to 3 V and 0.15 to 3 V. Note the appearance of a 0.8 V to the expense of the 1.2 V peak corresponding to the MO \leftrightarrow M conversion process, and of a large extra capacity located around 0.1 V.

The hypothesis was directly confirmed by magnetic measurements (Figure 7.9) that showed no changes in the sample magnetization (equivalent

to 80% of Co in the magnetic state), whether the composite electrode was in its charged or discharged state. In light of such results, it appeared that the measured capacity, once the CoO conversion process became inactive, must be due to the polymer-like forming film.

Among the remaining questions are whether, in addition to the key role played by the polymeric layer, these processes could also be rooted in: 1) the presence of Co surfaces electrochemically attractive to Li deposits at potential positive with respect to the Nernst potential (UPD-type processes) or, 2) in the feasibility of Co, in such highly divided electrodes, to electrochemically alloy with Li. Finding a clue to these questions depends on finding the exact nature and composition of the formed polymeric layer, a task presently being pursued by our group.

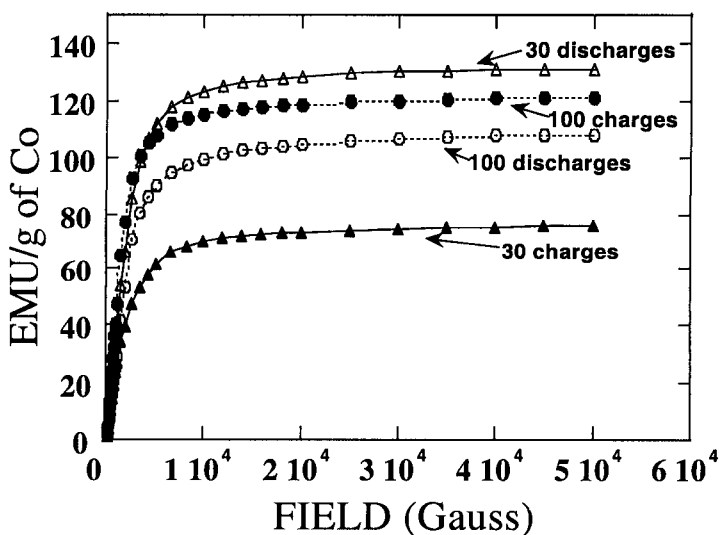


Figure 7.9. Variation of the room temperature remnant magnetization for fully charged and discharged CoO electrodes recovered from CoO/Li cells that were cycled 30 and 100 times, respectively, at a C rate over a 0.02 to 3 V voltage range.

Under any circumstances, and whatever the exact process, either a combination of UPD and Li-alloying processes or others, the main result is that reactivity of the 3d metal oxides towards Li stresses the profound effect that divided particles could have within the field of energy storage. Worth mentioning is that the described effect is not specific to Co electrodes, but also occurs with Cu, Fe, Ni and Mn (which, purely coincidentally, are frequently used as catalysts in Fischer-Tropsch type reactions, for instance). Furthermore, numerous classes of materials besides the 3d metal monoxides

(NiO, FeO, MnO, CuO), such as 3d metal sesquioxides (Co_3O_4),¹⁴ Li-based ternary oxides (LiCoO_2 , LiNiO_2 , ...), 3d metal sulphides (CoS)²⁷, or nitrides (Cu_3N),⁴⁰⁻⁴¹ were found to behave identically, leading to the formation/decomposition upon cycling of Li_2S and Li_3N , respectively, together with the formation of a polymeric gel-like layer. Similarly, there are recent reports describing the potential reactivity of 3d metal-based borates or phosphates in similar terms, thus suggesting the universality of such a proposed mechanism.

7.3.3. Practical Application Considerations

A fundamental understanding was of a great help in optimising these materials, so that 100% capacity retention was achieved with plasticized CoO electrodes containing 1-micron particles. Since the measured capacity, at least within the first hundred cycles, mainly comes from the $\text{CoO} \rightarrow \text{Co}$ conversion process, where two electrons are liberated, rules to increase the overall capacity were established. Hence the need to search for oxides in which the metal oxidation state was greater than 2 as well as our interest for Co_3O_4 , although numerous other spinels or layer oxides (LiCoO_2) could be used as well. We selected Co_3O_4 as our negative electrode, and went into the exercise of assembling Li-ion cells with Co_3O_4 as carbon alternative. The $\text{LiCoO}_2/\text{Co}_3\text{O}_4$ Li-ion cells cycled exceedingly (Figure 7.10) well at both RT and 55°C, since no capacity fade was observed.⁴² Furthermore, these cells, having a weight ratio of positive to negative of 8.5, delivered a 2.2 V output voltage, resulting in an energy density of about 130 Wh/kg. This value is not competitive with today's existing value of 180 Wh/kg for LiCoO_2/C cells, because the $\text{LiCoO}_2/\text{Co}_3\text{O}_4$ cells are penalized by both the voltage of the negative electrode, which is too high as compared to carbon, and the 20% irreversible capacity linked to the use of Co_3O_4 . These are not show-stoppers, since, through the large oxide family, there are compounds (MnO) having a reacting voltage of 0.5V vs. Li^+/Li^0 , and others ($\text{Li}_{1+x}\text{Mn}_2\text{O}_4$) that can be used as positive electrodes, while having a Li reservoir to compensate for the initial 20% capacity loss. In this respect, the $\text{Li}_{1+x}\text{Mn}_2\text{O}_4/\text{MnO}$ system is quite attractive, although still limited in power rate.

It should be realized that the appeal of the metal oxide negative electrodes is that their nano-structure is **internally** created during the first electrochemical reduction, producing pristine and compact nanoparticles, which are held together through Li_2O boundaries domains.⁴³ While it may be taken for granted, let's recall that a similar type of **internal** grinding occurs on the $\text{Ni}(\text{OH})_2$ electrode, widely used in today's Ni-based alkaline batteries. Indeed, during the first electrochemical oxidation, there is a drastic texture change in the $\text{Ni}(\text{OH})_2$ particles that evolve from monolithic to mosaic-type. Controlling the size of these electrochemically-made mosaic

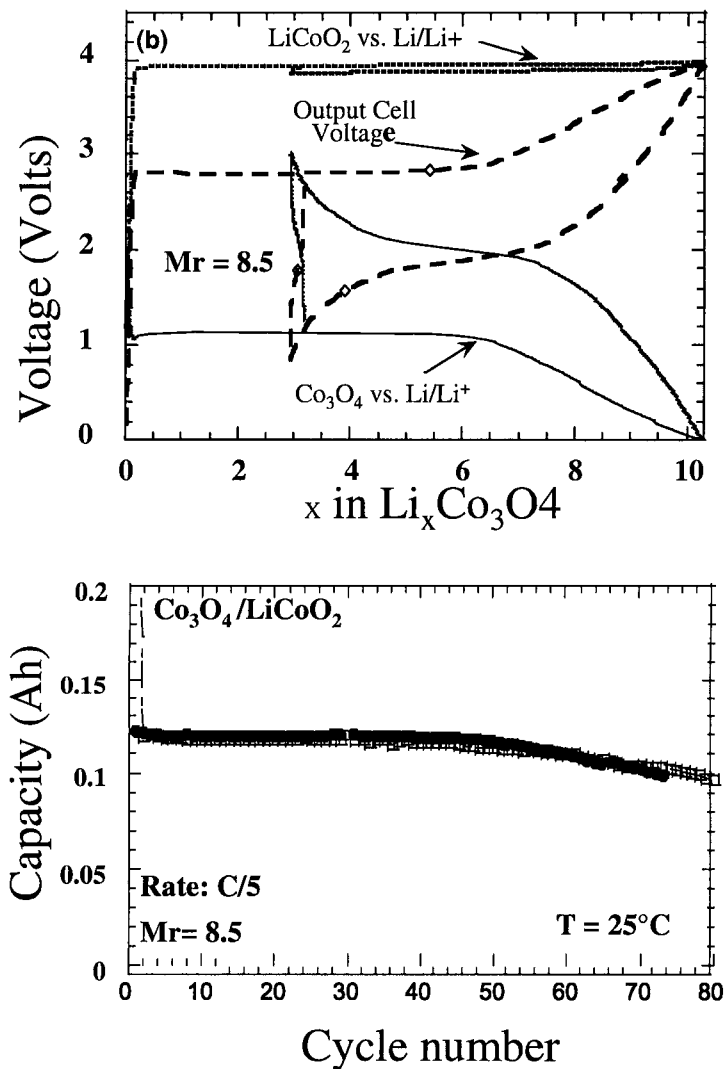


Figure 7.10. The first cycle of a $\text{LiCoO}_2/\text{Co}_3\text{O}_4$ cell cycled between 4.1 and 1.1V, as measured by means of three-electrode configuration, is shown in (a). The cell output voltage is of about 2 V and the weight ratio (M_r) of positive to negative equals 8.5. The capacity retention for such Li-ion cell is shown in (b).

domains, and in the same way the domain wall boundaries that act as a buffer layer, is crucial to the performance of this electrode, since, upon subsequent cycling, the so called “ $\text{Ni}(\text{OH})_2$ formation cycle” remains a valuable know-how specific to each battery manufacturers. This situation

differs from **externally**-made nanostructured powder, or electrodes that can be made either by chemical/physical means, with the greatest difficulty being to gain maximum control over the size and size dispersion of the resulting particles or cluster of atoms. Therefore there are recent reports of enhanced cycling performances obtained with nanostructured LiMn_2O_4 or LiFePO_4 electrodes made by ball milling. A remaining difficult task with externally made nanoparticles lies in the formation of densified electrodes, which are crucial for practical applications. Therefore, new densification methods, for instance Magnetic Pulse Compaction (MPC), may be of great help in densifying such highly divided electrode materials.

This novel reversible Li-reactivity mechanism, mediated through the formation of metal particles, underscores the possibility when working at the atomic level to radically change reaction kinetics and chemical/electrochemical reaction paths. Indeed, one must keep in mind that as particle size decreases, the amount of surface atoms adheres to that of the bulk, and becomes greater for particle size smaller than 20 Å. Thus, the basic considerations of the material electronic band structure or crystallographic voids are no longer valid. Our motivation to revisit well-known materials, that were previously disregarded, is investigated next.

7.3.4. Acting on Reaction Paths Through Particle Size

When the starting oxides correspond to the lowest initial oxidation state of the metal ion (CoO , NiO , Cu_2O), we showed that metallic clusters are formed as soon as the reduction process starts. In contrast, when starting from higher cationic oxidation states (Co_3O_4 , Fe_2O_3), one can expect intermediate reduced phases to be found in the early stage of the reduction process. Through all the above studies, we focused on the oxide decomposition reaction occurring at low voltage, using mainly metal oxides as precursor, with the exception of Co_3O_4 , which turned out to be one of the most promising negative electrode candidates as a carbon alternative. Indeed, this phase adopts the spinel-type structure, having empty tetrahedral or octahedral sites to host Li. It was then of special interest to really understand the interplay between decomposition and insertion reaction, when Co_3O_4 was fully reduced to 0 volt. There are early reports⁴⁴⁻⁴⁷ regarding the feasibility of electrochemically/chemically inserting Li ions in either Co_3O_4 or Mn_3O_4 , but the results were poorly reproducible, and the value of 'x' undetermined, due to the coexistence of secondary phases resulting from the lithiation process. A legitimate question was whether such issues could be related to particle size/morphology. We then initiated a study aimed at sensing how the particle size could influence insertion vs. decomposition reactions in oxides having open structures. Our results will be

presented through two pedagogical examples: Co_3O_4 ⁴⁸ and $\alpha\text{-Fe}_2\text{O}_3$.⁴⁹ Whatever the studied oxide, the first step towards such an approach consists in elaborating synthesis methods to enable the formation of tailor-made particles. Hence, each following section will begin with a material synthesis protocol.

7.3.4.1. Co_3O_4

Co_3O_4 tailored powders were prepared in two steps. First, crystallized Co^{+2} alkoxides were made from a derived polyol process that involved heating a solution of Co^{+2} acetate tetrahydrate in 1,2-propanediol. Secondly, the precipitated powders were recovered, washed with ethanol, and then fired at various temperatures ranging from 250°C to 800°C. These samples will be referred to as $\text{Co}_3\text{O}_{4(250)}$ and $\text{Co}_3\text{O}_{4(800)}$ samples, respectively. 250°C is the temperature needed (as determined by TGA measurement) to ensure a total combustion of the structural organic molecules. The x-ray powder patterns of the annealed samples indicated the appearance of broad peaks, characteristic of the spinel phase in the 250°C sample that increased in amplitude and sharpened with increasing temperature. From the Scherrer equation, we noted that the crystallite size evolved with temperature, and increased from about 150 Å to at least 800 Å. This particle coarsening resulted in a 60 m²/g to about 3 m²/g BET specific surface area decrease when increasing the sample annealing temperature. The most astonishing result concerns the maintenance (Figure 7.11) of the precursor spherical particles through the annealing process. Note also the very narrow size distribution of the particles constituting the agglomerates. Such tailor-made Co_3O_4 particles were the ingredient of our *in situ* X-ray electrochemical studies.

In situ X-ray $\text{Co}_3\text{O}_4/\text{Li}$ cells based on $\text{Co}_3\text{O}_{4(800)}$ powders were made and discharged at various current rates. We note (Figure 7.12) the appearance of a $\text{Li}_x\text{Co}_3\text{O}_4$ phase for discharging current rates ranging from C/6 to C/25, and its disappearance, at the expense of a CoO phase, as the discharge current was lowered to C/75. Similarly, *in situ* X-ray cells having Co_3O_4 samples, annealed at various temperatures, were discharged at the same (C/12) current rate. The XRD patterns collected during the discharge of a $\text{Co}_3\text{O}_{4(250)}/\text{Li}$ and $\text{Co}_3\text{O}_{4(800)}/\text{Li}$ cells exhibited, respectively, the sole presence of CoO Bragg peaks and $\text{Li}_x\text{Co}_3\text{O}_4$ Bragg peaks. A common denominator to these observed effects is the current density sensed by the particle, with the overall result being that high density favours Li insertion, to the expense of decomposition reactions. Hence Thackeray's difficulties encountered in achieving a pure

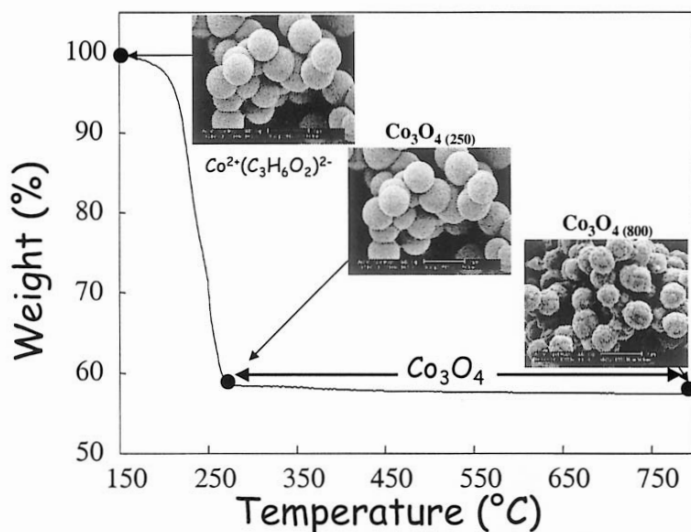


Figure 7.11. Weight loss, as determined by thermo gravimetric analysis, for a home synthesized Co glycolate precursor that was heated at a 10°C/min. rate. SEM micrographs shown for the initial precursors as well as for materials annealed at 250°C and 800°C, respectively.

lithium-phase, whatever the chemical used or electrochemical approaches. Under reducing conditions and using a strong reducing agent such as *n*-butyllithium, which to a certain extent mimics a cell short circuit (*e.g.*, high current density), his chemically prepared samples always contained large amounts of $\text{Li}_x\text{Co}_3\text{O}_4$.

These findings indicate that the nature of the intermediates, when Co_3O_4 is electrochemically reduced *vs.* Lithium, is rate/surface dependent. The intercalated $\text{Li}_x\text{Co}_3\text{O}_4$ formation suggests that kinetic limitations lower its stability voltage far below the over voltage of the $\text{Co}_3\text{O}_4 \rightarrow \text{CoO}$ reaction. Such a poor kinetic is nested in structural aspects that are peculiar to spinel structures. Indeed, the insertion of Li into Co_3O_4 necessitates the migration of Co ions from the 8a to the 16c sites (spinel \rightarrow rock-salt). This Li-driven migration of Co^{+2} from 8a to 16c sites is energetically costly, and competes with the Co_3O_4 decomposition reaction associated to the departure of oxygen leading to CoO, which will then decompose into Co. A similar path was shown to occur for Mn_3O_4 that either decomposes into MnO or intercalates Li to $\text{Li}_x\text{Mn}_3\text{O}_4$.

Thus, an open question is whether such findings regarding the importance of particle size on Li-driven reactivity paths could be generalized to other oxides differing from the spinel structure. As a tentative answer, we

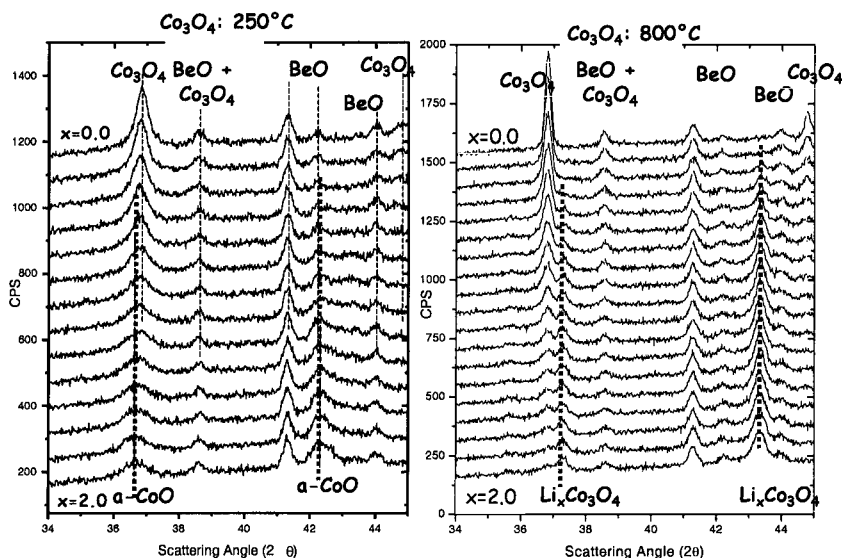


Figure 7.12. *In situ* X-ray data for CoO/Li cells discharged at very low current drains (C/12) close to equilibrium at a C rate. The cells contained either CoO_{250} or CoO_{800} electrodes.

decided to investigate Fe-based oxides, and more especially $\alpha\text{-Fe}_2\text{O}_3$ (hematite), which has the corundum structure, and is known to switch from a hexagonal compact to a cubic, close-packed oxygen array at a Li concentration lower than 0.1 per unit formula.

7.3.4.2. $\alpha\text{-Fe}_2\text{O}_3$

Two batches of $\alpha\text{-Fe}_2\text{O}_3$ (hematite), referred to as $M\text{-Fe}_2\text{O}_3$ (for micrometric) and $n\text{-Fe}_2\text{O}_3$ (for nanometric), were used in this study: $M\text{-Fe}_2\text{O}_3$ is a commercial sample (Aldrich or Prolabo), and $n\text{-Fe}_2\text{O}_3$ is a homemade powder prepared by forced hydrolysis in acidic medium. More specifically, ferric nitrate hydrate $\text{Fe}(\text{NO}_3)_3 \cdot 9\text{H}_2\text{O}$ was progressively dissolved in a HNO_3 aqueous solution that was heated in a glass vessel under magnetic stirring, and refluxed at boiling point for 24 hours. Then, the recovered reddish brown powder was thoroughly washed and dried prior to being investigated.

Aside from some slight deviations in the relative peaks intensities, the XRD patterns for $M\text{-Fe}_2\text{O}_3$ and $n\text{-Fe}_2\text{O}_3$ (Figure 7.13) perfectly match that of

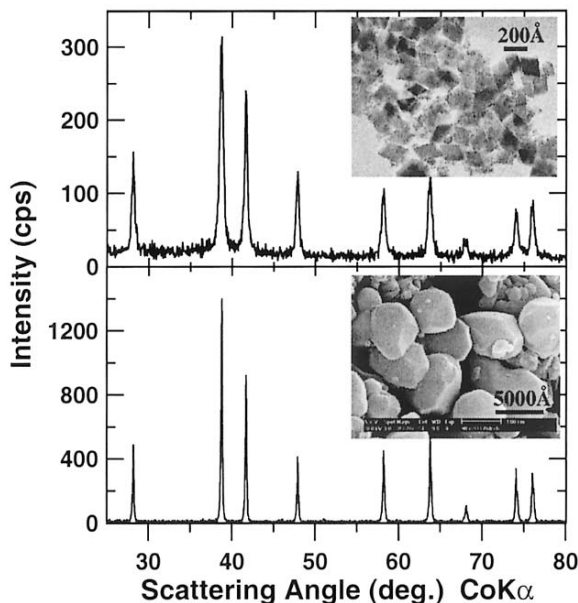


Figure 7.13. X-ray powder patterns for commercial and home-synthesized α - Fe_2O_3 together with, as inset, the SEM image for both samples.

α - Fe_2O_3 . While structurally similar, these two samples strongly differ in the width of their Bragg reflections. From the Scherrer's equation, we estimated the mean crystallite size at about 200 Å for n - Fe_2O_3 , and at least 1000 Å for M - Fe_2O_3 . By TEM, the lozenge-shaped n - Fe_2O_3 particles were found to be monolithic and very small (200 Å), in total agreement with the crystallite size deduced from XRD analysis. M - Fe_2O_3 particles are much larger (0.5 μm in mean diameter), as shown by SEM images. The measured BET specific surface areas are 60 m^2/g and 2 m^2/g for n - Fe_2O_3 and M - Fe_2O_3 .

The first electrochemical discharge curves collected at C/5 rate for the two hematite samples previously described are presented in Figure 7.14. When discharged down to 0 Volt, 7.2 Li per M - Fe_2O_3 and 8.3 Li per n - Fe_2O_3 can be reacted, corresponding to capacities of 1200 and 1400 mAh/g. Both discharge curves show a nicely developed and long voltage plateau lying below 1.0 Volt, until an x value of about 6 (x in " $\text{Li}_x\text{Fe}_2\text{O}_3$ "), in agreement with the theoretical capacity for the $\text{Fe}^{3+} \rightarrow \text{Fe}^0$ reaction, is reached. The larger excess in capacity measured for n - Fe_2O_3 is consistent with its much larger specific surface area, when compared to that of M - Fe_2O_3 .

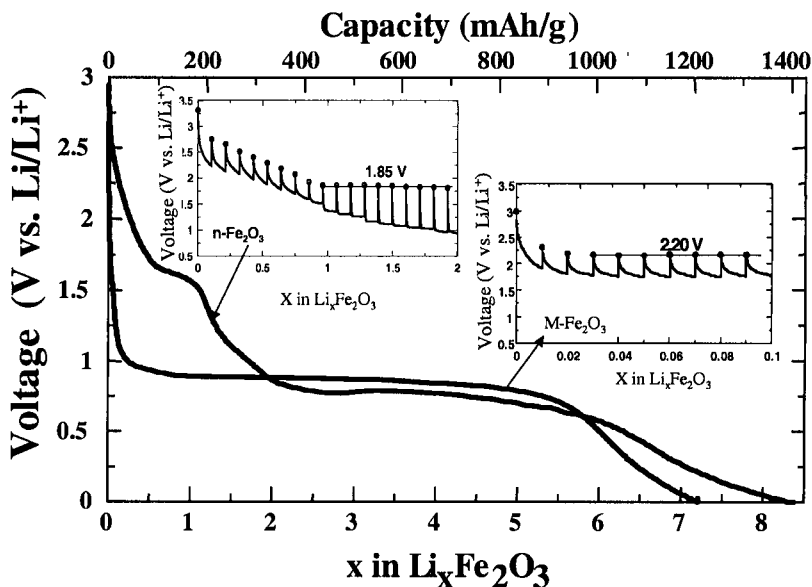


Figure 7.14. First discharge for α - Fe_2O_3 /Li cells, using bulk or nano α - Fe_2O_3 as positive electrode, together with, as insets, the open circuit voltage measurements for similar cells.

However, the most relevant part of the curve, with respect to the importance of nano particles, lies at low x values. Indeed, note that the onset of the 1 V plateau is very quickly reached for M - Fe_2O_3 ($x = 0.1$), while it occurs at $x=2$ for n - Fe_2O_3 , suggesting a different Li reactivity mechanism between the two samples. To better isolate such differences, PITT experiments were conducted on n - Fe_2O_3 and M - Fe_2O_3 up to $x=2$. Within this composition domain, the reduction of n - Fe_2O_3 clearly proceeds in two steps. First, a monophasic process characterized by a continuous decrease in the quasi-equilibrium OCV is observed up to x close to 1, and then a biphasic reaction characterized by a constant equilibrium voltage close to 1.85 Volts.

The Li reactivity difference was well diagnosed by *in situ* X-ray measurements (Figure 7.15), with a continuous shift of the hematite Bragg peaks towards low angles for the n - Fe_2O_3 sample, as compared to a progressive vanishing of the hematite Bragg peaks for M - Fe_2O_3 reflections, at the expense of a new set of reflections. These extra peaks, that were indexed within a cubic symmetry having an axis of 8.422 Å, were found to correspond to a Li-Fe-O rock-salt compound described by Thackeray *et al.*⁵⁰ and not to a FeO rock-salt phase (as confirmed by EXAFS and Mössbauer), that should have an a axis of 4.31 Å (*e.g.*, $2a = 8.62$ Å).

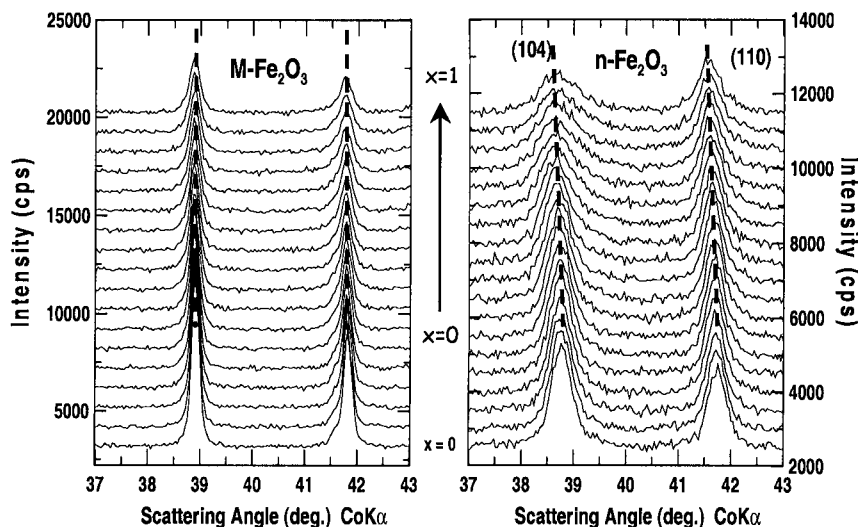


Figure 7.15. *In situ* X-ray data for $\alpha\text{-Fe}_2\text{O}_3/\text{Li}$ cells, using either bulk or nano $\alpha\text{-Fe}_2\text{O}_3$ as positive electrode. For reasons of clarity, only part of the pattern ($33^\circ < 2\theta < 43^\circ$) depicting the evolution of the 104 and 110 Bragg peaks as a function of the amount of reacted Li is shown. Note a disappearance of these peaks for the bulk sample, as compared to a shift for the nano-material.

Thus, from these measurements, it appears that up to one Li per formula unit can be inserted into the $\alpha\text{-Fe}_2\text{O}_3$ corundum structure of $n\text{-Fe}_2\text{O}_3$, resulting in a 1% volume expanded $\alpha\text{-LiFe}_2\text{O}_3$ end-member phase, having the lattice parameters $a=5.041(1)\text{ \AA}$ and $c=13.815(2)\text{ \AA}$, while no lithium can be significantly inserted into $M\text{-Fe}_2\text{O}_3$. The feasibility of inducing reversible insertion reactions in $n\text{-Fe}_2\text{O}_3$, and not in $M\text{-Fe}_2\text{O}_3$, is mainly nested in the fact that small particles can more easily and uniformly expand to accommodate strains resulting from insertion reactions than larger ones.

Finally, when either $\text{Li}/n\text{-Fe}_2\text{O}_3$ or $\text{Li}/M\text{-Fe}_2\text{O}_3$ cells were cycled at C/5 rate between 1 and 3.5 V, we observed (Figure 7.16), as expected, that the ones containing nanometric Fe_2O_3 display a nicely reversible and sustained capacity upon cycling, while the other cells did not exhibit any sign of reversibility.

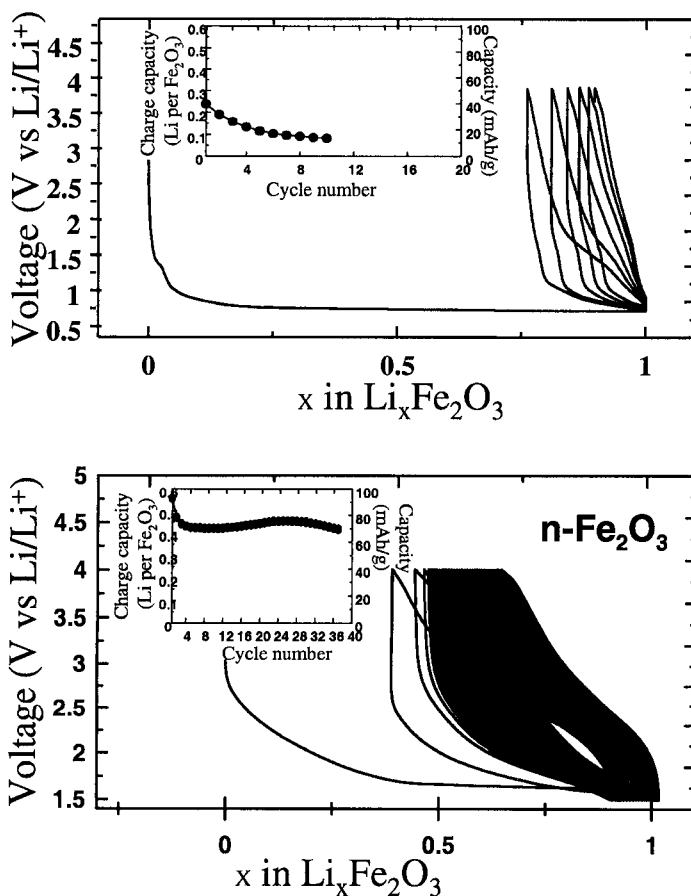


Figure 7-16. Voltage-composition profile for $\alpha\text{-Fe}_2\text{O}_3/\text{Li}$ cells, having bulk (upper) or nano (lower) $\alpha\text{-Fe}_2\text{O}_3$ as the positive electrode. Their capacity retention upon cycling is shown by the insets.

Worth mentioning is the large irreversibility displayed by the $\text{Li}/n\text{-Fe}_2\text{O}_3$ cell, whose origin still remains precisely undetermined, while there is strong suspicion for the presence of chemical groups, specific to the $n\text{-Fe}_2\text{O}_3$ synthesis process, that remain adsorbed at the surface of the highly divided powders. Further studies must be carried out to sort out this issue. Nevertheless, throughout this work we stressed the importance of particle size in controlling Li reactivity mechanisms. We also resolved to unravel potential electrode materials that were thus far disregarded. As time elapses, numerous examples, which further emphasise the wonders of nano compounds in igniting unexpected reactions, appear. They encompass

oxides, nitrides, fluorides and sulphides, and another family of materials like intermetallics. For instance, our group recently reported that the reactivity of CoSb_3 towards Li is reversible. Although Co-Sb bonds are broken during the discharging process, leading to a full disintegration of the CoSb_3 structural framework into Co and Li_3Sb nano particles, we show that upon recharge these destroyed bonds, due to the high reactivity of the divided metal nano particles, reformed and arranged to convert back to the initial CoSb_3 structure⁵¹. Such an example, also observed with Cu_6Sn_5 ⁵², further contrasts with previous beliefs that bond-breakings were prohibited for reversible Li-reactivity.

7.4. CONCLUSIONS

We have shown, through a few descriptive examples, how the field of nano materials can unravel novel reactivity mechanisms so far not expected to occur at the macroscopic scale. These mechanisms are of tremendous importance, since, for instance, the reported reversible reactivity of 3d metal oxides towards Li was shown to be universal, and to apply to a wide family of compounds. Furthermore, although we limited ourselves to electrode materials, size confinement can also positively affect other battery components, such as electrolyte, current collectors and others. On that issue, we recalled a few recent reports that dealt with the positive attributes of adding TiO_2 or Al_2O_3 nano-particles to polymer electrolyte. This would enhance their conductivity several times. Consider also the make-up of nano-structured electrodes to bypass electronic limitation. The awareness of the importance of nano materials is rapidly growing within the battery community. A new path of opportunities has been opened. In the quest for new electrode materials, we no longer need materials with good electronic conductivity or open structures. Thus, a large variety of previously disregarded compounds are worth revisiting. As a new field is opened, its understanding suffers from the lack of theoretical support to build on. Building this theoretical platform on nano driven Li electrochemistry stands as a great challenge that requires interactive studies between chemists, electrochemists and theorists. An exciting adventure awaits us....

ACKNOWLEDGMENTS

The authors would like to give special thanks to L. Dupont, M. Dollé, C. Payen, F. Badway, and I. Plitz for their contribution to some of the presented data.

REFERENCES

1. M.B. Armand, New Electrode Materials, in *Fast Ion Transport in Solids* (Van Gool, W., Ed., North Holland, Amsterdam) (1973) 665.
2. M. S. Whittingham, *Science* 192 (1976) 1226 .
3. D. W. Murphy, P.A. Christian, *Science* 205 (1979) 651.
4. A. R. Armstrong, P.G. Bruce, *Nature* 381 (1996) 499.
5. B. Ammundsen, J. Desilvestro, T. Groutso, D. Hassel, J.B. Metson, E. Regan, R. Steiner, P.J. Pichering, *ECS Fall Meeting*, Hawai, Abstract N°138 (1999).
6. A.K. Padhi, K.S. Nanjundaswamy, C. Masquelier, J.B. Goodenough, *J. Electrochem. Soc.* 144 (1997) 1609.
7. Y. Idota, T. Kubota, A. Matsufuji, Y. Maekawa, T. Miyasaka, *Science* 276 (1997) 1395 .
8. I.A. Courtney, J.R. Dahn, *J. Electrochem. Soc.* 144 (1997) 2045.
9. O. Mao, R.A. Dunlap, J.R. Dahn, *J. Electrochem. Soc.* 146 (1999) 405.
10. K.D. Kepler, J.T. Vaghey, M.M. Thackeray, *Electrochem. Solid-State Lett.* 7 (1999) 307.
11. N. Pereira, L.C. Klein, G.G.Amatucci, *J. Electrochem. Soc.* 149 (2002) A262.
12. R. Alcantara, F. J. Fernandez-Madrigal, P. Lavela, J. L. Tirado, J-C. Jumas, J. Olivier-Fourcade, *J. Mater. Chem.* 9 (1999) 2517.
13. V. Pralong, D.C.S. Souza, K.T. Leung, L.F. Nazar, *Electrochem. Comm.* 4 (2002) 516.
14. P. Poizot, S. Laruelle, S. Grugeon, L. Dupont, J.-M. Tarascon., *Nature* 407 (2000) 496.
15. G.G. Amatucci, J.M. Tarascon, L.C. Klein, *J. Electrochem. Soc.* 143 (1996) 1114.
16. R. Bates, Y. Jumel, *Lithium batteries* J. P. Gabano Ed., Academic Press, London (1983).
17. Y. Matsuda, K. Teraji, Y. Takasu, *Denki Kagaku* 44 (1976) 363.
18. P. Novák, *Electrochim. Acta* 30 (1985) 1687.
19. C. Sigala, D. Guyomard, Y. Piffard, M. Tournoux, *C.R. Acad. Sci. Paris II* 320 (1995) 523.
20. P. Poizot, E. Baudrin, S. Laruelle, L. Dupont, M. Touboul, J-M. Tarascon, *Solid state Ionics* 138 (2000) 31.
21. E. Baudrin, S. Denis, F. Orsini, L. Seguin, M. Touboul, J-M. Tarascon, *J. Mater. Chem.* 9 (1999) 101.
22. S. Denis, E. Baudrin, F. Orsini, G. Ouvrard, M. Touboul, J-M. Tarascon, *J. Power Sources* 81-82 (1999) 79.
23. E. Baudrin, S. Denis, S. Laruelle, M. Touboul, J-M. Tarascon, *Solid State Ionics* 123 (1999) 139.
24. S. Laruelle, P. Poizot, E. Baudrin, V. Briois, M. Touboul, J-M.Tarascon, *J. Power Sources* 97-98 (2001) 251.
25. P. Poizot, S. Laruelle, S. Grugeon, L. Dupont, J.-M.Tarascon., *Nature* 407 (2000) 496.
26. P. Poizot, S. Laruelle, S. Grugeon, L. Dupont, B. Beaudoin, J-M. Tarascon, *C.R. Acad. Sci. Paris II*, 3 (2000) 681.
27. P. Poizot, S. Laruelle, S. Grugeon, L. Dupont, J-M. Tarascon, *Ionics* 6 (2000) 321.
28. S. Grugeon, S. Laruelle, R. Herrera-Urbina, L. Dupont, P. Poizot, J-M. Tarascon, *J. Electrochem. Soc.* 148 (2001) A285.
29. A. Débart, L. Dupont, P. Poizot, J-M. Tarascon, *J. Electrochem. Soc.* 148 (2001) A1266.
30. P. Poizot, S. Laruelle, E. Baudrin, S. Denis, M. Touboul, J.-M. Tarascon, *J. Power Sources* 97-98 (2001) 235.
31. N.N. Obrovac, R.A. Dunlap, R.J. Sanderson, J.R. Dahn, *J. Electrochem. Soc.* 148 (2001) A576.
32. M.M. Thackeray, W.I.F. David, J.B. Goodenough, *Mat. Res. Bull.* 17 (1982) 785.
33. M.M. Thackeray, W.I.F. David, J.B. Goodenough, *J. Solid-State Chem.* 55 (1984) 280.

34. *Standard Potentials in Aqueous Solution*, A.J. Bard, R. Parsons, J. Jordan, Eds., Marcel Dekker (1985).
35. O. Kubaschewski, C. B. Alcock, *Metallurgical Thermochemistry*, 5th Edition, Pergamon Press (1987)
36. S. Laruelle, S. Grugeon, P. Poizot, M. Dollé, L. Dupont, J.-M. Tarascon, *J. Electrochem. Soc.* 149 (2002) 627.
37. P. Poizot, S. Laruelle, S. Grugeon, J.-M. Tarascon, *J. Electrochem. Soc.* 149 (2002) 627.
38. M. Dollé, P. Poizot, L. Dupont, J.-M. Tarascon, *Electrochem. Solid-State Lett.* 5 (2002) A18.
39. S. Grugeon, S. Laruelle, J.-M. Tarascon, *J. Electrochem. Soc.* submitted (2002).
40. N. Pereira, L.C. Klein, G.G. Amatucci, *ECS and ISE Joint International Meeting*, San Francisco, CA, Sept. 2001, paper 203.
41. N. Pereira, L. Dupont, J.-M. Tarascon, L. Klein, G.G. Amatucci, *J. Electrochem. Soc.* (in press).
42. F. Badway, I. Plitz, S. Grugeon, S. Laruelle, M. Dollé, A.S. Gozdz, J.-M. Tarascon, *Electrochem. Solid-State Lett.* 5 (2002) A115.
43. A. Delahaye-Vidal, B. Beaudoin, M. Figlarz, *Reactivity Solids* 2 (1986) 223.
44. W.I.F. David, J.B. Goodenough, M.M. Thackeray, M.G.S.R. Thomas, *Rev. Chim. Miner.* 20 (1983) 636.
45. M.M. Thackeray, W.I.F. David, J.B. Goodenough, *Mat. Res. Bull.* 17 (1982) 785.
46. M.M. Thackeray, W.I.F. David, P.G. Bruce, J.B. Goodenough, *Mat. Res. Bull.* 18 (1983) 461.
47. M.M. Thackeray, S.D. Backer, K.T. Adendorff, *Solid State Ionics* 17 (1985) 175.
48. D. Larcher, G. Sudant, J.-B. Leriche, Y. Chabre, J.-M. Tarascon, *J. Electrochem. Soc.* 149 (2002) A234.
49. D. Larcher, C. Masquelier, D. Bonnin, Y. Chabre, V. Masson, J.-B. Leriche, J.-M. Tarascon, *J. Electrochem. Soc.* submitted (2002).
50. M.M. Thackeray, J. Coetzer, *Mat. Res. Bull.* 16 (1981) 591.
51. J.-M. Tarascon, M. Morcrette, L. Dupont, Y. Chabre, C. Payen, D. Larcher, V. Pralong, *J. Electrochem. Soc.* in press (2003).
52. D. Larcher, L.Y. Beaulieu, O. Mao, A.E. George, J.R. Dahn, *J. Electrochem. Soc.* 147 (2000) 1703.

Chapter 8

NITRIDE AND SILICIDE NEGATIVE ELECTRODES

G. G. Amatucci and N. Pereira

Telcordia Technologies, 331 Newman Springs Road, Red Bank, NJ 07701, U.S.A.

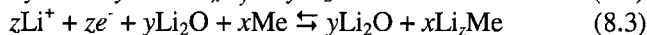
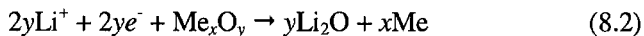
8.1. INTRODUCTION

The search for negative electrode materials which exhibit improved electrochemical properties relative to the widely used graphite intercalation materials has lead to a renaissance of research on inorganic negative electrodes.

The intercalation of Li^+ into graphite follows the basic topotactic insertion process:

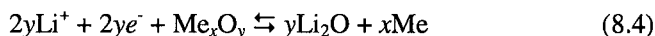


Beyond basic binary lithium alloys, a large focus has been on the development of conversion oxides. The conversion oxides Me_xO_y , as discussed in a previous chapter, consist of metals (Me) which can alloy with lithium. Upon the first lithiation, an electrochemically induced conversion process occurs creating a nanostructure consisting of nanodomains of Me in a matrix of nonstructured Li_2O (8.2):



The combination of the nanosized metal and buffer matrix of Li_2O leads to reversible alloying reactions (8.3) that have much improved reversibility than traditional Li_xMe alloys. More recent studies have focused on the use of Me_xO_y initial materials in which Me is a metal which does not support alloying reactions with Li. These materials were found to convert during the cathodic scan analogous to reaction (8.2); however this

conversion reaction was found to be reversible (8.4):



The quest for new inorganic anodes has recently proceeded into areas which have been largely ignored, namely, nontraditional Me_xX_y materials, where the anion X is N or P. The number of papers on these type of materials is relatively small, but nonetheless the electrochemistry is found to be surprisingly rich and somewhat exotic. In this chapter, we take a close look at the work that has been done to this point on binary and ternary metal nitrides along with a look at the often overlooked metal silicides.

8.2. THE NITRIDES

8.2.1. The Ternary Nitrides

8.2.1.1. The Antifluorites ($\text{Li}_{2x-1}\text{MN}_x$)

Metal nitrides have been investigated for their properties related to fast lithium ion conduction for the past two decades. The most famous of these nitrides is the highly conducting $\text{Li}_3\text{N}^{1-7}$ which exhibits ionic conductivity on the order of $1 \cdot 10^{-2}$ S/cm. A number of papers have been published on this material; however, because of its poor resistance to anodic decomposition at high potentials, it has found little use as a solid state ionic conductor in a practical cell. In spite of this drawback, the initial work spurred interest in the investigation of alternative nitrides that could also support appreciable ionic conductivity as a result of the low polarizability of the nitrogen anion. Many of these structures are related to $\text{Li}_{2x-1}\text{MN}_x$ which is based upon the antifluorite structure. Containing pathways for facile ion movement, these materials exhibited appreciable Li^+ conductivity. Materials such as Li_3BN_2 ,⁸ Li_5SiN_3 ,^{9,10} and Li_3AlN_2 all share this structure type and have well established ionic activity. Due to their electronically insulative properties, these materials were investigated solely for use as solid state ionic conductors.

The facile movement of the lithium ions within the antifluorite structure gave rise to the question whether such structures could be utilized as faradaic insertion intercalation electrodes for lithium batteries. This issue was addressed by the use of transition metals as a substitute for M in $\text{Li}_{2x-1}\text{MN}_x$. The resulting $\text{Li}_{2x-1}\text{MN}_x$ structure gained appreciable electronic conductivity to parallel the existing ionic conductivity. The materials, due to the substitution, were mixed conductors, opening the possibility for their use

as negative electrode materials. In light of this, the electrochemical activity of $\text{Li}_{2x-1}\text{Mn}_x\text{N}_x$ materials were investigated particularly for materials containing $\text{M} = \text{Mn}$ or Fe .

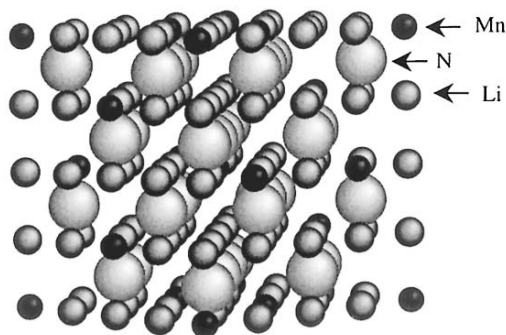


Figure 8.1. Crystal structure of Li_7MnN_4 from the [110] viewpoint. Dark spheres represent Mn.

Li_7MnN_4 can be fabricated through solid state reaction between Li_3N and Mn or Mn_4N in a N_2 atmosphere. The material crystallizes in the cubic antiperfluorite structure built of isolated MnN_4 tetrahedra where Mn and Li are located on tetrahedral sites (Figure 8.1). Li and Mn are present in ordered arrangements with clearly observable three dimensional pathways for diffusion. Despite the high formal charge associated with the Mn cation (Mn^{5+}), the structure is prelithiated; therefore, the cycling of the material commences with lithium extraction. This feature makes it particularly useful for Li-ion batteries utilizing non-lithiated positive electrodes. The delithiation of Li_7MnN_4 was found to proceed to $\text{Li}_{5.45}\text{MnN}_4$, centered on plateaus at approximately 1.15 V (Figure 8.2). The initial 0.625 lithium extracted corresponded to a two-phase delithiation in a unit cell with same symmetry but different lattice parameter. The remaining lithium was removed in a single-phase reaction. The structural transformations are reversible and the material cycles well with a stable 300 mAh/g specific capacity.

In Li_7MnN_4 the Mn cation exhibits an unusually high nominal charge of Mn^{5+} . Even more surprising, assuming an ionic model, the Mn cation proceeds to a mixed oxidation state of $\text{Mn}^{6+}/\text{Mn}^{7+}$ upon charge. These unusual electronic attributes combined with the material's relatively low insertion potential of 1.2 V spurred Suzuki and coworkers¹¹ to a deeper investigation of the electronic attributes of the material leading to its active electrochemistry.

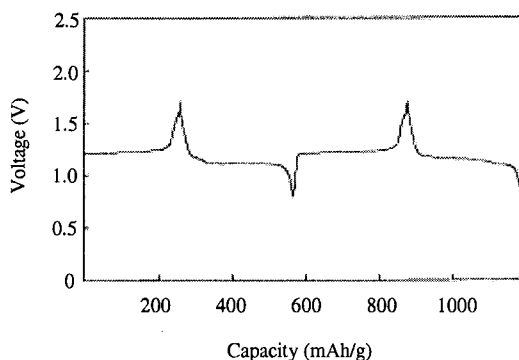


Figure 8.2. Voltage profile of Li_7MnN_4 (from Ref. 12).

The investigation was accomplished through the use of core level electron energy loss spectroscopy. It was found that in the ground state, there exist a number of holes on the N 2p band. This is consistent with the strong hybridization of the Mn 3d and N 2p orbitals associated with the covalency of the compound. Analysis of the lithium deintercalated $\text{Li}_{7-x}\text{MnN}_4$ where $x=1$ revealed a strong growth in the N-K spectra related to the amount of 2p unoccupied states. Simply stated, lithium deintercalation proceeds with an oxidation reaction introducing holes into the nitrogen 2p orbitals. This is in stark contrast to the classical situation where holes are introduced into the transition metal (manganese) 3d orbitals. Therefore, one can make the generalization that the electronic redox is centered on the N rather than Mn and explains the low redox voltages associated with the Li_7MnN_4 electrode materials.

As opposed to Li_7MnN_4 , Li_3FeN_2 crystallizes in orthorhombic symmetry. However, fundamental similarities exist as the structure is a distorted form of the antifluorite structure. The structure can be simply characterized as Fe_4N tetrahedra sharing edges to form one-dimensional chains along the c direction.

The structural evolution during delithiation was characterized in depth by Nishijima and coworkers.¹² Delithiation occurred at approximately 1.2 V in the range of Li_3FeN_2 to Li_2FeN_2 . Four phases appeared during the delithiation reaction, all were of orthorhombic symmetry. Relithiation occurred with systematic redevelopment of the phases evolved during delithiation. The reversible lithiation processes occurred with little over/under potential and the crystallinity of the material is maintained for $x < 1$. It should be noted that delithiating $\text{Li}_{3-x}\text{FeN}_2$ beyond Li_2FeN_2 resulted in the decomposition of the crystal structure.

Question still remains to the electronic basis of the redox reaction of Li_3FeN_2 . Nishijima *et al.* concluded that the redox was classical and centered on the reversible $\text{Fe}^{3+} \rightarrow \text{Fe}^{4+}$ reaction. This conclusion was centered on results of Mossbauer spectroscopy. Half a decade later, Suzuki *et al.* realized many similarities related to the structural electrochemical features of Li_3FeN_2 and believed the electronic reaction to be similar to that of Li_7MnN_4 (N centered electronic redox) although no supporting spectra was offered.

8.2.1.2. The Hexagonal $\text{Li}_2(\text{Li}_{1-x}\text{M}_x)\text{N}$ Structures

The second major class of ternary lithium transition metal nitrides exists in a structure which is isostructural with the well known Li_3N lithium ion conductor. These materials take the stoichiometric form of $\text{Li}_2(\text{Li}_{1-x}\text{M}_x)\text{N}$ or in its better known notation, $\text{Li}_{3-x}\text{M}_x\text{N}$, where $\text{M} = \text{Co}, \text{Cu}, \text{and Ni}$.¹³ The basic structure (Figure 8.3) can be simply envisioned as Li^+ between layers of Li_2N^{1-} . The transition metal cations substitute for the Li between the layers; however, it should be noted that this site is slightly unusual as it consists of a linear N-M-N bond along the c axis and is not octahedral or tetrahedral in nature. From an electrochemical standpoint, the most promising and most studied of the transition metal substitutions is Co.¹⁴

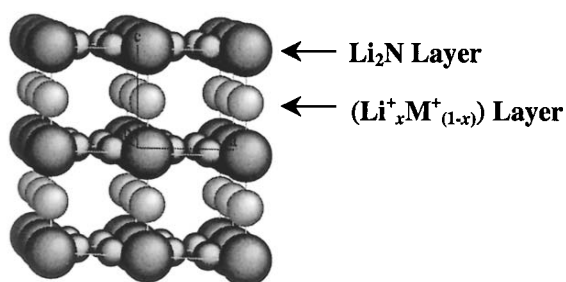


Figure 8.3. Schematic of $\text{Li}_2(\text{M}_{1-x}\text{M}_x)\text{N}$ structure.

$\text{Li}_{3-x}\text{Co}_x\text{N}$ materials can be prepared by the reaction of Li_3N and Co metal under a N_2 -based atmosphere. The solid solution range for $\text{Li}_{3-x}\text{Co}_x\text{N}$ is $0 \leq x \leq 0.5$. It was quickly identified that the optimum specific capacity could be realized from a composition of $\text{Li}_{2.6}\text{Co}_{0.4}\text{N}$.

Small amounts of Li can be inserted into $\text{Li}_{3-x}\text{Co}_x\text{N}$ during the initial discharge reaction between 0.5 and 0.1 V (Li/Li^+). The amount of lithium

inserted is related to Li vacancy population but the specific capacity does not exceed 100 mAh/g. Practically speaking, $\text{Li}_{2.6}\text{Co}_{0.4}\text{N}$ can be treated as being in the lithiated state; therefore, lithium must be deintercalated from the structure in an initial anodic oxidation. During the first charge, $\text{Li}_{2.6}\text{Co}_{0.4}\text{N}$ enables the removal of approximately 800 mAh/g of charge at an extended plateau at 1.1 V corresponding to a delithiated composition of approximately $\text{Li}_{1.0}\text{Co}_{0.4}\text{N}$. Subsequent discharge and charge results in the reversible insertion of 800 mAh/g from 1.5 to 0.1 V (Figure 8.4). After the initial delithiation cycle, subsequent delithiations remove capacity in a

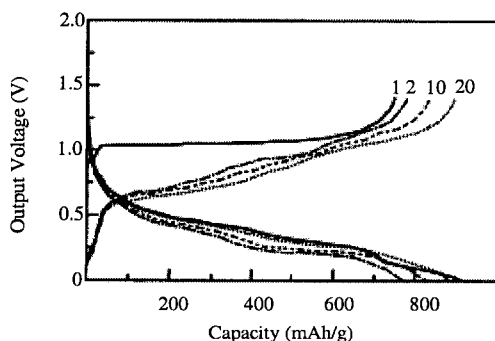


Figure 8.4. Voltage profile of $\text{Li}_{2.6}\text{Co}_{0.4}\text{N}$ vs. Li metal counter electrode. Cycle numbers are indicated (from Ref. 15).

pseudolinear profile at voltages between 0.5 and 1.1 V. Excellent cycling stability is observed for this material.

Ex-situ X-ray diffraction revealed that the delithiation reaction proceeds topotactically for $\Delta x=1$ in $\text{Li}_{2.6-x}\text{Co}_{0.4}\text{N}$. In this region the reversible specific capacity is 480 mAh/g and the crystal structure does tend to become amorphous with cycle number. More recent data¹⁵ suggests the initial delithiation reaction proceeds concurrent with a systematic and gradual loss of crystallinity. Regardless, extending the initial lithium removal to $\Delta x=1.46$ results in the systematic destruction of the crystal structure and formation of an X-ray amorphous compound. It is easy to understand from the inspection of the crystal structure (Figure 8.3) how excess Li^+ deintercalation can lead to its destabilization and loss of crystallinity. Subsequent cycles revealed an impressively stable specific capacity of approximately 800 mAh/g. To gain more insight on the faradaic activity leading to the electrochemical activity of $\text{Li}_{2.6}\text{Co}_{0.4}\text{N}$, a more localized investigation of the electronic structure of the material had to be taken by alternative techniques.

As with the Li_7MnN_4 antifluorite material discussed in the previous section, a number of mysteries exist with respect to the electronic structure of the optimized $\text{Li}_{2.6}\text{Co}_{0.4}\text{N}$. Utilizing a basic ionic stoichiometry model, the charge distribution of $\text{Li}_{2.6}\text{Co}_{0.4}\text{N}$ should be $\text{Li}^{1+}_{2.6}\text{Co}^{1+}_{0.4}\text{N}^{3-}$. Although monovalent cobalt is very rare, characterization by EELS¹⁶ revealed surprising data consistent with the existence of the monovalent cobalt cation. Utilizing this stoichiometric model, delithiation to $\text{Li}_{1.0}\text{Co}_{0.4}\text{N}$ would require Co to adopt the even more unusual Co^{5+} oxidation state. EELS measurements were performed on the fully delithiated sample. Figure 8.5 shows the N-K spectra of that sample. The band at 403.5 eV is ascribed to the hybridization of the nitrogen 3p band with the lithium 2s band. The

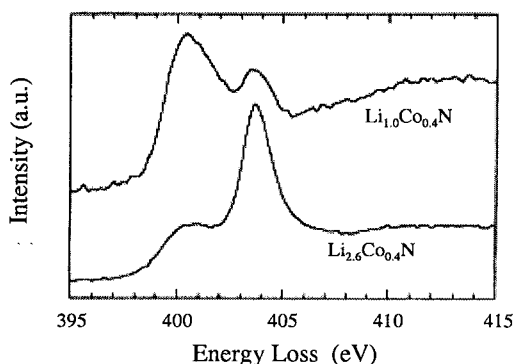


Figure 8.5. N-K EELS spectra of lithiated and delithiated $\text{Li}_{2.6}\text{Co}_{0.4}\text{N}$ (from Ref. 15).

delithiated $\text{Li}_{2.6-x}\text{Co}_{0.4}\text{N}$ sample reveals an expected decrease of the 403.5 eV peak consistent with the removal of Li and subsequent decrease of Li-N bonds.

The peak at 400 eV is associated to the unoccupied nitrogen 2p band. As lithium is removed the intensity increases drastically, consistent with the development of holes on the nitrogen 2p band during electrochemical delithiation. EELS analysis of the cobalt indicated the oxidation state to be approximately Co^{3+} after oxidation. This would require the removal of the remaining electrons from the nitrogen bands to effectively charge compensate. This interplay is clear from the schematic of the electronic structure of $\text{Li}_{2.6}\text{Co}_{0.4}\text{N}$. Therefore, like in the case of Li_7MnN_4 , the nitrogen anion plays a crucial role in the redox chemistry of $\text{Li}_{2.6}\text{Co}_{0.4}\text{N}$.

Other $\text{Li}_{3-x}\text{M}_x\text{N}$ based materials exist. Early on, $\text{Li}_{3-x}\text{M}_x\text{N}$ materials where $\text{M} = \text{Ni}$ or Cu were also investigated. These materials also crystallized in the space group of $P6/mmm$. The $\text{Li}_{2.6}\text{Cu}_{0.4}\text{N}$ sample exhibits good cycling

stability, on par with that of $\text{Li}_{2.6}\text{Co}_{0.4}\text{N}$. The copper compound revealed 650 mAh/g in the 0-1.3 V range. The Ni system, in contrast, was found to show a reversible specific capacity of only 180 mAh/g in the range of 0.0 to 1.4 V.

Most recently, a layered lithium nitride has been investigated in the pursuit of a less toxic and more cost effective negative electrode material.¹⁷ Li_4FeN_2 is a layered nitride with hexagonal Li_2N layers analogous to the $\text{Li}_{3-x}\text{M}_x\text{N}$ materials described above. A similar material $\text{Li}_2(\text{Li}_{0.7}\text{Fe}_{0.3})\text{N}$ ($\text{Li}_{2.7}\text{Fe}_{0.3}\text{N}$) was investigated for its electrochemical performance. The material exhibited 550 mAh/g at an average potential (between 0.05 and 1.2 V) of 0.6 V. Analogous to $\text{Li}_{2.6}\text{Co}_{0.4}\text{N}$, the structure decomposes to a quasi-amorphous state upon delithiation.

8.2.2. The Binary Nitrides

8.2.2.1. InN & Sn_3N_4

Some of the earliest work on binary nitrides as alternatives for graphite or Li has come by way of thin film work. One of the first compounds to be investigated was that of Sn_3N_4 .¹⁸ Sn_3N_4 films can be prepared by reactive sputtering of Sn in a Ar-N_2 gas mixture. The films crystallized in the hexagonal $P3m1$ space group expected for this material. Similarly, films of InN were deposited. The lithium reaction mechanism for both of these consisted of a straightforward conversion reaction to a Li_xSn or Li_xIn alloy embedded in a matrix of Li_3N . Subsequent specific capacity is developed through the alloying reaction with Sn or In, as Li_3N remains as a buffer matrix. As expected, the alloying reaction was found to give relatively poor cycling due to the electromechanical grinding induced by large volume changes within the alloy.

8.2.2.2. Ge_3N_4

Ge_3N_4 crystallizes in a hexagonal structure with large tunnels theoretically capable of lithium intercalation parallel to the c axis. Lithium was found to be able to reversibly react with Ge_3N_4 at a voltage of 0.25 V with a reversible capacity ranging from 500 to 1200 mAh/g depending on the crystallite size (Figure 8.6).¹⁹ Finer crystallites were found to offer much improved specific capacity. The low voltage at which Ge_3N_4 is electrochemically active makes it especially suitable for use as a negative electrode in Li-ion. The cycling stability of Ge_3N_4 was found to be quite good with less than 15% loss after 70 cycles (Figure 8.7). *In-situ* and *ex-situ*

XRD revealed that Ge_3N_4 experienced a large loss of crystallinity during the first discharge. This, combined with an irreversible loss of 30-50% active material and a 50% irreversible capacity loss, suggested a portion of the material converted during the first cycle concomitant with an alloy formation:

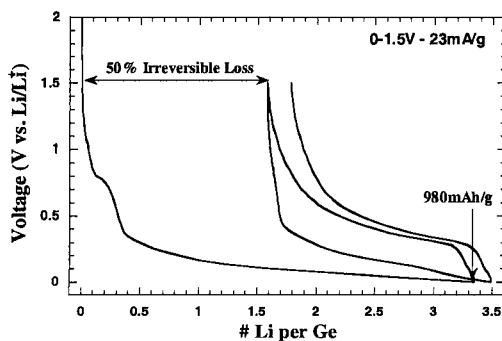
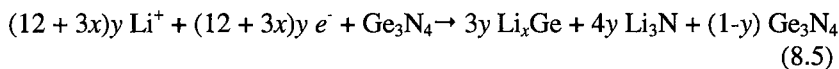


Figure 8.6. Voltage profile of crystalline Ge_3N_4 cycled vs. Li metal between 0 and 1.5 V at a constant current of 23 mA/g.

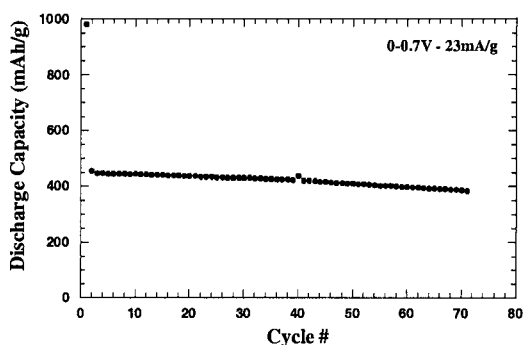
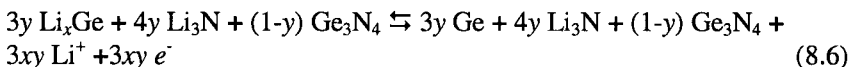


Figure 8.7. Cycle life of crystalline Ge_3N_4 cycled vs. Li metal between 0 and 0.7 V at a constant current of 23 mA/g.

The reaction products were of exceptionally low crystallinity and made characterization difficult.

The remaining cycles are believed to incorporate themselves within a reversible alloying reaction (8.6) (supported by selective area electron diffraction) on crystallites composed of alloy “shells” grown on core structures of unreacted Ge_3N_4 (Figure 8.8).



The X-ray amorphous nature of the alloy combined with a substrate of Ge_3N_4 is believed to bring about the uncharacteristically good cycling performance for an electrode based on lithium alloying.

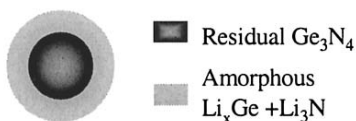
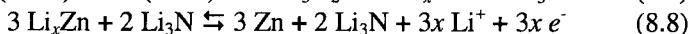
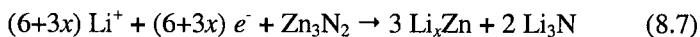


Figure 8.8. Schematic representation of a Ge_3N_4 particle exhibiting an unreacted Ge_3N_4 core surrounded by an electrochemically active converted shell.

8.2.2.3. Zn_3N_2

The electrochemical behavior of zinc nitride thin films versus metallic Li was first reported by Bates *et al.*²⁰ It was postulated that the reaction was similar to the irreversible conversion reaction taking advantage of the alloying properties of Zn. Zn metal alloys easily with Li and as such the Li-Zn phase diagram²¹ exhibits five alloys, LiZn_4 ,²² Li_2Zn_5 , LiZn_2 , Li_2Zn_3 and LiZn .



Recent analysis of powder Zn_3N_2 revealed finer attributes of the electrochemistry which was not initially obvious.²³ Zn_3N_2 reversibly reacts with lithium electrochemically, exhibiting a large reduction capacity of 1325 mAh/g corresponding to the insertion of 3.7 Li per Zn. Of this initial capacity, 555 mAh/g was found to be reversible. *In-situ* and *ex-situ* X-ray diffraction revealed the reaction mechanism with lithium was a conversion

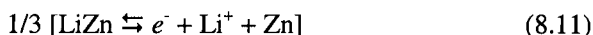
reaction of Zn_3N_2 into LiZn and a matrix of $\beta\text{Li}_3\text{N}$, the high-pressure analog of Li_3N :



Upon oxidation, LiZn transformed into metallic Zn, while $\beta\text{Li}_3\text{N}$ contributed to the transformation into LiZnN:



This reversible metal - Li_3N conversion mechanism is analogous to the mechanism (8.4) that was previously isolated to oxides and sulfides. Subsequent cycles proceed reversibly using the LiZnN and Zn as the precursor materials. Indeed, the true reaction could be best described as two parallel reactions, one consisting of the reversible alloying reaction of the base Zn material, and the second consisting of a reversible conversion of the LiZnN phase to the LiZn alloy plus Li_3N :



The formation of LiZnN as the new end member of the electrochemical reaction with lithium was identified as the cause of the irreversible loss observed during the first cycle. Therefore, LiZnN can be utilized as a negative electrode material from the beginning as it would exhibit 930 mAh/g with no initial irreversible capacity loss.

The cycle life of Zn_3N_2 was found to be poor. The poor cycle life was mainly attributed to the electromechanical grinding of the Li-Zn alloying reaction which contained appreciable volume change with alloy composition.

8.2.2.4. Cu_3N

Cu_3N crystallizes in the anti- ReO_3 cubic structure type. The structure consists of NCu_6 octahedra connected at the corners resulting in a 3D array with 3D tunnels. Cu_3N was found to involve a complex series of electrochemically induced transformations, of which the origins are not yet fully known.²⁴ The initial cathodic reduction of Cu_3N with Li^+ involved a three-step reaction mechanism (Figure 8.9). X-ray diffraction revealed that the lattice parameter was found to expand during the first step. This was

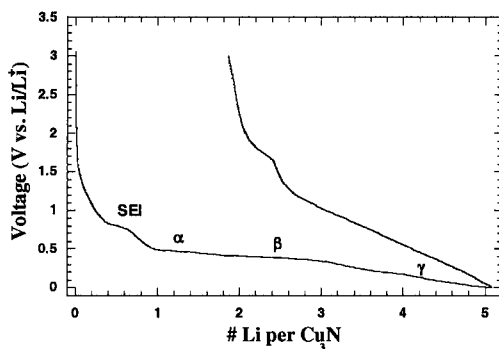
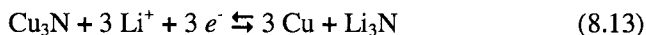


Figure 8.9. First cycle voltage profile of a Cu_3N electrode cycle vs. Li metal between 0 and 3 V at a constant current of 22.4 mA/g (equivalent to a C/6 rate).

consistent with lithium intercalation into the open structure of Cu_3N concurrent with copper displacement. Copper metal was detected by SAED in this region and the reaction was found to be irreversible. The second step of the electrochemical process was identified, using a combination of XRD, SAED and TEM, as the conversion of the remaining copper nitride into a $\text{Cu} + \text{Li}_3\text{N}$ nanocomposite which promoted the formation of an organic layer at the surface of the nanocomposite. The latter two processes were found to be reversible. The reversible nature of the $\text{Cu} + \text{Li}_3\text{N}$ nanocomposite is similar to that observed for the reversible nitride conversion mechanism of Zn_3N_2 .



Cu_3N electrodes showed excellent cycling efficiency at high rate (equivalent to 1.67 C) (Figure 8.10). Extended cycling seemed to promote the development of electrochemical processes above 2V during delithiation whereas the cycling stability of the copper nitride conversion process was found to be poor. These seem to be associated with the formation during delithiation of Cu_2O and CuO believed to be rooted in electrolyte degradation. The reversible copper oxide conversion processes may contribute to the increase in capacity with cycle number.

8.2.3. Summary - Nitrides

The metal nitrides exhibit an exceptionally wide range of reaction mechanisms with lithium, ranging from metal nitride conversion and subsequent lithium alloying, reversible conversion, redox reactions

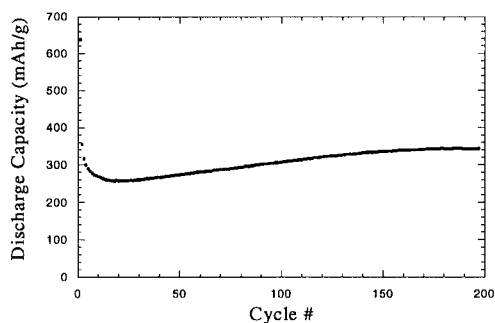


Figure 8.10. Cycle life of Cu_3N cycled vs. Li metal between 0 and 3 V at a rate equivalent to 1.67 C.

associated to the anion, to simple topotactic insertion. The reaction mechanisms of these materials are closely tied to the electronic configuration and thermodynamic stability of the phases upon reduction. Some of the metal nitrides' uniqueness is a result of the low electronegativity and covalent character of the nitrogen atom. This places the Fermi level close to that of the nitrogen 2p bands as opposed to the transition metal 3d bands normally encountered in oxides. These materials have also presented to the researchers an added complexity to material characterization to uncover these mechanisms as many of them occur within quasi-amorphous structures.

It is still too soon to comment on the expected viability of metal nitrides as negative electrodes in Li-ion batteries of the future. However, $\text{Li}_{2.6}\text{Co}_{0.4}\text{N}$ has shown its viability by being successfully implemented into Li-ion cells.²⁵ High specific capacities, exceptional cycling stability and good voltage profiles have been demonstrated within the metal nitrides discussed in this chapter. However, the combination of all of these attributes along with low air sensitivity and cost have yet to be demonstrated in one material. Regardless of the eventual outcome, the nitrides offer a new path towards next generation negative electrodes with a rich electrochemistry rivaled by few other materials.

8.3. SILICIDES

8.3.1. Introduction

Binary lithium alloys have long been considered as alternative negative electrode materials as they exhibit greater specific capacities,

especially volumetric capacities, than carbonaceous materials. The Li-Si system shows the highest theoretical capacity of over 4000 mAh/g with the

formation of $\text{Li}_{4.4}\text{Si}$. Unfortunately, the cycle life of binary alloys is poor as large volume changes are associated to repeated alloying/dealloying resulting in the pulverization of the electrode. One area of research to improve the performance of Li-Si alloys focuses on silicon-based nanocomposites. Silicon has been dispersed in different types of materials (carbonaceous materials, ductile metals, TiN, etc...).

An alternative approach to the silicon-based nanocomposite considers the investigation of silicides for use both at elevated and ambient temperature. The examination of several binary silicides^{26,27} showed only a few reacted with lithium significantly at ambient temperature. This section will mostly focus on magnesium silicide, Mg_2Si , which exhibits interesting electrochemical properties, such as high capacity and low potential, even at ambient temperature.

8.3.2. Ternary Li-Si-M Systems at Elevated Temperature

8.3.2.1. Thermodynamics

Anani and Huggins²⁸ proposed a methodology, based on the principles of ternary thermodynamics, to predict how the addition of a third component to a binary system could alter both the capacity and the potential of the binary counterpart. They aimed at ternary alloys, using Li-Si-M alloys for illustration, with improved electrochemical performance for use as negative electrodes in thermal batteries, using FeS_2 as cathode material and operating in the 400-450°C temperature range.

The reactions of an initial Si-M alloy with lithium were predicted using the isothermal equilibrium phase diagram of the Li-Si-M ternary system at the adequate temperature (400°C in this case). The construction of these phase diagrams was based on the free energy of formation, or Gibbs free energy, of all the binary and ternary phases known to exist in the Li-Si-M system. An estimation of the theoretical potential, at which the equilibrium reactions (or three-phase equilibria) should occur, was obtained using the Nernst relation. Table 8.1 shows the theoretical potential and the theoretical capacity of several M-Si alloys (where M = Ca, Cr, Mg, Mn, Mo, Nb, Ni, Ta, Ti and V) used as starting materials. The maximum theoretical specific energy (MTSE) values provided in the table were obtained as follows:

$$\text{MTSE} = (26.805 \cdot n \cdot E_{\text{av}}) / W \quad (8.14)$$

Table 8.1. Estimated thermodynamic properties of several Li-Si-M ternary systems (from Ref. 28).

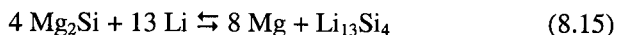
System ^a	Starting composition	Phases in equilibrium	Electrode potential (mV vs. Li)	Electrode capacity		MTSE (Wh/kg)
				Li/Si	Li/g (x10 ³)	
Li-Si	Li ₇ Si ₃	Li ₇ Si ₃ -Li ₁₃ Si ₄	158	0.92	18.1	428
A-Mg	Mg ₂ Si	Mg ₂ Si-Mg-Li ₁₃ Si ₄	60	3.25	32.7	574
A-Mn	MnSi	MnSi-Mn ₅ Si ₃ -Li ₇ Si ₃	163	0.93	10.4	316
	Mn ₅ Si ₃	Mn ₅ Si ₃ -Mn ₃ Si-Li ₁₃ Si ₄	45	1.44	11.1	350
	Mn ₃ Si	Mn ₃ Si-Mn-Li ₃₃ Si ₅	43	4.40	19.7	474
A-Mo	MoSi ₂	MoSi ₂ -Mo ₅ Si ₃ -Li ₁₃ Si ₄	120	2.28	24.8	502
	Mo ₅ Si ₃	Mo ₅ Si ₃ -Mo ₃ Si-Li ₂₂ Si ₅	3	1.96	9.7	328
A-Ni	Ni ₇ Si ₁₃	Ni ₇ Si ₁₃ -NiSi-Li ₁₂ Si ₇	316	0.79	12.1	317
A-Nb	NbSi ₂	NbSi ₂ -Nb ₅ Si ₃ -Li ₇ Si ₃	184	1.63	19.0	432
A-Ta	TaSi ₂	TaSi ₂ -Ta ₅ Si ₃ -Li ₇ Si ₃	211	1.63	12.6	344
A-V	VS ₂	VS ₂ -V ₅ Si ₃ -Li ₇ Si ₃	191	1.63	25.2	486
A-Ca	CaSi	CaSi-Ca ₂ Si-Li ₂₂ Si ₅	13	2.2	26.4	544
A-Cr	CrSi ₂	CrSi ₂ -CrSi-Li ₇ Si ₃	223	1.17	18.8	420
	CrSi	CrSi-Cr ₅ Si ₃ -Li ₇ Si ₃	205	0.93	10.8	315
	Cr ₅ Si ₃	Cr ₅ Si ₃ -Cr ₃ Si-Li ₁₃ Si ₄	138	1.44	11.6	341
A-Ti	TiSi	TiSi-Ti ₅ Si ₃ -Li ₇ Si ₃	182	1.55	11.3	328

^aA=Li-Si

where n is the number of moles of lithium involved in the reaction, E_{av} is the difference between the positive (FeS₂) and negative electrode (M-Si alloy) potentials and W is the weight of active material. Because the ternary Li-Si-Ca, Li-Si-Mo and Li-Si-Mg systems exhibited improved maximum theoretical specific energy (544, 502 and 574 Wh/kg, respectively) with respect to the binary Li-Si system (428 Wh/kg), they appeared as potential alternative negative electrode materials for thermal batteries.

8.3.2.2. The Li-Si-Mg System

The theoretical results provided in the previous section were verified experimentally using the ternary Li-Si-Mg system.^{29,30} Mg₂Si is the only intermetallic compound existing in the Mg-Si system. Thermodynamics predicted a three-phase equilibrium at 400°C that can be depicted by the following reaction:



According to equation (8.15), the theoretical potential and capacity of Mg₂Si upon reaction with lithium correspond to 0.06 V vs. Li/Li⁺ and 876

mAh/g, respectively. Coulometric titration techniques with current densities in the 5-20 mA/cm² range were performed at 440°C using three-electrode cells. Mg₂Si was used as working electrode and a 44% Li-Si alloy served as counter and reference electrode while the electrolyte consisted of a LiCl-KCl eutectic. The resulting Mg₂Si voltage profiles showed a specific capacity of 788 mAh/g at an average potential of 0.07 V vs. Li/Li⁺; these data agree well with the theoretical values predicted by thermodynamics (Table 8.1). In light of these results, the use of Mg₂Si as negative electrode would provide a cell of higher specific energy than a cell utilizing a Li-Si binary alloy (based on the Li₇Si₃-Li₁₃Si₄ equilibrium).

8.3.3. Silicides at Ambient Temperature

8.3.3.1. Mg₂Si

Two conflicting mechanisms have been found for the reaction of Mg₂Si with lithium at ambient temperature. One scenario involves the intercalation of lithium into Mg₂Si to form Li₁Mg₂Si while the formation of a unique ternary Li₂MgSi phase intervenes in the second scheme.

8.3.3.1.1. Formation of Li₁Mg₂Si

Huang *et al.*^{31,32} reported the insertion of up to 2 lithium per Mg₂Si that is equivalent to a specific capacity of 700 mAh/g. The working electrode, constituted of 98 wt% Mg₂Si active material and 2 wt% ethylene-propylene-diene binder, was tested versus lithium metal down to 0 V at 0.0158 mA/cm². X-ray diffraction showed the material maintained its crystalline structure upon reaction with up to one lithium but became amorphous thereafter. As opposed to the results predicted by thermodynamics at 400°C, there was no evidence of Mg and Li₁₃Mg₄ phases at ambient temperature. In the ternary Li-Si-Mg isothermal equilibrium phase diagram at ambient temperature, a line that does not exist at 400°C connects Mg₂Si to Li. Mg₂Si crystallizes in an antifluorite structure where Si occupies the octahedral sites to form a face-centered cubic arrangement while Mg occupies the tetrahedral sites. This structure offers vacant octahedral sites favorable for lithium intercalation that supports the theory of a single-phase intercalation process with the formation of a Li₁Mg₂Si phase.

Kim *et al.*³³ investigated the electrochemistry of Mg₂Si versus lithium in more detail as it exhibited an initial capacity of 1370 mAh/g corresponding to the insertion of up to 3.9 lithium (Figure 8.11). This value far exceeded the capacity reported by Huang *et al.*^{31, 32} at ambient

temperature (2 lithium) and also the capacity predicted by Anani and Huggins^{29,30} at elevated temperature (3.25 lithium) (Table 1.1). Although the

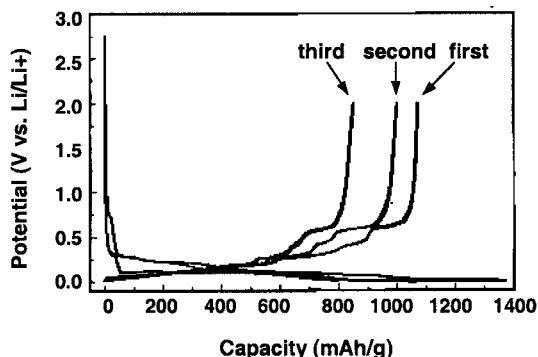


Figure 8.11. First three cycles voltage profile of an Mg_2Si electrode cycled vs. Li metal between 0 and 2 V at a constant current of 10 mA/g (from Ref. 33).

electrode exhibited high initial cycling efficiency (78.4% in the first cycle), the electrode failed within 10 cycles.

The evolution of the structure was examined using *ex-situ* X-ray diffraction. The Mg_2Si structure, which remained crystalline during cycling, expanded during lithiation and contracted during delithiation. The expansion/contraction of the lattice with cycling was consistent with an intercalation process. The emergence of Mg metal at 0.17 V and a Li-Mg alloy on further lithiation suggested the decomposition of the $\text{Li}_x\text{Mg}_2\text{Si}$ phase. Although no evidence of any Li-Si phase was obtained by XRD, Auger electron spectroscopy performed in the lithiated state revealed the co-existence of a $\text{Li}_x\text{Mg}_2\text{Si}$ phase with Li-Si and Li-Mg alloys. Similarities in the differential capacity plots of the Mg_2Si electrodes with the ones obtained for Si-based materials, such as Si metal and SiO , and Mg also suggested the formation of Li-Si and Li-Mg alloys, respectively. In brief, lithium was proposed to intercalate into the vacant octahedral sites of the Mg_2Si antifluorite structure until the concentration of lithium in the $\text{Li}_x\text{Mg}_2\text{Si}$ reached a critical value. At this point, the material decomposes into Li-Si alloys and Mg, which alloys with lithium on further lithiation.

The rapid degradation of Mg_2Si electrodes was proposed to result from the large volume changes associated to the Li-Si and Li-Mg alloying reactions. Scanning electron microscopy revealed cracking and crumbling after 10 cycles while XRD analyses showed an increase of the amount of residual Mg metal and Li-Mg with respect to the Mg_2Si phase with cycle number.

8.3.3.1.2. Formation of a Ternary Li_2MgSi Phase

Moriga *et al.*³⁴ proposed a two-step reaction mechanism for the reaction of Mg_2Si with lithium at ambient temperature that differed from the

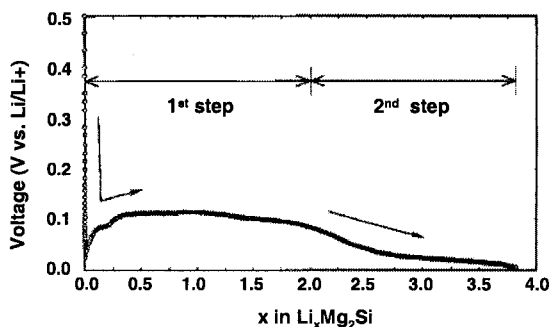
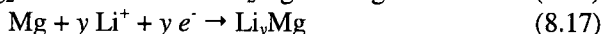


Figure 8.12. First discharge voltage profile of an Mg_2Si electrode cycled vs. Li metal at a constant current of 0.5 mA/cm^2 (from Ref. 34).

one described above. The first discharge voltage profile in Figure 8.12 shows the voltage remained quite flat during the insertion of the first two lithium while it gradually decreased during further lithiation. The first step was believed to involve the extraction of Mg from Mg_2Si concomitant to the formation of a ternary Li_2MgSi phase (equation 8.16). The second step was associated to the alloying reaction of lithium with the extracted Mg metal (equation 8.17).



XRD patterns obtained at various points of discharge revealed Mg metal and a new cubic phase emerged while Mg_2Si vanished. The new cubic phase was associated to Li_2MgSi based on the XRD pattern simulations of $\text{Mg}_{2.5}\text{Si}$ with half-occupation of the 8c Mg sites. On further lithiation, Mg metal disappeared and a body-centered cubic Li phase identified as a Li-Mg alloy appeared. Good correlation existed between the XRD pattern obtained experimentally upon insertion of 3.5 Li and the XRD pattern obtained by simulation using the Li_2MgSi structure with a $Fm\bar{3}m$ space group depicted in Figure 8.13. The later has a $2a_F \times 2a_F \times 2a_F$ structure, where a_F is the lattice parameter of the initial Mg_2Si cubic structure. In the proposed structure, two

units of Li_2MgSi were alternatively arranged. The second unit was obtained by rotating the first one clockwise for 90° about the a axis. Finally, DV- $X\alpha$ calculations revealed electrons were introduced in the Mg 3s orbitals for charge compensation during lithium insertion, resulting in the reduction of Mg^{2+} ions. This was consistent with the extraction of Mg (supported by XRD) from Mg_2Si .

More recently, Roberts *et al.*³⁵ confirmed the formation of Mg metal and Li_2MgSi by XRD during lithiation of Mg_2Si . Because the reconstitution reactions in the Li-Si system are kinetically hindered at ambient temperature and only selective equilibrium is achieved,³⁶ the Li-Si alloys may be difficult to detect using XRD. Therefore, although the structural characterization of the electrode at different points of charge and discharge showed no evidence of Li-Si alloy formation, the authors proposed electrochemical evidence for Li-Si alloying with extensive cycling. The anodic differential capacity plot of an Mg_2Si electrode lithiated down to 5 mV exhibited a peak in the same voltage range as obtained for pure silicon. Finally, the material was shown to transform back to Mg_2Si during delithiation.

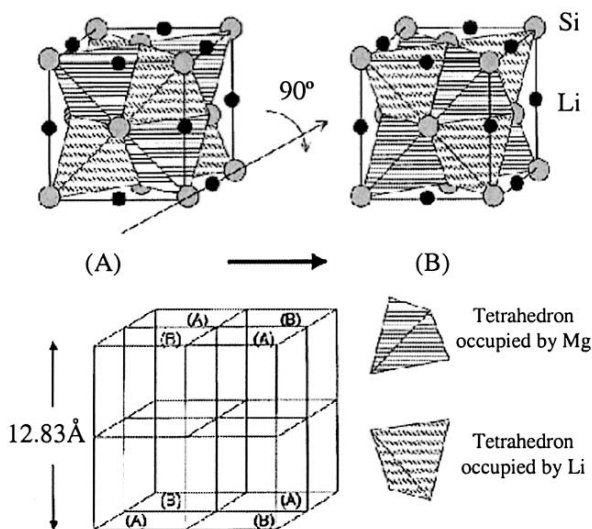


Figure 8.13. Schematic illustration of Li_2MgSi structure (from Ref. 34).

8.3.3.2. CrSi_2

Lithium was found to intercalate into the CrSi_2 structure.³⁶ Because the

electrochemical insertion of lithium into CrSi_2 is very slow at ambient temperature, ternary Li-Si-Cr samples were fabricated by reaction of pure lithium with CrSi_2 at 360°C using various initial Li: CrSi_2 stoichiometry ratios. The resulting materials were characterized by XRD in order to identify the chemical reactions of CrSi_2 with lithium. Table 8.2 exhibits the assumed chemical reactions along with the initial Li: CrSi_2 ratio at which the different phases were observed. It also provides the theoretical capacity associated to these reactions and the experimental delithiation capacity. Lithium intercalation occurs for initial stoichiometry ratios up to 60:40. A further increase in the initial lithium content results first in the formation of Cr_5Si_3 and Li_7Si_3 , then Cr_5Si_3 transforms into Cr_3Si and finally $\text{Li}_{13}\text{Si}_4$ and $\text{Li}_{21}\text{Si}_5$ were observed. No ternary phase was found.

The Li-Si-Cr samples prepared by solid-state reaction were tested versus lithium metal under a constant current equivalent to a C/60 rate. The samples exhibited lithiation capacities ranging from 661 to 811 mAh/g and reversible delithiation capacities of up to 800 mAh/g that are rooted in binary Li-Si alloying reactions. Although the theoretical specific capacities of ternary Li-Si-Cr system are smaller than the binary Li-Si system, the capacities obtained experimentally for the ternary system

Table 8.2. Reconstitution reactions as found from X-ray diffraction analyses after chemical lithiation of CrSi_2 (from Ref. 36).

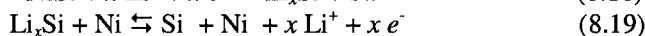
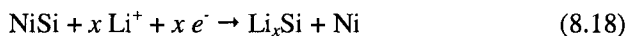
Assumed chemical reaction	Found for initial stoichiometry ratio of Li: CrSi_2	Calculated capacity (mAh/g)	Experimental delithiation capacity (mAh/g)
Lithium intercalation into CrSi_2	up to 60:40	-	-
$15 \text{ CrSi}_2 + 49 \text{ Li} \rightarrow 3 \text{ Cr}_5\text{Si}_3 + 7 \text{ Li}_7\text{Si}_3$	75:25	669	-
$9 \text{ CrSi}_2 + 35 \text{ Li} \rightarrow 3 \text{ Cr}_3\text{Si} + 5 \text{ Li}_7\text{Si}_3$	80:20	771	496
$12 \text{ CrSi}_2 + 65 \text{ Li} \rightarrow 4 \text{ Cr}_3\text{Si} + 5 \text{ Li}_{13}\text{Si}_4$	85:15	996	682
$3 \text{ CrSi}_2 + 21 \text{ Li} \rightarrow \text{Cr}_3\text{Si} + \text{Li}_{21}\text{Si}_5$	88:12	1197	836

exceeded the ones obtained with the binary system. This benefit in capacity may be related to the Cr-Si phases. The latter remain mostly electrochemically inactive after the first discharge and may act as stabilizing conductive matrix.

8.3.3.3. NiSi

Preliminary results showed nanosize NiSi synthesized by high-energy milling reacts with lithium reversibly.³⁷ The material consisted of agglomerates of small particles with an average crystallite size of 4-6 nm as

determined from the width of Bragg peaks using the Scherrer equation. The discharge voltage profile (Figure 8.14), which is smooth and approximately follows a half parabolic curve down to 0 V, shows high initial capacity, 1180 mAh/g. Even though 80% of the initial discharge capacity was reversible, the capacity fade during cycling is significant as NiSi electrodes retained only 65% of the initial discharge capacity after 25 cycles. Based on previous reports of Sn-Sb materials, NiSi was proposed to decompose into Li-Si alloys and Ni during the first lithiation (equation 8.18). In subsequent charge and discharge, the Li-Si alloys reversibly transform into Si metal, which constitutes the active center of the electrode, while Ni metal remains electrochemically inactive (equation 8.19).



8.3.4. Summary – Silicides

Several binary silicides have been examined as potential negative electrode materials first for thermal batteries and then for batteries operating

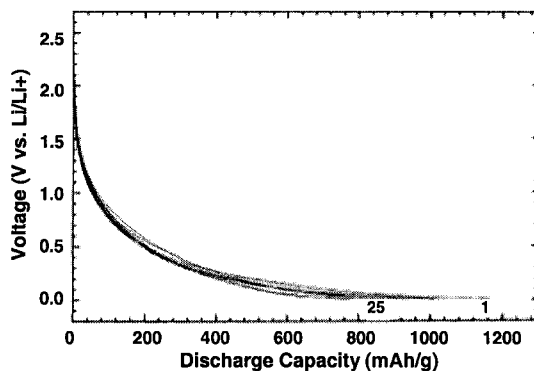


Figure 8.14. Discharge voltage profile of a nanosize NiSi electrode cycled vs. Li metal at a constant current of 0.08 mA/cm² (from Ref. 37).

at ambient temperature. Using Mg₂Si as an illustration, thermodynamics was proven to be an excellent tool for screening silicides with improved specific capacity and energy with respect to the binary Li-Si system for use in

thermal batteries operating in the 400-450°C temperature range. Mg_2Si was also found to react with lithium reversibly at ambient temperature. Even though this system exhibits initial high capacity, its short cycle life limits its utilization in commercial applications. The rapid failure of the electrode was attributed to the large volume changes associated to the Li-Mg and Li-Si repeated alloying/dealloying reactions occurring during cycling. These alloys result from the decomposition of a $\text{Li}_x\text{Mg}_2\text{Si}$ solid solution or a ternary Li_2MgSi phase during lithiation. There still exist a conflict as for the actual reaction mechanism of Mg_2Si with lithium at ambient temperature. CrSi_2 and NiSi were also investigated. In general, silicides show high capacity at low potentials that make them very attractive as negative electrodes for Li-ion batteries; however their poor cycle life needs to be improved.

REFERENCES

1. B. Knutz, S. Skaarup, *Solid State Ionics* 9&10 (1983) 371.
2. P. M. Richards, *J. Solid State Chem.* 33 (1980) 127.
3. R. Bittihn, *Solid State Ionics* 8 (1983) 83.
4. M. Meyer, H. Rickert, U. Schwaitzer, *Solid State Ionics* 9&10 (1983) 689.
5. M. F. Bell, A. Breitschwerdt, U. Alpen, *Mater. Res. Bull.* 16 (1981) 267.
6. J. R. Rea, D.L. Foster, *Mater. Res. Bull.* 14 (1979) 841.
7. B. A. Boukamp, R. A. Huggins, *Mater. Res. Bull.* 13 (1978) 23.
8. H. Yamane, S. Kikkawa, M. Horiguchi, M. Koizumi, *J. Solid State Chem.* 65 (1986) 6.
9. R. Juza, H. H. Weber, E. Meyer-Simon, *Z. Anorg. Allg. Chem.* 48 (1953) 273.
10. H. Yamane, S. Kikkawa, M. Koizumi, *Solid State Ionics* 25 (1987) 183.
11. S. Suzuki, T. Sodai, *Solid State Ionics* 116 (1999) 1.
12. M. Nishijima, Y. Takeda, N. Imanishi, O. Yamamoto, N. Takano, *J. Solid State Chem.* 113 (1994) 205.
13. T. Asai, K. Nishida, S. Kawai, *Mat. Res. Bull.* 19 (1984) 1377.
14. M. Nishijima, T. Kagohashi, M. Imanishi, Y. Takeda, O. Yamamoto, S. Kondo, *Solid State Ionics* 83 (1996) 107.
15. T. Shodai, Y. Sakurai, T. Suzuki, *Solid State Ionics* 122 (1999) 85.
16. S. Suzuki, T. Shodai, J. Yamaki, *J. Phys. Chem. Solids* 59 (1998) 331.
17. J. Rowsell, V. Pralong, L. Nazar, *J. Am. Chem. Soc.* 123 (2001) 8598.
18. B. Neudecker, R. Zuhr, *Electrochemical Society Proceedings* 99-24, p. 295.
19. N. Pereira, M. Balasubramanian, L. Dupont, J. McBreen, L.C. Klein, G.G. Amatucci, submitted, *J. Electrochem. Soc.* (2002).
20. J.B. Bates, N.J. Dudney, B. Neudecker, A. Ueda, C.D. Evans, *Solid State Ionics* 135 (2000) 33.
21. A. D. Pelton, *J. Phase Equilibria* 12 (1991) 42.
22. E. Zintl, A. Schneider, *Z. Elektrochem.* 41 (1935) 764.
23. N. Pereira, L. C. Klein, G.G. Amatucci, *J. Electrochem. Soc.* 149 (2002) A262.
24. N. Pereira, L. Dupont, J.M. Tarascon, L.C. Klein, G.G. Amatucci, submitted, *J. Electrochem. Soc.* (2002).

25. Y. Takeda, M. Nishijima, M. Yamahata, K. Takeda, N. Imanishi, O. Yamamoto, *Solid State Ionics* 130 (2000) 61.
26. R.A. Huggins, *Solid State Ionics*, in press (2002).
27. N. Pereira, Ph-D thesis, Rutgers University, December 2001.
28. A. Anani, R.A. Huggins, *J. Power Sources* 38 (1992) 351.
29. A. Anani, R.A. Huggins, *J. Power Sources* 38 (1992) 363.
30. US Patent 4,950,566.
31. C.K. Huang, B.V. Ratnakumar, S. Surampudi, G. Halpert, *The Electrochemical Society Proceedings*, Vol. 94-28, 361.
32. US Patent 5,294,503.
33. H. Kim, J. Choi, H.J. Sohn, T. Kang, *J. Electrochem. Soc.* 146 (1999) 4401.
34. T. Moriga, K. Watanabe, D. Tsuji, S. Massaki, I. Nakabayashi, *J. Solid State Chem.* 153 (2000) 386.
35. G.A. Roberts, E.J. Cairns, J.A. Reimer, *J. Power Sources* in press (2002).
36. W. J. Weydanz, M. Wohlfahrt-Mehrens, R.A. Huggins, *J. Power Sources* 81-82 (1999) 237.
37. W. G.X. Wand, L. Sun, D.H. Bradhurst, S. Zhong, S.X. Dou, H.K. Liu, *J. Alloys and Comp.* 306 (2000) 249.

Chapter 9

ALLOYS AND INTERMETALLIC ANODES

R. A. Huggins

Faculty of Engineering, University of Kiel, Kaiserstrasse 2, D-24143 Kiel, Germany

9.1. INTRODUCTION

Early work on the commercial development of rechargeable lithium batteries to operate at or near ambient temperatures involved the use of elemental lithium as the negative electrode reactant. Binary phases, generally involving a solid solution of lithium in one of the forms of carbon, are currently employed on the negative side of lithium cells.

There is considerable interest in finding alternative materials that might be more attractive than the lithium-carbons. Improvements might involve the ability to operate safely at higher current densities, less first cycle irreversible capacity loss, better cycling behavior, reduced specific volume, and lower cost.

A number of possible alternative negative electrode materials are discussed in other chapters of this book. The intent of this chapter is not to present a catalog of possible materials and their properties. Instead, emphasis will be placed upon the principles involved in understanding the behavior of simple multi-component alloys, starting with their equilibrium or near-equilibrium behavior at both elevated and ambient temperatures. Information relating to equilibrium conditions provides the theoretical limits of the potentials and capacities of electrodes in electrochemical systems. The properties that are actually observed under operating conditions will, of course, deviate from these values due to kinetic factors.

Especially interesting have been recent results on materials that demonstrate significant deviations from equilibrium behavior, including the formation of amorphous structures, at low temperatures. The use of materials in which amorphous silicon is formed *in situ* during cycling appears to be particularly attractive.

9.2. ALLOYS AS AN ALTERNATIVE TO PURE LITHIUM

Attention has been given to the use of lithium alloys as an alternative to elemental lithium for some time. Groups working on batteries with molten salt electrolytes that operate at temperatures of 400-450°C, well above the melting point of lithium, were especially interested in this possibility. Two major directions evolved. One involved the use of lithium-aluminum alloys,^{1,2} whereas another was concerned with lithium-silicon alloys.³⁻⁵

Whereas this approach can avoid the problems related to lithium melting, as well as the others mentioned in the literature, there are always at least two disadvantages related to the use of alloys. Because they reduce the activity of the lithium, they necessarily reduce the cell voltage. In addition, the presence of additional species that are not directly involved in the electrochemical reaction always brings additional weight and, often, volume. Thus the maximum theoretical values of the specific energy are always reduced compared to what might be attained with pure lithium. The energy density is also often reduced. But lithium has a large specific volume, so that this is not always the case.

In practical cases, however, the excess weight and volume due to the use of alloys may not be very far from those required with pure lithium electrodes. It is generally necessary to have a large amount of excess lithium in rechargeable cells in order to make up for the capacity loss related to the dendrite or filament growth problem upon cycling.

Lithium alloys have been used for a number of years in the high temperature "thermal batteries" that are produced commercially for military purposes. These devices are designed to be stored for long times at ambient temperatures before use, where their self-discharge kinetic behavior is very slow. They must be heated to elevated temperatures when their energy output is desired. An example is the Li alloy/FeS₂ battery system that employs a chloride molten salt electrolyte. In order to operate, the temperature must be raised to over the melting point of the electrolyte. This type of cell typically uses either Li-Si or Li-Al alloys in the negative electrode.

The first use of lithium alloys as negative electrodes in commercial batteries to operate at ambient temperatures was the employment of Wood's metal alloys in lithium-conducting button type cells by Matsushita in Japan. Development work on the use of these alloys started in 1983,⁶ and they became commercially available somewhat later.

9.2.1. Lithium - Carbon Alloys

It was also shown in 1983 that lithium can be reversibly inserted into

graphite at room temperatures when using a polymeric electrolyte.⁷ Prior experiments with liquid electrolytes were unsuccessful due to co-intercalation of species from the organic electrolytes that were used at that time. This problem has been subsequently solved by the use of other electrolytes.

There has been a large amount of work on the development of graphites and related carbon-containing materials for use as negative electrode materials in lithium batteries in recent years. This is due in large part to the successful development by Sony of commercial rechargeable batteries containing negative electrodes based upon materials of this family.

Lithium-carbon materials are, in principle, no different from other lithium-containing alloys. However, since this topic is treated in more detail elsewhere, only a few points will be briefly discussed here.

One is that the behavior of these materials is very dependent upon the details of both the nanostructure and the microstructure. Therefore, the composition and the thermal and mechanical treatment all play important roles in determining the resulting thermodynamic and kinetic properties. Materials with a more graphitic structure have more negative potentials, whereas those with less well organized structures typically operate over much wider potential ranges, resulting in a cell voltage that is both lower and more state-of-charge dependent.

Another important consideration in the use of carbonaceous materials as negative electrodes in lithium cells is the common observation of a considerable loss of capacity during the first charge-discharge cycle due to irreversible lithium absorption into the structure. This has the distinct disadvantage that it requires that an additional amount of lithium be initially present in the cell. If this irreversible lithium is supplied from the positive electrode, an extra amount of the positive electrode reactant material must be put into the cell during its fabrication. As the positive electrode reactant materials often have relatively low specific capacities, *e.g.*, around 140 mAh/g, this irreversible capacity in the negative electrode leads to a requirement for an appreciable amount of extra reactant material weight and volume in the total cell.

There are some other matters that should be considered when comparing normal metallic lithium alloys with the lithium-carbons. The specific volume of some of the metallic alloys can be considerably lower than that of the carbonaceous materials.

9.3. PRINCIPLES DETERMINING THE POTENTIALS AND CAPACITIES OF ALLOY ELECTRODES UNDER EQUILIBRIUM CONDITIONS

The theoretical basis for understanding and predicting the potentials

and capacities of both binary (two element) and ternary (three element) lithium alloys under equilibrium and near-equilibrium conditions has now been established. Under these conditions, these important practical parameters are directly related to the thermodynamic properties and compositional ranges of the pertinent phases in the respective alloy systems.

One can often understand their behavior under dynamic conditions in terms of simple deviations from such equilibrium conditions. In other cases, however, metastable phases, either crystalline or amorphous, may be present whose properties are considerably different from those of the thermodynamically stable phases and compositions.

9.3.1. Relations Between Phase Diagrams, the Composition-Dependence of the Potential, and the Capacity of Electrodes

Phase diagrams are figures that graphically represent the equilibrium state of a chemical system. They can be very useful thinking tools to help understand the fundamental electrochemical properties of electrodes. There are various types of phase diagrams, but in the most common case they are two-dimensional plots that indicate the temperature and compositional conditions for the stability of various phases under equilibrium conditions.

A binary phase diagram is a plot of temperature versus the overall composition for alloys composed of two different elements. It shows the temperature-composition conditions for the stability of the various phases that can form in a given system, and is commonly used in materials science. It will be seen that there are regions in which only a single phase is stable, and regions in which two phases are stable. Although not of particular importance to electrochemical experiments, there are also special conditions under which it is possible for three phases to be present in a binary system. According to the Gibbs Phase Rule, this can only happen at a specific temperature. At both above and below that unique temperature only one-phase and two-phase regions are possible. This means that at that particular temperature the three phases in equilibrium must contact a horizontal (constant temperature) line in the diagram. Two will touch it at the ends, and the third will only do so at a single composition between them.

In the construction of binary phase diagrams the same rules apply whether the phases present in the relevant ranges of temperature and composition are liquids or solids. At any fixed temperature single phase regions are always separated by two-phase regions, and in two-phase regions a change in the overall composition is accomplished by variation of the relative amounts of the two phases at its limits, each of which maintains a

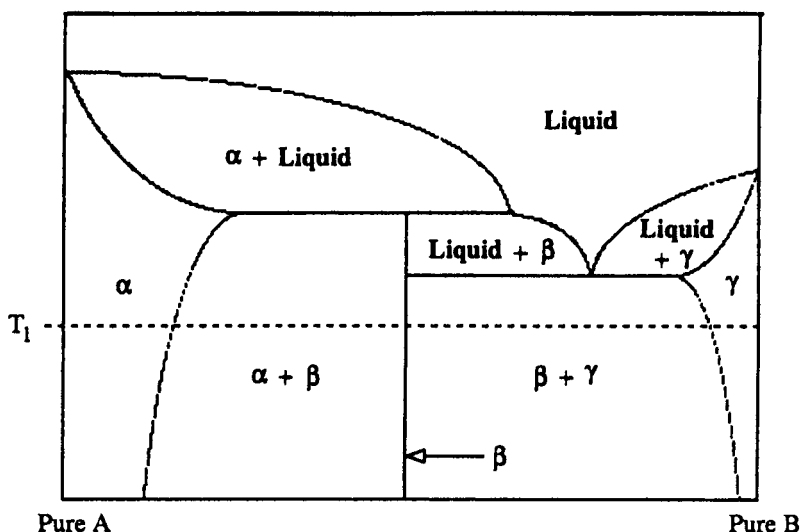


Figure 9.1. Schematic binary phase diagram with an intermediate phase β , and solid solubility in terminal phases α and γ .

fixed-composition.

A schematic diagram for a hypothetical binary alloy system A-B is shown in Figure 9.1. In this case there are four 1-phase regions. The solid phases are designated as phases α , β and γ . In addition, there is a liquid phase at higher temperatures. It can be seen in the figure that the single phases are all separated by 2-phase regions as the composition moves horizontally (isothermally) across the diagram.

According to the Gibbs phase rule all intensive properties, including the electrical potential, vary continually with the composition within single phase regions in a binary system. Correspondingly, the intensive properties are composition-independent when two phases are present in a binary system. Since the equilibrium electrical potential of such an electrode, E , in an electrochemical cell is determined by the lithium activity, it also varies with composition within single phase regions, and is composition-independent when there are two phases present under the equilibrium conditions that are assumed here.

The variation of the electrical potential difference V (voltage between the electrode and some reference potential) with the overall composition in this hypothetical system at temperature T_1 is shown in Figure 9.2. It is seen that it alternately goes through composition regions in which it is constant (potential plateaus) and those in which it varies. If B atoms are added to pure element A the overall composition is initially in the solid solution phase α and the electrical potential varies with composition. When the solubility limit is

reached, the addition of more B causes the nucleation and growth of the β phase. Two phases are then present, and the potential maintains a fixed value. When the overall composition reaches composition at the $\alpha+\beta/\beta$ line all of the α phase will have been consumed and there will only be phase β present. Upon further compositional change within the β phase, which is assumed to

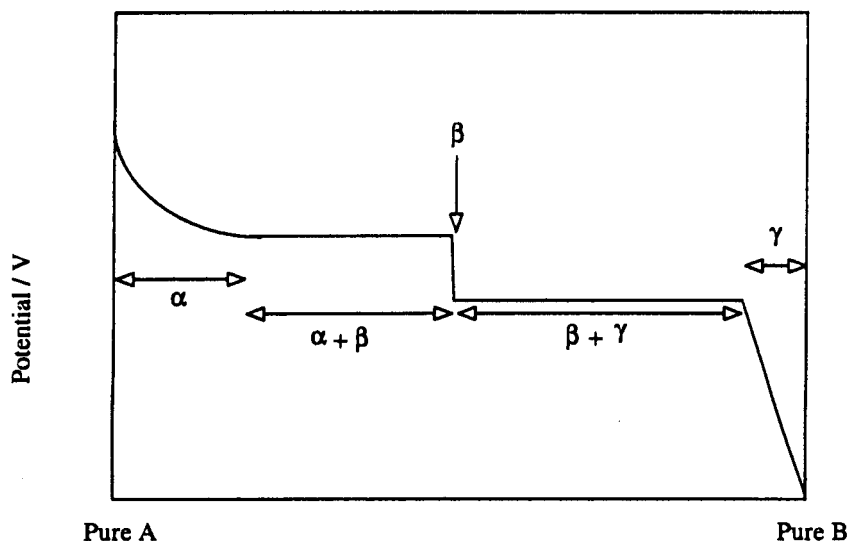


Figure 9.2. Variation of electrical potential with composition across the binary phase diagram shown in Figure 9.1.

have a very narrow range of composition in this illustration, the electrical potential again becomes composition-dependent. When the upper compositional limit of the β phase is reached, the overall composition again enters a 2-phase (β and γ) range and the potential is again composition-independent. Upon reaching composition at the $\beta+\gamma/\gamma$ line the potential again varies with composition.

9.3.2. An Example, the Lithium-Antimony System

As a concrete example to demonstrate these principles consider the Li-Sb system, which has been studied both experimentally and theoretically in some detail.⁸⁻¹⁰ The phase diagram is shown in Figure 9.3.

Below 615°C there are two intermediate phases between Sb and Li, Li_2Sb and Li_3Sb . Both have rather narrow ranges of composition and are represented simply as vertical lines in the phase diagram. Thus, if an electrode starts as pure Sb and lithium is added, it successively goes through two

different reactions. The first involves the formation of the phase Li_2Sb , and can be written as:



Upon the addition of more lithium a second reaction will occur that results in the formation of the second intermediate phase from the first. This

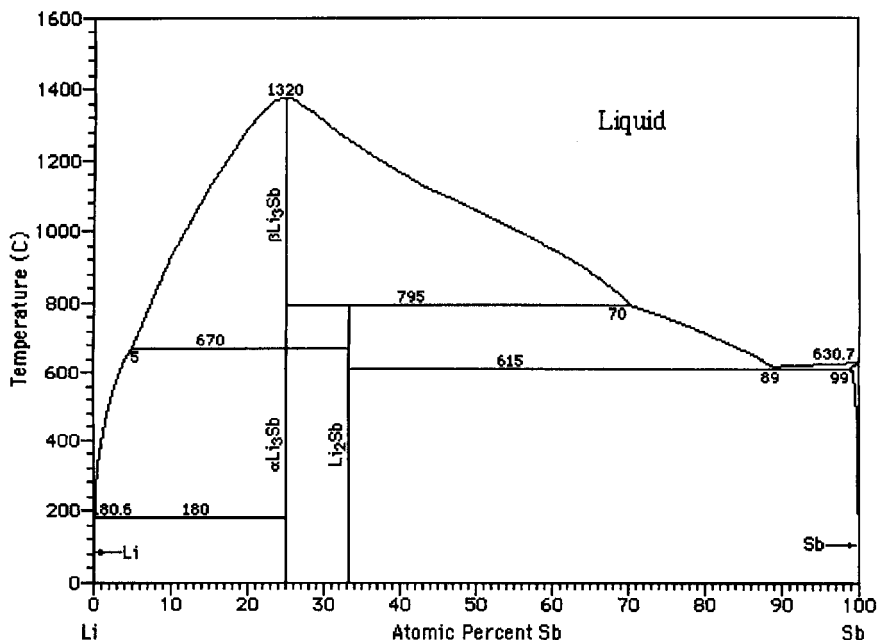


Figure 9.3. Lithium-antimony phase diagram.

can be written as:



This process can be studied experimentally by the use of a simple electrochemical cell whose initial configuration is similar to that shown schematically in Figure 9.4.

By driving current through this cell from an external source that causes the voltage between the two electrodes to be reduced, lithium will leave the negative electrode, pass through the electrolyte, and arrive at the positive electrode. If the chemical diffusion rate within the Li_xSb electrode is sufficiently high relative to the rate at which lithium ions arrive at the electrode surface, this lithium will be incorporated into the bulk of the

electrode crystal structure, changing its composition. That is, the value of x in the positive electrode material Li_xSb will increase.

If the lithium is either added very slowly, or stepwise, allowing equilibrium to be attained within the positive electrode material after each

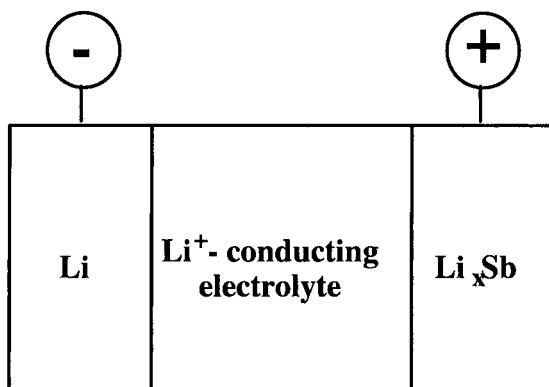


Figure 9.4. Schematic drawing of the electrochemical cell used to study the Li-Sb system.

step, the influence of the lithium concentration in the positive electrode upon its potential under equilibrium or near-equilibrium conditions can be investigated. This procedure was called electrochemical titration by Wagner, who first used it to study the properties of the phase " Ag_2S " as a function of the Ag/S ratio.¹¹ The result of such an experiment on the Li-Sb system, performed at 360°C , is shown schematically in Figure 9.5.¹⁰

We can understand these results by consideration of the Gibbs phase rule, which was mentioned earlier. It can be written simply as:

$$F = C - P + 2 \quad (9.3)$$

where F is the total number of degrees of freedom, C the number of components, and P the number of phases. In this case there are two components, Li and Sb. In an experiment conducted at constant temperature and pressure two degrees of freedom are specified. Thus, if two phases are present, the number of residual degrees of freedom will be zero, and all intensive variables will be fixed, independent of the overall composition. In this case, this means that the electrical potential will be constant over compositional interval where two phases are present in the phase diagram. On the other hand, the potential will vary with the concentration in composition regions in which only one phase is present in the phase diagram. After an initial, invisibly narrow, range of solid solution, the first plateau in Figure 9.5 corresponds to compositions in the phase diagram in which both (almost pure) Sb and the phase Li_2Sb are present. Thus it is related to the reaction in

equation (9.1).

There is also a very narrow composition range in which only one phase, Li_2Sb , is present and the potential varies. Upon the addition of further Li the

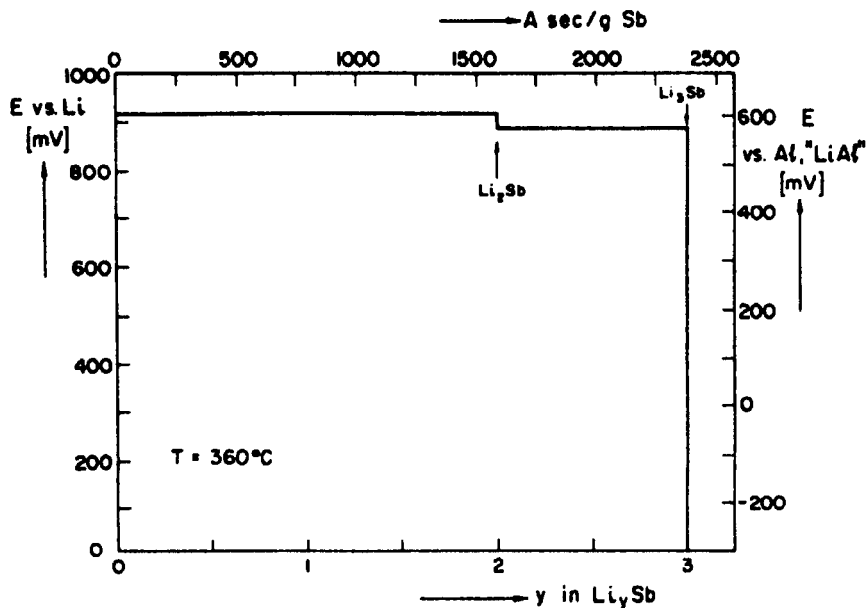


Figure 9.5. Results of coulometric titration experiment on Li-Sb system.

overall composition moves into the region of the phase diagram in which two phases are again present, in this case Li_2Sb and Li_3Sb , and the potential follows along a second plateau related to Equation (9.2).

9.3.3. Relation Between the Potentials and Thermodynamic Data

The potentials of the two plateaus in Figure 9.5 can be calculated from thermodynamic data on the standard Gibbs free energies of formation of the two phases, Li_2Sb and Li_3Sb . According to Ref. 10, these values are - 176.0 kJ/mol and - 260.1 kJ/mol, respectively, at that temperature.

The standard Gibbs free energy change, ΔG_r° , related to reaction (9.1) is simply the standard Gibbs free energy of formation of the phase Li_2Sb , $\Delta G_f^\circ(\text{Li}_2\text{Sb})$. From this we can calculate the potential of the first plateau from:

$$E - E^\circ = [(-\Delta G_r^\circ)/(2F)] \quad (9.4)$$

where E° is the potential of pure Li. This is found to be 912 mV.

The potential of the second plateau is related to virtual reaction (9.2), where:

$$\Delta G_r^\circ = \Delta G_f^\circ(\text{Li}_3\text{Sb}) - \Delta G_f^\circ(\text{Li}_2\text{Sb}) \quad (9.5)$$

and in this case:

$$E - E^\circ = [(-\Delta G_r^\circ)/F] \quad (9.6)$$

The result is that the potential of this plateau is 871 mV vs. pure Li.

This is the same result that would be found if it were assumed that the intermediate phase, Li_2Sb , did not form, and that there is only one voltage plateau. If the electrochemical titration curve were calculated from this value of energy, it would have only a single plateau, at a voltage that is the weighted average of the voltages of the two reactions. This is false, due to the lack of recognition of the existence of the intermediate phase. Thus one has to be careful to be aware of all of the stable phases when making predictions from thermodynamic data.

This discussion has assumed that thermodynamic data are available, and that one wants to predict the electrochemical properties. The opposite can also be done, of course; experimental measurements can provide information about the relevant phase diagram and the thermodynamic properties of the related phases.

Similar experiments have been made on a number of other binary metallic systems under conditions such that equilibrium can be reached. This requirement is fulfilled within reasonable times much more easily at elevated temperatures. In some cases, however, equilibrium data can also be obtained at ambient temperatures, albeit with a bit more patience. Elevated temperature data for a number of phases in the Li-Al, Li-Bi, Li-Cd, Li-Ga, Li-In, Li-Pb, Li-Sb, Li-Si, and Li-Sn binary lithium alloy systems, made using a LiCl-KCl molten salt electrolyte, are listed in Table 9.1.

9.3.4. Temperature Dependence of the Equilibrium Potential

In addition to the experiments in the LiCl-KCl molten salt electrolyte, measurements have also been made on some of these systems using lower temperature molten salts, $\text{LiNO}_3\text{-KNO}_3$ ²⁰, and also with organic electrolytes at ambient temperature. This provided information on the temperature dependence of the potentials and capacities.

The results of experiments carried out on materials in the Li-Sb and Li-Bi systems over a wide range of temperature demonstrate the principles involved. Each of these systems has two intermediate phases at low temperatures. The data are shown in Figure 9.6.

The temperature dependence of the potentials of the plateaus due to the presence of two-phase equilibria in the Li-Sb system was straightforward,

falling upon two straight lines, corresponding to the reactions of equations (9.1) and (9.2) above.

Table 9.1. Plateau potentials and composition ranges of a number of binary Li alloys at elevated temperatures.

Voltage vs. Li/Li ⁺ , V	System	Range of y	Temperature °C	Ref.
0.047	Li _y Si	3.25 - 4.4	400	12
0.058	Li _y Cd	1.65 - 2.33	400	13
0.080	Li _y In	2.08 - 2.67	400	14
0.089	Li _y Pb	3.8 - 4.4	400	15
0.09	Li _y Ga	1.53 - 1.93	400	16
0.122	Li _y Ga	1.28 - 1.48	400	16
0.145	Li _y In	1.74 - 1.92	400	14
0.156	Li _y Si	2.67 - 3.25	400	12
0.170	Li _y Sn	3.5 - 4.4	400	17
0.237	Li _y Pb	3.0 - 3.5	400	15
0.271	Li _y Pb	2.67 - 3.0	400	15
0.283	Li _y Si	2 - 2.67	400	12
0.283	Li _y Sn	2.6 - 3.5	400	17
0.300	Li _y Al	0.08 - 0.9	400	18
0.332	Li _y Si	0 - 2	400	12
0.373	Li _y Cd	0.33 - 0.45	400	13
0.375	Li _y Pb	1.1 - 2.67	400	15
0.387	Li _y Sn	2.5 - 2.6	400	17
0.430	Li _y Sn	2.33 - 2.5	400	17
0.455	Li _y Sn	1.0 - 2.33	400	17
0.495	Li _y In	0.22 - 0.86	400	14
0.507	Li _y Pb	0 - 1.0	400	15
0.558	Li _y Cd	0.12 - 0.21	400	13
0.565	Li _y Ga	0.15 - 0.82	400	16
0.570	Li _y Sn	0.57 - 1.0	400	17
0.750	Li _y Bi	1.0 - 2.82	400	19
0.750	Li _y Bi	1.0 - 2.82	400	19
0.760	Li _y Bi	0.6 - 1.0	400	19
0.875	Li _y Sb	2.0 - 3.0	400	19
0.910	Li _y Sb	0 - 2.0	400	19

In the Li-Bi case, however, where the comparable reactions are:



and:



the temperature dependence of the plateau potentials is different. There is a

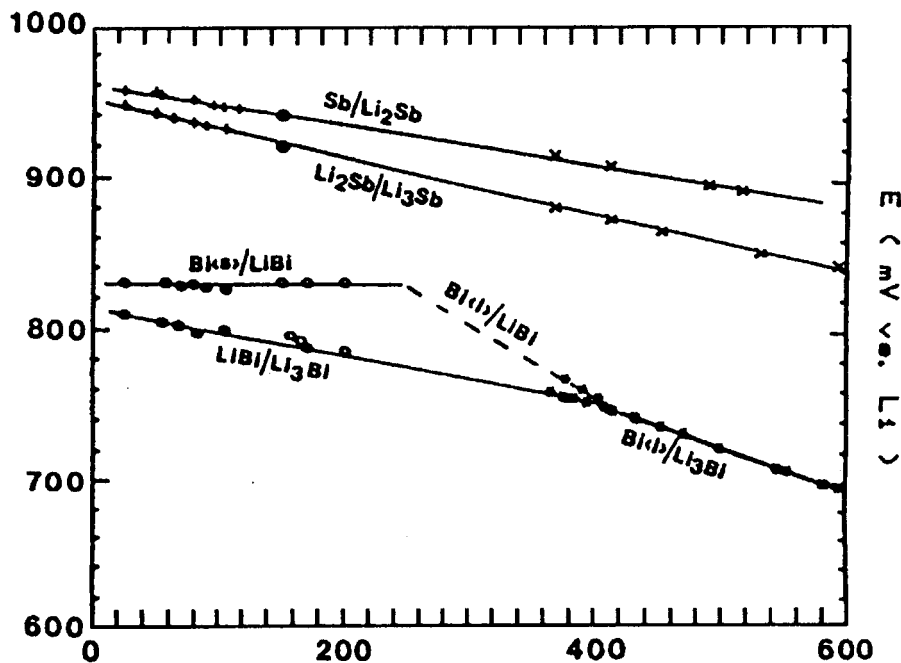


Figure 9.6. Temperature dependence of the potentials of the two-phase plateaus in the Li-Sb and Li-Bi systems.

change in slope at the eutectic melting point (243°C), and the data for the two plateaus converge at about 420°C, which corresponds to the fact that the LiBi phase is no longer stable above that temperature. These features can be seen in the phase diagram for that system, shown in Figure 9.7. At higher temperatures there is only a single reaction:



In addition, the potentials of the second reaction fall along two straight line segments, depending upon the temperature range. There is a significant change in slope at about 210°C, resulting in a negligible temperature dependence of the potential at low temperatures, due to the melting of bismuth.

As before, all the potentials are related to the standard Gibbs free energy changes ΔG_r° relating to the relevant reactions.

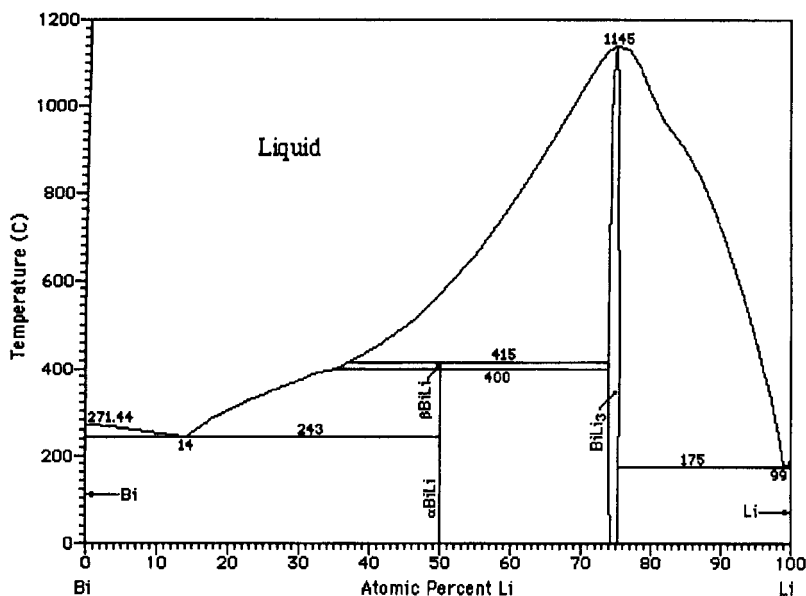


Figure 9.7. Lithium-bismuth binary phase diagram.

The temperature dependence of the values of ΔG_r° can be seen from the defining equation:

$$\Delta G_r^\circ = \Delta H_r^\circ - T\Delta S_r^\circ \quad (9.10)$$

where ΔH_r° is the change in the standard enthalpy and ΔS_r° is the change in the standard entropy resulting from the corresponding reaction. Thus it can be seen that:

$$[(d\Delta G_r^\circ)/(dT)] = \Delta S_r^\circ \quad (9.11)$$

From these data, one can obtain values of the standard molar entropy changes involved in these several reactions. They are shown in Table 9.2. This allows the prediction of the potentials at any temperature within this range.

Table 9.2. Reaction entropies in the lithium-antimony and lithium-bismuth systems.

Reaction	Molar Entropy of Reaction (J/K mol)	Temperature Range (°C)
$2 \text{ Li} + \text{Sb} = \text{Li}_2\text{Sb}$	- 31.9	25 - 500
$\text{Li} + \text{Li}_2\text{Sb} = \text{Li}_3\text{Sb}$	- 46.5	25 - 600
$\text{Li} + \text{Bi} = \text{LiBi}$	0	25 - 200
$2 \text{ Li} + \text{LiBi} = \text{Li}_3\text{Bi}$	- 36.4	25 - 400

9.3.5. Experiments at Ambient Temperature

Experiments have also been performed to determine the equilibrium values of the electrochemical potentials and capacities in a number of binary lithium systems at ambient temperatures.^{21,22} Because of slower kinetics at lower temperatures, these experiments took longer to perform. Data are presented in Table 9.3.

9.4. LIQUID BINARY ALLOYS

Although the discussion here has involved solid lithium alloys, similar considerations apply to those based on sodium or other species. In addition, it is not necessary that the active material be solid. The same principles hold for liquids.

Table 9.3. Plateau potentials and composition ranges of lithium alloys at low temperatures under equilibrium conditions.

Voltage vs. Li/Li ⁺ , V	System	Range of y	Temperature°C	Ref.
0.005	Li _y Zn	1 - 1.5	25	21
0.055	Li _y Cd	1.5 - 2.9	25	21
0.157	Li _y Zn	0.67 - 1.0	25	21
0.219	Li _y Zn	0.5 - 0.67	25	21
0.256	Li _y Zn	0.4 - 0.5	25	21
0.292	Li _y Pb	3.2 - 4.5	25	21
0.352	Li _y Cd	0.3 - 0.6	25	21
0.374	Li _y Pb	3.0 - 3.2	25	21
0.380	Li _y Sn	3.5 - 4.4	25	22
0.42	Li _y Sn	2.6 - 3.5	25	22
0.449	Li _y Pb	1 - 3.0	25	21
0.485	Li _y Sn	2.33 - 2.63	25	22
0.530	Li _y Sn	0.7 - 2.33	25	22
0.601	Li _y Pb	0 - 1	25	21
0.660	Li _y Sn	0.4 - 0.7	25	22
0.680	Li _y Cd	0 - 0.3	25	21
0.810	Li _y Bi	1 - 3	25	22
0.828	Li _y Bi	0 - 1	25	22
0.948	Li _y Sb	2 - 3	25	22
0.956	Li _y Sb	1 - 2	25	22

An example that was of great interest some years ago involved the so-called sodium-sulfur battery that operates at about 300°C. In this case, both of the electrodes are liquids, and the electrolyte is a solid sodium ion conductor, commonly called sodium beta alumina. This configuration can be described as an L/S/L system. It is the inverse of conventional systems with solid electrodes and a liquid electrolyte, S/L/S systems. The negative electrode is molten sodium, and the positive electrode is the product of the reaction of sodium with liquid sulfur. Thus the basic reaction can be simply written as:



The potential of the sodium electrode is constant, independent of the amount of sodium present. The composition of the positive electrode changes

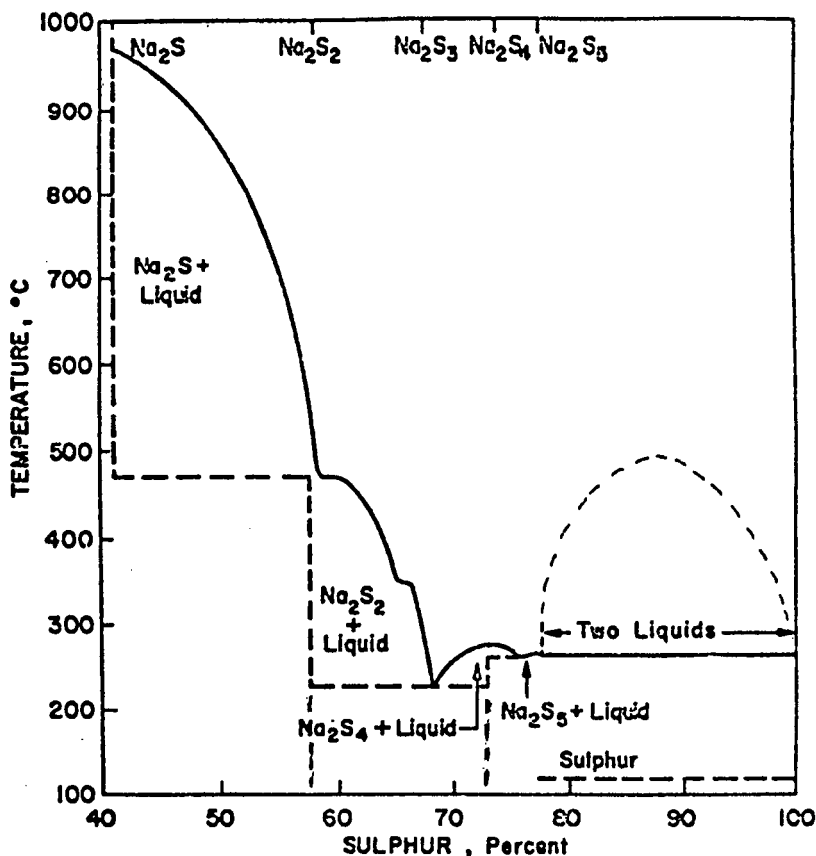


Figure 9.8. Part of the sodium-sulfur phase diagram.

as the sodium concentration varies, however. Thus its potential is composition-dependent.

The relevant portion of the Na-S phase diagram is shown in Figure 9.8. It is seen that at about 300°C a relatively small amount of sodium can be dissolved in liquid sulfur. When this concentration is exceeded, a second liquid phase with a composition of about 78 atomic percent Na is nucleated. This has a composition that is roughly $\text{Na}_{0.4}\text{S}$. As more sodium is added, the overall composition traverses the two-phase region, and the amount of this liquid phase increases relative to the amount of the sulfur-rich liquid phase. Thus a potential plateau is expected over this composition range. When the sodium concentration exceeds that corresponding to about $\text{Na}_{0.4}\text{S}$ the overall composition moves into a single phase liquid range, and thus the potential varies. The maximum amount of sodium that can be used in this electrode corresponds roughly to $\text{Na}_{0.67}\text{S}$. At higher sodium concentrations, a solid second phase begins to form from the liquid solution. This tends to form at the interface between the solid electrolyte and the liquid electrode, and prevents the ingress of more sodium, thus blocking the reaction. The variation of the potential with the composition of the electrode is shown in Figure 9.9.

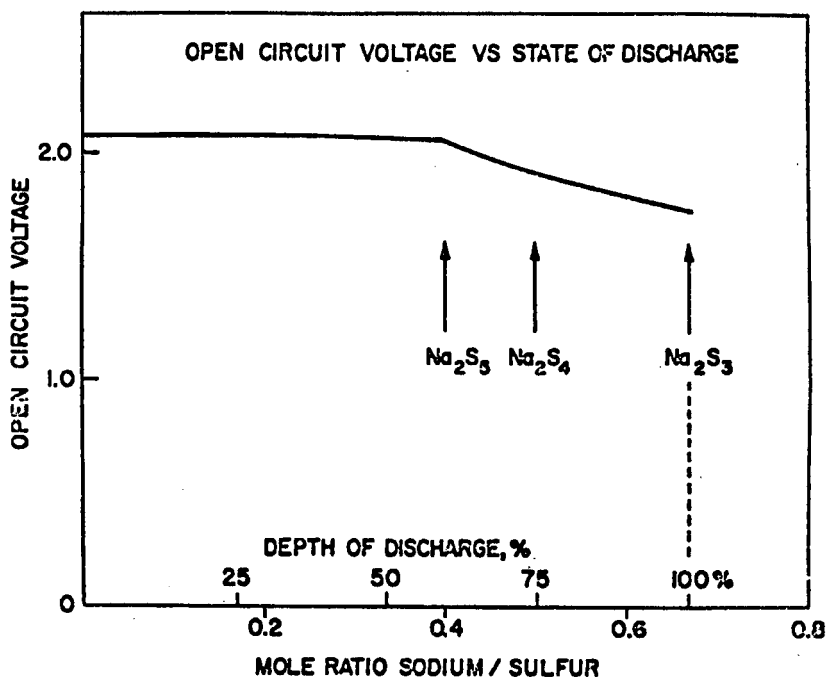


Figure 9.9. Voltage versus sodium as a function of the composition of the positive electrode.

9.5. MIXED-CONDUCTOR MATRIX ELECTRODES

In order to be able to achieve appreciable macroscopic current densities while maintaining low local microscopic charge and particle flux densities, many battery electrodes that are used in conjunction with liquid electrolytes are produced with porous microstructures containing very fine particles of the solid reactant materials. This high reactant surface area porous structure is permeated with the electrolyte.

This porous fine-particle approach has several characteristic disadvantages. Among these are difficulties in producing uniform and reproducible microstructures, and limited mechanical strength when the structure is highly porous. In addition, they often suffer Ostwald ripening, sintering, or other time-dependent changes in both microstructure and properties during cyclic operation.

Furthermore, it is often necessary to have an additional material present in order to improve the electronic transport within an electrode. Various highly dispersed carbons are often used for this purpose.

A quite different approach was introduced some years ago²³⁻²⁵ in which it was demonstrated that a dense solid electrode can be fabricated which has a composite microstructure in which particles of the reactant phase or phases are finely dispersed within a solid electronically-conducting matrix in which the electroactive species is also mobile, *i.e.* within a mixed conductor. There is thus a large internal reactant/mixed-conducting matrix interfacial area. The electroactive species is transported through the solid matrix to this interfacial region, where it undergoes the chemical part of the electrode reaction. Since the matrix material is also an electronic conductor, it can also act as the electrode's current collector. The electrochemical part of the reaction takes place on the outer surface of the composite electrode.

When such an electrode is discharged by deletion of the electroactive species, the residual particles of the reactant phase remain as relics in the microstructure. This provides fixed permanent locations for the reaction to take place during following cycles, when the electroactive species again enters the structure. Thus this type of configuration has the additional advantage that it can provide a mechanism for the achievement of true microstructural reversibility.

In order for this concept to be applicable, the matrix and the reactant phases must be thermodynamically stable in contact with each other. One can evaluate this possibility if one has information about the relevant phase diagrams as well as the titration curves of the component binary systems. The stability window of the matrix phase must span the reaction potential of the reactant material. It has been shown that one can evaluate the possibility that these conditions are met from knowledge of the binary titration curves.

Since there is generally a common component, these two binaries can also be treated as a ternary system. Although ternary systems are not explicitly discussed here, it can be simply stated that the two materials must lie at corners of the same constant-potential tie triangle in the relevant isothermal ternary phase diagram in order to not interact. The potential of the tie triangle determines the electrode reaction potential, of course. An additional requirement is that the reactant material must have two phases present in the tie triangle, but the matrix phase only one.

The kinetic requirements for a successful application of this concept are readily understandable. The primary issue is the rate at which the electroactive species can reach the matrix/reactant interfaces. The critical parameter is the chemical diffusion coefficient of the electroactive species in the matrix phase. This can be determined by various techniques, as discussed elsewhere.

The first example that was demonstrated was the use of the phase with the nominal composition $\text{Li}_{13}\text{Sn}_5$ as the matrix, in conjunction with reactant phases in the lithium-silicon system at temperatures near 400°C . This is an especially favorable case, due to the very high chemical diffusion coefficient of lithium in the $\text{Li}_{13}\text{Sn}_5$ phase.

The relation between the potential-composition data for these two systems under equilibrium conditions is shown in Figure 9.10. It is seen that the phase $\text{Li}_{2.6}\text{Sn}$ ($\text{Li}_{13}\text{Sn}_5$) is stable over a potential range that includes the upper two-phase reconstitution reaction plateau in the lithium-silicon system.

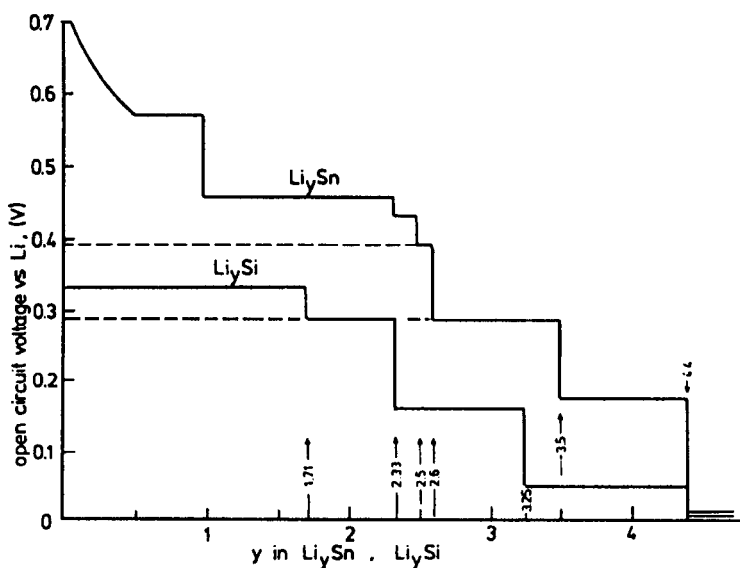


Figure 9.10. Composition dependence of the potential in the Li-Sn and Li-Si systems.

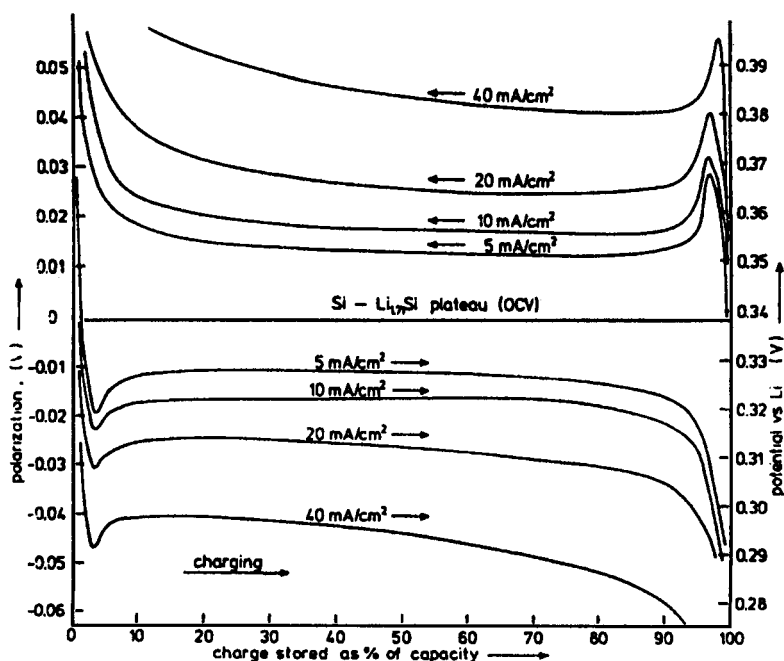


Figure 9.11. Charge and discharge curves of the Li-Si alloy in the matrix of the electrochemically inert mixed-conducting Li-Sn alloy at different current densities.

Therefore, lithium can react with Si to form the phase $\text{Li}_{1.7}\text{Si}$ ($\text{Li}_{12}\text{Si}_7$) inside an all-solid composite electrode containing the $\text{Li}_{2.6}\text{Sn}$ phase, which acts as a lithium-transporting, but electrochemically inert matrix.

Figure 9.11 shows the relatively small polarization that is observed during the charge and discharge of this electrode, even at relatively high current densities. It is seen that there is a potential overshoot due to the free energy involved in the nucleation of a new second phase if the reaction goes to completion in each direction. On the other hand, if the composition is not driven quite so far, this nucleation-related potential overshoot does not appear, as seen in Figure 9.12.

This concept has also been demonstrated at ambient temperature in the case of the Li-Sn-Cd system.^{26,27} The composition-dependence of the potentials in the two binary systems at ambient temperature is shown in Figure 9.13, and the calculated phase stability diagram for this ternary system is shown in Figure 9.14. It was shown that the phase $\text{Li}_{4.4}\text{Sn}$, which has fast chemical diffusion for lithium, is stable at the potentials of two of the Li-Cd reconstitution reaction plateaus, and therefore can be used as a matrix phase.

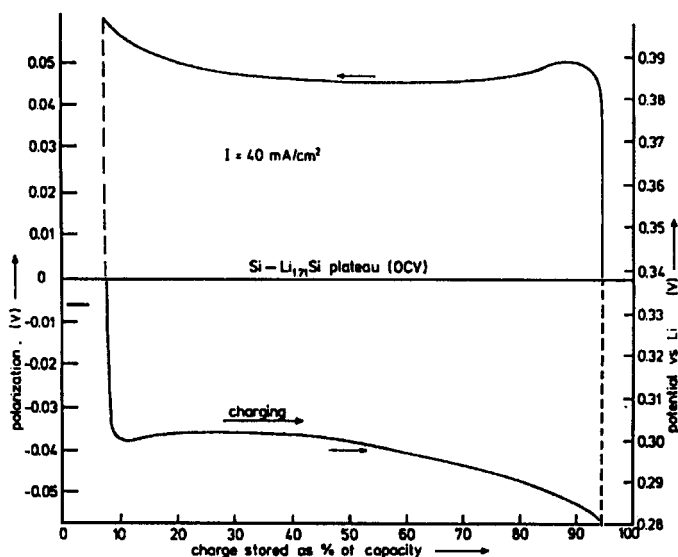


Figure 9.12. Charge and discharge curves of the Li-Si, Li-Sn composite if the capacity is limited so that the reaction does not go to completion in either direction. There is no large nucleation overshoot in this case.

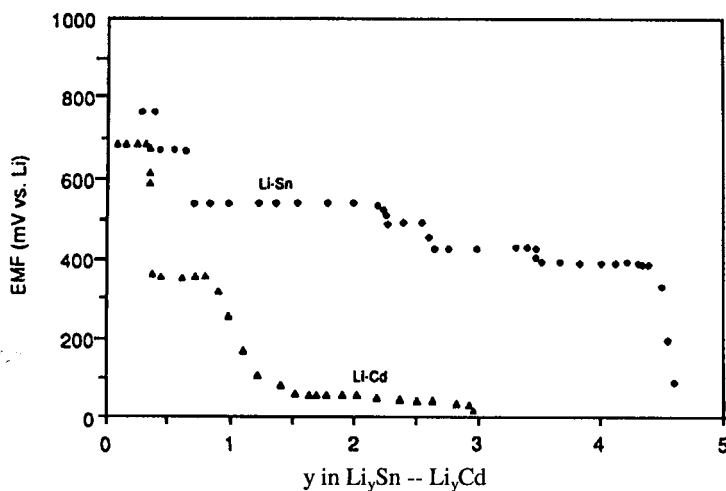


Figure 9.13. Potential versus composition for Li-Sn and Li-Cd systems at ambient temperature.

The behavior of this composite electrode, in which Li reacts with the Cd phases inside of the Li-Sn phase, is shown in Figure 9.15.

In order to achieve good reversibility, the composite electrode

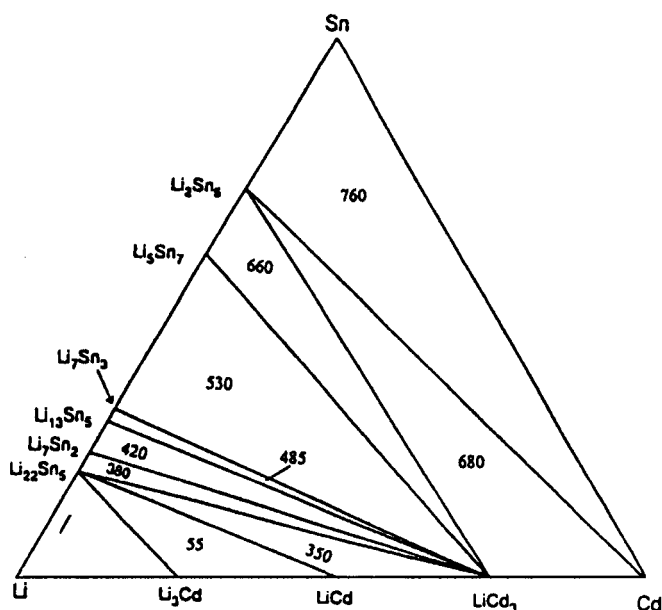


Figure 9.14. Calculated phase stability diagram for the Li-Cd-Sn system at ambient temperature. Numbers are voltages vs. Li.

microstructure must have the ability to accommodate any volume changes that might result from the reaction that takes place internally. This can be taken care of by clever microstructural design and alloy fabrication techniques.

9.6. DECREPITATION

A phenomenon called “decrepitation” can occur in materials that undergo significant volume changes upon the insertion of guest species. It is also sometimes called “crumbling”. These dimensional changes cause mechanical strain in the microstructure, often resulting in the fracture of particles in an electrode into smaller pieces.

This can be a striking, and sometimes disastrous, phenomenon, for it is not specifically related to fine particles, or even to electrochemical systems. As an example, it has been shown that some bulk solid metals can be caused to fracture, and can even be converted into powders by repeated exposure to hydrogen gas if they form metal hydrides under the particular thermodynamic conditions present. This is, of course, different from the hydrogen embrittlement problem in metals with body-centered cubic crystal structures,

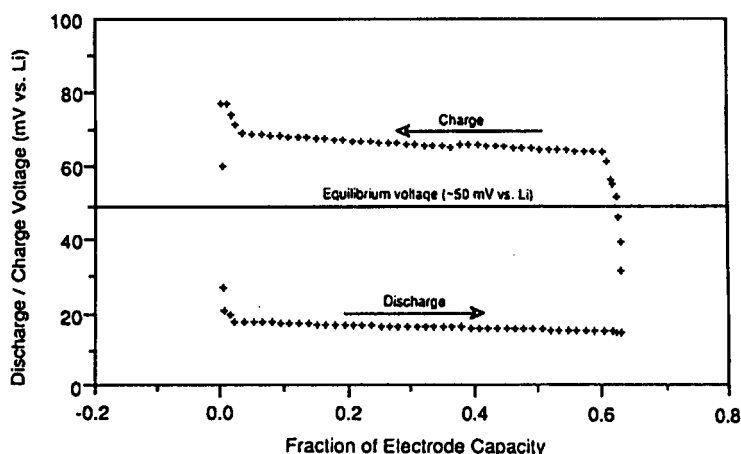


Figure 9.15. Charge-discharge curve of the Li-Cd system with a fast mixed-conducting phase in the lithium-tin system at a current density of 0.1 mA/cm^2 (ambient temperature).

which involves the segregation of hydrogen to dislocations within the microstructure, influencing their mobility.

Decrepitation is often particularly evident during cycling of electrochemical systems. It can readily result in the loss of electronic contact between reactive constituents in the microstructure and the current collector. As a consequence, the reversible capacity decreases.

This phenomenon has long been recognized in some electrochemical systems in which metal hydrides are employed as negative electrode reactants. Similar phenomena also occur in lithium systems employing alloy electrodes, some of which undergo very large changes in specific volume if the composition is varied over a wide range in order to achieve a large capacity.

Because of its potentially large capacity, a considerable amount of attention has been given recently to the Li-Sn system, which is a fine example of this phenomenon. The phase diagram of the Li-Sn system shows that there are six intermediate phases. The thermodynamic and kinetic properties of the different phases in this system were investigated some time ago at elevated temperatures^{17,28} and also at ambient temperatures.^{21,22,26,27} The volume changes that occur in connection with phase changes in this alloy system are large. The phase that forms at the highest lithium concentration, $\text{Li}_{4.4}\text{Sn}$, has a specific volume that is 283% of that of pure tin. Thus Li-Sn electrodes swell and shrink, or “breathe”, a lot as lithium is added or deleted.

Observations on metal hydrides that undergo larger volume changes have shown that this process does not continue indefinitely. Instead, it is found that there is a terminal particle size that is characteristic of a particular material. Particles with smaller sizes do not fracture further.

Experiments on lithium alloy electrodes have also shown that the electrochemical cycling behavior is significantly improved if the initial particle size is already very small,²⁹ and it is reasonable to conclude that this is related to the terminal particle size phenomenon.

A theoretical paper on the mechanism and the influence of the important parameters related to decrepitation appeared recently.³⁰ It uses a simple one-dimensional model which allows the calculation of the conditions under which fracture will be caused to occur in a two-phase structure due to specific volume mismatch. This model predicts that there will be a terminal particle size below which further fracture will not occur. The value of this characteristic dimension is material-specific, depending upon two parameters, the magnitude of a strain parameter related to the volume mismatch and the fracture toughness of the lower-specific-volume phase. For the same value of volume mismatch, the tendency to fracture will be reduced and the terminal particle size will be larger the greater the toughness of the material. The results of this model calculation are shown in Figure 9.16.

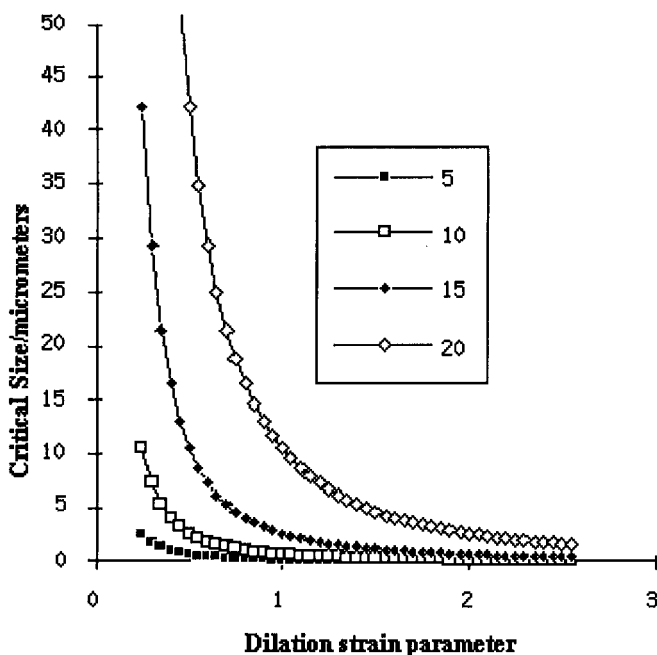


Figure 9.16. Variation of the critical particle size as a function of the dilation strain and the fracture toughness of the phase in tension.

9.7. FORMATION OF AMORPHOUS PRODUCTS AT AMBIENT TEMPERATURE

This chapter has been primarily concerned with understanding the behavior of alloys under equilibrium or near-equilibrium conditions, from which the potential and capacity limits can be determined. Actual behavior in real applications always deviates from these limiting values, of course.

There have been a number of observations that the operation of oxide or alloy electrodes at very high lithium activities can result in the formation of amorphous, rather than crystalline, products, whose properties are different from those of the corresponding crystalline materials.

The spectrum of materials in which amorphous phases have been formed under electrochemical conditions is now quite broad, and include materials of potential interest as positive electrode reactants, such as some vanadium-based materials with the general formula RVO_4 , where R is Al, Cr, Fe, In, or Y.³¹

A group of interesting nitride alloys with structures related to that of Li_3N , which is known to be a fast ionic conductor for lithium, but in which some of the lithium is replaced by a transition metal, such as Co, have been found to become amorphous upon the first insertion of lithium.³²⁻³⁵

Experimental evidence for the electrochemical amorphization of alloys in the Li-Si, Li-Sn or Li-Ag systems was studied by Limthongkul.³⁶ In the latter two cases, this was only a transient phenomenon.

Especially interesting, however, have been experiments that gave evidence for the formation of amorphous silicon during the initial lithiation of a number of silicon-containing precursors, including SiB_3 , SiO , $CaSi_2$ and $NiSi_2$.³⁷⁻³⁹ The electrochemical behavior of these materials after the initial lithiation cycle was essentially the same as that found in Si powder that was initially amorphous. There was, however, an appreciable amount of irreversible capacity in the first cycles of these precursors, about 1 mol of Li in the case of SiB_3 and the disilicides, which was evidently due to an irreversible displacement reaction with Li to form one mol of amorphous silicon. In the case of SiO the irreversible capacity amounted to about two mols of Li, which was surely related to the irreversible formation of Li_2O as well as the amorphous silicon. Some of these materials with amorphous Si are

Table 9.4. Reversible capacity of several materials that contain amorphous silicon.

Material	Reversible Capacity, mAh/g
SiB_3	440
SiO	675
Amorphous Si	>1000

of considerable potential interest as negative electrode reactants in lithium systems, as their charge/discharge curves are in an attractive potential range, they have reasonable kinetics, and their reversible capacities are very high, as shown in Table 9.4.

9.8. SUMMARY

Because of safety and cycle life problems with the use of elemental lithium, essentially all rechargeable lithium batteries use lithium alloys as negative electrode reactants today. The theoretical limits of the potentials and capacities of such electrodes can be determined from a combination of thermodynamic data and phase diagrams. This has been demonstrated for several examples of binary systems.

There are two general types of reactions that can take place: homophase reactions, in which guest atoms are inserted into an existing phase, often topotactically, and reconstitution reactions in which phases nucleate and grow in heterophase microstructures. The potential varies with the overall composition of an electrode in the insertion reaction homophase case, but is composition-independent when reconstitution reactions take place in heterophase microstructures.

The electrochemical titration method can be used to investigate the relevant parameters experimentally. Experimental results are now available for a number of systems, both at elevated temperatures and at ambient temperatures.

Under equilibrium, or near-equilibrium, conditions the potentials are directly related to the standard Gibbs free energies of formation of the phases involved. Thus thermodynamic data can predict experimental results. Likewise, experiments can provide thermodynamic data. As an example, the temperature dependence of potential plateaus can be used to determine the standard entropy changes in the relevant reaction. These experimental data also correlate with the stability of phases in the phase diagram. Furthermore, the maximum theoretical specific energy of an electrochemical system can also be determined from the equilibrium electrochemical titration curve and the related thermodynamic data.

These principles are applicable to liquid, as well as solid, binary materials. An example is the Na-S system, which is the basis for a high temperature L/S/L battery system that uses sodium beta alumina as a solid electrolyte.

Composite multiphase microstructures can be useful in some cases, if the thermodynamic and kinetic properties of one binary system are compatible with those of another binary system. The critical question is the potential range in which the desired reaction takes place. It must be within

the stability range of the other phase with fast kinetics. Experiments have demonstrated that this mixed-conductor matrix concept can be used at both elevated temperatures and ambient temperatures.

One of the practical problems with a number of alloy systems in which large values of capacity are achieved by the use of large composition changes is related to the corresponding volume changes. This can lead to decrepitation and electronic disconnection of reactant particles. The general features of this behavior, and the importance of the particle size and the mechanical properties of the respective phases are now understood in principle.

An interesting recent development relating to alloys has been the appearance of experimental results showing that electrochemical lithiation can cause the appearance of amorphous phases with quite different properties from those of the equilibrium phases. Especially interesting, and potentially important, is the observation that displacement reactions can take place during lithiation of some materials containing silicon that result in the formation of amorphous silicon as a product. This amorphous silicon can then react reversibly with lithium at attractive potentials and with a high capacity.

REFERENCES

1. N. P. Yao, L.A. Heredy and R.C. Saunders, *J. Electrochem. Soc.* 118 (1971) 1039.
2. E.C. Gay, D.R. Vissers, F.J. Martino and K.E. Anderson, *J. Electrochem. Soc.* 123 (1976) 1591.
3. S.C. Lai, *J. Electrochem. Soc.* 123 (1976) 1196.
4. R.A. Sharma and R.N. Seefurth, *J. Electrochem. Soc.* 123 (1976) 1763.
5. R.N. Seefurth and R.A. Sharma, *J. Electrochem. Soc.* 124 (1977) 1207.
6. H. Ogawa, *2nd IMLB*, (Elsevier Sequoia) (1984), p. 259.
7. R. Yazami and P. Touzain, *J. Power Sources* 9 (1983) 365.
8. W. Weppner and R.A. Huggins, *Symposium on Electrode Materials and Processes for Energy Conversion and Storage*, J.D.E. McIntyre, S. Srinivasan and F.G. Will, Eds., *Electrochem. Soc.* (1977), p. 833.
9. W. Weppner and R.A. Huggins, *Z. Phys. Chem. N.F.* 108 (1977) 105.
10. W. Weppner and R.A. Huggins, *J. Electrochem. Soc.* 125 (1978) 7.
11. C. Wagner, *J. Chem. Phys.* 21 (1953) 1819.
12. C.J. Wen and R.A. Huggins, *J. Solid State Chem.* 37 (1981) 271.
13. C.J. Wen, *Ph.D. Dissertation*, Stanford University (1980).
14. C.J. Wen and R.A. Huggins, *Mat. Res. Bull.* 15 (1980) 1225.
15. M.L. Saboungi, J.J. Marr, K. Anderson and D.R. Vissers, *J. Electrochem. Soc.* 126 (1979) 322.
16. C.J. Wen and R.A. Huggins, *J. Electrochem. Soc.* 128 (1981) 1636.
17. C.J. Wen and R.A. Huggins, *J. Electrochem. Soc.* 128 (1981) 1181.
18. C.J. Wen, B.A. Boukamp and R.A. Huggins, *J. Electrochem. Soc.* 126 (1979) 2258.
19. W. Weppner and R.A. Huggins, *J. Electrochem. Soc.* 125 (1978) 7.
20. J.P. Doench and R.A. Huggins, *J. Electrochem. Soc.* 129 (1982) 341C.
21. J. Wang, P. King and R.A. Huggins, *Solid State Ionics* 20 (1986) 185.
22. J. Wang, I.D. Raistrick and R.A. Huggins, *J. Electrochem. Soc.* 133 (1986) 457.
23. B.A. Boukamp, G.C. Lesh and R.A. Huggins, *J. Electrochem. Soc.* 128 (1981) 725.
24. B.A. Boukamp, G.C. Lesh and R.A. Huggins, in *Proc. Lithium Batteries*,

- H.V. Venkatasetty, Ed., *Electrochem. Soc.* (1981), p. 467.
25. R.A. Huggins and B.A. Boukamp, *US Patent* 4,436,796.
26. A. Anani, S. Crouch-Baker and R.A. Huggins, in *Lithium Batteries*, A. N. Dey, Ed., *Electrochem. Soc.* (1987), p. 382.
27. A. Anani, S. Crouch-Baker and R.A. Huggins, *J. Electrochem. Soc.* 135 (1988) 2103.
28. C. J. Wen and R. A. Huggins, *J. Solid State Chem.* 35 (1980) 376.
29. J. Yang, M. Winter and J. O. Besenhard, *Solid State Ionics* 90 (1996) 281.
30. R. A. Huggins and W. D. Nix, *Ionics* 6 (2000) 57.
31. Y. Piffard, F. Leroux, D. Guyomard, J.-L. Mansot and M. Tournoux, *J. Power Sources* 68 (1997) 698.
32. M. Nishijima, T. Kagohashi, N. Imanishi, Y. Takeda, O. Yamamoto and S. Kondo, *Solid State Ionics* 83 (1996) 107.
33. T. Shodai, S. Okada, S-i. Tobishima, and J-i. Yamaki, *Solid State Ionics* 86-88 (1996) 785.
34. M. Nishijima, T. Kagohashi, Y. Takeda, N. Imanishi and O. Yamamoto, *8th IMLB* (1996), p. 402.
35. T. Shodai, S. Okada, S. Tobishima and J. Yamaki, *8th IMLB* (1996), p. 404.
36. P. Limthongkul, *Ph.D. Thesis*, Mass. Inst. of Tech. (2002).
37. B. Klausnitzer, *Ph.D. Thesis*, University of Ulm (2000).
38. A. Netz, *Ph.D. Thesis*, University of Kiel (2001).
39. A. Netz, R.A. Huggins and W. Weppner, *11th IMLB* (2002), Abstract No. 47.

Chapter 10

CURRENT ISSUES OF METALLIC LITHIUM ANODE

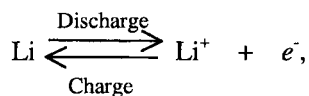
M. Ishikawa and M. Morita

*Department of Applied Chemistry and Chemical Engineering,
Faculty of Engineering, Yamaguchi University, Yamaguchi, Japan*

10.1. INTRINSIC ADVANTAGES AND DRAWBACKS OF METALLIC LITHIUM ANODE

Metallic lithium has the highest theoretical specific capacity (3860 mAh/g) and the most negative redox potential among all metals. These features have attracted the interest of battery investigators, who have attempted to put lithium metal into practical use in rechargeable battery systems. Its poor charge-discharge cycleability, however, and its potential fire hazards have hindered thus far the development of cells with a metallic lithium anode.¹

The essential reaction of metallic lithium anode is very simple:



but, in spite of this simplicity, the practical application of Li metal to a rechargeable anode has been very difficult due to some crucial issues. The most important one is that Li metal usually tends to deposit as a dendritic or mossy structure during charge, and the disordered metallic deposit gives rise to a poor coulombic efficiency. This happens because such a fine Li metal often acts as an active site inducing reductive decomposition of electrolyte components. Part of the deposit may become electrically isolated and shedding may also occur. Furthermore, the fine metallic Li can easily penetrate into the separator and eventually cause internal short, this resulting in heat generation and contingent ignition. To turn batteries with a metallic Li anode into actual utilization more efforts should be made to overcome these problems.

10.2. HISTORICAL ASPECTS IN RECHARGEABLE METALLIC LITHIUM BATTERIES

Before the successful commercialization of Li-ion batteries, *i.e.*, around 1990, in prototype and commercialized secondary Li metal-based batteries, major strategies to compensate for poor Li cycling efficiency could be categorized into two ways. They were: (i) compensation for the low charge-discharge reversibility of the Li anode by loading excess amount of Li metal, and: (ii) suppression of irregular (mossy or dendritic) Li deposition by using a Li-alloy anode as listed in Table 10.1.

Although these schemes could somewhat make up for the poor cycleability of Li metal, their effects were still unsatisfactory. The use of excess amount of Li (scheme i) resulted in an increase of the total weight of batteries. Furthermore, even with excess metallic Li, cycling life was still short: 200-300 cycles.

On the other hand, Li-alloy anodes (scheme ii) were applied mainly to coin-type cells for memory back-up. Cells with Li-alloy anodes could stand approximately 1000 cycles because memory back-up applications do not demand deep charge-discharge cycles.^{2,3} However, a secondary metal alloyed with Li increases the total anode weight, and induces a positive shift of the potential; for instance, Li-Al alloy anodes typically have a redox potential of 0.3-0.5 V *vs.* Li/Li⁺. The energy density of cells containing a Li-alloy anode was usually much lower even than that of cells with an excess amount of Li metal. In addition, such Li-alloy anodes cannot be applied to cylindrical cells, which need wound electrodes, because the Li-alloy anodes are too brittle and hard to be wound.

Besides Al, some metals can form with Li intermetallic compounds acting as Li-alloy anodes, which can be easily handled and control the morphology of the Li deposit.⁴ Unfortunately, however, such anodes have crucial problems; the change in electrode volume during charge-discharge is remarkably large, and the electrodes gradually become pulverized, limiting the cycle life. "Wood's metal alloy" is a eutectic alloy consisting of Bi, Pb, Cd and Sn, and can form an intermetallic compound with Li.⁵ However, the pulverization of Wood's metal is still inevitable like most Li-alloy anodes.

To overcome this problem we might assemble a cell using "originally" pulverized alloy powders instead of an intact alloy sheet as an anode. Generally, however, it is very difficult to optimize their binding and dispersion conditions, and there is severe trade-off between their long cycle life and high energy density.

Table 10.1. Rechargeable lithium batteries in commercialization or test production before 1990.

Type	Battery system	Electrolyte	Energy density	Cycle life	Makers
	Anode-Cathode		Wh/kg		
Coin	Li/Wood's metal alloy-Carbon cathode	PC+ α -LiClO ₄	2.3	1000	Matsushita Battery Industrial
	Li/Al alloy-TiS ₂	4MeDOL/DME/HMPA LiPF ₆	1.8	1000	Hitachi Maxell
	Li/Linear graphite-Amorphous V ₂ O ₅	PC-LiClO ₄	5.4	1000	Toshiba Battery
	Li/Al alloy-Polyaniline	DME LiBF ₄	8.3	1000	Bridgestone
	Li/Al alloy-LiOH/ MnO ₂	-	18	200	Sanyo Electric
	Li/Al alloy-V ₂ O ₅	-	20	100	Matsushita Battery Industrial
AA Size	Li-MoS ₂	EC PC	50	400	MOLI
		LiAsF ₆	70	100	
	Li-MnO ₂ composite oxide	-	106	200	Sony Energytec
	Li-NbSe ₃	-	95	250	ATT
	Li-TiS ₂	MeTHF/THF LiAsF ₆	89	75-200	Grace
	Li-CuCl ₂	Inorganic electrolyte	ca. 100	200	Altus
	Li-MoO ₃	-	81	300	FDK

Table 10.2. Lithium metal rechargeable batteries developed after 1990.

Application	Anode-Cathode	Electrolyte	Energy density Wh/kg	Average operating voltage V
Load leveling ¹	Li-LiV ₂ O ₄	-	120	-
Vehicle ²	Li(+Ga)-LiMn ₂ O ₄ (+Cu)	LiPF ₆ /EC+DME	132	3.1
Electric vehicle (high-temperature operation polymer battery) ³	Li-VO ₂	-	-	-
Vehicle (high-temperature operation) ⁴	Li(alloy)-FeS or FeS ₂	LiCl+KCl	80-180	1.7
Small electronics (polymer gel battery) ⁵	Li-Disulfide+PAN	Acrylate derivatives	630	3.4
Small electronics (polymer gel battery) ⁶	Li alloy-V ₆ O ₁₃	PEO derivatives	-	2.5
Small electronics (polymer gel battery) ⁷	Li-sulf-composite materials	Acrylate derivatives	-	-

¹Yusasa Battery/CRIEPI (Central Research Institute of Electric Power Industry, Japan); ²NEDO/DENSO; ³USABC/Hydro-Quebec/3M; ⁴USABC/ANL/Westinghouse/SAFT-America; ⁵Matsushita Battery Industrial; ⁶Lithium Technology; ⁷PolyPlus

back-up coin-type cells, research activity for such alloy electrodes is now being diminished. In Europe, nonetheless, Besenhard and co-workers continue basic studies on alloy electrodes,⁶ and in the USA mainly USABC is developing rechargeable batteries for high-temperature applications with a Li-Al anode for vehicles.⁷

10.3. RECENT TRENDS IN THE DEVELOPMENT OF BATTERIES WITH A Li ANODE

After the start of commercial production of Li-ion batteries, the goal of developing rechargeable batteries with a metallic Li anode became more definite than that before the '90s: the performance of Li metal batteries must somehow exceed that of batteries with a carbon anode in practical use. Table 10.2 shows batteries under development with a Li metal anode. In Japan there have been projects utilizing a Li metal anode conducted by "NEDO" (New Energy and Industrial Technology Development Organization) aiming at power sources both for transportation and stationary applications.⁸

One of the fields where a Li metal anode is attracting much interest is that of polymer battery systems. These systems are considered promising not only for portable electronics but also for electric vehicles. As just described, the practical use of Li metal anode is still considered to be worth the effort. On the other hand, with respect to investigations on the basic chemistry of Li metal electrode behavior, several important factors affecting the reversibility of Li cycling have become fairly clear based on electrochemical tests (ac impedance spectroscopy and scanning vibrating electrode technique [SVET]), chemical tests (typically ESCA [XPS] and IR), and microscopic tests (TEM, SEM and AFM, analyses of Li anode surface). On the basis of such characterizations, novel electrolyte systems as well as electrolyte additives compatible with a Li anode have been proposed. Details will be given in the next section.

10.4. OPTIMIZATION OF THE LITHIUM ANODE INTERFACE

10.4.1. Fundamentals

An essential strategy to obtain a satisfactory performance from a metallic Li anode is to optimize chemically as well as physically the interfacial structure between Li anode and electrolyte. Without a design based on this strategy, it is practically impossible to have a practical Li

anode showing high coulombic efficiency and adequate safety.

Since the reducing power of Li metal is extremely high, *i.e.*, its thermodynamic redox potential is very low, reductive decomposition of an electrolytic solvent and/or salt occurs at the pristine Li interface as soon as

Table 10.3. Chemical composition of passivation films on Li metal.

Electrolyte	Passivation film
Without electrolyte (native film)	LiOH, Li ₂ CO ₃ , Li ₂ O
General PC systems	CH ₃ CH(OCO ₂ Li)CH ₂ OCO ₂ Li
PC/LiPF ₆	LiF, Li ₂ O, LiOH
PC/LiClO ₄	Li ₂ CO ₃ , LiOH, Li ₂ O, LiCl, ROCO ₂ Li, LiCHClCHCl, LiCH ₂ CHClCH ₂ Cl
General EC systems	(CH ₂ OCO ₂ Li) ₂
General DMC systems	CH ₃ OCO ₂ Li
General DEC systems	CH ₃ CH ₂ OCO ₂ Li, CH ₃ CH ₂ OLi
SO ₂ /LiAlCl ₄	Li ₂ S ₂ O ₄ , Li ₂ SO ₃ , LiS _n O ₆ , Li ₂ S ₂ O ₅
General THF systems	BuOLi
THF/LiAsF ₆	BuOLi, RLi, -As-O-As-, ROLi, -O(CH ₂) ₄ -THF ⁺ , F ₂ -As-O-As-F ₂
General 2MeTHF systems	Li pentoxides
2MeTHF/LiAsF ₆	(-As-O-) _n , LiAs(OR) _n F _{6-n} , AsO _n F _{5-n} , As(OR) _n F _{3-n}
General DME systems	CH ₃ OLi
DME/LiAsF ₆	CH ₃ OLi, LiF
General BL systems	C ₃ H ₇ OCO ₂ Li, cyclic <i>b</i> -keto ester
General DOL systems	CH ₃ OLi, C ₂ H ₅ OLi, LiOC ₂ H ₄ (OCH ₂) _n OX (X=Oli, H, OR)

they get in contact. Some components of the decomposition products form the so-called solid electrolyte interface (SEI). If the latter can protect against further electrolyte decomposition, as does a passivation layer in a corrosion process of some metal, the SEI can prevent perpetual side reactions of an electrolyte with Li, and hence even the thermodynamically unstable Li metal can get pseudo-stability in an organic electrolyte.

With regard to a rechargeable Li anode interface, however, it should be not only protective against side reactions, but should also not impede the diffusion of Li ions across the interface during cycling. As the components of an interface layer depend obviously on the nature of electrolytes (see Table 10.3), appropriate electrolytes have to be selected to favor Li cycling. The surface layer is known to crucially affect the morphology of Li metal and the charge/discharge efficiency. It is recognized that a grained or lumpy surface structure can lead to a high efficiency of Li cycling, while a dendritic or mossy Li structure is undesirable.

For instance, LiPF_6 , an electrolytic salt with perfluoro anion, leads to the formation of a LiF layer at a metallic Li interface.⁹⁻¹¹ This layer has a good protective ability, and if its thickness is appropriate, the morphology of deposited Li becomes grainy, resulting in an improved cycling efficiency.

Table 10.4. Additives used to enhance the cycling efficiency of Li metal.

Group	Additive	Major acting mechanism
Inorganic	HF	Formation of LiF layer
	AlI_3 , MgI_2 , SnI_2	Formation of Li-alloy layer
	S_x^{2-}	Formation of protecting film
Organic	2Me-furan, 2Me-THF, Pyridine derivatives, Dipyridyl derivatives	Surface adsorption, formation of organic protecting film, solvation of Li^+
	Cetyltrimethylammonium chloride	Electrode surface adsorption
	Nonionic surfactants, Crown ethers	Electrode surface adsorption, solvation of Li^+
	Benzene	Electrode surface adsorption
Gas	CO_2	Formation of Li_2CO_3 layer
	N_2O , CO	Formation of protecting film

10.4.2. Effect of Additives

Another approach to the improvement of Li cycling efficiency is including some additives in the electrolyte formulation. This method can control or modify the thickness, morphology and chemical composition of the Li surface layer. The main additives so far investigated for rechargeable Li battery electrolytes are listed in Table 10.4.

These organic, inorganic and gaseous additives can improve the cycling efficiency of a Li anode. They can be categorized roughly into two groups with different mechanisms: (i) formation of a protective surface layer by reaction of Li with an additive, (ii) formation of a protective quasi-layer by adsorption of a non-reactive additive.

Not only major components but also minor impurities in the electrolytes can have a serious influence on the surface composition via their reactions with Li, and hence a change in cycleability can occur. In addition, trace impurities in the controlled atmosphere used to form a Li sheet would also affect the Li surface. Usually, a Li metal sheet is made in an atmosphere containing CO_2 to provide a Li_2CO_3 layer as a “native” interface at a Li sheet surface, while oxygen and moisture must be thoroughly excluded from the atmosphere. The Li_2CO_3 interface is widely known to be favorable for Li cycling.¹²⁻¹⁵

Addition of a small amount (5% or less) of another metal to bulk Li was reported as an alternative method for improving Li surface properties. This scheme is different from the utilization of “conventional” Li-alloys containing relatively large amounts of another metal. Few percents of Al, Sn, Ga, etc. can decrease the interfacial resistance between anode and electrolyte. These anodes may modify the morphology and interfacial impedance of deposited Li while keeping their redox potentials as low as that of pure Li.¹⁶

10.5. PHYSICAL FACTORS AFFECTING THE LITHIUM INTERFACE

Besides chemical factors such as electrolytes and additives, some physical factors have an influence on the Li interface structure. Temperature and stacking pressure on the anode have long been known as such factors. It was reported that cycling a metallic Li anode under a certain pressure can improve Li morphology and hence can provide a good cycling efficiency.¹⁷ With respect to the temperature effect, a uniform surface morphology and a higher cycling efficiency can be obtained cycling Li in some low-temperature electrolytes (*e.g.*, LiPF_6 -based binary carbonate-type electrolytes: LiPF_6 -PC/DMC, LiPF_6 -EC/DMC) in comparison with that in

the corresponding electrolytes at ambient-temperature.^{18,19} Furthermore, a high efficiency can be obtained at ambient-temperature after low-temperature “precycling” in such electrolytes. This result suggests that there is a “hysteresis effect” of electrolyte temperature upon Li anode performance.^{18,19}

10.6. RECENT ADVANCES IN THE RESEARCH ON METALLIC LITHIUM ANODE

Besides the above instances, many efforts have been focused on suitable electrolytes for the improvement of metallic Li anode. Fringant *et al.* studied multi-solvent electrolytes containing a mixture of PC and EC, high-permittivity solvents, with DMC, a low-viscosity co-solvent which contributes to a good cycleability of metallic Li anode.²⁰ As an electrolytic salt, LiAsF₆ has been widely known to provide high Li cycling efficiency, although it has a serious drawback, high toxicity.

Aurbach *et al.* have investigated the relationship among electrolyte composition, corresponding Li surface chemistry, ionic conductivity at the surface layer and morphology of Li deposit.^{19, 21-23} They suggested that

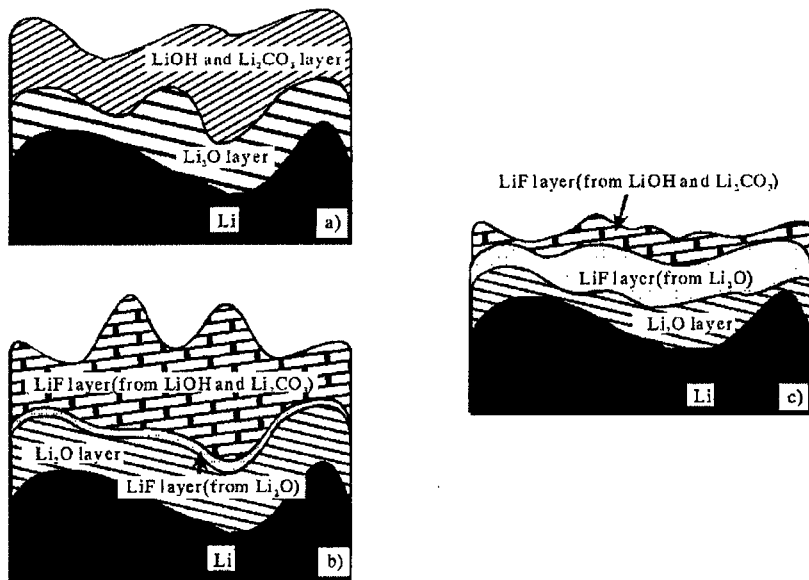


Figure 10.1. Chemical structure of passivation films on Li metal anode, a) under Ar atmosphere, b) immersion in 1.0 M LiBF_4 / PC or γ -BL for 3 days, c) immersion in 1.0 M LiPF_6 / PC or γ -BL for 3 days.

alkylcarbonate-type electrolytes, such as PC, first give lithium alkylcarbonate, which then react with some impurities to form Li_2CO_3 and Li_2O . It is notable that a reaction leading to a surface layer tends to be dominated by a solvent component in mixed-solvent electrolytes.

Kanamura *et al.* have investigated the relationship between inorganic components at a Li surface and the composition of electrolytes by XPS analysis,^{10,24} and proposed chemical models with a multi-layer structure consisting of inorganic components as shown in Figure 10.1. Furthermore, based on such information, they reported the treatment of Li metal surface with HF to suppress Li dendrite formation.^{25,26}

Another topic of research on salts suitable for a Li anode is the utilization of new salts with an organic anion as alternatives to conventional inorganic salts. Among them, lithium bis(perfluoroalkylsulfonyl)imides have especially proved interesting. They have been tested in various cell systems, where a Li imide has been used not only as a single electrolytic salt but also in mixture with another salt, *e.g.*, $\text{LiN}(\text{SO}_2\text{C}_2\text{F}_5)_2$ with LiPF_6 . Many useful imides have two perfluoroalkylsulfonyl groups linked to a central nitrogen atom asymmetrically [*e.g.*, $\text{LiN}(\text{SO}_2\text{C}_2\text{F}_5)(\text{SO}_2\text{C}_3\text{F}_7)$], as well as symmetrically [*e.g.*, $\text{LiN}(\text{SO}_2\text{C}_2\text{F}_5)_2$], with the exception of lithium bis(trifluoromethylsulfonyl)imide [$\text{LiN}(\text{SO}_2\text{CF}_3)_2$], which is known to cause a severe corrosion of the aluminum substrate at the cathode.

Naoi *et al.* reported that electrolytes containing some lithium

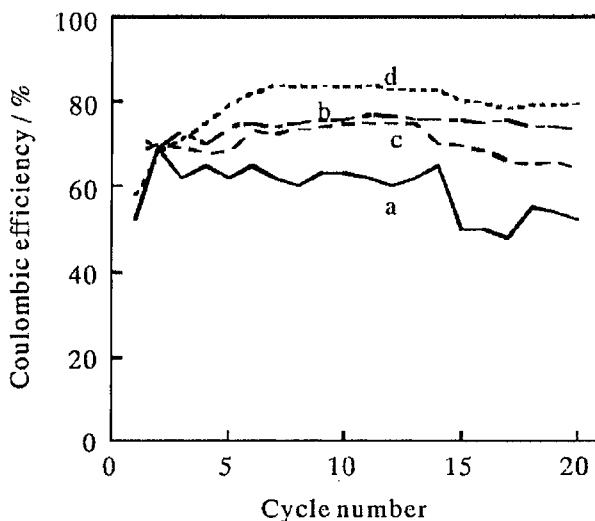


Figure 10. 2. Addition effects of 2MeF, 2MeTp, and benzene on coulombic efficiency of Li in PC with LiClO_4 (1 mol/dm³); current density: 1.0 mA/cm²; charged: 0.1 C/cm²; a: PC, b: PC + 2MeF (0.5 vol %), c: PC + 2MeTp (0.5 vol %), d: PC + benzene.

bis(perfluoroalkylsulfonyl)imides provide a LiF layer which is thinner than that derived from electrolytes containing LiPF_6 ; this thinner layer can protect

the Li surface and promote efficient Li cycling.²⁷ They emphasized that the formation mechanism of the LiF layer in lithium imide-based electrolytes should be completely different from that of LiF layer in LiPF_6 -based electrolytes. In the latter, LiF is formed thanks to the small amount of HF contained in the LiPF_6 systems, while in the imide systems LiF comes from the direct reaction of the imide anion with Li metal.

To modify a metallic Li surface, as already stated, some additives to electrolytes have been investigated. Figure 10.2 shows the effect of several representative additives, 2-methylfuran (2MeF), 2-methylthiophene (2MeTp), and benzene, on the coulombic efficiency of Li cycling in LiClO_4 -PC.

The addition of 2MeF and 2MeTp can restrain a decrease in Li cycling efficiency.²⁸ On the other hand, a positive effect of benzene addition appears at a higher concentration when compared to the effective concentration of 2MeF and 2MeTp. According to interface analyses such as *ac* impedance measurement, the origin of the positive effect of these additives can be explained with the help of Figure 10.3.²⁸

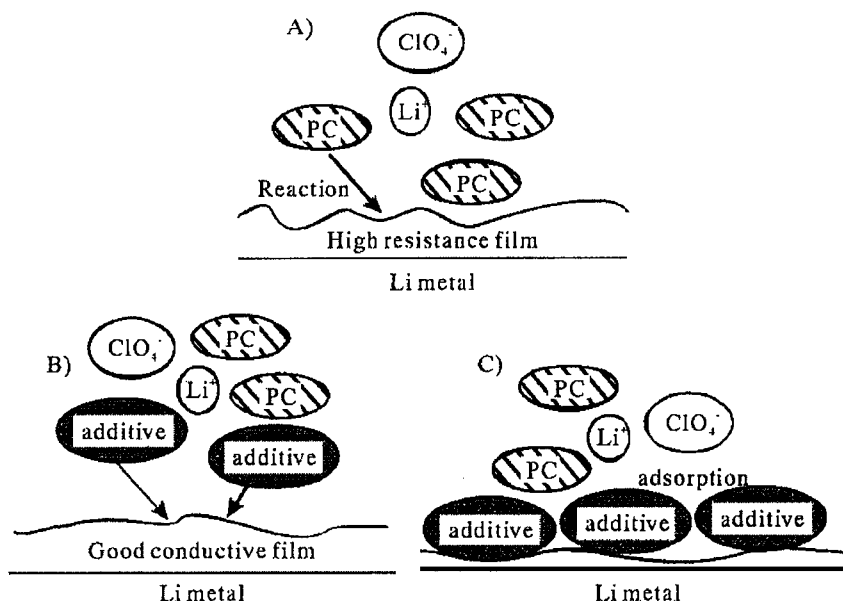


Figure 10.3. Working mechanisms of organic additives, A) without additive, B) reactive additive such as 2MeF or 2MeTp, C) adsorption-type additive such as benzene.

2MeF and 2MeTp react with Li metal to form an ion-conductive protective layer which provides uniform Li deposition at the Li surface. On the other hand, although benzene does not react with Li metal, it is accumulated, or adsorbed, at the Li interface due to its low polarity, and the resulting quasi-layer acts as a barrier separating electrolyte components from Li metal.

Figure 10.4 shows the effect of adding a small amount of metal ion (Al^{3+} and Sn^{2+}).²⁹ A positive effect of these additives on the Li cycling efficiency can be clearly observed. Here, it should be significant to know the difference in ionic current distribution on the Li metal anode with

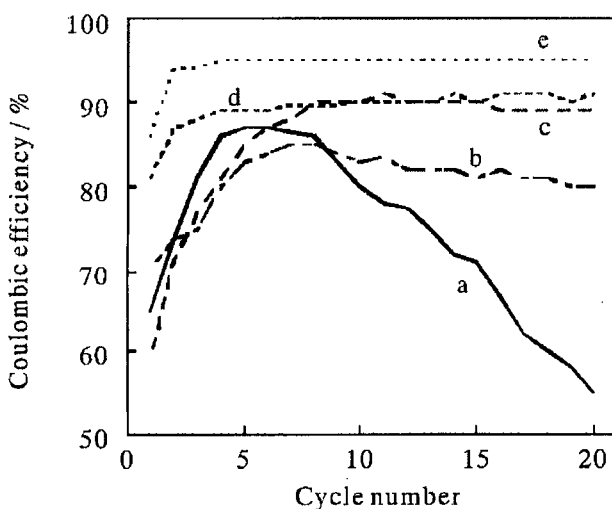


Figure 10.4. Addition effects of LiI, SnI_2 , AlI_3 , and $\text{AlI}_3 + 2\text{MeF}$ on coulombic efficiency of Li in PC with LiClO_4 (1 mol/l); current density: 2.0 mA/cm^2 ; charged electricity: 0.2 C/cm^2 ; a: PC, b: PC + LiI (I⁻ 300 ppm), c: PC + SnI_2 (Sn^{2+} 100 ppm), d: PC + AlI_3 (Al^{3+} 100 ppm), e: PC + AlI_3 (Al^{3+} 100 ppm) + 2MeF (0.5 vol %).

and without additives; to observe this, the scanning vibrating electrode technique (SVET) was applied.^{29,30} The outline of the in situ SVET system is drawn in Figure 10.5; this system can offer potential gradient profiles induced by the Li ionic currents on the surface of the Li-deposited electrode during discharge. The scanning vibrating (SV) electrode (a Pt wire electrode) attached to a sensor probe is vibrated (with a certain frequency between 100-1000 Hz) along a vertical axis (Z-direction) in the vicinity of a test specimen electrode surface by a piezoelectric oscillator; typical distance

electrode. The distance between the highest and the lowest positions was on the sub-micron order: say 0.5 μm . In this case, therefore, the potential gradient values correspond to the potential gaps along a distance of 0.5 μm in the vertical axis on the test electrode surface. This potential gradient is proportional to the ionic current in the vicinity of the electrolyte-test electrode interface because the resistance of the electrolytes can be

regarded as a constant. The X-Y stage, on which the SV electrode is mounted, is moved horizontally by a stepping motor. By gathering the potential gradient values at various X-Y positions, a two-dimensional potential gradient map on the test electrode can be obtained. After all, on the basis of the above measurement criterion, a potential gradient map must correlate directly with ionic current distribution on a test electrode.

Figure 10.6 indicates the potential gradient maps of Li metal anode surface with anodic polarization with and without additives. When the metals (Al and Sn) deposit at Li metal surface with cathodic polarization, they change into a thin Li-alloy surface layer, which can ease the irregularity of Li anode interface. Thus the distribution of Li ionic current becomes relatively regular at the surface with anodic polarization as shown in Figure 10.6. Ishikawa *et al.* revealed the compatibility of metal ion additives with electrolytes; for example, an additive such as AlI_3 can fairly enhance the cycleability of the Li metal anode especially in lithium imide-based electrolytes.^{31,32}

On the other hand, as for gaseous additives, Osaka *et al.* analyzed the effect of saturating electrolytes with CO_2 upon Li metal cycle performance on the basis of *ac* impedance measurement, and found this addition effective in the enhancement of Li anode cycleability.^{14,15} Furthermore, some surfactants were reported to have such an enhancement effect.^{33,34}

Again, representative mechanisms of the aforementioned additives can be briefly summarized as follows: (a) formation of organic polymer passive layer with a good ionic conductivity as a protective interface derived from organic compounds such as 2-methylfuran (2MeF) or its analogues,²⁸ (b) adsorption of inactive additives at a Li interface to inhibit a reaction forming a low-conductive passivation films resulting in uneven Li deposition, *i.e.*, nonpolar additives such as benzene and dekaline²⁸ as well as (ionic or nonionic) polymer or oligomer additives such as surfactants,^{33,34} (c) Li-alloy layer formation by co-deposition of Li with another metal such as Al from an electrolyte containing a small amount of metal salt additive, *e.g.*, AlI_3 , to control the morphology of Li deposit (in other words, to suppress dendritic deposition of Li),²⁹⁻³² (d) formation of an uniform inorganic protective layer from a dissolved gas such as CO_2 ¹²⁻¹⁵ or inorganic acid, *e.g.*, HF .^{25,26}

These working mechanisms appear to have independent origins, so

that we are likely to observe “synergistic effects” when we use some additives with different mechanisms simultaneously. In fact, the simultaneous use of AlI_3 and 2MeF results in a better Li cycleability when compared to the effect of each additive (Figure 10.4).²⁹ In addition, some of

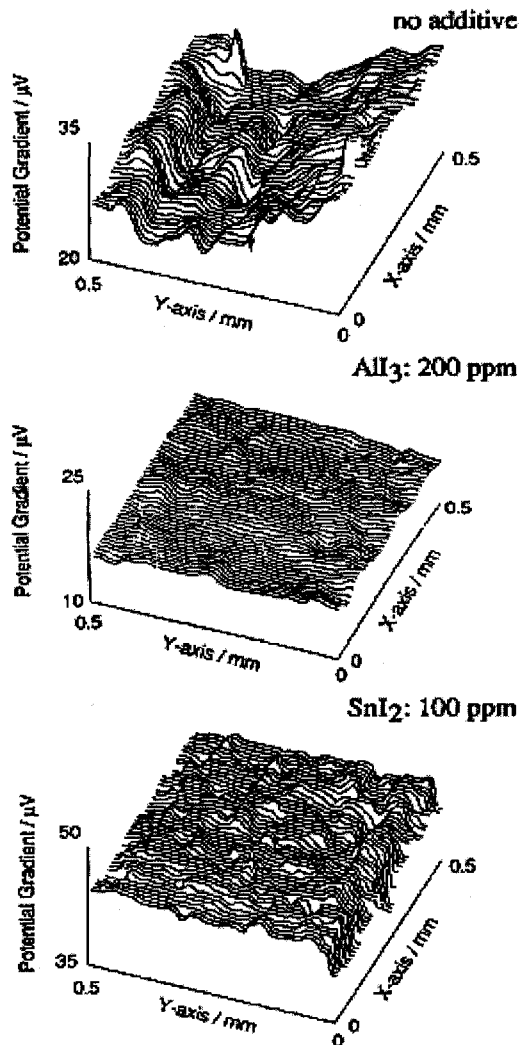


Figure 10.6. Potential gradient maps of Li-deposited Ni substrate (X-Y plate) in PC + 2Me-THF/ LiClO_4 during discharge (25 mV vs. Li/Li^+); 2 mA/cm^2 and 0.2 C/cm^2 for Li-deposition.

the above additives have been known to provide “sustained” effect, even after transfer of a Li anode from an electrolyte with an additive to another electrolyte without additives, the Li anode “treated” with the additive, in some cases, still retains the effect of the additive.³⁵

This means that “pretreatment” of a Li anode with some additives may enhance the cycling efficiency in the subsequent cycles in a “clean” electrolyte without additives.³⁵ This treatment sequence may be promising because we could avoid some undesirable effects of such additives upon other battery components: for instance, internal self-discharge originated from the shuttle effect of redox active additives between anode and cathode, or an unforeseen negative effect of the additives on cathode performance.

REFERENCES

1. E. Peled, *J. Electrochem. Soc.* 126 (1979) 2047.
2. T.B. Reddy, S. Hossain, “Rechargeable Lithium Batteries (Ambient Temperature)” in D. Linden, T.B. Reddy Eds., *Handbook of Batteries*, 3rd Edition, McGraw-Hill, New York, 2002, Chapter 34, pp. 34.1-34.62.
3. J.O. Besenhard, *J. Electrochem. Soc.* 94 (1978) 77.
4. R.A. Huggins, “Lithium Alloy Anodes” in J.O. Besenhard Ed., *Handbook of Battery Materials*, Wiley-VCH, Weinheim, 1999, pp. 359-381.
5. Y. Toyoguchi, J. Yamaura, T. Matsui, T. Iijima, *Proc. Electrochem. Soc.* 88-6 (1986) 659.
6. J.O. Besenhard, J. Yang, M. Winter, *J. Power Sources* 68 (1997) 87.
7. G.L. Henriksen, A.N. Jansen, “Lithium/Iron Sulfide Batteries” in D. Linden, T.B. Reddy Eds., *Handbook of Batteries*, 3rd Edition, McGraw-Hill, New York, 2002, Chapter 41, pp. 41.1-41.23.
8. P. C. Symons, P. C. Butler, “Advanced Batteries for Electric Vehicles and Emerging Applications-Introduction” in D. Linden, T.B. Reddy Eds., *Handbook of Batteries*, 3rd Edition, McGraw-Hill, New York, 2002, Chapter 37, pp. 37.1-37.25.
9. K. Kanamura, H. Tamura, Z. Takehara, *J. Electroanal. Chem.* 333 (1992) 127.
10. K. Kanamura, H. Tamura, S. Shiraishi, Z. Takehara, *Electrochim. Acta* 40 (1995) 913.
11. K. Kanamura, S. Shiraishi, Z. Takehara, *J. Electrochem. Soc.* 141 (1994) 2379.
12. Y. Malik, D. Aurbach, P. Dan, A. Meitav, *J. Electroanal. Chem.* 282 (1990) 73.
13. D. Aurbach, O. Chusid, *J. Electrochem. Soc.* 140 (1993) L155.
14. T. Osaka, T. Momma, T. Tajima, Y. Matsumoto, *Denki Kagaku* 62 (1994) 451.
15. T. Osaka, T. Momma, T. Tajima, Y. Matsumoto, *J. Electrochem. Soc.* 142 (1995) 1057.
16. M. Ishikawa, K. Otani, M. Morita, Y. Matsuda, *Electrochim. Acta* 41 (1996) 1253.
17. T. Hirai, I. Yoshimitsu, J. Yamaki, *J. Electrochem. Soc.* 141 (1994) 611.
18. M. Ishikawa, Y. Takaki, M. Morita, Y. Matsuda, *J. Electrochem. Soc.* 144 (1997) L90.
19. M. Ishikawa, M. Kanemoto, M. Morita, *J. Power Sources* 81-82 (1999) 217.

20. C. Fringant, A. Tranchant, R. Messina, *Electrochim. Acta* 40 (1995) 513.
21. D. Aurbach, Y. Ein-Eli, A. Zaban, *J. Electrochem. Soc.* 141 (1994) L1.
22. D. Aurbach, A. Zaban, Y. Gofer, Y. Ein-Eli, I. Weissman, O. Chusid, O. Abramson, *J. Power Sources* 54 (1995) 76.
23. D. Aurbach, A. Zaban, Y. Gofer, O. Abramson, M. Ben-Zion, *J. Electrochem. Soc.* 142 (1995) 687.
24. K. Kanamura, H. Tamura, S. Shiraishi, Z. Takehara, *J. Electrochem. Soc.* 142 (1995) 340.
25. K. Kanamura, S. Shiraishi, Z. Takehara, *J. Electrochem. Soc.* 143 (1996) 2187.
26. S. Shiraishi, K. Kanamura, Z. Takihara, *Langmuir* 13 (1997) 3542.
27. K. Naoi, M. Mori, Y. Naruoka, W.M. Lamanna, R. Atanasoski, *J. Electrochem. Soc.* 146 (1999) 462.
28. M. Morita, S. Aoki, Y. Matsuda, *Electrochim. Acta* 37 (1992) 119.
29. M. Ishikawa, S. Yoshitake, M. Morita, Y. Matsuda, *J. Electrochem. Soc.* 141 (1994) L159.
30. Y. Matsuda, M. Ishikawa, S. Yoshitake, M. Morita, *J. Power Sources* 54 (1995) 301.
31. M. Ishikawa, S. Machino, M. Morita, *J. Electroanal. Chem.* 473 (1999) 279.
32. M. Ishikawa, S. Machino, M. Morita, *Electrochem.* 67 (1999) 1200.
33. T. Hirai, I. Yoshimitsu, J. Yamaki, *J. Electrochem. Soc.* 141 (1994) 2300.
34. K. Naoi, M. Mori, M. Inoue, T. Wakabayashi, K. Yamauchi, *J. Electrochem. Soc.* 147 (2000) 813.
35. M. Morita, M. Ishikawa, *Final Report on Electrochemistry of Ordered Interfaces*: by Grant-in-Aid for Scientific Research on Priority Area (No. 282) from The Ministry of Education, Science, Sports, Culture, Japan, 2000, 57.

Chapter 11

TRENDS IN CATHODE MATERIALS FOR RECHARGEABLE BATTERIES

M. Pasquali¹, S. Passerini² and G. Pistoia³

¹*Dipartimento ICMMPM, Università di Roma La Sapienza, Rome, Italy*

²*Enea Casaccia, Rome, Italy*

³*Consultant, Rome, Italy (E-mail: pistoia@libero.it)*

11.1. INTRODUCTION

This chapter will not provide an exhaustive review of the work on cathodes for rechargeable Li batteries, but will try to focus on the most significant recent advances in both fundamentals and applications.

Commercial Li-ion batteries were successfully introduced into the market by Sony in 1991.¹ They used LiCoO₂ as a cathode and more than a decade later this is still the cathode of choice. Nonetheless, the research on cathode materials has been more intense than ever and remarkable success has been met both at the practical and at the theoretical level. Improving the LiCoO₂ synthesis has contributed to double the specific energy of commercial batteries in 10 years: from 80 to 165 Wh/kg. A new cathode, LiMn₂O₄, has been introduced by NEC^{2-4a} in 1996 and Sanyo^{4b} in 2001, although for a limited market. Some other materials, derived from LiCoO₂, e.g. LiNi_{1-x-y}Co_xM_yO₂ ($x+y < 0.25$, M=Mg or Al, preferably), have become serious candidates as future cathodes.

A wealth of knowledge has been acquired in terms of: synthesis techniques, reaction mechanisms, effect of particle size, interfaces, structural modifications, effect of doping, electrochemical and thermal stability, etc. This knowledge has allowed to revisit the criteria of choice of an efficient cathode. The classical criteria based on thermodynamic and kinetic considerations are:

1. The cathode must intercalate (if layered) or insert (for mono- and tri-dimensional structures) Li⁺.
2. To show a high OCV, it has to have low electron energy (hence low Fermi level) and low site energy for Li⁺.
3. The electrode potential should have limited variations as a function

of Li^+ content.

4. The number of sites for Li^+ has to be high and the hosting molecule has to feature low weight and high density (high gravimetric and volumetric capacity).
5. The coupled diffusion of electrons and Li^+ in the host, as a function of concentration gradient, must be fast enough to grant a good rate capability (high power).
6. The Li^+ intercalation/insertion has to be reversible, *i.e.*, with no or reversible structural changes, to allow cyclability.
7. The cathode must be stable towards the electrolyte over the entire operating voltage range.

To these criteria, one has to add the prerequisites of:

8. Low cost.
9. Lack of toxicity.
10. Ease of synthesis.

However, it is becoming evident that the above are necessary but non sufficient criteria. One has also to add:

11. A favourable interface formed in contact with the electrolyte (a cathode may be stable in a given electrolyte, but affected by a highly resistive interface).
12. The synthesis has to be not only simple, but also reproducible and must allow the production of a material with the desired particle size (the latter feature being of the utmost importance).
13. It should be possible to prepare a material encapsulated by another one to protect it from unwanted reactions with the electrolyte.
14. The material has to be easily processed into a practical electrode. Indeed, some materials may be difficult to fabricate as sheets (*e.g.*, a LiNiO_2 slurry tends to be thixotropic).

Furthermore, the choice of a cathode is oriented by the applications. For instance, in portable devices, a material can be tolerated which is relatively expensive and moderately performing at high rates; conversely for high power applications, such as in EV, cheapness and rate capability are mandatory.

In Table 11.1, materials which have particularly attracted the attention of researchers in the last 10-15 years are reported together with their operating voltage ranges. More details on them will be given in the appropriate sections. Before starting the description of selected cathode materials, we think it useful reviewing the principal methods of synthesis. This section will be followed by two other sections dealing with the effect of particle size on cathode performance and with the properties of the cathode-solution interfaces. These aspects are of a general character and can apply to all cathode materials.

Table 11.1. Cathode materials of interest and their V range.

V Range	Typical Materials
5	$\text{LiMn}_{2-x}\text{M}_x\text{O}_4$ ($x \geq 0.5$)
4	LiNiO_2 , LiCoO_2 , $\text{LiCo}_{1-x-y}\text{Ni}_x\text{M}_y\text{O}_2$, LiMn_2O_4 , $\text{Li}_{1+y}\text{Mn}_{2-x}\text{M}_x\text{O}_4$ (low x and y)
4-3	LiMnO_2 , $\text{Li}_x\text{Mn}_{1-y}\text{M}_y\text{O}_2$, $\text{Li}[\text{Li}_x\text{M}_y\text{Mn}_{1-x-y}]\text{O}_2$
3.5	LiFePO_4
3	Mn Spinel, Li_xMnO_2 , $\text{Li}_x\text{V}_y\text{O}_z$
2	S and Polysulfides
1.5	FeS_2

11.2. METHODS OF SYNTHESIS

For many years, the only way of synthesizing cathode materials was by thermal treatment at high temperatures of mixtures of reactants. Diffusion limitations in the solid state impose both long reaction times and regrinding between subsequent firings. Even so, the possibility of having less than pure final products remains high. This can be partially alleviated if a reactant has a low melting point, so that the melt can impregnate the solid (melt impregnation technique). However, especially if the solid reactant has large particles and limited porosity, the core of the solid may not be reached by the viscous melt, again leading to incomplete reactions.

Since the 90's, alternative methods of synthesis have been proposed. In general, they tend to form a better mixture of the precursors and to reduce both the time and temperature of the reaction. The most popular of these processes is sol-gel synthesis. Originally, this term was used for the hydrolysis of an alkoxide and subsequent heating of the hydrolysis product to give an oxide. At present, we call solution-sol-gel (or sol-gel, for short) any process in which a solution gives, through a chemical reaction, a sol which converts into a gel. The latter is typically converted by annealing or solvent-exchange into the desired ceramic (normally an oxide).

The sol-gel process allows a high degree of control over the physico-chemical characteristics of the product obtained with high purity and homogeneity. This is made possible by the initial solution step, as the intermixing of the reactants may reach the molecular level. Then, lower temperatures and shorter firing times are necessary to achieve materials with

good electrochemical characteristics. Quite often, this approach allows one to obtain small particle size materials and, so, faster reactions through faster diffusion of intercalating ions. However, the particle size issue is a rather delicate one, as lowering this parameter may bring about such shortcomings as low packing density, poor thermal stability, higher reactivity with the electrolytes and enhanced solubility. We shall return to this topic in the following sections.

In a typical sol-gel process, a mixture of reactants is dissolved in water, and a solution with a chelating agent is then added and mixed. Slow evaporation of the solvent generates a sol and moderate heating of the latter gives a gel, which is then calcinated at the appropriate temperature. An example of sol-gel process is reported in Figure 11.1 for a synthesis of LiMn_2O_4 , using adipic acid as a chelating agent.⁵

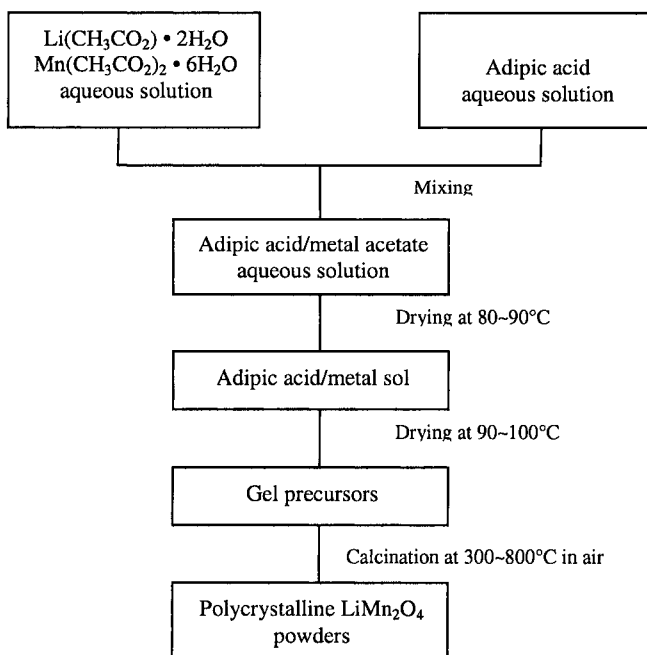


Figure 11.1. Typical sol-gel scheme (from Ref. 5).

Control of the pH and concentration of the chelating agent is required for optimized characteristics. Several chelants have been proposed, *e.g.* poly(acrylic acid) (PAA), poly(vinylalcohol) (PVA), and monomeric acids as succinic, adipic, glycolic, stearic, citric, propionic, oxalic. A technique recently described is the so-called combustion synthesis. The reactants (*e.g.*

Li and Mn nitrate in the case of Mn spinel) are dissolved in a solution together with a fuel (*e.g.*, urea or PAA). The powder formed on reaction is dried and then calcined at the appropriate temperature while igniting. Combustion is thought to accelerate the reaction and to bring it to completion.⁶⁻⁹

A peculiar technique combining the features of sol-gel and combustion is the so-called Pechini process applied to Mn spinels.¹⁰ To a solution containing Li and Mn compounds, a solution of citric acid and ethylene glycol is added. The polymeric gel obtained is pre-ignited at relatively low temperature before being calcined. As in the case of sol-gel synthesis, particles in the submicron range, with surface areas higher than those typical of thermal treatments, are obtained.

Solution techniques with reduction or oxidation processes have also been exploited.¹¹ For instance, Mn spinel can be obtained by reduction of the permanganate with such reducing agents as fumaric acid¹² or Mn^{2+} .¹³ Conversely, Mn^{2+} aqueous solutions can be oxidized with lithium peroxide, at room temperature and in the presence of LiOH, and the precursors can be fired at $t < 500^\circ\text{C}$ to give $\text{Li}_4\text{Mn}_5\text{O}_{12}$ with unusually good performance in the 3 V range (Figure 11.2).¹⁴ A material which can be prepared by reduction in solution and shows excellent electrochemical behaviour is $\text{VO}_2(\text{B})$.¹⁵ Indeed, the nanocrystalline product so obtained can insert into its

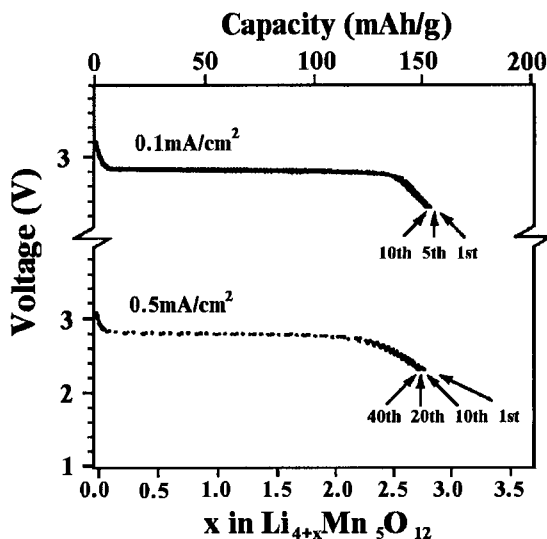


Figure 11.2. Discharge curves of $\text{Li}_4\text{Mn}_5\text{O}_{12}$, synthesized by a solution technique, in the 3 V range (adapted from Ref. 14).

monodimensional tunnels 0.9 Li per vanadium (290 mAh/g) vs. 0.5 Li per vanadium for the thermally prepared analog.¹⁶

A peculiar synthesis of LiNiO_2 (and $\text{LiNi}_{1-x}\text{Co}_x\text{O}_2$) is carried out by oxidizing, in a LiOH solution, Ni(OH)_2 to NiOOH with $\text{Na}_2\text{S}_2\text{O}_8$, followed by the H^+/Li^+ exchange in the same solution.¹⁷ This form of LiNiO_2 shows a two-electron redox reaction ($\text{Ni}^{4+} \rightarrow \text{Ni}^{2+}$) to which a specific capacity of 300 mAh/g corresponds in the potential range 4.2-1.5 V. 30 cycles at 0.9 mA/cm² are reported, with a final capacity of 260 mAh/g.

Ion-exchange has been frequently exploited in the last years, especially to obtain LiMnO_2 or similar materials. Orthorhombic LiMnO_2 was first prepared by Dahn *et al.* by ion exchange in an acetonitrile solution from MnOOH and LiOH.¹⁸ Bruce *et al.* have substituted Li for Na in NaMnO_2 and $\text{Na}_{0.44}\text{MnO}_2$ by ion exchange in alcoholic solutions at moderate temperatures.¹⁹⁻²¹ The products so obtained show high capacities and long cycle lives. They will be more extensively treated in another section of this chapter.

An interesting solution procedure, sometimes utilised to tailor materials with structures otherwise difficult to achieve, is hydrothermal synthesis.²²⁻²⁵ By controlling such parameters as the pH of the medium, temperature, solvent, time and, optionally, size of the templating cation (if a special architecture is sought), modified oxide cathodes may be obtained. An example is the layered $\text{M}_x\text{Mn}_{1-y}\text{Co}_y\text{O}_2$ ($\text{M}=\text{Na}$ or K) which has an electronic conductivity two orders of magnitude higher than pure K_xMnO_2 .²⁴ Also, a layered Mn oxide can be stabilized by placing pillars (*e.g.*, of vanadium oxide) between the MnO_2 sheets.²⁶ The opposite is also possible, that is stabilizing the layered structure of a vanadium oxide with Mn ions.²⁶

Other peculiar synthesis techniques include spray drying²⁷, emulsion drying²⁸ and freeze drying.²⁹ In all of them the precursors are initially dissolved (suspended) in aqueous solutions enabling the formation of sub-micron particles. Whether or not these rather complex techniques can really be useful is difficult to say as limited data on battery cycling have been reported.

Recently, the synthesis of Li cobaltate³⁰ and Mn spinels^{31,32} by microwaves has been reported. The former has been cycled for over 300 cycles in a lithium-ion cell. Li-rich and fluorinated spinels have been synthesised in a domestic microwave oven in less than 40 minutes.³² Unfortunately, no electrochemical data were provided.

A technique which has been emerging in the last few years is mechanochemistry. LiMO_2 ($\text{M}=\text{Ti}, \text{Mn}, \text{Fe}$)³³ and spinels^{34,35} have been synthesized by ball milling mixtures of Li compounds and Mn oxides. It is surprising that a definite compound may be formed in a limited milling time. For instance, in 10 minutes Li_2CO_3 and MnO_2 give rise to spinel formation.³⁴ Acceleration of the solid state reaction is due to the close contact of the reagents imposed by grinding and plastic deformation of particles.

Subsequent thermal treatment to the desired stoichiometry and degree of crystallinity may be carried out. Tarascon's group has shown a satisfactory first cycle even for a non-annealed spinel after 8 hrs of grinding. Sub-micron particles of high surface area ($12\text{--}18\text{ m}^2/\text{g}$) are obtained.^{35a}

11.3. EFFECT OF PARTICLE SIZE AND MORPHOLOGY ON CATHODE BEHAVIOR

The choice of a synthesis technique to produce a cathode material of potential use in Li batteries should take into account the kind of particles obtained by that technique. Indeed, the size (and its distribution), morphology and density of the particles play a fundamental role on their performance. It is also possible to modify the particle size by simple grinding after the synthesis and, in some instances, the behaviour of the modified material may be surprisingly different.

When evaluating if a material with given particle characteristics is suitable as a cathode, one has to assess its behaviour not only in typical room temperature cycling but also in high temperature storage and cycling. Indeed, in these latter conditions, unwelcome reactions with the electrolytes, *e.g.*, decomposition and dissolution processes, may more easily be identified. A check of its thermal stability is also necessary, as this important parameter may deteriorate with smaller particle sizes.

Compounds based on nanoparticles constitute a relatively new class of cathodes with, at least, one excellent characteristic, *i.e.*, elevated cyclability. This comes from much shorter diffusion paths for Li^+ diffusion and the occurrence of smaller dimensional changes upon cycling. Some examples are provided below.

Nanosized V_2O_5 , synthesized by the combustion flame-chemical vapor condensation process giving particles of $\sim 40\text{ nm}$,³⁶ has a capacity of 170 mAh/g (14 cycles), while coarse V_2O_5 has only 130 mAh/g . Furthermore, the irreversible capacity loss after the first charge is negligible for the former, but 16% for the latter.

LiMn_2O_4 cannot be cycled in the 3 V range, as the Jahn-Teller (J-T) effect changes the cubic phase ($c/a=1$) into a tetragonal one ($c/a=1.16$). The resulting large volume increase causes particle fracture and loss of contact. Recently, this problem was alleviated by using spinels having a $\text{Mn}^{4+}/\text{Mn}^{3+}$ ratio higher than 1, such as $\text{Li}_4\text{Mn}_5\text{O}_{12}$.¹¹ However, a surprising result has been reported by Goodenough *et al.* who could cycle a nearly stoichiometric spinel ($\text{Li}_{1.03}\text{Mn}_{1.91}\text{O}_4$, Mn oxidation state=3.64), after ball milling, in spite of an apparent J-T distortion.^{37,38} It has been observed that ballmilling (1-2 hrs) produces three effects: generation of lattice strains, partial oxidation of Mn (to 3.76) and formation of nanosized grains within the particles. The strain induced by the J-T effect is supposed to be better accommodated in

the small particles, *i.e.*, it is less anisotropic also by virtue of the pre-existing strain.

A similar effect has been reported for a spinel created by the electrochemical cycling of orthorhombic LiMnO_2 (*o*- LiMnO_2) obtained at high temperature.³⁹ This spinel has a nanodomain structure with particles of 20-50 nm within the pristine particles. At low rates (3.3 mA/g), a capacity of 272 mAh/g can be obtained, which is 95% of the theoretical value. According to the authors, the J-T effect is suppressed in this case due to cation disorder (partial occupation of the lithiated spinel tetrahedral sites) and the occurrence of nanodomains.

The above mentioned excellent cyclability of *o*- LiMnO_2 could only be observed after several cycles. Indeed, the initial capacity was below 40 mAh/g and reached a steady value after 30-40 cycles. Lee and Yoshio have also prepared *o*- LiMnO_2 by high temperature synthesis (1000°C followed by quenching) and observed the same low initial capacities.⁴⁰ However, after a ball milling to bring the surface area from 0.55 to 9.25 m²/g, these authors could obtain a material providing 193 mAh/g in the first cycle. The diffusional limitations due to the relatively large particles (5-15 μm) were overcome with the smaller ones obtained by milling.

The above positive effects stemming from the use of small particles are balanced by the drawbacks mentioned in the previous section. In practical batteries, relatively large particles are now preferred. For instance, the Li-ion cells by Sony have LiCoO_2 produced by a synthesis process using Co_3O_4 , Li_2CO_3 and PVA resin as precursors, so to obtain a material with particles of 20 μm , instead of the 1-3 μm which are obtainable in the conventional synthesis.⁴¹ In this way, a better packing density and an enhanced safety are obtained.

The importance of particles with a predetermined shape and size is stressed in some articles related to $\text{LiNi}_x\text{Co}_{1-x}\text{O}_2$. Cho *et al.* were able to synthesize this material starting from coprecipitated $\text{Ni}_x\text{Co}_{1-x}(\text{OH})_2$ with spherical particles.⁴² Reaction of the latter with LiOH at 650-750°C produces $\text{LiNi}_x\text{Co}_{1-x}\text{O}_2$ with the same spherical particles of ~15 μm and a tap density of 2.9 g/cm³ (vs. 2.6 g/cm³ for the analogous product obtained by thermal synthesis). This material cycles much better than the one obtained by ordinary thermal synthesis and, furthermore, has a higher volumetric energy density as the uniform spherical particles improve the packing density.

The same cathode material (with the exact composition $\text{LiNi}_{0.74}\text{Co}_{0.26}\text{O}_2$) was investigated, in its electrochemical and thermal behavior, with 3 different particles sizes, namely 5, 13 and 25 μm .⁴³ When cycled at the 1C rate, the 5- μm material shows a fairly constant capacity of 180 mAh/g for 70 cycles. Under the same conditions, the cathodes with 13 and 25 μm show a final capacity of 160 mAh/g, which is still remarkable at the high rate used. On the other hand, DSC experiments have shown a large

exothermic peak for the 5- μm material, while the heat evolved by the two other materials is rather limited. The conclusion is that the large surface area (2.75 m^2/g) of the 5- μm cathode and the subsequent reaction with the electrolyte prevent its use in practical batteries.

A similar solution technique ("controlled crystallization") was used by Ying *et al.* to obtain spherical $\text{LiNi}_{0.8}\text{Co}_{0.2}\text{O}_2$.⁴⁴ These authors could obtain particles with a very high tap density (3.24 g/cm^3), while a commercial sample not based on spherical particles has a density of 2.27 g/cm^3 . The former material could maintain a stable capacity of 170 mAh/g when cycled at 0.5 mA/cm^2 for 50 cycles.

A study of commercial Mn spinels has again stressed the importance of the morphology factor in determining the electrochemical performance. Among the different samples, those having uniform spherical particles resulting from the agglomeration of spherical crystallites showed better cyclability.⁴⁵

The issue of capacity fading for the Mn spinel upon storing and cycling, especially at high temperatures, has received a wealth of attention. Here we wish to point out the reported implication of the spinel particle size on this phenomenon. Tarascon *et al.* have investigated in detail this aspect and found a correlation between surface area and capacity loss on storing or cycling at 55°C.⁴⁶ They prepared samples with different surface areas and found that as this parameter increases the irreversible self discharge also increases, due to the enhancement of both electrolyte oxidation and Mn dissolution. A low surface area of 0.5-1 m^2/g is considered optimal by these authors.

The issue of spinel surface area vs. capacity fading has also been addressed by Cho through measurements of the surface area by both a conventional BET method and methylene blue (MB) method.⁴⁷ With the first, the area is measured through N_2 adsorption, while the second is based on the adsorption of MB molecules. The difference between the two lies on the fact that N_2 can access the nanopores of the particles, while the larger MB molecules, having the same size of the electrolyte molecules, ~ 15 Å, cannot. When evaluating the electrochemical characteristics of 5 samples with particles in the 5 to 50 μm range, a precise correlation was found between irreversible first cycle capacity (and capacity fading) vs. MB surface area. As the latter increased, higher values for the irreversible capacity and capacity fading on cycling were measured. Interestingly, BET and MB surface areas did not correlate and even had opposite trends for the samples in the 13-25 μm range.

There are some discrepancies in the literature about the influence of particle surface area on storing and cycling the spinel at high temperatures, as some authors have noticed a better performance with higher surface areas.^{48,49} It seems that these disagreements may be partly reconciled if one takes into account the fact that the BET measurements do not provide a value of

the real area accessible by the electrolyte. On this basis, one may perhaps rationalise the results of Yoshio *et al.* on cycling at 55°C Li-rich spinels of surface areas 1.2 and 6.2 m²/g.⁵⁰ In 100 cycles, the former had a 5% capacity loss, while the latter had a loss of 8%. With a 5/1 ratio in surface areas, one might have expected a larger difference. It may be conceivable that the two samples, prepared by different techniques, have a different pore structure in terms of number and size.

All of the above remarks emphasise that any synthesis or post-synthesis process should produce particles with an appropriate size and morphology if they are to be used successfully in rechargeable batteries. Techniques leading to compounds with exceedingly high surface area or broad particle size distribution are unlikely to be of practical interest.

11.4. NATURAL VS. ARTIFICIAL CATHODIC FILMS

Any cathode in an electrolyte solution is covered by a film, which largely determines its electrochemical behavior. There are now several techniques enabling the characterization of such films, *e.g.*, SEM, TEM (and STEM, HRTEM), electron diffraction, AFM, FTIR, XPS, EDAX, EIS and other electrochemical techniques.

The most reactive materials, *e.g.*, LiNiO₂, have a pristine film mostly based on Li₂CO₃ from the reaction with atmospheric CO₂.⁵¹ However, the nature of the film changes in contact with the electrolyte. Aurbach's and Tarascon's groups have explored this topic, taking into consideration especially LiNiO₂ and LiMn₂O₄.⁵¹⁻⁵³ According to its own reactivity and the type of electrolyte, each material tends to form a film with specific characteristics. For instance, the highly nucleophilic LiNiO₂ is very reactive towards the electrophilic alkyl carbonates and tends to form thick resistive films comprising LiF and Li-alkyl carbonates of general formula ROCO₂Li. In comparison, LiMn₂O₄ is less reactive, as shown by FTIR and impedance tests, but it is covered by a complex layer containing, in a LiPF₆-based electrolyte, LiF⁵¹, moieties with P (*e.g.*, Li₂PO₃F)^{51,54} and a protonated, Mn-defective form of λ-MnO₂ (λ-H_zMn_{2-z}O₄).⁵⁵

Li ions migrate through the surface layer before reaching the active material for the charge transfer process. So, it is obvious that the characteristics of the film, especially its conductivity, play a fundamental role in the kinetics of the cathode. LiF is reported to be highly resistive and this explains why, in LiPF₆-based electrolytes, the impedance is higher than in other electrolytes.⁵¹ The surface layer, besides allowing Li⁺ migration, has to permit electron tunneling. It has also been proposed that this layer is an electronic conductor, so that the charge transfer may occur at the interface between the electrolyte and the surface layer.⁵⁶

As the cathode-electrolyte reaction is a surface process, it is magnified

in high surface area materials. This has especially been observed for Mn spinels.⁵⁵ A sample with a surface area of 5 m²/g, prepared from LiNO₃ as a lithiating agent, was stored at 100°C in solutions of EC-DMC containing different Li salts (LiPF₆, LiBF₄, LiAsF₆ or LiClO₄). With LiPF₆, remarkable Mn dissolution was observed, which was larger for the oxidized state (λ -MnO₂) in comparison with the reduced state (LiMn₂O₄). The organic/inorganic layer observed by IR was connected with the dissolution process and the underlying electrolyte reaction at the cathode. HF, present in solution as an impurity or formed at the cathode by a secondary reaction,⁵⁵ is responsible for the spinel dissolution and the increase of Mn concentration in the electrolyte. This process, which is believed to be the main cause of the spinel capacity fading upon cycling at high temperature, will be dealt with later in more detail.

Under proper conditions, the formation of a surface film on the spinel may be beneficial with regard to the capacity loss on storage. Pistoia *et al.* have shown that both undoped and Ga-doped spinels, if stored in the charged state for several days at 55°C in a LiBF₄-EC/PC solution, have a much lower capacity loss on extended cycling than samples stored only few days.⁵⁷ It seems that, with time, the gradual construction of an interface occurs, as shown by impedance measurements, which to a large extent preserves the electrochemical characteristics.

Once it is ascertained that the performance of a cathode largely depends on the type of layer formed in contact with the electrolyte, and, more generally, on the interactions with the electrolyte, it is conceivable to artificially create a film which can modify such interactions. Tarascon *et al.* have applied this concept to LiMn₂O₄ in an attempt to reduce the loss of capacity on storing and cycling at high temperature. They have attempted to encapsulate the spinel particles with B-containing glasses through such techniques as: ball-milling the spinel with Li₂O·2B₂O₃ and firing at 800°C or soaking the spinel with H₃BO₃ followed by annealing at the same temperature. Alternatively, the spinel was treated with acetylacetone, which formed a monolayer around each particle.⁵³ The treatment at 800°C obviously decomposed acetylacetone, but it was proposed that its chelating/dissolving effect on Mn would leave a surface layer mainly composed of Li₂MnO₃. The tetravalent Mn of the latter is resistant to dissolution. Storage of these surface-modified spinels at 55°C (4 weeks) brought the capacity loss from 45-50% to 18-23%. Cycling was not improved over the uncoated sample.⁵³ Spinel surface modification could also be obtained by the use of composite LiMn₂O₄-polypyrrole cathodes, possibly through partial Mn dissolution preventing further capacity fading. Such cathodes have a higher capacity and a better cyclability at 55°C.⁵⁸

Cho's group has extensively investigated the coating of several cathode materials. In particular, for the Mn spinel they proposed a coating based on such Co-containing molecules as LiCoO₂^{59a} and Co₃O₄.^{59b} A

thermally prepared spinel was coated by sol-gel solutions from which, by firing at the appropriate temperature, the above materials were obtained. Analyses of the particles by X-Ray diffraction and electron probe have shown that the pure spinel transforms into $\text{LiMn}_{2-x}\text{Co}_x\text{O}_4$, with a higher Co concentration at the particle surface. In other words, a Co-rich coating was formed, which preserved the particles from the dissolution reaction with HF in LiPF_6 -containing solutions at high temperature. As a consequence, a greatly improved cyclability was observed. For instance, a coated spinel could sustain 50 cycles at 60°C without showing an appreciable loss, while the uncoated one lost 41% of its initial capacity. It has been shown that Mn dissolution and capacity loss is accompanied by major structural changes.^{59b} The spinels tend to approach compositions of the type $\text{Li}_2\text{Mn}_4\text{O}_9$ and $\text{Li}_4\text{Mn}_5\text{O}_{12}$, characterized by low values of the cubic parameter a (e.g., 8.12–8.18 Å). The uncoated spinel shows, after cycling, $a=8.12$ Å vs. an initial value of 8.23 Å, while no change was observed for the coated one.^{59b} A spinel coated with $\text{LiNi}_{1-x}\text{Co}_x\text{O}_2$ ($x=0.2$ and 1) has also shown improved storage and cycling characteristics at 65°C .⁶⁰

The technique of reducing (or eliminating) electrode/electrolyte secondary reactions has successfully been applied to other cathodes. Both LiCoO_2 and LiNiO_2 were covered by CVD with a carbon layer (diamond-like for the former, amorphous for the latter).^{61,62} In such a way, it was possible to charge both cathodes up to 4.6 V without electrolyte decomposition. As a result, initial capacities above 200 mAh/g were obtained for both compounds. However, in limited cycling experiments (5 cycles), only LiNiO_2 showed a very low capacity loss.

Coating of LiCoO_2 was also addressed by applying such oxides as SnO_2 , Al_2O_3 , and ZrO_2 on the cathode surface.^{63–66} Li_xCoO_2 , when delithiated, undergoes several phase transitions. In particular, at $x=0.5$, a hexagonal-monoclinic transition ($H \rightarrow M$) is observed which gives a substantial contribution (about 50%) to the total anisotropic expansion along the c axis (about 2.6% with respect to the initial c value). It is accepted that the phase transitions in delithiating LiCoO_2 are reversible up to the CoO_2 composition.^{67a} Nonetheless, the large anisotropic volume changes cannot be tolerated by the particles, so that fractures and contact losses ensue. Furthermore, a remarkable Co dissolution at high potentials has been evidenced.^{67(a-c)} This is why commercial cells are only charged up to about 4.1 V. Coating with the oxides mentioned above changes the surface of LiCoO_2 and this has a dramatic effect on the cycle life performance even if the charge cut-off voltage is brought well above 4.2 V. For instance, a stable capacity of 168 mAh/g was obtained for 70 cycles with ZrO_2 coating in the cycling range 4.4–2.75 V.^{63a} In Refs. 63a–65, this behavior is attributed to a coating-induced structural stabilization. In particular, the best oxides, e.g. ZrO_2 and Al_2O_3 , would greatly limit or even suppress expansion along the c axis, thanks to a strain-preventing shell formed around the LiCoO_2 particles.

This view was rejected by Chen and Dahn, who found, for nanocrystalline ZrO_2 -coated LiCoO_2 , the same variation of the c axis measured for the uncoated sample.⁶⁶ According to these authors, the excellent electrochemical performance of this material has to be possibly connected with a reduction of side reactions involving oxygen loss from Li_xCoO_2 to the electrolyte.

A reconsideration of the effect of coating LiCoO_2 with oxides has led Cho's group to attribute the capacity stabilization to a reduced Co dissolution at high potentials.^{63b} Even after charging to 4.8 V, ZrO_2 -coated LiCoO_2 showed a much lower Co dissolution with respect to the uncoated one.

A final example of performance improvement by cathode coating is provided by o - LiMnO_2 . On cycling, this material transforms into a spinel-like oxide of general formula $\text{Li}_{1-x}\text{Mn}_{2-x}\text{O}_4$ ($0 < x \leq 0.33$; the upper limit corresponding to $\text{Li}_4\text{Mn}_5\text{O}_{12}$). As cycling goes on in the extended range 4.5–2.0 V, formation of the rock salt phase $\text{Li}_2\text{Mn}_2\text{O}_4$ occurs, with all Mn in the trivalent state and, so, quite prone to dissolution through a disproportionation reaction producing Li_2MnO_3 and MnO . An uncoated o - LiMnO_2 does indeed show after 50 cycles the presence of the Li_2MnO_3 peak, while a significant decrease of this peak was observed in a sample coated with CoO or Al_2O_3 .^{68,69} The stabilization of the spinel formed upon cycling results in a capacity of about 170 mAh/g after 50 cycles, while a bare sample gives 120 mAh/g.

11.5. SPECIFIC CATHODE MATERIALS

11.5.1. LiNiO_2 and LiCoO_2

The early report by Goodenough *et al.* on a new layered compound, LiCoO_2 , cyclable at 4 V, received limited attention in 1980 as there were not, at the time, electrolytes suitable for that potential range.^{70a} However, a decade later, LiCoO_2 became the cathode used in the first commercial Li-ion batteries and is still in use.

The structural features of LiCoO_2 , and of its homologous LiNiO_2 , have received a great deal of attention. They are built of MO_2 slabs (with M in octahedral coordination) separated by Li layers (with Li also octahedrally coordinated), as shown in Figure 11.3a. Li^+ can entirely be removed from the layers of the $\text{O}3$ hexagonal structures, through different phase changes. The most generally accepted phase-composition diagrams are shown in Figure 11.4a,b. Li^+ removal from LiCoO_2 or LiNiO_2 causes an enlargement of the interlayer distance (equal to $c/3$), due to slabs repulsion, for up to ~50% delithiation, followed by a decrease. This is depicted in Figure 11.4c,d.

The large variations along the c axis cause volume reductions of 6–

8% at full delithiation. This is too much to grant a practical reversibility and, therefore, the utilisation of the full capacity (273 mAh/g). It has been pointed out that both CoO_2 and NiO_2 , obtained by electrochemical delithiation, can reinsert 90-95% of Li in a low-rate discharge.^{67a} This means that the phase transitions, and the related volume changes, are reversible. However, as pointed out in the previous section, volume expansion causes particles breaking and contact losses impairing true reversibility in practical conditions, this adding to other unpleasant effects as electrolyte decomposition and partial cathode dissolution at high potentials. This last phenomenon has especially been evidenced for LiCoO_2 .^{67a} Lee *et al.* have noticed a remarkable reduction of cobalt dissolution by preparing solid solutions of LiCoO_2 with Li_2SnO_3 .^{67b} Aurbach *et al.* have obtained similar results by using a boron-based additive which forms a protecting film on LiCoO_2 .^{67c}

In the following, we shall review interesting findings regarding the structural characteristics and electrochemical behavior of LiCoO_2 , LiNiO_2 and their derivatives. Stoichiometric LiCoO_2 is easily prepared by soft chemistry or high temperature processes. The preparation of LiNiO_2 , however, is not straightforward, as it tends to become Li-deficient while divalent Ni is present in both the Li^+ layers and NiO_2 slabs. Ni^{2+} in the Li^+ layers has detrimental effects. Indeed, in the early oxidation stages it gives rise to the smaller Ni^{3+} ($r=0.56 \text{ \AA}$ vs. 0.65 \AA for Ni^{2+}), so that the structure collapses around this ion and the following Li^+ intercalation is hindered, as also shown by the irreversible capacity loss in the first cycle.^{73,74} Other unpleasant features of LiNiO_2 are: limited thermal stability in the oxidized state and poor capacity retention during cycling. This is the reason why, in spite of its lower price and toxicity with respect to LiCoO_2 , the latter is the cathode of choice for practical batteries. However, in recent years the synthesis of nearly stoichiometric LiNiO_2 has been reported.⁷⁴ This material may cycle fairly well for as many as 1200 cycles, without showing structural modifications.⁷⁵ However, the safety issue remains, as a large exothermic peak is manifested by the charged cathode at about 200°C (the exact temperature depending on the state of charge).⁷⁶ Therefore, only compounds with partial Ni substitution are of practical interest. Before going into the details of LiNiO_2 or LiCoO_2 derivatives, we wish to stress that the structural changes of the pure materials upon Li^+ removal is still a matter of debate. Mc Breen *et al.*, by *in situ* XRD experiments using a synchrotron X-ray source, have questioned the formation of monoclinic phases in LiNiO_2 (Figure 11.4a). According to these authors, the first-order transitions give rise to 3 phases with hexagonal structure.⁷¹ Bianchi *et al.*⁷⁴ have pointed out that phase coexistence and the extent of the unit cell volume change upon delithiation strongly depend on the Ni^{2+} content in the Li^+ layers. By removing 60% of Li^+ from $\text{Li}_{0.975}\text{Ni}_{1.025}\text{O}_2$, the volume decreases by 1.4%, while with $\text{Li}_{0.992}\text{Ni}_{1.008}\text{O}_2$ the variation is only 0.4%.⁷⁴

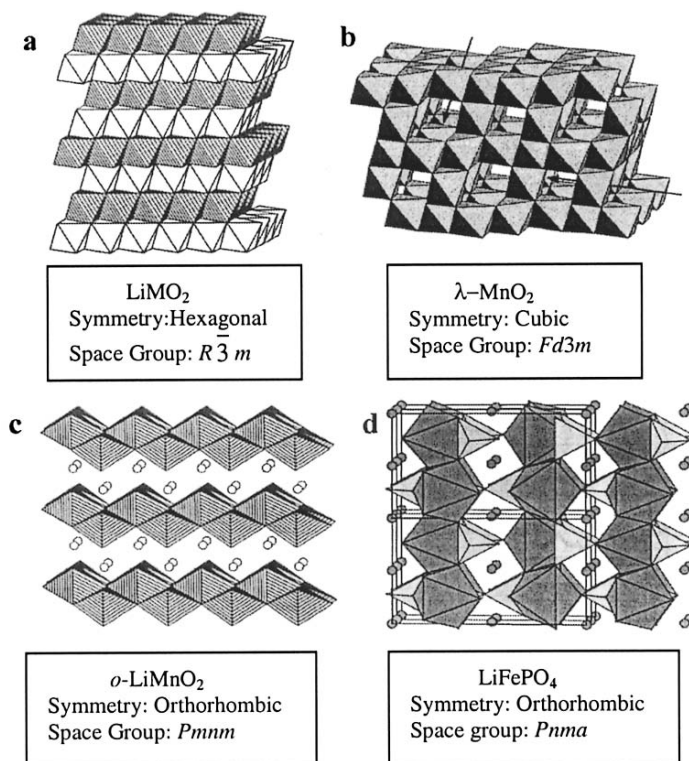


Figure 11.3. a) shaded octahedra: MO_6 , white octahedra: LiO_6 ; b) note two of the pathways for Li^+ transport; c) hatched octahedra: MnO_6 , circles: Li^+ ; d) tetrahedra: PO_4 , octahedra: FeO_6 , circles: Li^+ (in octahedral sites). a-c) from Ref. 70b; d) from Ref. 70c.

For LiCoO_2 , the second monoclinic phase at low Li^+ content (Figure 11.4b) is not observed by Mc Breen *et al.*,⁷¹ who found instead another hexagonal phase. The phase composition above ~ 4.3 V has recently been reconsidered by other authors. Chen and Dahn^{77a} have found that the hexagonal O3 structure* becomes a stage-2 compound of formula $\text{Li}_{0.12}\text{CoO}_2$, also hexagonal as previously proposed by Ceder *et al.*^{77b} At full delithiation, CoO_2 with an O1 structure is formed. This latter finding is in agreement with the results of Yang *et al.*^{77c} and Tarascon *et al.*^{67a} The latter authors, in a subsequent paper, assign a mixture of two O1 phases to CoO_2 .⁷⁸ However,

* In O1 and O3 structures, Li is in octahedral (O) coordination and the unit cell contains 1 or 3 CoO_2 sheets, respectively. In P3, Li has prismatic (P) coordination and the unit cell has 3 sheets.

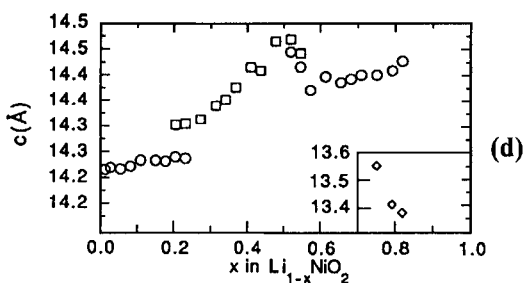
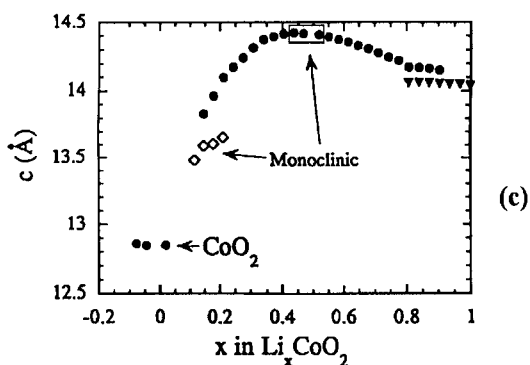
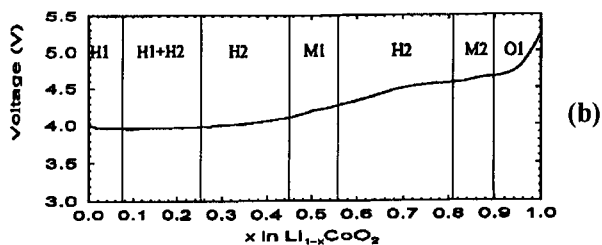
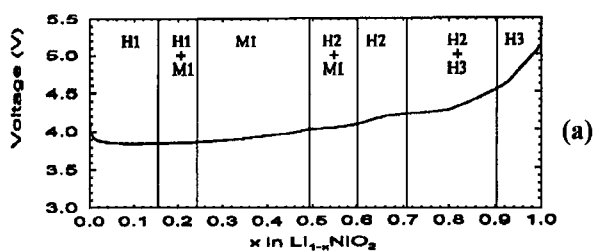


Figure 11.4. (a) Phase diagram of $\text{Li}_{1-x}\text{NiO}_2$ (from ref.71); (b) Phase diagram of $\text{Li}_{1-x}\text{CoO}_2$ (from Ref. 71); (c) Variation of the c axis during delithiation of LiCoO_2 (negative x values: electrolyte decomposition) (from Ref. 67a); (d) Variation of the c axis during delithiation of LiNiO_2 (from Ref. 72).

according to Venkatraman and Manthiram, CoO_2 has the P3 structure.⁷⁹ These authors observe formation of a P3 phase for $x=0.45$ in Li_xCoO_2 , which coexists with the O3 phase in the range $0.2 < x < 0.45$ and is characterized by a faster decrease of the c axis as x decreases. The P3 phase loses oxygen more rapidly than the O3 phase (P3-like CoO_2 should be written as $\text{CoO}_{1.7}$) and this can be connected with the practically usable capacity of LiCoO_2 .

Examples of the cyclability of pure LiNiO_2 and LiCoO_2 are given in some of the references of the next sub-sections as well as in the references dealing with coated LiCoO_2 in Section 11.4.

We have already noted that LiCoO_2 is the cathode used in most of the presently commercialised Li-ion batteries. LiMn_2O_4 -based cells have a marginal market. Batteries with LiCoO_2 have now reached energy densities in excess of 150 Wh/kg and 350 Wh/l, cycle lives in excess of 1000 cycles and low self-discharges (<3%/month). The industrial processes are well established and high levels of mass production of portable batteries have been achieved through huge investments. On this basis, it is very difficult to consider the substitution of LiCoO_2 with another cathode, unless the alternative is highly attractive in terms of performance and price. One has also to consider that the price of cobalt has been drastically decreasing in recent years and that in small portable batteries the relative cost of active materials is lower.

11.5.1.1. $\text{LiNi}_{1-x}\text{Co}_x\text{O}_2$ Solid Solutions

Taking LiNiO_2 as a reference, a number of cations have been used to substitute Ni, *e.g.*, Co, Mg, Al, Fe, Ti, Ga. In some cases, O has partly been replaced by F or S. Co is the most obvious substitute for Ni as they form the $\text{LiNi}_{1-x}\text{Co}_x\text{O}_2$ solid solution at all x values. In view of the need of exploiting the potentialities of LiNiO_2 , Ni-rich stoichiometries (70-80% Ni) have especially been investigated. For $x > 0.3$, $\text{LiNi}_{1-x}\text{Co}_x\text{O}_2$ are strictly layered materials, with no Ni^{2+} in the Li^+ layers.⁷⁵ Delmas' group has extensively studied this system, with special emphasis to the structural evolution upon charging. These authors have reported that, in the mixed Ni/Co oxide, Ni ions are first oxidized.⁷⁵ By further NMR experiments of the same authors, a compound of formula $\text{Li}_x\text{Ni}_{0.3}\text{Co}_{0.7}\text{O}_2$, was said to have only Ni^{3+} oxidized in the range $0.85 < x < 1$. However, in the following $0.70 < x < 0.85$ range, Ni/Co hopping was evident ($\text{Ni}^{4+} + \text{Co}^{3+} \rightarrow \text{Ni}^{3+} + \text{Co}^{4+}$) so that the question as to which ion is preferentially oxidized on delithiation becomes less relevant.⁸⁰ The prevailing charge carriers are electron holes and even at $x=0.40$, where pure LiCoO_2 is a metallic conductor, the presence of Ni hinders long range electronic delocalization.⁸⁰ By using XANES spectra, Mc Breen *et al.*⁸¹ have concluded that Ni is first oxidized, while, with the same technique, Lee and

Kim⁸² have found that both ions are simultaneously oxidized. These latter authors have also examined the relationship between irreversible capacity loss and depth of first charge. They found that most of the capacity is lost at the beginning of the first charge and is not influenced by the phase transitions occurring during further charging/discharging. The presence of Co reduces the irreversible capacity, which is due to the oxidation of Ni^{2+} in the Li^+ layers and preferential removal of Li^+ around the Ni ions, this causing a local structural collapse.⁸²

Co not only improves the layered characteristics of LiNiO_2 , but also increases its thermal stability in the charged state. This is because the Co-O bond is stronger than the Ni-O bond (binding energies: 1067 KJ/mol for CoO_2 and 1029 KJ/mol for NiO_2).⁸³ As a consequence, a thermogravimetric analysis has shown progressively reduced weight losses to 1000°C as Co replaces Ni in $\text{LiNi}_{1-x}\text{Co}_x\text{O}_2$.⁸³ The stronger Co-O bonds also contribute to stabilize the structure during Li^+ intercalation/deintercalation. In addition to Co, Li excess helps to reduce the amount of Ni^{2+} in the Li^+ layers, as these are saturated by Li^+ , and thus a limited irreversible capacity in the first cycle and a good cyclability are observed.⁸³

An investigation on the thermal stability of delithiated $\text{Li}_{1-y}\text{Ni}_{1-x}\text{Co}_x\text{O}_2$ ($0 \leq x \leq 0.3$), has produced surprising results. All samples have shown structural damages on storage, demonstrated by a decrease of the c/a ratio even at temperatures as low as 50°C. The rate of change of the c/a ratio increases with time (several days), temperature and oxidation degree, and decreases with the Co content: a Ni-free sample does not show any variation.⁸⁴ The thermal stabilization of oxidized $\text{Li}_{1-y}\text{Ni}_{1-x}\text{Co}_x\text{O}_2$ at higher Co contents is confirmed by DSC experiments. In samples charged to 4.2-4.3 V, the large exothermic peak at about 195°C of pure $\text{Li}_{1-y}\text{NiO}_2$ is transformed into a small peak centred at 220°C for $\text{Li}_{1-y}\text{Ni}_{0.7}\text{Co}_{0.3}\text{O}_2$.⁸⁵ Cyclic voltammetry tests of this latter compound have shown the disappearance of the hexagonal-monoclinic phase transitions and delithiation seems to occur in a single phase up to 4.4 V.⁸⁵ Several authors have attributed the improved electrochemical stability of the Co-containing cathodes to this feature.^{86,87}

According to Ref. 79, the original O3 phase coexists, for $x < 0.25$ in $\text{Li}_x\text{Ni}_{0.85}\text{Co}_{0.15}\text{O}_2$, with another hexagonal phase, O3'. At full delithiation, only the new O3' phase exists. Oxygen loss would occur only after formation of this phase. This behaviour is different from that of LiCoO_2 (oxygen loss at $x < 0.45$, see Section 11.5.1) and would explain why $\text{Li}_x\text{Ni}_{0.85}\text{Co}_{0.15}\text{O}_2$ can reach a practical capacity of 180 mAh/g vs. 140 mAh/g for LiCoO_2 .

The references of this sub-section give details on the best syntheses to produce efficient materials. Here, we only wish to point out an unusual low-temperature synthesis based on the reaction at 400°C (instead of the usual 700-800°C) between $\beta\text{-Ni}_{1-x}\text{Co}_x\text{OOH}$ and LiNO_3 .⁸⁶ Since Ni is already in the trivalent state in the starting material, a lower temperature may be used. A

$\text{LiNi}_{0.85}\text{Co}_{0.15}\text{O}_2$ composition gives in a one-phase discharge (*i.e.*, with no $H \rightarrow M$ transitions) 190 mAh/g at 0.5 mA/cm² and a very limited capacity loss on cycling.

11.5.1.2. Partial Substitutions in $\text{LiNi}_{1-x}\text{Co}_x\text{O}_2$

To further improve the electrochemical and thermal stability of LiNiO_2 , several cations have been proposed for partially substituting Co/Ni, while S and F have been proposed for O. A cation of particular interest is Mg, used by several authors at low concentrations (around 0.05 atoms/mol) in compounds of the type $\text{Li}(\text{Ni}_{0.75}\text{Co}_{0.25})_{1-x}\text{Mg}_x\text{O}_2$.⁸⁷⁻⁹⁰ The role of this ion is debated in the literature, even after carrying out Rietveld analyses to determine the site occupancies. Delmas *et al.* found that in $\text{LiNi}_{0.86}\text{Co}_{0.09}\text{Mg}_{0.05}\text{O}_2$, part of Mg (0.02 atoms/mol) resides in the Li layers, with the remaining Mg is in the Co/Ni slabs.⁸⁸ Mg^{2+} , whose radius (0.72 Å) is similar to that of Li^+ (0.73 Å), prevents occupancy of the Li^+ layers by Ni^{2+} and, as it cannot be oxidized, does not cause any local structural

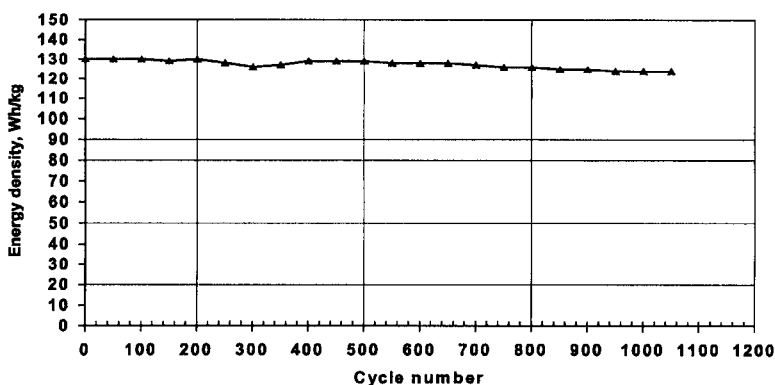


Figure 11.5. Cycling of a 40 Ah Li-ion SAFT battery with a $\text{LiNi}_{1-x-y}\text{Co}_x\text{Al}_y\text{O}_2$ cathode ($\text{Ni} > 75\%$). C/3, 80% DOD (from Ref. 95b).

collapse and, so, is beneficial for the electrochemical behaviour. Furthermore, during an extended cycling, all of the Mg ions migrate (with some Ni) from the Co/Ni slabs to the Li^+ layers. In a Li-ion cell cycled 500 times at 1 C rate, the capacity loss was strongly reduced, while the Mg-free homologous showed a rapid decline. At the end of cycling, an XRD analysis showed limited variations of the cell parameters for the Mg-containing compound, in agreement with the low capacity fading. Chowdari *et al.*, studying the cathode $\text{LiNi}_{0.8}\text{Co}_{0.2-2x}\text{Ti}_x\text{Mg}_x\text{O}_2$, also inferred the

presence of Mg in the interslab sites from the relative heights of the (003) and (104) peaks in the diffractograms: a lower (003)/(104) ratio for $x=0.05$ and 0.075 was taken as a proof of the distribution of Mg between Li and Ni/Co layers.⁹¹

Conversely, Cho *et al.*⁸⁹ and Chang *et al.*⁹⁰ have refuted the presence of Mg in the 3b sites. According to the former authors, as the Mg content increases from 0 to 0.06 atoms/mol, the Mg and Ni occupancy of the Li sites becomes negligible (Rietveld analysis). Chang *et al.* also found a very low Mg concentration in the Li sites, through Rietveld, chemical and thermogravimetric analyses. Despite the disagreement regarding Mg occupancy, all of the authors agree that these materials have excellent cyclabilities with high and stable capacities (*e.g.* 160-170 mAh/g⁸⁹).

Mn, Ti and Al substitutions also give excellent cyclability.⁹²⁻⁹⁵ $\text{LiNi}_{1-x-y}\text{Co}_x\text{Al}_y\text{O}_2$ is now receiving special attention at the technological level as it is believed to be a candidate for a new generation of Li-ion batteries.⁹⁵ Indeed, it can be produced on a large scale and is commercially available. A 10 Ah Li-ion cell was cycled at AEA for 270 cycles (C/5) with a 90% capacity retention. The specific energy of this cell was 150 Wh/kg in a "soft-packaged" version.^{95a} A similar performance (up to 145 Wh/kg) was reported by SAFT for a 40 Ah cell.^{95b,c} This cell can be long cycled with a rather constant energy output - see Figure 11.5.

Dahn *et al.* have reported the structure and electrochemical behaviour of $\text{Li}[\text{Ni}_x\text{Co}_{1-2x}\text{Mn}_x]\text{O}_2$ ($x=1/4$ and $3/8$), prepared by substituting Ni^{2+} and Mn^{4+} for Co^{3+} in LiCoO_2 .^{92a} This new compound, which maintains the α - NaFeO_2 structure of LiCoO_2 , can deliver a stable capacity of 160 mAh/g between 2.5 and 4.4 V, and proves more thermally stable than LiCoO_2 .

The double cationic and anionic substitution in LiNiO_2 has also been proposed, *e.g.*, in: $\text{Li}_{1.075}\text{Ni}_{0.755}\text{Co}_{0.17}\text{O}_{1.9}\text{F}_{0.1}$.⁹⁶ This material has an initial capacity of 182 mAh/g and a capacity fading of 2.6% in 100 cycles at 1 mA/cm².

11.5.1.3. $\text{LiNi}_{1-x}\text{M}_x\text{O}_2$ or $\text{LiCo}_{1-x}\text{M}_x\text{O}_2$ ($\text{M} \neq \text{Co}$ or Ni)

Delmas' group has partly substituted Ni in LiNiO_2 with such ions as Fe, Al or Mg.^{73,75} They confirm the presence of the last ion in the Li^+ layers through Rietveld analysis of XRD data and magnetic measurements: only the diamagnetic Mg^{2+} , and not the paramagnetic Ni^{2+} , is found in the layers. A substitution of 5% Mg for Ni is enough to suppress lithium/vacancy ordering in the interslab space and, so, all phase transitions observed upon delithiation.⁷³ A limited amount of Mg substitution (<0.02 atoms/mol) resulted in capacities of 150 mAh/g.

Al has been used by several authors for substituting both Ni and

Co.^{97,98} Ohzuku *et al.* have found that Al in $\text{Li}_{1-x}\text{Al}_{1/4}\text{Ni}_{3/4}\text{O}_2$ produces a single-phase behaviour and allows charging up to 4.5 V with excellent reversibility of the 160 mAh/g initial capacity.⁹⁷ The presence of non-oxidizable Al^{3+} limits the degree of Ni^{3+} oxidation, thus avoiding the considerable shrinking of the *c* axis at high *x* values and consequent loss of capacity. In contrast, Al substitution in LiCoO_2 does not have a positive effect and fast capacity fading is observed. Al substitution increases the voltage in both LiNiO_2 (by ~0.1 V) and LiCoO_2 (by ~0.2 V).

Instead of counterbalancing the tendency of Ni^{3+} to form Ni^{2+} in LiNiO_2 with di- or tri-valent ions, in one report Ti^{4+} was used to compensate for the electric charge deficiency and structural instability due to Ni^{2+} .⁹⁹ The cyclability of $\text{LiNi}_{1-x}\text{Ti}_x\text{O}_2$ ($0.025 \leq x \leq 0.2$) was rather good with initial capacities ranging from 170 to 240 mAh/g as a function of *x*.

A double Mg-Ti substitution has been reported to have a dramatic effect on the thermal stability of LiNiO_2 . Indeed, compounds of formula $\text{LiNi}_{1-x}\text{Ti}_{x/2}\text{Mg}_{x/2}\text{O}_2$ show a progressive disappearance of the large exothermic peak of pure, fully oxidized LiNiO_2 as *x* increases. For *x*=0.3, no exotherm was observed.^{76a} These materials, however, have large irreversible capacities. Including Co among the dopants, the materials become highly stoichiometric (99% Li^+ in the Li^+ layers for $\text{LiNi}_{0.7}\text{Co}_{0.2}\text{Ti}_{0.05}\text{Mg}_{0.05}\text{O}_2$) and show an excellent cycle performance in addition to thermal stability.^{76b} This last feature has been explained by arguing that the highly ionized Ti^{4+} and Mg^{2+} (plus unremovable Li^+) increase the ionic character of these compounds and prevent depletion of electrons from the oxygen sites during charge.^{76c}

There are reports of O substitution with $\text{F}^{96,100}$ or S^{101} . The latter seems to be particularly effective in stabilizing the capacity of a compound with formula $\text{Li}_{1.01}\text{NiO}_{1.98}\text{S}_{0.02}$ at ~140 mAh/g in 100 cycles at 0.4 mA/cm².

11.5.2. Manganese Spinel

The advantages of a Mn spinel cathode (structure in Figure 11.3b) over LiCoO_2 are well known: lower price, lack of toxicity and better thermal stability. On the other hand, the spinel has a lower specific capacity (around 110-120 mAh/g vs. 130-140 for the cobaltate) and serious problems in storage and cycle life at high temperatures. Some years after the first commercial release (1996), NEC has introduced a second generation of spinel batteries with improved capacity and high temperature cyclability.^{2-4a} Figure 11.6 depicts the cycling behaviour of a battery for HEV applications.^{4a} Note that, at 60°C, 87% of the initial capacity was retained after 500 cycles.

Sanyo has also developed in 2001 a Li-ion polymer battery with a

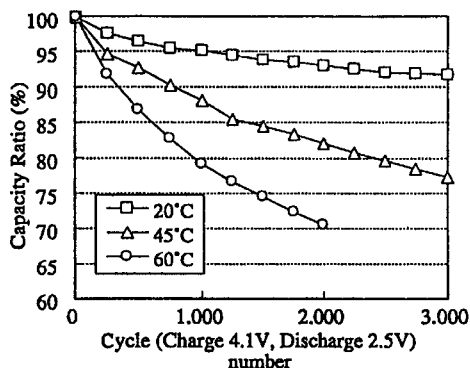


Figure 11.6. Cycling of a NEC battery with a Mn spinel cathode. Rate: 1 C (from Ref. 4a).

cathode based on Mn spinel. This cathode also contains LiCoO_2 which controls the gas evolution during storage at high temperature. A good cycling performance at room temperature for 2000 cycles is reported.^{4b}

Thus far, such batteries have found only a niche in the high-tech market (computers, cellular phones, cameras, etc.), but will probably find wide acceptance in industrial and EV/HEV applications.^{4a,95b}

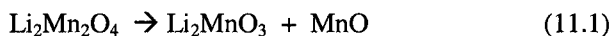
Researchers in this area are steadily working to better understand the complexity of this material and to overcome the problems cited above. The vast literature on this material presents several discrepancies with regards to such aspects as: phase transition of the as-prepared material just below room temperature; phase transition upon delithiation in the 4 V range; origins of the capacity fading during storage/cycling; Mn dissolution as a function of the state of charge and products formed during dissolution.

LiMn_2O_4 undergoes a structural phase transition at ~ 280 K. Even the mechanism of this process is debated. Some authors have supposed, as a consequence of the Jahn-Teller effect, the formation of a tetragonal phase,^{71,102} while others have reached the conclusion that a cubic-orthorhombic transition occurs.^{103,104} Substitution of a small amount of Mn^{3+} with foreign ions, *e.g.*, Li, Ni, Co, Cr, lowers the $\text{Mn}^{3+}/\text{Mn}^{4+}$ ratio below unity, which suppresses the transition.^{103,104} However, Basu and Seshadri have rejected the view of a transition linked to a J-T effect and suggest that it is instead due to charge (holes and electrons) ordering.¹⁰⁵ Yoshio *et al.* have pointed out that oxygen deficiency is the primary cause of the transition.¹⁰⁶

The simple delithiation, *i.e.* Li^+ removal from the tetrahedral 8a sites during charge, is also much debated and has been variously interpreted as a process involving one, two or three phases. Mc Breen *et al.* have shed light on this question.¹⁰⁶ *In situ* X-Ray data have shown that stoichiometric spinel $\text{Li}_x\text{Mn}_2\text{O}_4$ gives rise to a single phase for $0.5 < x < 1$ and to a two-phase system

for $x < 0.5$. Li-rich spinels (and spinels doped with another ion) are single phase throughout the entire x range, and, finally, oxygen-defective spinels ($\text{Li}_x\text{Mn}_2\text{O}_{4-\delta}$) show two biphasic plateaux separated by a voltage knee at $x = 0.5$. The two-phase regions show the fastest capacity decay on cycling.

Much debate is also ongoing regarding the failure mechanisms upon storage or cycling at high temperature. The hypotheses are: 1) Mn^{2+} dissolution; 2) J-T effect with formation of the tetragonal spinel $\text{Li}_2\text{Mn}_2\text{O}_4$; 3) structural instability and 4) decomposition reaction of the electrolyte at high voltage. It is quite possible that such effects are interrelated. For instance, points 1-3 can occur if the following sequence is considered: in a discharge down to ~ 3 V under non-equilibrium conditions, $\text{Li}_2\text{Mn}_2\text{O}_4$ is formed; this can then disproportionate according to the reaction:



and the latter dissolves in the solution; as a consequence, a structural reorganization has to occur which can greatly impair the cyclability. Reaction (11.1) is thought to be more important at low voltages, *i.e.*, when the ratio $\text{Mn}^{3+}/\text{Mn}^{4+}$ is maximized. Indeed, several authors report higher Mn solubility values in the fully discharged state,^{107,108} or at low states of charge (20%).^{109,110} However, others report higher solubility at full charge.^{111,112} In this case, dissolution implies a complex reaction mechanism based on electrolyte decomposition and reaction with λ - MnO_2 . The cathode would then be covered by such by-products as MnF_2 , $\text{Li}_{0.5}\text{MnO}_2$, Li_2POF_3 ⁵⁴ and LiF .⁵¹ In all cases, the particle surface is modified and a polarization ensues that contribute to degrade the electrochemical characteristics. Impedance tests have been particularly useful in showing the resistance increase due to formation of surface layers.^{52,113}

It has been demonstrated that the amount of dissolved Mn^{2+} is normally limited. Inoue and Sano report a weight loss of 1.1% for a totally discharged spinel exposed to a LiPF_6 -based solution at 80°C for 2 days.¹⁰⁸ However, this spinel has a capacity loss of 59% after storage. According to these authors, the modest solubility has a dramatic effect on the structural integrity, creating lattice defects that adversely affect the Li^+ diffusion paths. In addition, structural degradation during the first charge, especially at high rates, has been suggested as a cause of performance loss for stoichiometric spinels.¹¹⁴

Another proposed mechanism for rationalizing the capacity fade on storage at high temperature is the formation of a partially protonated, inactive λ - MnO_2 in solutions containing LiPF_6 , where HF is easily formed by decomposition.⁵⁵ In this study, by Tarascon *et al.*, the protonated phase (probably Mn-defective) was found to form both in the charged and in the discharged state. Gradual accumulation of λ - MnO_2 was also noticed

by White *et al.* in prolonged cycling (up to 700 cycles) at room temperature of a 1 Ah Li-ion battery with a spinel cathode.¹¹⁵ These authors have also found evidence, by EDAX experiments, that Mn metal plated onto the C anode, as a consequence of the dissolution promoted by HF generated during electrolyte oxidation.

The Mn spinel structure undergoes considerable contraction/expansion during delithiation/lithiation, regardless of the number of phase transformations involved. The cubic parameter a typically contracts from 8.24 to 8.05 Å (2.5%). As a general rule, this level of contraction/expansion may create problems with the integrity of the particles and their interconnection. By substituting Mn with other metals (*e.g.*, Ni, Co, Al), it is possible to limit the variation of a , and, so, of the lattice volume. Doped spinels showing lower volume changes also show reduced capacity losses.^{116a} This has been confirmed by Shin and Manthiram.^{116b} They have measured the Δa difference between the two cubic phases formed for $x \sim 0.5$ in $\text{Li}_x\text{Mn}_2\text{O}_4$. Lower capacity losses correspond to lower Δa , the latter being favored by such substituents as Li, Co or Ni.

Other effects brought about by metal dopants will be later discussed.

We have stressed in Section 11.4 the role of the surfaces in determining the cathode characteristics. The surface changes stemming from storage and/or cycling of the Mn spinels have been the subject of extensive investigations aiming at understanding the reaction mechanisms and their products. Direct evidence of electrolyte decomposition during room-temperature storage at high voltages in $\text{LiBF}_4\text{-EC/PC}$ was obtained by SEM experiments showing spinel grains heavily covered by fibers.⁵⁷ In $\text{LiPF}_6\text{-EC/DMC}$, the original 100-nm grains of fully charged cathodes were covered, after storage at 70°C, by fine structures of 10-30 nm.¹¹⁷ XPS analyses have shown that MnF_2 was formed on the surface and that the oxidation state of Mn changed from MnO_2 to MnO .

The surface composition after cycling was examined by several authors. There is a general consensus on the formation of tetragonal spinel $\text{Li}_2\text{Mn}_2\text{O}_4$, as also indicated by electron diffraction.^{118a} According to Cho and Thackeray,^{118b} reaction (11.1) then occurs, this accounting for the formation and dissolution of Mn^{2+} . Other authors suppose that the Mn^{+4} compounds formed in the disproportionation are cation-defective spinels of the type $\text{Li}_2\text{Mn}_4\text{O}_9$.¹⁰⁷ According to Yoshio *et al.*, an oxygen-defective spinel, $\text{LiMn}_2\text{O}_{4-z}$, would be formed.¹¹⁹

The approaches taken to counteract the capacity fading include: adding additives to the solution or to the cathode, encapsulating the particles with a protective layer or doping the spinel with foreign ions.

A soluble additive suggested by Sano *et al.* is $(\text{CH}_3)_3\text{SiNHSi}(\text{CH}_3)_3$, a molecule able to react with water traces to produce NH_3 which can neutralize HF. Mn dissolution was drastically reduced with this additive and so was the

capacity fading on storage at high temperatures.¹²⁰ The cathode of the above mentioned NEC battery is formed by blending the Mn spinel with 10-15% $\text{LiNi}_{0.8}\text{Co}_{0.2}\text{O}_2$.^{3,121} The latter material acts as a scavenger for HF, thus suppressing Mn dissolution.

We have already mentioned the effect of coating the spinel particles with such materials as Co_3O_4 or LiCoO_2 prepared by sol-gel synthesis.⁵⁹ The thin layer formed on the spinel, possibly with the $\text{LiMn}_{2-x}\text{Co}_x\text{O}_4$ composition, is resistant to HF attack and prevents Mn dissolution. As a result, a steady capacity of 105 mAh/g was obtained on cycling at 60°C.

Substituting part of Mn^{3+} with other ions was suggested by the inference of a J-T effect in the 4 V range. The spinel was initially doped with divalent ions as Mg^{2+} or Zn^{2+} .^{122,123} The capacity was indeed stabilized although a penalty in its absolute value was paid, as the amount of Mn^{3+} which determines the capacity was decreased, according to the general formula: $\text{Li}[\text{M}^{n+}_x\text{Mn}^{3+}_{1+(n-4)x}\text{Mn}^{4+}_{1-(n-3)x}]\text{O}_4$. The numerous reports on this topic have shown that the doping ions also have other beneficial effects: they reduce the Mn solubility in the electrolyte;¹²⁴ often give higher energies for the M-O bond;¹²⁵ limit the extraction of Li^+ , and give rise to a single-phase charge-discharge process.¹²⁶ All the above effects contribute to the structure stabilization, which is ultimately the basis for a good cyclability.

Several elements have been used as dopants. Substitution with Li is the most obvious choice: it is generally agreed that Li^+ replaces Mn^{3+} in the 16d octahedral sites, from which it cannot be extracted. However, Howard *et al.*, by observing that Li^+ -doped spinels have an experimental capacity larger than the theoretical one, have suggested, also on the basis of neutron diffraction data, that Li^+ may also reside in tetrahedral 8b sites.¹²⁷ In another report, occupancy of octahedral 16c sites is suggested.¹²⁸ $\text{Li}_{1+x}\text{Mn}_{2-x}\text{O}_4$ spinels, even though showing a better cyclability than the undoped one, show problems on storage at high temperature, with an enhanced formation of $\text{Li}_2\text{MnO}_3/\text{Li}_2\text{Mn}_4\text{O}_9$,¹⁰⁷ and do not compare favourably with other doped spinels in terms of capacity retention.¹²⁹

Divalent metals, as Zn and Ni, or trivalent as Co, Cr, Ga and Al show the best performance. Ni and Cr are particularly effective in reducing the Mn dissolution and, so, the spinel instability.¹²⁴ Capacity losses as low as 0.02-0.03 mAh/g/cycle at room temperature and 50°C have been measured during long cycling.^{129,130,132,133} Reports indicate that Al, Zn and Ga may reside in the 8a tetrahedral sites.^{131,132} In principle, they could create diffusion problems for Li^+ along the 8a-16c-8a paths, but, at least for the limited substitutions considered, this does not occur and, instead, both show a well stabilized capacity.^{129,132,133} According to Thackeray *et al.*¹³¹ substitution in tetrahedral sites may retard the Mn diffusion to these sites, a phenomenon accompanying its dissolution.

Excellent data have often been reported for double doping. Not only

may different cations be used to replace Mn, *e.g.*, Ga-Cr,⁵⁷ but S or F may be used to partially replace O. Tarascon *et al.* have proposed $\text{LiAl}_{0.2}\text{Mn}_{1.8}\text{O}_{4-\delta}\text{F}_z$

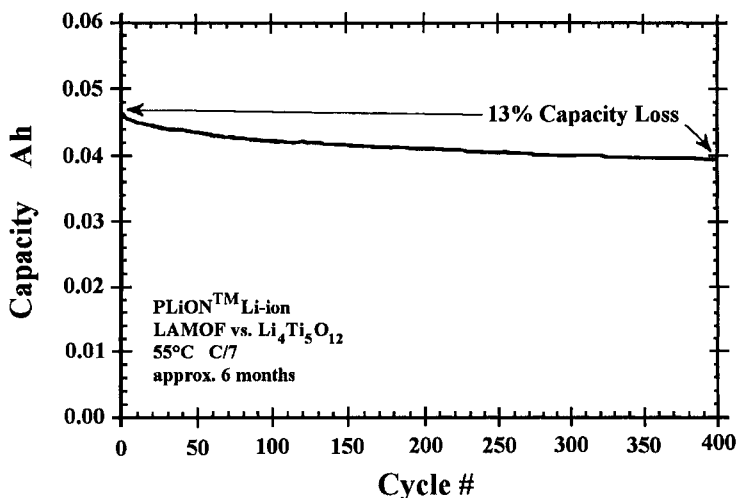


Figure 11.7. Cycling of a Li-ion cell with $\text{LiAl}_{0.2}\text{Mn}_{1.8}\text{O}_{4-\delta}\text{F}_z$ as a cathode (from Ref. 134).

(with $z \approx 0.5$).¹³⁴ The improvement of cyclability of this material at 55°C over a Li-doped spinel is dramatic as shown in Figure 11.7, where cycling of a polymer Li-ion cell at 55°C is reported.

Sun *et al.* have substituted O with a limited amount of S: $\text{LiAl}_{0.24}\text{Mn}_{1.76}\text{O}_{3.98}\text{S}_{0.02}$.¹³⁵ Al stabilizes cycling in the 4 V range, whereas S is effective in stabilizing cycling in the 3 V range. Overall, capacities exceeding 200 mAh/g could be obtained. Leaving aside for the moment the practical interest of a cathode showing a sharp voltage drop of 1 V, the stability in the 3 V range is highly surprising. Furthermore, the authors have shown that, even upon long cycling down to 2.3 V, the cubic structure of the initial spinel is preserved, *i.e.*, there is no J-T effect causing the tetragonal distortion, perhaps due to a more flexible structure of the oxysulphide. A similar result has been found by using Cr instead of Al.¹³⁶ Kang and Goodenough have commented on these results. According to them, sulphur ions ($r = 1.70 \text{ \AA}$ vs. 1.26 \AA for oxygen) would only reside on the spinel surface and the J-T distortion should be present as the 3 V plateau does occur.¹³⁷

Yoshio *et al.* have shown that heavily doping the spinel with Co or Ni, *e.g.*, in $\text{LiM}_{0.5}\text{Mn}_{1.5}\text{O}_4$, also provides a good stabilization of the 3 V capacity.¹³⁸

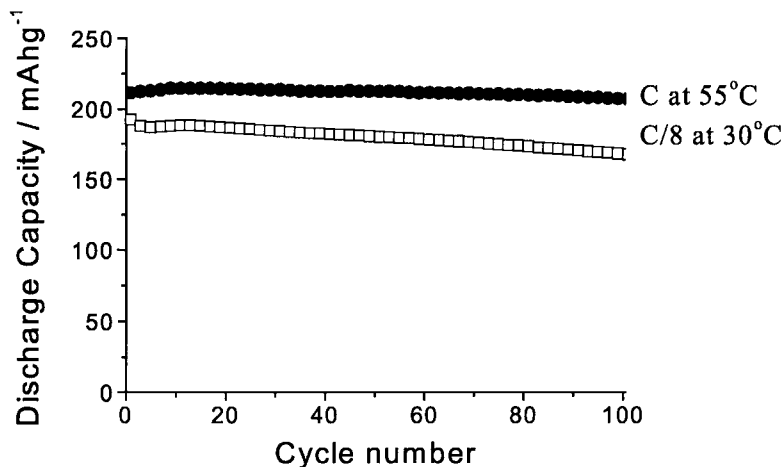


Figure 11.8. Cycling of a cell with a $\text{Li}_x\text{Mn}_{0.975}\text{Li}_{0.025}\text{O}_2$ cathode (from Ref. 21c).

11.5.3. Layered Li_xMnO_2 and Similar Cathodes

A LiMnO_2 compound with the same layered structure as LiNiO_2 and LiCoO_2 would give a theoretical capacity of 285 mAh/g based on the $\text{Mn}^{3+}/\text{Mn}^{4+}$ couple. However, LiMnO_2 is not thermodynamically stable as the layered structure, but as the orthorhombic phase, *o*- LiMnO_2 , of space group *Pnmm*. Layered LiMnO_2 can be prepared by soft chemistry routes or by adding stabilizing ions during the thermal synthesis. This material does not have the α - NaFeO_2 structure of LiCoO_2 (hexagonal symmetry), but rather a monoclinic symmetry with space group *C2/m*. This occurs because the J-T effect brought about by the Mn^{3+} ion (d^4 with a single electron on the e_g level) causes a cooperative distortion of the MnO_6 octahedra.

A number of syntheses have been reported to prepare LiMnO_2 and similar materials. The work done until 2001 has been reviewed by Ammundsen and Paulsen.¹³⁹

According to Ceder and Mishra, the orthorhombic structure is more stable than the layered one due to the strong antiferromagnetic interactions between Mn^{3+} ions and the ensuing localization of the electronic states.¹⁴⁰ So, if one could partly substitute Mn^{3+} with non-magnetic ions, the layered structure could be stabilized. Following this suggestions, layered LiMnO_2 has been prepared by ceramic synthesis by slightly doping the material with ions such as Al or Cr.^{139,141} Doping levels of 3-5% allow one to obtain LiMnO_2 with enhanced cyclability in the voltage range 4.4-2.0 V. Both *o*- LiMnO_2 and layered LiMnO_2 transform when cycled into a more stable

spinel-like structure, through a minor cation rearrangement, as all of these compounds have the same cubic close packed sublattice of oxygen ions. Al-doped layered LiMnO_2 is no exception to this rule, as shown by the characteristic two-plateau discharge curve. Cr-doped LiMnO_2 , however, does not convert into a spinel, although showing some phase transitions.

Capacities as high as 160-190 mAh/g could be obtained at 55°C at the rate of 30 mA/g, with Cr giving higher capacities than Al. The reason why Cr does not favour transformation into spinel lies in its strong octahedral site stabilization energy.¹³⁹ Whether or not a spinel is formed is important, as the 1 V drop between the two plateaux would prevent applications in practical batteries.

We have already mentioned the relevant work of Jang,³⁹ Cho,^{68,69} and Yoshio⁴⁰ on *o*- LiMnO_2 , which also has high and stabilized capacities. *o*- LiMnO_2 is not a true layer structure as it is formed by alternate corrugated layers of Li and Mn (see Figure 11.3c).

A truly layered LiMnO_2 can be obtained at low temperature by ion exchange from NaMnO_2 with LiBr in hexanol.^{21a} This material however does not cycle well and subsequent work by Bruce *et al.* was devoted to compounds partially doped with Li, Ni or Co. These have the α - NaFeO_2 structure of LiCoO_2 (space group $R\bar{3}m$) with Li in the 3b sites, Mn and the doping ion in the 3a sites and O in the 6c sites. The performance of these compounds of general formula $\text{Li}_x\text{Mn}_{1-y}\text{M}_y\text{O}_2$ depends upon the starting Na compound used, degree of doping and ion exchange procedure.^{21(b,c),142,143} It has been found that a Na compound of formula $\text{Na}_{0.518}\text{Mn}_{0.908}\text{Co}_{0.025}\text{O}_2$, ion-exchanged with Li by refluxing in ethanol at 80°C, cycles fairly well. This is attributed to the presence of Na^+ and transition metal vacancies in the final compound, which facilitates the relief of strains induced by the J-T effect in particles composed of nanodomains.²⁰ When the ion exchange is carried out in hexanol at 150°C, the amount of defects is quite limited and the structure is less prone to accommodate the J-T effect, so that the electrochemical behavior is poorer.¹⁴³ In Figure 11.8, the cyclability of layered $\text{Li}_x\text{Mn}_{0.975}\text{Li}_{0.025}\text{O}_2$, prepared by Bruce *et al.* using low-temperature ion exchange, is reported.^{21b}

By using different Na precursors, both layered and non-layered Li derivatives may be obtained. Doeff *et al.*,¹⁴⁴ and Bruce *et al.*¹⁹ starting from $\text{Na}_{0.44}\text{MnO}_2$ with a tunnel structure, have obtained by ion exchange the corresponding Li compounds which could insert Li^+ with capacities of 100-120 mAh/g. Jeong and Manthiram have shown that this Na compound, which more correctly should be written as $\text{Na}_{0.5}\text{MnO}_{2+\delta}$, is obtained with a layered structure if fired below 500°C and with a tunnel structure above 600°C. The layered ion-exchanged samples have a better cycling life than the tunnel ones (225 mAh/g of initial capacity vs. 170 mAh/g) and better capacity retention.¹⁴⁵

Ohzuku's group has thoroughly investigated layered $\text{Li}[\text{Ni}_{1/2}\text{Mn}_{1/2}]\text{O}_2$ obtained by ceramic synthesis.¹⁴⁶⁻¹⁴⁸ Its XRD is closely related to that of LiNiO_2 but both the structure and the electrochemical behavior are different. This material gives a stable capacity of ~ 200 mAh/g when cycled at low rate between 2.5 and 4.5 V. The synthesis of this material is critical and requires, in particular, the use of a double Mn-Ni hydroxide with an exact 1:1 ratio for the two ions.^{148b} An improved behavior, with enhanced rate capability, was shown by $\text{Li}[\text{Co}_{1/3}\text{Ni}_{1/3}\text{Mn}_{1/3}]\text{O}_2$.^{148c} This material has the peculiar characteristic of showing a zero-volume change up to a deintercalation of $0.67 \text{ Li}^+/\text{mol}$.

Dahn *et al.* have devoted particular attention to doped layered LiMnO_2 having the O2 structure instead of the O3 typical of $\text{LiCoO}_2/\text{LiNiO}_2$ and doped LiMnO_2 .¹⁴⁹⁻¹⁵² A layered O2 structure consists of 2 MnO_2 sheets enclosed in the unit cell, instead of 3 for O3. We have already pointed out that the O3 layered structure of monoclinic LiMnO_2 is easily converted into that of the lithiated spinel. The O2 structure, however, is quite different. From P2-type sodium manganese oxides, O2 layered lithium oxides may be obtained which do not convert into spinel, as this would require a rearrangement of the oxygen lattice - a very unlikely event at room temperature. Several O2 phases have been prepared as $\text{Li}_{2/3}[\text{Li}_{1/6}\text{Mn}_{5/6}]\text{O}_2$, $\text{Li}_{2/3}[\text{Co}_{0.15}\text{Mn}_{0.85}]\text{O}_2$,¹⁴⁹ and $\text{Li}_{2/3}[\text{Ni}_{1/3}\text{Mn}_{2/3}]\text{O}_2$.¹⁵⁰ They show specific capacity of 150-180 mAh/g at low rates (typically C/40).

Stabilization of the O3 layered structure of LiMnO_2 has been attempted with the use of solid solutions between Li_2MnO_3 and LiMO_2 ($\text{M}=\text{Cr}, \text{Ni}, \text{Co}$). Dahn *et al.* have prepared materials of general formula $\text{Li}[\text{Ni}_x\text{Li}_{(1/3-2x/3)}\text{Mn}_{(2/3-x/3)}]\text{O}_2$, that may be thought of as derived from $\text{Li}[\text{Li}_{1/3}\text{Mn}_{2/3}]\text{O}_2$, i.e. Li_2MnO_3 , by partial substitution of Li^+ and Mn^{4+} with Ni^{2+} , while maintaining the remaining Mn as Mn^{4+} . These compounds have the O3 structure of LiCoO_2 when synthesised at temperatures above 800°C .^{153(a-d)} Charging them up to 4.8 V, Ni^{2+} is first oxidized to Ni^{4+} and, then, oxygen is lost while more Li^+ is extracted in a plateau between 4.5 and 4.7 V. These oxygen-deficient cathodes, with $x=1/4, 1/3, 5/12$, can reversibly intercalate Li^+ with capacities as high as 225 mAh/g to 2V. Excellent rate capabilities are also reported. According to the authors, considerations of performance, safety and cost candidate these materials as possible substitutes for LiCoO_2 . However, from the data on cyclability, a loss of 0.25 mAh/g/cycle may be calculated. This value is too high for practical use and needs to be improved.

The same solid solution between Li_2MnO_3 and LiNiO_2 has been used by Sun *et al.* to prepare a material with formula $\text{Li}[\text{Li}_{0.13}\text{Ni}_{0.30}\text{Mn}_{0.57}]\text{O}_2$, which can provide a stable specific capacity of 190 mAh/g when cycled between 2.0 and 4.6 V.^{153e} A further improvement can be obtained if Al is used to partially replace Ni and Mn, as in $\text{Li}[\text{Li}_{0.15}\text{Ni}_x\text{Al}_{0.55-2x}\text{Mn}_{0.3+x}]\text{O}_2$.^{153f}

The solid solution between Li_2MnO_3 and LiCrO_2 has also received much attention and, in particular, $\text{Li}[\text{Li}_{0.2}\text{Cr}_{0.4}\text{Mn}_{0.4}]\text{O}_2$ has proved attractive.¹³⁹ Just like for the other solid solutions, the doping transition metal is the electrochemically active species ($\text{Cr}^{3+} \rightarrow \text{Cr}^{6+}$ in this case), while Li and Mn form an inert matrix.

11.5.4. 3 V Cathodes

11.5.4.1. Manganese Oxides

During the early 90's, a cylindrical rechargeable battery with a Li anode, a $\text{Li}_{0.3}\text{MnO}_2$ cathode and a solution based on dioxolane was commercialized.¹⁵⁴ This battery, whose safety resulted from the polymerisation of the solvent at 125°C (thermal shutdown), could deliver 300 cycles but only at low charging rates ($<C/9$). At higher rates, a failure mechanism based on the reaction of small Li grains with the electrolyte was observed.¹⁵⁵

In spite of this failure (and of the previous ones), the development of a Li-anode rechargeable battery remains a realistic goal, *e.g.*, through the realization of a glassy film to protect the anode.¹⁵⁶ Also in view of this perspective, the research on 3 V cathodes has been actively ongoing, especially for Mn-based oxides. Both layered (*e.g.*, buserite and birnessite) and tunnel structures of MnO_2 (*e.g.*, ramsdellite/rutile, α - MnO_2 , hollandite, todorokite), have been reconsidered.¹⁵⁷⁻¹⁶¹ These compounds are characterized by a high initial capacity which rapidly decreases in the next few cycles, but recently some reports on the stabilization of the capacity have appeared. For instance, Franger *et al.* have found that a sol-gel Co-doped birnessite can deliver a stable capacity of 177 mAh/g in 40 cycles.¹⁵⁹ Johnson and Thackeray have reported that α - MnO_2 stabilised by doping with Li_2O and treated with NH_3 can deliver 150-220 mAh/g (depending on the rate).¹⁶⁰

More interest has been devoted to lithiated Mn oxides. Yoshio *et al.* have tried to resolve the uncertainty linked to the actual composition of what is conventionally called CDMO (composite dimensional manganese oxide).¹⁶² A single orthorhombic phase, $\text{Li}_{0.33}\text{MnO}_2$, can be obtained by heating a $\text{LiNO}_3/\text{MnO}_2$ mixture (Li/Mn ratio = 1/3) at a temperature lower than 350°C for less than 30 hours. Higher Li/Mn ratios, temperatures and times favor the formation of Mn spinel. The latter was indeed observed by Thackeray *et al.*¹⁶³ $\text{Li}_{0.33}\text{MnO}_2$ obtained under the conditions described above delivers a stable capacity of 180 mAh/g. However, an even better performance is reported by Yoshio *et al.* with orthorhombic $\text{Li}_{0.5}\text{MnO}_2$ obtained by lithiating MnO_2 with LiI (Li/Mn ratio = 1) at 150-200°C. The

authors report capacities of ~ 250 mAh/g while cycling at 0.4 mA/cm² in the 4.5–2.0 V range.¹⁶⁴

Recently, Li-rich spinels (*e.g.*, $\text{Li}_4\text{Mn}_5\text{O}_{12}$) and O-rich spinels have been reconsidered as 3 V cathodes. The former has been examined by Manthiram (see Section 11.2),¹¹ while the latter, with a typical composition $\text{LiMn}_2\text{O}_{4.54}$, has been shown by Kilroy *et al.* to cycle with capacities above 200 mAh/g.¹⁶⁵

Surprisingly stable capacities have been reported for the Mn spinel in the 3 V range by Goodenough *et al.* These authors have prepared a nearly stoichiometric spinel by a sol-gel synthesis with glycolic acid, producing a material with an average particle size of 0.8 μm .¹³⁷ Cycling at 1 mA/cm², capacities of ~ 110 mAh/g have been obtained in spite of the evident two-phase behaviour testifying to a J-T effect. The authors, although unable to provide a sound explanation of this unusual behaviour, tended to attribute it to the small particle size. Indeed, the same authors made experiments on ball-milled spinel samples obtained by both sol-gel and thermal syntheses and found even higher and stable 3 V capacities. In this work, also mentioned in Section 11.3, the conclusion was reached that the J-T distortion could be accommodated by strained, nanosized particles.³⁷ Excellent cycling behavior was also reported at 60°C and 80°C .

11.5.4.2. Cr and V Oxides

Vanadium oxides, *e.g.*, V_2O_5 , V_6O_{13} and LiV_3O_8 , have long been investigated as cathodes for 3 V batteries with a Li anode.

V_2O_5 is very amenable to sol-gel processing by different routes. Using the well known ion-exchange process that yields a precursor HVO_3 solution that self-assembles into the V_2O_5 hydrogel, a variety of materials of different porosity have been synthesized in form of films, powders and free-standing membranes. In the gel stage, the V_2O_5 solid network is bicontinuous with interconnected pores filled with water. Depending on the way the liquid solvent is removed (drying process) any of the following three types of solid, amorphous vanadium pentoxide can be produced:

1. Xerogel (XRG): nominal surface area = $1\text{--}10$ m²/g.
2. Aerogel (ARG): nominal surface area = $350\text{--}450$ m²/g.
3. Aerogel-like (ARG-like): nominal surface area = $100\text{--}300$ m²/g.¹⁶⁶

All materials are reported to have high specific capacities (see Table 11.2) in near-equilibrium or very slow insertion/release tests.¹⁶⁷ However, as the rate increased the capacity of xerogel decreased to 380 mAh/g (at C/20), 320 mAh/g (at C/5), and 200 mAh/g (at 1C). The dependence of the capacity on the rate indicates that diffusion limitations are key factors determining the performance of the xerogel material.

In an effort to further improve the intercalation kinetics and rate capability of these materials, there has been some investigation of the doping in the precursor hydrogel. Reaction of the hydrogel V_2O_5 with metallic Cu, Ag, Al, Ni, Mg, and Zn has been found to enhance the electronic conductivity by up to three orders of magnitude.¹⁶⁸ X-Ray absorption spectroscopy studies have shown the formation of metallic copper nanoclusters upon lithium insertion in $Cu_{0.1}V_2O_5$ xerogel.¹⁶⁹ The process is completely reversible at the atomic level and the starting compound is regenerated upon releasing the inserted lithium. $Cu_{0.1}V_2O_5$ aerogel-like based electrodes in coin cell batteries were found to have capacities of 170 mAh/g (active material) at 1 C rate for more than 400 cycles.¹⁷⁰ $Cu_{0.1}V_2O_5$ xerogel showed similar capacity-cycle life behavior. In addition the latter material

Table 11.2. Specific capacities of amorphous vanadium pentoxides prepared by sol-gel processes. For comparison, the specific capacity of crystalline V_2O_5 is also indicated. Data obtained in low rate discharges (C/100).

Material	Typical Specific Capacity
V_2O_5 XRG	560 mAh/g
Cu-doped V_2O_5 XRG	300 mAh/g
V_2O_5 ARG	560 - 780 ^a mAh/g
V_2O_5 ARG-Like	560 mAh/g
c- V_2O_5	148 mAh/g

a. Obtained by chemical lithiation

showed very good performance in pulsed insertion test.¹⁷¹

V_2O_5 is the cathode most used when investigating organic-inorganic hybrid materials.²⁶ In its layered structure it can even intercalate large molecules as polyaniline.¹⁷² However, both the electrochemical and thermal stability of these composites need to be improved.

LiV_3O_8 is a pseudo-layered material formed by V_3O_8 ⁻ puckered sheets pinned by non-mobile Li^+ ions residing in octahedral sites.¹⁷³ It can be prepared by both solution and ceramic techniques, and, in both cases, optimized syntheses lead to high (well above 200 mAh/g) and reversible capacities.¹⁷⁴⁻¹⁷⁷ Particularly effective is the introduction of H_2O and CO_2 molecules between the layers, which allows their expansion and, so, an increased mobility and enhanced distribution of Li^+ .¹⁷⁴ A sample prepared in this manner has an initial capacity approaching 300 mAh/g (at C/3) and can still deliver 260 mAh/g after 200 cycles.

Interesting results have also been obtained with the isostructural NaV_3O_8 ^{178,179} and $\text{Na}_{1-x}\text{K}_x\text{V}_3\text{O}_8$ ($x < 0.4$),¹⁸⁰ while KV_3O_8 gives poor results.¹⁸¹ The latter, however, is not the only composition in the phase diagram between V_2O_5 and KVO_3 . One of the four possible compositions, *i.e.* KV_5O_{13} , also gives rechargeable capacities in excess of 200 mAh/g.¹⁸¹

K-containing vanadates have also been prepared by hydrothermal reactions between KMnO_4 and hydrated VOSO_4 .¹⁸² Depending upon the reactant ratios and the mixture pH, two different layered materials can be obtained, *i.e.* $\text{K}_{0.16}\text{Mn}_{0.04}\text{V}_2\text{O}_{4.94} \cdot 14\text{H}_2\text{O}$ and $\text{K}_{0.44}\text{V}_2\text{O}_{4.96}$. It seems that at a pH value of 2.3 both phases coexist and provide the optimum reversible capacity of 190-200 mAh/g. Another interesting vanadate is the Al-doped $\text{Co}_3\text{V}_6\text{O}_{17}$, providing more than 250 mAh/g at low rates (C/10).¹⁸³

All the above vanadium oxides do not contain removable Li^+ and can only be used in cells with a Li anode. However, chemical lithiation has been reported for both LiV_3O_8 and NaV_3O_8 to obtain $\text{Li}_4\text{V}_3\text{O}_8$ and $\text{Li}_3\text{NaV}_3\text{O}_8$, respectively.^{177,178} $\text{Li}_4\text{V}_3\text{O}_8$ was obtained by using Li_2S as a lithiating agent, whereas $\text{Li}_3\text{NaV}_3\text{O}_8$ was obtained with butyllithium. Li can be reversibly extracted from both compounds, enabling them to be used in lithium-ion cells. For instance, with $\text{Li}_3\text{NaV}_3\text{O}_8$, capacities of 210-230 mAh/g could be obtained on cycling at 25-50 mA/g.¹⁷⁸

In comparison to V oxides, the search on Cr oxides has been more limited. Starting from CrO_3 , Arora *et al.* could prepare, by decomposition in an autoclave under O_2 pressure, CrO_x and, by lithiating the latter with LiI, LiCrO_x .^{184a} Both compounds can give high capacities but only at low rates. However, a moderate doping with Co (typically 0.2 atoms/mol) is effective in stabilizing both structures, so enhancing the rate capability and allowing to obtain capacities of 230-250 mAh/g.^{184b}

11.5.5. A Special Case: LiFePO_4

Lithium iron phosphate, LiFePO_4 , with the phospho-olivine structure (Figure 11.3d) is emerging as a promising cathode for lithium and lithium-ion batteries. Its high theoretical capacity (170 mAh/g), flat voltage at ~3.4 V, low cost and safety (low toxicity and environmental impact) make this material very appealing.

The interest on this material was raised by Padhi *et al.*¹⁸⁵ that showed the possibility of chemically remove lithium from the structure of LiFePO_4 thus leaving a new phase, FePO_4 , isostructural with heterosite, $\text{Fe}_{0.65}\text{Mn}_{0.35}\text{PO}_4$. The lithium electrochemical extraction from LiFePO_4 proceeds via a bi-phasic process in which the final FePO_4 structure is obtained through minimum displacements of the ordered phospho-olivine framework. Nevertheless, the lithium electrochemical extraction/insertion in

this material is limited to 0.6 Li⁺/mol even if driven at a very low specific current (2.1 mA/g, *i.e.*, C/81 rate).

Ravet *et al.*¹⁸⁶ renewed the interest on LiFePO₄ by improving its electrochemical performance via a new synthetic route. They added sucrose to the precursors to act as a source of carbon to be formed during the thermal synthesis (700°C). In such a way they were able to produce LiFePO₄ particles covered with a carbon layer. This material, cycled at 80°C in polymer electrolyte cells, delivered about the theoretical capacity even at high current rates.

Andersson *et al.* have investigated the electrochemical lithium release and insertion processes in thermally synthesised, additive-free LiFePO₄ by in situ X-ray diffractometry and Mossbauer spectroscopy.¹⁸⁷ They found that 20-25% of LiFePO₄ remains unaltered depending on the material particle size and surface area. In a following work, they showed that the amount of lithium involved in the first extraction is larger than in the second.¹⁸⁸ Furthermore, they found a direct correlation between the temperature and the extracted amount of lithium. On these bases they proposed that lithium diffusion within each particle is the limiting step.

Following this finding, research groups at NTT and Sony have investigated the effect of synthesis temperature on the electrochemical properties of LiFePO₄.^{189,190} They found that the reduction of the synthesis temperature decreased the material particle size (ranging from 0.2 to 30 µm), increased the specific surface area (about 10 m²/g) and enhanced the electrochemical performance (160 mAh/g for a material synthesised at 550°C).

Similar results have been obtained by Prosini *et al.* that have synthesised LiFePO₄ in the presence of high surface area carbon.^{191,192} The addition of carbon was found to reduce the particle size to less than 10 µm. The authors report an enhancement of the electrochemical performance in terms of high rate delivered capacity while the theoretical capacity (170 mAh/g) was obtained in tests performed at 80°C and C/10 rate. According to these authors, the rate limitations in LiFePO₄ could be due to the poor lithium diffusion or the poor electronic conductivity of the material. They proposed that the addition of carbon has a beneficial effect because it reduces the particle size and increases the overall electronic conductivity of the material.

The effect of the particle size reduction (*i.e.*, the shortening of the solid phase path for ions and electrons) has been also evidenced by Goodenough on hydrothermally synthesised LiFePO₄.¹⁹³ Croce *et al.*¹⁹⁴ have tried a different approach that consisted of the dispersion of a very fine metallic powder (copper and silver) in the LiFePO₄ precursors following a process earlier reported.^{168,169} The authors stated that the metallic particles act as nucleation sites (thus reducing the active material particle size) and enhance the electronic conductivity, thus allowing the improvement of the

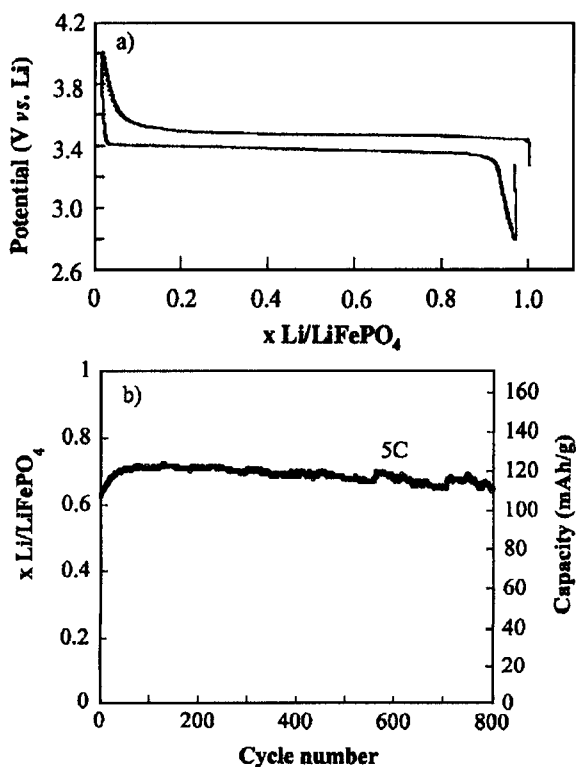


Figure 11.9. a) First cycle of a cell with a LiFePO₄ cathode (C/10); b) Prolonged cycling at 5 C (from Ref. 196).

performance. Prosini *et al.* reported the synthesis of nanocrystalline LiFePO₄ by heating its amorphous form, the latter being prepared by chemical lithiation of FePO₄.¹⁹⁵ The nanocrystalline material had a globular structure with a grain size of about 100-150 nm and delivered a capacity of 162 mAh/g at 17 mA/g (room temperature).

Following this reasoning, Nazar *et al.* have synthesised a LiFePO₄/C composite with active material particles in the scale of nanometers, via a sol-gel synthesis.¹⁹⁶ Such a composite was able to deliver about 90% of the theoretical capacity at C/2 rate and ambient temperature. The reported cycle life of this material is also extremely good with about 90% of the theoretical capacity delivered at the 100th cycle at C/5 rate. Even more impressive is the result of the combined rate performance-cycle life test performed at 5C rate in which the material was able to deliver 70% of the theoretical capacity (about 110 mAh/g) at the 800th cycle (see Figure 11.9). These results

clearly confirm that the reduction of the material particle size and the improvement of the electronic conductivity lead to a better electrochemical performance of LiFePO_4 .

11.5.6. Sulphur and Organic or Inorganic Sulphides

Integrated circuits for microelectronics which can be powered by 2 V sources, instead of 3 V, have been developed. This makes it possible to use electrochemical couples thus far neglected, provided that they can deliver high capacities and are cheap and safe.

Sulphur can provide a specific capacity of 1675 mAh/g and an energy of 2600 Wh/kg in a Li/S cell. However, realization of an efficient cathode has been rather elusive thus far due to the low conductivity and high solubility of sulphur. In recent years, efforts to exploit its potentialities have been renewed and interesting results reported.

Sulphur is reduced in two steps. During the first, at ~ 2.4 V, several Li polysulphides are formed, *e.g.*, Li_2S_4 , Li_2S_8 , etc., while in the second step, at 1.8–2.0 V, Li_2S is formed.¹⁹⁷ The sulphides are soluble and can diffuse to the cathode where they are reduced. The reduced forms can diffuse back to the cathode and reoxidize.¹⁹⁷ A proper cathode formulation, including an electronic conductor and a binder, affords capacities as high as 1364 mAh/g at room temperature (82% utilization).¹⁹⁸ A further improvement is reported with the use of filamentary nickel. By ball-milling the Ni with S, NiS is formed and the so-modified electrode can retain 99% of its initial capacity after 110 cycles.¹⁹⁹

The sulphur electrode has stimulated considerable interest at the industrial level. Prototypes with a relatively high cathode loading, >4 mAh/cm² vs. 2.5–3 mAh/cm² for commercial lithium-ion batteries, have been realized and provide about 370 mAh/g on extended cycling. It has been suggested that a stable passivation layer on Li forms, resulting in gravimetric and volumetric energy densities, in liquid and polymeric electrolytes, comparable with those of commercial batteries.²⁰⁰

In a recent development, the S cathode is coupled with a Li electrode obtained by deposition and separated by a glass electrolyte film from the electrolyte.²⁰¹ The interfacial resistance of Li/glass/electrolyte is much lower and more stable than that of unprotected Li and seems to offer the potential for practical secondary batteries with a Li anode. The combination of this protected Li and S (Li_2S_x) is rather promising. In a flat-type cell, this chemistry has afforded specific energies of 420 Wh/kg and 520 Wh/l, allowing the developers to foresee viable marketing possibilities.^{201a}

Organo-sulphur cathode materials have also been investigated, *e.g.*, poly(carbon sulphides) obtainable in various forms according to the

synthesis procedures.²⁰² These compounds have been tested in prototype batteries under conditions simulating those typical of cellular phones. A poly(phenylenedithiazol) has also been reported, whose electrochemical activity is based on an S-S bond and an unsaturated dithiazolium ring.²⁰³ Its excellent first-discharge capacity (420 mAh/g at low rate) was only partly reversible, perhaps due to solubility problems.

Peled's group has investigated in detail the Li/FeS₂ couple in a composite polymeric electrolyte based on PEO.^{204,205} Thin-cathode batteries, discharging at the mean potential of 1.7 V (at 135°C), have a reversible capacity of 625 mAh/g (2.8 Li/FeS₂) and a projected specific energy of 170 Wh/kg in a bipolar configuration. 500 cycles with 100% DOD have been reported. The Li/FeS₂ couple has been proposed as a good candidate for EV applications. The same couple has also been cycled at room temperature in a polymeric electrolyte based on PVdF.²⁰⁶

11.5.7. High Voltage Materials

Another way to increase the energy output of lithium batteries is by focusing on materials having redox reactions above ~4.3 V (a commercial Li-ion battery based on LiCoO₂ has an average potential of 3.65 V on discharge). Heavily doped Mn spinels, LiM_xMn_{2-x}O₄ (M=Fe,Cr,Ni,Co,Cu and their mixtures), have been identified as the compounds which may offer this possibility. All of these materials retain the spinel space group *Fd3m* and take advantage of the redox reaction of the doping ion. West *et al.* have examined several substituted spinels and found that some of the Co-substituted ones, *e.g.*, Li₂Co_{0.8}Mn_{3.2}O₈ and LiCoMnO₄, give the best results.^{207,208} In them, the Co³⁺/Co⁴⁺ couple creates a discharge plateau at about 5 V, in addition to the 4 V plateau of Mn³⁺/Mn⁴⁺. Initial capacities of these compounds are 135 and 105 mAh/g, respectively, with moderate decrements after 35 cycles at 0.5 mA/cm².

Ohzuku's group has examined the low-rate first cycle of the spinels Li[M_{1/2}Mn_{2/3}]O₄ (M=Ni,Co,Cr,Fe,Cu) and found capacities of 120-125 mAh/g for the Fe and Ni spinel, with the latter providing most of its capacity in a single 4.5 V plateau.²⁰⁹ The promising behaviour of Ni-spinels has been confirmed in subsequent reports. Hernan *et al.* have examined spinels of composition LiM_{0.3}Mn_{1.7}O₄ (M=Fe,Co,Ni).²¹⁰ XPS data have shown that Ni is in a divalent state. Its oxidation to the tetravalent state results in high capacities (around 120 mAh/g at 4.5 V). Thackeray *et al.* have studied spinels of composition LiNi_xCu_{0.5-x}Mn_{1.5}O₄ (0 ≤ x ≤ 0.5).²¹¹ With increasing Ni concentration, the capacity increases (to a maximum of 117 mAh/g) while the upper-plateau potential decreases (from 4.9 V to 4.6 V). In the last two references the cathodes were cycled for about 50 cycles at 0.25 mA/cm². We have calculated for these tests capacity losses of 0.4 mAh/g cycle

(~0.33%/cycle), a very high value in comparison with that shown by the conventional 4 V cathodes (0.01-0.05%/cycle). A better capacity retention has recently been reported for sol-gel spinel $\text{LiNi}_{0.5}\text{Mn}_{1.5}\text{O}_4$.^{212,213} In particular, in Ref. 214 the synthesis was optimized by first firing the gel at 850°C and annealing at 600°C to reduce oxygen loss and improve Ni content. The material so obtained has an initial capacity of 127 mAh/g at 0.5 mA/cm², which is only reduced to 124 mAh/g after 60 cycles. This is explained by the low surface area of the annealed spinel (2 m²/g), so that electrolyte ($\text{LiPF}_6\text{-PC}$) decomposition is minimized.

Recently, a remarkable improvement has been reported for the cyclability of $\text{LiNi}_{0.5}\text{Mn}_{1.5}\text{O}_4$. In a first report, Yoshio *et al.*²¹⁴ have reported that this material, prepared by a sol-gel technique and coated with nanosized ZnO, could be cycled at C/3 and 55°C for 50 cycles with a stable capacity of 137 mAh/g. ZnO is proposed to protect the spinel from the electrolyte and, in particular, to act as a HF scavenger. In a subsequent report, Yoshio *et al.*²¹⁵ have described an improved synthesis technique for $\text{LiNi}_{0.5}\text{Mn}_{1.5}\text{O}_4$, the so-called composite carbonate process, allowing to obtain a more homogeneous material formed by agglomerated nanoparticles of 50-100 nm. As a result, it shows an excellent performance at high temperature without the ZnO-coating: 96% capacity retention in 50 cycles.

11.6. CONCLUDING REMARKS

The research on rechargeable cathode materials has been very fruitful since the introduction of the first commercial Li-ion batteries. Here, we shall try to summarize the most important advances.

LiCoO_2 , the cathode still used in mass production, has been optimized in its preparation, especially as far as particle size is concerned (~20 μm).⁴¹ Interesting reports on the coating of this cathode to improve the thermal stability and to allow the use at higher voltages (with higher capacities) have appeared.^{59,63} As mentioned in Section 11.5, the price of this material has been decreasing, consolidating its predominant position in batteries for portable electronics. In 2002, the price of LiCoO_2 was about twice that of $\text{LiNi}_{1-x}\text{Co}_x\text{O}_2$ and about four times that of LiMn_2O_4 , the two major candidates for future developments. However, if the price is related to the energy (Wh) of a given battery, a LiCoO_2 -based battery is only 30% more expensive than batteries with cathodes containing Ni or Mn.^{95b} This can be tolerated in small cells, but not in the large ones intended for EV and industrial applications. Indeed, in view of the fact that for such large batteries mass production processes are not as well established as for the small ones, it can be foreseen that only Ni- and/or Mn-based cathodes will be used.

As already mentioned, small Li-ion batteries based on Mn spinel are also commercialized, although to a limited market share. The lower spinel capacity with respect to LiCoO_2 does not allow to foresee a higher energy. The limited cyclability at high temperature has recently been improved, thanks to the use of additives.⁴ The safety has also been improved but needs further efforts. A remarkable advancement is represented by the cyclability in the previously prohibitive 3 V range.^{37,137}

Perhaps, the most rapidly emerging material is now $\text{LiNi}_{1-x-y}\text{Co}_x\text{Al}_y\text{O}_2$.⁹⁵ It contains more than 75% of the relatively cheap Ni, can be prepared on a large scale and affords high and stable capacities. LiFePO_4 also appears of great interest, as shown in Section 11.5.5. Close attention are also receiving layered Mn-containing materials, such as $\text{Li}[\text{Li}_{0.2}\text{Cr}_{0.4}\text{Mn}_{0.4}]\text{O}_2$ (with the $\text{Cr}^{3+}/\text{Cr}^{6+}$ couple)¹³⁹ and $\text{Li}[\text{Ni}_x\text{Li}_{(1/3-2x/3)}\text{Mn}_{(2/3-x/3)}]\text{O}_2$ (with the $\text{Ni}^{2+}/\text{Ni}^{4+}$ couple)¹⁵³.

Broussely has calculated that an optimized Li-ion cell based on a C anode of 350 Ah/kg and a LiCoO_2 cathode of 140 Ah/kg would give 166 Wh/kg and 412 Wh/l.^{95b} These values are not far from those attainable in the present generation of Li-ion batteries. They may be taken as a benchmark for possible new batteries based on different cathodes, especially those having lower or higher voltages than C/ LiCoO_2 (3.6 V). So, a new cathode with an average 2.5 V (usable in the newly developed integrated circuits) should have a capacity of at least 250 Ah/Kg and a density higher than 6.5 g/cm³ to outperform C/ LiCoO_2 . Some new cathodes mentioned in Section 11.5 have such high capacities but none are so dense.

On the other hand, a cathode discharging at 4.25 V should be better than 115 Ah/kg and 5 g/cm³. Capacities well in excess of the above value have been reported for heavily doped spinels (up to 140 mAh/g at >4.5 V)²¹⁵, while their density should be similar to that of pure spinel (~4.2 g/cm³). Electrolyte decomposition at the cathode could negatively affects the performance, but this problem can be tackled with improved syntheses and the coating techniques.^{214,215} Therefore, the new generation of high voltage cathodes looks quite promising.

In the meantime, the presently available cathode materials perform well enough if one notes that, in only 10 years, Li-ion batteries have gained a 70% share of the market for portable devices.

REFERENCES

1. T. Nagaura, K. Tozawa, *Prog. Batt. Solar Cells* 9 (1990) 209.
2. T. Numata, C. Amemiya, J. Iriyama, T. Miura, M. Shirakata, *NEC R&D* 41 (2000) 8.
3. M. Tsunoda, Y. Oshima, M. Yoshinaga, T. Shirasu, *NEC R&D* 41 (2000) 13.
4. (a) C. Amemiya, J. Kurihara, M. Yonezawa, *NEC R&D* 42 (2001) 241; (b) S. Narukawa, I. Nakane, N. Imachi, S. Fukuoka, M. Yamasaki, 11th *IMLB*, Monterey, CA, USA, June

- 2002, Abs. 2.
5. Y.-S. Lee, Y.-K. Sun, K.-S. Nahm, *Solid State Ionics* 109 (1998) 285.
6. H.-B. Park, J. Kim, C.-W. Lee, *J. Power Sources* 92 (2001) 124.
7. C. Julien, M.A. Camacho-Lopez, T. Mohan, S. Chitra, P. Kalyani, S. Gopukumar, *Solid State Ionics* 135 (2000) 241.
8. S. Chitra, P. Kalyani, T. Mohan, R. Gangadharan, B. Yebka, S. Castro-Garcia, M. Massot, C. Julien, M. Eddrief, *J. Electroceram.* 3:4 (1999) 433.
9. W. Yang, G. Zhang, J. Xie, L. Yang, Q. Liu, *J. Power Sources* 81-82 (1999) 412.
10. Y.-S. Han, H.G. Kim, *J. Power Sources* 88 (2000) 161.
11. A. Manthiram, J. Kim, *Chem. Mater.* 10 (1998) 2895.
12. S. Bach, J.P. Pereira-Ramos, N. Baffier, *Solid State Ionics* 80 (1995) 151.
13. Q. Feng, H. Kanoh, K. Ooi, M. Tani, Y. Nakacho, *J. Electrochem. Soc.* 141 (1994) L135.
14. J. Kim, A. Manthiram, *J. Electrochem. Soc.* 145 (1998) L53.
15. A. Manthiram, A. Dananjay, Y. Zhu, *Chem. Mater.* 6 (1994) 1601.
16. C. Tsang, A. Manthiram, *J. Electrochem. Soc.* 144 (1997) 520.
17. J. Maruta, H. Yasuda, M. Yamachi, *J. Power Sources* 90 (2000) 89.
18. J.N. Reimers, E.W. Fuller, E. Rossen, J.R. Dahn, *J. Electrochem. Soc.* 140 (1993) 3396.
19. A.R. Armstrong, H. Huang, R.A. Jennings, P. G. Bruce, *J. Mater. Chem.* 8 (1998) 255.
20. A.D. Robertson, A.R. Armstrong, P.G. Bruce, *Chem. Mater.* 13 (2001) 2380.
21. (a) A.R. Armstrong, P. G. Bruce, *Nature* 381 (1996) 499; (b) A.D. Robertson, A.R. Armstrong, A.J. Peterson, M.J. Duncan, P.G. Bruce, *2001 ECS and ISE Joint International Meeting*, San Francisco, CA, USA, September 2001; (c) A.D. Robertson, A.R. Armstrong, A.J. Peterson, M.J. Duncan, P.G. Bruce, *11th IMLB*, Monterey, CA, USA, June 2002, Abs. 74.
22. M.S. Whittingham, J.-D. Guo, R. Chen, T. Chirayil, G. Janauer, P. Zavalij, *Solid State Ionics* 75 (1995) 257.
23. M.S. Whittingham, S. Yang, K. Ngala, P. Zavalij, *2001 ECS and ISE Joint International Meeting*, San Francisco, CA, USA, September 2001.
24. P.K. Sharma, G.J. Moore, F. Zhang, P. Zavalij, M.S. Whittingham, *Electrochem. Solid-State Lett.* 2 (1999) 494.
25. R. Chen, M.S. Whittingham, *J. Electrochem. Soc.* 144 (1997) L64.
26. M.S. Whittingham, *Solid State Ionics* 134 (2000) 169.
27. (a) Y. Li, C. Wan, Y. Wu, C. Jiang, Y. Zhu, *J. Power Sources* 85 (2000) 294; (b) K. Konstantinov, G.X. Wang, J. Yao, H.K. Liu, S.X. Dou, *11th IMLB*, Monterey, CA, USA, June 2002, Abs. 100.
28. (a) S.-T. Myung, H.-T. Chung, *J. Power Sources* 84 (1999) 32; (b) S.-T. Myung, S. Komaba, N. Hirotsaki, N. Kumagai, K. Arai, T. Kodama, Y. Terada, I. Nakai, *11th IMLB*, Monterey, CA, USA, June 2002, Abs. 90.
29. Y.-M. Chiang, Y.-I. Jang, H. Wang, B. Huang, D. Sadoway, P. Ye, *J. Electrochem. Soc.* 145 (1998) 887.
30. H. Yan, X. Huang, H. Li, L. Chen, *Solid State Ionics* 113 (1998) 11.
31. H. Yan, X. Huang, L. Chen, *J. Power Sources* 81-82 (1999) 647.
32. P.S. Whitfield and I.J. Davidson, *J. Electrochem. Soc.* 147 (2000) 4476.
33. M.N. Obrovac, O. Mao, J.R. Dahn, *Solid State Ionics* 112 (1998) 9.
34. N.V. Kosova, N.F. Uvarov, E.T. Devyatkina, E.G. Avvakumov, *Solid State Ionics* 135 (2000) 107.
35. (a) S. Soiron, A. Rougier, L. Aymard, J.-M. Tarascon, *J. Power Sources* 97-98 (2001) 402; (b) W.T. Jeong, J.H. Joo, K.S. Lee, *11th IMLB*, Monterey, CA, USA, June 2002, Abs. 68.
36. A. Singhal, G. Skandan, G. Amatucci and N. Pereira, *Electrochemical Society Proceedings Volume 2000-36*, A.R. Landgrebe and R.J. Klinger, Eds., p. 244, 2001.
37. S.-H. Kang, J.B. Goodenough, L.K. Rabenberg, *Chem. Mater.* 13 (2001) 1758.

38. S.-H. Kang, J.B. Goodenough, L.K. Rabenberg, *Electrochem. Solid-State Lett.* 4 (2001) A49.
39. Y.-I. Jang, B. Huang, H. Wang, D. R. Sadoway, Y.-M. Chiang, *J. Electrochem. Soc.* 146 (1999) 3217.
40. Y. S. Lee, M. Yoshio, *Electrochem. Solid-State Lett.* 4 (2001) A166.
41. Y. Nishi, *J. Power Sources* 100 (2001) 101.
42. J. Cho, G. Kim, H.S. Lim, *J. Electrochem. Soc.* 146 (1999) 3571.
43. J. Cho, B. Park, *J. Power Sources* 92 (2001) 35.
44. J. Ying, C. Wan, C. Jiang, Y. Li, *J. Power Sources* 99 (2001) 78.
45. H. Huang, C.H. Chen, R.C. Perego, E.M. Kelder, L. Chen, J. Schoonman, W.J. Weydanz, D.W. Nielsen, *Solid State Ionics* 127 (2000) 31.
46. G. Amatucci, C.N. Schmutz, A. Blyr, C. Sigala, A.S. Gozdz, D. Larcher, J.-M. Tarascon, *J. Power Sources* 69 (1997) 11.
47. J. Cho, *Solid State Ionics* 138 (2001) 267.
48. V. Manev, T. Faulkner, J. Engel, in: *Proceedings of the 1st Hawaii Battery Conference*, January 1998.
49. H. Huang, C.A. Vincent, P.G. Bruce, *J. Electrochem. Soc.* 146 (1999) 481.
50. Y. Xia, N. Kumada, M. Yoshio, *J. Power Sources* 90 (2000) 135.
51. D. Aurbach, *J. Power Sources* 89 (2000) 206.
52. D. Aurbach, K. Gamolsky, B. Markovsky, G. Salitra, Y. Gofer, U. Heider, R. Oesten, M. Schmidt, *J. Electrochem. Soc.* 147 (2000) 1322.
53. G. Amatucci, A. Du Pasquier, A. Blyr, T. Zheng, J.-M. Tarascon, *Electrochim. Acta* 45 (1999) 255.
54. T. Aoshima, K. Okahara, C. Kiyohara, K. Shizuka, *J. Power Sources* 97-98 (2001) 377.
55. A. Du Pasquier, A. Blyr, A. Cressent, C. Lenain, G. Amatucci, J.-M. Tarascon, *J. Power Sources* 81-82 (1999) 54.
56. C.H. Chen, J. Liu, K. Amine, *J. Power Sources* 96 (2001) 321.
57. A. Antonini, C. Bellitto, M. Pasquali, G. Pistoia, *J. Electrochem. Soc.* 145 (1998) 2726.
58. A. Du Pasquier, F. Orsini, A.S. Gozdz, J.-M. Tarascon, *J. Power Sources* 81-82 (1999) 607.
59. (a) J. Cho, G.B. Kim, H.S. Lim, C.-S. Kim, S.-I. Yoo, *Electrochem. Solid-State Lett.* 2 (1999) 607; (b) J. Cho, T.-J. Kim, Y.J. Kim, B. Park, *Chem. Comm.* 2001, 1074.
60. S.-C. Park, Y.-M. Kim, S.-C. Han, S. Ahn, C.-H. Ku, J.-Y. Lee, *J. Power Sources* 107 (2002) 42.
61. E. Endo, T. Yasuda, A. Kita, K. Yamaura, K. Sekai, *J. Electrochem. Soc.* 147 (2000) 1291.
62. E. Endo, T. Yasuda, K. Yamaura, A. Kita, K. Sekai, *J. Power Sources* 93 (2001) 87.
63. (a) J. Cho, Y. J. Kim, T.-J. Kim, B. Park, *Angew. Chem. Int. Ed.* 40 (2001) 3367; (b) Y. J. Park, personal communication.
64. (a) J. Cho, Y. J. Kim, B. Park, *Chem. Mater.* 12 (2000) 3788; (b) J. Cho, Y. J. Kim, B. Park, *J. Electrochem. Soc.* 148 (2001) A1110.
65. J. Cho, C.-S. Kim, S.-I. Yoo, *Electrochem. Solid-State Lett.* 3 (2000) 362.
66. Z. Chen, J. R. Dahn, *Electrochem. Solid-State Lett.*, 5 (2002) A213.
67. (a) G. Amatucci, J.-M. Tarascon, L.C. Klein, *J. Electrochem. Soc.* 143 (1996) 1114; (b) J.H. Lee, H.S. Kim, K.T. Lee, S.M. Oh, *11th IMLB*, Monterey, CA, USA, June 2002, Abs. 102; (c) B. Markovsky, A. Rodkin, Y. S. Cohen, E. Levi, D. Aurbach, H.-J. Kim, M. Schmidt, U. Heider, *11th IMLB*, Monterey, CA, USA, June 2002, Abs. 327.
68. J. Cho, *Chem. Mater.* 13 (2001) 4537.
69. J. Cho, Y. J. Kim, T.-J. Kim, B. Park, *Chem. Mater.* 13 (2001) 18.
70. (a) K. Mizushima, P.C. Jones, P.J. Wiseman, J.B. Goodenough, *Mater. Res. Bull.* 15 (1980) 783; (b) M.M. Thackeray, "The Structural Stability of Transition Metal Oxide Insertion Electrodes for Lithium Batteries", in *Handbook of Battery Materials*, J.O. Besenhard Ed., Wiley-VCH, 1999; (c) A.S. Andersson, J.O. Thomas, *J. Power Sources*

- 97-98 (2001) 498.
71. J. McBreen, X.-Q. Yang, M. Balasubramanian, X. Sun, *Electrochemical Society Proceedings Volume 2000-36*, A.R. Landgrebe and R.J. Klinger, Eds., p. 252, 2001.
 72. W. Li, J.N. Reimers, J.R. Dahn, *Solid State Ionics* 67 (1993) 123.
 73. C. Pouillierie, L. Croguennec, Ph. Biensan, P. Willmann, C. Delmas, *J. Electrochem. Soc.* 147 (2000) 2061.
 74. V. Bianchi, S. Bach, C. Belhomme, J. Farcy, J.P. Pereira-Ramos, D. Caurant, N. Baffier, P. Willmann, *Electrochim. Acta* 46 (2001) 999.
 75. C. Delmas, M. Ménétrier, L. Croguennec, I. Saadoune, A. Rougier, C. Pouillierie, G. Prado, M. Grune, L. Fournès, *Electrochim. Acta* 45 (1999) 243.
 76. (a) Y. Gao, M. V. Yakovleva, W.B. Ebner, *Electrochem. Solid-State Lett.* 1 (1998) 117; (b) M.V. Yakovleva, Y. Gao, *11th IMLB*, Monterey, CA, USA, June 2002, Abs. 209; (c) Y. Gao, M.V. Yakovleva, *11th IMLB*, Monterey, CA, USA, June 2002, Abs. 315.
 77. (a) Z. Chen, J.R. Dahn, *202nd ECS Meeting*, Salt Lake City, Utah, USA, October 2002; (b) A. Van der Van, M.K. Aydinol, G. Ceder, *J. Electrochem. Soc.* 145 (1998) 2149; (c) X.Q. Yang, X. Sun, J. McBreen, *Electrochem. Comm.* 2 (2000) 100.
 78. J.-M. Tarascon, G. Vaughan, Y. Chabre, L. Seguin, M. Anne, P. Strobel, G. Amatucci, *J. Solid State Chem.* 147 (1999) 410.
 79. S. Venkatraman, A. Manthiram, *202nd ECS Meeting*, Salt Lake City, Utah, USA, October 2002
 80. D. Carlier, M. Ménétrier, C. Delmas, *J. Mater. Chem.* 11 (2001) 594.
 81. M. Balasubramanian, X. Sun, X.Q. Yang, J. McBreen, *J. Electrochem. Soc.* 147 (2000) 2903.
 82. K.-K. Lee, K.-B. Kim, *J. Electrochem. Soc.* 147 (2000) 1709.
 83. G.X. Wang, J. Horvat, D.H. Bradhurst, H.K. Liu, S.X. Dou, *J. Power Sources* 85 (2000) 279.
 84. R.V. Chebiam, F. Prado, A. Manthiram, *J. Electrochem. Soc.* 148 (2001) A49.
 85. J. Cho, H. Jung, Y. Park, G. Kim, H. Lim, *J. Electrochem. Soc.* 147 (2000) 15.
 86. Y. Fujita, K. Amine, J. Maruta, H. Yasuda, *J. Power Sources* 68 (1997) 126.
 87. M. Broussely, P. Biensan, B. Simon, *Electrochim. Acta* 45 (1999) 3.
 88. C. Pouillierie, F. Pertion, Ph. Biensan, J.P. Pérès, M. Broussely, C. Delmas, *J. Power Sources* 96 (2001) 293.
 89. J. Cho, *Chem. Mater.* 12 (2000) 3089.
 90. C.-C. Chang, J. Y. Kim, P.N. Kumta, *J. Power Sources* 89 (2000) 56.
 91. B.V.R. Chowdari, G.V. Subba Rao, S.Y. Chow, *Solid State Ionics* 140 (2001) 55.
 92. (a) Z. Lu, D.D. MacNeil, J.R. Dahn, *Electrochem. Solid-State Lett.* 4 (2001) A200; (b) M. Yoshio, H. Noguchi, J. Itoh, M. Okada, T. Mouri, *J. Power Sources* 90 (2000) 176.
 93. H. Arai, M. Tsuda, Y. Sakurai, *J. Power Sources* 90 (2000) 76.
 94. S. Madhavi, G.V. Subba Rao, B.V.R. Chowdari, S.F.Y. Li, *J. Power Sources* 93 (2001) 156.
 95. (a) J.S. Weaving, F. Coowar, D.A. Teagle, J. Cullen, V. Dass, P. Bindin, R. Green, W.J. Macklin, *J. Power Sources* 97-98 (2001) 733; (b) M. Broussely, *Lithium Battery Discussion*, Arcachon (France), May 2001; (c) M. Broussely, *11th IMLB*, Monterey, CA, USA, June 2002, Abs. 415.
 96. K. Kubo, S. Arai, S. Yamada, M. Kanda, *J. Power Sources* 81-82 (1999) 599.
 97. T. Ohzuku, K. Nakura, T. Aoki, *Electrochim. Acta*, 45 (1999) 151.
 98. S. H. Park, K.S. Park, Y. K. Sun, K. S. Nahm, Y.S. Lee, M. Yoshio, *Electrochim. Acta* 46 (2001) 1215.
 99. J. Kim, K. Amine, *Electrochem. Comm.* 3 (2001) 52.
 100. A.R. Naghash, J. Li, *Electrochim. Acta* 46 (2001) 2293.
 101. S. H. Park, K.S. Park, Y. K. Sun, K. S. Nahm, Y.S. Lee, M. Yoshio, Y.K. Lee, K.W. Han, *Electrochemical Society Proceedings Volume 2000-21*, M. Doyle, E. Takeuchi and K.M. Abraham, Eds., p. 45, 2001.

102. A. Yamada, M. Tanaka, K. Tanaka, K. Sekai, *J. Power Sources*, 81-82 (1999) 73.
103. C.-H. Shen, R. Gundakaram, R.-S. Liu, H.-S. Sheu, *J. Chem. Soc. Dalton Trans.* 2001, 37
104. (a) D. Capsoni, M. Bini, G. Chiodelli, V. Massarotti, C. Azzoni, M.C. Mozzati, A. Comin, *Phys. Chem. Chem. Phys.* 3 (2001) 2162; (b) G. Rousse, C. Masquelier, J. Rodriguez-Carvajal, E. Elkaim, J.P. Lauriat, J.L. Martinez, *Chem. Mater.* 11 (1999) 3629.
105. R. Basu, R. Seshadri, *J. Mater. Chem.* 10 (2000) 507.
106. Y. Xia, T. Sakai, T. Fujieda, X.Q. Yang, X. Sun, Z.F. Ma, J. McBreen, M. Yoshio, *J. Electrochem. Soc.* 148 (2001) A723.
107. A. Blyr, C. Sigala, G. Amatucci, D. Guyomard, Y. Chabre, J.-M. Tarascon, *J. Electrochem. Soc.* 145 (1998) 194.
108. T. Inoue, M. Sano, *J. Electrochem. Soc.* 145 (1998) 3704.
109. Y. Kogetsu, M. Kohno, T. Hatanaka, T. Saito, J. Yamaura, 2001 ECS and ISE Joint International Meeting, San Francisco, CA, USA, September 2001.
110. T. Saito, M. Machida, Y. Yamamoto, M. Nagamine, 2001 ECS and ISE Joint International Meeting, San Francisco, CA, USA, September 2001.
111. N. Nishimura, T. Douzono, M. Kasai, H. Andou, Y. Muranaka, Y. Kozono, *J. Power Sources*, 81-82 (1999) 420.
112. D.H. Jang, Y.J. Shin, S.M. Oh, *J. Electrochem. Soc.* 143 (1996) 2204.
113. G. Pistoia, A. Antonini, R. Rosati, D. Zane, *Electrochim. Acta*, 41 (1996) 2683.
114. H. Huang, C.A. Vincent, P.G. Bruce, *J. Electrochem. Soc.* 146 (1999) 3649.
115. R. Premanand, A. Durairajan, B. Haran, R. White, B. Popov, *J. Electrochem. Soc.* 149 (2002) A54.
116. (a) J. Lee, J. K. Hong, D.H. Jang, Y.-K. Sun, S.M. Oh, *J. Power Sources*, 89 (2000) 7; (b) Y. Shin, A. Manthiram, 202nd ECS Meeting, Salt Lake City, Utah, USA, October 2002.
117. F.T. Quinlan, K. Sano, T. Willey, R. Vidu, K. Tasaki, P. Stroeve, *Chem. Mater.* 13 (2001) 4207.
118. (a) M.M. Thackeray, C.S. Johnson, A.J. Kahaian, K.D. Kepler, J.T. Vaughney, Y. Shao-Horn, S.A. Hackney, *J. Power Sources* 81-82 (1999) 60; (b) J. Cho, M.M. Thackeray, *J. Electrochem. Soc.* 146 (1999) 3577.
119. S. Ma, H. Noguchi, M. Yoshio, *J. Power Sources* 97-98 (2001) 385.
120. H. Yamane, T. Inoue, M. Fujita, M. Sano, *J. Power Sources* 99 (2001) 60.
121. T. Numata, C. Amemiya, T. Kumeuchi, M. Shirakata, M. Yonezawa, *J. Power Sources* 97-98 (2001) 358.
122. R.J. Gummow, A. de Kock, M.M. Thackeray, *Solid State Ionics* 69 (1994) 59.
123. A. de Kock, E. Ferg, R.J. Gummow, *J. Power Sources* 70 (1998) 247.
124. E. Iwata, K. Takahashi, K. Maeda, T. Mouri, *J. Power Sources* 81-82 (1999) 430.
125. D. Song, H. Ikuta, T. Uchida, M. Wakihara, *Solid State Ionics* 117 (1999) 151.
126. G. Pistoia, G. Wang, *Solid State Ionics* 66 (1993) 135.
127. H.F. Howard, S.W. Sheargold, P.M. Story, D. Zhang, *Electrochemical Society Proceedings Volume* 2000-36, A.R. Landgrebe and R.J. Klingner, Eds., p. 36, 2001.
128. C. Vogler, A. Butz, H. Dittrich, G. Arnold, M. Wohlfahrt-Mehrens, *J. Power Sources* 84 (1999) 243.
129. G. Pistoia, A. Antonini, R. Rosati, C. Bellitto, G.M. Ingo, *Chem. Mater.* 9 (1997) 1443.
130. Y.-K. Sun, C.S. Yoon, C.K. Kim, S.G. Yoon, Y.-S. Lee, M. Yoshio, I.-H. Oh, *J. Mater. Chem.* 11 (2001) 2519.
131. J.-S. Kim, J.T. Vaughney, C.S. Johnson, M.M. Thackeray, 202nd ECS Meeting, Salt Lake City, Utah, USA, October 2002.
132. (a) M. Yoshio, H. Noguchi, Y. Todorov, Y. Hideshima, *Denki Kagaku*, 66 (1998) 1198; (b) H. Noguchi, H. Nakamura, M. Yoshio, *Electrochemical Society Proceedings Volume*

- 2000-21, M. Doyle, E. Takeuchi and K.M. Abraham, Eds., p. 18, 2001.
133. C. Bellitto, M. Pasquali, to be published.
 134. G. Amatucci, N. Pereira, T. Zheng, I. Plitz, J.-M. Tarascon, *J. Power Sources*, 81-82 (1999) 39.
 135. Y.-K. Sun, Y.-S. Jeon, *J. Mater. Chem.* 9 (1999) 3147.
 136. Y.-K. Sun, I.-H. Oh, *J. Power Sources* 94 (2001) 132.
 137. S.-H. Kang, J.B. Goodenough, *J. Electrochem. Soc.* 147 (2000) 3621.
 138. M. Okada, Y.-S. Lee, M. Yoshio, *J. Power Sources* 90 (2000) 196.
 139. (a) B. Ammundsen, J. Paulsen, *Adv. Mater.* 13 (2001) 943; (b) B. Ammundsen, J. Paulsen, I. Davidson, C.-H. Shen, J.-M. Chen, L.-Y. Jang, Y.-F. Lee, *J. Electrochem. Soc.* 149 (2002) A436.
 140. G. Ceder and S.K. Mishra, *Electrochem. Solid-State Lett.* 2 (1999) 550.
 141. B. Ammundsen, J. Desilvestro, T. Groutso, D. Hassel, J.B. Metson, E. Reagan, R. Steiner, P.J. Pickering, *J. Electrochem. Soc.* 147 (2000) 4078.
 142. T.E. Quine, M.J. Duncan, A.R. Armstrong, A.D. Robertson, P.G. Bruce, *J. Mater. Chem.* 10 (2000) 2838.
 143. A. Robertson, A.R. Armstrong, A. J. Fowkes, P.G. Bruce, *J. Mater. Chem.* 11 (2001) 113.
 144. M.M. Doeff, A. Anapolsky, L. Edman, T.J. Richardson, L.C. De Jonghe, *J. Electrochem. Soc.* 148 (2001) A230.
 145. Y. U. Jeong, A. Manthiram, *Electrochem. Solid-State Lett.* 2 (1999) 421.
 146. T. Ohzuku, Y. Makimura, *Chem. Lett.* 2001, 744.
 147. T. Ohzuku, Y. Makimura, *2001 ECS and ISE Joint International Meeting*, San Francisco, CA, USA, September 2001.
 148. (a) T. Ohzuku, D. Endo, Y. Makimura, *42nd Battery Symposium in Japan*, Yokohama, November 2001, p.118; (b) Y. Makimura, T. Ohzuku, *11th IMLB*, Monterey, CA, USA, June 2002, Abs. 117; (c) N. Yabuuchi, T. Ohzuku, *11th IMLB*, Monterey, CA, USA, June 2002, Abs. 122.
 149. J.M. Paulsen, C.L. Thomas, J.R. Dahn, *J. Electrochem. Soc.* 146 (1999) 3560.
 150. J.M. Paulsen, C.L. Thomas, J.R. Dahn, *J. Electrochem. Soc.* 147 (2000) 861.
 151. J.M. Paulsen, J.R. Dahn, *J. Electrochem. Soc.* 147 (2000) 2478.
 152. J.M. Paulsen, D. Larcher, J.R. Dahn, *J. Electrochem. Soc.* 147 (2000) 2862.
 153. (a) Z. Lu, D.D. MacNeil, J.R. Dahn, *42nd Battery Symposium in Japan*, Yokohama, November 2001, p. 42; (b) Z. Lu, D.D. MacNeil, J.R. Dahn, *Electrochem. Solid-State Lett.* 4 (2001) A191; (c) Z. Lu, L.Y. Beaulieu, R.A. Donabarger, C.L. Thomas, J.R. Dahn, *J. Electrochem. Soc.* 149 (2002) A778; (d) Z. Lu, J.R. Dahn, *J. Electrochem. Soc.* 149 (2002) A815; (e) Y.-K. Sun, S.H. Park, S.S. Shin, C.W. Park, *11th IMLB*, Monterey, CA, USA, June 2002, Abs. 287; (f) S.H. Park, S.S. Shin, Y.-K. Sun, *11th IMLB*, Monterey, CA, USA, June 2002, Abs. 76.
 154. P. Dan, E. Mengeritsky, Y. Geronov, D. Aurbach, I. Weissman, *J. Power Sources* 54 (1995) 143.
 155. D. Aurbach, E. Zinigrad, H. Teller, P. Dan, *J. Electrochem. Soc.* 147 (2000) 1274.
 156. J.-M. Tarascon, M. Armand, *Nature* 414 (2001) 359.
 157. M.S. Whittingham, P.Y. Zavalij, *Solid State Ionics*, 131 (2000) 109.
 158. M.J. Duncan, F. Leroux, J.M. Corbett, L.F. Nazar, *J. Electrochem. Soc.* 145 (1998) 3746.
 159. S. Franger, S. Bach, J. Farcy, J.-P. Pereira-Ramos, N. Baffier, *2001 ECS and ISE Joint International Meeting*, San Francisco, CA, USA, September 2001.
 160. C.S. Johnson, M.M. Thackeray, *J. Power Sources* 97-98 (2001) 437.
 161. S. Jouanneau, S. Sarciaux, A. Le Gal La Salle, D. Guyomard, *Solid State Ionics* 140 (2001) 223.
 162. M. Yoshio, H. Nakamura, Y. Xia, *Electrochim. Acta* 45 (1999) 273.
 163. M.M. Thackeray, M.H. Rossouw, R.J. Gummow, D.C. Liles, K. Pearch, A. de Kock, W.I.F. David, S. Hull, *Electrochim. Acta* 38 (1993) 1259.

164. H. Nakamura, K. Motooka, H. Noguchi, M. Yoshio, *J. Power Sources* 81-82 (1999) 632.
165. W.P. Kilroy, W.A. Ferrando, S. Dallek, *J. Power Sources* 97-98 (2001) 336.
166. B.B. Owens, S. Passerini, W.H. Smyrl, *Electrochim. Acta* 45 (1999) 215.
167. B.B. Owens, W.H. Smyrl in *Electrochemical Microsystems Technology*, J. W. Schultze, T. Osaka and M. Datta, Eds., Taylor & Francis, London/New York (2002).
168. F. Coustier, J. Hill, B.B. Owens, S. Passerini, W.H. Smyrl, *J. Electrochem. Soc.* 146 (1999) 1355.
169. M. Giorgetti, S. Mukerjee, S. Passerini, J. McBreen, W.H. Smyrl, *J. Electrochem. Soc.* 148 (2001) A768.
170. F. Coustier, J.-M. Lee, S. Passerini, W.H. Smyrl, *Solid State Ionics* 116 (1999) 279.
171. F. Coustier, G. Jarero, S. Passerini, W.H. Smyrl, *J. Power Sources* 83 (1999) 9.
172. M. Lira-Cantù, P. Gomez-Romero, *J. Electrochem. Soc.* 146 (1999) 2029.
173. A.D. Wadsley, *Acta Crystallogr.* 10 (1957) 261.
174. G. Pistoia, M. Pasquali, G. Wang, L. Li, *J. Electrochem. Soc.* 137 (1990) 2365.
175. V. Manev, A. Momchilov, A. Nassalevska, G. Pistoia, M. Pasquali, *J. Power Sources* 54 (1995) 501.
176. A. Yu, N. Kumagai, Z. Liu, J.Y. Lee, *J. Power Sources* 74 (1998) 117.
177. B. Chaloner-Gill, D.R. Shackle, T. N. Andersen, *J. Electrochem. Soc.* 147 (2000) 3575.
178. M.E. Spahr, P. Novak, W. Scheifele, O. Haas, R. Nesper, *J. Electrochem. Soc.* 145 (1998) 421.
179. M. Pasquali, G. Pistoia, *Electrochim. Acta* 36 (1991) 1549.
180. G. Pistoia, G. Wang, D. Zane, *Solid State Ionics* 76 (1995) 285.
181. V. Manev, A. Momchilov, A. Nassalevska, G. Pistoia, M. Pasquali, *J. Power Sources* 43-44 (1993) 561.
182. P. Liu, J.-G. Zhang, J.A. Turner, *J. Power Sources* 92 (2001) 204.
183. E. Andrukaitis, I.R. Hill, G.L. Torlone, *J. Power Sources* 97-98 (2001) 494.
184. (a) P. Arora, D. Zhang, B.N. Popov, R.E. White, *Electrochem. Solid-State Lett.* 1 (1998) 249; (b) D. Zhang, B.N. Popov, Y.M. Podrazhansky, P. Arora, R.E. White, *J. Power Sources* 83 (1999) 121.
185. A.K. Padhi, K.S. Nanjundaswamy, J.B. Goodenough, *J. Electrochem. Soc.* 144, (1997) 1188.
186. N. Ravet, J.B. Goodenough, S. Besner, M. Simoneau, P. Hovington, M. Armand, *196th ECS Meeting*, Hawaii, October 1999.
187. A.S. Andersson, B. Kalska, L. Häggström and J.O. Thomas, *Solid State Ionics* 130 (2000) 41.
188. A.S. Andersson, J.O. Thomas, B. Kalska, L. Häggström, *Electrochem. Solid-State Lett.* 3 (2000) 66.
189. M. Takahashi, S. Tobishima, K. Takei, Y. Sakurai, *J. Power Sources* 508 (2001) 97.
190. Yamada, S.C. Chung, K. Hinokuma, *J. Electrochem. Soc.* 148 (2001) A224.
191. P.P. Prosini, D. Zane, M. Pasquali, *Electrochim. Acta* 46 (2001) 3517.
192. P.P. Prosini, M. Lisi, D. Zane, M. Pasquali, *Solid State Ionics* 148 (2002) 45.
193. J.B. Goodenough, V. Manivannam, *Denki Kagaku* 66 (1998) 1173.
194. F. Croce, A. D'Epifanio, J. Hassoun, A. Deptula, T. Olczac, B. Scrosati, *Electrochem. Solid-State Lett.* 5 (2002) A47.
195. P.P. Prosini, M. Carewska, S. Scaccia, P. Wisniewski, S. Passerini, M. Pasquali, *J. Electrochem. Soc.* 149 (2002) A886.
196. H. Huang, S.-C. Yin, F. Nazar, *Electrochem. Solid-State Lett.* 4 (2001) A170.
197. J. Shim, K.A. Striebel, E.J. Cairns, *2001 ECS and ISE Joint International Meeting*, San Francisco, CA, USA, September 2001.
198. H.S. Ryu, K.Y. Kang, K.W. Kim, B.Y. Hur, J.H. Ahn, J.Y. Lee, H.J. Ahn, *2001 ECS and ISE Joint International Meeting*, San Francisco, CA, USA, September 2001.
199. S.-C. Han, H.-S. Kim, Y.-M. Kang, H.-J. Ahn, J.-Y. Lee, *2001 ECS and ISE Joint*

- International Meeting*, San Francisco, CA, USA, September 2001.
200. H. Kim, *18th International Seminar&Exhibit on Primary&Secondary Batteries*, March 2001, Fort Lauderdale, Florida, USA.
201. (a) S.J. Visco, *18th International Seminar&Exhibit on Primary&Secondary Batteries*, March 2001, Fort Lauderdale, Florida, USA; (b) E.S. Nimon, M. Sukeshini, S.J. Visco, *11th IMLB*, Monterey, CA, USA, June 2002, Abs. 221.
202. J. Broadhead, T. Skotheim, *J. Power Sources* 65 (1997) 213.
203. H. Uemachi, Y. Iwasa, T. Mitani, *Electrochim. Acta* 46 (2001) 2305.
204. E. Peled, D. Golodnitsky, E. Strauss, J. Lang, Y. Lavi, *Electrochim. Acta* 43 (1998) 1593.
205. E. Strauss, D. Golodnitsky, E. Peled, *Electrochim. Acta* 45 (2000) 1519.
206. E. Shembel, O. Chervacov, D. Reisner, L. Neduzhko, Y. Polischuk, I. Maksyuta, N. Globa, T. Pastushkin, K.K. Kylyvnyk, P. Novak, *11th IMLB*, Monterey, CA, USA, June 2002, Abs. 419.
207. H. Kawai, M. Nagata, H. Kageyama, H. Tukamoto, A.R. West, *Electrochim. Acta* 45 (1999) 315.
208. H. Kawai, M. Nagata, H. Tukamoto, A.R. West, *J. Power Sources* 81-82 (1999) 67.
209. T. Ohzuku, S. Takeda, M. Iwanaga, *J. Power Sources* 81-82 (1999) 90.
210. L. Hernan, J. Morales, L. Sanchez, E. Rodriguez Castellon, M.A.G. Aranda, *J. Mater. Chem.* 12 (2002) 734.
211. Y. Ein-Eli, J.T. Vaughney, M.M. Thackeray, S. Mukerjee, X.Q. Yang, J. McBreen, *J. Electrochem. Soc.* 146 (1999) 908.
212. H. Narai, Y. Idemoto, N. Koura, *42nd Battery Symposium in Japan*, Yokohama, November 2001, p. 42.
213. X. Wu, S.B. Kim, *J. Power Sources* 109 (2002) 53.
214. Y.-K. Sun, Y.-S. Lee, M. Yoshio, K. Amine, *Electrochem. Solid-State Lett.* 205 (2002) A99.
215. Y.S. Lee, Y.K. Sun, S. Ota, T. Miyashita, M. Yoshio, *Electrochem. Comm.* 4 (2002) 989.

Chapter 12

SPINEL CATHODE MATERIALS FOR LITHIUM-ION BATTERIES

Y. Xia^a and M. Yoshio^b

^a*Department of Chemistry, Fudan University, Shanghai, China*

^b*Department of Applied Chemistry, Saga University, Saga 840-8502, Japan*

12.1. INTRODUCTION

Secondary lithium batteries have long been studied because they exhibit the highest specific energy among all rechargeable batteries. Nevertheless, the limited safety and rechargeability associated with the use of metallic lithium has prevented their widespread acceptance in the market. Unsatisfactory results with lithium metal have directed the research towards the development of the so called “rocking-chair” or “lithium-ion” batteries (LIB), based on a transition metal oxide cathode and a carbon anode.¹⁻³ In 1990, Sony Energytec Inc. commercialized this type of batteries.³ Today, lithium ion batteries are used in cellular phones, notebook-size personal computers, video cameras, and, to a limited extent, in electric vehicle (EV) applications. Most commonly, the negative electrode acts as a “lithium sink” and the positive LiA_xB_y electrode acts as a “lithium source”. Layered lithium transition metal oxides and spinel lithium manganese oxide have been selected as preferred cathode materials for lithium-ion batteries. Table 12.1 summarizes the cathode materials that have been, or possibly will be, used in LIB. LiCoO_2 is the cathode of choice for small-size batteries. In view of the economic and environmental advantages, spinel-structured manganese oxides have demonstrated to be the most promising positive electrode materials for large-size batteries for EV and industrial applications, as they are cheaper, less toxic, and show higher safety.

In this chapter, we will describe the fundamental aspects of spinel

Table 12.1. Cathode Materials for Li-ion Batteries

Material	Pr. Cap. (mAh/g)	Density (g/cm ³)	En.Dens. (mAh/cm ³)	Shape of Discharge Curve	Safety	Cost	Comment
LiCoO ₂	160	5.05	808	Flat	Fair	High	Small-size LIB
LiNiO ₂	220	4.80	1056	Sloping	Poor	Fair	Impossible
LiMn ₂ O ₄	110	4.20	462	Flat	Good	Low	HEV, EV
LiCo _{0.2} Ni _{0.8} O ₂	180	4.85	873	Sloping	Fair	Fair	LIP? Small Scale
LiMn _{0.5} Ni _{0.5} O ₂	160	4.70	752	Sloping	Good	Low	?
LiFePO ₄	160	3.70	592	Flat	Good	Low	Low cond.

cathode materials with emphasis on their electrochemical performance. Firstly, the structure of LiMn₂O₄ and metal-ion substituted spinels LiM_xMn_{2-x}O₄, and their Li insertion/extraction characteristics, will be introduced, followed by addressing the issue of how to optimize cycleability and capacity. Finally, the capacity fading at elevated temperature will be discussed, together with the new finding of oxygen-deficient spinels.

12.2. LiMn₂O₄ AND METAL-ION DOPED SPINELS LiM_xMn_{2-x}O₄

The structure of stoichiometric spinel LiMn₂O₄ has been refined with space group *Fd3m*, that can be described as layers of close-packed oxygen atoms, in which lithium and manganese ions occupy tetrahedral (8a) and octahedral (16d) sites, respectively, as shown in Figure 12.1. Li ions in the 8a tetrahedral sites can be removed during charge in the 4 V range, and LiMn₂O₄ transforms into λ -MnO₂, also having a cubic unit cell.⁴ During discharge to 3 V, Li ions are inserted into the 16c octahedral sites, and Li₂Mn₂O₄ with a tetragonal lattice is formed.⁵ A fundamental problem prohibiting a wider use of the Mn spinel as a 4 V cathode for lithium-ion batteries is a remarkable capacity fading at elevated temperatures. Doping with foreign metal ions, including Li⁺, Mg²⁺, Ga³⁺, Zn²⁺, Al³⁺, Ni²⁺, Cu²⁺, Co³⁺, Cr³⁺ and Fe³⁺ has been suggested to stabilize its structure, thus improving the elevated temperature performance.⁶⁻¹¹ The doping ions substitute for Mn³⁺ and, so, they reduce the capacity delivered at 4 V. A heavy doping results in a manganese oxidation state approaching 4+. These heavily doped compounds

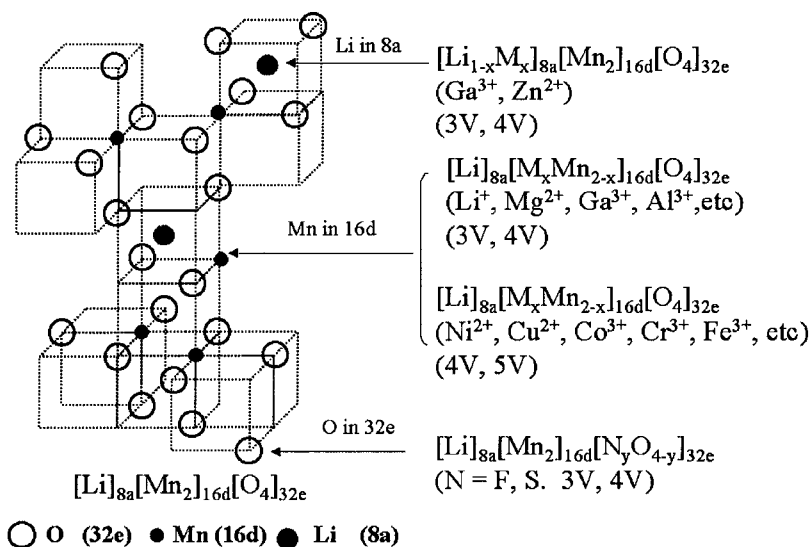
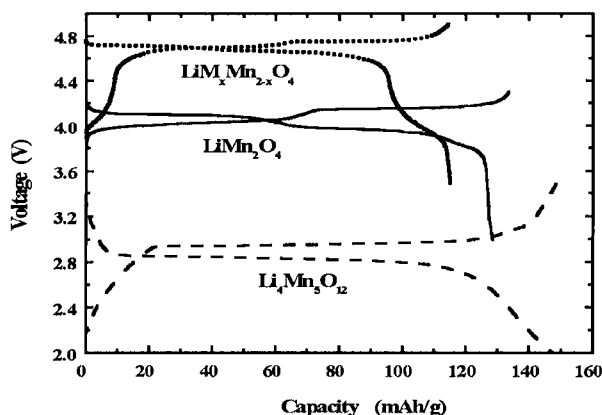

 Figure 12.1. Structure of spinel LiMn_2O_4 .


Figure 12.2. Typical charge/discharge curves of three kinds of spinel structures.

deliver no capacity at 4 V, but show a capacity at 3 V or 5 V. Figure 12.2 shows a typical charge/discharge for three kinds of cubic-structured spinel electrodes. In this case, M is an ion which can be further oxidized.

$\text{Li}_4\text{Mn}_5\text{O}_{12}$ ($\text{Li}[\text{Li}_{0.33}\text{Mn}_{1.67}]\text{O}_4$) is the upper limit of $\text{Li}_{1+x}\text{Mn}_{2-x}\text{O}_4$.

Lithium insertion into its structure occurs at 2.8 V with a rechargeable capacity of 140 mAh/g.¹²⁻¹⁴ Recently, it has been demonstrated that this nonstoichiometric spinel has the potential for use in true solid-state lithium/polymer batteries.¹⁵

LiMn_2O_4 shows a poorer cyclability in the 3 V region than in the 4 V, which is considered to be due to the cubic/tetragonal phase transition. The capacity can be stabilized by cation substitution in 16d sites and optimization of particle size, morphology and microstructure. Figure 12.3 shows the cycle life of $\text{LiAl}_{0.1}\text{Mn}_{1.9}\text{O}_4$ synthesized from two different Mn_3O_4 precursors: one from Tosoh, prepared by hydrothermal method, has a much finer particle size of $<0.1\ \mu\text{m}$, and another from Chuo, prepared by heating MnO_2 or MnSO_4 , has a particle size of $<1\ \mu\text{m}$. Although XRD analysis indicates virtually no structural differences among the two spinels, TEM and SEM analysis reveal subtle differences in the microstructure, which result in different reversible capacities of the electrochemical cells. XRD and TEM analysis confirm that $\text{LiAl}_{0.1}\text{Mn}_{1.9}\text{O}_4$ prepared with Mn_3O_4 from Chuo, showing a better capacity retention, has a lower tetragonal/cubic phase ratio after cycling,¹⁶ in spite of the fact that lithium insertion causes the average Mn oxidation state to fall below 3.5 (e.g., 3.3).^{17a-c}

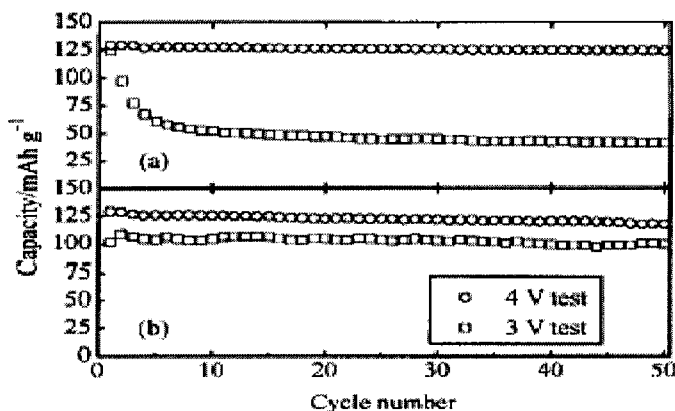


Figure 12.3. Cycle tests of $\text{LiAl}_{0.1}\text{Mn}_{1.9}\text{O}_4$ in the 4 V region (3.0-4.3V) and 3 V region (2.2-3.6V) at 1/3 C rate: (a) using Tosoh Mn_3O_4 ; (b) using Chuo Mn_3O_4 .

The end-member of a doped spinel $\text{Li}[\text{M}_x\text{Mn}_{2-x}]\text{O}_4$ is $\text{LiMn}_{0.5}\text{Mn}_{1.5}\text{O}_4$ for a divalent cation, e.g., $\text{LiNi}_{0.5}\text{MnO}_4$ ^{18,19}, $\text{LiCu}_{0.5}\text{Mn}_{1.5}\text{O}_4$ ²⁰, and LiMMnO_4 for a

trivalent cation, *e.g.*, LiCoMnO_4 and LiCrMnO_4 .²¹ If the substituent is an oxidizable ion, like Ni^{2+} , Co^{3+} , Cr^{3+} , Fe^{3+} , Cu^{2+} ,^{22-26(a-e)} lithium deintercalation is accompanied by oxidation of Mn^{3+} to Mn^{4+} at 4 V and oxidation of M ions at ~ 5 V, *e.g.*, Ni^{2+} to Ni^{4+} in $\text{LiNi}_{0.5}\text{MnO}_4$ and Co^{3+} to Co^{4+} in LiCoMnO_4 . The exact potential depends on the type of dopant used. Among them, $\text{LiNi}_{0.5}\text{Mn}_{1.5}\text{O}_4$ shows the best cycleability even at 50°C, particularly if prepared by the composite carbonate process.^{26b} Moreover, it seems that doping the other 5 V materials with Ni increases the cycleability, *e.g.*, in LiCrMnO_4 transformed into $\text{LiMn}_{1.25}\text{Cr}_{0.5}\text{Ni}_{0.25}\text{O}_4$.^{19,26c} According to *in situ* EXAFS studies, poor cycleability of LiCrMnO_4 would be due to the existence of Cr(VI) at a high charge state.^{26d,26e}

However, some samples prepared by classical techniques show faster capacity fading when cycled at high voltage and elevated temperature. This is the case of sol-gel $\text{LiNi}_{0.5}\text{Mn}_{1.5}\text{O}_4$. When cycled at 55°C, this spinel retains only 27% of its capacity after 50 cycles.²⁷ A most useful approach consists in the coating of $\text{LiNi}_{0.5}\text{Mn}_{1.5}\text{O}_4$ with nano-sized ZnO.²⁷ This allows a capacity

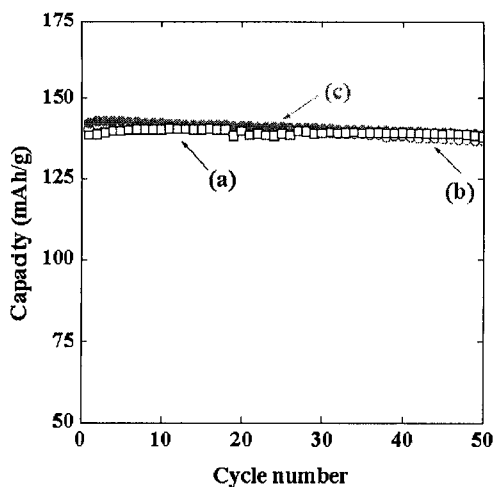


Figure 12.4. Specific capacity vs. cycle number for the $\text{Li}/1\text{M LiPF}_6\text{-EC/DMC/ZnO-coated LiNi}_{0.5}\text{Mn}_{1.5}\text{O}_4$ cell at 1/3 C rate [cathode obtained by sol-gel method] ((a) at 55°C) and for $\text{Li}/1\text{M LiPF}_6\text{-EC/DMC/LiNi}_{0.5}\text{Mn}_{1.5}\text{O}_4$ [cathode obtained by the composite carbonate process] ((b) 50°C and (c) 25°C).

retention of 99% in the same conditions. ZnO is proposed to act as a HF-scavenger to protect from Mn dissolution and electrolyte decomposition. However, as anticipated above, a significant improvement can be achieved with a proper synthesis technique. Figure 12.4 shows the cycle life at high temperature of uncoated $\text{LiNi}_{0.5}\text{Mn}_{1.5}\text{O}_4$, prepared by the composite carbonate process,^{26b} and ZnO-coated one, prepared by sol-gel. The capacity retention of the former, characterized by high homogeneity and nanosized particles, approaches that of the latter.

These 5 V cathode materials have an advantage when used in combination with such electrode materials as SnO, SnMe_x , $\text{Li}_4\text{Ti}_5\text{O}_{12}$, as they compensate for the loss of energy density due to the high intercalation potential of the anode.^{28,29}

Cations with an octahedral-site preference (*e.g.*, Ni^{2+} , Cu^{2+} , Co^{3+} , Cr^{3+}) are expected to occupy the 16d sites, whereas cations with a high preference for tetrahedral site occupation (*e.g.*, Ga^{3+} and Zn^{2+}) are expected to occupy the 8a sites, as confirmed by Rietveld analysis.^{30,31} However, it has to be stressed that Zn occupies tetrahedral sites only, whereas Ga distributes over both tetrahedral and octahedral sites.^{30,31} Both Ga- and Zn-doped spinels show an improved cycling performance at elevated temperature.

12.3. OPTIMIZING THE CAPACITY AND RECHARGEABILITY BY USING A Li-Mn-O PHASE DIAGRAM

The theoretical capacity of LiMn_2O_4 is 148 mAh/g, corresponding to 1 Li^+ extracted from LiMn_2O_4 , which is accompanied by the oxidation of Mn^{3+} to Mn^{4+} . However, a remarkable capacity decline is observed during cycling. As mentioned above, the capacity fading is alleviated by using lithium, divalent and trivalent metal ion-doped spinels. Normally, the oxidation state of the substituents is less than 4+, thus increasing the average oxidation state of remaining manganese. This leads to a reduction of the delivered capacity and, consequently, raises the question: how to optimize both the capacity and rechargeability of a spinel to be used as a practical 4 V positive electrode for Li-ion batteries? The capacity at 4 V for the metal-modified $\text{LiM}_y\text{Mn}_{2-y}\text{O}_4$ can be estimated by the equation:

$$C = 26.8 [1 - (4 - z)y] / MW \text{ (Ah/g)} \quad (12.1)$$

where z is the valence of the doping ion and MW is the molecular weight of $\text{LiM}_y\text{Mn}_{2-y}\text{O}_4$.³² The relationship between the capacity and the doping ion oxidation state with two levels of doping is presented in Figure 12.5. For a given doping level, a lower oxidation state of the doping ion gives rise to a lower capacity.

Herein we further discuss in detail the relationship between the capacity and cycleability of lithium-ion doped spinels. A nonstoichiometric spinel may be "lithium-rich" or "vacancy-rich". $\text{Li}_4\text{Mn}_5\text{O}_{12}$ is the limit composition of the "lithium-rich" series, and $\text{Li}_2\text{Mn}_4\text{O}_9$ of the "vacancy-rich" series, both with a Mn valence of 4.

The Li-Mn-O phase diagram is displayed in Figure 12.6, where the length of the straight line xy is assumed to represent the Li/Mn molar ratio and the average Mn valence, xz the average Mn valence, and yz the Li/Mn molar ratio.

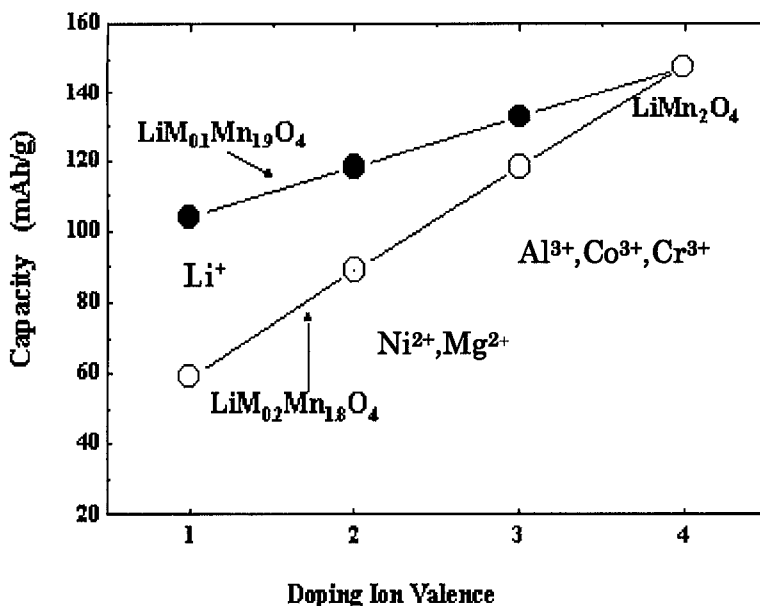
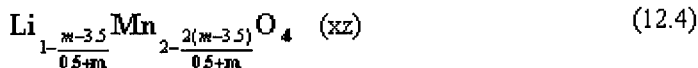
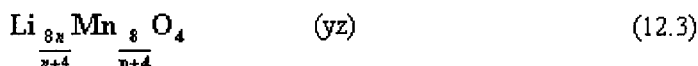
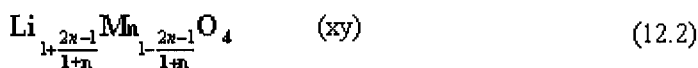


Figure 12.5. Relationship between capacity and doping level and oxidation state of doping metal ions.

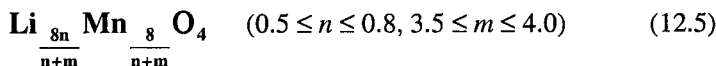
The lines parallel to the line yz show changes in the average Mn valence from 3.5 to 4.0, and the lines parallel to the line xz variations of Li/Mn molar

ratio from 0.5 to 0.8. It is evident that the stoichiometric spinel LiMn_2O_4 and the nonstoichiometric spinels, $\text{Li}_2\text{Mn}_4\text{O}_9$ and $\text{Li}_4\text{Mn}_5\text{O}_{12}$, are on the three vertices of the equilateral triangle.²⁸ If the Li/Mn molar ratio is represented as n , and the average Mn valence as m :

(i) the composition of each compound on the straight lines xy , xz and yz can be expressed as:



and (ii) any compound lying within the xyz triangle can be written as:



Each compound in the LiMn_2O_4 - $\text{Li}_4\text{Mn}_5\text{O}_{12}$ - $\text{Li}_2\text{Mn}_4\text{O}_9$ triangle plane can be synthesized directly by a solid-solid reaction in which Li/Mn molar ratio, reaction temperature and time are all controlled. It should be noted that high heating temperatures may result in an oxygen deficient spinel $\text{LiMn}_2\text{O}_{4-y}$. Also for “lithium-rich” spinels it is very difficult to obtain a formula $\text{Li}_{1+x}\text{Mn}_{2-x}\text{O}_4$, as reported in the literatures,^{37,38} in which the total number of Mn and Li atoms is just equal to 3 per formula unit. In fact, the number of Li and Mn atoms per formula unit depends not only on the Li/Mn molar ratio in the starting materials but also on the oxygen content, as the compounds located on the line xz have the same Li/Mn molar ratio ($\text{Li/Mn}=0.50$) but have a different composition as a result of different heating temperatures. Therefore the chemical formula of “lithium-rich” spinels should be referred to as $\text{Li}_{1+x}\text{Mn}_{2-y}\text{O}_4$ ($y \geq x$).

The initial capacity can be evaluated through the knowledge of the Li/Mn molar ratio, n , and the average Mn valence, m [equation (12.6)]:

$$C = 1184(4-m)/(m+n) \text{ (mAh/g)} \quad (12.6)$$

The capacity decreases with increasing vacancy rate or lithium content in the spinel matrix, while the rechargeability is improved. This indicates that

large capacity and good rechargeability cannot coexist in these materials, *e.g.*, for a spinel with a Li/Mn molar ratio of 0.55, the capacity may be limited to 120 mAh/g. Despite this, it should be possible to optimize both of them in terms of the Li-Mn-O phase diagram given above. For example, if the optimum spinel electrode requires a capacity in the range 110-125 mAh/g and a good rechargeability, its formula should be located in the shaded area.

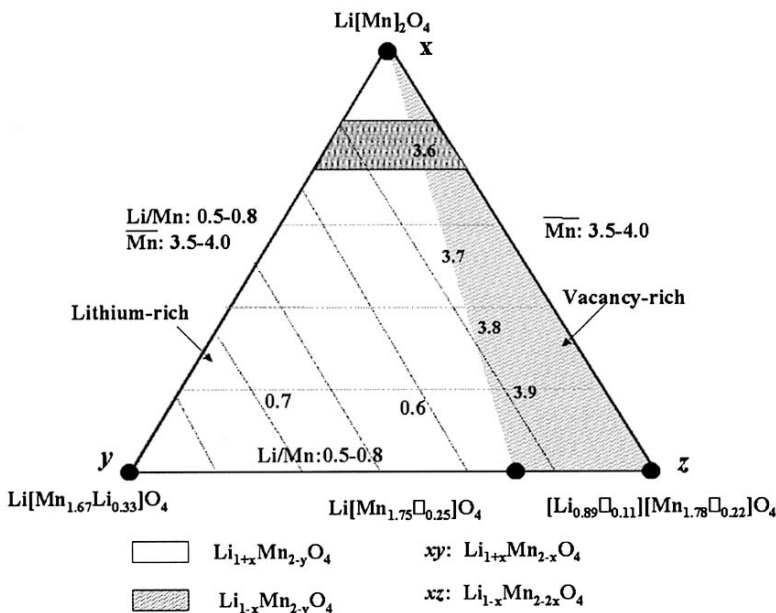


Figure 12.6. Semiquantitative Li-Mn-O phase diagram for optimization of the capacity and cycleability.

12.4. CAPACITY FADING ON CYCLING

A fundamental problem prohibiting a wider use of spinels as cathodes for lithium-ion batteries is that their capacity fades when they are cycled in an broad voltage range. Several factors that contribute to the fading have been discussed in the literature: (i) electrochemical oxidation of the electrolyte at high voltage;³⁹⁻⁴² (ii) dissolution of Mn²⁺ from LiMn₂O₄ into the electrolyte solution;³¹⁻⁴² (iii) structural failure in the two-phase (4.2 V) region,³⁹ with transformation to a more stable defect spinel;^{39,43} (iv) fracture of the particle surface due to local Jahn-Teller distortion at high discharge rates,⁴⁴ and (v) Li/Mn site exchange,⁴⁵ etc. It can be envisaged that all above suggested

mechanisms will also to some extent occur in metal-ion doped spinels, with a difference in their insertion/extraction reactions (two-phase for the former vs. one-phase for the latter). Capacity fading has to be referred primarily to the spinel structure. Lithium-ion intercalation in the stoichiometric LiMn_2O_4 framework leads to a one-phase reaction (cubic $a = 8.163$ to 8.247 Å) in the range $0 < x < 0.55$ in $\text{Li}_{1-x}\text{Mn}_2\text{O}_4$ (4.0 V plateau), and a two-phase reaction (cubic $a = 8.154$ and 8.072 Å) in the range $0.55 < x < 0.9$ (4.2 V plateau), while for the lithium-rich compound $\text{Li}_{1+x}\text{Mn}_2\text{O}_{4+y}$, with a high capacity stabilization, a one-phase reaction (cubic $a = 8.105$ – 8.223 Å) was observed over the entire intercalation range $0.25 < \text{Li} < 1.04$.^{33,46} Moreover, the cycleability of LiMn_2O_4 critically depends on the operating temperature. LiMn_2O_4 loses less capacity during cycling at 0°C .³⁹ *In situ* XRD experiments confirmed that split peaks were still observed after 50 cycles at 0°C (corresponding to two phases in the high voltage region), indicating that the two-phase structure is more stable for lithium ion insertion/extraction at this temperature. On the other hand, during cycling at 50°C , split peaks were hardly detected and each diffraction line shifted almost continuously to higher diffraction angles, indicating a continuous contraction of the unit cell. Figure 12.7 shows the cell lattice parameter changes as a function of

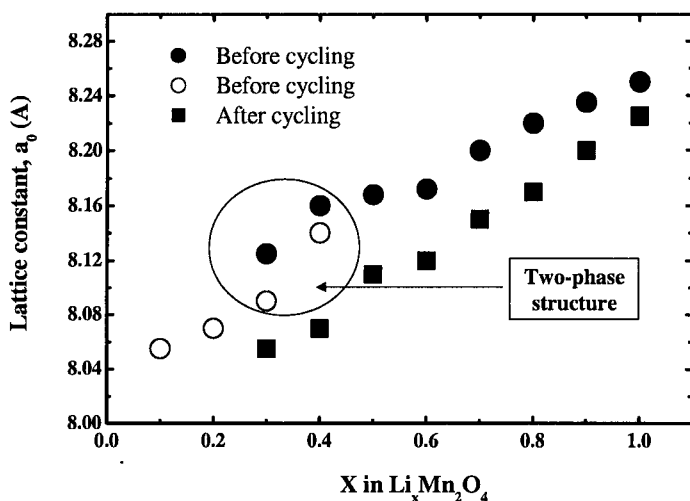


Figure 12.7. Variation of the cubic lattice parameter as a function of oxidation depth of spinel in the first charge and after 50 cycles at 50°C (1/3 C rate).

oxidation depth (in the first charge and after cycling at 50°C for 50 cycles). Furthermore, the lattice parameter, a , decrease from 8.246 Å of original LiMn_2O_4 to 8.235 Å after cycling at 50°C. Both results are consistent with a change to a defect structure, in which more Mn vacancies are present in 16d sites, *e.g.*, “lithium-rich” or “vacancy-rich” spinels are formed. Mn dissolution and structural changes are facilitated at high temperature.^{47, 48} Apparently, all above proposed mechanisms are mainly associated with the crystal structure and morphology. Accordingly, many researches have been devoted to these aspects. The most common way to stabilize the structure is by doping with metal ions, as previously discussed. A second way is to reduce the Mn dissolution by minimizing the LiMn_2O_4 /electrolyte interface through the synthesis of spinels with small surface area,^{49(a,b),50} coating with $\text{Li}_2\text{O} \cdot \text{B}_2\text{O}_3$,⁵¹ ZnO ²⁷ or LiCoO_2 ,^{52a,b} using a salt containing less HF, *e.g.* LiBF_4 ^{53a} or Li bisoxalatoborate (LiBOB)^{53b} instead of LiPF_6 ; or using $(\text{CH}_3)_3\text{SiNHSi}(\text{CH}_3)_3$ ⁵⁴ which is able to react with water traces to act as a scavenger for HF, thus suppressing Mn dissolution.

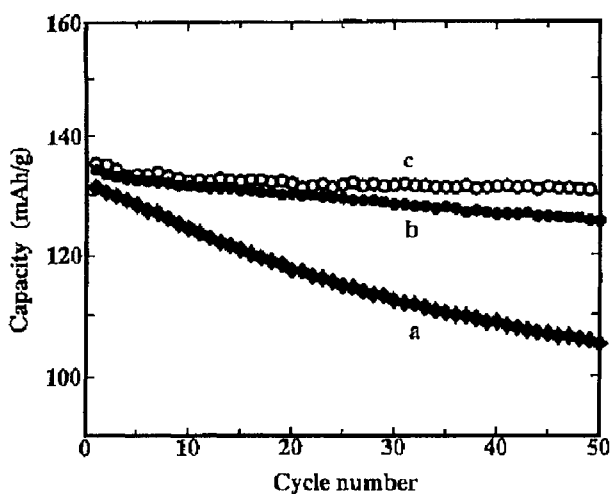


Figure 12.8. Effect of the surface area on the cycle profile of spinel electrode materials at 50°C (1/3 C rate). (a) LiMn_2O_4 (3.0 m^2/g), (b) $\text{Li}_{1.1}\text{Mn}_2\text{O}_{4.19}$ (6.3 m^2/g) and (c) $\text{Li}_{1.1}\text{Mn}_2\text{O}_{4.17}$ (1.2 m^2/g).

Figure 12.8 shows cycling of a stoichiometric spinel and two lithium-rich spinels, prepared by different methods, with the same chemical

composition of $\text{Li}_{1.1}\text{Mn}_2\text{O}_{4.2}$ but different surface areas. Stoichiometric spinel loses, as expected, much of its initial capacity. The spinel with the small surface area of $1.22 \text{ m}^2/\text{g}$ loses 5% of its initial capacity over the first 100 cycles compared to 8% of the one with an area of $6.2 \text{ m}^2/\text{g}$.^{49a} The different synthesis techniques may have reduced the difference between the two spinels, but low surface area is beneficial especially in terms of Mn dissolution. The solubility of the common spinel is reported around 70 ppm,^{53b} but highly optimized metal ion doped spinels with surface area of $0.2\text{--}0.3 \text{ m}^2/\text{g}$ show solubilities of 2–3 ppm after storage in the electrolyte at 60°C for 4 weeks.

We have recently prepared spinels with a high stabilization at elevated temperatures by taking into account three factors: low surface area, doping with metal ions, oxygen stoichiometry. A two-step process has been developed based on the: 1) synthesis at relatively high temperature to keep the surface area low, thus reducing Mn dissolution, 2) annealing at lower temperature under O_2 atmosphere, so to have spinels with a stoichiometric amount, or a slight excess, of oxygen.^{49b} Figure 12.9 shows charge-discharge tests of lithium-ion cells carried out at 60°C . The cathodes consisted of either a quasi-stoichiometric spinel $(\text{Li,Mn,Mg})_3\text{O}_{4+\delta}$ ($0 \leq \delta \leq 0.02$), prepared as above, or a spinel with an oxygen defect $(\text{Li,Mn,Mg})_3\text{O}_{4-\delta}$.

Even at 60°C , the spinel prepared according to the two-step process shows a remarkably constant capacity. In the following, the problems created by an oxygen deficiency will be stressed.

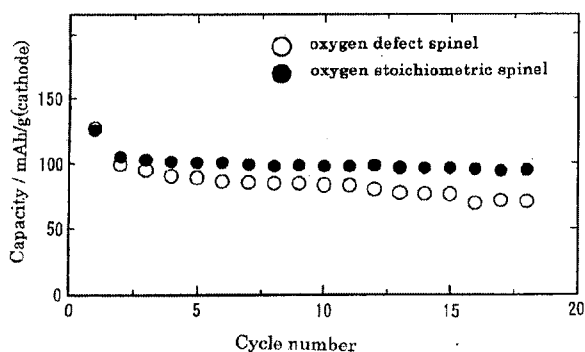


Figure 12.9. Cycle performance of Li-ion batteries at 60°C : (●) oxygen quasi-stoichiometric spinel, $(\text{Li,Mn,Mg})_3\text{O}_{4+\delta}$, and (○) oxygen-deficient spinel $(\text{Li,Mn,Mg})_3\text{O}_{4-\delta}$, as a cathode at $1/3 \text{ C}$ rate. Anode: graphitized mesophase carbon (MCMB6-28). CR2032 type coin cells.

12.5. OXYGEN-DEFICIENT SPINEL $\text{LiMn}_2\text{O}_{4-y}$

LiMn_2O_4 has commonly been synthesized using solid-state reactions, and solvent-process techniques, *e.g.*, sol-gel, precipitation, and Pechini process. In fact, it is quite difficult to obtain the truly stoichiometric LiMn_2O_4 without anion or cation vacancies. The spinel synthesis mechanism involves formation of a defect spinel at $<600^\circ\text{C}$ (the temperature is dependent on the reaction process, with particular reference to the lithium salt), followed by a transformation from a defect to a well-ordered spinel proceeding *via* a loss of oxygen. When the annealing temperature is as high as 800°C , LiMn_2O_4 loses oxygen to give an oxygen-deficient spinel $\text{LiMn}_2\text{O}_{4-y}$ and, on further heating to 1000°C , LiMnO_2 is formed.⁴⁶ During cooling, oxygen can reversibly be taken up, but the lost oxygen cannot completely be recovered. The net oxygen weight loss increases with increasing annealing temperature.^{36,46} The temperature corresponding to transformation into an oxygen-deficient spinel from a well-ordered spinel is lower as the lithium content in the starting material is higher.³⁸ This is why no general consensus on the mechanism of capacity fading on cycling has yet been reached. The structural and electrochemical results vary from sample to sample, even for samples claimed as stoichiometric LiMn_2O_4 by means of chemical analysis. The key factor determining these different results is oxygen stoichiometry. The oxygen stoichiometry plays a very important role in the structures and electrochemical properties of LiMn_2O_4 spinel materials. Herein, the charge/discharge profile, phase transition during lithium-ion insertion/extraction, and low-temperature phase transition will be related to the oxygen stoichiometry.

12.5.1. Charge/Discharge Profile of Spinel with Different Li/Mn Ratios and Oxygen Contents

Figure 12.10 shows charge/discharge curves of four kinds of $\text{Li}_{1\pm\delta}\text{Mn}_2\text{O}_{4\pm\delta}$ spinels with different Li/Mn ratios (obtained by varying the Li/Mn ratio in the starting materials) and various oxygen contents (by controlling the synthesis conditions, including temperature, heat treatment time and atmosphere, during both the solid state reaction and annealing), *i.e.*, sample A is quasi-stoichiometric spinel $\text{Li}_{0.99}\text{Mn}_2\text{O}_{4.02}$, sample B oxygen-deficient $\text{Li}_{0.98}\text{Mn}_2\text{O}_{3.97}$, sample C lithium- and oxygen-rich

$\text{Li}_{1.05}\text{Mn}_2\text{O}_{4.10}$, and sample D lithium-rich but oxygen-deficient $\text{Li}_{1.05}\text{Mn}_2\text{O}_{3.92}$. The capacity fading of the quasi-stoichiometric spinel mainly occurs on the 4.2 V plateau. In contrast, fading occurs on both 4.0 V and 4.2 V plateaus for the compounds with an oxygen-deficiency (samples B and D). The lithium- and oxygen-rich compound shows the highest capacity stabilization (sample C). Capacity fading in oxygen-deficient samples is much faster than in those without an oxygen-deficiency.⁵⁵ For the samples with an oxygen deficiency, a very small discharge plateau at about 3.2 V was also observed (B and D).³⁸ A recent research reported that there is a linear relationship between the capacity at 3.2 V (or 4.5 V) and oxygen deficiency.⁵⁶ The two arrows in Figure 10B show that the oxygen-deficient spinel loses capacity in both the low voltage and the high voltage region.

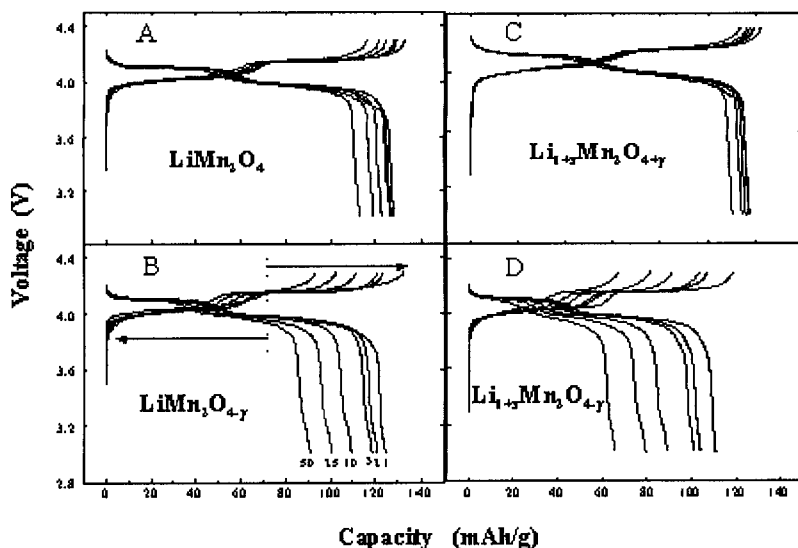


Figure 12.10. Charge/discharge curves of four kinds of $\text{Li}_{1\pm\gamma}\text{Mn}_2\text{O}_{4\pm\delta}$ spinels at 1/3 C rate. Sample A: stoichiometric spinel $\text{Li}_{0.99}\text{Mn}_2\text{O}_{4.02}$, Sample B: oxygen-deficient $\text{Li}_{0.98}\text{Mn}_2\text{O}_{3.97}$, Sample C: lithium and oxygen-rich $\text{Li}_{1.05}\text{Mn}_2\text{O}_{4.10}$, and Sample D: lithium-rich but oxygen-deficient $\text{Li}_{1.05}\text{Mn}_2\text{O}_{3.92}$.

12.5.2. Phase Transitions During Charge/Discharge

It has been demonstrated that the capacity loss for stoichiometric spinel LiMn_2O_4 is mainly due to the unstable two-phase region of the 4.2 V plateau. As shown above, this two-phase characteristic, and the capacity fading, can be suppressed by making the sample lithium-rich (one-phase model).³³ Moreover, a three-phase model was also proposed in the literature.⁵⁷ Recent research based on systematic *in situ* XRD studies has shown that the phase transition critically depends on the oxygen stoichiometry, this affecting the cycling profile.⁵⁵ When a lithium-rich compound is heat-treated to yield an oxygen-deficient compound, it shows clear evidence of two biphasic regions in both the 4.0 V and 4.2 V plateaus, and significant capacity fading was observed for both plateaus. In the compound with no oxygen deficiency, the two-phase regions were suppressed, and the capacity fading was also reduced. These results provide strong evidence relating the capacity fading during cycling to the transitions among three cubic phases.

12.5.3. Phase Transition at Low Temperature

In 1995, Yamada and Tanaka found that stoichiometric LiMn_2O_4 undergoes a first-order phase transition from a cubic ($Fd3m$) to a tetragonal ($I4_1/amd$) structure during cooling (at about 280 K) attributed to a Jahn-Teller distortion.⁵⁸ They concluded that the mass fraction of the tetragonal phase increases with decreasing temperature, but saturates below 260 K at a value of 65%. On the other hand, other research groups proposed a low temperature phase with ~100% orthorhombic symmetry ($Fddd$) at temperatures below 250 K.^{59, 60} More recently, it has been demonstrated that this phase transition is closely related to the population of oxygen vacancies.^{55, 61} The existence of oxygen vacancies is the sole and necessary condition for this phase transition. In other words, if this phase transition is observed, the sample is not an oxygen-stoichiometric one, but contains oxygen vacancies. Equivalently, in a strictly stoichiometric sample, this phase transition should not occur.

Figure 12.11 shows the DSC traces for four kinds of compounds between -30°C and 50°C. For the spinel sample with composition close to the

stoichiometric LiMn_2O_4 (sample A), no exothermic and endothermic peaks were observed in the DSC curves. On the other hand, oxygen-deficient $\text{LiMn}_2\text{O}_{3.97}$ (sample B) shows a phase transition. For lithium-rich $\text{Li}_{1.05}\text{Mn}_2\text{O}_{4.10}$ (sample C), no exothermic or endothermic peaks were detected.

This is in agreement with Yamada's data.⁵⁸ However, after an oxygen-deficiency was created by heat treatment, $\text{Li}_{1.05}\text{Mn}_2\text{O}_{3.97}$ (sample D) shows clear exothermic and endothermic peaks. The peak amplitude increases with increasing degree of oxygen deficiency. Therefore, the disappearance of the phase transition observed in the lithium-rich samples was actually due to the elimination of the oxygen-deficiency. As soon as the oxygen-deficiency was created, the phase transition reappeared. Therefore, the oxygen-deficiency is the primary condition and the content of lithium is only a secondary factor.

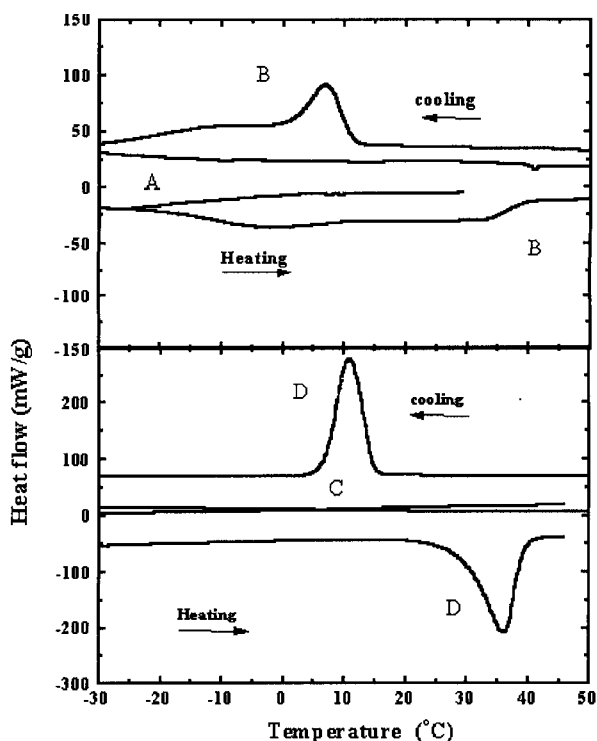


Figure 12.11. DSC traces between -30°C and 50°C for four kinds of $\text{Li}_{1\pm y}\text{Mn}_2\text{O}_{4\pm 8}$ spinels: Sample A ($\text{Li}_{0.99}\text{Mn}_2\text{O}_{4.02}$), Sample B ($\text{Li}_{0.98}\text{Mn}_2\text{O}_{3.97}$), Sample C ($\text{Li}_{1.05}\text{Mn}_2\text{O}_{4.10}$), and Sample D ($\text{Li}_{1.05}\text{Mn}_2\text{O}_{3.92}$).

12.6. SUMMARY

The capacity fading on cycling of spinel cathode materials, especially at high temperatures, is mainly due to structural instability and Mn dissolution, which can be improved by metal-ion substitution and morphology modification. It is possible to obtain spinel cathode materials with high capacity stabilization by controlling the Li/Mn (or Li/M+Mn) ratio, the heat treatment temperature and time, and the atmosphere during both the solid state reaction and annealing. In particular, the oxygen deficiency should be avoided, as it is the primary factor affecting the structural stability. The capacity fading on cycling of spinel cathode materials is not only dependent on the spinel material itself, but also on the electrolyte and anode materials. Remarkable progresses have recently been made, this allowing the realization of practical batteries.

For instance, a spinel material with a capacity of 110 mAh/g has been used in a Li-ion battery developed by Shinkobe Inc. for Nissan Hypermini EV and Tino HEV.^{62a,b} Recently, it has also been applied in 2.5-3 Ah medium-size batteries with soft cover for electrically assisted bicycles by Panasonic Inc.⁶³ One of the advantages of using spinel for EV or HEV applications is the high rate capability, up to 50 C, which is twice that of MH batteries or Ni-based Li-ion batteries. Spinel used in HEV and bicycles are oxygen-stoichiometric samples with low surface area, to improve the high temperature performance.

A cooperative research among electrochemists, inorganic and organic chemists, ceramists, and among research groups, material makers and battery makers may provide new advancements in this field. We foresee that high safety, low-cost lithium-ion batteries with Mn-based materials will grow fast in the market in the near future.

REFERENCES

1. M. Armand, in *Materials for Advanced Batteries*, D.W. Murphy, J. Broadhead and C.H. Steele, Eds., Plenum Press, New York, 1980, p.145.
2. T. Nagura, K. Tozawa, *Prog. Batteries Solar Cells* 9 (1990) 209.
3. K. Brandt, 7th IMLB, Boston, MA, USA, May 1994, Abstract FRI-30.
4. J. Hunter, *J. Solid State Chem.* 39 (1981) 142.
5. M. M. Thackeray, A. De Kock, M. H. Rossouw, D. C. Liles, D. Hoge, R. Bittihn, *J.*

- Electrochem. Soc.* 139 (1992) 363.
6. G Li, H. Ikuta, T. Uccida, M. Wakihara, *J. Electrochem. Soc.* 143 (1996) 178.
 7. M. Yoshio, Y. Xia, N. Kumada, S. Ma, *J. Power Sources* 101 (2001) 79.
 8. J. M. Tarascon, E. Wang, F. K. Shokoohi, W. R. McKinnon, S. Colson, *J. Electrochem. Soc.* 138 (1991) 2859.
 9. A. D. Robertson, S. H. Lu, W. F. Averill, W. F. Howard, Jr., *J. Electrochem. Soc.* 144 (1997) 3500.
 10. G Pistoia, A. Antonini, R. Rosati, C. Belletto, G.M. Ingo, *Chem. Mater.* 9 (1997) 1443.
 11. G Pistoia, A. Antonini, R. Rosati, C. Bellitto, *J. Electroanal. Chem.* 410 (1997) 115.
 12. M. M. Thackeray, A. De Kock, *Mat. Res. Bull.* 28 (1993) 1041.
 13. M. H. Rossouw, A. De Kock, L. A. de Picciotto, M. M. Thackeray, *Mat. Res. Bull.* 25 (1990) 173.
 14. A. De Kock, M. H. Rossouw, L. A. de Picciotto, M. M. Thackeray, *Mat. Res. Bull.* 25 (1990) 657.
 15. Y. Xia, T. Sakai, C. X. Wang, T. Fujieda, K. Tatsumi, K. Takahashi, A. Mori, M. Yoshio, *J. Electrochem. Soc.* 148 (2001) A112.
 16. Y.-K. Sun, C.S. Yoon, C.K. Kim, S.G. Youn, Y.-S. Lee, M. Yoshio, I.-H. Oh, *J. Power Sources* 108 (2002) 97.
 - 17a. Y.- S. Lee, Y.- K. Sun, M. Yoshio, *Chem. Lett.* 498 (2001).
 - 17b. Y.- S. Lee, C.S.Yoon, Y.- K. Sun, M. Yoshio, *Electrochem. Solid-State Lett.* 5 (2002) A1.
 - 17c. Y.-S. Lee, M. Yoshio, *Electrochem. Solid-State Lett.* 4 (2001) A155 .
 18. Q. Zhong, A. Bonakdarpour, M. Zhang, Y. Gao, J. R. Dahn, *J. Electrochem. Soc.* 144 (1997) 205.
 19. Y. Todorov, C. Wang, B. I. Banov, M. Yoshio, *Batteries for Portable Applications and Electric Vehicles*, C. F. Holmes and A. R. Landgrebe, Eds., The Electrochem. Soc. Inc., Pennington, NJ, 1997, PV97-18, p. 176.
 20. Y. Ein-Eli, W. F. Howard, Jr., *J. Electrochem. Soc.* 144 (1997) L205 .
 21. Y. Todorov, *Ph.D. Thesis*, Saga University, Japan, 1999.
 22. T. Ohzuku, S. Takeda, M. Iwanaga, *J. Power Sources* 81-82 (1999) 90 .
 23. J. H. Lee, J. K. Hong, D. H. Jang, Y. K. Sun, S. M. Oh, *J. Power Sources* 89 (2000) 7.
 24. K. Amine, H. Tukamoto, H. Yasuda, Y. Fujita, *J. Electrochem. Soc.* 143 (1996) 1607.
 25. Y. Gao, K. Myrtle, M. Zhang, J. N. Reimers, J. R. Dahn, *Phys. Rev. B* 54 (1996) 3878 .
 - 26a. H. Kawai, M. Nagata, H. Tukamoto, A. R. West, *J. Power Sources* 81-82 (1999) 67.
 - 26b. Y.S.Lee, Y.K.Sun, S.Ota, T.Miyashita, M.Yoshio, *Electrochem. Comm.* 4 (2002) 989.
 - 26c. Y.-S. Lee, Y.M.Todorov, K.Konishi, M. Yoshio, *ITE Lett.* 1 (2000) 883.
 - 26d. Y. Terada, K. Yasaka, F. Nishikawa, T. Konishi, M. Yoshio, I. Nakai, *J. Solid State Chem.* 156 (2001) 286.
 - 26e. K.Yasaka, *Master Thesis*, Science University of Tokyo (2001).

27. Y.-K. Sun, Y.-S. Lee, M. Yoshio, K. Amine, *Electrochem. Solid-State Lett.* 5 (2002) A99.
28. Y. Xia, T. Sakai, T. Fujieda, M. Wada, H. Yoshinaga, *J. Electrochem. Soc.* 4 (2001) A9.
29. T. Ohzuku, K. Ariyoshi, S. Yamamoto, Y. Makimura, *Chem. Lett.* 1270 (2001).
30. M. Yoshio, H. Noguchi, Y. Todorov, Y. Hideshima, *Denki Kagaku* 66 (1998) 1198.
31. H. Noguchi, H. Nakamura, M. Yoshio, *Electrochemical Society Proceedings Volume 2000-21*, M. Doyle, E. Takeuchi, K.M. Abraham, Eds., p. 18, 2001.
32. Y. Xia, M. Okada, M. Nagano, M. Yoshio, *Batteries for Portable Applications and Electric Vehicles*, C. F. Holmes and A. R. Landgrebe, Eds., The Electrochem. Soc. Inc., Pennington, NJ, 1997, PV97-18, p. 494.
33. Y. Xia, M. Yoshio, *J. Electrochem. Soc.* 143 (1996) 825.
34. Y. Xia, M. Yoshio, *J. Power Sources* 57 (1995) 125.
35. R.J. Gummow, A. de Kock, M.M. Thackeray, *Solid State Ionics* 69 (1994) 59.
36. Y. Xia, M. Yoshio, *J. Electrochem. Soc.* 144 (1997) 4186.
37. M.M. Thackeray, L.A. de Picciotto, A. de Kock, P. Johnson, V. Nicholas, K. Adendorff, *Mater. Res. Bull.* 21 (1987) 1.
38. Y. Gao, J.R. Dahn, *J. Electrochem. Soc.* 143 (1996) 100.
39. Y. Xia, Y. Zhou, M. Yoshio, *J. Electrochem. Soc.* 144 (1997) 2593.
40. D. H. Jang, Y. J. Shin, S. M. Oh, *J. Electrochem. Soc.* 143 (1996) 2204.
41. D. Guyomard, J. M. Tarascon, *Solid State Ionics* 69 (1994) 222.
42. G. Pistoia, A. Antonini, R. Rosati, D. Zane, *Electrochim. Acta* 41 (1996) 2683.
43. S. J. Wen, T. J. Richardson, L. Ma, K. A. Striebel, P. N. Ross, Jr., E. J. Cairns, *J. Electrochem. Soc.* 143 (1996) L136.
44. M. M. Thackeray, Y. Shao-Horn, A. J. Kahaian, K. D. Kepler, E. Skinner, J. T. Vaughney, and S. A. Hackney, *Electrochem. Solid-State Lett.* 1 (1998) 7.
45. J. M. Tarascon, W. R. McKinnon, F. Coowar, T. N. Bowmer, G. Amatucci, and D. Guyomard, *J. Electrochem. Soc.* 141 (1994) 1421.
46. Y. Xia, H. Noguchi, M. Yoshio, *J. Solid State Chem.* 119 (1995) 216.
47. X. Wang, Y. Yagi, Y.-S. Lee, M. Yoshio, Y. Xia, T. Sakai, *J. Power Sources* 97-98 (2001) 427.
48. T. Inoue, M. Sano, *J. Electrochem. Soc.* 145 (1998) 3704.
- 49a. Y. Xia, N. Kumada, N. Yoshio, *J. Power Sources* 90 (2000) 135.
- 49b. M. Yoshio, X. Wang, H. Nakamura, *203rd ECS Meeting*, to be presented (2003).
50. G. G. Amatucci, C.N. Schmutz, A. Blyr, C. Sigala, A.S. Gozdz, D. Larcher, J. M. Tarascon, *J. Power Sources* 69 (1997) 11.
51. G. G. Amatucci, A. Blyr, C. Sigala, P. Alfone, J. M. Tarascon, *Solid State Ionics* 104 (1997) 13.
- 52a. J. Cho, G.B. Kim, H.S. Lim, C.-S. Kim, S.-In. Yoo, *Electrochem. Solid-State Lett.* 2 (1999) 607.
- 52b. S.-C. Park, Y.-S. Han, Y.-Skang, P.S. Lee, S. Ahn, H.-M. Lee, J.-Y. Lee, *J. Electrochem.*

- Soc. 148 (2001) A680.
- 53a. Y. Xia, Y. Hideshima, N. Kumada, M. Nagano, M. Yoshio, *J. Power Sources* 74 (1998) 24
- 53b. J. Liu, K. Xu, T. R. Jow, K. Amine, *202nd ECS Meeting*, Abs. No. 135 (2002).
54. H. Yamane, T. Inoue, M. Fujita, M. Sano, *J. Power Sources* 99 (2001) 60.
55. Y. Xia, T. Sakai, T. Fujieda, X. Q. Yang, X. Sun, Z. F. Ma, J. McBreen, M. Yoshio, *J. Electrochem. Soc.* 148 (2001) A723.
56. Y. Yagi, Y. Hideshima, M. Sugita, H. Noguch, M. Yoshio, *Jpn. Electrochem.* 68 (2000) 252.
57. X. Q. Yang, X. Sun, S. J. Lee, J. McBreen, S. Mukerjee, M. L. Daroux, X. K. Xing, *Electrochem. Solid-State Lett.* 2 (1999) 157.
58. A. Yamada, *J. Solid State Chem.* 122 (1996) 160.
59. K. Oikawa, T. Kamiyama, F. Izumi, B. Chakoumakos, H. Ituka, M. Wakihara, J. Li, Y. Matsui, *Solid State Ionics* 109 (1998) 35.
60. J. Rodriguez-Carvajal, G. Rousse, C. Masquelier, M. Hervieu, *Phys. Rev. Lett.* 81 (1998) 4660.
61. X. Q. Yang, X. Sun, M. Balasubramanian, J. McBreen, Y. Xia, T. Sakai, M. Yoshio, *Electrochem. Solid-State Lett.* 4 (2001) A117.
- 62a. K. Hironaka, T. Aiba, T. Kai, T. Matumura, K. Koseki, T. Horiba, Y. Muranaka, *Shin-Kobe Tech. Report* 10 (2000) 3.
- 62b. T. Kai, H. Ando, Y. Muranaka, T. Horiba, K. Hironaka, *Shin-Kobe Tech. Report* 11 (2001) 9.
63. <http://www.panabyco.co.jp/>

Chapter 13

LAYERED MANGANESE OXIDES AS CATHODES

B. Ammundsen

Pacific Lithium New Zealand Limited, PO Box 90725, Auckland, New Zealand

13.1. INTRODUCTION

The first commercial lithium-ion batteries used LiCoO_2 as the cathode active material, and this material continues to be used in most lithium-ion batteries manufactured despite the high cost and safety hazards associated with cobalt. Apart from LiCoO_2 , only the isostructural nickelate LiNiO_2 , and more particularly the Co-substituted nickelate $\text{LiCo}_x\text{Ni}_{1-x}\text{O}_2$, have been considered to have sufficient energy density and cycling stability to be of commercial interest. However the nickelates present safety and toxicity concerns which are still greater than LiCoO_2 . Manganese oxides offer lower cost and toxicity than cobalt or nickel, and have been demonstrated to be safer on overcharge. A lithium manganese oxide based cathode should therefore, at least in principle, provide significant technological advantages in a lithium-ion system over LiCoO_2 , LiNiO_2 , or $\text{LiCo}_x\text{Ni}_{1-x}\text{O}_2$.

One of the reasons that LiCoO_2 functions so well as a lithium-ion cathode material is that it has a well-ordered and stable layered crystal structure which is easily prepared and handled in air, and enables a fast and reversible lithium intercalation. Nickelates also have a layered crystal structure, although the synthesis conditions are more difficult, requiring calcination and sintering under a controlled oxygen-rich atmosphere. The most readily prepared lithium manganese oxide is LiMn_2O_4 , which does not have a layered crystal structure but a spinel structure (refer previous chapters in this volume). Although the spinel crystal structure of LiMn_2O_4 permits rapid intercalation of lithium ions, its stoichiometry means that it has a lower capacity than LiCoO_2 . Furthermore, the stoichiometric spinel LiMn_2O_4 shows a large capacity fade with cycling. Lithium-rich spinel compositions $\text{Li}[\text{Li}_x\text{Mn}_{2-x}]\text{O}_4$ or materials substituted with cations such as Co, Cr, Al,

Mg or Zn provide better cycling stability and are therefore generally applied in preference to the stoichiometric material. However the Li-rich and substituted materials give capacities only around 115 mAh/g, and even stabilized formulations may still exhibit stability problems in a Li-ion battery with a carbon anode. These disadvantages have not yet been fully overcome, and have limited the application of spinel in commercial lithium-ion batteries.

A layered lithium manganese oxide cathode material with the stoichiometry LiMnO_2 would be expected to overcome at least some of the limitations of the spinel manganese oxides. Layered crystal structures based on lithium manganese oxide have therefore been widely investigated over the last few years as an alternative to spinel. The underlying idea is to combine the electrochemical properties of the layered structures, particularly the higher theoretical capacity, with the advantages of a manganese-based chemistry. The problem with layered LiMnO_2 , however, is that its synthesis is not trivial.

The structural chemistry of manganese oxides is very complex – more complex than that of cobalt or nickel oxides. Even the binary oxide MnO_2 exists in a variety of structures, as well as intergrowths of these structures. Therefore it is not surprising that lithiated manganese oxides can also be prepared in a variety of structures. Thermodynamically stable spinel compounds have been reported with a range of different cation distributions within the compositional range LiMn_2O_4 – $\text{Li}_2\text{Mn}_4\text{O}_9$ – $\text{Li}_4\text{Mn}_5\text{O}_{12}$. Other readily prepared lithium manganese oxides are an orthorhombic form of LiMnO_2 and a monoclinic phase Li_2MnO_3 . However LiMnO_2 with a layered crystal structure analogous to LiCoO_2 is not thermodynamically stable, and therefore cannot be simply prepared using the high temperature processing routes used to manufacture other lithium manganese oxides, LiCoO_2 , or lithium nickelates.

This chapter examines the various approaches that have been taken to prepare and stabilize the layer structure for lithium manganese oxide in order to develop high energy storage capacity and cycling stability in lithium-ion cells. Strategies have included preparation by soft chemistry synthesis or by selective substitution, but neither approach has fully successfully dealt with the instability of the layered manganese oxide structure when cycled. As an understanding of the relationships between crystal structural chemistry and electrochemical performance has developed, recent work has focused on using the properties of tetravalent rather than trivalent Mn as a basis for developing novel complex or solid-solution cathode materials with improved capacity, cycling stability and safety. This latter approach provides a technological solution to many of the stability issues that have previously prevented layered lithium manganese oxides from entering into commercial applications.

13.2. OVERVIEW OF THE STRUCTURE AND STABILITY OF LAYERED MANGANESE OXIDES

13.2.1. Layered vs. Orthorhombic Structure of LiMnO_2

When prepared by typical high temperature solid state methods, LiCoO_2 has the well-ordered $\alpha\text{-NaFeO}_2$ rocksalt structure with $R\bar{3}m$ symmetry shown in Figure 13.1(left). The stacking sequence of the oxygen sublattice in the rocksalt structure is ABCABCABC. The cations are located in octahedral sites, ordered to make alternating layers of transition metal and lithium, thus yielding $A\gamma B$ a $C\beta A$ c $B\alpha C$ (where greek letters denote transition metal layers and small latin letters denote Li layers). The transition metal cations (M) and oxygen anions form rigid $\text{MO}_2^{(-)}$ sheets. The Li^+ ions between the sheets are more mobile, and can be reversibly extracted and reinserted electrochemically.

LiMnO_2 is not thermodynamically stable as the layered structure. Under equilibrium high temperature synthesis conditions, preparations of stoichiometric LiMnO_2 crystallize in the orthorhombic structure (space group $Pmmn$) illustrated in Figure 13.1(right). In this structure, which is unique among lithiated transition metal oxides, Li and Mn ions occupy octahedral sites arranged in an alternating zig-zag configuration of edge-sharing $[\text{LiO}_6]$ and $[\text{MnO}_6]$ octahedra. The phase with this structure is commonly referred to as “orthorhombic LiMnO_2 ”, or $o\text{-LiMnO}_2$.

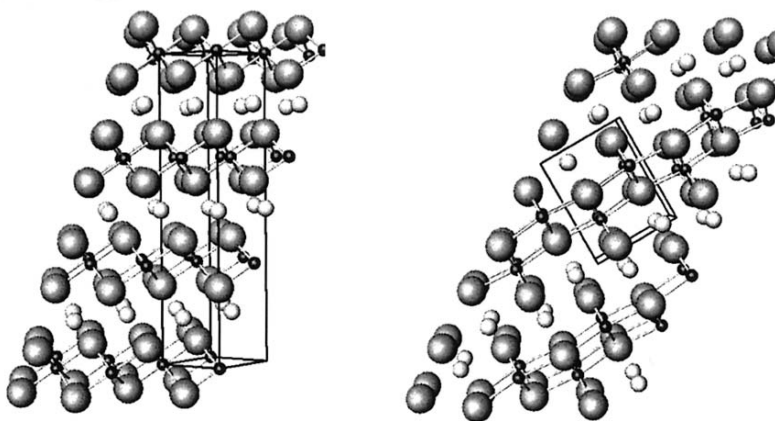


Figure 13.1. Crystal structures of layered LiCoO_2 (left) and $o\text{-LiMnO}_2$ (right). Small white spheres represent Li ions, small black spheres represent transition metal ions, and large gray spheres represent oxygen.

However, the difference in stability between the orthorhombic and layered structures is rather small, and soft chemical routes such as ion exchange or hydrothermal syntheses can yield layered LiMnO_2 .¹⁻³ These synthesis methods are described in more detail below in Section 13.3.2. The resulting materials do not have a perfect $\alpha\text{-NaFeO}_2$ structure. The trivalent d^4 Mn ions cause a cooperative distortion of the MnO_6 octahedra due to Jahn-Teller stabilization, leading to a monoclinic unit cell (space group $C2/m$) with angles and lattice constants distorted from the higher rhombohedral symmetry.

The physical principles underlying the thermodynamic stability of orthorhombic LiMnO_2 over the layered structure have been examined using first-principles structure calculations.⁴ Mn^{3+} ions introduce two features which distinguish LiMnO_2 from other lithiated transition metal oxides: a large magnetic moment (four unpaired electrons in the high-spin configuration), and Jahn-Teller distortion of the MnO_6 octahedron due to the single occupancy of an e_g level. Structure calculations show that although the layered monoclinic structure should be more stable based on ionic size considerations, strong antiferromagnetic interactions between Mn^{3+} ions, and the consequent localization of electronic states, stabilize the orthorhombic structure of LiMnO_2 over the layered structure. Chemical substitution of LiMnO_2 by either nonmagnetic ions or ions with valence other than $3+$ could therefore stabilize the layered structure by perturbing the magnetic Mn-Mn interaction and/or electronic charge on the Mn ion. This approach has been successfully implemented in practice using several different chemical species, as described in Section 13.3.3 below.

13.2.2. Instability with Respect to the Spinel Structure

Although strategies have been developed to synthesize layered lithium manganese oxides, a further stability problem arises when the materials are used as cathodes. When LiMnO_2 materials are cycled, layered (and also orthorhombic) structures tend to transform toward the spinel structure. Spinel LiMn_2O_4 differs from the layered LiMnO_2 by having a three-dimensional crystal structure rather than the two-dimensional layered crystal structure. The Li ions reside in tetrahedral sites in channels of the spinel MnO_2 crystal structure, rather than the interlayer octahedral sites of the layered LiMnO_2 . However the transformation between a layered or orthorhombic structure and a spinel structure requires only relatively minor rearrangement of the cations. Figure 13.2 shows the spinel crystal structure of LiMn_2O_4 , drawn with the oxygen planes in the same relative orientation as the structures in Figure 13.1 to illustrate the similarity between the basic structures. In relation to the $R\bar{3}m$ layered structure, the spinel structure can

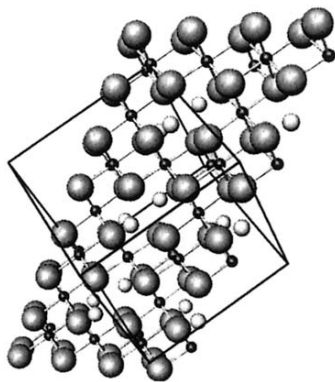


Figure 13.2. Crystal structure of spinel LiMn_2O_4 (refer Figure 13.1 for key).

be viewed as having cation layers with octahedral sites alternately filled three-quarters and one-quarter by Mn, resulting in three-dimensional channels with Li ions in tetrahedral sites.

Structure calculations have also helped to understand this instability of layered and orthorhombic manganese oxide structures with respect to the transformation to spinel. Calculations have shown that the spinel structure is energetically preferred over the layered or orthorhombic structure for most lithiated transition metal oxides when the stoichiometry $\text{Li}_{0.5}\text{MO}_2$ is reached during extraction of Li.^{5,6} This is true for cobalt oxide as well as manganese oxide, and yet cobalt oxide cycles well without showing spinel transformation. This suggests that the transformation to spinel occurs more readily in manganese oxide due to different kinetic factors. *Ab initio* calculations suggest that delithiated Li_xMnO_2 layered materials transform to spinel in a two stage process.⁷ In the first stage a portion of the Mn and Li ions rapidly migrate into tetrahedral sites surrounded by Li vacancies. The activation barriers for this are low, partly because the migration of Mn into a tetrahedral site is assisted by a stabilization gained by charge disproportionation of Mn^{3+} into Mn^{2+} (tetrahedral) and Mn^{4+} (octahedral) species. By comparison, in LiCoO_2 the activation energy for the same process was calculated to be prohibitively high. The second stage of the layered-to-spinel transformation involves a more difficult coordinated rearrangement of Mn and Li ions to form spinel, which takes place more slowly due its complexity and higher activation barriers. This calculated model agrees with experimental observations of LiMnO_2 cathodes examined by diffraction and X-ray absorption experiments. Experimental data typically show that significant structural rearrangements to a disordered, less two-dimensional structure take place during the first charge (delithiation) of the cathode material, followed by a gradual re-ordering into an increasingly

spinel-like structure over subsequent cycles.⁸⁻¹¹

Figure 13.3(A) in Section 13.3.3 shows the consequence of the phase transformation toward the spinel structure on the discharge voltage profile of a typical LiMnO_2 material (here shown for $o\text{-LiMnO}_2$ prepared by high temperature processing). The transformation toward the spinel structure is accompanied by evolution of a voltage profile characteristic of spinel manganese oxide, which drops sharply from approximately 4 V vs. Li/Li^+ to just below 3 V near the $\text{Li}_{0.5}\text{MnO}_2$ stoichiometry, *i.e.* at the halfway point of discharge. The voltage step in the spinel structure is associated with a change in intercalation mechanism. For $0 < x < 1$ in spinel $\text{Li}_x\text{Mn}_2\text{O}_4$, Li ions are inserted directly into tetrahedral sites with high binding energy for lithium, a process which takes place around 4 V vs. Li/Li^+ . For $1 < x < 2$ in spinel $\text{Li}_x\text{Mn}_2\text{O}_4$, Li ions are inserted into octahedral sites to form a tetragonally-distorted rock salt structure of stoichiometry $\text{Li}_2\text{Mn}_2\text{O}_4$ ($=\text{LiMnO}_2$) in a two-phase process which occurs at a potential of just below 3 V vs. Li/Li^+ . Such a large drop in voltage midway through discharge poses problems for power management in actual systems. Furthermore, while a crystalline spinel structure provides fast diffusion for lithium into tetrahedral sites at around 4 V, conversion of LiMnO_2 materials can lead to a less ordered spinel structure with lower 4 V capacity and poorer rate capability. Additionally, the two-phase process that occurs at around 3 V typically has much poorer kinetics than the insertion process at 4 V, manifesting as polarization of the voltage and incomplete discharge as the current rate is increased. This also poses problems for practical constant-power applications that require higher current rates as the voltage lowers toward the end of discharge.

On the other hand, spinel-type cathodes formed *in situ* by cycling LiMnO_2 materials often show better cycling stability over a large lithiation range (up to nearly LiMnO_2 or $\text{Li}_2\text{Mn}_2\text{O}_4$) than spinel materials prepared *ex situ* by conventional methods. The retention of high capacity – in many cases more than 200 cycles have been reported – is surprising considering that conventionally prepared LiMn_2O_4 spinel materials almost always show large irreversible capacity loss over only a few cycles when cycled over both the 4 and 3 V regions. Data from high resolution electron microscopy have shown that the cycling stability may largely result from the formation of antiphase nanodomains (at a length scale of 20-50 nm) in cathode materials starting from LiMnO_2 phases.^{12,13} The antiphase nanodomains arise from nucleation of the spinel structure at different points in the original crystal structure, followed by growth of the spinel domains from the point of nucleation to meet at phase boundaries where there is incoherence of the spinel crystal structure between neighboring domains. The formation of this nanodomain structure, in which there is a high density of phase boundaries, provides an elasticity which can better accommodate transformation strains and anisotropic changes in volume arising from cycling the material over such a wide voltage range. Some cation inversion (Mn ions in tetrahedral Li sites)

has also been found in the spinel structure obtained from LiMnO_2 phases, which is also considered to contribute to the cycling stability,¹³ but would have an adverse effect on rate capability.

It has been pointed out that substitution of LiMnO_2 with species having strong octahedral site stabilization energies could hinder the second stage of the layered-to-spinel transformation, *i.e.* the stage that requires cooperative re-arrangement of transition metal ions in the structure.⁷ This approach has been shown to be partially successful for materials made by both soft chemistry routes and high temperature processing (see below).

13.2.3. Alternative Layered Structures

In the materials described above, the transformation to spinel is possible because the layered, orthorhombic, and spinel structures have the same close-packed oxygen sublattice, so that only relatively minor cation re-arrangements are needed for the transformation. An alternative approach has been to prepare a layered lithium manganese oxide with a different oxygen sublattice, so that transformation to spinel would require a coordinated lattice rearrangement impossible to achieve at ambient temperature. Such a material can be prepared by soft chemistry routes,¹⁴ as described in Section 13.3.4 below. The material with the different oxygen sublattice in this case is designated an O2 structure following the notation for layered structures given by Delmas *et al.*,¹⁵ in which the letter refers to the type of site occupied by the alkali metal cation (in this case Li in octahedral sites), and the number refers to the number of $\text{MO}_2^{(-)}$ layers included in the unit cell. By contrast the $R\bar{3}m$ layered structure is an O3 structure in which the oxygen stacking is essentially the same as in the stable spinel structure.

It has been shown experimentally that O2 layered lithium manganese oxides do not convert to the spinel structure during cycling.¹⁴ However the materials were at first found to have relatively poor current rate capability, which was attributed to poor crystallinity caused by high densities of stacking faults, resulting from the ion-exchange process used to make the materials. More crystalline O2 materials with improved electrochemical properties have since been prepared using Ni and Co substitution.^{14,16,17}

The collapse of a layered to a spinel structure could also be hindered by substituting larger cations in the Li layers to “pillar” the oxide. Such an approach has been described, for example using K ions as the pillaring species.¹⁸ However a problem remains that species such as K ions tend to be extracted during the charge cycles.

13.2.4. Layered Lithium Manganese Oxides with Tetravalent Manganese

A lithium manganese oxide phase which is layered, thermodynamically stable and easy to prepare, but until recently frequently overlooked, is Li_2MnO_3 . Unlike LiMnO_2 , the manganese in Li_2MnO_3 is tetravalent. The structure of Li_2MnO_3 can be viewed as a rocksalt phase with alternating Li and $[\text{Li}_{1/3}\text{Mn}_{2/3}]$ layers, allowing the formula to be written as $\text{Li}[\text{Li}_{1/3}\text{Mn}_{2/3}]\text{O}_2$. In this phase the $[\text{Li}_{1/3}\text{Mn}_{2/3}]$ layers show a honeycomb-type ordering of the cations. The material can be prepared very simply by high temperature solid state processing in air. The layer structure of Li_2MnO_3 is stabilized compared with LiMnO_2 partly by the smaller ionic radius of tetravalent Mn compared with trivalent Mn, partly by energy-lowering effect of the ordering of Li ions in the $[\text{Li}_{1/3}\text{Mn}_{2/3}]$ layers, and also by less strong magnetic interactions between Mn ions.

$\text{Li}[\text{Li}_{1/3}\text{Mn}_{2/3}]\text{O}_2$ is, however, electrochemically inactive – the extraction of any lithium would normally require highly oxidized manganese which is not observed in these types of structures. $\text{Li}[\text{Li}_{1/3}\text{Mn}_{2/3}]\text{O}_2$ has been used as a precursor to prepare layered manganese oxides by acid leaching of the lithium out of the structure, and the resulting materials have been shown to be able to reversibly insert lithium in lithium cells.^{19,20} In some cases the materials seem to convert more slowly to a spinel-type phase than LiMnO_2 materials, which may be due to a unique protonated and hydrogen-bonded layer structure formed during acid-leaching.²¹ However, the materials still cycle on a $\text{Mn}^{3+}/\text{Mn}^{4+}$ redox couple, which ultimately leads to spinel formation. Furthermore, the acid-leached materials require lithiation before they can be used with a carbon anode.

Although tetravalent Mn cannot itself be oxidized in layered oxides, it can be combined with other oxidizable transition metals in solid solutions to give layered oxides having interesting properties as cathode materials. It is only just now beginning to be appreciated that this type of approach can be applied to provide at least part of the benefits of manganese in terms of cost, safety and non-toxicity, while avoiding the instability issues associated with LiMnO_2 materials. As described above, the first stage of the transformation of layered LiMnO_2 to spinel is associated with the disproportionation of trivalent Mn to Mn^{2+} and Mn^{4+} within the crystal structure, allowing Mn to migrate through tetrahedral sites as Mn^{2+} . On the other hand, Mn^{4+} has a very high activation barrier for diffusion through the tetrahedral site. Layered oxides containing only tetravalent Mn are therefore expected to be stable in the layered structure. Practical applications of this approach are described in Section 13.4.

13.3. LAYERED MANGANESE OXIDES BASED ON LiMnO_2

13.3.1. Orthorhombic LiMnO_2

The structure of the orthorhombic phase $o\text{-LiMnO}_2$ is sometimes considered to be “layered”, and the material will be discussed briefly here because the LiMnO_2 stoichiometry means that it shares certain common characteristics with other layered LiMnO_2 systems.

The synthesis and electrochemical properties of $o\text{-LiMnO}_2$ materials have been investigated in detail by various groups over the past decade. The orthorhombic phase being the thermodynamically stable structural form for the LiMnO_2 stoichiometry, its preparation is relatively straightforward as long as excess oxygen is excluded. Any oxidation gives rise to spinel and Li_2MnO_3 phases. The electrochemical performance of $o\text{-LiMnO}_2$ materials is however very dependent on material microstructure, and therefore dependent on the synthesis approach. $o\text{-LiMnO}_2$ materials can be broadly categorized into those made by low temperature routes, and those made by high temperature processing.

Many low temperature synthesis methods have been reported, with the objective of increasing the electrochemical activity of the $o\text{-LiMnO}_2$ material. Ohzuku *et al.* were the first to report a relatively high capacity of 190 mAh/g over a voltage range of 4.25 – 2.0 V for an $o\text{-LiMnO}_2$ product prepared by heating an equimolar mixture of $\gamma\text{-MnOOH}$ and LiOH at 300 – 450 °C under dry nitrogen.²² Reimers *et al.* also reported high capacities for $o\text{-LiMnO}_2$ products synthesized by an ion-exchange reaction of $\gamma\text{-MnOOH}$ in boiling LiOH solution with subsequent drying at 105 °C in air, or heating at 200 °C under argon.²³ However, in all cases the crystal structure of the materials was found to transform on charging the cell (delithiation of the LiMnO_2) to give a disordered crystal structure of the spinel type and a discharge voltage profile of the kind shown in Figure 13.3(A). Electrochemical and X-ray diffraction data have shown that several charge-discharge cycles are generally required to complete the transformation to the spinel structure – depending on current rate and voltage limits the transformation is more or less fast. In particular, charging cells to higher voltage (more complete delithiation of the cathode) has been found to increase the speed of the transformation.²⁴ However the capacity retention on extended cycling of the cathode materials formed from $o\text{-LiMnO}_2$ materials prepared by low temperature routes has generally been poor.

$o\text{-LiMnO}_2$ materials made using high temperature processing have generally been prepared by solid state reaction of a manganese oxide and lithium salt under an inert atmosphere. These $o\text{-LiMnO}_2$ materials also transform to spinel-type structures when delithiated during charging, but

generally show better cycling stability over a wide voltage window than the materials prepared at low temperature. Gummow *et al.* prepared *o*-LiMnO₂ products by solid state reaction of γ -MnO₂ with LiOH at 600 – 620°C in an argon atmosphere in the presence of carbon black as a reducing agent, and obtained capacities of up to 160 mAh/g over 4.45 – 2.5 V.²⁵ Davidson *et al.* obtained capacities up to 140 mAh/g over 4.4 – 2.0 V for HT *o*-LiMnO₂ products prepared by reaction of MnO₂ and Li₂CO₃ at 800 – 1000°C under argon.²⁶ Croguennec *et al.* examined in detail the effect of crystallinity on the electrochemical performance of HT *o*-LiMnO₂ phases, using solid state reactions between Mn₂O₃ and LiOH.H₂O at 700°C designed to produce materials with very small crystallites (<0.5 μ m).^{27,28} Capacities up to 200 mAh/g were obtained for materials with crystallite sizes of around 0.3 μ m.²⁹ The small-crystallite-size *o*-LiMnO₂ phases were characterized by cationic disorder identified as stacking faults in the crystal structure, which were considered to be important for the electrochemical activity.³⁰ However Jang *et al.* later reported high capacities for *o*-LiMnO₂ materials prepared by a controlled high temperature synthesis process giving small crystallite size but a low content of stacking faults, indicating that crystallite size is the most critical parameter in determining the electrochemical performance of *o*-LiMnO₂ materials.³¹

The problem for application of *o*-LiMnO₂ as a cathode material remains its instability in transforming to a disordered spinel structure during cycling. To the best of our knowledge the stabilization of the *o*-LiMnO₂ structure against transformation to a spinel-type structure has never been reported. The speed of transformation to spinel, and the rate capability problem on the 3 V plateau, can both be controlled to some extent by modifying the microstructure of the *o*-LiMnO₂ material. However the sharp voltage drop in the middle of discharge remains a problem for applications.

13.3.2. Lithium Manganese Oxide with the O3 Layered Structure Prepared by “Soft Chemistry” Routes

Although LiMnO₂ with a layered-type crystal structure is metastable with respect to the orthorhombic phase, it has been prepared successfully by “soft” chemistry methods involving low temperature processing such as ion-exchange. As explained in Section 13.2.1, the layered LiMnO₂ materials do not crystallize in the $R\bar{3}m$ space group, but show a monoclinic distortion of the lattice (space group $C2/m$) due to cooperative ordering of Jahn-Teller distorted [Mn³⁺O₆] octahedra. Monoclinic LiMnO₂ shows similar behavior to *o*-LiMnO₂ when used as a lithium-ion cathode. Spinel phase nucleates in the material on first charge, and transformation to a disordered spinel phase is usually complete within a few charge-discharge cycles. The consequences

for the discharge voltage profile and rate capability are analogous to those found for the orthorhombic material.

Despite its large commercial and scientific interest, it took more than ten years of development before layered LiMnO_2 was successfully prepared. In the early 1980's Delmas *et al.* investigated ion exchange reactions and extraction/insertion in layered transition metal oxide bronzes.¹⁵ Two groups of structures denoted O3, O1, O6 and P3, and the other of structures denoted P2 and O2. In the first group all MO_2 layers have the same orientation, while in the latter the orientation alternates. Phase transitions are possible between members of the same group by gliding of the layers, but the orientation of the layers cannot change. The concept was successfully demonstrated using different LiCoO_2 and Na_xCO_2 phases.^{32,33} Due to the smaller ionic radius of Li, Li-Na exchange is energetically preferred and in principle it should be straightforward to prepare layered LiMnO_2 (which has the O3 structure) by ion exchanging Li for Na in O3 NaMnO_2 .

However, Li-Na exchange in molten salt was not successful. A collapse of the layered toward a three dimensional structure was reported and attributed to the use of relatively high temperatures for the exchange reactions.³⁴ Success was eventually achieved by Capitaine *et al.* through ion exchange of NaMnO_2 in LiCl dissolved in methanol at 90°C , however the ion exchange kinetics were poor, and the process required around one month.¹ More rapid and complete ion exchange was reported by Armstrong and Bruce by refluxing NaMnO_2 in LiBr , dissolved in n-hexanol, at 150°C .² However the layered LiMnO_2 material did not cycle well. A large amount of lithium could be extracted on first charge, but subsequent discharges showed poor and declining capacity. Later investigations of cycled material by neutron diffraction and electron microscopy confirmed that the material undergoes structural transformation to a disordered spinel over only a few cycles.¹⁰ During the first charge cycle Li is initially removed in a two-phase process where both the original monoclinic layered and a hexagonal phase co-exist. After approximately 30% of the lithium is removed, a single hexagonal phase is observed up until almost complete delithiation of the Li_xMnO_2 . At the very end of the first charge cycle a collapse of the interlayer spacing was observed. Subsequent cycling showed increasing amounts of spinel phase appearing in the material.

Armstrong *et al.* have subsequently reported that partial substitution of Co or Ni for Mn in the NaMnO_2 precursor can significantly improve the cycling properties of the LiMnO_2 material obtained by ion exchange.³⁵ The substitution of around 10% Co or Ni results in a slightly Li-deficient $\text{LiM}_x\text{Mn}_{1-x}\text{O}_2$ material with a $R\bar{3}m$ lattice symmetry rather than monoclinic distortion. Although the materials still transform to a spinel structure with cycling, the transformation is slowed and the resulting materials show

improved capacity, rate capability and cycling stability relative to non-substituted LiMnO_2 . Recent advances in the conditions required for synthesis have also been reported, including lower temperatures and the use of alternative solvents such as ethanol³⁶ or NMP.³⁷ The results are interesting but the ion exchange process of manufacture remains a complex and challenging process for large scale manufacture, and synthesis of the doped sodium bronze precursor materials is not trivial in itself.

The structural variety of manganese oxides, and the small stability differences in free enthalpy between the stable and metastable phases allow a variety of different structures and intergrowth structures to be prepared by low temperature processing routes. Some reported products can be described as layered structures. Tabuchi *et al.* reported hydrothermal synthesis of layered monoclinic LiMnO_2 .³

Whereas LiMnO_2 materials prepared at high temperatures often have rate capability limitations, the low temperature materials may show much better capacities and rate capabilities. This often originates from shorter diffusion lengths for Li in such materials, which typically have lower crystallinity and higher surface areas than materials sintered at high temperature. If the diffusion lengths are short, then lithium may be inserted and extracted at crystallographic sizes and into defects that would not be accessible in crystalline materials, contributing to large capacities. On the other hand such materials often have low volumetric densities, diminishing the energy density of the cathode and the battery. Furthermore large surface areas can speed up unwanted reactions on the interface between electrolyte and cathode, leading to poor safety and poor cycling stability. These problems can counter the often impressive capacities reported for cathodes prepared by low temperature routes. At present such cathode materials have yet to be applied in commercial lithium-ion batteries.

13.3.3. Substituted LiMnO_2 with the O3 Layered Structure Prepared by High Temperature Processing

Chemical substitution in LiMnO_2 not only slows the transformation from the layered structure to spinel during cycling of the cathodes. Substitution can also stabilize the layered structure over the orthorhombic structure in the initial preparation of the LiMnO_2 material, allowing the layered phase to be directly obtained using high temperature processing. As mentioned in Section 13.2.1, this occurs by perturbing the magnetic Mn-Mn interactions and/or by changing the electronic charge on the Mn ions. In practice, as little as 3–5% substitution has been found to be sufficient to destabilize the orthorhombic structure in favor of the layered $C2/m$ monoclinic structure. Based on theoretical considerations, a number of

cations should be able to perform this function, but only Al, Cr and Ga have been shown to work in practice. This is at least partly because the high temperature conditions using inert atmosphere are not suitable for the use of substituting elements like Co and Ni, which tend to reduce to divalent oxides during the attempted synthesis. Al, Cr and Ga have in common that the trivalent oxidation state is stable under the synthesis conditions.

The stabilization of the layered structure over the orthorhombic structure in a high temperature process was first reported by Davidson *et al.*, using Cr substitution.³⁸ Substitution of as little as 5% of the Mn by Cr^{3+} in LiMnO_2 resulted in crystallization of a layered monoclinic phase by a simple solid state reaction at 1000°C under argon. The original report was unclear in identifying the crystal structure of the material, but subsequent work confirmed that it was indeed layered with the same monoclinic $C2/m$ structure reported for LiMnO_2 obtained by ion-exchange.³⁹ It was reported that the Cr-substituted material seemed to convert to a spinel-type structure with cycling, but extended cycling data was not shown.

Later, Jang *et al.* reported that monoclinic layer-structure LiMnO_2 could also be crystallized in a stable form at high temperature (*ca.* 950°C) by substituting 5–10% of the Mn with Al.⁴⁰ The materials were synthesized from a precursor powder prepared by atomizing and freeze-drying a suspension of Al and Mn hydroxide, coprecipitated from nitrate precursors, in LiOH solution. During cycling, the Al-substituted materials were again found to convert to a spinel-type structure. Despite the transformation of the structure and consequent evolution of the discharge voltage profile, however, the Al-substituted cathodes could be cycled over the voltage range 4.4 – 2.0 V with good retention of capacity, and showed unusually good cycling stability at 55°C .⁴¹

The formation of monoclinic layered oxides by high temperature processing was investigated in further detail by Ammundsen *et al.*^{42,43} Layered monoclinic LiMnO_2 was successfully prepared by substituting between 3 and 10% Al^{3+} , Ga^{3+} , or Cr^{3+} in simple low-cost solid state methods of preparation which could be implemented on an industrial scale.⁴⁴ The monoclinic unit cell parameters for the substituted materials showed a systematic decrease in unit cell volume and in the extent of the monoclinic distortion by comparison with non-substituted LiMnO_2 prepared by ion-exchange.

Al- and Cr-substituted materials were evaluated as cathodes to determine whether stabilization of the layered crystal structure in a well-ordered highly crystalline material through chemical substitution could translate to increased stability of the layered structure against transformation to spinel during cycling.^{42,43} Figure 13.3 shows the discharge voltage curves for monoclinic layered materials substituted with 5% Al and 3% Cr, compared with the *o*- LiMnO_2 material prepared under the same high temperature processing conditions in the absence of a substituting element.

The o -LiMnO₂ cathode undergoes rapid conversion to spinel-type structure, with the 4 V and 3 V voltage steps clearly defined in the discharge by cycle 16. The results for Al-substituted LiMnO₂ prepared by the high temperature solid state methods agree with those of Chiang *et al.*,⁴¹ showing that substitution by Al serves to slow the transformation of the crystal structure from layered to spinel-type, but does not prevent it from occurring. The results for the Al-substituted material prepared at high temperature are qualitatively similar to those observed for O3 layered materials prepared by Na-Li ion-exchange in lattices substituted with Co or Ni.

The quite different evolution of the discharge voltage curves for Cr-substituted material compared with those for o -LiMnO₂ or the Al-substituted

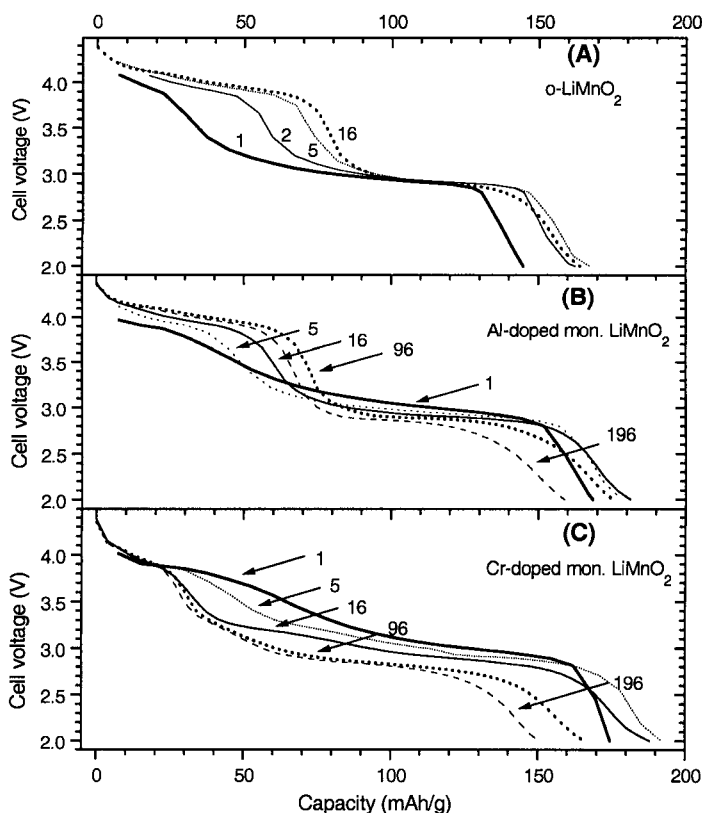


Figure 13.3. Discharge voltage profiles for LiMnO₂ phases prepared by high temperature processing: (A) o -LiMnO₂, (B) monoclinic layered LiMnO₂ with 5% Al substitution, (C) monoclinic layered LiMnO₂ with 3% Cr substitution. Data recorded in lithium cells cycled between 4.4 and 2.0 V at 55°C, 30 mA/g current rate. Cycle numbers are indicated.

material indicates that something different occurs during cycling. Little additional capacity is evolved at 4 V for the Cr-substituted LiMnO_2 , even after 200 cycles, indicating little formation of spinel-type tetrahedral insertion sites for Li ions. X-ray diffraction on cycled cathodes confirmed the absence of spinel phase in the cycled Cr-substituted materials.⁴³ Subsequent work by other authors has confirmed that Cr substitution is peculiarly effective in blocking the transformation to spinel structure with cycling.^{45,46} Instead a quasi-layered phase with some disordered displacement of a portion of the Mn ions out of their original octahedral layer sites seems to form. This is similar to the intermediate structure proposed by structure calculations for a layered material which has undergone the first stage of the transformation toward a spinel-type structure, but which has been unable to complete the second stage of coordinated rearrangement of the cations to form a true spinel structure, as described in Section 13.2.1.

To summarize, substituted O3 layered LiMnO_2 materials prepared at high temperature, like layered LiMnO_2 materials prepared by soft chemistry routes, also undergo structural phase changes with cycling to form defective spinel-type structures, with consequent changes in the voltage profile. Substitution with Cr has been demonstrated to be particularly effective in inhibiting transformation of the layered structure to spinel, but the Cr-substituted LiMnO_2 materials still undergo structural rearrangements away from an ideal ordered $R\bar{3}m$ structure. More work will be needed to successfully stabilize a true layered LiMnO_2 structure by this approach.

13.3.4. O2 Layered Structures

As an alternative to preparing layered lithium manganese oxide with a LiCoO_2 -type (O3) crystal structure, it is possible to synthesize a layered oxide with a different oxygen sublattice, so that transformation to spinel would require a coordinated lattice rearrangement impossible to achieve at ambient temperature. While the direct preparation of a lithium manganese oxide with the latter kind of structure has never been reported, the structural variety of sodium manganese bronzes allows such compounds to be made using ion-exchange methods.

Preparation of lithium manganese oxides with O2 layered structures was first reported by Paulsen *et al.*, who synthesized materials by ion exchanging P2-structure layered sodium manganese oxides ("P" in this case designating prismatic Na sites).¹⁴ However, although it was demonstrated that the O2 materials do not convert to spinel during cycling, the materials nonetheless cycled poorly with insufficient rate capability. This was attributed to poor crystallinity caused by high densities of stacking faults

resulting from the ion-exchange process. During Na-Li exchange, the $\text{MO}_2^{(-)}$ sheets glide with respect to one another, creating the stacking faults.

However substitution of a fraction of the Mn with Co or Ni improves both the ion exchange kinetics and the electrochemical properties. A layered material of composition $\text{Li}_{2/3}[\text{Mn}_{0.85}\text{Co}_{0.15}]\text{O}_2$ showed a smoothly sloping voltage profile and good cycling performance without transforming to spinel.¹⁴ Substitution with Ni allowed a successful ion exchange at room temperature resulting in a crystalline layered phase with a novel T2 type structure.¹⁶ T2 $\text{Li}_{2/3}[\text{Ni}_{1/3}\text{Mn}_{2/3}]\text{O}_2$ shows $\text{Ni}_{1/3}\text{Mn}_{2/3}$ honeycomb type ordering in the transition metal planes and unusual occupation of tetrahedral-type layer sites by Li ions.⁴⁷ On first charge the material converts to the O2 structure. The material can then be cycled in the O2 structure over hundreds of cycles without collapse of the layer structure, with capacities of up to 180 mAh/g if cycled between 2.5 and 4.6 V. However, unlike the Co-substituted material, only one-third Li per formula unit $\text{Li}_{2/3}[\text{Ni}_{1/3}\text{Mn}_{2/3}]\text{O}_2$ (*i.e.* half the available Li) can be removed from the lattice on charge. In order to obtain a capacity of 180 mAh/g, an additional 1/3 Li needs to be inserted into the lattice on discharge (requiring an additional source of Li not normally available in lithium-ion cells). Furthermore, although the 1/3 Li removed on first charge is reversibly re-intercalated at around 3.8 V, the additional 1/3 Li is intercalated at around 2.8 V. Although the material does not convert to a spinel, the voltage profile is almost the same as that of O3 phases that do convert to spinel. In the case of $\text{Li}_{2/3}[\text{Ni}_{1/3}\text{Mn}_{2/3}]\text{O}_2$ the two steps with a 1 V drop in the middle are due to different redox couples being involved. The 3.8 V intercalation is related to reduction of nickel, while the 2.8 V intercalation corresponds to reduction of Mn^{4+} to Mn^{3+} .

Substitution of Co for Ni in $\text{Li}_{2/3}[\text{Ni}_{1/3}\text{Mn}_{2/3}]\text{O}_2$ has been found to result in formation of a stacking faulted O2 structure with incomplete Li-Na exchange.^{48,49} However substitution of Co for both Ni and Mn allows ion exchange to go to completion to give materials of composition $\text{Li}_{2/3}[\text{Co}_x\text{Ni}_{1/3-x/2}\text{Mn}_{2/3-x/2}]\text{O}_2$, and allows increased amounts of Li to be extracted on first charge, enlarging the reversible capacity available in a sloping discharge between 4.5 and 3.8 V.¹⁷

The O2 layered cathode materials are still far from commercialization due to the complicated methods of preparation, and lower capacity at higher current rates in their current state of development. Although the substitution by Ni and/or Co improves the rate performance, the resulting T2 and O2 materials need to be cycled over a wide voltage range and require an additional source of Li to capture their full capacity, which is delivered in two steps with a large voltage drop mid-discharge.

The structural studies carried out on the O2 and T2 layered oxides do, however, provide interesting data on the behavior of Mn, Ni and Co ions when sharing the same oxide lattice. In particular, the data show that best structural and electrochemical results are achieved when Mn is fully

tetravalent in the initial material. Ni in the T2 layered manganese compounds is divalent, while Co is trivalent. These observations have bearing on the subject matter of Section 13.4.

13.4. LAYERED SOLID SOLUTION CATHODE MATERIALS BASED ON TETRAVALENT MANGANESE

13.4.1. Overview of Solid Solution Approaches

In order to facilitate the preparation of layered LiMnO_2 and to attempt to improve the stabilization of the layered structure of the delithiated phases against transformation to spinel, there have been many investigations of higher levels of substitution by elements such as Cr, Co and Ni. This type of approach overlaps to some extent with that of investigators who have tried to lower the cost and improve the safety properties of LiCoO_2 and LiNiO_2 by heavily substituting these materials with manganese. The underlying idea behind all these different approaches is the same: to combine the cost and safety advantages of manganese oxide with the thermodynamic preference of other LiMO_2 phases to stabilize in a layered structure and, in the case of Co and Ni, to include something of the electrochemical performance of the LiMO_2 phases.

The last few years have seen an increasing emphasis on layered complex oxides of manganese with Cr, Co and Ni which are “lithium-rich”, i.e. where the molar ratio of lithium to transition metal is higher than one. A general trend is that “lithium-rich” solid solution compositions are easier to prepare than stoichiometric $\text{LiMn}_{1-x}\text{M}_x\text{O}_2$ compounds, and the “lithium-rich” materials have improved electrochemical properties. It is now clear that these properties, which include improved rate capability and better structural stability on cycling, are associated with a stable tetravalent state for manganese.

The ability of the layered rock salt structure of complex oxides to absorb an excess of Li ions is associated with Mn, because Mn is able to adopt a tetravalent oxidation state in the as-prepared compounds to compensate the charge. The excess Li ions appear in the transition metal layer, as observed for Li_2MnO_3 . The chemistry of these lithium-rich layered oxides therefore relates to the crystal chemistry of Li_2MnO_3 . As already explained in Section 13.2.4, Li_2MnO_3 is an easily prepared layered oxide $\text{Li}[\text{Li}_{1/3}\text{Mn}_{2/3}]\text{O}_2$ in which cation planes alternate as lithium layers and layers which are one-third lithium and two-thirds manganese. Ammundsen and Paulsen⁵⁰ proposed a useful classification of solid solution layered oxides based on manganese according to their position within the triangle

$\text{Li}[\text{Li}_{1/3}\text{Mn}_{2/3}]\text{O}_2 - \text{LiMnO}_2 - \text{LiMO}_2$, shown in Figure 13.4. Solid solutions on the line between LiMnO_2 and LiMO_2 (*i.e.* $\text{Li}[\text{Mn}_x\text{M}_{1-x}]\text{O}_2$), where the Li/transition metal ratio is equal to one, are denoted “lithium stoichiometric”. Solid solutions on the line between Li_2MnO_3 and LiMO_2 (*i.e.* $\text{Li}[\text{Mn}_x\text{Li}_{x/2}\text{M}_{1-3x/2}]\text{O}_2$), where the maximum amount of Li is incorporated into the transition metal layers, are denoted “lithium saturated”. Solid solutions within the triangle (*i.e.* $\text{Li}[\text{Li}_y\text{Mn}_x\text{M}_{1-x-y}]\text{O}_2$ with $y < x/2$), where different amounts of Li are incorporated into the transition metal layers, are called “lithium-rich”. The metal M in LiMO_2 can be a single species, or a mixture of transition metals such as Ti, Cr, Co, Ni or Fe, and/or non-transition metals such as Mg, Al, or Ga. A number of these systems will be described in this section.

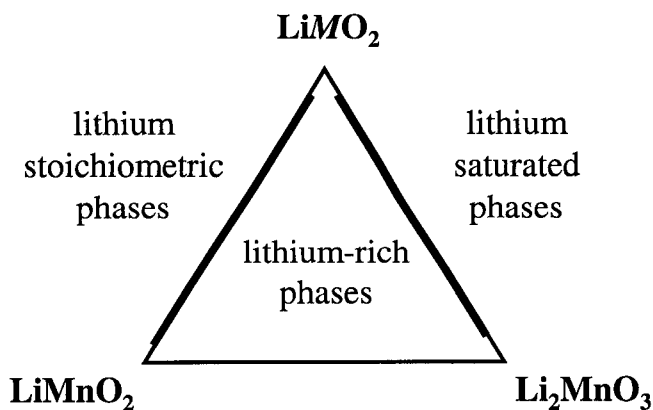


Figure 13.4. The $\text{Li}_2\text{MnO}_3 - \text{LiMnO}_2 - \text{LiMO}_2$ solid solution system showing the classification of phases according to their lithium stoichiometry.

All compounds within the phase triangle shown in Figure 13.4 obey the rules described by Dahn *et al.* for these layered rock salt solid solution phases.⁵¹ Firstly, the sum of the cation occupations on the sites in the transition metal layers (the 3b sites in the space group $R\bar{3}m$) is equal to one. Secondly, the sum of the cation oxidation state times the cation occupations of the transition metal layer sites equals three.

It should be noted that the results of different investigations into solid solutions over the past decade have shown considerable variation, depending strongly on the conditions used to prepare the materials. These variations can

lead to some confusion about the intrinsic performance of certain chemistries. A general trend in complex layered oxides based on solid solutions is that solid state reactions using simple binary oxides or salts as starting materials often do not lead to the desired phases or to phases with the desired electrochemical activity. Increasingly, more complex synthesis methods are applied, such as sol-gel, coprecipitation, or ball milling methods, which allow the preparation of well-mixed solid solution phases with superior electrochemical performance.

Another important factor influencing the outcome of any solid solution preparation is the conditions of temperature and atmosphere used. Solid solutions based on trivalent Mn tend to only be achievable using oxygen-free atmospheres, but oxygen-free atmospheres are not normally good conditions for forming materials with trivalent Co or Ni. On the other hand, solid solutions based on tetravalent Mn are easily achieved in air atmospheres, up to 1000°C.

The examples that follow have in common that the as-prepared materials contain tetravalent Mn in combination with a high proportion of one or more other, redox-active, elements. In these materials the Mn remains stable in the tetravalent state during charge and discharge, while the other element(s) change(s) oxidation state. The situation is therefore very different from the compounds described in preceding sections, which depend on the reversible oxidation of Mn^{3+} to Mn^{4+} for their activity as lithium-ion cathode materials. The Mn in the materials described in this section therefore takes a passive role as a framework element, providing an inert and stable matrix for the overall material. The resulting materials benefit from the manganese oxide component in terms of cost, thermal stability and safety, without suffering from the structural instabilities associated with trivalent Mn. This approach of developing solid solution materials based on tetravalent manganese therefore shows highest promise for practical application of the “layered manganese oxide” concept.

13.4.2. Solid Solutions with LiCrO_2

One of the first demonstrations of the improvement in electrochemical properties that can be gained through “lithium-rich” preparations was in solid solutions with LiCrO_2 .

As described in Section 13.3.3, Davidson *et al.* showed that single-phase layered materials could be made in the solid solution $(1-x)\text{LiMnO}_2 - x\text{LiCrO}_2$ for any value of x down to $x=0.05$, providing the preparations are made under oxygen-free atmospheres.^{38,39} Practically the whole solid solution range is achievable because the mechanism is a simple substitution of Mn^{3+} for Cr^{3+} . Compounds with $x < 0.7$ crystallize in the monoclinic $C2/m$

layered structure, showing clearly that the Mn in these compounds is trivalent, producing a Jahn-Teller cooperative distortion. Only compounds with $x \geq 0.7$ adopt the layered $R\bar{3}m$ structure of LiCrO_2 , due to sufficient dilution of Mn^{3+} ions to prevent cooperative ordering of the distorted MnO_6 octahedra. (Dahn *et al.* have shown that materials with $0.5 < x < 0.75$ can be prepared with hexagonal layered structures by using sol-gel precursors and lower synthesis temperatures of 700°C ,⁵² but it is likely that these lower temperature preparations result in cation vacancies compensated by some Mn^{4+}).

Cathode materials in the solid solution $\text{LiMnO}_2 - \text{LiCrO}_2$ undergo nearly complete delithiation on first charge, similar to that observed for the monoclinic LiMnO_2 materials described in Section 13.3. This indicates that both Mn and Cr are oxidized from 3+ to 4+ states in these materials. During first charge any monoclinic phase is first converted to hexagonal phase, and then the hexagonal phase is delithiated in a single-phase process. The disappearance of monoclinic phase in the first part of charge suggests that Mn^{3+} is oxidized before Cr^{3+} . Materials of composition around the mid-member of the $\text{LiMnO}_2 - \text{LiCrO}_2$ solid solution, $\text{LiCr}_{0.5}\text{Mn}_{0.5}\text{O}_2$, can be cycled with reversible capacities around 150 mAh/g between 4.4 and 2.5 V, delivered in a sloping discharge profile with an average voltage of about 3.3 V. However the capacity drops off rapidly to below 100 mA/g when current rates are increased to provide discharges over two hours or less. Furthermore, the voltage profile evolves with cycling in a manner similar to that described in Section 13.3.3 for lightly Cr-substituted LiMnO_2 . $\text{LiCr}_x\text{Mn}_{1-x}\text{O}_2$ materials with compositions $x \geq 0.75$ were found to have more stable voltage profiles with cycling, but cells containing cathodes based on these compositions show large impedance and lower capacities, <100 mAh/g even at low current rates.

The substitution of additional lithium ions into solid solutions with LiCrO_2 to give lithium-rich compositions changes and improves the structural and electrochemical properties of the materials.^{53,54} Results are particularly interesting for lithium-saturated compositions in the $\text{Li}_2\text{MnO}_3 - \text{LiCrO}_2$ system. In particular the stability of the crystal structure with cycling is markedly improved over “stoichiometric” $\text{LiMn}_{1-x}\text{Cr}_x\text{O}_2$ compositions, providing a monotonic discharge voltage profile that does not evolve with cycling. Detailed structural studies of the mid-member of the lithium saturated solid solution $\text{Li}_2\text{MnO}_3 - \text{LiCrO}_2$ (*i.e.* $\text{Li}[\text{Li}_{0.2}\text{Cr}_{0.4}\text{Mn}_{0.4}]\text{O}_2$), using XAFS and NMR, have shown that the material contains both Li_2MnO_3 -like and LiCrO_2 -like structure at the local level, although the material is single-phase to X-ray diffraction.^{55,56}

What was initially surprising is the high reversible capacities which can be achieved for lithium-saturated $\text{Li}_2\text{MnO}_3 - \text{LiCrO}_2$ materials, up to 220 mAh/g in the voltage range 4.4 – 2.5 V. Figure 13.5 shows charge

and discharge curves for the first two cycles of a $\text{Li}[\text{Li}_{0.2}\text{Cr}_{0.4}\text{Mn}_{0.4}]\text{O}_2$ material. It is clear from these curves that an irreversible process occurs on the first charge, giving rise to around 25% capacity loss that is not recovered on the first discharge. Subsequent cycling however is nearly 100% efficient, with very little capacity loss or change in voltage profile over more than 200 cycles, even at 55°C.⁵⁵

X-ray absorption spectroscopy data have shown that the high capacity obtained from these materials is due to Cr being oxidized to higher than a 4+ state during charge.^{55,57} Cycling oxidizes and reduces Cr ions between 6+ and 3+ states, while the Li_2MnO_3 component acts as an inert matrix. The Mn remains tetravalent throughout cycling, which means that Mn ions remain locked into the Li_2MnO_3 -type structure throughout charge and discharge. The situation is different from LiMnO_2 – LiCrO_2 solid solutions, where the presence of Mn^{3+} allows Mn to migrate out of the transition metal layer sites during cycling. In fact, in Li_2MnO_3 – LiCrO_2 materials it is likely that the Cr ions are the mobile species, owing to the large changes in oxidation state.

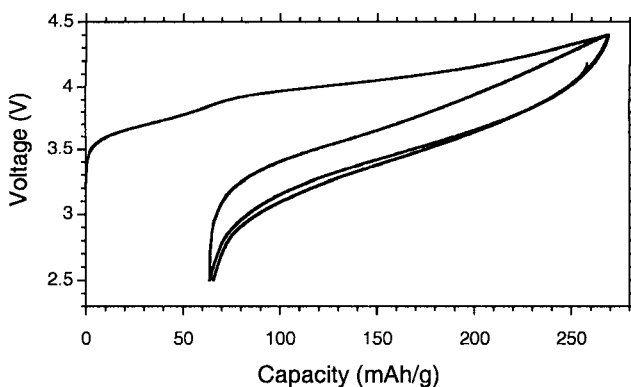


Figure 13.5. First and second cycle charge-discharge voltage curves for a material of composition $\text{Li}[\text{Li}_{0.2}\text{Cr}_{0.4}\text{Mn}_{0.4}]\text{O}_2$ cycled between 4.4 and 2.5 V (3 mA/g current rate, 25°C).

The ability of the Li_2MnO_3 -type layered matrix to support reversible oxidation of Cr between 3+ and 6+ states without significant loss of structural integrity is quite remarkable, and illustrates a significant advantage of using Li_2MnO_3 as a base for solid solution compounds rather than LiMnO_2 .

The capacity retention of Li_2MnO_3 – LiCrO_2 materials when cycled at 55°C illustrates another interesting feature of materials based on tetravalent rather than trivalent manganese. The poor cyclability of manganese oxides at

high temperatures is frequently attributed to manganese dissolution through a mechanism that requires Mn^{3+} to be present at the surface of the material. If Li_2MnO_3 is used as the solid solution, trivalent Mn ions are not present and the material is less susceptible to dissolution processes.

13.4.3. Lithium-Rich Solid Solutions with LiCoO_2

Since LiCoO_2 is the dominant commercial lithium-ion cathode product, the solid solution $\text{LiCoO}_2 - \text{LiMnO}_2$ is of obvious interest. LiCoO_2 is known to stabilize the layer structure and significantly improve the electrochemical properties of LiNiO_2 . Beneficial effects of Co substitution on the stability and rate capability of monoclinic LiMnO_2 prepared by low temperature soft chemistry methods have also been reported.³⁵ However a thermodynamically stable layered material prepared at higher temperatures based on a $\text{LiCoO}_2 - \text{LiMnO}_2$ solid solution has never been reported. This is most probably due to phase separation of spinel lithium manganese oxide phases when preparations are made in air, or of CoO when preparations are made in inert atmospheres.

On the other hand, using Li_2MnO_3 as the base of the solid solution allows stable single-phase materials to be prepared by simple high temperature processing in air.^{58,59} This is because although compounds in which both Co and Mn are trivalent cannot be prepared, LiCoO_2 can be prepared with tetravalent Mn in combination with charge-compensating Li in the transition metal layer.

However the solid solution $\text{Li}_2\text{MnO}_3 - \text{LiCoO}_2$ differs in one important regard from the $\text{Li}_2\text{MnO}_3 - \text{LiCrO}_2$ system. Unlike Cr, the oxidation state achievable by Co on charge is limited to Co^{4+} . This represents a basic limitation in realizable capacity for the $\text{Li}_2\text{MnO}_3 - \text{LiCoO}_2$ system. For the mid-member $\text{Li}[\text{Li}_{0.2}\text{Co}_{0.4}\text{Mn}_{0.4}]\text{O}_2$ the maximum capacity that could be expected would be around 125 mAh/g, corresponding to 0.4 moles of Li extracted, at which point both Co and Mn would be in their maximum achievable oxidation states of 4+. The achievable capacities reported in practice have been lower, and the system is therefore of less interest for practical applications.

13.4.4. Solid Solutions with LiNiO_2 and $\text{LiCo}_x\text{Ni}_{1-x}\text{O}_2$

Unlike the $\text{LiCoO}_2 - \text{LiMnO}_2$ system, single-phase compositions can be prepared in the $(1-x)\text{LiNiO}_2 - x\text{LiMnO}_2$ system up to $x=0.5$. Solid solution materials of this type were first investigated by Rossen *et al.*,⁶⁰ who reported reversible capacities of around 150 mAh/g in the voltage range

4.3 – 2.5 V, delivered in a smooth sloping discharge profile, although with significant rate limitations. Spahr *et al.*⁶¹ described $\text{LiMn}_{0.5}\text{Ni}_{0.5}\text{O}_2$ prepared by an oxidative coprecipitation process which showed similar characteristics, but cycling data reported for the material showed poor capacity retention. Ohzuku *et al.*⁶² and Lu *et al.*⁶³ have recently reported data for layered $\text{LiMn}_{0.5}\text{Ni}_{0.5}\text{O}_2$ materials prepared from coprecipitated precursors of Ni and Mn salt, calcined and then sintered at temperatures of 1000°C and 900°C, respectively. The resulting materials again show smooth discharge voltage profiles, and reversible capacities between 150 and 180 mAh/g, depending on charge voltage cutoff and discharge current rate.

It is interesting to understand why compositions in the solid solution $\text{LiNiO}_2 - \text{LiMnO}_2$ can be prepared up to $x=0.5$, while $\text{LiCoO}_2 - \text{LiMnO}_2$ materials cannot be synthesized. It now seems that the answer lies in different oxidation states that Co and Ni ions prefer to adopt when sharing the LiMO_2 lattice with Mn. Recent theoretical calculations [64], as well as X-ray absorption and NMR data,⁶⁵ have shown that the Ni in $\text{LiMn}_{0.5}\text{Ni}_{0.5}\text{O}_2$ is mainly divalent, while the Mn is tetravalent. Substitution of Mn into LiNiO_2 therefore takes place with Mn going into the lattice as Mn^{4+} , requiring reduction of an equivalent number of Ni^{3+} ions to Ni^{2+} . This process explains why substitution is limited to a maximum Mn/Ni ratio of 1. Presumably Mn cannot be easily substituted into LiCoO_2 because the $\text{Co}^{2+}/\text{Mn}^{4+}$ oxidation states are not adopted. The chemistry of the $\text{LiMnO}_2 - \text{LiNiO}_2$ system is also different from that of $\text{LiMnO}_2 - \text{LiCrO}_2$, where Mn^{3+} substitutes for Cr^{3+} across the full solid solution range. And because Mn substitutes into LiNiO_2 as Mn^{4+} rather than Mn^{3+} , the resulting as-prepared materials retain hexagonal symmetry, whereas stoichiometric materials in the $x\text{LiMnO}_2 - (1-x)\text{LiCrO}_2$ solid solution adopt a monoclinic symmetry above $x=0.3$ due to the trivalent Mn ions.

The important consequence of the $\text{Mn}^{4+}/\text{Ni}^{2+}$ oxidation state of $\text{LiMn}_{0.5}\text{Ni}_{0.5}\text{O}_2$ is that Mn remains stable in the tetravalent state during cycling of the material. The reversible capacity is due to oxidation and reduction of Ni between the 2+ and 4+ states. $\text{LiMn}_{0.5}\text{Ni}_{0.5}\text{O}_2$ materials can therefore be cycled without conversion from a layered to a spinel-type crystal structure. As with $\text{Li}_2\text{MnO}_3 - \text{LiCrO}_2$ solid solution materials, $\text{LiMn}_{0.5}\text{Ni}_{0.5}\text{O}_2$ remains kinetically stable against transformation to spinel because Mn is not present in oxidation states lower than 4+. An advantage of the $\text{LiMnO}_2 - \text{LiNiO}_2$ system is that oxidation of Ni^{2+} to Ni^{4+} can occur without changes in the Ni site, whereas the oxidation of Cr^{3+} to Cr^{6+} results in displacements of Cr due to the preference of Cr^{6+} for a tetrahedral rather than an octahedral coordination.

Another interesting feature of the $\text{LiMn}_{0.5}\text{Ni}_{0.5}\text{O}_2$ materials is that the voltage curves are almost identical to those of LiNiO_2 , although different redox couples are active. In $\text{LiMn}_{0.5}\text{Ni}_{0.5}\text{O}_2$, the charge and discharge capacities can only be explained by a reversible oxidation of Ni^{2+} to Ni^{4+} ,

whereas in LiNiO_2 Ni cycles between 3+ and 4+ oxidation states. Hence the potential for $\text{LiMn}_{0.5}\text{Ni}_{0.5}\text{O}_2$ might be expected to be lower than for LiNiO_2 . Even if Mn participated in the redox process the higher potential would be difficult to explain, since the redox potential of $\text{Mn}^{3+}/\text{Mn}^{4+}$ is below that of $\text{Ni}^{3+}/\text{Ni}^{4+}$. Theoretical calculations have suggested that the surprisingly high potential for the $\text{Ni}^{2+}/\text{Ni}^{4+}$ redox in $\text{LiMn}_{0.5}\text{Ni}_{0.5}\text{O}_2$ may be due to changes in the Mn-Ni interactions as the oxidation states change from 4+/2+ to 4+/4+.⁶⁴ In the lattice containing Mn^{4+} and Ni^{2+} the Mn-Ni interactions are essentially attractive, while they are repulsive for Mn^{4+} - Ni^{4+} , effectively introducing an additional energy term for the intercalation of Li that would increase the potential.

Materials of composition $\text{LiNi}_{0.5}\text{Mn}_{0.5}\text{O}_2$ have however proven difficult to prepare reliably, and often show evidence of spinel lithium manganese oxide secondary phases. It is also difficult to prevent Ni^{2+} ions from appearing in the Li layers, which degrades the performance of the materials as cathodes. Incorporating excess Li has been shown to address both these problems.^{63,66,67} The main benefit of lithium rich compositions is an improvement in the ordering of the layered structure compared with the stoichiometric materials, *i.e.* less transition metal (mainly Ni^{2+}) on lithium layers. Best results have been achieved for phases with a limited amount of excess lithium. In the $\text{Li}_2\text{MnO}_3 - \text{LiMnO}_2 - \text{LiNiO}_2$ system there is basically a balance between increasing the quantity of Li_2MnO_3 , to obtain improved layer character, and not adding so much that the capacity of the material is lowered below practical values. On the other hand, an interesting feature of the lithium-rich compositions is that if the cathodes are first charged to a relatively high voltage, an irreversible plateau appears at around 4.5 V at capacities beyond that which can be accounted for by oxidation of all the Ni to Ni^{4+} .⁶³ The length of the plateau seems to be correlated to the amount of lithium in the transition metal layer. The plateau disappears during subsequent cycles, but allows higher capacities to be achieved in subsequent cycling by reversible insertion of some additional Li around 3.3 V, correlating with reduction of a portion of the Mn^{4+} to Mn^{3+} .

Solid solutions in the $\text{Li}_2\text{MnO}_3 - \text{LiMnO}_2 - \text{LiNiO}_2$ system have also been investigated when Co is introduced.^{51,66,67} In fact, even though $\text{LiCoO}_2 - \text{LiMnO}_2$ materials cannot be prepared, it is possible to substitute Co into lithium-stoichiometric $\text{LiMnO}_2 - \text{LiNiO}_2$ materials. The result is particularly effective when the Mn/Ni ratio is maintained equal to 1, giving materials of capability, and improved cyclability. In this case the Co serves a similar role as it does in $\text{LiCo}_x\text{Ni}_{1-x}\text{O}_2$ materials. Ohzuku *et al.* have shown particularly good electrochemical results for the composition $\text{Li}[\text{Co}_{1/3}\text{Mn}_{1/3}\text{Ni}_{1/3}]\text{O}_2$, where it is assumed that the transition metal ions are ordered in a "superlattice" structure.^{62,69}

Paulsen *et al.* have shown that lithium-rich formulations in the $\text{Li}_2\text{MnO}_3 - \text{LiMnO}_2 - \text{LiNiO}_2$ system also benefit from addition of Co.^{66,67}

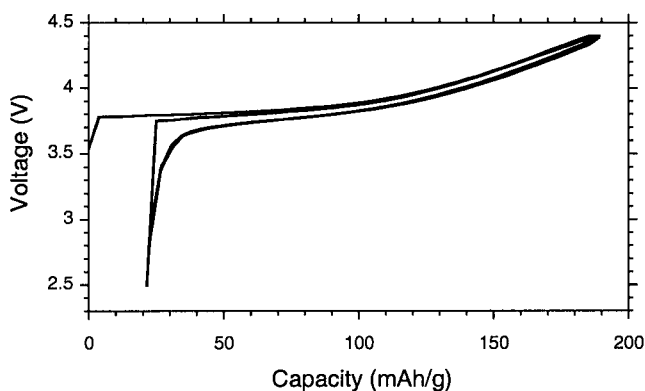


Figure 13.6. First and second cycle charge-discharge voltage curves for a material of composition $\text{Li}[\text{Li}_{0.05}\text{Co}_{0.15}\text{Mn}_{0.4}\text{Ni}_{0.4}]\text{O}_2$ cycled between 4.4 and 2.5 V (30 mA/g current rate, 25°C).

These complex oxides contain Co^{3+} , Mn^{4+} , Ni^{2+} and Ni^{3+} . As with lithium-stoichiometric compositions, good electrochemical results have been obtained for materials in which the Mn/Ni ratio is near to 1. Again, the effect of the Co is to further improve the layered structure, and consequently the reversible capacity, rate capability, and cyclability. Representative first cycle charge and discharge profiles are shown in Figure 13.6 for a lithium-rich composition comprising approximately 15% Co.

Materials based on the $\text{Li}_2\text{MnO}_3 - \text{LiMnO}_2 - \text{LiNiO}_2$ solid solution system show attractive characteristics for practical applications as cathodes in lithium-ion batteries. The manganese component inherently lowers the cost of production relative to cobaltates and nickelates. The capacities which can be achieved in a lithium-ion cell are close to those of LiCoO_2 in a similar operating voltage range. Unlike LiCoO_2 and $\text{LiCo}_x\text{Ni}_{1-x}\text{O}_2$ materials which require strict voltage control to prevent charge above 4.2 V for safety and stability reasons, it has been shown that cells containing cathode materials in the $\text{Li}_2\text{MnO}_3 - \text{LiMnO}_2 - \text{LiNiO}_2$ solid solution system, both with and without addition of Co, can be charged to higher voltages without compromising safety, thereby allowing higher capacities to be achieved. The thermal stability of the charged cathodes in contact with electrolyte has been demonstrated by both DSC and ARC measurements.^{51,63,66-68} Remarkably, as little as 5% $[\text{Mn}_{0.5}\text{Ni}_{0.5}]$ in LiCoO_2 has been found to significantly improve the thermal stability relative to LiCoO_2 .⁶⁸ The impressive safety characteristics, derived from the Mn component, make these types of materials particularly attractive for use in larger battery formats.

The impressive electrochemical properties of these types of materials, markedly superior to that currently provided by LiMnO_2 materials, means

that they are likely to be the first “layered manganese oxide” materials to be used in commercial applications.

13.4.5. Further Work

The advantages of preparing solid solution materials based on tetravalent rather than trivalent manganese have been demonstrated for a number of compositions. In these materials Mn has given up its role as an electrochemically active center and is present as a stabilizing framework element. Based on this concept, other innovative cathode materials could be engineered. It has been pointed out that other elements that can take on the 4+ oxidation state in layered oxides might also be selected on the basis of cost, weight, processability and non-toxicity, as a substitute for Mn, taking the role of stabilizing component.⁶⁴ An example of such an approach has been reported using a small amount of Li_2TiO_3 , which is isostructural with Li_2MnO_3 , to stabilize layered $\text{LiMn}_{0.5}\text{Ni}_{0.5}\text{O}_2$.⁷⁰

13.5. SUMMARY AND OUTLOOK

Technological interest in manganese-based cathode materials will continue as battery manufacturers seek to distinguish their products in an increasingly competitive market by lower pricing, improved safety and lower toxicity, as well as increased energy density and performance. Furthermore, over the next few years manufacturers will seek to deliver lithium-ion batteries into new markets beyond portable electronics, and in particular into markets requiring larger cells and batteries. The cost and safety requirements of large cells are likely to require a manganese-based cathode solution. Although intensive efforts are still under way to commercialize batteries using spinel lithium manganese oxide, alternative manganese-based materials that can offer improvements in capacity and cycling stability will be required to be competitive in commercial applications.

Although layered LiMnO_2 materials offer the higher capacity, their major drawback remains the structural instability against transformation towards disordered spinel structures, low density, and/or poor rate capability. Light substitution helps to improve the electrochemical properties, but the fundamental instability associated with the trivalent Mn is still a problem.

Solid solution materials using a stable tetravalent manganese oxide matrix to enhance the structural stability during cycling represent the most likely near-term solution for commercialization of the “layered lithium manganese oxide” concept. In particular, layered complex oxides in the

$\text{Li}_2\text{MnO}_3 - \text{LiMnO}_2 - \text{LiNiO}_2$ system, with or without added cobalt, show strong near-term promise with competitive capacities, good cycling stability, and smooth voltage profiles with high average voltage. These materials offer significant cost and safety advantages over materials such as LiCoO_2 and $\text{LiCo}_x\text{Ni}_{1-x}\text{O}_2$.

REFERENCES

1. F. Capitaine, P. Gravereau, C. Delmas, *Solid State Ionics* 89 (1996) 197.
2. A. R. Armstrong, P. G. Bruce, *Nature* 381 (1996) 499.
3. M. Tabuchi, K. Ado, H. Kobayashi, H. Kageyama, C. Masquelier, A. Kondo, R. Kanno, *J. Electrochem. Soc.* 145 (1998) L49.
4. G. Ceder, S.K. Mishra, *Electrochem. Solid-State Lett.* 2 (1999) 550.
5. G. Ceder, A. Van der Ven, *Electrochim. Acta.* 45 (1999) 131.
6. C. Wolverton, A. Zunger, *J. Electrochem. Soc.* 145 (1998) 2424.
7. J. Reed, G. Ceder, A. Van Der Ven, *Electrochem. Solid-State Lett.* 4 (2001) A78.
8. G. Vitins, K. West, *J. Electrochem. Soc.* 144 (1997) 2587.
9. I. M. Koetschau, J. R. Dahn, *J. Electrochem. Soc.* 145 (1998) 2672.
10. Y. Shao-Horn, S. A. Hackney, A. R. Armstrong, P. G. Bruce, R. Gitzendanner, C. S. Johnson, M. M. Thackeray, *J. Electrochem. Soc.* 146 (1999) 2404.
11. S.-J. Hwang, H.-S. Park, J.-H. Choy, G. Campet, *Chem. Mater.* 12 (2000) 1818.
12. Y.-I. Jang, B. Huang, H. Wang, D. R. Sadoway, Y.-M. Chiang, *J. Electrochem. Soc.* 146 (1999) 3217.
13. H. Wang, Y.-I. Jang, Y.-M. Chiang, *Electrochem. Solid State Lett.* 2 (1999) 490.
14. J. M. Paulsen, C. L. Thomas, J. R. Dahn, *J. Electrochem. Soc.* 146 (1999) 3560.
15. C. Delmas, J. Braconnier, A. Maazaz, P. Hagenmueller, *Rev. Chim. Miner.* 19 (1982) 343.
16. J. M. Paulsen, C. L. Thomas, J. R. Dahn, *J. Electrochem. Soc.* 147 (2000) 861.
17. Z. Lu, R. A. Donabarger, C. L. Thomas, J. R. Dahn, *J. Electrochem. Soc.* 149 (2002) A1083.
18. R. Chen, M. S. Whittingham, *J. Electrochem. Soc.* 144 (1997) L64.
19. M. H. Rossouw, M. M. Thackeray, *Mater. Res. Bull.* 26 (1991) 463.
20. C. S. Johnson, S. D. Korte, J. T. Vaughey, M. M. Thackeray, T. E. Bofinger, Y. Shao-Horn, S. A. Hackney, *J. Power Sources* 81-82 (1999) 491.
21. Y. Paik, C. P. Grey, C. S. Johnson, J.-S. Kim, M. M. Thackeray, *Chem. Mater.* (2002) in press.
22. T. Ohzuku, A. Ueda, T. Hirai, *Chem. Express* 7 (1992) 193.
23. J. N. Reimers, E. W. Fuller, E. Rossen, J. R. Dahn, *J. Electrochem. Soc.* 140 (1993) 3396.
24. I. Koetschau, M. N. Richard, J. R. Dahn, J. B. Soupart, J.-C. Rousche, *J. Electrochem. Soc.* 142 (1995) 2906.
25. R. J. Gummow, D. C. Liles, M. M. Thackeray, *Mater. Res. Bull.* 28 (1993) 1249.
26. I. J. Davidson, R. S. McMillan, J. J. Murray, J. E. Greedan, *J. Power Sources* 54 (1995) 232.
27. L. Croguennec, P. Deniard, R. Brec, A. Lecerf, *J. Mater. Chem.* 5 (1995) 1919.
28. L. Croguennec, P. Deniard, R. Brec, P. Biensan, M. Broussely, *Solid State Ionics* 89 (1996) 127.
29. L. Croguennec, P. Deniard, R. Brec, *J. Electrochem. Soc.* 144 (1997) 3323.

30. L. Croguennec, P. Deniard, R. Brec, A. Lecerf, *J. Mater. Chem.* 7 (1997) 511.
31. Y.-I. Jang, B. Huang, H. Wang, D. R. Sadoway, Y.-M. Chiang, *ECS Meeting Abstracts Vol. MA 98-2* (1998) p.132.
32. C. Delmas, J. Braconnier, P. Hagenmueller, *Mater. Res. Bull.* 17 (1982) 117.
33. A. Mendiboure, C. Delmas, P. Hagenmueller, *Mater. Res. Bull.* 19 (1984) 1383.
34. B. Fuchs, S. Kemmler-Sack, *Solid State Ionics* 68 (1994) 279.
35. A. R. Armstrong, R. Gitzendanner, A. D. Robertson, P. G. Bruce, *Chem. Commun.* (1998) 1833.
36. T. E. Quine, M. J. Duncan, A. R. Armstrong, A. D. Robertson, P. G. Bruce, *J. Mater. Chem.* 10 (2000) 2838.
37. F. Coowar, *PCT International Publication No. WO 00/15557* (2000).
38. I. J. Davidson, R. S. McMillan, J. J. Murray, *J. Power Sources* 54 (1995) 205.
39. I. J. Davidson, R. S. McMillan, H. Slegr, B. Luan, I. Kargina, J. J. Murray, I. P. Swainson, *J. Power Sources* 81-82 (1999) 406.
40. Y.-I. Jang, B. Huang, Y.-M. Chiang, D. R. Sadoway, *Electrochem. Solid-State Lett.* 1 (1998) 13.
41. Y.-M. Chiang, D. R. Sadoway, Y.-I. Jang, B. Huang, H. Wang, *Electrochem. Solid-State Lett.* 2 (1999) 107.
42. B. Ammundsen, J. Desilvestro, T. Groutso, D. Hassell, J. B. Metson, E. Regan, R. Steiner, P. J. Pickering, in *New Materials for Batteries and Fuel Cells*, D. H. Dougherty, L. F. Nazar, M. Arakawa, H.-P. Brack, K. Naoi, Eds., *Mat. Res. Soc. Symp. Proc. Vol. 575*, Materials Research Society (2000), pp 49-58.
43. B. Ammundsen, J. Desilvestro, T. Groutso, D. Hassell, J. B. Metson, E. Regan, R. Steiner, P. J. Pickering, *J. Electrochem. Soc.* 147 (2000) 4078.
44. B. Ammundsen, W. Gao, D. Hassell, Z.-Y. Liu, J. B. Metson, R. Steiner, P. J. Pickering, *PCT International Publication No. WO 00/23380* (2000).
45. S.-J. Hwang, H.-S. Park, J.-H. Choy, G. Campet, *J. Phys. Chem. B* 104 (2000) 7612.
46. S. Choi, A. Manthiram, *J. Electrochem. Soc.* 149 (2002) A1157.
47. J. M. Paulsen, R. A. Donaberger, J. R. Dahn, *Chem. Mater.* 12 (2000) 2257.
48. Z. Lu, R. A. Donaberger, J. R. Dahn, *Chem. Mater.* 12 (2000) 3583.
49. Z. Lu, J. R. Dahn, *J. Electrochem. Soc.* 148 (2001) A237.
50. B. Ammundsen, J. M. Paulsen, *Adv. Mater.* 13 (2001) 943.
51. Z. Lu, D. D. MacNeil, J. R. Dahn, *Electrochem. Solid-State Lett.* 4 (2001) A200.
52. J. R. Dahn, T. Zheng, C. L. Thomas, *J. Electrochem. Soc.* 145 (1998) 851.
53. C. Storey, I. Kargina, Y. Grincourt, I. J. Davidson, Y. Yoo, D. Y. Seung, *J. Power Sources* 97-98 (2001) 541.
54. Y. Grincourt, C. Storey, I. J. Davidson, *J. Power Sources* 97-98 (2001) 711.
55. B. Ammundsen, J. Paulsen, I. Davidson, R.-S. Liu, C.-H. Shen, J.-M. Chen, L.-Y. Jang, J.-F. Lee, *J. Electrochem. Soc.* 149 (2002) A431.
56. C. Pan, Y. J. Lee, B. Ammundsen, C. P. Grey, *Chem. Mater.* 14 (2002) 2289.
57. M. Balasubramanian, J. McBreen, I. J. Davidson, P. S. Whitfield, I. Kargina, *J. Electrochem. Soc.* 149 (2002) A176.
58. K. Numata, C. Sakaki, S. Yamanaka, *Chem. Lett.* (1997) 725.
59. K. Numata, C. Sakaki, S. Yamanaka, *Solid State Ionics* 117 (1999) 257.
60. E. Rossen, C. D. W. Jones, J. R. Dahn, *Solid State Ionics* 57 (1992) 311.
61. M. E. Spahr, P. Novak, B. Schnyder, O. Haas, R. Nesper, *J. Electrochem. Soc.* 145 (1998) 1113.
62. T. Ohzuku, Y. Makimura, *Chem. Lett.* (2001) 642.
63. Z. Lu, D. D. MacNeil, J. R. Dahn, *Electrochem. Solid-State Lett.* 4 (2001) A191.
64. J. Reed, G. Ceder, *Electrochem. Solid-State Lett.* 5 (2002) A145.

65. W.-S. Yoon, Y. Paik, X.-Q. Yang, M. Balasubramanian, J. McBreen, C. P. Grey, *Electrochem. Solid-State Lett.* 5 (2002) A263.
66. J. M. Paulsen, B. Ammundsen, L. Kieu, European Patent Application No. EP 1 189 296 A2 (2002).
67. J. M. Paulsen, B. Ammundsen, S. Argue, *11thIMLB*, Abstract 208, Monterey, CA (2002).
68. D. D. MacNeil, Z. Lu, S. D. Beattie, G. D. Murphy, J. R. Dahn, *11thIMLB*, Abstract 109, Monterey, CA (2002).
69. Y. Koyama, I. Tanaka, H. Adachi, Y. Makimura, N. Yabuuchi, T. Ohzuku, *11thIMLB*, Abstract 121, Monterey, CA (2002).
70. C. S. Johnson, J.-S. Kim, A. J. Croft, A. J. Kahaian, J. T. Vaughey, M. M. Thackeray, *Electrochem. Comm.* 4 (2002) 492.

Chapter 14

CATHODES BASED ON LiCoO_2 AND LiNiO_2

Byungwoo Park¹, Yong Jeong Kim¹, and Jaephil Cho²

¹*School of Materials Science and Engineering, and Research Center for Energy Conversion and Storage, Seoul National University, Seoul, Korea*

²*Department of Applied Chemistry, Kumoh National Institute of Technology, Gumi, Korea*

14.1. LiCoO_2 CATHODE MATERIALS

14.1.1. Introduction

Li-ion cells consisting of LiMeO_2 (Me: a 3d-transition metal element) and carbon materials have been of interest because of their capability to be safely operated for thousands of cycles whilst retaining a high energy density. Materials with the above formula more extensively examined for positive electrodes include LiCoO_2 , LiNiO_2 , $\text{LiCo}_{1-x}\text{Ni}_x\text{O}_2$, and LiMnO_2 . Among these, more research has been done on LiCoO_2 because of its high energy density and good cycling performance. The electrochemical properties of cathodes based on LiCoO_2 are shown in Table 14.1.¹⁻⁵ LiCoO_2 has served as an archetypal cathode material for secondary Li batteries ever since the discovery by Mizushima *et al.*⁶ that Li can be reversibly removed (deintercalated) from and reinserted (intercalated) into Li_xCoO_2 . The layered form of LiCoO_2 , which has a rhombohedral symmetry belonging to the space group $R\bar{3}m$, is ideally suited to accommodate large changes of the Li content, x . This crystal structure consists of close-packed oxygen layers stacked in an $ABCABC$ sequence with Co and Li ions residing in octahedral sites in alternating layers between the oxygen planes.⁷ Figure 14.1 illustrates the crystal structure of LiCoO_2 . As the Li concentration is changed in Li_xCoO_2 , vacancies are either created or filled within the Li planes.

Table 14.1. Cycling stability of cathodes based on LiCoO_2 .

Cathode Material	Capacity	Voltage Range/ Current Density	Ref.
LiCoO_2	157 mAh/g (initial)	4.35 - 2.5 V	1
	120 mAh/g (50 cycles)	0.4 mA/cm ²	
	151 mAh/g (initial)	4.3 - 3.0 V	2
	128 mAh/g (30 cycles)	0.5 mA/cm ²	
$\text{LiAl}_{0.25}\text{Co}_{0.75}\text{O}_2$	127 mAh/g (initial)	4.5 - 2.0 V	3
	64 mAh/g (9 cycles)	0.4 mA/cm ²	
	80 mAh/g (initial)	4.3 - 2.5 V	4
	35 mAh/g (10 cycles)	0.4 mA/cm ²	
$\text{LiMg}_{0.05}\text{Co}_{0.95}\text{O}_2$	143 mAh/g (initial)	4.3 - 3.0 V	2
	125 mAh/g (30 cycles)	0.5 mA/cm ²	
	158 mAh/g (initial)	4.3 - 2.9 V	5
	141 mAh/g (30 cycles)	0.5 mA/cm ²	

Li_xCoO_2 exhibits many of the essential properties required for a reliable cathode material. The voltage of Li_xCoO_2 is sufficiently high to guarantee a high-energy density, although it is not too high to cause electrolyte decomposition. Furthermore, Li_xCoO_2 undergoes small structural changes as Li is deintercalated to a concentration of approximately 0.5. In addition to its favorable electrochemical properties, Li_xCoO_2 also exhibits phase transformations that are typical of many intercalation compounds.

Figure 14.2 shows the evolution of the lattice constants a and c as a function of x in Li_xCoO_2 , and the global phase diagram for Li_xCoO_2 .²⁸ *In-situ* X-ray diffraction indicates a sequence of three distinct phase transitions as x is varied from 1 to 0.4. Two of the transitions are situated slightly above and below $x=0.5$, and are caused by an order-disorder transition of the lithium ions.^{8,9} Reimers and Dahn,⁸ for example, observed that Li ions are ordered in rows at $x=0.5$. They carefully measured the stability region of this ordered phase and determined its order-disorder transition temperature to be approximately 60°C (Figure 14.2). The order-disorder (monoclinic-hexagonal phase) transition has been studied as a function of temperature, allowing the determination of an order-disorder diagram. The other phase transition is shown to be first order (hexagonal I + II) involving a significant expansion of the lattice constant c of the hexagonal unit cell.^{8,9}

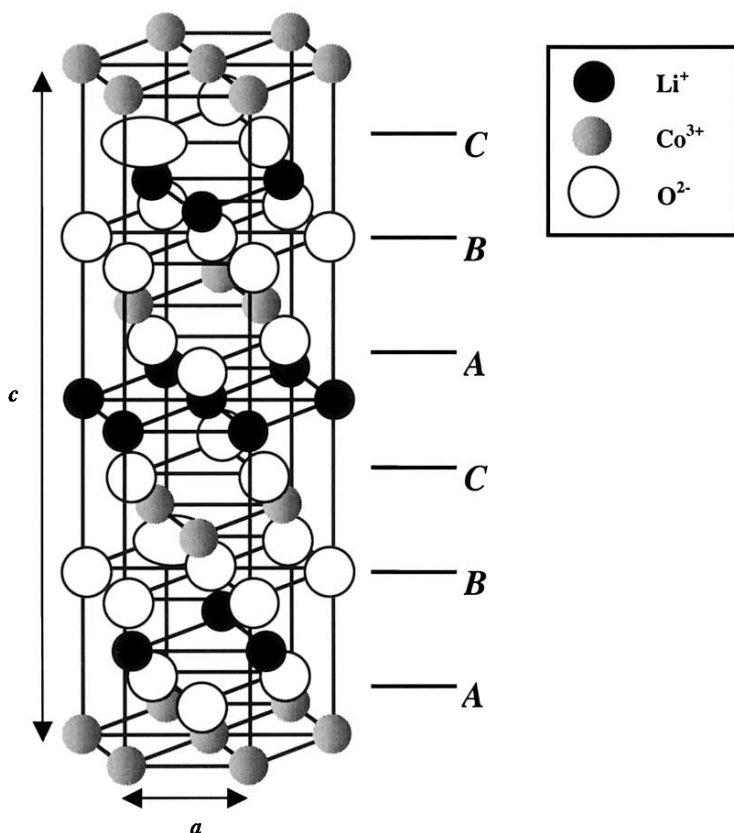


Figure 14.1. Schematic diagram of the layered LiCoO_2 structure.

Another transformation of an electronic nature occurs at a high Li concentration: LiCoO_2 is a semiconductor¹⁰ while Li_xCoO_2 at concentrations below $x=0.75$ is metallic,¹¹ suggesting that a metal-insulator transition occurs at the intermediate Li concentration. Intriguingly, superimposed on this metal-insulator transition is the two-phase coexistence region between two crystallographically identical host hexagonal structures. At room temperature, this two-phase coexistence region is found to exist between the Li concentrations of $x=0.75$ and 0.93 ,^{8,9} as shown in Figure 14.2. Amatucci *et al.*¹² reported that Li_xCoO_2

can be completely and reversibly deintercalated to form CoO_2 . They found that in the CoO_2 phase the different O-Co-O slabs, held together by van der Waals forces, slide with respect to each other, so that the close-packed oxygen layers have an *ABAB* stacking sequence, as opposed to the *ABCABC* sequence of LiCoO_2 .

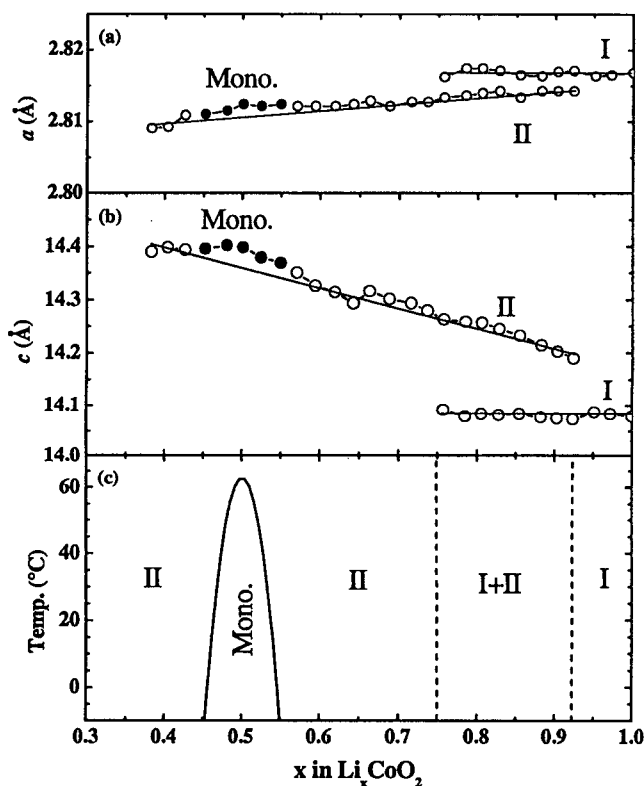


Figure 14.2. Lattice constants a (a) and c (b) as a function of the lithium concentration, x , in Li_xCoO_2 . (c) Phase diagram for Li_xCoO_2 (Ref. 8).

14.1.2. Capacity Fading Mechanisms in LiCoO_2 Cathode Materials

The theoretical capacity of a LiCoO_2 cathode is 274 mAh/g. However, in practical cells, the capacity is limited to about 140 mAh/g. This value corresponds to the range $0.5 < x < 1$ in Li_xCoO_2 , with the cutoff voltage of approximately 4.2 V (with respect to a Li metal). To achieve more than 50% of its theoretical capacity, one must charge the Li_xCoO_2 to above 4.2 V. However, this generally causes a rapid loss of capacity with increasing cycle number. Cycling above 4.2 V leads to a dramatic increase in the capacity fade, which has been closely related to structural changes involving a decrease in the unit-cell volume,^{1,13-19} and an increase of cobalt dissolution into the electrolyte.²⁰

As shown in Figure 14.2 [(a) and (b)], the lattice constant a shows only minor changes during Li deintercalation. This is quite the opposite to the lattice constant c , which exhibits an expansion of up to 2-3% at $x \approx 0.5$, followed by a decrease for larger x .^{9,12} Therefore, the lattice strain is both anisotropic and directly correlated with the lithium concentration. A LiCoO_2 cathode, like most oxides, can tolerate some elastic strain prior to fracture.¹ This property has been mainly attributed to the mechanical failure associated with the large lattice expansion along the c axis direction. Figure 14.3 shows individual highly-strained particles where microcracks are clearly visible (indicated by arrows), after 50 cycles between 2.5 and 4.35 V.¹ It is also observed that the fractured particles sometimes contain an unstrained region, apparently relieved from the stress by the fracture event (Figure 14.3(b)).

LiCoO_2 /liquid electrolyte/Li cells were cycled to upper voltages in the range 4.1 - 4.5 V. The cells were then floated at each voltage for two weeks to allow the system to reach equilibrium. The cells were disassembled and quantitatively analyzed for the presence of cobalt on the anode through the use of atomic absorption spectroscopy. Figure 14.4 shows that for voltages of 4.1 and 4.2 V versus Li metal, cobalt dissolution in the liquid electrolyte (1 M LiPF_6 in ethylene carbonate (EC): dimethyl carbonate (DMC) (67:33 vol.%)) is very low, as is the capacity fade.²⁰ However, a marked increase in cobalt loss is found when the cells are cycled to 4.3 V. Cycling to 4.4 V further increases the cobalt loss, and 4.5 V shows another sharp increase in the amount of cobalt dissolution. Cobalt dissolution is indeed related to the capacity loss with cycling above the traditional reversible voltage limit of 4.2 V.

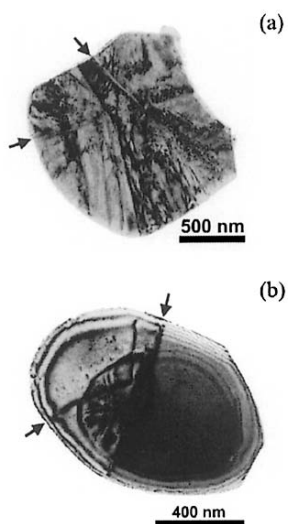


Figure 14.3. Severely damaged LiCoO_2 particles from a cycled cathode showing microfractures (arrows) and a strong diffraction contrast from the internal strain and extended defects (Ref. 1).

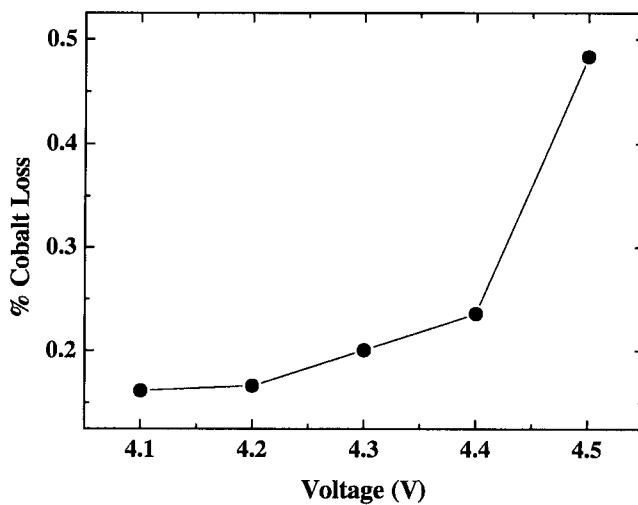


Figure 14.4. Cobalt loss (percentage) as a function of cycling voltage (Ref. 20).

14.1.3. Electrochemical Properties of LiCoO_2 Cathode

LiCoO_2 powders are typically prepared by reacting a mixture of $\text{LiOH} \cdot \text{H}_2\text{O}$ and Co_3O_4 in the mole ratio of 1.05:1 at 900°C for 24 h. An excess amount of $\text{LiOH} \cdot \text{H}_2\text{O}$ is used to compensate for the loss of Li during firing. Figure 14.5 shows the XRD patterns of LiCoO_2 powders before cycling. The starting materials have a well-ordered $\alpha\text{-NaFeO}_2$ structure.

Figure 14.6 shows the first charge and discharge curves for LiCoO_2 , which indicate an initial capacity of 174 mAh/g between 4.4 and 2.75 V at a rate of 0.1 C (14 mA/g) in the half cell Li/LiCoO_2 . The flat potential plateau at ~ 3.93 V is characteristic of the two-hexagonal-phase region.^{8,9} Two additional plateaus at ~ 4.1 and ~ 4.2 V are attributed to the order-disorder transition (changes between monoclinic and hexagonal phases) occurring at $x \approx 0.5$.^{8,9} Figure 14.7 shows the cycle-life performance of a LiCoO_2 cathode with charge cutoff voltages of 4.4 V, 4.2 V, and 4.1 V at a rate of 0.5 C. The capacity losses at the charge cutoff voltage of 4.4 V, 4.2 V, and 4.1 V are $\sim 52\%$, $\sim 20\%$, and $\sim 6\%$, respectively, after 50 cycles.

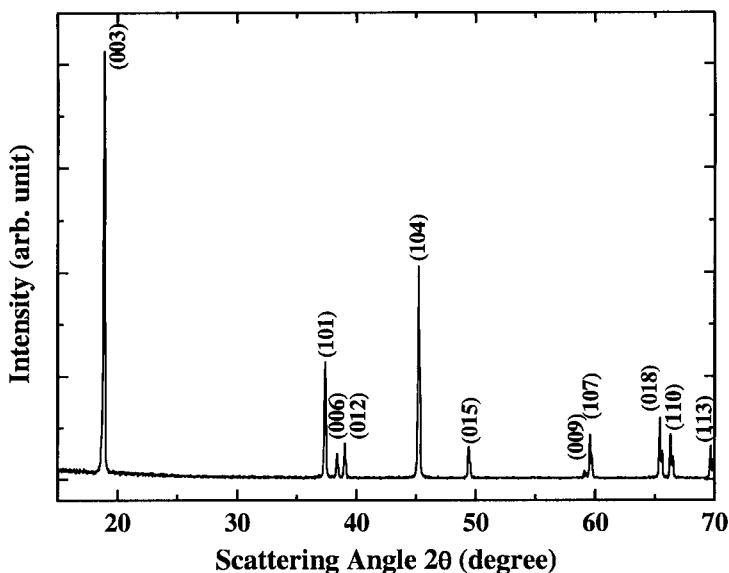


Figure 14.5. XRD patterns of the LiCoO_2 powders before cycling.

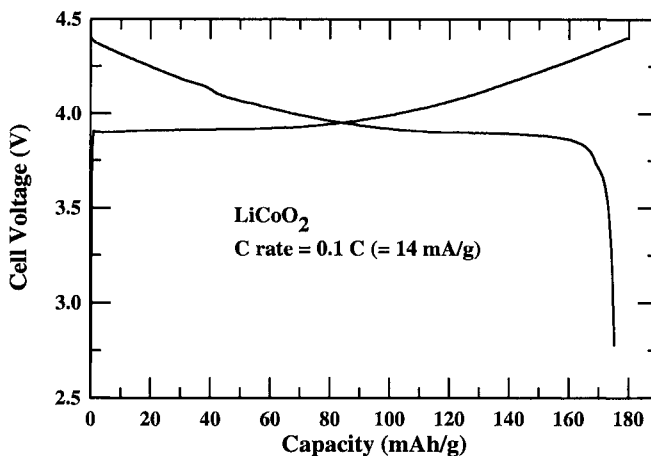


Figure 14.6. Voltage profiles of the LiCoO_2 cathode at a rate of 0.1 C (4.4 - 2.75 V).

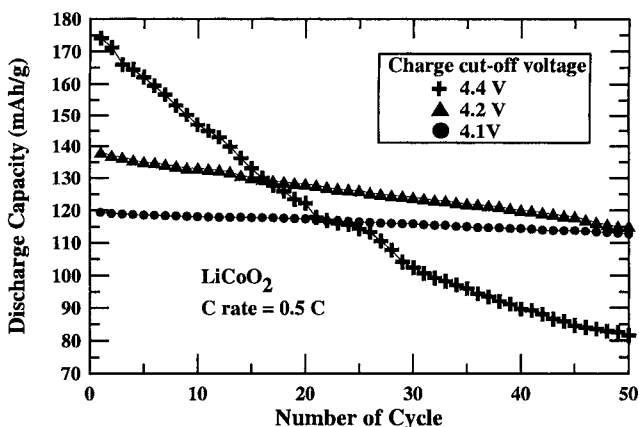


Figure 14.7. Cycle-life performance of the LiCoO_2 cathode with a charge cutoff voltage of 4.4 V, 4.2 V, and 4.1 V at the rate of 0.5 C. The discharge cutoff voltage is 2.75 V.

An evaluation of the cycle-life performance of LiCoO_2 was also carried out between 4.4 and 2.75 V in a coin-type Li-ion cell (C/ LiCoO_2) (Figure 14.8). The lower initial capacities of the C/ LiCoO_2 cells (154 mAh/g) compared to the half-cells are due to the irreversible capacity loss of the mesophase pitch-based carbon fiber (MCF) anode.

For measuring the rate capability of a LiCoO_2 cathode, the charge rate is fixed at 0.5 C, and the discharge rates are increased from 0.2 to 0.5, 1, 2, and 3 C (Figure 14.9). At higher C rates, the discharge voltage decreases more appreciably than the initial capacity.

Figure 14.10 shows the cyclic voltammograms (CVs) of LiCoO_2 conducted up to the second cycle. In this figure, *H* and *M* represent the hexagonal and monoclinic phases, respectively. Li diffusion in the oxide is a key factor that determines the rate at which a battery can be charged and discharged. With increasing interest in higher power density batteries, understanding the mechanisms of diffusion in insertion electrodes is important. The dependence of the Li^+ diffusion coefficient in the LiCoO_2 particles on the electrode potential is shown in Figure 14.11—note the variation from $\sim 3 \times 10^{-10}$ to $\sim 7 \times 10^{-8} \text{ cm}^2/\text{sec}$.²¹ The Li diffusivities in the anodic (Li deintercalation) and cathodic (Li intercalation) scans are quite similar. Three minimum values corresponding to the CV peaks in Figure 14.10 can be observed. It should be noted that the Li diffusivities exhibit minimum values at these peak potentials.

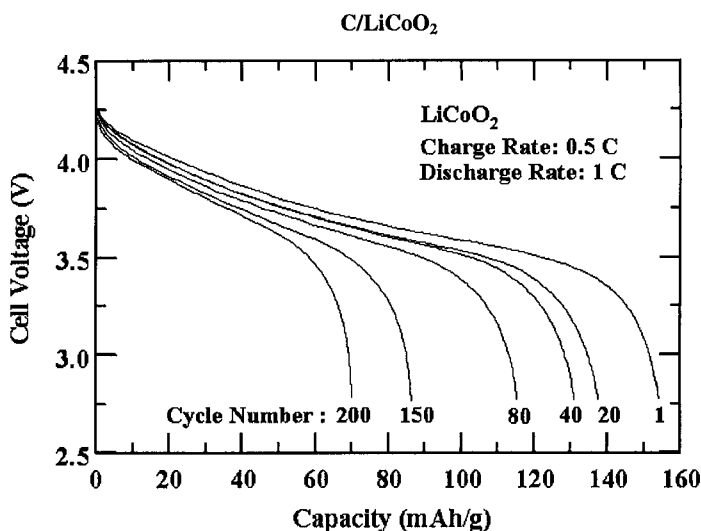


Figure 14.8. Plots of the capacity retention for C/LiCoO_2 cells as a function of cycle number. The charge and discharge rates are 0.5 and 1 C, respectively.

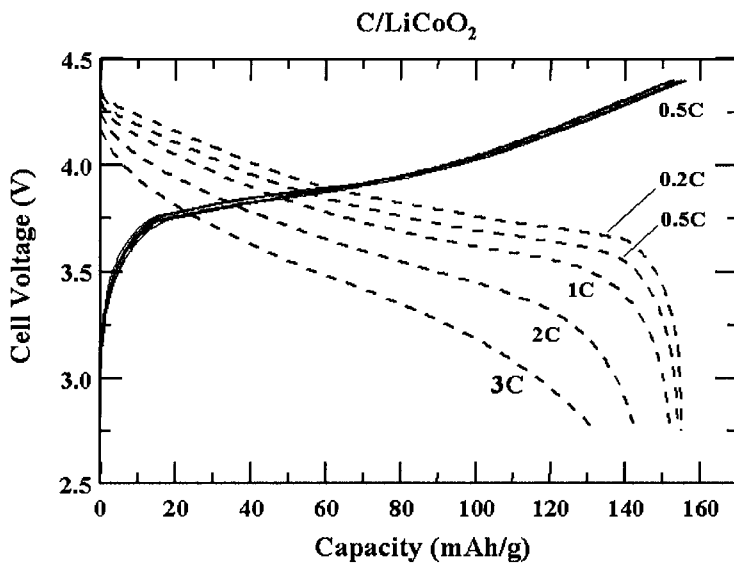


Figure 14.9. Rate capabilities of LiCoO_2 at various discharge rates of 0.2, 0.5, 1, 2, and 3 C. The charge rate was fixed at 0.5 C.

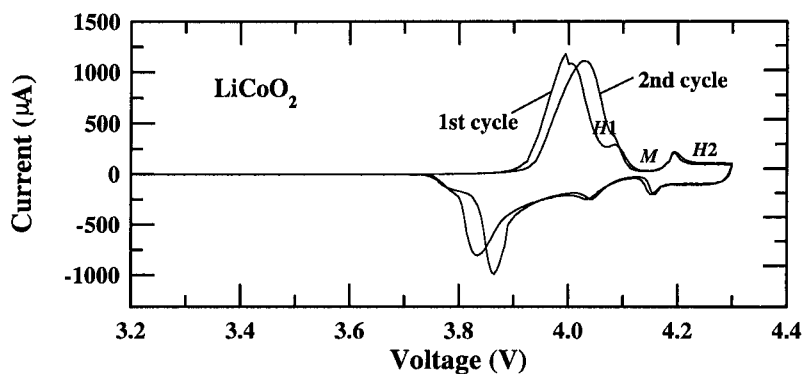


Figure 14.10. Cyclic voltammograms of a LiCoO_2 cathode. Scan rate: 0.02 mV/sec. The symbols H and M denote the hexagonal and monoclinic phase, respectively.

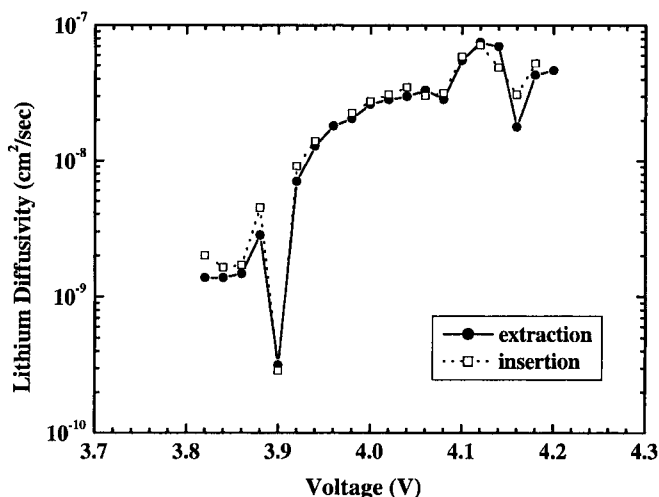


Figure 14.11. Dependence of the apparent diffusion coefficient of Li in the LiCoO_2 particles on the electrode potential (with a Li anode) (Ref. 21).

14.1.4. Doping the LiCoO_2 Cathode

Although LiCoO_2 has excellent electrochemical properties, other materials such as LiNiO_2 and LiMn_2O_4 are being extensively studied as lower-cost and more environmentally-friendly substitutes. Efforts have also been made to synthesize solid solutions of $\text{LiM}_y\text{Co}_{1-y}\text{O}_2$ ($\text{M} = \text{Al}, \text{Mg}$, etc.) isostructural with LiCoO_2 .^{2-5,13,22,23} Ceder *et al.*²² reported that first-principles calculations could orient the search for possible cathode materials. Through such calculations, they have identified a large class of new candidate materials in which non-transition metals are substituted for cobalt. For one such material, $\text{LiAl}_y\text{Co}_{1-y}\text{O}_2$, they have predicted and experimentally verified that Al substitution raises the cell voltage while decreasing both the density of the material and its cost.

Figure 14.12 shows the open-circuit voltage (equilibrium potential) as a function of the Li content in LiCoO_2 , $\text{LiAl}_{0.25}\text{Co}_{0.75}\text{O}_2$, and $\text{LiAl}_{0.5}\text{Co}_{0.5}\text{O}_2$.³ The open-circuit voltage of the cells increases systematically with increasing Al content in the oxide. As shown in Figure 14.13, during the first charge of $\text{LiAl}_{0.25}\text{Co}_{0.75}\text{O}_2$ between 2.0 and

4.5 V at 0.4 mA/cm^2 , 182 mAh/g is extracted at room temperature, and 219 mAh/g at 55°C , which corresponds to 61 and 73% of the theoretical, respectively. The first discharge capacities are 127 mAh/g and 144 mAh/g at room temperature and 55°C , respectively. Rapid capacity fade is observed upon cycling at room temperature. After nine cycles, the discharge capacity decreases to 51% of the initial value. The Al-doped LiCoO_2 cathode shows both a reduced initial capacity relative to LiCoO_2 , and a deteriorated capacity retention during cycling.

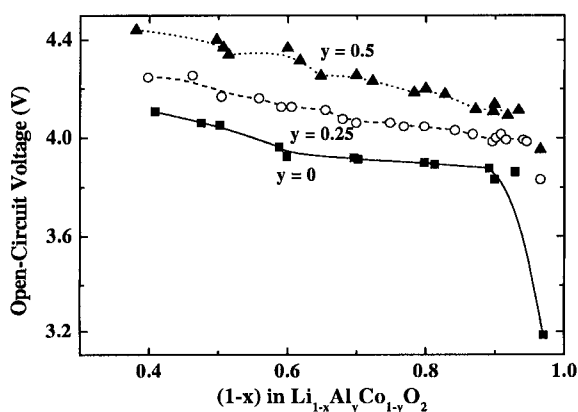


Figure 14.12. Open-circuit voltage (OCV) as a function of the Li content in pure LiCoO_2 and in Al-doped materials (Ref. 3).

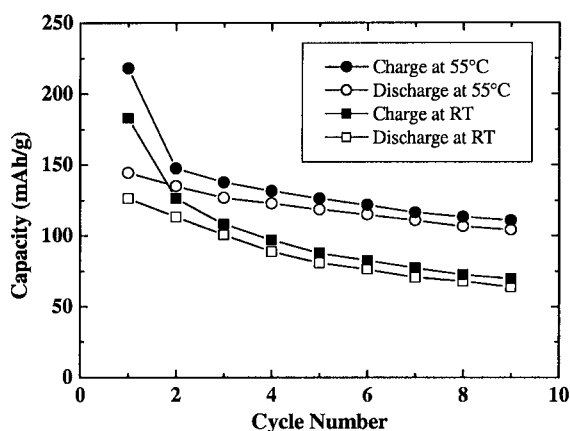


Figure 14.13. Specific capacity vs. cycle number for $\text{LiAl}_{0.25}\text{Co}_{0.75}\text{O}_2$, tested against a Li-metal anode at 0.4 mA/cm^2 between 2.0 and 4.5 V at room temperature and 55°C (Ref. 3).

14.2. LiNiO₂ CATHODE MATERIALS

14.2.1. Introduction

Compared to LiCoO₂, LiNiO₂ is cheaper and less toxic. It delivers a larger reversible capacity with a comparable cycle life. It is considered to be one of the best cathode materials for Li-ion cells, and is used in graphite-based cells. The electrochemical properties of cathodes based on LiNiO₂ are shown in Table 14.2.²⁴⁻²⁷ However, its synthesis requires special care to obtain good and reproducible performances. Its structural and electrochemical behavior has been reviewed.^{24,25,28-30}

Table 14.2. Cycling stability of cathodes based on LiNiO₂.

Cathode Material	Capacity	Voltage Range/ Current Density	Ref.
LiNiO ₂	220 mAh/g (initial) 70 mAh/g (100 cycles)	4.3 - 3.0 V 1 mA/cm ²	24
	195 mAh/g (initial) 150 mAh/g (30 cycles)	4.4 - 3.1 V 1 mA/cm ²	25
LiNi _{0.70} Co _{0.30} O ₂	160 mAh/g (initial) 108 mAh/g (100 cycles)	4.3 - 2.75 V 2 mA/cm ²	26
LiNi _{0.25} Co _{0.50} Mn _{0.25} O ₂	166 mAh/g (initial) 157 mAh/g (25 cycles)	4.4 - 2.5 V 0.6 mA/cm ²	27

14.2.2. Structure of LiNiO₂

The ideal structure of LiNiO₂ is layered, isostructural with LiCoO₂. The XRD patterns of LiNiO₂ are indexed to a hexagonal symmetry with the space group $R\bar{3}m$, as shown in Figure 14.14. However, the Li-Ni-O system is characterized by the existence of a Li_{1-z}Ni_{1+z}O₂ (0 < z < 1) solid solution. At low z values (0 < z < 0.2), the structure can still be described as a layered structure with the presence of Ni²⁺ cations within the Li layers. The amount, z, of interlayer Ni²⁺ cations depends on the

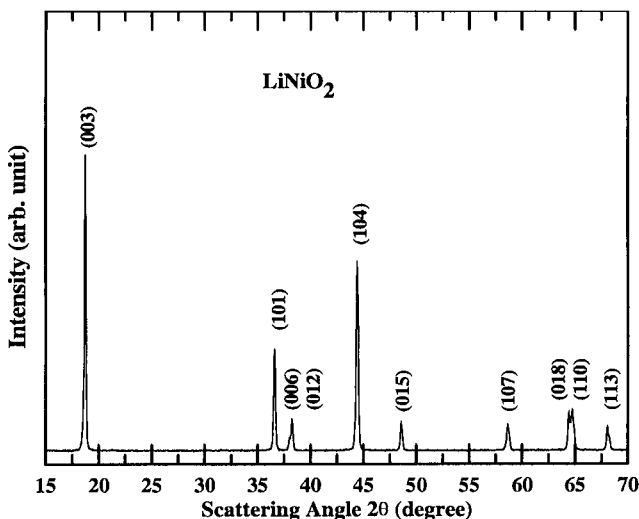


Figure 14.14. XRD patterns of the LiNiO_2 powders, before cycling.

synthesis conditions, and is lowered when using oxidizing atmospheres for the synthesis because of the stabilization of Ni^{3+} . The extra interlayer Ni^{2+} cations are strongly detrimental to the electrochemical performance, as they induce a lower capacity and larger polarization (voltage difference between the charge and discharge curves).³¹⁻³⁵

14.2.3. Electrochemical Properties and Capacity Fading Mechanisms of LiNiO_2

As shown in Figure 14.15, LiNiO_2 exhibits quite a large irreversible capacity loss during electrochemical cycling, much larger than that of LiCoO_2 . Most of the irreversibility is observed at the end of the first charge, and a model based on the formation of inactive domains was proposed.³⁶ Another model,^{33,37} based on a local collapse of the interlayer space due to the oxidation of interlayer Ni^{2+} to smaller size Ni^{3+} cations ($r_{\text{Ni}^{2+}} = 0.68 \text{ \AA}$; $r_{\text{Ni}^{3+}} = 0.56 \text{ \AA}$), was proposed. Such a local contraction would impede Li reintercalation in the six close-neighboring sites of interlayer Ni^{3+} cations, due to the larger size of the Li^+ ion ($r_{\text{Li}^+} = 0.74 \text{ \AA}$), which would lead to a fast increase of the irreversible capacity with increasing quantities of initial interlayer cations.

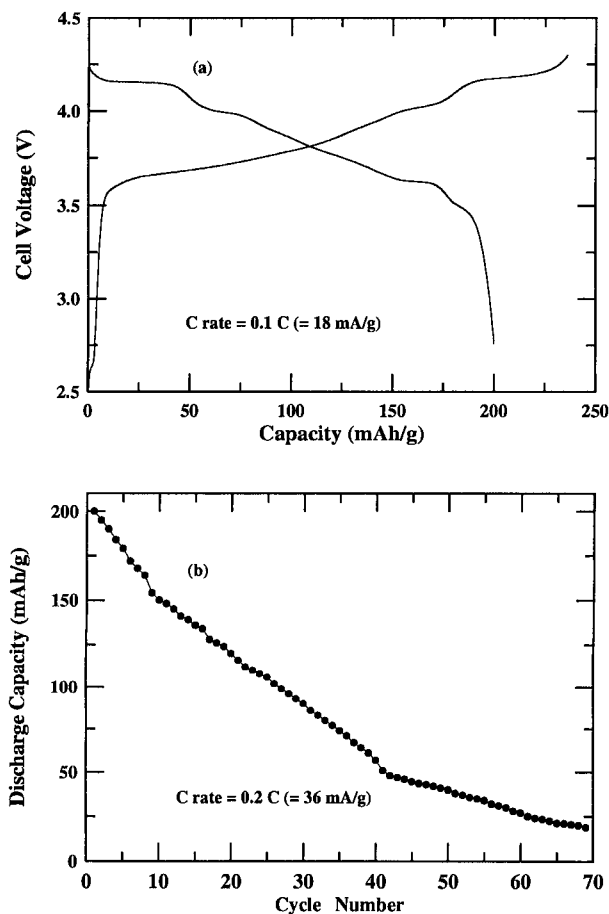


Figure 14.15. (a) Initial voltage profiles of LiNiO_2 between 4.3 and 2.75 V at a rate of 0.1 C (18 mA/g), and (b) cycle life of LiNiO_2 at a rate of 0.2 C (36 mA/g).

Several reversible structural transitions occur upon Li deintercalation,^{31,34,38} which are different from those occurring in $\text{Li}_{1-x}\text{CoO}_2$ (Figure 14.16). CVs up to 4.4 V show $H1 \leftrightarrow M \leftrightarrow H2 \leftrightarrow H3$ transformations and high initial charge and discharge capacities. However, a large capacity fade on long-term cycling was also observed (Figure 14.15(b)). This behavior can be attributed to the migration of Ni cations from the layers to the interlayer space, thereby altering the subsequent electrochemical behavior.^{12,39} In addition, since metal oxides with a low ductility undergo mechanically-induced microcracks resulting from lattice strains, the reversibility of Li intercalation sharply

deteriorates. Microcrack formation in each LiNiO_2 particle is induced by anisotropic lattice changes along the a and c axis in the initial hexagonal phase (Figure 14.17).^{38,40} A similar behavior is observed in LiCoO_2 .

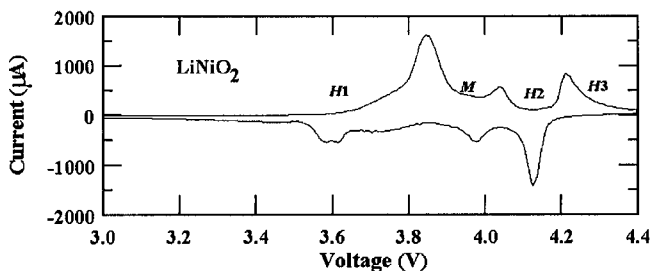


Figure 14.16. Cyclic voltammograms of LiNiO_2 . The scan rate was 0.02 mV/sec.

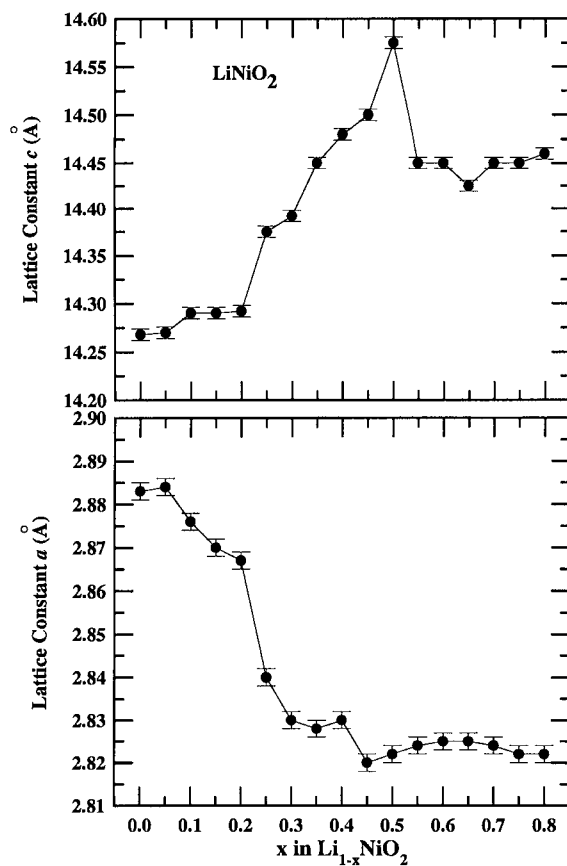


Figure 14.17. Evolution of the lattice constants a and c as a function of x in $\text{Li}_{1-x}\text{NiO}_2$.

14.3. METAL-OXIDE COATING ON LiCoO_2 POWDERS

14.3.1. Introduction

The electrochemical cycling of LiCoO_2 at a high cutoff voltage results in a significant deterioration of the stability of the cathode. As commented above, this capacity loss is related to non-uniform structural changes^{1,13-19} and an increase in cobalt dissolution into the electrolyte.²⁰ To improve the electrochemical performance of LiCoO_2 above 4.2 V, an innovative approach was adopted. This involved coating the particles with some metal oxides to avoid the unwanted surface reactions and protect the bulk.^{5,16-19,41-47} This method changes the surface properties of the cathode materials. Aurbach *et al.*⁴⁸ reported that the electrochemical behavior of Li_xMO_y ($\text{M} = \text{Ni}, \text{Mn}$) cathode materials is strongly dependent on their surface chemistry. Recent reports on surface modifications to cathode materials such as LiCoO_2 and LiNiO_2 with Al_2O_3 , ZrO_2 , MgO , ZnO_2 , Ga_2O_3 , and SnO_2 have shown that surface coating is an effective way to stabilize the structure of the materials and improve their electrochemical performance.

14.3.2. Preparation of Metal-Oxide Coated LiCoO_2 Powders

A sol-gel coating of various metal oxides having a wide range of fracture toughness (ZrO_2 , Al_2O_3 , TiO_2 , B_2O_3 , and SiO_2)⁴⁹⁻⁵¹ is applied on the LiCoO_2 particle surfaces. Metal ethylhexanate-diisopropoxide ($\text{M}(\text{OOC}_8\text{H}_{15})(\text{OC}_3\text{H}_7)_2$) is dissolved in 2-propanol, followed by continuous stirring at RT. The LiCoO_2 powder (average particle size of $\sim 10 \mu\text{m}$) is then mixed with the coating solution such that the total concentration of metal in the coating solution corresponds to 5 wt% of the LiCoO_2 powders used. The resulting solution is further aged at 50°C to allow the M-OR groups to react with the LiCoO_2 surface-OH groups, leading to strong bonds between the metal-oxide gel and the LiCoO_2 particle surface. After drying, each coated LiCoO_2 powder is fired at 400°C for some hours. Field-emission SEM confirms that the metal-oxide coating is continuous. X-ray diffraction of the as-prepared samples show a single-phase $\alpha\text{-NaFeO}_2$ structure ($R\bar{3}m$), where the cobalt and lithium

ions are located at the 3a and 3b octahedral sites, respectively, in a close-packed oxygen array. However, the XRD patterns of the coated samples do not show any evidence of a crystalline metal oxide. Enhanced electrochemical results have been observed by a metal-oxide coating from Dahn's group.⁴² However, they have shown that the coating layer contains nanocrystalline ZrO_2 (15-25 nm) on the surface of the LiCoO_2 powders through their XRD pattern and TEM image. This discrepancy may be due to the difference in the coating precursors. The coating solutions used by Dahn's group are a zirconium oxide polymeric precursor or an aqueous solution of $\text{ZrO}(\text{NO}_3)_2 \cdot x\text{H}_2\text{O}$.

14.3.3. Cycle-Life Performance of Metal-Oxide Coated LiCoO_2

To test the cycle-life performance of each cathode material, coin-type half cells (Li/LiCoO_2) are cycled at the 0.1 C rate (14 mA/g) for the first 2 cycles between 4.4 and 2.75 V. Cycling is then continued at the 0.5 C rate for up to 70 cycles. As shown in Figure 14.18, the initial discharge capacities of the ZrO_2 - and Al_2O_3 -coated samples are similar to that of the uncoated one, and the cycle-life performance trend is consistent with the fracture toughness of the coated metal oxide ($\text{ZrO}_2 > \text{Al}_2\text{O}_3 > \text{TiO}_2 > \text{B}_2\text{O}_3 > \text{SiO}_2$). In addition, the ZrO_2 -coated sample does not show any noticeable capacity fading over 70 cycles. In contrast, bare LiCoO_2 loses ~40% of its original capacity after only 30 cycles.

The lattice constant c as a function of x in the hexagonal $\text{Li}_{1-x}\text{CoO}_2$ from $x=0$ to 0.7 during the first charge is shown in Figure 14.19. Even though the lattice constant a shows a slight variation during charging in both the bare and coated $\text{Li}_{1-x}\text{CoO}_2$, the lattice-constant c shifts depend on the choice of the metal-oxide coating. The stability of the c -axis dimension correlates well with the fracture toughness of the coated oxides, and occurs in the order of $\text{ZrO}_2 > \text{Al}_2\text{O}_3 > \text{TiO}_2 > \text{B}_2\text{O}_3 > \text{SiO}_2$. This result confirms that suppressing the non-uniform strain during the delithiation produces a new-class of cathode materials, which are extremely tolerant to electrochemical cycling. Note that the lattice constant c of the ZrO_2 -coated LiCoO_2 exhibits a negligible shift in the range $0 < x < 0.7$. In addition, a sol-gel coating of ZrO_2 can effectively inhibit cobalt dissolution from the LiCoO_2 cathodes. As shown in Figure 14.20, cobalt dissolution in ZrO_2 -coated LiCoO_2 is greatly reduced (~140 ppm), compared to that of an uncoated LiCoO_2 (~730 ppm), after a charge

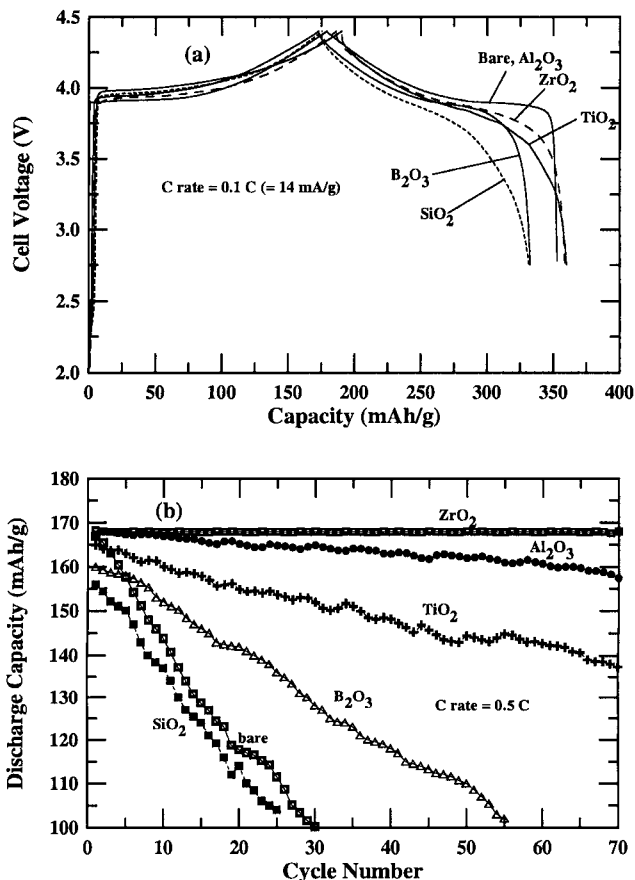


Figure 14.18. (a) Initial charge and discharge curves for various metal-oxide coated LiCoO_2 , and comparison with uncoated LiCoO_2 (first cycle). (b) Cycle-life performances for ZrO_2 -, Al_2O_3 -, TiO_2 -, B_2O_3 -, SiO_2 -coated, and uncoated LiCoO_2 . The cells were cycled at a rate of 0.1 C for the first two cycles, followed by a 0.5 C rate between 4.4 and 2.75 V at 21°C.

to 4.8 V and one-week storage at 25°C. Amatucci *et al.* reported that an increase in cobalt dissolution above 4.4 V is related to the lattice changes induced by removal of the binding lithium.¹² Figure 14.21 depicts how enclosing the LiCoO_2 particles in a fracture-toughened metal-oxide coating layer can effectively suppress the non-uniform lattice-constant changes during Li deintercalation. It should be noted that, in thin film LiCoO_2 (both bare and metal-oxide coated), the lattice constants as a function of the cell voltage from OCV to 4.4 V show negligible *c* axis

expansion (details in Section 14.4.2.5). Dahn's group suggests that a ZrO_2 coating on the powder has no effect on Li_xCoO_2 expansion although the ZrO_2 -coated LiCoO_2 powders exhibit an improved cycling behavior to 4.5 V.⁴² This disagreement is probably due to the difference in the coating solution. Dahn's group assumes that a ZrO_2 coating may inhibit side reactions involving oxygen loss from the Li_xCoO_2 to the electrolyte and hence improve the cycling stability.

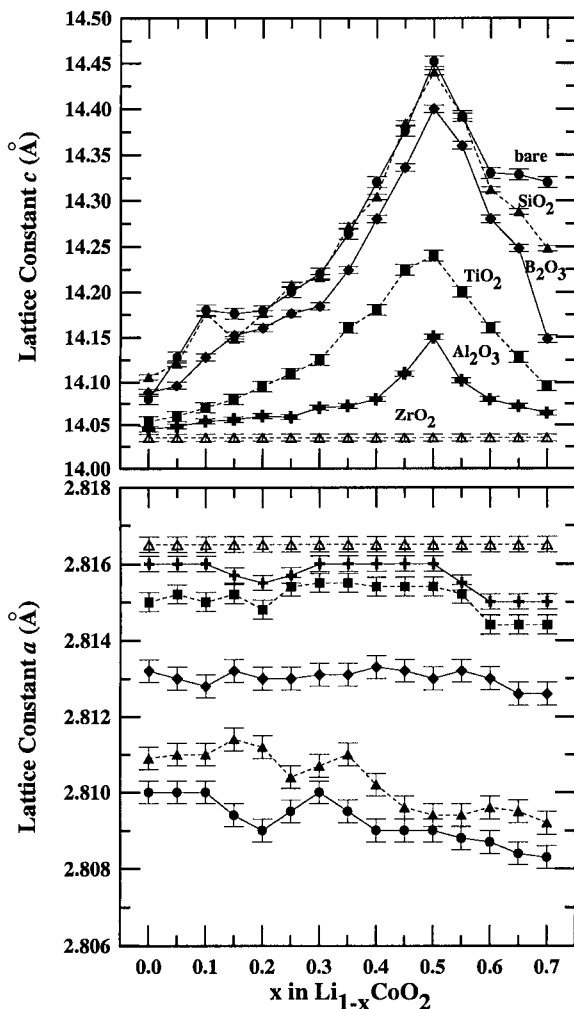


Figure 14.19. Lattice constants a and c in ZrO_2 -, Al_2O_3 -, TiO_2 -, B_2O_3 -, SiO_2 -coated, and bare LiCoO_2 as a function of x in $\text{Li}_{1-x}\text{CoO}_2$ during the first charge. The precursor is metal ethylhexanate-diisopropoxide ($\text{M}(\text{OOC}_8\text{H}_{15})(\text{OC}_3\text{H}_7)_2$) dissolved in 2-propanol.

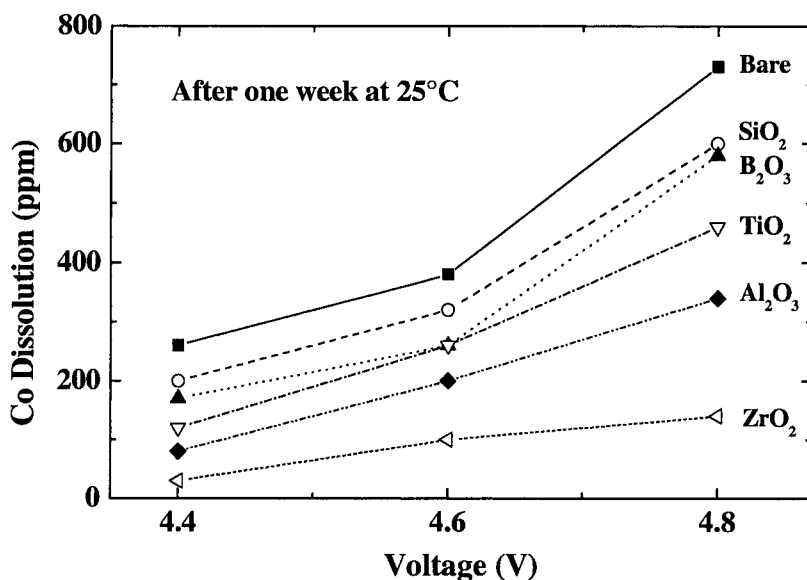


Figure 14.20. The amount of cobalt dissolution in the electrolyte (1 M LiPF₆-EC/DMC), from various metal-oxide coated and uncoated LiCoO₂, after an initial charge and being immersed for one week at 25°C.

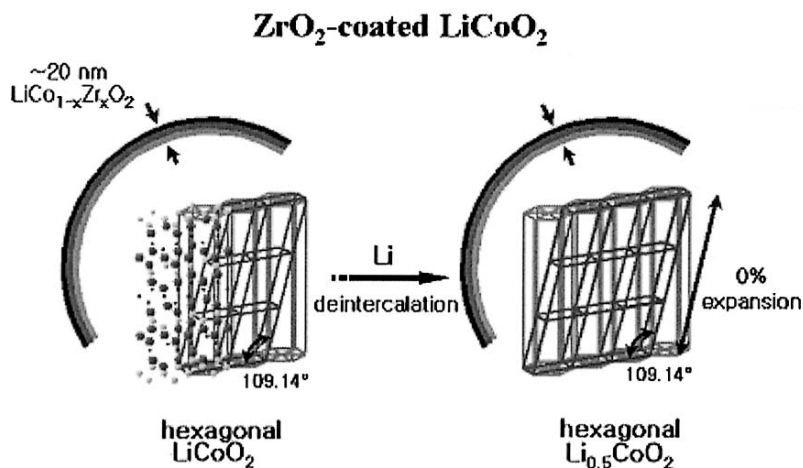


Figure 14.21. Schematic illustration of the suppression of lattice expansion from hexagonal to monoclinic phase by a nanoscale metal-oxide coating.

14.4. THIN-FILM LiCoO_2 CATHODES

14.4.1. Introduction

Thin film microbatteries⁵²⁻⁵⁴ have potential applications in microelectronics. In particular, the fabrication of lithiated intercalation oxides in a thin-film form is of great interest because of their possible use as a positive electrode in all-solid-state lithium rechargeable microbatteries. This is due to the need to miniaturize various electronic devices, such as monolithic hybridization with CMOS-RAM, back-up power systems for computer chips, small sensors, and hazard cards.⁵⁵⁻⁵⁸ Thin-film cathodes have also received a great deal of attention as they allow to study the intrinsic electrochemical properties of lithiated transition-metal oxides. Indeed, composite powders with polymer binders and carbon blacks may not represent the characteristic electrochemical properties of these oxides.⁵⁷⁻⁶⁷

14.4.2. Electrochemical Properties of Al_2O_3 -Coated LiCoO_2 Thin Films

14.4.2.1. Cycle-Life Performance of Al_2O_3 -Coated LiCoO_2 Thin Films

To test the cycle-life performance of bare and 30 nm-thick Al_2O_3 -coated LiCoO_2 thin films on a Pt/Si substrate, half cells are cycled in the voltage range 2.75 - 4.4 V at 0.2 mA/cm², as shown in Figure 14.22. A 30 nm-thick Al_2O_3 coating significantly improves the electrochemical stability of the LiCoO_2 thin-film cathodes. The charge and discharge capacities of bare LiCoO_2 get deteriorated to only ~3% and ~25% of the original capacity after 100 cycles (Figure 14.22(a)), while Al_2O_3 -coated LiCoO_2 retains ~64% and ~75% of the initial capacity at a current rate of 0.2 mA/cm² (Figure 14.22(b)). The charge capacities of the bare LiCoO_2 films (Li deintercalation) exhibit faster deterioration than the discharge capacities (Li intercalation). The effect of an Al_2O_3 coating on the cycle-life performance is more pronounced at a higher-current rate (Figure 14.23). The insets in Figure 14.22 show the same cycle-life performance, including the extra capacity from the constant voltage mode (at 4.4 V and 2.75 V).

In the bare samples, most of the charge capacity after ~40 cycles comes from the constant voltage charge of 4.4 V, indicating that the Li

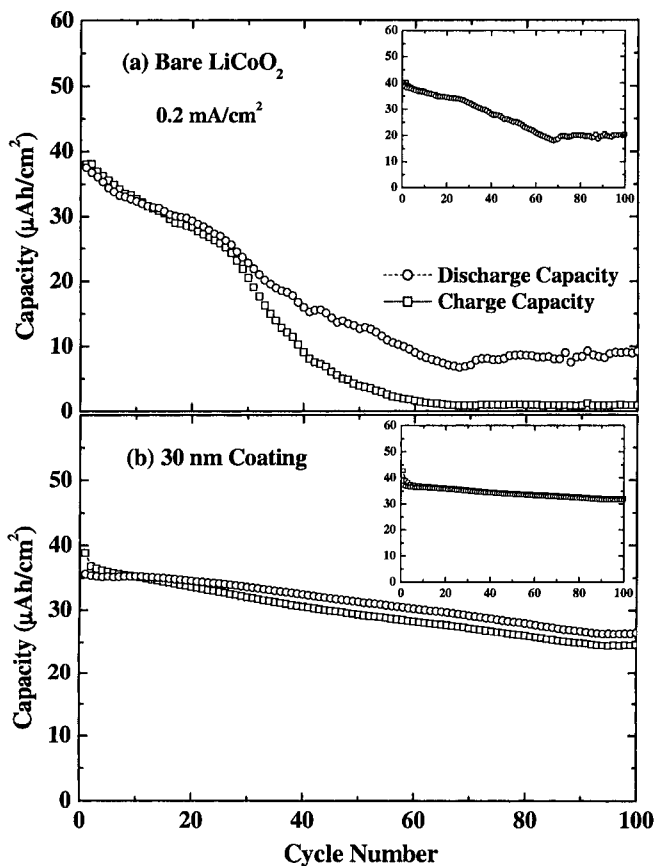


Figure 14.22. Cycle-life performance (charge and discharge capacities vs. cycle number) of (a) bare, and (b) 30 nm-thick Al₂O₃-coated LiCoO₂ thin films between 4.4 and 2.75 V at 0.2 mA/cm² (≈ 6 C). The inset shows the same cycle-life performance, including the extra capacity from the constant-voltage mode.

deintercalation kinetics are slower than the Li intercalation kinetics. On the other hand, the Al₂O₃-coated samples exhibit similar charge and discharge capacities, and the curve in the inset of Figure 22(b) has an almost constant slope. This means that Li intercalation and deintercalation in the coated films become more symmetrical. The Al₂O₃ coating on the surface modifies the properties of the cathode surface exposed to the electrolyte and changes the Li-diffusion kinetics. The voltage profiles of the bare and 30 nm-thick Al₂O₃-coated LiCoO₂ thin films are shown in Figure 14.24. The profiles of the bare LiCoO₂ thin films become steeper with increasing the cycling number up to 80 cycles

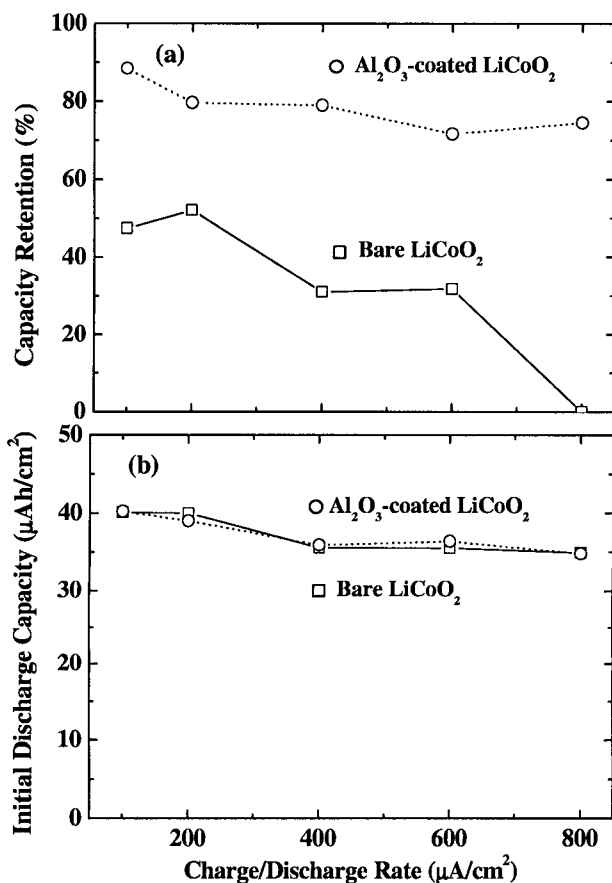


Figure 14.23. (a) Capacity retention vs. current rate after 100 cycles, and (b) initial discharge capacity vs. current rate of uncoated and Al_2O_3 -coated LiCoO_2 thin films.

at $0.2 \text{ mA}/\text{cm}^2$. In contrast, the change in the voltage profiles of the Al_2O_3 -coated LiCoO_2 thin films during 80 cycles is more gradual. However, compared with the cycling profiles of bare LiCoO_2 thin films, a slight increase in cell potential is observed in the initial cycle of Al_2O_3 -coated cathodes. This is attributed to the insulating effect of the aluminum-oxide layer. From the 2nd cycle on, the polarization in the charge and discharge processes of coated sample is not significant, as the Li-Al-O coating layer on LiCoO_2 acts as a solid electrolyte (details in Section 14.4.2.2).

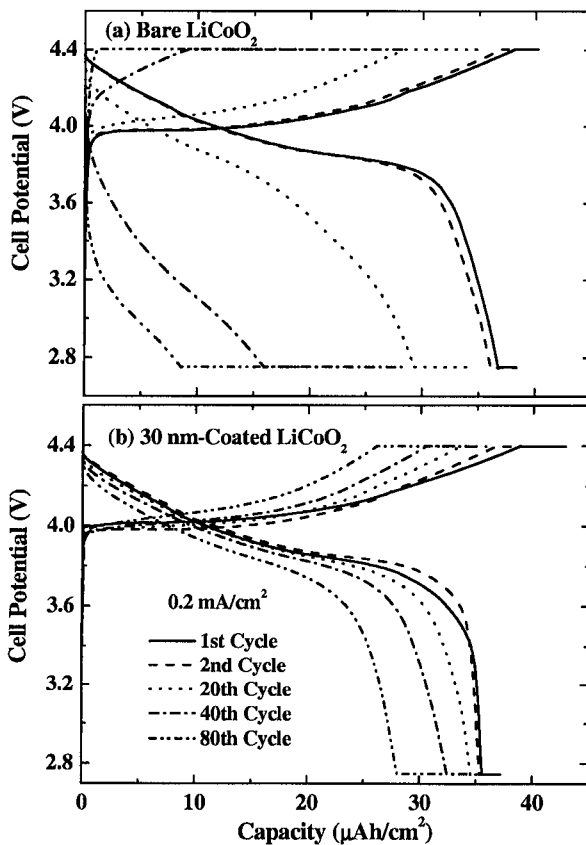


Figure 14.24. Voltage profiles of (a) uncoated, and (b) 30 nm-thick Al₂O₃-coated LiCoO₂ films between 4.4 and 2.75 V at a rate of 0.2 mA/cm². At each charge/discharge cutoff step, the cell voltage was potentiostated until the current decreased to 0.02 mA/cm².

14.4.2.2. Al₂O₃ Coating Layer Acting as a Solid Electrolyte

The Al₂O₃-coating thicknesses were varied from 10 nm to 300 nm to examine the possible questions of electronic insulation and Li migration through the Al₂O₃ layer. Figure 14.25(a) shows that the initial discharge capacities are almost independent of the coating thickness (0-300 nm range). In addition, the variation in the Al₂O₃ thickness ranging from 10 nm to 300 nm does not affect the capacity retention: ~70% and ~60% retention, respectively, at 0.2 and 0.4 mA/cm², while the capacity retention

of the uncoated LiCoO_2 thin film is only $\sim 25\%$ after 100 cycles, as shown in Figure 14.25(b). This is possibly because the Al_2O_3 coating layer acts as a solid electrolyte with a low electronic conductivity and a reasonably high Li-ion conductivity. For example, the Li-ion conductivity of a $0.7\text{Li}_2\text{O}-0.3\text{Al}_2\text{O}_3$ solid electrolyte is $\sim 10^{-7}$ S/cm at room temperature.⁶⁸

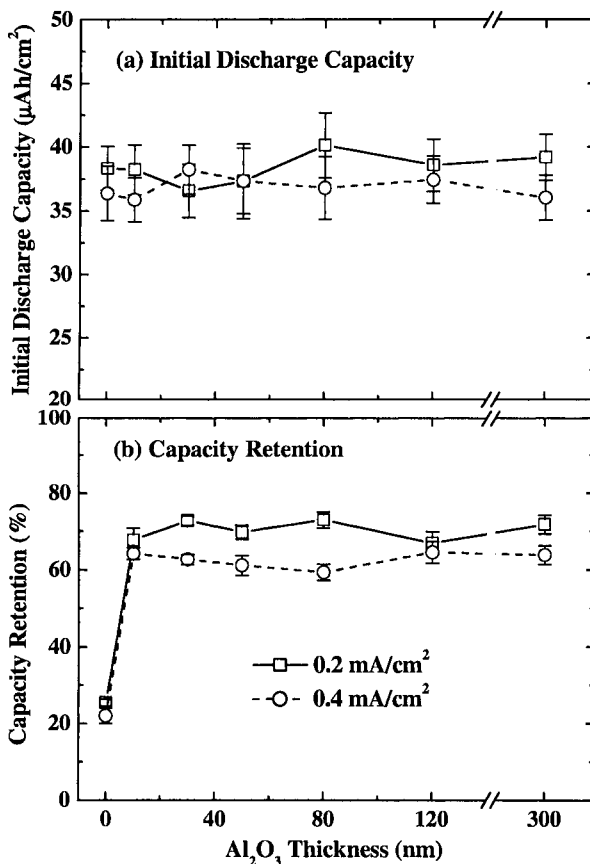


Figure 14.25. The effect of the Al_2O_3 -coating thickness on (a) initial discharge capacity and (b), capacity retention after 100 cycles, all excluding the extra capacity from the constant-voltage mode. The cells were cycled between 4.4 and 2.75 V at 0.2 and 0.4 mA/cm^2 .

14.4.2.3. Suppression of Cobalt Dissolution by Al_2O_3 Coating

To clarify the reason why the Al_2O_3 -coated LiCoO_2 thin films showed better electrochemical performance than the bare ones, inductively coupled plasma-mass spectroscopy (ICP-MS) analysis was carried out after floating at 4.2 V, 4.4 V, 4.5 V, 4.6 V, and 4.7 V, respectively, for 12 days. As shown in Figure 14.26, the amount of cobalt dissolution from the uncoated LiCoO_2 films significantly increases with increasing the charge-cutoff voltages, while an increase in cobalt dissolution from the Al_2O_3 -coated ones is not significant. An increase in the fraction of Co^{4+} in $\text{Li}_{1-x}\text{CoO}_2$ augments the reactivity with the electrolytes and HF, if present. An Al_2O_3 coating can effectively reduce cobalt dissolution, even at 4.7 V, to a much smaller level (~ 100 ppm) than that of the uncoated LiCoO_2 films (~ 1000 ppm).

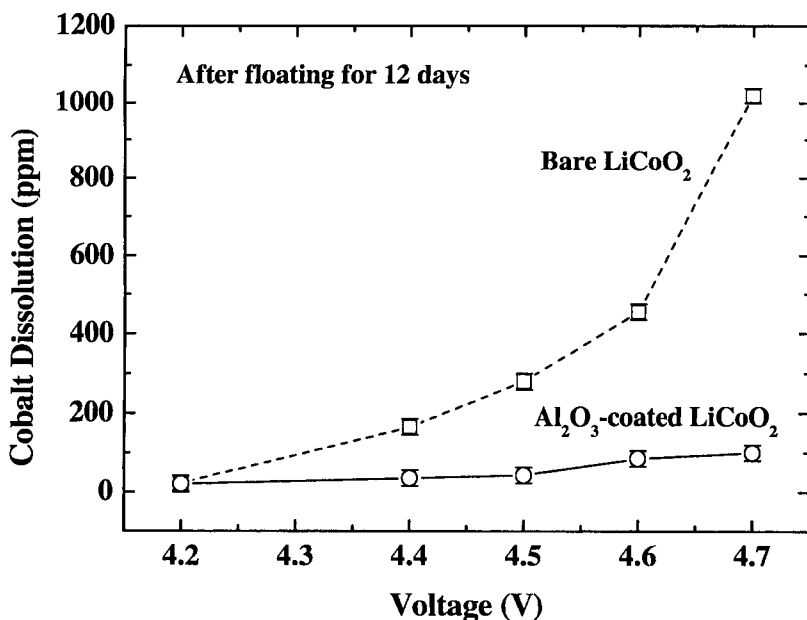


Figure 14.26. The amount of cobalt dissolution in the electrolyte, from bare and Al_2O_3 -coated LiCoO_2 , after an initial charge and being immersed for 12 days at 25°C.

14.4.2.4. CV Measurement of Al_2O_3 -Coated LiCoO_2 Thin Films

Figure 14.27 shows the cyclic voltammograms of the bare and 30 nm-thick Al_2O_3 -coated LiCoO_2 thin films at a scan rate of 0.1 mV/sec, carried out during the 1st cycle, and after the 40th and 80th charging/discharging cycles. The CVs of the Al_2O_3 -coated LiCoO_2 thin films during the 1st cycle clearly show three sets of well-defined current peaks, *i.e.* ~ 3.96 and ~ 3.87 V (a , a'), ~ 4.07 and ~ 4.05 V (b , b'), ~ 4.19 and ~ 4.16 V (c , c'). The first set is due to the first-order phase transition between the two hexagonal phases, and the second and third sets are caused by the phase transition between the hexagonal and monoclinic phases.^{8,9} These values are in good agreement with those obtained from the uncoated LiCoO_2 films and powders. However, these thin-film results are different from the CVs of Al_2O_3 -coated LiCoO_2 powders,^{16,18} and the reasons for this disparity need to be identified. The cathodic peak (~ 3.87 V at a') of the Al_2O_3 -coated film during the 1st cycle is narrower than that of the bare one, although the anodic peaks (~ 3.96 V at a) are similar. In addition, in the bare LiCoO_2 thin films, the widths of both the cathodic and anodic peaks are remarkably broadened, and the peak positions become more separated as the cycle number increases to 80, while the widths of the cathodic and anodic peaks of the Al_2O_3 -coated samples are relatively sharp. This indicates that the Al_2O_3 -coated LiCoO_2 thin films are more reversible than the bare ones, which is probably related to the suppression of cobalt dissolution from the cathode (Figure 14.26).

14.4.2.5. Changes in the Lattice Constants c as a Function of the Cell Potential

Figure 14.28 shows the changes in the lattice constants c as a function of the cell potential during the first charge in the $\text{Li}_{1-x}\text{CoO}_2$ thin films and powders.¹⁶⁻¹⁸ Both the bare and Al_2O_3 -coated LiCoO_2 thin films exhibit negligible c axis expansion even with a strong (003) texture.⁶⁷ This is in contrast to the LiCoO_2 powders, which exhibit $\sim 2.6\%$ c axis expansion at ~ 4.17 V. Further studies are necessary to identify the mechanisms allowing LiCoO_2 thin films to have a limited c axis expansion.

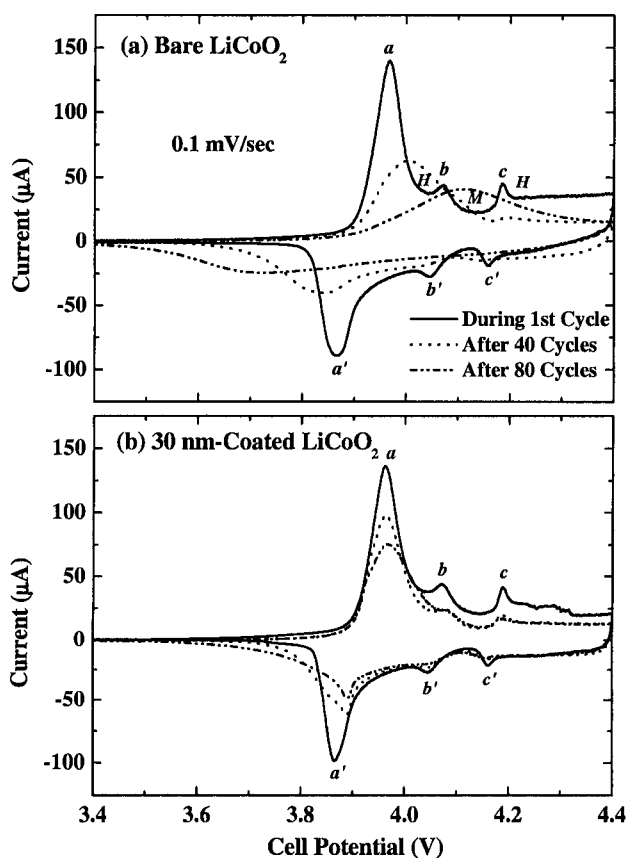


Figure 14.27. Cyclic voltammograms of (a) bare, and (b) 30 nm-thick Al_2O_3 -coated LiCoO_2 thin films, during the 1st cycle, and after the 40th and 80th cycle. The sweep rate was 0.1 mV/sec between 3.0 and 4.4 V. The symbols *H* and *M* denote the hexagonal and monoclinic phases, respectively.

14.4.2.6. Li Diffusivities of Al_2O_3 -Coated LiCoO_2 Thin Films

Figures 14.29 and 14.30 show the apparent Li diffusivities as a function of the cell potential of the $\text{Li}_{1-x}\text{CoO}_2$ cathodes during Li deintercalation (charging) and intercalation (discharging), respectively. The Li diffusivities of Al_2O_3 -coated LiCoO_2 are slightly lower than those of bare one during the 1st Li deintercalation, as shown in Figure 14.29.

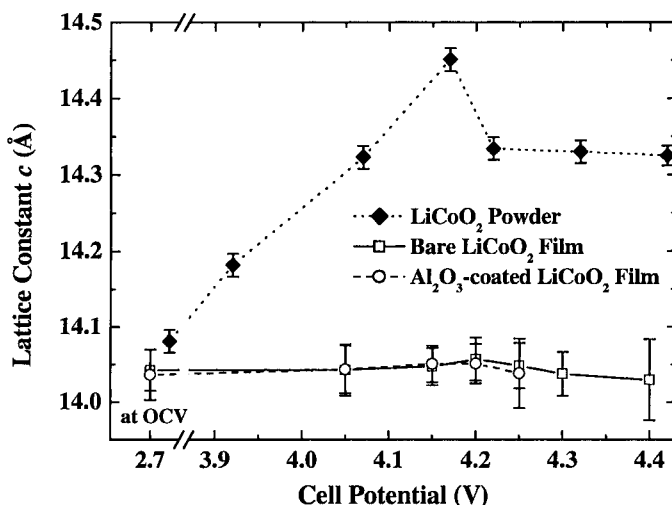


Figure 14.28. Changes in the lattice constants c as a function of the cell potential for bare and Al_2O_3 -coated LiCoO_2 thin films during the first charge, with a comparison with powder samples. For thin films, each cell was charged at a 0.1 mA/cm^2 rate to the predetermined voltages, then potentiostated until the current density decreased to $1 \mu\text{A/cm}^2$.

The Li diffusivities in the bare LiCoO_2 thin films during Li deintercalation (Figure 14.29) are in good agreement with the previous results obtained using either thin-film $\text{Li}_{1-x}\text{CoO}_2$ cathodes^{57,58,62,69} or powder electrodes.⁷⁰⁻⁷² Note that the plots of Li diffusivity vs. cell potential show maxima at $\sim 4.13 \text{ V}$, corresponding to the monoclinic phase. In addition, two minima are observed at the cell potential corresponding to the phase transition between the hexagonal and monoclinic phase, in agreement with previous reports by Jang *et al.*⁶⁰

As the cycle number increases, the Li diffusivity decreases owing to the degradation of the thin-film LiCoO_2 cathodes. As shown in Figure 14.29, during Li deintercalation the Li diffusivities of the bare LiCoO_2 thin films (in the range of approximately 4.15 and 4.3 V) decrease to $\sim 5 \times 10^{-12} \text{ cm}^2/\text{sec}$ after 80 cycles, compared to $\sim 2 \times 10^{-11} \text{ cm}^2/\text{sec}$ in the coated films. During Li intercalation, the Li diffusivities in bare samples

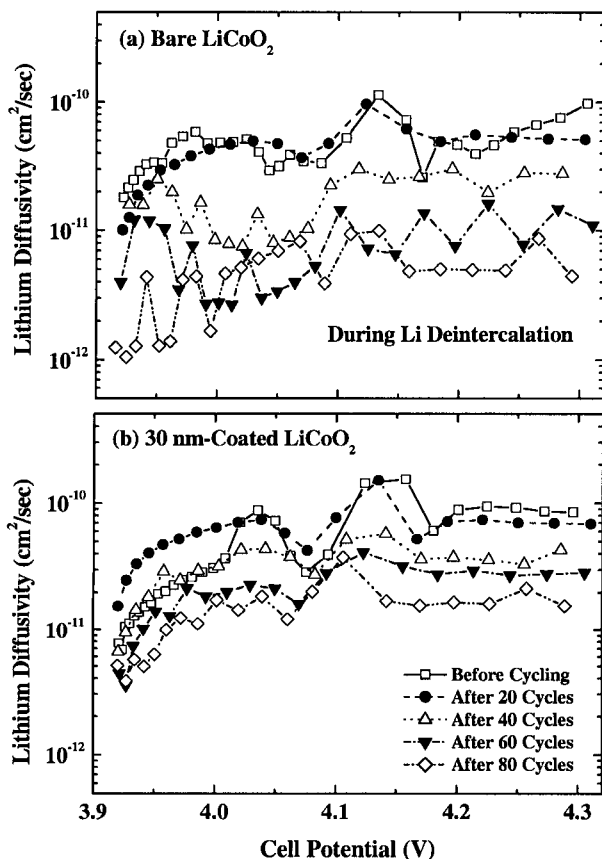


Figure 14.29. Lithium diffusivities as a function of cell potential for (a) bare, and (b) 30 nm-thick Al_2O_3 -coated LiCoO_2 thin films, determined by GITT during Li deintercalation (charging).

are $\sim 1 \times 10^{-11} \text{ cm}^2/\text{sec}$ after 80 cycles, while the deterioration of the Li diffusivities in the coated ones remains at $\sim 3 \times 10^{-11} \text{ cm}^2/\text{sec}$ (Figure 14.30). These results suggest that an Al_2O_3 coating on the LiCoO_2 thin films can tolerate the electrochemical cycling with a high cutoff voltage of 4.4 V, thanks to the suppression of cobalt dissolution by Al_2O_3 coating.

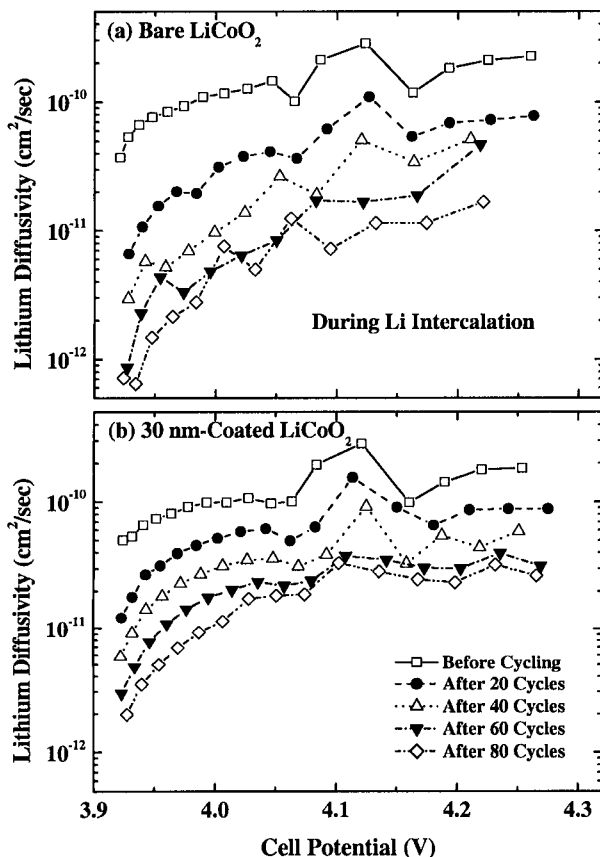


Figure 14.30. Lithium diffusivities as a function of cell potential for (a) bare, and (b) 30 nm-thick Al_2O_3 -coated LiCoO_2 thin films, as determined by GITT during Li intercalation (discharging).

14.4.3. Future Work

Further studies to detail the effect of a metal-oxide coating on the surface reactions, such as the microstructural changes in $\text{Li}_{1-x}\text{CoO}_2$, the composition profile of the Li-Al-O coating layer, and the electric-potential distribution near the interface between the LiCoO_2 cathode and the Li-Al-O coating layer, are currently underway. Also, the coating effects of various oxides need to be identified.

ACKNOWLEDGEMENT

We are grateful to Joon-Gon Lee, Hyemin Kim, Tae-Joon Kim, and Byoungsoo Kim for their help to improve the clarity of this manuscript.

REFERENCES

1. H. Wang, Y.-I. Jang, B. Huang, D. R. Sadoway, Y.-M. Chiang, *J. Electrochem. Soc.* 146 (1999) 473.
2. H. Tukamoto, A. R. West, *J. Electrochem. Soc.* 144 (1997) 3164.
3. Y.-I. Jang, B. Huang, H. Wang, D. R. Sadoway, G. Ceder, Y.-M. Chiang, H. Liu, H. Tamura, *J. Electrochem. Soc.* 146 (1999) 862.
4. W.-S. Yoon, K.-K. Lee, K.-B. Kim, *J. Electrochem. Soc.* 147 (2000) 2023.
5. M. Mladenov, R. Stoyanova, E. Zhecheva, S. Vassilev, *Electrochem. Commun.* 3 (2001) 410.
6. K. Mizushima, P. C. Jones, P. J. Wiseman, J. B. Goodenough, *Mater. Res. Bull.* 15 (1980) 783.
7. H. J. Orman, P. J. Wiseman, *Acta Crystallogr., Sect. C: Cryst. Struct. Commun.* 40 (1980) 12.
8. J. N. Reimers, J. R. Dahn, *J. Electrochem. Soc.* 139 (1992) 2091.
9. T. Ohzuku, A. Ueda, *J. Electrochem. Soc.* 141 (1994) 2972.
10. J. van Elp, J. L. Wieland, H. Eskes, P. Kuiper, G. A. Sawatzky, F. M. F. de Groot, T. S. Turner, *Phys. Rev. B* 44 (1991) 6090.
11. J. Molenda, A. Stoklosa, T. Bak, *Solid State Ionics* 36 (1989) 53.
12. G. G. Amatucci, J. M. Tarascon, L. C. Klein, *J. Electrochem. Soc.* 143 (1996) 1114.
13. H. Wang, Y.-I. Jang, B. Huang, D. R. Sadoway, Y.-M. Chiang, *J. Power Sources* 81-82 (1999) 594.
14. Y.-K. Sun, *J. Power Sources* 83 (1999) 223.
15. Y.-M. Choi, S.-I. Pyun, *Solid State Ionics* 99 (1997) 173.
16. J. Cho, Y. J. Kim, B. Park, *Chem. Mater.* 12 (2000) 3788.
17. J. Cho, Y. J. Kim, T.-J. Kim, B. Park, *Angew. Chem. Int. Ed.* 40 (2001) 3367.
18. J. Cho, Y. J. Kim, B. Park, *J. Electrochem. Soc.* 148 (2001) A1110.
19. J. Cho, C.-S. Kim, S.-I. Yoo, *Electrochem. Solid-State Lett.* 3 (2000) 362.
20. G. G. Amatucci, J. M. Tarascon, L. C. Klein, *Solid State Ionics* 83 (1996) 167.
21. K. Dokko, M. Mohamede, Y. Fujita, T. Itoh, M. Nishizawa, M. Umeda, I. Uchida, *J. Electrochem. Soc.* 148 (2001) A442.
22. G. Ceder, Y.-M. Chiang, D. R. Sadoway, M. K. Aydinol, Y.-I. Jang, B. Huang, *Nature* 392 (1998) 694.

23. S.-T. Myung, N. Kumagai, S. Komaba, H.-T. Chung, *Solid State Ionics* 139 (2001) 47.
24. K. Kubo, M. Fujiwara, S. Yamada, S. Arai, M. Kanda, *J. Power Sources* 68 (1997) 553.
25. C.-C. Chang, J. Y. Kim, P. N. Kumta, *J. Electrochem. Soc.* 149 (2002) A331.
26. J. Cho, G. Kim, H. S. Lim, *J. Electrochem. Soc.* 146 (1999) 3571.
27. Z. Lu, D. D. MacNeil, J. R. Dahn, *Electrochem. Solid-State Lett.* 4 (2001) A200.
28. M. M. Thackeray, *J. Electrochem. Soc.* 142 (1995) 2558.
29. P. G. Bruce, *Chem. Commun.*, 1817 (1997).
30. P. Koksang, J. Barker, H. Shi, M. Y. Sakdi, *Solid State Ionics* 84 (1996) 1.
31. H. Arai, S. Okada, H. Ohtsuka, M. Ichimura, J. Yamaki, *Solid State Ionics* 80 (1995) 261.
32. T. Ohzuku, A. Ueda, M. Nagayama, *J. Electrochem. Soc.* 140 (1993) 1862.
33. A. Rougier, P. Gravereau, C. Delmas, *J. Electrochem. Soc.* 143 (1996) 1168.
34. J. Barker, R. Koksang, M. Y. Saidi, *Solid State Ionics* 89 (1996) 25.
35. R. V. Moshtev, P. Zlatilova, V. Manev, A. Sato, *J. Power Sources* 54 (1995) 329.
36. H. Arai, S. Okada, Y. Sakurai, J. I. Yamaki, *Solid State Ionics* 95 (1997) 275.
37. J. P. Peres, PhD thesis, Univ. of Bordeaux I, France, (1996).
38. W. Li, J. N. Reimers, J. R. Dahn, *Solid State Ionics* 67 (1993) 123.
39. T. Ohzuku, A. Ueda, M. Kouguchi, *J. Electrochem. Soc.* 142 (1995) 4033.
40. J. Cho, H. Jung, Y. Park, G. Kim, H. Lim, *J. Electrochem. Soc.* 147 (2000) 10.
41. Z. Wang, C. Wu, L. Liu, F. Wu, L. Chen, X. Huang, *J. Electrochem. Soc.* 149 (2000) A466.
42. Z. Chen, J. R. Dahn, *Electrochem. Solid-State Lett.* 5 (2002) A213.
43. Z. Wang, L. Liu, L. Chen, X. Huang, *Solid State Ionics* 148 (2002) 335.
44. J. Cho, T.-J. Kim, Y. J. Kim, B. Park, *Electrochem. Solid-State Lett.* 4 (2001) A159.
45. D. Rahner, W. Plieth, M. Kloss, "Modified electrode material and its use," U.S. Patent No. 6348259, March 30, 1999.
46. T. Miyasaka, "Non-aqueous lithium ion secondary battery," U.S. Patent No. 6037095, March 30, 1998.
47. H.-J. Kwon, G.-B. Kim, D.-G. Park, "Positive active material for rechargeable lithium battery and method of preparing same," U.S. Patent No. 6183911, October 29, 1999.
48. D. Aurbach, K. Gamosky, B. Markovsky, G. Salitra, Y. Gofer, U. Heider, R. Oesten, M. Schmidt, *J. Electrochem. Soc.* 147 (2000) 1322.
49. W. D. Jr. Callister, *Materials Science and Engineering: An Introduction*, John Wiley & Sons: New York, 4th ed., Appendix C, p. 787 (1997).
50. M. C. Fredel, A. R. Boccaccini, *J. Mater. Sci.* 31 (1996) 4375.
51. J. Sehgal, S. Ito, *J. Non-Cryst. Solids* 253 (1999) 126.
52. P. Birke, W. F. Chu, W. Weppner, *Solid State Ionics* 93 (1997) 1.
53. J. B. Bates, G. R. Gruzalski, N. J. Dudney, C. F. Luck, X. Yu, *Solid State Ionics* 70-71 (1994) 619.

54. C. Julien, G.-A. Nazri, *Solid State Batteries: Materials Design and Optimization*, Kluwer Academic, Boston, 1994.
55. C. Wolverton, A. Zunger, *J. Electrochem. Soc.* 145 (1998) 2424.
56. D. G. Fauteux, A. Massucco, J. Shi, C. Lampe-Onnerud, *J. Appl. Electrochem.* 27 (1997) 543.
57. B. Wang, J. B. Bates, F. X. Hart, B. C. Sales, R. A. Zuhr, J. D. Robertson, *J. Electrochem. Soc.* 143 (1996) 3203.
58. J. B. Bates, N. J. Dudney, B. J. Neudecker, F. X. Hart, H. P. Jun, S. A. Hackney, *J. Electrochem. Soc.* 147 (2000) 59.
59. M. Antaya, J. R. Dahn, J. S. Preston, E. Rossen, J. N. Reimers, *J. Electrochem. Soc.* 140 (1993) 575.
60. Y.-I. Jang, B. J. Neudecker, N. J. Dudney, *Electrochem. Solid-State Lett.* 4 (2001) A74.
61. J.-K. Lee, S.-J. Lee, H.-K. Baik, H.-Y. Lee, S.-W. Jang, S.-M. Lee, *Electrochem. Solid-State Lett.* 2 (1999) 512.
62. K. A. Striebel, C. Z. Deng, S. J. Wen, E. J. Cairns, *J. Electrochem. Soc.* 143 (1996) 1821.
63. Y. Iriyama, M. Inaba, T. Abe, Z. Ogumi, *J. Power Sources* 94 (2001) 175.
64. J. D. Perkins, C. S. Bahn, J. M. McGraw, P. A. Parilla, D. S. Ginley, *J. Electrochem. Soc.* 148 (2001) A1302.
65. P. J. Bouwman, B. A. Boukamp, H. J. M. Bouwmeester, P. H. L. Notten, *J. Electrochem. Soc.* 149 (2002) A699.
66. J. D. Perkins, C. S. Bahn, P. A. Parilla, J. M. McGraw, M. L. Fu, M. Duncan, H. Yu, D. S. Ginley, *J. Power Sources* 81-82 (1999) 675.
67. Y. J. Kim, T.-J. Kim, J. W. Shin, B. Park, J. Cho, *J. Electrochem. Soc.* 149 (2002) 1337.
68. A. M. Glass, K. Nassau, *J. Appl. Phys.* 51 (1980) 3756.
69. J. M. McGraw, C. S. Bahn, P. A. Parilla, J. D. Perkins, D. W. Readey, D. S. Ginley, *Electrochim. Acta* 45 (1999) 187.
70. J.-S. Hong, J. R. Selman, *J. Electrochem. Soc.* 147 (2000) 3190.
71. M. D. Levi, K. Gamolsky, D. Aurbach, U. Heider, R. Oesten, *J. Electroanal. Chem.* 477 (1999) 32.
72. D. Aurbach, D. L. Levi, E. Levi, H. Teller, B. Markovsky, G. Salitra, *J. Electrochem. Soc.* 145 (1998) 3024.

Chapter 15

POLYANION-BASED POSITIVE ELECTRODE MATERIALS

C. Masquelier, S. Patoux, C. Wurm and M. Morcrette

Laboratoire de Réactivité et Chimie des Solides, UMR CNRS 6007, Université Picardie Jules Verne, 33, rue Saint-Leu, 80000 Amiens, France

15.1. INTRODUCTION: FROM OXIDES TO IONICALLY CONDUCTING POLYANIONIC FRAMEWORKS

Over the last 15 years the vast majority of fundamental and technological contributions on the search for better positive electrode materials has been devoted to transition metal oxides such as Li_xMO_2 ($\text{M} = \text{Co}, \text{Ni}, \text{Mn}$), $\text{Li}_x\text{Mn}_2\text{O}_4$, $\text{Li}_x\text{V}_2\text{O}_5$ or $\text{Li}_x\text{V}_3\text{O}_8$.¹ The first two classes of materials, built on close-packed oxygen stacking adopt bi-dimensional and tri-dimensional crystal structures, respectively. Lithium ions may be easily intercalated or extracted from these structures in a reversible manner. These oxides are reasonably good ionic and electronic conductors and lithium insertion/extraction proceeds while operating on the $\text{M}^{4+}/\text{M}^{3+}$ redox, located at around 4V vs. Li^+/Li . Cost considerations brought some special attention to the possible use of LiFeO_2 that may be prepared in the same crystallographic arrangement as of LiCoO_2 through ion exchange from $\alpha\text{-NaFeO}_2$.² Electrochemical extraction of lithium would give access to the $\text{Fe}^{4+}/\text{Fe}^{3+}$ redox couple but no stability of $\text{Li}_{1-x}\text{FeO}_2$ was successfully demonstrated yet.

The peculiar structure of the two-dimensional oxides $\text{Li}_{1-x}\text{MO}_2$ ($\text{M} = \text{Co}, \text{Ni}, \text{Fe}, \text{Mn}$) lead to structural instabilities when the number x of extracted lithium is high (end of charge). Irreversible motion of transition metals within the lithium layers may occur and lead to important capacity loss on cycling. In practical use, for instance, only 150 mAh/g out of the theoretical 273 mAh/g is used for LiCoO_2 in commercial Li-ion batteries.

For this reason, Goodenough³ and Thackeray⁴⁻⁶ had envisioned in the early eighties the possible use of three-dimensional oxides such as the spinel $\text{Li}[\text{Mn}_2]\text{O}_4$. In such spinel structure, MnO_6 octahedra are strongly connected to each other through edge-sharing and delimitate a three-dimensional

network of conduction paths for lithium motion. One of the major problems with the spinel LiMn_2O_4 , though, is that there is a $\sim 1\text{V}$ difference for the same $\text{Mn}^{4+}/\text{Mn}^{3+}$ couple between the extraction of lithium from the tetrahedral 8a sites ($\sim 4\text{V}$ vs. Li^+/Li) and the insertion of lithium in the octahedral 16c sites ($\sim 3\text{V}$ vs. Li^+/Li). This limits then the theoretical capacity at 4V on lithium extraction from LiMn_2O_4 (equivalent to $\text{Li}_{0.5}\text{MnO}_2$) to values similar to the practical capacities delivered by LiCoO_2 or LiNiO_2 .

The concept of three-dimensional insertion/extraction positive electrodes was then extended in the late 80's to new families of 3-D framework structures, by Goodenough's group^{7,8} and by Delmas.^{9,10} These framework structures are not built from close-packing of oxygen atoms but built on polyanions such as tetrahedral XO_4^{n-} groups ($\text{X} = \text{P}, \text{Mo}, \text{W}, \text{S}$).

The NASICON framework (Natrium Super Ionic CONductor), which will be described in much details through this contribution was considered as particularly attractive from structural stability and fast ion transport considerations. The originality of the idea of using this class of materials as insertion electrodes comes from the fact that previous studies had been focusing on developing NASICON compositions as solid electrolytes in Na/S type batteries.

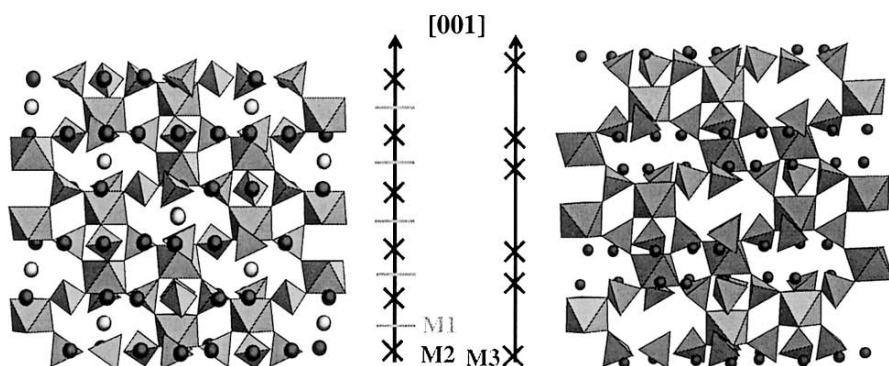


Figure 15.1. Schematic representation of two NASICON compositions $\text{Na}_3\text{Fe}_2(\text{PO}_4)_3$ (left) and $\text{Li}_3\text{Fe}_2(\text{PO}_4)_3$ (right).

The NASICON structure of general formula $\text{A}_x\text{MM}'(\text{XO}_4)_3$ is built on a three-dimensional framework of MO_6 and $\text{M}'\text{O}_6$ octahedra sharing all their corners with XO_4 tetrahedra and vice versa (Figure 15.1). The basic $\text{MM}'(\text{XO}_4)_3$ repeating unit, named as “lantern”, is made of three tetrahedra connected to two octahedra. Each lantern is connected to six other lanterns which generates overall a large interstitial space that may accommodate between 0 to 4 alkali cations per structural formula. The exceptional adaptability of this structural arrangement to numerous chemical substitutions

onto the A^{n+} , $M^{n'+}$ or $X^{n''+}$ sites has been widely demonstrated. Importantly, the number of alkali cations per structural formula may be adjusted depending on the stable oxidation states of transition metals and on the X element chosen. Below, the elements which may give NASICON compositions are listed:

- A = Li, Na, Mg, Ca
- M or M' = Sc, Ti, V, Cr, Mn, Fe, Zr, Nb, In
- X = Si, P, S, As

M or M' elements form octahedra, while X elements form tetrahedra.

For instance, niobium, titanium and iron, mostly stable in air at their oxidation states +5, +4 and +3 respectively lead, when combined with the PO_4^{3-} anion, to compositions such as $NbTi(PO_4)_3$, $LiTi_2(PO_4)_3$, $Na_2FeTi(PO_4)_3$ and $Na_3Fe_2(PO_4)_3$ that all adopt the NASICON structure and are easy to prepare as pure powders. Other examples include $Fe_2(SO_4)_3$ and $Na_4Zr_2(SiO_4)_3$.

The preparation of these numerous compositions is well documented in the literature and was aimed at trying to establish close relationships between crystal structures, alkali ion contents within the interstitial space, chemical nature of substituting elements, and ionic conduction.¹¹ Within the $Na_{1+x}Zr_2P_3-xSi_xO_{12}$ ($0 \leq x \leq 3$) solid solution, a pronounced maximum of ionic conductivity had been first discovered by Hong¹² for $x=2$ while the two end members $NaZr_2(PO_4)_3$ ($x=0$,¹³) and $Na_4Zr_2(SiO_4)_3$ ($x=3$,¹⁴) are poor ionic conductors. The chemical and structural characteristics responsible for the fast ion transport in the NASICON structure were clearly addressed in a fundamental contribution of Goodenough¹⁵ and are summarized as follows :

- Highly covalent three-dimensional framework generating a large interstitial space,
- Elasticity of the framework for better accommodation of local compositional changes,
- Weak framework – alkali cation interactions,
- Electrostatic interactions between neighbouring alkali cations,
- Three-dimensional network of interconnected conduction pathways,
- Non reducible transition element when in contact with metallic alkali cation.

If the transition metal, located in octahedral environment in the present case, may be reduced or oxidized, the above considerations indicate that the NASICON structure is very interesting as well as a host for reversible alkali ion insertion/extraction.

As will be developed in this contribution one of the major drawbacks of this structure as an insertion electrode is its very poor intrinsic electronic conductivity (major advantage for an electrolyte !!): no direct ..-M-O-M-..

electronic delocalization is possible as the MO_6 octahedra are isolated from each other and separated by the XO_4 groups (Figure 15.1). As an example, the Zr-Zr distance in $\text{NaZr}_2(\text{PO}_4)_3$ is of 4.75 Å. An interesting study aiming at modifying the electronic conduction within mixed-valence NASICON structures was reported by Tillement.¹⁶ In this pioneer work, Tillement describes in much details the possibility of preparing NASICON structures with unusual oxidation states for transition elements, such as Nb^{IV} , Ti^{III} , Fe^{II} . This was achieved either through synthesis in sealed container under vacuum or through electrochemical insertion of Na^+ ions. We will develop in further details these important early results on the localization of $\text{Nb}^{5+/4+}$, $\text{Ti}^{4+/3+}$ and $\text{Fe}^{3+/2+}$ redox couples vs. Na^+/Na .¹⁷⁻¹⁹

In this contribution, we will attempt to establish an overall review as complete as possible on the ongoing research on alkali insertion/extraction within three dimensional framework structures of transition metal elements. The NASICON structure will be used first as a didactic example to illustrate two key concepts brought to our attention from the recent works of Padhi :

- The influence of the chemical nature of the XO_4^{n-} anion ($\text{X} = \text{P}, \text{As}, \text{S}, \text{Mo}, \text{W}$) on the position of a given $\text{M}^{n+}/\text{M}^{(n-1)+}$ redox couple vs. Li^+/Li . This was first addressed in 1989 by Manthiram⁸
- For a given XO_4^{n-} polyanion, the relative positions of several transition metal redox couples.

The concept of using polyanionic structure materials as positive electrodes in rechargeable lithium batteries will then be discussed through various structures that were examined recently such as LiMPO_4 ($\text{M} = \text{Fe}, \text{Co}, \text{Mn}$), $\text{Li}_x\text{MM}'(\text{XO}_4)_3$ ($\text{M}, \text{M}' = \text{Nb}, \text{Ti}, \text{Fe}, \text{V}$; $\text{X} = \text{S}, \text{P}, \text{As}$), $\text{Li}_x\text{MX}_2\text{O}_7$ ($\text{M} = \text{Fe}, \text{V}, \text{Ti}$; $\text{X} = \text{P}, \text{As}$), Li_xMOXO_4 ($\text{M} = \text{V}, \text{Nb}$; $\text{X} = \text{P}, \text{As}, \text{S}$), $\text{FePO}_4 \cdot n\text{H}_2\text{O}$, $\text{Fe}_4(\text{P}_2\text{O}_7)_3$. Depending on the M/X ratio, these materials offer theoretical capacities ranging from 170 mAh/g ($\text{Li}_{1-x}\text{FePO}_4$) to 128 mAh/g ($\text{Li}_{1+x}\text{Fe}_2(\text{PO}_4)_3$) to 116 mAh/g ($\text{Li}_{1+x}\text{FeP}_2\text{O}_7$).

15.2. TUNING THE $\text{M}^{n+}/\text{M}^{(n-1)+}$ REDOX COUPLE IN THE NASICON STRUCTURE BY CHANGING THE CHEMICAL NATURE OF THE XO_4^{n-} GROUPS : INDUCTIVE EFFECT

The first reports dealing with lithium or sodium electrochemical insertion in a NASICON-type polyanionic framework are those of Nadiri,²⁰ Reiff,²¹ Torardi²² and Manthiram⁷ on molybdates and tungstates $\text{Li}_x\text{Fe}_2(\text{MO}_4)_3$ ($\text{M} = \text{Mo}, \text{W}$). Electrochemical insertion of lithium operates on the $\text{Fe}^{3+}/\text{Fe}^{2+}$ redox couple, located at 3V vs. Li^+/Li for the whole compositional range ($0 < x < 2$). A two-phase reaction takes place between the monoclinic ($\text{P}2_1/a$)

form of $\text{Fe}_2(\text{MoO}_4)_3$ and the orthorhombic (*Pnma*) form of $\text{Li}_2\text{Fe}_2(\text{MoO}_4)_3$. This latter phase may be prepared by chemical lithiation using LiI .

Bruce²³ undertook a similar study on the insertion of Na^+ in defect garnet compositions and confirmed the similar behavior of $\text{Fe}_2(\text{MoO}_4)_3$ and $\text{Fe}_2(\text{WO}_4)_3$. Interestingly, the cell voltage is of 2.7 V, as measured vs. Na^+/Na , *i.e.* 0.3 V lower than when lithium is inserted vs. Li^+/Li . This indicates that the $\text{Fe}^{3+}/\text{Fe}^{2+}$ redox couple is located at the same value, the 0.3 V difference being directly related to the difference between the Li^+/Li and Na^+/Na redox couples (Figure 15.2a). This observation is a clear signature on the weak interactions between the alkali cations and the oxygen atoms of the NASICON framework, which is of importance for good ionic conduction.

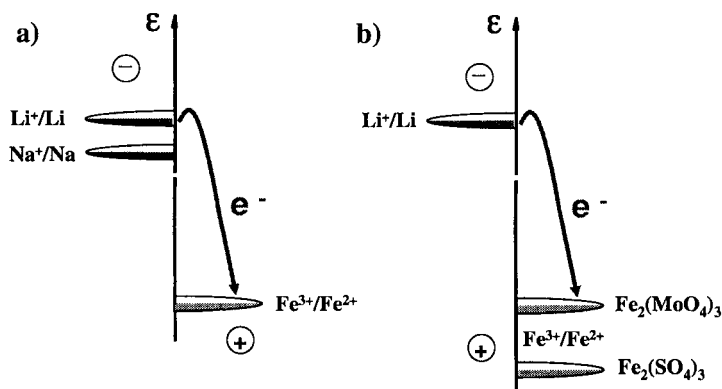


Figure 15.2. Illustration of the cell voltages measured for a) lithium or sodium insertion into $\text{Fe}_2(\text{MoO}_4)_3$ and b) lithium insertion into $\text{Fe}_2(\text{MoO}_4)_3$ and $\text{Fe}_2(\text{SO}_4)_3$.

A significant early contribution on the evaluation of the insertion properties of polyanionic structures was given by Manthiram⁸ who demonstrated the good reversibility of the $\text{Fe}_2(\text{SO}_4)_3/\text{Li}_2\text{Fe}_2(\text{SO}_4)_3$ system, operating once again on the $\text{Fe}^{3+}/\text{Fe}^{2+}$ redox couple, located this time at 3.6 V vs. Li^+/Li . A 0.6 V difference was hence pointed out for the same redox couple into same structural arrangements that differ only in the nature of the XO_4^{n-} polyanion (Figure 15.2b). This was explained in a convincing manner as a signature of the inductive effect of XO_4 groups that, depending on the electronegativity of X, weakens or strengthens the covalency of the Fe-O bonds. In the NASICON structure, each transition metal is involved in six M-O-X sequences. As a result, substitution of S for Mo or W weakens the Fe-O bonds and increases the difference between the $\text{Fe}^{3+}/\text{Fe}^{2+}$ and Li^+/Li couples.⁸

A further illustration of the inductive effect on the position of the $\text{Fe}^{3+}/\text{Fe}^{2+}$ couple in the NASICON structure is given from the rhombohedral form of $\text{Li}_3\text{Fe}_2(\text{PO}_4)_3$ that may be prepared through ion exchange from the

sodium counterpart $\text{Na}_3\text{Fe}_2(\text{PO}_4)_3$.²⁴⁻²⁶ In this case, lithium insertion proceeds as a complicated series of subtle phase transitions located at an average potential of 2.8 V vs. Li^+/Li ,²⁷⁻²⁹ for the complete reduction of Fe^{3+} into Fe^{2+} . A strong shift in the position of the $\text{Fe}^{3+}/\text{Fe}^{2+}$ couple (0.8 V) is hence observed on going from SO_4^{2-} to PO_4^{3-} groups. The polarization of the O^{2-} anion towards P^{V} is weaker than towards S^{VI} and this leads to Fe-O bond strengths greater in $\text{Li}_3\text{Fe}_2(\text{PO}_4)_3$ than in $\text{Fe}_2(\text{SO}_4)_3$. One should note that the above comparison is drawn for NASICON structures that host different amounts of lithium ions ($0 \leq x \leq 2$ for $\text{Li}_x\text{Fe}_2(\text{SO}_4)_3$; $3 \leq x \leq 5$ for $\text{Li}_x\text{Fe}_2(\text{PO}_4)_3$). This could have a small impact on the relative positions of the $\text{Fe}^{3+}/\text{Fe}^{2+}$ couples. Padhi showed,³⁰ additionally, that lithium insertion in the mixed composition $\text{LiFe}_2(\text{SO}_4)_2(\text{PO}_4)$ occurred at ~ 3.3 V vs. Li^+/Li , i.e. at intermediate values between the pure sulfate (3.6 V) and the pure phosphate (2.8 V).

These early considerations have prompted the identification of new positive electrode materials with attractive operating voltage for the $\text{Fe}^{3+}/\text{Fe}^{2+}$ couple in lithium batteries and theoretical capacities in the range of 120 mAh/g. They provided as well an elegant measure of Fe-O bond strengths modified by XO_4^{n-} polyanions through the inductive effect, summarized below (Figure 15.3):

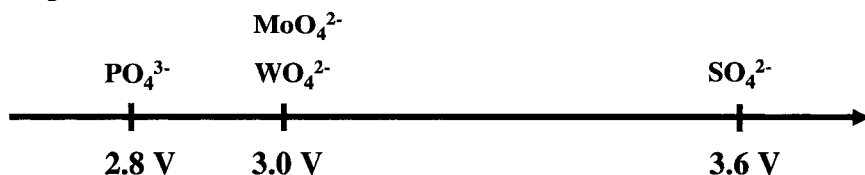


Figure 15.3. Positions of the $\text{Fe}^{3+}/\text{Fe}^{2+}$ redox couple vs. Li^+/Li in NASICON compositions $\text{Li}_x\text{Fe}_2(\text{XO}_4)_3$.

15.2.1. Relative Positions of Various $\text{M}^{n+}/\text{M}^{(n-1)+}$ Redox Couples ($\text{M} = \text{Fe}, \text{Ti}, \text{V}, \text{Nb}$) in Nasicon Phosphates

We indicated above how the value of a given redox couple ($\text{Fe}^{3+}/\text{Fe}^{2+}$) would be influenced by the chemical nature of the tetrahedral XO_4^{n-} group. In this section, we fix the XO_4^{n-} polyanion as a phosphate PO_4^{3-} group. A very rich variety of $\text{A}_x\text{MM}'(\text{PO}_4)_3$ compositions having the NASICON structure is accessible and the number x ($0 \leq x \leq 5$) of alkali cations is governed by the chemical nature and the oxidation states of M and M' . Besides the considerable amount of contributions in the literature on how the ionic conduction of NASICON compositions would be influenced by the amount of alkali cations and by the nature of (M, M') , only few studies have been devoted so far on their behavior as hosts for reversible alkali

insertion/extraction.³¹ The major advances were reported by the groups of Delmas, Quarton and Goodenough and are summarized below.

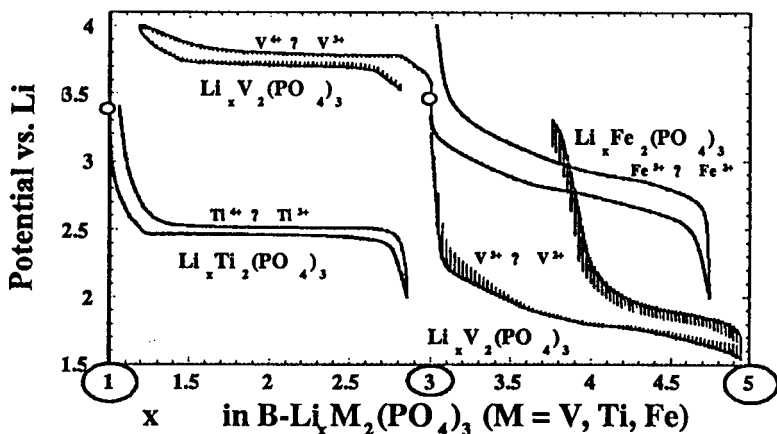


Figure 15.4. Voltage – composition profiles recorded vs. Li^+/Li during lithium insertion/extraction into/from various NASICON compositions $\text{Li}_x\text{M}_2(\text{PO}_4)_3$ ($\text{M} = \text{Fe}, \text{V}, \text{Ti}$)

15.2.2. Position of the $\text{Ti}^{4+}/\text{Ti}^{3+}$ Couple vs. Li^+/Li and Na^+/Na

Delmas^{9,10,32} showed the possible insertion of lithium or sodium into $\text{LiTi}_2(\text{PO}_4)_3$ and $\text{NaTi}_2(\text{PO}_4)_3$, respectively, to reach the end-members $\text{A}_3\text{Ti}_2(\text{PO}_4)_3$ ($\text{A} = \text{Li}, \text{Na}$) into which titanium is at the oxidation state +III. Delmas determined first,³² recently confirmed by Aatiq³³ and Patoux that lithium insertion into $\text{LiTi}_2(\text{PO}_4)_3$ occurs at 2.48 V vs. Li^+/Li for the $\text{Ti}^{4+}/\text{Ti}^{3+}$ redox couple according to a two-phase mechanism between $\text{LiTi}_2(\text{PO}_4)_3$ and $\text{Li}_3\text{Ti}_2(\text{PO}_4)_3$ (Figure 15.4). The *in situ* X-ray diffraction data³³ of Figure 15.5 show on discharge the progressive disappearance of $\text{LiTi}_2(\text{PO}_4)_3$ peaks at the benefit of those of $\text{Li}_3\text{Ti}_2(\text{PO}_4)_3$.

For $\text{Li}_3\text{Ti}_2(\text{PO}_4)_3$, the appearance of an XRD peak at around $2\theta \sim 39.0^\circ$ ($d = 2.30 \text{ \AA}$, (303)) indicates that the space group $R\bar{3}c$ (into which $\text{LiTi}_2(\text{PO}_4)_3$ crystallizes) is no longer valid. On going from $\text{LiTi}_2(\text{PO}_4)_3$ to $\text{Li}_3\text{Ti}_2(\text{PO}_4)_3$, Delmas pointed out a remarkable increase in the c/a ratio of the hexagonal unit-cell, due to stronger electrostatic repulsions between $[\text{Ti}_2(\text{PO}_4)_3]$ lanterns along [001] when the M1 site, located halfway between two lanterns, is emptied (Figure 15.1).

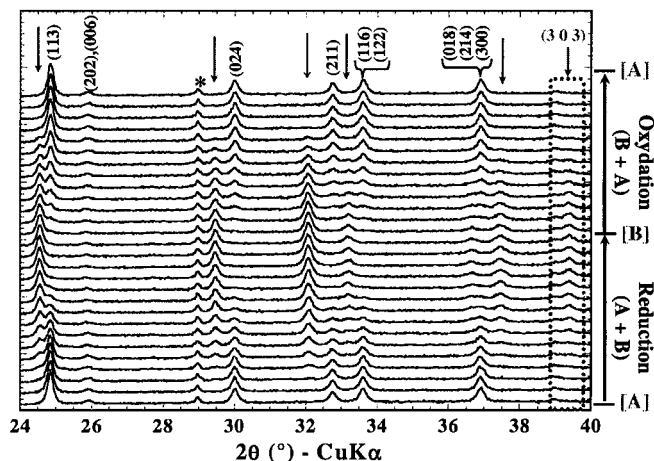


Figure 15.5. In situ X-ray diffraction patterns recorded during a full discharge and charge cycle of a $\text{LiTi}_2(\text{PO}_4)_3 / \text{Li}$ cell.

In a first approach, $\text{Li}_3\text{Ti}_2(\text{PO}_4)_3$ adopts the crystal structure of $\text{Li}_3\text{Fe}_2(\text{PO}_4)_3$ determined by Masquelier³⁴ where Li^+ ions occupy a set of tetrahedral sites labelled as M3, shifted by $\sim 0.8 \text{ \AA}$ along [001] from the M2 position. From a careful investigation coupling solid state Li NMR and powder neutron diffraction, Aatiq *et al.*³³ indicate that the situation is even more complex as lithium appears to be distributed on two similar tetrahedral sites M3' and M3'', occupied in the ratio 2/3 and 1/3, respectively.

As shown in Figure 15.6, the isotopic composition $\text{NaTi}_2(\text{PO}_4)_3$ is also active towards the electrochemical insertion of sodium according once again to a two-phase mechanism. The reversible redox process occurs at 2.15 V vs. Na^+/Na for the $\text{Ti}^{4+}/\text{Ti}^{3+}$ couple. This value is once again a clear demonstration of very weak interactions between the alkali cations and the framework in the NASICON structure as the $\sim 0.3\text{V}$ difference between the operating voltages of $\text{Li}/\text{Li}_{1+x}\text{Ti}_2(\text{PO}_4)_3$ and $\text{Na}/\text{Na}_{1+x}\text{Ti}_2(\text{PO}_4)_3$ reflects the difference between the Li^+/Li and Na^+/Na couples. Patoux showed recently³⁵ that sodium insertion into $\text{NaTi}_2(\text{PO}_4)_3$ results into $\text{Na}_3\text{Ti}_2(\text{PO}_4)_3$ isostructural with $\text{Na}_3\text{Fe}_2(\text{PO}_4)_3$ where the M(1) site is still fully occupied and M(2) at 2/3.

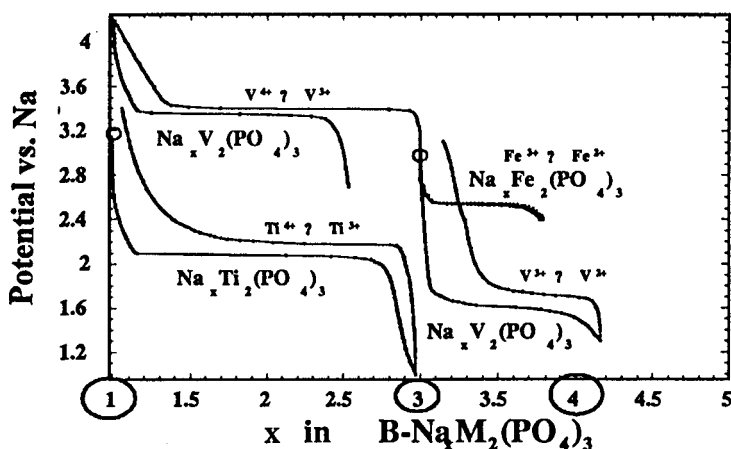


Figure 15.6. Voltage – composition profiles recorded vs. Na^+/Na during sodium insertion/extraction into/from various NASICON compositions $\text{Na}_x\text{M}_2(\text{PO}_4)_3$ ($\text{M} = \text{Fe}, \text{V}, \text{Ti}$).

15.2.3. Relative Positions of the $\text{Ti}^{4+}/\text{Ti}^{3+}$, $\text{Fe}^{3+}/\text{Fe}^{2+}$, $\text{Nb}^{5+}/\text{Nb}^{4+}$, $\text{Nb}^{4+}/\text{Nb}^{3+}$, $\text{V}^{4+}/\text{V}^{3+}$ and $\text{V}^{3+}/\text{V}^{2+}$ Couples vs. Na^+/Na and Li^+/Li in the NASICON Structure

A first series of detailed investigations had been conducted in the early 90's by Quaroni's group who demonstrated Na^+ reversible insertion into several mixed NASICON compositions $\text{Na}_x\text{MM}'(\text{PO}_4)_3$ ($\text{M} = \text{Fe}, \text{Ti}, \text{Nb}, \text{Sc}$).¹⁶⁻¹⁹ Peculiar attention was given to the compositions $\text{Na}_x\text{TiNb}(\text{PO}_4)_3$,^{17,18} $\text{Na}_{1+x}\text{FeNb}(\text{PO}_4)_3$,^{18,19} $\text{Na}_{1+x}\text{ScNb}(\text{PO}_4)_3$ ³⁶ and $\text{Na}_{2+x}\text{FeTi}(\text{PO}_4)_3$.^{16,19} An important result was that the position of a given $\text{M}^{n+}/\text{M}^{(n-1)+}$ redox couple is mostly independent of the chemical nature of the second transition metal element M' , due to the absence of direct connectivity between two $(\text{M}, \text{M}')\text{O}_6$ octahedra. For instance, the $\text{Ti}^{4+}/\text{Ti}^{3+}$ couple was found to lie at the same value of ~ 2.2 V vs. Na^+/Na in $\text{Na}_x\text{TiNb}(\text{PO}_4)_3$, $\text{Na}_{2+x}\text{FeTi}(\text{PO}_4)_3$ and $\text{Na}_{1+x}\text{Ti}_2(\text{PO}_4)_3$. Additional experiments performed recently by Patoux³³ on $\text{Na}_{2+x}\text{TiM}(\text{PO}_4)_3$ ($\text{M} = \text{Fe}, \text{Cr}$) are depicted in Figure 15.7.

The case of $\text{Na}_{2+x}\text{FeTi}(\text{PO}_4)_3$ is instructive as $\text{Fe}^{3+} \rightarrow \text{Fe}^{2+}$ reduction occurs first at ~ 2.45 V vs. Na^+/Na before reduction of $\text{Ti}^{4+} \rightarrow \text{Ti}^{3+}$ at 2.2 V. The data obtained for $\text{Na}_{1+x}\text{FeNb}(\text{PO}_4)_3$ ¹⁹ and $\text{Na}_{3+x}\text{Fe}_2(\text{PO}_4)_3$ (Figure 15.6) confirm the position of $\text{Fe}^{3+}/\text{Fe}^{2+}$ vs. Na at ~ 2.5 V. Besides this, it is of importance to note that only one sodium ion may be intercalated into

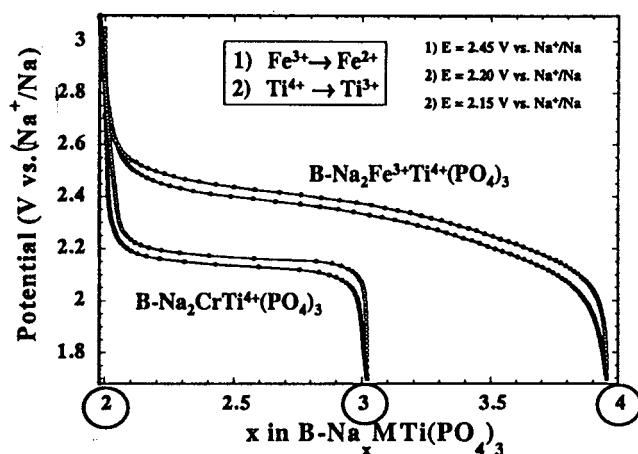


Figure 15.7. Voltage – composition profiles recorded vs. Na^+/Na during sodium insertion/extraction into/from NASICON $\text{Na}_{2+x}\text{TiM}(\text{PO}_4)_3$ ($M = \text{Fe}, \text{Cr}$).

$\text{Na}_3\text{Fe}_2(\text{PO}_4)_3$ as a result of the complete filling of both $M(1)$ and $M(2)$ sites.³⁵ Tillement was the first to locate the $\text{Nb}^{5+}/\text{Nb}^{4+}$ and $\text{Nb}^{4+}/\text{Nb}^{3+}$ redox couples in the NASICON structure, at 1.90 V and 1.20 V vs. Na, respectively.

As shown in Figure 15.6, the NASICON composition $\text{Na}_3\text{V}_2(\text{PO}_4)_3$ may lead to either oxidation of $\text{V}^{3+} \rightarrow \text{V}^{4+}$ through sodium extraction³⁶ or to partial reduction of $\text{V}^{3+} \rightarrow \text{V}^{2+}$ through sodium insertion. The difference between these two couples is of 1.8 V (3.4 V and 1.6 V vs. Na^+/Na , respectively). From *in situ* X-ray diffraction during cell operation, Patoux showed that the extraction of sodium from $\text{Na}_3\text{V}_2(\text{PO}_4)_3$ to $\text{NaV}_2(\text{PO}_4)_3$ is a two phase reaction, the latter phase being isotypical with $\text{NaTi}_2(\text{PO}_4)_3$.

A similar approach was followed by Goodenough's group to evaluate the relative positions of these same transition elements couples when lithium is inserted or extracted into/from the NASICON framework. To this end, $\text{Li}_x\text{MM}'(\text{PO}_4)_3$ compositions were prepared through $\text{Na}^+ \leftrightarrow \text{Li}^+$ ion exchange from the stable sodium analogs immersed in molten LiNO_3 at 300°C. $\text{LiFeNb}(\text{PO}_4)_3$,³⁷⁻³⁹ $\text{Li}_2\text{FeTi}(\text{PO}_4)_3$,³⁷⁻³⁹ $\text{Li}_3\text{Fe}_2(\text{PO}_4)_3$,^{27-29,40} and $\text{Li}_3\text{V}_2(\text{PO}_4)_3$ ⁴¹⁻⁴³ are among the most significant examples.

Recent neutron diffraction^{41(a,b),44} and *in situ* X-ray diffraction experiments⁴⁵ demonstrated that the the composition $\text{Li}_3\text{V}_2(\text{PO}_4)_3$ is isostructural with $\text{Li}_3\text{Fe}_2(\text{PO}_4)_3$ and $\text{Li}_3\text{Ti}_2(\text{PO}_4)_3$. Lithium extraction leads to $\text{LiV}_2(\text{PO}_4)_3$ isostructural with $\text{LiTi}_2(\text{PO}_4)_3$ (Figure 15.8). This occurs at an interesting potential of 3.75 V vs. Li^+/Li , among the highest for polyanionic structures. The overall data relative to lithium insertion or extraction is perfectly consistent with the one obtained for sodium

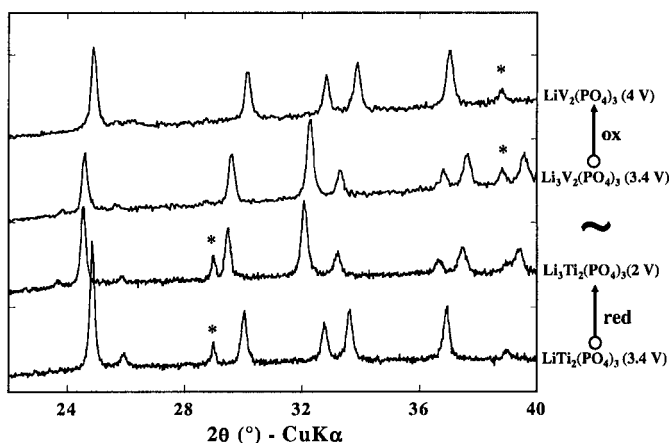


Figure 15.8. X-ray diffraction patterns collected *in situ* for NASICON $\text{LiM}_2(\text{PO}_4)_3$ and $\text{Li}_3\text{M}_2(\text{PO}_4)_3$ ($\text{M} = \text{Ti}, \text{V}$)

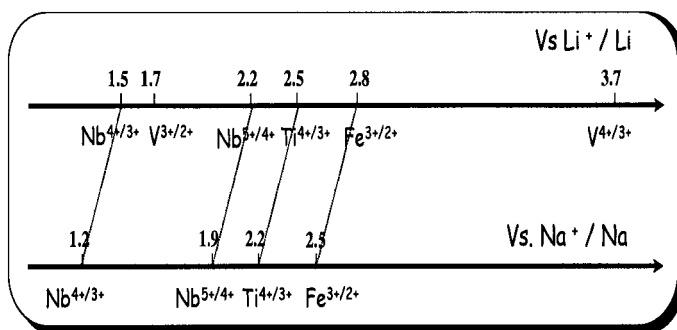


Figure 15.9. Positions of $\text{M}^{n+}/\text{M}^{(n-1)+}$ redox couples in NASICON $\text{A}_x\text{MM}'(\text{PO}_4)_3$.

insertion/extraction and is summarized in Figure 15.4 and Figure 15.9.

All these studies, summarized in Figure 15.10, have identified a wide variety of redox potentials for the NASICON frameworks containing reducible /oxidizable transition metals. The values of these couples are strongly dependent on the nature of the XO_4 tetrahedral polyanion and on the transition metal itself. The NASICON framework, additionally, is found to be remarkably stable over a large range of alkali ion content. Electrochemical insertion of lithium has allowed for instance to isolate for the first time NASICON structures ($\text{Li}_5\text{Fe}_2(\text{PO}_4)_3$ and $\text{Li}_5\text{V}_2(\text{PO}_4)_3$) containing 5 alkali cations per structural formula.^{27,40}

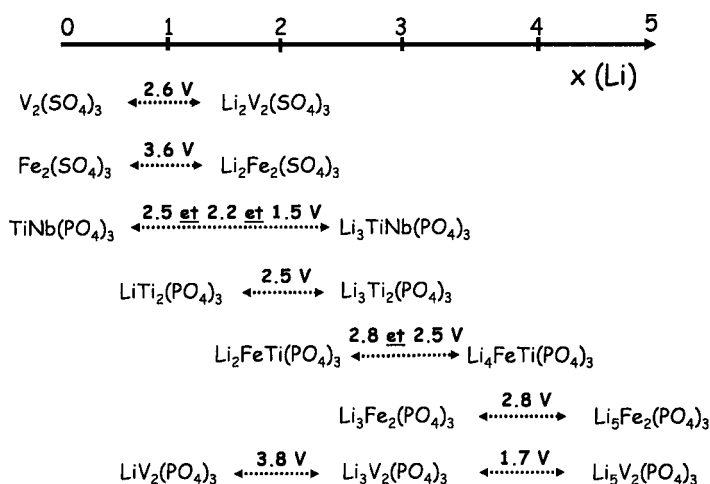


Figure 15.10. Selected examples of NASICON compositions obtained electrochemically (in black) from various starting electrodes (in blue).

15.3. EXTENSION OF THE CONCEPT TO OTHER POLYANIONIC STRUCTURES

The third part of this contribution deals with a review, as complete as possible, on latest discoveries and achievements in shifting the concept of using polyanionic insertion hosts, from an academic curiosity to attractive candidates for real systems. As stated above, these materials take full benefit of the inductive effect that, for a given transition element redox couple, lead to higher operating voltages than for “simple” oxides. The presence of the “heavy” XO_4 groups is of course penalizing, compared to the oxides, in terms of theoretical specific capacity that can be achieved. However, as we showed for the “didactic” NASICON family, this is partly compensated by the high stability of these frameworks that allow to fully extract or insert lithium without irreversible structural changes.⁴⁶ The theoretical capacity of 138 mAh/g for the reaction $\text{LiTi}_2(\text{PO}_4)_3 \leftrightarrow \text{Li}_3\text{Ti}_2(\text{PO}_4)_3$ at 2.5 V vs. Li^+/Li is effectively attained experimentally, once smart electrode preparation is performed to favor electron transport into these mostly insulating materials. The most exciting example, developed in details further below is that of LiFePO_4 out of which several groups have recently succeeded in obtaining experimental capacities very close to the theoretical value of 170 mAh/g.

Table 15.1. Selected examples of iron-containing phosphate structures that reversibly insert lithium at potentials ranging from 2.5 to 3.5 V vs. Li^+/Li .

	Formula	M (g.mol ⁻¹)	Théor. Cap. (mAh/g)	Operating Voltage vs. Li^+/Li
M/P = 1	LiFePO_4	157.8	170	$\text{Fe}^{3+/2+}$: 3.45 V
M/P = 1	$\text{FePO}_4 \cdot 2\text{H}_2\text{O}$	186.8	147	$\text{Fe}^{3+/2+}$: 3.00 V
M/P = 2/3	$\text{Fe}_4(\text{P}_2\text{O}_7)_3 \cdot 4\text{H}_2\text{O}$	745.2	144	$\text{Fe}^{3+/2+}$: 3.20 V
M/P = 2/3	$\text{Li}_3\text{Fe}_2(\text{PO}_4)_3$	417.4	128	$\text{Fe}^{3+/2+}$: 2.80 V
M/P = 1/2	LiFeP_2O_7	231.7	116	$\text{Fe}^{3+/2+}$: 2.90 V

The selected examples given in Table 15.1 are relative to a same given $\text{Fe}^{3+}/\text{Fe}^{2+}$ redox couple for two kinds of polyanions, PO_4^{3-} and $\text{P}_2\text{O}_7^{4-}$. This illustrates the wide variety of potentials accessible depending on the crystal structure, as previously addressed by Padhi.³⁸ Table 15.1 illustrates as well the obvious penalty in terms of theoretical capacity when the Fe/P ratio decreases from LiFePO_4 to LiFeP_2O_7 .

The examples developed below include several structural families, mostly phosphates, of iron, vanadium, titanium and niobium.

15.3.1. The Monoclinic Forms of $\text{Fe}_2(\text{SO}_4)_3$ and $\text{Li}_3\text{M}_2(\text{XO}_4)_3$ (M = Fe, V, X = P, As)

Depending on the preparation procedure, $\text{Fe}_2(\text{SO}_4)_3$ may adopt two distinct crystal structures where the $\text{Fe}_2(\text{SO}_4)_3$ lantern units are stacked differently in three-dimension. The rhombohedral form is of NASICON structure, fully described in the space group $R\bar{3}$.⁴⁷ The lantern units are stacked parallel to the [001] direction of the hexagonal unit-cell. In the monoclinic form, space group $P2_1/n$,⁴⁸ the lantern units are stacked antiparallel, alternately along the directions $\sim(2b \pm c)$ of the monoclinic unit-cell.^{49,50} This arrangement of MO_6 octahedra and SO_4 tetrahedra results in a less open structure than in the NASICON form, less favourable for alkali ion transport. This is illustrated by the schematic representations of Figure 15.11

that differentiate the bottlenecks in both monoclinic and NASICON forms of $\text{Fe}_2(\text{SO}_4)_3$: 6-membered “rings” for the monoclinic form, 8-membered “rings” for the NASICON form.

The monoclinic forms of $\text{Li}_3\text{Fe}_2(\text{PO}_4)_3$,^{24,51,52,53} $\text{Li}_3\text{Fe}_2(\text{AsO}_4)_3$ ^{54,27} and $\text{Li}_3\text{V}_2(\text{PO}_4)_3$ ^{55,56} are easily prepared by solid state reaction at 700-900°C. They are isostructural with $\text{Li}_3\text{In}_2(\text{PO}_4)_3$.⁴⁹

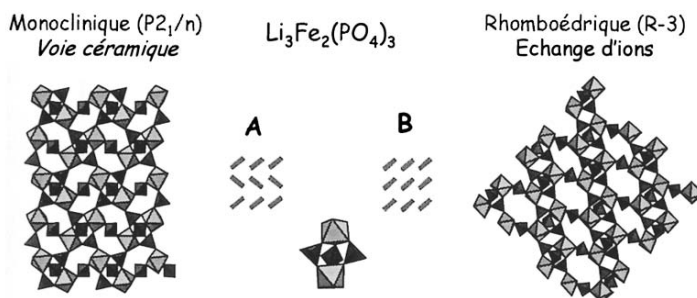


Figure 15.11. Schematic representations of the monoclinic (left) and hexagonal-NASICON (right) forms of $\text{Fe}_2(\text{SO}_4)_3$.

Manthiram⁸ was the first to report on the insertion of lithium into monoclinic $\text{Fe}_2(\text{SO}_4)_3$ at an attractive potential of 3.6 V vs. Li^+/Li . Okada⁵⁶ showed that NASICON and monoclinic $\text{Fe}_2(\text{SO}_4)_3$ had similar electrochemical signatures. Insertion of lithium into monoclinic $\text{Fe}_2(\text{SO}_4)_3$ occurs through a two-phase reaction, the end-member $\text{Li}_2\text{Fe}_2(\text{SO}_4)_3$ being of orthorhombic symmetry (*Pcan*).⁵⁷

In the same study, Okada investigated for the first time the behavior of monoclinic $\text{Li}_3\text{Fe}_2(\text{PO}_4)_3$ and located the $\text{Fe}^{3+}/\text{Fe}^{2+}$ couple at 2.8 V vs. Li^+/Li . At this point, $\text{Li}_3\text{Fe}_2(\text{PO}_4)_3$ was envisaged as an interesting buffer material to be mixed with $\text{Fe}_2(\text{SO}_4)_3$ for protection against overdischarge. More detailed investigations,^{27,29} revealed though that two bi-phasic reactions take place at 2.88 V and 2.73 V vs. Li^+/Li with the existence of a definite composition $\text{Li}_4\text{Fe}_2(\text{PO}_4)_3$ in between. *In situ* X-ray diffraction during a discharge process⁵⁶ revealed that the framework is very well-maintained and that the intermediate phases involved are extremely similar to the pristine one. From Potentiodynamic Cycling with Galvanostatic Acceleration technique, Morcrette determined²⁹ that these phase transitions are kinetically limited more by electron transport within each phase rather than from phase front migration (Li diffusion) (Figure 15.12).

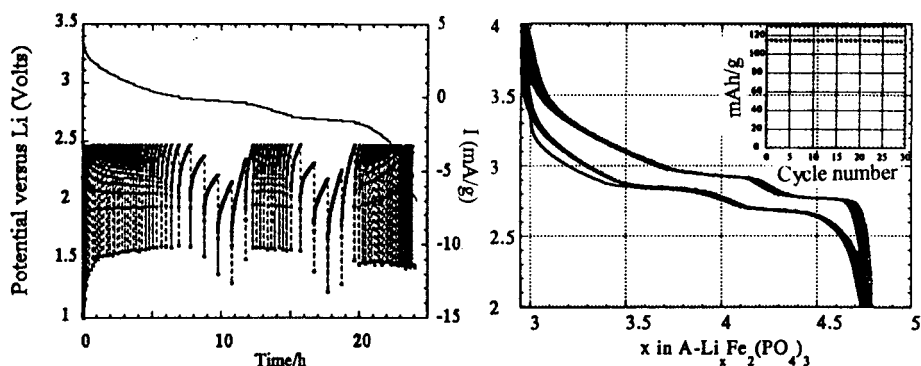


Figure 15.12. Discharge in PCGA mode (left) and galvanostatic cycling at C/10 (right) of a monoclinic $\text{Li}_3\text{Fe}_2(\text{PO}_4)_3$ / Li cell.²⁹

Additionally, Morcrette showed that reversible capacities as high as 115 mAh/g at C/10 regime could be attained with an excellent capacity retention once particle sizes and surface were optimized. Tailored particles were obtained chemically by a low temperature synthetic route and their surface was then modified by ball milling of carbon/ $\text{Li}_3\text{Fe}_2(\text{PO}_4)_3$ mixtures.

Much attention has been given recently to the monoclinic $\text{Li}_3\text{V}_2(\text{PO}_4)_3$ that can be oxidized through lithium extraction at potentials ranging from 3.4 V to 4.6 V vs. Li^+/Li .^{55,56,58-60} $\text{Li}_3\text{V}_2(\text{PO}_4)_3$ shows a complicated series of four successive two-phase transitions on Li extraction towards $\text{Li}_{0.1}\text{V}_2(\text{PO}_4)_3$ (Figure 15.13). From *in situ* X-ray diffraction, Morcrette⁴⁵ identified that all the intermediate compositions were fully indexed in the monoclinic space group $P2_1/n$, with a unit-cell contraction of $\Delta V/V = -6.8\%$ between $\text{Li}_3\text{V}_2(\text{PO}_4)_3$ and $\text{LiV}_2(\text{PO}_4)_3$ and a slight increase on further oxidation to $\text{Li}_{0.1}\text{V}_2(\text{PO}_4)_3$. Despite these numerous phase transitions and non-negligible volume changes, the monoclinic $\text{Li}_3\text{V}_2(\text{PO}_4)_3$ system is structurally highly reversible and, once vanadium dissolution in the electrolyte will have been prevented, will stand as a promising positive electrode for Li-rechargeable batteries.

Lithium may be inserted as well into the monoclinic arsenate $\text{Li}_3\text{Fe}_2(\text{AsO}_4)_3$, towards $\text{Li}_3\text{Fe}_2(\text{AsO}_4)_3$ through reduction of Fe^{3+} into Fe^{2+} . The shape of the potential-composition curve²⁷ is very similar to that of $\text{Li}_3\text{Fe}_2(\text{PO}_4)_3$, with the existence of an intermediate composition $\text{Li}_4\text{Fe}_2(\text{AsO}_4)_3$ between two two-phase reactions. These reactions take place at 2.91V and 2.62V vs. Li^+/Li , i.e. are better separated than for $\text{Li}_3\text{Fe}_2(\text{PO}_4)_3$ but the average voltage is very similar. Substitution of AsO_4^{3-} for PO_4^{3-} has very minor influence on the global inductive effect on iron due to the similar electronegativities of As and P. This was confirmed by Gaubicher^{61,62} who

found same redox potential values (4.0 V vs. Li^+/Li) for the $\text{V}^{5+}/\text{V}^{4+}$ couple in Li_xVOPO_4 and $\text{Li}_x\text{VOAsO}_4$.

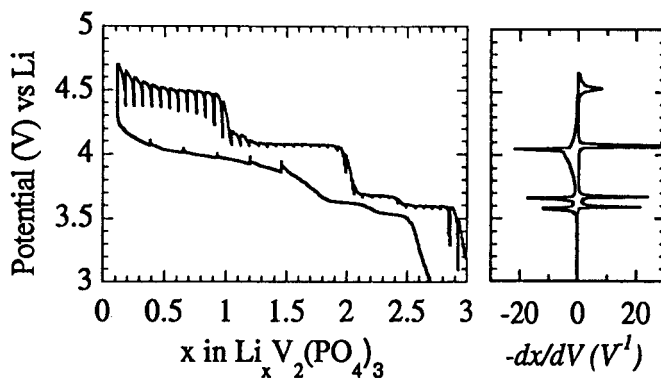


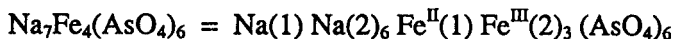
Figure 15.13. Cycling of a monoclinic $\text{Li}_3\text{V}_2(\text{PO}_4)_3 / \text{Li}$ cell in GITT mode (left) and corresponding derivative curves (right).⁴⁵

15.3.2. The Rhombohedral Form of $\text{Li}_3\text{Fe}_2(\text{AsO}_4)_3$

A second form of $\text{Li}_3\text{Fe}_2(\text{AsO}_4)_3$ may be prepared through ion exchange from the sodium analog $\text{Na}_3\text{Fe}_2(\text{AsO}_4)_3$.^{63,64} This structure is unusual for being built on Fe_4O_{18} clusters into which one $\text{Fe}(1)\text{O}_6$ octahedron is surrounded by three $\text{Fe}(2)\text{O}_6$ octahedra through edge sharing. Alkali cations are distributed on two independent crystallographic sites, A(1) fully occupied, and A(2) occupied at 5/6 according to the structural formula :



d'Yvoire⁶⁴ and Masquelier⁶⁵ showed that partial chemical reduction of Fe^{3+} into Fe^{2+} could occur through adding of extra sodium ions in the interstitial space according to the structural formula :



The electrochemical insertion of lithium into this unusual form of $\text{Li}_3\text{Fe}_2(\text{AsO}_4)_3$ allowed to demonstrate the preferential reduction of $\text{Fe}(1)$. During the first discharge, two clearly distinct redox processes occur as intercalation plateaus located at 3.1 and 2.4 V vs. Li^+/Li . As seen in the inset, the first process at 3.1 V is highly reversible. It corresponds to the insertion of 0.5 Li^+ per $\text{Li}_3\text{Fe}_2(\text{AsO}_4)_3$ unit, hence to the total occupation of the A(2) site

and hence, by analogy with the sodium analog, to the reduction of $\text{Fe}^{\text{III}}(1)$ into $\text{Fe}^{\text{II}}(1)$. The second process corresponds to reduction of Fe on the Fe(2) sites but irreversible structural changes occur.

15.3.3. The Diphosphates and Diarsenates $\text{Li}_x\text{MX}_2\text{O}_7$ ($\text{M} = \text{Fe, V, Ti}$; $\text{X} = \text{P, As}$)

As Table 15.1 indicates, $\text{Li}_x\text{MX}_2\text{O}_7$ compositions^{66,67} are clearly not competitive electrode materials in terms of theoretical capacities to be delivered. They provide however an interesting panel of crystal structure arrangements and electrochemical insertion mechanisms that deserve to be shortly mentioned here. In a comparative study, Wurm⁶⁸ described the preparation of LiFeP_2O_7 , $\text{LiFeAs}_2\text{O}_7$ and LiVP_2O_7 as pure microcrystalline powders via an aqueous solution route that allowed the formation of finely dispersed small particles.

The redox couples that are accessible are $\text{Fe}^{3+}/\text{Fe}^{2+}$ for $\text{Li}_{1+x}\text{FeX}_2\text{O}_7$ and, interestingly, $\text{V}^{4+}/\text{V}^{3+}$ and $\text{V}^{3+}/\text{V}^{2+}$ for $\text{Li}_{1\pm x}\text{VP}_2\text{O}_7$.⁶⁷ Patoux³³ showed the complete reduction of Ti^{4+} to Ti^{3+} from TiP_2O_7 to LiTiP_2O_7 . LiFeP_2O_7 and LiVP_2O_7 are isostructural^{49,69,70} and crystallize in the space group $P2_1$. As shown in Figure 15.14a, each FeO_6 (or VO_6) octahedron is linked to five different P_2O_7 groups, one of them acting as a “chelating” sequence around Fe (or V). $\text{LiFeAs}_2\text{O}_7$ adopts its own crystal structure,⁷¹ described in the space group $C2$. There is in this case no bidentate corner sharing, and thus each FeO_6 octahedron is linked to six different As_2O_7 groups (Figure 15.14b).

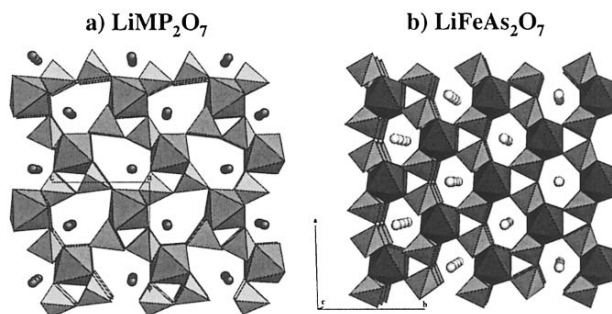


Figure 15.14. Partial representation of the crystal structures of (a) LiMP_2O_7 ($\text{M} = \text{Fe, V}$) and (b) $\text{LiFeAs}_2\text{O}_7$.

Padhi showed first³⁷ that the electrochemical insertion of lithium into LiFeP_2O_7 occurred at 2.9 V vs. Li^+/Li *i.e.* at a slightly higher operating voltage than for $\text{Li}_3\text{Fe}_2(\text{PO}_4)_3$. However, at this early stage of investigations on polyanionic structures, only part of the theoretical capacity (~60%) was

obtained due to the poor electronic conductivity of such material. Wurm⁶⁸ showed that the electrochemical activity of these materials is drastically enhanced by an intimate mixing of finely divided particles of pristine materials with conductive carbon, through ball milling.

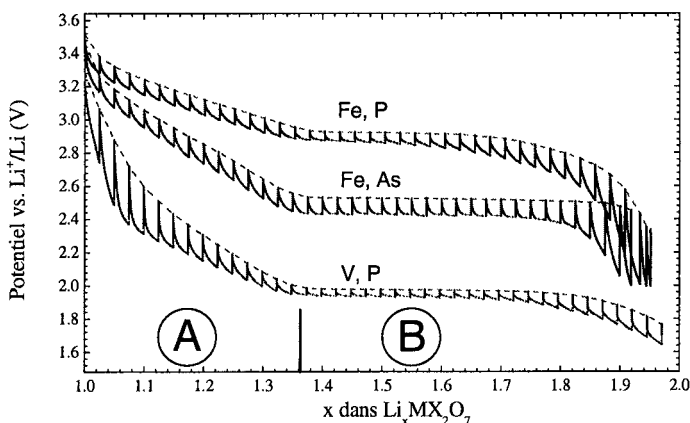


Figure 15.15. Potential-composition curves recorded in GITT mode during the first discharge of $\text{Li}_{1+x}\text{MX}_2\text{O}_7$ ($\text{M} = \text{Fe}, \text{V}$; $\text{X} = \text{P}, \text{As}$) / Li cells.

This mandatory step resulted in producing amorphous Li-M-X-O domains at the surface of crystalline LiMX_2O_7 crystallites and a continuous voltage decrease is first observed as lithium insertion proceeds into the amorphous part of the composite electrodes ("A" region of Figure 15.15).

Crystalline LiMX_2O_7 particles react with lithium through two-phase mechanisms, characterized by insertion plateaus located at 2.90 V for LiFeP_2O_7 ($\text{Fe}^{3+}/\text{Fe}^{2+}$ couple), 1.99 V for LiVP_2O_7 ($\text{V}^{3+}/\text{V}^{2+}$ couple) and 2.55 V for $\text{LiFeAs}_2\text{O}_7$ on first discharge. The Li-driven second phase is crystalline, with a larger unit-cell in the case of isostructural $\text{Li}_{1+x}\text{MP}_2\text{O}_7$ ($\text{M} = \text{Fe}, \text{V}$). It is amorphous in the case of $\text{Li}_{1+x}\text{FeAs}_2\text{O}_7$ that shows, interestingly, a recrystallisation process on charge (when Li is extracted from $\text{Li}_2\text{FeAs}_2\text{O}_7$) and subsequent cycling at ~ 2.90 V.

As for $\text{Li}_3\text{V}_2(\text{PO}_4)_3$, LiVP_2O_7 offers the possibility of operating on the $\text{V}^{4+}/\text{V}^{3+}$ redox couple if lithium is extracted. The electrochemical extraction of one lithium from LiVP_2O_7 occurs as a two-phase process at a relatively high equilibrium potential of 4.26V vs. Li^+/Li (Figure 15.16). The compound obtained at the end of the oxidation (either electrochemically or chemically) is totally exempt of lithium and the transformation between LiVP_2O_7 and VP_2O_7 is displacive, *i.e.* without breaking of V-O and P-O bonds. The crystal structure of VP_2O_7 was determined from Synchrotron X-Ray powder diffraction.⁷² The framework of LiVP_2O_7 is maintained upon lithium

extraction, and VP_2O_7 crystallizes in space group $P2_1$. Compared to LiVP_2O_7 , there is a very large cell distortion due to a modification of the shape of the tunnels that contained lithium ions along with an oxidation of the vanadium V^{III} to V^{IV} that induces shorter V-O bond lengths.

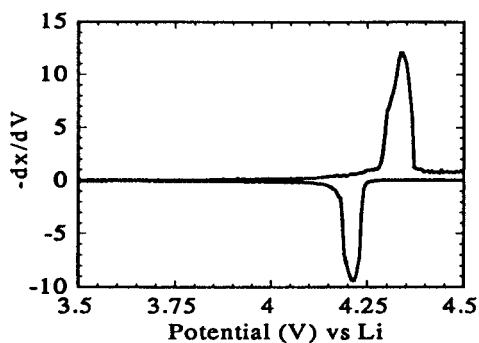


Figure 15.16. Electrochemical data recorded in PITT mode during lithium extraction/insertion from/into LiVP_2O_7 .⁶⁸

Patoux³³ showed the reversible insertion of lithium into $\text{Li}_x\text{TiP}_2\text{O}_7$,^{73, 74} that proceeds through two reversible redox processes, at 2.63 V and 2.57 V vs. Li^+/Li (Figure 15.17). From potentiodynamic intermittent titration technique and *in situ* XRD, a complex series of phase transitions was reported in details. The formation of $\text{Li}_{0.96}\text{TiP}_2\text{O}_7$ at the end of discharge corresponds to a global unit cell volume expansion of $\Delta V/V = +4.4\%$ from the pristine material TiP_2O_7 . The *in situ* XRD data revealed the good reversibility of the system as the XRD pattern of the pristine material TiP_2O_7 was recovered at the end of the first oxidation. This is a common feature to many polyanionic framework structures built on phosphate groups that easily accommodate relatively large volume expansions/contractions over extensive electrochemical cycling.

15.3.4. Amorphous or Crystalline Iron Phosphates: $\text{FePO}_4 \cdot n\text{H}_2\text{O}$ and $\text{Fe}_4(\text{P}_2\text{O}_7)_3 \cdot 4\text{H}_2\text{O}$

Recent contributions from Whittingham's⁷⁵ and Masquelier's⁷⁶ groups as well as those of Hong⁷⁷ and Prosini⁷⁸ indicate reversible insertion of lithium into amorphous hydrated Fe^{III} phosphates such as $\text{FePO}_4 \cdot 2\text{H}_2\text{O}$ and $\text{Fe}_4(\text{P}_2\text{O}_7)_3 \cdot 4\text{H}_2\text{O}$. As seen in Table 15.1, these compositions present attractive theoretical capacities, among the highest for iron phosphates. Such compounds are easily prepared from precipitation in aqueous media which leads to powders of submicronic particle size with high surface area.

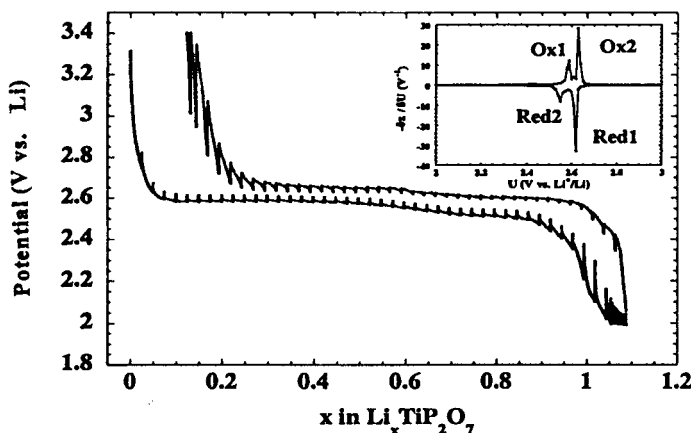


Figure 15.17. Potential-composition curve of TiP_2O_7 recorded in a GITT mode vs. Li^+/Li . The inset plot draws the incremental capacity voltammogram.⁴²

As stated by Morcrette²⁹ and Masquelier,⁷⁶ the poor electronic conduction of Fe^{III} phosphates may be partly compensated by selecting highly divided powders intimately mixed, or “coated” (through ball-milling) to conductive carbon. The beneficial role of constitutional water, that may act as a promoter for faster ionic diffusion has been demonstrated. Within the operating voltage window used (2V–4V vs. Li) these water molecules look unaffected as very good electrochemical stability was demonstrated for extensive cycling. This stability suggests that, as for the crystalline form of $\text{FePO}_4 \cdot 2\text{H}_2\text{O}$, where the 6-fold coordination of Fe is ensured by 4 oxygen belonging to PO_4 groups + 2 oxygen belonging to H_2O groups, a similar local arrangement occurs for the amorphous $\text{FePO}_4 \cdot n\text{H}_2\text{O}$ powders.

Despite a whole panel of kinetic responses that depend strongly on extrinsic parameters such as powder crystallinity, morphology, texture, and electrode preparation, all the materials investigated in Ref. 76 lead to a very similar operating voltage vs. Li, *i.e.* comprised mainly between 3.4 V and 2.6 V. As for crystalline LiFePO_4 and $\text{Li}_3\text{Fe}_2(\text{PO}_4)_3$, the position of the $\text{Fe}^{3+}/\text{Fe}^{2+}$ redox couple is thus strongly modified by the inductive effect of the PO_4 groups that diminishes the strength of the Fe–O bonds, even for amorphous compositions.

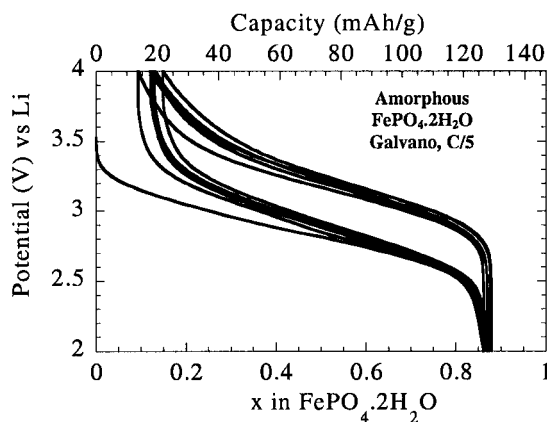


Figure 15.18. Li insertion in amorphous $\text{FePO}_4 \cdot 2\text{H}_2\text{O}$ at a C/5 regime. Electrolyte: LiPF_6 EC:DEC (1:1).

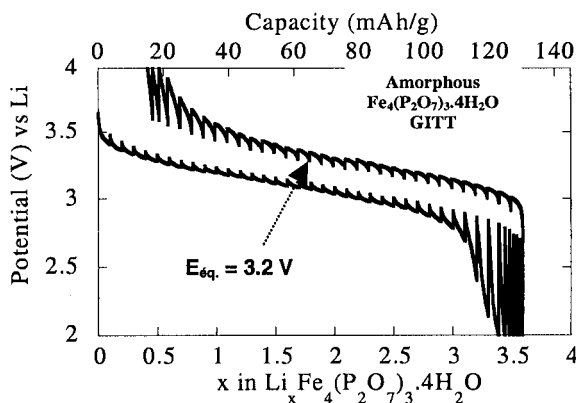


Figure 15.19. Potential-composition curve of amorphous $\text{Fe}_4(\text{P}_2\text{O}_7)_3 \cdot 4\text{H}_2\text{O}$ recorded in a GITT mode vs. Li^+/Li .⁷⁷

Both profiles of Figures 15.18 and 15.19 show S-shape voltage profiles without any well-defined intercalation plateau over the whole composition ranges. The position of the $\text{Fe}^{3+}/\text{Fe}^{2+}$ redox couples for both materials were then determined, after a first full cycle in GITT mode, by measuring the equilibrium potential after relaxing the battery for 2 days at half state of discharge. The obtained values are 3.0 V and 3.2 V for amorphous $\text{FePO}_4 \cdot 2\text{H}_2\text{O}$ and $\text{Fe}_4(\text{P}_2\text{O}_7)_3 \cdot 4\text{H}_2\text{O}$, respectively. This difference may arise from different local environments around Fe atoms. In this regard, it is interesting to note that the higher position of the $\text{Fe}^{3+}/\text{Fe}^{2+}$ redox couple in $\text{Fe}_4(\text{P}_2\text{O}_7)_3 \cdot 4\text{H}_2\text{O}$ (Fe/P = 2/3) may be related to the fact that Fe is statistically surrounded

by more PO_4 groups than in $\text{FePO}_4 \cdot 2\text{H}_2\text{O}$ ($\text{Fe/P} = 1$): it is therefore more affected by the inductive effect.

15.3.5. $\text{V}^{5+}/\text{V}^{4+}$ and $\text{V}^{4+}/\text{V}^{3+}$ Couples in Li_xVOXO_4 ($\text{X} = \text{P, As}$)

A very complete series of studies was initiated by Gaubicher^{61,62,79,80} and followed by Dupré^{81,82} and Kerr⁸³ on various Li_xVOXO_4 structures^{84,85} hosts for the reversible insertion of lithium. As for the NASICON structure, the inductive effect of XO_4^{n-} polyanion generates attractive operating voltages for the $\text{V}^{5+}/\text{V}^{4+}$ and $\text{V}^{4+}/\text{V}^{3+}$ redox couples in lithium batteries. However, as we'll discuss extensively, each MO_6 octahedron is connected to 4 XO_4 tetrahedra only, instead of 6 for the NASICON structure. This generates weaker global inductive effect in VOXO_4 -type structures than in $\text{A}_x\text{M}_2(\text{XO}_4)_3$.

We will focus here on the relative positions of these couples as a function of the crystal structure and of the chemical nature of the polyanion.

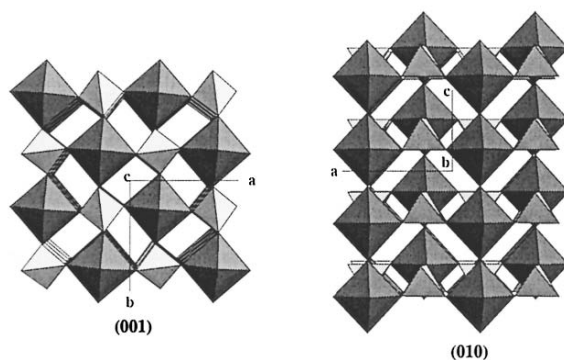


Figure 15.20. Schematic representation of the crystal structure of $\alpha\text{-VOPO}_4$. VO_6 octahedra are larger, PO_4 tetrahedra smaller.

From a structural point of view, two main classes of VOXO_4 ($\text{X} = \text{P, As, S}$) compositions, noted as α and β should be distinguished. The $\alpha\text{-VOPO}_4$ structure (Figure 15.20) is tetragonal, space group $P4/n$ and is built of $[\text{VO}_5]_\infty$ chains of VO_6 octahedra sharing corners along the quaternary axis $[001]$.^{86,87} The four remaining oxygen corners of the VO_6 octahedra each belong to a different XO_4 tetrahedron. VOAsO_4 adopts only the α form. The $\beta\text{-VOPO}_4$ structure (Figure 15.21) is orthorhombic, space group $Pnma$. The VO_6 octahedra are strongly distorted and form chains along $[100]$.

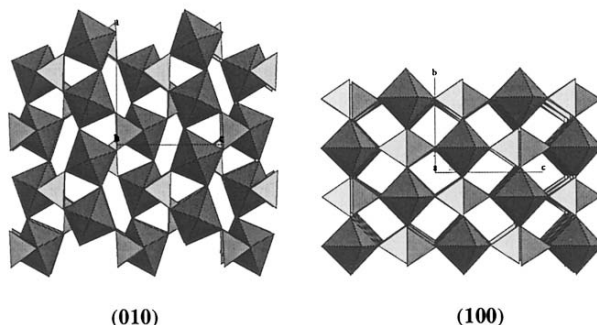


Figure 15.21. Schematic representation of the crystal structure of β -VOPO₄. VO₆ octahedra are larger, PO₄ tetrahedra smaller.

As mentioned earlier, only VOPO₄ may be prepared in the β form. Gaubicher indicated however⁸⁰ that this form may be stabilized for X = As by preparing β -LiVOAsO₄ from a mixture of VOAsO₄·2H₂O and Li₂CO₃ heated under Ar up to 600°C. As a consequence, the position of the V⁵⁺/V⁴⁺ redox couple in this structure could be determined by i) electrochemical insertion of lithium into VOPO₄ or ii) electrochemical extraction of lithium from LiVOAsO₄. For the two above reactions, the experimental values are extremely close, equal to 3.98 V and 4.02 V, respectively. This is an additional signature of the same electronegativities of P and As. The location of the V⁵⁺/V⁴⁺ couple at ~4V vs. Li⁺/Li is at an intermediate value between what was found for LiV₂(PO₄)₃ → V₂(PO₄)₃ (>4.5 V) and what is known for V₂O₅ (~3.4 V). This was interpreted in details by Gaubicher⁶¹ as a result of the peculiar structural arrangement in β -VOPO₄, itself intermediate between a NASICON structure (only ...V-O-X... sequences) and an infinite oxide (only ...V-O-V...) sequences.

15.3.6. Nb⁵⁺/Nb⁴⁺ Couple in Li_xNbPO₅

The chemical and electrochemical insertions of lithium into two structural forms of NbPO₅, α -NbOPO₄ (*P4/n*) and β -NbPO₅ (*P2₁/c*) was recently communicated by Patoux.³⁵

Among the complex polyanionic framework groups built of MO₆ octahedra (M = Nb, W, Mo, V...) and XO₄ tetrahedra (X = P, S, Mo...), the crystal structure of α -NbOPO₄ is built on one of the simplest arrangements.⁸⁶ It is described in the space group *P4/n* (*Z* = 2) with *a* = 6.388(1) Å and *c* = 4.118(1) Å and consists of PO₄ tetrahedra sharing their corners with NbO₆ octahedra, which themselves share four vertices with tetrahedra and two with other similar octahedra along [001] (Figure 15.22). Thus, the α -NbOPO₄

structure can be described as ..O-Nb-O-Nb-O... type chains, which are cross-linked by PO_4 forming a three-dimensional network.⁸⁷ The formulation $\text{NbO}(\text{PO}_4)$ accounts for this peculiar connectivity. The NbO_6 octahedra are distorted with 4 medium Nb-O(P) bond lengths (1.97 Å) in the (*a*, *b*) plane, one longer (2.32 Å) and one shorter (1.78 Å) alternately along the *c* axis (-O-Nb-O- sequences). Similar features are encountered for VOPO_4 and MoOPO_4 , which are isostructural with $\alpha\text{-NbOPO}_4$.

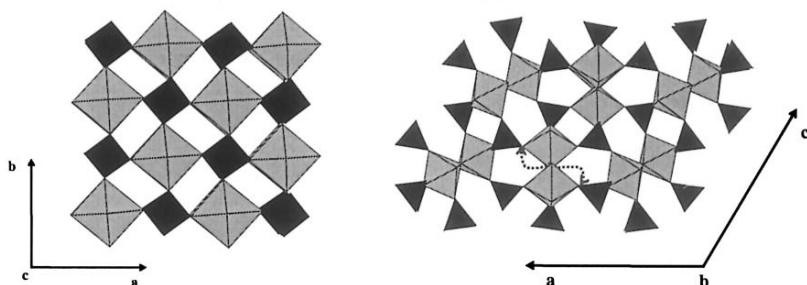


Figure 15.22. Schematic representation of the crystal structures of $\alpha\text{-NbOPO}_4$ (left) and $\beta\text{-NbPO}_5$ (right).

On the other hand, two kinds of more regular NbO_6 octahedra are encountered in $\beta\text{-NbPO}_5$ that crystallises in the monoclinic space group $P2_1/c$ ($Z = 8$) with $a = 13.028(1)$ Å, $b = 5.278(1)$ Å, $c = 13.225(1)$ Å and $\beta = 120.17(1)^\circ$.^{88,89} This second high temperature form, is characterised as the member $m=2$ of the “*MonoPhosphate Tungsten Bronze with pentagonal tunnels*” (MPTB_p) family of general formula $\text{A}_x(\text{NbO}_3)_{2m}(\text{PO}_2)_4$; ($\text{A} = \text{Li}, \text{Na}, \text{Ag}$)⁹⁰ The structure is described as ReO_3 -type chains of NbO_6 octahedra, separated by slabs of PO_4 tetrahedra delimiting pentagonal tunnels (Figure 15.22). In this structure, double strings of NbO_6 octahedra parallel to the *b* axis are isolated, and linked to others by tetrahedra only.

Both structures present distinct behaviours with regard to lithium insertion (Figure 15.23). $\beta\text{-Li}_x\text{NbPO}_5$ rapidly and reversibly uptakes lithium leading to a sustained capacity of 90–120 mAh/g (*i.e.* operating to the $\text{Nb}^{5+}/\text{Nb}^{4+}$ couple) for more than 100 cycles at ~ 2 V vs. Li^+/Li . This reversibility was confirmed by *in situ* X-ray diffraction in the range $0 \leq x \leq 0.7$ that additionally revealed a series of single- and two-phase insertion mechanisms. On the other hand, $\alpha\text{-Li}_x\text{NbOPO}_4$ displays an insertion plateau at ~ 1.7 V vs. Li^+/Li indicative of a two-phase process that was found to be poorly reversible. Both materials, when discharged at voltages lower than 1 V, present irreversible reactions with complete amorphization and reduction to metallic Niobium.

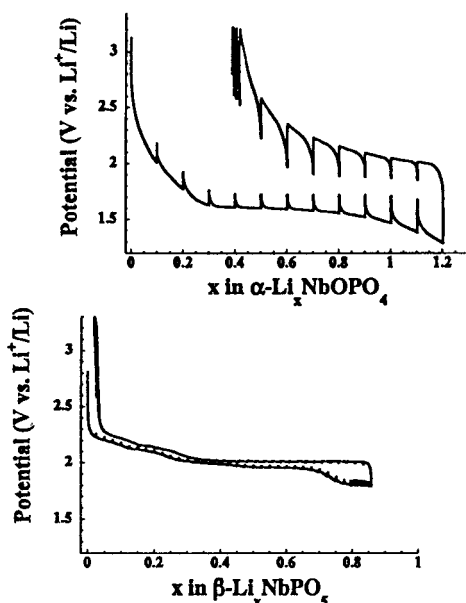


Figure 15.23. Potential-composition plots of GITT data recorded during Li insertion into α -NbOPO₄ (left) and β -NbPO₅ (right).

15.3.7. The Olivine LiMPO₄ (M = Fe, Mn, Co)

Since the demonstration by Padhi *et al.*^{39,91} that lithium can be extracted reversibly from triphylite at ~3.5V vs. Li⁺/Li, the material of choice for Li insertion/extraction among the so-called polyanionic structures is with no doubt the triphylite LiFePO₄. Lithium is extracted from the octahedral sites in a two phase process which, although very attractive for providing a very flat voltage plateau at 3.44V vs. Li⁺/Li, is penalizing through a kinetically limited front phase migration between LiFePO₄ and FePO₄.⁴¹

The triphylite LiFePO₄ adopts the olivine structure-type, built on an oxygen hexagonal packing into which Li⁺ and Fe²⁺ occupy half of the octahedral sites and P 1/8th of the tetrahedral sites. The peculiar distribution of Li⁺ and Fe²⁺ within the octahedral sites generates [FeO₆] layers as shown in Figure 15.24. This connectivity has a special impact on both electronic and ionic conductivity in LiFePO₄. FeO₆ octahedra share corners between each

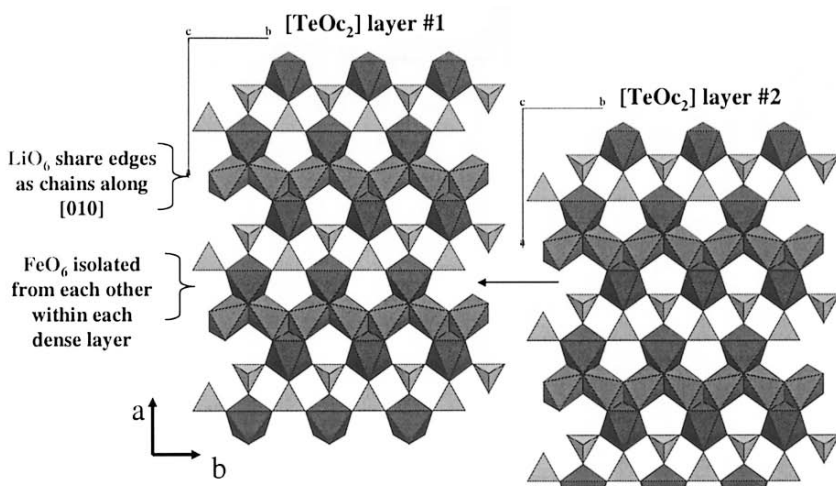


Figure 15.24. Structure representation of LiFePO_4 .

other, not edges, and electronic delocalization is made difficult. Lithium conductivity is not three-dimensional and proceeds mostly along [001]. Anderson demonstrated, by means of *in situ* Mössbauer spectroscopy and *in situ* X-ray diffraction, the two-phase character of the electrochemical extraction of lithium.^{92,93}

The theoretical capacity of 170 mAh/g at a flat potential plateau, the non toxicity and the cost of iron makes it a very good candidate to be used in industrial lithium batteries. Several patents have been published recently⁹⁴, Sony, HQ. Since Ravet's public announcement of reaching this theoretical capacity at high charge/discharge rates,⁹⁵ many efforts have focused on increasing the electronic conductivity at the surface of the mostly insulating LiFePO_4 . Recent significant advances have focused on

- i) increasing the electronic conductivity of composite electrodes through carbon coating.^{96,97,98,99}
- ii) lowering the synthesis temperature to $\sim 500^\circ\text{C}$.¹⁰⁰
- iii) using hydrothermal reaction,¹⁰¹⁻¹⁰³ or solution routes^{104,105}
- iv) adding foreign metallic elements such as Cu or Ag¹⁰⁶ or Nb.¹⁰⁷ Note that in this last case,¹⁰⁷ the term "doping" may be inappropriate to explain the dramatic increase in electronic conductivity of $\text{LiFePO}_4/\text{Nb}$ compared to that of LiFePO_4 .

Careful synthesis procedures are needed to stabilise Fe^{2+} in the

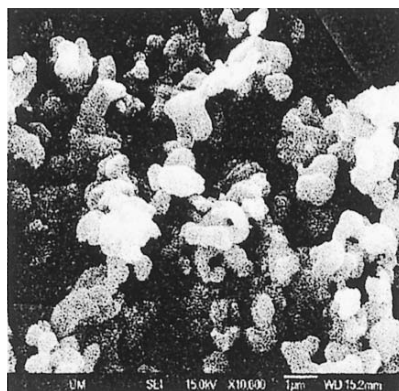


Figure 15.25. SEM image of optimized LiFePO_4 particles ($\sim 1\mu\text{m}$).¹⁰⁸

structure: i) prevent the formation of stable Fe^{III} phosphates such as LiFeP_2O_7 , $\text{Li}_3\text{Fe}_2(\text{PO}_4)_3$ and/or amorphous Fe^{III} phosphates if low temperature synthesis is chosen for producing small particles, ii) avoid the formation of iron phosphures such as Fe_2P if high temperature is chosen for improving the carbon-coated electronic conductivity.

Pure LiFePO_4 may be easily obtained at 500°C by annealing under reducing atmosphere the solid resulting from the evaporation ($\sim 150^\circ\text{C}$) of an aqueous solution containing lithium and iron (III) precursors. The particles thus produced are around $1\mu\text{m}$ in their largest dimension (against $50\mu\text{m}$ for the solid route presented by Padhi *et al.*) (Figure 15.25). A classical hand milling with carbon black to prepare the electrode gives very poor electrochemical performances. These are much enhanced by mechanical ball milling¹⁰⁹ which had to be optimised (duration, absence of oxygen in the container, etc...).

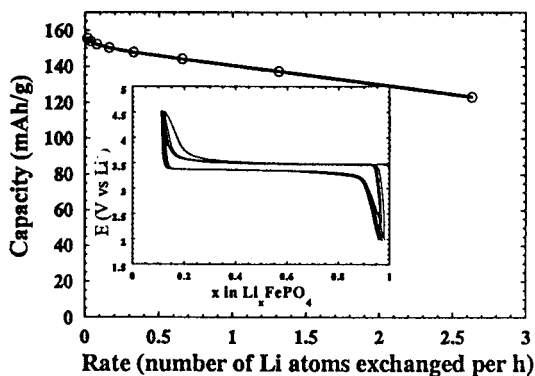


Figure 15.26. Galvanostatic cycling of a $\text{LiFePO}_4/\text{Li}$ cell at various rates at room at 20°C .

A similar “solution” route was used to coat chemically carbon at the surface of LiFePO_4 in an *in situ* way. Acrylonitrile was introduced in the initial aqueous solution with all the precursors needed for its polymerisation. Evaporation and polymerisation occur at the same time on first heating in air, after which the polymer is decomposed into carbon particles coated at the surface of LiFePO_4 . The electrochemical performances (Figure 15.26) are enhanced in this case as well, given appropriate thermal treatment of the composite electrode is done : at sufficient temperature to produce conductive carbon, not too high though to avoid reduction of Fe^{II} in Fe^0 .

For a carefully optimized LiFePO_4/C composite electrode, Morcrette *et al.* showed the complete transformation of LiFePO_4 into FePO_4 by means of *in situ* X-ray diffraction.¹⁰⁹ The diffractogram obtained at the end of charge of such electrode is compared to that obtained from a non-optimized electrode in Figure 15.27.

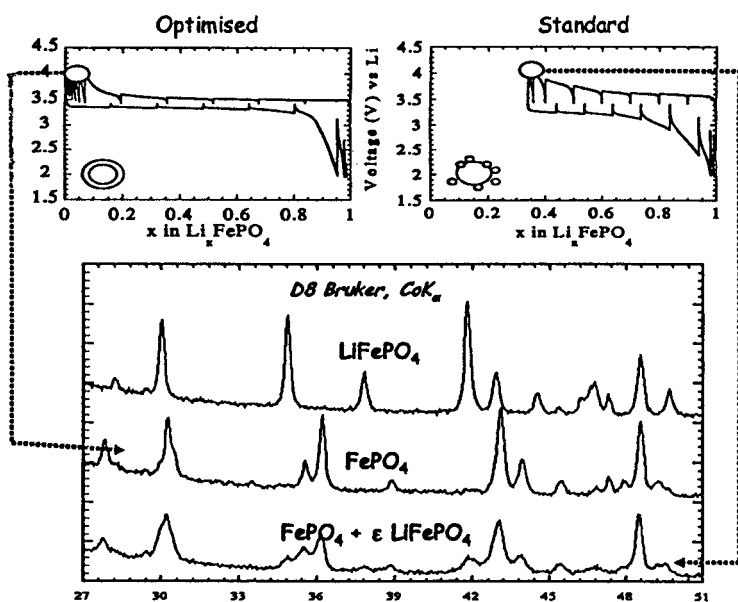


Figure 15.27. X-ray diffraction patterns of LiFePO_4/C pristine electrode and at the end of charge for two different electrodes.¹¹⁰

Padhi showed as well³⁸ that lithium extraction from isostructural compositions $\text{LiFe}_{1-x}\text{Mn}_x\text{PO}_4$ was also possible, locating the $\text{Mn}^{4+}/\text{Mn}^{3+}$ redox couple at 4.1 V vs. Li^+/Li . Since then, Yamada¹¹¹⁻¹¹³ reinvestigated the $\text{Li}_{1-x}\text{Fe}_{1-x}\text{Mn}_x\text{PO}_4$ phase diagram in details. Li did as well¹¹⁴⁻¹¹⁶ and reported good capacity ($\sim 140 \text{ mAh/g}$) for pure LiMnPO_4 ¹¹⁷ coated with carbon black. These

published results appear however difficult to reproduce. Investigations by Amine,¹¹⁸ Lloris¹¹⁹ and Okada¹²⁰ on $\text{Li}_{1-x}\text{CoPO}_4$ located the $\text{Co}^{4+}/\text{Co}^{3+}$ redox couple at 4.8 V vs. Li, too high to be sustained by the electrolytes presently available.

15.4. CONCLUSIONS

Polyanionic structures built on transition metal MO_6 octahedra and XO_4 tetrahedra offer a wide variety of crystalline structures hosts for the reversible insertion/extraction of alkali cations. We tried through this contribution to demonstrate that these structures are progressively shifting from a conceptual curiosity to possible candidates for new generations of positive electrode materials for lithium batteries.

As illustrated in Figure 15.28, $\text{V}^{4+}/\text{V}^{3+}$ and $\text{Fe}^{3+}/\text{Fe}^{2+}$ redox couples have been identified in various structural types and are the most interesting ones if high potential vs. Li^+/Li is desired. Depending on the type of application chosen though, titanium-containing phosphates are also attractive in terms of stable potential delivered at 2.5 V vs. Li. This offers a very wide variety of operating voltage for individual cells, tuned by the inductive effect of the XO_4 groups and by the crystal structure as well.

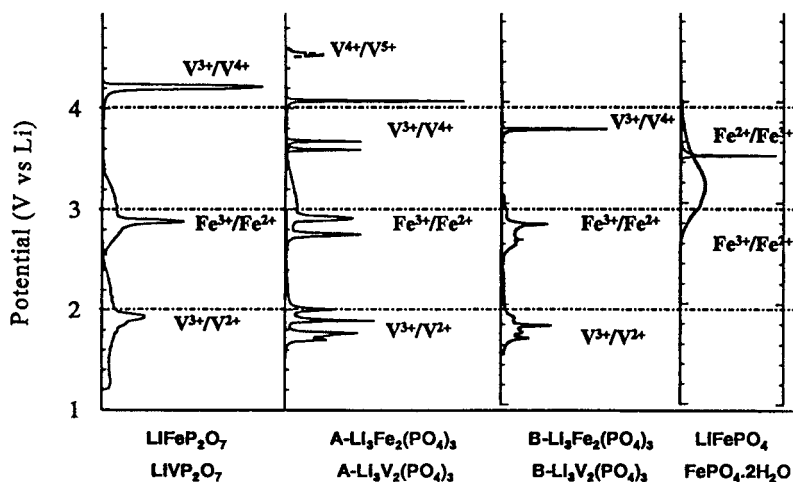


Figure 15.28. Derivative of potentiodynamic curves obtained for several polyanionic structures.

The extensive work undertaken since 2000 on coating the olivine LiFePO_4 with conductive carbon has led to the successful use of this material at ~100% of its theoretical capacity. As evoked by Chen though⁹⁹ efforts

shall still have to be focused on increasing the tap density of these composite electrodes for their use in practical systems.

REFERENCES

1. D. Guyomard, in "New Trends in Electrochemical Technology : Energy Storage Systems for Electronics", T. Osaka and M. Datta (Editors), Gordon & Breach Science Publishers, Chapter 9 p. 253 (2000).
2. V. B. Nalbandyan, I. L. Shukaev, *Russ. J. Inorg. Chem.* 32 (1987) 3.
3. J. B. Goodenough, M. M. Thackeray, W. I. F. David, P. G. Bruce, *Rev. Chim. Minér.* 21 (1984) 435.
4. M. M. Thackeray, W. I. F. David, J. B. Goodenough, *Mater. Res. Bull.* 17 (1983) 785.
5. M. M. Thackeray, W. I. F. David, P. G. Bruce, J. B. Goodenough, *Mater. Res. Bull.* 18 (1983) 461.
6. M. M. Thackeray, P. J. Johnson, L. A. de Picciotto, P. G. Bruce, J. B. Goodenough, *Mater. Res. Bull.* 19 (1984) 179.
7. A. Manthiram, J. B. Goodenough, *J. Solid State Chem.* 71 (1987) 349.
8. A. Manthiram, J. B. Goodenough, *J. Power Sources* 26 (1989) 403.
9. C. Delmas, F. Cherkaoui, A. Nadiri, P. Hagenmuller, *Mat. Res. Bull.* 22 (1987) 631.
10. C. Delmas, A. Nadiri, *Mat. Res. Bull.* 23 (1988) 65.
11. G. Collin, J.P. Boilot, in "Superionic Solids and Solid Electrolytes", Academic Press, (1989) p 227.
12. H.Y-P. Hong, *Mat. Res. Bull.* 11 (1976) 173; L. Hagman, P. Kierkegaard, *Acta Chem. Scand.* 22 (1968) 1822.
13. L. Hagman, P. Kierkegaard, *Acta Chem. Scand.* 22 (1968) 1822.
14. R. G. Sizova, A. A. Vronkov, N. G. Shumyatskaya, V. V. Pynkhin, N. V. Belov, *Dokl. Akad. Nauk SSSR*, Ser. 205, Issue 1 (1972) 90.
15. O. Tillement, Thèse de doctorat de l'Université Paris VI, Mars 1992.
16. J. B. Goodenough, H. Y-P. Hong, J. A. Kafalas, *Mat. Res. Bull.* 11 (1976) 203.
17. O. Tillement, J. Angenault, J.C. Couturier, M. Quarton, *Solid State Ionics* 44 (1991) 299.
18. O. Tillement, J.C. Couturier, J. Angenault, M. Quarton, *Solid State Ionics* 48 (1991) 249.
19. O. Tillement, J. Angenault, J.C. Couturier, M. Quarton, *Solid State Ionics* 53-56 (1992) 391.
20. A. Nadiri, C. Delmas, R. Salmon, P. Hagenmuller, *Rev. Chim. Minér.* 21 (1984) 537.
21. W. M. Reiff, J.H. Zhang, C.C. Torardi, *J. Solid State Chem.* 62 (1986) 231.
22. C.C. Torardi, E. Prince, *Mat. Res. Bull.* 21 (1986) 719.
23. P. G. Bruce, G. Miln, *J. Solid State Chem.* 89 (1990) 162.
24. F. d'Yvoire, M. Pintard Scrépel, E. Bretey, M. de la Rochère, *Solid State Ionics* 9&10 (1983) 851.
25. M. Pintard-Scrépel, F. d'Yvoire et Francis Rémy, *C. R. Acad. Sc. Paris* 286 (1978) 381.
26. C. Delmas, R. Olazcuaga, F. Cherkaoui, R. Brochu, G. Le Flem, *C. R. Acad. Sc. Paris* 287 (1978) 169.
27. C. Masquelier, A. K. Padhi, K. S. Nanjundaswamy, J. B. Goodenough, *J. Solid State Chem.* 135 (1998) 228.
28. A.S. Andersson, B. Kalska, P. Eyob, D. Aernout, L. Häggström, J.O. Thomas, *Solid State Ionics* 140 (2001) 63.
29. M. Morcrette, C. Wurm, C. Masquelier, *Solid State Sciences* 4 (2002) 239.
30. A. K. Padhi, V. Manivannan, J. B. Goodenough, *J. Electrochem. Soc.* 145 (1998) 1518.
31. K. Rangan, J. Gopalakrishnan, *Inorg. Chem.* 34 (1995) 1969.

32. C. Delmas, A. Nadiri, J. L. Soubeyroux, *Solid State Ionics* 28-30 (1988) 419.
33. A. Aatiq, M. Ménétrier, L. Croguennec, E. Suard, C. Delmas, *GFECL, Orléans, March 2002* ; *J. Mater. Chem.* 2002, in press
34. C. Masquelier, C. Wurm, J. Rodríguez-Carvajal, J. Gaubicher, L.F. Nazar, *Chem. Mater.* 12 (2000) 525.
35. S. Patoux, C. Masquelier, *Chem. Mater.* 14(5 (2002) 2334.
36. L. Znaidi, S. Launay, M. Quarton, *Solid State Ionics* 93 (1997) 273.
37. J. Gopalakrishnan, K. Rangan, *Chem. Mater.* 4 (1992)745.
38. A. K. Padhi, K. S. Nanjundaswamy, C. Masquelier, J.B. Goodenough, *J. Electrochem. Soc.* 144 (1997) 2581.
39. A. K. Padhi, K. S. Nanjundaswamy, J. B. Goodenough, *J. Electrochem. Soc.* 144 (1997) 1188.
40. P. Eyob, A.S. Andersson, J. O. Thomas, *J. Mater. Chem.* 12, (2000)1.
41. (a) J. Gaubicher, C. Wurm, G. Goward, C. Masquelier, L. Nazar, *Chem. Mater.* 12 (2000) 3240; (b) J. Gaubicher, F. Orsini, T. Le Mercier, S. Llorente, A. Villesuzanne, J. Angenault, M. Quarton, *J. Solid State Chem.* 150 (2000) 250.
42. S. Patoux, C. Masquelier, *Chem. Mater.* in press (2002)
43. B. L. Cushing, J. B. Goodenough, *J. Solid State Chem.* 162 (2001) 176.
44. C. Masquelier, G. Rousse, S. Patoux, C. Wurm, M. Morcrette, submitted to *Chem. Mater.* (2003).
45. M. Morcrette, J. B. Leriche, S. Patoux, C. Wurm, C. Masquelier, submitted to *Elec. Solid State Letters*, 2002
46. K. S. Nanjundaswamy, A. K. Padhi, J.B. Goodenough, S. Okada, H. Ohtsuka, H. Arai, J. Yamaki, *Solid State Ionics* 92 (1996) 1.
47. P.C. Christidis, P.J. Rentzeperis, *Z. für Kristallographie* 144 (1976) 341.
48. P.C. Christidis, P.J. Rentzeperis, *Z. für Kristallographie* 141 (1975) 233.
49. D. Tran Qui, S. Hamdoune, Y. Le Page, *Acta Cryst.* C43 (1987) 201.
50. D. Tran Qui, S. Hamdoune, *Acta Cryst.* C43 (1987) 397.
51. B. A. Maksimov, L. A. Muradyan, E. A. Genkina, V. I. Simonov, *Sov. Phys. Dokl.* 31(5) (1985) 370 .
52. A. B. Bykov, A.P. Chirkin, L. N. Demyanets, S. N. Doronin, *Solid State Ionics* 38 (1990) 31.
53. G. Rousse, J. Rodríguez-Carvajal, C. Wurm, C. Masquelier, *Chem. Mater.* 13 (2001) 4527.
54. J. M. Winand, A. Rulmont, P. Tarte, *J. Solid State Chem.* 87 (1990) 83.
55. M. Sato, H. Ohkawa, K. Yoshida, M. Saito, K. Uematsu, K. Toda, *Solid State Ionics* 135 (2000) 137.
56. S. Patoux, C. Wurm, M. Morcrette, G. Rousse, C. Masquelier, *11th International Meeting on Lithium Batteries*, Monterey, CA (2002), accepted for publication into *J. Power Sources*.
57. S. Okada, K. S. Nanjundaswamy, A. Manthiram, J. B. Goodenough, *36th Power Sources Conf.*, June 6-9 (1994).
58. J. Barker, M.Y. Saidi, *US Patent* 6,203,946 (March 20, 2001).
59. M.Y. Saidi, J. Barker, H. Huang, J.L. Swoyer, G. Adamson, *Electrochem. Solid State Lett.* 5(7) (2002) A149.
60. L. Nazar, H. Huang, S.-C. Yin, T. Kerr, *11th International Meeting on Lithium Batteries*, Monterey, CA (2002).
61. J. Gaubicher, T. Le Mercier, Y. Chabre, J. Angenault, M. Quarton, *J. Electrochem. Soc.* 146(12) (1999) 4375.
62. J. Gaubicher, F. Orsini, T. Le Mercier, S. Llorente, A. Villesuzanne, J. Angenault, M. Quarton, *J. Solid State Chem.* 150 (2000) 250.
63. F. d'Yvoire, M. Pintard-Scrépel, E. Bretey, *Solid State Ionics* 18&19 (1986) 502.
64. F. d'Yvoire, E. Bretey, G. Collin, *Solid State Ionics* 28-30 (1988) 1259.

65. C. Masquelier, F. d'Yvoire, G. Collin, *Journal of Solid State Chemistry* 118 (1995) 33.
66. M. Gabelica-Robert, P. Tarte, *Solid State Chem., Proceedings of the 2nd European Conf. 7-9 June 1982*, p.475.
67. J. Belkouch, L. Monceaux, E. Bordes, P. Courtine, *Mat. Res. Bull.* 30 (1995) 149.
68. C. Wurm, M. Morcrette, L. Dupont, G. Rousse, C. Masquelier, *Chem. Mater.* 14(7) (2002) 2701.
69. D. Riou, N. Nguyen, R. Benloucif, B. Raveau, *Mat. Res. Bull.* 25 (1990) pp 1363.
70. K. H. Lii, Y. P. Wang, Y. B. Chen, S. L. Wang, *J. Solid State Chem.* 86 (1990) 143.
71. S. Wang, C. Wu, S. Liu, *J. Solid State Chem.* 113 (1) (1994) 37.
72. G. Rousse, C. Wurm, J. Rodriguez Carvajal, M. Morcrette, C. Masquelier, *Int. J. Inorg. Mater.* 3 (2001) 881.
73. V. V. Pechkovskii, E. D. Dzyuba, G. I. Salonen, V. N. Yaglov, A. I. Volkov, *Rus. J. Inorg. Chem.* 20(3) (1975) 329.
74. J. Sanz, J.E. Iglesias, J. Soria, E. R. Losilla, M. A. G. Aranda, S. Bruque, *Chem. Mater.* 9 (1997) 996.
75. Y. Song, S. Yang, P.Y. Zavalij, M.S. Whittingham, *Mater. Res. Bull.* 37 (2002) 1249.
76. C. Masquelier, P. Reale, M. Morcrette, C. Wurm, L. Dupont, D. Larcher, *J. Electrochem. Soc.* 149(8) (2002) A1037.
77. Y.S. Hong, K.S. Ryu, Y.J. Park, M.G. Kim, J.M. Lee, S.H. Chang, *J. Mater. Chem.* 12 (2002) 1870.
78. P.P. Prosini, M. Lisi, S. Scaccia, M. Carewska, F. Cardellini, M. Pasquali, *J. Electrochem. Soc.* 149(3) (2002) A297.
79. J. Gaubicher, Y. Chabre, J. Angenault, A. Lautié, M. Querton, *J. of Alloys and Compounds* 262-263 (1997) 34-38.
80. J. Gaubicher, Thèse de Doctorat, Université Pierre & Marie Curie, Paris (1998).
81. N. Dupré, J. Gaubicher, J. Angenault, G. Wallez, M. Querton, *J. Power Sources* 97-98 (2001) 532.
82. N. Dupré, J. Gaubicher, T. Le Mercier, G. Wallez, J. Angenault, M. Querton, *Solid State Ionics* 140 (2001) 209.
83. T. A. Kerr, J. Gaubicher, L.F. Nazar, *Electrochem. Solid State Lett.* 3(10) (2000) 460.
84. A. V. Lavrov, V. P. Nikolaev, G. G. Sadikov, M. A. Porai-Koshits, *Sov. Phys. Dokl.* 27(9) (1982) 680.
85. K.H. Lii, C.H. Lii, C.Y. Cheng, S. L. Wang, *J. Solid State Chem.*, 95 (1991) 352.
86. J. M. Longo, P. Kierkegaard, *Acta Chem. Scand.* 20 (1966) 72.
87. T. G. Amos, A. Yokochi, A. W. Sleight, *J. Solid State Chem.* 14 (1998) 303.
88. T. G. Amos, A. W. Sleight, *J. Solid State Chem.* 160 (2001) 230.
89. A. Leclair, H. Chahboun, D. Groult, B. Raveau, *Z. für Kristallographie* 177 (1986).
90. H. Chahboun, D. Groult, M. Hervieu, B. Raveau, *J. Solid State Chem.* 65 (1986) 331.
91. A. K. Padhi, K. S. Nanjundaswamy, C. Masquelier, S. Okada, J.B. Goodenough, *J. Electrochem. Soc.* 144(5) (1997) 1609.
92. A.S. Andersson, B. Kalska, L. Häggström, J.O. Thomas, *Solid State Ionics* 130 (2000) 41.
93. A.S. Andersson, J.O. Thomas, B. Kalska, L. Häggström, *Electrochem. Solid State Lett.* 3(2), (2000) 66.
94. J.B. Goodenough, A.K. Padhi, K.S. Nanjundaswamy, C. Masquelier, *US Patent #5,910,382* (1999).
95. N. Ravet, J. B. Goodenough, S. Besner, M. Simoneau, P. Hovington, M. Armand, Abstract # 127, *196th Meeting of the Electrochemical Society*, Hawai, Oct. (1999).
96. N. Ravet, Y. Chouinard, J. F. Magnan, S. Besner, M. Gauthier, M. Armand, *J. Power Sources* 97-98 (2001) 503.
97. H. Huang, S. C. Yin, L. F. Nazar, *Electrochem. Solid State Lett.* 4(10) (2001), A170.
98. R. Dominico, M. Gaberscek, J. Drofenik, M. Bele, S. Pejovnik, *Elec. Solid State Lett.* 4(11) (2001) A187.

99. Z. Chen, J.R. Dahn, *J. Electrochem. Soc.* 149(9), (2002) A1184.
100. A. Yamada, S.C. Chung, K. Hinokuna, *J. Electrochem. Soc.* 148 (3) (2001) A224 .
101. S. Yang, P.Y. Zavalij, M.S. Whittingham, *Electrochemistry Communications* 3 (2001) 505.
102. S. Yang, Y. Song, P.Y. Zavalij, M.S. Whittingham, *Electrochemistry Communications* 4 (2002) 239.
103. S. Franger, F. Le Cras, C. Bourbon, H. Rouault, *Electrochem. Solid State Lett.* 5(10) (2002) A231.
104. P. P. Prosini, D. Zane, M. Pasquali, *Electrochimica Acta* 46 (2001) 3517.
105. P.P. Prosini, M. Carewska, S. Scaccia, P. Wisniewski, S. Passerini, M. Pasquali, *J. Electrochem. Soc.* 149(7) (2002) A886.
106. F. Croce, A.D. Epifanio, J. Hassoun, A. Deptula, T. Olczac, B. Scrosati, *Electrochem. Solid State Lett.* 5(3) (2002) A47.
107. S.Y. Chung, J. T. Bloking, Y.M. Chiang, *Nature materials* 1 (2002) 123.
108. C. Wurm, Thèse de doctorat, Université Paris-XI Orsay, July 2002 .
109. M. Morcrette, C. Wurm, J. Gaubicher, C. Masquelier, Proceedings of the 1st Lithium Battery Discussions, Arcachon (France), 27-30 May 2001 .
110. M. Morcrette, Y. Chabre, G. Vaughan, G. Amatucci, J-B. Leriche, S. Patoux, C. Masquelier, J-M. Tarascon, *Electrochimica Acta* 47 (2002) 3137.
111. A. Yamada, Y. Kudo, K.Y. Liu, *J. Electrochem. Soc.* 148 (7) (2001) A747.
112. A. Yamada, S.C. Chung, *J. Electrochem. Soc.* 148 (8) (2001) A960.
113. A. Yamada, Y. Kudo, K. Y. Liu, *J. Electrochem. Soc.* 148 (10) (2001) A1153.
114. G. Li, H. Azuma, M. Tohda, *Electrochemical and Solid State Letters* 5(6) (2002) A135.
115. G. Li, H. Azuma, M. Tohda, *J. Electrochem. Soc.* 149(6) (2002) A743.
116. G. Li, Y. Kudo, K. Y. Liu, H. Azuma, M. Tohda, *J. Electrochem. Soc.* 149(11) (2002) A1414.
117. S. Geller, J. L. Durand, *Acta Cryst.* 13 (1960) 325.
118. K. Amine, H. Yasuda, M. Yamachi, *Electrochem. Solid State Lett.* 3(4),(2000) 178.
119. J. M. Lloris, C. Pérez Vicente, J. L. Tirado, *Electrochemical and Solid State Letters* 5(10) (2002) A234.
120. S. Okada, S. Sawa, M. Egashira, J. Yamaki, M. Tabuchi, H. Kageyama, T. Konishii, A. Yoshino, *J. Power Sources*, 97-98 (2001) 430.

Chapter 16

UNDERSTANDING PHASE TRANSFORMATIONS IN LITHIUM BATTERY MATERIALS BY TRANSMISSION ELECTRON MICROSCOPY

Y. Shao-Horn

*Massachusetts Institute of Technology
Cambridge, Massachusetts 02139*

16.1. INTRODUCTION

Downsizing of electronic components demands energy storage systems with high energy and power densities, and thus continuously drives the research and development efforts. The most commonly used batteries in portable computers and cellular phones are lithium rechargeable batteries¹. In these batteries, chemical energy stored in the positive electrode is released and converted into electrical energy during discharge through an intercalation (insertion) process by which lithium ions are incorporated within the host structure of the positive electrode materials. During charge, the process is reversed (de-intercalation) and electric energy is applied to remove lithium ions from the positive electrode. Lithium transition metal oxides that host mobile lithium ions on the interstitial sites have been studied as positive electrode materials and the intercalation and de-intercalation processes of lithium ions are accompanied by redox of transition metal ions. The energy output of lithium rechargeable batteries is dependent on the voltage upon which lithium ions are inserted and the number of interstitial sites that can accommodate lithium ions in the host structure. Ideally, intercalation and de-intercalation of lithium ions and redox of transition metal ions, should leave the host structure intact. In practice, however, variation in lithium contents in the host structure leads to lattice expansion or contraction, migration of transition metal ions and local or global lattice distortion as a result of ordering of lithium and vacancies or Jahn-Teller distortion of transition metal ions. These structural changes can 1) induce stresses and strains within lithium transition metal oxide crystals, 2) affect the electronic conductivities of lithium battery materials, and 3) lead to irreversible phase changes and thus

decrease in energy outputs of lithium batteries. Therefore, much research has been focused on characterizing structural changes of lithium transition metal oxides associated with lithium intercalation and de-intercalation, and modifying material chemistry to suppress phase transformations and to optimize lithium battery performance.

Layered O3 Li_xCoO_2 ²⁻⁴, Li_xNiO_2 ⁵⁻⁸ and Li_xMnO_2 ⁹⁻¹¹, spinel $\text{Li}_x\text{Mn}_2\text{O}_4$ ¹²⁻¹⁴ and olivine Li_xFePO_4 ¹⁵ are the most studied positive electrode materials in the last two decades^{16,17}. Layered Li_xCoO_2 and Li_xNiO_2 are stable upon lithium intercalation or de-intercalation despite the fact that several phase transformations are observed from lithium composition $x = 1$ to $x = 0$. Of significance, lithium and vacancy ordering³, Jahn-Teller induced¹⁸, and metal-insulator¹⁹ transformations have been reported. On the other hand, layered Li_xMnO_2 host structure is not stable upon lithium intercalation or de-intercalation and it transforms a spinel-related structure²⁰⁻²². Spinel $\text{Li}_x\text{Mn}_2\text{O}_4$ structure is stable upon electrochemical cycling but it can undergo many interesting phase transformations induced by Jahn-Teller distortion¹³ or charge ordering²³⁻²⁵. Extensive research efforts have focused on understanding the structural changes underwent in these lithium transition metal oxides and their effects on lithium battery performance.

Conventional bulk analytical techniques, such as X-ray, neutron powder diffraction and electrochemical characterization, are used routinely to provide overall, averaged chemical and structural information of lithium battery electrodes. Although the bulk diffraction techniques enable accurate determination of distances and angles of atoms in the volume-averaged crystal structures, they are insensitive to spatially localized phase transformations and ordering transitions of lithium and vacancy or charges in lithium electrode materials. In particular, Garcia-Adeva *et al.* have recently pointed out the ambiguities in revealing nanoscale heterogeneity or aperiodic phase separation by conventional powder diffraction techniques²⁶. Electrochemical methods, such as lithium cell voltage monitoring, are very sensitive to changes of local environments available for lithium ions at the electrode-electrolyte interface but they provide little information on the details of structural features responsible for the electrochemical responses. Therefore, bulk analytical techniques alone are inadequate to identify critical material features and phase transformations in lithium electrode materials that limit battery performance. Combination of transmission electron microscopy (TEM) analyses, bulk diffraction and electrochemical techniques has proven invaluable in this regard. TEM and associated techniques enable microstructural characterization of lithium battery materials from both local structural and chemistry points of view.

Although TEM techniques have been used extensively in materials science, solid state chemistry and mineral science²⁷⁻³⁰, application of these techniques in lithium battery research has been comparatively recent^{21,31-52}.

TEM techniques provide high-spatial resolution single-crystal diffraction information from individual lithium transition metal oxide crystals complementary to X-ray and neutron powder diffraction as electrons can be focused easily. In addition, one can use TEM imaging to detect the phase distribution in the electrode that provides valuable insights to heterogeneous phase transformation mechanisms, and imperfections in the lithium transition metal oxide crystals, which is introduced either during material synthesis or electrochemical cycling. Moreover, high-resolution TEM imaging and image simulation can permit direct visualization of atomic arrangements and modifications associated with structural defects and modifications, as shown in understanding stacking faults in orthorhombic LiMnO_2 ⁴⁸ and imaging of lithium ions in LiCoO_2 ³⁹. Furthermore, recent electron energy loss spectroscopy (EELS) studies have provided evidence for charge compensation mechanisms of Li_xCoO_2 ⁵¹ and $\text{Li}_x\text{Ni}_{0.8}\text{Co}_{0.2}\text{O}_2$ ⁴⁹, and transition metal clustering in $\text{LiNi}_{1-x}\text{Al}_x\text{O}_2$ ⁵³. Therefore, combination of bulk analytical studies and TEM studies has led to significant advances in identifying phase transformation mechanisms of lithium electrode materials, understanding of structure-property relationships, and providing directions to design of new battery materials.

In this chapter, we focus on understanding phase transformations of O3 and O2 layered Li_xCoO_2 , O3 Li_xNiO_2 , O3 Li_xMnO_2 and spinel $\text{Li}_x[\text{Mn}]_2\text{O}_4$ underwent during electrochemical cycling or upon materials synthesis. Much of our information is derived from electron diffraction data obtained in the transmission electron microscope (TEM). We begin with an overview of commonly used TEM techniques. We then illustrate how TEM techniques can be used to reveal and understand electrochemically induced phase transformations in lithium electrode materials and understand their effects on the electrochemical performance of lithium batteries. Electron diffraction has provided first experimental evidence for order-disorder phenomena of lithium and vacancy in O3 and O2 derived Li_xCoO_2 and O3 derived Li_xNiO_2 . In addition, high spatial resolution of TEM techniques is powerful in identifying localized phase transitions such as revealing the presence of tetragonal, Jahn-Teller distorted $\text{Li}_2[\text{Mn}_2]\text{O}_4$ in $\text{Li}_x[\text{Mn}_2]\text{O}_4$ electrodes discharged to 3.0 V and above, which supports one of previously proposed hypotheses responsible for capacity degradation of 4 V $\text{Li}_x[\text{Mn}_2]\text{O}_4$ electrodes during electrochemical cycling. Moreover, electron diffraction has revealed and quantified intermediate cation configurations between the spinel and the layered configurations in as-prepared low-temperature LiCoO_2 (LT- LiCoO_2) and cycled layered O3 Li_xMnO_2 electrodes, which leads to electrochemical properties of LT- Li_xCoO_2 and Li_xMnO_2 electrodes significantly different from layered O3 Li_xCoO_2 . A rapid, irreversible phase transformation from the layered to a spinel-related structure in cycled Li_xMnO_2 electrodes leads to significant modification in the electrochemical voltage profile and reduction

in reversible capacity, which limits the commercialization of layered Li_xMnO_2 in lithium batteries. In all these cases, TEM techniques identify critical phase transformations in lithium transition metal oxides that control the electrochemical performance of lithium batteries.

16.2. TRANSMISSION ELECTRON MICROSCOPY

Electron diffraction and TEM imaging are effective in probing localized structural modifications in lithium electrode materials on the nanometer-scale.

16.2.1. Electron Diffraction of Crystals

Kinematical theory that assumes that electron beam is scattered weakly by the material (the amplitude of the scattered electron wave is much less than the incident electron wave) is used here. We begin with scattering of electrons from atoms. The wave function ψ of the electron at non-relativistic velocities satisfies the time independent Schrodinger equation, for stationary states:

$$\frac{h^2}{8\pi^2 m_0 e} \nabla^2 \psi + (E + V)\psi = 0 \quad (1)$$

Where eE is the total energy of the electron and $-eV$ is the potential energy. Within the kinematical approximation, the amplitude of the wave scattered from an atom at a point P (at \mathbf{r} from the origin) can be expressed by:

$$\psi_s = \frac{2\pi m_0 e}{h^2} \frac{\exp(2\pi i \mathbf{k} \mathbf{r}_i)}{r} \int_{atom} V(\mathbf{r}_i) \exp(2\pi i \mathbf{K}' \mathbf{r}_i) d\tau_i \quad (2)$$

where $V(\mathbf{r}_i)$ is the atomic potential at a point \mathbf{r}_i , \mathbf{k} is the wave vector and $\mathbf{K}' = \mathbf{K} - \mathbf{k}$. Using the Born approximation, we obtain the atomic scattering amplitude for electrons:

$$f_{electrons}(\theta) = \frac{m_0 e^2}{2h^2} \left(\frac{\lambda}{\sin \theta} \right)^2 (\mathbf{Z} - \mathbf{f}_x) \quad (3)$$

where \mathbf{f}_x is the atomic scattering amplitude for X-rays and \mathbf{Z} is the atomic number. The interaction between the atom and electrons consists of scattering from both nucleus and the electron cloud. This is different from X-ray diffraction, which interacts with atomic electrons and the atomic scattering factor for X-rays can be expressed by:

$$f_{x\text{-rays}}(\theta) = \frac{e^2}{m_0 c^2} f_x \quad (4)$$

As shown in Equations 3 and 4, the scattering power of atoms for electrons is therefore much greater than for X-rays. In addition, the atomic scattering factors for electrons increase smoothly with atomic number except at low scattering angles but not as quickly as X-rays. Therefore, electron diffraction is more sensitive in detecting light atomic number elements than X-ray diffraction. It should be noted that the electron scattering factor of lithium relative to transition metals is significantly larger than that of X-rays as a result of strong interactions between electrons and atoms, as shown in Figure 16.1.. Therefore, electron diffraction can be used to probe the presence of superstructures induced by ordering of light elements or charges, which is typically proven difficult for X-ray or neutron powder diffraction.

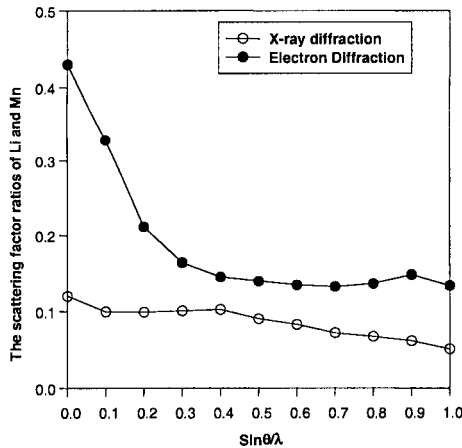


Figure 16.1. The ratios between the X-ray and electron scattering factors of lithium to manganese atoms ($f_{\text{Li}}/f_{\text{Mn}}$) as a function of $\text{Sin}\theta/\lambda$. Note that the ratio, $f_{\text{Li}}/f_{\text{Mn}}$, for electron diffraction is considerably larger than that of X-ray diffraction.

The scattered electron wave from one crystal can be described by:

$$\psi_s = \frac{\exp(2\pi i \mathbf{k} \cdot \mathbf{r}_i)}{r} \sum_i^N f_i(\theta) \exp(-2\pi i \mathbf{K}' \cdot \mathbf{r}_i) \quad (5)$$

where $f_i(\theta)$ is the atomic electron scattering factor of site i in the crystal. The absolute intensity of the scattered wave can be obtained by taking the product of the wave function with its complex conjugate.

Electron diffraction patterns of a powder sample can be obtained by selected area electron diffraction from regions as small as 0.5 μm or by

nanodiffraction or convergent beam electron diffraction, in which focused electron beam is used to obtain diffraction patterns from regions down to 1 nm. Single-crystal electron diffraction data obtained from lithium transition metal oxide crystals can be viewed as planes in its reciprocal space, which consists of the transmitted electron beam and individual diffraction spots. Detailed procedures on electron diffraction pattern indexing can be found in the TEM textbook by Fultz and Howe²⁹. Because of strong dynamic diffraction effects in electron diffraction of most crystals, electron diffraction intensities are often used qualitatively, and quantitative analysis of electron diffraction intensities is less reliable than X-ray diffraction and neutron diffraction.

16.2.2. TEM Imaging

Diffraction contrast in the TEM images results from the variation in the diffracted intensity of the material. Bright-field images (the transmitted beam intensity) and dark-field images (the diffracted beam intensity) provide information about microstructure features of the materials. Imperfections such as dislocations, stacking faults, domain and phase boundaries within the crystal displace the unit cell and thus introduce a phase change in the scattered wave, which leads to intensity variation in the dark-field and bright field images. Dark-field imaging has been particularly useful to show and study domain structures within lithium transition metal oxide crystals induced by lithium intercalation or de-intercalation.

In addition to diffraction contrast, imaging of lattice fringes has been commonly used in studying phase transformations in lithium battery materials on the nanometer scale. The intensity distribution of the incident beam and one diffracted beam gives a modulation with the spacing of the plane being diffracted for a given crystal orientation and thickness, which reveals the lattice of the lithium electrode material in form of sine fringes as shown as follows:

$$I = 1 + R^2 - 2R \sin\left(\frac{2\pi x}{d} - s_0\right) \quad (6)$$

Where d is the spacing of the plane being diffracted, x is the direction of modulation in the image, and R and S_0 are constants for a given thickness and crystal orientation). It should be noted that the positions of the lattice fringes bear no apparent relation to the position of atomic planes. Further detailed information on lattice image formation can be found in the TEM textbooks^{27,30}.

16.2.3. TEM Sample Preparation

The requirements of a good TEM sample include 1) electron beam transparency, which limits maximum thickness to 5 μm , and 2) clean surface (free of contaminants). Lithium transition metal oxides used in lithium batteries are in form of powder and the crystal sizes are dependent on synthesis routes, typically in the range of 20 nm to 10 μm . TEM samples of these oxides can be obtained from the following preparation procedure: 1) grind the powder in agate mortar and pestle, 2) suspend the powder in an organic solvent in an ultrasonic bath, 3) deposit suspended particles onto a TEM copper grid coated with lacey carbon. If crystal sizes of lithium electrode materials are significantly greater than 1 μm , mechanically thinning of these crystals is needed. Microtoming is an effective method to produce thin TEM sections of as-prepared lithium transition metal oxides. The material is first embedded in epoxy resin. Ultrathin sections on the order of 60 nm cut with diamond knives using an ultramicrotome are floated on water and then transferred to TEM copper grids with lacey carbon support.

16.2.4. Caveats to TEM Techniques

Although electron diffraction and TEM imaging techniques are powerful in probing localized structural defects and phase transitions, they have a few limitations in comparison to bulk analytic techniques. Three of the most important are 1) the sampling statistics is very poor, 2) only crystals with thickness less than 1 μm can be analyzed and 3) kinematical theory is only qualitative. Therefore, in order to ensure the fact that crystals analyzed in the TEM are representative of the bulk materials, it is necessary to combine TEM results with bulk analytical information including X-ray powder diffraction and electrochemical data. In addition, there are concerns with regard to the stability of materials during TEM sample preparation and under electron beam. This is a serious issue when studying highly de-intercalated lithium battery materials in the TEM. Performing TEM data collection at liquid nitrogen temperature can remove some materials instability problems related to thermal breakdown under electron beam.

16.3. LITHIUM AND VACANCY ORDERING

Ordering of lithium and vacancy has been first proposed in intercalation compounds of layered chalcogenides such as Li_xTiS_2 ⁵⁴ and Li_xTaS_2 ⁵⁵. At room temperature, lithium ions that reside in octahedral sites are mobile. Lithium ions are constrained to occupy certain sites preferentially as a result of long-range, repulsive, Coulomb interactions among lithium ions, which leads to

formation of superlattices at various lithium contents parallel to the transition metal layers. Although direction observation of lithium ordering by X-ray diffraction is difficult, characteristic peaks in the incremental capacity dx/dV vs. x plots are observed at specific lithium compositions where ordering is expected in Li_xTiS_2 ⁵⁴. As a similar electrochemical feature is noted in $\text{Li}/\text{Li}_x\text{CoO}_2$ cells where x is near 0.5, Reimers and Dahn³ have proposed lithium and vacancy ordering in $\text{Li}_{0.5}\text{CoO}_2$ obtained from lithium de-intercalation of layered O3 LiCoO_2 . First direct experimental evidence of lithium ordering is the presence of superstructures in the electron diffraction patterns of layered Li_xNiO_2 ^{42,56}. Subsequently electron diffraction and TEM imaging have successfully revealed order-disorder phenomena of lithium and vacancy in layered O3- $\text{Li}_{0.5}\text{CoO}_2$ ³⁷ and O2- Li_xCoO_2 ³⁸ electrode materials. Moreover, first-principles studies support the concept of lithium and vacancy ordering in these layered compounds⁵⁷⁻⁶⁴. Van der Ven and Ceder have shown that lithium ordering reduces lithium ion mobility as evidenced by a two-order magnitude of reduction in the chemical diffusion coefficient in Li_xCoO_2 at ordered compositions⁵⁷. Lithium and vacancy ordering can be suppressed by metal substitution in the transition metal layers^{65,66}, which eliminates phase transformations and greatly affects electrochemical cycling of lithium batteries. Therefore, understanding order-disorder phenomena of lithium and vacancy in lithium battery materials is not only essential to further improve the cycling performance of lithium rechargeable batteries but also important to provide new insights to lithium-lithium interactions in these transition metal oxides, its impact on their kinetic properties and design of better lithium electrode materials. In this section, we focus on understanding order-disorder transformations of lithium and vacancy in these layered materials by electron diffraction.

16.3.1. Lithium and Vacancy Ordering in O3 Li_xNiO_2

O3 layered LiNiO_2 consists of lithium and nickel sheets stacked alternatively in-between AB CA BC AB close-packed oxygen arrays. The structure is typically defined in a hexagonal cell that has a trigonal symmetry with space group $R\bar{3}m$. Lithium de-intercalation from LiNiO_2 leads to many phase transformations that occur as a function of lithium concentration⁶⁷⁻⁶⁹. Electron diffraction of Li_xNiO_2 has lent to first experimental evidence of lithium and vacancy ordering in lithium transition metal oxides at various lithium concentrations, $x = 0.25, 0.33$ and 0.65 , as shown in Figure 16.2.^{42,56} It should be noted that at lithium compositions of $x = 0.25$ and $x = 0.33$, order-disorder of lithium and vacancy is associated with noticeable inflexion points in the voltage profile of $\text{Li}/\text{Li}_x\text{NiO}_2$ cells, similar to lithium ordering in Li_xTiS_2 ⁵⁴. However, lithium ordering in Li_xNiO_2 near $x = 0.65$ is different and no pronounced modification in the voltage profile is associated with this

ordering transformation. X-ray powder diffraction studies^{42,67-69} of Li_xNiO_2 show that this composition falls in the wide monoclinic, single-phase region with the lithium composition the range of $0.5 \leq x \leq 0.75$. The stability of the monoclinic phase, important to electrochemical performance, has been a subject of debate.

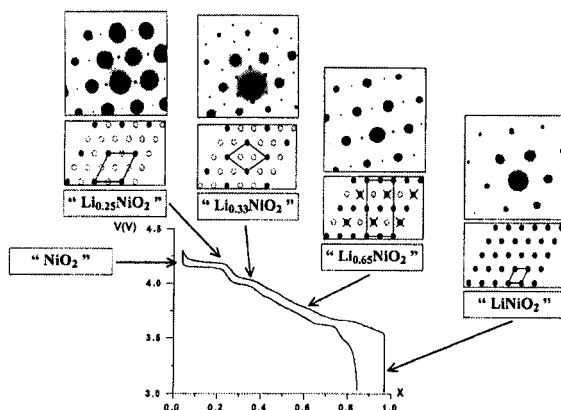


Figure 16.2. The voltage profile of Li_xNiO_2 vs. lithium as a function of lithium content x from Delmas *et al.*⁵⁶. Note that the electron diffraction patterns obtained from various points in the voltage profile show different superstructures, which is not visible in the X-ray powder diffraction patterns of Li_xNiO_2 samples.

It has been proposed that this symmetry reduction to monoclinic is driven and stabilized by either a cooperative Jahn-Teller induced distortion of NiO_2 octahedra⁶⁸ or ordering of lithium and vacancy⁴². Using selected area electron diffraction, Peres *et al.* have provided experimental evidence of a $2 \times 2 \times 2$ superstructure of ordered lithium and vacancy in the monoclinic phase (not detectable in the X-ray powder diffraction patterns) in a $\text{Li}_{0.63}\text{Ni}_{1.02}\text{O}_2$ sample. This superstructural model can be used to accommodate a range of lithium concentrations, in which lithium ordering stabilizes the monoclinic phase⁴². Recent first-principle studies⁶⁴ of layered Li_xNiO_2 have shown that lithium and vacancy ordering is coupled with monoclinicity and weak Jahn-Teller distortion of Ni^{3+} ions in this phase region. In contrast to the $2 \times 2 \times 2$ superstructure of the monoclinic cell found by electron diffraction studies⁴², different superstructures have been predicted from first-principles studies⁶³: one superstructure with $2 \times 1 \times 1$ of the monoclinic cell at $\text{Li}_{0.75}\text{NiO}_2$ and the other with $\sqrt{3} \times \sqrt{7} \times 1$ of the parent hexagonal cell at $\text{Li}_{0.4}\text{NiO}_2$. In addition to superstructures in the monoclinic phase region, one $2\sqrt{3} \times 2\sqrt{3} \times 1$ superstructure⁶³ of the hexagonal cell is found at $\text{Li}_{0.5}\text{NiO}_2$ via computation but no experimental evidence is found for this composition at this time.

Therefore, discrepancy exists in the detailed nature of the superstructures of ordered lithium and vacancy in the monoclinic Li_xNiO_2 between first-principles and electron diffraction results and further investigations are needed.

16.3.2. Lithium and Vacancy Ordering in O3 Li_xCoO_2

O3 layered LiCoO_2 , isostructural to O3 LiNiO_2 , has become the most commonly used positive electrode material in lithium rechargeable batteries since the concept of reversible lithium removal from and insertion into LiCoO_2 was first introduced by Goodenough *et al.*². Intensive research and development efforts have been devoted to understanding the physical properties and phase transformations of Li_xCoO_2 ($0 \leq x \leq 1$) in order to improve the energy output and cycle life of lithium batteries^{3,4,19,44,59,70-76}. Lithium de-intercalation from LiCoO_2 lead to several phase transformations as detailed as follows: 1) $0.75 \leq x \leq 0.94$, a first-order transformation from a rhombohedral insulating $\text{Li}_{0.94}\text{CoO}_2$ phase to a rhombohedral metallic $\text{Li}_{0.75}\text{CoO}_2$ phase^{3,4,19,73}; 2) $x \approx 0.5$, a phase transformation from the rhombohedral to monoclinic symmetry^{3,4}; 3) $0.17 < x < 0.33$, a phase transformation from O3 rhombohedral to H1-3^{77,78} and 4) $0 < x < 0.12$, a phase transformation from H1-3 to O1^{75,77,78}. Of particular interest has been to understand the phase transformation from the rhombohedral to monoclinic symmetry in Li_xCoO_2 at $x \approx 0.5$, which has been attributed to the ordering of lithium ions and vacancies within the layers (in-plane ordering) by X-ray powder diffraction experiments³ and by first-principle studies^{58,78}, as shown in Figure 16.3..

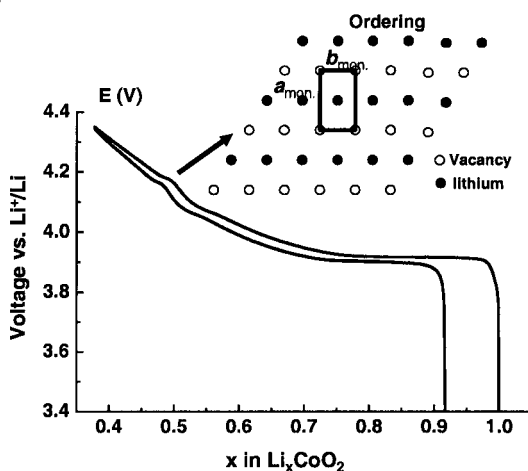


Figure 16.3. Typical voltage profiles of $\text{Li}/\text{Li}_x\text{CoO}_2$ cells and the inflexion point is correlated with order-disorder of lithium and vacancy in Li_xCoO_2 ($x \approx 0.5$)^{3,37}.

Experimental electron diffraction analysis³⁷ of Li_xCoO_2 with $x \approx 0.5$ and electron diffraction simulation of disordered $\text{Li}_{0.5}\text{CoO}_2$ with space group $C2/m$ and ordered $\text{Li}_{0.5}\text{CoO}_2$ with space group $P2/m$ have confirmed the proposed in-plane lithium ordering. The in-plane ordering long the $[110]_{\text{hex}}$ and equivalent directions allows the formation of mazed crystals and electron diffraction patterns with appearance that resembles those of the spinel structure can be fully explained by lithium and vacancy ordering and coexistence of two or three variants, as shown in Figure 16.4.³⁷ Therefore, it is believed that electron diffraction data³⁷ do not suggest the layered to spinel transformation in the Li_xCoO_2 , and the stability of the layered Li_xCoO_2 upon lithium removal is in agreement with the excellent cycling performance of $\text{Li}/\text{Li}_x\text{CoO}_2$ batteries. In addition to in-plane lithium ordering, evidence of ordering of lithium and vacancy arrangements perpendicular to the c axis of the hexagonal parent cell is also found, which is consistent with first-principles predication⁷⁸.

We now compare and discuss the difference in lithium ordering arrangements between Li_xNiO_2 and Li_xCoO_2 systems. The number of ordered lithium arrangements found in Li_xNiO_2 obtained from electron diffraction and first-principles is significantly more than Li_xCoO_2 . Lithium ordering occurs at Li_xCoO_2 with $x = 0.5$ and $x = 1/3$ where lithium ordering in Li_xNiO_2 has been proposed at $x = 0.25, 0.4, 1/3, 0.5, 0.6$ and 0.75 ^{42,63}. In theory, in-plane ordering of lithium and vacancy should lead to deviation in the a/b ratio of the rhombohedral layered structure as the electrostatic interactions of lithium ions along the a and b directions are different. The deviation in the a/b ratio from the ideal value (1.732) decreases the crystal symmetry from rhombohedral to monoclinic, where the crystal structure can be modified by varying the a/b ratio and/or β . It is interesting to note that the structural changes associated with lithium ordering at the $\text{Li}_{0.5}\text{CoO}_2$ composition and in the Li_xNiO_2 ($0.50 \leq x \leq 0.75$) system are different. Changes in the a/b ratio would considerably modify the cobalt-oxygen bonds and distort the CoO_6 octahedra, which is energetically unfavorable as both Co^{3+} and Co^{4+} ions prefer to occupy ideal or nearly ideal octahedra. Therefore, the $\text{Li}_{0.5}\text{CoO}_2$ layered structure adopts a negligible change in the a/b ratio (1.733) but a significantly different β (107.89°) value from the rhombohedral symmetry upon lithium and vacancy ordering. In contrast, the Li_xNiO_2 ($0.50 \leq x \leq 0.75$) structure has a small change in β (109.75°) but a large increase in the a/b ratio (1.764) as Jahn-Teller distorted Ni^{3+} ions can accommodate the distortion in the a and b direction upon lithium and vacancy ordering.

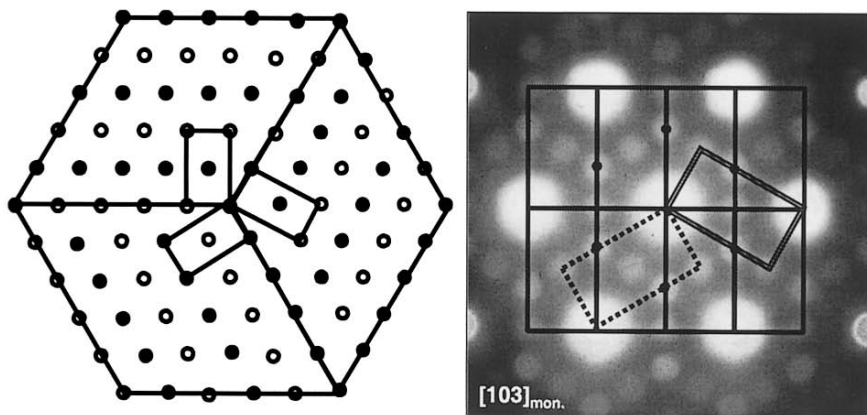


Figure 16.4. Left, three possible orientations for lithium and vacancy ordering in the lithium layers and the monoclinic unit cell of $\text{Li}_{0.5}\text{CoO}_2$ and right, an experimental diffraction pattern along the $[103]_{\text{mon.}}$ zone axis of the monoclinic unit cell or the $[001]_{\text{hex.}}$ zone axis of the hexagonal unit cell, which revealed the reflections associated with lithium and vacancy ordering from all three variants³⁷.

16.3.3. Lithium Ordering in O2 derived Li_xCoO_2

Layered O2 LiCoO_2 with a unique AB CB AB oxygen packing, first reported by Delmas *et al.*⁷⁹, is metastable to layered O3 LiCoO_2 with O3-type AB CA BC oxygen packing. Recently O2 LiMO_2 ($\text{M} = \text{Ni}, \text{Mn}, \text{Co}$, etc.) compounds have been reinvestigated for lithium rechargeable battery applications⁸⁰⁻⁸⁹ as their structural derivatives upon lithium de-intercalation and intercalation are stable with respect to the spinel-related framework. Lithium removal from O2- LiCoO_2 leads to the formation of various novel phases as shown by X-ray powder diffraction, $\text{T}^{\#}2$, $\text{T}^{\#}2'$ and O6, which are closely related to the O2 crystal structure^{82,86,90}, as shown in Figure 16.5.. Of particular interest is the $\text{T}^{\#}2\text{-Li}_x\text{CoO}_2$ phase that is stable over a large compositional range ($0.52 < x \leq 0.72$) and the stability of this structure is not clearly understood. The $\text{T}^{\#}2$ structure has an orthorhombic unit cell and space group Cmca , for instance, ' $\text{Li}_{0.61}\text{CoO}_2$ ' with $a_{\text{orth.}} = 2.8097 \text{ \AA}$, $b_{\text{orth.}} = 4.8500 \text{ \AA}$, and $c_{\text{orth.}} = 9.9082 \text{ \AA}$ ⁸². Previous studies⁸⁷ have reported that lithium ions are located on the 8e type tetrahedral sites in the $\text{T}^{\#}2$ structure, where two 8e sites are available per cobalt ions and fewer than half of the 8e sites are occupied by lithium ions. As simultaneous occupancy of adjacent 8e sites is unlikely due to small site-to-site distances (1.4 \AA and 2.4 \AA), lithium ordering on the 8e sites is expected in the $\text{T}^{\#}2$ structure. Nevertheless, it should be noted that the voltage-capacity profile for the entire $\text{T}^{\#}2$ compositional range is relatively smooth (Figure 16.5.). The absence of

inflexion points in the voltage profile is significantly different from lithium and vacancy ordering at specific lithium compositions in O3- Li_xNiO_2 and O3- Li_xCoO_2 systems (such as $x = 0.25$ and 0.33 in Figure 16.2. and $x = 0.5$ in Figure 16.3.), where pronounced modification in the lithium intercalation voltage is noted.

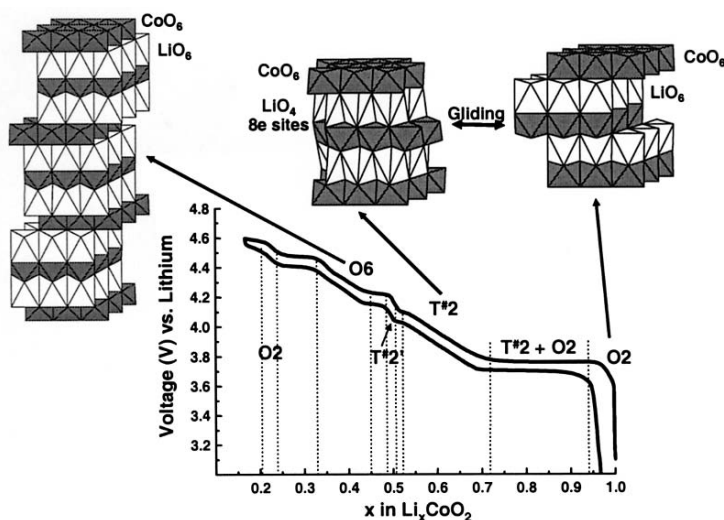


Figure 16.5. Typical galvanostatic charge and discharge voltage profiles of Li/O₂-Li_xCoO₂ cells and schematics of the O₂-LiCoO₂ structure with both lithium and cobalt ions on the octahedral sites, the T^{#2}-Li_xCoO₂ structure with cobalt ions on the octahedral sites and lithium on the 8e tetrahedral sites and the O₆-Li_xCoO₂ structure with both lithium and cobalt ions on the octahedral sites³⁸.

Although no superlattice reflection is found in X-ray and neutron powder diffraction patterns of the T^{#2} phase, electron diffraction has revealed evidence of several commensurate and incommensurate superstructures in the T^{#2} phase³⁸. A $2a_{\text{orth.}} \times 2b_{\text{orth.}} \times 2c_{\text{orth.}}$, a $2a_{\text{orth.}} \times b_{\text{orth.}} \times c_{\text{orth.}}$ and an incommensurate with $q = \gamma a_{\text{orth.}}^*$ ($\gamma = 0.23$ and 0.36) superstructures have been identified, which can be explained by different lithium and vacancy ordering configurations. For instance, superreflections present half way between the diffraction center and the fundamental reflections in the $[51\bar{2}]_{\text{orth.}}$ and the $[02\bar{1}]_{\text{orth.}}$ diffraction patterns collected from a ' $\text{Li}_{0.7}\text{CoO}_2$ ' sample reveal the presence of the $2a_{\text{orth.}} \times 2b_{\text{orth.}} \times 2c_{\text{orth.}}$ superstructure and one lithium ordering scheme is proposed to explain this superstructure, as shown in Figure 16.6³⁸.

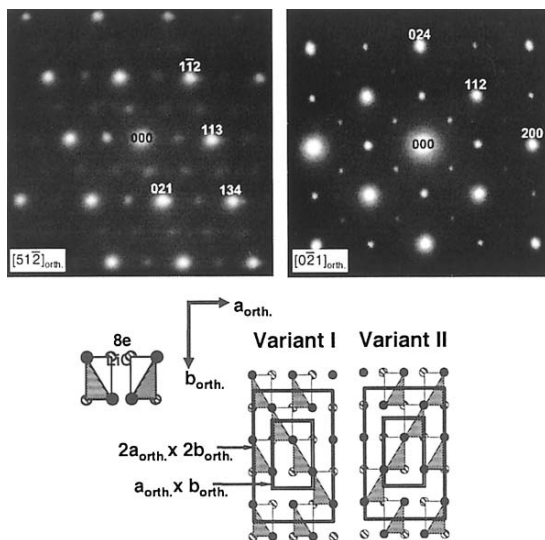


Figure 16.6. The $[51\bar{2}]_{\text{orth.}}$ and the $[02\bar{1}]_{\text{orth.}}$ diffraction patterns collected from the ‘ $\text{Li}_{0.7}\text{CoO}_2$ ’ sample reveal the presence of the $2a_{\text{orth.}} \times 2b_{\text{orth.}} \times 2c_{\text{orth.}}$ superstructure, in which only fundamental reflections are indexed. Lithium and vacancy ordering configurations needed to describe the doubling of the $a_{\text{orth.}}$ and $b_{\text{orth.}}$ cell parameters are presented. Note that two variants are allowed as two possible orientations exist for the 8e LiO_4 tetrahedra. The doubling of the $c_{\text{orth.}}$ cell parameter results from the alternation of these variants in the interslab space along the $c_{\text{orth.}}$ axis³⁸.

In addition to commensurate superstructures, incommensurate periodicities, $q = 0.36 \cdot a_{\text{orth.}}^*$ and $0.23 \cdot a_{\text{orth.}}^*$, are found in the $[0\bar{1}1]_{\text{orth.}}$ and $[001]_{\text{orth.}}$ electron diffraction patterns collected from the ‘ $\text{Li}_{0.63}\text{CoO}_2$ ’ samples, respectively, as shown in Figure 16.7.³⁸ The presence of these incommensurate superstructures suggests that 1) incommensurate lithium and vacancy ordering is preferred to commensurate ordering of lithium and vacancy in large superstructures such as $3a_{\text{orth.}} \times b_{\text{orth.}} \times c_{\text{orth.}}$ and $4a_{\text{orth.}} \times b_{\text{orth.}} \times c_{\text{orth.}}$ and 2) the lithium-lithium interaction can be fairly long range, greater than 10 \AA , in the $\text{T}^{\#2}$ structure. In addition, it is of significance to point out that combination of transmission electron microscopy and electron diffraction showed that two or three $\text{T}^{\#2}$ variants could coexist in different regions within one $\text{T}^{\#2}$ crystal, which led to the development of a domain (mazed) microstructure similar to what has been observed in $\text{Li}_{0.5}\text{CoO}_2$ (Figure 16.4.).

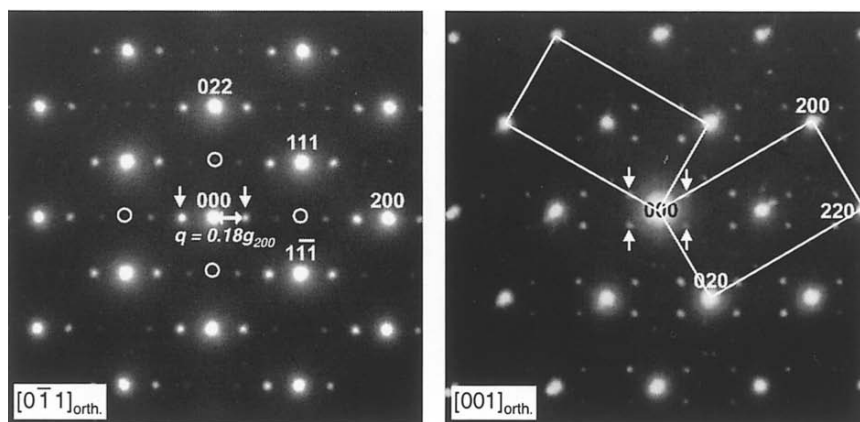


Figure 16.7. The $[0\bar{1}1]_{\text{orth.}}$ and $[001]_{\text{orth.}}$ electron diffraction patterns collected from the 'Li_{0.63}CoO₂' samples, where the first-order, incommensurate reflections are marked by arrows³⁸. Two variants of the incommensurately ordered structure are highlighted in the $[001]_{\text{orth.}}$ electron diffraction pattern.

The lack of substantial peaks of ordering transitions within the single-phase T[#]2-Li_xCoO₂ domain in the differential capacity versus voltage curve could be attributed to the presence of a large number of commensurate and incommensurate superstructures with similar Gibbs free energies of different chemical compositions³⁸. The presence of many ordered phases in the T[#]2 region is supported by a recent first-principles study⁶². It is believed that the presence of various lithium and vacancy ordering configurations improves the stability of the T[#]2 structure over a range of lithium compositions. Nevertheless, it should be mentioned that the nature of superstructures present and possible lithium ordering configurations in T[#]2-Li_xCoO₂ were complex and further investigations are needed.

Many fundamental questions with regard to lithium and vacancy ordering in layered intercalation compounds remain to be answered: 1) what are the strain and the stress concentrations in the crystals induced by lithium and vacancy order-disorder transitions and formation of domains, and 2) how do ordering transformations directly affect the cycling of lithium batteries.

16.4. SPATIALLY LOCALIZED PHASE TRANSITIONS

As electrons can be focused much easier than X-rays, combination of TEM imaging and electron diffraction can provide structural information from regions as small as the probe size of electron beam, which can be focused down to 5 nm. As electrochemical reactions occur at the interface between the

electrode materials and the electrolyte, the performance of lithium batteries is very sensitive to any phase transformations on the surfaces of electrode materials, in which the secondary phase often cannot be detected by X-ray or neutron powder diffraction due to a low volume fraction in the electrode. TEM techniques have shown particularly powerful in detecting new phases formed in lithium intercalation compounds during electrochemical cycling as reported by Thackeray *et al.*^{34,40} and Dupont *et al.*⁹¹.

16.4.1 Jahn-Teller Induced Phase Transition in $\text{Li}_x[\text{Mn}_2]\text{O}_4$

$\text{Li}/\text{Li}_x[\text{Mn}_2]\text{O}_4$ batteries cycle poorly between 3 and 4 V plateaus and the poor cycling performance results from destruction of the spinel framework by a cubic-tetragonal phase transition induced by cooperative Jahn-Teller distortion at 3 V vs. lithium¹³. Gradual loss in capacity is still observed if $\text{Li}/\text{Li}_x[\text{Mn}_2]\text{O}_4$ batteries are cycled within the 4 V plateau (the cubic phase domain)^{92,93}. It has been proposed that the capacity loss of 4 V $\text{Li}/\text{Li}_x[\text{Mn}_2]\text{O}_4$ cells at room temperature is at least partially attributed to the formation of tetragonal $\text{Li}_2[\text{Mn}_2]\text{O}_4$ transformed from cubic $\text{Li}[\text{Mn}_2]\text{O}_4$ at the end of discharge⁹². However, the tetragonal $\text{Li}_2[\text{Mn}_2]\text{O}_4$ phase is not detected by X-ray powder diffraction of the cycled $\text{Li}_x[\text{Mn}_2]\text{O}_4$ electrodes in the 4 V range. If the cubic-tetragonal transition is localized, especially on the surface of crystals, it can considerably affect the reversibility of the lithium intercalation process even though the volume fraction of the tetragonal phase is insignificant in the $\text{Li}_x[\text{Mn}_2]\text{O}_4$ electrode. Using high-spatial resolution TEM techniques, the presence of localized tetragonal domains at the surface of cubic $\text{Li}_x[\text{Mn}_2]\text{O}_4$ spinel crystals in cycled electrodes^{34,40} is confirmed.

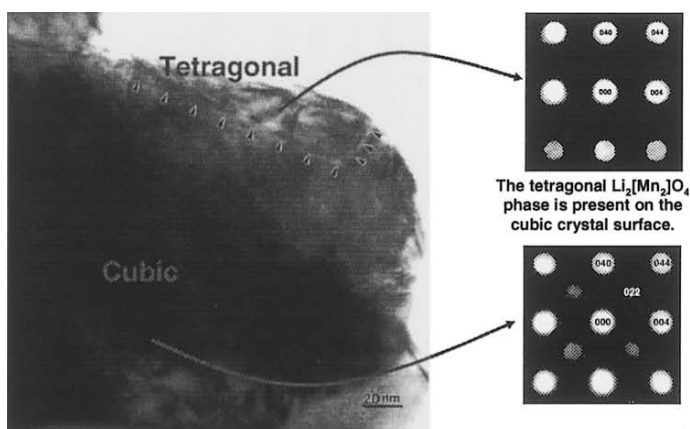


Figure 16.8 A transmission electron microscope image of a $\text{Li}_x[\text{Mn}_2]\text{O}_4$ crystal, extracted from a $\text{Li}/\text{Li}_x[\text{Mn}_2]\text{O}_4$ cell discharged to 3.3 V vs. lithium, showing a phase boundary near the surface of the crystal marked by arrows. The electron diffraction patterns collected from the surface and the center of the crystal using a 20 nm electron beam probe are shown on the right⁴⁰.

TEM data of a spinel $\text{Li}_x[\text{Mn}_2]\text{O}_4$ crystal, extracted from a $\text{Li}/\text{Li}_x[\text{Mn}_2]\text{O}_4$ cell discharged to 3.3 V vs. lithium, are presented in Figure 16.8. The dark fringes in the image marked by arrows are associated with the cubic and tetragonal phase boundary. The phase change across the boundary is confirmed by electron diffraction analysis of two regions. The diffraction pattern obtained from the crystal center (right bottom) has a four-fold symmetry, corresponding to the cubic phase. In contrast, the pattern from the crystal surface (right top) exhibits a two-fold symmetry, corresponding to the tetragonal phase. In addition, the absence of $\{220\}$ reflections and the non-equivalence of the (040) and (004) reflections are consistent with tetragonal rock-salt $\text{Li}_2[\text{Mn}_2]\text{O}_4$. Therefore, TEM analysis has provided direct experimental evidence for localized, cubic to tetragonal transformation induced by the Jahn-Teller distortion of Mn^{3+} during cycling of 4V $\text{Li}/\text{Li}_x[\text{Mn}_2]\text{O}_4$ batteries. Substitution of monovalent, divalent and trivalent ions in $\text{Li}[\text{M}_x\text{Mn}_{2-x}]\text{O}_4$ can increase the average valence state of Mn ions, suppress the cooperative Jahn-Teller distortion of Mn^{3+} ions and thus the cubic-tetragonal transition, and eventually improve the cycling performance of 4V $\text{Li}[\text{M}_x\text{Mn}_{2-x}]\text{O}_4$ spinel electrodes⁹². Although TEM studies have revealed the formation of tetragonal $\text{Li}_2[\text{Mn}_2]\text{O}_4$, further research is still needed to correlate this phase transformation to capacity fading of $\text{Li}/\text{Li}_x[\text{Mn}_2]\text{O}_4$ cells during electrochemical cycling.

16.5. Phase Transformations Between 2D Layered And 3D Spinel-Related Configurations

The layered structure and the lithiated-spinel structures have close-packed oxygen arrays (which, in practice, usually deviate slightly from ideal cubic-close-packing) but differ in the arrangement of the transition metal and lithium ions. The layered LiMO_2 structure has one set of unique close-packed planes, i.e., the (001) planes, which is parallel to one of four equivalent close-packed planes of the lithiated-spinel $\text{Li}_2[\text{M}_2]\text{O}_4$ structure, i.e., the (111), $(\bar{1}\bar{1}1)$, $(1\bar{1}\bar{1})$ and $(\bar{1}\bar{1}\bar{1})$ planes. In the lithiated-spinel $\text{Li}_2[\text{M}_2]\text{O}_4$ structure, the transition metal ions are distributed between the alternate close-packed oxygen layers in a 3:1 ratio. Therefore, if one-quarter of the transition metal ions in the lithiated-spinel structure is transposed with one-quarter of the lithium ions, the lithiated-spinel structure is then transformed to the layered structure. An intermediate cation distribution occurs if these transition metal ions are partially transposed with the lithium ions. X-ray and neutron powder diffraction patterns of layered LiMO_2 and lithiated-spinel $\text{Li}_2[\text{M}_2]\text{O}_4$ structures (M = transition metal cation) often share strong resemblance, particularly when the c/a ratio approaches 4.899, which leads to

ambiguity in identifying whether the cation configuration in lithium electrode materials is 2D layered or 3D spinel-related. In the case of layered O3-LiCoO₂ with a c/a ratio of 4.99, it is reasonably easy to distinguish the layered structure. It is especially difficult to distinguish structures with cation distributions intermediate between those of the ideal layered and ideal spinel configurations by X-ray powder diffraction. Single-crystal electron diffraction analyses of individual crystals provide phase relationships among different atomic planes, which can determine whether the structure is layered or spinel-related. In addition, the electron scattering intensity can be used to quantify intermediate cation distributions in lithium transition metal oxides.

The lithiated-spinel structure can be converted to the layered structure if the four transition metal ions on the 16d sites with coordinates $(\frac{1}{4}, \frac{1}{2}, \frac{1}{4})$, $(\frac{1}{4}, 0, \frac{3}{4})$, $(\frac{3}{4}, \frac{1}{2}, \frac{3}{4})$ and $(\frac{3}{4}, 0, \frac{1}{4})$, are transposed with the four lithium atoms on the 16c sites with coordinates $(\frac{1}{4}, 0, \frac{1}{4})$, $(\frac{1}{4}, \frac{1}{2}, \frac{3}{4})$, $(\frac{3}{4}, 0, \frac{3}{4})$ and $(\frac{3}{4}, \frac{1}{2}, \frac{1}{4})$ ⁹⁴. An intermediate structure is produced when a fraction of these transition metal and lithium ions are transposed and such an intermediate structure can be determined quantitatively by examining and comparing the intensities of four sets of the {111} planes in the lithiated-spinel structure and the (003) planes in the layered structure.

The structure factor $F_{(003)}$ of the (003) atomic planes in the layered structure with space group symmetry $R\bar{3}m$ and with a cubic close-packed oxygen array and the oxygen ions located at (0, 0, 0.24) have the following relationships:

$$F_{(003)} = 3(f_M - f_{Li}) + 1.124 f_O \quad (7)$$

Where f_M is the scattering factor of a transition metal ion, f_O is the scattering factor of an oxygen and f_{Li} is the scattering factor of a lithium ion. When considering an equivalent number of atoms in the layered structure to the number of atoms in one unit cell of the lithiated-spinel structure and ignoring the scattering of oxygen ($1.124f_O$ is significantly smaller than $3f_M$), then

$$F'_{(003)} = 16(f_M - f_{Li}) \quad (8)$$

and the total scattering intensity of the (003) planes in the layered structure is

$$I'_{(003)} \propto 2(F'_{(003)})^2 = 512(f_M - f_{Li})^2 \quad (9)$$

In the case of an ideal lithiated-spinel Li₁₆[M₁₆]O₃₂ structure with space group $Fd\bar{3}m$, the structure factor $F_{\{111\}}$ and the total scattering intensity $I_{\{111\}}$ for the {111} atomic planes have the following relationships (the scattering of oxygen is neglected):

$$F_{\{111\}} = 8(f_M - f_{Li}) \quad (10)$$

$$I_{\{111\}} \propto 8(F_{\{111\}})^2 = 512(f_M - f_{Li})^2 \quad (11)$$

These equations indicate that the total scattering intensity from the (003) reflections in the layered structure equals that from the {111} reflections of the lithiated-spinel structure.

Now we consider intermediate cation distributions that deviate from the ideal lithiated-spinel and layered configurations, which can be described by the following formula: $\{(\text{Li}_{16-4x})_{16c}[\text{Li}_{4x}]_{16d}\}_{\text{layer1}}\{(\text{M}_{16-4x})_{16d}[\text{M}_{4x}]_{16c}\}_{\text{layer2}}\text{O}_{32}$ in spinel notation. When $x = 0$, the structure has the ideal lithiated-spinel configuration, $(\text{Li}_{16})_{16c}[\text{M}_{16}]_{16d}\text{O}_{32}$, or $(\text{Li}_2)_{16c}[\text{M}_2]_{16d}\text{O}_4$. When $x = 1$, it has the layered configuration, $\{(\text{Li}_{12})_{16c}[\text{Li}_4]_{16d}\}_{\text{layer1}}\{(\text{M}_{12})_{16d}[\text{M}_4]_{16c}\}_{\text{layer2}}\text{O}_{32}$ (alternatively, in the layered notation, $(\text{Li}_3)_{3a}[\text{M}_3]_{3b}\text{O}_6$). The magnitude of the structure factor and the scattering intensity for the set of the {111} planes with increasing transition metal density, *e.g.*, the $(1\bar{1}1)$ reflection can be described as a function of x :

$$F_{(1\bar{1}1)} = (8f_M + 8xf_M - 8f_{\text{Li}} - 8xf_{\text{Li}}) \quad (12)$$

The magnitudes of the structure factors and the scattering intensities for each of the other three sets of the {111} planes with decreasing transition metal densities, can also be described as a function of x :

$$F_{(111)} = (8f_M - 8xf_M - 8f_{\text{Li}} + 8xf_{\text{Li}}) \quad (13)$$

The ratio between the scattering intensities of the (111) and $(1\bar{1}1)$ planes, denoted as m , can be related to x by the following equation:

$$m = \frac{I_{(111)}}{I_{(1\bar{1}1)}} = \frac{(1-x)^2}{(1+x)^2} \quad (14)$$

As shown in Figure 16.10., m decreases as x increases, *i.e.*, where the specific occupancies of lithium and transition metal ions in the structure vary from the lithiated-spinel to the layered configuration.

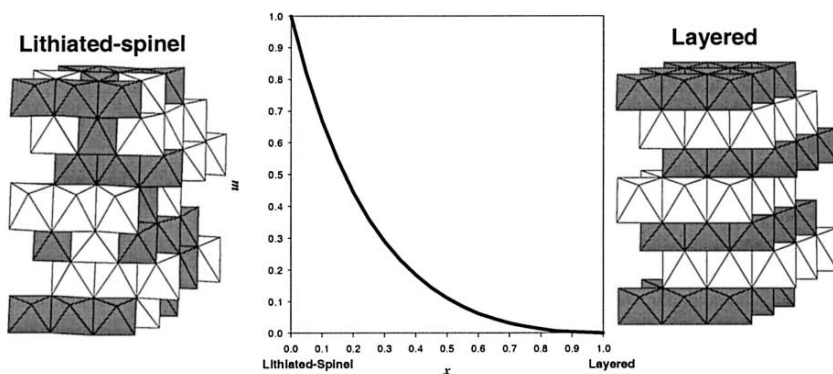


Figure 16.9. The scattering intensity ratio of the (111) and $(1\bar{1}1)$ planes, m , decreases as the cation distribution varies from the ideal lithiated-spinel to the ideal layered configuration³¹.

One can determine the values of x , the degree of cation distribution between the layered and the lithiated-spinel configurations, by measuring the relative intensity ratios of the $\{111\}$ reflections. The caveat to this approach is that the dynamical diffraction conditions often encountered in transmission electron microscopy studies would tend to reduce the intensity differences among the $\{111\}$ reflections. Taken together with the experimental fact that the variations in the $\{111\}$ scattering intensity are observed, it is apparent that the diffraction conditions of thin crystals with slight deviation from the exact zone axis are consistent with the kinematical approximation. This approach has proven particularly powerful in analyzing the structural features of LT-LiCoO₂ upon heat-treatments^{31,35} and the structural stability of layered O3 Li_xMnO₂ during electrochemical cycling²¹.

16.5.1. Intermediate Layered-Spinel Cation Configurations in LT-LiCoO₂

LT-LiCoO₂ synthesized at 400 °C has been studied extensively as a positive electrode material for lithium batteries⁹⁵. X-ray powder diffraction data and vibration spectroscopy studies have determined that LT-LiCoO₂ has the lithiated-spinel Li₂[Co₂]O₄ structure (space group $Fd\bar{3}m$)^{96,97}. LT-LiCoO₂ electrodes do not perform well in lithium cells, and there is considerable hysteresis between the lithium de-intercalation and intercalation processes, which contrasts with the superior electrochemical performance of electrodes with layered O3 LiCoO₂ structure (space group $R\bar{3}m$)⁹⁵. In addition, the voltage profile of Li/LT-Li_xCoO₂ cells is considerably different from that of Li/Li_x[Mn₂]O₄ spinel cells, which calls into question the ideal lithiated-spinel cation configuration of LT-LiCoO₂. TEM analyses of LT-LiCoO₂ crystals have shown that the cobalt distribution in LT-LiCoO₂ samples is not ideal, and that it can be considered to be intermediate between an ideal layered (Li)_{3a}{Co}_{3b}O₂ configuration and an ideal lithiated-spinel (Li₂)_{16c}[Co₂]_{16d}O₄ configuration³¹.

Crystal morphology of LT-LiCoO₂ crystals and two single-crystal electron diffraction patterns collected from two different LT-LiCoO₂ crystal are shown in Figure 16.10.. TEM imaging reveals that the average crystal size of LT-LiCoO₂ is on the order of 20 nm, which supports that the kinematical approximation can be used in electron diffraction intensity analysis. Both diffraction patterns are indexed according to the lithiated-spinel structure with cubic symmetry ($Fd\bar{3}m$) along the $[10\bar{1}]$ direction; they cannot be indexed consistently with trigonal symmetry ($R\bar{3}m$). The (111) and $(1\bar{1}1)$ reciprocal points in one pattern (top right of Figure 16.10.) have similar scattering intensities with an intensity ratio of 0.95, as expected for an

ideal lithiated-spinel structure. In contrast, the (111) and $(1\bar{1}1)$ reflections in the other pattern (bottom left of Figure 16.10.) have significantly different scattering intensities with an intensity ratio of 0.25. The scattering intensity variation observed in the $\{111\}$ planes, which can be quantified digitally from the electron diffraction patterns, is then used to determine x , the parameter to describe non-ideal cation distribution intermediate between the layered and lithiated-spinel structures based on Equations 12-14 and Figure 16.9.. There are significantly more crystals that have a configuration closer to the lithiated-spinel structure ($x < 0.5$) than to the layered structure ($x > 0.5$) in LT-LiCoO₂, as shown in bottom right of Figure 16.10.. These electron diffraction results not only confirm that the lithiated-spinel structure is the major phase in LT-LiCoO₂ products but also provide an explanation for the previously reported, poor electrochemical properties of LT-LiCoO₂ in lithium batteries. The mixing of cobalt and lithium ions in layered or lithiated-spinel LiCoO₂ structures will restrict the two-dimensional or three-dimensional pathways for lithium diffusion that are normally accessible in the ideal layered and ideal spinel structures, respectively. Therefore, the poor electrochemical behavior of Li/LT-LiCoO₂ cells can be attributed to the intermediate cation distribution between the layered and the lithiated-spinel structures in LT-LiCoO₂.

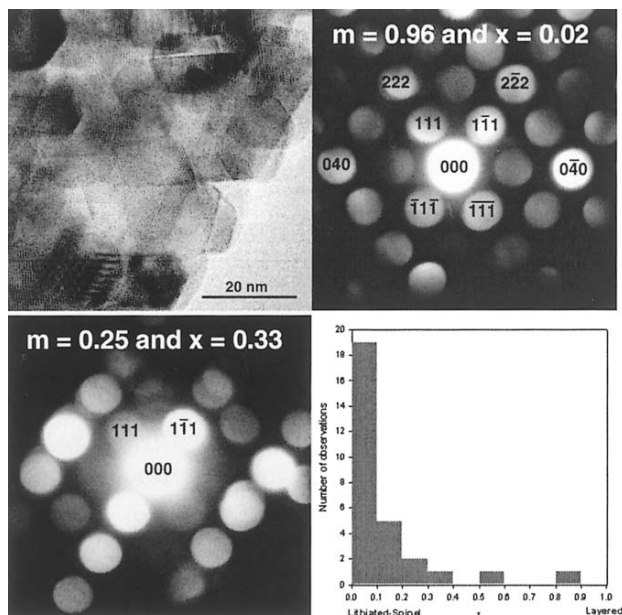


Figure 16.10. A high-resolution TEM image (top left) of LT-LiCoO₂ crystals showing the average crystal size on the order of 20 nm, and two single-crystal electron diffraction patterns with dissimilar scattering intensity ratios of the (111) and $(1\bar{1}1)$ planes³¹. The number of crystals analyzed in the LT-LiCoO₂ sample is plotted as a function of x (bottom right).

16.5.2. Layered to Spinel Transformation in Cycled Li_xMnO_2

Extensive research efforts have been focused on developing layered O_3 LiMnO_2 , isostructural to layered O_3 LiCoO_2 in order to reduce the cost and improve the safety aspects of positive electrode materials in lithium batteries^{9,11}. The voltage profile of $\text{Li}/\text{Li}_x\text{MnO}_2$ cells is modified considerably upon first intercalation process and subsequent voltage profiles of cycled $\text{Li}/\text{Li}_x\text{MnO}_2$ cells resemble those of the layered and the spinel compounds²¹. It is believed that some Mn ions in the MnO_2 slabs migrate into the lithium plane during lithium de-intercalation, resulting in localized, spinel-type cation arrangements. However, similarities between the X-ray powder diffraction patterns of the lithium-spinel $\text{Li}_2[\text{Mn}_2]\text{O}_4$ and layered Li_xMnO_2 phases lead to ambiguities in understanding phase transformations underwent in Li_xMnO_2 electrodes, which prevents confirmation of the spinel-type configuration with certainty. Combination of high-resolution lattice imaging and electron diffraction²¹ has been able to reveal the formation of localized, spinel domains in the cycled Li_xMnO_2 .

A typical high resolution TEM image and the corresponding electron diffraction pattern of one as-prepared LiMnO_2 crystal and a randomly selected crystal in the $\text{Li}_{0.5}\text{MnO}_2$ electrode obtained after one charge and one partial discharge are compared in Figure 16.12.. It should be pointed out that two sets of lattice fringes and the corresponding reflections (right of Figure 16.11.) indicate the presence of two sets of close-packed planes in the Li_xMnO_2 structure in contrast to one allowed in the layered LiMnO_2 structure (left of Figure 16.11.). The occurrence of more than one set of close-packed Mn planes corresponds to the presence of the spinel-type configuration. As some manganese ions have migrated into lithium planes during lithium de-intercalation and they are trapped in the lithium layers upon lithium re-intercalation, therefore, localized cation distributions resemble that of the spinel. In addition, it can be argued that the non-equivalent scattering intensity of the $\{111\}$ reflections of the spinel-type structure in the Li_xMnO_2 sample can be attributed to a non-uniform cation distribution within individual Li_xMnO_2 crystal with discrete domains, where each domain has a cation distribution of either the layered or the spinel-type configuration. The averaged cation distribution over each crystal can be regarded as being intermediate between that of the layered and the lithiated-spinel structures, which can be quantified according to Equation 12-14 and Figure 16.9.. Therefore, combination of high-resolution TEM imaging and electron diffraction has clearly revealed the structural instability of layered Li_xMnO_2 structure and provided direct evidence of the spinel-type atomic arrangements in the cycled Li_xMnO_2 electrode materials. Furthermore, Chiang *et al.*⁴⁶ have proposed the formation of antiphase boundaries upon transformation from

layered LiMnO_2 to the spinel configuration during electrochemical cycling. Further high-resolution TEM imaging and theoretical calculations are needed to verify the presence and the energetic of nano-meter-scale antiphase domains in lithium transition metal oxides.

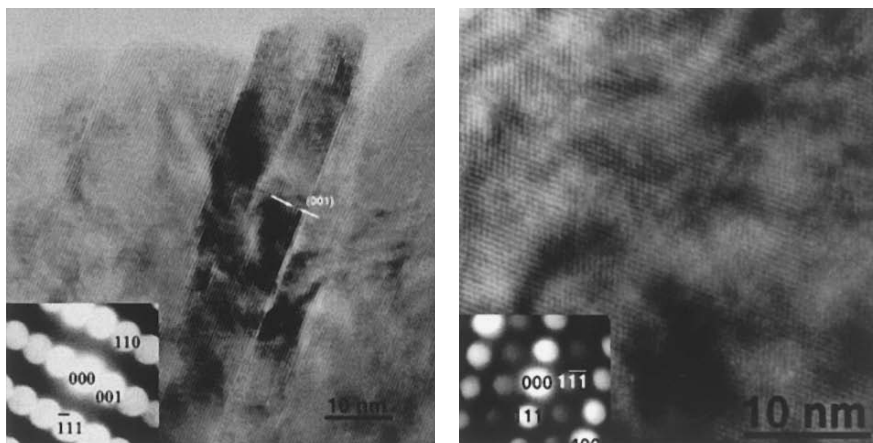


Figure 16.11. Left: A typical high-resolution TEM micrograph and the corresponding electron diffraction pattern $\{[1\ \bar{1}\ 0]_{\text{layered}} \text{ zone axis}\}$ of layered LiMnO_2 crystals and Right: A high-resolution TEM image and the corresponding electron diffraction pattern $\{[0\ \bar{1}\ 1]_{\text{spinel}} \text{ zone axis}\}$ of a randomly selected crystal in the $\text{Li}_{0.5}\text{MnO}_2$ electrode after one charge and one partial discharge²¹.

16.6. PERSPECTIVES

Conventional TEM imaging and electron diffraction studies of lithium battery materials have been invaluable in revealing phase transformations that occur in lithium battery materials during lithium de-intercalation or intercalation. The information has led to improved understanding of structure-property relationships of lithium intercalation compounds and optimization of battery performance and design of new electrode materials. Here we discuss several recently developed TEM techniques that can be used to further improve our fundamental understanding of lithium intercalation compounds in lithium batteries.

16.6.1. High-Resolution TEM Imaging and Simulation

Although X-ray and neutron powder diffraction techniques are insensitive to lithium ion arrangements, columns of lithium in host structures can potentially be imaged (along with the columns of other atoms present) by making use of their interactions with an electron beam in the high-resolution

TEM (HRTEM). The results of the electrons' interaction with lithium transition metal oxide lattice are encoded on the emergent electron wave as changes in the phase (and, to a lesser extent, the amplitude) of the original incident electron wave. The phase of this exit-surface wave (ESW) is a function of the oxide potential projected in the direction of the incident electron beam⁹⁸. In the HRTEM, the ESW phase is imaged with an objective lens that imposes additional phase changes due to aberrations such as defect of focus (defocus) and spherical aberration. Focal-series reconstruction (FSR) of the ESW from a series of images obtained over a range of defocus values⁹⁹ can mitigate the effects of spherical aberration, and move beyond the native resolution of a TEM to its information limit⁹⁸. This method has achieved resolution of oxygen atoms in staurolite¹⁰⁰ and BaTiO₃¹⁰¹, and recently it has been used to successfully image and resolve individual lithium ions in layered O3 LiCoO₂.

As shown in Figure 16.12., image simulation via the “weak-phase-object” approximation indicates that resolutions higher than 1 Å are needed to resolve individual lithium ions in layered CoO₂ matrix³⁹. The ESW phase image reconstructed from experimental images of a thin edge of a LiCoO₂ crystal along the [110] zone axis shows all three types of atoms in LiCoO₂ (Figure 16.12., right a)³⁹. Comparison with a simulated ESW phase image based on a crystal model of 17 unit cells thick (48 Å) at 0.9 Å resolution (Figure 16.12., right b), reveals that all the atom peaks have the characteristics predicted by the simulations. The O-Co-O units can clearly be distinguished in the experimental image, with each fuzzy cobalt peak flanked by a pair of bright oxygen atoms, and the weak spots lying between them can be identified as the electron scattering intensities of the lithium ions (arrowed).

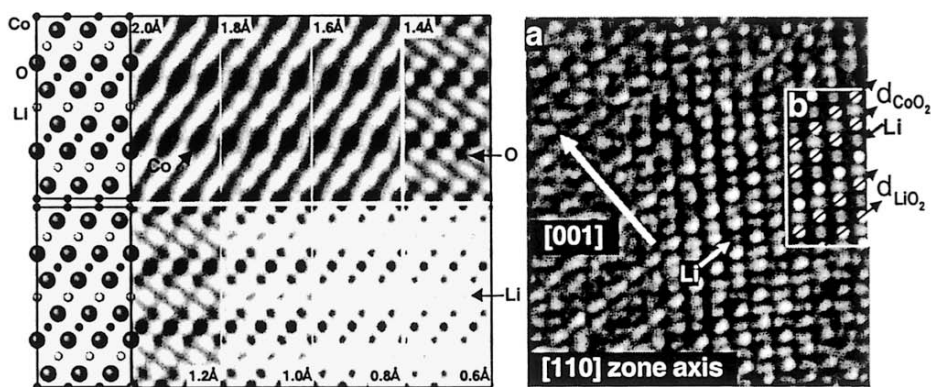


Figure 16.12. Left: Simulated Images of LiCoO₂ in the [110] zone axis under thin-crystal (“weak-phase-object”) conditions for increasing resolution (marked) show that atoms of cobalt should be visible at 2 Å resolution, oxygen at 1.4 Å, and lithium at 1 Å. Right: Experimental imaging of Li columns confirmed by simulation a) LiCoO₂ ESW-phase image, reconstructed from 20 experimental images, shows lithium ions in rows (arrowed) between O-Co-O groups. b) ESW-phase simulation for 48 Å thickness and 0.9 Å resolution³⁹.

Studies with such atomic details can provide knowledge of the distribution of vacancies and light atoms such as lithium and oxygen in lithium transition metal oxides, which is invaluable to engineering of lithium storage materials.

16.6.2. EELS Analysis and Imaging

Much attention has been focused on characterizing localized atomic arrangements and phase transformations by electron diffraction and imaging techniques. It is also important to analyze the chemical and electronic properties of lithium battery materials upon lithium intercalation or de-intercalation. Although high-resolution images are sensitive to differences in structural factors, the combined effect of differences in structural factors and deviation from the exact Bragg condition leads to ambiguity in revealing differences in local chemical compositions from TEM images. EELS could provide quantitative information on light elements such as lithium and oxygen, and determine the valence states of transition metal and oxygen ions in lithium transition metal oxides. Recently Graetz et al.^{49,51} have used EELS analyses to study and confirm charge compensation mechanisms in layered Li_xCoO_2 and $\text{Li}_x\text{Ni}_{0.8}\text{Co}_{0.2}\text{O}_2$ upon lithium de-intercalation, which has been previously predicted from first-principle studies^{60,78}. In addition, imaging with EELS can provide information about how different ions are distributed in lithium transition metal oxides on the nanometer-scale. Combination information on the chemistry, structure and electronic properties of localized domains in lithium battery materials will enable us to optimize and advance lithium battery performance.

16.6.3. In-Situ TEM imaging

One way that offers the possibility of overcoming material stability and handling limitations of TEM sample preparation is to develop *in-situ* TEM characterization and observe the phase transformations in electrode materials in an electrochemical cell *in-situ*. The *in-situ* cell could be built containing solid or liquid electrolytes. The difficulties in design of *in-situ* electrochemical cells reside in the facts that the whole cell has to be thin enough to be electron transparent and hermetically sealed. Ross recently reported a preliminary design of a liquid *in-situ* cell to study the electroplating process, which is a critical step in integrated circuit fabrication¹⁰². Although it was found too thick to be electron transparent, it held promise for real-time studies of electrochemical systems. More importantly, *in-situ* characterization would offer an effective route to study many interfacial phenomena between

the electrode and electrolyte, and provides directions to improve the safety and storage aspects of battery systems. Interfacial reactions may include the formation of the solid electrolyte interface on the negative and/or positive electrode before electrochemical reactions, the chemical stability of electrode materials at the electrolyte-electrode interface during electrochemical reactions and storage, *etc.* At present, these interfacial reactions are not well studied nor clearly understood. Observations *in-situ* before, during and after electrochemical reactions would provide information essential to better understanding of these phenomena.

Acknowledgments

The author is grateful to A. Mayes, G. Ceder, A. Van der Ven and C. Delmas for comments insightful discussions. The International Research Fellow Award INT 0000-429 from National Science Foundation and partial support from Department of Mechanical Engineering at the Massachusetts Institute of Technology and Office of Naval Research Young Investigator Award N00014-03-10448 are greatly acknowledged.

REFERENCES

1. D. Linden & T. Reddy (eds.) *Handbook of Batteries* (McGraw-Hill, New York, 2002).
2. K. Mizushima, P. C. Jones, P. J. Wiseman & J. B. Goodenough, *Materials Research Bulletin* **15**, 783-789 (1980).
3. J. N. Reimers & J. R. Dahn, *J. Electrochem. Soc.* **139**, 2091-2097 (1992).
4. T. Ohzuku & A. Ueda, *J. Electrochem. Soc.* **141**, 2972-2977 (1994).
5. J. Morales, C. Pérez-Vicente & J. L. Tirado, *Materials Research Bulletin* **25**, 623-630 (1990).
6. J. R. Dahn, U. Von Sacken, M. W. Juskow & H. Al-Janaby, *J. Electrochem. Soc.* **138**, 2207-2211 (1991).
7. M. Broussely, F. Pertion, P. Biensan, J. M. Bodet, J. Labat, A. Lecerf, C. Delmas, A. Rougier & J. P. Pérès, *Journal of Power Sources* **54**, 109-114 (1995).
8. C. Delmas, M. Ménétrier, L. Croguennec, I. Saadoune, A. Rougier, C. Pouillier, G. Prado, M. Grune & L. Fournès, *Electrochimica Acta* **45**, 243-253 (1999).
9. A. R. Armstrong & P. G. Bruce, *Nature* **381**, 499-500 (1996).
10. P. G. Bruce, A. R. Armstrong & H. Huang, *Journal of Power Sources* **68**, 19-23 (1997).
11. F. Capitaine, P. Gravereau & C. Delmas, *Solid State Ionics* **89**, 197 (1996).
12. M. M. Thackeray, P. J. Johnson, L. A. De Picciotto, P. G. Bruce & J. B. Goodenough, *Materials Research Bulletin* **19**, 179 (1984).
13. W. I. F. David, M. M. Thackeray, L. A. De Picciotto & J. B. Goodenough, *Journal of Solid State Chemistry* **67**, 316-323 (1987).
14. M. M. Thackeray, W. I. F. David, P. G. Bruce & J. B. Goodenough, *Materials Research Bulletin* **18**, 461 (1983).
15. A. K. Padhi, K. S. Nanjundaswamy & J. B. Goodenough, *Journal of the Electrochemical Society* **144**, 1188 (1997).
16. J.-M. Tarascon & M. Armand, *Nature* **414**, 359 (2001).
17. M. M. Thackeray, J. O. Thomas & M. S. Whittingham, *MRS Bulletin*, 39 (2000).

18. C. Delmas, J. P. Pérès, A. Rougier, A. Demourgues, F. Weill, A. Chadwick, M. Broussely, F. Perton, P. Biensan & P. Willmann, *Journal of Power Sources* **68**, 120-125 (1997).
19. M. Ménétrier, I. Saadoune, S. Levasseur & C. Delmas, *Journal of Materials Chemistry* **9**, 1135-1140 (1999).
20. G. Vitins & K. West, *Journal of the Electrochemical Society* **144**, 2587-2592 (1997).
21. Y. Shao-Horn, S. A. Hackney, A. R. Armstrong, P. G. Bruce, R. Gitzendanner, C. S. Johnson & M. M. Thackeray, *J. Electrochem. Soc.* **146**, 2404-2412 (1999).
22. H. F. Wang, Y. I. Jang & Y. M. Chiang, *Electrochemical and Solid State Letters* **2**, 490-493 (1999).
23. J. Rodriguez-Carjaval, G. Rousse, C. Masquelier & M. Hervieux, *Physical Review Letters* **81**, 4660 (1998).
24. G. Rousse, C. Masquelier, J. Rodriguez-Carjaval & M. Hervieu, *Electrochemical and Solid-State Letters* **2**, 6-8 (1999).
25. G. Rousse, C. Masquelier, J. Rodriguezcarvajal, E. Elkaim, J. P. Lauriat & J. L. Martinez, *Chemistry of Materials* **11**, 3629-3635 (1999).
26. A. J. Garcia-Adeva, D. R. Conradson, P. Vilella & S. D. Conradson, *J. Phys. Chem. B*, **107** (28), , 2003 **107**, 6704 -6716 (2003).
27. P. Hirsch, A. Howie, R. Nicholson, D. W. Pashley & M. J. Whelan. *Electron Microscopy of Thin Crystals* (Krieger Publishing Company, 1977).
28. D. B. Williams & C. B. Carter. *Transmission Electron Microscopy - A Textbook for Materials Science* (Plenum Press, New York, 1996).
29. B. Fultz & J. M. Howe. *Transmission Electron Microscopy and Diffractometry of Materials* (Springer, Berlin, 2002).
30. P. R. Buseck, J. M. Cowley & L. Eyring (eds.) *High-Resolution Transmission Electron Microscopy and Associated Techniques* (Oxford Science Publications, 1992).
31. Y. Shao-Horn, S. A. Hackney, C. S. Johnson, A. J. Kahaian & M. M. Tackeray, *Journal of Solid State Chemistry* **140**, 116-127 (1998).
32. Y. Shao-Horn, S. A. Hackney, C. S. Johnson & M. M. Thackeray, *J. Electrochem. Soc.* **145**, 582-589 (1998).
33. Y. Shao-Horn, Ph.D dissertation, Michigan Technological University, Houghton, Michigan, USA (1998).
34. Y. Shao-Horn, S. A. Hackney, A. J. Kahaian, K. D. Kepler, E. Skinner, J. T. Vaughey & M. M. Thackeray, *Journal of Power Sources* **81-82**, 496 (1999).
35. Y. Shao-Horn, S. A. Hackney, A. J. Kahaian & M. M. Thackeray, *Journal of Solid State Chemistry* **168**, 60 (2002).
36. Y. Shao-Horn, M. A. O'Keefe, E. C. Nelson, L. Croguennec & C. Delmas. in *Fall Meeting of the Materials Research Society, Symposium G, Boston, Massachusetts* (2002).
37. Y. Shao-Horn, S. Levasseur, F. Weill & C. Delmas, *J. Electrochem. Soc.* **150**, A366-A373 (2003).
38. Y. Shao-Horn, L. Croguennec, D. Carlier, F. Weill, M. Menetrier & C. Delmas, *Chemistry of Materials* **15**, 2977-2983 (2003).
39. Y. Shao-Horn, L. Croguennec, C. Delmas, E. C. Nelson & M. A. O'Keefe, *Nature Materials* **2**, 464-467 (2003).
40. M. M. Thackeray, Y. Shao-Horn, A. J. Kahaian, K. D. Kepler, E. Skinner, J. T. Vaughey & S. A. Hackney, *Electrochemical and Solid-State Letters* **1**, 7-9 (1998).
41. M. M. Thackeray, C. S. Johnson, Kahaian, A.J., K. D. Kepler, J. T. Vaughey, Y. Shao-Horn & S. A. Hackney, *J. Power Sources* **81-82**, 60 (1999).
42. J. P. Pérès, F. Weill & C. Delmas, *Solid State Ionics* **116**, 19 (1999).
43. H. Wang, Y. I. Jang, B. Huang, D. R. Sadoway & Y. M. Chiang. in *9th International Symposium on Intercalation Compounds* abstract N°111 (Molecular Crystals and Liquid Crystals Science and Technology, Arcachon (FRANCE), 1998).
44. H. F. Wang, Y. I. Jang, B. Y. Huang, D. R. Sadoway & Y. T. Chiang, *J. Electrochem. Soc.* **146**, 473-480 (1999).

45. H. F. Wang, Y. I. Jang, B. Y. Huang, D. R. Sadoway & Y. M. Chiang, *Journal of Power Sources* **82**, 594-598 (1999).
46. Y. Chiang, H. F. Wang & Y. I. Jang, *Chemistry of Materials* **13**, 53-63 (2001).
47. Gabrisch H., R. Yazami & B. Fultz, *Electrochemical and Solid State Letters* **5**, A111 (2002).
48. L. Croguennec, P. Deniard, R. Brec, M. T. Caldes Ricos & L. Brohan, *Mol. Cryst. Liq. Cryst.* **311**, 101-108 (1998).
49. J. Graetz, C. C. Ahn, R. Yazami & B. Fultz, *Journal of Physical Chemistry B* **107**, 2887-2891 (2003).
50. H. Gabrisch, R. Yazami & B. Fultz, *Electrochemical and Solid State Letters* **5**, A111-A114 (2002).
51. J. Graetz, A. Hightower, C. C. Ahn, R. Yazami, P. Rez & B. Fultz, *Journal of Physical Chemistry B* **106**, 1286-1289 (2002).
52. A. Hightower, C. C. Ahn, B. Fultz & P. Rez, *Applied Physics Letters* **77**, 238-240 (2000).
53. Y. Shao-Horn, L. Croguennec, A. Gloter, M. Guilmard, C. Colliex & C. Delmas, *Chemistry of Materials*, submitted (2003).
54. A. H. Thompson, *Physical Review Letters* **40**, 1511-1514 (1978).
55. W. R. McKinnon & J. R. Dahn, *Solid State Communications* **48**, 43-45 (1983).
56. C. Delmas, M. Ménétrier, L. Croguennec, S. Levasseur, J. P. Pérès, C. Poullierie, G. Prado, L. Fournès & F. Weill, *Inter. J. of Inorg. Mater.* **1**, 11 (1999).
57. A. Van der Ven & G. Ceder, *Electrochemical and Solid State Letters* **3**, 301-304 (2000).
58. M. Catti, *Physical Review B* **61**, 1795-1803 (2000).
59. C. Wolverton & A. Zunger, *Physical Review B - Condensed Matter* **57**, 2242-2252 (1998).
60. C. Wolverton & A. Zunger, *Physical Review Letters* **81**, 606-609 (1998).
61. C. Wolverton & A. Zunger, *Journal of Power Sources* **82**, 680-684 (1999).
62. D. Carlier, A. Van der Ven, C. Delmas & G. Ceder, *Chemistry of Materials* **15**, 2651-2660 (2003).
63. M. de Dompablo, A. Van der Ven & G. Ceder, *Physical Review B* **66**, art. no.-064112 (2002).
64. M. E. Arroyo y de Dompablo & G. Ceder, *Chemistry of Materials* **15**, 63-67 (2003).
65. I. Saadoune & C. Delmas, *Journal of Solid State Chemistry* **136**, 8-15 (1998).
66. S. Levasseur, M. Menetrier, E. Suard & C. Delmas, *Solid State Ionics* **128**, 11-24 (2000).
67. W. Li, J. N. Reimers & J. R. Dahn, *Solid State Ionics* **67**, 123-130 (1993).
68. T. Ohzuku, A. Ueda & M. Nagayama, *J. Electrochem. Soc.* **140**, 1862-1870 (1993).
69. A. Hirano, R. Kanno, Y. Kawamoto, Y. Takeda, K. Yamaura, M. Takano, K. Ohyama, M. Ohashi & Y. Yamaguchi, *Solid State Ionics* **78**, 123-131 (1995).
70. M. G. S. R. Thomas, P. G. Bruce & J. B. Goodenough, *Solid State Ionics* **17**, 13-19 (1985).
71. S. Kikkawa, S. Miyazaki & M. Koizumi, *Journal of Solid State Chemistry* **62**, 35 (1986).
72. E. Plichta, M. Salomon, S. Slane, M. Uchiyama, D. Chua, W. B. Ebner & H. W. Lin, *Journal of Power Sources* **21**, 25-31 (1987).
73. J. Molenda, A. Stoklosa & T. Bak, *Solid State Ionics* **36**, 53-58 (1989).
74. J. P. Kemp & P. A. Cox, *J. Phys.: Condens. Matter* **2**, 9653-9667 (1990).
75. G. G. Amatucci, J. M. Tarascon & L. C. Klein, *J. Electrochem. Soc.* **143**, 1114-1123 (1996).
76. M. K. Aydinol, A. F. Kohan & G. Ceder, *Journal of Power Sources* **68**, 664-668 (1997).
77. A. Van der Ven, M. K. Aydinol & G. Ceder, *J. Electrochem. Soc.* **145**, 2149-2155 (1998).
78. A. Van der Ven, M. K. Aydinol, G. Ceder, G. Kresse & J. Hafner, *Physical Review B* **58**, 2975-2987 (1998).
79. C. Delmas, J. J. Braconnier & P. Hagenmuller, *Materials Research Bulletin* **17**, 117 (1982).
80. R. Siegel, J. Hirschinger, D. Carlier, S. Matar, M. Ménétrier & C. Delmas, *J Phys. Chem. B* **105**, 4166 (2001).

81. D. Carlier, I. Saadoune, E. Suard, L. Croguennec, M. Ménétrier & C. Delmas, *Solid State Ionics* **144**, 263 (2001).
82. D. Carlier, I. Saadoune, M. Ménétrier & C. Delmas, *J. Electrochem. Soc.* **149**, A1310 (2002).
83. J. M. Paulsen, C. L. Thomas & J. R. Dahn, *J. Electrochem. Soc.* **147**, 861 (2000).
84. J. M. Paulsen & J. R. Dahn, *J. Electrochem. Soc.* **147**, 2478 (2000).
85. J. M. Paulsen, C. L. Thomas & J. R. Dahn, *J. Electrochem. Soc.* **147**, 2862 (2000).
86. J. M. Paulsen, J. R. Mueller-Neuhaus & J. R. Dahn, *J. Electrochem. Soc.* **147**, 508 (2000).
87. J. M. Paulsen, R. A. Donaberger & J. R. Dahn, *Chem. Mater.* **12**, 2257 (2000).
88. Z. Lu & J. R. Dahn, *J. Electrochem. Soc.* **148**, A710 (2001).
89. Z. Lu & J. R. Dahn, *J. Electrochem. Soc.* **148**, A237 (2001).
90. A. Mendiboure, C. Delmas & P. Hagenmuller, *Materials Research Bulletin* **19**, 1383 (1984).
91. L. Dupont, M. Hervieu, G. Rousse, C. Masquelier, M. R. Palacin, Y. Chabre & J. M. Tarascon, *Journal of Solid State Chemistry* **155**, 394 (2000).
92. R. J. Gummow, A. De Kock & M. M. Thackeray, *Solid State Ionics* **69**, 59-67 (1994).
93. J.-M. Tarascon, E. Wang, F. K. Shokoohi, W. R. McKinnon & S. Colson, *Journal of the Electrochemical Society*, 2859 (1991).
94. R. J. Gummow, Ph.D dissertation, University of Cape Town (1993).
95. R. J. Gummow, M. M. Thackeray, D. Wif & S. Hull, *Materials Research Bulletin* **27**, 327-337 (1992).
96. W. Li, J. N. Reimers & J. R. Dahn, *Physical Review B* **49**, 826 (1994).
97. W. Huang & R. Frech, *Solid State Ionics* **86-88**, 395-400 (1996).
98. M. A. O'Keefe, *Ultramicroscopy* **47**, 282-297 (1992).
99. P. Schiske, in *Image Processing And Computer-Aided Design* (ed. Hawkes, P. W.) 82-90 (Acad. Press, London, 1973).
100. K. H. Downing, M. Hu, H. Wenk & M. A. O'Keefe, *Nature* **348**, 525-528 (1990).
101. C. L. Jia & A. Thust, *Phys. Rev. Letts* **82**, 5052-5055 (1999).
102. F. M. Ross, *IBM J. Res. Develop.* **44**, 489 (2000).

Chapter 17

LIQUID ELECTROLYTES: SOME THEORETICAL AND PRACTICAL ASPECTS

M. Nazri

University of Windsor, Department of Chemistry, Windsor, Ontario, N9B 3P4, Canada

17.1. INTRODUCTION TO SOLVENTS

The basic requirements of a suitable electrolyte for electrochemical devices are high ionic conductivity, low melting and high boiling points, chemical and electrochemical stability, and safety. Electrolyte conductivity and electrochemical stability are key parameters in selecting an electrolyte for modern electrochemical devices such as advanced batteries, fuel cells, super-capacitors, sensors, and electrochromic displays. These parameters, conductivity and electrochemical stability, will receive particular attention in this chapter. Although progress has been made in enhancing the conductivity of solid electrolytes, particularly the polymeric ones, liquid electrolytes are still used in most electrochemical systems. The solvent properties, and dynamics of ion solvent interactions, must be understood in designing new electrolytes. In this chapter, a short but general introduction to properties of solvents and ion-solvent dynamics is discussed.

The history of electrolyte development goes as far back as the work of Greek philosophers in search for a universal solvent, the so-called "Alkahest". In search of Alkahest, many solvents and chemical rules were discovered such as "like dissolves like" (*similia similibus solvuntur*) as shown in Table 17.1. Later, the theory of osmotic pressure by van't Hoff (1852-1911), and the theory of electrolyte dissociation by Arrhenius (1859-1927) were discovered. Many speculations about the nature of solute-solvent interactions and the influence of solvent media on the rate of chemical reaction were proposed in the early eighteen-century. The role of solvents on chemical equilibrium, on tautomerism (*i.e.* keto-enol tautomerism), and the phenomenon of solvatochromism (shift of UV/Vis absorption bands due to the changes of the index of refraction) were discovered.^{1,2} Scheibe *et al.* have

correlated the solvating ability of solvents to their degree of influence on reaction rate, chemical equilibrium, and shift in absorption spectra.³

In the early 19th century, it was much argued that solvents and electrolytes should not be considered as a continuum, usually characterized by their physical properties such as dielectric constant, density, index of refraction, etc., but as a discontinuum with mutually interacting molecules. It was discovered in many instances that the density of the solvent in solvation shells around small cations is greater than that of the bulk solvent, due to the strong ion-solvent interactions. The interaction forces between solvent molecules are too big to treat them like gases but not significant enough to consider them as solids. Although the nearest neighbor distances in liquid and solids are very close, the volume of liquid is about 10% greater than the solid forms, due to the significant defects that exist in the coordination number of ions in the liquid state.

Table 17.1. Various solvents with different degree of hydrophobicity.

Compound		Well soluble in
Hydrocarbons	hydrophobic	Hydrocarbons, Ethers, Halohydrocarbons
Halohydrocarbons		
Ethers		
Amines		
Esters		Carboxylic Esters
Nitrohydrocarbons		
Nitriles		
Ketones		Alcohols, 1,4-Dioxane Acetic Acid
Aldehydes		
Phenols		Alcohols, Water
Amides		
Alcohols		
Carboxylic Acids		
Sulfonic Acids	hydrophilic	Water
Salts		

In addition, the solvent molecules in the solvation shell of an ion have a short residency time, and the dynamics of solvent exchange processes vary in a wide range, depending on the size and charge of the ions and the chemical nature of the solvent. In some cases the solvation shell is stable enough that the complex can be considered as a molecular entity, *e.g.* $[\text{Co}(\text{NH}_3)_6]^{2+}$. On the other hand, in some cases the solvent exchange is faster than the time scale of NMR, and solvent molecules in the solvation shell cannot be distinguished from those in bulk solution. The complexity of interactions in liquid state makes the theoretical treatment of electrolyte

structure a difficult task, and still most reliable data are those obtained experimentally, using NMR, vibrational spectroscopy, and fast spectroscopy techniques.

When dealing with mixed solvents, the solubility parameter relates to the molar enthalpy of vaporization for a gas of zero pressure by⁴

$$\text{Hildebrand parameter} = \delta = [(\Delta H_v - RT)/V_m]^{1/2} \quad (17.1)$$

where, V_m is the molar volume and ΔH_v is the molar enthalpy of vaporization. The δ is the measure of work necessary to separate solvent molecules to create a cavity to accommodate the solute.

17.2. COLUMBIC FORCES BETWEEN IONS AND DIPOLAR SOLVENTS

In addition to the intermolecular forces, such as van der Waals forces and the well-known hydrogen bonding forces responsible for the non-ideal behavior of solvents and electrolytes, there are other important forces between ions and neutral molecules with permanent dipole moments (dipolar solvents) that can alter the physical and chemical properties of solvents. The most important forces which exist between solvent molecules and solute-solvents are discussed in the following section.

17.2.1. Ion-Dipole Forces

Solvents with unsymmetrical charge distribution (dipolar solvents) possess a permanent dipole moment, μ . The magnitude of the dipole moment depends on the value of charges on the opposite sides of the molecule and their separation distance as defined by $\mu = q \cdot r$, where q is the charge (assuming equal value of charge on each side of the molecule), and r is the separation distance between charges.⁵ Most organic solvents have permanent dipole moment in a wide range from 0 to 18×10^{-30} Coulomb-meters (Cm). In particular, cyclic and linear organic carbonates, used in lithium batteries and particularly dealt with here, have a large difference in permanent dipole moment, (*i.e.* $\mu_{\text{propylene carbonate}} = 16.7 \times 10^{-30}$ Cm, and $\mu_{\text{diethyl carbonate}} = 3 \times 10^{-30}$ Cm). The dipole moment, relative dielectric constant, melting point, and boiling point of several common organic solvents are listed in Table 17.2. The water molecule is also listed as a reference for comparison.

Table 17.2. Common dipolar organic solvents and their physical properties.⁶⁻⁸

Solvent	$t_{mp}/^{\circ}\text{C}$	$t_{bp}/^{\circ}\text{C}$	ϵ	μ (10^{-30}Cm)
Water	0.0	100	78.30	
Formamide	2.55	210.5	111.0	11.2
Methanol	-97.7	64.5	32.66	5.7
Ethanol	-114.5	78.3	24.55	5.8
Acetic acid	16.7	117.9	6.17	5.6
Cyclohexanol	25.15	161.1	15.0	6.2
Propylene Carbonate	-54.5	241.7	64.92	16.5
Nitromethane	-28.55	101.2	35.94	11.9
Acetonitrile	-43.8	81.6	35.94	11.8
Dimethyl sulfoxide	18.5	189.0	46.45	13.5
Aniline	-6.0	184.4	6.71	5.0
Sulfolane	28.45	287.3	43.3	16.0
Acetone	-94.7	56.1	20.56	9.0
Cyanobenzene	-12.75	191.1	25.20	13.4
Nitrobenzene	5.8	210.8	34.78	13.3
Hexamethylphosphoric				
Acid triamide	7.2	233	29.6	18.5
Acetophenone	19.6	202.0	17.39	9.8
Pyridine	-41.55	115.25	12.91	7.9
Methyl acetate	-98.05	56.9	6.68	5.7
Cyclohexanone	-32.1	155.65	16.10	10.3
Quinoline	-14.85	237.1	8.95	7.3
Tetrahydrofuran	-108.4	66.0	7.58	5.8
Diethyl carbonate	-43.0	126.8	2.82	3.15
Dimethyl carbonate	4	90	3.12	2.95
Methyl-propyl carbonate	-49	130	3	4.84
Methyl-isopropyl carbonate	-76	117	3	4.92
Ethyl-propyl carbonate	-81	148	3	5.25
Ethyl-isopropyl carbonate	-132	135	3	
Ethylene carbonate	36.4	238	89	4.87
1,4-Dioxane	11.8	101.3	2.21	1.54
Trichloroethene	-86.4	87.2	3.42	2.7
Diethyl ether	-116.3	34.4	4.20	3.8
Benzene	5.5	80.1	2.27	0.0
Toluene	-95.0	110.6	2.38	1.0
Carbon disulfide	-111.6	46.2	2.64	0.0
Tetrachloromethane	-22.8	76.6	2.23	0.0
n-Hexane	-95.3	68.7	1.88	0.0

t_{mp} = melting point, t_{bp} = boiling point, ϵ = dielectric constant, μ = dipole moment.

A solvent molecule with a permanent dipole when placed in the field of an ion, orients itself to minimize its mutual potential energy so that the attractive end of the solvent becomes directed toward the ion and the repulsive end orients itself away from the ion. The ion-dipole interaction energy is given by⁹

$$U_{\text{ion-solvent}} = - (ze\mu \cos \theta) / (4 \pi \epsilon_0) r^2 \quad (17.2)$$

where ze is the charge of the ion, θ is the dipole angle relative the line joining the ion to the center of dipole, and ϵ_0 is the vacuum permittivity. For a monodendate ion-solvent configuration, the solvent molecule and the ion are aligned on the same line, and $\theta = 0$. The ion-dipole forces are very important on the relative stability of the solvation shells. It also plays a major role on preferred solvation when multi-component solvents are used.

17.2.2. Dipole-Dipole Interactions

Solvent molecules with permanent dipole moments interact with each other via directional electrostatic interactions. The dipole-dipole orientation is strongly temperature dependent, and thermal energy prevents optimum orientation of solvents toward each other. The dipole orientation is statistically favored, and at higher temperatures all other dipole orientations become more populated. The dipolar interaction is mainly responsible for the association of dipolar solvents.^{10,11} The dipole-dipole interaction is given by¹²

$$U_{\text{dipole-dipole}} = - (2\mu_1^2 \mu_2^2) / (4 \pi \epsilon_0) 3K_B T r^6 \quad (17.3)$$

where K_B is the Boltzmann constant, and T is the absolute temperature.

17.2.3. Dipole-Induced Dipole Interactions

A solvent with permanent dipole moment can induce a dipole moment in its neighboring solvents. The magnitude of the induced dipole moment depends on the polarizability of the solvents, α , and is defined as¹³

$$\mu_{\text{induced}} = 4 \pi \epsilon_0 \alpha E \quad (17.4)$$

where E is the electric field strength. The induced moment is directional and lies along the induced dipoles. The energy of dipole-induced dipole interaction between solvent molecules is given by the following equation¹³

$$U_{\text{dipole-induced dipole}} = -(\alpha_1 \mu_2^2 + \alpha_2 \mu_1^2)/(4 \pi \epsilon_0) r^6 \quad (17.5)$$

In addition to the solvent-solvent molecules induced dipole moment interaction, there is also strong induced polarization of solvent by ions in the electrolytes. The magnitude of the ion-solvent induced polarization depends on the polarizability of the solvent molecules and the degree of distortion of the molecule's electron cloud. The energy of ion-induced dipole interaction is defined as¹³

$$U_{\text{ion-induced dipole}} = -(z^2 e^2 \alpha)/(4 \pi \epsilon_0) 2 r^4 \quad (17.6)$$

17.2.4. Instantaneous Dipole-Induced Dipole Interaction Forces

In general, the electron movement in one species (atom or molecule) induces a small dipole moment that polarizes the electron cloud in its neighboring system. This induced interaction is called the dispersion interaction and strongly depends on polarizability and ionization potential of interacting species according to the following equation¹⁴

$$U_{\text{dispersion}} = -(3\alpha_1\alpha_2)(I_1I_2)/(I_1+I_2)2 r^6 \quad (17.7)$$

where I is the ionization potential. The dispersion energy between two similar molecules then will be reduced to

$$U_{\text{dispersion}} = -(3\alpha^2 I)/4 r^6 \quad (17.8)$$

The dispersion energies are very short range as expressed in $1/r^6$. This is very important for molecules with polarizable π electrons. The molecular aggregation of polyaromatic molecules are mainly related to the dispersion energy among polyaromatic molecules with conjugated π electrons. From the equations above, it is clear that the dispersion energy is also important for the cohesion of molecules with high polarizability values. For example, the dispersion interaction energy of two molecules with $\alpha = 3 \times 10^{-30} \text{ m}^3$, $I = 20 \times 10^{-19} \text{ J}$, and $r = 3 \times 10^{-10} \text{ m}$ is calculated to be -11.3 kJ/mol or -2.7 kcal/mol . For a similar molecular system the dipole-dipole energy is only -5.3 kJ/mol or -1.1 kcal/mol .¹⁵

The dispersion forces depend highly on the polarizability of the solvent. The polarizability is also connected to the refractive index according to the Lorenz-Lorenz equation¹⁶

$$\frac{n^2 - 1}{n^2 + 2} V_M = \frac{4\pi N \alpha}{3} = \text{Molar - refractive - index} \quad (17.9)$$

where V_M is the molar volume. For the low frequency radiation, the static dielectric constant is related to the refractive index by the Maxwell derived equation, $n^2 = \epsilon$.

Solvents with large index of refraction and large optical polarizability should have a large value of dispersion forces. Most aromatic and polyaromatic molecules have a large refractive index, *e.g.* quinoline ($n = 1.6273$), diphenyl ether ($n = 1.5763$). In general, solvents with high polarizability are good solvents for anions with high polarizability. This is important, particularly when designing a salt with a high cation transference number and a low anion transference number under an electric field. In a liquid electrolyte, the ionic conduction is related to both the anion and the cation mobility and their transference number. The total cation and anion transference number is equal to unity¹⁷

$$t_+ + t_- = 1 \quad (17.10)$$

where t_+ and t_- are the transference numbers, the portion of charge carried by cations or anions respectively.

17.2.5. Hydrogen Bonding

Hydrogen bonding is significant for molecules possessing hydroxyl or other groups in which hydrogen is connected to an electronegative atom. The abnormally high boiling points of many solvents with high degree of hydrogen bonding are well known. The hydrogen bonding can occur between two similar molecules to form homo-intermolecular hydrogen bonds or between two different solvent molecules (hetero-intermolecular hydrogen bonds). The hydrogen bonds can also be formed either intermolecularly or intramolecularly. For example in 2-nitrophenol, depending on Lewis basicity of the solvent, inter- and intra-molecular hydrogen bonds are formed. Various conformations of hydrogen bonds are possible depending on the nature of solvents and solutes.

Dipolar organic solvents, usually with a large dielectric constant and a rather high dipole moment, do not strongly participate in hydrogen bonding, when their hydrogen is not connected to a strong electronegative atom (O, N, S, etc.). Their C-H bond is not strongly polarized. However, they may participate in electron pair donors (EPD), electron pair acceptor (EPA) process.

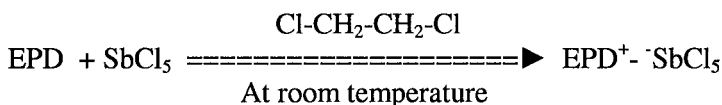
17.3. ELECTRON PAIR DONOR-ELECTRON PAIR ACCEPTOR INTERACTIONS (EPD/EPA INTERACTIONS)

Molecules with high energy, occupied orbitals, and molecules with a sufficiently low energy unoccupied orbitals, form electron pair donor/electron acceptor complexes. The long-wavelength absorption nature of EPD/EPA complexes is associated with the electron transfer from the donor molecule to the acceptor. This type of optical absorption is called the "charge-transfer" or CT absorption. Three classes of EPD molecules have been accepted based on the involvement of n , σ , and π orbitals. For the n -group, the highest energy orbital is the lone-pair of a heteroatom (R_2O , R_3N , R_2SO , etc.). The σ types are the involvement of the σ -type bond ($R-Hal$), and the π -type association is the involvement of a pair of π -electrons of unsaturated molecules (alkyl benzenes, polycyclic aromatics, etc.).

A similar classification also exists for electron acceptor molecules, when n , σ , or π orbitals are involved. Therefore nine different combination of EPD/EPA association have been distinguished. The reaction enthalpy of the EPD/EPA associations is used as their bond strength, and varies between -42 to 188 kJ/mol (-10 to 45 kcal/mole).¹⁸ The enthalpy of formation of a n -EPD/ σ -EPA, such as Et_2O-BF_3 , is -50 kJ/mole, -11.9 kcal/mole, and for a π -EPD/ π -EPA such as benzene/1,3,5-trinitobenzene is -8 kJ/mole or -1.9 kcal/mole.

The n -donor solvents strongly solvate cations in electrolytes. They are good solvents for salts and they are known as coordinating solvents.¹⁹ The n -donor solvents are good media for inorganic reactions. Examples of n -donor solvents are pyridine, dimethyl sulfoxide, triamide, N,N -dimethylformamide, acetone, methanol, and water.

Gutmann and coworkers^{20,21} have developed a semi-quantitative scale for the degree of nucleophilic properties of EPD-solvents, called the donor number (DN) or donicity. The donicity is defined as the negative ΔH value for 1:1 adduct formation between the antimony pentachloride ($SbCl_5$) and the electron pair donor solvent (EPD), in a dilute solution of non-coordinating 1,2 dichloroethane solvent, according to the following equation



The solvent Donor Number = DN=Donicity = $-\Delta H_{\text{EPD-SbCl}_5}$ (kcal/mole)

The donor number is a very useful concept and correlates well with the electrochemical half-wave redox potentials, kinetic rates, and the NMR chemical shift signals for various EDP solvents.²⁰⁻²⁶ The donor numbers of some common organic solvents are listed in Table 18.3 of Chapter 18.

A quantitative electron accepting ability (accepting number, AN) for electron pair acceptor solvents has also been developed to determine their electrophilic properties. This concept is developed by Gutmann and coworkers based on ^{31}P -NMR chemical shift of triethylphosphine oxide ($\text{Et}_3\text{P}=\text{O}$) in presence of an EPA-solvents at room temperature.²⁷⁻²⁹ The equation used to determine the acceptor number AN is

$$AN = \frac{\delta_{\text{corr}}(A) - \delta_{\text{corr}}(n - \text{C}_6\text{H}_{14})}{\delta_{\text{corr}}(\text{Et}_3\text{PO} - \text{SbCl}_5) - \delta(n - \text{C}_6\text{H}_{14})} \cdot 100 = \Delta\delta_{\text{corr}} \cdot 2.348 / \text{ppm} \quad (17.11)$$

AN is obtained from the relative ^{31}P -NMR chemical shift values related to the 1:1-adduct $\text{Et}_3\text{P}=\text{O} - \text{SbCl}_5$ dissolved in 1,2-dichloroethane. The chemical shift for n-hexane has been used as reference, $AN_{\text{n-hexane}} = 0$. The AN values of a number of common organic solvents are also listed in Table 18.3 of chapter 18. The acceptor numbers are dimensionless number relative to those of SbCl_5 .

17.4. SOLVATION

The interaction between ions and solvent molecules is important in electrolytic media. The shell formed around the ions by solvent molecule is termed solvation (hydration in aqueous electrolytes). The energy of solvation is the change in Gibbs energy when an ion is transferred from vacuum into a solvent: $\Delta G_{\text{solvation}}$, is the solvation ability of the solvent. In order to dissolve a salt in a solvent, the interaction energies between solvent molecules, including the all-electrostatic, polarization, and dispersion energies, as well as the lattice energy of the salt, must be overcome.

The electrostatic field that solvent molecule experience in close proximity of the ion in a solvation shell is in the order of 10^6 – 10^7 V/cm. This

enormous field increases the density of the solvent in a solvation shell as compared to that of the bulk solution. The effect of solvation in different media on chemical reaction rates is well known, and in most cases the solvent media need to be mentioned in defining the reaction kinetics. Criss and Salomon have provided a comprehensive compilation of Gibbs free energies of solvation.³⁰

17.4.1 Solvation Number

The solvation number is the number of solvent molecules in the primary shell attached to the ion in a way that their translational and rotational motions exhibit changes from the bulk solution. In some cases, the solvent molecules in the second sphere around the ion are also considered as solvation number. The residency time of a solvent molecule in the solvation shells is short, so that in most cases they can be monitored in the time scale of NMR spectroscopy. The ^{17}O -NMR spectroscopy of Al^{3+} and alkali ions in aqueous solution has indicated a slower than $10^4/\text{sec}$ solvent exchange for Al^{3+} and faster than $10^4/\text{sec}$ exchange for the alkali ion hydration.^{31,32} NMR spectroscopy has proved to be a very useful tool for studying the dynamic of solvent molecule in solvation shells of various ions.

The solvation number is usually measured by electrolytic transport methods. The solvation number is higher for the harder ions (small size), as compared to the softer ions (large size), with similar charge.^{33,34} The data from electrolytic transport measurement and from conductance measurements indicate that solvation numbers increase according to: $\text{Li}^+ > \text{Na}^+ > \text{K}^+ > \text{Rb}^+ > \text{Cs}^+$; the alkaline earth ions are more solvated than the alkali ions and their order is: $\text{Mg}^{++} > \text{Ca}^{++} > \text{Sr}^{++} > \text{Ba}^{++}$. Anion solvation numbers for halogen ions follow the order: $\text{F}^- > \text{Cl}^- > \text{Br}^- > \text{I}^-$.³⁵

17.4.2. Selective or Preferred Solvation

In mixed solvents containing salt, *e.g.* binary or ternary solvent electrolytes, the interaction of solvent-solvent molecules and ion-solvent interactions are complicated. It is often observed that the ratio of solvent molecules in the solvation shell is different from that of the bulk solution. The ions in the electrolyte tend to solvate themselves more with the solvent molecules that produce more negative Gibbs energy of solvation, $\Delta G_{\text{solvation}}$. This preferred solvation results in lack of homogeneity in the solvation shell and in the bulk of mixed solvent electrolytes. When the cation and the anion are preferentially solvated with the same solvent, it is called homoselective

solvation, and when the cation is solvated preferentially by one solvent and the anion by other solvent molecules, it is called heteroselective solvation.^{36,37}

Several methods have been developed to study selective solvation in multicomponent electrolytes. The IR and NMR spectroscopy have been used most by spectroscopists and the conductance method and Hittorf transference measurements by electrochemists.³⁶

17.5. THE BASIC REQUIREMENTS OF ELECTROLYTES FOR LITHIUM BATTERIES

A suitable electrolyte for lithium batteries must have the following characteristics:

1. High ionic conductivity to minimize the cell resistance and resistive heating of the device.
2. High chemical stability to prevent decomposition of electrolyte on the surface of a highly reducing anode materials, *e.g.* metallic lithium or lithiated graphite, LiC_6 , and a highly oxidizing cathode material such a delithiated $\text{Li}_{1-x}\text{MO}_2$ electrodes, where $\text{M} = \text{Co}, \text{Ni}, \text{Mn}$, or mixed transition metals.
3. Electrochemical stability to tolerate the high voltage difference between anode and cathode (>4 V). Not many organic solvent can tolerate such wide voltage range without being reduced or oxidized.
4. Low melting point to provide sufficient conductivity at sub-ambient temperatures and prevent solidification and phase separation.
5. High boiling point to provide safety and prevent explosions resulting from high pressure build-up in the cell.
6. Non toxicity to be accepted environmentally for ease of handling, mass production, and waste treatment.
7. Low cost to be affordable and compete with existing power sources using aqueous electrolytes.

17.5.1. Electrolyte Conductivity

We wish to stress in the final part of this chapter points 1 and 3 of the above list. To this end, some data on the anodic stability of several carbonates and their conductivity in a broad temperature range will be presented here.

Among various solvents presented in Table 17.2, the organic carbonates, particularly the cyclic carbonates, are the most suitable solvents for application in a battery electrolyte. However, the viscosity of the cyclic carbonates is high and needs to be modified to improve their low temperature performances. Addition of a linear carbonate with high fluidity enhances the ionic conductivity of multi-solvent blend electrolytes. The conductivity of several organic carbonates at various salt concentrations and at different temperatures has been measured. The salt concentration was chosen from 0.4M to 1M LiPF_6 . Normally, below 0.4M salt concentration a marked decrease in conductivity of the electrolyte is observed and considered not to be practical. Above the 1M concentration, there is significant salt precipitation at low temperatures, $t < -20^\circ\text{C}$, that is detrimental to most electrochemical devices. The temperature range was selected from -40 to 50°C in our experiments. This is a practical temperature range for most electrochemical devices. It has been shown that there is no electrolyte with a single solvent that can provide all the requirements of a practical electrolyte. Therefore multi component electrolytes containing multi-blend solvents are used. Several binary and ternary organic carbonate solvents are used to enhance the performance of the electrolytes, particularly their low temperature conductivity. In fluid dynamics, the mixing rules for the viscosity and dielectric constant have been defined³⁸

$$\text{Log } \eta_{\text{mixture}} = x_1 \log \eta_1 + x_2 \log \eta_2 + x_3 \log \eta_3 + \dots \quad (17.12)$$

where x_i is the mole fraction of solvent I and η_i is the viscosity of the component i.

$$\epsilon_m = y_1 \epsilon_1 + y_2 \epsilon_2 + y_3 \epsilon_3 + \dots \quad (17.13)$$

where $y_i = x_i V_i / V_m$ = volume fraction of component I, and V_i is the molar volume fraction of component i, and V_m is the molar volume of mixture (cm^3/mole)

$$V_m = x_1 V_1 + x_2 V_2 + \dots \quad (17.14)$$

There are several reviews concerning the conductivity and properties of nonaqueous electrolyte solutions.³⁹⁻⁴³ Electrolytes are composed of a

lithium salt (LiClO_4 , LiPF_6 , LiCF_3SO_3 , etc) dissolved in high purity cyclic and linear organic carbonates. The salt used in lithium batteries also must be stable in a wide voltage range (0-4.5 volts). LiPF_6 is the most studied salt and is used in almost all advanced high voltage lithium cells. LiPF_6 has a satisfactory electrochemical stability, but its thermal stability is of concern, being stable up to *ca.* 150°C as shown by thermogravimetric analysis. LiPF_6 is also extremely moisture sensitive and reacts with residual water in the electrolyte and forms HF that is detrimental to the performance of the cell, particularly on the cathode side. The released HF also reacts with the anode to form LiF, which is a poorly ionic conductor and increases the impedance of the electrode/electrolyte interface. There is an extensive search to develop novel lithium salts for lithium batteries.⁴⁴⁻⁵²

Binary and ternary solvents containing LiPF_6 have been studied in an attempt to improve the low-temperature conductivities of electrolytes to be used in Li batteries. Table 17.3 shows the various solvents and electrolytes examined by the author from the conductivity point of view.

Table 17.3. Solvents and electrolytes.

EC	DEC	DMC	PC	EMC
EC: LiPF_6	DEC: LiPF_6	DMC:EC	PC: LiPF_6	EMC: LiPF_6
EC:DEC: LiPF_6	DEC: EC: LiPF_6	DMC:DEC	PC:DEC: LiPF_6	EMC:EC: LiPF_6
EC:DMC: LiPF_6	DEC:PC: LiPF_6	DMC: LiPF_6	PC:DMC: LiPF_6	EMC:PC: LiPF_6
EC:PC: LiPF_6	DEC:EC:PC: LiPF_6	DMC:PC: LiPF_6	PC:EC:DMC: LiPF_6	EMC:EC:PC: LiPF_6

17.5.1.1. Conductivity of Single Solvents vs. Concentrations and Temperatures

The first class of electrolytes contained only single carbonate solvents with different concentration of salt. PC- DMC- and EMC-based electrolytes have been particularly investigated.

Among them, LiPF_6 -EMC has proven quite interesting. The conductivity of this asymmetric linear carbonate solvent containing various amounts of LiPF_6 is shown in Figure 17.1. The conductivity of ethyl methyl carbonate (EMC) based electrolytes containing LiPF_6 remain high even at low temperatures (-40°C). This solvent has a very low melting point. It is interesting that substituting one of the methyl groups in DMC with another alkyl group significantly affects the melting and boiling temperatures of DMC-based electrolytes (Table 17.2). This substitution introduces significant disorder in the electrolyte system that markedly changes the glass transition and the fluidity of this solvent. Asymmetric solvents such as EMC are good

candidates for low temperature electrolyte and investigation of the electrochemical properties of materials at low temperatures.

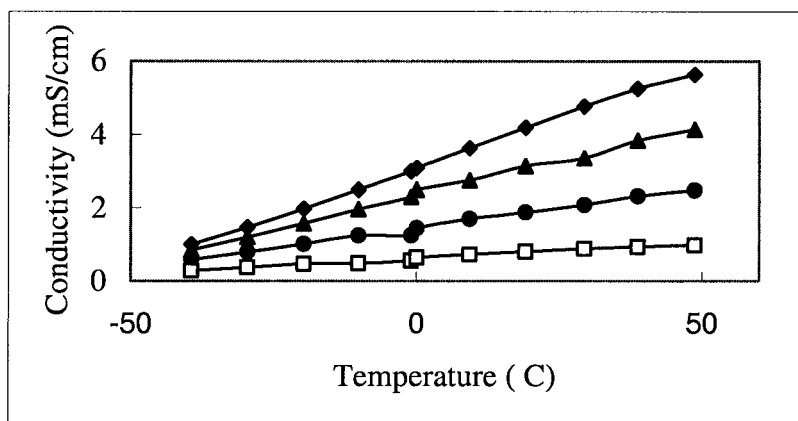


Figure 17.1. Conductivity of ethyl methyl carbonate (EMC) containing, (♦) 1M, (▲) 0.8M, (●) 0.6M, and (□) 0.4M LiPF_6 .

17.5.1.2. Conductivity of Binary Solvents– LiPF_6 Electrolytes vs. Concentrations and Temperatures

It is almost impossible to find a single solvent electrolyte meeting all the requirements for application in practical devices. This is why mixed organic carbonates have been more often investigated. According to the Walden rule, the conductivity of an electrolyte is inversely proportional to its viscosity. Therefore, multi-blend electrolytes with solvents of different viscosities are preferred. Data on the conductivities of mixtures of cyclic and linear carbonate solvents are here reported.

Figure 17.2 shows the conductivity of EC-DMC-based electrolyte for various salt concentrations and in a wide temperature range (-40 – 50°C). It is remarkable that the conductivity of this mixture is very different than the single solvent electrolyte. DMC– LiPF_6 has very poor conductivity below -10°C and that of EC– LiPF_6 is very negligible below 30°C , as EC melts at 39°C . However, the mixed solvent is fluid down to -30°C , and has significant conductivity from -30 to 50°C .

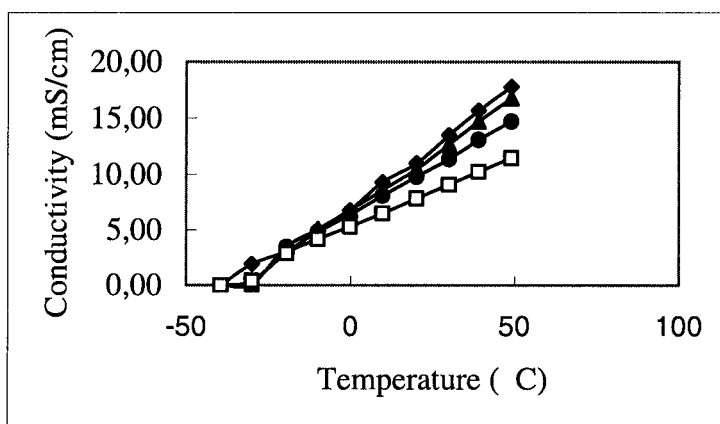


Figure 17.2. Conductivity of ethylene carbonate – dimethyl carbonate (EC-DMC) containing (♦) 1M, (▲) 0.8M, (●) 0.6M, and (□) 0.4M LiPF₆.

The conductivity of EC-EMC containing various amounts of LiPF₆ from -40 to 50°C is shown in Figure 17.3. Again, high ionic conductivity was observed at temperatures well below the melting point of the EC solvent. This mutual interaction of solvents in mixed electrolytes has opened a new area in search of electrolytes with unique properties for low temperature electrochemistry.

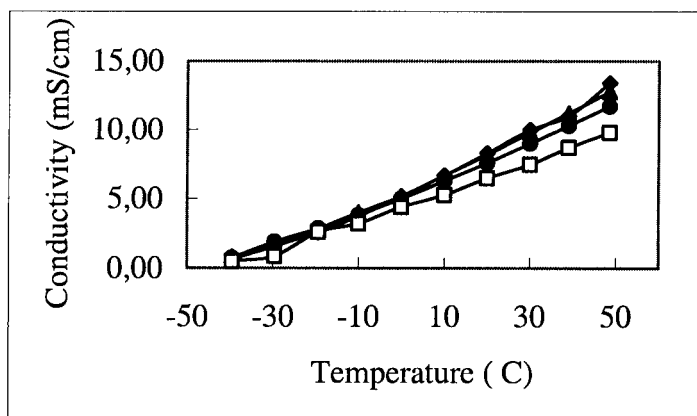


Figure 17.3. Conductivity of ethylene carbonate – ethyl methyl carbonate (EC-EMC) containing, (♦) 1M, (▲) 0.8M, (●) 0.6M, and (□) 0.4M LiPF₆.

The most striking feature of the EC-EMC mixed electrolyte is that its conductivity does not change significantly for 1M, 0.8M, and 0.6M LiPF_6 salt concentrations, even at high temperatures. Using this remarkable electrolyte, the cost of salt can be reduced by 40%. The other remarkable property of this electrolyte is that the EC with melting point of 39°C does not phase separate at temperatures significantly below its melting point.

17.5.1.3. Conductivity of Ternary Solvents – LiPF_6 Electrolytes vs. Concentrations and Temperatures

In order to optimize the performance of the electrolyte in lithium batteries, several electrolytes with a ternary solvent mixture have been studied. The conductivity of PC-EC-DMC containing various amounts of LiPF_6 as a function of temperature is shown in Figure 17.4. Several interesting observations are worth mentioning. First, the conductivity of solutions with 1M, 0.8M and 0.6M LiPF_6 are almost the same over the entire temperature range of -40 to 50°C . Second, the overall conductivity of the ternary solvent is higher than that of the single and binary solvent electrolytes. Third, there is no effect of salt precipitation and phase separation of EC. The conductivity for 0.4M solution is markedly lower than the 0.6-1M solutions. This ternary solvent is suitable for an advanced lithium battery, because it provides sufficient conductivity at low temperatures. It also contains ethylene carbonate, which selectively solvates the lithium ion, and its decomposition on the lithiated graphite anode provides a good protective SEI layer. The nature of the SEI film formed in

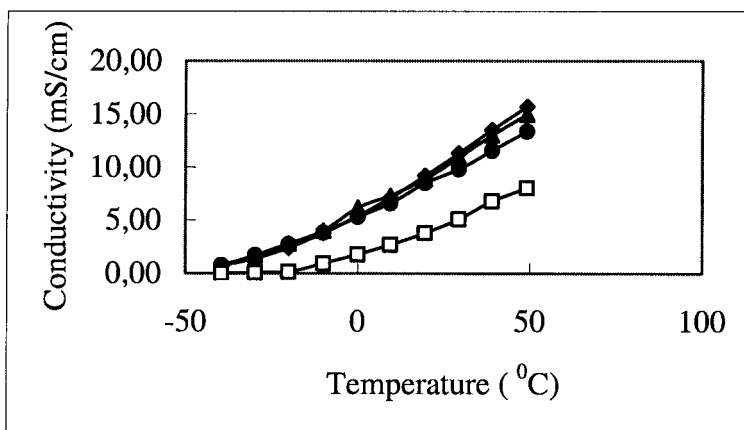


Figure 17.4. Conductivity of propylene carbonate - ethylene carbonate - dimethyl carbonate (PC-EC-DMC) containing, (♦) 1M, (▲) 0.8M, (●) 0.6M, and (□) 0.4M LiPF_6 .

this electrolyte is discussed in Chapter 5. Further, the electrolyte contains sufficient EC concentration that can be used with a graphite anode, because this solvent does not co-intercalate between the graphite layers. The ternary solvents can be tailored to reduce the amount of lithium salt used in lithium batteries.

The conductivity of multicomponent electrolytes with PC-EC-EMC is shown in Figure 17.5. The conductivity values for salt concentrations in the range of 1M to 0.6M are very similar between -40 and 50°C , making these electrolytes quite interesting for applications in Li batteries.

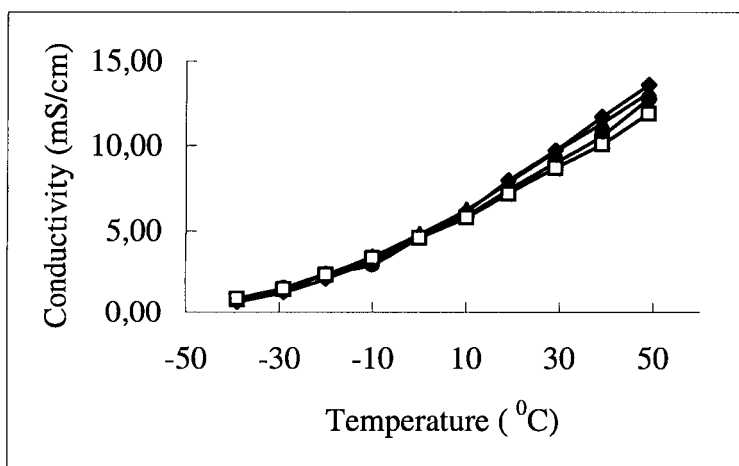
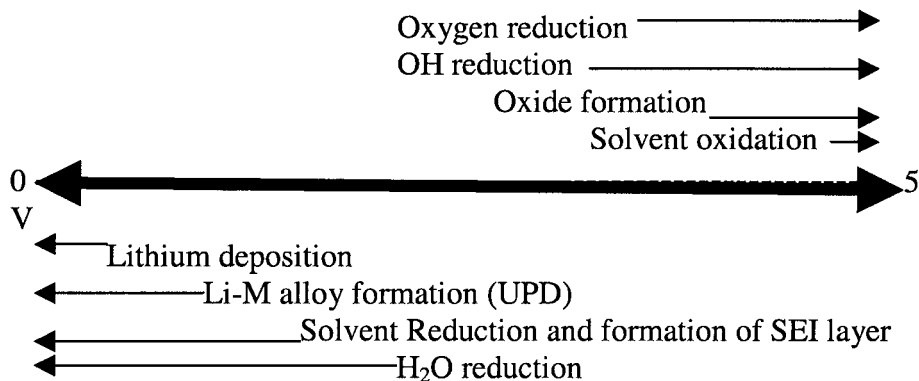


Figure 17.5. Conductivity of propylene carbonate - ethylene carbonate - ethyl methyl carbonate (PC-EC-EMC) containing, (♦) 1M, (▲) 0.8M, (●) 0.6M, and (□) 0.4M LiPF_6 .

The multi-blend solvent provides the opportunity to use less salt and reduce the overall cost of the lithium battery. In most commercial cells, electrolytes with 1M LiPF_6 are still in use. This high salt concentration is even detrimental to the performance of the cells at low temperatures (-30 – 40°C), due to the possibility of salt precipitation.

17.5.2. The Electrochemical Stability of Organic Electrolytes

When cycling a Li battery, several electrochemical reactions may take place at the electrodes as a function of the voltage range. In general, by taking into account all compounds that may be present in a cell, we have the following scheme:



Scheme 17.1. Schematic of various electrochemical reactions and their voltage ranges.

The data collected on scheme 17.1 refer to a platinum microelectrode during a voltage scan from the cathodic to the anodic region.

The decomposition of organic electrolytes at the negative electrode has been a major concern, as there is no organic electrolyte that can tolerate the reducing power of metallic lithium or lithium doped graphite. In fact, the reason that current anodes work so well is mainly because of the formation of a protective layer on the surface of anode. This protective layer is formed by decomposition of organic solvents (SEI layer). The nature of SEI depends on the organic solvents used in the battery. The SEI is electronically insulating, but has significant lithium ion conductivity and allows the lithium ions to reach the anode. The SEI layers that are formed in carbonate-based electrolytes are remarkable in their protection of the anode.

There have been extensive investigations to find a stable organic electrolyte above 4 V. The carbonates have shown stability even exceeding 5 V (Table 17.3) and this remarkable stability provides the opportunity to use high voltage cathodes materials (layered LiCoO_2 and 3-D spinel LiMn_2O_4 cathodes). The average voltage of a Li-ion battery ($\text{LiC}_6/\text{LiCoO}_2$) is 3.75V and its operating voltage range is between 3 to 4.5 V.

Anodic stability tests have been performed in electrolytes containing 1M and 0.8M LiPF_6 (Pt microelectrode, Li reference and counter, 70°C). The onset of electrolyte oxidation for each solvent is reported in Table 17.4.

Table 17.4. Oxidation potentials of organic solvents used for lithium battery applications.⁵³

Electrolyte solvent	Oxidation potential (V)
Propylene carbonate	4.3
Ethylene carbonate	5.2
Dimethyl carbonate	5.1
Diethyl carbonate	5.2
Methyl ethyl carbonate	5.2
Gamma-butyrolactone	5.2
Diethoxyethane	4.5
Tetrahydrofuran	4.1
2-methyltetrahydrofuran	4.3
1,3 dioxolane	4.2
Acetonitrile	3.8

17.6. CONCLUSIONS

Some fundamental properties of single solvents, mixtures and salt-solvent(s) combinations have been discussed. There is a complex interplay among the electrolyte components linked to the ion-solvent and solvent-solvent interactions. Such factors as ion-dipole and dipole-dipole interaction, and ion solvation determine the suitability of a given solution from the standpoint of its transport properties. However, the parameters making a given electrolyte usable in a given battery are numerous and this chapter has listed those for electrolytes to be used in Li batteries. Among them, conductivity and anodic stability have been stressed here.

Conductivity data for different combinations of cyclic and linear carbonates have shown the interesting behavior of electrolytes containing the asymmetric linear ethyl methyl carbonate. Especially the ternary mixture EC-PC-EMC (with LiPF_6 as a salt) shows good conductivities over a wide temperature range. Furthermore, lowering the LiPF_6 concentration from 1 M to 0.6-0.4 M does not cause a loss of conductivity, this obviously having a positive implication on the battery cost. The carbonates have excellent anodic stabilities (above 5 V vs. Li^+/Li , with the exception of PC), this allowing their use not only in the present generation of Li-ion batteries but also in the 5 V batteries now being widely investigated.

REFERENCES

1. M. Magat, *J. Phys. Chem.* A162 (1932) 432.
2. S. E. Sheppard, *Chem. Abstr.* 37 (1943)1654.
3. G. Scheibe, E. Felger, G. RoBler, *Ber. Dtsch. Chem. Ges.* 60 (1927) 1406.

4. J.H. Hildebrand, J. M. Prausnitz, R. L. Scott, *Regular and Related Solutions*, VanNorstrand-Reinhold, Princeton, (1970).
5. C. J. F. Bottcher, *Theory of Electric Polarization*, Vol. I, Second Edition, Elsevier Scientific Publishing Co., New York (1973).
6. R. C. Weast, M. J. Astle, *CRC Handbook of Data on Organic Compounds*, Vol I and II, CRC Press, Florida, (1985).
7. R. C. Weast, (ed.), *Handbook of Chemistry and Physics*, 66th Edition, CRC Press, Florida (1986).
8. A. L. McClellan, *Table of Experimental Dipole Moments*, Freeman Co., San Francisco, (1963).
9. N. H. March, M. P. Tosi, *Coulomb Liquids*, Academic Press, New York 1984.
10. R. L. Amev, *J. Phys. Chem.* 72 (1968) 3358.
11. M. Rabinowiz, A. Pines, *J. Am. Chem. Soc.* 91 (1969) 1585.
12. W. H. Keesom, *Z. Physik* 23 (1922) 225.
13. P. Debye, *Z. Physik* 22 (1921) 302.
14. J.H. Mahanty, B.W. Ninham, *Dispersion Forces*, Academic Press, New York (1977).
15. C. H. Yoder, *J. Chem. Educ.* 54 (1977) 402.
16. N.E. Hill, W.E. Vaughan, A.H. Price, M. Davice, *Dielectric Properties and Molecular Behaviour*, Van Norstrand Reinhold Co., London (1969).
17. K.E. Thomas, R.M. Darling, J. Newman, *Mathematical Modeling of Lithium Batteries, in Advances in Lithium-ion Batteries*, (eds. Schalkwijk, W.A., Scrosati, B.), Kluwer Academic / Plenum Publishers, Boston (2002).
18. R. Paetzold, *Z. Chem.* 15 (1975) 377.
19. R. S. Drago, L.B. Parr, C.S. Chamberlain, *J. Am. Chem. Soc.* 99 (1977) 3203.
20. V. Gutmann, *Coordination Chemistry in Non-Aqueous Solvents*, Springer, Wien, NY (1968).
21. V. Gutmann,, *Coord. Chem. Rev.* 2 (1967) 239.
22. U. Mayer, *Pure Appl. Chem.* 41 (1975) 291.
23. V. Gutmann, *Pure Appl. Chem.* 15 (1973) 141.
24. U. Mayer, *Pure Appl. Chem.* 51 (1979) 1697.
25. R. Schmid, V. A. Sapunov, *Chemie Verlag Nethreland*(1982).
26. C.J. Bender, *Chem. Soc. Rev.* 1986, 201.
27. U. Mayer, V. Gutmann, W. Gerger, *Pure Appl. Chem.* 51 (1979) 1697.
28. R. Schmid, *J. Sol. Chem.* 12 (1983) 135.
29. U. Mayer, *Pure Appl. Chem.* 51 (1979) 1697.
30. C. M. Criss, Salomon, M., *Thermodynamic Measurements – Interpretation of Thermodynamic Data*, in A. K. Covington, T. Dickinson, (eds): *Physical Chemistry of Organic Solvent Systems*, Plenum Press, London, NY (1973).
31. J. E. Gordon, *The Organic Chemistry of Electrolyte Solutions*, Wiley, New York (1975).
32. J. A. Jackson, J. F. Lemons, H. Taube, M. Alei, J. A. Jackson, *J. Chem. Phys.* 41 (1964) 3402.
33. E. S. Amis, J. F. Hinton, *Solvent Effects on Chemical Phenomena*, Vol.1, Academic Press, New York (1973).
34. E. S. Amis, *Solvation of Ions, in Solutions and Solubilities*, Vol. III, Part 1, of the series *Techniques of Chemistry*, M. R. J. Dack, (ed.), Wiley-Interscience, NewYork (1975).
35. J. F. Hinton, E. S. Amis, *Chem. Rev.* 71 (1971) 627.
36. H. Strehlow, H. Schneider, W. Knoche, *Ber Bunsenges. Phys. Chem.* 77 (1973) 760, and *Pure Appl. Chem.* 25 (1971) 327.
37. H. Strehlow, H. Koepp, H. Schneider, *Z. Phys. Chem.* 44 (1966) 49.
38. G. E. Blomgren, *J. Power Sources* 14 (1985) 39.
42. K.; M. Abraham, M. J. Alamgir, *J. Electrochem. Soc.* 137 (1990) 1657.
43. B. Klessen, R. Aroca, G. A. Nazri, *J. Phys. Chem.* 100 (1996) 9334.

44. G. E. Bloomgren, in *Lithium Batteries*, (ed): J. Gabano, Academic Press, New York 1983, p13.
45. H. J. Gores, J. Barthal, *J. Solution Chem.* 9 (1980) 939.
46. Y. Matsuda, *J. Power Sources* 19 (1987) 20.
47. J. T. Dudley, D. P. Wilkinson, G. Thomas, R. LeVae, Woo, H. Blom, C. Horvath, M. W. Juzkow, B. Denis, P. Juric, P. Aghakinan, J. R. Dahn, *J. Power Sources* 35 (1991) 59.
48. H. Watanabae, T. Nohma, I. Nakane, S. Yoshimura, K. Nishio, T. Saito, *J. Power Sources* 217 (1993) 43.
49. P. V. S. S. Prabhu, T. P. Kumar, P. N. N. Namboodiri, R. J. Gangadharan, *Appl. Electrochem.* 23 (1993) 151.
50. D. Aurbach, M. Daroux; P. Faguy, E. B. Yeager, *J. Electroanal. Chem.* 225 (1991) 297.
51. S. K. Lee, Y. Zu, A. Hermann, Y. Geerts, K. Mullen, A. J. Bard, *J. Am Chem.Soc.* 121 (1999) 3513.
52. R. Oesten, U. Heider, M. Schmidt, *Solid State Ionics* 148 (2002) 391.
53. J-I. Yamaki, *Liquid Electrolytes*, in *Advances in Lithium-ion Batteries*, (W.A. Van Schalkwijk, Scrosati, B., Eds.), Kluwer Academic Plenum Publishers, Boston (2002).

Chapter 18

ADVANCED LIQUID ELECTROLYTE SOLUTIONS

D. Aurbach and A. Schechter

Department of Chemistry, Bar-Ilan University, Ramat-Gan 52900, Israel

18.1. INTRODUCTION

18.1.1. Types of Advanced Liquid Electrolyte Solutions

18.1.1.1. Organic Polar Aprotic Solvents

The major families of this class are ethers, esters, and alkyl carbonates, which are highly important for the field of high energy density batteries. These solvents and their formulas are summarized in Figure 18.1. Other important solvents are acetonitrile (AN), dimethylsulfoxide (DMSO), N-N dimethyl formamide (DMF), methylene chloride and nitromethane. The latter five solvents are mainly important for electroanalytical use and organic synthesis. As discussed later in this chapter, the type of salt plays a major role in determining the electrochemical window of a polar aprotic system. Commonly used anions, in conjunction with Li^+ , are PF_6^- , ClO_4^- and BF_4^- . All polar aprotic solutions may contain atmospheric contaminants such as O_2 , H_2O and CO_2 , which are reactive and may play an important role in determining the electrochemical behavior.

18.1.1.2. Inorganic Polar Aprotic Solvents

Oxyhalide solvents such as SOCl_2 , SO_2Cl_2 , and SO_2 are used in electrochemical systems together with a salt such as LiAlCl_4 . Their major use is for batteries.¹ These species may serve as both the electrolyte solvent and the cathode active material in Li batteries. There are reports on the study of electrochemical reactions in SO_2 as a solvent.² There are many solvents of

the MO_yX_z type ($\text{M}=\text{S}, \text{P}, \text{N}$, and even metals such as V and Cr ; $\text{X}=\text{Cl}^-, \text{Br}^-, \text{F}^-$) that were mentioned in the literature in connection with possible battery applications. However, SOCl_2 and SO_2 seem to be the most important solvents in this group for electrochemical systems.¹

18.1.1.3. Nonpolar Electrolyte Solutions

As shown by Gileady *et al.*,³ it is possible to form non-polar electrolyte solutions based on aromatic hydrocarbons such as ethyl benzene, toluene, benzene and mesitylene. The electrolyte comprises Al_2Br_6 and KBr .⁴ By using a nearly molar concentration of these species, it is possible to obtain specific conductivities of the same order of magnitude as that measured in




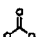
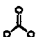
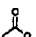
<u>ETHERS</u>	
Diethyl ether (DEE)	$\text{CH}_3\text{CH}_2\text{OCH}_2\text{CH}_3$
Tetrahydrofuran (THF)	
2-Methyl-THF (2Me-THF)	
Diethoxyethane	$\text{CH}_3\text{CH}_2\text{OCH}_2\text{CH}_2\text{OCH}_2\text{CH}_3$
1-3 Dioxolane	
<u>ALKYL CARBONATES</u>	
Ethylene carbonate (EC)	
Propylene carbonate (PC)	
Dimethyl carbonate (DMC)	$\text{CH}_3\text{O}\overset{\text{O}}{\parallel}\text{COCH}_3$
Diethyl carbonate (DEC)	$\text{CH}_3\text{CH}_2\text{O}\overset{\text{O}}{\parallel}\text{COCH}_2\text{CH}_3$
Ethyl methyl carbonate (EMC)	$\text{CH}_3\text{CH}_2\text{O}\overset{\text{O}}{\parallel}\text{COCH}_3$
<u>ESTERS</u>	
Methyl formate (MF)	HCOCH_3
γ -Butyrolactone (BL)	
Methylacetate	CH_3COCH_3
(a)	

Figure 18.1. The most important organic polar aprotic solvents for Li batteries.

polar aprotic solutions (around 5 mS/cm) at ambient temperature. It was found that these electrolytes do not dissolve in the above solvents to form ions or ion pairs, but rather they form clusters which are charged aggregates of species such as $\text{Al}_2\text{Br}_7^-\text{K}^+$.

18.1.1.4. Molten Salts⁵

Molten salt electrolyte systems comprise salts in the liquid state (molten), which form ionic phases and are highly ionically conductive, have a wide potential range of stability, and thus reach specific conductivities comparable to those of room temperature, concentrated aqueous solutions ($0.1 < \chi < 10$ S/cm). These systems can be divided into two classes:

1. High temperature molten salts.
2. Ambient temperature molten salts.

18.1.2. Scope of Subjects of Interest

Dealing with nonaqueous electrolyte solutions, the most important issues for discussion are the following:

1. Physical properties.
2. Factors that determine solution conductivity and diffusion of the ions.
3. The electrochemical windows of the solutions.
4. The major electrode reactions of the electrolyte solutions and the factors that influence them: the nature of the solvent, the cation and anion used, the level of contamination, and the importance of the electrode's material.
5. The most important applications and what the directions are for improvement of existing systems in order to meet current and future needs.

This chapter is written in light of the above points of interest.

18.2. GENERAL PROPERTIES OF LIQUID ELECTROLYTE SOLUTIONS

18.2.1. On the Physical Properties of Polar Aprotic Electrolyte Solutions

Table 18.1, prepared by Blomgren,⁶ presents physical properties of interest for a number of important polar and nonpolar aprotic solvents.

Table 18.1. Physical properties of solvents at 25°C (unless noted). Taken from Blomgren.⁶

Solvent	Acronym	Melting point(°C)	Boiling point(°C)	Dielectric permittivity	Viscosity (cP)	Density (g/cm ³)	Dipole moment (D)
<i>N,N</i> -diethylacetamide	DEA	-	184	30.4	1.226	0.904	3.69
<i>N,N</i> -dimethylformamide	DMF	-60.44	153.0	36.71	0.794	0.9439	3.86
Dimethyl sulfoxide	DMSO	18.54	189.0	46.5	1.99	1.0955	3.9
Hexamethylphosphoric triamide	HMPA	7.2	233	29.6	3.22	1.0201	5.54
<i>N</i> -Methyl-2-pyrrolidinone	NMP	-24.4	202	32.0	1.663	1.0268	4.09
Pyridine	Py	-41.55	115.256	12.4@21°C	0.884	0.97824	2.37
Sulfolane	TMS	28.45	287.3	43.3@30°C	1.262@30°C	4.81	4.81
Acetone		-94.7	56.29	20.56	0.303	0.7843	2.69
Acetonitrile	AN	-48.835	81.60	35.95	0.341	0.7767	3.44
Benzonitrile	BN	-12.75	191.10	25.20	1.237	1.0006	4.05
γ -Butyrolactone	GBL	-43.53	204	39.1	1.7315	1.1242	4.12
Diethyl carbonate	DEC	-43.0	126.8	2.820@20°C	0.748	0.9693	0.90
Diethyl sulfite	DES	-	157	15.6@20°C	0.839	1.0829@20°C	2.96
Dimethyl carbonate	DMC	3	90	3.12	0.585	-	-
Ethyl acetate	EA	-84.0	71.1	6.02	0.426	0.8946	1.88
Ethylene carbonate	EC	36.5	238	90.36@40°C	1.9@40°C	1.321@40°C	4.87
Ethylene glycol sulfite	EGS	-11	173	39.6	2.056	1.4158	-
Methyl acetate	MA	-98.05	56.868	6.68	0.364	0.9279	1.61
Methyl formate	MF	-99.0	31.75	8.5@20°C	0.328	0.9664	1.77
Nitromethane	NM	-28.55	101.20	38.0	0.62	1.131	3.56

Table 18.1. Physical properties of solvents at 25°C (unless noted). Taken from Blomgren.⁶ (continued)

Propylene carbonate	PC	-54.53	242	64.95	2.51	1.1996	4.98
Trimethyl phosphite	TMP	-46.0	197.2	22.3	2.03	1.0695@20°C	3.02
Diethyl ether	DEE	-116.3	34.55	4.23	0.242	0.70760	1.15
Diglyme	DG	-64	163	7.23	1.06	0.9440	1.97
1,2-Dimethoxyethane	DME	-58	84.50	7.075	0.407	0.8612	1.71
1,4-Dioxane	DX	11.80	101.32	2.21	1.20	1.0280	0.45
1,3-Dioxolane	DIOX	-97.22	75.6	7.13	0.589	1.0647@20°C	1.47
2-Methyl-tetrahydrofuran	Me-THF	-137.2	79.9	6.97	0.467	0.848	-
Tetrahydrofuran	THF	-108.5	65.965	7.43	0.459	0.8819	1.75
Tetrahydropyran	THP	-45	88	5.61	0.764		
Triglyme		-45	216	7.5			
Benzene		5.533	80.07	2.274	0.6028	0.87360	0.00
Carbon tetrachloride		-23.0	76.8	2.22793	0.905	1.5844	0.00
Chloroform		-63.6	61.2	4.7218	0.540	1.4799	1.15
1,1-Dichloroethane	1,1-DCB	-97.0	57.28	9.90	0.464	1.1757	2.06
Methylene chloride		-95.14	39.75	8.93	0.413	1.31678	1.14
Toluene		-95.0	110.6	2.379	0.552	0.8623	0.31
Trichloroethylene		-86.4	87.19	3.42@16°C	0.532	1.4514@30°C	0.8
Cyclohexane		6.544	80.725	2.01714	0.898	0.77374	0.00
n-Heptane		-90.582	98.424	1.9246@20°C	0.3967	0.67946	0.0
n-Hexane		-95.5	68.7	2.0231	0.299	0.6548	0.09
Sulfur dioxide		-75.46	-10.02	14.1@20°C	0.291	1.3695	1.60
Sulfuryl chloride		-54.1	69.4	11.5	0.674	1.657	-
Thionyl chloride		-104.5	75.8	9.25@20°C	0.603@20°C	1.629@20°C	1.38

A critical property of solvents for electrolyte solutions is their ability to dissolve salts and completely separate the ions from each other. This ability depends on the solvent polarity. The parameters related to this polarity, which are easily available and which appear in Table 18.1, are the dielectric constant and the dipole moment. The dielectric constant usually decreases as the temperature increases.⁷ However, these parameters are not sufficient for determining and ranking the ability of solvents to form ion-conducting electrolyte solutions. Other parameters had to be invented for that purpose, as summarized in the next section.

18.2.2. How to Evaluate Solvents for Electrolyte Solutions

The solvating power of a solvent is a fairly complex quantity that depends on various factors, such as solvent basicity, acidity, polarity, structure, etc., whose relative contributions may vary considerably with the substrate under consideration. In other words, different reactions may respond differently to the same changes in a solvent environment. The initial or fundamental requirement for the development of a more generally applicable solvent concept is the need to try to separate the various factors responsible for the solvating power of a solvent. It is important to find criteria for the solvent classification that can be correlated not only to salt solubility and apparent conductivity, but also to the impact of the solvents on the thermodynamics and kinetics of the electrochemical reactions. There are several approaches to defining a typical solvent property that can represent its polarity and can be correlated to the thermodynamics and kinetics of reactions conducted in its solutions (*i.e.*, a linear free-energy relationship). In a comprehensive review of such approaches by C. Reichardt,⁸ he divides them into three categories:

1. Comparative equilibrium measurements of reactions in solvents.
2. Comparative spectroscopic measurements based on solvatochromic effects of solvents.
3. Comparative measurements of reaction rates in various solvents.

Table 18.2, taken from Reichardt's review, describes representative corresponding data from the above three categories. Especially interesting are the parameters: donor number (DN),⁹ acceptor number (AN),⁹ and E_T30 , which appear in this table.

Refs. 8,10,11 present both the compound, whose solvatochromic effect defines the polarity scale E_T30 , and the typical absorption in the UV-VIS of this compound in three different solvents of different polarities (in decreasing order): ethanol, acetonitrile, and 1-4 dioxane. It was clearly demonstrated therein that as the solvent is less polar, the absorption of the 2,6-diphenyl-4-(2,4,6-triphenyl-1-pyridino) phenolate in the visible, which defines the

Table 18.2. Typical approaches for defining solvent polarity. Taken from Reichardt⁽⁸⁾.

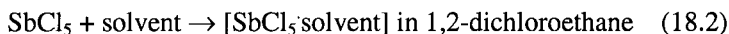
Symbol (name)	Physical quantity measured	Solvent-dependent standard process
<u>From equilibrium measurements</u>		
<i>L</i> (desmotropic constant)	Equilibrium constant	Keto-enol tautomerism equilibrium of ethyl acetoacetate at <i>ca.</i> 20 °C
$-\Delta G^\circ$	Free energy of the reaction reaction in standard state	NH/OH tautomerism equilibrium of Schiff Bases of pyridoxal-5'-phosphate at 25 °C.
<i>DN</i> (Donor number)	Reaction enthalpy $-\Delta H_{\text{EPD-SbCl}_5}$	1:1 Adduct formation between antimonyl(V) chloride as standard EOA and EPD solvents in 1,2-dichloroethane at 25 °C.
<u>From measurements of reaction rates</u>		
<i>Y</i>	Relative rate constant k_1	S_N1 Solvolysis of <i>tert</i> -butyl chloride at 25 °C.
<i>X</i>	Relative rate constant k_2	S_E2 reaction of tetramethyltin with bromine at 20 °C
Ω	<i>Endo-exo</i> product ratio	Diels-Alder [$\pi 4 + \pi 2$] cycloaddition of cyclopentadiene to methyl acrylate at 30 °C.
<u>From spectroscopic measurements</u>		
<i>Z</i>	Molar transition energy	Charge-transfer absorption of 1-ethyl-4-methoxycarbonylpyridinium at 25 °C.
E_n , E_{T30}	Molar transition energy	$\pi-\pi^*$ Absorption of pyridinio-phenolate at 25 °C.
Z^R	Molar transition energy	$\pi-\pi^*$ Absorption of a positively solvatochromic undecamethine-merocyanine dye at 25 °C
Z^B	Molar transition energy	$\pi-\pi^*$ Absorption of a negatively solvatochromic nonamethine-merocyanine dye at 25 °C.
π^*	Absorption wave number	$\pi-\pi^*$ Absorption of several compounds particularly nitro-substituted arenes (e.g. 4-nitro-anisole (1-methoxy-4-nitro-benzene)).
<i>S</i>	Equilibrium constant, rate constant, molar transition energy	Mixed parameter, calculated from various solvent dependent processes.
<i>P</i>	Relative ^{19}F -NMR chemical shift	^{19}F -NMR absorption of 1-fluoro-4-nitrosobenzene.
<i>AN</i> (acceptor number)	Relative ^{31}P -NMR chemical shift	^{31}P -NMR absorption of triethylphosphane oxide.

E_{T30} scale, appears at a lower wave number. The scale itself is defined by the following equation:

$$E_{T30} \text{ (kcal/mole)} = hc\bar{\nu}L \quad (18.1)$$

where h is Plank's constant, c is the speed of light, $\bar{\nu}$ is the absorption's wave number, and L is Avogadro's number. The importance of this solvent parameter lies in the ease of its measurement and the widely successful experience obtained to date in correlating this parameter to reaction rate coefficients and equilibrium constants in many solvent systems.

The donor number (DN), introduced by Gutmann and Mayer,^{9,12,13} represents the measure of the donor properties of solvents and is defined as the numerical value of the heat of adduct formation between the donor molecule and the reference acceptor SbCl_5 in diluted 1,2-dichloroethane solution:



The values range between zero and about 60 kcal/mole. Polar solvents such as nitromethane are very weak donors. Solvents such as acetonitrile and propylenecarbonate are moderately strong donors. Ketone, ester, and ether solvents show medium donor properties. Amides and sulfones are strongly basic solvents with donor numbers of 25 to 30, and aliphatic amines are very strong donors.

The characterization of the *acceptor* properties of solvents is a more difficult problem. The definition of an analogous thermochemical quantity is not possible because many solvents contain atoms with lone pair electrons, and thus may undergo adduct formation with strong reference acceptors.

This problem was solved by Mayer^{9,12} by the use of triethylphosphine Et_3P oxide ($\text{Et}_3\text{P}^{\delta+} \cdots \text{O}^{\delta-}$) as a basic reference donor, in a solvent acting as an acceptor.

Triethylphosphine oxide contains a highly basic oxygen atom, which is easily accessible to solvent electrophilic attack. This causes a polarization of the $\text{P} = \text{O}$ bond and a downfield shift of the ^{31}P NMR signal. The observed chemical shifts (δ) referred to the reference solvent *n*-hexane, and extrapolated to infinite dilution, may be taken as a measure of the acceptor properties of the solvents. The acceptor number (AN) is defined as follows:

$$\text{AN} = \frac{\delta(\text{Et}_3\text{PO in solvent S}) - \delta(\text{Et}_3\text{PO in hexane})}{\delta(\text{SbCl}_5 \cdot \text{Et}_3\text{PO in C}_2\text{H}_4\text{Cl}_2)} \quad (18.3)$$

The importance of solvent parameters such as DN and AN and the advantage of their use over physical-electrostatic parameters was further demonstrated by Mayer *et al.*,¹⁴ who studied correlations between the DN and AN of solvents and thermodynamic properties of reactions carried out in them. These include redox potentials, equilibrium constants, and parameters of ion pair equilibria. According to the Born theory, redox potentials should depend linearly on the reciprocal of the solvent's dielectric constant.¹³

However, when plotting $E_{1/2}$ values of a redox couple such as Cd/Cd^{2+} vs. $1/\epsilon$ of the solvents, the results provide a very scattered picture. In contrast, it has been clearly shown by Mayer *et al.* that redox potentials of metals (e.g., Zn/Zn^{2+} , Cd/Cd^{2+} , Eu/Eu^{2+}) can be nicely correlated to the donor numbers of the solvents, and that the $E_{1/2}$ values measured behave linearly vs. the solvents' DN.⁹

Table 18.3, taken from Refs. 8 and 9, lists some solvent evaluation parameters, in light of the above discussions and the definitions in Table 18.2, for a number of solvents of interest.

In conclusion, extensive work on solvent properties has revealed that simple physical properties, such as dielectric constant or dipole moment, are not adequate measures for solvent polarity (which can correlate well with the influence of solvents on thermodynamic and kinetic reaction parameters in them). Better solvent parameters, which correlate well with the impact of the chosen solvent on electrochemical and chemical reactions, are donor and acceptor numbers or parameters based on solvatochromic effects, because these reflect not only pure electrostatic effects, but rather the entire electronic properties of a solvent. We should also mention the efforts to develop tools

Table 18.3. $E_{\text{T}30}$ values, donor numbers (DN), and acceptor numbers (AN) of various solvents. Taken from Refs. 8 and 9.

Solvent	$E_{\text{T}30}$	DN	AN
Acetic acid	51.2	-	52.9
Acetone (AC)	42.2	17.0	12.5
Benzene	34.5	0.1	8.2
1,2-Dichloroethane (DCE)	39.4	0.0	16.7
Diethylamine	35.4	-	9.4
Diethyl ether	34.6	19.2	3.9
<i>N,N</i> -Dimethylformamide (DMF)	43.8	26.6	16.0
Dimethyl sulfoxide (DMSO)	45	29.8	19.3
Ethanol (ET)		-	37.9
Formamide	51.9	24	39.8
<i>N</i> -Hexane	56.6	0.0	0.0
Methyl acetate		16.5	10.7
<i>N</i> -Methyl-2-pyrrolidone (NMP)		27.3	13.3
Propylene carbonate	46.6	15.1	18.3
Propionitrile	43.6	16.1	-
Thionyl chloride		0.4	-
Water	63.1	16.4	54.8

for the prediction of solution properties in polar aprotic solvents based on some characteristic measurements of thermodynamic properties in reference solvents (*e.g.*, the concept of transfer parameters, ΔG , ΔH , ΔS of solution, as developed by Coetzee,¹⁵ and also demonstrated by others¹⁶).

18.2.3. On the Conductivity of Polar Aprotic Solutions and Diffusion of Ions in Them

The elementary condition for obtaining conductivity in solutions is obviously the dissolution of the electrolyte and considerable charge separation. The most common and important conduction mechanism relates to the motion of separated ions in the liquid medium, retarded by friction (solvent-solute and ion-ion interactions). The ions thus reach a constant drift speed (S) under the electric field (Stock's law¹⁷).

The mobility of ions in solutions (*i.e.*, the proportion between their speed and the electric field applied to the solution) is proportional (at constant temperature) to their diffusion coefficient (Einstein equation¹⁷). Basic properties of solutions are their specific (χ) and molar ($\Lambda = \chi/C$, C =concentration of the electrolyte) conductivity, resulting from the sum of the contributions of the various ions. The molar conductivity of solutions with strong electrolytes depends slightly on the concentration ($\propto \sqrt{C}$).^{17,18} When there is no full dissociation of the electrolytes in solutions, either in cases of weak electrolytes or solvents of low polarity, we observe a variety of complicated phenomena, including formation of solvated and unsolvated ion pairs, triple ions, etc. The behavior of polar aprotic solutions with complicated inter-ion and ion solvent interactions is well covered in theory (*e.g.*, Fuoss,¹⁹ Shedlovsky,²⁰ and Venkatesetty²¹).

An important approach to forming conductive nonaqueous solutions is the use of solvent mixtures. There are many important highly polar aprotic solvents whose polarity leads to strong, intermolecular interactions, and thus to high viscosity. Hence, the advantage of the high electrolyte dissociation due to the high polarity is balanced by the high viscosity, which leads to the relatively low conductivity, since the latter property depends inversely on the solvent viscosity.^{17,18} Combining solvents of low dielectric constant and low viscosity with solvents of high dielectric constant but high viscosity may form mixtures of higher conductivity, compared with the single solvent systems. Typical examples are mixtures of alkyl carbonates and ethers that, together with Li salts, form highly conductive electrolyte solutions for lithium batteries. In most cases, the conductivity of these systems *vs.* the molar ratio of the solvents has a maximum around equimolar concentrations of the solvents.

The dependence of the conductivity on the salt concentration may also be complicated. As the salt concentration increases, the total amount of charge carriers in the solution increases. However, high salt concentration leads to high viscosity and strong ion interactions, which increase the friction to ion mobility under the electric field. Thus, in many cases the dependence of the conductivity of polar aprotic solutions on the salt concentration is a function with a maximum.

It should be noted that there are well-established theories that calculate the effect of salt concentration and temperature on the specific conductivity of polar aprotic electrolyte solutions (*e.g.*, a summary by Blomgren,⁶ the Casteel-Amis equation,²² Angell *et al.*,²³ and Barthel and coworkers²⁴).

A special challenge is the development of electrolyte solutions for low temperatures.²⁵ For instance, nonaqueous batteries are required to function at temperatures as low as -40°C . It was found that some ternary and quaternary mixtures of solvents, *e.g.*, cyclic or linear alkyl carbonates (EC, PC, DMC, DEC, EMC) and esters (MF, methyl propionate) with salts such as LiPF_6 , LiBF_4 , etc., can function as electrolyte solutions for Li-ion batteries at very low temperatures ($<-30^{\circ}\text{C}$).²⁵ However, when preparing electrolyte solutions for batteries, one should take into account that the most important factor related to the battery performance is the stability of the electrode-

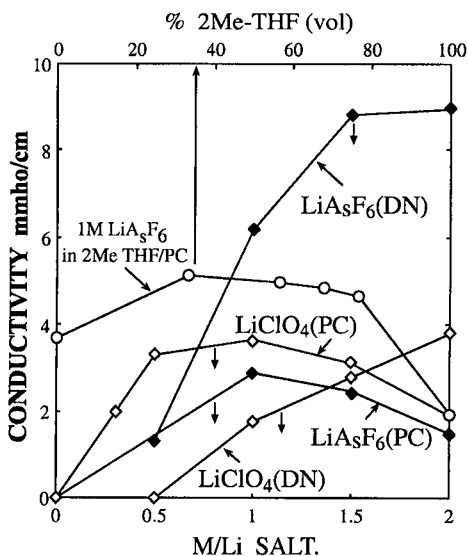


Figure 18.2. Examples of the variation in the conductivity of polar aprotic solutions as a function of solvent ratio and salt concentration. LiAsF_6 and LiClO_4 solutions in PC and DN, and LiAsF_6 solutions in mixtures of PC and 2MeTHF, as indicated. Refs. 26 and 27.

solution interfaces. Hence, some esters that can have a positive impact on the conductivity may interfere badly with the passivation of Li or Li-C anodes. Thus, the choice of solvent mixtures for low temperature applications requires a rigorous study of the electrodes' surface chemistry and stability in these mixtures at ambient and high temperatures. Figure 18.2 shows typical examples of the behavior of polar aprotic solutions showing dependence of the conductivity on the salt concentration, and on the solvent ratio, in binary solutions containing low dielectric constant-low viscosity and high dielectric constant-high viscosity solvents (*e.g.*, 2Me-THF and PC).^{26,27}

Table 18.4²⁸ shows typical parameters related to the conductivity of selected polar aprotic solutions and demonstrates the effects of salts, solvents, solvent mixtures, and temperature. There are many publications dealing with the conductivity of polar aprotic solutions. Typical examples are Refs. 29-32.

18.3. ELECTROCHEMICAL WINDOWS OF NONAQUEOUS ELECTROLYTE SOLUTIONS

In order to review briefly the electrochemical stability of nonaqueous electrolyte solutions, classification of the electrode types used is very important. The relevant electrodes may be divided into the following categories.

A. Noble metal electrodes and special carbon electrodes

Noble metal electrodes include metals (M) whose redox couple M/M^{z+} is not involved in direct electrochemical reactions in all nonaqueous systems of interest. Typical examples that are the most important, practically speaking, are gold, platinum, and glassy carbon. Conductive-doped diamond electrodes³³ also belong to this category, since the carbon material in these cases is not involved in redox reactions.

B. Reactive metal electrodes

Reactive electrodes refer mostly to metals from the alkaline (*e.g.*, Li, Na) and the alkaline earth (*e.g.*, Ca, Mg) groups. These metals may react spontaneously with most of the nonaqueous polar solvents, salt anions containing elements in a high oxidation state (*e.g.*, ClO_4^- , AsF_6^- , PF_6^- , SO_3CF_3^-) and atmospheric components (O_2 , CO_2 , H_2O , N_2). Note that all the

Table 18.4. Ionic conductivity of some 1 M organic liquid electrolytes used in secondary lithium battery systems. Taken from Ref. 28. (Conductivities at °C, mS/cm).

Salt	Solvents	Solvent vol %	-40	-20	-0	20	40	60	80
LiPF ₆	EC/PC	50/50	0.23	1.36	3.45	6.56	10.34	14.63	19.35
	2Me-THF/EC/PC	75/12.5/12.5	2.43	4.46	6.75	9.24	11.64	14.00	16.22
	EC/DME	33/67	-	1.2	5.0	10.0	-	20.0	-
	EC/DME	33/67	-	8.0	13.6	18.1	25.2	31.9	-
LiAsF ₆	EC/DEC	33/67	-	2.5	4.4	7.0	9.7	12.9	-
	EC/DME	50/50	Freeze	5.27	9.50	14.52	20.64	26.65	32.57
	PC/DME	50/50	Freeze	4.43	8.37	13.15	18.46	23.92	28.18
	2Me-THF/EC/PC	75/12.5/12.5	2.54	4.67	6.91	9.90	12.76	15.52	18.18
LiCF ₃ SO ₃	EC/PC	50/50	0.02	0.55	1.24	2.22	3.45	4.88	6.43
	DME/PC	50/50	-	2.61	4.17	5.88	7.46	9.07	10.61
	DME/PC	50/50	-	Freeze	5.32	7.41	9.43	11.44	13.20
	2Me-THF/EC/PC	75/12.5/12.5	0.50	0.93	1.34	1.78	2.31	2.81	3.30
LiN(CF ₃ SO ₂) ₂	EC/PC	50/50	0.28	1.21	2.80	5.12	7.69	10.70	13.86
	EC/DME	50/50	-	Freeze	7.87	12.08	16.58	21.25	25.97
	PC/DME	50/50	-	3.92	7.19	11.23	15.51	19.88	24.30
	2Me-THF/EC/PC	75/12.5/12.5	2.07	3.40	5.12	7.06	8.71	10.41	12.02
LiBF ₄	EC/PC	50/50	0.19	1.11	2.41	4.25	6.27	8.51	10.79
	2Me-THF/EC/PC	75/12.5/12.5	-	0.38	0.92	1.64	2.53	3.43	4.29
	EC/DME	33/67	-	1.3	3.5	4.9	6.4	7.8	-
	EC/DEC	33/67	-	1.2	2.0	3.2	4.4	5.5	-
	EC/DME	33/67	-	6.7	9.9	12.7	15.6	18.5	-

Table 18.4. Ionic conductivity of some 1 M organic liquid electrolytes used in secondary lithium battery systems. Taken from Ref. 28. (Conductivities at °C, mS/cm). (continued)

LiClO ₄	EC/DMC EC/DEC EC/DME	33/67 33/67 33/67	- - -	1.0 1.8 8.4	5.7 3.5 12.3	8.4 5.2 16.5	11.0 7.3 20.3	13.9 9.4 23.9	- - -
LiPF ₆	EC/PC 2Me-THF/EC/PC EC/DMC EC/DME EC/DEC	50/50 75/12.5/12.5 33/67 33/67 33/67	0.23 2.43 - - -	1.36 4.46 1.2 8.0 2.5	3.45 6.75 5.0 13.6 4.4	6.56 9.24 10.0 18.1 7.0	10.34 11.64 - 25.2 9.7	14.63 14.00 20.0 31.9 12.9	19.35 16.22 - - -
LiAsF ₆	EC/DME PC/DME 2Me-THF/EC/PC	50/50 50/50 75/12.5/12.5	Freeze Freeze 2.54	5.27 4.43 4.67	9.50 8.37 6.91	14.52 13.15 9.90	20.64 18.46 12.76	26.65 23.92 15.52	32.57 28.18 18.18
LiCF ₃ SO ₃	EC/PC DME/PC DME/PC 2Me-THF/EC/PC	50/50 50/50 50/50 75/12.5/12.5	0.02 - - 0.50	0.55 2.61 Freeze 0.93	1.24 4.17 5.32 1.34	2.22 5.88 7.41 1.78	3.45 7.46 9.43 2.31	4.88 9.07 11.44 2.81	6.43 10.61 13.20 3.30
LiN(CF ₃ SO ₂) ₂	EC/PC EC/DME PC/DME 2Me-THF/EC/PC	50/50 50/50 50/50 75/12.5/12.5	0.28 - - 2.07	1.21 Freeze 3.92 3.40	2.80 7.87 7.19 5.12	5.12 12.08 11.23 7.06	7.69 16.58 15.51 8.71	10.70 21.25 19.88 10.41	13.86 25.97 24.30 12.02
LiBF ₄	EC/PC 2Me-THF/EC/PC EC/DMC EC/DEC EC/DME	50/50 75/12.5/12.5 33/67 33/67 33/67	0.19 - - - -	1.11 0.38 1.3 1.2 6.7	2.41 0.92 3.5 2.0 9.9	4.25 1.64 4.9 3.2 12.7	6.27 2.53 4.4 4.4 15.6	8.51 3.43 7.8 5.5 18.5	10.79 4.29 - - -

polar solvents have groups that may contain C-O, C-S, C-N, C-Cl, C-F, S-O, S-Cl, etc. These bonds can be attacked by active metals to form ionic species, and thus the electrode-solution reactions may produce reduction products that are more thermodynamically stable than the mother solution components and much less soluble. Consequently, active metals in nonaqueous systems are always covered by surface films.³⁴

When introduced to the solutions, active metals are usually already covered by 'native' films (formed by reactions with atmospheric species), and then these initial layers are replaced by surface species formed by the reduction of solution components.³⁵ In most of these cases, the open circuit potentials of these metals reflect the potential of the $M/MX/M^{z+}$ half-cell, where MX refers to the metal salts/oxide/hydroxide/carbonates which comprise the surface films. The potential of these half-cells may be close to that of the M/M^{z+} couple.

At potentials positive to the OCV, the electrochemical window may be very limited because dissolution of the active metal takes place either via migration of M^{z+} ions through the surface films or by the breakdown of the surface films, exposing the active metal to the solution and enabling a 'direct' dissolution process.³⁶ At potentials lower than the OCV, the situation is more complicated. Since there is no possibility of a cathodic breakdown mechanism of the surface films, the possibility of obtaining active metal deposition depends either on the feasibility of migration of the M^{z+} ion through the surface films, or on electron tunneling through them to form metal deposits outside the surface layer. Consequently, in the case of alkaline earth metals (Ca, Mg, etc.) whose ions are bivalent, and whose migration through thin layers of their salts is difficult (if not impossible), there may be no possibility of metal deposition.^{37,38} In such cases, the cathodic limit of the electrochemical window may be determined by reduction reactions of solutions components. In the case of alkaline metals such as lithium, the electrochemical window is very narrow because Li dissolution and deposition take place above and below the OCV at very low overpotentials, as Li ions migrate through the surface films that cover Li electrodes.³⁹

C. Non-active/slightly reactive metal electrodes

Nonactive/slightly reactive electrode materials include metals whose reactivity towards the solution components is much lower as compared with active metals, and thus, there are no spontaneous reactions between them and the solution species. On the other hand, they are not noble, and therefore their anodic dissolution may be the positive limit of the electrochemical windows of many nonaqueous solutions. Typical examples are mercury, silver, nickel, copper, etc. It is possible to add to this list both aluminum and iron, which may react by themselves spontaneously with nonaqueous solvent

molecules or salt anions containing central atoms of high oxidation states.⁴⁰ However, they are not reactive due to passivation phenomena. Hence, the electrochemical window of nonaqueous solutions with electrodes such as aluminum or stainless steel may be determined by the electrochemical reaction of the solution components.⁴¹

A typical example is aluminum, which is used as a current collector for cathodes in lithium batteries. The stability of aluminum in many Li salt solutions at potentials as high as 4.5 V vs. Li/Li⁺ is due to the formation of highly insoluble Al halides on the aluminum surface, which remain stable and thus protect this active metal from corrosion.⁴²

D. Intercalation electrodes

Intercalation electrodes may include either carbon electrodes or transition metal oxide and sulfide electrodes, which intercalate with solution components such as metal cations. The most important example is intercalation of lithium ions into many types of carbonaceous materials at low potentials (0-1.5 V vs. Li/Li⁺)⁴³ and transition metal oxides and sulfides at high potentials (2.5-4.5 V vs. Li/Li⁺)⁴⁴. These electrochemical intercalation reactions are the basis for rechargeable Li ion battery systems and are usually the limiting anodic reactions in the Li salt solutions/Li_xMO_y or Li_xMS_y systems.

E. Red-ox electrodes

Redox electrode materials mostly include electronically conducting polymers such as polypyrrole, polythiophene, or polyaniline that may undergo reversible oxidation-reduction reactions accompanied by doping of the polymer with the counter-ion that balances the charge.⁴⁵ These processes are the anodic limit for these electrodes in many nonaqueous systems. In some cases, such as conductive polythiophene or polyparaphenylene electrodes, it is also possible to dope the polymer at low potentials and thus charge it negatively, when this negative doping is charge balanced by the entrance of cations into the polymer's matrix.⁴⁵ The electrochemical window of these systems may be determined solely by the redox activity of the electrode materials, which may leave a wide range of potentials between the two processes in which the electrode is electrochemically inert.

18.3.1. On Cathodic Reactions of Polar Aprotic Electrolyte Solutions

The cation used in the electrolyte plays an important role in

determining the cathodic behavior of polar aprotic solutions. Figure 18.3 shows typical cyclic voltammograms of ether (THF), alkyl carbonate (PC), and ester (BL) solutions with tetrabutylammonium perchlorate (TBAClO₄) and gold electrodes, and a CV of a Li salt in BL with a gold working electrode (WE).⁴⁶ The comparison among the CVs in Figure 18.3 is highly important because it demonstrates very clearly the effect of the salt cation on the electrochemical behavior of these solutions. In TBA salt solutions, as well as in any nonaqueous tetraalkylammonium salt solutions, there is no passivation of non-active electrodes. The high cathodic currents seen for the relevant CVs in Figure 18.3 reflect massive reduction of solution species. In the case of ethers, TBA is reduced. When the solvents are alkyl

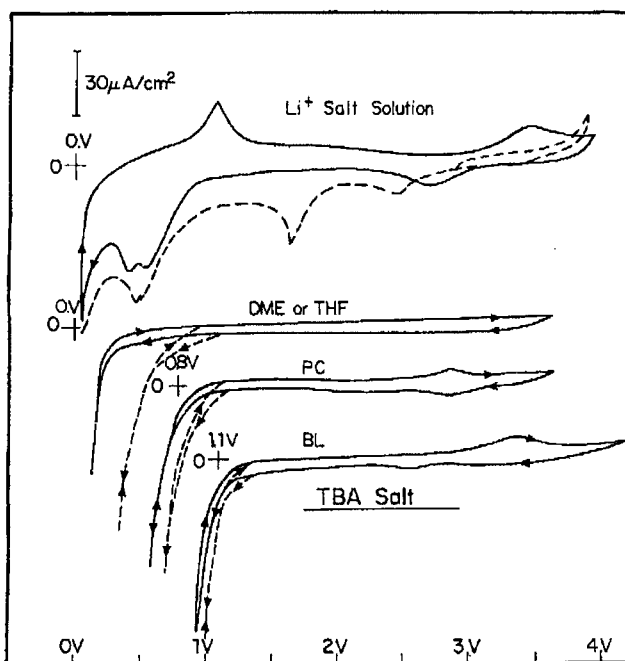


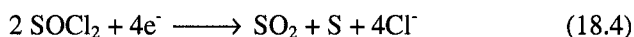
Figure 18.3. Steady state cyclic voltammograms obtained with four electrolyte solutions. The three lower ones were obtained from 0.2 M TBAP solutions with THF, BL and PC, as indicated. The upper one was obtained from 0.2 M LiAsF₆ or LiClO₄ solutions in BL. The potential scale refers to the Li/Li⁺ 0.1 M reference electrode. The potential sweep rate was 20 mV/s. The current scale is common to all CVs. Solid lines: dry solutions (~15-30 ppm of H₂O); dashed line: water contaminated solutions (0.001 M). The potential scan in all cases started from open circuit potential (2.7-3 V in these systems). Ref. 46.

carbonates or esters, which are more reactive than ethers, the major cathodic reactions in TBA salt solutions relate to solvent reduction.⁴⁶

When the cations belong to the alkaline metals (Li, Na, K), reduction of trace oxygen, water, CO₂ solvents, and salt anions form insoluble oxides, hydroxides, carbonates, halides, and organic salts, which passivate the electrodes and form surface films that block massive reduction of solution species.⁴⁷⁻⁵³ Hence, a first polarization of a non-active electrode in a polar aprotic Li (or Na) salt solution from open circuit potentials (usually around 3 V vs. Li/Li⁺) to low potentials, is characterized by irreversible cathodic peaks around 2 V and 1.5 V (corresponding to traces of O₂⁵⁴ and H₂O⁵⁵ reduction) superimposed on a broad cathodic wave related to reduction of solvent molecules and salt anions, which form surface films.⁴⁶⁻⁵⁶

The steady state voltammetric response of Li (and Na) salt solutions with non-active electrodes includes mostly underpotential deposition and stripping of the active metal on/from the noble metal electrode, possible alloy formation and decomposition (active metal + non-active metal), and bulk deposition-dissolution of the active metal. As discussed in detail and well-established in the literature, UPD processes and alloy formation depend on the nature of both the host (substrate) and the deposited metals.^{46,51,52} Schemes 18.1-3 show reaction paths of alkyl carbonates, commonly used salt anions and contaminants, respectively, in the presence of Li-ions with Li metal, lithiated carbon and/or non-active metals and carbons at low potentials, as well as the product distribution, based on Refs. 26, 27, 46-53, 56, 67.

Finally, we mention the fundamental basic cathodic reactions of the two most important polar aprotic inorganic solvents, thionyl chloride and SO₂ (due to their application for Li batteries¹), as listed below:



18.3.2. Oxidation Reactions in Polar Aprotic Electrolyte Solutions

18.3.2.1. Introduction

The study of the oxidation reactions of polar aprotic solutions and

Scheme 18.1: Possible reduction patterns of alkyl carbonate on Li (Refs. 27, 49, 50, 59, 61, 67)

- a. $\text{PC} + \text{e}^- + \text{Li}^+ \longrightarrow \text{CH}_3\dot{\text{C}}\text{HCH}_2\text{OCO}_2^-\text{Li}^+(\text{PC}^-\text{Li}^+)$ supported
- b. $\text{CH}_3\dot{\text{C}}\text{HCH}_2\text{OCO}_2\text{Li} + \text{H} \xrightarrow{?} \text{CH}_3\text{CH}_2\text{CH}_2\text{OCO}_2\text{Li}$ not supported
- c. $2\text{CH}_3\dot{\text{C}}\text{HCH}_2\text{OCO}_2\text{Li} \xrightarrow{?} (\text{CH}_3\text{-CH-CH}_2\text{OCO}_2\text{Li})_2$ not supported
- d. $2\text{CH}_3\dot{\text{C}}\text{HCH}_2\text{OCO}_2\text{Li} \longrightarrow \text{CH}_3\text{CH}(\text{OCO}_2\text{Li})\text{CH}_2\text{OCO}_2\text{Li} \downarrow + \text{CH}_3\text{CH}=\text{CH}_2 \uparrow$ supported
- e. $2\text{EC} \xrightarrow{2\text{e}^-, 2\text{Li}^+} (\text{CH}_2\text{OCO}_2\text{Li})_2 \downarrow + \text{CH}_2=\text{CH}_2 \uparrow$ supported
- f. $2\text{EC} \xrightarrow{2\text{e}^-, 2\text{Li}^+} \text{LiOCO}_2(\text{CH}_2)_4\text{OCO}_2\text{Li}$ not supported
- g. $\text{Li}_2\text{O} + \text{EC} \xrightarrow{?} \text{LiOCH}_2\text{CH}_2\text{OCO}_2\text{Li}$

Nucleophilic Mechanism (relevant to PC as well):

- h. $\text{RO}^- \curvearrowright \begin{array}{c} \text{CH}_2\text{-O} \\ | \\ \text{CH}_2\text{-O} \end{array} \text{C=O} \xrightarrow{\text{Li}^+} \text{ROCH}_2\text{-CH}_2\text{-OCO}_2\text{Li}$ poor nucleophile
- i. $\begin{array}{c} \text{RO-CH}_2 \\ | \\ \text{CH}_2\text{-OCO}_2\text{Li} \end{array} \xrightarrow{\text{second nucleophilic attack}} \text{ROCH}_2\text{CH}_2\text{OR} + \begin{array}{c} \text{O} \\ || \\ \delta^-\text{O}-\text{C}-\text{O}-\delta^- \\ | \\ \text{Li}^+ \end{array}$ nucleophile
- j. $\begin{array}{c} \text{O} \\ || \\ \delta^-\text{O}-\text{C}-\text{O}-\delta^- \\ | \\ \text{Li}^+ \end{array} \xrightarrow{\text{Li}^+} \text{Li}_2\text{CO}_3 \downarrow$ ion pairing
 competition
 $\xrightarrow{\text{EC}} \begin{array}{c} \text{CH}_2\text{-OCO}_2\text{Li} \\ | \\ \text{CH}_2\text{-OCO}_2\text{Li} \end{array} \downarrow$ nucleophilic attack
- k. $\text{EC} + 2\text{e}^- \xrightarrow{\text{Li}^+} \begin{array}{c} \text{CH}_2 \\ || \\ \text{CH}_2 \end{array} + \text{CO}_3^-(\text{Li}^+) \xrightarrow{\text{EC}, \text{Li}^+} \begin{array}{c} \text{H}_2\text{C}-\text{OCO}_2\text{Li} \\ | \\ \text{H}_2\text{C}-\text{OCO}_2\text{Li} \end{array} \downarrow$ high C_{EC}
- (Relevant to PC as well)
- $\begin{array}{c} \text{O} \\ || \\ \text{CH}_3\text{OCOCH}_3 \end{array} + \text{e}^- + \text{Li}^+ \xrightarrow{\text{Li}^+} \text{CH}_3\text{OCO}_2\text{Li} \downarrow + \text{CH}_3\cdot \text{ or } \text{CH}_3\text{OLi} \downarrow + \text{CH}_3\text{OCO}\cdot$
- $\xrightarrow{\text{Li}^+} \text{Li}_2\text{CO}_3 \downarrow$ low C_{EC}
- (In a similar manner other acyclic alkyl carbonates: DEC, EMC, PMC reacts).
- m. $2\text{ROCO}_2\text{Li} + \text{H}_2\text{O} \longrightarrow \text{Li}_2\text{CO}_3 + 2\text{ROH} + \text{CO}_2$
- n. $\text{ROCO}_2\text{Li}, \text{Li}_2\text{CO}_3 \xrightarrow{\text{HF}} \text{LiF} + \text{H}_2\text{CO}_3, \text{ROCO}_2\text{H}$
- o. $\text{R}\cdot + \text{Li}^0 \longrightarrow \text{R-Li}$

Scheme 18.2: Surface reactions of commonly used Li salts (Refs. 26, 49, 50, 53, 57, 58, 61-67)

- a) $\text{LiAsF}_6 + 2\text{Li}^+ + 2\text{e}^- \rightarrow 3\text{LiF} \downarrow + \text{AsF}_3 (\text{sol})$
- b) $\text{AsF}_3 + 2x\text{Li}^+ + 2x\text{e}^- \rightarrow \text{Li}_x\text{AsF}_{3-x} \downarrow + x\text{LiF} \uparrow$
- c) $\text{PF}_6^- + 3\text{Li}^+ + 2\text{e}^- \rightarrow 3\text{LiF} \downarrow + \text{PF}_3$
- d) $\text{LiPF}_6 \rightleftharpoons \text{LiF} + \text{PF}_5$
- e) $\text{PF}_5 + \text{H}_2\text{O} \rightarrow \text{PF}_3\text{O} + 2\text{HF}$
- f) $\text{PF}_5 + 2x\text{Li}^+ + 2x\text{e}^- \rightarrow \text{Li}_x\text{PF}_{5-x} \downarrow + x\text{LiF} \downarrow$
- g) $\text{PF}_3\text{O} + 2x\text{Li}^+ + 2x\text{e}^- \rightarrow \text{Li}_x\text{PF}_{3-x}\text{O} \downarrow + x\text{LiF} \downarrow$
- h) $\text{BF}_4^- \xrightarrow{\text{Li}^+, \text{e}^-} \text{LiF} \downarrow, \text{Li}_x\text{BF}_y \downarrow (\text{in general})$
- i) $\text{LiClO}_4 + 8\text{Li}^+ + 8\text{e}^- \rightarrow 4\text{Li}_2\text{O} + \text{LiCl}$
- j) $\text{LiClO}_4 + x\text{Li}^+ + x\text{e}^- \rightarrow \text{LiClO}_{(4-1/2x)} + 1/2x\text{Li}_2\text{O}. (x = 2, 4, 6)$
- k) $\text{LiN}(\text{SO}_2\text{CF}_3)_2 + n\text{e}^- + n\text{Li}^+ \rightarrow \text{Li}_3\text{N} + \text{Li}_2\text{S}_2\text{O}_4 + \text{LiF} + \text{C}_2\text{F}_x\text{Li}_y$
- l) $\text{LiN}(\text{SO}_2\text{CF}_3)_2 + 2\text{e}^- + 2\text{Li}^+ \rightarrow \text{Li}_2\text{NSO}_2\text{CF}_3 + \text{CF}_3\text{SO}_2\text{Li}$
- m) $\text{Li}_2\text{S}_2\text{O}_4 + 10\text{e}^- + 10\text{Li}^+ \rightarrow 2\text{Li}_2\text{S} + 4\text{Li}_2\text{O}$
- n) $\text{LiC}(\text{SO}_2\text{CF}_3)_3 + 2\text{e}^- + 2\text{Li}^+ \rightarrow \text{Li}_2\text{C}(\text{SO}_2\text{CF}_3)_2 + \text{LiSO}_2\text{CF}_3, \text{ etc.}$
- o) $\text{Li}_2\text{S}_2\text{O}_4 + 4\text{e}^- + 4\text{Li}^+ \rightarrow \text{Li}_2\text{SO}_3 + \text{Li}_2\text{S} + \text{Li}_2\text{O}$
- p) $2\text{LiSO}_3\text{CF}_3 + 2\text{Li}^+ + 2\text{e}^- \rightarrow 2\text{Li}_2\text{SO}_3 + \text{C}_2\text{F}_6$
- q) $\text{R-CF}_3 + 2\text{Li}^+ + 2\text{e}^- \rightarrow \text{RCF}_2\text{Li} + \text{LiF}$
- r) $\text{Li}_2\text{SO}_3 + 6\text{Li}^+ + 6\text{e}^- \rightarrow \text{Li}_2\text{S} + 3\text{Li}_2\text{O}$

Scheme 18.3: Reaction patterns of common contaminants (Refs. 26, 47, 48, 50, 51, 53-55, 61, 62, 64-66)

- a. $\text{CO}_2 + \text{e}^- + \text{Li}^+ \rightarrow \dot{\text{C}}\text{O}_2\text{Li}$
 $\dot{\text{C}}\text{O}_2\text{Li} + \text{CO}_2 \rightarrow \text{O} = \dot{\text{C}}\text{-O-CO}_2\text{Li}$
 $\text{O} = \dot{\text{C}}\text{-O-CO}_2\text{Li} + \text{e}^- + \text{Li}^+ \rightarrow \text{CO} \uparrow + \text{Li}_2\text{CO}_3 \downarrow$
 $2\text{LiOH} \downarrow + \text{CO}_2 \rightarrow \text{Li}_2\text{CO}_3 \downarrow + \text{H}_2\text{O}$
 $\text{Li}_2\text{O} \downarrow + \text{CO}_2 \rightarrow \text{Li}_2\text{CO}_3 \downarrow$
 $\text{ROLi} \downarrow + \text{CO}_2 \rightarrow \text{ROCO}_2\text{Li} \downarrow$
- b. $\text{H}_2\text{O} + \text{e}^- + \text{Li}^+ \rightarrow \text{LiOH} + 1/2 \text{H}_2$
 $\text{LiOH} + \text{Li}^+ + \text{e}^- \rightarrow \text{Li}_2\text{O} + 1/2 \text{H}_2$
 $\text{H} + \text{e}^- + \text{Li}^+ \rightarrow \text{LiH}$

- a. $\text{N}_2 + 6\text{e}^- + 6\text{Li}^+ \rightarrow 2\text{Li}_3\text{N}$
- b. $\text{O}_2 + \text{e}^- + \text{Li}^+ \rightarrow \text{LiO}_2$
 $\text{LiO}_2 + \text{e}^- + \text{Li}^+ \rightarrow \text{Li}_2\text{O}_2$
 $\text{Li}_2\text{O}_2 + 2\text{e}^- + 2\text{Li}^+ \rightarrow 2\text{Li}_2\text{O}$
- c. $\text{HF} + \text{e}^- + \text{Li}^+ \rightarrow \text{LiF} + \frac{1}{2} \text{H}_2$

R&D of solutions with high anodic stability have become very important in recent years due to the R&D of Li-ion batteries with cathode redox potentials as high as 5 V. In recent years we have seen intensive efforts to study rigorously the oxidation reactions of polar aprotic electrolyte solutions, important in the field of Li batteries.^{41,68-71} These have included mostly mixtures of alkyl carbonates and commonly used Li salts. Of especial importance for these studies has been the application of spectroscopic tools such as *in situ* FTIR spectroscopy and mass spectrometry.^{70,71} In general, the identification of the specific oxidation reactions of nonaqueous solutions is much more difficult than the identification of the cathodic reactions of the same solutions. This is due to the fact that oxidation of most of the polar aprotic solutions usually forms species that are soluble in the mother solutions and cannot be easily separated from them for identification. In contrast, cathodic reactions of polar aprotic solutions usually form gases and surface films which can be identified by spectroscopic means, as described in the previous section, as well as described in the relevant references listed therein. In the case of ethers and alkyl carbonate solutions, oxidation forms soluble polymers.^{71,72} The solutions whose oxidation was studied most rigorously were alkyl carbonates and ethereal systems.⁶⁸⁻⁷⁵

With noble metal electrodes, small scale oxidation processes of alkyl carbonate solutions may be detected at potentials above 3.5 V (Li/Li⁺),⁷¹ while massive, intensive oxidation processes occur at potentials >4.5 V⁴¹.

During oxidation of alkyl carbonates, evolution of CO₂ was clearly detected by DEMS. Ring opening and a change in the nature of the carbonyl group as an intermediate step were suggested, following *in situ* FTIR measurements.⁷⁶ As shown by Eggert and Heitbaum in DEMS studies,⁷⁵ when an LiClO₄ electrolyte is used, the anion is also involved in the oxidation process of the system at the 4-4.5 V potential range, and intermediates such as ClO₂ and radical or molecular oxygen are then formed. Traces of water were also identified (by DEMS) among the oxidation products of a PC-LiClO₄ solution. This product may be formed through hydrogen abstraction by an oxygen radical from the solvent molecules.

In the case of BF₄⁻ or PF₆⁻ salts, the oxidation products also include

fluorinated derivatives of propylene and/or propylene oxide (in the case of PC solutions).⁷⁶ Another solvent whose electrochemical oxidation was rigorously investigated was 1-3 dioxolane (DN).⁷⁷ It was found that when this ketal is diluted with other ethers, it exhibits high anodic stability, similar to THF ($4.5\text{ V} > E_{\text{ox}} > 4\text{ V}$ vs. Li/Li^+). However, since this solvent is a ketal, it is highly sensitive to Lewis acids and thus can polymerize at potentials as low as 3 V in the single solvent solutions of salts such as LiClO_4 . At these potentials, adsorbed hydrogen on the electrode (formed by trace water reduction) is oxidized to H^+ , which readily initiates polymerization of dioxolane.

18.3.2.2. On the Role of the Electrode's Material

The electrode's material has a high impact on the anodic stability of electrochemical systems based on polar aprotic solutions, as summarized below:

- a. It is only with noble metals such as Au and Pt and doped (conducting) diamond that the electrode's material is not involved in the anodic reactions of the electrochemical systems.
- b. With electrodes such as Ag, Ca, Ni, etc., metal dissolution may be the major anodic process that limits the electrochemical window of the system.
- c. Graphite electrodes can intercalate with commonly used anions at potentials $>4\text{ V}$ (Li/Li^+). Such an intercalation process, when possible, becomes the limiting anodic reaction.⁷⁸
- d. In the case of transition metal oxides or sulfide electrodes and Li salt solutions, the limiting anodic process is, of course, Li insertion into the electrode's active mass. It is important to note that we have evidence that massive oxidation of solution species is largely inhibited with commonly used transition metal oxide cathodes, even at high potentials ($>4.5\text{ V}$), due to passivation phenomena.⁷⁹
- e. With active metal electrodes such as Li, Na, Mg, and Ca, the limiting anodic reactions are, of course, dissolution of the active metal. However, since these electrodes are always covered by surface films, their processes are complicated. The surface films on Li or Na may conduct the monovalent cations and, thus, Li and Na dissolution occurs at low overpotentials.⁵²
- f. Aluminum, which is also an active metal, demonstrates high anodic stability in most of the commonly used polar aprotic solutions, due to passivation phenomena (e.g., by Al halides). Therefore, the metal is widely used as a current collector for cathodes in Li and Li-ion batteries.⁴²

18.3.3. A Short Summary of the Anodic Limit of Nonaqueous Electrolyte Solutions

Table 18.5 provides oxidation potentials of a number of Li salt solutions with three types of electrodes: Pt, glassy carbon and composite carbon black.⁸⁰ An expected correlation between the donor number of the solvent and its oxidation potential was found: the higher the donor number, the lower is the oxidation potential.⁸¹ Further comprehensive data on the electrochemical windows of polar aprotic solutions can be found in Refs. 82,83.

Some conclusions related to the data in Refs. 80-83 are listed below.

1. In general, the determination of oxidation potentials is not trivial, since all of the relevant reactions are irreversible. Therefore, oxidation potentials may relate to arbitrary decisions; normally, the potential is determined at a point where the anodic current of a system is significantly high.
2. Some of the early data in the literature refer to aqueous SCE or Ag/Ag⁺ reference electrodes,⁸⁵ whereas more recent data, such as that presented in Table 18.5, refer to the non-aqueous Li/Li⁺ reference electrode. However, as shown by Auburn and Ciemieki,⁸⁴ the SCE electrode potential is 3.24 V vs. Li/Li⁺ and thus data from different sources can be compared. It appears that the early data provided by Mann⁸⁵ relating to aqueous reference electrodes correspond well to later data relating to non-aqueous reference electrodes (for the same solvents and salts).
3. Alkyl carbonates have a much higher anodic stability than do ethers (>1 V difference).
4. The anion and the electrode material have a pronounced effect on the oxidation potentials of the non-aqueous systems. The metals to which the highest potentials can be applied in non-aqueous systems are obviously the noble metals (Pt, Au). The limiting reaction when the anions are halides (Cl⁻, Br⁻, I⁻) was found to be their oxidation to the elemental form. When the anion is ClO₄⁻, its oxidation onset at potentials above 1.5 vs. Ag/Ag⁺ may promote further intensive solvent degradation, as in the case of AN. It is important to note that using BF₄⁻ instead of ClO₄⁻ in AN (which is an important and useful non-aqueous solvent in electrochemistry) extends its anodic stability by 2 V. Similar results were obtained from Pt and glassy carbon electrodes, indicating that no catalytic effects take place in the electrochemical oxidation of polar aprotic solutions.⁸²
5. It appears that acetonitrile is one of the polar aprotic solvents of the highest anodic stability.

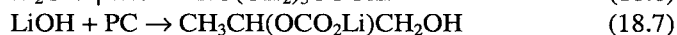
6. The order of anodic stability found for commonly used Li salts is $\text{LiAsF}_6, \text{LiBF}_4, \text{LiPF}_6 > \text{LiClO}_4, \text{LiSO}_3\text{CF}_3, \text{LiN}(\text{SO}_2\text{CF}_3)_2$.

18.4. LIQUID ELECTROLYTE SOLUTIONS FOR RECHARGEABLE Li (METAL) BATTERIES

18.4.1. Problems with the Use of Li Metal Anodes

Li surfaces are naturally covered by bilayer surface films. The inner part is comprised mostly of Li_2O , while the outer part is comprised of a mixture of LiOH and Li_2CO_3 . When Li electrodes are introduced into electrolyte solutions, the following changes take place.

1. Solvent molecules can percolate through the surface films and react with the active metal.
2. Species such as LiOH , Li_3N , Li_2O , and even Li carbonate, which are part of the native passive layer, may be highly nucleophilic in aprotic media and react with electrophilic solvent molecules such as esters and alkyl carbonates.^{48,86} For instance:



3. Part of the pristine surface species and the products of the nucleophilic reactions above dissolve in the solution, thus allowing other solution species to react with the active metal.
4. Traces of water may hydrate most of the surface species formed on Li, and hence, diffuse through the surface films and react with the active metal to form LiOH , Li_2O , LiH and H_2 .⁸⁷
5. Consequently, the surface films become very non-uniform at the micrometric and nanometric scales (both laterally and vertically).
6. When fresh Li is exposed to a solution, there is an immediate reaction with solution species under highly non-selective conditions. The solution reduction products precipitate and form an initial surface layer through which electron transfer to solution species continues at an increasing level of selectivity.

As the film reaches a certain thickness, it blocks electron transfer and the electrode reaches passivation. Further reduction of surface species may continue within the surface films. In addition, at the outer solution side of the films, there is a continuous dissolution-precipitation of surface species, secondary reactions of surface species with solution components, and highly

Table 18.5. Oxidation potentials (V vs. Li/Li⁺) for several electrolyte solutions. Taken from Ref. 128 and Refs. therein.

Solvent	Salt	Pt	GC ^a	TAB ^b
PC	LiClO ₄	5.3	5.3	4.7
PC-DME (90/10)	LiClO ₄	4.5	4.5	
PC-DME (75/25)	LiClO ₄	4.5	4.5	
PC-DME (50/50)	LiClO ₄	4.6	4.7	4.6
DME	LiClO ₄	4.5	4.5	4.6
2Me-THF/THF/2-MeF ^{c,d} (49/49/2)	LiClO ₄	4.1	4.0	
2Me-THF/THF (50/50)	LiClO ₄	4.1	4.0	
2Me-THF/THF (90/10)	LiClO ₄	3.9	4.0	
2Me-THF	LiClO ₄	4.0	4.2	
THF	LiClO ₄	4.2		
PC LiClO ₄	LiAsF ₆	5.6	5.2	
PC/DME (90/10)	LiAsF ₆	4.9	4.9	
PC/DME (75/25)	LiAsF ₆	4.7	4.8	
PC/DME (50/50)	LiAsF ₆	4.7	4.7	
DME	LiAsF ₆	4.6	4.6	
2Me-THF/THF/2-MeF (49/49/2)	LiAsF ₆	4.0	3.9	4.0
2Me-THF/THF (90/10)	LiAsF ₆	4.0	4.1	
2Me-THF/THF (75/25)	LiAsF ₆	4.0	4.0	
2Me-THF/THF (50/50)	LiAsF ₆	4.0	4.1	
2Me-THF	LiAsF ₆	4.1	4.1	
THF	LiAsF ₆	4.2	4.2	
2MF (50/50)	LiAsF ₆	5.0	4.9	
MF	LiAsF ₆	4.9		

^a GC= glassy carbon; ^b TAB = Teflonized acetylene black.; ^c MF = methyl formate; ^d 2MeF = 2-methyl furan.

selective reduction of solution species by electron tunneling through the surface films at certain locations of high electrical conductivity. The result of this description is, again, highly non-uniform, multilayer films that comprise a compact, inner part, which contains species of very low oxidation states (Li₂O, Li-C, Li₃N, LiH, Li halides, etc.), a middle part that contains surface species of higher oxidation states (ROCO₂Li, Li₂CO₃, ROLi, LiOH, RCOOLi, etc.), and a porous outer part of the surface films' solution interface.^{88,92} The surface species formed on Li, which are all Li salts, precipitate as thin films (submicronic thickness⁹³) that can conduct Li ions. Therefore, when an electrical field is applied, the surface films formed on Li in any polar aprotic solution behave like a solid electrolyte interphase³⁹ (see the famous, well-established SEI model in Ref. 94)

Hence, a general property of Li electrodes in solutions based on solvents such as esters, ethers, alkyl carbonates, DMSO, SO_2 , and SOCl_2 , is that, on a thermodynamic basis, the Li electrodes are unstable because all reduction processes of polar aprotic solvents by Li are thermodynamically favorable. However, kinetically speaking, Li electrodes are apparently stable due to passivation by the surface films. In most cases, the surface films are Li-ion conductive and, therefore, Li deposition-dissolution in polar aprotic solutions can be driven easily at relatively low overpotentials. However, as described above, the surface films are highly non-uniform and, thus, the current distribution of Li deposition-dissolution processes is very non-uniform. Thereby, in most polar aprotic solutions, Li dissolution leads to a breakdown and repair of the surface films and forms holes and cracks that

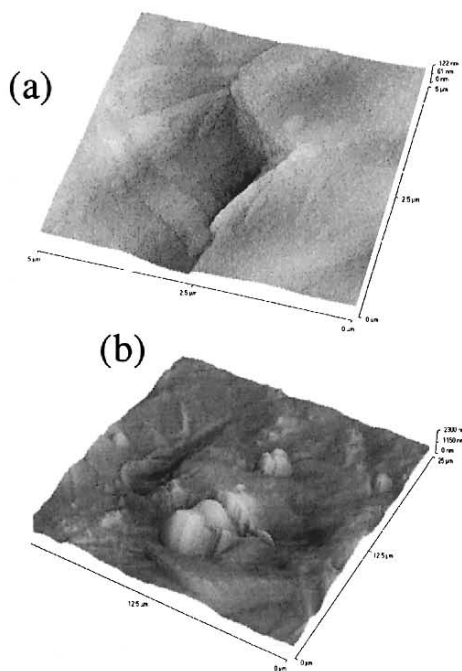


Figure 18.4. Non-uniform Li deposition and dissolution in polar aprotic solutions. (a) A typical AFM image of non-uniform Li dissolution ($5 \times 5 \mu\text{m}$, 122 nm height difference) in a PC- LiPF_6 solution. Ref. 96. (b) A typical AFM image of non-uniform Li deposition ($25 \times 25 \mu\text{m}$, 230 nm height difference) in an EC-DMC $\text{LiC}(\text{SO}_2\text{CF}_3)_3$ solution. Ref. 97.

expose fresh Li to solution, and Li deposition is dendritic. Figure 18.4 presents AFM images that demonstrate typical, non-uniform Li deposition and dissolution processes.⁹⁵⁻⁹⁷

Dendritic Li deposition and non-uniform Li dissolution is a major problem in the use of Li metal anodes in rechargeable batteries when using most of the commonly available polar aprotic solutions. There are only a few electrolyte solutions in which Li deposition/dissolution is sufficiently uniform for battery application.

18.4.2. On the Choice of Electrolyte Solutions for Rechargeable Li (Metal) Batteries

In the early stages of R&D of Li batteries it already became clear that Li deposition is dendritic in most of the relevant polar aprotic solutions.⁹⁸ It was discovered that LiAsF_6 is a superior salt for the reversibility and high cycling efficiency of Li electrodes.⁹⁹ It was suggested that reduction of the AsF_6^- anion or species such as AsF_3 or AsF_5 in ethereal solutions form, together with ether reduction products, polymeric films that improve the passivation of lithium anodes (the “brown film” concept).¹⁰⁰ Later on, it was suggested that reduction of AsF_6^- forms a variety of species: LiF , Li_3As , As^0 , Li_xAsF_y , all of which dope the Li surface and reduce its reactivity.^{57,77,101}

Over the years, a large variety of electrolyte solutions containing different solvents, salts and additives were tested in connection with the cycling efficiency of Li electrodes.¹⁰²⁻¹⁰⁴ The solvents included cyclic ethers,¹⁰⁵ esters,¹⁰⁶ alkyl carbonates,¹⁰⁷ SO_2 ¹⁰⁸ and sulfolane.¹⁰⁹ The salts included LiClO_4 , LiAsF_6 , LiBF_4 , $\text{LiN}(\text{SO}_2\text{CF}_3)_2$ and $\text{LiC}(\text{SO}_2\text{CF}_3)_3$, and the additives included active gases (e.g., CO_2),⁵⁰ metal cations (e.g., Ga^{3+} , Mg^{2+}),¹¹⁰ and organic species (alkanes, aromatic compounds).¹¹¹ It was found that modifying lithium surface films with very small quantities of Li_3N ¹¹² or a second metal such as aluminum¹¹³ may improve its performance as an anode material. Also, application of pressure to Li electrodes (e.g., using compact electrochemical cells in which the separator presses on the Li electrodes), suppresses dendritic Li deposition and increases Li cycling efficiency.¹¹⁴

It became clear that the major problem of Li electrodes relates to the fact that the surface films formed on Li in most of the commonly used electrolyte solutions cannot accommodate the volume and morphological changes of the Li metal during dissolution or deposition, as illustrated in Figure 18.5.¹¹⁵ In cases where the surface films are comprised mostly of Li salts, they are not elastic enough to protect the active metal in conditions of non-uniform Li dissolution or deposition. Only in cases where the surface

films contain elastomers, as is the case of 1-3 dioxolane solutions, the surface films are elastic and provide good passivation to the Li electrodes in the dynamic situation of Li electrochemical deposition/dissolution cycling (see Figure 18.5).^{77,115}

Highly important and critical in the use of Li metal anodes in rechargeable batteries are safety considerations. Abuse cases, such as short circuit of Li batteries, which means an immediate, very high current flow, lead to a pronounced heat dissipation. A rapid release of heat inside a lithium battery can drive highly dangerous, exothermic redox reactions between Li and the solution components. The lithium in the battery can very easily reach its melting point, which should accelerate the thermal reactions in the cell. Such a scenario is called “thermal runaway” and results in the explosion of shorted Li batteries.¹¹⁶ As a Li battery is cycled, the Li surface may be rougher, and hence, internal thermal reaction inside the battery in abuse cases should be more intensive and dangerous. Dangerous “thermal runaway” situations of Li batteries can also occur upon overcharging and overdischarging of secondary Li batteries.¹¹⁶ Hence, even in cases where the performance of Li batteries is excellent in terms of cycling efficiency and rates and temperature range of operation, the above safety considerations may be a critical limitation in their practical use.

Over the years, there were three electrolyte solutions that were considered as suitable for the practical development of rechargeable Li (metal) batteries, and each deserves special discussion.

18.4.2.1. EC-PC/LiAsF₆, MOLI Energy Inc. Li-MoS₂ Cells¹¹⁷

With this electrolyte solution, the Li passivation is dominated by the EC reduction products (*e.g.*, CH₂OCO₂Li)₂)⁵⁰ plus doping by the reduction products of AsF₆⁻, as explained above. We attribute the possibility to obtain sufficient Li cycling efficiency for practical battery application in this solution to the stack pressure applied to the Li anodes in the AA-“jelly rolled” configuration of the batteries produced by MOLI Inc.¹¹⁴ However, MOLI’s Li-MoS₂ batteries could not be fully commercialized due to safety problems.¹¹⁷

18.4.2.2. THF, 2Me-THF, 2-Methyl Furane/LiAsF₆^{118,119}

This solution was also found to be very good for reversible, high cycling efficiency of Li anodes. While relatively high cycling efficiency

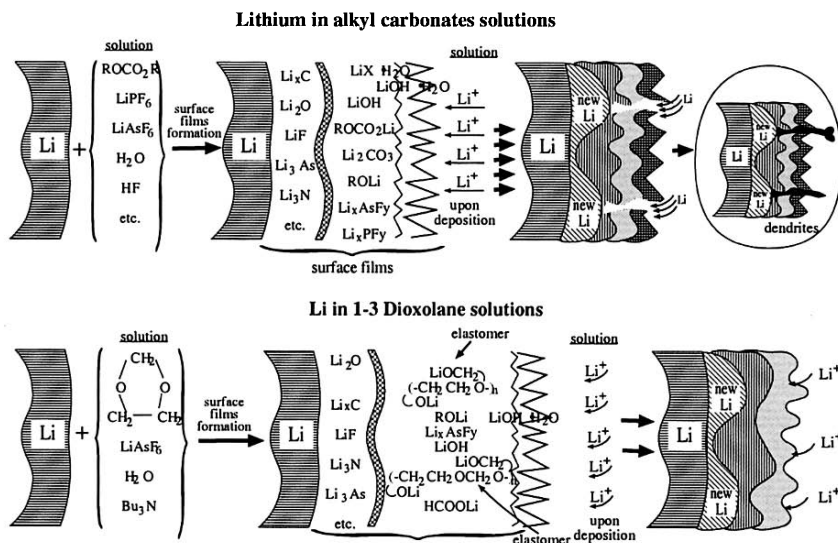


Figure 18.5. A schematic illustration of surface film formation on lithium electrodes in alkyl carbonates and in 1-3 dioxolane solutions. Ref. 115.

could be measured with Li anodes in 2Me-THF/ LiAsF_6 ,¹²⁰ the combination of the three-solvent mixture (2Me-furan in a few percent by volume) was found to be superior. The identified surface species formed on Li in these solutions include Li-alkoxides, which are the reduction products of THF and 2Me-THF, and salt anion reduction products (LiF , Li_xAsF_y , possibly including Li_3As and As^0).¹²¹ 2Me-furan may be reduced on the Li surface to form polymeric species. It also acts as a scavenger for trace Lewis acids in solutions. Another component in the surface films on Li in this system may be the brown film (As-O-R) cross-linked polymer.¹⁰⁰

JPL (Pasadena, USA) developed prototypes of AA rechargeable Li- TiS_2 batteries with these electrolyte solutions.¹²² In spite of their high energy density, these batteries could not be commercialized, due to safety limitations, as explained above, and the possible danger in the use of such batteries in abuse cases.

18.4.2.3. 1-3 Dioxolane/ LiAsF_6 /Tributylamine⁷⁷

From early studies of secondary Li battery systems, 1-3 dioxolane (DN) was considered to be a "magic" solvent in which Li anodes behave highly reversibly. The morphology of Li deposition in DN solutions was

found to be very smooth and dendrite free.¹²³ The surface films formed on Li in this solvent include Li formate, alkoxides such as $\text{CH}_3\text{CH}_2\text{OCH}_2\text{OLi}$ and oligomers of polyDN with $-\text{OLi}$ edge groups. We believe that the presence of these oligomers makes the surface films elastic, and thereby, enhances their passivating properties.¹¹⁵

When the salt is LiAsF_6 , doping of Li surfaces by the various possible Li_xAsF_y products further improves the passivation of the Li electrodes. However, DN, which is a ketal, readily polymerizes in the presence of trace Lewis acids such as AsF_3 (which may be unavoidably present in LiAsF_6 solutions). Therefore, it is necessary to stabilize the DN/ LiAsF_6 solution with a base such as three-butyl amine (TBA).⁷⁷ In addition to the excellent cycling efficiency of Li electrodes in these solutions, this electrolyte system also provides a unique, intrinsic safety mechanism for Li batteries, that works as follows.¹²⁴ Up to 120°C , Li with DN/ LiAsF_6 /TBA is stable, and Li is fully passivated. At temperatures above 120°C , DN reacts with LiAsF_6 (a thermal redox reaction). One of the products of the reaction is HF. As it is formed, it leads to a very fast polymerization of the solvent, which shuts down the electrochemical system because of the relatively low electrical conductivity of the solid-gel matrix in which polyDN is a major component. Commercial Li- $\text{Li}_{0.3}\text{MnO}_2$ AA batteries containing this solution were produced and distributed.¹²⁵ In any case of short circuit, high currents flow and heat up the battery so that its internal temperature exceeds 120°C , solvent (DN) polymerization occurs, as explained above, and the battery shuts down before thermal runaway takes place (see Figure 18.6a). Upon overcharging, the TBA stabilizer is electrolyzed (>3.6 V vs. Li/Li^+),⁷⁷ trace Lewis acids are formed, the solvent is polymerized by the acidic species thus formed, and the battery again shuts down before any thermal runaway can occur (see Figure 18.6b). These batteries possess high energy density (>140 Wh/Kg, practical), high power density upon discharge, a wide temperature range of operation ($-30^\circ\text{C} \rightarrow 60^\circ\text{C}$), and extended cycle life (300-400 cycles at 100% DOD).

A major disadvantage of these batteries has been their requirement for slow charging (C/9-12 hrs). At too high charging rates, Li is deposited in small grains, which facilitate side reactions between Li deposits and solution species (no dendrite formation and internal shorts by Li deposits). The cycle life decreases as the charging rate increases, because the electrolyte solution disappears by continuous reaction with Li deposits.¹²⁶ Tadiran Inc. gave up the mass production of these batteries because they could not compete with Li-ion battery technology that allows for very fast charging rates with no low cycle life penalty.

While there are reports from time to time on research on rechargeable Li metal battery systems, we have come to the conclusion that there is no future in secondary batteries with Li metal anodes and liquid electrolyte

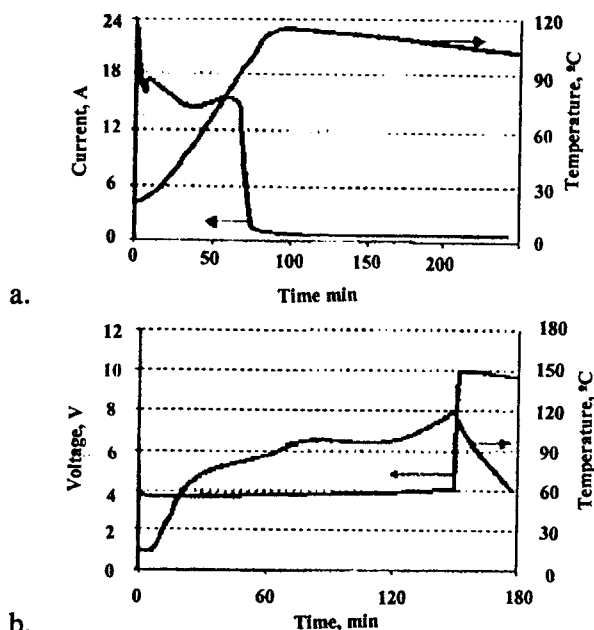


Figure 18.6. (a) Short-circuit behavior of practical AA Li/DN, LiAsF₆, TBA/LiMnO₂ batteries after 30 cycles. (b) Overcharged behavior of the same cells at a current of 1 A after 60 cycles. Ref. 125.

solutions based on the current state-of-the-art technology. There is no way to avoid side reactions between any liquid electrolyte solution and Li deposits (even in the absence of dendrite formation), especially at high charging rates.¹²⁷ Li metal anodes, however, can be used in rechargeable batteries with polymeric/solid or gel electrolytes¹²⁸ (a full discussion of which is beyond the scope of this chapter).

18.5. LIQUID ELECTROLYTE SOLUTIONS FOR RECHARGEABLE LI-ION BATTERIES

18.5.1. The Requirements of Suitable Solutions for Li-Ion Batteries

In Li-ion batteries, Li metal anodes are replaced by Li-C intercalation compounds. Li-ion batteries use high voltage cathodes: LiNiO₂, LiCoO₂, LiMn₂O₄, etc., whose redox potentials are above 4 V.¹²⁹ LiMn₂O₄ doped with

metals such as Cr and Cu have redox activity around 5 V.^{130,131} Hence, the electrolyte solutions for these batteries should have high anodic stability. The anodic side, *i.e.*, the Li-C/solution interface, also requires special properties of the electrolyte solutions in terms of their low potential surface chemistry.

So far, the most commonly used anode materials for Li-ion batteries are graphitic carbons. All graphitic carbons have a weak lattice comprising graphene planes bound together in layered structures by relatively weak bonds. Graphitic lattices can be easily destroyed during intercalation of lithium by phenomena such as co-intercalation of solvent molecules,¹³² and a build-up of internal pressure due to surface reactions that form gaseous products.¹³³ Hence, the stability and reversibility of graphite electrodes upon Li intercalation depends mostly on passivation phenomena.

As explained in Section 18.3 above, polarization of any carbon electrode to low potential in any polar aprotic, Li salt solution leads to intensive reduction processes of solution species on the electrode's surface, and the precipitation of surface films. These surface films consist mostly of Li salts, and they conduct Li-ions (and thus, do not interfere badly with Li insertion-deinsertion into/from the carbon). A mandatory condition for the use of an electrolyte solutions for Li-C anodes is that the reduction of the solution species on the carbon surface occurs at potentials higher than that of Li insertion potentials.¹³⁴ The products of solution reduction should have a good cohesion and a strong adhesion to the carbon surface. Hence, they should precipitate as quickly as possible to form passivating surface films, which efficiently block electron transfer from the negatively charged electrode to solution species.

Finally, it should be noted that the 3D structure of the carbon and the morphology of the particles plays a major role in determining its performance as a Li insertion anode material.¹³⁵ Disordered carbons are much more robust than graphitic carbons, and hence, the reversibility of Li insertion into them is much less dependent on the solution composition.¹³⁶ The smoother the surface through which Li is inserted into the carbon (*e.g.*, the edge plane facets of graphite particles), the faster are the surface film formation processes, and the better the passivation. As a graphitic carbon includes more turbostratic disorder in its 3D structure, it is more robust, and hence, it is influenced less by solution-related detrimental processes during intercalation with lithium.¹³⁵

18.5.2. Standard Electrolyte Solutions for Li-ion Batteries

Over the years, a large matrix of solvents, salts and additives was tested with graphite electrodes.¹³⁶⁻¹³⁸ As explained in the previous section, graphite is the most sensitive carbon material. Composite electrodes consisting of

synthetic graphite flakes seem to be the best probe to test suitable solutions for Li-ion batteries, because what works well with these electrodes should work even better with other types of graphite and with disordered carbons.¹³⁵ These intensive studies converged into the development of standard electrolyte solutions which are commonly used throughout the world in the mass production of commercial Li-ion batteries. These solutions include LiPF_6 as the electrolyte and alkyl carbonate solvents. EC is an obvious component,¹³⁹ together with cosolvents that are acyclic alkyl carbonates from the DEC,¹⁴⁰ DMC,¹⁴¹ EMC,⁵⁹ and PMC⁶⁰ list. The alkyl carbonate solvents are the most suitable because their anodic stability is higher than that of other families of solvents such as ethers and esters. Also, at low potentials both Li and Li-C compounds reach a very good passivation in a variety of alkyl carbonate solutions. It should be noted that neither ethers nor esters promote good passivation of Li-C electrodes.¹³²⁻¹³⁸ In the case of ethers, these solvents are not sufficiently reactive to form passivation layers at high enough potentials. Thus, ether molecules can easily cointercalate into graphite with Li-ions, which leads to the destruction of the graphite's structure (exfoliation).¹³³ The reduction products of esters are not cohesive and adhesive enough to form sufficiently passivating surface films on carbon electrodes.

Highly interesting, and deserving of discussion herein, is the failure of graphite electrodes in PC solutions. No graphite carbons can insert Li reversibly in pure PC solutions with Li salts.¹³⁴ It appears that some destructive processes take place at relatively high potentials (in which PC is reduced, 1.5-0.8 vs. Li/Li^+), and the electrodes cannot reach all of the Li intercalation stages.¹³² Reversible behavior of Li-graphite electrodes is obtained in mixtures of ethers and PC, PC solutions containing crown ethers (e.g., 12 Cr 4),¹⁴² and in EC-PC mixtures¹⁴³. In the latter solutions, the irreversible capacity is very strongly dependent on the morphology and degree of disorder of the graphite particles.¹³⁵ The fact that in solutions based on EC, which is similar in structure to PC, the behavior of Li-graphite electrodes is so reversible, is striking. PC is reduced on graphite below 1.5 V to species such as $\text{CH}_3\text{CH}(\text{OCO}_2\text{Li})\text{CH}_2\text{OCO}_2\text{Li}$ and $\text{CH}_3\text{CH}=\text{CH}_2$ (propylene gas), while EC is reduced to species such as $(\text{CH}_2\text{OCO}_2\text{Li})_2$ and ethylene gas.^{46,50} The EC reduction products, when formed, precipitate quickly on the graphite surface to form cohesive and adhesive surface films that passivate the electrode and block electron transfer, thus preventing any major surface reactions except for Li insertion (which include Li-ion migration through the surface films). The fast precipitation of the surface films in this case prevents detrimental side processes such as cointercalation of solvent molecules.

In the case of PC, its reduction product contains the methyl group, which interferes badly with the good cohesion and adhesion of the surface

species and formation of compact Li_2CO_3 film, as seen in the case of EC-formed surface film. As a result, an intensive PC reduction takes place at low potentials before passivation is completed. This allows a build up of internal pressure (due to propylene gas formation), which cracks the graphite particles and prevents their passivation by stable surface films.¹³⁵ The surface films in this case rather lead to electrical isolation of a great part of the active mass.^{133,135} Figure 18.7 illustrates the behavior of graphite electrodes in PC and EC solutions.¹³⁵ In PC-ether solutions, the surface chemistry of graphite electrodes is different: Li_2CO_3 , which is an excellent passivating agent, becomes a dominant surface species, and thus, efficient electrode passivation can be developed in these solutions.⁸⁶

The change in the surface chemistry in these cases relates to the possible formation of carbonate ion ($\text{CO}_3^{=}$ or LiCO_3^-), which may be a strong nucleophile in aprotic media. At high PC concentration, it attacks another PC molecule nucleophilically to form $\text{CH}_3\text{CH}(\text{OCO}_2\text{Li})\text{CH}_2\text{OCO}_2\text{Li}$, while at a low enough PC concentration it interacts with Li-ions and precipitates as Li_2CO_3 .⁸⁶ The difference in the behavior of graphite electrodes in PC and EC solutions, as well as the conclusion on the impact of the surface chemistry/surface film composition of the electrodes' behavior, serves as a good tool for understanding the failure and stabilization of graphite electrodes in solutions, and for designing optimized electrolyte solutions. A key issue is the formation of passivating, compact and stable surface films of high Li-ion conductivity at high enough potentials, before detrimental processes such as solvent cointercalation, build up of internal pressure, and exfoliation/cracking of graphite particles take place.

Regarding the choice of electrolyte, LiPF_6 was selected as the standard salt, which is commonly used in Li-ion batteries. Below we list some reasons for this, some of which relate to problems with alternative salts.

1. This salt is much less poisonous than LiAsF_6 , which is commercially better for both Li and Li-C anodes.
2. A very good passivation of the aluminum current collectors used for the cathodes is reached in LiPF_6 solutions, probably by AlF_3 (e.g., by reactions of trace HF, unavoidably present in all LiPF_6 solutions, with aluminum).⁴²
3. The conductivity of alkyl carbonates/ LiPF_6 solutions is relatively high. (See Table 18.4.)
4. The thermal stability of battery systems based on LiPF_6 solutions is acceptable, compared with systems containing LiClO_4 (a very good salt in terms of electrode performance at ambient temperatures), which are explosive.¹⁴⁴
5. The mass production of LiPF_6 is relatively easy and its price is acceptable.

However, LiPF_6 solutions have a pronounced disadvantage, which is

their unavoidable contamination with HF.¹⁴⁵ LiPF_6 decomposes into LiF and PF_5 in an equilibrium reaction.¹⁴⁶ The latter species readily hydrolyzes with protic substances to form PO_xF_y , $\text{P(OR)}_x\text{F}_y$ species and HF, which reacts with ROLi or ROCO_2Li surface species formed by alkyl carbonate reduction, and replaces them with highly resistive LiF surface films. HF also reacts with the Li_xMO_y cathode materials. The impact of the HF reactions on the electrodes' passivation is negative and the electrodes' impedance increases as HF surface reactions are more intensive.

In conclusion, the standard electrolyte solutions for Li-ion batteries are LiPF_6 solutions in mixtures of alkyl carbonates that always contain EC as a highly polar component and a precursor for very good passivating agents (e.g., $(\text{CH}_2\text{OCO}_2\text{Li})_2$)^{61,62} and solvents from the DMC, EMC, DEC list.¹³⁹⁻¹⁴¹ It should be emphasized that ternary mixtures such as EC-DMC-DEC enable a very good low temperature conductivity of LiPF_6 solutions to be reached.²⁵ The choice of these systems is mostly due to an acceptable passivation and stabilization of both anodes and cathodes for Li-ion batteries and a wide electrochemical window (*i.e.*, high anodic stability > 4.5 V *vs.* Li/Li^+ with lithiated transition metal oxide cathodes).⁴¹ Major problems with the use of these solutions in practical batteries relate mostly to HF contamination, which interferes badly with the electrodes' passivation. In addition, at elevated temperatures there are accelerated surface reactions on both anodes and cathodes, which increases their impedance and lead to apparent capacity-fading of Li-ion batteries.^{147,148} There is, therefore, a strong driving force for R&D of improved electrolyte solutions for Li-ion batteries, as summarized in the next section.

18.5.3. Advanced Electrolyte Solutions for Li-ion Batteries

Special challenges in R&D of new electrolyte solutions for Li-ion batteries include the following:

1. Increasing the anodic stability.
2. Increasing low temperature conductivity.
3. R&D of non-flammable solvents.
4. The use of acid scavengers.
5. R&D of more stable, non-contaminating salts.
6. Enhancing the passivation of the electrodes, especially at elevated temperatures.
7. Overcharge protection.

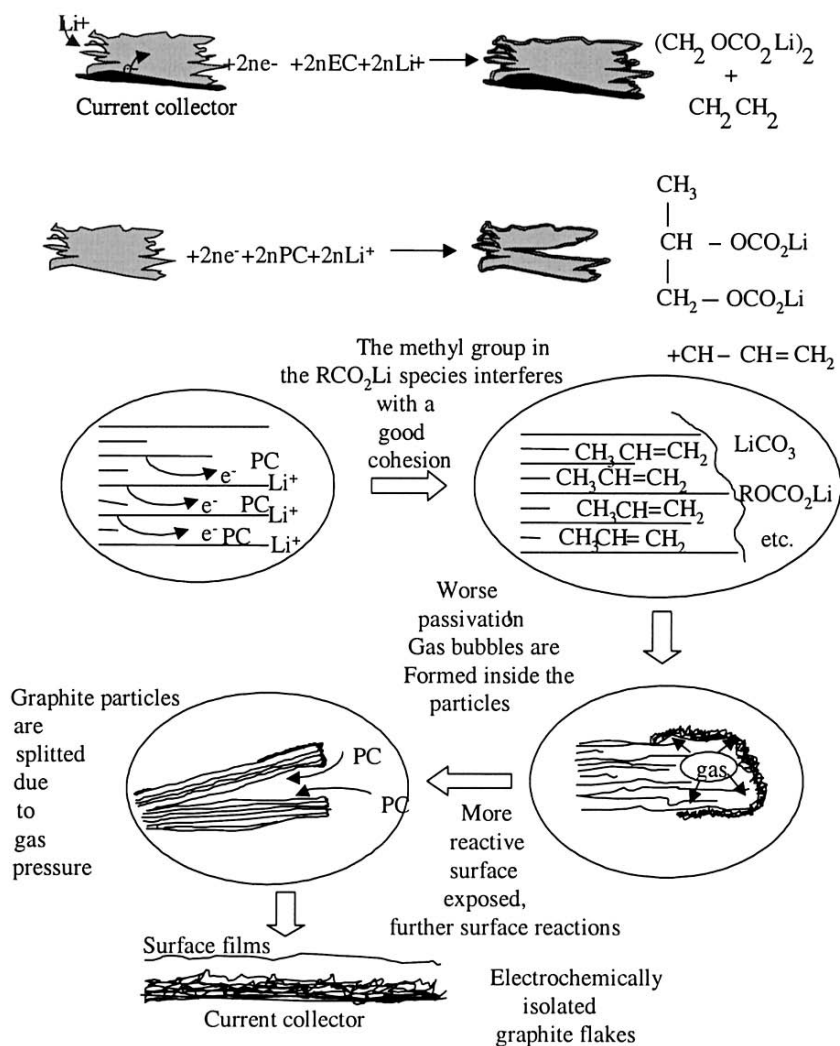


Figure 18.7. A schematic presentation of stabilization and failure mechanisms of graphite electrodes in alkyl carbonate solutions as indicated. Ref. 135.

It should be emphasized that the possibility of finding replacements for the currently used alkyl carbonate solvents and $LiPF_6$ is difficult. Much easier is the use of functional additives that improve the electrodes' interfaces and enhance conductivity. The R&D of special additives for Li-ion

battery solutions is indeed highly innovative, and opens the door for pronounced improvements in the battery's performance and safety features. Below we list typical solvents, salts, and additives that were suggested in recent years as desirable components in electrolyte solutions for Li-ion batteries.

We find in the literature a number of reports on substituted alkyl carbonate solvents that improve performance. Trans butylene carbonate was found to be a suitable single solvent in which graphite electrodes behave highly reversibly.¹⁴⁹ Chlorinated and fluorinated alkyl carbonates were also found to be very suitable^{150,151} for graphite anodes. The major importance of these solvents is their use as a replacement for EC, whose freezing point is too high (RT). There are studies of pyrocarbonates ($\text{ROCO}_2\text{CO}_2\text{R}$) and bicarbonates ($\text{ROCO}_2\text{ROCO}_2\text{R}$)¹⁵² as cosolvents. Their major advantage relates to modification of the surface chemistry of both anodes and cathodes and an improvement of the high temperature performance. Alkyl, aryl and allyl sulfites were tested as cosolvents that react predominantly on the anodes' surface, enhance passivation, and decrease the irreversible capacity of lithiated carbon anodes.¹⁵³ Alkyl nitrates,¹⁵⁴ sulfates¹⁵⁵ and phosphonates¹⁵⁶ were also suggested as passivation-improving additives whose presence in standard solutions reduces the irreversible capacity of Li-C anodes. Another additive that was the focus of attention is vinylene carbonate (VC).¹⁵⁷ VC is more reactive than EC on both anodes and cathodes. It is reduced on the anodes to ROCO_2Li and poly Li alkyl carbonate species, and may polymerize on the LiMO_x cathodes to form polycarbonates. The presence of VC in solutions reduces irreversible capacity and increases stability, especially at elevated temperatures.¹⁵⁷ Alkyl phosphates and phosphazenes were also suggested as non-flammable solvents for Li-ion batteries.¹⁵⁸ Alkyl phosphates were suggested recently as stabilizers for LiPF_6 solutions at high temperatures.¹⁵⁹

Aromatic species such as biphenyl were suggested as overcharging protection agents.¹⁶⁰ At excessive potentials, they may be reduced into radical anions at the negative or oxidize to radical cations at the positive electrode, after which the radical ions migrate/diffuse to the counter electrode to reversibly form the pristine compounds. We should also mention additives such as alkyl silanes¹⁶¹ and Li_2CO_3 , which can be considered as an acid scavenger.¹⁶² Active gases were also tested as additives for electrolyte solutions. CO_2 in solutions reacts on Li-C surfaces to form Li_2CO_3 , an excellent passivating agent.¹³⁷ SO_2 solutions react on Li-C to form Li_2S , Li_2SO_3 , $\text{Li}_2\text{S}_2\text{O}_4$, and Li_2O , which are also good passivating agents.¹⁶³ Recently, Li organo borate complexes were suggested as promising additives for improving high temperature performance.¹⁶⁴ What is described above in fact includes only a few typical examples of R&D of new additives for Li-ion battery solutions. In recent years we have seen intensive efforts to

develop additives that improve the passivation of the Li-ion battery electrodes.

Finally, we should review attempts to introduce new families of salts. Merck developed the $\text{LiPF}_3(\text{CF}_2\text{CF}_3)_3$ (LiFAP) salt.¹⁶⁵ It was proven that this salt is much more stable than LiPF_6 . Its solution is less acidic and more thermally stable than LiPF_6 solutions.¹⁶⁶ Both graphite anodes, LiCoO_2 and LiMn_2O_4 cathodes, behave better in LiFAP solutions than in LiPF_6 solutions, especially at elevated temperatures. The $\text{LiN}(\text{SO}_2\text{CF}_2\text{CF}_3)_2$ (BETI) salt was also introduced.¹⁶⁷ However, we found that for Li-ion battery systems its solutions are inferior in their electrochemical performance to LiPF_6 or LiFAP solutions.¹⁶⁶

Recently, the ‘LiBOB’, Li bis(oxalo)borate salt was suggested as a stable, non-acidic electrolyte.¹⁶⁸ Both Li-C and Li_xMO_y cathodes seem to behave highly reversibly in its solution. However, more work is needed to confirm that this salt is really an alternative to LiPF_6 .

18.6. MOLTEN SALTS

18.6.1. Introduction

Molten salts may be useful non-aqueous electrolyte systems for a variety of applications, including batteries.^{169,170} Ionic liquids of anhydrous salts, namely molten salts, usually have high conductivity and wide stability over large potential ranges.¹⁷¹

Especially important are the room temperature molten salts. The most widely studied are the chloroaluminate melts with organic cations such as methyl-ethylimidazolium, N-butyl pyridinium, pentamethylimidazolium, and 1,2-dimethyl-1,2,4 triazolium.¹⁷²

Regarding the conductivity of molten salts, unlike conventional nonaqueous solutions, where the medium is almost unaffected by the electrical field, in molten salts the properties of a medium which consists only of ions are affected by the applied electric field. It is often found that the equivalent conductivity increases as the electrical field applied is higher, up to a certain point where a plateau is reached.¹⁷³ Regarding the conductivity of molten salts, several conduction mechanisms have been proposed to explain their high electrical conductivity.^{174,175} With organic RT molten salts, a maximum conductivity is usually reached with neutral systems.¹⁷⁶

18.6.2. Electrochemical Properties of Molten Salt Solutions and Battery Applications

The potential windows of molten salts are very important for their electrochemical applications. The limiting potentials depend on the composition of the melts and the temperature, which affect the standard potential of reduction and oxidation of their components.

In the case of room temperature molten salts, the anion is typically a mixture of aluminum halide complexes in equilibrium. These anions can undergo several oxidation reactions, depending on the composition of the melt. The cathodic reactions may involve reductions of the organic cations.¹⁷⁷

It was possible to obtain reversible Li and Al dissolution and deposition in some RT organic molten salts.¹⁷² Hence, these molten salts may be considered as possible electrolyte systems for rechargeable nonaqueous lithium and aluminum batteries.

Recent work on the behavior of cathodes for Li batteries (e.g., Li_xMO_y , $\text{M}=\text{Mn, Co}$)^{178,179} clearly demonstrates that RT molten salts may be promising electrolytes for secondary Li-ion batteries as well, comprising cations such as ethyl methyl imidazolium and anions such as Cl^- , BF_4^- , and AlCl_4^- .

Finally, there are reports on the use of these systems in super (EDL) capacitors.¹⁸⁰

REFERENCES

1. C. R. Schlaikjer, in *Lithium Batteries*, J. P. Gabano, Ed., Academic Press, London (1983), Chapter 13, p. 304.
2. E. Garcia, A. J. Bard, *Chem. Phys. Lett.* 120 (1985) 437.
3. M. Elam, E. Peled, E. Gileadi, *J. Electrochem. Soc.* 131 (1984) 2058.
4. E. Peled, M. Brand, E. Gileadi, *J. Electrochem. Soc.* 128 (1981) 1697.
5. I. Galasio, R. Galasio, J. Thonstad, in *Nonaqueous Electrochemistry*, Wiley-VCH, Weinheim (2002), Chapter 12, p. 342.
6. G. Blomgren, in *Nonaqueous Electrochemistry*, D. Aurbach, Ed., Marcel Dekker, N.J. (1999), Chapter 2, p. 53.
7. M. Swarc, in *Ions and Ion Pairs in Organic Reactions*, Vol. 1, M. Swarc, Ed., Wiley-Interscience, New York, (1972), Chapter 1.
8. C. Reichardt, *Angew. Chem. Int. Ed. Engl.* 18 (1979) 87.
9. U. Mayer, in *Proceedings of the Workshop on Lithium Nonaqueous Battery Electrochemistry*, E. B. Yeager, B. Schumm, Jr., G. Blomgren, D. R. Blankenship, V. Leger, J. Akridge, Eds., The Electrochemical Society, Inc., PV 80-7, 1980, p. 13.
10. K. Dimrot, C. Reichardt, T. Siepmann, F. Bohlmann, *Justus Liebig's Ann. Chem.* 661 (1963) 2; K. Dimrot, C. Reichardt, *ibid.* 727 (1969) 93.

11. Z. B. Maksimovic, C. Reichardt, A. Spiric, *ibid.* 270 (1974) 100.
12. U. Mayer, *Pure Appl. Chem.* 51 (1979) 1697.
13. V. Gutmann, *The Donor-Acceptor Approach to Molecular Interactions*, Plenum Press, New York, 1978.
14. U. Mayer, *Monatsch. Chem.* 108 (1977) 1479.
15. J. F. Coetzee, in *Proceedings of the Workshop on Lithium Nonaqueous Battery Electrochemistry*, E. B. Yeager, B. Schumm, Jr., G. Blomgren, D. R. Blankenship, V. Leger, J. Akridge, Eds., The Electrochemical Society, Inc., softbound series PV 80-7, 1980, p. 70.
16. G. R. Hedwig, D. A. Owensby, A. J. Parker, *J. Am. Chem. Soc.* 97 (1975) 3888.
17. P. W. Atkins and J. D. Paula, *Physical Chemistry*, 7th ed. Oxford University Press, Oxford, Melbourne, Tokyo, 2002, Chapter 24.
18. S. H. Maron, J. B. Lando, *Fundamentals of Physical Chemistry*, Macmillan, New York; Collier Macmillan, London, 1974, Chapter 13, Eq. 40.
19. R. M. Fuoss, *J. Am. Chem. Soc.* 80 (1958) 5059.
20. R. M. Fuoss, T. Shedlovsky, *J. Am. Chem. Soc.* 71 (1949) 1496.
21. H. V. Venkatesetty, in *Proceedings of the Workshop on Lithium Nonaqueous Battery Electrochemistry*, E. B. Yeager, B. Schumm, Jr., G. Blomgren, D. R. Blankenship, V. Leger, J. Akridge, Eds., The Electrochemical Society, Inc., softbound series PV 80-7, 1980, p. 46.
22. J. F. Casteel, E. A. Amis, *J. Chem. Eng. Data* 17 (1972) 55.
23. C. A. Angell, J. C. Tucker, *J. Phys. Chem.* 78 (1974) 278.
24. J. Barthel, H. G. Gores, P. Carlier, F. Feuerlein, M. Utz, *Ber. Bunsenges. Phys. Chem.* 87 (1983) 436.
25. M. C. Smart, B. V. Ratnakumar, S. Surampudi, *J. Electrochem. Soc.* 146 (1999) 486; M. C. Smart, B. V. Ratnakumar, S. Surampudi, *ibid.* 149 (2002) A361.
26. O. Youngman (Chusid), Y. Gofer, A. Meitav, P. Dan, D. Aurbach, *Electrochim. Acta* 35 (1990) 625.
27. D. Aurbach, Y. Gofer, *J. Electrochem. Soc.* 138 (1991) 3529.
28. T. B. Reddy, S. Hossain, in *Handbook of Batteries*, 3rd Edition, D. Linden and T. B. Reddy, Eds., McGraw Hill, Inc., N.Y., 2002, Chapter 34.
29. J. Barthel, H.-J. Gores, in *Chemistry of Nonaqueous Solutions*, G. Mamantov and A. I. Popov, Eds., VCH, New York, 1994, p. 1.
30. J. T. Dudley, D. P. Wilkinson, G. Thomas, R. LeVae, S. Woo, H. Blom, C. Horvath, M. W. Juzkow, B. Denis, P. Aghakian, J. R. Dahn, *J. Power Sources* 35 (1991) 59.
31. M. Salomon, E. J. Plichta, *Electrochim. Acta* 30 (1985) 113.
32. K. Hayashi, Y. Nemoto, S. Tobishima, J. Yamaki, *Electrochim. Acta* 44 (1999) 2337.
33. G. M. Swain, A. B. Anderson, J. C. Angus, *MRS Bulletin* 23 (1998) 56.
34. D. Aurbach, in *Nonaqueous Electrochemistry*, D. Aurbach, Ed., Marcel Dekker, N.Y. 1999, Chapter 6, p. 289.
35. J. O. Besenhard, G. Eichinger, *J. Electroanal. Chem.* 60 (1976) 1.
36. M. W. Verbrugge, B. J. Koch, *J. Electrochem. Soc.* 141 (1994) 3053.
37. D. Aurbach, R. Skaletsky, Y. Gofer, *J. Electrochem. Soc.* 138 (1991) 3536.
38. Z. Lu, A. Schechter, M. Moshkovich, D. Aurbach, *J. Electroanal. Chem.* 466 (1999) 203.
39. E. Peled, in *Li Batteries*, J. P. Gabano, Ed., Academic Press, N.Y. and London 1983, Chapter 3, p. 43.
40. D. A. Shifler, P. J. Moran, J. Kruger, *Electrochim. Acta* 42 (1997) 567.
41. K. Kanamura, *J. Power Sources* 81-82 (1999) 123.
42. M. Morita, T. Shibata, N. Yoshimoto, M. Ishikawa, *Electrochim. Acta* 47 (2002) 2787.
43. J. R. Dahn, A. K. Sleight, H. Shi, B. M. Way, W. J. Weydanz, J. N. Reimers, Q. Zhong, U. von Sacken, *Lithium Batteries – New Materials, Developments and Perspectives*, G. Pistoia, Ed., Elsevier-North Holland, Amsterdam 1992, p. 1.

44. T. Ohzuku, A. Veda, M. Nagayama, Y. Iwakoshi, H. Komori, *Electrochim. Acta* 38 (1993) 1159.
45. P. Novak, K. Muller, K. S. V. Santhanam, O. Hass, *Chem. Rev.*, 97, 207 (1997); M. Gazard in *Handbook of Conducting Polymers*, Vol. 1, T. A. Skotheim, Ed., Marcel Dekker, New York, 1988, Chapter 19.
46. D. Aurbach, H. E. Gottlieb, *Electrochim. Acta* 34 (1989) 141.
47. D. Aurbach, *J. Electrochem. Soc.* 136 (1989) 906.
48. D. Aurbach, *J. Electrochem. Soc.* 136 (1989) 1606.
49. D. Aurbach, M. L. Daroux, P. Faguy, E. Yeager, *J. Electrochem. Soc.* 134 (1987) 1611.
50. D. Aurbach, Y. Gofer, M. Ben-Zion, P. Aped. *J. Electroanal. Chem.* 339 (1992) 451.
51. D. Aurbach, M. L. Daroux, P. Faguy, E. Yeager, *J. Electroanal. Chem.* 297 (1991) 225.
52. D. Aurbach, M. Moshkovich, Y. Gofer, *J. Electrochem. Soc.* 148 (2001) E155.
53. D. Aurbach, Y. Ein-Eli, *Langmuir* 8 (1992) 1845.
54. D. T. Sawyer, G. Chlericato, C. T. Angelsi, E. J. Nanni, T. Tsuchiya, *Anal. Chem.* 54 (1982) 1720.
55. B. Burrows, S. Kirkland, *J. Electrochem. Soc.* 115 (1968) 1164.
56. Y. Ein-Eli, B. Markovsky, D. Aurbach, *J. Power Sources* 54 (1995) 281.
57. D. Aurbach, A. Zaban, O. Chusid, I. Weismann, *Electrochimica Acta* 39 (1994) 51.
58. D. Aurbach, E. Granot, *Electrochimica Acta* 42 (1997) 697.
59. D. Aurbach, A. Schechter, B. Markovsky, Y. Ein-Eli, V. Koch, *J. Electrochem. Soc.* 143 (1996) L273.
60. Y. Ein-Eli, S. F. McDevitt, B. Markovsky, A. Schechter, D. Aurbach, *J. Electrochem. Soc.* 144 (1997) L 180.
61. D. Aurbach, A. Zaban, A. Schechter, Y. Ein-Eli, E. Zinigrad, B. Markovsky. *J. Electrochem. Soc.* 142 (1995) 2873.
62. D. Aurbach, B. Markovsky, A. Schechter, Y. Ein-Eli, H. Cohen, *J. Electrochem. Soc.* 143 (1996) 3809.
63. D. Aurbach, O. Chusid, I. Weissman, *Electrochimica Acta* 41 (1996) 747.
64. E. Goren, O. Chusid, D. Aurbach, *J. Electrochem. Soc.* 138 (1991) L6.
65. O. Chusid (Youngman), D. Aurbach, *J. Electrochem. Soc.* 140 (1993) L1.
66. D. Aurbach, O. Chusid, *J. Electrochem. Soc.* 140 (1993) L155.
67. D. Aurbach, Y. Ein-Eli, and A. Zaban, *J. Electrochem. Soc.* 141 (1994) L1.
68. M. Arakawa, J. I. Yamaki, *J. Power Sources* 54 (1995) 250.
69. G. Eggert, J. Heitbaum, *Electrochim. Acta* 31 (1986) 1443.
70. F. Joho, P. Novak, *Electrochim. Acta*, 45 (2000) 3589.
71. M. Moshkovich, M. Cojocar, H. E. Gottlieb, D. Aurbach, *J. Electroanal. Chem.* 497 (2001) 84.
72. J. E. Dubois, G. Tourillon, P. C. Lacaze, *J. Electrochem. Soc.* 125 (1978) 1257.
73. D. H. Jang, S. M. Oh, *J. Electrochem. Soc.* 144 (1997) 3344.
74. K. Kanamura, S. Toriyama, S. Shiraishi, Z. Takehara, *J. Electrochem. Soc.* 143 (1996) 2548.
75. G. Eggert, J. Heitbaum, *Electrochim. Acta* 31 (1986) 1443.
76. B. Rasch, E. Cattaneo, P. Novak, W. Vielstich, *Electrochim. Acta* 36 (1991) 1397.
77. D. Aurbach, Y. Gofer, M. Ben-Zion, *J. Power Sources* 39 (1992) 163.
78. J. A. Seel, J. R. Dahn, *J. Electrochem. Soc.* 147 (2000) 892.
79. D. Aurbach, B. Markovsky, M. D. Levi, E. Levi, A. Schechter, M. Moshkovich, Y. Cohen, *J. Power Sources* 81-82 (1999) 95.
80. F. Ossola, G. Pistoia, R. Seeber, P. Ugo, *Electrochim. Acta* 33 (1988) 47.
81. L. A. Zvat'kova, V. N. Atanasev, G. A. Krestov, T. V. Ivanova, *Elektrokhimiya* 29 (1993) 946.
82. R. Herr, *Electrochim. Acta* 35 (1990) 1257.
83. M. Ue, K. Ida, S. Mori, *J. Electrochem. Soc.* 141 (1994) 2989.

84. K. T. Ciemieki and J. A. Auburn, in *Proceedings of the Symposium on Lithium Batteries*, A. N. Dey, Ed., ECS Meeting, Washington, The Electrochemical Society, Inc., softbound series PV 84-1, The Electrochemical Society, Inc., Pennington, N.J., 1984, p. 363.
85. C. K. Mann, in *Electroanalytical Chemistry*, A. J. Bard, Ed., Marcel Dekker, New York, 1970, Vol. 3.
86. D. Aurbach, M. D. Levi, E. Levi, A. Schechter, *J. Phys. Chem. B* 101 (1997) 2195.
87. K. Wang, P. N. Ross, Jr., F. Kong, F. McLarnon, *J. Electrochem. Soc.* 143 (1996) 422.
88. D. Aurbach, E. Zinigrad, A. Zaban, *J. Phys. Chem.* 100 (1996) 3089.
89. A. Schechter, D. Aurbach, *Langmuir* 15 (1999) 3334.
90. K. Kanamura, H. Tamura, Z.-I. Takehara, *J. Electroanal. Chem.* 333 (1992) 127.
91. K. Kanamura, S. Shiraishi, Z.-I. Takehara, *J. Electrochem. Soc.* 143 (1996) 2187.
92. K. Kanamura, S. Shiraishi, H. Tamura, and Z.-I. Takehara, *J. Electrochem. Soc.* 141 (1994) 2379.
93. E. Peled, D. Golodnitsky, and J. Penciner, in *Handbook of Battery Materials*, J. O. Besenhard, Ed., Wiley-VCH, New York, 1999, Chapter 6, p. 419.
94. E. Peled, *J. Electrochem. Soc.* 126 (1979) 2047.
95. D. Aurbach, Y. Gofer, Y. Langzam, *J. Electrochem. Soc.* 136 (1989) 3198.
96. D. Aurbach, Y. Cohen, *Electrochem. Solid-State Lett.* 2 (1999) 16.
97. D. Aurbach, Yaron Cohen, *J. Phys. Chem. B* 104 (51) (2000) 12282.
98. V. S. Bagotzky, A. M. Skundin, *Russ. J. Electrochem.* 31 (1995) 308; translated from *Elektrokhimiya* 31 (1995) 342.
99. K. M. Abraham, S. B. Brummer, in *Li Batteries*, J. P. Gabano, Ed., Academic Press, N.Y. and London 1983, Chapter 14, p. 371.
100. V. R. Koch, J. L. Goldman, D. L. Natwing, *J. Electrochem. Soc.* 129 (1982) 1.
101. D. Aurbach, I. Weissman, A. Schechter, H. Cohen, *Langmuir* 12 (1996) 3991.
102. S. Tobishima, M. Arakawa, T. Hirai, J. Yamaki, *J. Power Sources* 28 (1989) 449.
103. K. M. Abraham, J. L. Goldman, D. L. Natwig, *J. Electrochem. Soc.* 129 (1982) 2404.
104. D. P. Wilkinson, H. Blom, K. Brandt, D. Wainwright, *J. Electroanal. Chem.* 355 (1993) 193.
105. V. R. Koch, R. H. Young, *Science* 204 (1979) 499.
106. E. Plichta, M. Salomon, S. Shane, M. Uchiyama, *J. Power Sources* 21 (1987) 25.
107. Y. Matsuda, M. Morita, *J. Power Sources* 26 (1989) 579.
108. I. R. Hill, B. G. Anderson, M. Goledzinowski, R. J. Dore, *J. Electrochem. Soc.* 142 (1995) 3267.
109. B. J. Carter, B. Jeffries, S. P. S. Yen, in *Proceedings of the Symposium on Lithium Batteries*, A. N. Dey, Ed., The Electrochemical Society, Inc., softbound series PV 87-1, 1987, p. 145.
110. Y. Matsuda, M. Morita, H. Nigo, in *Proceedings of the Symposium on Primary and Secondary Lithium Batteries*, K. M. Abraham and M. Salomon, Eds., The Electrochemical Society, Inc., softbound series PV 91-3, 1991, p. 272.
111. J. Yamaki, S. Tobishima, in *Proceedings of the Symposium on Primary and Secondary Lithium Batteries*, K. M. Abraham and M. Salomon, Eds., The Electrochemical Society, Inc., softbound series PV 91-3, 1991, p. 235.
112. C. D. Desjardins, T. G. Green, G. K. Maclean, *J. Power Sources* 12 (1988) 489.
113. N. Kumagai, Y. Kikuchi, K. Tanno, *J. Appl. Electrochem.* 22 (1992) 620.
114. D. P. Wilkinson, D. Wainwright, *J. Electroanal. Chem.* 335 (1993) 193.
115. D. Aurbach, *J. Power Sources* 89 (2000) 206.
116. P. Biensan, B. Simon, J. P. Peres, A. de Guibert, M. Broussely, J. M. Bodet, *J. Power Sources* 81-82 (1999) 906.
117. L. Dominey, in *Nonaqueous Electrochemistry*, D. Aurbach, Ed., Marcel Dekker, N.Y. 1999, Chapter 8, p. 437.
118. K. M. Abraham, D. M. Pasquariello, F. J. Martin, *J. Electrochem. Soc.* 133 (1986) 662.
119. K. M. Abraham, D. M. Pasquariello, D. A. Schwartz, *J. Power Sources* 26 (1989) 247.

120. C. D. Desjardins, T. G Cadger, R. S. Salter, G. Donaldson, E. J. Casey, *J. Electrochem. Soc.* 132 (1985) 529.
121. D. Aurbach, A. Zaban, Y. Gofer, O. Abramson, M. Ben-Zion, *J. Electrochem. Soc.* 142 (1995) 687.
122. K. M. Abraham, *J. Power Sources* 14 (1985) 179.
123. J. L. Goodman, L. A. Dominey, V. Koch, *J. Power Sources* 26 (1989) 519.
124. D. Aurbach, I. Weissman, A. Zaban, Y. Ein-Eli, E. Mengeritsky, P. Dan, *J. Electrochem. Soc.* 143 (1996) 2110.
125. P. Dan, E. Mengeritsky, Y. Geronov, D. Aurbach, I. Weissman. *J. Power Sources* 54 (1995) 143.
126. D. Aurbach, E. Zinigrad, H. Teller, P. Dan, *J. Electrochem. Soc.* 147 (2000) 2486.
127. D. Aurbach, E. Zinigrad, H. Teller, Y. Cohen, G. Salitra, *J. Electrochem. Soc.* 149 (2002) A1267.
128. T. Osaka, in *Nonaqueous Electrochemistry*, D. Aurbach. Ed., Marcel Dekker, N.Y. 1993, Chapter 7, p. 441.
129. J. B. Goodenough, in *Advances in Li-ion Batteries*, W. A. Van Schalkwijk and B. Scrosati, Eds., Kluwer Academic/Plenum Publishers, N.Y., London and Moscow 2002, Chapter 4, p. 135.
130. D. D. MacNeil, Z. Lu, J. R Dahn, *J. Electrochem. Soc.* 149 (2002) A1332.
131. Y. Ein-Eli, M. A. Rzeznik, S. Mukerjee, X. Q. Yang, J. McBreen, *J. Electrochem. Soc.* 145 (1998) 3383.
132. M. Winter, J. O. Besenhard, in *Handbook of Battery Materials*, J. O. Besenhard, Ed., Wiley-VCH, Weinheim, New York, Chapter 5, 1990, p. 383.
133. D. Aurbach, B. Markovsky, K. Gamolsky, E. Levi, Y. Ein-Eli, *Electrochimica Acta*, 45 (1999) 67.
134. E. Buie, and J. R. Dahn, *Electrochim. Acta* 45 (1999) 121.
135. D. Aurbach, H. Teller, E. Levi. *J. Electrochem. Soc.* 149 (2002) A1255.
136. D. Aurbach, O. Youngman Chusid, Y. Carmeli, M. Babai, Y. Ein-Eli, *J. Power Sources* 43 (1993) 47.
137. D. Aurbach, B. Markovsky, Y. Ein-Eli, Y. Carmeli, H. Yamin, S. Luski, *Electrochim. Acta* 39 (1994) 2559.
138. R. Yazami, *Electrochim. Acta* 45 (1999) 87.
139. D. Guyomard, J. M. Tarascon, *J. Power Sources* 54 (1995) 92.
140. J. M. Tarascon, and D. Guyomard, *Solid State Ionics* 69 (1994) 293.
141. D. Guyomard, J. M. Tarascon, *J. Electrochem. Soc.* 140 (1993) 3071.
142. Z. X. Shu, R. S. McMillan, J. J. Murray, *J. Electrochem. Soc.* 140 (1993) 922.
143. R. Fong, U. Von Sacken, J. R. Dahn, *J. Electrochem. Soc.* 137 (1990) 2009.
144. M. N. Richard, J. R. Dahn, *J. Electrochem. Soc.* 146 (1999) 2068.
145. U. Heider, R. Oesten, M. Jungnitz, *J. Power Sources* 81-82 (1999) 119.
146. S. E. Sloop, J. K. Pugh, S. Wang, J. B. Kerr, K. Kinoshita, *Electrochem. Solid-State Lett.* 4 (2001) A42.
147. D. Aurbach, B. Markovsky, A. Rodkin, M. Cojocaru, E. Levi, H. J. Kim, *Electrochim. Acta* 47 (2002) 1899.
148. M. Broussely, in *Advances in Li-ion Batteries*, W. A. Van Schalkwijk and B. Scrosati, Eds., Kluwer Academic/Plenum Publishers, N.Y., London and Moscow 2002, Chapter 13, p. 393.
149. G. C. Chung, H. J. Kim, S. H. Jun, J. W. Choi, M. H. Kim, *J. Electrochem. Soc.* 147 (2000) 4398.
150. X. Z. Shu, R. S. McMillan, J. J. Murray, J. J. Davidson, *J. Electrochem. Soc.* 142 (1995) L161.
151. M. Inaba, Y. Kawatate, A. Funabiki, S. K. Jeong, T. Abe, Z. Ogumi, *Electrochim. Acta* 45 (1999) 99.
152. H. Gan, E. S. Takeuchi, "Dicarbonate Additives for Nonaqueous Electrolyte

- Rechargeable Cells," (Wilson Greatbatch Ltd., USA), Application for US Patent, N. 2001:45110.
153. G. H. Wrodnigg, J. O. Besenhard, M. Winter, *J. Power Sources* 97-98 (2002) 592.
154. H. Gan and E. S. Takeuchi, "Nitrate Additives for Nonaqueous Electrolyte Rechargeable Cells," (Wilson Greatbatch Ltd., USA), Application for US Patent, N. 2000:752090.
155. H. Gan and E. S. Takeuchi, "Sulfate Additives for Nonaqueous Electrolyte Rechargeable Cells," (Wilson Greatbatch Ltd., USA), Application for Eur. Patent Appl. Ep./2001, N. 2001:451045 7.
156. H. Gan and E. S. Takeuchi, "Phosphonate Additives for Nonaqueous Electrolyte Rechargeable Cells," (Wilson Greatbatch Ltd., USA), US Patent Application, US 2002, N. 2001:453468; US Patent 6,200,701.
157. D. Aurbach, K. Gamolsky, B. Markovsky, Y. Gofer, *Electrochim. Acta* 47 (2002) 1423.
158. K. Xu, M. S. Ding, S. Zhang, J. L. Allen, T. R. Jow, *J. Electrochem. Soc.* 149 (2002) A622.
159. S. S. Zhang, J. Ku, T. R. Jow, *Electrochem. Solid-State Lett.* 5 (2002) A206.
160. H. Mao, "Polymerizable Aromatic Additives for Overcharge Protection in Secondary Nonaqueous Lithium Batteries," (MOLI Energy (1990) Ltd. Can.): Eur. Pat. Appl.; Ep./1997, An. 1997:257375.
161. H. Buqa, M. V. S. Alvarez, J. O. Besenhard, M. Winter, *J. Power Sources* 97-98 (2001) 126.
162. A. M. Stux and J. Barker, "Carbonate Additive for Inhibiting Decomposition of Lithium Salts in Nonaqueous Battery Electrolyte and Electrolytes Containing this Additive," (Valence Technology, Inc., USA). US Patent Application, US, 1998, An. 1998:44815.
163. Y. Ein-Eli, S. R. Thomas, V. R. Koch, *J. Electrochem. Soc.* 143 (1996) L195.
164. D. Aurbach, B. Markovsky, K. Gamolsky, M. Koltypin, U. Heider, M. Schmidt, *ITE Battery Letters*, Vol. 2, No. 3, B46 (2001).
165. M. Schmidt, U. Heider, A. Kuehner, R. Oesten, M. Jungnitz, N. Ignat'ev, P. Sartori, *J. Power Sources* 97-98 (2001) 557.
166. J. S. Gnanaraj, M. D. Levi, Y. Gofer, and D. Aurbach, *J. Electrochem. Soc.* (2002), in press.
167. K. Naoi, M. Nori, Y. Naruoka, W. M. Lamanna, R. Atanasoski, *J. Electrochem. Soc.* 146 (1999) 462.
168. K. Xu, S. S. Zhang, R. R. Jow, W. Xu, C. A. Angell, *Electrochem. Solid-State Lett.* 5 (2002) A26.
169. E. J. Cairns, R. K. Steunenbergh, in "Progress in High Temperature Physics and Chemistry," Vol. 5, C. A. Rouse, Ed., Pergamon Press, New York, 1973, p. 63.
170. E. J. Cairns, "Batteries in Molten Salt Technology," D. G. Lovering, Ed. Plenum Press, N.Y. (1972), p. 287.
171. C. L. Hussey, in *Advances in Molten Salt Chemistry*, Vol. 5, G. Mamantov and C. B. Mamantov, Eds., Elsevier, Amsterdam, 1983, pp. 55-78.
172. A. Webber, G. E. Blomgren, in *Advances in Li-ion Batteries*, W. A. Van Schalkwijk and B. Scrosati, Eds., Kluwer Academic/Plenum Publishers, N.Y., London and Moscow, Chapter 6, p. 185.
173. T. A. Zawodzinski, R. A. Osteryoung, *Inorg. Chem.* 29 (1990) 2842.
174. B. R. Sundheim, in *Fused Salts*, B. R. Sundheim, Ed., McGraw-Hill, New York, 1964, Chapter 3.
175. G. J. Janz, *Molten Salts Handbook*, Academic Press, New York, 1967, p. 344.
176. J. S. Wilkes, J. A. Levisky, R. A. Wilson, C. Li Hussey, *Inorg. Chem.* 21 (1982) 1263.
177. P. R. Gifford, J. B. Palmisano, *J. Electrochem. Soc.* 134 (1987) 610.
178. Y. S. Fung, R. Q. Zhou, *J. Power Sources* 81-82 (1999) 891.
179. K. Vi, N. Koura, Y. Idemoto, K. Iyzuka, *Denki Kagaku* 65 (1997) 161.
180. A. B. McEwen, H. K. Ngo, K. Le Compte, J. L. Goldman, *J. Electrochem. Soc.* 146 (1996) 1687.

Chapter 19

POLYMERIC ELECTROLYTES: AN OVERVIEW

J. B. Kerr

Lawrence Berkeley National Laboratory, Berkeley, California, 94720, USA

19.1. INTRODUCTION

Ionically conducting polymers have been the focus of much fundamental and applied research for many years. Polyelectrolyte membranes have found significant technological use in the production of chlorine and caustic soda,¹ as separators in fuel cells^{2,3} and in electrodialysis^{4,5} for example. The discovery of ionic conductivity in polyethylene oxide solutions of alkali metal salts^{6,7} led the way for the introduction of polymer electrolyte in devices such as lithium batteries and electrochromic windows.^{8,9} Since those early days many books,¹⁰⁻¹³ book chapters⁸ and reviews^{9,14-19} have been published on these materials and the reader is referred to these for more detailed information.

In a recent article Scrosati and Vincent¹⁵ have listed the desired properties of a polymer electrolyte for use in lithium batteries. These are adequate conductivity, high cation mobility, good mechanical properties, good interfacial contact with electrodes, wide electrochemical stability, chemical and thermal stability, safety and ease of processing. This set of properties is understandably difficult to obtain in a single material and a number of different classes of polymer electrolyte materials have been defined which possess most but not all of the desired properties. Wright¹⁴ has further elaborated on this classification and defined them as:

1. Solvent-containing gel and hybrid systems.
2. Solvent-free, ion-coupled systems.
3. "Single-ion" systems and systems with reduced anion mobility.
4. Decoupled systems.

These classifications are useful for distinguishing different mechanisms of ion transport in the bulk separator. However, the complete

property requirements are most easily appreciated in the context of the lithium battery application and it is a purpose of this chapter to attempt to link the theoretical considerations of ion transport with the practical requirements of the battery in order to provide a rationale for material selection. For this we shall explore a mix of quantum chemistry, molecular dynamics, synthesis, mechanical and transport property measurements with system modeling and chemical reactivity considerations. Although this is by no means an exhaustive survey of useful techniques and approaches, it is hoped that it will provide an overview of the methods available to study the problems involved in preparation and use of polymer electrolytes.

19.2. LITHIUM ION TRANSPORT IN LITHIUM BATTERIES

Rigorous performance demands are made by battery engineers on organic electrolyte solutions in rechargeable lithium batteries. These materials, whether liquids, gels or polymers, are in intimate contact with strongly reducing lithium metal or lithiated carbon and with reactive, highly oxidizing metal oxides related to materials widely used for catalysis in other fields of technology. Figure 19.1 shows a schematic diagram of a typical lithium battery system which shows the basic components and the role of the

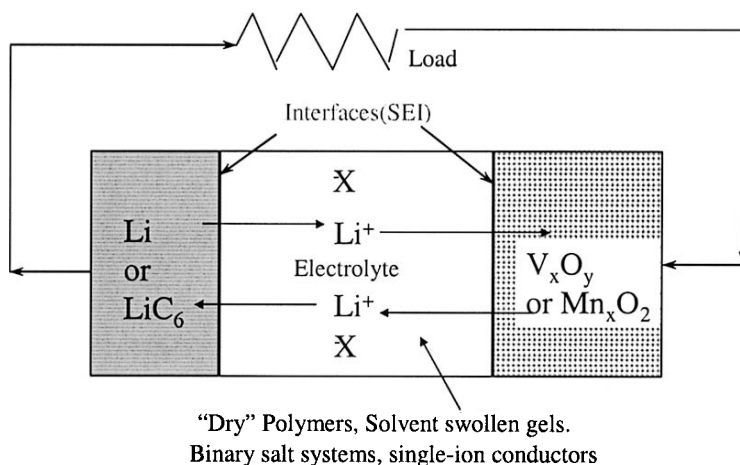


Figure 19.1. Schematic diagram of a rechargeable lithium battery (relative thickness of the electrolyte exaggerated relative to the electrodes).

electrolyte in separating the electrodes while facilitating the passage of lithium ions between them.

In any rechargeable lithium battery capable of achieving desirable performance three main processes must occur. Lithium ions must pass from the anode into the solution, ions must be transported across the separator efficiently (good lithium ion transport properties) and react or be intercalated efficiently and reversibly at the cathode. Since the battery should be recharged, the process must be reversed with very high efficiency (>99.99%) in order to achieve a high cycle life. In addition the electrolyte must not react with the electrodes while the battery is at open circuit thereby providing a long calendar life (15 years for electric vehicle use). Since no organic compound is thermodynamically stable to 0 volts *vs.* lithium metal, these requirements are stiff indeed! Fortunately, the formation of surface films at the electrodes limits the extent of these reactions and reduces the rates to levels that allow the useful cycle and calendar life of the battery to be achieved. An extensive review on this topic has recently appeared²⁰ to which the reader is referred. For the present discussion however, it is important to note that these surface films provide layers with very different transport properties from the bulk electrolyte and through which the lithium ions must pass. These layers are frequently referred to as the solid electrolyte interphase or SEI and they play a crucial role in both the cycle life and also in the rate capability of the battery.

Although chemical and thermal stability of the bulk electrolyte would seem to be a prerequisite for long life, the most commonly used liquid electrolytes in Li-ion batteries (ethylene carbonate/dimethyl carbonate/LiPF₆) are not stable on standing.²¹ They have been shown to react on standing to form transesterification products, a reaction that is catalyzed by the presence of acids or bases in the electrolytes. Such acids and bases can be formed through oxidation or reduction reactions at the electrodes or they may be present in the electrolyte itself either as an impurity (HF) or an intrinsic property of one of the components. LiPF₆, LiBF₄ and LiAsF₆ have all been shown to generate the Lewis acids PF₅, BF₃ and AsF₅ which are known to catalyze the ring-opening polymerization of ethylene carbonate²² to polyethylene ether carbonates and other polymer materials with the accompanying production of CO₂ gas. Even though these electrolytes appear to be unacceptably reactive, the reactions play an important role in the formation of the SEI and hence the cycle and calendar life of the battery.

Prior to the development of intercalation anodes for lithium ion batteries, much attention was given to the behavior of the rechargeable lithium metal electrode with liquid electrolytes such as 1,3-dioxolane,²³⁻²⁵ THF and 2-methyltetrahydrofuran (2-MeTHF)²⁵⁻²⁷ containing LiClO₄, LiBR₄ and LiAsF₆ salts. The Lewis acidity of the AsF₅ formed from the AsF₆⁻ was found to play a crucial role in forming surface layers that enhance the cycling

efficiency. Impressive cycle lifetimes were obtained for the lithium electrode under certain conditions ($\text{Li}_{\text{FOM}} > 100$). Parameters such as the purity of the electrolyte and the lithium metal, prior history (exposure to heat or light), presence of surface-active additives or impurities and cell stack pressure were all found to affect the results. With lithium metal electrodes, loss of capacity was found to be due to chemical reactions and morphological changes that convert the lithium into a form that is not easily recoverable. This can be insoluble lithium salts or isolation of lithium metal through dendrite growth that produces “mossy” lithium. The suppression of lithium dendrite growth was and still remains a critical safety and reliability issue that could not be easily solved with liquid electrolytes. The reaction of volatile and flammable organic solvents with finely divided lithium powder was found to be an insurmountable safety problem. Polymer electrolytes, however, are not volatile and although they do react with lithium metal and oxidizing metal oxides²⁸ the slow delivery of fuel to the reaction site limits the rate of reaction and prevents runaway reactions. This safety feature plus a perception that polymer electrolytes inhibit dendrite growth have lead to the intense interest in solvent-free materials over the last twenty years.

19.2.1. Solvent-Free, Ion-Coupled Systems

The commonest polymer electrolyte investigated has been based on polyethylene oxide which is commercially available in a relatively pure state at reasonable cost. It was found by Wright that the polymer could dissolve alkali metal salts to provide ionic conductivity. Figure 19.2 illustrates how the polymer achieves the dissolution of the salts by complexation of the metal ions via binding interactions between the ether oxygens and the metal ions. As shown in Figure 19.2 it is possible to bind the ions via one or more chains depending on the metal ion and the structure of the polymer chain itself. The figure shows that the number of donor atoms bound to the metal ion may also vary and in a dynamic fashion that gives rise to the movement of the ions along the polymer chains. The interaction of the anion is also shown where the anion binds or is ion-paired to the cation to form a neutral or even a negatively charged cluster species. The figure shows contact ion-pairs although solvent separated ion pairs are also possible. Intuitively, it is expected that the conductivity of the material will be favored by the formation of a higher concentration of charged species. Reduction of the ion-pair binding strength may be achieved by the use of anions such as bis(trifluoromethylsulfonyl) imide ($((\text{CF}_3\text{SO}_2)_2\text{N}^-)$), often referred to as TFSI or imide, which delocalize the negative charge over the large anion structure.²⁹ The anion in this case is dissociated from the cation and does not interact significantly with the polymer chains. Its motion requires free

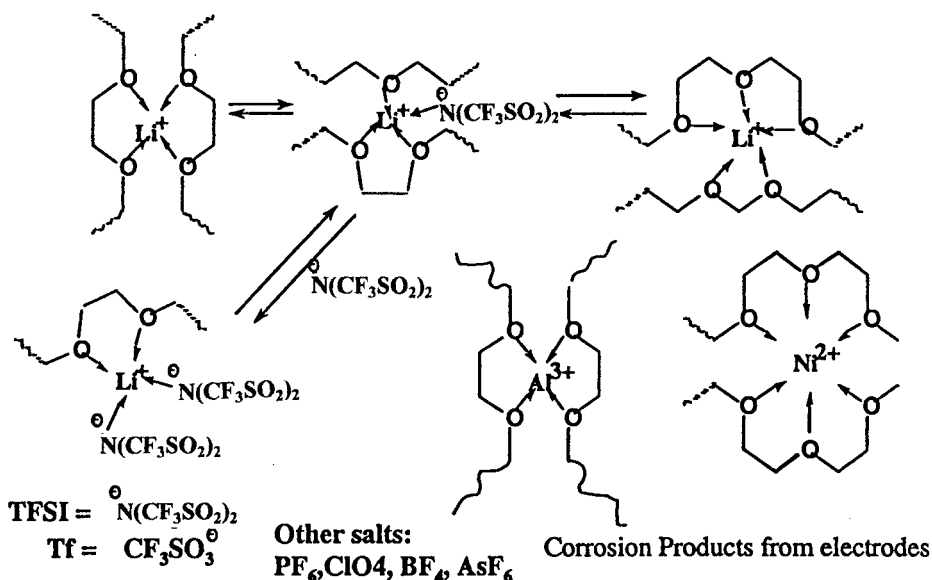


Figure 19.2. Solvation of lithium and other metal ions by polyethylene oxide.

volume between the polymer chains.

In parallel with the decreased binding of the lithium ion with the anion, the strength of binding (or solvation) to the polymer increases. Thus, although there is a higher concentration of free lithium ions, they are more tightly bound to the polymer and mobility is restricted by the need to break the stronger bond in order to move along the polymer chain or from one chain to another. It was found early in the study of polymer electrolyte salt solutions that the most significant contribution to conductivity occurred through the amorphous phase where there is segmental motion of the polymer chains. Although the crystalline phases are of significant interest in order to understand the thermodynamics and conformations of the ion-polymer complexes,^{30,31} the ionic conduction through these immobile phases is much slower. Thus the semi-crystalline PEO-lithium salt electrolytes exhibit reduced conductivities at temperatures below the melting point of the complex. Similarly, the conductivity falls precipitously at temperatures below the glass transition temperature (t_g) where the segmental motion of the polymer ceases and the chains are immobilized. This evidence demonstrates the strong coupling between the polymer chain motion and the mobility of the lithium ions.

A rule of thumb for the design of a polymer electrolyte is therefore to prevent crystallization and to reduce the t_g as much as possible. The larger the difference in temperature between the operating temperature and the t_g ,

the more vigorous is the segmental motion. Unfortunately, both crystallinity and high t_g are linked to good mechanical properties (shear modulus, tensile strength, creep compliance), which are necessary to prepare practical materials that will act as separators as well as electrolytes. A major goal of polymer electrolyte design is to de-couple the ion transport from the mechanical properties.

19.2.2. Effect of Polymer Molecular Structure (Architecture)

PEO :- $\text{-(CH}_2\text{CH}_2\text{-O)-}_n$ M.Wt. $> 10^6$ \$4-8/lb

PEMO :- M.Wt. $\sim 150k$
- Oxymethylene-linked PEG400

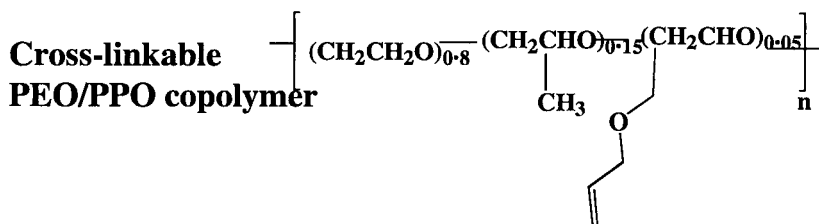
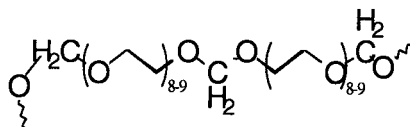


Figure 19. 3. Linear chain polymers.

A first approach is then to alter the structure of the polymer to remove the crystallinity, at least in the temperature range of interest. Figure 19.3 shows the chemical structures of commercial PEO, PEMO (also known as oxymethylene-linked polyethylene glycol 400 or amorphous PEO³²) and a PEO/PPO/AGE co-polymer patented by HydroQuebec³³ (PPO = polypropylene oxide; AGE = allyl glycidyl ether). These are all linear chain polymers and the latter two polymers exhibit significantly less crystallinity and lower melting points than PEO. In fact, the polymer complexes with LiTFSI exhibit no sign of a melting transition in DSC measurements down to -100°C . The introduction of the oxymethylene link, the propylene oxide group or the allyl ether group prevent crystallization due to the irregularity of the chains that disrupts the packing of the chains into regular forms necessary

for crystallization. The glass transition temperatures of these linear polymers are all less than -65°C and hence they are viscous liquids with moderate mechanical properties for high M.Wt. ($> 500\text{k}$) samples.

All of the polymers shown in Figure 19.3 may be cross-linked after film formation by reaction with radical species such as those provided by AIBN or UV radiation. However, this is quite uncontrolled chemistry that may result in a non-uniform material as the reactive radical intermediates are quite unselective. Over reaction results in a high density of cross-links, leading to an increase in t_g , reduced segmental motion and lower conductivity. Non-uniform cross-linking (or curing) yields non-uniform current densities through the membrane which will lead to rapid failure (*e.g.* dendrite growth). The allyl ether group, however, may be selectively reacted with hydrosilyl cross-linkers^{34,35} to provide uniform films from the more controlled and selective chemistry. It is worth noting that commercially available PEO contains butylated hydroxytoluene (BHT) to inhibit attack on the polyether chains by radical species formed from oxygen or light. Higher M.Wt. grades of PEO are actually prepared by radiation cleavage of very high M.Wt. PEO ($5\text{--}8 \cdot 10^6$) which illustrates the sensitivity of these materials to radiation.

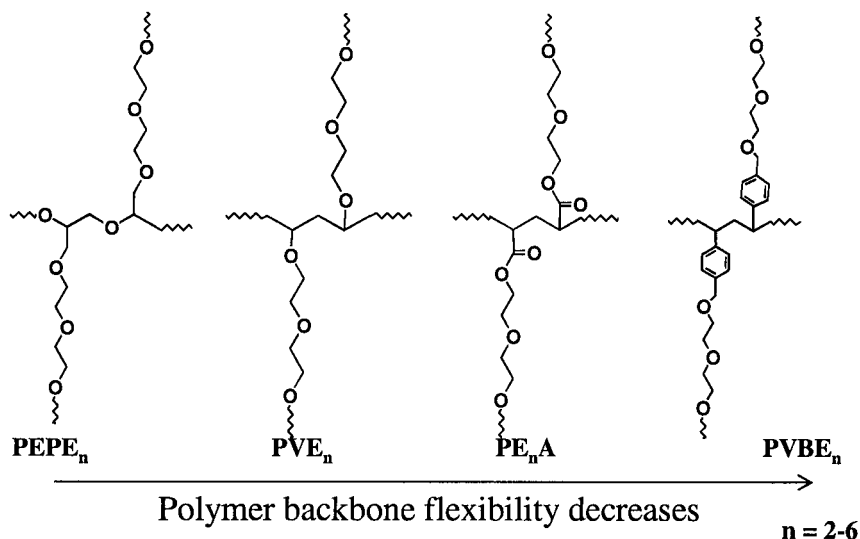
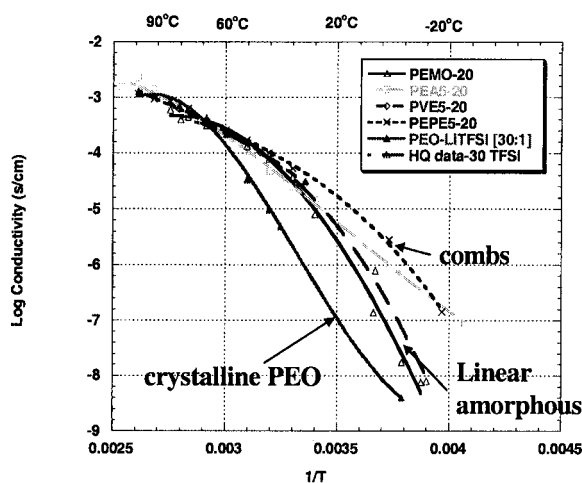


Figure 19. 4. Comb Polymers. Optimum side chain length = 5-6 EO units.

Figure 19.4 shows a series of comb polymers with different backbones and side chains containing ethylene oxide (EO) units similar to those in PEO.

The materials are completely amorphous at all temperatures. The optimum length of the side chains is found to be between 5-6 EO units due to the appearance of crystallinity as the length of the side chains grows and resembles PEO. For shorter side chains the influence of the backbone is stronger and leads to lower conductivity. The polymer backbone influences the conductivity due to the stiffness (polystyrene) and polarizability (polyacrylate). In these cases short side chains (2-4 EO units) lead to reduced conductivity.^{36,37} The PEPE_x and PVE_x polymers show less sensitivity to the side chain length as their backbones are more flexible.³⁸⁻⁴⁴ Polyphosphazene⁴⁵⁻⁴⁷ and polysiloxane^{48,49} backbones exhibit similar properties as do highly branched polymer architectures.⁵⁰⁻⁵³ The t_g values for the comb polymers are lower than for the linear polymers and their mechanical properties are much more liquid-like due to the molecular shape.

The conductivities of the polymers in Figures 19.3 and 19.4 are shown in Figure 19.5 as a function of temperature for polymer-salt complexes with lithium TFSI at a salt concentration of one lithium ion to 20 or 30 oxygens in the polymer. One can immediately note the lower conductivity of the PEO electrolyte at low temperatures due to the crystallinity. The linear amorphous polymer solutions show higher conductivity at low temperatures consistent with the lack of crystallinity while the comb materials show even higher conductivity at low temperature, which is consistent with greater segmental motion due to the more freely moving side chains that have free end groups.⁵¹ All of the materials show the familiar convex, bent shape that has the VTF form related to the polymer chain motion. For rechargeable lithium batteries, acceptable performance for electric vehicle and typical consumer



PEO = Polyethylene Oxide
 PEA = Polyacrylate ether
 PVE = Polyvinylether
 PEPE = Polyepoxide ether
 PEO = oxymethylene
 linked PEG400
 HQ = EO/PO copolymer

Figure 19.5. Comparison of conductivities of comb-branch polymer electrolytes (20:1 LiTFSI) with linear and networked co-polymers (HQ data, USP #5,755,985).

applications requires a conductivity of between 10^{-4} and 10^{-3} S/cm. Thus PEO performs adequately at 80°C but no system provides acceptable transport properties at ambient temperatures. In order to provide adequate performance at low temperatures it is important to elucidate the factors that control the dependence of transport properties on temperature.

19.2.3. Effect of Polymer Solvation Structure

The foregoing results provide an example of how change of the molecular structure may lead to improved ion transport through an increase of the polymer chain mobility. Much research effort has been expended in the synthesis of novel polymer structures to increase the lithium ion mobility but no true, dry polymer electrolyte has been shown to provide better performance than the comb materials shown here. The effects of the architecture change upon the conductivities are generally greatest at temperatures below 40°C . Above this temperature one may note that all the materials exhibit nearly identical conductivity dependence with temperature. This is Arrhenius dependence and is consistent with a process with an activation energy involving the making and breaking of chemical bonds. Since all of the polymers use ethylene oxide units (EO) to solvate the lithium ions it seems reasonable that the rate determining process involves breaking and forming oxygen-lithium bonds that occur in the same way for all polymers containing EO solvation units. Thus, at low temperatures close to

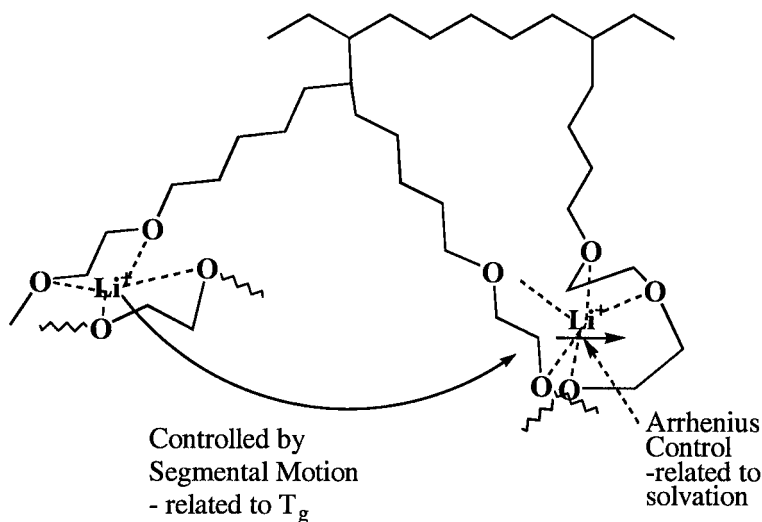


Figure 19.6. Schematic contributions of segmental motion and solvation to ionic mobility.

the glass transition the segmental motion of the polymer chains is the slow process. At higher temperatures this motion increases to a point where the rearrangement of the solvation sphere becomes rate determining. This is illustrated schematically in Figure 19.6 which shows an exaggerated motion of a comb polymer side chain combined with the solvent rearrangement as the ion moves from one chain to the next. Recent neutron scattering experiments have provided support for this scheme⁵⁴⁻⁵⁶ through the identification of two distinct types of relaxation.

The mechanism of the solvent reorganization around the ion is of crucial importance as it controls the height of the activation barrier to movement of the bound ion and hence the slope of the temperature dependence of conductivity. In order for the ion to move the solvated ion passes through an activated complex. This may be formed by dissociation of an oxygen-lithium bond to form a less coordinated complex followed by formation of a new $\text{Li}^+\text{-O}$ bond to a different point in the chain or on a new chain. An alternative mechanism would involve an increase in the coordination number in the activated complex with either the same chain or a second chain (or segment). The rearrangement involving multiple chains will be slower as a result of the decreased entropy of the intermediate complex in the case of either mechanism and may imply that chain to chain transfer is rate determining.

If the nature of the solvation is rate determining for ion mobility there should be a change in the temperature dependence of the conductivity upon a change of the groups involved. Figure 19.7 shows a comparison of a number of polymers complexed with LiTFSI. In particular, those that contain propylene oxide units ($\text{CH}_2\text{CH}(\text{CH}_3)\text{O}$), carbonate (OCOO) and trimethylene oxide (TMO, $\text{CH}_2\text{CH}_2\text{CH}_2\text{O}$) appear to show different temperature dependences at temperatures above 40°C where segmental motion is not rate determining. In comparison, a liquid or gel electrolyte shows less pronounced temperature dependence in this range than any of these electrolytes due to the vehicular mechanism of ion transport. For liquids and gels the solvent molecules travel with the ions so the bond breaking and forming is less important to the ion transport.

These results indicate that there is scope to improve the ambient temperature performance of polymer electrolytes by variation of the solvating groups. However, this involves considerable synthetic effort to introduce new groups such as TMO, carbonate or new donor atoms such as nitrogen, sulfur or phosphorus. The use of molecular modeling is an invaluable aid to guide the synthesis direction since it may eliminate unpromising structures before an extensive effort is made to prepare appropriate polymers. There is an extensive literature on different levels of modeling for polymer electrolytes.^{10,17,57-62} Among this work are some calculations relevant to the polymer structures whose conductivities are

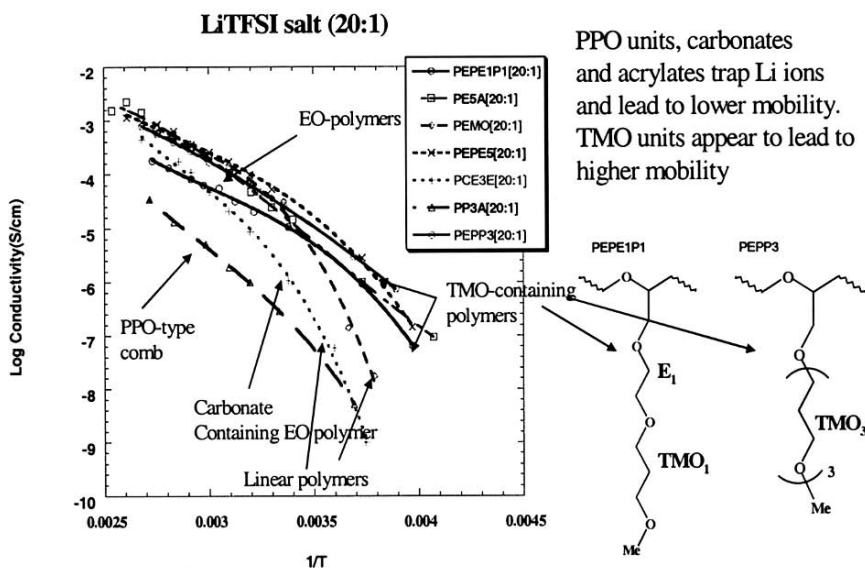


Figure 19.7. Temperature dependence of conductivity for polymer electrolytes containing different solvation groups.

shown in Figure 19.7. Quantum chemical calculations have been carried out to estimate the binding strength of lithium ions to polyalkyl oxides as a function of the coordination number (1-6) and the nature of the solvating group (EO, PO and TMO).⁶³ These calculations show that the binding energy of the TMO groups are higher for TMO than for PO and EO at coordination numbers up to 6 when the steric crowding of the TMO forces a longer Li–O bond length and the binding energies drop below those of the EO and PO. This is consistent with early literature reports that polyTMO polymers did not dissolve lithium salts.⁶⁴ Methods of estimating the height of the activation barrier for movement of the lithium ion along the polymer chain have been developed based on a mechanism that involves an intermediate with a lower coordination number^{65,66} and a comparison of polymer structures containing EO and TMO groups indicates that the barriers are lower for the TMO polymers.⁶⁷ Figure 19.8 illustrates the movement of the lithium ions along the polymer chain where the arrow points to the lithium ion and illustrates the method of calculation.

The theoretical calculations indicate that the migration of the lithium ion along the polymer chain will be faster for a TMO polymer compared to an EO polymer. Comb polymers have been prepared with varying contents of

EO and TMO units and the temperature dependence of conductivity, the glass transition temperature as a function of salt concentration are shown in

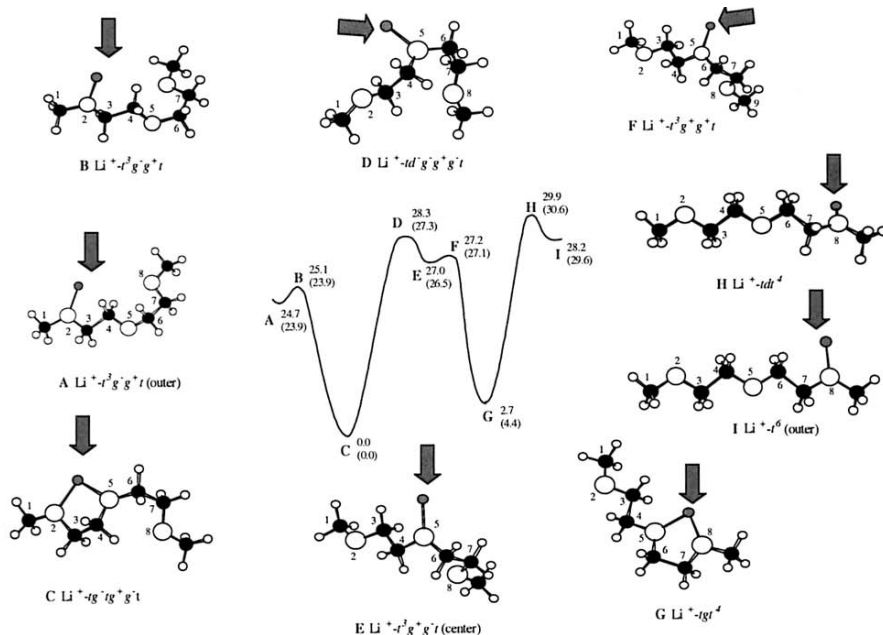


Figure 19.8. Calculated reaction pathway for migration of the lithium cation along a polyethylene oxide (PEO) chain. The PEO is modeled by diglyme and the cation moves by making and breaking Li-O bonds. The energies are in kcal/mol from HF/6-31G* calculations.^{63,67}

Figure 19.9. The polymers in this case are the polyepoxide ether polymers with different proportions of EO and TMO units in the side chains which vary from all EO to all TMO units.^{67,68} It can be clearly seen that as the proportion of TMO in the polymer increases the low temperature conductivity increases and the dependence of t_g upon the salt concentration decreases. However, it is very striking that the temperature dependence of the conductivity above 40°C is unaffected indicating that the motion along the chain as calculated is not rate determining.

There are a number of significant differences between these comb polymers (presence of PO units in the backbone, chain ends with OH groups) and the linear polymer chain used for the calculations but it appears that the mechanism used in the calculations does not dominate the rate. Measurements of the linear PTMO-LiTFSI complexes show a slightly

shallower slope but no overall increase in conductivity over the linear PEO systems which indicates that the differences in the comb structure are not significant. The decreased dependence of the t_g on salt concentration observed for both comb and linear TMO polymers indicates that the ionic cross-linking between chains is reduced with TMO. Although this does not solve the problem of how to obtain high conductivity at room temperature, it is an important result as the TMO structures may be used to mitigate the effects of salt concentration gradients that occur in lithium-polymer batteries, particularly in the presence of surfaces such as electrodes or ceramic filler particles.

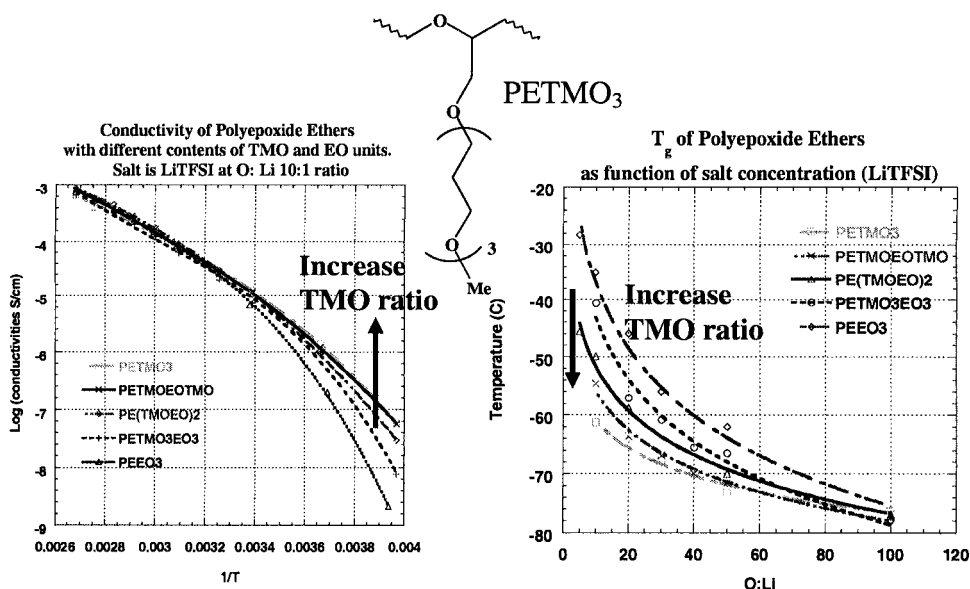


Figure 19.9. Conductivity as a function of temperature and glass transition temperature as a function of Li TFSI salt concentration for comb polymers with structures like the PETMO₃ shown but with some or all of the TMO units exchanged for EO.

The results of these combined synthetic and theoretical efforts have yet to establish the physical phenomena that limit the mobility of the ions. However, the possibilities have barely been explored as there are many structures such as carbonates, polyethylene imide (PEI) and polyalkylsulfide (PES)⁶¹ that may be synthesized to test the limitations of these electrolyte systems. To date, the barrier to ion transport remains undefined in the simple systems. Efforts have been made to investigate the influence of different phases such as the use of block copolymers⁶⁹⁻⁷⁴ that provide different

environments for the solvated ions, rigid polymer systems such as glassy⁷⁵ or crystalline⁷⁶ electrolytes that contain defects as well as “polymer-in-salt” systems.⁷⁷ These approaches show promise to provide information that will elucidate the nature of the limiting process in the ionic motion although they do introduce further complexity into the system. The presence and effect of different phases on the behavior of the polymer electrolyte is of great interest not only for the effect on ionic mobility but also for the understanding of the interfacial behavior at electrode surfaces.

19.2.4. Effect of Surfaces on Polymer Electrolyte Behavior

There has been much interest in the behavior of polymer electrolytes in combination with fillers such as nano-particulate fumed silica, alumina and other ceramic materials.⁷⁸⁻⁸⁴ Most of these studies have been carried out with high M.Wt. PEO and have reported improvements in conductivity, transference number and interfacial behavior with lithium metal electrodes upon addition of the ceramic fillers. The effect of the fillers has been shown to be partly due to a suppression of the crystallinity of the PEO electrolyte but increases in conductivity have been observed at temperatures above the melting point of the polymer system which indicate some different mechanism is in play. It was noted many years ago that the method of electrolyte preparation and the presence of fillers could alter the mechanical and transport properties^{85,86} and the presence of solvent impurities and the thermal history of the semi-crystalline materials can lead to wide variations in the measured properties. Unfortunately, most of the studies are complicated by the fact that commercial PEO already contains about 3% fumed silica plus some residual calcium salts from the manufacturing process. The fumed silica is added as a desiccant and binds impurities such as water and other solvents to its surfaces.

The observation of increased ion transport with added nanoparticles at higher temperatures is not universal. Johansson and co-workers observed no increase upon the addition of fumed silica to LiTFSI solutions in PEO and PEO.⁸⁴ Their observation is more consistent with reports in the rheology literature that would lead one to expect a decrease in ion transport properties. For example, Tsagaropoulos and Eisenberg have reported on the observation of a second glass transition at higher temperatures upon addition of fumed silica nano-particles to various polymers.^{87,88} They have ascribed this behavior to the inhibition of polymer segmental motion by interactions between the polymer and the particle surface which leads to the development of immobile layers. As the proportion of filler particles increases the immobile layers overlap leading to a distinct phase from the polymers in the bulk of the material and hence to the observation of a second T_g at values as

much as 100°C above the first one (see Figure 19.10). The second T_g was observed using dynamic mechanical analysis but the behavior has been confirmed by recent neutron scattering measurements which showed the existence of two distinct relaxation processes in the presence of the fillers.⁸⁹ The behavior is dependent upon the nature of the polymer-surface interaction, the polymer molecular weight and any cross-linking, be it covalent or ionic as in the case of a polymer electrolyte. It has been reported that for high M.Wt. polymers the second T_g is not observed but the T_g increases due to the restriction of the polymer chain motion by multiple particles.⁹⁰ As has been noted by Eisenberg these effects are not confined to solid polymer systems but also play a role in polymer gel systems and hence are likely to influence transport properties in composite electrolytes and electrodes in lithium ion and lithium-polymer gel batteries as well as solid “dry” polymer electrolytes.

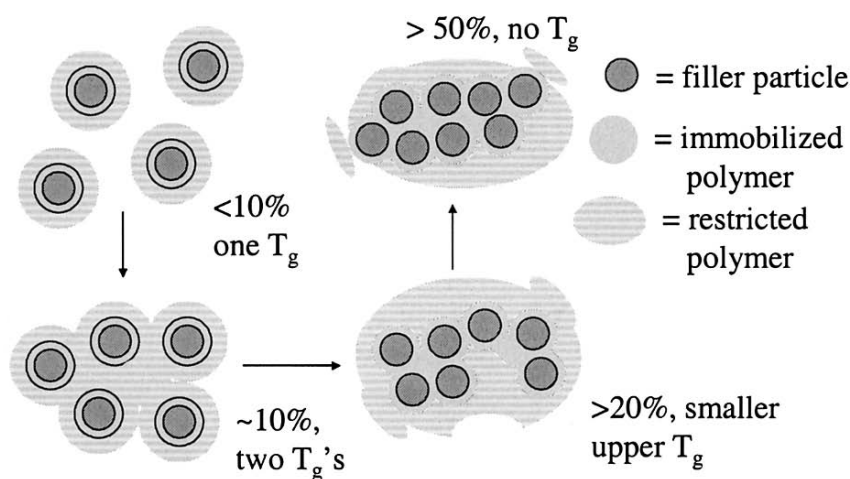


Figure 19.10. Eisenberg model of the effect of nanoparticles on the mobility of polymer chains.

The effect of surfaces and thin film geometries on the properties of polymers⁹¹⁻⁹⁷ is of general interest to materials scientists due to the relevance to the properties of composites, laminates and the field of adhesion.^{98,99} In general these effects derive from the inhibition of the polymer motion by the surface either through formation of some form of binding or by geometric restriction of some modes of motion. This accounts for the inhibition of crystallization and may in some cases result in an increase in mobility of the polymer chains close to the surface compared to the bulk. The nature of the interaction between the surface and the polymer may lead to increases of the

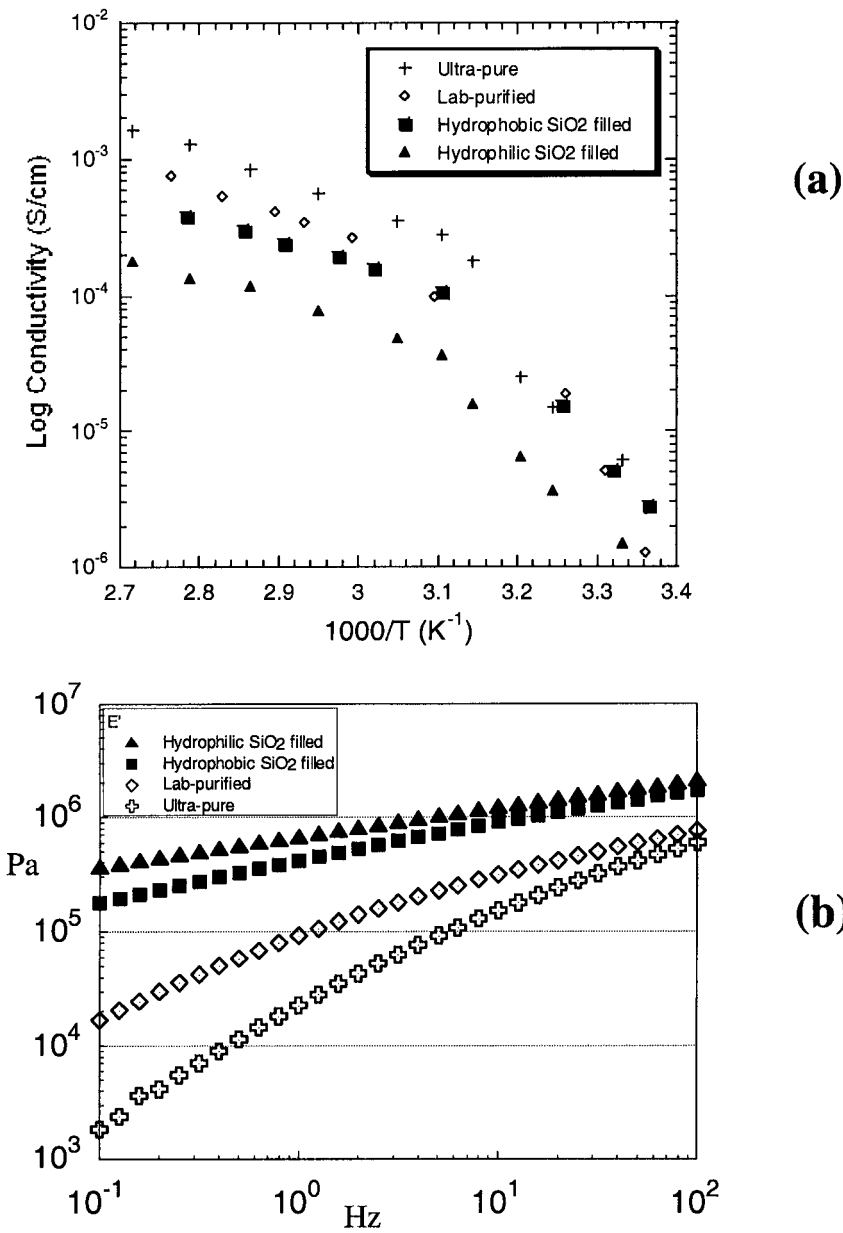


Figure 19.11: (a) Conductivity; (b) compression elastic modulus of low molecular weight (2×10^5) P(EO)₂₀LiTFSI at 80°C. Amount of fumed silica added is 10%.

chain motion and lower t_g values if the surface is appropriately treated to minimize the polymer-surface interaction.⁹² On the other hand very strong polymer-surface interactions can lead to the formation of an immobile layer at the surface. If this surface happens to be an electrode it implies that the mechanism of ion transport through the surface layers at the electrode is different from the bulk polymer where segmental motion predominates. The study of nano-particle fillers may therefore be useful for understanding some of the complex processes that occur at the electrode surface in the SEI layers.

A recent study of the effects of added nanoparticles upon the ion transport and mechanical properties of PEO electrolytes has provided results that allow reconciliation of the apparently contradictory mechanical and conductivity measurements.¹⁰⁰ Firstly, PEO was purified to remove the fumed silica added by the manufacturer to provide a true measure of the PEO properties when complexed with lithium salts. This material was compared with commercial PEO containing the 3% fumed silica (lab-purified) and with commercial PEO containing added nanoparticles fillers (hydrophilic Aerosil A200 and hydrophobic Aerosil R805), 10% by weight. The conductivities are plotted against temperature in Figure 19.11a for the LiTFSI solutions in these PEO samples while Figure 19.11b shows the compression elastic modulus as a function of frequency at 80°C for the same LiTFSI-PEO samples.

The results clearly show that the conductivity is higher in the absence of nanoparticles while the modulus is lower. Crystallization occurs below 60°C as seen by the break in the conductivity curve in Figure 19.11(a) and the presence of the filler materials does not suppress this. The compression modulus increases and the conductivity decreases as fillers are added in these experiments where care was taken to exclude moisture. A striking result, however, is that the addition of the hydrophobic filler material provides almost as much increase in mechanical strength as the hydrophilic material yet the conductivity decrease is much smaller, indicating the different effects of the surface groups. In this case the hydrophilic filler has SiOH groups on the surface while with the hydrophobic group the surface OH groups are capped with octyl groups to provide the hydrophobicity. The results illustrate the effects of the polymer-surface interaction upon the segmental motion and in this case the ionic motion appears to largely avoid the hydrophobic surface layers. It might be noted that similar interfacial effects might be expected with diblock copolymers that promote microphase separation and generate a polar/non-polar interface.^{70,72-74,101}

Addition of impurities such as water through exposure of the samples to atmosphere has been shown to have an effect on conductivity for certain salt systems. In the case of the LiTFSI-PEO system exposure of the membranes to atmosphere did not result in appreciable changes in the conductivity in the presence or absence of ceramic fillers. However, for lithium triflate and lithium perchlorate systems such exposure led to an

increase in the conductivity particularly in the presence of the ceramic fillers. The effect appears to be greater at low temperatures where crystallization is inhibited although increase of conductivity was observed above the melting point. Clearly, adventitious water is absorbed by the filler material to create a layer on the surface of the particles that can provide a pathway for the ions to move more easily than through the bulk of the polymer. Addition of filler particles such as activated alumina have long been used to scavenge residual water in organic solvents and electrolytes^{102,103} and this desiccant effect is likely the source of the reported improvements in interfacial behavior with lithium electrodes. The concentration of the water and other polar impurities on the filler surfaces provides a physical basis for the proposal of Kumar that there is a change in dipoles at the interface⁸³ and is consistent with some of the other observations concerning Lewis acidity of the surfaces^{78,104}.

These composite and multiphase systems are intrinsically interesting for the insight they provide into ion transport mechanisms in solid polymer electrolytes. Studies on this behavior also provide valuable information on how the electrolytes behave next to electrode surfaces and how the composite electrode structures should be formulated to obtain the best mass transport conditions in the electrolyte in confined spaces. Since similar interfacial issues arise with gels and liquids the issues raised here for the solid polymer systems are relevant for gel polymer and liquid lithium ion systems as well as fuel cell electrodes where the desired power densities and rates are very much higher.

19.2.5. Gel Polymer Systems

The introduction of small molecule additives or plasticizers into a solid polymer electrolyte system leads us into the area of polymer gel electrolytes. These are electrolyte systems that consist of a polymer matrix combined with a solvent system. The salt may be dissolved in the solvent or may be attached to the polymer framework as is the case in the familiar polyelectrolyte membrane, Nafion[®], used in chlor-alkali electrolyzers and in fuel cells. Two articles have recently appeared that describe polymer gel systems^{105,106} of the former type where polymer matrices selected from PVDF, PAN and PEO are used to form a gel with liquid electrolyte systems that are commonly used in lithium ion systems. Two types of polymer gel battery systems are generally under investigation. One is where a polymer gel is sandwiched between lithium ion battery electrodes where a different polymer (PVDF) from the separator is used as binder in the electrode.^{107,108} The second type is often referred to as the Bellcore system and refers to a porous polymer gel system prepared from copolymers of vinylidene fluoride with hexafluoropropylene, PVDF-HFP, and typical lithium ion battery electrolytes, LiPF₆/EC-DMC.¹⁰⁹

¹¹³ In this case the polymer binder in the electrodes is identical to the polymer in the separator and the co-polymer formulation is chosen to reduce the crystallinity and optimize the uptake of solvent into the separator and electrodes. These gels often contain fumed silica particles to provide improved mechanical properties.¹¹⁴⁻¹¹⁶ In fact, gel electrolytes with excellent mechanical properties and liquid-like transport properties have been prepared with only the presence of fumed silica particles which form a network structure that contains a polyethylene glycol dimethylether (PEGDME) solution of LiTFSI salts.¹¹⁷⁻¹²⁰ These systems show great promise as they combine excellent mechanical properties with high rate capability and the potential for good chemical and electrochemical stability with the electrodes while providing enhanced safety, lower cost and more flexibility in packaging than a conventional lithium ion cell.

The operation of the gel polymers is dependent upon the presence of the solvent molecules that travel with the ions just as occurs in a liquid. Thus, the conductivity and salt diffusion coefficients approach those of liquid electrolytes ($>10^{-3}\text{S/cm}$, $10^{-7}\text{cm}^2/\text{s}$ at room temperature).^{111,121,122} The polymers and ceramic networks provide the mechanical strength by forming networks through which the liquid is able to migrate. This network formation is a function of the properties of the polymer or particle surface and how it interacts with the solvent cluster as it moves through the matrix. The best known system for this is the presence of clusters and multiplets that form lamellar pathways in polyelectrolyte gels as is well known for Nafion[®] and other polyelectrolyte membranes.^{3,123} As such these solvent-network interactions and gel-electrode interactions are simply extensions of the issues considered above for the effect of surfaces on dry polymers and consequently many of the considerations are similar. The ability of the network system to completely contain the liquid and prevent leakage is of great importance as is the potential for the gel to retard reactions, prevent thermal runaway and enhance safety. From a manufacturing point of view polymer gel systems are of interest as the gel precursors can be introduced into the cell as a liquid and gelled in place, thereby greatly simplifying the manufacturing process. There are, however, a number of drawbacks with this procedure that will be more apparent after discussion of the design needs of practical lithium batteries in the next section.

19.3. POLYMER ELECTROLYTES IN LITHIUM BATTERIES

Since the intense interest in polymer electrolytes is nearly always justified by the use of these materials as separators in lithium batteries, it is

clearly important to bear in mind the requirements of this application. Our schematic of a lithium battery in Figure 19.1 may be elaborated upon as shown in Figure 19.12 to provide us with more insight into the conditions that the polymer electrolyte is expected to operate under. Inspection of the figure shows a lithium metal anode in contact with a polymer electrolyte where the polymer chains are represented by the thin lines and the salt ions are dispersed through the electrolyte. The lithium metal thickness and the electrolyte separator are each on the order of $30\text{--}50\mu\text{m}$ thick. The composite cathode is represented by the mixture of large cathode particles (vanadium, manganese or cobalt oxides) which are about $1\text{--}10\mu\text{m}$ in diameter, carbon black nanoparticles ($10\text{--}100\text{nm}$ diameter), polymer chains and salt ions in a layer that is about $50\text{--}100\mu\text{m}$ thick. The purpose of the carbon nanoparticles is to provide an electronic conduction path from the current collector to the cathode particles. The polymer electrolyte has to function as a binder for the cathode particles so that they remain in electronic contact as well as to provide a pathway for ionic conduction through the electrode to the surfaces of the cathode particles. In the case of a gel polymer the ions with their accompanying solvent molecules must travel through the confined spaces between the electrode particles while for a dry polymer system, the polymer

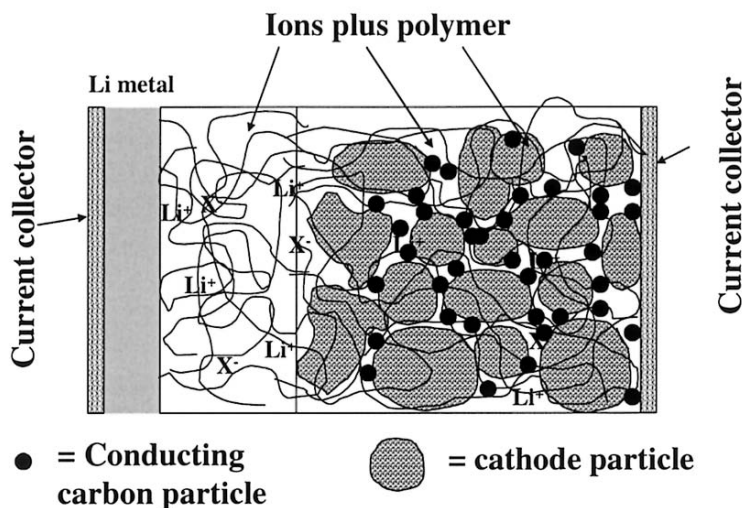


Figure 19.12. Schematic of a lithium polymer-metal oxide battery showing the environment for the operation of the polymer electrolyte.

segmental motion must be maintained in the restricted spaces to provide ionic mobility or some other mechanism of ionic transport may operate.

Consideration of these requirements immediately provides some perspectives on the approaches that have been used to improve the

conductivity of polymer electrolytes. The barriers to ionic transport occur more in the composite electrodes than in the separator.^{110,111,124,125} Hence, one can immediately see the difficulties for the introduction into a composite electrode of glassy polymers,⁷⁵ composite systems with more particles^{78,82,83,115} or regular structures such as layered⁷²⁻⁷⁴ or crystalline^{30,76} phases. It would be unreasonable to expect similar behavior in the composite electrode as is observed in the bulk separator. As we have seen from our discussion of the effects of surfaces on polymer dynamics, this is equally true for polymer electrolytes that depend on segmental motion or vehicular motion of solvent. While battery engineers continue to use composite electrodes this will be a challenge. However, Sadoway and Mayes have pointed out the possibilities of thin-film battery systems¹²⁶ and these novel systems may become more practical as large-area, thin-film technology is developed for applications such as organic and polymer light emitting diodes for area lighting for example.¹²⁷ In either composite or thin-film electrode systems the electrolyte will continue to have an interfacial region and therefore the study of composite polymer electrolytes will continue to provide invaluable information.

In addition to the physical changes that the electrode surfaces may impose upon the electrolytes one must also consider chemical changes that occur due to interactions between the electrodes and the electrolytes. In the case of lithium metal one can expect cleavage of carbon-oxygen bonds to occur leading to lithium alkoxides and alkyl-lithium compounds on the electrode surfaces.^{20,26,128} If these lithium compounds remain connected to polymer chains the resulting strong interaction will lead to immobilization of the polymer chain close to the surface. The complex surface reactions are critical for the formation of effective SEI layers at both lithium metal, carbon and alloy electrodes²⁰ and indeed there is evidence that the salt anions may be more reactive than the polymers under some circumstances.¹²⁹ Corresponding oxidation chemistry is expected to occur at the cathode surfaces. Ethers are known to be oxidized at potentials less than 4 V vs. Li¹³⁰⁻¹³² and, while carbonate solvents appear to be electrochemically stable to greater than 5 V,¹³³ preceding chemical reactions may occur to yield more easily oxidized species.^{21,134} In any event, side reactions that involve oxidation of electrolyte at the cathode will likely generate hydrogen ions that may initiate further reactions in the organic medium which can lead to further bond formation or cross-linking. These reactions can drastically change the nature of the electrolyte-surface interaction and as we have seen this can have significant effects on polymer dynamics close to the electrodes.

The surface effects combine with the mechanical and transport properties of the bulk polymer electrolyte to provide a complicated system that is best approached from a system model point of view.¹²⁵ Consideration of how the system behaves in the application can be related back to the

molecular models of transport and reactivity to help guide the selection and design of the appropriate materials that can provide the desired improved performance.⁶⁸

19.3.1. The Effect of Transport Properties on Cell Performance

In the previous discussion on lithium ion mobility, the conductivity was primarily used as a measure of the effects of the various structural changes. To properly describe the transport properties of an electrolyte containing n components requires knowledge of $(n/2)(n-1)$ transport properties. For a binary salt polymer electrolyte system these properties are conductivity (σ), salt diffusion coefficient (D_s) and transference number (t_+^0) where the transference number is defined as the number of moles of ion constituent crossing a reference plane fixed with respect to the solvent when one Faraday of current is passed.¹³⁵ For a gel electrolyte six transport properties would be required while for a polyelectrolyte only one is required, the conductivity. The impact of the transport properties results from the

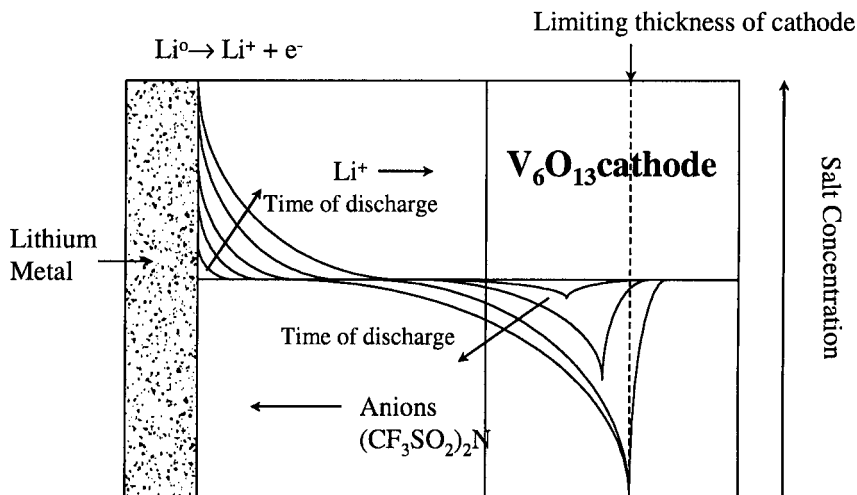


Figure 19.13. Effects of transference number and salt diffusion coefficient on salt concentration profiles upon Li-polymer cell discharge.

electrode processes in the cell. In most lithium ion battery systems only the lithium ion undergoes any reaction at the electrode while the anion does not undergo a reaction. Thus, when the lithium ion is removed from solution by

intercalation into or deposition on to the electrode, the anion will move towards the other electrode and tend to accumulate there. This will set up a concentration gradient next to the electrode which will be relaxed by diffusion. A system with a large salt diffusion coefficient such as a liquid electrolyte will be able to relax the concentration gradient sufficiently to prevent concentration polarization from becoming a problem. The higher the current density or power requirement, the larger this needs to be in order to prevent voltage losses due to concentration polarization. The development of the concentration gradients in the lithium-polymer battery is shown schematically in Figure 19.13.

The figure shows the development of an increase in salt concentration at the anode with time of discharge while within the cathode there is a depletion of salt concentration until it reaches zero. This limits the accessibility of the cathode towards the back of the electrode. These processes are complex and have been exhaustively analyzed by the Newman group^{125,136-141} and the reader is referred to this body of work for detailed information. On recharging the battery the salt concentration is depleted next to the lithium electrode while the concentration increases occurs within the composite electrode. The only way to avoid these concentration gradients is to immobilize the anion on the polymer to form a polyelectrolyte where $t_+^0=1$. The system modeling uses concentrated electrolyte theory and porous electrode theory¹³⁵ to predict the behavior of the batteries and to successfully accomplish this requires knowledge of the transport properties in the bulk of the separator and also within the composite electrodes. Rigorous methods for measurement of transport properties in the bulk of the polymer electrolyte separator have been developed^{121,122,142-144} and these have been used to provide values for a number of important systems.^{142, 145-148} The values of the transference numbers and salt diffusion coefficients are found to vary with salt concentration and temperature for any particular system and the values for the PEMO-LiTFSI system are shown in Figure 19.14. It has been found that the values are affected by phase changes in the electrolyte at high concentrations and by side reactions with the lithium metal electrodes at low concentrations. However, the values in the concentration range 0.5-2.5 M appear to be quite usable as they accurately predict cell behavior (*e.g.* limiting current at various temperatures). These numbers were used to model the lithium/polymer/ V_6O_{13} system^{124,125} and to predict the energy and power density of the system. The analysis demonstrated that the transport properties of the PEMO-LiTFSI system at 85°C were adequate to obtain the energy and power density that is desired for electric vehicle use but that performance at

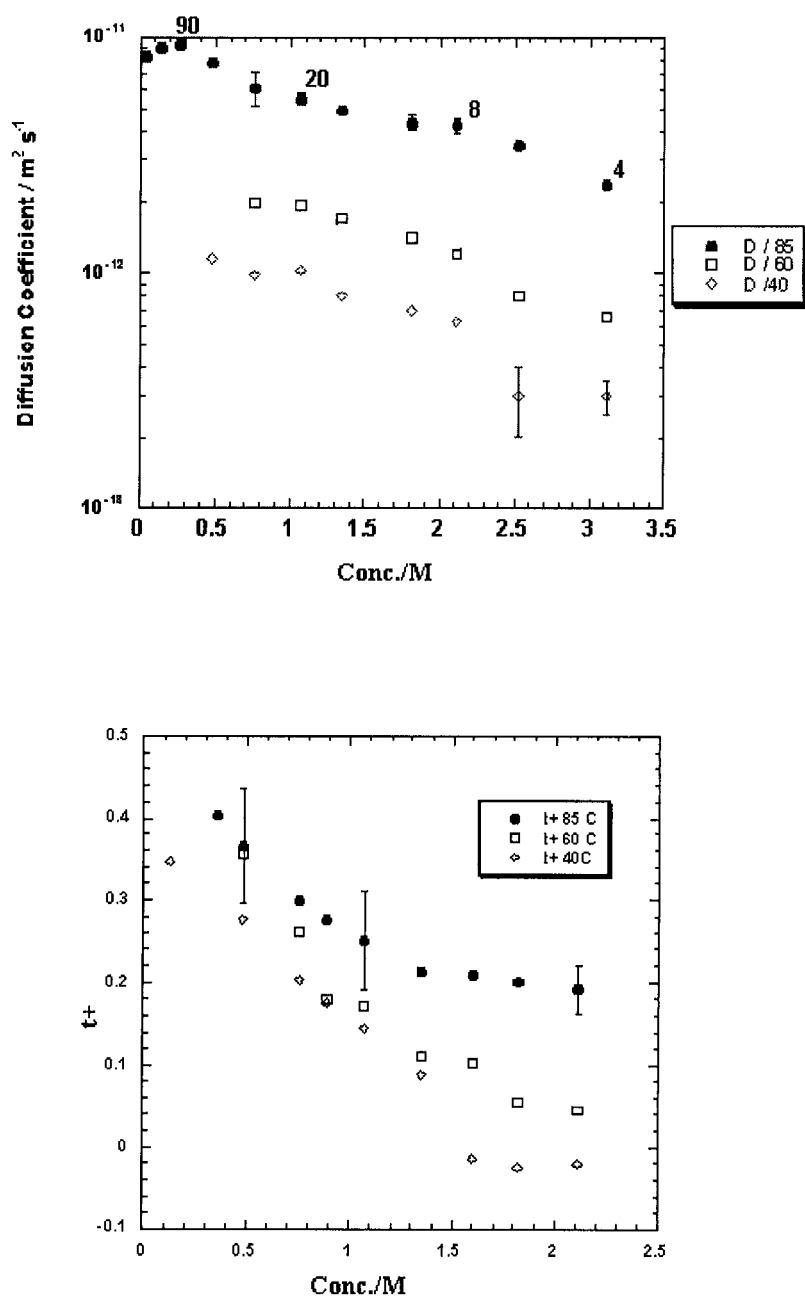


Figure 19.14. Salt diffusion coefficient (D_s) and transference number (t_+) for LiTFSI-PEMO as a function of salt concentration and temperature (40, 80 and 85°C).

lower temperatures was seriously inadequate. It is from analyses such as these that the conductivity goal of polymer electrolytes of 10^{-3} S/cm at room temperature has evolved but it is necessary to measure all the relevant transport properties to correctly predict battery performance. From the earlier discussion on the effects of surfaces and nano-particles on the polymer dynamics, it is not unreasonable to expect that the transport properties of the polymer electrolyte may be altered within the composite electrodes and that this may lead to performance that is different from the model predictions, particularly at high rates where the diffusional relaxation may be significantly altered by the presence of nano-particles. Some hint of this phenomenon has been noted in the comparison of the performance of Bellcore gel polymer batteries with model predictions.¹¹¹ Reduction of the salt diffusion coefficient by a factor of two or more was necessary in order to fit the model predictions to the high rate behavior. A similar comparison of model predictions with discharge and charge behavior has not yet been completed for lithium-polymer systems. However, examination of the cell cycling behavior by current interruption techniques indicates that the mass transport effects are very significant. Figure 19.15 shows the voltage profiles of discharging and charging of a lithium metal/PEO-LiTFSI/ V_6O_{13} while the current is interrupted for one hour after ten minutes of current flow at 0.1 mA/cm². The insets in the figure show the relaxation of the cell at the top of charge and at the bottom of discharge. One can observe significantly larger

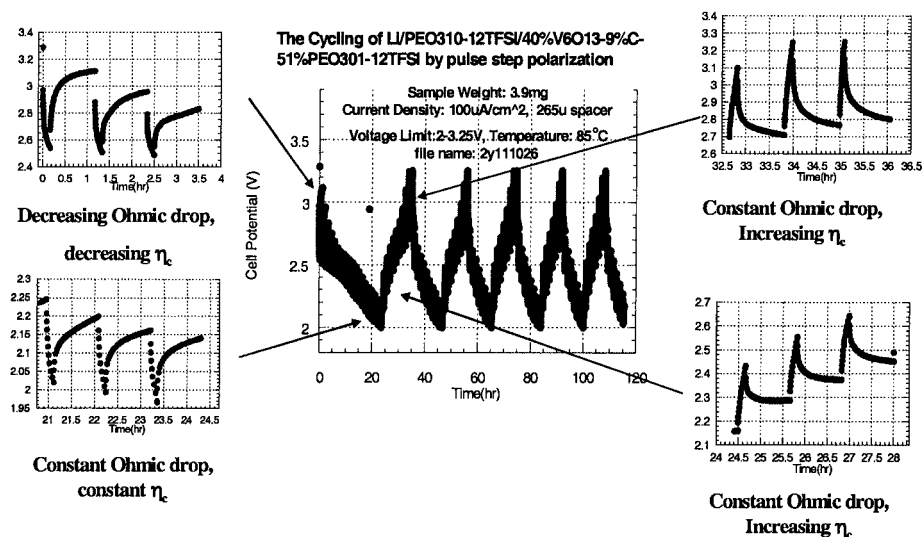


Figure 19.15. Pulse polarization of a Li metal/PEO-LiTFSI/ V_6O_{13} in discharge and charge modes. The cell is charged or discharged for 10 minutes followed by a 1 hour relaxation.

concentration polarizations at the top of charge which is consistent with the increase of salt concentration within the cathode structure that is relaxed more slowly due to the change in transport properties within the composite. The discharge capacity declines rapidly under these cycling conditions. The correlation of capacity fading with poor transport properties has also been demonstrated for a number of electrolytes with manganese oxide cells¹⁴⁹ and the formulation of the composite electrode system has to take into account the potential effects of surface-polymer interactions on the polymer dynamics. It has been noted that modification of the carbon particle surfaces with PEG chains leads to improved cycle life¹⁵⁰ and it is common practice to include surfactants in the cathode mix that improve the cycle behavior¹⁴⁹ presumably by modifying the carbon-polymer interaction.

Impedance measurements taken during the course of the cell cycling demonstrates steady increase of impedances (see Figure 19.16) that are generally identified as the interfacial or charge transfer impedance. Modeling of the impedance response of cells is a complex subject,¹⁵¹ especially as the response is a mixture of the two electrodes unless steps are taken to introduce a reference electrode. The response can be controlled by solid-state diffusion or electronic conductivity within an electrode, ionic diffusion in the electrolyte phase or interfacial, charge transfer kinetics. In Figure 19.16 one can observe changes in the impedance as a function of state of charge and the development of several impedances which may be related to processes going on at either or both electrodes. Even more interesting is the observation of dependence of the impedance on the time that the measurement is taken after current is turned off. Figure 19.17 shows the impedance plots for a lithium/PEO-LiTFSI/lithium cell that is polarized five times in the same direction at 0.2 mA/cm^2 for 2 coulombs of charge/cm². The impedance of the cell is taken 30 seconds after the current is turned off (a) and then again after one hour (b). The “charge transfer” impedance is observed to change with time, indicating that some of this impedance is due to salt concentration gradients close to the electrode surface. In some cases the impedance actually decreases with time while in other cases it increases. It can be observed that the impedance appears to return to a similar value indicating that no irreversible process has occurred that would indicate growth of the SEI layer through chemical reactions or the growth of dendrites. In this case, the current density used (0.2 mA/cm^2) was well below the limiting current ($>2 \text{ mA/cm}^2$) as calculated from the transport properties and cell geometry. It can further be noted, from the time dependence of the impedance spectrum and the increasing polarization observed on passing current, that one hour is still not enough time for the concentration gradients to completely relax.

These observations illustrate that the performance of lithium polymer batteries is dependant upon the behavior of the electrolyte at the interfaces. As noted previously, the polymer dynamics in composite systems is

influenced by the nature of the electrolyte-surface interaction and by the restriction of movement that the presence of the surface causes. Even in the case of the planar lithium metal electrode we have observed significant effects. The salt concentration gradients that build up on the electrodes can lead to depletion on one electrode and very high concentrations that can lead to salt precipitation on the other. Effects of high concentration may also be felt long before actual precipitation occurs. Figure 19.9 shows that as the salt concentration increases the glass transition temperature of the polymer

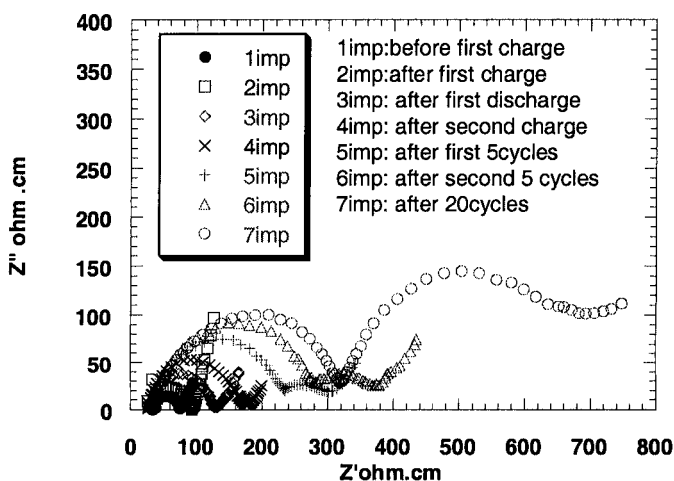


Figure 19.16. The evolution of impedance in Li/PEO-LiTFSI/V₆O₁₃ cells cycled at 100 $\mu\text{A}/\text{cm}^2$.

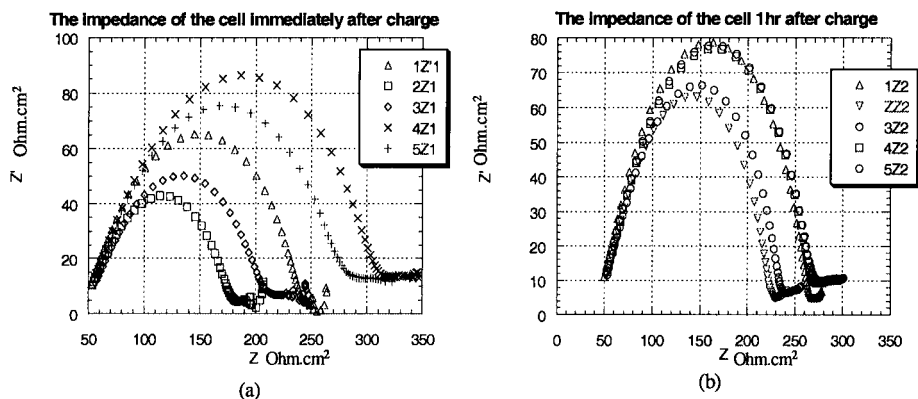


Figure 19.17. Impedance of a Li/PEO-LiTFSI(1:30)/Li cell at 85°C polarized at 0.2 mA/cm² for 2 coulombs of charge. Impedance recorded after (a) 30 seconds and (b) one hour after current stopped. Five separate polarizations designated 1-5Z in order.

electrolyte increases. This effect is more severe for EO-containing polymers and is even more pronounced for linear PEO and PPO polymers than the comb polymers shown in Figure 19.9. The combination of high salt concentration and the interaction with the electrode surface indicates that the electrolyte layer next to the electrode is likely to be very restricted in motion if not actually a glass. This implies that the mechanism of ion transport through these surface layers is different from the bulk and that these layers contribute to the interfacial impedance observed in the polarized cells. Understanding of how ions move such layers is of great importance and the study of ion transport in less mobile polymer systems takes on added relevance in this context.^{75, 76}

Figure 19.9 shows that the dependence of the glass transition temperature upon concentration is much reduced for the TMO-containing polymers and hence they would be expected to generate less interfacial impedance. This is observed at lithium metal electrodes where the TMO comb polymers with LiTFSI typically give an interfacial impedance of about 50 ohm-cm² compared to 100 ohm-cm² for PEO-LiTFSI. As mentioned above, although the introduction of the TMO groups was disappointing in terms of producing an increase in the bulk conductivity of the polymer electrolytes, the t_g salt-dependence provides very valuable properties that can lead to greatly improved cell performance by reduction of the interfacial

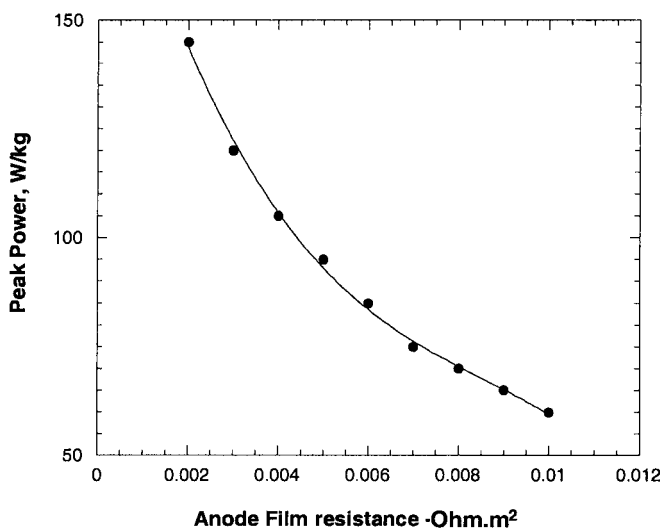


Figure 19.18. Dependence of peak power on anode film (SEI) resistance.¹⁵²

impedance. The importance of interfacial impedance on cell performance can be appreciated by use of system modeling. In the Li/PEMO-LiTFSI/V₆O₁₃ model calculations referred to above,¹²⁴ the interfacial impedances were accounted for by use of a value for the anode film resistance which was taken to be 0.01 ohm-m² or 100 ohm-cm². It was found that the peak power that could be obtained from the cell is very dependent on the value that is selected. The results of calculations of peak power that varied this resistance are shown in Figure 19.18.¹⁵² The decrease in interfacial impedance observed on replacing EO polymers with TMO would lead to a near doubling in the peak power capability. More sobering, however, is the effect of an increase in the interfacial impedance. Since reduction of the cell operating temperature to 25°C typically results in an increase in interfacial impedance to greater than 1 ohm-m² even for TMO polymers, this indicates that useful rates of discharge with a polymer electrolyte will not be possible even with high room temperature conductivity unless the interfacial impedance problem is also solved. Thus, the studies of the effects of surfaces on the transport properties take on an even greater importance for all types of batteries and fuel cells.

19.3.2. Polyelectrolyte Single-Ion Conductors

The properties demanded of polymer electrolytes for good performance in lithium batteries that we have discussed now include a forbidding list. In addition to chemical and electrochemical stability, adequate transport properties are necessary both in the bulk of the separator and at the electrode surfaces. This is difficult to attain if the electrochemical processes lead to the development of concentration gradients at the surfaces and the transport properties are degraded at extremes of concentration. A way to avoid this is to use polyelectrolyte single-ion conductor materials which have a transference number $t_+^0=1$. With these materials no concentration gradients will develop as the anions are unable to move and accumulate on one side of the cell. However, the loss of anionic mobility results in lower conductivity. The electrolyte portion of the cell is therefore limited by ohmic resistance rather than the concentration polarization. Here again modeling provides invaluable guidance for the design of materials and for targeting appropriate performance goals.

The best known polyelectrolyte material is Nafion[®], an ionomeric comb polymer with a PTFE backbone and fluorinated ethylene oxide side chains that are terminated with sulfonate anion groups. A number of similar fluorinated materials have been examined for gel polymer systems quite recently¹⁵³⁻¹⁵⁵ where the ionomeric membrane is swollen with a solvent.

Conductivities greater than 10^{-4} S/cm have been reported. Several attempts have been made to prepare lithium and sodium polyelectrolytes for use in solvent free systems¹⁵⁶⁻¹⁶⁹ and the most successful of these have the comb structure with a pendant anion similar to the structures shown in Figure 19.19. A typical comb structure will have several comb side chains with no attached anion for every side chain with an attached anion and this allows the concentration of ions to be controlled.^{163, 167} The best conductivities for these polyelectrolytes approach 10^{-5} S/cm at room temperature. The nature of the anion has been shown to play a role through its ability to delocalize the negative charge and hence reduce the strength of ion-pairing to the lithium or sodium ions. Strong ion-pairing as occurs with the alkylsulfonate anion tends to bind the cation and slow its motion through the electrolyte. Replacement of the sulfonate group with fluoroalkylsulfonates leads to a significant increase in conductivity.¹⁶³

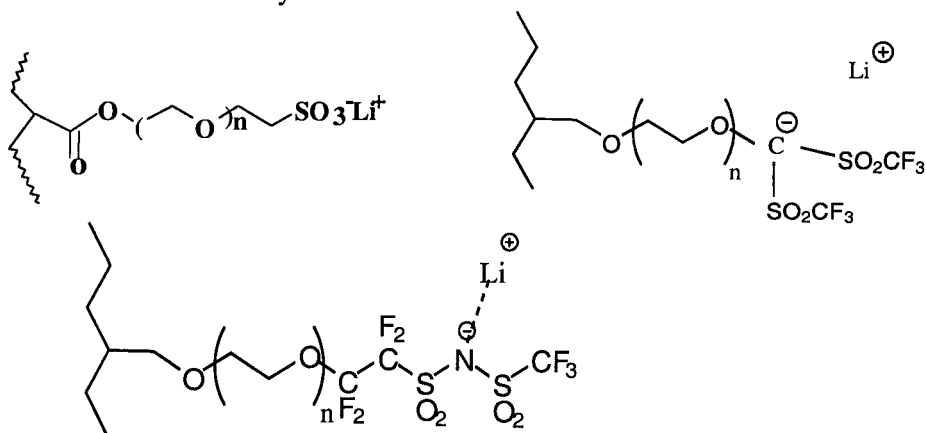


Figure 19.19. Examples of pendant anions on comb structures for single-ion conductors.

Molecular modeling has been carried out on polyelectrolyte systems using Monte Carlo methods.^{170, 171} The results of this modeling imply that the comb-type systems are the optimal architecture when combined with appropriate anions and that the ideal length of the side chains can also be estimated. Comparison with the behavior of the corresponding binary salt systems also allows prediction of the optimum salt concentration for bulk conductivity. It turns out that the optimum ionomer salt concentration is about half that of the binary salt system. This is an important result as the lower salt concentration can lead to lower costs of the electrolyte and

probably to better interfacial behavior. A controlling factor in the behavior of the polyelectrolyte is the value of the glass transition temperature. As the ionic concentration increases so does the glass transition temperature and the mobility of the side chains is accordingly diminished. With higher salt concentration there are more charge carriers so that conductivity is increased. Thus an optimum is reached where the ion concentration is maximized before the effect of the rising glass transition temperature reduces the polymer mobility. Here again, introduction of more flexible backbones and side chains such as the TMO units should depress the t_g while allowing a higher concentration of ions to be used.

Unfortunately, little work has been reported on the behavior of single-ion conductors in real lithium batteries. Most reports refer only to efforts to increase the conductivities usually because the conductivities are so low as to be impractical. One report exists on the impedance behavior of a polyelectrolyte with sodium electrodes¹⁶⁹ but little satisfactory data has been obtained on the interfacial behavior of polyelectrolytes. System modeling has been employed to estimate the behavior of polyelectrolytes in real cells and to determine the conductivity that is actually needed. The system modeled was the $\text{Li/V}_6\text{O}_{13}$ cell and the results were compared with the binary salt system using the transport properties shown in Figure 19.14. For both systems an “ideal” polymer material was modeled and this was the binary salt system at 85°C and a polyelectrolyte system with conductivity of 10^{-4} S/cm. An “available” polymer was the binary system at 40°C and a polyelectrolyte with a conductivity of 4×10^{-6} S/cm which is the conductivity at 40°C of the fluorinated methide anion system shown in Figure 19.19. The results of the modeling¹²⁴ show no clear advantage for either system and both provide rather poor power capability due to the effect of the interfacial resistance. It was also noted that increased power and energy density results from increasing the voltage of the cell which highlights the need to maximize the stability of the electrolyte to high voltage cathodes. The modeling exercise does demonstrate that achievement of lithium polyelectrolyte conductivity between 10^{-4} to 10^{-3} S/cm at ambient temperatures is a worthwhile goal provided that the interfacial impedance is kept below 50 ohm-cm².

19.3.3. Chemical and Electrochemical Stability of Polymer Electrolytes

As we have discussed, the delivery of the lithium ions to the electrode surface is a complicated process. Once there, the dynamics of the layers at the electrode surface is even more difficult to unravel and yet they are critical

for the efficiency of the electrochemical reaction. Large surface resistances to electron or ion transfer will lead to slow kinetics, large activation polarizations and side reactions. Side reactions lead to loss of cycling efficiency, capacity fading and an increase of interfacial impedance due to deposition of products at the interface or soluble products that may migrate to other surfaces where reactions may occur that reduce efficiency. Given the inherent reactivity of organic materials to 0 V versus Li, it is indeed remarkable that any lithium battery is feasible. The critical role of the SEI layers on the electrodes is the subject of intense investigations.²⁰ These layers must possess a remarkable set of properties. They must not react with the electrode itself and they must separate the reactive electrode from the sensitive electrolyte. However, the SEI layer must allow the passage of lithium ions with a minimum of resistance. To achieve this degree of selectivity it is necessary that the layers behave as single-ion conductors and that the mechanism of ion conduction is different from the bulk of the solution. The SEI layers must also accommodate changing geometry of the electrode under different states of charge. For intercalation electrodes this involves volume changes as the lithium ion intercalates while for lithium metal shape changes and dendrite growth must be accommodated. In the latter case, changes in the surface area of the electrode occur that expose the electrolyte to fresh lithium metal. The electrolyte must then participate in the formation of fresh SEI layer to protect against further reaction.

From the previous discussion concerning the effect of surfaces on polymer dynamics, one can appreciate that the passage of the lithium ions through the surface layers is complex indeed. The presence of resistive layers may lead to depletion of ions at the electrode to levels where their concentration can no longer support the current demanded. In such cases electrons must be injected into or removed from other species present in the solution. These species can include the anions of the salt (C-F bond breaking, for example) or the solvent molecules themselves. Detection of fluoride ion demonstrates the reduction of the anion with triflate or TFSI salts. The formation of products from side reactions removes lithium ions from use in the battery and leads to reduced capacity, particularly if the electrode capacities are balanced. Often, however, one electrode is in large excess (*e.g.* lithium metal) and the loss of lithium is not noticed.

Our understanding of the electrode dynamics may be helped by the chemical side reactions that do occur. The reactive intermediates which lead to irreversible bond cleavage may be related to the mode of electron transfer. It has been shown in the past that electrochemical and chemical reactions may involve different reactive intermediates and these lead to different product distributions.¹²⁸ The existence of trapped solvated electrons has been postulated during electrochemically driven electron transfer¹⁷² which will lead to bond cleavage (*e.g.* carbon-oxygen bonds) once localized on a single

solvent molecule. Since a reaction involving an unpaired electron will favor certain structures such as tertiary carbons over secondary or primary carbons, detection of products corresponding to this will support the intermediacy of a radical reactive species. Anionic cleavage will favor secondary over tertiary carbons and this might be expected to occur when two electrons are injected simultaneously as may occur during a chemical reaction between lithium metal surface and solvent molecules. From an analysis of the products formed from suitable solvent molecules (*e.g.* 2-MeTHF) one can sometimes gain insight into the electrode processes and any corrosion processes that may reduce the capacity of the battery. This understanding can then be used to design electrolytes that are resistant to the side reactions or which have groups deliberately introduced that lead to the formation of desired SEI layers upon reaction.

For linear polymer electrolytes the effect of bond cleavage is to change the molecular weight by breaking the chains and to immobilize the chains on the electrode, possibly leading to poorer ion transport through the surface layer. The detection of changes in molecular weight and mechanical properties are about all that can be gained from linear polymers. Comb polymers are more useful for the investigation of side reactions at electrodes as bond cleavage leads to small fragments that can be detected and quantified by conventional chemical analysis techniques (surface and bulk spectroscopy, gas and liquid chromatography, mass spectroscopy). Figure 19.20 shows the structure of a comb and how bond cleavage reactions at a negative electrode yield small fragments. Similar reasoning can be applied to oxidation reactions. Different reactive intermediates will favor certain reaction pathways. For example a radical intermediate will favor cleavage of the tertiary carbon in the backbone next to the oxygen while anionic intermediates will favor secondary carbons. Thus electrochemically driven reactions may favor injection of one electron at a time through electron trapping and lead to cleavage at the tertiary carbon and hence the production of fragments that are the full side chain length while corrosion reactions may involve injection of two electrons simultaneously through chemical reaction with the metal surface and yield fragments that result from bond cleavage all along the side chains. The product distribution would then contain products consistent with the preferred point of bond cleavage in the side chain. One may also expect that the cleaved lithium alkoxide fragments will contribute to the SEI layer and influence the behavior of the electrode. The structure of the electrolyte may therefore be designed to provide fragments that promote good interfacial performance and provide a means for SEI layer repair during the battery lifetime. The well known but not understood difference in the interfacial behavior of ethylene carbonate versus propylene carbonate at carbon anodes is an excellent example of this.

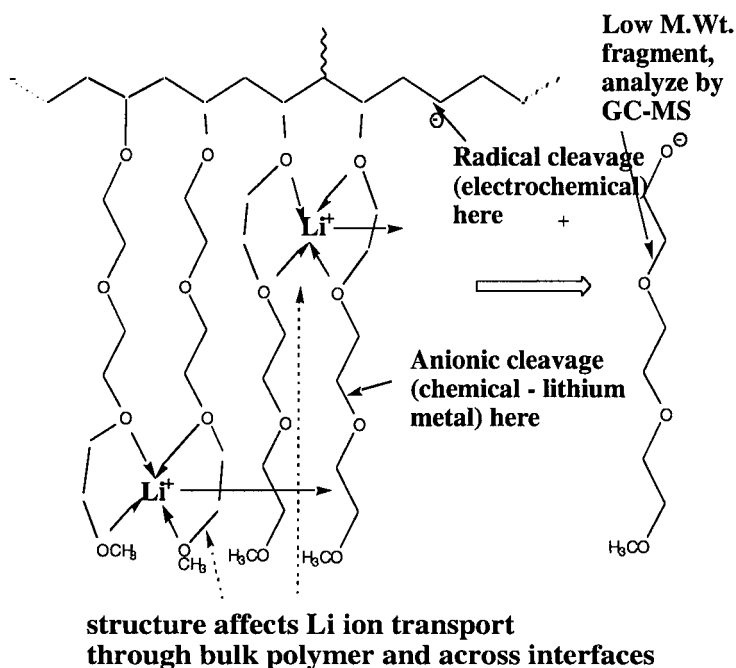


Figure 19.20. Degradation pathways of polymers at lithium electrodes.

The incorporation of functional groups other than ethers in the electrolyte structure has been long studied. Substitution of nitrogen or sulfur for the oxygen^{61,173,174} not only alters the dielectric constant but also the strength of the donor atom interaction with the lithium ion leading to different solvation energies and different energy barriers to lithium ion movement. As always, however, the reactivity with the electrodes is critical to successful use of a material. The imine and sulfide functions are more easily reduced at the anode than the ether groups and hence the presence of a robust SEI layer is required. As is well known, however, the highly reactive cyclic carbonates are used successfully in lithium ion batteries due to the formation of a remarkable SEI layer.²⁰ However, other desirable functional groups such as nitrile (*e.g.* acetonitrile) appear to be unable to form a satisfactory film on lithium metal or on carbon and therefore have very restricted use in lithium batteries.

The ether function reacts with lithium metal also. Figure 19.21(a) shows some vigorous cycling at 85°C of a symmetrical lithium/lithium cell containing the comb branch polymer PE(TMO)₃ (structure shown in Figure 19.9) with LiTFSI salt in a 10:1 oxygen:lithium concentration ratio. The cell

Prior to the cycling at 0.4 mA/cm^2 shown in Figure 19.21(a) the cell had been cycled at 0.2 mA/cm^2 for two days to pass a total of 134 coulombs (37.22 mAh) with little visible change in the impedance (<5% increase in the interfacial impedance). The cell had been cycled during this time at a rate that was below the limiting current where the transport properties were sufficient to ensure an adequate supply of lithium ions. The limiting current I_{lim} may be calculated according to the following equation¹³⁵:

$$I_{\text{lim}} = FD_s \Delta c / (1 - t_+^0) L$$

Where F = Faraday's constant, D_s = salt diffusion constant in cm^2/s , Δc = the concentration difference across the cell in moles/cm^3 , t_+^0 = the lithium ion transference number and L = the membrane thickness in cm. The salt diffusion coefficient had been measured for this electrolyte using the restricted diffusion method.¹⁴³ Estimation of the transference number at about 0.3 allows one to calculate the limiting current and it is found that 0.4 mA/cm^2 is above this value, leading to the observation of the transition time shown in Figure 19.21(a).

While the cell is cycled at values below the limiting current the interfacial impedance does not change appreciably except for concentration effects as shown in Figure 19.17. This indicates that the SEI layer that is initially formed (Li_2O , LiOH , Li_2CO_3 , LiF , LiOR) is preventing appreciable reactions between the newly plated lithium and the electrolyte components. However, as soon as the limiting current is reached where insufficient lithium ion is delivered, electrons are injected into the solvent molecules leading to reactions and dendrite growth is initiated. Dendrite growth increases the surface area and reduces the inter-electrode distance therefore increasing the limiting current that may be supported. However, the dendrites frequently grow completely across the gap leading to a short circuit and failure of the cell as shown in Figure 19.21(a).

19.3.4. Dendrite Growth

The role of the transport properties in the initiation and growth of dendrites is well known when the limiting current is exceeded and technological advantage is taken of this to electrodeposit metal powders.¹⁷⁵ If this was the only factor in dendrite growth one could simply ensure that the limiting current was never exceeded and a major problem for lithium metal batteries would be solved. Unfortunately, dendrites also grow at current densities below the calculated limiting current and lead to failure of the cell. Considerable attention has been given to the dendrite problem for both liquid

and polymer electrolytes and it remains the most significant issue preventing the commercialization of lithium metal polymer batteries.^{16,25,27,176-182} The unpredictable nature of the dendrite growth leads to unacceptable reliability problems as well as safety issues due to the formation of “mossy” lithium deposits. A lot of work has been carried out on liquid electrolyte systems to study lithium dendrite growth but until the last few years the published reports on dendrite growth in polymer electrolytes have been much sparser. Recently a number of excellent *in situ* studies of dendrite growth in PEO electrolytes have appeared¹⁸³⁻¹⁹³ that demonstrate the growth of dendrites in polymer electrolytes even at current densities that are well below the calculated limiting current. The topic of dendrite growth is covered in detail in a separate chapter in this book so this discussion will be confined to the role of the polymer properties in dendrite growth.

During studies of rechargeable lithium metal anodes in liquid electrolyte systems it was noted that stack pressure on the cells led to improvements in lithium metal cycling.^{25,27,194,195} The liquid electrolyte cells contained a microporous separator and through this the pressure was transmitted to the anode surface. These observations led to assumptions that polymer electrolytes would also provide better cycling of the lithium metal electrode. However, the commonly used polymer system, PEO, is a viscous liquid under the typical operation conditions and is not a solid. Some of the recent *in situ* studies have amply demonstrated that dendrites grow rapidly in viscous liquids^{183,186,188} at current densities well below the limiting current. In experiments carried out in the author’s laboratory, dendrite growth has been observed at virtually any current density provide that the polarization continues for long enough. The rate of initiation and propagation of dendrite growth appears to be sensitive to a number of factors including the presence of impurities,¹²⁹ the transport properties and concentration of the salt,³⁸ capacity of the charge cycle,⁶⁸ the presence of filler particles and the molecular weight which influence the mechanical properties.¹⁰⁰

For these viscous liquid polymer systems pressure cannot be applied without the aid of a supporting separator network. This can be supplied by use of a microporous separator, addition of nano-particle fillers or by cross-linking the polymer itself. Cross-linking is required^{33,68,196,197} to form a true solid electrolyte with the mechanical properties of a solid to inhibit dendrite growth. With an electrolyte with sufficient mechanical strength pressure may be applied to the anode^{33,198} and the dendrite growth further inhibited. Unfortunately, the presence of filler particles and cross-linking tends to raise the glass transition temperature, reduce the mobility of the polymer^{33,68,100} and the transport properties of the electrolyte decline, leading to a lower limiting current. A further consequence is that any modification of the polymer mechanical properties must be uniform across the membrane. If non-uniform cross-linking or dispersion of particles occurs the current

distribution at the anode will be non-uniform and this will encourage dendrite growth. Thus, poorly controlled chemistry such as UV and thermal radical initiated cross-linking is likely to lead to non-uniformity in the polymer membrane and cause problems during cycling particularly at high rates. This is one reason why *in situ* curing of polymer gel systems may not be wise. Development of alternate cross-linking chemistry that is more controllable^{35,197} is critical to the production of quality lithium polymer batteries.

The previous discussion on the effects of surfaces on the polymer dynamics is pertinent to recall at this time. One may recall that the glass transition temperature of polymer electrolytes rises with increasing salt concentration (see Figure 19.9). During discharge of a lithium metal cell with a binary salt system, the concentration gradients at the lithium metal electrode rise to levels that induce phase changes (glass formation, precipitation) and leads to changes in interfacial impedance (Figure 19.17). These changes will be enhanced by the presence of filler particles and cross-links in the polymer and inhomogeneities in the membrane will induce non-uniform current distribution which may encourage dendrite initiation at the opposite electrode in a symmetrical lithium/lithium cell. On charging of the lithium metal electrode in a lithium /polymer/metal oxide cell, the depletion of salt concentration at the plating electrode will lead to a lower t_g , higher mobility at the electrode surface and the ability to sustain a higher current density. During the charging cycle strong mechanical properties are desired at the plating electrode surface to restrain dendrite growth.^{33,68} However, in the metal oxide electrode, salt concentration rises, leading to a higher t_g , decreased mobility and high interfacial impedance. The presence of strongly-interacting particles such as carbon black or cross-linking in the polymer electrolyte, binder or polymers formed from electrolyte solvents during the calendar or cycle life will lead to decreased transport properties in the composite electrode. This will be the case for dry polymer, gels and liquid systems and will result in high impedance and low rate capability. The consequence of a non-uniform composite electrode composition will be a very uneven current distribution which will encourage the initiation of dendrite growth at the lithium metal counter electrode.

There is a well-developed literature on morphological instability during electrodeposition of a variety of metals, which indicates that even a small perturbation on the surface will initiate dendrites.¹⁹⁹⁻²⁰³ The case of lithium is complicated by the reactivity of the metal and the need for a protective film on the surface, commonly known as the SEI. A physical example of a perturbation would be non-uniformity in the SEI that can give rise to instability and dendrite growth. It is obvious from our discussion on polymer dynamics at surfaces how perturbations may arise from the changing properties of the polymer electrolyte during cycling and that any design of

polymer electrolytes must take these factors into account. There is much scope for modeling of the effects of such perturbations and how they can induce dendrite growth as cycling is continued. It should be noted that the basis of these models assumes that the surface is fundamentally unstable and that dendrite growth is inevitable. The goal will be to understand how to limit and control the dendrite growth sufficiently for useful battery life.

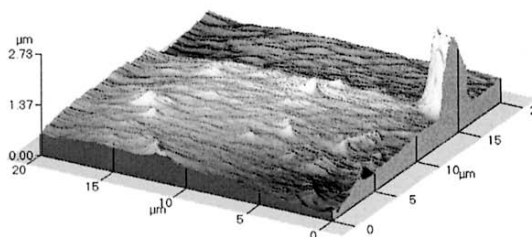
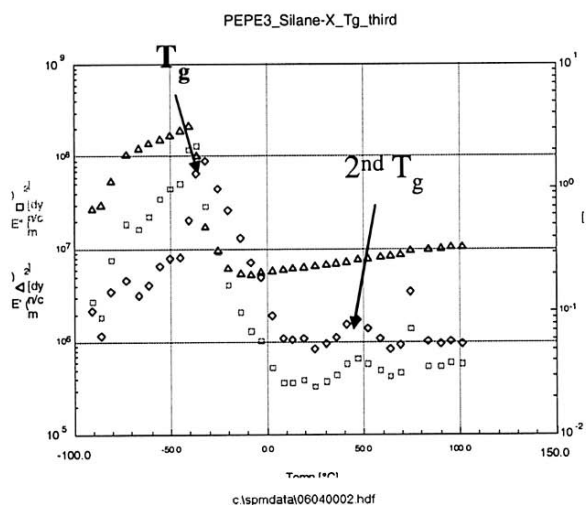
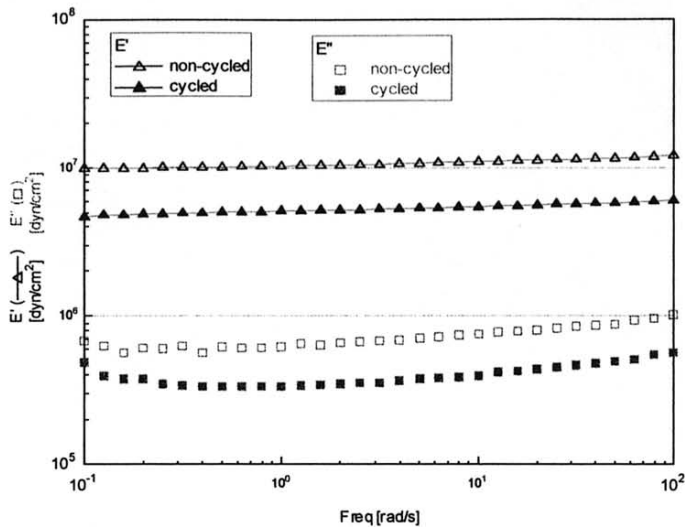


Figure 19.22. Polymer membranes prepared by cross-linking the co-polymer EPE₃ and AGE (10%) using hydrosilylation;³⁵ (a) DMTA in compression mode at 10Hz. The elastic (E') and viscous (E'') moduli and the $\tan \delta$ response are shown as a function of temperature. (b) AFM in contact mode.

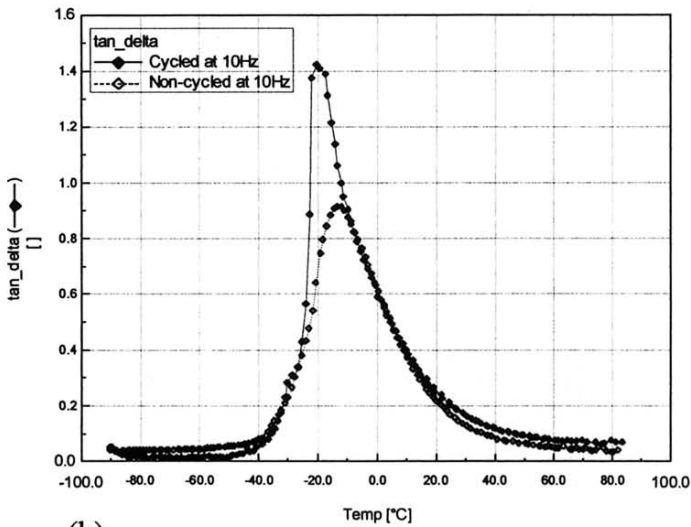
19.3.5. Mechanical Properties

The foregoing discussion on dendrite growth highlights the need for better understanding and control of the mechanical properties of the electrolytes. The inevitable desire to push the battery to the limits of its performance will impose great stress on the polymer electrolytes that will rapidly expose any weaknesses. Since the mechanical properties of the polymer electrolytes are closely coupled with the transport properties, the design of the polymer systems needs to take close account of whether it will be used next to a lithium metal electrode, in the bulk of the separator or in a composite electrode. Even the seemingly simple process of cross-linking the polymer membrane can introduce undesirable properties. For example, Figure 19.22(a) shows the dynamic mechanical thermal analysis (DMTA) of a cross-linked polymer membrane of co-polymer EPE₃ and AGE (10%) with LiTFSI(20:1) that shows the presence of a second t_g indicating non-uniformity in the material.²⁰⁴ Examination of the film by contact mode atomic force microscopy (AFM) is shown in Figure 19.22(b), which shows the presence of non-uniform areas. Phase imaging AFM in tapping mode has been shown to be even more useful for the study of membrane morphology for fuel cell membranes²⁰⁵ and clearly these are very useful techniques for quality control of membranes.

In this case the non-uniformity of the membrane is due to the non-random nature of the co-polymer. During the co-polymerization it was noted that the AGE and EPE₃ monomers disappeared at different rates indicating that the polymer was a block co-polymer and hence the cross-linking was concentrated in the AGE blocks. The membrane showed rapid formation of dendrites when it was cycled in a symmetrical lithium/lithium cell and this can be ascribed to the non-uniformity of the membrane and the fact that the membrane was very thick (400 μ m) so that the limiting current was low. Unfortunately the requirements for quantitative mechanical measurements (~1mm thickness) are difficult to reconcile with the need for thin membranes (<50 μ m) for lithium batteries. Nevertheless, useful results can still be obtained if the membrane can be separated from the electrodes after cycling. Figure 19.23 shows the frequency sweep (a) and dynamic mechanical thermal analysis (b) of a composite membrane consisting of the cross-linked co-polymer of EPE₃ and AGE (X-PEPE₃), LiTFSI (20:1) and A200 Aerosil fumed silica before and after cycling at 85°C in a lithium/lithium cell at 0.2 mA/cm². The membrane in this case was about 300 μ m thick²⁰⁴ and the calculated limiting current was about 1 mA/cm² based on the transport properties measured in the absence of cross-linking and filler particles. The frequency sweep experiments show a decrease in the moduli after cycling while the DMTA shows an increase in the area under the $\tan \delta$ peak, indicating an increase in the proportion of polymer undergoing the transition,



(a)



(b)

Figure 19.23. Mechanical measurements on X-linked PEPE₃-LiTFSI(20:1)-A200 Aerosil (10%) before and after cycling in a Li/Li cell at 85°C. (a) Frequency sweep; (b) dynamic mechanical thermal analysis at 10Hz.²⁰⁴

a decrease in the t_g , indicating increased mobility and the growth of a shoulder on the low temperature side that is a β -transition associated with the movement of the side chains. Extraction of the membrane and analysis by gas chromatography showed the presence of peaks corresponding to cleavage of the side chains and this is consistent with the growth of the β -transition and the loss of mechanical strength from cleavage of the cross-links.

These results are consistent with the occurrence of bond cleavage during cycling of the lithium metal. Both cross-linking and the presence of strongly interacting filler particles leads to poorer transport and the salt diffusion coefficient was measured to be reduced by nearly four times by the presence of the cross-linking and the filler particles. Thus, the current density was close to the limiting current and the extent of the damage to the electrolyte may be explained by injection of electrons directly into the polymer under conditions where the supply of lithium ions was insufficient to maintain the current. The loss of mechanical strength observed after cycling shows that chemical reactions at the electrodes can degrade the structure of the membrane during the life of the cell. In this case the degradation appears to be caused by the unexpectedly large decrease in the transport properties due to cross-linking and filler particles which are present to inhibit dendrite growth. This is an apt demonstration of the need to balance transport properties with mechanical properties in lithium batteries as the consequences of chemical reactions with the high energy electrodes is very unforgiving.

19.4. CONCLUSIONS

The design of polymer electrolytes for lithium batteries is a complex problem that needs to be approached with a combination of sophisticated modeling, diagnostic techniques and significantly greater synthetic effort than has been applied in the past. Molecular modeling is needed to predict the molecular features desired in an electrolyte to attain the transport properties required to support the desired rate capability and to provide the necessary mechanical strength to act as a separator, inhibit dendrites and to bind together the particles of the composite electrodes. These molecular features must also be stabilized towards reaction at the electrodes by the formation of an SEI layer with almost magical properties. System modeling is needed to set the performance goals of the materials that need to be designed and rigorous comparison of the model predictions with experiment is necessary. Failure analysis must be accomplished by a combination of sophisticated diagnostic techniques together with reaction modeling and synthesis of model materials designed to test the modes of failure. Only then can the rates of side reactions be related to lifetime issues.

It is clear that this task is daunting for dry polymer systems and is likely to prove difficult for polymer gels if demands are put upon them beyond acting as an adhesive to hold lithium ion electrodes together as is mostly practiced today. Our survey of polymer electrolyte properties has demonstrated that the desired properties depend critically upon the component of the cell where the electrolyte has to function. The electrolyte next to lithium metal has to have sufficient mechanical strength to inhibit dendrite growth but the means of attaining this should not reduce the transport properties. The polymer electrolyte in the composite electrodes should have much more flexibility as the surface effects of the electrodes lead to major difficulties with ion transport. This is true in dry polymer, gel and liquid systems where polymers are expected to bind the particles together. These polymer systems also have to resist reactions with these electrodes over the life of the battery so that these desirable properties do not change and degrade the performance of the battery.

Given all of these rigorous requirements, it is hardly surprising that the introduction of the lithium metal polymer battery has not yet been successful. In fact, it is more surprising that progress has been as successful as it has been given how primitive have been the polymer systems used so far in comparison to the severity of the demands placed on them by battery engineers. This chapter has attempted to illustrate how modeling, diagnostics and synthesis can be used to design better materials for the application. Many of these methods have only become available in recent years so there is much exciting work to be done in the coming years. The lithium metal system is particularly difficult due to the dendrite issue but holds the most promise for a very high energy density, particularly if ways can be found to increase the cell voltage to 4 volts or more. This will require the development of multi-layer systems that have a layer resistant to lithium metal on the lithium with high mechanical strength and a polymer in the cathode that is stable to four volts. Since no single material can combine these chemical properties different materials will be necessary in different parts of the cell. As we have seen, it is necessary for the electrolyte to possess different mechanical properties in different parts of the cell anyway. The nature of these multilayers next to electrodes will be the subject of much research and it is encouraging to note that already attempts are being made to design and fabricate protective layers on both anodes and cathodes.²⁰⁶⁻²⁰⁸ Such efforts are likely only the beginning of an exciting new chapter in the development of lithium batteries which will lead to more realistic demands on the battery materials and better designed materials for the applications.

ACKNOWLEDGEMENT

This work was supported by the Assistant Secretary for Energy Efficiency and Renewable Energy, Office of FreedomCAR and Vehicle Technologies of the U.S. Department of Energy under Contract No. DE-AC03-76SF00098.

REFERENCES

1. R. T. Leah, N. P. Brandon, V. Vesovic, G. H. Kelsall, *J. Electrochem. Soc.* 147 (2000) 4173.
2. J. A. Kerres, *J. Membrane Science* 185 (2001) 3.
3. K. D. Kreuer, *J. Membrane Science* 185 (2001) 29.
4. S. Mazrou, H. Kerdjoudj, A. T. Cherif, A. Elmidaoui, *J. Molenat, New J. Chem.* 22 (1998) 355.
5. L. Bazinet, F. Lamarche, D. Ippersiel, *Trends Food Sci. Tech.* 9 (1998) 107
6. D. E. Fenton, J. M. Parker, P. V. Wright, *Polymer* 14 (1973) 589 .
7. P. V. Wright, *Br. Polymer J.* 7 (1975) 319.
8. M. Armand, J. Y. Sanchez, M. Gauthier, Y. Choquette, in *Electrochemistry of Novel Materials* (J. Lipkowski and P.N. Ross, eds.), VCH, New York, NY, (1994) p. 65.
9. M. Armand, *Solid State Ionics* 69 (1994) 309 .
10. M. A. Ratner, (J. R. MacCallum, C. A. Vincent, eds.), Elsevier Applied Science, London (1987).
11. J. R. MacCallum, C. A. Vincent, *Polymer electrolyte reviews--2*, Elsevier Applied Science, London ; New York, (1989).
12. F. M. Gray, *Solid polymer electrolytes : fundamentals and technological applications*, VCH, New York (1991).
13. F. M. Gray, Royal Society of Chemistry (Great Britain), *Polymer electrolytes*, Royal Society of Chemistry, Cambridge, 1997.
14. P. V. Wright, *MRS Bulletin* 27 (2002) 597 .
15. B. Scrosati, C. A. Vincent, *MRS Bulletin* 25 (2000) 28 .
16. D. Fauteux, A. Massucco, M. McLin, M. Vanburen, *J. Shi, Electrochim. Acta* 40 (1995) 2185.
17. M. A. Ratner, P. Johansson, D. F. Shriver, *MRS Bulletin* 25 (2000) 31 .
18. M. A. Ratner, D. F. Shriver, *MRS Bulletin* 39 (1989).
19. A. Hooper, M. Gauthier, A. Belanger, *Electrochem. Sci. Technol. Polym.* 2 (1990) 237.
20. D. Aurbach, in *Advances in lithium-ion batteries* (W. A. v. Schalkwijk and B. Scrosati, eds.), Kluwer Academic/Plenum Publishers, New York, NY, (2002) p. 7.
21. S. E. Sloop, J. K. Pugh, S. Wang, J. B. Kerr, K. Kinoshita, *Electrochem. Solid-State Lett.* 4 (2001) A42.
22. L. Vogdanis, B. Martens, H. Uchtmann, F. Hensel, W. Heitz, *Makromol. Chem.* 191 (1990) 465 .
23. J. L. Goldman, L. A. Dominey, V. R. Koch, *J. Power Sources* 26 (1989) 519.
24. Y. Gofer, M. Benzion, D. Aurbach, *J. Power Sources* 39 (1992) 163.
25. K. M. Abraham, *Electrochim. Acta* 38 (1993) 1233.
26. V. R. Koch, *J. Electrochem. Soc.* 128 (1981) 1293.
27. K. M. Abraham, J. S. Foos, J. L. Goldman, *J. Electrochem. Soc.* 131(1984) 2197.

28. S.-J. Wen, J. Kerr, M. Rubin, J. Slack, K. von Rottkay, *Solar Energy Materials & Solar Cells* 56 (1999) 299.
29. G. Oradd, L. Edman, A. Ferry, *Solid State Ionics* 152 (2002) 131.
30. Y. G. Andreev, P. G. Bruce, *Electrochim. Acta* 45 (2000) 1417.
31. Y. G. Andreev, P. G. Bruce, *J. Physics-Condensed Matter* 13 (2001) 8245.
32. D. J. Wilson, C. V. Nicholas, R. H. Mobbs, C. Booth, *Br. Polymer J.* 22 (1990) 129.
33. A. Vallee, M. Duval, F. Brochu, M. Kono, E. Hayashi, T. Sada, *US Patent* 5,755,985, 1998.
34. H. R. Allcock, *Chem. Mater.* 6 (1994) 1476.
35. H. R. Allcock, D. E. Smith, Y. B. Kim, J. J. Fitzgerald, *Macromolecules* 27 (1994) 5206.
36. J. M. G. Cowie, V. M. C. Reid, I. J. McEwen, *Br. Polymer J.* 23 (1990) 353.
37. J. M. G. Cowie, A. C. S. Martin, *Polymer* 32 (1991) 2411.
38. O. Buriez, Y. B. Han, J. Hou, J. B. Kerr, J. Qiao, S. E. Sloop, M. M. Tian, S. G. Wang, *J. Power Sources* 89 (2000) 149.
39. S. Pantaloni, S. Passerini, F. Croce, B. Scrosati, F. Roggero, M. Andrei, *Electrochim. Acta* 34 (1989) 635.
40. L. Marchese, M. Andrei, A. Roggero, S. Passerini, P. Prosperi, B. Scrosati, *Electrochim. Acta* 37 (1992) 1559.
41. M. Andrei, L. Marchese, S. Passerini, A. Roggero, B. Scrosati, *US Patent*, 5,162,174, (1992).
42. M. Andrei, L. Marchese, P. Prosperi, A. Roggero, *US Patent* 5,173,205, (1992).
43. M. Andrei, L. Marchese, A. Roggero, P. Prosperi, *Solid State Ionics* 72 (1994) 140.
44. J. M. G. Cowie, K. Sadaghianizadeh, *Solid State Ionics* 42 (1990) 243.
45. P. M. Blonsky, D. F. Shriver, P. Austin, H. R. Allcock, *J. Am. Chem. Soc.* 106 (1984) 6854.
46. H. R. Allcock, S. J. M. Oconnor, D. L. Olmeijer, M. E. Napierala, C. G. Cameron, *Macromolecules* 29 (1996) 7544.
47. H. R. Allcock, D. L. Olmeijer, S. J. M. Oconnor, *Macromolecules* 31 (1998) 753.
48. Z. C. Zhang, S. B. Fang, *Electrochim. Acta* 45 (2000) 2131.
49. R. Hooper, L. J. Lyons, D. A. Moline, R. West, *Organometallics* 18 (1999) 3249.
50. A. Nishimoto, M. Watanabe, Y. Ikeda, S. Kohjiya, *Electrochim. Acta* 43 (1998) 1177.
51. M. Kono, E. Hayashi, M. Watanabe, *J. Electrochem. Soc.* 145 (1998) 1521.
52. M. Watanabe, T. Endo, A. Nishimoto, K. Miura, M. Yanagida, *J. Power Sources* 82 (1999) 786.
53. A. Nishimoto, K. Agehara, N. Furuya, T. Watanabe, M. Watanabe, *Macromolecules* 32 (1999) 154.
54. G. M. Mao, R. F. Perea, W. S. Howells, D. L. Price, M. L. Saboungi, *Nature* 405 (2000) 163.
55. G. M. Mao, M. L. Saboungi, D. L. Price, M. B. Armand, W. S. Howells, *Phys. Rev. Lett.* 84 (2000) 5536.
56. M. L. Saboungi, D. L. Price, G. M. Mao, R. Fernandez-Perea, O. Borodin, G. D. Smith, M. Armand, W. S. Howells, *Solid State Ionics* 147 (2002) 225.
57. J. W. Halley, Y. H. Duan, *J. Power Sources* 89 (2000) 139.
58. O. Borodin, G. D. Smith, R. L. Jaffe, *J. Comput. Chem.* 22 (2001) 641.
59. A. Aabloo, M. Klintonberg, J. O. Thomas, *Electrochim. Acta* 45 (2000) 1425.
60. H. Kasemagi, M. Klintonberg, A. Aabloo, J. O. Thomas, *Solid State Ionics* 147 (2002) 367.
61. P. Johansson, *Polymer* 42 (2001) 4367.
62. G. J. Kearley, P. Johansson, R. G. Delaplane, J. Lindgren, *Solid State Ionics* 147 (2002) 237.
63. P. C. Redfern, L. A. Curtiss, *J. Power Sources* 110 (2002) 401.

64. J. M. G. Cowie, (J. R. MacCallum, C. A. Vincent, eds.), Elsevier Applied Science, London ; New York, (1987).
65. A. Sutjianto, L. A. Curtiss, *J. Phys. Chem.* 102 (1998) 968.
66. A. G. Baboul, P. C. Redfern, A. Sutjianto, L. A. Curtiss, *J. Am. Chem. Soc.* 121 (1999) 7220.
67. J. B. Kerr, G. Liu, L. A. Curtiss, P. C. Redfern, *Electrochim. Acta* In press (2003).
68. J. B. Kerr, S. E. Sloop, G. Liu, Y. B. Han, J. Hou, S. Wang, *J. Power Sources* 110 (2002) 389.
69. A. V. G. Ruzette, P. P. Soo, D. R. Sadoway, A. M. Mayes, *J. Electrochem. Soc.* 148 (2001) A537 .
70. P. P. Soo, B. Y. Huang, Y. I. Jang, Y. M. Chiang, D. R. Sadoway, A. M. Mayes, *J. Electrochem. Soc.* 146 (1999) 32.
71. P. E. Trapa, B. Y. Huang, Y. Y. Won, D. R. Sadoway, A. M. Mayes, *Electrochem. Solid-State Lett.* 5 (2002) A85.
72. Y. Zheng, F. Chia, G. Ungar, P. V. Wright, *J. Power Sources* 97-98 (2001) 641.
73. Y. G. Zheng, F. S. Chia, G. Ungar, T. H. Richardson, P. V. Wright, *Electrochim. Acta* 46 (2001) 1397.
74. F. S. Chia, Y. Zheng, J. Liu, G. Ungar, P. V. Wright, *Solid State Ionics* 147 (2002) 275.
75. X. Y. Wei, D. F. Shriver, *Chem. Mater.* 10 (1998) 2307.
76. Z. Gadjourova, Y. G. Andreev, D. P. Tunstall, P. G. Bruce, *Nature* 412 (2001) 520.
77. M. G. McLin, C. A. Angell, *Solid State Ionics* 53-56 (1992) 1027.
78. F. Croce, G. B. Appetecchi, L. Persi, B. Scrosati, *Nature* V394 (1998) 456.
79. L. Persi, F. Croce, B. Scrosati, E. Plichta, M. A. Hendrickson, *J. Electrochem. Soc.* V149 (2002) A212.
80. D. Golodnitsky, G. Ardel, E. Strauss, E. Peled, Y. Lareah, Y. Rosenberg, *J. Electrochem. Soc.* V144 (1997) 3484.
81. D. Golodnitsky, G. Ardel, E. Peled, *Solid State Ionics* V147 (2002) 141.
82. B. Kumar, L. G. Scanlon, *J. Electroceram.* V5 (2000) 127.
83. B. Kumar, L. G. Scanlon, R. J. Spry, *J. Power Sources* 96 (2001) 337.
84. P. Johansson, M. A. Ratner, D. F. Shriver, *J. Phys. Chem. B* 105 (2001) 9016
85. J. E. Weston, B. C. H. Steele, *Solid State Ionics* 7 (1982) 81.
86. J. E. Weston, B. C. H. Steele, *Solid State Ionics* 7 (1982).
87. G. Tsagaropoulos, A. Eisenberg, *Macromolecules* 28 (1995) 396.
88. G. Tsagaropoulos, A. Eisenberg, *Macromolecules* 28 (1995) 6067.
89. S. Gagliardi, V. Arrighi, R. Ferguson, M. T. F. Telling, *Physica B* 301 (2001) 110.
90. A. Zhu and S. S. Sternstein, in *MRS Proc. Vol. 661* (A. I. Nakatani, R. P. Hjelm, M. Gerspacher, R. Krishnamoorti, eds.), MRS, Boston, MA, (2000) p. KK4.3.1.
91. W. E. Wallace, D. A. Fischer, K. Efimenko, W. L. Wu, J. Genzer, *Macromolecules* 34 (2001) 5081.
92. W. E. Wallace, J. H. Vanzanten, W. L. Wu, *Phys. Rev. A* 52 (1995) R3329.
93. J. H. Vanzanten, W. E. Wallace, W. L. Wu, *Phys. Rev. A* 53 (1996) R2053.
94. J. A. Forrest, J. Mattsson, *Phys. Rev. E* 61 (2000) R53.
95. J. A. Forrest, J. Mattsson, L. Borjesson, *Eur. Phys. J. A* 8 (2002) 129.
96. J. A. Forrest, K. Dalnoki-Veress, J. R. Stevens, J. R. Dutcher, *Phys. Rev. Lett.* 77 (1996) 2002.
97. J. A. Forrest, K. Dalnoki-Veress, *Advances in Colloid & Interface Science* 94 (2001) 167.
98. V. L. Vakula, L. M. Pritykin, *Polymer Adhesion: Physico-Chemical Principles*, E. Horwood, London, (1991).
99. S. H. Anastasiadis, A. Karim, G. S. Ferguson, *Interfaces, Adhesion and Processing in polymer systems* : symposium held April 24-27, (2000), San Francisco, California, U.S.A, *Materials Research Society, Warrendale, Penn.* (2001).

100. J. B. Kerr, J. Xie, R. Duan, *J. Electrochem. Soc.*, Submitted (2003).
101. D. R. Sadoway, B. Y. Huang, P. E. Trapa, P. P. Soo, P. Bannerjee, A. M. Mayes, *J. Power Sources* 97-8 (2001) 621 .
102. H. Lund, O. Hammerich, *Organic Electrochemistry: an Introduction and a Guide*, Marcel Dekker, New York, 2001.
103. O. Hammerich, V. D. Parker, *Electrochim. Acta* 18 (1973) 537 .
104. G. B. Appetecchi, F. Croce, L. Persi, F. Ronci, B. Scrosati, *Electrochim. Acta* V45 (2000) 1481.
105. Y. Nishi, in *Advances in lithium-ion batteries* (W. A. v. Schalkwijk and B. Scrosati, eds.), Kluwer Academic/Plenum Publishers, New York, (2002) p. 233.
106. B. Scrosati, in *Advances in lithium-ion batteries* (W. A. v. Schalkwijk and B. Scrosati, eds.), Kluwer Academic/Plenum Publishers, New York, (2002) p. 251.
107. M. Kono, E. Hayashi, M. Watanabe, *J. Electrochem. Soc.* 146 (1999) 1626.
108. M. Kono, E. Hayashi, M. Nishiura, M. Watanabe, *J. Electrochem. Soc.* 147 (2000) 2517.
109. A. S. Gozdz, C. N. Schmutz, J.-M. Tarascon, US Patent (1994).
110. M. Doyle, J. Newman, A. S. Gozdz, C. N. Schmutz, J. M. Tarascon, *J. Electrochem. Soc.* 143 (1996) 1890.
111. P. Arora, M. Doyle, A. S. Gozdz, R. E. White, J. Newman, *J. Power Sources* 88 (2000) 219 .
112. A. Du Pasquier, P. C. Warren, D. Culver, A. S. Gozdz, G. G. Amatucci, J. M. Tarascon, *Solid State Ionics* 135 (2000) 249.
113. A. Du Pasquier, T. Zheng, G. G. Amatucci, A. S. Gozdz, *J. Power Sources* 97-8 (2001) 758.
114. Y. Aihara, G. B. Appetecchi, B. Scrosati, K. Hayamizu, *Phys. Chem. Chem. Phys.* 4 (2002) 3443.
115. Y. Aihara, G. B. Appetecchi, B. Scrosati, *J. Electrochem. Soc.* 149 (2002) A849 .
116. J. M. Tarascon, A. S. Gozdz, C. Schmutz, F. Shokoohi, P. C. Warren, *Solid State Ionics* 86-8 (1996) 49.
117. S. A. Khan, G. L. Baker, S. Colson, *Chem. Mater.* V6 (1994) 2359 .
118. J. Fan, S. R. Raghavan, X. Y. Yu, S. A. Khan, P. S. Fedkiw, J. Hou, G. L. Baker, *Solid State Ionics* 111 (1998) 117 .
119. S. R. Raghavan, M. W. Riley, P. S. Fedkiw, S. A. Khan, *Chem. Mater.* 10 (1998) 244 .
120. H. J. Walls, J. Zhou, J. A. Yarian, P. S. Fedkiw, S. A. Khan, M. K. Stowe, G. L. Baker, *J. Power Sources* 89 (2000) 156 .
121. H. L. Dai, T. A. Zawodzinski, *J. Electrochem. Soc.* 143L (1996) 107.
122. H. L. Dai, T. A. Zawodzinski, *J. Electroanal. Chem.* 459 (1998) 111.
123. A. Eisenberg, J.-S. Kim, *Introduction to Ionomers*, Wiley, New York, (1998).
124. K. E. Thomas, S. E. Sloop, J. B. Kerr, J. Newman, *J. Power Sources* 89 (2000) 132
125. K. E. Thomas, R. M. Darling, J. Newman, in *Advances in lithium-ion batteries* (W. A. v. Schalkwijk and B. Scrosati, eds.), Kluwer Academic/Plenum Publishers, New York, (2002) p. 345.
126. D. R. Sadoway, A. M. Mayes, *MRS Bulletin* 27 (2002) 590 .
127. P. N. Powell, *Laser Focus World* 37 (2001) 41.
128. J. B. Kerr, *J. Electrochem. Soc.* 132 (1985) 2839 .
129. O. Chusid, Y. Gofer, D. Aurbach, M. Watanabe, T. Momma, T. Osaka, *J. Power Sources* 97-98 (2001) 632 .
130. W. Schmidt, E. Steckhan, *Angew. Chem.* 91 (1979) 850 .
131. W. Schmidt, E. Steckhan, *Angew. Chem.* 90 (1978) 717 .
132. J. W. Boyd, P. Schmahl, L. L. Miller, *J. Am. Chem. Soc.* 102 (1980) 3856 .
133. X. R. Zhang, J. K. Pugh, P. N. Ross, *J. Electrochem. Soc.* 148 (2001) E183 .
134. M. Moshkovich, M. Cojocar, H. E. Gottlieb, D. Aurbach, *J. Electroanal. Chem.* 497 (2001) 84 .

135. J. Newman, *Electrochemical Systems*, Prentice-Hall, Englewood Cliffs, NJ, (1991).
136. M. Doyle, J. Newman, *J. Power Sources* 54 (1995) 46.
137. M. Doyle, J. Newman, *Electrochim. Acta* 40 (1995) 2191.
138. M. Doyle, T. F. Fuller, J. Newman, *Electrochim. Acta* 39 (1994) 2073.
139. T. F. Fuller, M. Doyle, J. Newman, *J. Electrochem. Soc.* 141 (1994) 1.
140. T. F. Fuller, M. Doyle, J. Newman, *J. Electrochem. Soc.* 141 (1994) 982.
141. M. Doyle, T. F. Fuller, J. Newman, *J. Electrochem. Soc.* 140 (1993) 1526.
142. A. Ferry, M. M. Doeff, L. C. Dejonghe, *Electrochim. Acta* 43 (1998) 1387.
143. Y. P. Ma, M. Doyle, T. F. Fuller, M. M. Doeff, L. C. Dejonghe, J. Newman, *J. Electrochem. Soc.* 142 (1995) 1859.
144. H. J. Walls, T. A. Zawodzinski, *Electrochem. Solid-State Lett.* 3 (2000) 321.
145. A. Ferry, M. M. Doeff, L. C. Dejonghe, *J. Electrochem. Soc.* 145 (1998) 1586.
146. M. M. Doeff, P. Georen, J. Qiao, J. Kerr, L. C. De Jonghe, *J. Electrochem. Soc.* 146 (1999) 2024.
147. M. M. Doeff, L. Edman, S. E. Sloop, J. Kerr, L. C. De Jonghe, *J. Power Sources* 89 (2000) 227.
148. L. Edman, M. M. Doeff, A. Ferry, J. Kerr, L. C. De Jonghe, *J. Phys. Chem. B* 104 (2000) 3476.
149. M. M. Doeff, A. Ferry, Y. P. Ma, L. Ding, L. C. Dejonghe, *J. Electrochem. Soc.* 144 (1997) L20.
150. L. F. Nazar, G. Goward, F. Leroux, M. Duncan, H. Huang, T. Kerr, J. Gaubicher, *Int. J. Inorg. Mater.* 3 (2001) 191.
151. M. Doyle, J. P. Meyers, J. Newman, *J. Electrochem. Soc.* 147 (2000) 99.
152. E. Rivero, K. O. Thomas, J. Newman, Unpublished results 2002.
153. M. Doyle, M. E. Lewittes, M. G. Roelofs, S. A. Perusich, *J. Phys. Chem. B* 105 (2001) 9387.
154. M. Doyle, M. E. Lewittes, M. G. Roelofs, S. A. Perusich, R. E. Lowrey, *J. Membrane Science* 184 (2001) 257.
155. A. E. Feiring, S. K. Choi, M. Doyle, E. R. Wonchoba, *Macromolecules* 33 (2000) 9262.
156. D. P. Siska, D. F. Shriver, *Chem. Mater.* 13 (2001) 4698.
157. T. Fujinami, A. Tokimune, M. A. Mehta, D. F. Shriver, G. C. Rawsy, *Chem. Mater.* 9 (1997) 2236.
158. K. Matsushita, Y. Shimazaki, M. A. Mehta, T. Fujinami, *Solid State Ionics* 133 (2000) 295.
159. M. A. Mehta, T. Fujinami, *Chem. Lett.* 915 (1997).
160. G. C. Rawsy, T. Fujinami, D. F. Shriver, *Chem. Mater.* 6 (1994) 2208.
161. D. Benrabah, M. Armand, D. Delabouglise, *US Patent* 5,696,224, (1997).
162. D. Benrabah, S. Sylla, F. Alloin, M. Armand, *Electrochim. Acta* 40 (1995) 2259.
163. J. M. G. Cowie, G. H. Spence, *Solid State Ionics* 123 (1999) 233.
164. D. D. Desmarteau, *J. Fluorine Chem.* 72 (1995) 203.
165. L. Q. Hu, D. D. Desmarteau, *Inorg. Chem.* 32 (1993) 5007.
166. W. Xu, K. S. Siow, Z. Gao, S. Y. Lee, *Chem. Mater.* 10 (1998) 1951.
167. S. S. Zhang, G. X. Wan, *J. Appl. Polymer Sci.* 48 (1993) 405.
168. S. S. Zhang, L. L. Yang, Q. G. Liu, *Solid State Ionics* 76 (1995) 121.
169. S. S. Zhang, L. L. Yang, Q. G. Liu, *Solid State Ionics* 76 (1995) 127.
170. J. F. Snyder, M. A. Ratner, D. F. Shriver, *Solid State Ionics* 147 (2002) 249.
171. J. F. Snyder, M. A. Ratner, D. F. Shriver, *J. Electrochem. Soc.* 148 (2001) A858.
172. D. Rahner, *J. Power Sources* 82 (1999) 358.
173. R. E. A. Dillon, D. F. Shriver, *Chem. Mater.* 13 (2001) 1369.
174. S. York, R. Frech, A. Snow, D. Glatzhofer, *Electrochim. Acta* 46 (2001) 1533.
175. M. Paunovic, M. Schlesinger, *Electrochemical Society, Fundamentals of Electrochemical Deposition*, Wiley, New York, 1998.

176. D. Aurbach, E. Zinigrad, H. Teller, P. Dan, *J. Electrochem. Soc.* 147 (2000) 1274 .
177. J. O. Besenhard, J. Guertler, P. Komenda, M. Josowicz, *Proc. - Electrochem. Soc.* 88-6 (1988) 618 .
178. D. Fauteux, *Electrochim. Acta* 38 (1993) 1199 .
179. D. Fauteux, R. Koksang, *J. Appl. Electrochem.* 23 (1993) 1 .
180. K. Kanamura, *Erekutoronikusu* 43 (1998) 60 .
181. Z.-i. Takehara, *J. Power Sources* 68 (1997) 82 .
182. J.-i. Yamaki, S.-i. Tobishima, K. Hayashi, K. Saito, Y. Nemoto, M. Arakawa, *J. Power Sources* 74 (1998) 219 .
183. M. Rosso, T. Gobron, C. Brissot, J. N. Chazalviel, S. Lascaud, *J. Power Sources* 97-98 (2001) 804 .
184. C. Brissot, M. Rosso, J. N. Chazalviel, S. Lascaud, *J. Power Sources* 94 (2001) 212
185. C. Brissot, M. Rosso, J. N. Chazalviel, S. Lascaud, *J. Electrochem. Soc.* 146 (1999) 4393 .
186. C. Brissot, M. Rosso, J. N. Chazalviel, S. Lascaud, *J. Power Sources* 82 (1999) 925 .
187. C. Brissot, M. Rosso, J. N. Chazalviel, P. Baudry, S. Lascaud, *Electrochim. Acta* 43 (1998) 1569 .
188. M. Dolle, L. Sannier, B. Beaudoin, M. Trentin, J. M. Tarascon, *Electrochem. Solid-State Lett.* 5 (2002) A286 .
189. F. Orsini, L. Dupont, B. Beaudoin, S. Grugeon, J. M. Tarascon, *International Journal of Inorg. Mater.* 2 (2000) 701 .
190. F. Orsini, M. Dolle, J. M. Tarascon, *Solid State Ionics* 135 (2000) 213.
191. F. Orsini, A. du Pasquier, B. Beaudoin, J. M. Tarascon, M. Trentin, N. Langenhuiizen, E. de Beer, P. Notten, *J. Power Sources* 82 (1999) 918 .
192. F. Orsini, A. Dupasquier, B. Beaudoin, J. M. Tarascon, M. Trentin, N. Langenhuiizen, E. Debeer, P. Notten, *J. Power Sources* 76 (1998) 19 .
193. T. Osaka, T. Homma, T. Momma, H. Yarimizu, *J. Electroanal. Chem.* 421 (1997) 153 .
194. J. A. R. Stiles, K. Brandt, D. S. Wainwright, K. C. Lee, *US Patent* 4,587,182, (1986).
195. E. Eweka, J. R. Owen, A. Ritchie, *J. Power Sources* 65 (1997) 247 .
196. T. Tatsuma, M. Taguchi, N. Oyama, *Electrochim. Acta* 46 (2001) 1201 .
197. C. Michot, A. Vallee, P.-E. Harvey, M. Gauthier, M. Armand, *US Patent* 6,492,449, (2002)
198. M. Gauthier, A. Belanger, A. Vallee, *US Patent* 6,007,935, (1999).
199. J. Elezgaray, C. Leger, F. Argoul, *J. Electrochem. Soc.* 145 (1998) 2016 .
200. D. S. Louch, M. D. Pritzker, *J. Electroanal. Chem. Interfac. Electrochem.* 319 (1991) 33.
201. D. S. Louch, M. D. Pritzker, *J. Electroanal. Chem.* 346 (1993) 211.
202. L. G. Sundstrom, F. H. Bark, *Electrochim. Acta* 40 (1995) 599 .
203. M. D. Pritzker, T. Z. Fahidy, *Electrochim. Acta* 37 (1992) 103 .
204. J. Xie, G. Liu, Y. B. Han, K. J.B., Unpublished results (2003).
205. F. Wang, M. Hickner, Y. S. Kim, T. A. Zawodzinski, J. E. McGrath, *J. Membrane Science* 197 (2002) 231 .
206. S. J. Visco, F. Y. Tsang, *US Patent* 6,432,584, (2002)
207. S. J. Visco, M.-Y. Chu, *US Patent* 6,025,094, (2000)
208. N. J. Dudney, *J. Power Sources* 89 (2000) 176.

Chapter 20

GLASS AND CERAMIC ELECTROLYTES FOR LITHIUM AND LITHIUM-ION BATTERIES

N. J. Dudney

*Solid State Division, Oak Ridge National Laboratory, P. O. Box 2008, Oak Ridge,
Tennessee 37831-6030, U.S.A.*

20.1. INTRODUCTION

In recent years there have been important advances in the stability, safety, and performance of lithium and lithium-ion batteries. Many of the electrolyte materials being examined are based on organic liquids or polymers, although solid inorganic electrolytes still have an important role for a variety of applications. There are numerous reports of new compositions, advanced synthesis routes, and novel cell architecture for the glass and ceramic electrolytes.

For any rechargeable lithium battery, the electrolyte material must permit the repeated and rapid transfer of Li^+ ions between the anode and cathode over the expected range of operating conditions (voltage, temperature, and current), without significant deterioration. Additionally, the ideal electrolyte material would be an electronic insulator, ultra-thin, lightweight, free of hazards and inexpensive. The inorganic solid electrolytes offer both advantages and disadvantages over liquid and organic polymer electrolytes. For the required rapid transport of Li^+ across the electrolyte, the product of the resistivity and electrolyte thickness must be minimized. Typical room temperature conductivities are 10^{-1} S/cm for liquids, 10^{-2} S/cm for superionic conductors such as β -alumina, 10^{-3} to 10^{-6} S/cm for various gel and solvent-free (dry) polymers, and 10^{-4} to 10^{-8} S/cm for typical glass and ceramic solid electrolytes. If formed as a very thin film of less than about $1\text{ }\mu\text{m}$, even a rather resistive material may compete favorably when compared to a much thicker cast polymer or liquid-filled porous separator membrane. An ultra-thin electrolyte also provides a considerable savings in terms of volume and mass for the battery, if not offset by the need for a thick inactive support material. It comes as a

surprise to many that 1-10 μm thick glass and ceramic sheets are quite flexible.

One of the principle advantages of the inorganic solid electrolytes is that these materials are generally single ion conductors, meaning that only the Li^+ ions have an appreciable mobility, while the anions and other cations form a rigid framework. This has many beneficial consequences. Eliminating the anionic concentration gradient across the electrolyte may help suppress undesirable side reactions or decomposition of the electrolyte. The single ion conductor expands the choice of electrode materials and permits operation at higher voltages. Few polymer electrolytes mimic this single ion behavior and they are usually associated with a higher resistivity.¹ Likewise, a negligible electron transport across the electrolyte is necessary to prevent self-discharge of the battery. For a shelf life of months or years, the electrolyte must be an excellent insulator with an electronic conductivity $< 10^{-12}$ S/cm. Conductive electron paths may be formed along lithium dendrites for liquid or polymer electrolytes, while grain boundaries, pores, or cracks may become electronic paths for glass and ceramic electrolytes. Significant concentrations of multivalent ions in inorganic electrolytes may also contribute to electronic transport. Ideally, the lithium ion transference and transport numbers should be as close as possible to identically 1.0.

The resistance of the solid electrolyte-electrode interface is just as important and often as large as the bulk resistivity of the electrolyte. Because of this, reports of an electrolyte's properties are insufficient without an evaluation in contact with reversible electrodes comparable to those for the Li-ion battery. One might assume that ion exchange across the solid electrolyte-electrode interface would be more resistive than that with a liquid or soft polymer electrolyte. This is not necessarily the case, due to the formation of a "solid electrolyte interphase" (SEI) reaction layer, which adds to the interface resistivity for most liquid or polymer electrolytes. The solid electrode-electrolyte interface has the added advantage of providing a dense, hard surface that maintains its integrity and inhibits roughening of the microstructure that leads to mossy or dendritic deposits. Without good adhesion however, stresses may cause a rigid interface to form permanent cracks or voids.

The nature of the highly active lithium battery chemistry places severe electrochemical requirements on the electrolyte. Many of the glass and ceramic electrolytes proposed in the literature decompose under high voltages or react with lithium, but some are indeed believed to be thermodynamically stable. The organic electrolytes, on the other hand, invariably rely on the formation of a protective SEI layer to limit the reaction or decomposition rate.

As there are hundreds of different electrolyte compositions in the literature, this chapter will cover work published since 1995 or 1997, including newly investigated electrolytes, as well as known electrolytes that

continue to be used and studied for experimental batteries. The discussion will also focus on electrolytes for low and ambient temperature conditions, of primary interest for lithium-ion batteries. In 1995, publication of two chapters summarized the compositions, properties, and battery applications of glassy lithium electrolytes.^{2,3} The most recent review of crystalline ceramic lithium electrolytes appeared in 1997.⁴ An earlier overview addressing the motion of the lithium ions through either the amorphous or crystalline environment was presented in 1993.⁵

The compositions and properties of glassy and ceramic electrolytes to be discussed in this chapter have been summarized in Tables 20.1-2 at the end of this chapter. Not every composition is included, only representative examples of each class of electrolyte. The cited literature should be consulted for a thorough listing. Likewise, many reports cover a range of compositions, but for simplicity, the tabulated compositions are limited to those giving the maximum observed lithium conductivity. The table includes the synthesis process, the electrolyte thickness, the Li^+ ion and electronic transport properties, and the electrochemical stability. No doubt, in all cases the electrolyte could be formed as a thinner layer, but the tabulated values establish the current art. The stability range is given as reported by the authors, although in some studies, it appears that currents larger than that attributable to an electronic carrier were observed well before an obvious breakdown voltage. Very few studies evaluate the interface resistance with reversible lithium electrodes; these results will be noted in the text.

20.2. GLASS ELECTROLYTES

With many glassy lithium conductors already in the literature, the majority of recent work is tending away from the traditional glass processing to explore twin roller, vapor deposition, high-energy mechanochemical milling, or even explosive glass forming processes. These processes expand the normal glass-forming region. A number of studies reveal that compositions with a higher concentration of the Li modifier, *e.g.* Li_2O and Li_2S , give a higher conductivity and lower activation energy for Li^+ transport. For many compositions, the glass is almost fully depolymerized.

Commonly perceived advantages of glassy electrolytes over crystalline ceramic materials include: isotropic conductivity, ease of fabrication as dense thin films, and lack of grain boundaries. Grain boundaries in polycrystalline or granular electrolytes have an inherently lower density, higher defect concentration, space charge polarization, and segregated impurities. These may form resistive barriers for Li^+ but fast paths for other species, increasing the likelihood of an internal short circuit, a precipitated Li metal dendrite, or breakdown related to electrochemical stress. The nature and effect of boundaries in glass electrolytes formed as pressed compacts of crushed glass powder has not been determined.

20.2.1. Oxide Glasses

Compared to earlier reviews, fewer pure oxide glasses have been reported in recent years. This is likely due to their unexceptional conductivity. The big advantage of the lithium oxide glasses is that, although they may be hygroscopic, they are relatively stable in air. This simplifies the synthesis and handling of the material.

As illustrated by the first entry in Table 20.1, glasses with mixed formers, such as Se and B, have a reasonable conductivity.⁵ If formed as very thin films, such glass compositions may prove to be promising electrolytes. Unfortunately, this selenate-borate glass has not been evaluated as a thin film or with Li-ion electrodes. The second oxide glass is a vitrified form of a crystalline Li electrolyte with a nasicon structure to be discussed below.⁶ It was included to illustrate that even when doped with the LiCl modifier salt, the conductivity of the glass is an order of magnitude lower than that of the polycrystalline material with an open network structure that facilitates the Li transport. For other Li compounds, such as Li_3PO_4 and Li_2SiS_3 , the situation may reverse as the amorphous phase is indeed orders of magnitude more conductive than compact crystalline phases.

20.2.2. Oxynitride Glasses and Lipon

The phosphorus oxynitride glass, commonly referred to as 'lipon,' was pioneered at Oak Ridge National Laboratory (ORNL) in 1991⁷ and more fully characterized by ORNL researchers in later years.⁸ Subsequent publications number roughly 20 from several research institutions. Lipon films, about 1 μm thick, are typically deposited by *rf* magnetron sputtering from a high purity Li_3PO_4 ceramic target in nitrogen plasma. Attempts to fabricate glasses of similar compositions from the melt have been unsuccessful suggesting that vapor deposition is equivalent to a rapid quench preventing separation of a Li-rich phase. The small amount of N incorporated into the films from the plasma effectively stabilizes the material in contact with metallic lithium and enhances the ionic transport by 40-fold compared to amorphous Li_3PO_4 films also prepared by sputtering. Lipon has proven highly successful for Li and Li-ion thin film batteries fabricated at ORNL.⁹ Lipon is being investigated by a number of groups for a variety of electrochemical applications including: thin film batteries,^{10,11,12} CO_2 sensors,¹³ thin film capacitors,¹⁴ and electrochromic windows.

Deposition rates achieved by magnetron sputtering just exceed 10 nm/m.¹⁵ Because this is rather slow for a practical commercial process, researchers at Tufts have reported using a nitrogen ion beam and thermal

evaporation source in a so-called ion beam directed assembly (IBDA) process to deposit lipon at >30 nm/m.¹⁰ The IBDA deposited lipon has good conductivity and electrochemical properties, but appears to be prone to crack due to a residual tensile stress.¹⁶ A similarly high deposition rate is achieved by pulsed laser ablation which yields amorphous film of comparable conductivity.¹⁷ Some researchers report a variation of composition and conductivity as lipon is deposited by sputtering at higher rates, both detrimental¹⁸ and advantageous,¹⁹ although neither has been observed at Tuffs and ORNL. Variation in results from group to group is not surprising for this non-equilibrium synthesis. Film thickness is commonly about $1\text{ }\mu\text{m}$ as needed for good coverage of rough underlying electrode films. If the lipon were deposited onto a smooth and crack free surface, a continuous pinhole free film might be obtained with a submicron film, however a great improvement in cell performance would likely be thwarted without a comparable reduction in the interface resistance. Much is yet to be learned about control of the vapor deposition processes.

Compositions of the lipon films ($\sim 0.1\text{ mg/cm}^2$) are difficult to determine with accuracy greater than about $\pm 10\%$, so a clear analysis of the variation of conductivity and activation energy with composition is lacking. It is certain that a small substitution of N for O in the amorphous Li_3PO_4 material greatly enhances the Li mobility, due to either the formation of additional cross-linking between phosphate groups or a decrease of the electrostatic energy when P-O is replaced by P-N bonds.²⁰ The maximum reported conductivity is $2.3 \cdot 10^{-6}$ S/cm for compositions of about $\text{Li}_{2.9}\text{PO}_{3.3}\text{N}_{0.46}$. Variations in the conductivity upon further N substitution or the addition of N + Li are more subtle and difficult to quantify. Equally important for the conductivity is the relaxation of the structure. Increases of 2 to 4 times in the conductivity may occur when the lipon film is annealed briefly at temperatures of $150\text{--}250^\circ\text{C}$.

For a successful solid electrolyte, the electrochemical stability and electronic resistivity is as important as the Li ion conductivity. These properties are often assessed by current-voltage measurements with lithium and a blocking electrode, but the best evaluation is the long-term stability of a high voltage lithium cell. As reported at recent meetings, Li/LiCoO₂ batteries with a lipon electrolyte show a negligible self discharge rate at both fully charged (4.2V) and fully discharged (3V) conditions when stored for a year or more.²¹ Based on these results, the estimated electronic resistivity must exceed 10^{14} ohm-cm. The chemical stability of lipon in contact with Li metal may be attributed to the reducing character of the oxynitride glass matrix.²² Preliminary results for a similar sputter deposited lithium boron oxynitride electrolyte film have also been reported.²³ The electrochemical stability has not been assessed, but may be comparable to that of the phosphate material.

20.2.3. Sulfide and Oxsulfide Glasses

Original work on highly conductive Li sulfide glasses based on SiS_2 , P_2S_5 , and B_2S_3 , was reported 15 years ago.^{24,25} The impressive conductivities and low activation energies compared to the oxide glasses were attributed to the weaker bonding of Li with the non-bridging sulfur anions, due to the higher polarizability and softer basicity of the sulfide ion. As for the oxide glasses, the maximum conductivities were identified with large concentrations of the glass modifier allowing only a minimal degree of polymerization. These glasses have not been widely used largely because they are quite difficult to handle. Being both highly reactive with air and highly corrosive with silica containers, great care and a highly efficient glove box are required to synthesize and fabricate the sulfide glasses. Renewed interests by several Japanese groups in recent years have led to the modified processing and compositions summarized in Table 20.1.

The use of mechanochemical milling was first demonstrated for $\text{Li}_2\text{S}\cdot\text{SiS}_2$ compositions²⁶ and then expanded to the $\text{Li}_2\text{S}\cdot\text{P}_2\text{S}_5$ ²⁷ and various oxsulfide compositions. This process uses a high-energy planetary ball-mill to amorphize the mixed sulfide reactants at room temperature under a dry N_2 or Ar atmosphere. Achieving complete amorphization, as indicated by X-ray diffraction, generally required milling times of about 20 hours, but the total energy consumed was still less than that used in a traditional melt-quench process. A further advantage of this process is that the resulting fine-grained powder was ready to fabricate directly as a pressed pellet or as the electrolyte layer in a compacted solid state battery. In comparison, the lithium ion conductivities achieved by the ball-milling were as high or nearly as high as that of glasses prepared by twin-roller rapid quench of the same composition. There are also examples of an expanded glass forming region being achieved by the mechanochemical milling process.²⁷

Addition of a small amount, ~5 mole%, of a variety of different lithium metal oxides (silicate, phosphate, and germanate) was found to stabilize the sulfide glass structure as evidenced by an increase in the difference between the crystallization temperature and the glass transition temperature.²⁸ Results from NMR and XPS show the oxygen to be primarily bonded as a bridging anion. Larger additions of these lithium metal oxides become detrimental to the thermal stability and lithium ion conductivity, as increasing amounts of oxygen are found in a non-bridging coordination which impede the mobility of the lithium ions. Alternatively, additions of various group IVA, VA, VIA, and VB sulfides greatly enhance the thermal stability of the $\text{Li}_2\text{S}\cdot\text{SiS}_2$ glass.²⁹ Even when slow cooled or annealed, many

of the compositions remained vitreous with a high lithium conductivity near 1 mS/cm. This allowed for the fabrication of glass plates rather than pelletized samples of glass flakes or powders. The electronic conductivity is

clearly small, but the precise effect of the transition metals on the electronic conductivity has not been assessed.

All solid state batteries, In/LiCoO₂ and Li/LiCoO₂, have been prepared using the lithium silicon oxysulfide electrolyte compositions shown in Table 20.1.^{30,31,32} The cells were formed by compacting the ground electrolyte powder together with the cathode mixture and In or Li foil in a 1-cm diameter insulating tube. After several initial cycles, the cycling proceeded with a 100% coulomb efficiency for 100 cycles indicating good electrochemical stability. Although the electrolyte thickness was not given, the observed cell resistance (0.7-2 kohm) was higher than anticipated for an estimated 0.5 mm thick layer of the highly conductive electrolyte. This high internal resistance was attributed to the electrode interfaces, an important issue discussed briefly below. The reversible capacity was only 60 mAh per gram LiCoO₂ when using the In anode, while a higher capacity of 80-90 mAh/g is reported for the Li cell. A variety of cathode materials including LiVS₂ and Li₂FeCl₄ were evaluated with this same tubular cell construction of compacted powders.³³ These cathode materials, which had been deemed poorly reversible in liquid cell experiments, were shown to cycle with good capacity and efficiency in the cells using the glassy solid electrolyte.

20.2.4. Thionitride Glasses

Highly conductive thionitride glasses are also reported.^{34,35} These are formed by rapid quench or high energy mechanical milling processes as described for several of the sulfide glasses. Although the maximum conductivity is reported for material milled for 20 hours, a conductivity of 0.1 mS/cm is reported after only 20 minutes. Significant oxygen contamination is attributed to the milling media. A single voltammetric sweep (-0.5 to 10 V) indicates a wide stability range; however, the data plots are too coarse to ascertain the absence of significant tarnishing or interface reactions. It is clear that the electrochemical stability far exceeds that of Li₃N.

20.2.5. Lithium Halide Doped Glasses

In recent years, little additional work has been reported for Li halide doped glass compositions, although numerous compositions were reviewed earlier.¹ The most conductive Li electrolyte reported to date, >2 mS/cm, is a

LiI doped sulfide glass of 60Li₂S•40SiS₂•2.8TaS₂•4LiI.²⁹ One old composition, xLiI•(1-x)[0.6Li₂S•0.4B₂S₃] was revisited to evaluate the influence of the LiI on the lithium motion in light of recent models for the

ionic transport.³⁶ The mechanism of ion transport in the glassy structure continues to be a topic of experimental and theoretical research.

20.3. CRYSTALLINE CERAMIC ELECTROLYTES

Many ceramic electrolytes have been investigated, although few have been evaluated in actual electrochemical cells. A notable exception is LiI-based electrolytes for Li/I₂ batteries which are in commercial use to power cardiac pace makers. Ceramic electrolyte materials include oxides, sulfides, nitrides, halides, and a variety of polyanion compositions. Although some impressive lithium conductivities are reported, fabrication and stability issues require further attention.

The ceramic electrolyte materials were reviewed in 1997 for the application in high temperature lithium batteries.³ The materials requirements differ from those for the Li-ion battery only with regard to the activation energy. For the high temperature applications, high activation energy offers the advantage of a thermal switch for the cell, whereas a Li-ion battery electrolyte should ideally have a low activation energy. To avoid duplication, this discussion will highlight only very recent reports, emphasizing the electrolytes formed as films or with valuable insight concerning the electrochemical stability and electronic conduction. These are summarized in Table 20.2.

Several important issues arise for each class of crystalline electrolyte: electrochemical stability, grain boundaries, and fabrication as thin sheets. The stability is an important issue as many compositions contain transition metal cations which may compensate for lithiation or de-lithiation reactions. Depending on the composition and lattice, such reactions may result in a significant electronic conduction through the material. For the superionic conductive crystal phases, the disorder accompanying grain boundaries generally *impedes* the ion transport and decreases the conductivity. The electrolytes are hence very sensitive to processing factors affecting the density and grain size. On the other hand, for materials that conduct via lattice defects, such as vacancies and interstitials, the ion transport is often *enhanced* by the presence of grain boundaries, a dispersed second phase, or other extended defects. Most studies report results for cold-pressed and sintered ceramic pieces, while few present results for thin layers which would be far more appropriate to battery applications. Presumably, controlling the microstructure in thinner cast, spun or sprayed layers poses additional difficulties.

20.3.1. Perovskite Electrolytes

There has been a flurry of research on polycrystalline lithium electrolytes with the perovskite crystalline structure in recent years (Refs. 37,38 and references therein). In excess of 20 different compositions have been reported. Three of the simplest and most conductive compositions are reported in Table 20.2. The perovskite structure, with the general formula ABO_3 , has a remarkable tolerance for ion substitution, both aliovalent and isovalent, on both the A and B lattice sites. This can be exploited to create open lattice structures and compositions with large vacancy concentrations on the A sublattice. For the Li conductors, up to as much as $1/6^{\text{th}}$ mole of Li^+ ions are substituted into various A-deficient compositions. The lithium conductivity depends on a variety of factors, including: the lithium and vacancy concentrations on the A sites, the degree of cation ordering, the size and symmetry of the unit cell. Even when all the A sites are filled, there may still be appreciable Li conductivity, suggesting the availability of additional sites for the lithium.³⁷ The highest reported conductivity is $1.5 \cdot 10^{-3} \text{ S/cm}$ for $\text{La}_{2/3-x}\text{Li}_{1/3+x}\text{TiO}_3$, with $x \sim 0.11$.³⁹ Generally, substitution of the La by other rare-earth cations reduces the conductivity, as does substitution of the Ti with other tetra- or penta-valent cations. There is some variability in the grain boundary contribution to the total resistance.^{38,40} For some materials the grain boundary contribution to the resistivity is 10 to 100-fold higher than that of the crystal lattice (bulk), as evaluated by the frequency scans of the complex impedance. In most reports, these materials are prepared as pressed and sintered pellets of powders produced by solid state reaction.

So far, the perovskite electrolytes have not been used in any lithium or lithium-ion batteries. One potential difficulty is that additional Li can be intercalated into the lattice upon contact with metallic lithium or other lithium anode materials with a low electrochemical potential versus Li/Li^+ .⁴¹ This may result in a significant electronic conductivity due to the reduction of Ti^{4+} cations. The Ta-perovskites with a stable +5 oxidation state, however, are expected to be more stable than those with Ti.⁴² On the other hand, the cyclic voltammetry study of a Nb-perovskite⁴⁰ shows that reduction does indeed commence at voltages below 2.0 versus metallic Li, a reaction that is not fully reversible. This reaction effectively eliminates this Nb composition as a candidate for any Li-ion battery under current consideration. There is far too little research on the electrochemical stability and electronic conductivity of these materials to assess whether other perovskites are electrochemically stable towards the lithium intercalation. If a stable composition is identified, a perovskite electrolyte may prove highly conductive and relatively easy to fabricate and handle in air.

20.3.2. Nasicon-Type Phosphates

Another widely studied class is the lithium analogues of the so-called Nasicon phase (Na SuperIonic conductor). The general composition is $\text{Li}_{1+x}\text{M}_2(\text{PO}_4)_3$ with $0 < x < 3$. More than a dozen formulas containing different combinations of M cations have been reported. The structure consists of PO_4 and MO_6 polyhedra linked at corners to form open 3D tunnels in the crystal. The original sodium material contained $\text{M}=\text{Zr}$, however the smaller tunnels formed with $\text{M}=\text{Ti}$ were a better fit for the lithium conductors giving a bulk (lattice) conductivity of 3 mS/cm.⁴³ Although controversial in earlier work, it now appears clear that lower conductivities of $<10^{-4}$ are attributed to a grain boundary contribution to the total impedance. A reasonable conductivity has also been reported for thin films formed by several cycles of ultrasonic spray pyrolysis followed by an 800-1000°C anneal.⁴⁴

As for the perovskites, the potential for lithium insertion compensated by the reduction of the M cation may prohibit their use with most lithium anode materials. Again the Ti^{4+} is readily reducible, but the Al,Ta or Al,Ge compositions are expected to be electrochemically stable with Li.^{45,46} Unfortunately, this has not been evaluated by either cell fabrication or voltammetry studies. The results in Table 2 for the Al,Ti material show the only experimental evaluation of this Li insertion reaction, which occurs at 2.4 V versus Li/Li^+ .⁴⁷ Because this lithiation reaction was slow, the researchers were encouraged to add a $\text{LiBO}_2 \cdot \text{LiF}$ sintering aid which blocked the electronic conductivity while only reducing the lithium conductivity 2-fold. With this composite electrolyte, they succeeded in preparing and cycling a $\text{Li}_4\text{Ti}_5\text{O}_{12}/\text{LiMn}_2\text{O}_4$ battery. Numerous other compositions have been studied,^{48,49} largely to elucidate the relation between the structure and ion mobility. Several with high conductivities are presented in Table 20.2, including two with a Li-rich composition.

In additional publications, researchers report the properties and synthesis of several glass-ceramic lithium electrolytes for which the ceramic phase has the Nasicon-type crystal structure. The anticipated advantages of such a glass ceramic include: a reduced grain boundary resistance, dense microstructure, and greater ease of fabrication. Conductivities as high or higher than the sintered ceramic material have been reported for the Al,Ti and Al,Ge Nasicon grains crystallized from the mother glasses.^{50,51} As the anneal temperature is increased, grain growth leads to enhanced conductivity and reduced activation energy. Using a different approach, grains of $\text{LiTi}_2(\text{PO}_4)_3$ were mixed with powders of the $\text{Li}_2\text{S} \cdot \text{SiS}_2 \cdot \text{Li}_3\text{PO}_4$ glass discussed above.⁵² Small amounts of the ceramic powder, ≤ 10 wt.%, had little effect on the conductivity of the sulfide glass.

20.3.3. Lisicon-Type Materials

Lithium superionic conductors have an ABO_4 composition and a structure known as $\gamma\text{Li}_3\text{PO}_4$ in which the B tetrahedra share corners with clusters of three AO_4 tetrahedra. Solid solutions are formed with mixed cations at both the A and B sites, commonly Li and Zn at A sites, and V and Ge at B sites, but other combinations as well. One of the few thin film electrolytes of this phase is reported in Table 20.2.⁵³ In the bulk material, the composition is $\text{Li}_{3.4}(\text{V}_{0.6}\text{Si}_{0.4})\text{O}_4$ with a good (1 mS/cm) lithium conductivity and low electronic component ($t_e=10^{-7}$). However, when deposited as a thin film by sputtering, a large excess of Li_2O is incorporated in the highly disordered material which compromises the electron transference number. Appreciable self-discharge currents were observed for thin film batteries of Li versus Mo, W, or Mn oxide cathodes. The authors were optimistic about improving this performance, however a disordered structure with transition metal cations will likely always be susceptible to leakage currents.

A number of sulfide compounds with a lisicon structure are newly reported.^{54,55} As with the sulfide glasses, care must be taken to protect the reactive materials from the air and oxide containers. The compositions giving the maximum conductivity for two different solid solutions are given in Table 20.2, the Ge,P solid solution being most attractive. A Hebb-Wagner analysis for the phosphorus compound indicates a low electronic transference number when polarized up to 2V. The authors report electrochemical stability with lithium metal and for polarization up to ~5V versus Li, although the results are difficult to read and the current appears to be $\sim 10\mu\text{A}/\text{cm}^2$ at 5V suggesting a significant reaction. Batteries formed of compacted In/LiCoO_2 with the more resistive Ge,Ga electrolyte give an initial discharge capacity of $\sim 80\text{ mAh/g}$ of LiCoO_2 at low currents. These so-called 'thio-lisicon' materials deserve further investigation.

20.3.4. Lithium Metal Halides, Nitrides, and Phosphides

Earlier reports of halide compositions were mainly: (1) inverse spinels, $\text{Li}[\text{LiM}]\text{Cl}_4$, with M being a wide variety of divalent transition metals; (2) various combinations of metal nitrides with Li_3N , *e.g.* Li_8SiN_4 ; and (3) several mixed Li_3P - Li_3N compositions.³ Many of these have good conductivities at higher temperatures, but are prone to decompose at low voltages versus lithium making them unlikely candidates for Li-ion batteries. Several different structures identified in recent publications are highlighted in Table 2. In all cases, the materials must be carefully dried and prepared in a protective atmosphere. None of the studies have advanced to the point of testing electrochemical cells or forming the electrolyte as a thin layer. The

antifluorite structure of doped- $\text{Li}_9\text{N}_2\text{Cl}_3$, and the unidentified structure of $\text{Li}_9\text{Bi}_2\text{Cl}_3$ both have modest low temperature lithium conductivity and electrochemical stability up to 1.5-2.5 V versus Li.^{56,57} A higher room temperature conductivity is reported for the Li_3InBr_6 , which is considered a superionic conductor.⁵⁸ In the absence of a superion conducting phase, composite materials may show high conductivity attributed to the disorder and space charge layers formed at phase boundaries, grain boundaries, and other extended defects. This has been demonstrated for $\text{Li}_3\text{P} + 3\text{LiCl}$ composite electrolyte.⁵⁹ The last electrolyte in the table is a soft solid, hence not really a ceramic electrolyte. The combination of a lithium salt and strong Lewis acid gives a good low temperature conductor that might readily form a good interface contact with high surface area electrode materials.⁶⁰

20.3.5. Other Compositions

Two families of electrolytes that received detailed coverage in the earlier review,³ are not included here. For the electrolytes formed of Li_2SO_4 and related phases, an adequate lithium transport is limited to the high temperature phase making ambient temperature batteries with these electrolytes impractical. In the second case, no new research has been reported for electrolytes formed of solid solutions with lithium orthosilicate, Li_4SiO_4 . Earlier work reported a large number of these electrolytes doped with a variety of penta-, tri-, and di-valent cations producing large concentrations of mobile lithium defects. Although conductivities are modest, some compositions have proven electrochemically stable and good electronic insulators as was demonstrated for $\text{Li}_9\text{SiAlO}_8$.⁶¹

A final electrolyte, which eluded the earlier reviewer, is the lithia-doped boron phosphate $x\text{Li}_2\text{O} \cdot \text{BPO}_4$.⁶² These researchers adopted refreshingly unique and practical approaches to both forming the electrolyte, by various soft-chemical syntheses, and a complete solid state battery, by the dynamic compaction of laminated sheets.⁶³ Unfortunately, the completed batteries have so far proven more resistive than anticipated from studies of the electrolyte.

20.4. MODELS FOR ION CONDUCTION

Building on earlier models,⁴ new work continues to explore ion motion in a disordered structure.⁶⁴⁻⁶⁸ This includes ion motion in crystalline electrolytes lacking long range order of the lithium, as well as in the glassy electrolytes. The description of ion transport as the random walk of thermally activated point defects is not appropriate in these systems. Most

attention has focused on describing the power-law frequency dispersion of the conductance and NMR studies. Experimental conductivity data span many orders of magnitude in frequency (*dc* to far infrared) and a wide range of temperature.⁶⁴ Scaling the conductivity isotherms by a single activation energy collapses the data onto a single universal curve, good evidence that the charge carrier concentration is not thermally activated.

The model emerging⁶⁴ to describe the dispersion at moderate temperatures, where the conductivity exceeds the *dc* value, is of an ion hopping backwards and forward many times without contributing to a net *dc* conductivity. A productive hop occurs only when the neighboring ions relax to favor the new site over the old, before the ion can hop backwards. For glass electrolytes, there is experimental evidence for the existence of two types of target sites, one being more optimally configured for the mobile ion. These optimum sites form stepping stones for the ion through the network or lattice.⁶⁴ Models of the short-range ordering in lithium glassy electrolytes predict such weak structural inhomogeneities.^{65,66} Although these are associated mainly with the distribution of a lithium modifier salt, such as LiCl, similar inhomogeneities likely occur in other glass compositions. The site relaxation model has also been applied to the perovskite lithium electrolytes in which lithium is disordered over the vacant A sites.⁶⁷ A different dispersion is observed at very low temperatures for both glassy electrolytes and the lithium perovskites.^{64,68} The ion conductivity becomes proportional to the frequency, forming the so-call 'nearly constant loss' region, which is believed to reflect the ions vibrating within their potential wells.

Ion transport across the electrolyte – electrode interface has received much less attention, but is critically important for achieving low resistance solid state batteries. Simulations and model calculations for the case of a glassy electrolyte-crystalline electrode, highlight the importance of the interface energy barrier, the mismatched hopping frequencies,⁶⁹ and easy diffusion paths provided by favorable orientation of the crystal lattice or grain boundaries.⁷⁰

20.5. CONCLUSION

At the most recent International Meeting on Lithium Batteries (IMLB11, July 2002), ceramic and glass electrolytes accounted for only a small percentage of the contributions. Attention is clearly focused on the performance of polymer, gel and polymer composite electrolytes, while liquid electrolytes continue to be used for most routine electrode studies. For the most part, cells with the organic electrolytes are cheaper and faster to fabricate and have acceptable internal resistance and cycle life due to good progress in controlling the solid electrolyte interphase (SEI) layer formed at

the electrode - electrolyte interfaces. Although the consumer Li-ion batteries will likely continue to use organic electrolytes, other applications may benefit from the introduction of ceramic or glass electrolytes, including applications requiring extreme (high or low) operating temperatures, maximum lifetimes, negligible self-discharge, and extremely thin profiles.

Most research on ceramic and glass electrolytes still falls short of what is needed to address practical application of the materials. Results of the electrochemical stability have been most neglected and this can only be fully evaluated by actually making and cycling complete Li or Li-ion cells. Also missing are reports of fabrication techniques with an emphasis on minimizing the thickness of the electrolyte layer. Of the materials reviewed in this chapter, several stand out as particularly promising, including: the sputter deposited Lipon thin films, the slow quenched $\text{Li}_2\text{S}\cdot\text{SiS}_2$ glasses stabilized with a few percent Ta or Sn sulfide, and the $\text{Li}_{1.4}\text{Ge}_{1.6}\text{Al}_{0.4}(\text{PO}_4)_3$ glass ceramics. The thio-lisicon also looks interesting, but requires additional research.

Another valuable approach is to create laminated electrolytes using the ceramic or glass electrolytes in conjunction with a liquid or polymer electrolyte. This has been demonstrated using lipon-coated separator membranes, lipon-coated cathode films, and glass-coated metallic lithium anodes.^{71,72} The addition of such a mechanically hard, single-ion electrolyte film to the liquid or polymer electrolyte layer may eliminate the formation of lithium dendrites, inhibit chemical and dissolution reactions of the electrode materials, and reduce the concentration gradients that form due to anion diffusion within organic electrolytes. In addition, ceramic electrolyte powders are obvious candidates for the filler particles of composite polymer electrolytes.

ACKNOWLEDGEMENT

I wish to thank Dr. Young-Il Jang for assistance in preparation of this manuscript and the Department of Energy for supporting our research on lipon, composite, and β -alumina lithium electrolytes through contract DE-AC05-00OR22725 with UT-Battelle, LLC.

REFERENCES

1. C.-H. Lee, K. H. Joo, J. H. Kim, J. H. Woo, H.-J. Sohn, T. Kang, Y. Park, J. Y. Oh, *Solid State Ionics* 149 (2002) 59.
2. K. J. Rao, M. Ganguli, "Lithium Ion Conducting Glasses", in *Handbook of Solid State Batteries and Capacitors*, M. Z. A. Munshi, Ed., Singapore, World Scientific, 1995.
3. S. D. Jones, J. R. Akridge, "Lithium Glassy Electrolyte Batteries", in *Handbook of Solid State Batteries and Capacitors*, M. Z. A. Munshi, Ed. Singapore, World Scientific, 1995.
4. A. D. Robertson, A. R. West, A. G. Ritchie, *Solid State Ionics* 104 (1997) 1.
5. K. Funke, *Prog. Solid State Chem.* 22 (1993) 111.
6. N. Imanaka, T. Shimizu, G. Adachi, *Solid State Ionic* 62 (1993) 167.
7. J. B. Bates, N. J. Dudney, G. R. Gruzalski, R. A. Zuhr, A. Choudhury, C. F. Luck, J. D. Robertson, *J. Power Sources* 43-44 (1993) 103.
8. X. Yu, J. B. Bates, G. E. Jellison Jr., R. X. Hart, *J. Electrochem. Soc.* 144 (1997) 524.
9. J. B. Bates, N. J. Dudney, B. J. Neudecker, A. Ueda, C. D. Evans, *Solid State Ionics* 135 (2000) 33.
10. F. Vereda, R. B. Goldner, T. E. Haas, P. Zerigian, *Electrochem. Solid-State Lett.* 5 (2002) A239.
11. Y.-S. Park, S.-H. Lee, B.-I. Lee, S.-K. Joo, *Electrochem. Solid-State Lett.* 2 (1999) 58.
12. E. J. Jeon, Y. W. Shin, S. C. Nam, W. I. Cho, Y. S. Yoon, *J. Electrochem. Soc.* 148 (2001) A318.
13. C. Lee, S. A. Akbar, C. O. Park, *Sensor Actuat. B-Chem.* 80 (2001) 234.
14. Y. S. Yoon, W. I. Cho, J. H. Lim, D. J. Choi, *J. Power Sources* 101 (2001) 126.
15. N. J. Dudney, B. J. Neudecker, *Curr. Opin. Solid State Mater. Sci.* 4 (1999) 479.
16. F. Vereda, N. Clay, A. Gerouki, R. B. Goldner, T. Haas, P. Zerigian, *J. Power Sources* 89 (2000) 201.
17. S. Zhao, Z. Fu, Q. Qin, *Thin Solid Films* 415 (2002) 108.
18. C. H. Choi, W. I. Cho, B. W. Cho, H. S. Kim, Y. S. Yoon, Y. S. Tak, *Electrochem. Solid-State Lett.* 5 (2002) A14.
19. N.-S. Roh, S.-D. Lee, H.-S. Kwon, *Scripta Mater.* 42 (2000) 43.
20. B. Wang, B. S. Kwak, B. C. Sales, J. B. Bates, *J. Non-Cryst. Solids* 183 (1995) 297.
21. N. J. Dudney, in preparation.
22. A. Le Sauze, E. Gueguen, R. Marchand, *J. Non-Cryst. Solids* 217 (1997) 83.
23. P. Birke, W. F. Chu, W. Weppner, *Solid State Ionics* 93 (1996) 1.
24. J. H. Kennedy, Z. Zhang, *J. Electrochem. Soc.* 136 (1989) 2441.
25. Z. Zhang, J. H. Kennedy, *Solid State Ionics* 38 (1990) 217.
26. H. Morimoto, H. Yamashita, M. Tatsumisago, T. Minami, *J. Am. Ceram. Soc.* 82 (1999) 1352.
27. A. Hayashi, S. Hama, H. Morimoto, M. Tatsumisago, T. Minami, *J. Amer. Ceram. Soc.* 84 (2001) 477.
28. T. Minami, A. Hayashi, M. Tatsumisago, *Solid State Ionics* 136-137 (2000) 1015.
29. R. F. Bartholomew, D. M. Young, A. J. G. Ellison, *J. Non-Cryst. Sol.* 257 (1999) 242.
30. A. Hayashi, H. Yamashita, M. Tatsumisago, T. Minami, *Solid State Ionics* 148 (2002) 381.
31. R. Komiya, A. Hayashi, H. Morimoto, M. Tatsumisago, T. Minami, *Solid State Ionics* 140 (2001) 83.
32. K. Takada, N. Aotani, K. Iwamoto, S. Kondo, *Solid State Ionics* 79 (1995) 284.
33. K. Takada, T. Inada, A. Kajiyama, M. Kouguchi, S. Kondo, M. Watanabe, *J. Power Sources* 97-98 (2001) 762.
34. R. Sakamoto, M. Tatsumisago, T. Minami, *J. Phys. Chem. B* 103 (1999) 4029.
35. K. Iio, A. Hayashi, H. Morimoto, M. Tatsumisago, T. Minami, *Chem. Mater.* 14 (2002) 2444.
36. P. Vinatier, M. Ménétrier, A. Levasseur, *Solid State Ionics* 116 (1999) 35.
37. J. Ibarra, A. Várez, C. León, J. Santamaría, M. Torres-Martínez, J. Sanz, *Solid State Ionics* 134 (2000) 219.

38. K. Mizumoto, S. Hayashi, *Solid State Ionics* 127 (2000) 241.
39. Y. Inaguma, L.Q. Chen, M. Itoh, T. Nakamura, T. Uchida, H. Ikuta, M. Wakihara, *Solid State Commun.* 86 (1993) 689.
40. S. García-Martín, J.M. Rojo, H. Tsukamoto, E. Morán, M.A. Alario-Franco, *Solid State Ionics* 116 (1999) 11.
41. O. Bohnke, C. Bohnke, J.L. Fourquet, *Solid State Ionics* 91 (1996) 21.
42. H. Watanabe, J. Kuwano, *J. Power Sources* 68 (1997) 421.
43. H. Aono, E. Sugimoto, Y. Sadaoka, N. Imanaka, G. Adachi, *J. Electrochem. Soc.* 136 (1989) 590.
44. A.K. Ivanov-Schitz, A.V. Nistuk, L.N. Demianets, N.G. Chaban, *Solid State Ionics* 144 (2001) 133.
45. V. Thangadurai, A.K. Shukla, J. Gopalakrishnan, *J. Mater. Chem.* 9 (1999) 739.
46. H. Yamamoto, M. Tabuchi, T. Takeuchi, H. Kageyama, O. Nakamura, *J. Power Sources* 68 (1997) 397.
47. P. Birke, F. Salam, S. Döring, W. Weppner, *Solid State Ionics* 118 (1999) 149.
48. R. Sobiestianskas, A. Dindune, Z. Kanepe, J. Ronis, A. Kezionis, E. Kazakevicius, A. Orluikas, *Mat. Sci. Eng. B-Solid* B76 (2000) 184.
49. T. Suzuki, K. Yoshida, D. Uematsu, T. Kodama, K. Toda, Z.-G. Ye, M. Sato, *Solid State Ionics* 104 (1997) 27.
50. J. Fu, *Solid State Ionics* 96 (1997) 195.
51. B. V. R. Chowdari, G. V. S. Rao, G. Y. H. Lee, *Solid State Ionics* 136-137 (2000) 1067.
52. K. Takada, M. Tansho, I. Yanase, T. Inada, A. Kajiyama, M. Kouguchi, S. Kondo, M. Watanabe, *Solid State Ionics* 139 (2001) 241.
53. J. Yamaki, H. Ohtsuka, T. Shodai, *Solid State Ionics* 86-88 (1996) 1279.
54. R. Kanno, T. Hata, Y. Kawamoto, M. Irie, *Solid State Ionics* 130 (2000) 97.
55. R. Kanno, M. Murayama, *J. Electrochem. Soc.* 148 (2001) A742.
56. Y. Jia, J. Yang, *Solid State Ionics* 96 (1997) 113.
57. J. Yang, Y. Jia, Z. Yao, *Solid State Ionics* 96 (1997) 215.
58. Y. Tomita, H. Ohki, K. Yamada, T. Okuda, *Z Naturforsch. A* 55 (2000) 117.
59. G.A. Nazri, R.A. Conell, C. Julien, *Solid State Ionics* 86-88 (1996) 99.
60. X. Wei, D.F. Shriver, *Solid State Ionics* 133 (2000) 233.
61. B.J. Neudecker, W. Weppner, *J. Electrochem. Soc.* 143 (1996) 2198.
62. E.M. Kelder, M. J. G. Jak, F. de Lange, J. Schoonman, *Solid State Ionics* 85 (1996) 285.
63. M. J. G. Jak, F. G. B. Ooms, E.M. Kelder, W.J. Legerstee, J. Schoonman, A. Weisenburger, *J. Power Sources* 80 (1999) 83.
64. K. Funke, C. Cramer, B. Rolin, *Glastech. Ber. Glass Sci. Technol.* 73 (2000) 244.
65. J. Swenson, C. Karlsson, L. Börjesson, R.K. Heenan, *Phys. Rev. B* 64 (2001) 134.
66. P. Vinatier, M. Ménétrier, A. Levasseur, *Solid State Ionics* 136 (1999) 35.
67. K. Mizumoto, S. Hayashi, *Solid State Ionics* 127 (2000) 241.
68. A. Rivera, A. Várez, J. Sanz, J. Santamaría, C. León, *J. Alloys Compds.* 323-324 (2001) 545.
69. J Deppe, R.F. Wallis, I. Nachev, M. Balkanski, *J. Phys. Chem. Solids* 55 (1994) 759.
70. S.H. Garofalini, P. Shadwell, *J. Power Sources* 89 (2000) 190.
71. N.J. Dudney, *J. Power Sources* 89 (2000) 176.
72. E.S. Nimon, M. Sukeshini, S.J. Visco, Presentation No. 221, International Meeting on Lithium Batteries, June 23-28, 2002, Monterey, California (to be published within *J. Power Sources*).

Table 20.1. Glass electrolytes

Composition (mole ratio)	Synthesis	σ at 25°C (S/cm)	d (mm)	E_a^1 (kJ/mol)	t_e^2	ΔV^3 (V)	ΔV measured by	Ref.
$\text{Li}_2\text{O} \cdot \text{SeO}_2 \cdot \text{B}_2\text{O}_3$ (0.5, 0.25, 0.25)	quenched in steel mold	8×10^{-7}	0.3- 0.5			0/5	2 mV/s, Li/Au	[5]
$\text{LiCl} \cdot \text{Li}_{1.4}\text{M}_2(\text{PO}_3)_4$ M=Al+Ti+Ge (0.15, 0.85)	'exploded' droplets into LN_2	7×10^{-6}		49				[6]
$\text{Li}_x\text{PO}_y\text{N}_z$ ($x=2.9, y=3.3, z=0.46$, typical) ($0.24 < z < 1.2$)	rf sputter in N_2 plasma	2×10^{-6}	0.001	55	$< 10^{-8}$	0/5.5	1 mV/s, Li/Pt & dc polarization	[7,8]
$\text{Li}_x\text{PO}_y\text{N}_z$	thermal evaporation + N-ion beam	2×10^{-6}	0.001	53-56	$< 10^{-8}$	0/6	dc polarization TiN/Cu	[10]
$\text{Li}_x\text{BO}_y\text{N}_z$	rf sputter in N_2 plasma	6×10^{-8}	0.001	81				[23]
$\text{Li}_2\text{S} \cdot \text{P}_2\text{S}_5$ (0.75, 0.25)	mechanical mill & pressed	2×10^{-4}	1	37	10^{-4}	0/>>1	dc polarization	[26]

¹ E_a , activation energy for Li conduction from simple Arrhenius relation near room temperature. Those shown in () were estimated from the published graphs.

² t_e , transference number for these single ion conductors, generally by Wagner dc polarization.

³ ΔV , low/high voltage range of the electrochemical window with respect to Li^+/Li .

Table 20.1 (continued)

$\text{Li}_2\text{S}\cdot\text{SiS}_2$ (0.6, 0.4)	mechanical mill & pressed	1×10^{-4}	1	30	10^{-4}			[27]
$\text{Li}_2\text{S}\cdot\text{SiS}_2\cdot\text{Li}_x\text{MO}_4$ M=Si, P, Ge (0.57, 0.38, 0.05)	twin roller quench & pressed	1×10^{-3}	(0.5) est.	30	10^{-4}	0/>10	5 mV/s sweep	[30]
$\text{Li}_2\text{S}\cdot\text{SiS}_2\cdot\text{Li}_x\text{MO}_4$ M=Si, P, Ge (0.57, 0.38, 0.05)	mechanical mill & pressed	1×10^{-4}	(0.5) est.	35				[30]
$\text{Li}_2\text{S}\cdot\text{SiS}_2\cdot\text{Li}_3\text{PO}_4$ (0.63, 0.36, 0.01)	twin roller quench & pelletized	1.5×10^{-3}		29		0/4.5	Li-LiCoO ₂ cell	[32, 33]
$\text{Li}_2\text{S}\cdot\text{SiS}_2\cdot x\text{MS}_y$ M=Sn, Ta, Ti, etc. (0.6, 0.4, 0.01-0.05)	melt, slow cool or cast	$0.6-1.6 \times 10^{-3}$	1-9	26-30	$< 10^{-2}$			[29]
$\text{Li}_2\text{S}\cdot\text{SiS}_2\cdot\text{Li}_3\text{N}$ (0.55, 0.40, 0.03)	fast quenched & pelletized	1.5×10^{-3}		27	10^{-4}	0/10	cyclic voltammetry, Pt / Li-In	[34]
$\text{Li}_3\text{N}\cdot\text{SiS}_2$ (0.4, 0.6)	mechanical mill & pressed	2.7×10^{-4}		29	10^{-4}	0/10	cyclic voltammetry, Pt / Li-In	[35]

Table 20.2. Ceramic electrolytes.

Composition (mole ratio)	Synthesis	σ at 25°C (S/cm)	d (mm)	E_a (kJ/mol)	t_e	ΔV (V)	ΔV meas. by	Ref
$\text{La}_{0.75}\text{-Li}_{0.25}\text{TiO}_3$ $0.03 \leq x \leq 0.167$	solid state reaction & pressed	1×10^{-3} $x=0.13$	0.7	28 ± 2	10^{-6}	$1.5 > 4$	cyclic voltammetry & titration	[37, 41]
$\text{La}_{1/2}\text{-Li}_{1/2}\text{TaO}_3$ $0.025 \leq x \leq 0.167$	solid state reaction & pressed	9×10^{-6} $x=0.06$	2		10^{-4}			[38]
$\text{La}_{1/2}\text{-Li}_{1/2}\text{NbO}_3$ $0 \leq x \leq 0.06$	solid state reaction & pressed	4×10^{-3} $x=0.04$	2	35 ± 3		$1.8?$	cyclic voltammetry vs. Li	[40]
$\text{Li}_{1.3}\text{Ti}_{1.7}\text{Al}_{0.3}(\text{PO}_4)_3$	solid state reaction & pressed	3×10^{-4} $(3 \times 10^{-3})^*$	0.2-0.3			$2.4?$ see text	Coulometric titration vs. Li	[47]
$\text{LiAlTa}(\text{PO}_4)_3$	solid state reaction & pressed	6.5×10^{-7}		45				[45]
$\text{LiAl}_{0.4}\text{Ge}_{1.6}(\text{PO}_4)_3$	solid state reaction & pressed	1.3×10^{-4}		42				[46]
$\text{Li}_{1.4}\text{Ti}_{1.6}\text{Y}_{0.4}(\text{PO}_4)_3$	solid state reaction & pressed	4.5×10^{-3} $(1.8 \times 10^{-3})^*$						[48]

Table 20.2. Ceramic electrolytes. (continued)

$\text{Li}_{1-x}(\text{Sc}_{1-x}\text{M}_x)_2(\text{PO}_4)_3$ M = Zr, Ti, x=0.1, 0.2	solid state reaction & pressed	1×10^{-5}	1					[49]	
$\text{Li}_3\text{Sc}_{1-x}\text{Fe}_x(\text{PO}_4)_3$	spray pyrolysis & anneal >800°C	5×10^{-6}	0.003- 0.005	50				[44]	
$\text{Li}_{4.1}\text{V}_{0.61}\text{Si}_{0.39}\text{O}_{3.36}$	sputtered	1×10^{-4}	0.001	48		10^{-4}	0/3.5	Li-MO _x cells (M=V, Mo, Mn)	[53]
$\text{Li}_{4-x}\text{Ge}_{1-x}\text{Ga}_x\text{S}_4$ (x=0.25)	solid state reaction & pressed	6×10^{-5}	1-2	55		0.001	0/-5	1mV/s sweep Li-Au	[54]
$\text{Li}_{4-x}\text{Ge}_{1-x}\text{P}_x\text{S}_4$ (x=0.65)	solid state reaction & pressed	2×10^{-3}	1-2	20		10^{-6}	0/-5	1mV/s sweep Li-Au	[55]
$\text{Li}_9\text{Bi}_2\text{Cl}_3$	solid state reaction & pressed	7×10^{-7}	2	45		10^{-4}	0/>1.5	voltage sweep, Mo-Mo	[57]
Li_3InBr_6	solid state reaction & pressed	1×10^{-3}		24					[58]
$\text{Li}_3\text{P} + 3\text{LiCl}$ composite	solid state reaction & pressed	1×10^{-4}							[59]
$\text{LiCF}_3\text{SO}_3 \cdot \text{NbF}_5$ (0.33, 0.37)	solid state reaction & pressed	1×10^{-4}		(~40)					[60]
$\text{Li}_9\text{SiAlO}_8$	solid state reaction & pressed	2×10^{-7}	0.2-0.5	54		10^{-4}	0/6.5V	50 mV/s, 500 sweeps	[61]
$\text{Li}_2\text{BPO}_{4+x/2}$ x = 0.07	soft-chemical & cast, pressed, or sprayed	2×10^{-6}	0.5	29					[62]

• Indicates the bulk or crystalline component of the total conductivity.

Chapter 21

LITHIUM-ION BATTERIES FOR EV, HEV AND OTHER INDUSTRIAL APPLICATIONS

M. Broussely

Saft BP 1039, 86060 Poitiers, France

21.1. INTRODUCTION

So called “industrial batteries” are generally sized in the range from one to hundreds of kWh, addressing a market roughly divided in two segments: transportation and stationary applications. This market is mainly addressed by lead-acid and NiCd systems. Large special batteries for space and defense generally use more advanced and sophisticated chemistries, such as nickel-hydrogen, silver-zinc, silver-aluminum oxide, etc. One of the most exciting questions in this battery business today is: will the “Li-ion revolution” which occurred in portable batteries extend to larger battery systems? Obviously, that would only occur if two main conditions were satisfied: better answer to a real need, and in a cost-effective way. This chapter will review the most important applications in which Li-ion might bring benefits, and will describe the technical status today.

Going back a little over the last 5 to 10 years, the possible use of Li-ion in large batteries was first considered in electric vehicles, for which high specific energy is crucial to grant a sufficient range. In parallel with the development of portable Li-ion, very important R&D programs started about 8 years ago aiming at demonstrating the feasibility of such batteries in electric vehicles. These programs were supported by a strong financial effort all over the world: European Commission and french government organizations in Europe, DOE / USABC in USA, MITI / NEDO / LIBES in Japan (addressing first the stationary batteries for home individual power sources). Saft was one of the few companies involved from the beginning. Then, with the fast developments of HEV's, Li-ion also had the opportunity to demonstrate its very high potential in terms of specific power and power density.

Very soon the numerous demonstrated advantages of Li-ion over other advanced systems established it as the best power source for satellites and other space applications, leading to specific developments and qualified battery systems. The introduction of Li-ion is now being considered in other applications, as actual complete battery systems of different kinds are being built.

21.1.1. Specific Properties Required of Industrial Li-Ion Batteries

As will be described in more detail in the following sections for each main application, the general specifications are often more demanding than those for consumer portable electronics. Beside very high power or energy, depending on the application, longer life is generally required of this high valued piece of equipment, which means in some cases large number of cycles (typically >1000), or long shelf life (10 to 15 years), sometimes in an uncontrolled temperature environment. The cost is also an important issue. Being newly introduced, Li-ion is still an expensive technology, largely because of material costs. Cost reduction, coming with an increase in manufactured quantities, is the main factor for future expansion of this new technology in industrial battery markets. As a consequence, once the minimum electrical specifications are met, low material cost is the main parameter that drives the designer's choices.

21.2. WHICH LI-ION CHEMISTRY FOR A LARGE BATTERY?

21.2.1. Positive Materials

This is certainly the critical part of a Li-ion cell that is responsible for large differences in cell properties. The use of lithiated transition metal oxides, *e.g.* LiNiO_2 and LiCoO_2 , as possible positive materials for electrochemical power sources was discovered more than 20 years ago.¹ Since then, these compounds were widely investigated as positive materials for rechargeable lithium cells.^{2,3} When LiCoO_2 became the undisputed cathode of the Li-ion,⁴ it was available in very small quantities, and LiNiO_2 simply did not exist. Studying the possible preparation processes for LiNiO_2 ,⁵ the difficulty of preparing a "good" electrochemically active material was pointed out. It was later found that the tendency for Ni^{2+} to occupy sites in the Li^+ layers introduces a structure distortion, which drastically affects its ability to de-insert/insert Li^+ ions.⁶ Therefore, in spite of

the potential advantage of LiNiO_2 in energy density and of its greater stability on overcharge, LiCoO_2 was chosen by almost all the battery manufacturers to start production of Li-ion batteries for portable applications. Due to the huge growth of portable phones and personal computers, this system is now established as a standard for Li-ion.

However, it was recognized very early that, due to the high and somewhat unpredictable price of cobalt, it would have been difficult to meet the cost requirements for large systems, particularly for the car industry. Two alternatives were consequently explored, using either manganese (spinel LiMn_2O_4) or nickel based oxides. Primarily because of the higher energy density expected in batteries with the nickel oxide, Saft chose this option early on.^{7,8} Indeed, lithiated nickel based oxides are generally able to release up to $0.7 \text{ Li}^+/\text{mol}$, at 4.1 V vs. Li/Li^+ without performance degradation on cycling. That represents a potential specific capacity of around 200 Ah/kg , compared to 150 Ah/kg for LiCoO_2 and 120 Ah/kg for LiMn_2O_4 , while maintaining an average voltage of about 3.7 V vs. the lithiated carbon anode.

21.2.1.1. From LiNiO_2 to $\text{LiNi}_{1-x-y}\text{Co}_x\text{Al}_y\text{O}_2$

Substitution by cobalt (ideally 20%)⁹ was early identified as a solution to avoid Ni^{2+} formation, allowing easy manufacturing of the appropriate structural form. In the frame of the LIBES program, the mixed Ni/Co material $\text{LiNi}_{0.7}\text{Co}_{0.3}\text{O}_2$ was studied by Sanyo¹⁰ to design a 76 Ah cylindrical cell dedicated to home load leveling systems.

For some years, many “doping” metallic ions were tested by numerous laboratories, showing interesting specific properties.¹¹ Aluminum¹² was found to produce a significant stabilization of the delithiated form, inducing a better thermal stability, as shown by differential scanning calorimetry (DSC) experiments.¹³

That discovery focused the research work, made jointly with material manufacturers, towards the definition of a mixed Ni/Co/Al material, which appears to exhibit excellent electrochemical properties, now recognized by several laboratories.¹⁴ The exact composition used by Saft is still proprietary, but the ratio of nickel to total metals (except lithium) is greater than 0.75, allowing the expectation of a reasonable cost of the raw material.

Unlike LiNiO_2 , $\text{LiNi}_{1-x-y}\text{Co}_x\text{Al}_y\text{O}_2$ does not exhibit monoclinic/hexagonal phase transformations during cycling. This may at least partly explain the excellent stability on cycling, as described later. The crystalline structure is very similar to that of LiCoO_2 , however the charge discharge curves are different, as shown in Figure 21.1.

Figure 21.2 describes a particular feature of nickel based compounds. Due to a small remaining quantity of Ni^{2+} , the first charge/discharge cycle is

not totally reversible, although better than LiNiO_2 . As a consequence, because the total excess of lithium is not consumed by the carbon passivation, the positive electrode limits the cell capacity. At the end of discharge at 2.5V, about 15% of the Li capacity remains in the carbon electrode. If the cell is discharged beyond this voltage limit, a voltage

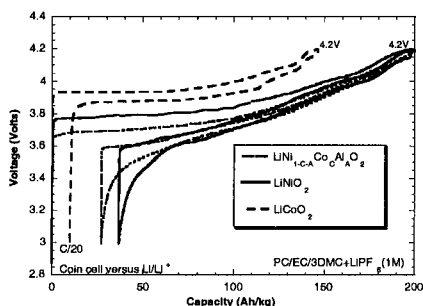


Figure 21.1. Compared voltage profiles of metal oxides at low rate (C/10, 25°C).

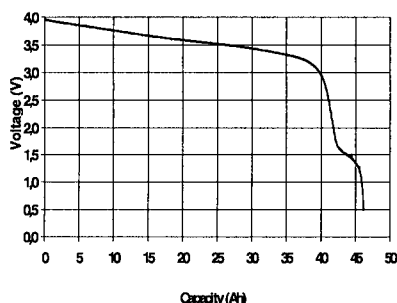


Figure 21.2. Deep DOD voltage profile of a $\text{LiNi}_{1-x-y}\text{Co}_x\text{Al}_y\text{O}_2/\text{graphite}$ cell at low rate (C/10). Ambient temperature.

plateau at about 1.5V is obtained where the lithium is completely consumed, as shown in Figure 21.2 for a 40 Ah cell. This interesting feature gives to the cell the ability to be deeply discharged even to 0 V without risk of copper corrosion unlike other positive materials (in this case the negative electrode is only at about 1.5V vs. Li/Li^+). For the same reason, the cell can be stored in the complete discharge state at 2.5V. It should be noted however that discharging the cell at elevated temperature (45°C or more, depending on the rate) allows the positive material to be totally reduced at high voltage, resulting in about 15% increase of the cell capacity, but coming back then to a negative limited cell.

This particular feature has also a noticeable impact on the cell shelf life. When the cell capacity is limited by the negative electrode, any loss of lithium directly impacts on the cell capacity, which is generally observed either on cycling or extended storage at elevated temperature, because the passivating layer is not a full electronic insulator.¹⁵ This induces also outstanding cell energy stability on cycling or storage, as will be described later.

Finally, the stabilizing property of Al ions on the delithiated form shifts the onset of thermal decomposition to a significantly higher temperature (about 100°C), thus reducing the risk of thermal runaway in case of overcharge. In the same manner, the reactivity towards electrolyte is reduced, and that might be also the reason for the good power retention during storage. Power loss is indeed generally attributed to electrolyte oxidation at the positive electrode interface.¹⁶ This behavior compares very

favorably to pure LiNiO_2 or LiCoO_2 , and is a big advantage over LiMn_2O_4 , for which interaction with electrolyte is still a major drawback.

21.2.1.2. LiMn_2O_4

There are two main reasons put forwards to promote the use of the LiMn_2O_4 spinel as the positive for a large Li-ion battery. The first usually mentioned is the cost, expected to be the lowest. However, the cost of MnO_2 used in primary dry cells is often given as example and goal, ignoring the necessary lithium salt and added processing costs. In addition, the pure material alone fails to provide the sufficient chemical stability to ensure the required long life time, and additional processes such as coating are necessary. Finally, as long as costs of other battery components are not drastically reduced, the final cost/Wh is strongly impaired by the lower energy density achieved, compared to nickel based materials. In high power cells, where the cost/W is more relevant, the lower relative amount of active materials reduces their influence on final cost. Finally, it is quite difficult today to predict which one of Mn or Ni based products will lead to the more cost effective system, but it can be anticipated that the difference would be marginal.

Safety is the second mentioned advantage, which is of a particular importance for large batteries. This aspect is described in more detail in another chapter of this book, and is only briefly discussed here. The totally delithiated phase, $\lambda\text{-MnO}_2$, which is the regular full state of charge, is actually thermodynamically stable. This is not the case of NiO_2 or CoO_2 , which are ultimately formed when LiNiO_2 or LiCoO_2 cells are fully overcharged. These non-stable forms may decompose via exothermic reactions with the electrolyte and can result in cell burning. This generally occurs when the cell starts to overheat because of electrolyte electrolysis, after the positive material is totally oxidized. The combustion is all the more reactive since lithium metal will have been deposited on carbon electrode, due to the excess of lithium extracted from the positive. Although there are different means provided for preventing all Li-ion batteries to go into overcharge, the better stability of LiMn_2O_4 provides an additional safety level.

That does not mean however that the cell is intrinsically safe and could be abused in any manner. The oxidized form, $\lambda\text{-MnO}_2$, is still a strong oxidizing agent and can react violently with organic solvents when overheated to about 300°C . This is usually studied using differential scanning calorimetry (DSC), and can be observed when the experiment involves a mixture of active material and electrolyte as in a real cell. Figure 21.3 describes the DSC heat output from 100% charged materials, in contact with electrolyte in proportions similar to a real cell. It must be pointed out

that the heat power (W) is not related, as is usual, to the weight of the sample, but to the quantity necessary to bring one Wh to the cell, which is closer to the real case.

The following comments can be made: 1) pure LiNiO_2 exhibits a low onset temperature for thermal runaway (temperature sharp peak), as low as about 200°C . 2) Although heating delithiated $\text{Li}_x\text{Mn}_2\text{O}_4$ alone would not produce any thermal effect, the presence of electrolyte leads, as expected, to a strong exothermal reaction at about 300°C . 3) Aluminum doping in the mixed Ni-based material brings a very significant improvement, ranking the material to an even better level than LiMn_2O_4 . Therefore, LiMn_2O_4 -based large batteries must be protected against overcharging, just like the other systems. Indeed, a high rate overcharge will produce heat as soon as electrolyte is oxidized, *i.e.* from the beginning of overcharge, and may reach the point where the positive material reacts with the flammable electrolyte. Heat transfer in cell design is also one of the key factors in improving battery safety, regardless of the electrochemical system.

Beside the advantages of a better safety, a LiMn_2O_4 -based system still suffers of poor calendar life even at moderately high temperature, which has been attributed to the tendency of Mn^{3+} ions to disproportionate into Mn^{4+} and Mn^{2+} . The problem comes from the solubility of Mn^{2+} ions in the electrolyte, which reacts on the negative side, and destroys the stability of the passivation layer on the carbon, which is the key point of Li-ion system viability. Although this can be tolerated for consumer batteries, whose life expectation is not too high and working temperature normally low, this is a real drawback for industrial batteries. Although improved solutions have been studied in the past years, the problem is not yet satisfactorily solved.

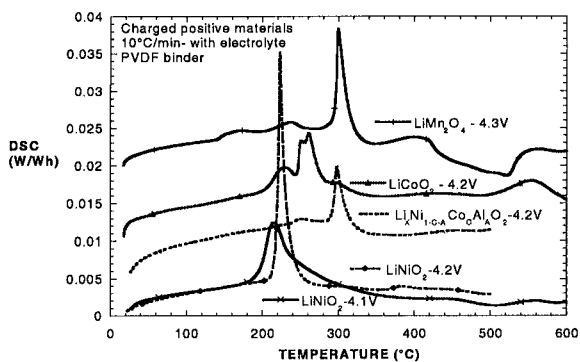


Figure 21.3. DSC of different positive materials at full state of charge in the presence of electrolyte. Stainless steel crimped sample vessels.

21.2.2. Negative Materials

There is a wide variety of carbons that can be used as negative electrode to make industrial Li-ion batteries, as with the small portable cells. However, because the material costs have a particular importance in the total battery costs in large systems, low cost graphites are generally preferred. One of the most important properties taken into consideration for the material selection is the ability to form a stable passivation layer, which is fundamental when long life is needed.

21.3. GENERAL TECHNOLOGY AND MANUFACTURING PROCESSES

Basically, there is no difference between the technology implemented in small portable Li-ion cells and large “industrial” cells. Electrode manufacturing processes consist of coating metallic foils (Al for positive and Cu for negative) with a slurry containing the active material, an electronic conductor (for the positive mix), and a binder dissolved in an appropriate solvent (generally PVDF/NMP). After drying, this coating is calendered to the desired thickness/density. The electrode thickness depends on the maximum power required. This is a very interesting feature of Li-ion battery technology, allowing a wide range of power/energy ratio designs with the same basic electrode manufacturing process. However, appropriate current collection and tabbing, cell shape and design are necessary.

There is also no significant difference in the nature of electrolytes, LiPF₆ being the only suitable salt, while cyclic or linear carbonates are the basis of the organic solvents. Separators, all in the form of thin (25 μ m or less) microporous membranes, may be either in polypropylene or polyethylene, or mixed polymers.

In most cases, the cell stack is built by rolling the electrodes in spiral, as is the case for small cells. Because of their small thickness, this is the most efficient way for assembling electrodes, compared to planar conventional stacking. The coil may be cylindrical, or flattened to make a prismatically shaped cell. Both designs have their own advantages and drawbacks and are currently being produced. Better volume filling in battery assembly is obtained with prismatic cells, which are however more sensitive to bulging on cycling or aging. The stronger mechanical characteristics of cylindrical cans give to the cell better dimensional stability, and homogeneous pressure within the electrode stack. The usual cell range proposed by battery manufacturers is from 3 Ah (high power design) to 100 Ah (high energy design).

21.3.1. General Considerations for Battery Assembly

Because of the large variety of possible applications, many types of battery assembly can be designed. These are greatly facilitated by two properties: the cell SOC/voltage dependence, which allows direct parallel connection to obtain the required capacity without any electronic component, and the cell ability to work in any position. On the other hand, as no overcharge shuttle mechanism exists in batteries with organic electrolyte, the end of charge and discharge voltages must be monitored for each cell or parallel grouping, which requires specific battery management features, especially when high voltages are involved (sometimes greater than 300 V).

Progress in high power electronics make this quite achievable, however, insuring very precise and stable battery characteristics, with cells in balance, etc. This control works much better than a chemical shuttle inside the cell, as in aqueous systems. Battery management systems may include sophisticated intelligent functions, which can communicate with the application. The most used information is the battery 'fuel' gauge, giving a real time read out of the state of charge.

Safety is also a major parameter taken into account at the battery level. The larger size of the battery makes this point even more crucial than for small batteries. Overcharge is the most critical situation to avoid, which can only happen in case of applying overvoltage to the cells. Redundant voltage thresholds are applied to prevent this situation in any circumstance. Overheating resulting from shorts or overloading is also avoided by limiting the maximum current, and by fuses and thermal sensors. Although all types of precaution are taken to avoid hazardous situations, the probability for ignition in a single cell (the non-aqueous electrolyte is flammable) should not be ignored. In such a case, the battery design should insure that fire would not propagate to the entire battery.

21.4. EV APPLICATIONS

Reducing the impact of road transportation on the environment is a mandatory task for the automotive industry all over the world. With no exhaust fumes, the electric vehicle is an optimum solution for urban transportation and goods delivery.

Electric vehicles have been traditionally powered by flooded lead-acid or nickel-cadmium batteries. These two technologies suffer from a low energy density that makes impractical a long-range vehicle, thus limiting public acceptance for such types of vehicles. Thanks to an energy density that is three to four times higher, Li-ion allows carmakers to design electric vehicles with very acceptable performance in term of range, top speed and acceleration.

21.4.1. EV Battery Requirements and Technology Comparison

21.4.1.1. Weight

The energy consumption of an electric vehicle is proportional to its weight. A typical figure for an EV is 120 Wh/ton/km. Since the allowable weight for the battery onboard a given vehicle is limited, the better the energy density, the larger will be the available energy and the vehicle range. A comparison of the different technologies is presented in Table 21.1.

Table 21.1. Comparison of different technologies of EV batteries for a typical size of 250 kg.

Technology	Pb Acid	NiCd	NiMH	Li-ion
Vehicle curb weight	1200 kg			
Battery weight allocation (typ.)	250 kg			
Battery structure cooling etc.	55 kg			
Module weight allocation	195 kg			
Energy density (module)	33 Wh/kg	45 Wh/kg	70 Wh/kg	120 Wh/kg
Onboard energy	6.4 kWh	8.8 kWh	13.0 kWh	23.4 kWh
Calc. range @ 120 Wh/ton/km	53 km	73 km	114 km	195 km

Table 21.2. Comparison of different technologies of EV batteries for a typical size of 200 liters.

Technology	Pb Acid	NiCd	NiMH	Li-ion
Battery volume allocation (typ.)	200 l			
Battery structure, cooling etc.	70 l			
Module volume allocation	130 l			
Volumetric Energy (module)	75 Wh/l	80 Wh/l	160 Wh/l	190 Wh/l
Onboard energy	9.8 kWh	10.4 kWh	20.8 kWh	24.7 kWh
Range @ 120 Wh/ton/km	81 km	87 km	173 km	206 km

21.4.1.2. Volume

It is obvious that the volume that can be allocated to a propulsion battery onboard a vehicle is limited. A typical performance comparison is described in Table 21.2.

21.4.1.3. Power

The vehicle's ability to accelerate and climb hills depends on the battery power, if it is not limited by the electric motor power. Here again, Li-ion exhibits superiority over the traditional chemistries, as described in Table

21.3.

Table 21.3. Power characteristics comparison for a 250 kg battery using different chemistries.

Technology	Pb Acid	NiCd	NiMH	Li-ion
Vehicle curb weight	1200 kg			
Battery weight allocation (typ.)	250 kg			
Battery structure cooling etc.	55 kg			
Module weight allocation	195 kg			
Power density (module)	75 W/kg	120 W/kg	170 W/kg	370 W/kg
Battery Power	15 kW	24 kW	33 kW	72 kW

21.4.1.4. Long Term Parking Capability

Aqueous electrolyte systems suffer from moderate to high self discharge that may reach several per cent of the rated energy per day. This phenomenon is reversible (the lost energy is recovered after the next charge) but it limits the long term parking capability of the vehicle. For some of these systems, a one-month stand at the airport parking for instance cannot be envisaged. A Li-ion battery, thanks to its low self-discharge rate (a few per cent per month), can be left, even at 20% state of charge, during extended periods of time without the need of recharge.

21.4.2. Battery Monitoring and Management**21.4.2.1. Fuel Gauge**

Electrochemistries using aqueous electrolytes (PbA, NiCd, NiMH) are difficult to manage since there is no direct way of measuring the battery state of charge. The faradic charge efficiency much lower than 100% (dependent on parameters such as temperature, state of charge, charge rate), the high self discharge rate, etc., make it difficult to assess correctly the battery state of charge by a coulometric method. When combined with the short-range of the vehicles that are equipped with these types of batteries, users suffer from a capacity gauge syndrome and experience shows that they barely use 50% of the onboard energy between two consecutive charges.

Li-ion exhibits an almost linear relationship between the open circuit voltage and the state of charge of the battery, the faradic charge efficiency is 100%, and the self-discharge is low. These facts make an accurate capacity gauge easy to implement, typically better than 5%. When associated with the long-range capability of the vehicles fitted with the Li-ion batteries, the fear of a flat battery should disappear.

21.4.2.2. Charge Monitoring

An economic drawback of the Li-ion technology is its lack of overcharge protection. It requires hardware to insure the monitoring of voltage of every group of cells in parallel to avoid any overcharge situation. However, the knowledge of every cell voltage (and therefore the state of charge) allows very precise battery management that helps to improve the battery life.

21.4.3. Li-Ion Technology for EV

21.4.3.1. Chemistries

As mentioned earlier, LiCoO_2 was soon abandoned in large cells for EV, because of its cost. Manganese-based or nickel-based are the two options presently considered for automotive applications. While LiMn_2O_4 is attractive for safety considerations, it has such disadvantages as a low practical specific capacity of about 110 Ah/kg increasing the potential cost/Wh of the battery, and a limited calendar life at moderately high temperature (see Section 21.2.1.2.). Most Japanese EV battery manufacturers are working on the manganese option¹⁷ while Saft adopted the “nickel solution”. Ongoing research programs on both sides, with the help of materials manufacturers, aim at finding the best material that would combine the best features of each option.

Each EV battery maker has its own proprietary choice of negative material and electrolyte solvent mixture. The use of LiPF_6 salt is a standard.

Cell general composition of Saft industrial Li-ion chemistry:

- Positive: $\text{LiNi}_x\text{Co}_y\text{Al}_z\text{O}_2$ + Carbon + PVDF, on Al substrate ($x > 0.75$).
- Negative: Graphite blend + non fluorinated binder on Cu substrate.
- Electrolytes: Carbonate blend, as a function of cell type, 1M LiPF_6 + VC.
- Separator: microporous PE or PP.

21.4.3.2. Cell Design

The general cell design is described in Section 21.3 All battery makers have selected the wound coil technology that is the optimum industrial solution to achieve a low process cost. These coils are then inserted into cylindrical or round-edge prismatic metallic cans. The can material may be nickel-plated steel or aluminum depending on which of the coil polarities is connected to the cell structure. A pressure release valve

Table 21.4. Main characteristics of high-energy Saft cells.

Cells		VL E	VL 41 M	VL 27 M
Nominal Voltage	V	3.55	3.55	3.55
Rated Capacity at C/3	Ah	45	41	27
Typical Power at 80% DOD, 30s pulse	W	450	700	420
Dimensions (Ø / h)	mm	54 / 222	54 / 222	54 / 163
Typical Weight	kg	1.07	1.07	0.77
Specific Energy	Wh/kg	150	135	125
Specific Power at 80% DOD	W/kg	420	650	550
Energy Density	Wh/l	310	285	275
Power Density at 80% DOD	W/l	880	1370	100

prevents cell bursting in case of overpressure.

For pure EV applications, the battery manufacturers have developed ranges of cells with individual capacities between 25 and 100 Ah. As an example, the main characteristics of high-energy cells manufactured by Saft are described in Table 21.4.

Shin Kobe Machinery¹⁷ has developed LiMn_2O_4 -based batteries for EV in collaboration with Hitachi Maxell. The performance characteristics of the cylindrical cell used to build 2.7 kWh modules, then assembled into batteries, are summarized in Table 21.5. Nissan has equipped vehicles with these batteries.

Japan Storage Battery developed a range of high-energy cells of elliptical cylindrical shape also using LiMn_2O_4 (Table 21.6).

Matsushita Batteries Industrial Co. Ltd designed a cylindrical 123 Ah cell in the frame of the LIBES program¹⁸ using LiMn_2O_4 and graphite. Its

Table 21.5. Main characteristics of Shin-Kobe high-energy cells.

Capacity	90 Ah
Nominal voltage	3.8 V
Wh/kg	107 Wh/kg
Wh/l	237 Wh/l
W/kg at 85% DOD	470 W/kg

Table 21.6. Main characteristics of JSB high-energy cells for EV (from JSB catalogue).

Model	Nominal Voltage (V)	Nominal Capacity (Ah)	Outer Dimensions (mm)			Weight (kg)	Specific Energy (Wh/kg)	Specific Power 80% DOD (W/kg)
			Width	Thick.	Height			
LEV6P	3.75	6	85.5	109	19	0.33	68	>500
LEV40P	3.75	40	133	170	47	2.1	71	>700
LEV95P	3.75	95	114	170	94	3.5	102	>700

characteristics are described in Table 21.7. A 30.4 V – 3 kWh module was designed using 8 of these cells connected in series. More recently, smaller sizes were also designed.

Table 21.7. Main characteristics of Panasonic high-energy cell for EV.

Capacity	123 Ah
Weight	3.34 kg
Dimensions	Ø65 x 410 mm
Voltage (V)	3.8 V

Table 21.8. Main characteristics of NGK Insulators cell.

Capacity	25 Ah
Energy	95 Wh
Energy density	200 Wh/l
Specific energy	110 Wh/kg

NGK Insulators¹⁹ designed a 25 Ah cylindrical cell using substituted manganese spinel, described in Table 21.8. The material and appropriate cell design allow to get a an improved safety behavior in severe abuse conditions, such as nail penetration and overcharge. High power cells are also developed (see 21.5.3.3).

21.4.3.3. Battery Design

The size of an EV battery design is of course dependent on the vehicle size. Typically, battery energy is in the range of 10 to 30 kWh, with a voltage of 300 V or more. The batteries are built from modules, each comprising a number of cells with total energy in the range of 1 to 2 kWh. Saft's EV module comprises 6 cells that may be configured in any series or parallel combination - see Figure 21.4. The module includes an electronic board that consolidates cell measurements and transmits data (voltage, temperature) to the battery controller. Because of the lack of an overcharge shuttle mechanism, differences in cell voltage in series are re-equilibrated by electronic means. The charge imbalance, caused by uneven self-discharge, is usually low in the Li-ion system. Re-equilibration is accomplished simply and automatically by slowly discharging cells with the highest voltages using resistors. This switching is included at the module level. The module is also designed to control cell temperature. The Li-ion chemistry has a very low entropy coefficient, and the temperature gradient inside a battery is not as critical as it is for some aqueous battery systems (NiMH for instance).



Figure 21.4. View of Saft EV Li-ion module and cells.

There is no extra heat on charge, and heat generation during a drive cycle is low. Air or liquid cooling can be used, the selection being left to the automotive manufacturer. Air-cooling is lighter and cheaper but tends to be noisy and does not allow for battery heating during cold temperature operation. The liquid cooling, using the car infrastructure, is more compact and quieter but heavier and more expensive. It allows for battery heating for cold temperature operation.

In the frame of the LIBES program, the Japanese battery makers, in collaboration with their automotive industry, selected the air cooling solution. In the frame of an European program, Saft in collaboration with EUCAR (European carmakers association) selected the liquid cooling solution. The modules are then assembled into batteries, to reach the size required by the customer. A standard battery system is composed of:

- An assembly of modules electrically connected in series
- A cooling system that may be limited to fans in case of air cooling and is composed of a pump, hydraulic manifolds, a thermal regulation valve and a liquid-to-air heat exchanger in case of liquid cooling
- A fuse to protect the battery against external short circuit
- A contactor to insulate the battery from the vehicle when parked. This contactor may also be connected to a vehicle shock detector to insulate the battery in case of an accident
- A ground fault detector which is mandatory for high voltage batteries

Most of these subsystems are managed by a battery controller that collects data coming from the module electronic boards, runs the various battery algorithms (charge, capacity gauge, protection against abuse, etc.) and communicates with the vehicle.

A picture of a battery used in the Daimler Chrysler EPIC van is shown in Figure 21.5. The battery characteristics are: 38.5 kWh, 315 V average voltage, >80 kW, 330 kg (excluding battery tray), 212 dm³. It provides to EPIC a 200-km⁺ range.

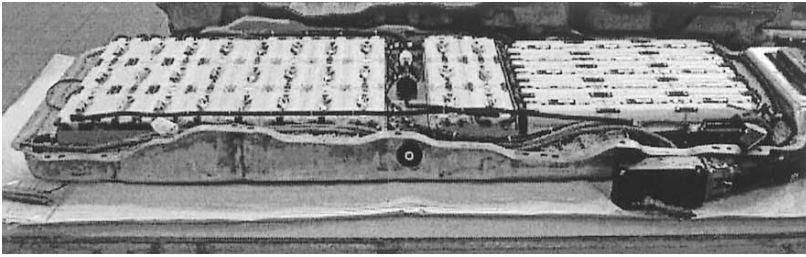


Figure 21.5. Open view of the Saft Li-ion battery for EPIC Daimler Chrysler van.

21.4.3.4. Typical Performances in Bench Tests

Figure 21.6 describes discharge curves of the Saft “VLE” cell at different discharge rates. It can be seen that even this high-energy cell (150 Wh/kg) still sustains high discharge rates.

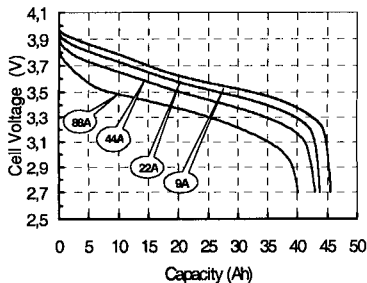


Figure 21.6. Discharge profile of high energy cells $\text{LiNi}_{1-x-y}\text{Co}_x\text{Al}_y\text{O}_2/\text{graphite}$ at different continuous rates. Ambient temperature. (EOCV = 4.0 V).

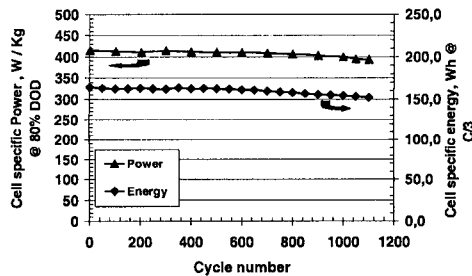


Figure 21.7. Specific energy and power of Saft “VLE” cells during cycling at 80% DOD DST cycle. Every 50 cycles, energy measured at 100% DOD - C/3, power measured at 80% DOD, 300A – 5mn pulse.

21.4.3.4.1. Cycle Life

The automotive industry considers that an EV battery reaches its end of life when it has lost 20% of its capacity/energy content or 20% of its power capability. Figure 21.7 shows the performance of high energy cells under cycling down to 80% DOD in a “DST” profile, which includes charge (regeneration) and discharge peaks at various rates, corresponding to an average rate of about C/3. For an electric vehicle capable of 150 km per each cycle, this corresponds to 150000 km that is comparable to the life achieved by most conventional vehicles.

Figure 21.7 also describes the energy and power delivered during diagnostic 100% DOD cycles at C/3, made every 50 cycles. As can be seen,

the energy remains remarkably stable during more than 1000 cycles, just like the power ability, measured with a 300 A pulse at 80% DOD. These results illustrate the good behavior of the positive material, as well as the stability of the passivating layer on the carbon, preventing lithium loss. As a matter of fact, Figure 21.2 describing the lithium excess has been recorded after 1000 cycles, which demonstrates the excellent stability of the layer, which is partly due to the patented VC additive.²⁰

21.4.3.4.2. Power capability

The nominal power of a Li-ion cell is not really an issue for EV applications. As described in the next section, much higher power densities can be obtained for HEV applications, through appropriate design. More important to the carmaker is how stable this power capability is, and how it varies with state of charge, temperature, cycling and aging.

Figure 21.8 shows typical specific power variations with SOC at different temperatures for the VLE Cell. This power, measured using pulses of 150 A for 30s, does not represent the maximum power available. Variations with SOC are derived mainly from the cell voltage.

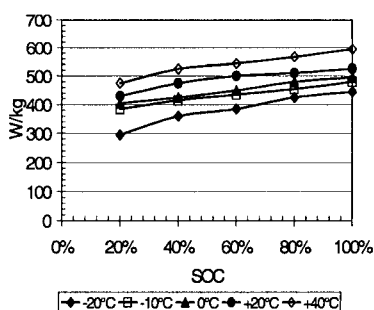


Figure 21.8. EV cell power as a function of SOC and temperature (Saft "VLE").

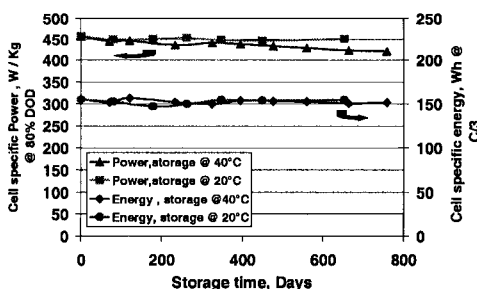


Figure 21.9. High energy "VLE" cell power and energy retention during floating at 4.0 V, @ 20 or 40°C.

Passivation layer stability on the carbon is an important parameter to insure a good shelf life of the Li-ion batteries. The chemistry selected by Saft, including the choice of electrolyte composition, graphite negative and $\text{LiNi}_x\text{Co}_y\text{Al}_z\text{O}_2$ positive, ensures an excellent calendar life. This important property is illustrated for example in Figure 21.9, showing the energy and power retention of high-energy cells, stored at a constant float voltage of 4.0 V, at 40°C. After more than 2 years in these conditions, both energy and power remain stable, similarly to what is observed on storage at 20°C.

From today's data, the life projection under average EV conditions is over 6 years. Accumulating more data will probably extend this value. The current life expectancy of manganese-based batteries seems to be limited to 3 to 4 years, due to the unsolved problem of partial dissolution of the positive material in the electrolyte.

21.4.3.4.3. Safety

As discussed in Sections 21.2 and 21.3.1, the main safety concern for a Li-ion battery is the fact that many of the components are flammable, starting with the electrolyte. Cell overheating may ultimately lead to battery ignition in the worst case, through active material decomposition. Therefore, better intrinsic cell stability would come from the discovery of a non- or less- flammable electrolyte, which is presently one of the most important research tasks for Li-ion throughout the world.

There are, however, means to prevent abusive situations at all levels, from cell to complete battery assembly. They usually include shutdown separators internal to the cell, fuses to avoid heavy short circuits, and voltage and temperature monitoring to shut down power in case of overvoltage or overheating. Ultimately, no explosion should ever occur, thanks to the case and safety vent design. Considering the worst case, should an individual cell ignite, the fire must be contained and/or extinguished, and not propagate to the whole battery. These are the considerations that are taken into account for battery design on a case-by-case basis.

Complete EV batteries have been subjected to abuse tests by carmakers in the frame of joint development programs. For example, a severe crash test was applied to the Saft battery for EPIC,²¹ simulating an accident where the battery bumps against a tree or a telegraph pole. The impact speed of the battery was 52 km/h. Sparks during crash resulted in a fire, as the electrolyte was burning. It was allowed to burn for about 15 min, then was extinguished without any problem.

The observations were as follows: there was no explosion, the fire was not dramatic and could have been easily extinguished in a short time, there was a very slow transmission to other modules. At the end of the experiment, only the modules of battery in the crash zone were destroyed. It must be emphasized that the crash with the battery system only was really a worst case. It is much worse than for a real crash with the same battery integrated properly in a vehicle. From this behavior the carmaker considered that the risk is acceptable and allows carrying on with the development of this technology for EV application.

21.4.3.5. Onboard Vehicle Experimentation

At the time this chapter is being written, the Li-ion for EV is not a commercially available product, and real life experience with EV Li-ion batteries is limited to fleet operations. More than one hundred vehicles using Li-ion batteries have now been put on the road by various carmakers. These batteries are coming from small production lines set up by the battery makers. Nissan initially experimented with Li-ion batteries using Sony (cobalt positive) batteries. After Sony stopped this battery activity, Shin Kobe (manganese positive) started supplying the batteries. Most European car manufacturers are experimenting with the Saft batteries. Some of these vehicles have achieved more than 40000 km and the batteries are still in good operation. A 200-km range on a single charge has been demonstrated both on a small Peugeot 106 and a large Chrysler Voyager minivan. Among all the vehicles running with these Li-ion batteries, not a single problem linked to the cells has been reported.

21.4.3.6. Cost

This is certainly a key point to consider when speculating about the probability of Li-ion becoming a very widely used system in EV and more generally in all industrial applications. Presently, the prices of large Li-ion EV batteries correspond to prototypes and small production volumes. Beyond the basic product cost, they often include R&D activities. They are now much greater than the targeted volume prices, which are about \$150/kWh for high energy and \$35/kWh for high power types.

Cost reduction is a permanent subject in development programs. Li-ion is still a new technology and a very important cost decrease occurred in the portable battery business during the last 5 years. The OEM selling price in large quantities is presently in the order of \$0.3/Wh²² and is expected to further fall down with competition, leading in turn to significant reductions in the cost of large batteries.

The battery assembly cost may vary significantly with the level of sophistication of the management system (thermal, electronics). The added cost is generally assessed to be in the range of 15 to 20% of the cell costs.

The onboard EV experimentation also demonstrates that Li-ion technology exhibits the lowest operating cost per kilometer among the four main competitive technologies. The reasons are:

- The energy efficiency (ratio between the discharged energy and the charged energy) of Li-ion is better than 90% while the energy efficiencies of aqueous batteries are in the 70-80% range. Therefore, for the same available energy put into the battery, less energy will be drained from the charging network.

- For the same onboard energy, a vehicle fitted with Li-ion will have a longer range thanks to the lighter weight of the battery.

Comparing two identical vehicles, one fitted with a Li-ion battery, and the other with a lead acid battery of the same energy, the lead acid powered vehicle consumes from the charging network twice the energy needed to the Li-ion vehicle to achieve the same driving range. Assuming an acceptable purchasing price, and taking into account zero maintenance costs and long operating life, Li-ion can be a very efficient technology based on life cycle cost.

21.5. HEV APPLICATIONS

The hybrid car concept is based on combining two or more different power sources in a vehicle, which would complement each other. The goal behind this approach is making cars more environmentally friendly by reducing emissions as well as improving gas mileage.

Usually the primary power source in the vehicle provides main propulsion and the second power source is only used when an additional power boost is needed, for example during vehicle acceleration. The primary source has long been considered to be a smaller, more economical internal combustion engine (ICE). In some more recent scenarios it is foreseen that the ICE could be replaced by a fuel cell. The second power source is a rechargeable battery capable of delivering the high power pulses needed for vehicle acceleration. In the early days of HEV, other technologies were considered as this second power source. Supercapacitors are capable of repeatedly delivering hundreds of thousands of high rate pulses even at low temperatures. However, the very low energy density of these devices, usually in the range of 3 to 5 Wh/kg, renders them unsuitable for this application. Another energy storage device considered for supplying the power for the acceleration burst was the flywheel. Although this technology has interesting potentialities, carmakers were not convinced of its ability to reach maturity due to its complexity, and the issue of containment. As a result, the rechargeable battery remains the only viable option that can meet the stringent requirements of the application.

21.5.1. Application Requirements

The battery needs to provide power on demand, normally manifested in short bursts of a few seconds, accept fast charging from regenerative braking, and last 15 years. Table 21.9 lists most of the important requirements for Power Assist HEV.²³

Table 21.9. Technical requirements of Power Assist HEV battery.

Characteristics	Units	Requirement
Pulse discharge power	KW	25 (18 sec)
Peak regenerative pulse power	KW	30 (2 sec)
Total available energy	KWh	0.3 (at C/1 rate)
Minimum roundtrip efficiency	%	90
Cold cranking power at -30°C	KW	5
Cycle life at 25Wh cycle energy	Cycles	300000
Calendar life	Years	15
Maximum weight/volume	kg/l	40/32
Operating voltage limits	V dc	$V_{MAX} \leq 440$ / $V_{MIN} \geq 0.5 * V_{MAX}$
Maximum allowable self-discharge	Wh/day	50
Temperature range	°C	
Operation		
Survival		

21.5.2. Competing Battery Technologies

The competing battery systems for future hybrid electric vehicles are lead-acid, Ni-MH and Li-ion technologies. Other technologies such as Ni-Zn have proven deficient in one or more critical performance aspects.

Lead-acid batteries have well established roots and traditions in the automotive industries. The main advantages are very low cost and proven high power capability. Drawbacks include low energy density, short life and limitations in charge acceptance at lower states-of-charge making this system poorly suited for traditional HEV.

Ni-MH batteries became popular as a replacement for Ni-Cd. They provide better energy density and their life, longer than that of Lead-acid batteries, is apparently sufficient to meet some of the life requirements in HEV application. The main disadvantages are their poor performance at extreme temperatures and high self-discharge rates.

A number of different types of hybrid vehicles are being considered by the automotive industry. Several Japanese carmakers have already introduced power-assist hybrid vehicles. These vehicles presently use NiMH batteries due to the more mature production status of this technology compared to Li-ion.

21.5.3. High Power Li-Ion Technology Challenges

From the very beginning Li-ion has promised and achieved great advantage in energy density and specific energy over existing technologies. However, due to the use of organic electrolytes with fairly low ionic

conductivity, its possible use in high power applications was not originally considered. Only in the last several years, R&D conducted for hybrid electric vehicles has proven that Li-ion can successfully compete in the high power rechargeable battery arena. The success of the development work has prompted interest from other industries which could use a light but powerful source of energy. Why is this possible? The main power limiting factors in Li-ion cells are indeed the low mobility of Li^+ in the organic electrolyte and low diffusion rate inside the active materials. The most practical way to increase the power is therefore to increase the electrodes surface area, by making them thinner, which also reduces the ionic pathway in the electrolyte (separator and electrode porosity).

Li-ion technology utilizes electrodes that are already much thinner than electrodes used in other rechargeable chemistries. Commercial Li-ion cells typically have negative and positive electrodes with thicknesses in the range of 200 microns. This means that coating, calendering, slitting and winding processes of thinner electrodes for high power cells must be controlled much more tightly than traditional mass-produced Li-ion cells.

Another technical challenge is associated with the need to carry much higher currents. Therefore, engineering of the high power cells must address internal electrode bussing as well as outside connections.

In order to meet the low temperature requirements, which commonly come by default with most high power applications, electrolyte properties must be specially tailored. High ionic conductivity, low freezing point and low viscosity enable low temperature discharge. This is accomplished through selection of appropriate solvents and optimizing salt molar content. However, selecting solvents that would improve low temperature performance may sometimes result in compromised stability at elevated temperature and reduced calendar and cycle life.

21.5.3.1. Performance of Saft Li-Ion HEV Battery Technology²⁴

The main feature of HEV batteries is the ability to deliver power on demand as well as to accept charge rapidly. Because of the voltage dependence on state of charge, the ability to deliver discharge power down to a minimum voltage limit decreases with decreasing state-of-charge. On the contrary, the ability to accept rapid charge to a maximum voltage limit increases with decreasing state-of-charge. In addition the power delivered over a short pulse is greater than the power delivered over a long pulse or over a complete discharge. Therefore, when talking about power it is important to specify both the state of charge and the duration of the pulse.

Table 21.10 describes the main characteristics of the cells presently available.

21.5.3.1.1. Power

A key parameter for a high power battery system is the point where the battery can deliver as much discharge power as it can accept charge. This point is called the “sweet spot”. Usually this point is around 50% SOC and is determined by conducting a series of discharge and charge pulse at different states-of-charge. Figure 21.10 shows the sweet spot for one of Saft’s high power cells.

A different way to characterize the power capability of a system is to subject it to a complete discharge at various rates. In addition to the voltage drop it is important to make sure that the cell does not overheat during the discharge because overheating will severely reduce its life. Figure 21.11 shows a set of discharge curves under different discharge loads. Figure 21.12 shows the cell temperature rise under 10C (6 min) discharge.

Table 21.10. Main characteristics of Saft Li-ion high power cells.

Cells		VL 8P	VL16 P
Nominal Voltage	V	3.6	3.6
Rated Capacity at C/3	Ah	8	16
Power 50% DOD, 18s pulse	W	513	904
Dimensions (Ø / h)	mm	47/104	47/178
Typical Weight	kg	0.38	0.67
Specific Energy	Wh/kg	75	85
Specific Power	W/kg	1350	1350
Energy Density	Wh/l	158	186
Power Density	W/l	2850	2900

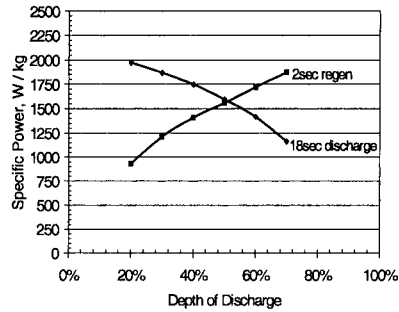


Figure 21.10. Sweet spot of a high power cell.

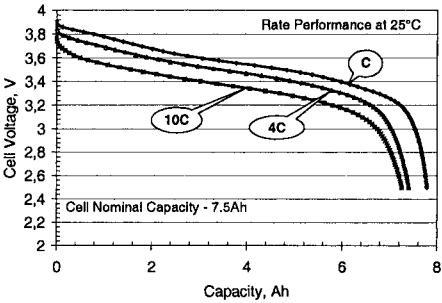


Figure 21.11. Complete discharge at different discharge rates.

Low temperature performance of high power cells is also critical. High current capability at low temperatures can be achieved through the use

of special electrolytes, optimized positive and negative active materials, and improved cell mechanical design. Figure 21.13 shows a sequence of three 2-second pulses separated by 10-second rest periods, called “cold cranking”, all conducted at -40°C .

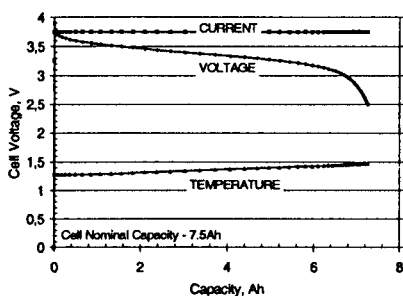


Figure 21.12. Temperature rise in a high power cell under 10C (6 min) load.

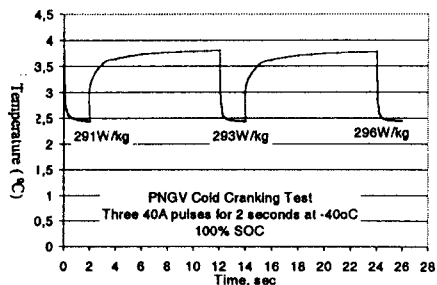


Figure 21.13. Cold cranking pulses of a high power cell at -40°C .

21.5.3.1.2. Cycle life

Cycle life of Li-ion like any other rechargeable system varies with depth of discharge, cycle rate and temperature. Figure 21.14 shows that Li-ion is capable of maintaining power and energy over 1 million shallow high rate cycles, representing the HEV utilization profile. Figure 21.15 displays the deep cycles recorded at C/1 rate. 5000 cycles are projected at an average ambient temperature of 20°C . Except for NiH_2 , which has much lower energy and power density (see Section 21.7.1.), this performance is unmatched by any other battery system. An evaluation of cycle life dependence on temperature still remains to be performed.

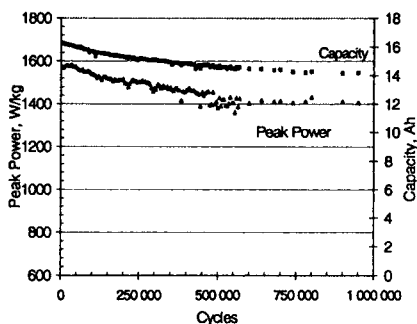


Figure 21.14. Deep cycling of a high power cell under HEV load profile (periodic 100% DOD diagnostic).

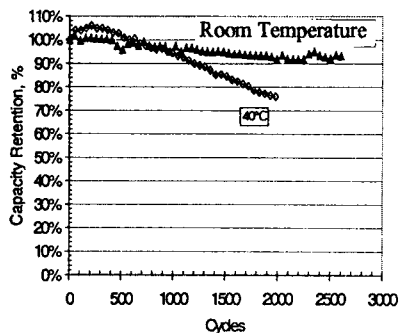


Figure 21.15. Cycle life of a high power cells (C rate, 100% DOD).

21.5.3.1.3. Calendar Life

Last but not least is the calendar life of the system. It has been projected that Saft HEV cells could maintain the required peak power and energy necessary for the HEV application over a period of 15 years. These estimates are based on actual data of cells stored at various temperatures and from projections based on the Arrhenius law. It has to be mentioned that the nature of the application, which requires the battery to be at around 50% state-of-charge, is very beneficial for achieving long calendar life in Li-ion. Figure 21.16 shows actual capacity and power fading from cells on storage at three different temperatures.

21.5.3.1.4. Abuse Behavior

Li-ion electrochemistry does not have metallic lithium, which makes it a safer system. However, it is still a high energy density system, and

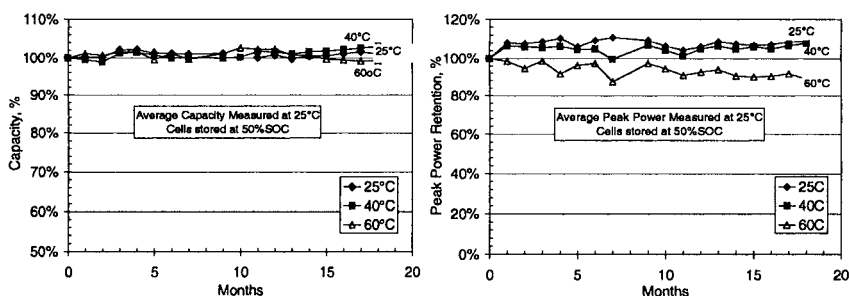


Figure 21.16. Capacity and power evolution of cells stored at 50% SOC at various temperatures.

contains flammable electrolytes. Under some severely abusive conditions such as overcharge, smoke and flame may be observed, as discussed in the general section. Because they contain relatively less active materials, and more inactive components (such as current collectors), high power cells are generally safer than high-energy designs.

Saft high power cells have an integrated fusible link preventing thermal runaway during external short circuit (the 8 Ah cell produces a peak short-circuit current of 1000 A). At the battery level, redundant protections are in place: by monitoring voltage, current and temperature, dangerous situations resulting from overcharge or overheating can be prevented. Table 21.11 describes the results of various abuse conditions.

21.5.3.2. Battery Configurations

Many battery configurations can be designed, depending on the required characteristics. Electronic systems for battery monitoring obey the same basic rules valid for high energy batteries (see previous section).

Active cooling is frequently required for these high power systems. Air-cooling is sufficient for most applications, but liquid cooling might sometimes be preferred. Figure 21.17 shows a Li-ion battery for a Power Assist HEV. The battery is 2.8 kWh, 8 Ah at 346 V, providing 50 kW for 18 seconds at 50% SOC. This particular battery is air-cooled and has integrated Battery Management System (BMS).

21.5.3.3. Other Li-Ion Battery Systems

As discussed in previous sections, LiMn_2O_4 is the other Li-ion chemistry proposed for HEV applications. Shin Kobe manufactures a high power cell for HEV. The small cylindrical 3.6 Ah cell demonstrates high

Table 21.11. Abuse test records on high power Li-ion cells.

Test description	Test results	Comments
External short VL8P VL16P	Vent of electrolyte, no smoke Vent of electrolyte, no smoke	Cell design with fusible link reacting at high power
Nail Test / Internal short VL8P VL16P	Smoke Smoke	A few “weld” sparks during penetration
Heat Test (ramp to 150°C in 30 min. Event after >45min) VL8P and VL16P	Smoke	
Crush VL8P VL16P	Vent only Smoke	
Impact Drop Test	No event	
High rate overcharge (100 A)	No event up to 4.6 V (>100% overcharged capacity). Smoke and flame if voltage not limited	Event start depends on charge rate.
Overdischarge (reversal)	No event	Typically the cell develops an internal short
Salt water immersion (8h)	No event	Terminal corrosion. End voltage: 3.4 V
Fuel fire (radiant heat 800°C)	Fire, no explosion	Case integrity fully kept.

power discharge capability,²⁵ as shown in Figure 21.18. A peak power of 2000 W/kg can be obtained at 50% SOC, 20°C.^{26,27}

Japan Storage Battery has also developed a high power design in batteries using LiMn_2O_4 . The 3 Ah cell exhibits 1500 W/kg on

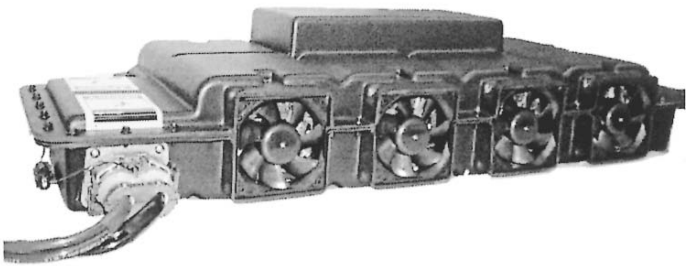


Figure 21.17. Example of 50 kW high power battery for power assist HEV (2.8 kWh, 8 Ah at 346 V).

charge and discharge at the 40% state of charge “sweet spot”. Good deep DOD cycle life is obtained at 1C rate at 25°C, while some capacity loss is observed at 60°C (Figure 21.19), as is typical of the Mn-based cells.

Using a substituted manganese spinel, NGK insulators¹⁹ developed recently a high power 4 Ah cylindrical cell of enhanced safety, exhibiting a specific power of 2500 W/kg at ambient temperature and 800 W/kg at -25°C. A medium size 12 Ah cell has been also designed for a 42 V battery.

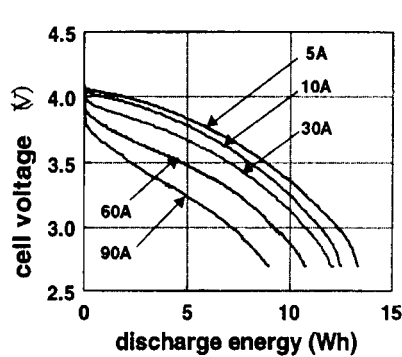


Figure 21.18. High rate discharge of LiMn₂O₄ Li-ion 3.6 Ah high power cell (Shin Kobe, from Ref. 25).

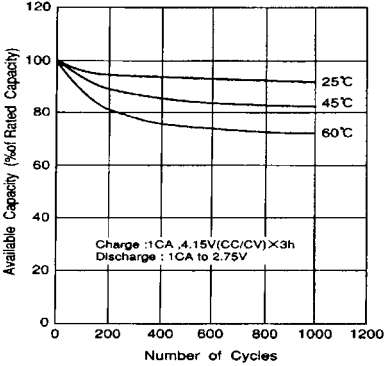


Figure 21.19. Available capacity on cycling at different temperature of LiMn₂O₄ Li-ion 3 Ah high power cell (from JSB catalogue).

Maintaining the power capability over a long period of time, including the high ambient temperature excursions during normal operation, is the main challenge for the technology in this application.

21.6. STATIONARY APPLICATIONS

Stationary battery applications can be categorized into broad subsets based on the way the battery is charged and discharged.

Standby (float) operation. The battery is maintained in a fully charged condition by a so-called ‘float’ or constant potential charger. The battery and the system loads are connected in parallel with the charger terminals. In this mode of operation, the charger supports continuous loads and the battery accepts whatever current is necessary to maintain it at a set voltage. If the charger output is lost, the battery immediately assumes the system loads.

Intermittent charging (cycling) operation. Batteries in these applications are charged only when the primary energy source is available. The primary energy may come from a solar (photovoltaic, or PV) panel, a wind turbine, an engine-driven generator, the utility grid, or some other source. When a load is connected and the primary source is unavailable or is inadequate to support the load, the battery is discharged.

Buffer operation. Halfway between the other application groups, the primary energy source in these applications is generally available but is frequently insufficient to supply the imposed loads. This may be because the loads exceed the rated output of the energy source, or because the rate of change in the loads exceeds the capability of the energy source to respond. When the load level falls below the rated output of the primary source the battery is recharged.

Each of these application sets imposes its own particular requirements on Li-ion batteries. The following sections describe the applications and their requirements in greater detail, and discuss the advantages and disadvantages of Li-ion batteries in meeting those requirements.

21.6.1. Standby (Float) Operation

Most applications in this subset incorporate a grid-connected charger/rectifier that is generally available and maintains the battery in a high state of charge. Examples of standby applications include:

- Telecommunications network switching
- Uninterruptible power supply (UPS) systems
- Power quality systems
- Safety/security systems, *e.g.*, emergency lighting, fire safety systems, intruder alarms
- Utility switching (transformer protection)
- Turbine control, *e.g.*, lube oil pumps
- Railway signaling
- Generator starting

The battery duty in these applications can be quite varied. Some duties require the battery to support a relatively constant load for a duration of several hours, such as telecommunications network switching or railway signaling. Others demand a short, high-rate discharge, such as in UPS systems or generator starting. A few applications feature a mixture of low-level continuous loads and short high-rate loads, such as utility switching systems.

Batteries may be located in controlled temperature environments, or may be subjected to extreme temperatures in outdoor cabinets. Battery designs that minimize high temperature aging and maximize low temperature performance are obviously beneficial in the latter case. The high volumetric energy density of Li-ion can be an important factor in some applications, particularly in cabinetized systems, but may be unimportant in others.

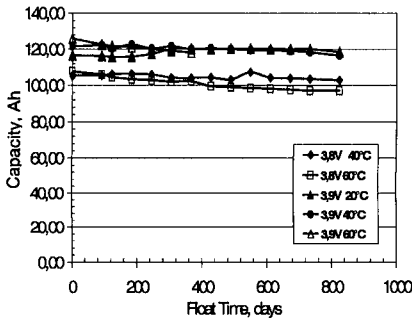


Figure 21.20. Residual capacity evolution of Saft high-energy Li-ion cells under float charge at various temperatures and voltages.

Although Li-ion batteries are more energy efficient than most other types, with better round-trip charge/discharge efficiency and lower power consumption on float, this feature is relatively unimportant in standby operation. More important is that the battery operates reliably over a long lifetime. A general good behavior of Li-ion batteries on continuous float charging has been demonstrated.^{28,29}

As an example, Figure 21.20 describes the residual capacity evolution, during 823 days at various temperatures and voltages, of Saft high-energy modules (3 cells in parallel) measured periodically at the floating temperature and at C/8 rate. The capacity retention is excellent, allowing life predictions of more than 15 years in service. The known failure mode of Li-ion, a slow increase of impedance and consequent energy decline, is a benefit in these applications since it makes battery health monitoring and life prediction easy. Full discharges may be quite rare, so a battery that requires periodic discharge tests or experiences sudden unexpected failure can be a major liability.

21.6.2. Intermittent Charging (Cycling) Applications

Stationary applications involving intermittent charging include many of the loads listed in the standby category. These applications are better categorized by the energy source, which can include:

- Renewables (wind, PV, etc.)
- Engine-driven generators (cyclic operation)
- Hybrid systems

As with standby applications, the battery may support longer energy-type loads, shorter power-type loads, or a mixture of the two. Li-ion batteries are particularly well suited for applications involving repeated discharges. This is not simply an issue of the cycle life of the technology, but also involves considerations of chargeability. With virtually no side reactions to compete with the main charging reaction, the process is highly efficient—the round trip energy efficiency typically exceeds 95%, compared with 60-75% for most other technologies. While this can be important from an economic point of view, particularly when the total available energy is limited, there is an even more important practical consideration.

The high efficiency and the voltage dependence of state of charge help to prevent severe mismatches in the state of charge of the positive and negative plates that can occur in aqueous battery systems. Such imbalances result from differences in charge efficiency between the plates and typically worsen as a battery is subjected to multiple discharges with partial recharges. The only solution in these cases is to subject the battery to a prolonged ‘finishing’ or ‘equalizing’ charge. Not only does this take the battery out of service until the charge can be completed, but in an off-grid system can result in prolonged and inefficient operation of generator units. Li-ion batteries are much more resistant to such imbalances and can be charged quickly and efficiently to a known state of charge.

21.6.3. Buffer Operation

This type of operation is expected to grow in significance in coming years as a new class of applications emerges. This is in the area of distributed generation, in which relatively small generators are sited close to the loads they supply. Distributed generators include microturbines and small fuel cell units. The latter are expected to be implemented as ‘micro-CHP’ (combined heat and power) systems in individual residences, producing both electrical power and heat for hot water or heat exchange systems. Both generator types are characterized by relatively slow response to load changes. Batteries can improve the load response for these units while also providing power for black starting.

It is worth noting that this type of buffer operation may also require a battery to absorb power as generator output is ramped down after a load has been abruptly terminated. It is likely that the most efficient way to accommodate this requirement will be to operate the battery in a less than fully charged state. This can be easily achieved with Li-ion batteries, with their relationship between open circuit voltage and state of charge.

21.6.4. Stationary Battery Trials

As the industry moves towards the commercialization of large size Li-ion batteries, trial sites are being set up to demonstrate the capabilities of this technology. These include high-energy batteries in telecommunications outside plant cabinets and high-power batteries for power quality and distributed generation support. Such demonstrations are critical to gaining acceptance of Li-ion technology in diverse applications, ready to take advantage of declining price levels as the batteries move into commercial production.

Japanese LIBES R&D program, sponsored by METI and NEDO addressed the home load leveling application.¹⁸ As for example, Sanyo³⁰ designed a 2 kWh-class module (117 Wh/kg, 177 Wh/l) using a 250 Wh cell, with a nickel-based positive, $\text{LiNi}_{0.7}\text{Co}_{0.3}\text{O}_2$, and graphite/coke mix as a negative. This cylindrical cell is described in Table 21.12.

Table 21.12. Main characteristics of Sanyo Li-ion cells (from Ref. 18).

Capacity	80 Ah
Dimensions	Ø64 x 312mm
Weight	2.19 kg
Voltage	3.5 V

Figure 21.21 shows a high-energy prototype Saft battery for telecommunications field trials. This battery is rated 70 Ah at 48 V. For higher power applications, Figure 21.22 shows a 14.5 kWh battery assembly capable of providing 100 kW for 1 minute.

21.7. SPACE APPLICATIONS

Since the start of the space era, rechargeable batteries were used to provide power to satellites during eclipse periods. In fact, solar panels are used to power the satellite payload (and recharge the batteries) when the sun illuminates them. Batteries take over from the solar panels

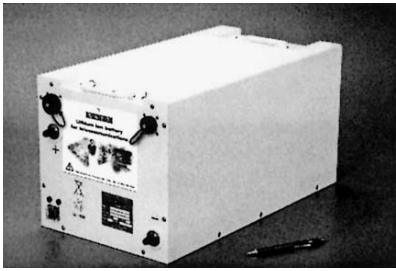


Figure 21.21. Prototype of a Li-ion battery for Telecoms.

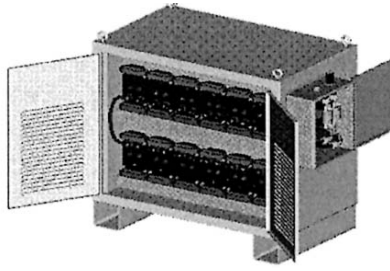


Figure 21.22. High power lithium ion battery assembly.

when the satellite enters into the earth's shadow. NiCd in the 60's, NiH₂ in the 90's and Li-ion now are the only three technologies for satellite use.

The telecommunication satellites that are presently in geosynchronous orbit (GEO), use nickel-hydrogen batteries. The size of telecommunication satellites, and, as a consequence, the electrical power demand during solar eclipses, is continuously increasing. In the 80's satellites weighing 0.5 ton, powered with nickel-cadmium batteries providing 0.5 kW were the standard. In the 90's, the prevailing design was 1 to 3 tons and 2 to 8 kW provided by nickel-hydrogen batteries. Now, satellites may weigh 5 tons with power demand in the range of 15 to 30 kW. With the current nickel-hydrogen technology, 30 kW of power leads to a battery weight of at least 800 kg corresponding to 15-20% of the total satellite weight! That means that the battery, which was already one of the heaviest pieces of equipment on board the satellite, is now reaching a critical size. Combined with the current price of 80-100 k\$ to place one kg in orbit, battery weight has become one of the main issues facing competitive telecommunication satellites.

Thanks to the Stentor project, started in '96, Saft has qualified Li-ion technology for the first time as the main power source of a satellite. Stentor is the first GEO satellite that will fly this promising new battery technology for space.

21.7.1. Battery Requirements for Satellites

Considering the battery constraints, two main satellite families can be considered.

21.7.1.1. GEO Satellites (Geostationary Earth Orbit)

Satellites in geosynchronous orbit are positioned over the equator and travel in the same direction as the earth rotates. They appear "fixed" with respect to a given spot on earth. Satellites in GEO orbit are 35786 km above the earth in the plane of equator. These satellites are mainly used for telecommunications (direct home TV broadcasting, voice and internet). Meteorological satellites are also positioned in geostationary orbits (meteosat family). The main parameters for GEO are an orbit duration of 24 hours, and a number of 90 eclipses per year. As the GEO satellite position is far from the earth, and due to the inclination of the earth's axis to the ecliptic plane, the satellite goes through the earth's shadow cone only once a day during the equinox periods (2 times 45 days per year). Eclipse duration is not constant but increases during the first 22 days up to 72 minutes and then decreases during the last 22 days of the eclipse period. The expected lifetime is 15 years, and the satellite power ranges from 5 to 25 kW.

21.7.1.2. LEO Satellites (Low Earth Orbit)

LEOs are either elliptical or (more usually) circular orbits at a height from 400 to 2000 km above the surface of the earth. The orbit period at these altitudes varies between 1.5 and 2 hours. As the altitude of the LEO satellites is low, their rotation speed is very high (>25000 km per hour). The maximum time during which a satellite in LEO orbit is above the local horizon for an observer on the earth is up to 20 minutes. A global communications system using this type of orbit (mainly due to the low propagation delay of 20-30ms) requires a large number of satellites in a number of different, inclined orbits. Most of the LEO satellites (except the constellations which are used for direct telecommunication systems: Iridium and Globalstar) are used for Earth or Space observation. The best examples of LEO satellites are the Hubble Space Telescope, the Spot family (Earth imaging and survey) and military satellites.

The key parameters are an orbit duration from 1.5 to 2 hours, and a number of 20 to 35 minutes eclipses per year from 4500 to 5500 depending on the satellite altitude. The expected life time is 5 to 8 years, and the satellite power vary from 10 to 3000 W. Two main LEO satellite families can be categorized: the "small" LEO (sometimes called nano- or micro satellites) and normal LEO

21.7.2. Competing Technologies

Table 21.13 compares the three main electrochemical systems for satellites: NiCd, NiH₂ and Li-ion.

The main advantage offered by Li-ion technology is weight reduction. As we can see in the table, weight benefits are achievable both at the battery and satellite level, because the lower thermal power and higher energy

Table 21.13. Performance comparison of NiCd, NiH₂ and Li-ion batteries for satellites.

	NiCd	NiH ₂	Li-ion	Impact of Li-ion on system
Energy density (Wh/kg)	30	60	125	Weight saving
Energy efficiency %	72	70	96	Less solar panel
Thermal power (scale 1-10)	8	10	3	Radiator reduction
Self discharge/day	1	10	0.3	No trickle and simple management at launch
Energy gauge	No	Pressure	Voltage	Better accuracy
Charge management	CC	CC	CC CV+balancing	More complex charge management
Modularity	No	No	Yes	One cell design

efficiency of Li-ion compared to NiH₂ impacts on solar panel and radiators sizes. Moreover, the lower self-discharge allows the launch operations to be simplified, thus avoiding battery recharge when the satellite is installed on the launcher. NiH₂ battery self discharge (10 times higher than for Li-ion) requires recharge of the battery right up to the final countdown. This recharging operation performed under the fuse cap is a critical phase of the launch mainly because of the thermal management of the battery. In orbit, therefore, management can be simplified as the necessary reconditioning operation of NiH₂ can be eliminated by using Li-ion. As discussed in the other sections, the direct relationship between voltage and state of charge induces here again the major benefits of a precise “fuel gauge”, and an easy directly assembly of the cells in parallel.

These numerous advantages of Li-ion compared to the two current nickel technologies lead to an increasing number of satellite projects adopting Li-ion batteries as base-line power source. The only drawback of the Li-ion is the need for more sophisticated electronic systems for battery management.

21.7.3. Saft Cell and Battery Designs

21.7.3.1. Cell Designs

Started at Saft in '95, the development of Li-ion cells for space took the advantage of the manufacturing line originally built for electric vehicles. The VES140 (140 Wh and 40 Ah) space cell has the same electrochemical stack (electrode assembly) as for the EV cell. The vital parts of the VES 140 cell are (Figure 21.23): the terminal, which must insure an extremely high level of hermeticity for the mission duration, and the support of the stack in the container, to withstand the high vibration levels during the launch phase.

The electrodes are made of substituted nickel-based oxide for the positive and mix of graphite for the negative. The specific properties of this electrochemistry, as described in previous sections, is particularly suitable for satellite needs: very long cycle and calendar life, enhanced by the “lithium reserve” of about 15%. The cell shape is cylindrical (250 mm height and 54 mm diameter) with a nominal weight of 1116 kg. Its specific energy is 125 Wh/kg. This number may appear low compared to other types of Li-ion cells. The difference mainly comes from the specific design for terminals and margins to insure higher reliability.

This cell design has been qualified either for GEO and LEO applications in January 2000 and has flown in 2002 on board Stentor. Two other cell designs are in the qualification process: VES100 (100 Wh and 26 Ah) which is similar to the VES140 but shorter (190 mm height) mainly dedicated to LEO missions, and MPS15S (15 Wh, 4.5 Ah) which has an elliptical prismatic shape and is mainly dedicated to “small” LEO satellites with low power (Figure 21.24).



Figure 21.23. The VES140 cell.



Figure 21.24. The MPS15S cell.

21.7.3.2. Battery Designs

STENTOR is a french technological satellite designed by the CNES (Centre National d'Etudes Spatiales) and manufactured by Alcatel Space Industries and Astrium. Its mission is to qualify new satellite technologies (solar panels, deployable radiators, electric propulsion, batteries, etc.) under orbital conditions. The emerging Li-ion system was proposed in 1995 by Saft to be included as the new power source, and considered as a strategic technology. The project objective was to qualify and fly a complete Li-ion battery design including charge management electronics (Figure 21.25). As the battery power is close to 3 kW, the battery is composed of 2 battery sets of 2P11S (2 cells mounted in parallel with 11 pairs connected in series). The Stentor battery meets all requirements (life time, thermal and mechanical

constraints, reliability) of the generic plate-forms Space Bus (Alcatel Space Industries) and Eurostar (Astrium). Stentor is the first GEO satellite to

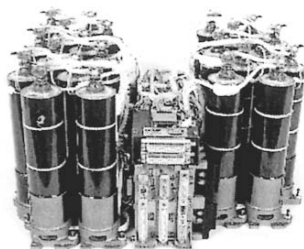


Figure 21.25. Stentor battery set.

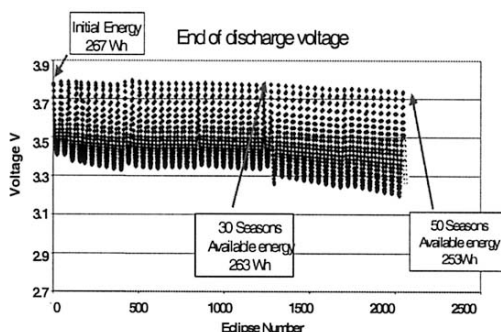


Figure 21.26. 56 GEO accelerated seasons on VES140 (82% DOD max).

experiment with Li-ion batteries.

From this experience, a range of modules has been designed to cover satellite manufacturers requirements for the near future (battery voltage, footprint, and power), suitable for GEO or LEO.

The module design from 3 to 12 parallel cells allows coverage of the range of satellite power from 5 to 30 kW. Assembling these modules in series offers the best modularity and simplification of the management system compared to the string of series cells in parallel design. In each module, a by-pass system and an electronic device interface with the satellite equipment. The main function of this electronic interface is to perform the balancing of the cells to guarantee the battery energy throughout its lifetime. The GEO batteries, delivering up to 108 Wh/kg, are generally 10 to 12 modules in series ("50 volts" bus), or 20 to 24 modules ("100 volts" bus). LEO satellites require less energy, and bus average voltage is 28 V corresponding to a 9S (9 modules in series).

22.7.3.3. Typical Performances and Life Expectation

Numerous life tests have been performed by ESA, CNES and satellite manufacturers to measure fading and calendar losses on Saft cells. For GEO, more than 25 life tests (accelerated or real time) have been conducted (some are still ongoing) with various DOD (from 50 to 90%), various end of charge voltages (from 3.9 to 4.1V), and with or without electric propulsion cycles.^{31,32}

More than 56 GEO seasons (corresponding to more than 26 years) have been completed on a 2P3S battery. The test conditions were:

- accelerated charge with currents from C/3 to C/6 (instead of C/10)
- discharge profile and currents identical to GEO mission, DOD ranging from 80 to 82%, at 20 °C.
- balancing system used before each season.

Figure 21.26 shows the end-of-discharge voltage during the 56 GEO seasons. Capacity was checked every season, and the energy loss at season 30, corresponding to the standard life time of GEO satellites (10 years), is less than 2%.

In addition, calendar loss is low, thanks to the system properties already described. Considering an average temperature of 20°C over 15 years (25°C during the equinox period to enhance energy and 15°C during solstice as the energy need is low), the calculated energy loss due to the storage is linked to the increase of the internal resistance and is less than 3%. So, the total energy loss for the 3 years of storage and 15 years in a GEO mission at 80% DOD is less than 5%. Considering an additional margin of 5%, the end-of-life (EOL) energy is 90% of the beginning-of-life (BOL) energy. VES140 cell LEO life tests are currently at more than 20000 cycles (equivalent to 4 years) at 20% DOD. The energy loss is less than 12%. Considering 3 years of storage and 8 years in a LEO mission at 20% DOD, the EOL energy represents 70% of the BOL energy.

21.7.4. Other Battery Designs

A few other battery manufacturers are addressing the space market with Li-ion batteries, using various designs and electrochemistries.

21.7.4.1. GS - Melco

Melco (Mitsubishi Electronic Corp) has developed the large capacity Li-ion battery shown in Figure 21.27 as an example of the families. The elliptic cylindrical 100 Ah cell specific for space has been jointly developed by Japan Storage Battery Co, Ltd (JSB) and Melco. The electrochemistry is based on LiCoO_2 , with other cell components similar to normal Li-ion types. The battery design includes paralleled cells mounted in series (P-S architecture), one by-pass system per package and electronics for balancing.

Figure 21.27 describes a 100 Ah battery module, using 10 cells in series. Rated at 3.6 kWh, this 35.9 kg module exhibits 100.3 Wh/kg.³³ The

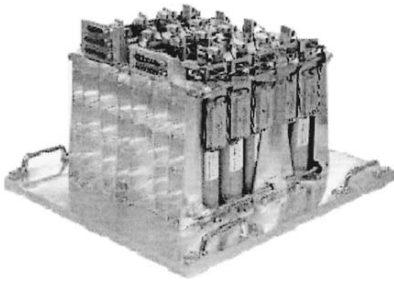


Figure 21.27. Melco 100Ahx10S battery module.

use of a larger cell size increases the battery specific energy and reduces the labor cost of manufacturing and tests. The wide range of cell capacities (50 to 190 Ah) will support the versatility to optimize battery size to the required power. Calendar and cycle life testing of these cells has been evaluated,³⁴ estimating a

76% capacity retention over a 15-year GEO mission + 3 years ground storage, and 59% retention over a 8-year LEO mission + 3 years ground storage.

21.7.4.2. AEA Technology plc/COM DEV Ltd

AEA Technology/COM DEV has made the opposite choice using specially selected small commercial cylindrical 1.5 Ah cells (18650HC manufactured by Sony).³⁵ LiCoO_2 is used as the positive material and hard carbon as the negative. Cells are connected in series strings to match the required voltage and these strings are assembled in parallel to achieve the required capacity. No electronics are required at the cell level, provided that the cell properties are uniform and well matched. This cell, originally designed for multipurpose use, includes a safety current breaker to prevent individual cell overcharge. There is no balancing, considering that the failure of one cell within a string should simply lead to the loss of one string. The number of strings is sized taking into account the probability of failures, to ensure the required battery life. Thanks to the small capacity increments, this configuration fits well the various needs for small spacecrafts and AEA Technology/COM DEV batteries have been selected for a number of microsat scientific projects.

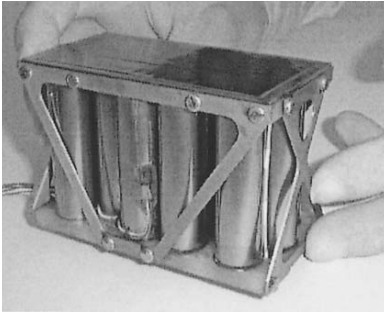


Figure 21.28. Rosetta Lander battery (one of the two modules) (courtesy of AEA Technology plc).

For example, a 3x(6s-11p) 1.07 kWh construction is designed for the ESA Rosetta platform, launched at the beginning of 2003 towards comet Wirtanen. Extension of this concept to larger battery configurations is being tested, in order to demonstrate adequate

reliability. Figure 21.28 shows half of the 151 Wh battery qualified for the CNES Rosetta Lander project.

21.7.4.3. Yardney Products/Lithion, Inc.

The Li-ion cell and battery design approach adopted by Yardney Technical Products/Lithion, Inc. utilizes a true parallel-plate prismatic design, and includes a mixed cobalt-nickel oxide as positive material (Figure 21.29). This design yields a highly gravimetrically and volumetrically efficient cell. High packing efficiencies are achievable with prismatic cells, and battery construction is simplified by constraining all cells in a single block.



Figure 21.29. 35 Ah Li-ion cell (courtesy of Yardney).

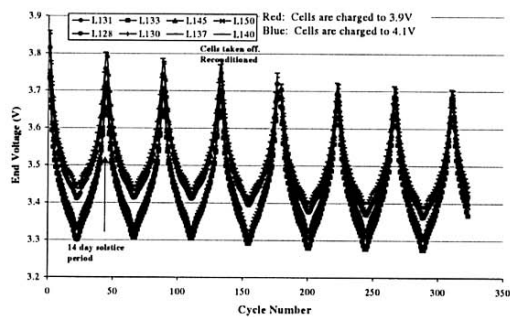


Figure 21.30. End of discharge voltage during GEO cycling of 35 Ah cells (60% DOD max) (courtesy of Yardney).

The 30 Ah cells developed for the 2001 Mars Lander Mission demonstrated over 144 Wh/kg specific energy and 345 Wh/l energy density. The 8-cell (28 V) battery constructed for this mission delivered 111 Wh/kg and 238 Wh/l. Life cycling of these cells have demonstrated over 12000 LEO-type cycles to 40% DOD and over 5 years of an accelerated GEO-type profile to 60% DOD, as shown in Figure 21.30. Upper curves are for charges to 4.1 V, lower curves to 3.9 V.

21.7.5. Launchers

Launchers also need batteries, mainly based today on NiCd or AgO/Zn technology. Here again, energy and power density of Li-ion are strong incentives. A new 1.26 kWh battery has been recently developed by Saft and is shown in Figure 21.31. A particular feature of this design is to withstand very drastic vibration conditions.

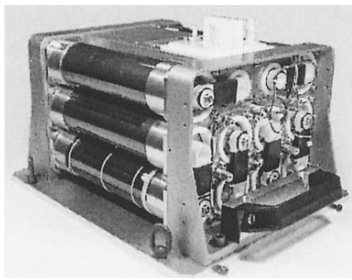


Figure 21.31. Saft Li-ion battery for a launcher.

Weight = 18 kg
Capacity = 35 Ah
Voltage = 36 V
Operating temperature: -20 to +30°C
Discharge profile is 600 Amp 100 ms +
340 Amp for 5 minutes

21.8. CONCLUSIONS

Li-ion electrochemistry has now demonstrated its ability to be used in large batteries for a very wide range of applications. The main features of these power sources are high energy or high power, extended cycling ability, long calendar life, and high reliability. Continuous technical improvements are expected, particularly in the field of safety, to enlarge the domain of utilization. Their superiority has already been proven in various applications through extended prototype testing such as EVs. The space industry, where Li-ion brings very substantial benefits, has already adopted and qualified this technology, which will progressively replace the existing NiH_2 batteries. There is no doubt that this system will very soon find its place in the industrial battery market. Opening the road to wide market segments, such as automotive where HEVs or new 42 V batteries are the biggest stakes, will greatly depend on cost reduction. Material costs and associated electronics represent the major part of the present costs, and should significantly decrease with increasing production level. Ultimately, Li-ion large batteries are expected to be competitive with the today's common systems on the basis of life cycle cost.

ACKNOWLEDGEMENT

This chapter has been written with the collaboration of Yannick Borthomieu, Guy Chagnon, Jim Mc Dowall, Louis D'Ussel, Kamen Nechev and Guy Sarre (all from Saft).

Note: The data on products presented here cannot be considered as a warranty from the manufacturers.

REFERENCES

1. K.Mizushima, P.C.Jones, P.J. Wiseman and J.B. Goodenough, *Mater. Res. Bull.* 17 (1980) 785.
2. E.Plichta, M.Salomon, S.Slane and M.Uchiyama, *J. Power Sources* 21 (1987) 25.
3. M.Broussely, F.Perton, J.Labat, R.J.Staniewicz and A.Romero, *J. Power Sources* 43-44 (1993) 65.
4. A. Yoshino, Asahi Kasei, JP 1989 293 (priority 1985), US Patent 4,668,595 (1987).
5. A.Lecerf, M.Broussely, and J.P.Gabano, EU Patent 0345 707, US Patent 4,980,080 (1989).
6. C. Delmas, J.P. Pérès, A. Rougier, A. Demourgues, F. Weill, A. Chadwick, M. Broussely, F. Perton, Ph. Biensan, and P. Willmann, *J. Power Sources* 54 (1995) 329.
7. G.Sarre, M.Broussely and R.J.Staniewicz, *Proceedings of EVS12*, Anaheim, USA (1994).

8. M. Broussely, G.Rigobert, J.P.Planchat and G.Sarre, *Proceedings of EVS13*, Osaka, Japan, I, 27-32, (1996).
9. C. Delmas and I. Saadoune, *Solid State Ionics* 53-56 (1992) 370.
10. A.Funahashi, Y.Kida, K.Yanagida, T.Nohma and I.Yonezu, *J.Power Sources* 104 (2002) 248.
11. Ph. Biensan, J.-P. Peres, and F. Perton, *ECS Fall Meeting*, Abstract 131, Honolulu, Hawaii (1999).
12. T. Ohzuku, T. Yanagawa and M. Kouguchi, *J. Electrochem. Soc* 142 (1995) 4033.
13. J.P.Pérès, C.Audry, Ph.Biensan, G.Blanc, J.P.Boeue, V.Dillay, M.Broussely and A.de Guibert, *Lithium Battery Discussion*, Proceedings, Abstract 32, Arcachon, France (2001).
14. C.H.Chen, J.Liu and K.Amine, Abstract 176, *ECS Fall Meeting*, San Francisco (2001).
15. M. Broussely, S.Herreyre, Ph.Biensan, P. Kaszlejna, K.Nechev and R.J.Staniewicz, *J. Power Sources* 97-98 (2001) 13.
16. M. Broussely, S.Herreyre, F.Bonhomme, Ph.Biensan, Ph.Blanchard, K.Nechev and G.Chagnon, *ECS Fall Meeting*, San Francisco (2001).
17. K.Nakai, T.Aiba, K.Hironaka, T.Matsumura, and T.Horiba, *41st Battery Symposium in Japan*, Nagoya, p. 350 (2000).
18. N.Terada, T.Yanagi, S.Arai, M.Yoshikawa, K.Ohta, N.Nakajima, A.Yanai and N.Arai, *J.Power Sources* 100 (2001) 80.
19. K.Kitoh and H.Nemoto, *J. Power Sources* 81-82 (1999) 887.
20. B.Simon, US Patent 5,626,981, EU Patent 0683537.
21. O.Bitsche, G.Gutmann, A.Schmloz and L.d'Ussel, *Proceedings of 18th Electric Vehicle Symposium (EVS18)*, Berlin, Germany (October 2001).
22. H.Takeshita, *19th International Seminar on Primary and Secondary Batteries*, Fort Lauderdale, USA (2002).
23. *PNGV Battery Test Manual*, Rev. 3 (February 2001).
24. K. Nechev, M. Saft, G. Chagnon and A. Romero, *2nd AABC*, Las Vegas, USA (2002).
25. T.Horiba, K.Hironaka, T.Matsumura, T.Kai, M.Koseki, and Y.Muranaka, *11th IMLB*, Monterey, USA, Abstract 418 (2002).
26. T.Horiba, *1st AABC*, session 5, Las Vegas, USA (2001).
27. T.Horiba, K.Hironaka, T.Matsumura, T.Kai, M.Koseki, and Y.Muranaka, *J. Power Sources* 97-98 (2001) 719.
28. M. Broussely, M. Perelle, J. McDowall, G. Sarre and J. Martaeng, *Proceedings of 22nd Int. Telecommunication Energy Conference*, Phoenix, USA, paper 12.1 (Intelec 2000).
29. T.Sasaki, M.Inaba, T.Abe, Z.Ogumi, *ECS Fall Meeting*, Abstract 271, San Francisco, USA (2001).
30. K.Yanagida, A. Yanai, A.Funahashi, K.Ohkita, T. Nohma and I.Yonezu, *40th Battery Symposium in Japan*, Kyoto, p.1 (1999).
31. Y.Borthomieu, M.Broussely and J.P.Planchat, *Proceedings 6th European Space Power Conference*, Porto, Portugal, p. 679 (May 2002).
32. G.Dudley, J.P.Planchat and P.Willmann, *Proceedings 6th European Space Power Conference*, Porto, Portugal, p. 673 (May 2002).
33. T.Gonai, T.Okamura and M.Goto, *Proceedings 19th Int. Communications Satellite Systems Conference*, Toulouse, France, p 147 (April 2001).
34. T.Inoue, N. Imamura, H.Yoshida, M.Mizutani and M.Goto, *Proceedings 19th Int. Communications Satellite Systems Conference*, Toulouse, France, p 186 (April 2001).
35. R.Spurrett, C.Thwaite, M.Slimm and D.Lizius, *Proceedings 6th European Space Power Conference*, Porto, Portugal, p. 476 (May 2002).

Chapter 22

LITHIUM BATTERIES FOR MEDICAL APPLICATIONS

E. S. Takeuchi¹, R. A. Leising¹, D. M. Spillman¹,
R. Rubino¹, H. Gan¹, K. J. Takeuchi² and A. C. Marschilok²

¹*Wilson Greatbatch Technologies, 10,000 Wehrle Drive, Clarence, NY 14031, U.S.A.*

²*Department of Chemistry, University at Buffalo, Buffalo, NY 14260, U.S.A.*

22.1. INTRODUCTION

This chapter on lithium batteries for medical applications is not meant to be an exhaustive review, but rather a broad overview of some of the different types of lithium batteries that power implantable medical devices. The battery systems described in this chapter fall into two major categories, primary or single use cells containing lithium metal anodes, and secondary or rechargeable systems utilizing lithium ion chemistry. Primary lithium batteries have been used for implantable devices such as cardiac pacemakers, drug pumps, neurostimulators and cardiac defibrillators. Secondary lithium ion batteries have been used with left ventricular assist devices, total artificial hearts, and implantable hearing assist devices.

The first human implant of a lithium battery, a lithium/iodine cell that powered an implantable cardiac pacemaker, was conducted thirty years ago.¹ Since that time several different lithium anode batteries have been developed and used successfully in a diverse set of implantable medical devices. The cells used in these devices are typically developed for the application and have used various combinations of cathode, electrolyte and separator, to meet the specific requirements of a device. Despite the various approaches that have been used, there are several power source characteristics that are desirable across all applications.

For all batteries that power implantable medical devices, the important considerations include the following:

- Safety (tolerance to electrical and mechanical abuse)
- Predictability of performance (voltage, current, and time relationships)
- Reliability (low variability of performance parameters)
- High energy density (also low battery weight and small battery size)
- Low self discharge (loss of capacity due to internal cell processes)
- End-of-life indication (usually loaded or unloaded voltage based).

In addition to the above considerations, charging safety and high cycle life are very important factors that must be addressed for rechargeable cells. As a part of this overview, the above considerations along with other pertinent design and performance information, will be discussed for the following lithium battery chemistries: iodine, thionyl chloride, CF_x , SVO, MnO_2 , and Li-ion.

22.2. PRIMARY BATTERIES

22.2.1. The Use of Lithium Metal as an Anode

The principal reason that lithium metal has been utilized as a battery anode material is the very high energy density that lithium can provide to batteries. Lithium possesses an electrochemical equivalence of 3860 mAh/g. For comparison, the electrochemical equivalences of the cathode materials to be discussed in this paper are listed in Table 22.1. As can be seen in this data set, Li has over 4 times the gravimetric capacity of the next closest material (CF_x at 860 mAh/g) and almost 30 times the capacity of LiCoO_2 (at 131 mAh/g).

Table 22.1. Gravimetric and volumetric capacities of cathode materials.

Cathode Material	Gravimetric Capacity (mAh/g)	Volumetric Capacity ^a (mAh/cc)
Iodine	211	1041
Thionyl chloride	451	746
CF_x	860	2322
SVO	315	1521
MnO_2	308	1540
LiCoO_2	131	668

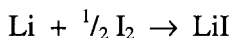
^a Volumetric capacity based on the true density of the active cathode materials.

Lithium metal also has a very low standard potential of -3.05 V at 25°C , which when combined with any of the cathode materials discussed here produces an electrochemical couple with high potential. These two factors, high capacity and low reduction potential, make lithium a good anode material for many batteries. However, there are some limitations. Most significant is lithium metal reactivity with water, which prohibits the use of aqueous electrolytes in lithium batteries under ordinary conditions. This typically limits lithium anode battery systems to the use of organic electrolytes or inorganic electrolytes/soluble cathodes. In using these nonaqueous electrolytes, the conductivity of the electrolyte is limited, leading to increased cell resistance. However, the self-discharge of the system is also typically low, which is important for long life in implanted devices. In general, despite the high energy and reactivity of lithium metal, lithium anode batteries can be designed to provide high safety and reliability for implantable medical applications, demonstrated by ample field data over the last thirty years.

22.2.2. Lithium/Iodine Systems and their Medical Applications

Lithium anode batteries have played a key role in making implantable biomedical devices viable therapy. The first implantable device to use a lithium battery was the cardiac pacemaker. The first implantable pacemaker was developed over forty years ago,² and a number of different types of power sources were used in early versions of the device. These included zinc/mercury (Mallory) cells, rechargeable NiCd batteries, nuclear batteries, and several lithium battery systems. However, for the last 30 years the lithium/iodine battery has been the dominant battery choice for powering implantable pacemakers.

The basic cell reaction in a lithium/iodine battery is:



The cathode contains a mixture of iodine and poly-2-vinylpyridine (PVP), which when reacted together at high temperature forms a conductive, charge transfer complex. In the most commonly used approach to the construction of a Li/I_2 cell, the molten cathode material is poured into the cell and a layer of LiI forms at the anode, producing a separator layer *in situ*. The energy density of the lithium/iodine-PVP system is high, due to the high energy density of I_2 , as illustrated in Table 22.1, and because separator material and electrolyte does not need to be added to the cell. During discharge of the Li/I_2 cell the LiI layer grows in thickness, which results in a rise in cell impedance. The

measurement techniques of microcalorimetry³ and AC impedance⁴ have been used extensively to study the discharge process in Li/I₂ cells.

Due to the solid electrolyte of the system, Li/I₂ cells typically supply low currents, in the μA range. This current output has been able to meet the requirement for implantable pacemakers over the last several decades. Additionally, the formation of a self-healing separator system, as well as high safety and reliability has made the Li/I₂ cell a good choice as a pacemaker power source. Li/I₂ cells have demonstrated very long life under usage conditions, as illustrated by the real time discharge data displayed in Figure 22.1 for a pacemaker battery on test for ~ 10 years. Other larger implantable Li/I₂ battery designs have demonstrated longevity under similar test conditions for over 14 years. The Li/I₂ battery from Figure 22.1 was constructed as previously described,⁵ using a complex mixture of iodine and poly-2-vinylpyridine as the cathode material. The cell was tested under a 100 kohm constant resistance load at 37°C. At the beginning of the discharge test, this load corresponds to $\sim 28 \mu\text{A}$ current drain on the battery.

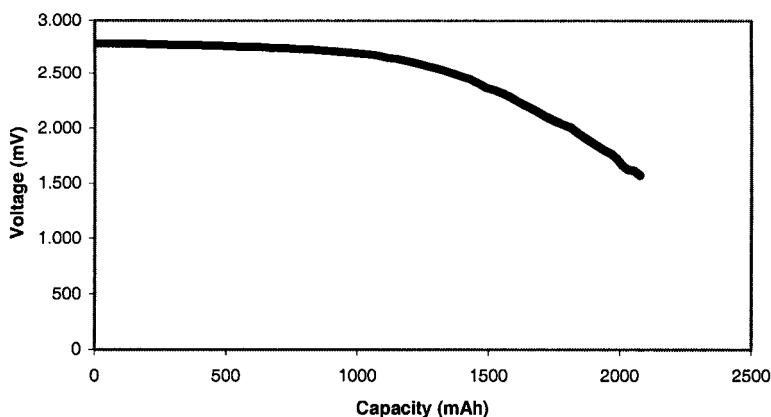


Figure 22.1. Discharge of a lithium/iodine-PVP battery under a 100 kohm load at 37°C.

22.2.3. Lithium/Thionyl Chloride Systems and their Medical Applications

While pacemakers have historically required power in the μW range, other implantable medical devices, such as drug pumps and neurostimulators, have higher power requirements, in the mW range. Thus, the current drains of these devices are too great for Li/I₂ batteries, and considerable work has been done to develop lithium/thionyl chloride (TC) as an implantable battery system.⁶ The discharge reaction for the Li/TC battery system is defined as:



where the thionyl chloride acts as both the electrolyte (in combination with a salt such as LiAlCl_4) as well as the active cathode material. In the physical construction of the cell a carbon black cathode is used to catalyze the electrochemical reaction of SOCl_2 . The theoretical capacity of thionyl chloride as a cathode material is high, as given in Table 22.1, and practical volumetric energy densities as high as 1.2 Wh/cc have been reported for small medical Li/TC batteries.⁶ A typical discharge curve for an implantable Li/TC battery is presented in Figure 22.2.

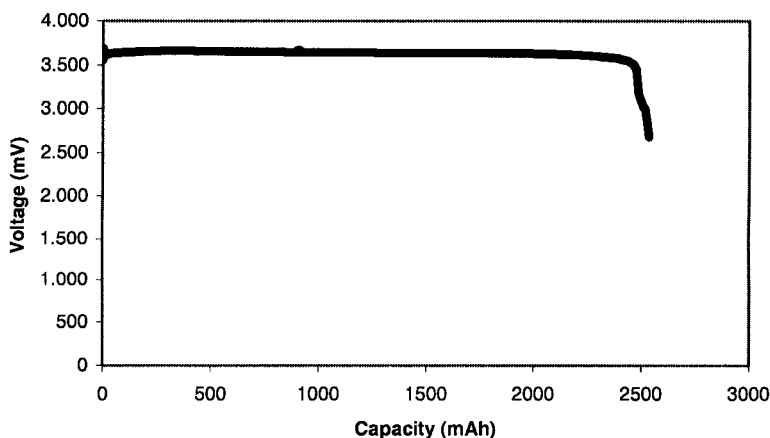


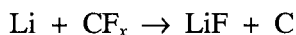
Figure 22.2. Discharge of a lithium/thionyl chloride battery under a 49.9 kohm load at 37°C.

Li/TC cells can display voltage delay after prolonged storage periods where the voltage of the cell is temporarily depressed, due to a passivation film on the anode. Techniques have been employed to minimize voltage delay, including careful attention to the purity of the electrolyte, the concentration and type of the electrolyte salt, and the use of additives.⁷

As noted in the introduction, an important aspect of battery systems for implantable medical devices is a state-of-charge, or end-of-life (EOL) indication. In practice this means that it is important for the battery to give warning significantly before all of the useable capacity is depleted. This is an important limitation of the Li/TC chemistry, since cells provide a flat discharge curve with a rapid loss of voltage at the end of the discharge curve, as illustrated in Figure 22.2. Several methods have been described to provide EOL indication, including using SO_2 discharge voltage as an indicator, as well as the use of lithium alloys.⁶

22.2.4. Lithium/CF_x Systems and their Medical Applications

Several implantable medical devices require a medium-rate power source, such as drug delivery pumps and neurostimulators as mentioned in the previous section. In addition, new advanced pacemakers which combine traditional pacing with other therapies, such as multi-site pacing for congestive heart failure (CHF) treatment, as well as telemetry and programmability features, can require a higher (mA) current output than can be provided by the Li/I₂ system. In addition to Li/TC cells, Li/CF_x cells have been developed to meet this need.^{8,9} CF_x is the notation for polycarbonmonofluoride, a solid state cathode material for lithium batteries. The use of fluorinated carbons as cathode materials was first reported by Watanabe and coworkers of Matsushita Electric Industrial Company.¹⁰ The overall electrochemical discharge reaction is described as:



although an intermediate phase consisting of carbon, fluoride ion, and solvated lithium ion is believed to decompose into the final LiF and C.¹¹

The construction of the Li/CF_x cell includes a solid cathode, consisting of CF_x mixed with a polymeric binder. Since CF_x is an insulator, an additive such as carbon black is mixed with the material to make the cathode conductive. A separator material, such as a film of polypropylene, separates the cathode pellet from the lithium anode. A non-aqueous electrolyte consisting of a lithium salt dissolved in an organic solvent (typically LiBF₄ in gamma-butyrolactone) is added to complete the cell. CF_x has a very high energy density, as illustrated in Table 22.1. Li/CF_x cells also have a high voltage of 3.1 V, and are characterized by internal impedance of about 10 ohms. An overlay of discharge curves for an implantable grade Li/CF_x battery is displayed in Figure 22.3. These curves were collected under constant resistance loads of 1, 2.7, 7.5, 32 and 100 kohms at 37°C. These loads correspond to current drains of ~2.8 mA to 0.03 mA, and illustrate the current capability of the Li/CF_x system.

22.2.5. Lithium/Silver-Vanadium-Oxide Systems and their Medical Applications

The implantable cardiac defibrillator (ICD) detects the onset of tachycardia (rapid heart beat) and attempts to provide pacing to regulate the heart rate.¹² If the tachycardia condition is not controlled by pacing, but

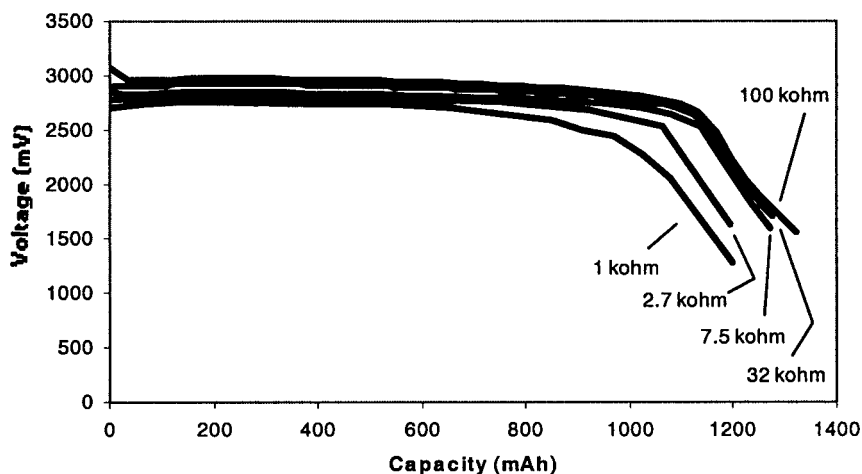
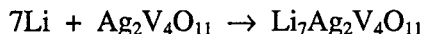


Figure 22.3. Discharge of a lithium/ CF_x battery under constant resistance loads of: 1, 2.7, 7.5, 32, and 100 kohm at 37°C .

deteriorates into ventricular fibrillation, the ICD provides a high-energy shock directly to the heart to stop fibrillation. Thus, ICDs are truly life saving devices. However, these devices also have unique power requirements, which include the need for continuous low current drain over the entire life of the device (several years) to power the monitoring circuitry. In addition, the device also requires very rapid deployment of high current pulses, typically on the order of 2 to 3 amps, when fibrillation is detected. Both of these requirements need to be provided in a small package with high safety and reliability.

The majority of ICDs implanted since the mid 1980s have used lithium/silver vanadium oxide (SVO) batteries. The active cathode material has a stoichiometry of $\text{Ag}_2\text{V}_4\text{O}_{11}$.¹³ The cell reaction is defined as:



The addition of 7 equivalents of Li to SVO corresponds to a theoretical energy density of 315 mAh/g for the material, as listed in Table 22.1, and results in an open circuit voltage of ~ 2 V at EOL. SVO has been found to accept additional equivalents of Li, but at a much lower running voltage, making this capacity unusable for a practical cathode. However, in this regard, metal vanadium oxides have been investigated as possible low voltage anode materials for lithium ion batteries.¹⁴

The discharge reaction of Li/SVO batteries has been studied in detail by a combination of physical and wet chemical methods.¹⁵ The reduction of

SVO resulted in the loss of crystallinity of the material over the range $0 < x < 2.4$ for $\text{Li}_x\text{Ag}_2\text{V}_4\text{O}_{11}$ with a concurrent reduction of Ag^+ to Ag^0 . The formation of metallic silver greatly increased the conductivity of the cathode material, which plays a role in the high current carrying capability of the Li/SVO system. At x values > 2.4 the reduction of V^{5+} to V^{4+} and V^{3+} was identified, and at $x > 3.8$ mixed valent materials were found, containing V^{3+} , V^{4+} , and V^{5+} in the same sample. The presence of several different oxidation states of vanadium, as well as silver reduction, in the discharge reaction of Li/SVO cells results in a stepped discharge curve. This step-wise change in voltage is predictable and provides state-of-charge indication for the battery when used in the implantable device.

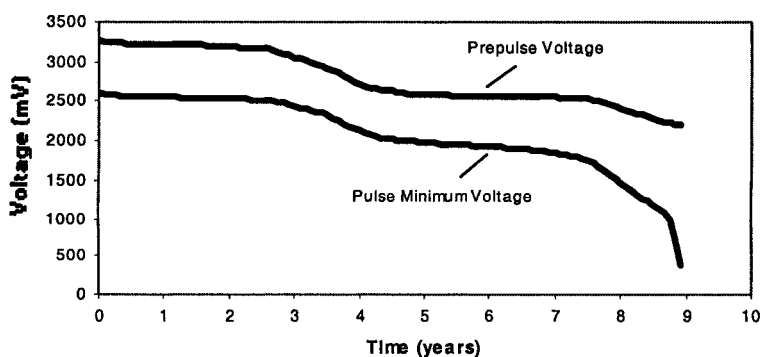


Figure 22.4. Discharge of a lithium/silver vanadium oxide battery under long-life test pulse conditions at 37°C . Four 10 sec, 2 Amp pulses are applied every 30 days, with a background load of 100 kohm applied continuously.

Li/SVO batteries typically use electrolytes based on the non-aqueous organic solvents such as propylene carbonate and dimethoxyethane. A lithium salt is dissolved in the electrolyte, and polypropylene or polyethylene separator is used in the system. The results of long term testing of a Li/SVO implantable grade battery are displayed in Figure 22.4. The Li/SVO discharged in this test was constructed in a prismatic cell configuration as previously described,¹⁶ using a multi-plate design. The test conditions combined a constant resistance background load of 100 kohm with sets of high rate pulses applied once every 30 days with the entire test conducted at 37°C . The high rate pulses of 2 A were each 10 sec in duration and applied in sets of four, 15 sec apart. As can be seen in Figure 22.4, the cell displayed good long life characteristics, with 9 years of real time data collected.

The evolution of ICDs has led to a significant decrease in size of these devices, and in turn has put greater demands on the power level provided by smaller Li/SVO batteries. Thus, several studies have been carried out to characterize the power capability of Li/SVO cells.^{17,18,19} In addition, the effect of electrolyte additives on minimizing voltage delay and resistance build-up in Li/SVO cells has been extensively studied.^{20,21,22} Electrolyte additives such as CO₂ or organic carbonates like dibenzyl carbonate (DBC) have a significant effect on the long term performance of Li/SVO batteries and are believed to reduce internal resistance by modifying the surface SEI layer at the lithium anode.

22.2.6. Lithium/MnO₂ Systems and their Medical Applications

In addition to SVO, another cathode system that has been used for ICD power sources is manganese dioxide (MnO₂). High rate lithium/manganese dioxide batteries have been produced where chromium oxide and lead oxide additives have been mixed with the MnO₂.^{23,24,25} These cells meet the requirements described in the section above. The use of chromium oxides (CrO_x, 2.5 < x < 2.7) and lead oxides (PbCrO₄, PbMoO₄ and PbO) in combination with manganese oxide provided for improved EOL indication for the Li/MnO₂ system.²³

For the ICD application, a double cell concept has been developed using the Li/MnO₂ system, which provides a 6 V running voltage.²⁶ The two cells were connected in series to provide the high voltage, and to avoid external inter-cell connection, the battery case was used as the electrical connector between the two cells.

Swelling of batteries during discharge is an important consideration for implantable devices, and the swelling of implantable Li/MnO₂ cells was studied under accelerated test conditions.²⁵ The swelling was found to depend on the voltage of the cells, and was attributed to decomposition of the organic electrolyte components.

22.3. SECONDARY BATTERIES

22.3.1. Lithium Ion Systems – General Considerations

While primary lithium batteries have been the subject of extensive research and enjoy continued commercial success in medical applications, secondary batteries employing lithium ion chemistry have begun to enter the medical power source market. Lithium ion batteries differ from primary

lithium in that the anodes are not lithium metal, which allows for safe recharging of this chemistry under controlled conditions. Lithium ion batteries also enjoy several distinct advantages over other secondary battery technologies such as nickel–cadmium (NiCd) or nickel metal hydride (NiMH), namely: 1) lithium ion cells possess a much higher discharge voltage of 3.6 V which is about three times the running voltage of NiCd and NiMH chemistries, 2) lithium ion cells display a much lower self-discharge rate, and 3) the memory effects of NiCd and NiMH systems are not present with lithium ion cells.^{27,30}

Lithium ion cells for implantable medical applications have mainly used LiCoO_2 cathodes with graphite anodes.²⁸ The gravimetric energy density of LiCoO_2 is listed in Table 22.1, and while the value of 131 mAh/g is the lowest in the table, the rechargeability of the material over several hundreds of cycles results in a much larger useable capacity over the life of the battery. The cycle life of a small (40 mAh) lithium ion cell designed for medical implantable application is displayed in Figure 22.5. Here the cell was

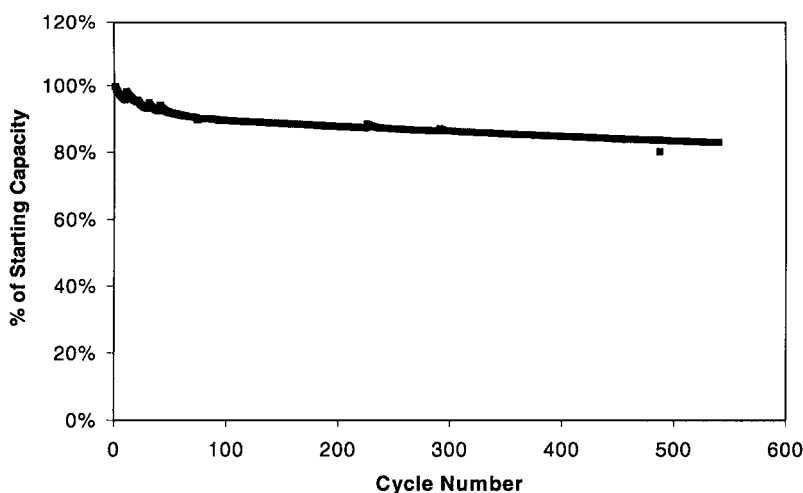


Figure 22.5. Discharge capacity for a small (40 mAh) lithium ion cell cycled between voltage limits of 4.10 V and 2.75 V using a charge and discharge current of 7 mA at 37°C.

charged and discharged at 37°C between voltage limits of 2.75 and 4.10 V, with a charge/discharge current of 7 mA, corresponding to a low rate of $\sim C/6$.³⁰ This cell design displayed good cycle life, with >80% of its initial capacity past 500 cycles. Larger lithium ion cells have also been designed for heart-assist applications. The cycle life curve for a 1.1 Ah cell charged at a $C/2$ rate and discharged at 1 C rate is displayed in Figure 22.6. This cell was again tested at 37°C, between voltage limits of 2.75 and 4.10 V, and displays

good capacity retention. The higher currents used in this test simulate faster charging (2 h) and high current drain that are a requirement for heart-assist applications, as outlined below.

Due to the rechargeable nature of lithium ion cells, it has become important to develop end of life (EOL) indicators for lithium ion batteries. For example, impedance spectroscopy has been tested as an EOL indicator

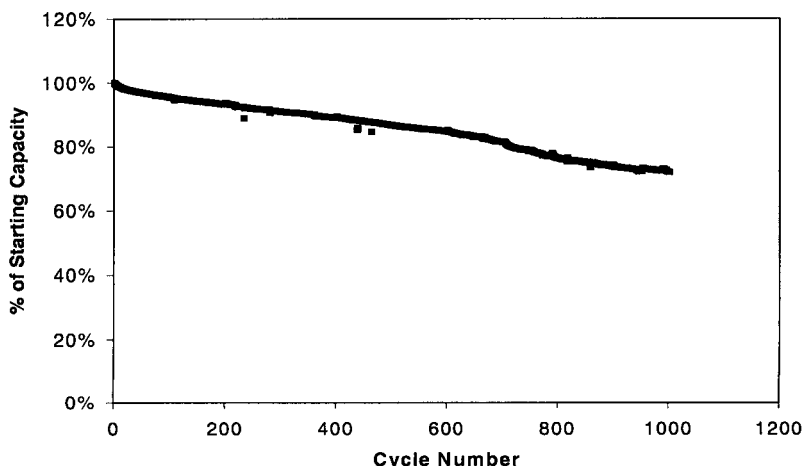


Figure 22.6. Discharge capacity for a 1.1 Ah lithium ion cell cycled between voltage limits of 4.10 V and 2.75 V using a charge current of 550 mA and a discharge current of 1100 mA at 37°C.

for lithium ion batteries.²⁹ Sealed prismatic Sanyo UF653467 cells with a nominal capacity of 930 mAh were cycled at a 1C charge-discharge rate. After 286 cycles, the battery capacity dropped from 1005 to 700 mAh. Impedance measurements of the fully discharged batteries were made and the Nyquist plots as a function of cycle number showed an increase in the size of the low frequency semicircle with the number of cycles, due to the increasing interfacial resistance of the cathode and anode. It was proposed therefore that impedance spectroscopy could be a good cycle life predictor for a sealed lithium ion battery.

The significant difference between lithium metal anodes and graphite anodes in secondary lithium ion cells is that lithium metal anodes suffer from lithium dendrite formation, while under controlled cycling conditions, graphite anodes do not. Lithium dendrite formation poses significant safety concerns, which ultimately results in a non-viable battery for medical applications. In addition to lithium dendrite concerns, safety considerations play a significant role in the design and testing of lithium-ion cells employed in medical applications^{27,30} Abuse testing for small lithium ion cells have

been defined by the International Electrotechnical Committee (IEC), Underwriter's Laboratories (UL), and the Japan Storage Battery Association (JSBA).³¹ A number of these abuse tests are conducted on lithium ion cells for medical applications to evaluate the safety of the design, including:

- Short circuit (on both fused and unfused cells)
- Overcharge
- Overdischarge
- Shock (or drop)
- Crush
- Nail penetration
- Hotbox type tests.

In addition, ARC (accelerating rate calorimetry) testing has been extensively studied for lithium ion cells to determine the thermal stability of materials and design.^{32,33}

Of particular concern for medical cells, the charging of lithium ion batteries must be carefully controlled, as evidenced by the results of overcharge tests.³⁸ Figure 22.7 displays the temperature and voltage curves obtained during overcharge abuse testing for a prismatic lithium ion cell designed for medical application. This cell was overcharged well past the normal 4.1 V cutoff, to the point of failure. When all lithium is extracted from the cathode (100% of charge in Figure 22.7), the cell temperature increased rapidly, resulting in thermal runaway and eventual cell venting. Thus, in medical applications it is critical that redundant over-voltage control be employed to avoid overcharge conditions.³⁰

22.3.2. Lithium Ion Systems – Current and Future Medical Applications

Several implantable biomedical devices possess power requirements which are so high that they preclude the use of a primary lithium battery. In these cases, rechargeable batteries offer a power source with small size that will also power the device for several years. Two examples of such devices are the left ventricular assist device (LVAD) and the total artificial heart (TAH). In both examples lithium ion cells have been developed for these applications due to the high energy density of this system.³⁴ Current versions of these devices are powered from external battery packs that can typically be worn on the patient's belt. However, there is also a desire to have an implanted back-up battery that will allow the patient to remove the external battery pack for a short period of time each day.

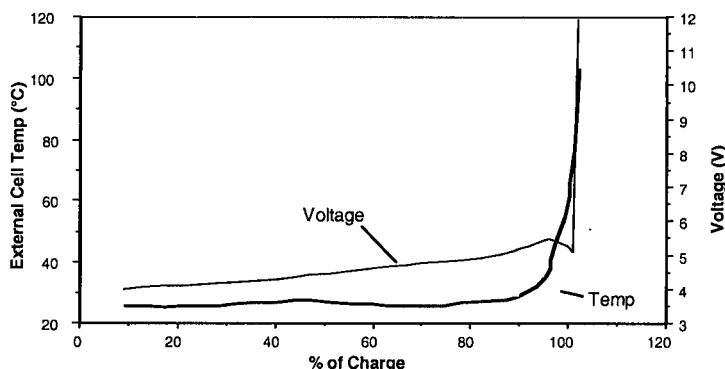


Figure 22.7. Temperature and voltage curves for a 1.5 Ah lithium ion cell under overcharge abuse conditions. The cell was charged at a constant current of 1.5 A (C-rate) at RT where 100% of charge equaled complete removal of lithium from the Li_xCoO_2 cathode material.

The left ventricular assist device is an implantable pumping mechanism that provides long-term circulatory support to patients with serious heart disease.³⁵ These devices are often used as a “bridge” to a heart transplant, where the LVAD assists the heart in pumping blood, while the heart remains in place in the patient. As a mechanical pump, the device requires high power for continuous operation. In one LVAD design the power load is described as ~10 W for a 12 V battery pack.³⁶ The total artificial heart is a mechanical pump that completely replaces the heart in the patient. Several experimental TAHs have been implanted in patients recently.³⁷ The design of this replacement heart contains two chambers, each capable of pumping over two gallons of blood per minute. This device utilizes an implantable Li-ion battery pack that is recharged through the skin without any wires or tubes penetrating the skin. The implantable batteries for these applications must meet all the requirements defined in the introduction, with additional safety requirements stemming from the charging steps involved with the lithium ion cells.³⁸

Small button-sized lithium ion cells have been developed for potential use in external medical devices such as common hearing aids (HAD), transdermal electrical nerve stimulation devices (TENS), and devices for the transdermal application of other drugs (TAD).³⁹ It has been proposed that these small lithium ion secondary cells could mitigate the cost, inconvenience, and environmental hazard associated with the continual replacement and disposal of small primary cells for external medical devices. The 0.45 g, 0.18 cm^3 miniature cells successfully completed 2700 cycles at 60% DOD and

discharge rates of 1-3 mA. The miniature cells had average energy densities of 200 Wh/l and specific energies of 75 Wh/kg, offering approximately 80% of the energy density and 70% of the specific energy of large, commercial lithium-ion batteries.

22.4. SUMMARY

Lithium batteries for implantable biomedical applications are in widespread use today. Lithium/iodine cells have the longest history, and by far the greatest number of implants, numbering into the millions as power sources for cardiac pacemakers. Lithium/thionyl chloride and lithium/CF_x batteries have found utility in medium-rate applications, such as neurostimulators and drug pumps, while lithium/SVO and lithium/manganese dioxide batteries provide the high rate capability needed to power implantable cardiac defibrillators. Rechargeable lithium ion cells have been suggested for a number of future implantable applications, where the high energy density in a rechargeable package lends itself to applications not currently served by primary cells.^{40,41} Lithium ion cells have already demonstrated utility in powering left ventricular assist devices as well as total artificial hearts. While all of these applications require small power sources with high energy density in order to keep the entire implantable device small, the requirements of safety, reliability and predictability of performance are the top priority.

REFERENCES

1. C.F. Holmes, *J. Power Sources* 97-98 (2001) 739.
2. W. Greatbatch, *The Making of the Pacemaker* (Prometheus Books, Amherst, NY, 2000) p. 119.
3. W. Greatbatch, R. McLean, W. Holmes, C. Holmes, *IEEE Trans. On Biomed. Eng.* BME-26 (1979) 306.
4. C.L. Schmidt, P. M. Skarstad, *J. Power Sources* 65 (1997) 121.
5. C.C. Liang, C.F. Holmes, *Prog. Batt. & Solar Cells* 2 (1979) 50.
6. P.M. Skarstad, in *Batteries for Implantable Biomedical Devices*, B.B. Owens, Ed., (Plenum Press, New York, 1986) p. 215.
7. C.R. Schlaikjer, in *Lithium Batteries*, J.-P. Gabano, Ed., (Academic Press, New York, 1983) p. 303.
8. E.S. Takeuchi, S.A. Smesko, in *7th Annual Battery Conference on Applications and Advances*, Long Beach, CA 1992.
9. W. Greatbatch, C.F. Holmes, E.S. Takeuchi, S.J. Ebel, in *Cardiostim 96*, Nice, France 1996.
10. N. Watanabe, M. Fukuda, U.S. Patent No. 3,536,532 (1970).
11. N. Watanabe, T. Nakajima, R. Hagiwara, *J. Power Sources* 20 (1987) 87.
12. E.S. Takeuchi, W.D.K. Clark, in *Implantable Cardioverter-Defibrillators, A Comprehensive Textbook*, N.A.M. Estes, A.S. Manolis and P. Wang, Eds., (Marcel Dekker, New York, 1994) p. 123.
13. K.J. Takeuchi, A.C. Marschilok, S.M. Davis, R.A. Leising, E.S. Takeuchi, *Coord.*

- Chem. Rev.* 219-221 (2001) 283.
14. Y. Piffard, F. Leroux, D. Guyomard, J.-L. Mansot, M. Tournoux, *J. Power Sources* 68 (1997) 698.
 15. R.A. Leising, W.C. Thiebolt, E.S. Takeuchi, *Inorg. Chem.* 33 (1994) 5733.
 16. E.S. Takeuchi, W.C. Thiebolt, *J. Electrochem. Soc.* 135 (1988) 2691.
 17. J. Norton, C. Schmidt in *Proceedings of the Symposium on Batteries for Portable Applications and Electric Vehicles*, C. F. Holmes and A.R. Landgrebe, Eds., PV 97-18, p.389.
 18. A. Crespi, C. Schmidt, J. Norton, K. Chen, P. Skarstad, *J. Electrochem. Soc.* 148 (2001) A30.
 19. C. Schmidt, G. Tam, E. Scott, J. Norton, K. Chen, *11th International Meeting on Lithium Batteries*, Monterey, CA, June 23-28, 2002, Abstract 422.
 20. H. Gan, E.S. Takeuchi, *J. Power Sources* 62 (1996) 45.
 21. H. Gan, E.S. Takeuchi, *ECS Joint International Meeting HI*, Oct. 17-22, 1999, Abstract 332.
 22. H. Gan, E.S. Takeuchi, *ECS Proceedings Volume 99-25*, p. 417.
 23. G. Fehrmann, R. Frommel, R. Wolf, U.S. Patent No. 5,587,258 (December 24, 1996).
 24. J. Drews, R. Wolf, G. Fehrmann, R. Staub, *J. Power Sources* 80 (1999) 107.
 25. J. Drews, G. Fehrmann, R. Staub, R. Wolf, *J. Power Sources* 97-98 (2001) 747.
 26. J. Drews, R. Wolf, G. Fehrmann, R. Staub, *J. Power Sources* 65 (1997) 129.
 27. D. M. Spillman, E. S. Takeuchi, *14th Annual Battery Conference on Applications and Advances*, Long Beach, CA, 1999.
 28. C.F. Holmes, R.A. Leising, D.M. Spillman, E.S. Takeuchi, *ITE Battery Letters* 1 (1999) 132.
 29. J. Li, E. Murphy, J. Winnick, P.A. Kohl. *J. Power Sources* 102 (2001) 294.
 30. R. S. Rubino, H. Gan, K. J. Takeuchi, *17th Annual Battery Conference on Applications and Advances*, Long Beach, CA, 2002.
 31. R. Spotnitz, in *Advances in Lithium-Ion Batteries*, W.A. van Schalkwijk and B. Scrosati, Eds., (Kluwer Academic/Plenum Publishers, New York, 2002) 433.
 32. P. Onnerud, J. Shi, R. Chamberlain, S.K. Singh, P. Ralbovsky, B. Barnett, C. Lampe-Onnerud, *201st Electrochemical Society Meeting*, Philadelphia, PA, May 12-17, 2002, Abstract No. 109.
 33. D.D. MacNeil, T.D. Hatchard, J. R. Dahn, *J. Electrochem. Soc.* 148 (2001) A663.
 34. G. Jacobs, J. Albright, E. Marlinski, C. Deirmengian, R. McClure, H. Valenta, E.S. Takeuchi, D. Tamez, J. Conger, O.H. Frazier, R. Jarvik, *ASAIO* 45 (1999) p.165.
 35. D. Tamez, J.L. Conger, G. Jacobs, I. Gregoric, R.W. Inman, B.R. Radovancevic, S.M. Moore, K. Eya, H. Eichstaedt, R.K. Jarvik, O.H. Frazier, *ASAIO* 46 (2000) p. 168.
 36. G.K. MacClean, P.A. Aiken, W.A. Adams, T. Mussivand, *J. Power Sources* 56 (1995) 69.
 37. For more information regarding TAH devices, see the Jewish Hospital, University of Louisville, Health Sciences Center. Website: www.heartpioneers.com
 38. R.A. Leising, M.J. Palazzo, E.S. Takeuchi, K.J. Takeuchi, *J. Electrochem. Soc.* 148 (2001) A838.
 39. S. Passerini, B.B. Owens, *J. Power Sources* 97-98 (2001) 750.
 40. C.L. Schmidt, P.M. Skarstad, *J. Power Sources* 97-98 (2001) 742.
 41. E.S. Takeuchi, R.A. Leising, *201st Electrochemical Society Meeting*, Philadelphia, PA, May 12-17, 2002, Abstract No. 260.

Chapter 23

CURRENT ISSUES AND MARKET TRENDS OF Li-ION BATTERIES FOR CONSUMER APPLICATIONS

D. MacArthur

CHEMAC International Corporation, Troy, Michigan 48043, U.S.A.

23.1. INTRODUCTION

The focus of this chapter is Li-Ion batteries in consumer applications. There is a long history and a large market of non Li-Ion batteries--many of them primary lithium batteries--but this other field is too extensive for inclusion here except to mention the recent apparent success to commercialize, after a long gestation period, the lithium metal-polymer electrolyte technology in the telecommunications backup application. The reader should also note that Li-Ion batteries are now finding their way into many non-consumer applications. This, too, is outside the scope of the present chapter.

The subject begins with the lithium metal/molybdenum disulfide system introduced by Moli Energy in the late 1970, early 1980 period. Other rechargeable lithium systems were introduced for consumer applications about this same time but the Moli cell was the first to reach wide spread use. As is very well known, the product encountered a safety issue. Was it just faulty construction or was the lithium metal-liquid electrolyte system so unstable as to be unacceptable for consumer applications? (And does the "dry" polymer electrolyte solve this problem?) Whatever the technical explanation, the technology gained a perceived image as unsafe and there was a need to move on. Sony researchers (and others) saw the opportunity and developed a high capacity carbon based anode. (Research into lithium intercalation in graphite has a much longer history but the capacities needed for practical use had generally not been observed.) This anode, along with a high voltage metal oxide cathode was key to what came to be called the Li-Ion battery, first officially described in 1991. The name was intended to dissociate the new system from the "unsafe" lithium battery. It is, of course, also to imply a "rocking chair" type battery (or the physicist's battery as

early on mentioned). The researchers, themselves, cannot be blamed for the ensuing confusion from the unfortunate use of “anode” and “cathode” in a rechargeable system. Not incidental to Sony’s development of Li-Ion technology was a need to leapfrog the nickel-metal hydride technology in the growing portable electronics market.

By early 1980, researchers interested in lithium batteries started holding meetings on just this subject for the exchange of information. Prior to this, much of the interest was in very high energy lithium batteries, many of military interest including molten salt systems. The first of the International Meetings on Lithium Batteries was held in Rome in 1982. Almost a decade later, the 5th International Meeting on Lithium Batteries was held in 1990 in Beijing, China and that is when the story of Li-Ion really begins. A summary of the meeting is contained in the first of the Powers Reports on Lithium Batteries. Moli Energy had just discontinued the Li/MoS₂ cell and was proceeding with Li/MnO₂ which was considered to be less hazardous. The Bell Labs Li/NbSe₃ system had been discontinued. Several groups had field tests of Li/V₆O₁₃ in “AA” and “C” size cells underway. Developers of Li/TiS₂ systems were promoting this technology and the Mead-Hope-Innovision (MHB) group was developing the Li/V₆O₁₃ cell with *in-situ* cross-linked doped polymer electrolyte. Honeywell was known to be working on a 4 volt Li/CoO₂ system. The Harwell consortium on lithium polymer batteries was developing the “dry” polymer electrolyte systems. And Sony EnergyTec had just dropped a highly publicized Li/MnO₂ system for a new unspecified system called Li-Ion. (Robert Powers, the author of the report, speculated it seemed to be a lithium-carbon fiber/CoO₂ system.) The Powers Reports continued to follow, at two year intervals, activities and progress in lithium batteries during the next decade.

23.2. LITHIUM-ION BATTERIES

23.2.1. The Market

The growth of the Li-Ion market has been huge, a matter which refutes the image of battery technology as slow-moving, out-of-date, and unresponsive. During the period of 1991 to 1999 growth of not just the Li-Ion market but the so-called advanced battery market closely paralleled that of the semiconductor industry, doubling and redoubling in periods of just a few years or less. By year 2000, however, growth had greatly diminished perhaps mostly because of the faltering world economy but perhaps also the result of reduction in number and significance of technical advances. The rapid growth and following slowdown is shown in the following Table 23.1.

Table 23.1. World annual sales of Li-Ion batteries.

	1992	1994	1996	1998	2000	2002
Quantity (millions of cells)	0	30	120	45	480	500
Value (millions of year 2000 US dollars)		300	1080	1880	2500	2450

Notes: Production in 1992 was entirely Sony captive. Value in the table is based on estimated factory cost. Data extracted from the Powers Reports.

At the same time reported manufacturing capacity grew even more rapidly (Tables 23.2-23.3). The number of companies establishing manufacturing has been surprising. By year 2002 there were 10 major manufacturers located in Japan, Taiwan or Korea and another 4-6 growing manufacturers most of which were located in the Republic of China. There is a shift in manufacturing to China where modern plants producing high quality product are rapidly appearing. SAFT, Matsushita, the newly formed in 2002 US Lithium Energetics, and several others were located in North America.

There is a large manufacturing overcapacity which places considerable stress on the industry.

Table 23.2. Growth in world Li-Ion manufacturing capacity (millions of cells per year at the end of the year).

	1992	1994	1996	1998	2000	2002 est.
Li-Ion	12	65	156	660	900	850
Li-Ion polymer					3	50

Notes: Data from the Powers Reports. Almost all Li-Ion polymer are of the *in-situ* polymerized type of a flat pack design intended for wireless telephones.

Table 23.3. Geographic distribution of Li-Ion manufacturing capacity (2001).

REGION	10 ⁶ units/month
Japan	65
China (including Taiwan)	5
Korea	3
North America and Europe	2

The large excess of manufacturing capacity has resulted in a highly competitive environment and falling prices. The opportunity for recovery of the high cost of introduction of technology, the high investment for production and high material costs of start-up is now small. An approximate cost breakdown of the Li-Ion technology is: cathode 25%, anode 10%,

packaging (includes electrolyte) 20%, electronics 18%, overhead 15%, all else 12%. Much of recent development is optimizing the technology for specific applications.

23.2.2. Different Technologies

Early constructions were 18650 (18 mm diameter, 650 mm long) jelly roll cells which, over the years, have grown from about 1 Ah capacity in 1992 to 2 Ah capacity in 2000. (The Molicell of 1998 which was “AA” size similar to the 18650 size had about 500 mAh capacity.) Much of the increase in capacity is the result of higher density carbon materials for the anode and better packing. By about 1995 there was a shift to 17650 cells of better fit to the thinner portable computers. About 300 million cells go to the wireless telephone market and about 200 million to the portable computer market. About 50% of Li-Ion production is now prismatic. In Table 23.4, the gain in energy content over the years is reported.

By 1998, there was growing interest in “flat packs” with superior packaging flexibility for wireless telephones. The introduction of polymer electrolytes follows a long history beginning even before the appearance of Li-Ion batteries. Several technologies have been developed: the “dry” polymer, the “solid state” *in-situ* cross-linked polymer, the gelled *in-situ* polymer, the extracted-activated polymer of the Bellcore technology. Early on the vision of the polymer technology was to make batteries like paper is made. The expectation of lower cost has not been fulfilled and the critical matter has become the form factor as the packages can be thin and shaped to fit within the contours of the telephone. By 2000 Li-Ion chemistry dominated the wireless telephone and portable computer markets but with the saturation of existing markets, if Li-Ion production is to increase there is a need to find new applications. Although the proliferation of portable electronic devices—information assistants, communicators, tools, and toys-- is growing it does not appear to predict a doubling in battery demand. A new market is needed. There is interest, in smaller sizes such as credit card sizes but Li-Ion technology is not well suited and many uses are served by primary technology. Much of the focus is on markets for larger sizes. This includes power backup, power tools and electric vehicles. The prospect of a huge hybrid vehicle market is very enticing. The challenges are cost and safety. Characteristics of small and large batteries are reported in Table 23.5

Table 23.4. Energy content of Li-Ion cells.

	1992	1994	1996	1998	2000	2002
Energy Density (Wh/l)	220	250	300	320	340	360
Specific Energy (Wh/kg)	95	105	110	110	125	130

Notes: The numbers are for commercial cells. The change in specific energy, year 2000, is related to introduction of the plastic envelope package. The change in energy density over the 1992-98 period was the result of changes in capacity of the anode and in packaging.

23.2.3. Targets: Small and Large Batteries

The growth of Li-Ion depends on being lighter, smaller and having longer charge retention than competitive products. But, the technology uses combustible electrolytes and clearly there is a safety issue here even though combustion inhibitors may be added. The overlap of electrode potentials with decomposition reactions of the system makes stability of the system dependent on inherently unstable materials such as the SEI layer, and the absence of a recombination system in overcharge forces use of sophisticated electronic controls. Yet, the technology is moving into applications of larger sizes. Nissan has used Li-Ion of the spinel manganese oxide type in electric vehicles since about 1998. Almost all automotive vehicle manufacturers are exploring Li-Ion batteries in hybrid vehicles. Li-Ion technology is well suited for long life where batteries are cycled in mid range of charge. JSB has reported 20K cycles at 20% DOD with only 22% capacity loss (of full capacity) with large Li-Ion cobalt oxide cells for space applications.¹ SAFT has reported on Li-Ion (40 Ah jelly roll cells in about 3.5 kWh installations) in telecommunications backup and has gained up to 5 years of experience.² Accelerated testing is indicating up to 11 year life which is an excellent result for this stage in development. As pricing declines into the fifty cents per Wh range and if no major safety events occur, these products may establish significant markets.

Table 23.5. Targets for market growth, Li-Ion type.

ATTRIBUTE	TARGET: SMALL BATTERIES	TARGET: LARGE BATTERIES
SE (Wh/kg)	150	150
ED (Wh/l)	400	400
PD (W/l) peak/sustained	800/400	1000/800
Life	7 years	10 years
Temperature Range (°C)	-20 to + 80	-30 to +60
Costs (\$/Wh)	<1	0.40
Safety/Robust	high	very high
Recycle	yes	yes

Adoption of new materials into the technology is expected to be slow now because of the low margins within the industry. This inertia provides an opportunity for startup companies which may be able to establish a base using newer technology. Most manufacturers are using graphite anodes although a few may be using a hard carbon. Carbon anodes, although more robust, have lower capacity per unit volume. Various pyrolyzed carbon materials with greater than the 372 mAh/g capacity of the Li-C₆ composition have been explored but as far as known are not in use. Carbon coated graphite materials may be used by some manufacturers. The higher capacity density micro alloy materials are not used in Li-Ion cells (although they may be in some primary cells) because of lower cycling capability. Each manufacturer seems to have a preferred electrolyte composition but all are based on the cyclic carbonates. Choices seem to be influenced by temperature range desired. Shutdown separators are widely used and some manufacturers may be using flame inhibitors. Most polymer electrolyte systems in use are of the thermally in-situ cross-linked type; the competing Bellcore process does not appear to be widely adopted. The liquid filled, *in-situ* cross-linked process has the advantage of compatibility with existing Li-Ion production. For the cathodes, most manufacturers are using a cobalt oxide material often with metal oxide doping; nickel oxide and manganese oxide materials, again with metal oxide doping are in use by a few manufacturers. The olivine lithium iron phosphate material is in development. Because of potential cost advantages it may be used in large cells; however, decrease in voltage and potentially lower cycle life may negate any cost advantage. Interest continues with manganese oxide based materials for cost, environmental, and safety reasons.

REFERENCES

1. N. Imamura, T. Inoue, H. Yoshida, M. Mizutani, M. Goto, *Power Sources Conference*, Cherry Hill, NJ, June 10-13, 2002, Paper 26-5.
2. J. McDowall, A. Brenier, M. Broussely, P. Laval, *INTELEC 2002 Conference*, Montreal Quebec, Sept. 30-Oct 3, 2002, Paper 22.2.

Subject Index

Additives for lithium battery 303, 174

Anode materials

Aluminides

Antimonides 116 121, 275

Cu-Sn 123

Graphite anodes 144

Intermetallic anodes 12, 125, 270

Lithiated carbons 146

Metallic lithium anode 297

Metal oxide anodes 129

Mg₂Si 127

Nitrides 132, 247

LiMN_x 248

InN 254

Sn₃N₄ 254

Ge₃N₄ 254

Cu₃N 257

Phosphides 134

Silicides 127, 247, 259

Li_xSi 260

Li-Si-Mg 261

CrSi₂ 265

NiSi 266

Silicon based composite 127

Tin anode 116

Tin oxide anode 117

Transition metal oxide 130

Anode synthesis 102

Battery buffer operation 673

Battery cost 662

Battery design 657

Battery market 702

Battery medical applications 686

Battery safety 661

Battery satellite applications 675

Battery stationary applications 671

Battery standby operation 671

Battery space applications 674

Carbonaceous anodes 114

Cathode materials, 315

Cr oxide cathode 345

LiNi_{1-x}Co_xO₂ 334, 410

First principle calculations 42

General electronic structure 45

Layered oxide cathodes 11, 24

LiCoO₂ 12, 410, 414

LiCo_xNi_{1-x}O₂ 333, 410

LiFePO₄ 99, 347, 445

LiFeP₂O₇ cathode 471

LiMXO₄ 445

Li₃M₂(XO₄)₃ cathodes 457

LiNiO₂ cathode 19

LiVO_x 33, 345

Polyanion cathodes 32

Role of bond covalency 64

Spinel oxide cathode 25, 30, 362

Spinel manganese oxide 26

Sulfides cathode 350

Synthesis of cathode materials

86, 317

Titanium disulfide 5, 90

V₆O₁₃ 34

Composite anodes 112

Covalent bonding in Li_xCoO₂

Crystal field stabilization energy 21

Electronic properties of LiNiO₂, 410

Decrepitation of alloy anodes 290

Electrode fabrication 200

Electron diffraction in crystals 481

Electrolytes related

Additives 174, 303

Alkyl carbonates 509, 531

Binary electrolytes 522

Cathodic reactions 545

Ceramic electrolytes 623

Dipole-dipole interactions 513

Electrochemical stability 525

Electron-pair donor (EPD) 516

Electron-pair acceptor (EPA)

Glass electrolytes 625

Gel electrolytes 591

Hydrogen bonding 515

516

Ion-dipole forces 511

Ion transport 575

Liquid electrolytes 509

Mixed electrolyte 509

Molten salts 567

Physical properties 532

Polar solvents 530

Polyelectrolytes 602

Polymer electrolytes 575

Selective solvation 518

Solvation 517

Stability 604

Ternary solvent blends 524

- EV-batteries 652
EV-battery requirements 653
- First principles methods 48
- GC-MS analysis 202
Gel electrolytes 591
Generalized gradient approximation 54
Glassy electrolytes 625
Graphitic carbon 148
- HEV-applications 663
HEV-batteries 645
Hydrothermal synthesis 93
- Industrial Li-ion batteries 646
Intercalation process 88
Intermetallic anodes 117
Intermittent battery charging 673
Ion exchange methods 95
- Jahn-Teller distortion 27, 493
- Launchers battery 683
Layered LiMnO_2 cathode 341, 381
Layered to spinel transformation 71, 78, 494
 LiMnO_2 instability 384
 LiPON 626
Lithium alloys 280, 283
Lithium flat cell 201
Lithium-ion battery technology 651
 LiPO_4 cathode 100
Lithiated carbon anode 146
Lithium metal anode 112
Lithium ordering in LiCoO_2 , 489
Lithium storage in carbon 148, 153, 160
Local density approximation (LDA) 54
- Manganese oxide cathode 344
Manganese spinel cathode 335
Market analysis for Li-ion batteries 701
Mechanochemistry 103
Metal oxide anode 130
Morphology and particle size 321
- Nasicon –type phosphate electrolytes 632
Non-graphitic carbon anodes 151
- Oxide glasses 626
Oxynitride Glassy electrolytes 626
Oxysulfide glassy electrolytes 628
- Perovskite electrolytes 631
Polyanion based cathodes 445
Polyelectrolytes 602
Polymer electrolytes 575
Primary batteries for medical applications 687
- Reactivity of lithiated carbons 167, 195
Reversible-irreversible capacity 157
- Safety issues of lithium battery 113, 661
Saft battery design 677
SEI layer on carbon anode 171, 176
 Infrared analysis 208
 Thermal analysis 216
Solvent co-intercalation 171
Space applications 674
Spin polarization 55
Spinel cathode 361, 381
Stabilization of layered oxide cathodes 97
Sulfide glasses 628
Synthesis
 Hydrothermal 93
 Ion exchange methods 95
 Mechanochemistry 103
 Soft chemistry routes 390
- TEM study of cathode materials 489
Thionitride glassy electrolytes 629
Tin compound anode 119
Tin oxide anode 117
Titanium disulfide 86
- Vacancy ordering in LiCoO_2 487
Vacancy ordering in oxide cathodes 484
Vacancy ordering in $\text{O}_3 \text{LiNiO}_2$ 485
- X-ray diffraction of graphite 199